

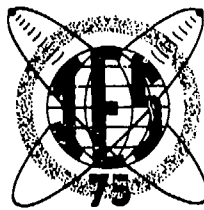
AD A023 510

# Effect of the Ionosphere on Space Systems and Communications

*Editor*

John M. Goodman

AD/A-023 510



*Based on*

**Ionosphere Effects Symposium**

*Held in*

**Crystal City, Arlington, Va.  
January 20-22, 1975**

REPRODUCED BY  
**NATIONAL TECHNICAL  
INFORMATION SERVICE**  
U. S. DEPARTMENT OF COMMERCE  
SPRINGFIELD, VA. 22161



**PRICES SUBJECT TO CHANGE**

**NAVAL RESEARCH LABORATORY  
Washington, D.C. 20375**

For sale by the Superintendent of Documents, U.S. Government Printing Office  
Washington, D.C. 20402 - Price \$10.20  
Stock Number 008-051-00064-0

ORGANIZING COMMITTEE

Dr. J.M. Goodman

Chairman

Mr. F.D. Clarke

Coordinator

Dr. L.B. Wetzel

Papers Committee Chairman

Mrs. R.A. Smithson

Secretary

Library of Congress Catalog Card No. 75-27352

## PREFACE

Since the advent of artificial earth satellites the nature of our global environment has come under considerable investigation resulting in a rapid growth in the knowledge of ionospheric structure and dynamical behavior. Satellite platforms have added a new dimension to study of the atmospheric environment which encompasses the earth and have contributed immeasurably to our understanding of the solar-terrestrial relationship. However this research has not always been pursued independently or without practical motivation. Early comprehension of the military significance of space platforms has fueled interest in the ionospheric environment because of the fact that many radio frequency systems are influenced by phenomena which are related to the presence of the ionosphere. Considering the quiescent ionosphere, gross effects such as refraction, group path delay, and Faraday fading are factors to be considered but may not be as important as scintillation, a generic term descriptive of fluctuation in either radio wave amplitude or phase. Using the considerable data base which has been accumulated, world-wide empirical models of the smoothed ionospheric electron density distribution have been developed over the last few years and recently considerable progress has been made in modelling the worldwide behavior of amplitude scintillation. In addition the problem of modelling the disturbed ionosphere, although immensely important, is in an incomplete state of development. At present there is no unassailable forecast capability in hand arising from these or kindred sub-models, but there is considerable DoD interest in producing such a capability for system application. Aside from the empirical modelling approaches which have been undertaken for sometime, efforts are now being directed toward the development of quasi-theoretical models using real-time solar data and certain classes of adaptive schemes for mitigation of effects. Indeed, at this juncture, it would appear that there is a horse race between the latter two approaches for real-time use in error-correction or forecasting, with the empirical modelling approaches relegated for use in systems design studies. Clearly the nature of the race depends upon the specified system for which the ionosphere may present a problem. In order to more clearly focus the energies of ionospheric researchers on the questions of relevance to DoD it was felt that a comprehensive symposium on the subject of ionospheric effects should be convened. This symposium would be timely and rewarding to both the ionospheric researchers and his eventual customers whether the customers be DoD systems houses with military requirements or civilian organizations with commercial or regulatory requirements.

Because of the need to eradicate the apparent disconnection between the ionospheric research and user communities, the Naval Research Laboratory accepted the responsibility to sponsor IES '75 and convene the sessions in the neighborhood of Washington, D. C. Technical Sessions were unclassified and were organized in such a way that a degree of coherence could be maintained throughout the symposium.

We were fortunate to have Dr. H.A. Friedman, the Superintendent of the Space Sciences Division at NRL and Chief Scientist of the Hulburt Center for Space Research, as our IES banquet speaker on January 21. Dr. Friedman delivered a banquet address entitled "Early Years of Ionospheric Research" which developed the history of ionospheric research with some emphasis on the NRL contribution to aeronomy and the solar-terrestrial relationship.

One of the unique features of IES '75 was the fact that we planned four keynote addresses instead of the usual one. This gave the meeting a wide-ranging array of viewpoints which were instrumental in setting the tone for the technical sessions which followed. The keynote speakers were Dr. John Allen of ODDR&E, Dr. Thomas Quinn of ONR, Dr. Fred Bond of DCA and H.A. Fiegleson of the Maritime Administration.

Besides the session chairman, keynote speakers, and authors, I would like to acknowledge Mr. F. D. Clarke for coordinating the symposium and special thanks to my secretary, Mrs. Rhea Smithson for carrying out numerous tasks leading up to the symposium and for registration during the symposium. Considerable help was provided by Mrs. Randleman and her staff of the Space Systems Division of NRL during registration. Mr. Warren Ramey, Mrs. Dora Wilbanks, Mrs. Mary Dickey, and Mr. D. E. Darr of the Technical Information Division of NRL are acknowledged for preparing the pre-print document. Clerical help was provided by the NRL personnel office and audio visual assistance was provided by Mr. John Otto of the Technical Information Division.

## TABLE OF CONTENTS

Preface .....	iii
Welcoming Address .....	ix
Alan Berman	
Keynote Addresses	
Ionospheric Research, Who Needs It? .....	x
John L. Allen	
Ionospheric Research, Navy Interest .....	xiii
Thomas P. Quinn	
The Ionosphere and Military Satellite Communications .....	xxv
Fred E. Bond	
Maritime Space Applications .....	xvi
Harry Feigieson	

### SESSION I

High Latitude Morphology of Ionospheric Scintillations .....	1
Jules Aarons	
A Synopsis of Radio and Photometric Effects Observed When the Ionosphere is Modified by a High-Power Ground-Based Transmitter .....	8
William F. Utlaut	
The Role of the Magnetosphere in Satellite and Radio-Star Scintillation .....	9
Henry G. Booker	
The Development of a Highly-Successful Worldwide Empirical Ionospheric Model and Its Use in Certain Aspects of Space Communications and Worldwide Total Electron Content Investigations ..	13
Rodney B. Bent, Sigrid K. Llewellyn, George Nesterczuk, and Paul E. Schmid	
A Review of the Recent Results of In Situ Ionospheric Irregularity Measurements and Their Relation to Electrostatic Instabilities .....	29
Michael C. Kelly and Forrest S. Mezer	
Recent Results from Theoretical and Numerical Modeling of E and F Region Irregularities .....	39
B.E. McDonnell, S.L. Ossakow, T.P. Coffey, R.N. Sudan, A.J. Scannapieco, and S.R. Goldman	
Spectra of Amplitude and Phase Scintillation .....	53
R.K. Crane	
First-Order Signal-Statistical Modeling of Scintillation .....	65
E.J. Fremouw and C.I. Rino	

### SESSION II

Morphology of Ionospheric Scintillation in the Auroral Zone .....	76
R.H. Wand and J.V. Evans	
F Layer Scintillations and the Aurora .....	84
Eileen Martin and Jules Aarons	
Amplitude and Fade Rate Statistics for Equatorial and Auroral Scintillations .....	91
Herbert E. Whitney and Charles Cantor	
Equatorial Scintillation at 136 MHz Observed over half a Sunspot Cycle .....	95
J.P. Mullen and Gerald S. Hawkins	



The Effect of Ionospheric Irregularities on the Reception of ATS-6 Signals .....	101
R. Sethuraman, S. Ganapathy, and M. Mukunda Rao	
Results of a Radio Holographic Study of Ionospheric Irregularities .....	107
G. Schmidt, J. Oksanen, and A. Tauriainen	
A Holographic Radio Camera Technique for the Three-Dimensional Reconstruction of Ionospheric Inhomogeneities .....	114
W. Ross Stone and Verne E. Hildebrand	
The Role of Large Scale Electric Fields and Field-Aligned Currents in Producing Field-Aligned Irregularities in the Magnetosphere and Ionosphere .....	123
K.D. Cole	
Effects of Ionospheric Scintillation on Two-Frequency Doppler Data .....	126
James R. Clynch and Arnold J. Tucker	
An Automatic Data Collection System for L-Band Ionospheric Scintillation Measurements .....	134
Roy E. Anderson, James R. Lewis, George Haroules, and Wilfred Brown	
Electron and Ion Density Studies with the NRL One-Dimensional Mid-Latitude Model of the Ionosphere .....	143
E.S. Oran, T.R. Young, D.F. Strobel, and T.P. Coffey	
High-Latitude Ionospheric Aurora Models .....	152
J.A. Fedder, J.H. Orens, and T.P. Coffey	
Computer Simulation of Embedded Electrically Small Scatterers .....	161
G. Bakalyar and E. Ziemba	

### SESSION III

Arecibo Heating Experiment .....	171
W.E. Gordon and H.C. Carlson, Jr.	
On the Size of the Irregularities Responsible for Heater-Generated Spread-F ... ..	180
G.D. Thome, E.M. Allen, and P.B. Rao	
Artificially Induced Enhancements in the Ionospheric Backscatter Spectrum Near Electron Gyrofrequency and Second Harmonic Plasma Line .....	185
Luiz Alberto Vieira Dias and William E. Gordon	
Ionospheric Perturbations Caused by Artificial Sources .....	190
G.L. Rao, R.J. Hung, R.E. Smith, and G.S. West	
Theoretical and Numerical Simulation Studies of Ionospheric Inhomogeneities Produced by Plasma Clouds .....	196
S.L. Ossakow, A.J. Scannapieco, S.R. Goldman, D.L. Book, and B.E. McDonald	
Experimental Studies of Lower Ionospheric Effects Resulting from High-Power Radio Waves ..	203
Glenn D. Falcon	
Pulsed Power Heating of the D-Region .....	204
William A. Seidler, II	

An Ionospheric F-Region Disturbance Induced by the Launch of Skylab Michael Mendillo, Gerald S. Hawkins, and John A. Klobuchar	206
Ionospheric Disturbances During Severe Weather Activities R.J. Hung, G.L. Rao, R.E. Smith, G.S. West, and B.B. Henson	212
Faraday Rotation and Angle of Arrival Measurements Using Beacon Satellites A.R. Webster and P.A. Forsyth	217
Prediction of Ionospheric Effects Associated with Solar Wind Disturbances Using Interplanetary Scintillation Observations at 34.3 MHz W.M. Cronyn, F. Erskine, S.D. Shewhan, B.L. Gotwols, and E.C. Roelof	223

#### SESSION IV

Non-Rician Statistics and Their Implications for Modeling Effects of Scintillation on Communication Channels V. Elaine Hatfield and Charles L. Rino	235
Some Unique Features of the Transionospheric Channel Charles L. Rino	242
Stochastic Stationarity of the Scintillating Equatorial Ionosphere Howard A. Blank and Gary J. Bream	250
Frequency Correlation and Coherent Bandwidth of Transionospheric Signals S.J. Ulaszek, D.H. Liu, and K.C. Yeh	256
Computer Simulation of Transionospheric Scintillation Communication Channels Based on Fade- Duration Statistics R.E. Zieman and W.F. Deckelman	267
Some Results of Scintillation Studies K.C. Yeh and C.H. Liu	276
Intensity Statistics for a Multiple-Scatter Model Via Computer Symbol Manipulation W.S. Ament	283
Exact Analysis of Ionospheric Inhomogeneities by the Reflection Coefficient Method Arthur K. Jordan and Saeyoung Ahn	286
Antenna Aperture Effects on Measurements of Propagation Through Turbulence Dennis L. Knepp	292
Observations of H.F. Scatter from F-Region Irregularities D.W. Cornelius, K.H. Joyner, P.L. Dyson, and E.C. Butcher	301
Comparison of Simultaneous Ionospheric Measurements During Auroral Conditions Glenn D. Falcon	310
Ray Tracing Through Realistic Ionosphere Gravity Wave Models: A Comparison with Experimental Data from Several Different Techniques E.A. Essex	311

#### SESSION V

Some Problems in Constructing Phenomenological Models of Ionospheric Electron Density Y.T. Chiu	324
--	-----

Modeling the Topside of the F Region .....	331
Richard S. Allen	
Deviaton of Total Electron Content for Real Time Global Applications .....	336
Thomas W. Flattery and Allan C. Ramsay	
Decimeter Modeling of Ionospheric Columnar Electron Content at S-Band Frequencies .....	345
K.W. Yip, F.B. Winn, M.S. Reid, and C.T. Stelzried	
Ionospheric Models Used in Ionogram Inversion Techniques .....	353
R.O. Conkright	
Solar Cycle Variations of the Total Electron Content at Low Latitude .....	355
Yinn-Nien Huang	
The Construction and Use of Storm-Time Corrections for Ionospheric F-Region Parameters .....	361
Michael Mendillo, Michael J. Buonsanto, and John A. Klobuchar	
Seasonal and Diurnal Variations in the Total Electron Content of the Ionosphere at Invariant Latitude 54 Degrees .....	372
Gerald S. Hawkins and John A. Klobuchar	
Limitations of Mapping Techniques to Predicting Total Electron Content at a Distant Point .....	397
Charles M. Rush	
Measurement of the Ionosphere Total Electron Content and Lower Layers Inhomogeneities Using Chirp Signals .....	402
Said E. El-Khamy	

#### SESSION VI

Ionospheric Effects in NAVSTAR GPS .....	403
C.K. Cretcher	
Observed Ionospheric Effects in an Experimental Satellite Ranging System .....	411
Roy E. Anderson	
On the Determination of Mid-Latitude Ionospheric Time Delay from foF2 .....	421
John A. Klobuchar and Gerald S. Hawkins	
Prediction Techniques for the Effect of the Ionosphere on Ranging from Satellites .....	427
M.M. Feen, V.L. Pisacane, and M. Sturmanis	
A Simulator for Evaluating the Accuracy of Various Techniques for Electron Content Determination from Satellite Transmissions .....	436
George H. Millman	
On the Effect of Ground Reflections on Faraday Rotation Measurement of ionospheric Structure . .	441
J. Jones and A.R. Webster	
A Pulsed Plasma Probe Technique for Simultaneous In-Situ Measurements of Density, Temperature, Density Fluctuation Power Spectra and Ambient Electric Fields .....	445
Edward P. Szczepczewicz and Julian C. Holmes	
Application of Electric Field and Fast Langmuir Probes for the In Situ Observation of Electrostatic Waves and Irregularities .....	452
Michael C. Kelly, C.W. Carlson, and F.S. Mozer	

The Morphology of Small Scale Thermal Ionization Irregularities at High Latitudes Deduced from ISIS-I Satellite Measurements .....	459
M. Ahmed, R.C. Sagalyn, and M. Smiddy	
In Situ Measurement of the Structure and Spectral Characteristics of Small Scale F Region Ionospheric Irregularities .....	468
M. Ahmed, A.D.R. Phelps, and R.C. Sagalyn	
<b>OTHER CONTRIBUTIONS</b>	
Integrated Studies on Inhomogeneities in the Equatorial Ionosphere Using Different Techniques ..	485
C.A. Reddy, C.V. Devasia, B.V. Krishna Murthy, and K.S.V. Subba Rao	
Ionospheric Refraction Errors in Position Fixing Using Satellites .....	488
A.B. Ghosh and Y.V. Somayajulu	
A Preliminary Evaluation of Scintillations Over India for ATS-6 Emissions .....	492
P.K. Pasricha, B.M. Reddy, and N.V.G. Sarma	

Dr. Alan Berman  
Director of Research  
Naval Research Laboratory

WELCOMING ADDRESS

Goodmorning; it gives me great pleasure to welcome you to the 1975 Symposium on the Effect of Ionosphere on Space Systems and Communications. I am particularly happy that NRL had the opportunity to sponsor this meeting. This symposium is attended by representatives from the Department of Defense, Universities, and private industry. I have been informed that we have a significant number of foreign guests. The total interest has been expressed by approximately 250 scientists, engineers, and other interested parties. As of Friday afternoon I was informed that approximately 160 people had been pre-registered. To me this indicates a considerable interest in the topics to be covered here. We anticipate that this interest will translate into a desire to address and eventually solve the myriad of problems which we presently face in the realm of DoD space system design and operation. Some of these problem areas will be alluded to in the keynote addresses which will follow. I think this conference is somewhat unique among any that NRL has ever sponsored. If you look at your program, you will note that we have four keynote speakers instead of the usual one. To make matters worse, Dr. Goodman had great difficulty in persuading me to have a five minute welcoming address rather than a fifteen minute address. Although I promised John I would behave myself, given a microphone and a podium it is hard to resist the temptation to comment about

an area that one feels strongly about. My view is that as space systems come of age, as communication requirements become more demanding, the direction of our ionospheric research programs, will change. For example, the ionosphere, has shown itself to affect both satellite communication channels and conventional HF communications, in a manner which I feel is presently and completely understood. This understanding will undoubtedly be improved through the years, as we conduct additional basic research. However, in response to the immediate challenge, physical models of the ionosphere and various instability mechanisms need to receive considerable attention and indeed they are. The object being to obtain a more truly predicted capability for application to radio propagation problems and in space communication channel design. This is but one example of course. We believe we must be more responsive and developing an even greater level in communication between the scientific community and the system design and user communities. There are definite signs that this process is now underway. Certainly this conference indicates some progress in that direction. Again I wish to welcome you to this symposium. I am sure that in the technical sessions, of the next few days, ideas will emerge which will be of assistance in the design of DoD and other systems. My best wishes for a successful symposium. Thank you.

Dr. John Allen  
Deputy Director of Defense Research  
and Engineering

#### IONOSPHERIC RESEARCH, WHO NEEDS IT?

It is a pleasure to follow Alan Berman again. I have been following Alan Berman for the last three years and today has started off like many others. Actually, it didn't. It started out in several rather bad fashions but I hope things are on the upswing as of now.

I woke up this morning to the same thing that everyone else did, finding the streets covered with water and snow, producing the usual traffic jam from Mt. Vernon to the Pentagon. Furthermore, I was welcomed to my office by finding out that during the period of time that I was gone last week we had moved down the corridor in the Pentagon six or seven bays. I got in to find the office stacked full of boxes and pictures to be hung and all that good stuff. That wouldn't be bad enough, but the absolute lifeblood of the system had collapsed around us in the meantime. We found that we had no telephones. I don't know whether that is a good sign or a bad sign, but it is one of the things that will make the day a little more complicated. But it is nice to have a chance to get out and especially nice to have the opportunity to come over and talk to you.

I want to talk to you about some problems that we have in DDR&E which directly bear upon ionospheric research — not exclusively — but certainly in a way that allows me to give you some philosophy and discuss with you some problem areas. In some respects it will sound like an enlargement of what Alan Berman just said. I will try to put it in a different context, however, and try to say a few more words about why we have the concerns that we do and what we might do about them.

I would like to commend the Naval Research Laboratory for their initiative in setting up this meeting, continuing to lead the pack in science as they have for so many years. I would especially like to express my appreciation to John Goodman for inviting me to speak here.

My job at the Pentagon can be roughly characterized as saying that I have the responsibility for what is called the Technology Base, which in Pentagon jargon means Research and Exploratory Development in some of the non-system-directed Advanced Development programs. I guess you would characterize what I am responsible for as saying that it is primarily our investment in the future as opposed to the attempt to deal with day-to-day problems of developing new systems.

The importance of this investment in the future is, I think, well-recognized by people that count, such as the Secretary of Defense who recently came forth with a ringing endorsement of the Technology Base in a statement that will go, or perhaps has already gone, to Congress, kicking off the FY 76 budget cycle. He says, and I quote, "we must vent every effort to sustain the health and vigor of the scientific and technology base." I will enlarge shortly on what he means by venting every effort. However, let

me say that we have the support of both the Secretary and Dr. Currie, the Director of Defense Research and Engineering, and this support translates into a thing which is the most tangible benefit to all of us; namely, money.

In the process of trying to figure out what to do with this money, and to best use it, there are a number of things that we have underway at DDR&E concerning the management of the Technology Base. I would like to touch on some of these and then hit very hard on a particular one because it bears precisely on what we are here for today. Part of the problem that we all have — you have it, we have it at DDR&E, and all laboratories have it — is how you make the output of this process, in which most of you here are engaged, available to those that are ultimately paying our bills. That is, how do we couple the Technology Base to the sort of things that represent useful products in the case of DoD or the military?

We have some new things going on here and some new programs. Furthermore, we are trying to change the flavor, in a fairly significant way, of how the DoD does business in development by making it a little bit easier to carry technological advances a bit farther and to carry forward more technological advances. We plan to make up the money for this by committing ourselves to fewer system developments, hopefully also using the technological approach to sort out what we really should be doing. This is something that we colloquially refer to as a "6.3A" or Advanced Technology Demonstration Programs. Hopefully, this approach will have some impact on you in years to come, since they will ultimately give you more of an output and also more of a tie between the research and the user end of the spectrum.

We, as you may be aware, also have given some careful consideration and are urging upon the Services some rather substantive changes in the way they do business with their laboratories and the way they manage their laboratory complexes. You will probably be hearing about that in the months to come.

We are quite concerned with the program content of the Technology Base. There are a number of aspects of that but primarily we must judge what is going on and hold people accountable for what is going on. You may be aware of the fact that, in the last few years, there has been more of an intense effort to surface and ventilate what is going on in the Technology Base. For those of you who are sponsored by DoD, you have probably encountered the syndrome of what we call Topical Reviews, about once each year, about this time of year, in which we try to review in depth about one-third of all the things that DoD is sponsoring. People who are working in the field get involved in these things and, by this method, hopefully you find out what your colleagues are doing; we find out what you are doing; users find out what others are doing and

have a chance to kibitz on this and offer remarks. That is the back-end of the process, however. That is the situation after things are well underway.

What I want to talk about today is the problem at the front-end of the process, i.e., how do we go about structuring programs in the first place? You may be aware that we instituted a major management innovation in the last four years or so in the Pentagon which goes by the initials "TCP," for Technology Coordinating Papers. This is an attempt to tie the whole process together, from the beginning of research to the ultimate use of the technology. In that sense, we see how this ties in with Dr. Bernam's comment. Those of you who have access to these documents (and not everybody does) I recommend to your reading the Environmental Sciences Technology Coordinating Paper, to see how this process goes. I will talk more about what goes into these papers a little bit later.

The thrust in trying to get the program better structured is the one that is typified by this kind of meeting, where we are trying to improve the interaction between the various communities involved. And that is the reason why I rather eagerly accepted the opportunity to give this talk today.

Our mission in the Technology Base is primarily just what you think it is, and that is the generation of new ideas. To generate new ideas you have to be able to start a new kind of work, and therein comes the crunch.

There are only two sources of money that are available in this world to us; one is fresh money and, if we can convince the Services and the Congress that we are worth more money in the Technology Base, hopefully we get it. That allows us to undertake or start some things we were not doing before. We have not, as you have noticed, been notably successful in this undertaking in the last few years and, while there are some hopeful signs on the horizon, there are also some rather dismal signs on the horizon. How we are going to come out in that regard, I do not know. Of course, the other possibility of new money is to stop things that are now going on.

To put this crunch into perspective and to point out to you what is happening as a result of the last few years, I think one can summarize it very succinctly. In the last ten years, the DoD Technology Base effort has decreased 40% since we have remained approximately level-funded. That is a manifestation of the bite that inflation has taken out of the Technology Base. We are trying to reverse this. We are trying to get new money into the system and, as I indicated earlier, both the Secretary of Defense and Dr. Currie are supporting this effort. We are currently in for a budget request of 13% above what we went in for last year.

You might say that if you are in for it, why don't you get it? Let me just point out that there are lots of pitfalls between here and there and all of them don't necessarily come from the people that you readily identify as where the problem might arise. How we are going to come out of this, I am not at all sure at this point.

We have fought our first set of enemies so to speak. Those are our colleagues in the Military Department who can always think of what they perceive to be better ways to spend our money, other than research and development.

We have fought that battle and, so far, we are in pretty good shape. Now we go up to Congress where we face, to make an understatement, a very uncertain set of events this year with a whole new host of characters. We don't know how we will come out, but we are trying.

We also have issued a directive to the Services for the ensuing three fiscal years. We want to increase research by 10% in real current dollars; that is, 10% plus inflation and to increase exploratory development by 5% in current dollars; that is, 5% plus inflation through fiscal year 1980. This is guidance that we intend to hold to and we trust that something will come of it. The Secretary supports this to the extent that he is indeed willing to see this money taken out of other places in the DoD Research, Development, Test and Evaluation part of the budget. Again, I emphasize that there are a lot of pitfalls between here and there, so we can only hope.

Meanwhile, while we are hoping for this new money, we do have the basic problem that I mentioned before. The only other way to get money in big chunks is to stop things that are going on. This indeed is our hardest problem, although it is not too difficult to philosophize about deciding what to fund and what not to fund.

There are, I think, only two valid criteria for the Department of Defense these days. First is the possibility that the work being considered will contribute to directly perceived military problems. That is, where we know we have problems, we certainly have to put priority in the use of funds for correcting those troubles. However, with any research, our ultimate payoff may be in things that we can't perceive. We do, in fact, very much like to protect some of this money and devote it to areas rather than specific projects, assuming that it is reasonable, or at least not unreasonable, to expect that there might be worthwhile contributions to some type of military problem. The thing that I emphasize in both of these areas is the question: Is the contribution there by intent, or is it there in a completely unexpected way in the application of military problems?

Since about four or five years ago, it has been thoroughly impressed in the Department of Defense that we are not the National Science Foundation. We get reminded of this periodically by our overseers all over the place. The problem that this gives us is that, to a large extent, history plays a very large part in the Technology Base program. I think, in some respects, it unfortunately plays a large part in the Technology Base program. Efforts that are undertaken and are continued for a large number of years tend to build up the constituency in terms of people involved in that kind of work and constituencies in terms of the fields of hardware which resulted from that kind of work and which have to be funded and maintained.

We are now starting into our fourth decade of post-World War II research, so it is not very surprising that we have built-up a large number of constituencies. This defines a problem which the managers of R&D face. We have to face-up to question as to whether it is proper or not, under the present budget constraints, to continue these various constituencies. The fact that they exist is not a sufficient reason for R&D. This problem is certainly cause for thought, which we do once in awhile.

Environmental science and general ionospheric research,

in particular, are certainly in the context of things that we have been doing for some time and certainly have built up a constituency, several hundred of which are sitting in the audience out here today.

Ionospheric research has a rich history which has made a significant contribution to the Department of Defense, both in terms of telling us how to better design our systems, and in terms of how to use the ones that we have already designed.

However, in the terms of having bad news and some good news, the bad news is the recognition that ionospheric research has been around long enough to provide us with an estimate of the likelihood of breakthroughs. Indeed, significant breakthroughs are probably rather unlikely. I think that, in terms of producing the unexpected, I cannot say it is not going to happen and neither can anyone else, but I would not place this particular area very high in the realm of things that are producing daily unexpected results. On the other hand, the good news is that there are certainly enough problems around that we recognize to keep this constituency, and I think even more, occupied for a goodly amount of time to come.

Scintillation problems in some of our communication systems, as you are well aware, are a critical interest to us at this point. We got caught somewhat asleep with TAC-SAT, you might say. In addition, we still have a large inventory of high frequency communications gear that we keep saying that we are not going to use anymore and we keep using year-after-year. Also, one of these days we are going to find out what OTH radar is really all about, maybe a little bit more on how to design it; maybe not, perhaps, but learn how to manage the thing so that it works a great deal better. So there are plenty of problems.

The question which arises, however, is: Of those of you that are sponsored by the DoD, are you really working on the right problem; indeed, are you working on problems at all? Research for research's sake, as I said, does not seem to be the bag of DoD these days. There is also in some circles — and I would accuse the environmental sciences area of being amongst the worst offenders in this regard — the tendency to often substitute research for insight.

The point is: Are we "guilty or not guilty?" The answer is: I am not sure. That is one of the reasons that we welcome this symposium. I have my agent, Colonel Al Kaehn, sitting in the back of the auditorium. I think he is going to be here for almost all or all of the symposium and this gives us a chance to sit in and find out what is going on.

What we basically seek to encourage here is what we might characterize as a customer-supplier relationship. We recognize that we have real problems. We very much need your help. We think that we know where those problems are, but we are not 100% convinced that we do. I don't want to say that I think there is no room at all for innovation in this business. It isn't simply writing out a work order and saying: Do this. If it were that simple, we wouldn't need to talk to you. Indeed, we would just write out a work order.

So we welcome this kind of symposium. It gives us an

opportunity to talk with you, to listen to you, and exchange views. Hopefully, we wish to get planted in your mind the idea of the customer-supplier relationship, the fact that we do have problems, we need help, we need people who are innovative in the current research in order to help us in solving these problems in what I would characterize as a user-oriented way.

John Goodman did not mention the title of my talk, but, basically, the title of the talk is: "Ionospheric Research, Who Needs It," and the answer is: "We need it and we need it very much." I am not sure that we need it all, but we need some of it. We are not perfect in defining what we need, so what we prefer to do is expose to the research people what our problems are and let you engage in the dialogue with us and help us to determine in the most enlightened way what our problems are and how we should go about solving them.

It does put a burden on you as researchers. It means that you have to get to know what your potential customers might be, what their problems are, and learn enough of their language to surmount the language barrier problem that invariably and unfortunately exists between technologists that work in different areas. In other words, to be a part of the solution instead of being part of the problem.

Keep these points in mind as you go through your symposium. We hope that this kind of meeting and other efforts that we are sponsoring — in particular that those of you who work for DoD (and I recognize that not all of you do) — will be able to help us in the course of the next few months to evolve a much better program, if there is room for improvement. Or, if we have a program which is near optimum now, convince ourselves that this is true.

With that note I would like to say again, I welcome the opportunity to give this talk, and commend NRL and all of you for getting together to have this symposium. You have my best wishes for a successful, stimulating, and informative symposium. Thank you.



Dr. Thomas P. Quinn  
Director Field Projects  
Office of Naval Research

#### IONOSPHERIC RESEARCH, NAVY INTERESTS

I think it might be interesting to reflect upon how we got to the point where there is enough interest in ionospheric effects on space systems communications that a major conference on the subject can be held. I don't think this would have been predicted ten years ago when the navy first became seriously interested in satellite communications. At that time DDR&E was pushing the services to get them involved in the development of satellite communications. I was on one of the early tri-service committees that looked into the applicability of satellites to the solution of DoD communications problems; and it's fair to say that the services entered into satellite communications, not necessarily dragged kicking and screaming, but in the case of the navy certainly with some reluctance.

Now one of the major reasons given at that time for developing a satellite capability was to get communications out of the high frequency band. Because HF depends on the ionosphere, which every communicator knows is uncooperative and unreliable, HF communications are viewed as being equally unreliable. So here was an opportunity to change that situation and have a communications system which did not depend on the ionosphere and therefore would be free of its influence. The predicted extremely high reliability, time availability, wide bandwidth; all those good things made a very attractive case for satellites. So the three services embarked on satellite communication programs, both strategic and tactical.

The first tactical satellites were to be UHF. One of the reasons for UHF was that the services had a tremendous investment in UHF equipment and there was of course an interest in how much of that investment could be salvaged by using existing equipment for satellite communications. The committee I mentioned looked into how much of that equipment could be used, and much to the chagrin of DDR&E, the answer was: essentially none of it. So that particular reason for using UHF was nullified, and the predicted high cost of shifting to satellite communications could not be eased by using existing equipment.

However, the fact that we would be rid of the ionosphere and its attendant problems would still make it worthwhile.

So it was concluded that, although expensive, satellites would give us a reliable non-ionospheric dependent system, and HF could finally be phased out. And things began to move in that direction, along with periodic recommendations that the navy phase out of HF completely.

Well, we have implemented satellite communications systems and some of them are now operational. So why are we back talking about ionospheric problems? Don't

we yet understand enough about the ionosphere to take it into account when we design new systems? Is it because we just don't apply what we already know? Or is it that there is a communications problem among the ionospheric scientists and communications systems engineers which is as much of a problem as the ionosphere itself. We are here no doubt, for all three of those reasons.

The fact of the matter is, the hoped for complete immunity of satellite communications to ionosphericly caused ills has not proven out. I don't mean that I think satellite communications systems have not been successful nor that they have not been an improvement over HF. I am rather dwelling on the problem areas.

For example, there are serious scintillation problems and, just as a switch to satellites was proposed as a cure-all to our HF problems, there are those who now suggest moving up in frequency as a simple cure-all for the scintillation problem. There are of course others who dispute that.

So the questions remain: How do we fix the current situation, and what do we do for the future? Do we know enough about the ionosphere to engineer a fix to the scintillation problem? Perhaps this conference can help answer that question. I certainly hope so or at least tell us what further it is we need to know.

One of the Navy's interests, and for that matter an interest of all the government agencies involved in satellite communications is to find an economical, technically acceptable and timely solution to the scintillation problem. I mentioned earlier the scientist/engineer communication problem. I think in order to develop a timely solution we are going to have to present the results of ionospheric research in a way that is useful to systems design and development engineers. We must try to establish better communications between these groups than we have had in the past.

Said another way, the Navy's interests really are in the excitation and propagation of electromagnetic waves through, under, within and especially in spite of the ionosphere, and not in the ionosphere for its own sake. So what is needed from a navy communications viewpoint is an adequate understanding of ionospheric effects on propagation under all conditions important to navy missions. The potential performance degradation due to ionospheric effects may then be properly taken into account during the systems design phase. To accomplish that will no doubt require some further ionospheric research; precisely what kind may very well not be completely resolved.

As I said earlier, past interest in ionospheric research has been primarily motivated by HF propagation problems. Current emphasis so far as HF is concerned is on what you might call improved HF circuit management. However, the emphasis on applied ionospheric research now is shifting away from attempting to cure HF propagation problems. This conference itself is an indication of that change. In fact it would appear that the Navy's interest in the frequency spectrum is moving away from HF in

both directions. We are implementing new VLF systems, developing an ELF system and conducting some research at ULF moving ever downward from HF. Moving upward, we are developing systems and conducting research from UHF through K band. I hope this conference will provide some useful guidance for us in this latter area; and toward that end I wish you all the best in having a most successful symposium over the next few days. Thank you.

Fred E. Bond  
Deputy Director, Military Satellite Communications Systems Office  
Defense Communications Agency

## THE IONOSPHERE AND MILITARY SATELLITE COMMUNICATIONS

Ever since the discovery of the means for generating and propagating radio waves, the various layers of charged particles surrounding the earth at altitudes ranging from 50 to 400 KM have played a highly significant role in radio communication beyond line-of-sight ranges. Military uses of this medium at frequencies in the lower end of the HF band had an early start. Fixed station operation over distances of a few hundred miles was used for CW as early as the World War I period. Applications were eventually extended to global networks, and vehicular, aircraft, shipborne and portable service. Also, the type of transmission began to include voice, teletype, and multiplexed combinations. By the time World War II occurred a number of sophisticated systems existed for communication via reflection from the ionosphere.

In retrospect, it is amazing to see how much was accomplished with such a small understanding of the basic transmission mechanism. Fading and static noise were accepted, and the use of different frequencies for day and night transmissions became a commonplace procedure. Eventually, antenna diversity combining systems were introduced to alleviate the effects of fading.

When the insatiable demand for more communications began to produce a crowded spectrum and the need for higher data rates, pressure began to mount for more efficient transmission. This inspired a concentrated effort to gain a significantly better understanding of the ionosphere, including its physical structure, and the effects on it produced by the sun, magnetic storms and artificially created environments. Meanwhile, more sophisticated modulation and coding techniques began to blossom and the use of sounding techniques evolved.

When satellite communication was discovered — or invented — it was first believed that we were at last free of the problems created by this capricious monster. Early military applications in the SHF range for fixed station

operation demonstrated feasibility of multichannel trunk transmission and wideband data with seemingly little problem. Early applications in the military UHF band for aircraft and ship terminals were also successful. However, as time progressed, severe scintillation fading was observed at the lower frequencies, especially at certain times of the year, certain hours of night, and in specific geographic locations. Further investigations revealed that it was present at higher frequencies as well but in smaller amounts. The cause of this problem? The same old devil-ionosphere. Early attempts at simple remedies such as space or frequency diversity, resulted in some unpleasant surprises. There is no easy solution. One might conclude from this that, we are, in a sense, back to the beginning of the 20th century when HF radio was in its rudimentary form and more of a curiosity than a utility; and ionosphere problems were just a modest nuisance. Unfortunately, the analogy breaks down. The insatiable appetite for more transmission and higher data rates is already pressing us in military communication satellites. Even without the scintillation problems, we are looking at all sorts of techniques to relieve congestion. This includes, frequency reuse, operation at higher frequencies, demand access, time division multiple access and a host of others. Meanwhile, the threat of deliberate enemy interference must be reckoned with right at the start of any system design.

So the pressure is already upon us for ways and means of mitigating the disturbing effects of the ionosphere in satellite communications. Fortunately, this time, we have a number of things in our favor; a good understanding of the medium, an excellent set of analytical tools, and several opportunities for experimental testing.

I want to wish you all a very successful symposium. I am sure that the results of the efforts reported in the next three days will go a long way in improving the quality and quantity of future military satellite communication systems.

Harry Fiegleson

MARITIME SPACE APPLICATIONS

Early operational use of maritime satellites for communications and follow-on users for position-determination make the need for as complete as possible knowledge of ionospheric effects as possible.

A brief summary of the development is provided. Emphasis is placed upon the economic consequences associated with assumptions regarding the effects of the ionospheric as well as its limiting effect on advanced applications.

## HIGH LATITUDE MORPHOLOGY OF IONOSPHERIC SCINTILLATIONS

Jules Aarons  
Air Force Cambridge Laboratory  
Bedford, MA. 01731

### INTRODUCTION

The interest in the study of ionospheric irregularities at F layer heights emanates from two directions. One is from the designer of systems in that portion of the spectrum which is affected by amplitude and phase fluctuations i.e., VHF to 1 GHz at high latitudes and VHF to S Band at equatorial latitudes. The other area served by the study of ionospheric scintillations is that of the physics of magnetospheric-ionospheric interactions. For aeronomic studies the recording of scintillations on beacon signals (and frequently measuring total electron content variations simultaneously) is one of the few ground methods of continuously observing changes in the ionosphere at F layer heights during magnetic storms.

This review is intended as a follow on of Global Morphology of Ionospheric Scintillations by Aarons, Whitney and Allen (1971), which will be referred to as Global Morphology I. Recent unpublished studies on scintillations at sub-auroral, auroral, and polar latitudes during magnetic storms have also been summarized.

Some of the text of this paper forms part of Global Morphology of Ionospheric Scintillations-II which will be printed in Proceedings of the Symposium of the Cospar Beacon Satellite Group held in Moscow, November 1974.

The global irregularity structure during magnetically quiet nights is pictured in an updated version of a figure used earlier by the author and his collaborators in Figure 1. Since the density of hatching is an attempt to describe the depth of fading it should be noted that equatorial scintillations

are of greater intensity than high latitude effects. Middle latitude scintillation is observed but is generally of lesser intensity than high or equatorial latitude fading.

The simple picture is deficient in many respects, because of the absence of the effects of solar flux variations, seasonal patterns and magnetic storm effects observations. For example, during years of low solar flux (Tao 1965) a mid-latitude region of spread F appears. This is apparent in scintillation records taken in 1972 in Camp Parks, California and in Athens, Greece. Another aspect of the picture

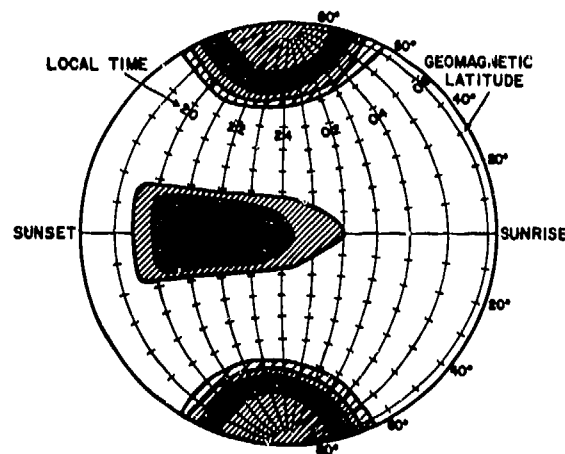


Fig. 1 A nighttime picture of the occurrence of deep fading. Equatorial scintillations show greater depth of fading than do scintillations observed at sub-auroral, auroral and polar latitudes. Daytime scintillations occur at high latitudes ( $>70^\circ$ ) but are low at equatorial latitudes.

that is deficient is the extent of the equatorial irregularity region during years of low and high sunspot number. Tao (1965) in his maps appears to indicate that the extent of the region (where it falls to half the occurrence of the maximum) is relatively constant whereas Singleton (1968) indicated a considerable increase in spread in the region during years of low solar flux. Recent measurements have shown, moreover, that the intensity of irregularities decreases during years of low solar flux. Clearly the true picture of scintillation activity is complex. We shall attempt to describe sub-auroral, auroral and polar morphology only.

#### MIDDLE AND SUB-AURORAL LATITUDE VARIATIONS

At latitudes below the auroral oval's position during both magnetically quiet and disturbed periods, various sets of data have yielded behavior indicating little correlation with magnetic conditions. Evans (1973) found no correlation of their 400 MHz radar return scintillations with magnetic index south of their station at  $56^\circ$  invariant latitude. Aarons and Martin (1974) found that during the August 4 - 10 1972 magnetic storms there was a negative correlation of scintillation and magnetic index for Athens, Greece and Camp Parks, California and little correlation for the  $45^\circ$  intersection of Aberystwyth, Wales. Bramley (1974) found that except for the December 1971 magnetic storm (when the irregularity region probably encompassed the intersection point of  $\sim 45^\circ$ ), there was no correlation between magnetic activity and scintillations.

This type of data essentially corroborates the early radio star observations in the U. K. which found little correlation with magnetic index except in paths to the north (with the exception of some intense magnetic storms).

For the middle latitude region the scintillation indices are low although there are high values reported at times. The diurnal pattern of weak scintillation shows little increase at night (Bramley, private communication). Some persistence of patches which recur or remain for two to three days running has been shown by Albrecht (1974).

#### HIGH LATITUDE IRREGULARITIES

It is now clear that the high latitude F layer irregularity structure has similarities with the morphology of the 100 km aurora - and differences. The irregularity region descends to its lowest latitude at night and moves close to the invariant latitude occupied by the aurora in the daytime sector. Its differences are that a detectable and significant fading can be observed equatorwards of the optical aurora and that the irregularities are intense in the polar regions. During magnetic storms in a manner similar to the aurora the irregularity region moves equatorwards of its quiet day position and in addition the irregularities gain in intensity.

##### (a) Models

As summarized by Pope (1974), the model developed in Fremouw and Rino (1973) considered several geographic regions separately. These regions are the equatorial ( $\pm 20^\circ$  geomagnetic), the mid latitude ( $20-60^\circ$ ), the high latitude ( $>60^\circ$ ) and the auroral regions ( $\sim 65^\circ - 70^\circ$ ). Suitable mathematical functional relations were assumed for each of the regions. Data pertaining to these regions were selected according to the weak scatter criterion that the phase shift introduced by the irregularities was less than 0.7 radians; these data were used to infer the appropriate coefficients. Pope (1974) made modifications to the high latitude term of the model and provided for variations in the position of the scintillation boundary with respect to magnetic activity. Another modification was made to represent the finding that the northern and southern polar regions of the scintillation activity are not symmetrical with the southern hemisphere boundary at higher invariant latitudes than the northern boundary (by about  $4^\circ$  in Pope's modification of the model).

##### (b) Radar Observations

Using 400 MHz radar signals obtained from skin tracking of satellites, a recent series of measurements was made by Evans (1974) at Millstone Hill, Massachusetts. He identified a scintil-

lation boundary, using the  $S_4$  value of .04 as the criterion as to whether the entry into the high latitude irregularity region had been reached. His results were similar to those of Aarons and Allen (1971) in that the lowest latitude of  $57^\circ$  was reached before midnight for this region.

He found that the probability of observing large scintillations increased during magnetically disturbed periods. The highest scintillation indices ( $S_4 \rightarrow 1.0$  and transverse angle scintillations  $\sigma_{TR} \geq 20$  m deg) were largely confined to periods when magnetic storms were in progress, including some in the daytime.

Evans found the amplitude during scintillation most closely followed a Nakagami m distribution with a Rayleigh distribution obtained when  $m = 1$ .

The mean scintillation index as a function of invariant latitude varied with magnetic activity. At latitudes above  $53^\circ$  a higher  $K_p$  is associated with increased scintillation, while below  $53^\circ$  there is a small decrease in scintillation with increasing  $K_p$ . The prediction of mean scintillation index from the model proposed by Fremouw and Rino (1973) was considerably lower than that observed at Millstone, probably due to problems of extrapolating 40 - 100 MHz data, some with effects of strong scattering, to the 400 MHz frequency.

#### (c) The Scintillation Boundary and the Trough

It was clear from earlier work that there were similarities between the electron density trough and the scintillation boundary. Both descended during the night and both moved equatorwards during magnetic storms. However, Aarons and Allen (1971) had pointed out several differences between the positions and the behavior of the two lines. Kersley et al (1972) found the scintillation boundary in general approximately one degree equatorwards of the trough minimum between 1700 and 0130 hours but after 0200 the positions were reversed until at 0700 the abrupt scintillation boundary was on average some three degrees poleward of the trough minimum. New analyses by Kersley and Van Eyken (1974) found that the trough latitude decreases from 1700 - 2000 with a possible very slow decrease to a minimum at 0600 followed by a rapid increase. Few troughs in total electron content were detected

in the afternoon sector. The dependence on magnetic activity of the trough is irregular whereas they found the scintillation boundary dependence on changing levels of magnetic activity more highly correlated.

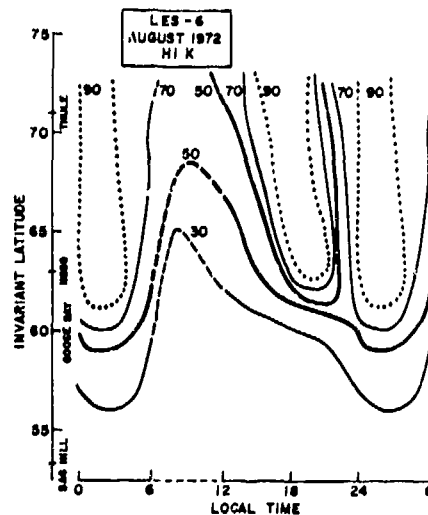
Evans (1973) by measuring total electron content using the Transit NNSS satellites found that there was no set spatial relationship between the position of the scintillation boundary and that of the trough when studied on a case by case basis. Statistically there were distinct differences as well.

McClure (1973) found that the poleward edge of the trough of ionospheric ions is almost always associated with the onset of soft auroral electron fluxes and large amplitude irregularities in  $N_1$ . He also found large amplitude auroral irregularities of ions near the dayside cusp related to fluxes of soft electrons (<300 ev).

#### (d) The Auroral Oval

##### (1) Night

The outlines of the intensity variations within the irregularity region are clear. At night during periods of magnetic quiet scintillation index increases several fold from the



2a. Contours of scintillations index as taken at four stations during the magnetic storms of August 1972. Frequency of observation is 254 MHz.

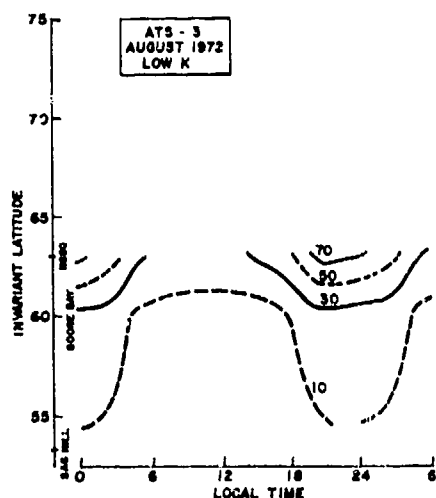


Fig. 2b. Contours of scintillation index at 136 MHz in August 1972 during periods of low magnetic activity.

boundary to the latitudes of the position of the optical auroral oval. Maximum index is recorded when the path traverses the auroral oval. A shallow minimum is then encountered with a second peak located near the corrected geomagnetic pole (Nielsen and Aarons 1973). Frihagen's (1971) data indicated a small trough poleward of the auroral oval. Higher magnetic indices increase intensity levels across the entire irregularity region as well as lower the boundary between the ordered F layer and the F layer encrusted with small scale irregularities.

One example that can be readily noted is that taken from the August 1972 magnetic storms. Figure 2a is a composite of data from the period August 3 - 10 when K indices were 5 or greater (Aarons and Martin, 1974). Quiet day contours of scintillation index (SI) are taken at 136 MHz (Figure 2b) while disturbed period indices are taken at 254 MHz (this presentation is used in order to reduce the effects of fading "saturation" shown at times when fading reaches levels indistinguishable from noise). Hawkins (1974) has shown that from one to two days after the onset of a period of magnetic quiet ( $A_p < 2$ ) scintillations disappear in the 50° to 65° invariant latitude range.

The time development of the irregularity spread from the auroral oval during magnetic storms has been studied by the author and his collaborators using a combination of synchronous satellite beacons, auroral photographs by the DMSP satellite, passes by the NIMBUS beacon, as well as local magnetograms.

The emergent picture is as follows: Storm Sudden Commencement produces immediate scintillation effects at invariant latitudes of 63° and for some storms at 60° invariant latitude. With the development of the main phase of the storm, the intensity of the irregularities spread to latitudes at times as low as 45°. The equatorwards boundary of the high latitude irregularities is a function of season, intensity of local magnetic displacement, and time of day. At local noon, effects have been shown to 57° invariant latitude.

One example of the development of effects of the storm can be noted in Figure 3 comparing magnetograms and scintillation indices at College, Alaska. Storm commencement at 1418 UT (local standard time ~0418) brought no increase of scintillation at the 350 km invariant intersection latitude. Only with the large variation in the H component during the day of ~1500  $\gamma$  at 17-18 UT (07 - 03 L.S.T.) and ~1100  $\gamma$  at 1930 UT did the daytime scintillations become dramatically large.

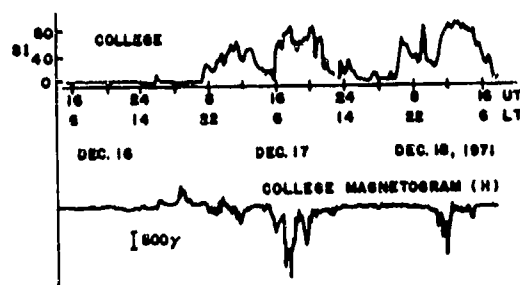


Fig. 3 Comparison of College, Alaska scintillation and magnetogram. The two paths (overhead for the magnetogram and the 350 km. intersection point to ATS-1) differ in latitude by approximately 8°.



Data from a series of stations, Thule and Narssarssuaq, Greenland; Goose Bay, Labrador; College, Alaska; Sagamore Hill, Massachusetts; Aberystwyth, Wales; and Lindau, Germany are leading to an ability to sort out local magnetic, diurnal, and seasonal variables.

An analysis of the U. S. Air Force DMSP satellite auroral photographs (Martin and Aarons, 1975) allowed the measurements of scintillation indices at times of aurora. The analysis showed that in the median when the diffuse edge of the aurora is  $4^\circ$  poleward of the path intersection, intense F layer irregularities are present. When the path intersection is polewards of the 100 km optical aurora, scintillation indices at 136 MHz of the same order of magnitude i.e. 25-50 ( $\sim 2-5$  dB peak to peak fading) were still noted.

## (2) Day

The daytime boundary is located between  $71^\circ$  and  $76^\circ$  for very low K indices ( $K = 0, 1$ ) and  $68^\circ-69^\circ$  for  $K = 2, 3$ . Increased magnetic activity brings higher levels of scintillations throughout the region for some magnetic storms.

Some new data (from Thule) are being studied which indicate that the cusp region about noon shows an unusually high occurrence of scintillation.

## (e) Polar Scintillations

There is clearly from in situ irregularity measurements, from spread F data, and from scintillation studies no polar cap cavity as there is in energetic electron precipitation. The spread F measurements indicated a permanent maximum (Penndorf (1962)). The in situ measurements of isotropic electric fields indicated a decrease in intensity over the dayside polar regions relative to the auroral oval measurements (Kelly and Mozer, 1972). Nielsen and Aarons (1973) using both 40 MHz and 150 MHz observations from Thule found high scintillations over the geomagnetic pole, even allowing for increases in scintillation index due to aspect sensitivity. The diurnal pattern over high latitudes differed from those at other latitudes; however, only brief periods of observations were available from this study.

The field of polar scintillation studies is relatively unexplored. 40 MHz observations show both multiple scattering effects and saturation of fading. Frequencies of the range of 136 to 400 MHz are needed; the DNA satellite with its unmodulated beacons will hopefully aid in the determination of the polar cap scintillation morphology.

## IN SITU MEASUREMENTS

Perhaps the largest contribution to new measurements of global morphology of irregularities in the period between 1970 and 1974 comes from the in situ measurements of various ionospheric parameters. These include electric fields, thermal electrons, suprathermal electrons, and ion density measurements.

Correlating in situ measurements with scintillations can only be done with several caveats. In situ measurements give no indication of thickness, an effect of importance on scintillation excursions (Singleton 1973). In situ measurements are frequently higher in altitude than the 350 km level found to be the predominant height of the (often) thin layer irregularities. In situ measurements unless configured carefully do not show the effects of irregularity elongation, field alignment or zenith angle. More basically, however, in situ measurements may measure the causal element for the production of the irregularities (suprathermal electrons) for example; therefore the ambient atmosphere must be taken into consideration.

One series of significant measurements were obtained with an electrostatic probe on ISIS-1; thermal positive ion observations were made (Sagalyn et al 1974). A spatial resolution of 150 meters was possible. The equatorial boundary of the irregularity region was defined as the latitude of onset of persistent small scale ionization irregularities extending over at least a few degrees in latitude with amplitudes amounting to 20% of more the mean background levels.

Comparisons with the topside sounder in the same vehicle showed that down to the minimum scale, irregularities map down to the peak of the F region. The boundary of the irregularity zone was found to be  $3^\circ-9^\circ$  closer to the pole in the southern hemisphere than in the northern hemisphere. The

seasonal variation of the mean location was small. At noon in the northern hemisphere the total seasonal variation is  $4^\circ$ ; at midnight,  $6^\circ$ . The boundary is closest to the pole in June and farthest in December. No poleward boundaries for the irregularity zone were found; the inhomogeneities extend across the pole. Sagalyn et al found that the equatorial boundary of the irregularity zone was  $3^\circ - 7^\circ$  equatorward of the auroral oval. Comparison of the irregularity boundary of this technique and that of the scintillation boundary was excellent at night and between 21-06 local time but differed at 1700 LT (Figure 4). Recent analysis of 40 MHz BEB results from Narssarssuaq (Mikkelsen and Aarons, private communication) indicate that the earlier boundaries found at this time period by data taken at  $57^\circ$  should be revised; the new contours will bring the scintillation boundary closer to Sagalyn's results.

The severe topside irregularity zone was observed using the ionosounder on ISIS 2 (Dyson and Winningham 1973). It is (probably) the topside observations of the same F layer irregularity zone (Pike 1971, 1972) observed by a flying sounder, where heavy spread F appears.

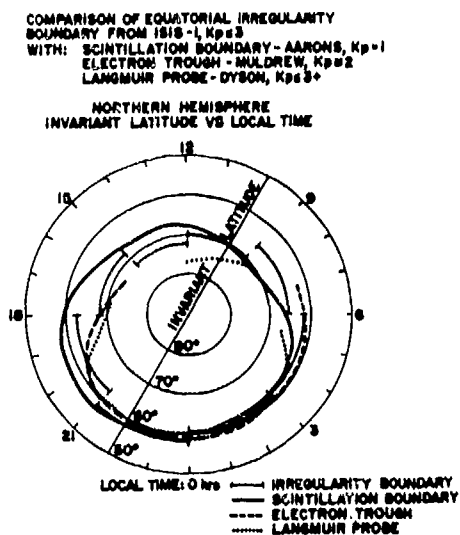


Fig. 4 Comparison of equatorward boundary from ISIS-I data with other boundaries (Sagalyn et al, 1974).

On the dayside of the earth the equatorward boundaries of this zone and of the  $< 300$  ev electron precipitation coincide. However, the boundary does not coincide with electron precipitation above 300 ev. The zone extends beyond the poleward boundary of the particle precipitation, probably due to magnetospheric convection transporting irregularities poleward of the region of production. It might be noted that the zone is coincident with the irregularities of the largest absolute (rather than relative) amplitude. On the dayside the zone and the cleft are coincident at times. In a significant number of cases the zone can begin equatorward of the cleft. There is no indication that it ever begins poleward of the cleft.

#### FUTURE STUDIES IN MORPHOLOGY

The mid-latitude scintillation picture will be helped by studies of ATS-6 40 MHz transmissions. At middle to sub-auroral latitudes there are indications of irregularities appearing a fair portion of the time.

One effect that is not as yet explored for its physical interpretation is that of mid-latitude and sub-auroral morphology. The plasmopause motions and the heating that produces Stable Auroral Red arcs must be a source for the creation of irregularities. Basu (1974) has shown correlation of scintillation and SAR arcs during magnetic storms. However, the occurrence of spread F and of scintillations at these latitudes during quiet periods has not as yet been explained.

At sub-auroral and auroral latitudes the picture is definitely clearing up with multi-frequency studies being made and with the aspect sensitivity more readily calculated. A detailed correlation with magnetic variations during some intense magnetic storms exists.

The polar irregularity structure is far from clear. The diurnal pattern, the effect of intense magnetic storms, and the quiet day pattern have not been correlated with other polar cap phenomena.

The seasonal behavior of sub-auroral and auroral scintillations is emerging. Maps of spread F occurrence and some seasonal statistics on scin-

tillation are available. For example, the winter pattern at auroral latitudes during magnetically quiet days has two peaks. Certainly this could be correlated with the complex electric field structure or with seasonal variations of suprathermal electrons.

The advent of ATS-6 with its beacons at 40 MHz, 140 MHz, and 360 MHz will aid the study of the global morphology of ionospheric scintillations. The 40 MHz signals will be valuable for mid-latitude observations, for frequency dependence studies, and for statistically observing multiple scattering while noting weak scattering (a comparison of 40, 140 and 360 MHz signals at high or equatorial latitudes during some periods). The 360 MHz signals will allow for observations at auroral latitudes during magnetic storms without encountering saturation too often.

Studies of phase scintillation of the small scale irregularities are needed. Recent interest in the field has added to the measurements, to the use of the data for systems design, and is beginning to add to the physics of magnetospheric ionospheric interactions.

#### REFERENCES

- Aarons, J. and R. S. Allen, J. Geophys. Res., **76**, 170 (1971).
- Aarons, J., H. E. Whitney and R. S. Allen, Proc. IEEE, **59**, 159 (1971).
- Aarons, J. and E. Martin, The Effects of the August 1972 Magnetic Storm on Ionospheric Scintillations, Submitted to Radio Science (1974).
- Albrecht, H. J., M. Piening and K. Rosenback, J. Atmos. Terr. Phys., **36**, 1527 (1974).
- Basu, Sunanda, J. Geophys. Res., **79**, 3155 (1974).
- Bramley, E. N., J. Atmos. Terr. Phys., **36**, 1503 (1974).
- Dyson, P. L. and J. D. Winningham, Scientific Report, University of Texas, Topside Ionospheric Spread F and Particle Precipitation in the Dayside Magnetospheric Clefts, AFCRL F19628-72-C-0230, July 1973.
- Evans, J. V., Technical Report 509, Lincoln Laboratory, MIT, 13 Nov 1973.
- Fremouw, E. J. and C. L. Rino, Radio Science, **8**, 213 (1973).
- Frihagen, J., J. Atmos. Terr. Phys., **33**, 21 (1971).
- Hawkins, G., Ionospheric Electron Content and Radio Scintillations During Magnetospherically Quiet Periods, AFCRL TR-74-0160, March 1974.
- Kelly, M. C. and F. S. Mozer, J. Geophys. Res., **77**, 4158 (1972).
- Kersley, L., D. B. Jenkins, and K. J. Edwards, Nature, **239**, 11, 1972.
- Kersley, L. and A. Van Eyken, The Mid-Latitude Trough and the Scintillation Boundary, Joint Satellite Studies Group, Report #5, Lannion, France, January (1974).
- Martin, E. and J. Aarons, F Layer Scintillations and the Aurora, Proceedings of NRL Ionospheric Effects Symposium of Washington, D. C., January (1975).
- McClure, J. P., Final Report for Contract NAS 5-23184, Goddard Space Flight Center, 1973.
- Nielson, E. and J. Aarons, J. Atmos. Terr. Phys., **36**, 159 (1974).
- Penndorf, R., J. Geophys. Res., **67**, 2279 (1962).
- Pike, C. P., J. Geophys. Res., **76**, 7745 (1971).
- Pike, C. P., J. Geophys. Res., **77**, 6911 (1972).
- Pope, J. H., Radio Science, **9**, 675 (1974).
- Sagalyn, R. C., M. Smiddy, M. Ahmed, J. Geophys. Res., **79**, 4252 (1974).
- Singleton, D. G., J. Geophys. Res., **73**, 295 (1968).
- Singleton, D. G., J. Atmos. Terr. Phys., **35**, 2253 (1973).
- Singleton, D. G., J. Atmos. Terr. Phys., **36**, 113 (1974).
- Tao, K., J. Radio Res. Lab., **12**, 317 (1965).

A SYNOPSIS OF RADIO AND PHOTOMETRIC EFFECTS OBSERVED  
WHEN THE IONOSPHERE IS MODIFIED BY A HIGH-POWER  
GROUND-BASED TRANSMITTER\*

William F. Utlaut  
Institute for Telecommunication Sciences  
Office of Telecommunications  
Boulder, Colorado 80302

ABSTRACT

High-power, HF, ground-based radio transmitters have been used to intentionally modify the electron temperature and density in the ionosphere since 1970. Transmitting facilities having power-aperture products of the order of  $10^4 \text{ MWm}^2$  have been used, and they provide a power density in the F region of a few tens of microwatts per square meter. Many unanticipated physical phenomena have been observed and new understanding has been gained in the field of plasma physics because of this ability to carry out experiments on the ionosphere. Perhaps more importantly, it has been shown that the modified region acts as a significant radio scatterer to radio frequencies at least as high as UHF. Thus, it has been possible to demonstrate a potential usefulness of ionospheric modification for telecommunication purposes. Voice, teletype, and facsimile transmissions have been sent, via the scattering region above the modifier, between ground terminals separated by several thousands of kilometers and using frequencies which would not otherwise have been useful for those paths. Surprisingly, it has also been shown that ionospheric modification and the creation of a significantly large scatterer in the ionosphere can be produced with relatively low power and simple antennas, a few hundred kilowatts and dipole antennas, for example.

This paper will provide a synoptic view of some of the salient effects observed during modification. The phenomena to be discussed include: 1) large-scale F-region irregularities, aligned with the geomagnetic field, that produce artificial spread F conditions; multiple, spatially distributed returns on high-resolution sky-maps; and enhanced scintillation of VHF and UHF satellite signals which have passed through the disturbed region, 2) modification of ambient airglow at 6300 Å, and 5577 Å, 3) small-scale, field-aligned F- and E-region irregularities that produce a large radar scattering cross section ( $\sim 10^5$  to  $10^8 \text{ m}^2$ ) which permits aspect-sensitive scattering of HF through UHF signals so that communications at those frequencies is possible over very long paths, 4) VHF and UHF signal scatter for which the received signal frequency is shifted upward and downward from that transmitted and which is believed to be caused by electron plasma waves and ion-acoustic waves generated by the HF modifier, and 5) D region modification.

---

\*Paper unavailable as of printing.

# THE ROLE OF THE MAGNETOSPHERE IN SATELLITE AND RADIO-STAR SCINTILLATION

Henry G. Booker

Department of Applied Physics and Information Science  
University of California, San Diego\*  
La Jolla, California 92037

## SUMMARY

A theory is developed to account for the scintillation phenomenon observed in equatorial regions when using communications satellites in the SHF band. The same theory is also used qualitatively to explain strong scintillations in the VHF band. Instead of confining irregularities to a narrow interval of height in the F region and assuming that they are strong, the alternative hypothesis is used that the irregularities are weak but extend from the F region upwards into the magnetosphere. It is suggested that the irregularities are field-aligned and extend at least up to an L shell of 1.3 and possibly up to 2 or more.

### 1. Introduction

It has long been established that weak scintillation of radio stars occurs in the F region of the ionosphere (Hewish, 1952). It has also been generally assumed that the same is true for strong scintillation in which the rms amplitude fluctuation is equal to the mean amplitude. In fact, however, the methods for assessing the height of occurrence of the irregularities are quite unsatisfactory for conditions of strong scintillation. In consequence, it is not established at this time that the imposition of strong scintillations in the VHF band is confined to a hundred or so kilometers in the vicinity of the level of maximum ionization-density in the F region.

In transferring one's attention from weak to strong scintillations in the VHF band, there are two main alternatives (see Figure 1): Either (1) One can confine attention to the same hundred or so kilometers of height near the level of maximum ionization-density in the F region

and increase the magnitude of the mean square fluctuation of ionization density by a power of ten or so. Or (2) One can continue to use roughly the same magnitude for the mean square fluctuation of ionization-density and increase the interval of height occupied by the irregularities by a power of ten or so.

Although the first of these alternatives is the one customarily chosen, there is no present observational reason for rejecting the second alternative. We therefore pursue the second alternative in this paper.

In recent years satellite scintillation phenomena have been observed in the SHF band (Craft and Westerlund 1972; Taur, 1973a; Crane 1974), and this phenomenon has also been interpreted on the basis of alternative 1 (Craft and Westerlund, 1972; Taur 1973a, 1973b; Crane, 1974; Wernik and Liu 1974; Rufenach, 1974).

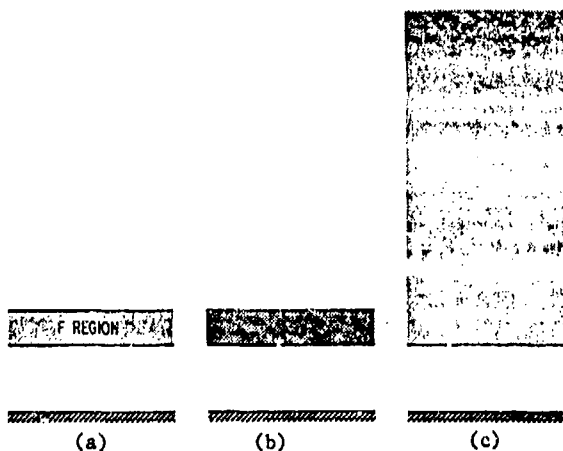


Figure 1. Illustrating (a) source of weak mid-latitude scintillations, and (b) and (c) two alternative hypotheses concerning the source of strong equatorial scintillations.

\*Much of this work was performed by the author as a consultant to the RAND Corporation, Santa Monica, California. The remainder was supported by National Aeronautics and Space Administration Grant NGR-05-009-076 and National Science Foundation Grants GA-20591 and 30628.

Characteristics of Field-Scintillations  
Observed at Ground Level (to 1974)

	Weak Mid-latitude Phenomenon (VHF only)	Strong Equatorial Phenomenon (Latitude < 25°, L < 1.3)
Statistical distribution	Roughly Gaussian	Gaussian at SHF Rayleigh at VHF
Shape	Roughly Isotropic	Extremely elongated N-S at VHF Undetermined at SHF
Outer Scale	Roughly 300 meters	50-500 meters E-W at VHF Undetermined at SHF
Spectrum	Power law ~ -4	Undetermined
Inner Scale	< 100 meters	Undetermined
Height of irregularities	F region	Undetermined
$\overline{(\Delta\phi)^2}$	$\propto \lambda^2$	Undetermined
$\overline{(\Delta A/A)^2}$	$\propto \lambda^4$ except for large zenith angles	$\propto \lambda^4$ at SHF $\propto \lambda^2$ at UHF ~ 1 at VHF

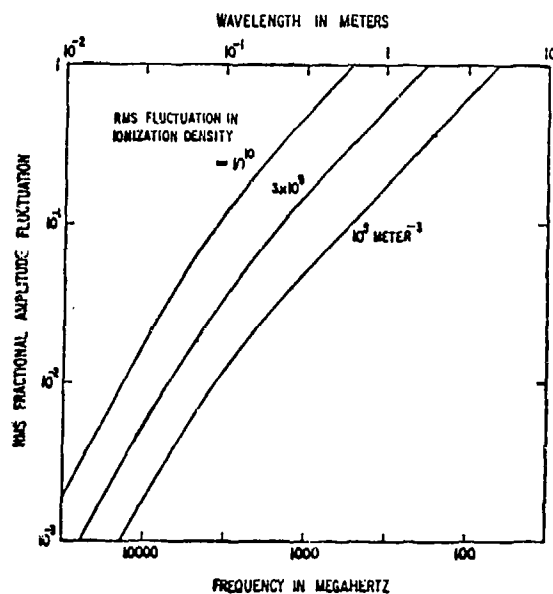


Figure 2. The frequency variation of rms fractional amplitude fluctuations at ground level for field-aligned irregularities of outer scale 300 meters existing in the plasmasphere to a height of 8000 kilometers. Vertical propagation at the equator is assumed.

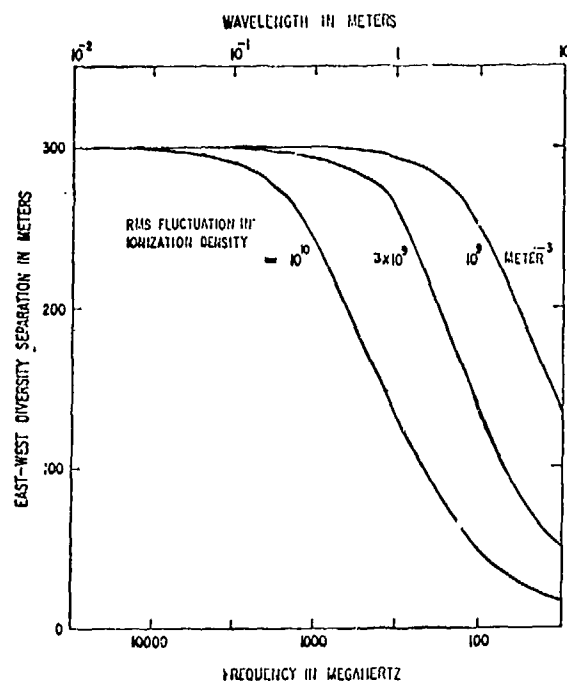


Figure 3. The frequency variation of an estimated east-west diversity separation for field-aligned irregularities of outer scale 300 meters existing in the plasmasphere to a height of 8000 kilometers. Vertical propagation at the equator is assumed.

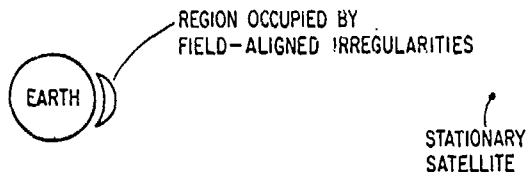


Figure 4. Illustrating the region that could be occupied by field-aligned irregularities involved in equatorial scintillation phenomena.

However, the Fresnel distance for irregularities that have a size of a few hundred meters is of the order of an earth's radius in the SHF band. Consequently, Fresnel filtering favors irregularities in the magnetosphere in comparison with irregularities in the ionosphere at SHF. It is alternative 2 therefore, rather than alternative 1, that provides irregularities at the height that are most effective in causing amplitude scintillation at ground level in the SHF band. Arbitrary concentration on alternative 1 therefore seems no longer to be justified. In consequence, we examine alternative 2 in this paper.

## 2. Experimental Facts

The experimental facts are summarized in the Table. It will be seen that, while the information concerning the weak mid-latitude VHF phenomenon is reasonably clear, this is by no means true for the strong equatorial phenomenon, especially at SHF. Such evidence as is available rests largely on the work of Koster (1963, 1966), of Craft and Westerlund (1972), and of Crane (1974), although numerous other workers have contributed.

## 3. Theory

The Table shows that the notion that strong equatorial scintillations might be due to a thick layer of relative weak irregularities as indicated in Figure 1(c) is not ruled out at this time by experimental observations of scintillation. The question therefore arises as to whether such an explanation is ruled out for theoretical reasons. This has been investigated by Booker (1975).

Booker considers a situation in which field aligned irregularities occupy an extensive range of height  $h$ . The transverse scale  $T$  of the irregularities, and the mean square fluctuation of ionization density  $(\Delta N)^2$  are assumed to be functions of height. The path of propagation from the satellite to the ground is supposed to make an angle  $\chi$  with the vertical and an angle  $\psi$  with the earth's magnetic field. At wavelength  $\lambda$  he calculates, on the basis of the Born approximation, the mean square fluctuation of phase and the mean square fractional fluctuation of amplitude at ground level as

tuation of phase and the mean square fractional fluctuation of amplitude at ground level as

$$\overline{(\Delta\phi)^2} = 4 r_e^2 \lambda^2 \int_0^\infty \frac{1 + \frac{1}{2} \left( \frac{h \sec \chi}{Z} \right)^2}{1 + \left( \frac{h \sec \chi}{Z} \right)^2} (\Delta N)^2 T \cos \psi \sec \chi \, dh \quad (1)$$

$$\overline{\left( \frac{\Delta A}{A} \right)^2} = 2 r_e^2 \lambda^2 \int_0^\infty \frac{\left( \frac{h \sec \chi}{Z} \right)^2}{1 + \left( \frac{h \sec \chi}{Z} \right)^2} (\Delta N)^2 T \cos \psi \sec \chi \, dh \quad (2)$$

where  $r_e$  is the classical radius of the electron ( $2.82 \times 10^{-15}$  meters) and  $Z$  is the Fresnel zone distance given by

$$Z = (8/3)^{1/2} \pi T^2 / \lambda \quad (3)$$

If  $(\Delta A/A)^2$  calculates to a value greater than unity, it should be replaced by unity. If  $(\Delta\phi)^2$  calculates to a value greater than unity, an extrapolation of the theory is involved.

For the case  $\chi=0$ ,  $\psi=\pi$ , Booker assumed that  $T$  is independent of height, and that  $(\Delta N)^2$  is constant from an ionospheric height up to a magnetospheric height that he determines by comparison with the experimental facts in the Table. The theoretical variation of  $(\Delta A/A)^2$  shows a change from a  $\lambda^4$  behavior at short wavelengths to a  $\lambda^2$  behavior at longer wavelengths, and Booker assumed, on the basis of the last entry in the third column of the Table, that this transitional wavelength is about 1.0 centimeters. Combining this with a value of the order of a few hundred meters for  $T$ , also derived from the Table, he deduces that weak field aligned irregularities would need to extend upwards from the F region into magnetosphere, perhaps to an L shell of the order of 1.3. With the particular parameters that he used, he arrived at the variation of  $(\Delta A/A)^2$  with  $\lambda$  shown in Figure 2. He also estimated by a rough argument that the variation of the east-west diversity separation with  $\lambda$  would be as shown in Figure 3.

It follows that there is no present difficulty in interpreting the available observations of equatorial scintillations in terms of a thick layer of weak irregularities as indicated in Figure 1(c).

## 4. Discussion

It is concluded that satellite experiments should be conducted and interpreted on the assumption that strong equatorial scintillations are due to field-aligned irregularities that may occupy a region that is not confined narrowly to the region of maximum ionization-

density in the F region, and that may extend upwards from the F region in the manner suggested by Figure 4. There is a need for more comprehensive scintillation observations in equatorial regions at VHF, UHF and SHF of the simple type carried out by Koster (1966), combined with observations of phase fluctuations.

#### REFERENCES

- Booker, H.G., 1975, Great Britain, Journal of Atmospheric and Terrestrial Physics (in press).
- Craft, H.D. and Westerlund, L.H., 1972, United States of America, AIAA 10th Aerospace Sciences Meeting, Paper 179.
- Crane, R.K., 1974, United States of America, AIAA 12th Aerospace Sciences Meeting, Paper 52.
- Gold, T., 1959, United States of America, Journal of Geophysical Research 64, 1219.
- Hewish, A., 1952, Great Britain, Proceedings of the Royal Society 214, 494.
- Koster, J.R., 1963, United States of America, Journal of Geophysical Research 68, 2579.
- Koster, J.R., 1966, France, Annales de Géophysique 22, 435.
- Taur, R.R., 1973a, United States of America, Comsat Technical Review 3, 145.
- Taur, R.R., 1973b, United States of America, Comsat Laboratories Technical Memorandum CL-29-73.
- Wernik, A.W and Liu, C.H., 1974, Great Britain, Journal of Atmospheric and Terrestrial Physics 36, 871.



THE DEVELOPMENT OF A HIGHLY-SUCCESSFUL WORLDWIDE EMPIRICAL IONOSPHERIC  
MODEL AND ITS USE IN CERTAIN ASPECTS OF SPACE COMMUNICATIONS AND WORLD-  
WIDE TOTAL ELECTRON CONTENT INVESTIGATIONS

Rodney B. Bent, Sigrid K. Llewellyn, George Nesterczuk  
Atlantic Science Corporation  
Indianapolis, Indiana

and  
Paul E. Schmid  
NASA/Goddard Space Flight Center  
Greenbelt, Maryland

Abstract

A global empirical ionospheric model has been developed that gives the electron density profile up to 3000 km as a function of latitude, longitude, time of day, season and solar flux. The model was derived from over 60,000 topside ionospheric soundings, 6000 satellite electron density profile measurements and over 400,000 bottomside soundings from solar minimum to solar maximum and is capable of prediction accuracies from 75-90%. A basic prediction routine is incorporated in the model as are routines to update the model as a function of daily solar flux as well as with actual measurements from distances up to 2000 km from the required prediction point.

The model has been used for many situations and results are shown giving ionospheric effects for Very Long Baseline Interferometry, satellite to satellite communications, satellite ranging and range rate, and satellite orbit determination. The variability of the ionosphere is discussed showing the statistical characteristics of total electron content at a low latitude site at solar maximum. Comparisons of the model are made with the Chapman profile and the capabilities that exist in the model to computer plot many ionospheric contours are described. A very simple worldwide model is also described which only requires a minimum of about 400 bits of storage.

IONOSPHERIC MODEL DEVELOPMENT

For several years scientists have investigated many different approaches to modeling the ionospheric profile on a theoretical basis. The names and types of these methods are well known and will not be discussed here, but it is

obvious after all the years that a good theoretical ionospheric profile still does not exist.

The object of our past investigations was to come up with an ionospheric profile that could give much improved results for refraction corrections in satellite communications to ground or to another satellite than had been obtained with the Chapman or many other theoretical profiles. It would have been pointless for us to sit down and investigate another theoretical approach when so many more competent scientists are working on this problem. For this reason we decided that in this present time of computers, an empirical model taken from a vast data base may provide us with the profile we were looking for.

It was our intention to acquire ionospheric data of any kind that helped us build up a data base covering minimum to maximum of solar cycle and providing information up to 3000 km. The lower layers of the ionosphere were neglected in terms of their irregularities although their electron content was added into the larger F layer; this was done to simplify the approach and as the prime objective was to obtain refraction corrections through the ionosphere, or at least to a point above 150 km, such an elimination would not be very detrimental.

Data from bottomside ionospheric sounders was obtained over the year 1962 through 1969 covering 14 stations approximately along the American longitudes having geographic latitudes 76 degrees to -12 degrees or magnetic latitudes 85 degrees to 0 degrees.

This data was in the form of hourly profiles of the ionosphere up to the  $f_o F2$  peak. Topside soundings were acquired for the year 1962 to 1968 covering the magnetic latitude range 85 degrees to -75 degrees and providing electron density profiles from about 3000 km down to a height just above maximum electron density. As only a small portion of this topside data was available near the solar maximum, electron density probe data was obtained from the Ariel 3 satellite over the period May 1967 to April 1968 from 70 degrees north to 70 degrees south geographic latitude and linked in real time to  $f_o F2$  values obtained from 13 stations on the ground.

### Ionospheric Profile

In order to analyze the vast amount of data that was obtained a number of assumptions had to be made. In the first case the topside sounding data did not geographically cover the entire globe and the bottomside data was only available for land masses and not over the oceans; however, as a local time effect is far more significant than a longitude effect, the data was analyzed as a function of latitude and local time. Geographic longitude was, however, taken into account for the determination of maximum electron density by using the ITS coefficients for  $f_o F2$  which are a function of latitude, longitude, time and solar activity. Secondly a theoretical profile was determined to which the data would fit. This profile is shown in Figure 1 and is the result of earlier work by Kazantsev (1956) and unpublished work of Bent (1967) while at the Radio and Space Research Station in England and requires the knowledge of the parameters  $k_1, k_2, k_3, k_4, k_5, y_1, y_2, f_o F2$ , and  $h_m$ . The equation of the upper topside is exponential, namely,

$$N = N_o e^{-kz},$$

the lower ionosphere is a bi-parabola,

$$N = N_m \left( 1 - \frac{b_1^2}{y_1^2} \right)^2,$$

and the top and bottomside are fit together with a parabola,

$$N = N_m \left( 1 - \frac{b_1^2}{y_1^2} \right),$$

where,

$N_m$  is the maximum value of electron density.

$y_1$  &  $y_2$  are the half-thicknesses of the lower and upper parabolic layers.

$k$  is the decay constant for an exponential profile.

The upper parabola extends from the

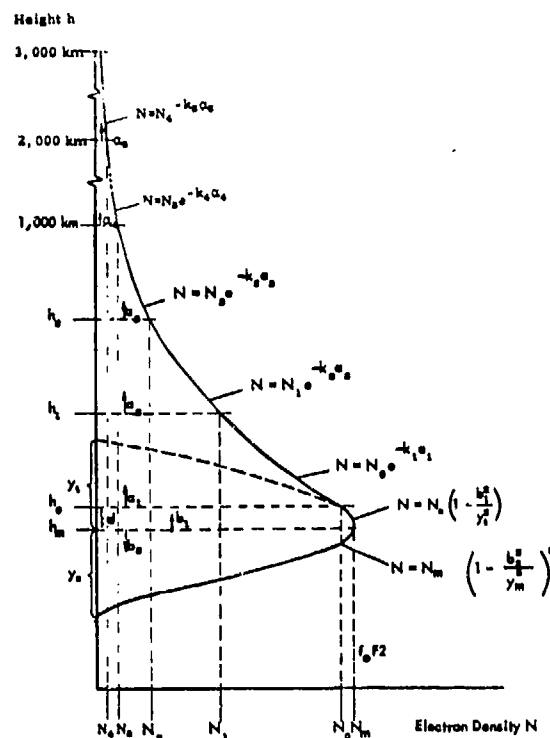


Fig. 1. The Exponential Parabolic & Bi-parabolic Profile

height of the maximum electron density up to the point where the slope of the parabola matches the slope of the exponential layer. The data investigated included over 60,000 topside soundings, 6,000 satellite electron density and related  $f_o F2$  measurements, and over 400,000 bottomside soundings.

### Topside Ionosphere

The initial approach was to take the topside soundings and break them down into zones 5 degrees of latitude by 40 minutes of local time eliminating data in the same zones that have similar times and profiles, and therefore are duplicated. This resulted in over 1,200 different areas in the northern and southern hemisphere with a reasonably constant density of data in each area. By these means it was possible to investigate the decay constant  $k$  in the exponential topside profile as a function of local time, latitude, solar flux, sunspot number and season. One of the major concerns was whether the decay constant  $k$  would be uniform for each sounding over the range 1,000km to the minimum height, and investigations showed that such an exponential profile does not exist. The layer was, therefore, divided into three equal height sections from 1,000km to the minimum recorded height, and two more

equal height sections from 1000 to 3000km; the exponent  $k$  was computed for the center point in each section. Figure 1 shows such a division where the values under investigation are the decay constants  $k_1, k_2, k_3, k_4, k_5$ . In most cases the topside soundings do not reach the height of maximum electron density and therefore the gradient at this lower point was mathematically equated to the point where the gradient of the 'nose' parabola was the same. Extensive analysis of the acquired data showed these gradients to be similar, on average, at a height  $y_m/4$  above the maximum electron density. At this point the value of the plasma frequency, which defines the lowest point of the topside sounding is approximately  $0.93 f_o F2$ .

Figure 2 shows the relationship between the five (5) decay constants  $k$  and magnetic latitude for all local times and season for the lower solar activity periods. Similar, but non-linear graphs exist for the solar flux values

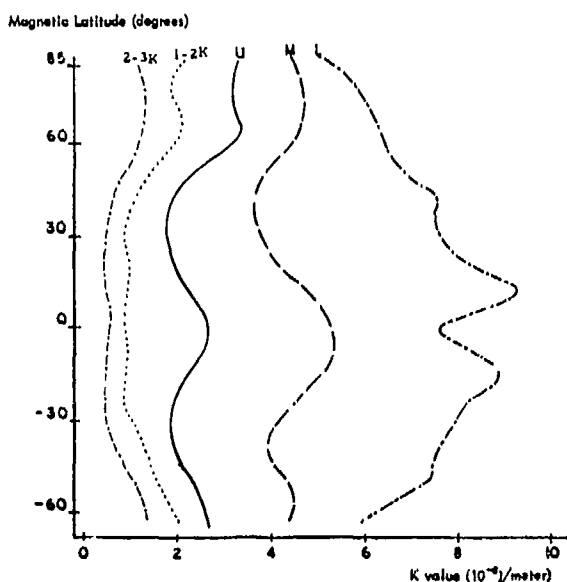


Fig. 2. The mean fluctuation of the decay constant  $k$  with magnetic latitude for the upper (U), middle (M) and lower (L) portions of the topside ionosphere below 1000 km and for the layers from 1000 to 2000 and 2000 to 3000 km.

between 120 and 250. The equatorial anomaly and a 40 degree trough show in the lower topside layer. The 65 degree trough is much more evident when the same analysis is done for certain local times.

It was found that correlations in  $k$  for specific  $f_o F2$  did not bear any further local

time correlation, but bore a significant variation with solar activity and magnetic latitude. However, the correlation with solar flux was considerably better than that with sunspot number, even allowing for the delay in the effects reaching the ionosphere, so all further correlations were computed with the Ottawa 10.7 cm solar flux. All these correlations were then plotted in graphical form to enable final interpolation.

Unfortunately the Alouette and Isis topside data did not cover the period at the peak of the solar cycle, but the Director of the U. K. Radio and Space Research Station made available electron density data from the Ariel 3 satellite to cover this period. This data had already been reduced thoroughly and the satellite electron density at about 550 km was provided with the sub-satellite  $f_o F2$  value obtained from ionosonde stations around the world. If the satellite was not directly over an ionosonde at the time of the observation, the  $f_o F2$  values from two or three transmitters in the general area had been interpolated in time and position to give the sub-satellite value. These interpolations had been carried out taking care to modify the values for ionospheric gradients. Data that was in doubt was eliminated. While these values did not give the five exponential decay constants at each point, it was found that for similar conditions of solar flux and position, the Ariel 3 data fit very closely to the profiles deduced from Alouette and Isis. Typical results from this overall analysis are shown in the graphs of Figure 3. The original data curves were less regular, but since the variations were mainly caused by the relatively low data density in each group after division of the large data base, the data was smoothed by the fitting of straight lines. In order to interpret these graphs and obtain a profile, we need the value of  $f_o F2$  and the magnetic latitude position. These values will indicate which graph to use in order to relate the 10.7 cm flux to the decay constants  $k$  for the topside ionosphere. Figure 3, therefore, shows the basis of obtaining the 5 independent slopes of the topside ionosphere as a function of  $f_o F2$ , latitude, and solar flux.

A correlation to investigate the seasonal effects on  $k$  was carried out with some 15,000 totally different Alouette soundings. Fluctuations in the  $k$  values of  $\pm 15\%$  were noted from the average spring and autumn values. The seasonal variation was monitored by observing the change in the daily maximum solar zenith angle from the equinoctial mid-day value, and corresponding seasonal update equations

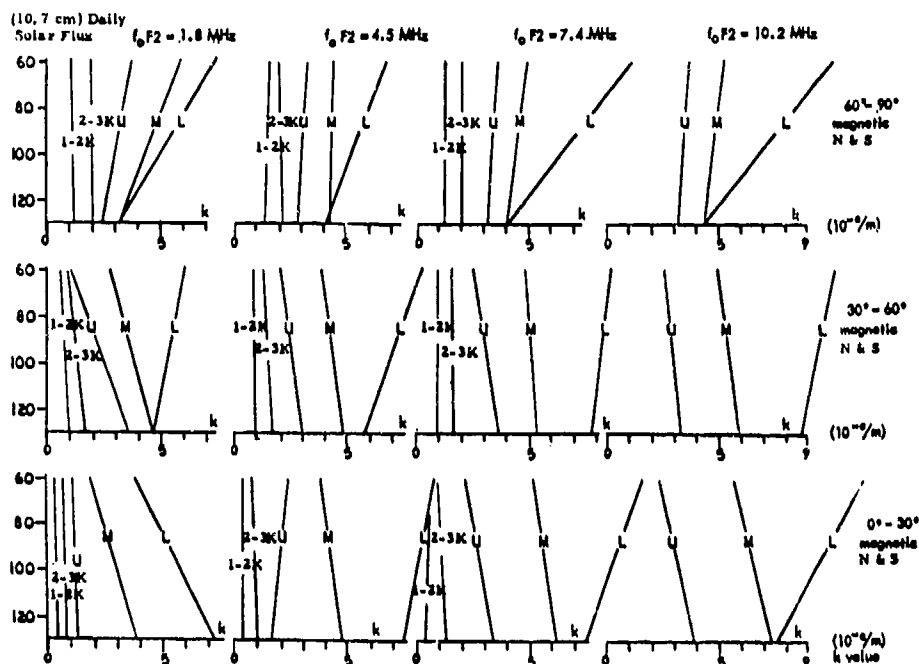


Fig 3. Variation of  $k$  for the upper (U), middle (M) and lower (L) topside profile below 1000 km and the layers from 1000 to 2000 and 2000 to 3000 km due to solar flux,  $f_o F2$  and magnetic latitude.

were derived and included in the model.

maximum electron density.

Investigation of the upper part of the 'nose' of the N-h profile is difficult because topside sounding information rarely gives any values in this region. Evidence from a number of scientists also implies that the topside profiles have about a +4% height error in the effective distance from the sounding satellite which places the topside profiles too low near the peak. This evidence is based on comparisons with two-frequency data, backscatter results, Faraday rotation and overlap tests, etc. Preliminary results in this empirical model showed that a parabola in this region gave the better comparison with integrated total electron content when compared with two-frequency and Faraday rotation data. A simple parabola having a half-thickness  $y_1$  was fitted between the bi-parabola and the exponential layer. The value of  $y_1$  was set equal to the half-thickness of the bi-parabola  $y_2$  for  $f_o F2$  values below 10.5 MHz, and  $y_1$  increases with  $f_o F2$  values rising above 10.5 MHz.

The final step in predicting the shape of the ionosphere is arranging for the gradient in the upper parabolic layer to be the same as the gradient in the lowest part of the topside exponential layer. This is the case at a distance  $d = 1/k[(1+y_1^2 k^2)^{1/2} - 1]$  above the height of the

#### Bottomside Ionosphere

Modeling the bottomside ionospheric profile was a somewhat easier task because for each profile the value of  $f_o F2$  was known and the electron density versus height profile from  $h_{min}$  to  $h_{max}$  was also known. Once more the geographic effect of longitude was eliminated and replaced with the more simple local time correlation. From Figure 1 we see that the equation of the lower layer is a parabola squared or a bi-parabola. This was found in general to fit the real profile somewhat better than a simple parabola. The unknown in this equation is the half-thickness of the layer  $y_2$  and in the reduction of the data the  $y_2$  value was treated in a similar way to a topside  $k$  value.

The irregularities in the ionosonde data due to the lower layers of the ionosphere were smoothed out because the prime objective of the work was to simplify the model, but keep the total content as accurate as possible. The sounding data was therefore integrated up to the peak electron density ( $N_m$ ) and made the same as the value of  $N_m$  deduced from integrating the bi-parabolic equation. In each instance the value of  $y_2$  was computed ready for further correlations.

Investigations, similar to those carried out for the topside decay constants, correlated  $y_m$  with solar flux  $f_oF2$ , local time and season. Surprisingly, no direct correlation was found between  $y_m$  and solar flux, but a definite correlation existed in local time and also in the solar zenith angle at local noon which represents the season.

Figure 4 indicates how  $y_m$  can be determined from local time and  $f_oF2$ . Seasonal update equations were also derived as a function of local time and solar zenith angle. In the cases where  $f_oF2$  was larger than 10 MHz the local time curve fluctuated very little from the 10 MHz curve. All of the curves displayed have not been hand smoothed; due to the large data base the average of all values taken every hour fit precisely on the lines shown.

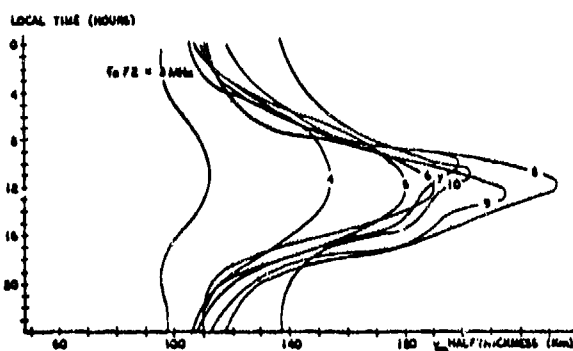


Fig. 4. Variation of  $y_m$  as a Function of  $f_oF2$  and Local Time.

A number of actual profiles from various stations at different local times were compared with the computed profile and excellent agreement found. A further 12,000 soundings from 14 stations were analyzed and the computed value of  $y_m$  compared to the actual measured value. These results are shown in Figure 5 along with the RMS errors. The two tests indicate that the bi-parabolic profile is, on average, in close agreement to the real profile.

The remaining unknowns which are needed to compute the profile are  $f_oF2$  and the height of that value; by far the most important of these being the value of  $f_oF2$ .

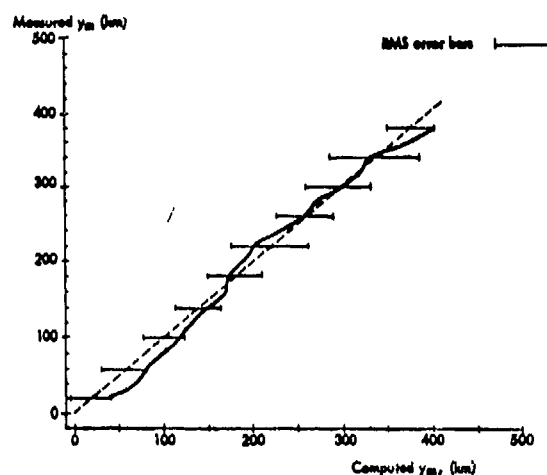


Fig. 5. The comparison of measured and predicted  $y_m$  for 12,000 profiles showing RMS error bars.

#### Predicting $f_oF2$

Severe horizontal gradients in  $f_oF2$  exist within the ionosphere as can be seen by examining Figure 6. In fact even if the value of  $f_oF2$  is known directly above a station, it can change considerably over the whole 'visible' ionosphere from that site. Figure 6 is a predicted status of  $f_oF2$  over the world at 6.0 a.m. during August, 1968, and two types of severe gradients are immediately noticeable, one due to sunrise causes rapid changes in  $f_oF2$  in an east to west direction and the other situated around the equatorial anomaly occurs primarily during the afternoon and early evening and causes severe gradients in the north to south direction. Two hypothetical stations, A and B, are marked on Figure 6 along with the ionosphere 'visible' from those sites. In case A the value of  $f_oF2$  changes from 11.5 MHz directly overhead to 5 MHz on the southern horizon. This change must be squared when converting to electron content hence a difference of a factor of over 5 in the vertical content arises before correcting for elevation angle effects. Similar gradients exist over half the earth's surface at some time of the day and it is therefore imperative to model these gradients in any ionospheric model.

For many years NOAA (formerly CRPL and ITSA) have been engaged in the development of numerical methods and computer programs for mapping and predicting characteristics of the ionosphere used in telecommunications. The most advanced method for producing an  $f_oF2$  model undoubtedly comes from their work. Jones, Graham & Leftin (1969) describe their techniques on how a monthly

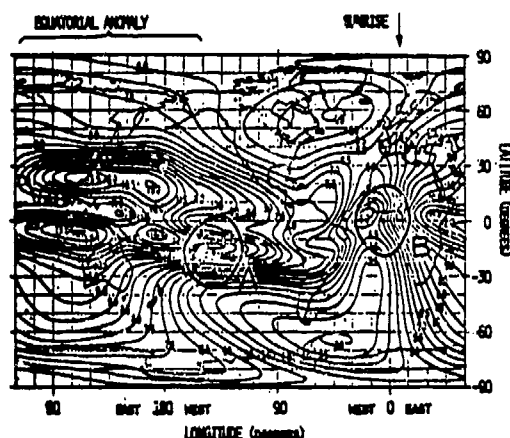


Fig. 6. The Predicted Global Status of a Monthly Median  $f_oF2$  at 6.0 a.m. UT August 1968 Showing Areas of Visibility for Two Hypothetical Ground Stations.

median of the F2 layer critical frequency ( $f_oF2$ ) was developed from an extremely large worldwide data base. In fact the gradient map shown in Figure 6 is a result of this work. We have already shown that it is important to include the horizontal gradients of  $f_oF2$  in any analysis and the work by Jones et al is undoubtedly the only satisfactory approach to this problem.

The document by Jones et al describing this work includes a Fortran program which, with monthly coefficients obtainable from NOAA, enables the monthly median value of  $f_oF2$  to be computed above any point in the world at any time. This program was primarily written to accept monthly coefficients using an average sunspot number, but more recent work by Jones & Obitts (1970) has described a more generalized set of coefficients which provides annual continuity and uses more extensive analysis.

For the ionospheric profile under discussion, it was decided to use the generalized  $f_oF2$  coefficients from NOAA incorporating solar flux thereby eliminating any need to continually obtain monthly data from them. The program was made self-contained and enabled a monthly median  $f_oF2$  to be produced above any surface position for any time of day or season and any twelve month running average of solar flux.

The question now arises as to how good these monthly median values are and how much error is introduced by day to day fluctuations. Many daily soundings were analyzed and the monthly median value computed; these were compared with the monthly median predicted

values and the actual day to day fluctuations. The monthly median predicted values were indeed very close to the actual measured value, but the day to day fluctuations can be as large as  $\pm 75\%$ . A technique therefore had to be derived to bring the computed monthly median value closer to the actual value.

It would be pointless to use the daily value of solar flux in the generalized coefficient set which had been built up using a twelve month running average, but it was thought possible that there may be a relation between the difference in  $f_oF2$  from monthly median to daily value and the difference in the 12-month running average of solar flux to the daily value.

#### Updating $f_oF2$

Approximately 24,000 real values of  $f_oF2$  from 13 stations widely spread in latitude, longitude, and solar cycle were compared with the predicted values using the NOAA solar flux method. A very surprising result emerged and can be explained by referring to Figure 7.

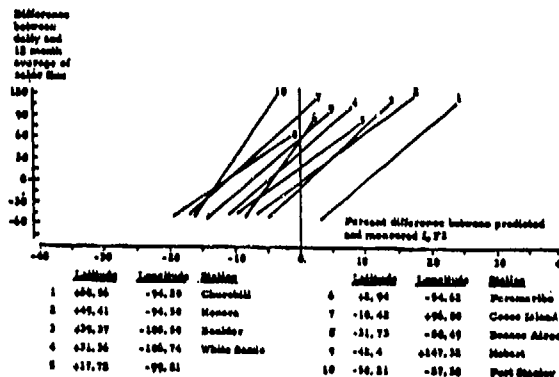


Fig. 7. Variability of Predicted  $f_oF2$  with Respect to Latitude and Daily Solar Flux.

Eliminating the data from stations close to the magnetic poles which did not quite follow the trend of the other stations a comparison between the difference in daily and 12-month flux value and the percentage difference of computer and measured  $f_oF2$  showed all stations having a very similar bias. The fact that the lines did not pass through the zero points in the graph undoubtedly indicates an erroneous bias in the NOAA predictions, but results help one to update substantially the monthly median  $f_oF2$  value on a daily basis. By these means it is possible to come somewhat nearer the actual

daily value of  $f_o F2$ .

Further accuracy in  $f_o F2$  can be derived by updating with data from stations within the general area. To determine the size of the area for which ionospheric values show similar deviations from normal, many comparisons of 3 and more stations were performed. Since similar variations in  $f_o F2$  were found consistently for distances of 2000 km or less, ionospheric data from within 2000 km of the evaluation site is, in general, considered of use for the update. When applying the same percent change to the ionosphere at the evaluation site as is found at the update station, the results achieved with data from nearby stations are excellent. However, where large distances are involved and when the ionospheric disturbances are not consistent over such distances, it has been observed that the basic predictions can be more accurate than the updated values. For this reason a distance weight has been introduced in conjunction with the update. Several possibilities have been considered as weights, both linear and exponential functions of the distance. Figure 8 shows the various weights along with the test results obtained from them. The best weighing function minimizing the residuals of

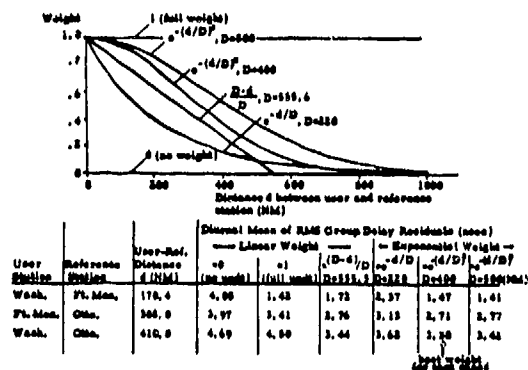


Fig. 8. Methods of Distance Weighting in the Update Procedure of the Ionospheric Model.

measured minus updated data is an exponential bell-shaped curve that gives almost full effect to the update from stations nearby and little effect to update over large distances. Figure 9 gives a typical example of monthly mean residuals achieved with this weighted update process.

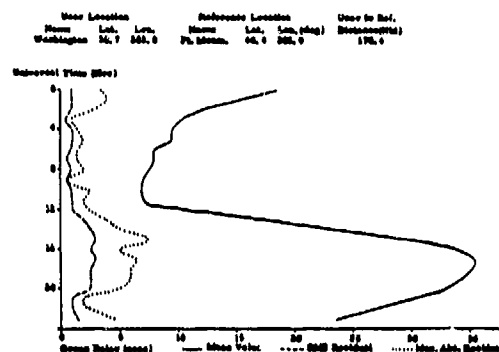


Fig. 9. Statistics Over Days of Month 3 of Year 58 Using  $e^{-(d/D)}$  Weighting in Update Procedure, D=400 NM.

### Predicting the Height of the Maximum Layer

In order to predict the real height of  $f_o F2$  the M(3000)F2 predictions from NOAA were used. To explain the terminology:

$$M(3000)F2 = M \text{ FACTOR} = MUF(3000)F2 / f_o F2,$$

where MUF(3000)F2 is the maximum useable frequency to propagate by reflection from the F2 layer a distance of 3,000km. The M(3000)F2 predictions can be calculated on a monthly basis from a generalized set issued by NOAA and provide the monthly median value as a function of sunspot number.

Knowledge of this factor along with the  $f_o F2$  value enables the height of the layer to be calculated using the equations of Appleton & Beynon (1940/47). If M is the M(3000)F2 factor and one assumes that  $y_p$  divided by the height of the bottom edge of the lower layer is greater than 0.4, then it is possible to derive the following polynomial,

$$h_p = 1346.92 - 526.40M + 59.825M^2,$$

where  $h_p$  is the required height.

### Model Accuracy

As a means of testing the accuracy of the model, an intense comparison with Faraday rotation data has been performed as well as tests with two frequency data, actual ionospheric profiles, and use in orbit determination programs.

Remarkable improvements have been noticed in precise orbit determination systems and the model has reduced the number of iterations needed for the program to converge as well as the size of the residuals by up to a factor of four. Excellent results have been noted with orbit programs using elevation angle, range and range rate systems.

The most extensive tests were carried out by comparing Faraday rotation data for seven stations from Hawaii to Puerto Rico to Alaska looking at the ATS1, ATS3, and SYNCOM3 satellites. In all, over 100 station months of continuous data were used during the years 1965 and 1967-1969 with data taken every hour. The integrated model data was compared with these actual results; update situations were also investigated. The results are shown in Figure 10 where the percentage of the ionosphere removed with the model is shown. In general, between 75 and 90% of the ionospheric effects are removed and these circumstances are for solar maximum conditions. The percentage accuracy is quoted as this remained reasonably constant throughout the diurnal and seasonal changes of the ionosphere.

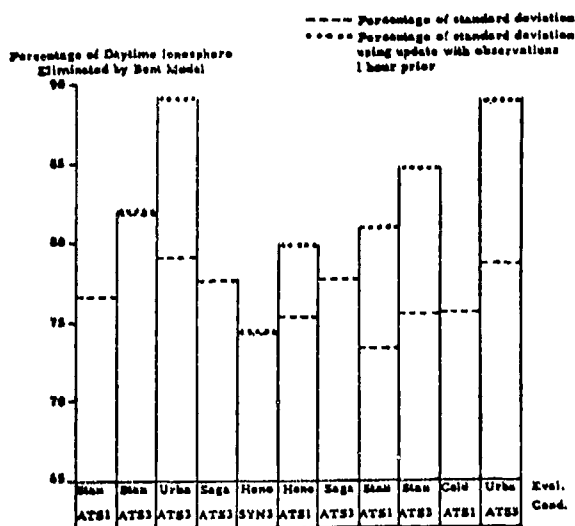


Fig. 10. Percentage of Daytime Ionosphere Eliminated for Different Evaluation Conditions.

## IONOSPHERIC INVESTIGATIONS

### Ionospheric Group Delay Measurements at Solar Maximum

The size of the ionospheric group delay errors at 1600 MHz that remain after application of several ionospheric models has been the subject of many reports. On average it is assumed that over the continental United States a residual RMS group delay (measured-predicted) for high solar activity varies between 2.6 and 3.3 nano-seconds using a good ionospheric model. For a point nearer the magnetic equator, such as Honolulu, this value can be as high as 6.8 to 9.0 nano-seconds. These figures, however, are extremely

deceptive.

Let us look initially at the ionospheric characteristics above Hawaii during 1968 when the solar activity was at its height during the last solar cycle. During the month of January and November large values of total ionospheric content existed. Figure 11 shows the minimum, mean, and maximum values recorded during January where the total electron content has been converted to group delay at 1600 MHz. It is immediately obvious that even with the best ionospheric model, without daily update, the predicted value can be 27 nano-seconds in error. It is highly unlikely that an ionospheric model will produce the same value as the mean and so the likely errors may be well in excess of 30 nano-seconds at vertical incidence.

### HONOLULU LOOKING AT ATS-1 31 DAYS OF JANUARY 1968

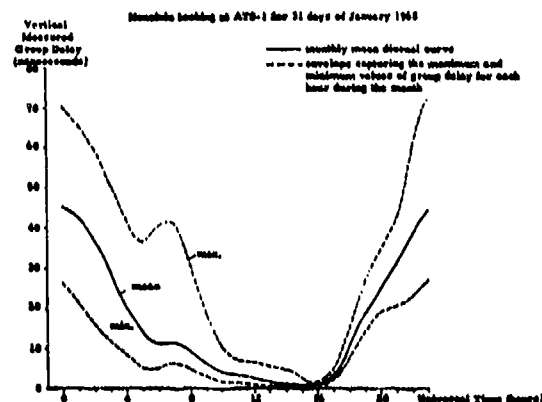


Fig. 11. Maximum, Minimum and Monthly Mean Values of Vertical Group Delay for Honolulu, January 1968.

More detailed data is shown in Figure 12 where the actual erratic values of vertical group delay are displayed on a day by day basis at local afternoon for November. Also shown are the corresponding updated values using the Bent Ionospheric Model. These updates use the critical frequency one hour old from Maui and are significantly correlated to the actual values.

This figure indicates that vertical group delay times of 70 nano-seconds or more were measured. Converting this value to the delay at 5 degrees elevation we must expect line of site delays of 210 nano-seconds which two days later may drop by 100 nano-seconds. One may ask the question, what would the maximum value be during a solar cycle where the activity was much higher as was the case during the previous cycle? With ionospheric 'no-update'



# IONOSPHERIC DELAY AT 1600 MHZ HONOLULU ATS-1, NOV 1968 0 HOURS UT

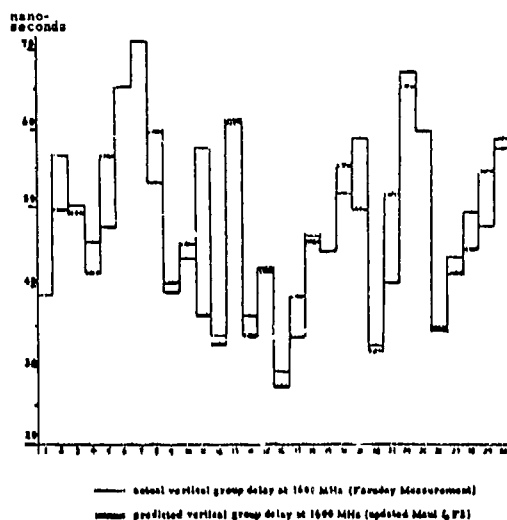


Fig. 12. Measured and Predicted Updated Vertical Group Delay at Honolulu, November 1968.

predictions, it is highly possible for a residual error (measured-predicted) of about 40 nano-seconds at vertical incidence to exist. At 5 degrees elevation, therefore, the residual error after application of a mean ionospheric model will be about 120 nano-seconds. With update from a nearby station, this residual can be reduced from about 40 nano-seconds to about 2 to 5 nano-seconds.

The continental United States has a much more stable ionosphere as it is some distance from the magnetic equator. In this region the maximum monthly RMS residual after applying a good ionospheric model will be about 6-7 nano-seconds during local afternoon. The actual daily residual, however, may rise to 4 times this value.

## Satellite to Satellite Communications

When two earth orbiting satellites are communicating with one another, certain configurations may induce serious ionospheric effects on their common radio link. The Bent Ionospheric Model is ideally suited for investigating such ionospheric problems where the electron density is required at certain heights and positions along the path. The integration to total electron content can be obtained from these values by numerically integrating with the Gaussian quadrature technique.

As an illustration of the different ionospheric effects, consider the situation where a

tracking data relay satellite (TDRS) is receiving data transmitted from a satellite moving from position A to position B shown in Figure 13. Within the space of a few minutes the line

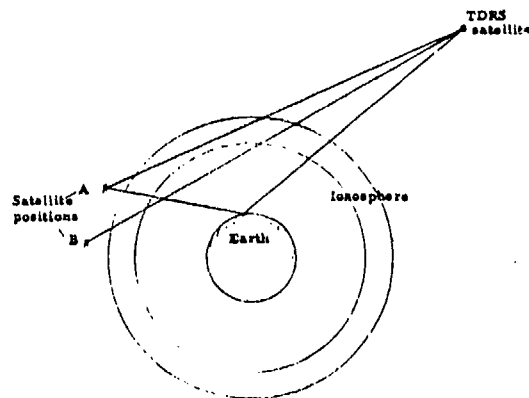


Fig. 13. Geometry of the Ionospheric Conditions Encountered in the Sat. to Sat. Tracking Problem.

of sight between the satellites has passed through a very thin ionosphere; then, at position A, it is transmitting along the line of maximum density, and when at B, it is transmitting through two totally different ionospheres.

Investigations of these ionospheric effects were carried out using a number of satellite orbits, with inclinations varying from equatorial to polar and with low satellite altitudes ranging from 200 to 1000 km. Specific cases were chosen to show the extreme situations of ionospheres with rapidly changing characteristics such as the equatorial anomaly and sunrise effect.

A slight shift in the position of the low satellite may make the difference in whether the ray between the two satellites rides along the height of the maximum electron density ( $h_m$ ) for long distances, or whether the ray hits the maximum at two separated points, or whether the ray passes through the ionosphere just above  $h_m$ . These slight shifts are likely to make enormous differences in total electron content, which emphasizes the need for an accurate ionospheric profile of electron density versus height including a good estimate of  $h_m$ . Figure 14 illustrates the results from such a situation. The high satellite is in stationary orbit over the equator, and approximately 111 degrees east of it is the low satellite in a polar orbit of 1000 km height. The ray path from the high satellite follows the other satellite as it is moving through the equatorial anomaly at an azimuth of about 130 degrees toward the

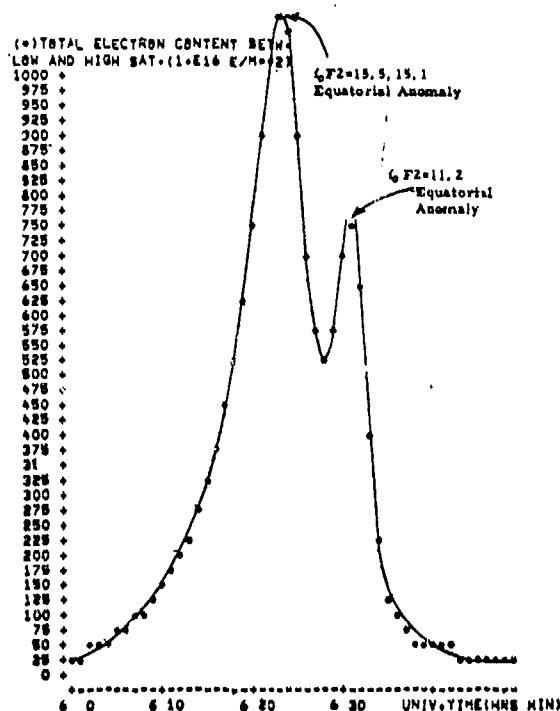


Fig. 14. Variation of the 'Satellite to Satellite' Electron Content in March 1970.

equator at 90 degree azimuth and onto the northern equatorial anomaly at an azimuth of about 50 degrees.

The two peaks in the electron content curve of Figure 14 correspond to the portions of the orbit where the low satellite is looking through the equatorial anomaly on both sides of the magnetic equator. In this region there are long periods when the ray from the low to the high satellite penetrates two ionospheres giving a high total electron content. The rapid rise of total electron content at about 6:18 UT occurs when the ray path approaches  $h_p$  and passes just below it as in the satellite A position in Figure 13. The two peaks of  $f_oF2$  are 15.5 and 15.1 MHz; these values are similar because the  $f_oF2$  gradients are almost parallel to the line of sight at this time and position. One reason for the large ionospheric effects is that a number of the ray paths in this example travel within 10 km of  $h_p$  for over 400 km because the height of  $h_p$  is changing rapidly in this region.

It has been shown that the line of sight electron density could often reach values much higher than  $10^{20} \text{ e/m}^2$  column. Under these or similar conditions, the attenuation of the signal reaching the tracking satellite could be larger than the signal it receives from a ground

reflected path as shown in Figure 13. This situation could mean that the tracking data relay satellite may lock onto the stronger ground reflected wave causing temporary problems in the amplitude and phase of the received signal.

#### Theoretical and Experimental Range Rate Problems

A problem can occur in computing range rate corrections through the ionosphere to a satellite. Many Doppler satellite tracking systems integrate cycle counts over a few seconds of time. The ionospheric corrections for such a technique are best obtained by range differencing the ionospheric corrections and dividing by the integration period; hence time, elevation and azimuth changes are incorporated. A typical ionospheric range rate correction can be significantly changed by the the sixth digit in the ionospheric range correction; precautions have therefore to be taken to ensure that no irregularities occur in computing the two adjacent range corrections. Furthermore, the ionospheric height at the ray intersection point must be computed to 1 km convergence in order to obtain a precise ionospheric latitude and longitude for  $f_oF2$  computations. An error of over 1 km in  $h_p F2$  will cause the  $f_oF2$  value to be very slightly different, and from this a change in the 5th or 6th digit in range can easily arise leading to very large errors in range rate. It is not claimed that  $h_p F2$  has to be accurate to 1 km as this is an impossible prediction, but the values of  $h_p F2$  should be consistent in their calculation to 1 km convergence.

The theoretical approach to range rate correction either by differentiating range or using the deviation angle of arrival at the satellite is in no way accurate. The differentiating technique yields a correction to an instantaneous measurement which can vary greatly from the correction to Doppler range rate measured over a finite time interval, from a fraction of a second up to over a minute's time. In addition, the range rate correction is not only influenced by the change in the satellite position, but also by the changing ionosphere below the moving satellite, which has mostly been neglected in either approach. To explain this fact, consider the range correction  $\Delta R$  as given by

$$\Delta R = \frac{KN_1}{\sin E} \quad \text{where } K = \frac{40.3}{f^2}$$

$N_1$  is the integrated vertical content and  $E$  is the local elevation angle in the ionosphere. Differentiating  $\Delta R$  while considering the case

where the satellite passes directly overhead where no azimuth change is observed;

$$\dot{\Delta R} = -KN_r \frac{\cos E}{\sin^3 E} \dot{E} + \frac{K}{\sin E} \frac{\delta N_r}{\delta E} \dot{E} + \frac{K}{\sin E} \frac{\delta N_r}{\delta t} \dot{t}$$

$t = \text{constant } E = \text{constant}$

In this equation the first term is in many cases the only one used, but it applies only to the instantaneous change in the satellite position. The other two terms are, however, often dominant. The second term is due to the positional change in the ionosphere and the last term represents the time variation of the ionosphere. For instance, with a high satellite moving east-west across the north-south ionospheric gradients at sunrise, the time variation is dominant as these gradients move towards the west with time. For a satellite moving north-south across the east-west ionospheric gradients near the equator, the time variation in the ionosphere is very small because the gradients change little in position while the ionosphere rotates with time. The second term which indicates positional change in the ionosphere is dominant for lower satellites where the ray path to the observer moves faster through the ionosphere. In cases where the satellite does not pass overhead, the azimuth change must also be considered.

To examine the relative importance of the three components of the range rate correction many orbits were examined for situations where tracking would be heavily effected by the equatorial anomaly and by the sunrise effect. Satellite heights between 500 and  $10^4$  km were considered, and the time intervals for range differencing were varied from 1/4 to 30 seconds. Figure 15 for example, shows the percent contributions for each of the range rate components to the total range rate values at various elevations. The station is near the equator at 218 degrees longitude, the satellite is at a height of  $10^4$  km, and range differencing over 30 second intervals is considered.

#### Very Long Baseline Interferometry

The model has been used to provide ionospheric corrections for the phase path measurements in very long baseline interferometry. It has been used primarily for baselines within the continental United States, but has also been used as a research tool for looking at problems that may arise on baselines between continents. A number of investigations were made of the ionospheric effects between Japan and Mojave, California. Over such a distance it is possible for one station to have low nighttime conditions and the other to have high daytime conditions with

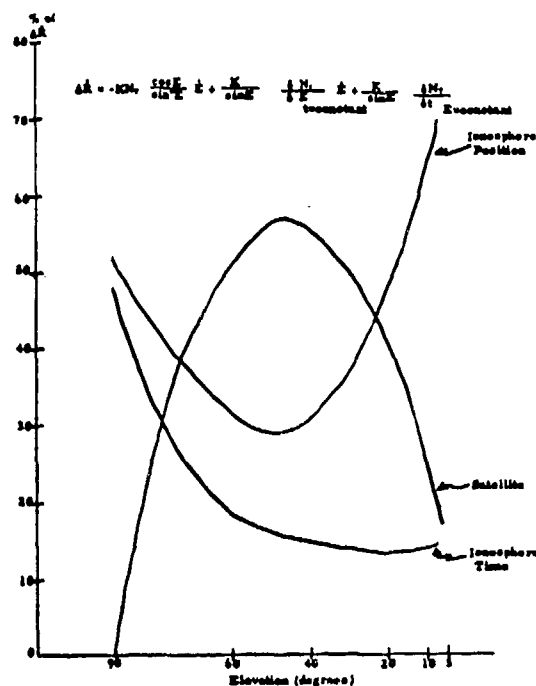


Fig. 15. Variation of the 3 Terms of the Ionospheric Range Rate Correction.

the sunrise effect between the sites. Figure 16 illustrates such a situation where Japan and

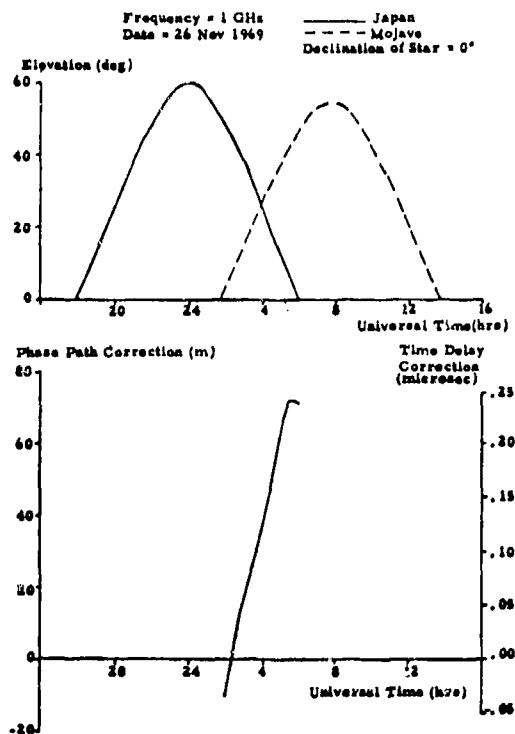


Fig. 16. Time Delay Correction for VLBL Experiments.

Mojave are receiving signals from a hypothetical radio star at 0 degrees declination.

The first part of Figure 16 shows the elevation angle of such a radio star from both sites and where the two curves overlap clearly the only time that interferometer measurements could be taken. The differential phase path and time delay corrections are shown in the second part of Figure 16 and the data has been reduced for a frequency of 1 GHz. Transposition to other frequencies is easily performed by multiplying or dividing by the square of the frequency of reception in GHz. Extremely large errors in time delay and phase caused by the ionosphere are evident and the gradient of these changes is very large.

Experiments involving very long base line interferometers have accuracy goals of a few cm at 5 GHz. Converting the ionospheric errors displayed in Figure 16 to this frequency it appears that the ionosphere can impose phase path errors of about 300 cm. The need for an accurate ionospheric model in such a reduction is therefore very evident.

#### Faraday Rotation Investigations

Faraday rotation measurements  $\Omega$  along an angular path are related to vertical electron content  $N_T$  by  $\Omega = \frac{K}{f^2} \bar{M} N_T$ , where  $f$  is the signal frequency,  $K$  a constant. The Faraday conversion factor  $\bar{M}$  is defined by,

$$\bar{M} = \frac{\int_0^h B \cos \theta \sec \chi N dh}{\int_0^h N dh},$$

$B$  is magnetic field strength,  $N$  electron density,  $\chi$  the zenith angle, and  $\theta$  the angle between the direction of propagation and the magnetic field. To compute  $\bar{M}$ , the integrals are numerically evaluated, after generating the functions under the integral sign of certain height intervals. The Bent Ionospheric Profile Model provides the electron densities as function of height.

The effects of many different conditions on the Faraday factor have been investigated. The test results point out the importance for modeling the Faraday factors correctly with respect to the station position, where the magnetic latitude is of most significance, and with respect to the direction of observation, since the elevation and azimuth angles determine the direction at which the magnetic field lines are intersected as well as the location at which the wave passes through the densest part of

the ionosphere. Less important are the specific season and diurnal influences producing variations of only about 2 to 6% in the Faraday factors, as well as the day to day prediction errors in  $f_oF_2$  having even less effect. However, prediction errors in ionospheric height could easily be caused by sudden day to day changes and can have a significant influence on the Faraday factors especially for observations along angular paths. Variations of  $\pm 100$  km in height are not uncommon particularly in the equatorial region. Errors of 5% in the Faraday factor are typical for paths at vertical incidence, but for angular paths errors of around 30% in the Faraday factor might occur resulting in proportionally large errors in  $N_T$ . The predicted values of the height of maximum electron density obtained from the Bent Model are on average within the accuracy of the measured values, which considering instrumental and reduction techniques, are about 15 km. However, the day to day variations are quite a bit larger, and on occasion, deviations in the predictions of 100 km from the height measurements have been noted.

To avoid errors in the computation of the Faraday factor, the angle  $\theta$  between the direction of propagation and the earth's magnetic field lines has to be carefully monitored along the ray path. When the condition  $89.5^\circ \leq \theta \leq 90.5^\circ$  occurs, the equation relating the Faraday rotation angle and vertical electron content no longer holds true. When  $\theta$  passes through  $90^\circ$  at a certain height, the wave experiences rotation of the polarization vector in one direction from the satellite down to that height, and rotation in the opposite direction below that height. Contributions to the rotation of the polarization vector in reversed directions cancel out, thus the measurement is not representative of the ionosphere between the satellite and the station.

There is some question as to what the upper integration limit should be for the computation of  $\bar{M}$ . Figure 17 shows the integrated electron content and Faraday rotation from ground up to height  $h$  as a percentage of the total values integrated to a satellite height of 33000 km. Faraday rotation is accumulated more rapid at lower heights than electron content; in the given cases 88 and 95% of the rotation are accumulated at 1000 km compared with 78 and 91% of the total content. The same condition is illustrated in Figure 18, only this time considering the percent of the total integrated values in each 100 km interval, and plotting the difference between these electron content and Faraday rotation contributions as a function of the interval height. For all

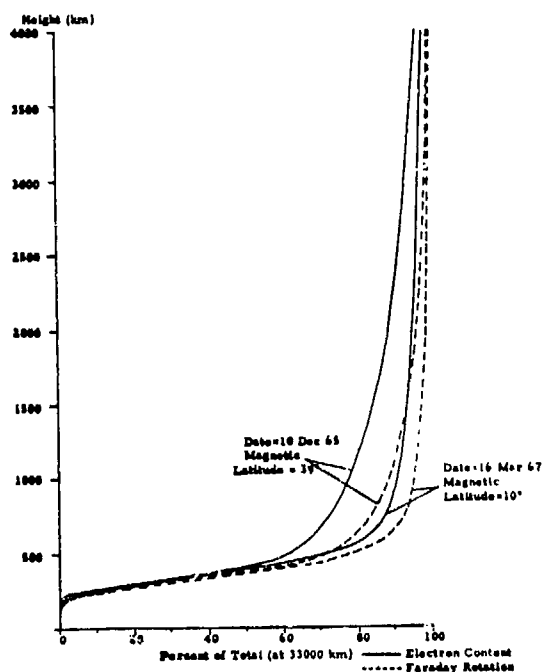


Fig. 17. Comparison of the Amount of EC and Far. Rotation Accumulated from Ground up to a Varying Height.

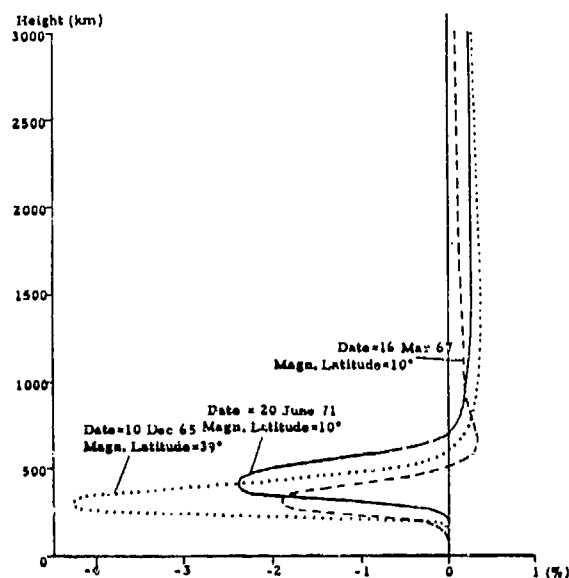


Fig. 18. Difference between Percent Contributions of Electron Content and Faraday Rotation in each 100 km Height Interval. Percentages are taken of the Total Values Integrated from 0 to 33000 km.

intervals below 500 to 600 km the contributions to the total rotation exceed the corresponding percentages of electron content, but at the higher altitudes the contributions to total content are considerably larger. This seems to indicate that the low altitude as well as the

high altitude portion have to be included in the integration process for the Faraday conversion factor, even though the amounts we are talking about are only of the same order or less than the instrumental errors. Excluding contributions above 1000 km from the computation by integrating only to a height of 1000 km and not all the way to the satellite would introduce a one-sided bias, and the resultant total content values would be consistently too small. The typical measurement errors of say  $\pm 10\%$  may become  $+2$  to  $-18\%$  if this one-sided bias is not taken account of.

#### Improvement of Satellite Orbit Determination

The Bent Ionospheric Model has been incorporated into several of the orbit determination programs at NASA/Goddard Space Flight Center to produce corrections to range, range rate and angular measurements. As a result, the overall measurement residuals of the statistical reduction process have been significantly lowered and the number of situations required for convergence has frequently decreased when comparing with the corresponding data reduction that does not consider the ionosphere. Thus an increased accuracy in the estimation of the orbit parameters as well as a reduction of the computer time have been gained.

Figure 19 shows the measured residuals

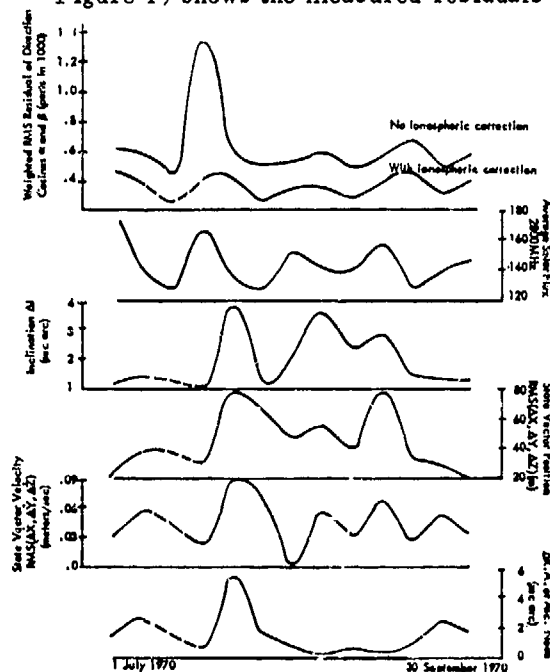


Fig. 19. Results of Orbit Determination Program on Three Months Minitrack Data from the BE-C Satellite. The top curve shows the improvement in the residuals when an ionospheric model is used and the lower curves indicate the difference in certain orbit parameters due to the ionosphere.

of the minitrack direction cosine data reduced by 30% after including ionospheric corrections, and the effects on the various orbit parameters. Another example is given in Figure 20 where

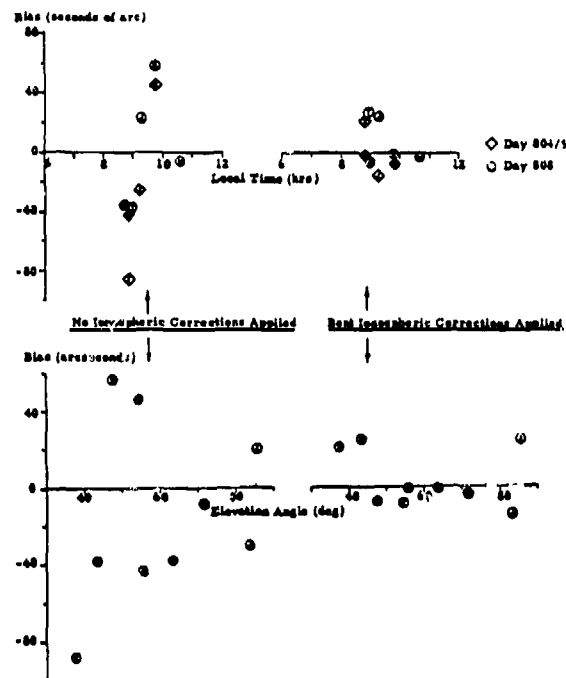


Fig. 20. Reduction of the Minitrack Observation Biases due to Ionospheric Corrections in the Goddard Trajectory Determination System. The Stations are Johannesburg, Tananarive, Orerai, Santiago, Winkfield.

the individual observation biases are shown for a number of stations, both with and without having ionospheric corrections applied. The very definite decrease in the biases is obvious.

#### Comparison with Chapman Profile

One of the ionospheric model subroutines plots the ionospheric profile of electron density versus height to 3000 km. A number of comparisons of profiles from the Bent Ionospheric Model with the Chapman profile have been made for different parts of the world at different times of the day, season, and solar cycle. The Chapman profile was given by the equation  $N = N_0 e^{1/2(1-z-e^{-z})}$  where  $z = (h-h_0)/H$  and  $H$  is the scale height. An accurate determination of scale height is very important for the Chapman equation, but no simple formulas exist which will provide the necessary accuracy. For the test situation, two formulas used at NASA/Goddard Space Flight Center were investigated. In these the scale height is defined by the equation,

$H = 1.66 (30 + a(h_0 - 200))$  where  $a$  is .075 in the first equation and .2 in the second. A

typical plot of these three models is shown in Figure 21. These profiles are plotted on a

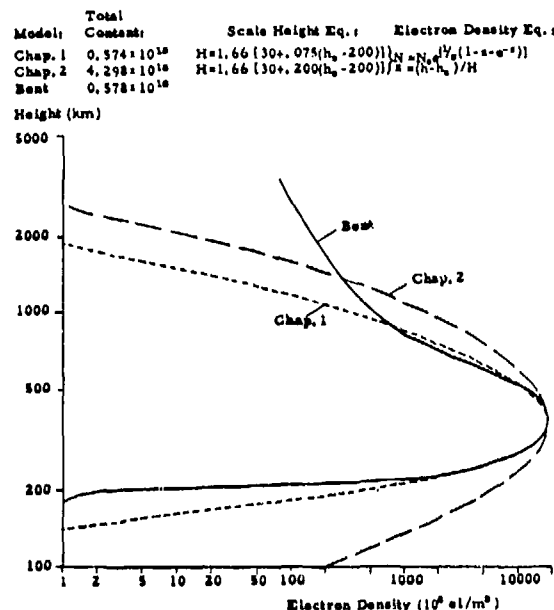


Fig. 21. Comparison of Bent Ionospheric Profile with Chapman Profiles at Quito, Ecuador on 15 January 1969 and 21 hours UT.

log-log scale to emphasize the maximum electron density region.

The integrated total electron content to 3000 km has also been analyzed. In all cases the profile described as Chapman 2, which uses 0.2 for the value of  $a$ , gave total contents a factor of 6-8 higher than Chapman 1 or the Bent Ionospheric Model. Large variations between the profiles are always evident in the lower and upper regions. In the many tests performed where widely varying times of day, latitude and longitude were investigated the profiles differed in ways similar to Figure 21, but the total content to 3000 km showed good comparison between the Bent Ionospheric Model and the Chapman profile described where  $a = .075$ .

#### THE DEVELOPMENT OF A VERY SIMPLE WORLDWIDE IONOSPHERIC MODEL

A simple technique requiring very little data and computations was tested for producing world wide ionospheric predictions. The simple model was developed using the Bent

Ionospheric Model as a data base. The basic data consists of ionospheric data values along one magnetic latitude line, the magnetic equator, and along one magnetic longitude line that passes through the densest section of the equatorial anomaly. The values along the two cross lines are chosen at 5 degree spacing, which adds up to a total of 107 numbers of 4 to 6 bits depending on the accuracy desired for each world map at a fixed time.

To generate world wide data from these values along the latitude-longitude cross lines, it is assumed that the ratios of the value at any given magnetic latitude to the value at the equator are the same along every magnetic longitude line. Specifically, these ratios are equal to the ratios formed for the magnetic longitude line for which data at 5 degree spacing is available. The condition around sunrise, however, does not follow this pattern; here the values of group delay are about the same at all latitudes along the same magnetic longitude line. Thus in this simple cross line technique, the values all along the magnetic longitude line just before sunrise are assumed to be the same as the equatorial value. To allow for a smooth transition between this and the proportionate ratio method, the results from both techniques are combined using linear weighting proportional to the respective distances for 75 degrees in magnetic longitude to both sides of the equal value longitude line. Figure 22 shows the map

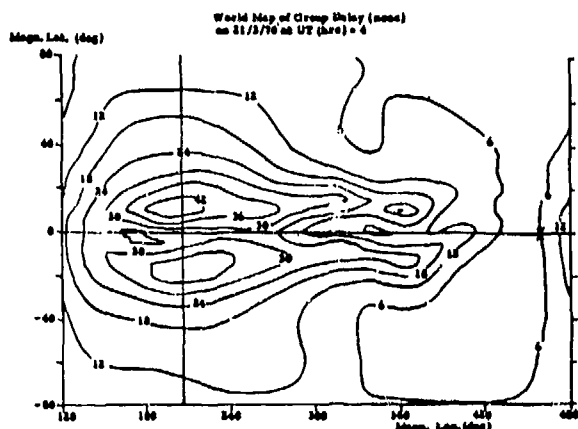


Fig. 22. Predictions from Bent Ionospheric Model Showing Cross-Lines.

with ionospheric group delay predictions from the Bent Model. The magnetic latitude and longitude lines that define the data base for the cross line technique are drawn in and the "X" defines the location of the equal value longitude line. The contour map resulting from the cross line computations is plotted in Figure 23.

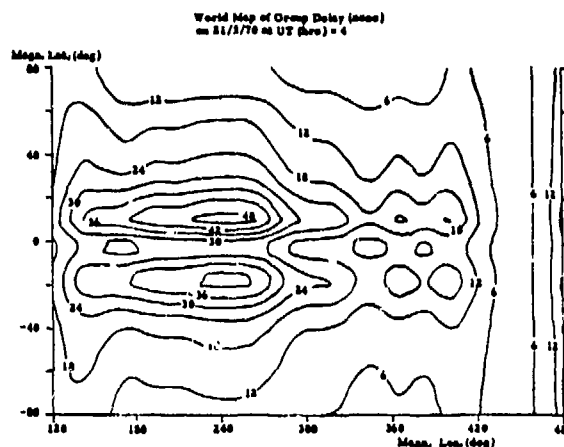


Fig. 23. Predictions from Latitude-Longitude Cross Line Technique.

For time adjustment the cross lines are rotated around the globe at a rate of 15 degrees per hour. However, since the contour lines of the ionospheric data are approximately symmetrical to the magnetic equator, causing the symmetry pattern to deviate notably from the geographic equator during parts of the day, an additional adjustment factor relating the geographic and magnetic equator is needed to achieve a diurnally stable accuracy. Such a simple model could take less than 450 bits of storage and estimate between 48 to 65% of the ionospheric effects. Depending on the circumstances, cross lines for a new map could be supplied on a monthly basis, or maps for two seasons could be stored permanently. The results for both seasons could be interpolated in time to any specific month and adjustments over a number of years could be incorporated with an additional transformation on a solar cycle basis.

## CONCLUSIONS

The Bent Ionospheric Model is an empirical world wide algorithm capable of accurately estimating the electron density profile and the associated delay and directional changes of a wave due to refraction. The model computes the electron density versus height profile from which the range, range rate, and the angular refraction corrections for the wave are obtained as well as the vertical and angular total electron content. Although the model is presented for ground to satellite and satellite to satellite communications, it is readily adaptable for ground to ground communications.

The only required inputs to the model are satellite and station position and time information and a limited amount of solar data.

For the model's additional capability of improving the ionospheric predictions by use of actual ionospheric observations, measured values of electron content or the critical frequency of the F2 layer,  $f_oF2$ , can be incorporated along with the observation station and time information. This update option uses a weighted mean technique that can accept, for the update, several measurements from different stations separated in time and space from the time and location at which the ionosphere is to be evaluated.

The model's prediction accuracy without update accounts for approximately 75 to 80 percent of the ionosphere which can improve with update to approximately 90 percent. The model, therefore, may be applied for future predictions or after the fact calculations. Since the model has been developed on a world-wide basis, predictions are not limited to any particular land mass or segment of the world. The model is applicable for determining wave refraction and ionospheric characteristics up to 3000 km in height and for all radio wave frequencies as long as the vertical component is slightly higher than critical frequency. Built into the model are the combined influences of geographical and geomagnetic effects, solar activity, local time, and seasonal variations.

Because of the flexibility of this model, it has been easily applied to a multitude of problems: range, range rate and elevation angle corrections, total electron content, and group delay reductions, very long baseline interferometry, Faraday factor analysis, satellite to satellite communications, and 3-dimensional ray tracing. Plot routines have been developed to produce vertical profiles of electron density versus height as well as cross sections of electron density or total electron content as functions of angular or geographic co-ordinates.

#### Acknowledgements

The majority of the work described herein has been performed under various contracts from NASA/Goddard Space Flight Center under the direction of Mr. Paul Schmid.

Further development and analysis has been performed under other contracts from the U. S. Government and private industry. The authors in particular are indebted to: Mr. J. Behuncik and Mr. J. Ryan, NASA/Goddard Space Flight Center; Mr. J. Klobuchar of U.S.A. F./Air Force Cambridge Research

Laboratories; Col. B. W. Parkinson, U.S.A. F. Space and Missiles Systems Organization; Mr. W. Melton, General Dynamics Electronics; Dr. B. Elrod, Mitre Corporation; and Dr. K. Cretcher, Aerospace Corporation.

The principal investigators were the authors of this paper, but we also acknowledge the help from our colleagues in the work described, namely Mr. J. Kozelsky, Mrs. M. Walloch, Mrs. L. A. Schleicher, and Mr. D. Robinson.

#### References

1. E. V. Appleton & W. J. G. Beynon, Proc. Phys. Soc. 52, Pt. I, 518 (1940); Proc. Phys. Soc. 59, Pt. II, 58 (1947).
2. W. B. Jones, R. P. Graham, M. Leftin, "Advances in Ionospheric Mapping by Numerical Methods," ESSA Technical Report ERL 107-ITS 75, (May 1969).
3. W. B. Jones & D. L. Obitts, "Global Representation of Annual and Solar Cycle Variation of  $f_oF2$  Monthly Median 1954-1958 OT/ITS Research Report No. 3 (Oct 1970).
4. A. N. Kazantsev, Tr. IRE AN SSSR, 2, 36, (1956).



A REVIEW OF THE RECENT RESULTS OF IN SITU IONOSPHERIC  
IRREGULARITY MEASUREMENTS AND THEIR RELATION TO  
ELECTROSTATIC INSTABILITIES

Michael C. Kelley  
School of Electrical Engineering  
Cornell University  
Ithaca, New York 14850

and

Forrest S. Mozer  
Department of Physics and Space Science Laboratory  
University of California  
Berkeley, California 94720

ABSTRACT

In situ measurements on rockets and satellites have greatly expanded our understanding of the location, causative factors and structure of ionospheric irregularities. In this paper results from electric field detectors and plasma density fluctuation probes will be presented, intercompared and discussed in relation to the electrostatic instabilities which create irregularities. The following phenomena have been studied in situ and are listed along with tentative instability mechanisms and the measurement techniques used:

Equatorial Electrojet (rocket):

Gradient Drift and

Two Stream  $\delta n_e/n_e$

Auroral Electrojet (rocket):

Two Stream  $\delta E, \delta n_e/n_e$

Equatorial Spread F (rocket & satellite):

Rayleigh Taylor  $\delta n_e/n_e$

High Latitude F Region Irregularities  
(rocket & satellite):

Convection Electric

Field Driven  $\delta E, \delta n_i/n_i$

Representative wave number spectra and amplitudes deduced from these studies will be presented and discussed.

Advancements in the explanations for such instabilities have proceeded fastest when plasma density gradients and flow patterns are also measured since the relative magnitude and direction of

these parameters play a key role in several instability mechanisms. Thus, future progress on the understanding of ionospheric irregularities must involve simultaneous measurements of fluctuation parameters as well as ionospheric parameters on well instrumented rockets and satellites, coupled with ground-based measurements of the earth fixed phase velocity and range time intensity profile of the waves via backscatter radar systems. For auroral studies simultaneous auroral photos taken from orbit are also highly desirable.

INTRODUCTION

Irregularities in the earth's ionosphere have been observed for more than two decades by a variety of ground-based and spacecraft techniques. In recent years these methods have become more sophisticated as have the theoretical basis for understanding the phenomena. The field has thus progressed from one of phenomenology to one more closely akin to the classical interplay of experimental and theoretical science.

The application of the principles of plasma physics, particularly with regard to electrostatic instabilities, has proven to be most fruitful. This is true since the phase velocities of such waves are comparable to the thermal and drift velocities of the plasma constituents. Energetic particles, on the other hand, interact more strongly with electromagnetic waves due to the higher characteristic velocities of such waves

and particles. In a collisionless plasma, electrostatic waves can cause collective interactions between particles which may replace binary collisions in the microscopic description of the physics involved. Thus in some cases knowledge of transport coefficients necessary for a macroscopic description of a given process requires information on the electrostatic waves present. Very often production of strong electrostatic waves which can significantly modify the transport coefficients only occurs after some initial condition is met. Further evolution, however, may proceed very rapidly. Thus one may have a physical condition which is stable under an MHD description evolve to a critical point where microscopic turbulence very rapidly destroys the equilibrium or modifies the electrical properties of the system.

Understanding of the physics thus requires knowledge both of the plasma conditions leading to instability as well as measurement of the frequency and wavelength spectra of the irregularities. Knowledge of the former has been aided by recent advances in measurement of the electric field and plasma motions in the ionosphere via incoherent scatter measurements of the ion flow velocity as well as balloon, rocket and satellite measurements of electric fields. Such flow measurements coupled with those of the plasma density and temperature and of the spatial variations in these quantities have been successful in determining the configurational state which leads to a number of instabilities.

Measurements of the irregularities themselves have been made by ground-based techniques as well as *in situ*. Particularly useful have been doppler shift measurements of radar waves back-scattered from the irregularities since such shifts yield the phase velocity of those irregularities in the plasma which have  $k = 4\pi/\lambda$  where  $\lambda$  is the radar wavelength. This phase velocity can be readily compared with theory. Such measurements have been performed most extensively via transmissions in the equatorial regions from Jicamarca, Peru, Thumba, India, and Natal, Brazil; and in the high latitude regions from Homer, Alaska, and recently from Ithaca, New York. *In situ* measurements of irregularities in the plasma density and electric fields, which are the fluctuating components of most electrostatic waves, have been performed on rockets and satellites and some of the results of these measurements are reviewed here. These measurements have an advantage over the radar in that a wide range in  $\omega$ ,  $k$  space can be instantaneously measured

although phase velocity measurements are more difficult due to usual high velocity of the vehicles with respect to the medium. A discussion of some recent developments in measurement techniques is presented elsewhere in this publication (Kelley et al., 1975a).

Irregularities are observed both in the E and F layers of the earth's ionosphere. In the E region strong instabilities are associated with the auroral and equatorial electrojets. In the F region irregularities are also observed in equatorial as well as high latitude regions. In both sectors the F region irregularities are present in a broader range of latitude than are the E region fluctuations. In the following pages, *in situ* measurements obtained in the equatorial and auroral electrojets will be discussed as will the equatorial and high latitude F region observations. No discussion of the temperate latitude E region irregularities associated with sporadic E will be made. As is usually done, the two altitude regions will be discussed separately. This simplification is probably justified in the equatorial zone since the magnetic field configuration is such that the narrow latitudinal region of equatorial E region irregularities cannot interact very efficiently with the higher altitudes. Such a separation at high latitudes is much less justified due to the direct linking of the two regions via highly conducting magnetic field lines. Theoretical work on equatorial irregularities has progressed farther than that concerning the high latitudes due to the relatively benign magnetic field geometry. *In situ* and radar measurements are in good agreement with many aspects of the equatorial theory and it is expected that considerable work on theory for the high latitudes will be encouraged by these successes.

## E REGION MEASUREMENTS

### Equatorial

Most of the *in situ* measurements of irregularities in the equatorial E region have been performed on sounding rockets by the Indian group under S. Prakash (Prakash et al., 1971; 1972). Satellite measurements are not very common at such altitudes and low altitude sounding rockets are the most useful since they pass rather slowly through the E region. Radar measurements have been used to catalogue two types of instability (I and II) on the basis of the characteristics of the returned doppler spectrum. Type I irregularities return a strong doppler shifted echo at a fre-

quency corresponding to the ion acoustic speed and have been explained as a two stream instability resulting when the magnetized electrons drift relative to the collision dominated ions at a speed in excess of the ion thermal speed (Buneman, 1963; Farley, 1963 a,b). Such conditions occur most often during the day at the equator and some rocket plasma density fluctuation data which bear this out are presented in Figure 1. The plasma density profile is smooth whereas the fluctuations are present on a layer at an altitude where electrons can  $E \times B$  drift freely while ion drifts are quenched by neutral collisions.

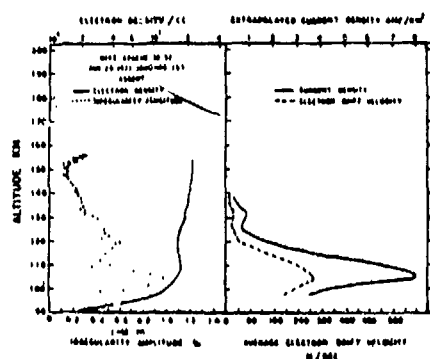


Fig. 1 E region density profile and irregularity intensity during a daytime rocket flight from Thumba, India. The right hand side shows an estimate of the electron drift profile deduced from magnetometer and plasma density measurements.

Both the theory and radar observations for Type II irregularities are more complicated and the rocket data has helped confirm that the gradient drift instability becomes important for drift speeds lower than the acoustic threshold. The rocket data taken from various publications by the Indian group and which is shown schematically in Figure 2 indicate that irregularities at night are typically present on only the top or the bottom side of a given E region density profile. The sense is such that topside (bottomside) irregularities are observed when the E region electrons are drifting westward (eastward), results which are in good agreement with the theory for the gradient drift instability which requires that the ambient electric field have a component parallel to the plasma density gradient.

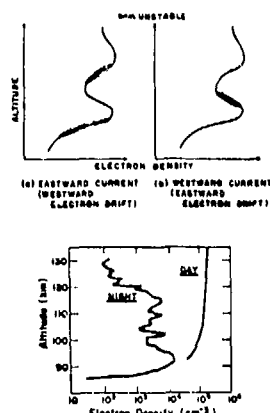


Fig. 2 Typical electron density profiles observed over Thumba, India near noon and midnight along with a schematic illustration of the unstable regions deduced from rocket data.

One feature of the Type I instability which is not yet fully explained is that the irregularity phase velocity is independent of the angle to the electrojet current direction. Rocket measurements of fluctuating electric fields as well as plasma density and temperature oscillations might help explain this peculiarity.

#### HIGH LATITUDE

Simultaneous electric field and plasma density measurements have been performed during a rocket flight into a very strong magnetic substorm (Kelley and Mozer, 1973). The altitude profile of the broadband  $\delta E$  and  $\delta n/n$  fluctuations are presented in Figure 3.

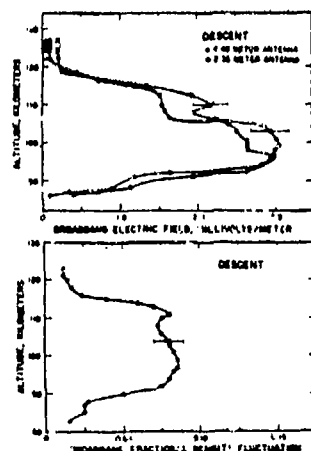


Fig. 3 Broadband electric field and plasma density fluctuation amplitudes observed in the auroral E region.

Since the electric field is a vector quantity it contains more information than does  $\delta n/n$  and since for electrostatic waves  $\delta E$  is parallel to  $k$ , the electric field can be used to determine the direction of wave propagation. In the case described here a single antenna was oriented perpendicular to the rocket spin axis which in turn was nearly parallel to  $B$ . Since the spin frequency was much less than the wave frequency, the ac electric field signal should peak twice per spin yielding the direction of  $k$  with an ambiguity of  $180^\circ$ . This direction is plotted in Figure 4 as the double ended dashed arrows. Since the  $E \times B$  velocity was also measured by the electric field detector and by barium releases carried aloft by the same vehicle, the magnitude and direction of the relative drift between E region ions and electrons could be calculated assuming a neutral atmosphere model. The direction of  $\delta E$  is seen to be in good agreement with direction of this drift giving good evidence for a drift driven instability. The density fluctuations were not spin modulated which is correct for this scalar quantity. The solid circle yields the magnitude of the ion thermal speed and shows that the differential drift greatly exceeded the threshold for the two stream instability. Since  $\delta E = -ik\phi$  and since  $\phi$  is related to  $\delta n/n$  for electrostatic waves, comparison of  $\delta E$  and  $\delta n/n$  as a function of frequency can be used to obtain information on the magnitude of  $k$  as a function of  $\omega$ . Such comparisons applied to these data showed that the assumption that  $\phi$  is proportional  $\delta n/n$ , which holds for example when electrons are in a Boltzmann distribution in the wave potential,

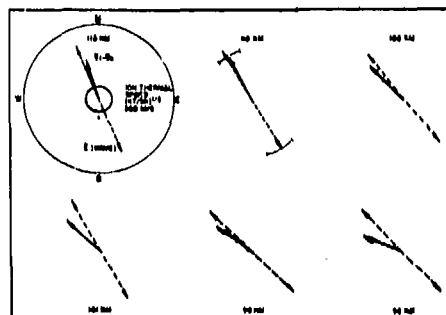


Fig. 4 The solid arrow represents the magnitude and direction of the difference between the ion and electron drift velocities in a geomagnetic coordinate system fixed to the earth for several altitudes on the upleg. The circle is the ion thermal speed, and the dashed arrow is the direction of the oscillating electric field detected on board the rocket.

is consistent with the data. If it is further assumed that there were no electron temperature fluctuations in the waves, the ratio of  $\delta E$  to  $\delta n/n$  can be used to determine the phase velocity which was found to be in good agreement with the ion acoustic speed. A non-varying electron temperature may not be a good approximation, however, and future experiments should measure this quantity also.

A frequency time spectrogram of the electric field signal observed during this event is presented in Figure 5. Waves with frequencies as high as those observed have been predicted when the electron drift velocity exceeds the ion thermal speed by several times as was the case here (Lee et al., 1971). The frequency spectrum of  $\delta E$  thus displayed shows intense signals from ten hertz to seven kilohertz which was near the lower hybrid resonance.

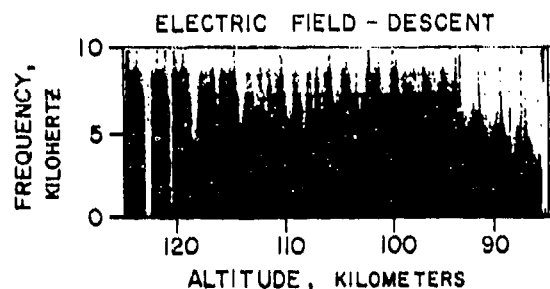


Fig. 5 A sonogram of the ac electric field detected in the E region by one of the double probe antennas.

Radar measurements of aurora at 3 m show complex doppler shift spectra and a displacement of maximum activity equatorward of visible aurora before midnight and poleward after midnight suggesting that strong currents may flow in regions other than visible aurora. The short wavelength F region irregularities observed near aurora and which are discussed below display a similar spatial relationship and simultaneous radar and in situ measurements are highly desirable.

## F REGION MEASUREMENTS

### Equatorial

Satellite and rocket data are both available in the F region. A plot of the percentage occurrence of irregularities as determined from the satellite ac electric field measurements on OV1-17 (Kelley, 1972) is given in Figure 6 as a function of geomagnetic latitude in the nightside. Also plotted is the percentage occurrence of spread F as evidenced by ionosonde ground studies

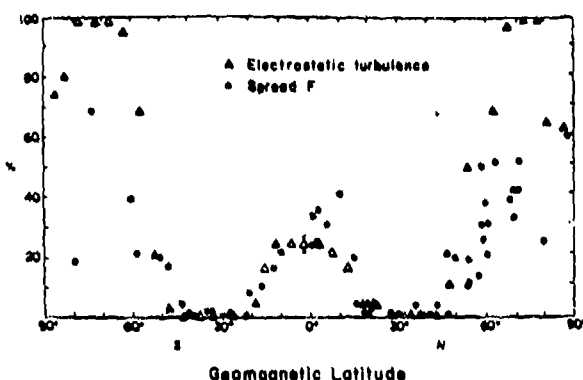


Fig. 6 Average percentage occurrence of spread F and fluctuating low frequency electric fields as functions of geomagnetic latitude.

(Shimazaki, 1959). Both sets of data display a local maximum in occurrence in a latitude range centered on the equator, a deep null in the mid-latitude range and a stronger maximum in the high latitudes. Similar patterns have been reported for in situ plasma density irregularity measurements (Dyson, 1969; Sagalyn et al., 1973; Dyson et al., 1974). An irregularity spectrum from such a probe flown on the OGO-6 satellite is presented on the right hand side of Figure 7 (Dyson et al., 1974) and several spectra from a recent rocket flight are plotted in Figure 8 (Kelley et al., 1975b). Both sets show an amplitude spectrum which peaks at small  $k$  and falls relatively smoothly as  $(k)^{-1}$  for large  $k$ . The broadband intensity of the irregularities are as high as 60% in the most intense rocket spectrum.

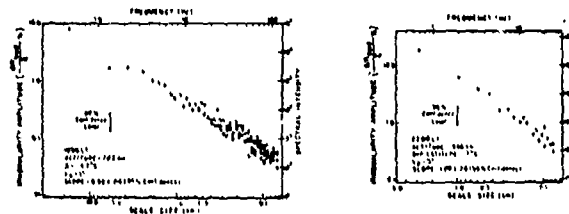


Fig. 7 Irregularity spectra obtained at high and equatorial latitudes by the plasma probe on OGO-6.

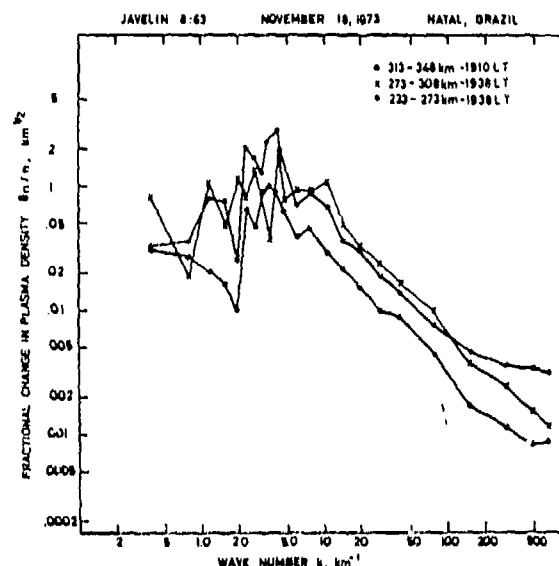


Fig. 8 Wave number spectra of the spread F irregularities for three different altitude ranges, one in the upleg and two in the downleg. The total rocket velocity was about 2.5 times the eastward component used in the analysis and which was 1000 meters/second.

A polar orbiting satellite such as OGO-6 or OV1-17 makes a rapid pass at a fixed local time and hence yields no information on the vertical structure nor the development in local time of the instability. The rocket in this experiment was launched eastward from Natal, Brazil and hence made two vertical profiles at local times differing by about one half hour in local time. It is important to point out that the development of equatorial irregularities, which result in the scattering of ionosonde signals (spread F), begins shortly after local sunset as the F region rises due to the usual post sunset enhancement of the vertical drift and as recombination reduces the plasma density at low altitudes. The disturbance can last well

into the night at a given site. In Figure 9 the up and downleg plasma density profiles are superimposed. Both

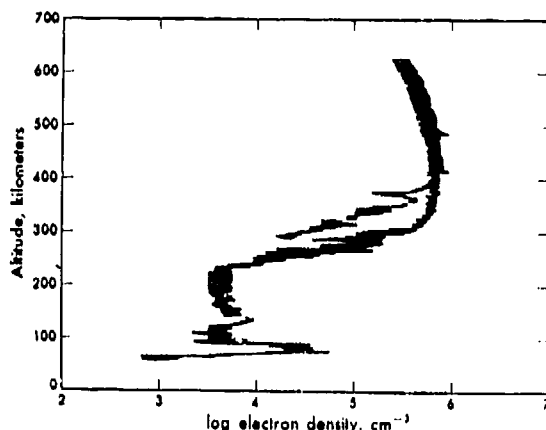


Fig. 9 Up and downleg plasma density profiles observed during a flight of a rocket launched east from Natal, Brazil during equatorial spread F conditions.

sets of data show a steep vertical gradient on the bottomside of the F peak which, in most theories for equatorial spread F, supplies the free energy for the instability. The profile which is displaced to lower altitudes is the one at a later local time which suggests that the instability evolved in such a way as to destroy the zero order gradient and hence to approach a lower energy state, as time passed, by filling in the plasma region at lower altitudes. This interpretation is upheld by barium cloud releases performed on the same rocket and which can be identified in the upleg profile by the enhancements in local plasma density at 425 km at 500 km. The drift of both clouds was upward during the twenty minutes of observation time. The Jicamarca radar facility did not, furthermore, detect the downward reversal of plasma flow until a local time of 2140 on this night. Thus the electric field driven flow was upward although the bottomside filled in. Comparison of the profile of irregularities observed during the up and downleg are presented in Figure 10. In addition to being more intense and located at lower altitudes, the irregularities display a distinctly asymmetric shape on either the eastward or the bottomside. Assuming the  $k$  vectors of the irregularities were in the east-west direction as is predicted by most linear theories, scale lengths  $(d(\ln n)/dx)^{-1}$  for density changes in excess of .5 e folds ranging from 12 m to 100 m were observed.

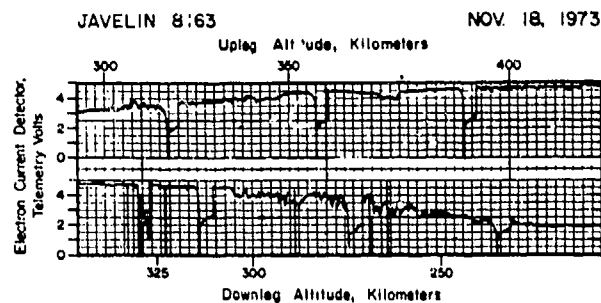


Fig. 10 Comparison of up and downleg irregularities detected by the electron probe. The downleg irregularities are more intense and display a steeper gradient on the down range edge.

These data are in reasonable good agreement with recent theoretical treatments of equatorial spread F (Haerendel, 1974; Hudson and Kennel, 1974) and an earlier one (Dungey, 1956) which show that the Rayleigh Taylor instability should be unstable on the bottomside of the F peak due to the anti-parallel configuration of  $\vec{g}$  and  $\vec{B}$ . The dc electric field pattern was such that the cross field instability configuration was also met during this event. Such mechanisms have been argued against by Farley et al., (1970) in light of spread F measurements made at 3 m by the powerful Jicamarca radar facility. However, backscatter measurements at 3 m made from Natal with a 15 kilowatt radar during the rocket flight showed strong F region backscatter near and well above the F peak but none associated with the very strong bottomside irregularities described here. Some of this radar data is presented in Figure 11 in a range time intensity format. All observed 3 m irregularities (white regions) were above 375 km altitude whereas the strong bottomside irregularities were below this altitude. (A region of 3 meter backscatter may have been associated with the particularly deep drop out in plasma density near the F peak on the upleg and is still under study). Balsley and Farley (private communication) have recently suggested that the powerful Jicamarca beam could backscatter in excess of incoherent levels from regions which were not unstable at 3 meters but merely imbedded with intense long wavelength irregularities which have steep gradients such as those in Figure 10. This observation taken with the Natal data thus indicate that theories for

bottomside equatorial spread F may not have to satisfy all the conditions imposed by the Jicamarca 3 m data and that a bonifide 3 m equatorial F region instability may follow a somewhat different morphology.

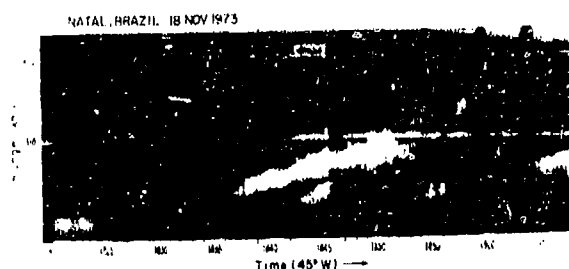


Fig. 11 Range time intensity profile of backscattered 50 MHz radar signals transmitted from Natal, Brazil during the night of the rocket flight. The rocket was launched at 1822 which was about 1902 true local time.

#### HIGH LATITUDE

As indicated in Figure 6, the high latitude F region is populated with irregularities virtually continuously. The sensitive ac electric field experiments on OV1-10, OGO-6 and OV1-17 and 18 have detected such fluctuations (Maynard and Heppner, 1970; Laaspere et al., 1971; Kelley and Mozer, 1972) as have a number of plasma density experiments (Dyson, 1969; Sagalyn et al., 1973; Dyson et al., 1974). An example of a high latitude spectrum from the OGO-6 plasma density experiment is presented in the left side of Figure 7. The spectrum for large  $k$  is typically  $k^{-1}$  for such a detector and is very similar to the equatorial spectrum on the right.

Typical data obtained during a polar pass of the OV1-17 electric field detector and from a nearly simultaneous pass of the OGO-6 magnetic search coil experiment are plotted in Figure 12. The signals at 500 hertz observed on the dayside are due to electromagnetic ELF hiss which has been extensively studied using the two spacecraft (Kelley and Tsurutani, 1975). The low frequency signal was electrostatic and was observed nearly continuously between two sharp boundaries at ( $68^\circ$ , 1800 M.L.T.) and at ( $52^\circ$ , 2400 M.L.T.). This pattern was observed on nearly every pass of OV1-17 and the position of the two boundaries

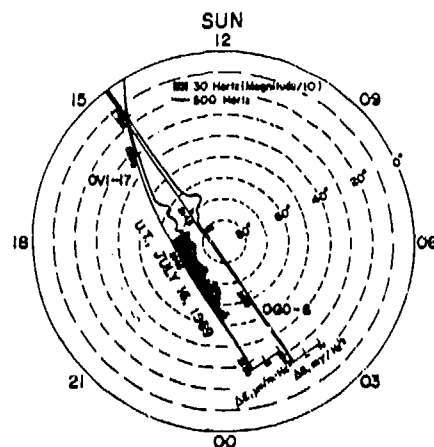


Fig. 12 Nearly simultaneous ac electric and magnetic field measurements made in the polar regions on OV1-17 and OGO-6.

are plotted in Figure 13 for 150 polar passes. The equatorward boundary as a function of local time is very similar to the boundary for scintillations which has been extensively studied by Aarons and co-workers (Aarons et al., 1969; Aarons and Allen, 1971).

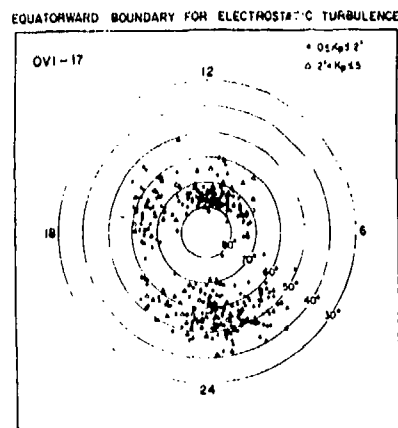


Fig. 13 Equatorward boundary for fluctuating electric fields as a function of magnetic local time and invariant latitude for two  $K_p$  ranges.

This region is also nearly identical to the region for large scale convective motion of the magnetospheric and ionospheric plasma. Evidence that this convection is related to the irregularities is presented in Figure 14. The upper two plots show the dc electric field in the vehicle reference frame with two different gain levels during a polar pass of OV1-17 while the lower plots display the ac signal at two

frequencies. The dc data includes the  $\nabla \times \mathbf{B}$  field in the satellite coordinate system and hence only deviations from

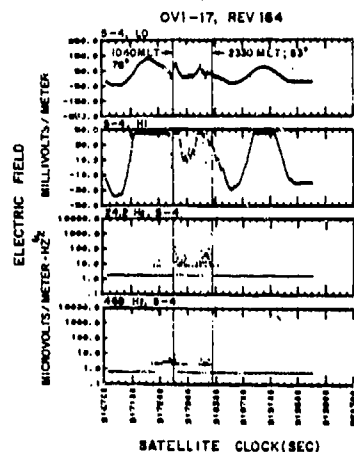


Fig. 14 Comparison of fluctuating quasi-dc and ac electric fields during a polar pass of OV1-17.

the smooth variation are due to ambient electric fields. The ac signals at 24 hertz seem to occur in the same region as the strong dc variations were observed. Variations in the dc field as intense as those observed in this pass are unusual, however, although the ac signals are very common. A more sensitive dc measurement must be made in conjunction with ac measurements in order to conclude that a definite relation exists between the dc and ac fields. Such measurements have been performed on sounding rockets near auroral arcs and do show a close relationship between shorter wavelength (1-12 m) waves and dc fluctuations. This is shown in Figure 15

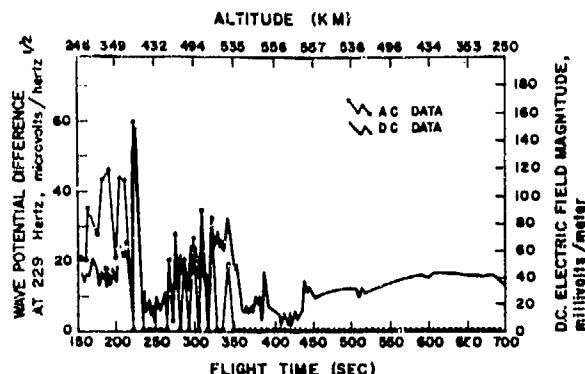


Fig. 15 Magnitude of the ambient dc electric field in an earth fixed frame along with the ac field observed with the same antenna near and above an auroral arc during a magnetic substorm.

where the magnitude of the dc electric field in an earth fixed frame and of the ac potential across a 3.9 m antenna at 229 hertz ( $\lambda$  of a few m if the irregularities are assumed to have low phase velocity) are plotted. It is of interest to note that the region of occurrence of short wavelength waves observed during the rocket flight agrees very well with that of 3 m waves in the E region reported by (Balsley et al., 1973). The relationship between these F region fluctuations and the aurora, as deduced from all sky camera data and from auroral particle detectors, is presented in Figure 16. The irregularities were much more intense equatorward of the arc as observed by Balsley et al. (1973) in pre-midnight conditions. Since the dc electric field pointed northward (toward the arc) in the equatorward region and since a large scale horizontal density gradient probably also pointed toward the arc, the  $\mathbf{E} \times \mathbf{B}$  Hall instability may have operated in the E region. Since the average pre(post)-midnight dc auroral zone electric field is north (south) such a mechanism also might explain the radar data. At such short wavelengths there is no direct communication between E and F region altitudes due to the small but finite resistivity parallel to the magnetic field lines, however, and hence separate mechanisms must be operating in the two regions. It is possible that long wavelength irregularities formed in the E region map up to F region heights where secondary instabilities create the shorter modes.

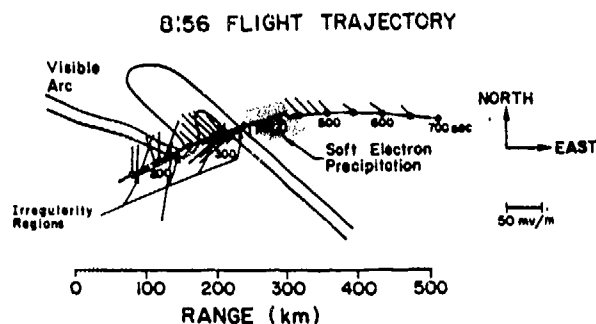


Fig. 16 Region of occurrence of F region turbulence relative to the position of the aurora and the dc electric field pattern.

Maynard and Heppner (1970) suggested that such fluctuations were due to variations in the convective field, presumably impressed from the magnetosphere,



rather than an ionospheric instability. Similarity to equatorial irregularities argues against this but further measurements are necessary. The fact that irregularities are present throughout the polar regions argues against local formation via particle precipitation since such fluxes are more narrowly defined in latitude than are the irregularities. It is possible, however, that precipitation related irregularities are formed in the auroral oval and distributed by the large scale convection motion.

The angular distribution of fluctuations observed at low frequencies by the various electric field detectors flown on satellites in polar orbit are difficult to understand. For an electrostatic wave with  $\omega/k \ll v_s$ , the relative velocity between plasma and satellite, fluctuations should only be observed when the antenna is parallel to  $v_s$ . Such a relationship was observed in the E and F region rocket electric field data described here but not in the satellite data where the fluctuations were nearly isotropic. The isotropy is further annoying since the long wavelength irregularities are known to be field-aligned. The satellite data was obtained primarily via long cylindrical antennas which interact with the medium over very long distances and hence have a complicated plasma sheath which varies along the probe. Such variations may make the probes more sensitive to variations in the plasma density due to the waves than in the potential variations (Fiala and Storey, 1970). The isotropy still requires that the electrode responses were uncorrelated. Satellite experiments utilizing spherical electrodes on long booms are planned and may help sort out this difficulty.

#### ACKNOWLEDGEMENTS

This work was supported by the Office of Naval Research under contract N00014-69-A-0200-1015. One of the authors (M.K.) was partially supported under an Alexander von Humboldt Fellowship at the Max-Planck-Institut für Physik und Astrophysik, Institut für extraterrestrische Physik, Garching, West Germany.

#### REFERENCES

- Aarons, J., J.P. Mullen, and H.E. Whitney, The scintillation boundary, J. Geophys. Res., **74**, 884, 1969.
- Aarons, J., and R.S. Allen, Scintillation boundary during quiet and disturbed magnetic conditions, J. Geophys. Res., **76**, 170, 1971.
- Balsley, B.B., W.L. Ecklund, and R.A. Greenwald, VHF Doppler spectra of radar echoes associated with a visual auroral form: observations and implications, J. Geophys. Res., **1681**, 1973.
- Buneman, O., Excitation of field-aligned sound waves by electron streams, Phys. Rev. Lett., **10**, 285, 1963.
- Dungey, J.W., Convective diffusion in the equatorial F region, J. Atmos. Terr. Phys., **9**, 304, 1956.
- Dyson, P.L., Direct measurements of the size and amplitude of irregularities in the topside ionosphere, J. Geophys. Res., **74**, 6291, 1969.
- Dyson, P.L., J.P. McClure and W.B. Hanson, In situ measurements of the spectral characteristics of F region irregularities, J. Geophys. Res., **79**, 1497, 1974.
- Farley, D.T., Jr., Two-stream plasma instability as a source of irregularities in the ionosphere, Phys. Rev. Lett., **10**, 279, 1963a.
- Farley, D.T., Jr., A plasma instability resulting in field-aligned irregularities in the ionosphere, J. Geophys. Res., **68**, 6083, 1963b.
- Farley, D.T., Jr., B.B. Balsley, R.F. Woodman, and J.P. McClure, Equatorial spread F: Implications of VHF Radar Observations, J. Geophys. Res., **75**, 7199, 1970.
- Fiala, V., and L.R.O. Storey, The response of a double-sphere dipole antenna to VLF electrostatic plasma waves, in Plasma Waves in Space and Laboratory vol. 2, edited by J.O. Thomas and B.J. Landmark, p. 411, Elsevier, New York, 1970.
- Haerendel, G., Theory of equatorial spread F, preprint, Max-Planck-Institut für Physik und Astrophysik, 1974.
- Hudson, M.K. and C.F. Kennel, Linear theory of equatorial spread F, submitted to J. Geophys. Res., 1975.
- Kelley, M.C., Relationship between electrostatic turbulence and spread F, J. Geophys. Res., **77**, 1327, 1972.
- Kelley, M.C., and F.S. Mozer, A satellite survey of vector electric fields in the ionosphere at frequencies from 10 to 500 hertz, 1. Isotropic, high latitude electrostatic emission, J. Geophys. Res., **77**, 4158, 1972.
- Kelley, M.C. and F.S. Mozer, Electric field and plasma density oscillations due to the high-frequency Hall current,

- two stream instability in the auroral E-region, J. Geophys. Res., 78, 2214, 1973.
- Kelley, M.C. and B. Tsurutani, Properties of ELF electromagnetic waves above the earth's ionosphere deduced from plasma wave experiments on the OV1-17 and OGO-6 satellites, submitted to J. Geophys. Res., 1975.
- Kelley, M.C., C.W. Carlson and F.S. Mozer, Application of electric field and fast Langmuir probes for the in situ observation of electrostatic waves and irregularities, Proceedings of the Symposium on the Effect of the Ionosphere on Space Systems and Communications (this volume), 1975a.
- Kelley, M.C., R. Balsley, C.W. Carlson, W. Ecklund, G. Haerendel, B. Häusler, H. Kappler, F.S. Mozer, E. Rieger, R. Torbert, and A. Valenzuela, A multi-experimental study of equatorial spread F, submitted to J. Geophys. Res., 1975b.
- Laaspere, T., W.C. Johnson, and L.C. Semperebon, Observations of auroral hiss, LHR noise, and other phenomena in the frequency range 20 Hz to 540 kHz on OGO-6, J. Geophys. Res., 76, 4477, 1971.
- Lee, K., C.F. Kennel, and J.M. Kindel, High-frequency Hall current instability, Radio Sci., 6, 209, 1971.
- Maynard, N.C., and J.P. Heppner, Variations in electric fields from polar orbiting satellites, in Particles and Fields in the Magnetosphere, edited by B. McCormac, p. 247, D. Reidel, Dordrecht, Netherlands, 1970.
- Prakash, S., S.P. Gupta, and B.H. Subbaraya, Experimental evidence for cross-field instability in the equatorial ionosphere, Space Res., 11, 1139, 1971.
- Prakash, S., B.H. Subbaraya, and S.P. Gupta, Rocket measurements of ionization irregularities in the equatorial ionosphere at Thumba and identification of plasma instabilities, Indian J. Radio and Space Phys., 1, 72, 1972.
- Sagaly, R., P. Wildman, S. Bredesen, L. Rao, and M. Ahmed, Topside ionospheric irregularities at high latitudes, Trans. Am. Geophys. Union, 54, 418, 1973.
- Shimazaki, T., A statistical study of world-wide occurrence probability of spread F., J. Radio Res. Labs., Japan, 6, 669, 1959.

RECENT RESULTS FROM THEORETICAL AND NUMERICAL MODELING OF E AND F  
REGION IRREGULARITIES

B. E. McDonald,<sup>†</sup> S. L. Ossakow,<sup>†</sup> T. P. Coffey,<sup>†</sup> R. N. Sudan,<sup>†\*</sup> A. J. Scannapieco,<sup>\*\*</sup>  
and S. R. Goldman<sup>\*\*</sup>

<sup>†</sup>U. S. Naval Research Laboratory, Washington, D. C. 20375

\*Permanent address: Cornell University, Ithaca, N.Y. 14850

\*\*Science Applications Incorporated, McLean, Va. 22101

**Abstract** The importance of ionospheric irregularities in the overall concept of dynamic ionospheric physics modeling is emphasized. In particular, ionospheric irregularities produce scintillation which cause communication and radar system degradation. The determination, classification and nonlinear development of such instabilities, in terms of theoretical and numerical simulation studies, is of fundamental importance in giving the Navy and other systems users a predictive capability in combating deleterious scintillation effects. This paper gives an overview of ionospheric irregularities and specific results in two areas. (i) nonlinear development of the type II E region equatorial electrojet instability; and (ii) scintillation causing F region irregularities.

I. INTRODUCTION

The general problem of ionospheric modeling, important for predictive capabilities in communication and radar systems, can be broken up into three categories: (1) data collection; (2) model development; and (3) systems applications. The general modeling category (2) can be broken up into the following subsections: (i) chemistry; (ii) neutral atmosphere; (iii) laminar ionosphere; and (iv) turbulent or irregular ionosphere. Study of the turbulent ionosphere requires a knowledge of the laminar ionosphere which in turn requires a knowledge of the chemistry and the neutral atmosphere. Thus, for a true predictive capability areas (i) - (iv) must be studied. A program addressing all of these areas is being developed. However, the work which will be reported on in this paper is an overview of the studies carried out in area (iv) which we call ionospheric plasma irregularities.

Initially the work involved the development of the capability to treat, computationally and theoretically, the non-linear dynamics of ionospheric plasmas. The capability, once developed, was then applied to several outstanding problems. Three of the problems are: (A) Type II E region equatorial electrojet instabilities; (B) Striations in plasma clouds and image formation in plasma cloud-ionosphere coupled systems; and (C) F region ionospheric irregularities causing scintillations and spread F. Radar backscatter [Balsley and Farley, 1973] observations of three major irregularities, i.e., electron density fluctuations,

in the geomagnetic equatorial E region electrojet have led us to study process A. Barium clouds [Rosenberg, 1971; Davis et al. 1973] released by rockets in the upper ionosphere and high altitude nuclear releases both of which exhibit field aligned striations, i.e., electron and ion density fluctuations, led us to the study of process B. Scintillation of radio signals from polar orbiting [Nielsen and Aarons, 1974] and equatorial satellites [Craft and Westerlund, 1972; Taur, 1973] and ionosonde data [Farley et al., 1970; Booker and Wells, 1958; Pitteway and Cohen, 1961] have led us to study process C (also due to electron density fluctuations). All three processes can cause scintillation or enhanced backscatter. These three processes are caused by plasma instabilities which depend on the fact that electrons and ions collide with neutral particles. In particular, the instabilities causing the first two processes (A and B) arise from having an electron density gradient and electron and ion-neutral drag effects transverse to the ambient magnetic field. This instability is called the E X B gradient drift instability [Simon, 1963, 1970; Linson and Workman, 1970; Maeda et al., 1963; Knox, 1964]. Process C, in the case of midlatitude spread F, is believed by Perkins [1973] to depend upon the fact that as the plasma in a flux tube is moved up or down in altitude it samples regions of different Pedersen conductivity. This is an alternative mechanism to the usual E X B instability. However, as we will show in a later section, the E X B gradient drift

instability can be quite effective causing F region irregularities which agree with scintillation and spread F data at middle to high latitudes. The inadequacy of linear perturbation theory to describe these phenomena has led us to study by theoretical and numerical simulation techniques the nonlinear development of these three process (plasma instabilities). However, in this paper we will present results for (A) and (C). The study listed under (B) will be presented in another paper in these proceedings.

## II. IMPORTANCE OF STUDIES

The basic importance of our studies on ionospheric irregularities can be catalogued as follows: (1) the instabilities degrade communications; (2) the instabilities degrade radar performance; and (3) the studies will enable us to obtain a predictive capability with respect to (1) and (2), i.e., where to expect these irregular structures and what their properties will be. At this juncture let us elaborate on (1).

The fact that time-varying irregular structure in the ionosphere (known as ionospheric scintillation) could affect radio signals emitted by stars has been known for some time [Hewish, 1952; Utlaut, 1974]. However, only recently, and then with some surprise, has it been found that the ionosphere can seriously perturb signals used for satellite communications [Utlaut, 1974]. The effect of irregular structure, i.e., irregularities of the refractive index, in the ionosphere is to superpose a random fluctuation of signal amplitude, phase and polarization. These deleterious effects may cause an intolerable number of errors in the received signal and produce unusable information. Utlaut [1974] has recently pointed out that (a) some of the orbiting meteorological satellites transmitting video weather data have experienced conditions during which the video data were nearly obscured as a result of scintillation; (b) a navigation satellite system has experienced difficulties inserting ephemeris data in the spacecraft at times because of scintillation; and (c) signals from geostationary satellites may also suffer deleterious effects, in regions other than the equatorial region, when transmitting to higher latitudes since the polar cap scintillating region is tipped with respect to the geographic pole (e.g., aircraft routes near midlatitude over the North Atlantic could experience difficulties communicating by way of geostationary satellites). Naturally occurring scintillation is strongest in the high latitude (auroral and polar regions) and equatorial regions [Utlaut, 1974; Hopkins and Paulson, 1974], although midlatitude scintillation also occurs [Aarons et al., 1971; Rufenach, 1972; Dyson et al., 1974]. However, these notions refer to natural scintillations. U. S. high altitude nuclear releases (e.g. Starfish) have produced

world wide spread F with attendant scintillation phenomena [Newman, et al., 1966; Maeda, et al., 1964; Heisler and Wilson, 1962]. Also, Russian releases at Novaya Zemlya, U.S.S.R. in October 1961 produced E and F region irregularities in the Scandinavian area [Stoffregen, 1972].

Although much of the scintillation observations have been restricted to VHF [Utlaut, 1974], recent results of equatorial scintillation in the 1-6 GHz regime [Craft and Westerland, 1972; Taur, 1973; Utlaut, 1974] show that one cannot merely go to higher frequencies to escape scintillation effects. Much of the scintillation observations come from ground based receivers (mostly in VHF and UHF regime, with a small amount of SHF data) although limited in situ measurements [Dyson, et al., 1974] are also available. These observations have provided valuable information about scintillation phenomena; however, the effects of variation of signal parameters important for system design or systems performance prediction is almost nonexistent. More fundamental is the lack of understanding of the basic physical processes involved in the formation of ionospheric irregularities which cause scintillation. The limited amount of observational data coupled with limited theoretical understanding make it impossible to now predict how communications systems will perform in natural or artificial scintillation environments. For the high data rate, broadband transmitters now planned for Navy, other DOD and commercial communication satellites it is imperative to understand scintillation phenomena, for severe scintillations over several seconds can mean loss of information (message).

Ionospheric physicists, systems designers, modelers and wave propagationists have noted [Utlaut, 1974; Fremouw, 1974] the need for theoretical studies to determine the underlying mechanisms responsible for ionospheric scintillation so that a true predictive capability can be achieved. The inadequacy of empirical modeling [Fremouw, 1974] of ionospheric scintillation, the recent in situ measurements of ionospheric scintillation [Dyson et al., 1974], and advances in theoretical and computational plasma physics [Perkins, 1973; Völk and Haerendel, 1971; Zabusky et al., 1973; Lloyd and Haerendel, 1973; Goldman et al., 1974; Scannapieco et al., 1974; Sudan et al., 1973; McDonald et al., 1974] make this a propitious time for further theoretical and numerical studies of scintillation phenomena. The theoretical and computational programs that we have at NRL are at a state, where we can generate detailed information on the causes and structure of ionospheric irregularities. The results of this work can provide a basis for interpretation of experimental data; suggest new experiments; aid in the design of new communication systems and provide a framework within which to improve the performance of existing systems.

### III. SIMPLIFIED SCINTILLATION GEOMETRY

Before proceeding with a description of examples of the work we are doing on ionospheric irregularities, we will give a brief discussion, albeit simple, on what is involved in scintillation phenomena. The interested reader can obtain a more complete understanding of propagation through ionospheric irregularities by consulting the references [Rufenach, 1972, 1974; Bowhill, 1961; Briggs and Parkin, 1963; Budden, 1965; Cronyn, 1970; Lovelace et al., 1970; Salpeter, 1967; Tatarski, 1961]

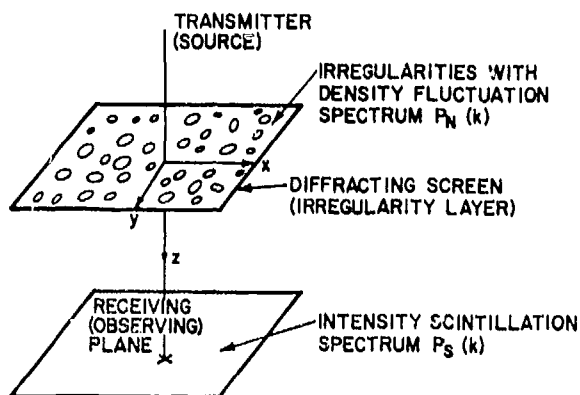


Fig. 1 Simplified scintillation geometry. A signal traveling in the z direction is incident on a layer of ionospheric irregularities (represented by ellipses). The scintillation power spectrum in the observing plane is related to the power spectrum of the irregularities in the irregularity layer.

Figure 1 shows a simplified view of what happens in scintillation phenomena. We consider a plane wave (signal) propagating in the z direction where it is emitted by a transmitter (source) and enters a layer where there are irregularities, i.e., density fluctuations, which are shown by ellipses (swiss cheese) in the x-y diffracting plane. On emergence from the irregularities layer, properties of the wave front are related to properties of the irregularities. In most cases of interest absorption in the layer is negligible. Also, the irregularity layer can usually be replaced by an equivalent thin screen of negligible thickness. Field fluctuations near the screen are of phase only; however, amplitude scintillations develop as the wave travels away from the screen. For these conditions the relationship between the intensity scintillation spectrum,  $P_S(k)$ , and the irregularities density fluctuation spectrum,  $P_N(k)$  is [Rufenach, 1974]

$$P_S(k) = 8\pi L(r_e \lambda)^2 P_N(k) \sin^2(k/k_f) \quad (1)$$

where  $L$  is the equivalent layer thickness,  $r_e$  is the classical radius of the electron ( $r_e = e^2/mc^2$ ),  $\lambda$  is the radio wavelength of the signal,  $k$  is the wavenumber of the irregularity of interest ( $k^2 = k_x^2 + k_y^2$ ),  $k_f$  is the Fresnel wavenumber ( $k_f^2 = 4\pi/\lambda z$ , where  $z$  is the mean height of the scattering layer). Equation 1 gives the expected two-dimensional diffraction pattern at the receiving plane.

Indeed the integral,  $2\pi \int_0^\infty P_S(k) k dk$  is

basically the scintillation index  $S_h$  used by ionospheric workers. The important point is that there exists a simple relationship between  $P_S(k)$  and the power spectrum  $P_N(k)$  of the irregularities (even for thick screens; see Rufenach, 1972).  $P_S(k)$  determines the diffraction pattern and  $P_N(k)$  determines  $P_S(k)$ . Thus, one of the things that we wish to find out from the theoretical and numerical simulation studies is the power spectrum,  $P_N(k)$ , of the density fluctuations. To date,  $P_N(k)$  is assumed by ionospheric workers (based on at best limited data on scintillation phenomena). To obtain  $P_N(k)$  from theoretical and numerical simulation analysis will aid in giving predictive capability for the scintillation problem.

### IV. IRREGULARITIES STUDIES - PARTICULAR EXAMPLES

Before proceeding to discuss our work on the type II E region electrojet instability and F region irregularities, as examples, in sections A and B below we will briefly outline the methods of solution which are involved and basically common to all three processes A, B, and C mentioned in Section I. The methods involved are (1) large scale numerical simulation of the appropriate system of coupled nonlinear differential equations which are derived theoretically and thought to represent the process being studied; (2) the geometry is basically two-dimensional, i.e., the dimension parallel to the ambient magnetic field,  $B_0$ , is integrated out; (3) there are continuity equations for the density and/or cross field (Pedersen) conductivity of the appropriate electron and ionic species; (4) momentum equations for the appropriate species; and (5) a potential-like equation arising from the fact that the divergence of the current is zero ( $\nabla \cdot \underline{J} = 0$ ).

The two dimensional geometry is a fairly good representation of the processes being studied. Full three dimensional studies would tax the capability of present day computers. The momentum equation in (4) usually reduces to an algebraic equation in which the velocity of the particular species is related to the transverse electric fields (and/or neutral winds) and ambient magnetic field by means of cross field mobilities. Assuming the electric

fields derivable from a potential (the electrostatic approximation valid for the ionosphere) results in a potential-like equation when the velocities are inserted into the current condition,  $\nabla \cdot \mathbf{J} = 0$ . All these ideas will become clearer in sections A and B below.

#### A. Equatorial E Region Electrojet - Type II Instability

To serve as a background for this section, Figure 2 shows a model of the daytime electrojet (see references Sugiura and Cain, 1966;

Sugiura and Poros, 1969) and how the radar views it. The electrojet is a highly conducting layer usually between 100 and 110 km located at the geomagnetic equator (within  $\pm 2^\circ$ ). The eastward field,  $E_D$ , results from atmospheric tidal motion and the vertical electric field,  $E_P$ , is the resulting vertical polarization field which suppresses vertical currents. This condition gives  $E_P = (\sigma_H / \sigma_P) E_D$ , where  $\sigma_H$  and  $\sigma_P$  are the Hall and Pedersen conductivities respectively and  $\sigma_H / \sigma_P \sim 20-30$ . It is this vertical field which drives the electrojet by Hall currents. Since the electron-neutral collision frequency is much less than the electron cyclotron frequency ( $\nu \ll \Omega$ ) and the ion-neutral collision frequency is much greater than the ion cyclotron frequency ( $\nu_i \gg \Omega_i$ ); ions are essentially at rest with respect to

the neutrals), the resulting electron-ion drift velocity is  $\mathbf{V}_0 \sim c\mathbf{E}_P/B$  (cgs units) and in the westward direction. This is essentially the electron drift so that the current is in the eastward direction. Also there is a positive vertical electron density gradient with a scale height  $(N/dN/dz) \sim 6-10$  km. (Note: at night the current reverses direction and the density gradient is irregular and changes sign within the layer.) The reason why the electrojet is localized in altitude is that above this region while  $N_0$  is increasing the collision frequency is decreasing and so the conductivity is low. However, below this region while the collision frequency is increasing the electron density is decreasing and so again the conductivity is low. The reason why the electrojet is located at the geomagnetic equator is deduced by considering the concept of a stratified ionosphere and the concept of layered conductivity [Baker and Martyn, 1953]. Basically the requirement that there be no vertical current reduces the  $3 \times 3$  conductivity tensor to a  $2 \times 2$  tensor representing a layered conductivity with horizontal flow. Into such an expression comes the dip angle (angle between the magnetic field and the horizontal direction). It can be shown that when the dip angle is zero the cross field conductivity becomes a maximum. Referring to Fig. 2 the radar observes the electrojet by backscatter so that a wave launched with wavevector  $\mathbf{k}_0$  sees a return with  $-\mathbf{k}_0$  and the relation between the radar wavelength and the irregularity wavelength is  $2|\mathbf{k}_0| = |\mathbf{k}_1|$  where  $k = 2\pi/\lambda$  and  $\lambda$  is the wavelength. (So that the radar wavelength is twice the wavelength of the irregularity that it samples). The radar at Jicamarca, Peru where the observations are made operates in the 15 MHz-150 MHz range (irregularity wavelengths 10 - 1 meter).

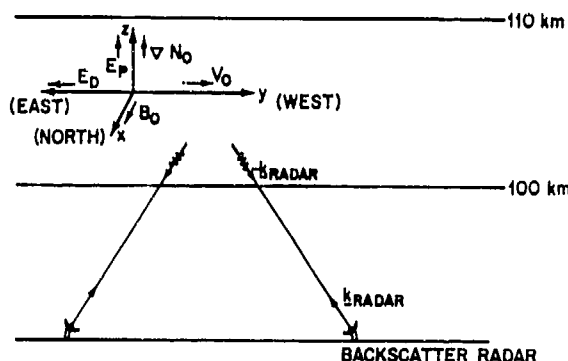


Fig. 2 Model of daytime equatorial electrojet geometry and observing backscatter radar. The atmospheric tidal electric field  $E_D$ , creates a vertical polarization electric field,  $E_P$ , which drives the relative electron-ion drift velocity,  $\mathbf{V}_0$ , by the Hall effect. This creates an eastward electrojet current. This region of high conductivity is located in the E region ionosphere usually between 100 and 110 km. The earth's ambient magnetic field is taken constant and in the x direc-

tion. There are two types of instabilities, producing density fluctuations, associated with the electrojet configuration shown in Fig. 2. In this paper we will be addressing the type II instability. This is excited when the electron current across  $B_0$  is less than the ion sound speed (i.e.,  $V_0 < \text{ion sound speed}$ ; type I occurs when  $V_0 > \text{ion sound speed}$ ). This instability has no velocity threshold and travels at the drift velocity of the electrons. The observed backscatter is generally believed to be due to this gradient drift instability [Maeda et al., 1963; Knox, 1964; Reid, 1968, Register and D'Angelo, 1970; Whitehead, 1971]. We will shortly see, however, that for the radar wavelengths observed, linear instability

theory cannot directly explain the phenomena. The basic equations governing the dynamics of the electrojet are [Sudan et al., 1973; McDonald et al., 1974 a,b]

$$\frac{\partial n_e}{\partial t} + \nabla \cdot (n_e \mathbf{V}_e) = 0 \quad (2)$$

$$\frac{e}{m_e} \left( \mathbf{E} + \frac{\mathbf{V}_e}{c} \times \mathbf{B}_0 \right) + \frac{U_e^2}{n_e} \nabla n_e + \nu_e \mathbf{V}_e = 0 \quad (3)$$

$$\frac{\partial n_i}{\partial t} + \nabla \cdot (n_i \mathbf{V}_i) = 0 \quad (4)$$

$$\left( \frac{\partial}{\partial t} + \mathbf{V}_i \cdot \nabla \right) \mathbf{V}_i = - \frac{U_i^2}{n_i} \nabla n_i + \frac{e}{m_i} \mathbf{E} - \nu_i \mathbf{V}_i \quad (5)$$

$$n_e = n_i = n \quad (6)$$

where the subscripts e and i refer to electrons and ions,  $U_e$  and  $\nu_e$  are the electron thermal speed and electron-neutral collision frequency, respectively,  $\mathbf{E} = -\nabla \phi$  is the electric field (electrostatic assumption),  $\mathbf{B}_0$  is the earth's magnetic field (assumed constant and in the x direction),  $n$  is density and  $\mathbf{V}$  is bulk velocity. The inclusion of the left hand side Eq. (5), i.e., ion inertia, is not really necessary for type II studies. However, it is important for type I studies ( $V >$  ion sound speed) and we retain it for generality. Equation (3) contains magnetic terms ( $\nu_e \ll \Omega_e$ ) showing the electrons are tied to the field lines, while Eq. (5) exhibits no such terms ( $\nu_i \gg \Omega_i$ ) showing the ions to be tied to the neutrals.

A linear stability analysis of Eqs. (2)-(6) with perturbations assumed to be of the form  $\exp i(k_y y - \omega t)$ , where  $\omega = \omega_r + i\gamma$  (so that positive  $\gamma$  represents the growth rate), has been performed. For electrojet parameters [Sudan et al., 1973; McDonald et al., 1974 a, b],  $\Omega_e = 5 \times 10^5 \text{ sec}^{-1}$ ,  $\nu_e = 4 \times 10^4 \text{ sec}^{-1}$ ,  $\nu_i = 2.5 \times 10^3 \text{ sec}^{-1}$ ,  $C_s^2 = 10^5 \text{ m}^2/\text{sec}^2$ , (where  $C_s^2 = U_i^2 + U_e^2 m_e/m_i$ )  $V_0 = 100 \text{ m/sec}$  ( $V_0 < C_s$ , ion sound) and  $(n/dn/dz) = 6 \times 10^3 \text{ a}$ , unstable gradient drift waves result in the y direction with a minimum wavelength of  $\sim 30$  meters (see Fig. 3). However, radar backscatter results [Balsley and Farley, 1973] show unstable waves, i.e., enhanced density fluctuations  $\sim 3$  meters. In order to resolve this dilemma, we have studied the nonlinear evolution of the electrojet equations (2) - (6), in the y-z plane, by numerical simulation [McDonald et al., 1974 a, b].

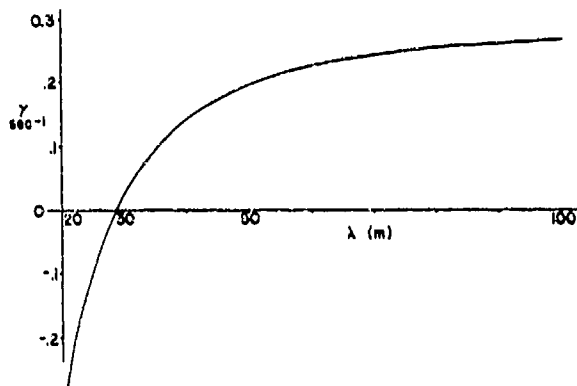


Fig. 3 Growth rate  $\gamma$  for horizontally propagating modes vs wavelength  $\lambda$  from linear analysis of gradient drift instability for equatorial electrojet. Positive  $\gamma$  indicates growth. For electrojet parameters,  $V_0 = 100 \text{ m/sec}$ ,  $\nu_e = 4 \times 10^4 \text{ sec}^{-1}$ ,  $\nu_i = 2.5 \times 10^3 \text{ sec}^{-1}$  and  $\Omega_e = 5 \times 10^5 \text{ sec}^{-1}$ , only waves greater than 28 meters are unstable.

Before proceeding with the numerical simulation, Eqs. (2) - (6) are recast using

$$\nabla \cdot \mathbf{J} = e \nabla \cdot [n (\mathbf{V}_i - \mathbf{V}_e)] = 0 \quad (7)$$

As stated previously Eq. (7) results in a Poisson-like equation by algebraically solving Eq. (3) for  $\mathbf{V}_e$  and using an effective potential,

$$\phi \equiv \frac{e}{m_e} \phi - U_e^2 \ln n \quad (8)$$

The resulting equation for  $\phi$  is

$$\nabla^2 \phi + \left[ \nabla \ln n - \frac{\Omega_e}{V_e} \times \nabla \ln n \right] \cdot \nabla \phi = \left( \nu_e + \frac{\Omega_e^2}{V_e^2} \right) \frac{1}{n} \nabla \cdot (n \mathbf{V}_i) \quad (9)$$

where  $\Omega_e = e B_0 / m_e c$ .

An initial density perturbation [Sudan et al., 1973; McDonald et al., 1974 a,b] of the form  $\delta n/n_0 = -0.03 \sin k_y y - 0.01 \sin k_z z$ , where  $k_y = k_z = 2\pi/72$  meters is put into the system at  $t = 0$  (see Fig. 4) and periodic boundary conditions are employed. We are essentially looking at a slice of the electrojet in the y-z plane which is  $75 \times 75$  meters. In Fig. 4 the density plot is on the left and

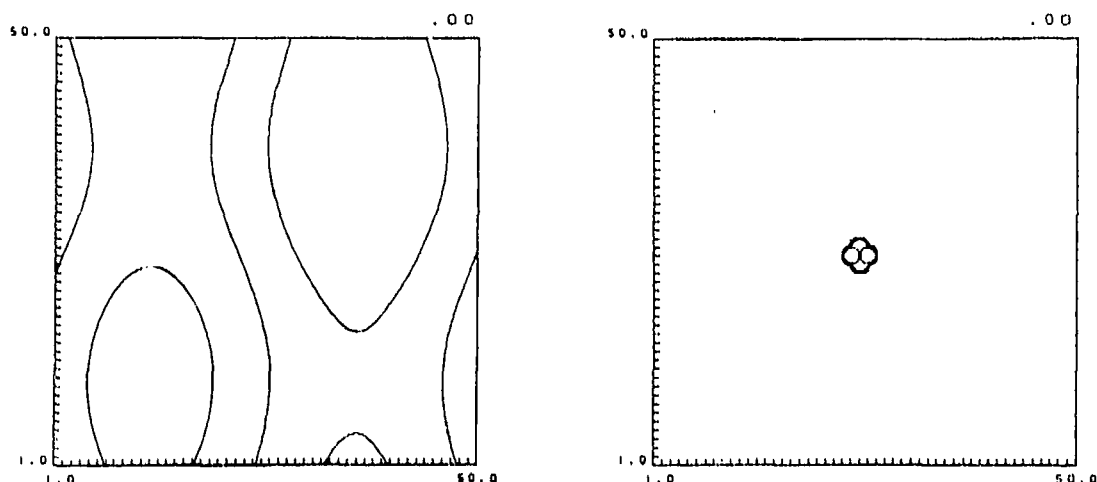


Fig. 4 Plasma density contours (left) in  $(y, z)$  space and spectral power contours (right in  $(k_y, k_z)$  space at  $t = 0$ . The isodensity contour spacing is 2.5% of ambient. The tick marks on the axes ( $z$  is vertical,  $y$  horizontal) are grid point locations. The  $50 \times 50$  grid points correspond to 0-75 meters (1.5 meter spacing between grid points). This is a slice of the electrojet and models the geometry depicted in Fig. 2. On the right, contours of constant  $|A(k)|^2$  are spaced in decades. The spectral grid interval is  $2\pi/72$  meters. The symmetry about the  $k$  origin (at the center of the plot) is due to the fact that  $A(k)$  is the Fourier transform of a real function.

the diagram accompanying it is a spectral power plot in two dimensional  $k$ -space. This spectral plot is a contour plot of  $|A(k_y, k_z)|^2$  where  $A$  is the complex Fourier transform of  $\delta n/n \equiv (n - n_0)/n_0$  (see McDonald et al., 1974b for more details). The initial condition consists of one delta-function spike on each of the positive  $y$  and positive  $z$  axes, corresponding to the two discrete Fourier modes of the initial density perturbation. We then numerically integrate Eqs. (4), (5) and (9) and carry it forward in time (see McDonald et al., 1974 a,b for a more complete discussion of the procedure used) and what results is a quasi-final state of turbulence as depicted in Fig. 5. The diagram accompanying the density plot is once again the  $k$ -space plot of  $|A(k_y, k_z)|^2$ . These numerical simulations were carried out on an IBM 360/195 using 240K bytes of core and the running time was 15 minutes.

The density contours depicted in Fig. 5 is the type of turbulent layer that a signal traversing the E region electrojet would see. The relevant information from the density contours is obtained by taking a direction average of  $|A(k)|^2$  for all  $k$  vectors with magnitudes between  $k$  and  $k + 2\pi/72$  meters. This is the power spectrum, i.e., the  $P_N(k)$  we spoke about in section III and is shown in Fig. 6. We note that this square of the density fluctuation spectral amplitude follows a power law for the shorter wavelengths which

agrees well with rocket observations through the equatorial electrojet [Prakash et al., 1969, 1970]. It is of interest to note that in situ measurements [Dyson et al., 1974] of F region irregularities and ground observed scintillation measurements [Rufenach, 1972, 1974] show similar power law dependence of the spectrum.

**Summary.** Type II electrojet results can be summarized as follows: (1) long wavelength ( $> 30$  meters) horizontally propagating gradient drift instabilities generate short wavelength ( $\sim 3$  meters) vertically propagating instabilities; (2) the quasi-final state is a highly turbulent two dimensional state with upward and downward moving irregularities with speeds of the order of the horizontal drift speeds; and (3) the power spectrum for density fluctuations in the short wavelength irregularities goes like  $k^{-3.5}$ . Result (1) agrees with the high resolution radar backscatter data [Balsley and Farley, 1973] and our basic theoretical ideas [Sudan et al., 1973; McDonald et al., 1974a,b]. It basically shows a cascading of energy from longer, linearly unstable wavelengths to shorter, linearly stable wavelengths. Result (2) also agrees well with the radar backscatter data [Balsley and Farley, 1973]. Result (3) agrees well with the rocket observations [Prakash et al., 1969, 1970] and dimensional arguments [Ott and Farley, 1974].



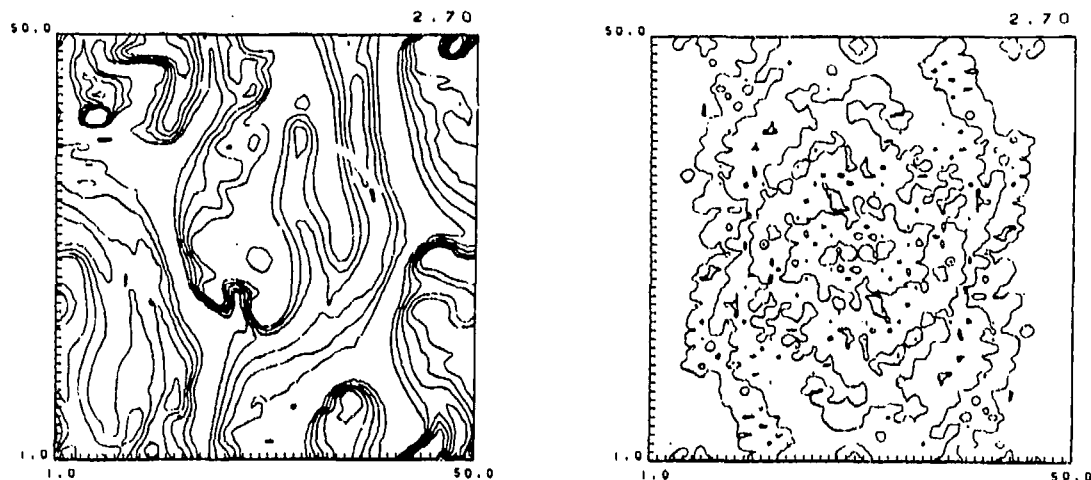


Fig. 5 Plasma density contours (left) in  $(y, z)$  space and spectral power contours (right) in  $(k_y, k_z)$  space at  $t = 2.7$  sec. The isodensity contour spacing is 2.5% of ambient. The tick marks on the axes ( $z$  is vertical,  $y$  horizontal) are grid point locations. The  $50 \times 50$  grid points correspond to 0-75 meters (1.5 meter spacing between grid points). This is a slice of the electrojet and models the geometry depicted in Fig. 2. On the right, contours of constant  $|A(k)|^2$  are spaced in decades. The spectral grid interval is  $2\pi/72$  meters. The symmetry about the  $k$  origin (at the center of the plot) is due to the fact that  $A(k)$  is the Fourier transform of a real function.

results (dots). The fall off from the line below about 5 meters is due to grid size resolution capabilities in this study.

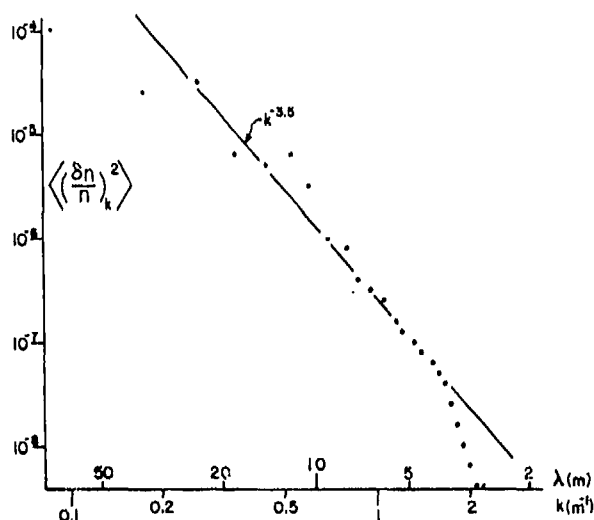


Fig. 6 Direction averaged power spectrum for type II electrojet irregularities taken from numerical simulation at 2.7 sec. Values of  $|A(k)|^2$  are averaged within concentric bands in discrete  $k$ -space and plotted on log-log coordinates as function of  $k$ , the mean band radius. The solid line is a least squares best fit to the simulation

This is the first numerical simulation ever done of the type II electrojet phenomena and has aided considerably in the understanding of such phenomena. Further simulations are on going to obtain finer resolution for the shorter wavelengths (see Fig. 6 and comments therein) and also increasing  $V_0$  so that the intermediate regime between type II and type I can be studied. The capability which has been developed for this problem can also be used to study the stability of the auroral electrojets.

#### B. F Region Irregularities

We will now discuss the work we have been doing on F region irregularities. Recently, Perkins [1973] set forth model equations in an attempt to describe the nighttime F region. Within the context of these equations and a particular form of the F region equilibrium (no gradients in total ion content or Pedersen conductivity transverse to the geomagnetic field) which satisfied these equations, Perkins performed a linear stability analysis. The analysis showed that if in addition to the supporting equilibrium eastward electric field, a north-south field existed then the nighttime F region would be unstable. The instability took the form of rising and falling sheets of ionization and had a growth rate  $\gamma \sim 3 \times 10^{-4} \nu_{in}^{-1}$  where  $\nu_{in}$  is the

ion-neutral collision frequency at the F region peak. Perkins [1973] argued that the results of his instability mechanism agreed with several of the temperate latitude spread F phenomenological observations [see Herman, 1966 for a thorough review on spread F]. Perkins noted, however, that his spread F instability mechanism would lead to Pedersen conductivity gradients transverse to the magnetic field and this in turn should be unstable to the usual  $\mathbf{E} \times \mathbf{B}$  gradient drift instability [Simon, 1963, 1970; Linson and Workman, 1970].

As an initial starting point for our F region irregularities studies we decided to investigate the nonlinear development of Perkins' [1973] nighttime F region equations, but for a spatially varying ionospheric equilibrium. This basically extends Perkins' work in two respects. First, we allow for east-west gradients in the Pedersen conductivity (this also satisfies Perkins' equations as we shall show) rather than assume the ionosphere to be constant transverse to the magnetic field. Second, we will look at the nonlinear dynamical evolution of the nighttime F region from this equilibrium (Perkins with his equilibrium only performed a linear stability analysis).

Instead of totally rederiving Perkins' set of equations we will outline how they were obtained. The geometry of the calculation is depicted in Fig. 7. The relation between the coordinates (upper part of figure) are as follows

$$h = x \cos D - z \sin D \quad (10)$$

$$k = x \sin D + z \cos D \quad (11)$$

Before proceeding to derive the equations Perkins makes the following assumptions: (1) the magnetic field is uniform, but makes a dip angle  $D$  with the horizontal; (2) the effect of gravity in pulling plasma down along the magnetic field line and in creating currents in the  $\mathbf{g} \times \mathbf{B}$  direction (eastward) is included; (3) the neutral atmosphere consists of a single species horizontally stratified and distributed in altitude according to a constant scale height  $H_n$ ; (4) electric fields and neutral winds give rise to Pedersen currents which by  $\mathbf{j} \times \mathbf{B}$  forces can support the ionosphere; (5) recombination and ion drag are neglected; (6) the plasma is high enough so that  $\Omega_i \gg \nu_i$  and the only important currents are Pedersen currents; (7) E region contributions to the ionospheric conductivity are neglected; and (8) the ions and electrons are isothermal.

The starting point are essentially equations (2)-(6) except that Eq. (5) now contains a  $\mathbf{v}_i \times \mathbf{B}$  term and a gravitational term  $\mathbf{g}$  on the right hand side and the left hand side is set equal to zero (neglect inertial terms).

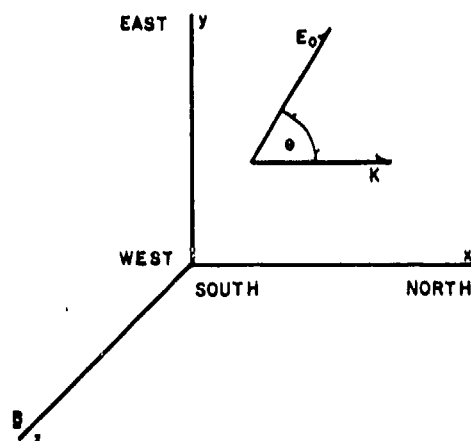
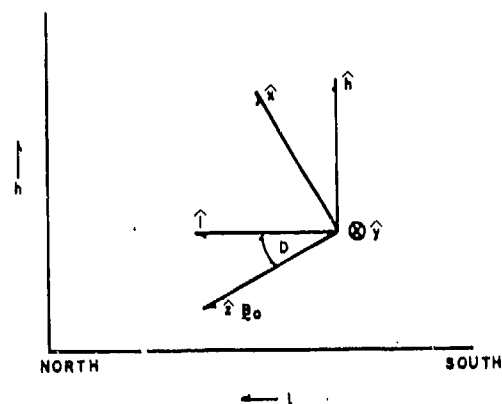


Fig. 7 Geometry for F region studies. (a) An eastward view in a northern hemisphere magnetic meridian plane. The unit vectors  $\hat{i}$  and  $\hat{h}$  are in the horizontal and vertical directions, respectively; whereas, the unit vectors  $\hat{j}$  and  $\hat{k}$  are parallel and perpendicular to the geomagnetic field  $\mathbf{B}$ .  $D$  is the dip angle which the magnetic field makes with the horizontal. (b) Orientation of ambient electric field,  $\mathbf{E}_0$  and wavenumber vector,  $\mathbf{k}$  for the initial perturbation considered in F region irregularities. There is also a zeroth order long wavelength variation in the Pedersen conductivity in the east-west direction.

One can then solve for the transverse velocities algebraically in terms of the fields and this becomes, remembering the geometry depicted by Fig. 7

$$\begin{aligned} \underline{v}_{\perp 1} = & \frac{c}{B} \frac{\kappa_1}{1+\kappa_1^2} \left[ \underline{E}_{\perp} + \frac{m_1 g_{\perp}}{e} - \frac{m_1 U_1^2}{e} \frac{\nabla n_1}{n_1} \right] \\ & + \frac{c}{B^2} \frac{\kappa_1^2}{1+\kappa_1^2} \left[ \underline{E}_{\perp} + \frac{m_1 g_{\perp}}{e} - \frac{m_1 U_1^2}{e} \frac{\nabla n_1}{n_1} \right] \times \underline{B} \end{aligned} \quad (12)$$

where  $\kappa_1 = \Omega_1 / \nu_1$ ,  $\Omega_1$  is the ion cyclotron frequency,  $\nu_1$  is the ion-neutral collision frequency,  $\perp$  denotes perpendicular to the magnetic field,  $m_1$  is the ion mass,  $g$  is gravity and  $e$  is the electronic charge. For the  $z$  component of the ion velocity we have

$$v_z = \frac{g \sin D}{\nu_1} - \frac{U_1^2}{\nu_1} \frac{1}{n_1} \frac{\partial n_1}{\partial z} \quad (13)$$

Then we set  $\underline{E}_{\perp} = -\nabla_{\perp} \phi$ , set  $m_1 U_1^2 = \frac{1}{2} m_1 v_a^2 = T$  (where  $T$  is in energy units), and set the relation between the potential  $\phi$  and the total electrostatic potential  $\psi$  as

$$\phi = \psi + \frac{T}{e} \ln(n/n_0) \quad (14)$$

where  $n_0$  is a reference electron density. If we use the quasi-neutrality condition Eq. (6), take

$$\underline{v}_{\perp e} = \frac{-c \nabla \phi \times \underline{z}}{B} \quad (15)$$

use Eqs. (4) and (7), remembering  $\Omega_1 \gg \nu_1$ , set  $\nu_1 \propto \exp[-z/H_n]$  which is assumption (3), and noticing because of the geometry that  $\nabla_{\perp}$  does not commute with  $\nu_1$ , we obtain by integrating Eqs. (4) and (7) along the  $z$  (magnetic field) direction

$$\frac{\partial N}{\partial t} + \frac{g}{\Omega_1} \cos D \frac{\partial N}{\partial y} - \nabla_{\perp} N \cdot \frac{\nabla_{\perp} \phi \times \underline{z} c}{B} = 0 \quad (16)$$

$$\begin{aligned} \nabla_{\perp} \cdot (\Sigma \nabla_{\perp} \phi) - \frac{\partial N}{\partial y} \frac{g \cos D}{\Omega_1} + \frac{2T}{e} \nabla_{\perp}^2 \Sigma \\ + \frac{\partial \Sigma}{\partial x} \cos D \left( \frac{2T}{e H_n} + \frac{m_1 g}{e} \right) = 0 \end{aligned} \quad (17)$$

In these equations we have introduced the two moments

$$N(x, y) = \int n dz \quad (18)$$

$$\Sigma(x, y) = \int dz \frac{n \nu_1 e c}{\Omega_1 B} \quad (19)$$

where  $\Sigma$  is the Pedersen conductivity. The moment equation for  $\Sigma$  is obtained by multiplying Eq. (4) by  $\nu_1 e c (\Omega_1 B)^{-1}$  and then integrating over  $z$  to obtain

$$\begin{aligned} \frac{\partial \Sigma}{\partial t} + \nabla_{\perp} \Sigma \cdot \left( \frac{g \times \underline{z}}{\Omega_1} - \frac{\nabla \phi \times \underline{z} c}{B} \right) \\ = \frac{e c \sin^2 D g N}{\Omega_1 B H_n} + \Sigma \frac{\partial \phi}{\partial y} \frac{c \cos D}{B H_n} \end{aligned} \quad (20)$$

Equations (16), (17), and (20) are two dimensional ( $x$ - $y$  plane). For a more complete description of the derivation of these equations see Perkins [1973].

We can then show that an equilibrium satisfying these equations with no north-south ( $x$ ) variation, but only an east-west ( $y$ ) variation exists. To do this we look at the equilibrium in a frame drifting with a velocity

$$\underline{v}_y = \frac{g \cos D}{\Omega_1} - \frac{c E_{ox}}{B} + \frac{2T}{e} \frac{c \cos D}{B H_n} \quad (21)$$

where the subscript zero refers to equilibrium. We then find, after integrating Eq. (17) once in  $y$  and then substituting into Eq. (20), that

$$\frac{\partial \phi}{\partial y} = - \frac{2T}{e} \frac{1}{\Sigma_0} \frac{\partial \Sigma_0}{\partial y} - \frac{N_0}{\Sigma_0} \frac{g \sin^2 D}{\Omega_1 \cos D} \quad (22)$$

This is a condition on the east-west component of the current and involves a Pedersen conductivity gradient in the east-west direction. If one neglects the small variation in  $N_0$  we have  $\partial N_0 / \partial t = 0$ .

If we now perform a linear perturbation analysis about this equilibrium with perturbed quantities proportional to  $\exp i[k_x x - \omega t]$  where  $\omega = \omega_r + i\gamma$  we find a growth rate

$$\begin{aligned} \gamma = \frac{c}{B} \left( \frac{B g \cos D}{\Omega_1 c} - E_{ox} \right) \frac{1}{\Sigma_0} \frac{\partial \Sigma_0}{\partial y} - \\ - \frac{c}{B H_n} E_{oy} \cos D \frac{\partial \Sigma_0}{\partial y} \end{aligned} \quad (23)$$

where we have

$$E_{oy} = \frac{eg \sin^2 D}{\Omega_1 \cos D} \frac{N_o}{\Sigma} \quad (24)$$

and we have taken

$$\Sigma_o = \bar{\Sigma} + \Sigma_1(y) \quad (25)$$

with  $\Sigma_1(y) < \bar{\Sigma}$ . Equation (25) shows that the equilibrium is made up of a spatially averaged homogeneous part,  $\bar{\Sigma}$  and an east-west (y) spatial variation  $\Sigma_1(y)$ . From Eq. (23) we see that the condition for a perturbation to grow in time is

$$\frac{c}{B} \left( \frac{gB \cos D}{\Omega_1 c} - E_{ox} \right) \frac{1}{\Sigma_o} \frac{\partial \Sigma_o}{\partial y} > \frac{c}{BH_n} E_{oy} \cos D \frac{\bar{\Sigma}}{\Sigma_o} \quad (26)$$

Consequently, we have shown that: (1) an equilibrium can exist when an east-west gradient in the Pedersen conductivity is present, along with the supporting east-west electric field; and (2) that perturbations about the equilibrium, whose wave vectors are in the north-south direction will grow provided there is a north-south electric field that is large enough (Eq. (26)).

The numerical simulations were initialized as follows:  $\Sigma_o(y) = \bar{\Sigma} + \bar{\Sigma} e^{-2} \sin k_y y$ ,  $k_y = 2\pi/30$  km,  $E_{oy} = N_o eg \sin^2 D / (\Omega_1 \cos D \bar{\Sigma})$ ,  $E_{ox} = \tan \theta E_{oy}$ ,  $\nabla \phi = -E_o + \nabla \phi^1$  with the initial perturbation taken as (see Fig. 1 for the geometry)  $\Sigma^1(x) = \bar{\Sigma} e^{-4} \sin k_x x$ ,  $k_x = 2\pi/10$  km. We have that  $\Sigma(x,y) = \Sigma_o + \Sigma^1(x)$ .

The moment Eqs. (17) and (20) can be rewritten, after transforming to a frame moving with the  $(E_o \times B)(c/B^2) + (g \times B)/(\Omega_1 B)$  drift velocity and defining,

$$\tilde{\Sigma} = \frac{\Sigma(x,y)}{\bar{\Sigma}} - \frac{\bar{\Sigma}}{\bar{\Sigma}} = \frac{\delta \Sigma}{\bar{\Sigma}} \quad (27)$$

as:

$$\frac{\partial \tilde{\Sigma}}{\partial t} - \nabla \tilde{\Sigma} \cdot \left( \nabla \phi^1 \times \frac{c}{B} \right) = \tilde{\Sigma} \left( \frac{\partial \phi^1}{\partial y} - E_{oy} \right) \frac{c \cos D}{BH_n} + \frac{\partial \phi^1}{\partial y} \frac{c \cos D}{BH_n} \quad (28)$$

$$\nabla^2 \phi^1 + \frac{\nabla \tilde{\Sigma} \cdot \nabla \phi^1}{1 + \tilde{\Sigma}} + \frac{\partial \tilde{\Sigma}}{\partial x} \cos D \left( \frac{2\tau}{eH_n} + \frac{m_1 g}{e} \right) + \frac{2\tau}{e} \frac{\nabla^2 \tilde{\Sigma}}{1 + \tilde{\Sigma}} - \frac{E_o}{1 + \tilde{\Sigma}} \cdot \nabla \tilde{\Sigma} = 0 \quad (29)$$

In the simulations the integrated ion number density was chosen to be constant in the spirit of the fact that there is no way to change the plasma content of the flux tube in the absence of ionization and recombination (see Perkins, 1973). The system of Eqs. (28) and (29) were solved on a rectangular mesh (x,y) using a grid  $32 \times 32$  km with  $\Delta x = \Delta y = 1$  km. An IBM 360/195 computer was used with 275K bytes of core and a typical running time of 5 minutes. The parameters chosen for the simulation were:  $D = 45^\circ$ ,  $N_o/\Sigma_o = 5 \times 10^{13}/.45 = (1/9) \times 10^{13}$  (mhos-cm<sup>2</sup>)<sup>-1</sup> resulting in  $v_i/\Omega_i = 2.8 \times 10^{-4}$ ,  $B = 0.5$  gauss,  $m_1 = 16 m_p$  ( $m_p$  is the proton mass),  $T = 916^\circ$  K, and  $H_n = 55$  km. The ionospheric parameters were chosen to correspond to an altitude  $\sim 350$  km (see Johnson, 1961; and Rishbeth and Garriott, 1969).

Figure 8 shows the time evolution of the Pedersen conductivity contours for the case in which the north-south mode is growing, i.e., for which

$$E_{ox} H_n = 9 E_{oy} \left| -\frac{1}{\Sigma_o} \frac{\partial \Sigma_o}{\partial y} \right|_{\max}^{-1}$$

For this case the linear growth rate is given approximately by  $\gamma = - (cE_{ox}/B) (\partial \Sigma_o / \partial y) (1/\Sigma_o)$ . Consequently, there should only be growth in those regions where the Pedersen conductivity gradient is negative and this is borne out in Fig. 8b in the region where the initial sinusoidal y variation is favorable. Figure 8c shows that, at late times, smaller scale structure develops from the initial large scale structure. This shows that there is a cascading of energy from long wavelength modes to shorter wavelength modes. This cascading of energy and an attendant power law for the power spectrum of the fluctuations (see Fig. 9) is reminiscent of the computer simulation results for type II irregularities presented in section IV A. In those E region studies and the present F region studies the basic generating mechanism is a form of the  $E \times B$  gradient drift instability. However, in the two cases the dynamical equations governing each region are different. From Fig. 8c we see that the late time structure looks sheet-like with orientation more in the east-west direction. Figure 9 represents a direction averaged power spectrum for the square of the amplitude of the Fourier transform of  $\delta \Sigma / \bar{\Sigma}$  corresponding to Fig. 8c. The straight line with a power law  $k^{-2}$  represents a least

squares fit to the simulation results. The reason that the dots fall off the straight line at short wavelengths is due to computer resolution capabilities in the present simulation.

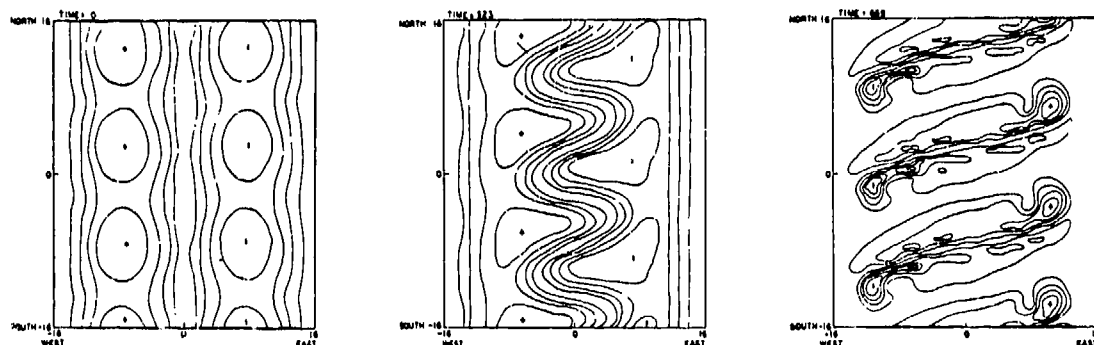


Fig. 8 Iso-Pedersen conductivity contours at times (a) 0, (b) 323 sec, and (c) 669 sec for the strong instability considered in the study. The contour spacing at  $t = 0$  is 3, 6, 9, and 12 above and below the spatially averaged constant background  $\Sigma$ . The plus and minus represent extremum above and below this background. As time progresses the contour values become larger. The frames represent a  $32 \times 32$  km slice of the F region which we have studied.

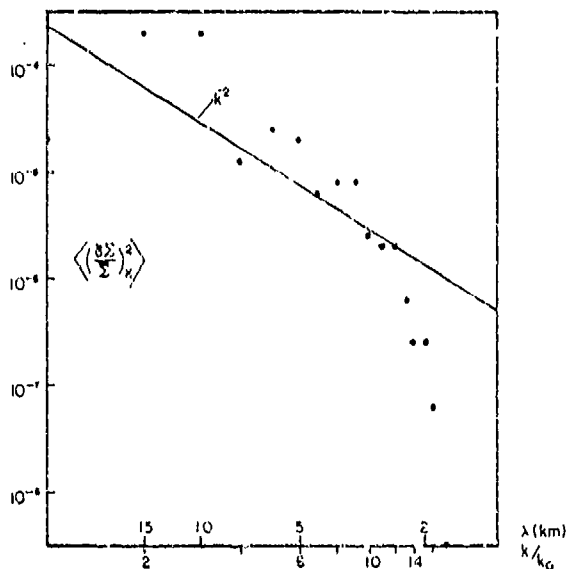


Fig. 9 Direction averaged power spectrum for the Pedersen conductivity fluctuations as obtained from Fig. 8c. The averaging procedure as in the E region electrojet studies was performed (see Fig. 6 and comments in text).  $k_0$  is the wavenumber

for the main long wavelength east-west variation.

**Summary.** F region irregularities results are as follows: (1) starting with Perkins' [1973] nighttime F region equations, a long wavelength variation in the Pedersen conductivity in the east-west direction produces instability in an initial shorter wavelength north-south perturbation instability via the E X B instability provided the north-south and east-west electric fields obey a certain criterion; (2) the linear instability criterion involves the neutral scale height  $H_n$  such that for fixed ratio of north-south to east-west electric field the instability is easier to excite at higher altitudes; (3) the nonlinear evolution of our system produces a power spectrum for the Pedersen conductivity fluctuations which goes as  $k^{-2}$ ; and (4) the quasi-final Pedersen conductivity contours resemble sheet-like structures with more of an east-west orientation.

Result (2) is in agreement with the idea that spread F is more common when the F region is high (Singleton, 1962). Result (3) is in good agreement with the in situ measurements of F region irregularities of Dyeon et al. [1974] which show a power law for the power spectrum proportional to  $k^{-2}$ . Result (4) is also in agreement with the power law power spectrum ( $k^{-n}$ , where  $n = 2$  to 3) deduced by Rufenach [1972] from scintillation observations

Result (4) is in agreement with the midlatitude winter scintillation observations of Singleton [1970] who deduced that the shape of F region irregularities showed east-west orientations.

We also wish to point out that this is the first nonlinear simulation of F region irregularities to be performed. However, we do not imply that our results can explain all spread F observations. We believe that further work dealing with the generation and nonlinear development of F region irregularities is warranted in order to gain an improved understanding of the relationship between these irregularities and spread F and scintillation phenomena.

#### V. CONCLUDING REMARKS

We have presented in Section IV A and B two classes of problems under the topic of ionospheric irregularities. We wish to reiterate that the theoretical and computational programs are at a stage where we can generate detailed information on the causes and structure of ionospheric irregularities, as

manifested in sections IV A and B. The problems remaining to be done can be accomplished, we believe, over a reasonable time period, i.e., we are applying existing technologies to gain a basic understanding of the causes and formation of ionospheric irregularities. The results we obtain provide a basis within which to interpret experimental data, suggest new experiments, and act as a vehicle for suggesting systems design. Understanding the results in terms of the physical processes involved leads to a true predictive capability, i.e., we can know what, when and where to expect irregularities. We can use our theoretical and computational modeling in areas where data is sparse or non-existent, after of course it has proven valid in areas where data exists. In the end, this predictive capability is very much needed for useful systems design. Our future goals in the study of ionospheric irregularities will include a determination, classification, and effects of the most important instabilities (including the study of the nonlinear development of such instabilities) which cause ionospheric scintillation effects.

#### REFERENCES

- Aarons, J., H. E. Whitney, and R. S. Allen, "Global Morphology of Ionospheric Scintillation," Proc. IEEE, 5, 159, 1971.
- Baker, W. G., and D. F. Martyn, "Electric Currents in the Ionosphere, I. The Conductivity," Phil. Trans. Roy. Soc. (London), A246, 36, 1953.
- Balsley, B. B., and D. T. Farley, "Radar Observations of Two-Dimensional Turbulence in the Equatorial Electrojet," J. Geophys. Res., 78, 7471, 1973.
- Booker, H. G., and H. W. Wells, "Scattering of Radio Waves by the F-Region of the Ionosphere," Terres. Magn., 43, 249, 1958.
- Bowhill, S. A., "Statistics of a Radio Wave Diffracted by a Random Ionosphere," J. Res. Nat. Bur. Stand., Sect. D., 65D, 275, 1961.
- Briggs, B. H., and I. A. Parkin, "On the Variation of Radio Star and Satellite Scintillations with Zenith Angle," J. Atmos. Terr. Phys., 25, 339, 1963.
- Budden, K. G., "The Amplitude Fluctuations of the Radio Wave Scattered from a Thick Ionospheric Layer with Weak Irregularities," J. Atmos. Terr. Phys., 27, 155, 1965.
- Craft, H. D., Jr., and L. H. Westerlund, "Scintillations at 4 and 6 GHz Caused by the Ionosphere," AIAA Pap. 72-179, Amer. Inst. of Aeronaut. and Astronaut. Libr., New York, 1972.
- Cronyn, W. M., "The Analysis of Radio Scattering and Space-Probe Observations of Small-Scale Structure in the Interplanetary Medium," Astrophys. J., 161, 755, 1970.
- Davis, T. N., G. J. Romick, E. M. Weacott, R. A. Jeffries, D. M. Kerr, and H. M. Peek, "Observations of the Development of Striations in Large Barium Ion Clouds," Planet. Space Sci., 22, 67, 1974.
- Dyson, P. L., J. P. McClure, and W. B. Hanson, "In Situ Measurements of the Spectral Characteristics of F Region Ionospheric Irregularities," J. Geophys. Res., 79, 1497, 1974.
- Farley, D. T., B. B. Balsley, R. F. Woodman, and J. P. McClure, "Equatorial Spread F: Implications of VHF Radar Observations," J. Geophys. Res., 75, 7199, 1970.
- Fremouw, E. J., "Modeling and Prediction of Ionospheric Scintillation," AIAA Pap. 74-54 AIAA 12th Aerospace Sciences Meeting, Jan 30-Feb. 1, 1974, Washington, D. C.
- Goldman, S. R., S. L. Ossakow, and D. L. Book, "On the Nonlinear Motion of a Small Barium Cloud in the Ionosphere," J. Geophys. Res., 79, 1471, 1974.
- Herman, J. R., "Spread F and Ionospheric F Region Irregularities," Rev. Geophys. Space Phys., 4, 255, 1966.
- Heisler, L. H., and L. D. Wilson, "Spread F Development Associated with a High Altitude Nuclear Explosion," Nature, 196, 258, 1962.

- Hewish, A., "The Diffraction of Galactic Radio Waves as a Method of Investigating the Irregular Structure of the Ionosphere," Proc. Roy. Soc., A214, 494, 1952.
- Hopkins, R. U. F., and M. R. Paulson, "Equatorial Scintillation," Naval Research Reviews pg. 17, May-June 1974.
- Johnson, F. S., Satellite Environment Handbook, Stanford Univ. Press, 1961, pgs. 19-21.
- Knox, F. B., "A Contribution to the Theory of the Production of Field-Aligned Ionization Irregularities in the Equatorial Electrojet," J. Atmos. Terr. Phys., 26, 239, 1964.
- Linson, L. M., and J. B. Workman, "Formation of Striations in Ionospheric Plasma Clouds," J. Geophys. Res., 75, 3211, 1970.
- Lloyd, K. H., and G. Haerendel, "Numerical Modeling of the Drift and Deformation of Ionospheric Plasma Clouds and of their Interaction with other Layers of the Ionosphere," J. Geophys. Res., 78, 7389, 1973.
- Lovelace, R. V. E., E. E. Salpeter, L. E. Sharp, and D. E. Harris, "Analysis of Observations of Interplanetary Scintillations," Astrophys. J., 159, 1047, 1970.
- Maeda, K., T. Tsuda, and H. Maeda, "Theoretical Interpretation of the Equatorial Sporadic E Layers," Rep. Ionos. Res. Space Res. Jap., 17, 3, 1963.
- Maeda, H., A. J. Shirgaokar, M. Yasuhara, and S. Matsushita, "On the Geomagnetic Effect of the Starfish High-Altitude Nuclear Explosion," J. Geophys. Res., 69, 917, 1964.
- McDonald, B. E., T. P. Coffey, S. Ossakow, and R. N. Sudan, "Preliminary Report of Numerical Simulation of Type 2 Irregularities in the Equatorial Electrojet," J. Geophys. Res., 79, 2551, 1974a.
- McDonald, B. E., T. P. Coffey, S. L. Ossakow, and R. N. Sudan, "Numerical Studies of Type 2 Equatorial Electrojet Irregularity Development," Radio Sci., 1974b (in press).
- Newman, P., B. Jones, and L. McCabe, "F-Region Irregularities After High Altitude Detonation of July 9, 1962" in Spread-F and its Effects Upon Radiowave Propagation and Communications, P. Newman ed., AGARDOGRAPH 95, Technivision, Maidenhead, England, 1966.
- Nielsen, E., and J. Aarons, "Satellite Scintillation Observations over the Northern High Latitude Regions," J. Atmos. Terr. Phys., 36, 159, 1974.
- Ott, E., and D. T. Farley, "The k-Spectrum of Ionospheric Irregularities," J. Geophys. Res., 79, 2469, 1974.
- Perkins, F., "Spread F and Ionospheric Currents," J. Geophys. Res., 78, 218, 1973.
- Prakash, S., S. P. Gupta, and B. H. Subbaraya, "Irregularities in the Equatorial E Region over Thumba," Radio Sci., 4, 791, 1969.
- Prakash, S., S. P. Gupta, and B. H. Subbaraya, "A Study of the Irregularities in the Night Time Equatorial E-Region Using a Langmuir Probe and Plasma Noise Probe," Planet. Space Sci., 18, 1307, 1970.
- Pitteway, M. L. V., and R. Cohen, "A Waveguide Interpretation of Temperate-Latitude Spread F on Equatorial Ionograms," J. Geophys. Res., 66, 3141, 1961.
- Reid, G. C., "The Formation of Small-Scale Irregularities in the Ionosphere," J. Geophys. Res., 72, 1627, 1968.
- Rishbeth, H., and O. K. Garriott, Introduction to Ionospheric Physics, Academic, New York, 1969, pgs. 118-119, 131 and 171.
- Rogister, A., and N. D'Angelo, "Type 2 Irregularities in the Equatorial Electrojet," J. Geophys. Res., 75, 3879, 1970.
- Rosenberg, N. W., "Observations of Striation Formation in a Barium Ion Cloud," J. Geophys. Res., 76, 6856, 1971.
- Rufenach, C. L., "Power-Law Wavenumber Spectrum Deduced from Ionospheric Scintillation Observations," J. Geophys. Res., 77, 4761, 1972.
- Rufenach, C. L., "Wavelength Dependence of Radio Scintillation: Ionosphere and Interplanetary Irregularities," J. Geophys. Res., 79, 1562, 1974.
- Salpeter, E. E., "Interplanetary Scintillations I. Theory," Astrophys. J., 147, 433, 1967.
- Scannapieco, A. J., S. L. Ossakow, D. L. Book, B. E. McDonald, and S. R. Goldman, "Conductivity Ratio Effects on the Drift and Deformation of F Region Barium Clouds Coupled to the E Region Ionosphere," J. Geophys. Res., 79, 2913, 1974.
- Simon, A., "Instability of a Partially Ionized Plasma in Crossed Electric and Magnetic Fields," Phys. Fluids, 6, 382, 1963.
- Simon, A., "Growth and Stability of Artificial Ion Clouds in the Ionosphere," J. Geophys. Res., 75, 6287, 1970.
- Singleton, D. G., "Spread-F and the Parameters of the F-Region Ionosphere, 2, Spread-F and F-Layer Height," J. Atmos. Terr. Phys., 24, 885, 1962.

Singleton, D. G., "Dependence of Satellite Scintillations on Zenith Angle and Azimuth," J. Atmos. Terr. Phys., 32, 789, 1970.

Stoffregen, W., "Travelling Ionospheric Disturbances Initiated by Low Altitude Nuclear Explosions," Paper 1972/73:14 presented at Specialist Meeting of Electromagnetic Wave Propagation, Wiesbaden, West Germany, 17-21 April 1972.

Sudan, R. N., J. Akinrimisi, and D. T. Farley, "Generation of Small-Scale Irregularities in the Equatorial Electrojet," J. Geophys. Res., 78, 240, 1973.

Sugiura, M., and J. C. Cain, "A Model Equatorial Electrojet," J. Geophys. Res., 71, 1869, 1966.

Sugiura, M., and D. J. Poros, "An Improved Model Equatorial Electrojet with a Meridional Current System," J. Geophys. Res., 74, 4025, 1969.

Tatarski, V. I., Wave Propagation in a Turbulent Medium, McGraw-Hill, New York, 1961.

Taur, R. R., "Ionospheric Scintillation at 4 and 6 GHz," Comsat Tech. Rev., 3, 145, 1973.

Utlaut, W. F., "Ionospheric Scintillations: A Potential Limitation to Satellite Communications - Important Unknown Scintillation Factors," AIAA Pap. 74-56, AIAA 12th Aerospace Sciences Meeting, Jan 30 - Feb 1, 1974, Washington, D. C.

Völk, H. J., and G. Haerendel, "Striations in Ionospheric Ion Clouds, 1," J. Geophys. Res., 76, 4541, 1971.

Whitehead, J. D., "The Equatorial Electrojet and the Gradient Instability," J. Geophys. Res., 76, 3116, 1971.

Zabusky, N. J., J. H. Doles III, and F. W. Perkins, "Deformation and Striation of Plasma Clouds in the Ionosphere, 2, Numerical Simulation of a Nonlinear Two-Dimensional Model," J. Geophys. Res., 78, 711, 1973.



## SPECTRA OF AMPLITUDE AND PHASE SCINTILLATION\*

R.K. Crane  
Lincoln Laboratory MIT  
Lexington, Massachusetts 02173

### ABSTRACT

Observations of amplitude and phase scintillation were made at Millstone Hill Radar facility using phase coherent sources at 150 and 400 MHz on the US Navy Navigation System satellites. These observations have been processed to yield power spectra of the fluctuations in the logarithm of the received power (log power) at each frequency, the fluctuations in phase path length difference (differential phase) between the two frequencies, and coherency between the log power fluctuations at each frequency. A theoretical analysis was performed to predict the log power and differential phase power spectra and the coherency spectra. The theoretical model was based upon weak scatter theory for a thick screen with a power-law power-spectrum representation for the electron density fluctuations. A -4 exponent for the power law best fit the observed spectra. For weak scintillation (rms fluctuations in log power less than 5 dB or  $S_4 < .9$ ) the theoretical calculations were in excellent agreement with the observations. For strong scintillation, saturation was observed and the measured spectra were broader than predicted based upon weak scatter theory.

### INTRODUCTION

Scintillation due to electron density fluctuations have been observed on line-of-sight paths through the ionosphere at frequencies ranging from 10 MHz to 6 GHz. Theoretical models have been developed over the past two decades to explain scintillation and provide equations for use in predicting the frequency dependence of rms fluctuations in received power. The theoretical models generally depend upon an assumption about the shape of the power spectrum of electron density fluctuations along the path. Early models assumed a Gaussian shape (Briggs and Parkin, 1963) and more recent models have used a power law form (Crane, 1974). This paper considers the shape of the power spectrum required to explain observed power spectra of amplitude and phase

made at several frequencies. The paper will also consider the frequency dependence of rms fluctuations of amplitude and phase.

Observations of amplitude and phase fluctuations were made using the US Navy Navigation System satellites. The satellites were in circumpolar orbit. Lines-of-sight to the satellite move rapidly through the ionosphere allowing a direct measurement of the spatial fluctuations of amplitude and phase. The spectra of the fluctuations of the logarithm of the received power (log power) and of differential phase path length (differential phase) between coherently related signals at 150 and 400 MHz were calculated and compared with theoretical estimates of the spectrum. The theoretical estimates and observations were for conditions of weak scintillation. The results of the observations show that the axial ratio for the electron density fluctuations is greater than two, a -4 exponent for the power law adequately explains the observations for scale sizes larger than 800m, and predictions of the frequency dependence of amplitude and phase fluctuations may be adequately estimated using the power law model for weak scintillation and frequencies lower than 1 GHz.

The observed spectra showed an unexpected increase in variance at spatial sizes ranging from 200 to 700m. The observations were in the far zone of irregularities of 700m size and smaller and showed identical structure at both 150 and 400 MHz. The increases in variance ranged to as much as an order of magnitude for some of the observations. At scale sizes smaller than for the region of increase, the spectrum again had a power law shape, but at an increased level relative to the power law for larger scale sizes. The power law form for regions above and below the region of increase had the same exponent corresponding to a value near -4 for the electron density fluctuations. The effect of the increase is negligible on the rms fluctuations of log power or phase for frequencies below 1 GHz. At higher frequencies, the region of increase corresponds to the peak of the Fresnel filter function, and increased rms fluctuation values will occur relative to those predicted using observations at lower

\*This work was sponsored by the Dept. of the Army.

frequencies. These small scale-size increases may explain the frequency dependence and two frequency correlation coefficients reported by Taur (1974) for observations at 1550 and 4000 MHz.

The wavelength dependence of rms fluctuations of log power, phase, doppler, and angle-of-arrival may be readily calculated using the single power law form for the power spectrum of electron density fluctuations for a finite observing time and weak scintillation conditions. The rms fluctuations of low power vary as  $\lambda^{1.5}$ , for phase and doppler the rms values vary as  $\lambda^{1.0}$ , and for angle-of-arrival, the rms values vary as  $\lambda^{2.0}$ . These predictions hold for frequencies below 1 GHz. The predictions were tested using log power and doppler observations at 150 and 400 MHz. For strong scintillation the rms fluctuations in log power approach a constant value that does not depend upon carrier frequency. The doppler spread (rms fluctuations of doppler) still varies with frequency in accordance with the weak scintillation theory estimate when strong scintillations occurs.

#### THEORETICAL ESTIMATION OF AMPLITUDE AND PHASE SPECTRA

Analytical expressions for the correlation functions and spectra describing the statistical fluctuations of amplitude and phase may be derived from analytical expressions for the received field. For the general problem of wave propagation through random media, analytical expressions for field quantities are not available. First order perturbation solutions for the field quantities are available and provide the basis for the weak scintillation (weak or single scattering) theory results. Two weak scattering models have been used, the single scattering or Born-approximation to the scalar wave equation (Budden, 1965), and the single scattering or Rytov-approximation to the equation for the logarithm of the amplitude of the wave (so called Rytov method or method of smooth perturbations, see Tatarski, 1967). These perturbation solutions are called the Born and Rytov solutions respectively and provide identical results in the limit of very weak scintillation. An ad hoc amalgamation of geometrical optics and diffraction theory has also been extensively used for an approximate description of scintillation effects. This approximation is termed the thin screen approximation, and in the limit of weak scattering also yields results identical to the perturbation solution results.

The Born and Rytov solutions for the scalar wave equation differ in their interpretation of the resultant expression for the fluctuating field quantity. The first order perturbation theory solution for a spherical wave source and random electron density fluctuations is

$$\psi(r) = r_e \int_{vol} e^{ik|\underline{r}-\underline{x}| + ik(\underline{x}-\underline{r})} \Delta N(\underline{x}) \frac{rd\underline{x}}{x|\underline{r}-\underline{x}|} (1)$$

where  $\psi(r) = X(r) + i\phi(r)$  = complex first order field perturbation at  $\underline{r}$

$\Delta N(\underline{x})$  = electron density fluctuation (departure from mean value) at  $\underline{x}$

$\underline{r}, \underline{x}$  = position vectors ( $r, x$  are magnitudes;  $\hat{r}, \hat{x}$  are unit vectors)

$k$  = wavenumber =  $2\pi/\lambda$ ,  $\lambda$  = wavelength

$r_e$  = classical electron radius.

For the Born approximation,  $\psi$  is interpreted as

$$\psi(r) = u_1(r)/u_0(r)$$

where  $u_1(r)$  = complex perturbation to received field values

$$u_0(r) = a_0(r)e^{i\phi_0(r)}$$

$a_0(r)$  = unperturbed (or averaged) amplitude

$\phi_0(r)$  = unperturbed phase.

For the Rytov method,

$$\psi(r) = \ln [1 + u_1(r)/u_0(r)]$$

In the Born approximation,  $\psi$  represents the in phase and quadrature fluctuations in the received field and in the Rytov approximation  $\psi$  represents fluctuation in the logarithm of received amplitude (log amplitude) and phase of the received field. For very small amplitude fluctuations, the quantities are identical.

Starting with  $\psi(r)$  which is a function of  $\Delta N(\underline{x})$ , the correlation function or spectra for  $X$  and  $\phi$  may be expressed as a function of the correlation function,  $B_N$ , or spectra,  $\Phi_N$ , of  $\Delta N$ . Using  $\Phi_N$  as the most convenient representation of the statistical fluctuations in  $\Delta N$ ,

$$B_{\frac{X}{\phi}}(d) = \frac{r_e^2}{k^2} \int_{L_1}^{L_2} \int_{-\infty}^{\infty} \int_{-\infty}^{\infty} \Phi_N(\rho; 0, \underline{s}) \frac{\sin \left( s^2 \beta - \underline{s} \cdot \underline{d} \frac{\rho}{L} \right)}{\cos \left( s^2 \beta \right)} \frac{\sin \left( s^2 \beta \right)}{\cos \left( s^2 \beta \right)} d\underline{s} d\rho \quad (2)$$

where  $\underline{d}$  = spatial separation between locations used in the evaluation of the correlation function

$\underline{s}$  = wave number =  $\{s_\rho, \underline{s}\}$

$\underline{s}$  = wave number perpendicular to ray path (two dimensional)

$s_\rho$  = wave number along path, taken as 0 in  $\phi_N(\rho; \underline{s})$

$\beta = z/2k$ ,  $z = \frac{\rho(L-e)}{L}$  = length of path,  $\rho$  position along path.

The expression for the power spectral density,  $S_\phi$  is given by

$$S_{\phi}(\kappa \hat{d}) = \frac{r_e^2}{k^2} \int_{L_1}^{L_2} \iiint_{-\infty}^{\infty} \phi_N(\rho; 0, \underline{s}) \frac{\sin(s^2 \beta - \underline{s} \cdot \hat{d} \frac{\rho}{L})}{\cos(s^2 \beta)} \frac{\sin(s^2 \beta)}{\cos(s^2 \beta)} e^{-i\kappa d} d\underline{s} d\rho \quad (3)$$

The expressions for the variance of  $X$  and the spectra for  $X$  and  $\phi$  may be simplified if the form of  $\phi_N$  is given. For a power-law spectrum with an outer scale represented by

$$\phi_N(\rho, \underline{s}) = \frac{\sigma_N^2(\rho) \alpha L_o^3 \Gamma(p/2)}{2\pi \Gamma(3/2) \Gamma\left(\frac{p-3}{2}\right) \left[1 + \left(\frac{L_o}{2\pi}\right)^2 (s_p^2 + \alpha^2 s_m^2)\right]^{p/2}} \quad (4)$$

where  $p$  = exponent of power law (assumed to be independent of  $\rho$ )

$\alpha$  = axial ratio (assumed to be independent of  $\rho$ )

$L_o$  = outer scale ( $\Sigma_o = 2\pi/L_o$  assumed to be independent of  $\rho$ )

$\sigma_N^2$  = variance of electron density fluctuations at  $\rho$  along path

$s_p, s_m$  = wave number perpendicular,  $p$ , and along,  $m$ , the geomagnetic field.

the variance in  $X$  is given by

$$\sigma_X^2 = B_X(0) = \frac{(4\pi)^2 r_e^2 \Sigma_o^{p-3} \Gamma(p/2)}{\Gamma(3/2) \Gamma\left(\frac{p-3}{2}\right)} f^2(\alpha, \psi) \frac{b_p I_p}{2^{p/2} k^{(p+4)/2}} \int_{L_1}^{L_2} \sigma_N^2(\rho) z^{\frac{p-2}{2}} d\rho \quad (5)$$

$$\text{where } f(\alpha, \psi) = \left[ \frac{\alpha}{2} \frac{1 + \cos^2 \psi + \alpha^2 \sin^2 \psi}{(\cos^2 \psi + \alpha^2 \sin^2 \psi)^{\frac{p-1}{2}}} \right]^{\frac{1}{2}}$$

$$b_p = \pi/2; p = 4$$

$$= -\Gamma\left(\frac{2-p}{2}\right) \cos\left(\frac{p-2}{4}\pi\right) 2^{\frac{p-4}{2}}; 2 < p < 5, p \neq 4$$

$$I_p = \frac{1}{2\pi} \int_0^{2\pi} \left[ (\cos^2 \psi + \alpha^2 \sin^2 \psi) \cos^2 \theta + \sin^2 \theta \right]^{\frac{p-2}{2}} d\theta$$

$$I_p = \frac{1 + \cos^2 \psi + \alpha^2 \sin^2 \psi}{2} \quad \text{for } p = 4$$

$\psi$  = propagation angle or angle between the geomagnetic field  $\hat{m}$  and the propagation deviation  $\hat{p}$  ( $\cos \psi = \hat{m} \cdot \hat{p}$ )

and the spectra of amplitude and phase are given by

$$S_{X/\phi}(\kappa) = \frac{r_0^2 (2\pi)^3 \alpha \Sigma_0^{p-3}}{k^2 \nu} \int_{L_1}^{L_2} \frac{\sigma_N^2(\rho) \left[ \frac{p-3}{2} + A \left( \frac{\kappa L}{\rho}, \psi \right) \right] d\rho}{\left( \frac{\kappa L}{\rho} \right)^{p-1} \left[ \left( \frac{\Sigma_0}{\frac{\kappa L}{\rho}} \right)^2 + \mu^2 \right]^{\frac{p-1}{2}}} \quad (6)$$

where 
$$A \left( \frac{\kappa L}{\rho}, \psi \right) = \frac{\Gamma(p-2)}{\Gamma(3/2) \Gamma(\frac{p-3}{2})} \int_0^\infty \frac{\cos(ux) \cos(sx^2 + t)}{(1 + x^2)^{p/2}} dx$$

$$u = \frac{z}{k} \left( \frac{\kappa L}{\rho} \right)^2 \frac{\gamma \mu}{\nu}$$

$$s = \frac{z}{2k} \left( \frac{\kappa L}{\rho} \right)^2 \left( \frac{\mu}{\nu} \right)^2$$

$$t = \frac{z}{2k} \left( \frac{\kappa L}{\rho} \right)^2 (1 + \alpha^2)$$

$$\gamma = (\alpha^2 - 1) \frac{\sin \xi \cos \xi \cos^2 \xi}{\nu^2}$$

$$\left( \frac{\mu}{\nu} \right)^2 = \frac{1 + (\alpha^2 - 1) \sin^2 \psi}{\nu^2}$$

$$\nu^2 = 1 + (\alpha^2 - 1) \cos^2 \xi \sin^2 \psi$$

$\xi$  = orientation angle or angle between the normal to the plane containing the geomagnetic field and the propagation direction and  $\hat{d}$ .

$$\cos \xi = \frac{\hat{p} \times \hat{m}}{|\hat{p} \times \hat{m}|} \cdot \hat{d}$$

( $\xi = 0$  for  $\hat{d}$  perpendicular to  $\hat{m}$ ,  $= 90^\circ$  for  $\hat{d}$  parallel to  $\hat{m}$ ).

In-situ observations of electron density fluctuations using the OGO-6 satellite (Dyson et al., 1974) showed that  $L_0 > 20$  km and that  $p$  was near 4 ( $3.5 \leq p \leq 4.3$ ). The value of 4 for  $p$  greatly simplifies the calculations as shown above. Numerical evaluation is still required of the integral represented by  $A$ . The circumpolar U.S. Navy Navigation System satellites passed rapidly overhead transferring the spatial fluctuations of received amplitude into readily observable temporal fluctuations. The expressions for the spatial spectra may be transformed to expressions for temporal spectra by substituting  $2\pi f/\nu(\rho)$  for  $\kappa L/\rho$  where  $f$  is the frequency of the statistical fluctuations and  $\nu(\rho)$  is the speed of the line-of-sight normal to its path through the ionosphere at  $\rho$  on the path ( $\hat{v}$  parallel to  $\hat{d}$ ). Using

$$f_0 = \nu(\rho)/\sqrt{2\pi\lambda z},$$

to normalize the frequency scale, the contribution to the power spectrum of received fluctuation of a thin layer at  $\rho$  may be parametrically represented for an exponent,  $p$ , of 4 as shown in Figures 1 and 2. In the limit of large  $\kappa$  or  $f$ ,  $A \rightarrow 0$  and the spectra has a  $f^{-3}$  (or  $\kappa^{-3}$ ) behavior. This behavior is identified by the high frequency asymptotes on each of the figures.

#### EXPERIMENTAL OBSERVATIONS

Scintillation observations were made using phase coherent transmissions at 150 and 400 MHz from the Navy Navigation System satellites and receivers at the Millstone Hill Radar Facility

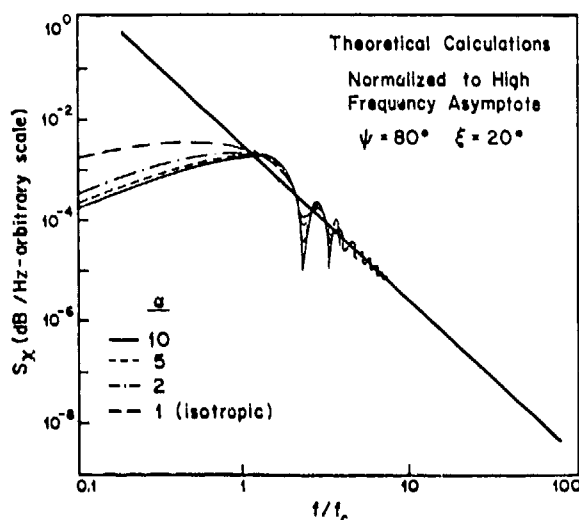


Figure 1. Theoretical spectra as a function of axial ratio.

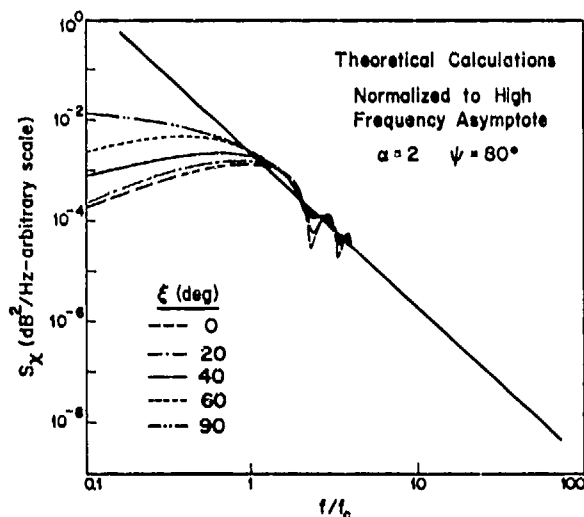


Figure 2. Theoretical spectra as a function of orientation angle.

(Ghiloni, 1973). The UHF (400 MHz) receiver system included the 84-foot Millstone antenna equipped for elevation and azimuth tracking, a phase lock receiver system, analog-to-digital converter, and digital tape recorder. The VHF receiver system included an 11-element yagi antenna mounted on one of the feed struts of the Millstone antenna, a coherent receiver providing in-phase and quadrature amplitudes referenced to the UHF signal, analog to digital converter and digital recording.

Data were normally sampled 15 times each second. For a limited number of observations, the data were sampled 1000 times a second. The UHF signal amplitude was determined by recording an AGC level. The UHF receiver had a

10 KHz predetection bandwidth and the AGC system had an effective bandwidth of 250 Hz (closed loop). The predetection bandwidth of the VHF receiver was 250 Hz. The received signal levels varied slowly during a satellite pass due to changing aspect angle at the satellite (satellite antenna pattern) and range to the satellite. For elevation angles below 40°, the signal-to-noise ratio varied by 10 dB. For optimum observing conditions, the signal-to-noise ratio was 50 dB at UHF and 35 dB at VHF. Both the UHF and VHF signals were phase modulated. The UHF phase modulation was used to remove the modulation at VHF. Residual signal level fluctuations still occurred in both the receiver outputs. The signal level to residual modulation variance was approximately 35 dB for both receivers.

The sampled data were transformed to time sequences of the logarithm of the received power (in dB) at each frequency, the phase path length difference (in radians at 150 MHz), the doppler frequency at 400 MHz (output from the phase lock receiver), the differential doppler frequency, the pointing angle at 400 MHz (constructed from antenna position encoders and the instantaneous value of the error signal), and in-phase and quadrature amplitudes at VHF. The data were blocked in time segments approximately eight seconds long (8196 samples at 1000 samples per second rate or 128 samples at 15 per second) spaced by one half a block length, detrended, weighted, and spectrally analyzed. The spectra were averaged over 13 successive blocks to provide estimates of the spectra for each minute with 21 degrees of freedom.

An example of spectra obtained for the logarithm of the amplitude (low power in dB) and differential phase for simultaneous 150 and 400 MHz observations are shown in Figure 3. The data were taken at the high sampling rate. The residual variance due to modulation is evident at frequencies above 10 Hz at VHF and above 40 Hz at UHF. For frequencies between 0 and 100 Hz, the modulation variance has a broad peak at 50.5 Hz and decreases to a minimum value at 0 and 101 Hz. For the spectra displayed on Figure 3, the effect of modulation is negligible for frequencies below 20 Hz at UHF and 8 Hz at VHF. The theoretical equations for the spectra (Eq. 6) show that the power spectral density should vary as wavelength squared in the limit of high frequencies. The VHF experimental power spectral density values were scaled by wavelength squared prior to plotting so the high frequency asymptotes would coincide. The differential phase data were also scaled by  $(20 \log_{10} e)^2$  so the high frequency asymptotes for all three spectra would coincide. The data for frequencies between 2 Hz and the upper frequency limit imposed by modulation variance follow the high frequency asymptote indicated by the straight line through the data.

Theoretical spectra are displayed on the figure for the propagation geometry of the

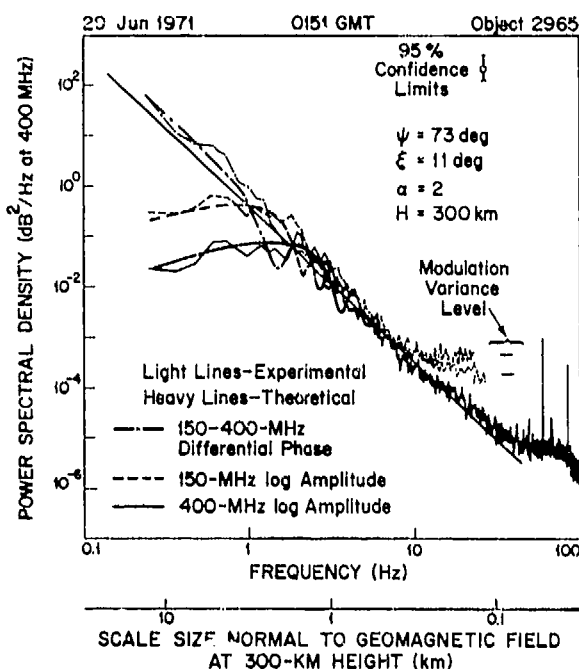


Figure 3. Experimental and theoretical spectra, log amplitude and phase.

observations ( $\psi$  and  $\xi$ ) and an axial ratio of two. For frequencies below the Fresnel zone cutoff ( $f_c$  on Figures 1 and 2) the effect of orientation angle is more important than axial ratio. For the same orientation angle, the spectra change little for axial ratios above two. The minima in the spectra at higher frequencies show both axial ratio and orientation angle dependence. The position of the minima also depend upon height through the value of  $f_c$ . For a thick irregularity region, the minima are filled in due to the variation of  $f_c$  with height. The null depths, therefore, cannot be used to estimate the axial ratio and due to the relative insensitivity of the spectra to axial ratio for values above two, a value of two was arbitrarily used for display.

The theoretical spectra were fit to the experimental data by selecting a best value for  $f_c$ . For the data on Figure 3, the  $f_c$  value corresponded to a height of 300 km for the lowest dominant irregularity layer. Due to satellite motion, the value of  $f_c$  increases monotonically with irregularity layer height. The theoretical spectra given in Figures 1 and 2 are for a differential scattering layer thicknesses at a height corresponding to  $f_c$ . For a thick region, the contributions from each height must be summed at each frequency. The higher heights contribute most at the higher frequencies and, for log amplitude fluctuations, the lower scattering layers dominate the summation at lower frequencies. The shape of the log amplitude spectra near its peak values will be most affected by the variation of electron density fluctuations with height. The log amplitude spectra shown in Figure 3

show good agreement with the theoretically estimated spectra in the region of the peak of each spectra suggesting a single dominant (probably thick) scattering layer.

The theoretical phase spectrum for 150 MHz is identified with the differential phase observations depicted on Figure 3. The power spectral density for phase fluctuations has a wavelength squared dependence. The contribution to the differential phase fluctuations contributed by the 400 MHz signal is, therefore, less than 14% of the observed value and is negligible in comparison with the statistical uncertainty of the estimate of the power spectral density. The estimation of phase variance is difficult due to the uncertainty in the power spectrum for electron density fluctuations at large scale sizes. The model used to estimate the theoretical phase spectra used an outer scale the order of 100 km and much larger than the 10-20 km scale size associated with the duration of the observations used to generate the spectra shown on Figure 3. The phase spectrum shows a continuous increase in power spectral density as the fluctuation frequency decreases in agreement with the model. Since the observing time is short compared with the time to traverse an outer scale size, the variance for the phase observations has a wavelength squared dependence. The variance in doppler found by integrating  $f^2 S_\phi(f)$  across the useful observation band also has a wavelength squared dependence.

#### ANALYSIS

The theoretical spectra were computed for  $X$  and  $\phi$ . These spectra may be interpreted as either log amplitude and phase or in-phase and quadrature amplitude as discussed above. The theoretical spectra are compared with log amplitude and phase observations on Figure 3 and show excellent agreement for all fluctuation frequencies not contaminated by modulation. The VHF data used to prepare Figure 3 were also used to generate in-phase, quadrature and complex spectra as shown in Figure 4. The in-phase and quadrature components were determined referenced to the smoothed phase values used to detrend the phase observations. The observations and the high frequency asymptote for the theoretical spectra ( $p = 4$ ) are shown on the figure. The shape of the in-phase (to be associated with  $X$ ) and quadrature (to be associated with  $\phi$ ) spectra do not match the theoretical estimates. The VHF data to compile Figures 3 and 4 correspond to weak scintillation conditions, the rms log power ( $\sigma_X$  in dB) was 2.2 dB ( $S_4 = 0.5$ ).  $\sigma_X$  was 0.5 dB at 400 MHz ( $S_4 = .1$ ). For scintillation of this intensity, the Rytov approach using the log amplitude and phase interpretation for  $X$  and  $\phi$  clearly fits the experimental observations best.

The in-phase and quadrature amplitude spectra show nearly equal spectral densities at a given frequency value except for

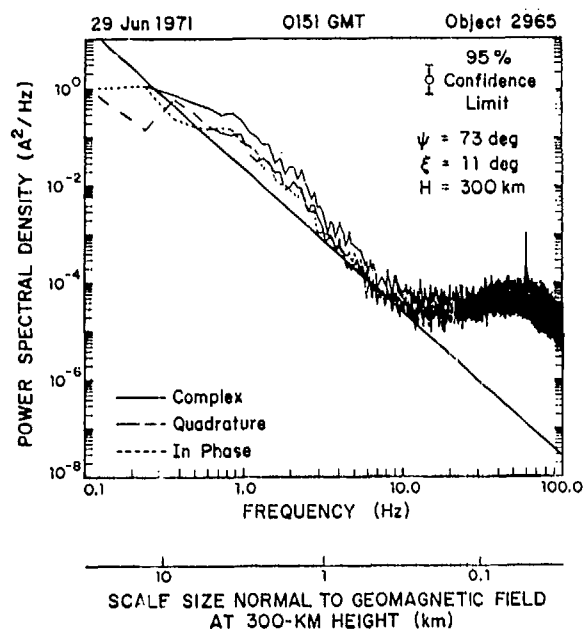


Figure 4. Experimental spectra in-phase and quadrature amplitude.

frequencies below 0.3 Hz which may be influenced by the detrending procedure. The data also show the complex spectra to be approximately equal to the sum of the in-phase and quadrature spectral density values suggesting no correlation between the in-phase and quadrature components. This last observation is strengthened by a coherency analysis which also shows no significant correlation. The in-phase and quadrature amplitude spectra approach the shape of the log amplitude and phase spectra as the intensity of the scintillation becomes smaller. For  $\sigma_X < 1.5$  dB ( $S_4 < 0.3$ ) the two interpretations of  $X$  and  $\phi$  yield identical results.

$S_4$  is generally used to describe amplitude fluctuations. Since the Rytov approach appears to provide a better fit to the data for an intermediate range of scintillation intensity values,  $\sigma_X$  where  $X$  is identified with log power provides a better basis for describing scintillation. The two measures of scintillation intensity,  $S_4$  and  $\sigma_X$  may be related if the amplitude distribution function is known. The theoretical construction of the perturbation solution does not provide any guidance as to the expected shape of the distribution function. Experimental observations show that the Nakagami-m distribution, although not identical with the observed distributions (Crane, 1974), does provide a reasonable approximation. Figure 5 shows the relationship between  $S_4$  and  $\sigma_X$  calculated using the Nakagami-m distribution and observed using estimates of  $\sigma_X$  and  $S_4$  based upon the same scintillation observations. The data follow the weak scatter limit for  $S_4 < 0.3$ ,

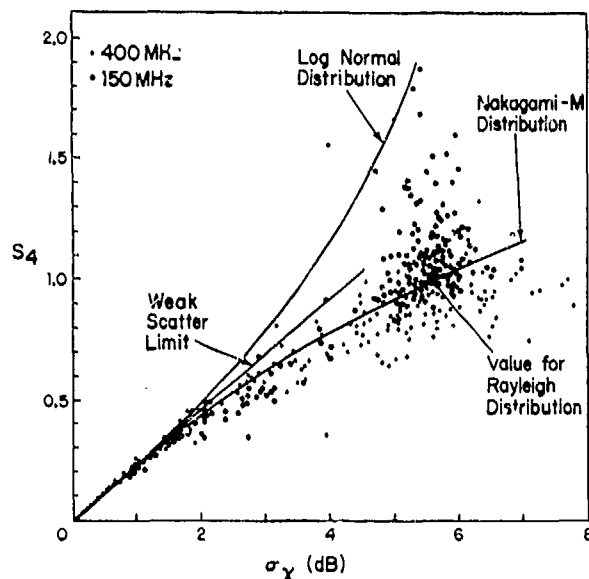


Figure 5.  $S_4$  vs  $\sigma_X$  for pass of object 3133 rising at 0411 GMT on 4 Aug. 1972.

a result consistent with the spectral shape observations. It is noted in the figure that the data do not follow a log-normal distribution function. Tatarski (1967) erroneously attributed a log normal behavior to the Rytov approximation. Because the Rytov solution is a single scattering solution, the law of large numbers does not lead to a log normal distribution function.

The range of validity of the Rytov solution may be investigated by comparing the  $\sigma_X$  values obtained simultaneously at two frequencies. Using the  $p = 4$  power law form for the electron density fluctuations, the  $\sigma_X$  values should follow a  $\lambda^{1.5}$  relationship. The first order perturbation solutions are secular predicting variances that increase linearly with increase in either the electron density variance or the extent of the irregularity region along the path. The predicted increases cannot continue indefinitely and higher order or multiple scattering corrections must occur. Using widely spaced frequencies, the break down of the first perturbation solution can be investigated. Figure 6 depicts the relationship between one minute averaged values of  $\sigma_X$  observed simultaneously at 150 and 400 MHz. The data were edited to remove cases of obvious surface multipath contamination at 150 MHz. The VHF system used an antenna with a 40° beamwidth and multipath contamination was evident for at least a portion of each track. The multipath was dominated by low frequency (less than 1-2 Hz) fluctuations, and could be identified using both the received signal time histories and the in-phase and quadrature spectra.

The results show good agreement between observation at 150 MHz and prediction at 150

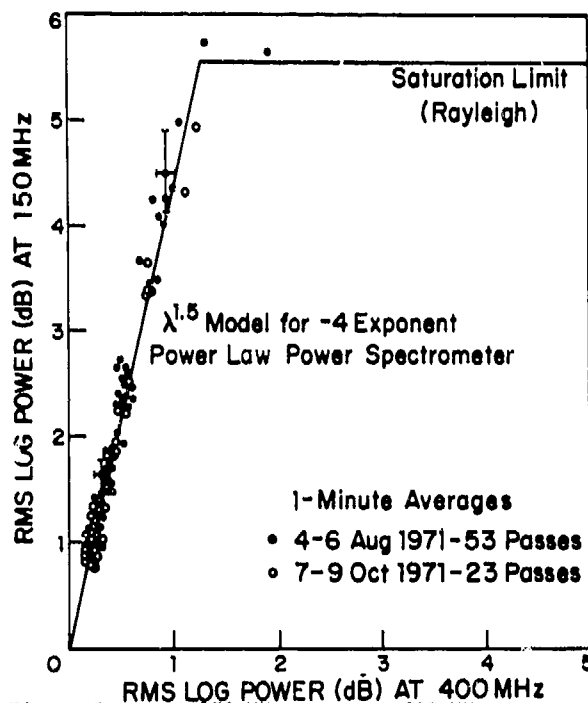


Figure 6.  $\sigma_X$  at 150 MHz vs  $\sigma_\psi$  at 400 MHz.

MHz based upon the Rytov approximation and 400 MHz observations. The data show that for  $\sigma_X < 5$  dB the first order perturbation model is in agreement with the observations. The data also show saturation at a value of  $\sigma_X = 5.56$  dB. At the saturation limit, the amplitude distributions test to be Rayleigh (Crane, 1974). The saturation limit therefore corresponds to multiple scattering. The data show a rather wide range of  $\sigma_X$  values for which the Rytov approximation holds, and that the range is significantly wider than for the Born approximation. The data shows a rather sudden transition to multiple scattering. Referring back to Figure 5, it is evident that the Born approximation begins to depart from the observations at  $\sigma_X = 1.5$  dB ( $S_4 = 0.3$ ) whereas the Rytov solution is valid up to  $\sigma_X = 5$  dB ( $S_4 = 0.9$ ).

A detailed two frequency comparison of  $\sigma_X$  and doppler spread is given in Figure 7 for the data used to compile Figure 5. The horizontal dot-dashed lines on the rms log power ( $\sigma_X$ ) plot are the saturation (Rayleigh) limits for scintillation at each frequency. The 150 MHz data were scaled to 400 MHz using the  $\lambda^{1.5}$  relationship. Except for several instances of multipath occurring between 0 and 4 minutes, the data at each frequency are in agreement within the  $\lambda^{1.5}$  scaling. Both data sets show saturation at later times. The doppler spread should follow the  $\lambda^{1.0}$  relationship discussed above. The 150 MHz doppler spread data were scaled to 400 MHz prior to plotting. The dot-dashed line indicates the limiting doppler spread value for the 150 MHz observations that occurs because the data were not sampled fast enough (these

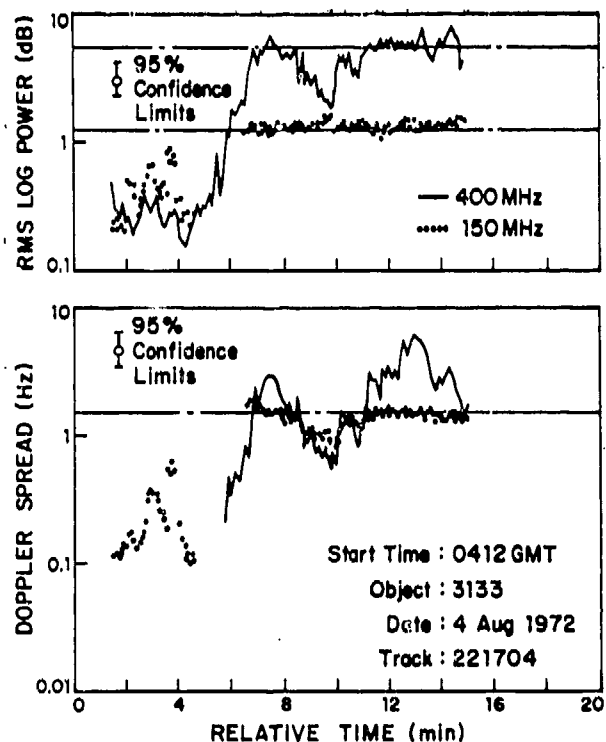


Figure 7.  $\sigma_X$  and doppler spread summaries for each pass of object 3133 rising at 0411 GMT on 4 Aug. 1972.

observations were taken at the lower 15 per second rate). Between 6 and 11 minutes the doppler spreads at the two frequencies followed the  $\lambda^{1.0}$  law predicted by the Rytov approximation for short observation times. The Rytov weak scatter solution holds even though saturation is evident in the amplitude data. Spectral observations show that when saturation occurs, the log amplitude spectra broadens, and the phase spectra for frequencies greater than  $f_c$  tend to flatten. The low frequency phase fluctuations, however, continue to increase as the electron density variance or extent of the irregularities along the path increases. These fluctuations dominate the phase and doppler variances causing the observed usefulness of the  $\lambda^{1.0}$  relationship for strong scintillation.

The spectra given above, although taken at the high sampling rate, are typical of all the low sampling rate observations. For frequencies below about 5 Hz they are typical of the higher sampling rate observations. At higher fluctuation frequencies, they are not. Figure 8 depicts typical spectra. For those observations, the dominant irregularity layer is at 450 km height. For an axial ratio of two and the observation propagation geometry, the theoretical spectra match the observed spectra for scale sizes larger than 500m. For smaller scale sizes, the observed spectra depart significantly from the predicted values. The departure from the high frequency asymptote is



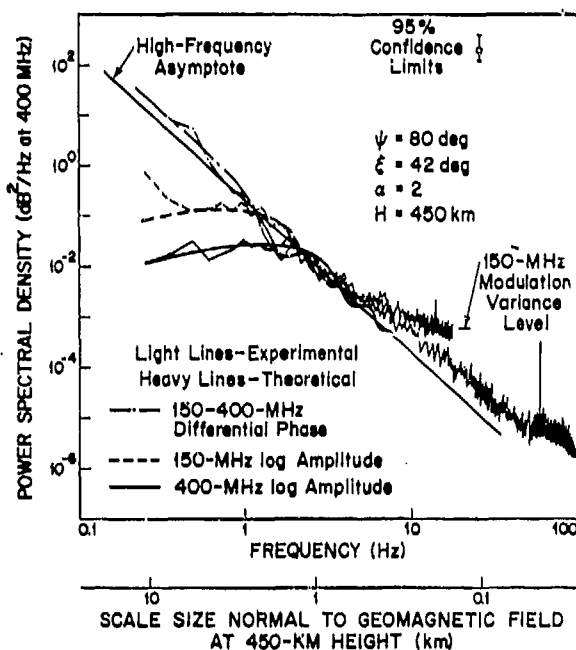


Figure 8. Phase and log amplitude spectra for 2336 GMT 5 April 1971.

identical at 150 and 400 MHz. Since the receiver is in the far zone for scatterers of this size, the observed spectra may be identified with  $s\phi_N$ , and the departure of the spectra from the expected values may be attributed to the spectra for electron density fluctuations. Simultaneous observation at two widely spaced frequencies indicates that the effect is caused by the medium, not the equipment. The data show an increase of better than a factor of two in power spectral density in the 400-600m scale size region and a  $s^{-4}$  behavior again at smaller scale sizes. The results are indicative of an energy input into the fluctuation spectra at a 500m scale size.

The energy input at small scale sizes has been observed in 70 percent of the 50 high sampling rate sets of spectra to date. The input scale sizes range from 200 to 800m and the variance increase ranges up to an order of magnitude. Figure 9 depicts three successive one minute observations of log amplitude spectra at 400 MHz, and Figure 10 depicts simultaneous 150 and 400 MHz observations of log amplitude spectra taken on another day. The 150 MHz data on Figure 10 were scaled both in power spectral density and wavelength so that the theoretical spectra would be the same for both wavelengths. The small scale spectral increase is evident in both figures. Using log amplitude spectra only, the increase could be confused with a change in power law as indicated on Figure 10. The change in slope of the asymptote is inconsistent with the simultaneous phase observations, as shown in Figure 8, indicating that only the small scale input interpretation is consistent with all the spectra.

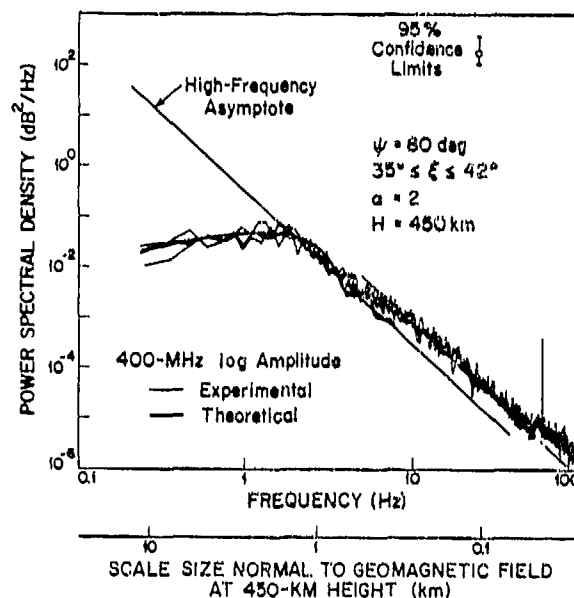


Figure 9. 400 MHz log amplitude spectra for 2334-2336 GMT 5 April 1971.

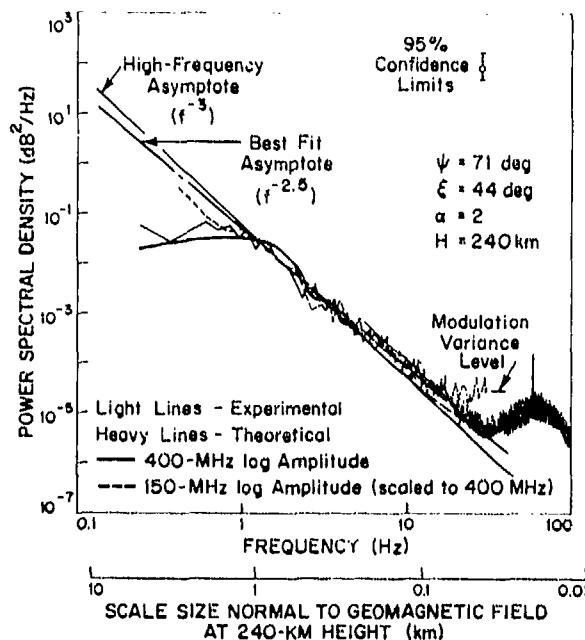


Figure 10. 150 and 400 MHz log amplitude spectra for 2032 GMT 20 April 1971.

The observed departure of the spectra from the simple power law model at small scale sizes indicates that the wavelength scaling laws described above do not hold. The variance observations, however, were consistent with these laws. The observations of spectral increases all occur at fluctuation frequencies too high

to significantly affect the variance value (integral of power spectral density across the frequency band). The 150 and 400 MHz scaling laws, therefore, are not affected by this small scale phenomena. As the wavelength decreases, however, the significance of the small scale phenomena increases. The frequency scaling laws, therefore, will tend to underestimate GHz scintillations. Using the spectra on Figure 9, for example, at 8 GHz the rms log amplitude fluctuations will be twice the value predicted using the frequency scaling laws given above. Wernik and Liu (1974) had to postulate small scale spectral increases to explain GHz scintillation. These observations show that such spectral increases do occur. These observations do not explain the apparent  $\lambda^2$  dependence reported by Craft and Westerlund (1972) because the observed spectra do not steepen sufficiently to obtain  $\lambda^2$ .

Occasionally spectra indicate that scintillation occurs in the E-region. Figure 11 shows such an occurrence. The height shown on the figure and the scale size legend corresponds to the spectra observed on both the minute before (Figure 10) and the minute after the displayed spectra. The high frequency asymptote and the best fit line displayed on Figure 10 are reproduced on Figure 11. As discussed above, although the  $f^{-2.5}$  curve fits the data depicted on Figure 11, it is not consistent with simultaneous phase observations. Two theoretical curves for orientation angles of  $40^\circ$  and  $60^\circ$  are displayed on the figure. For a dominant irregularity layer at 240 km height which was observed in the four other spectra for the same satellite pass, the experimental observations should lie between the two curves for frequencies below 1 Hz. Both the 150 and 400 MHz log amplitude spectra observations are significantly higher than the theoretical estimate at frequencies below 1 Hz indicative of a dominant irregularity layer at a significantly lower height. The experimental data indicate a layer at a height near 100 km. The UHF received signal record shown on Figure 12 corresponds to the data used to calculate the spectrum. The data show relatively long period amplitude fluctuations unlike typical ionospheric scintillation but consistent with the lower scattering layer height hypothesis. The UHF and VHF spectra on Figure 11 do not agree with each other for frequencies between 1 and 10 Hz. Since the UHF spectra agree with the expected asymptotic shape of the curve, the VHF data are considered spurious. Interference was noted at VHF for the time interval used to construct the spectra, and the most probable explanation for the observed increase in power spectral density above the expected level is the additive contribution of low level interference.

The first order perturbation theory used to derive the variance and power spectra for  $X$  and  $\phi$  can also be used to derive the two frequency correlation function for  $X$ . The results

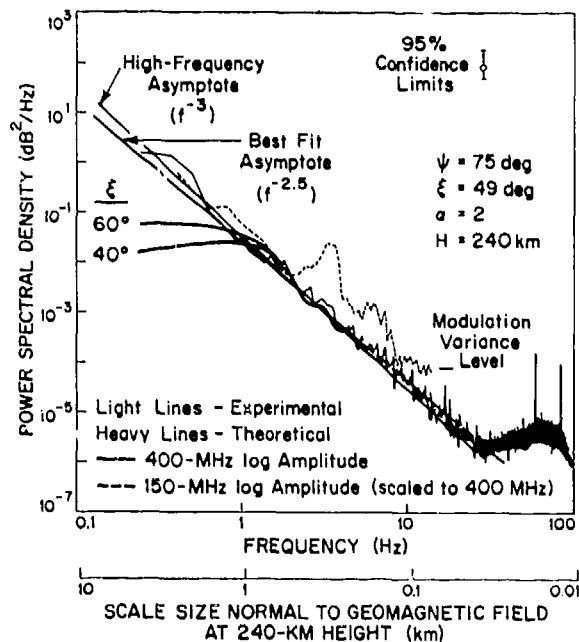


Figure 11. 150 and 400 MHz log amplitude spectra for 2033 GMT 20 April 1971.

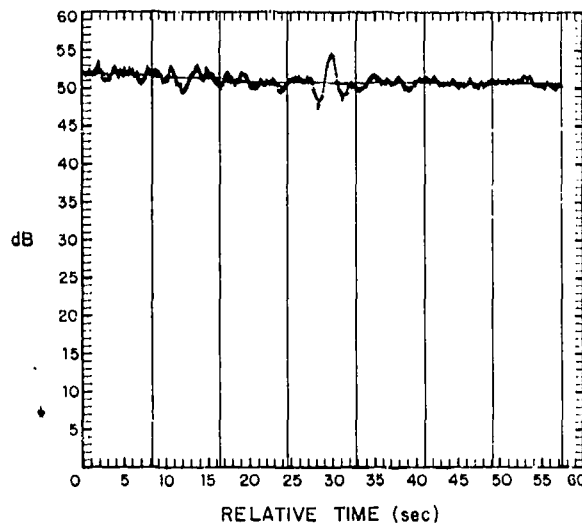


Figure 12. 400 MHz received power for 2033 GMT 20 April 1971.

of such an analysis are depicted on Figure 13 for three choices of  $p$ . The calculations show relatively high correlations for wide frequency spacings. Superimposed on the theoretical calculations are observations made by a number of authors. The 150 MHz observations were made at Millstone. Except for the Millstone Hill observations, the 113 MHz observations by Aarons et al (1967), and the 1500 MHz observations by Taur (1973), the data correspond in part to strong scintillation for which the weak scintillation predictions are not adequate. The

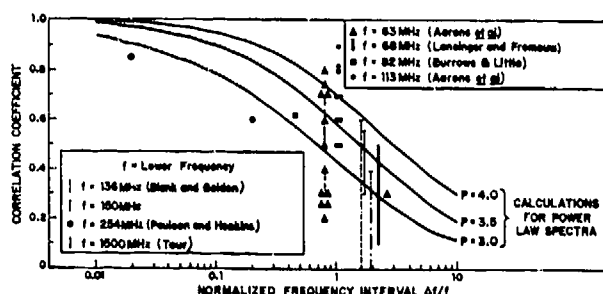


Figure 13. Two frequency correlation functions for amplitude fluctuations.

data by Aarons et al show good agreement with calculations using the value of  $p = 4$  required to explain the observations quoted above. The 1.5 GHz data of Taur show better agreement with  $p$  between 3 and 3.5. The spectra on Figures 10 and 11 show a best fit curve of  $f^{-2.5}$  corresponding to  $p = 3.5$  to explain the effect of the small scale size spectral increase. For the correlation coefficient between 1.5 and 4 GHz reported by Taur, the effect of the spectral increase should be important. The  $p = 3.0$  to 3.5 values compensate for the spectral increase showing that it is important to the equatorial GHz observations.

The correlation coefficients observed at Millstone span the range from 0 to 0.6 for conditions of weak scintillation. The theoretical estimate is 0.61. Two frequency correlation coefficients for a satellite pass on 3 Aug. 1971 are depicted on Figure 14 and show variable correlation coefficients with values between 0.2 and 0.5. The single-edge diffraction event is another E-region scintillation occurrence. The calculations were made assuming that the line-of-sight paths at both frequencies were coincident. Due to ionospheric refraction, the ray paths follow slightly different trajectories. At F-region heights and at an elevation angle of  $16^\circ$ , the ray path separation (normal to the rays) is the order of 400m (nighttime value). The ray separation, therefore, is a significant fraction of a Fresnel zone leading to additional decorrelation. The theoretical value for the correlation function displayed on Figure 13, therefore, should be interpreted only as an upper bound.

A coherency analysis was conducted for the Millstone two frequency observations to begin to investigate the effect of ray separation. Both the coherency values and the power spectral densities at both 150 and 400 MHz are displayed on Figure 15. The data were taken at the slow, 15 sample per second rate. The theoretical estimates of power spectral density for an axial ratio of two are displayed. The log amplitude spectra show reasonable agreement with the theoretical estimates for scale sizes larger than 500m. The coherency estimates show that the spectral components do not show significant correlation (coherency value below

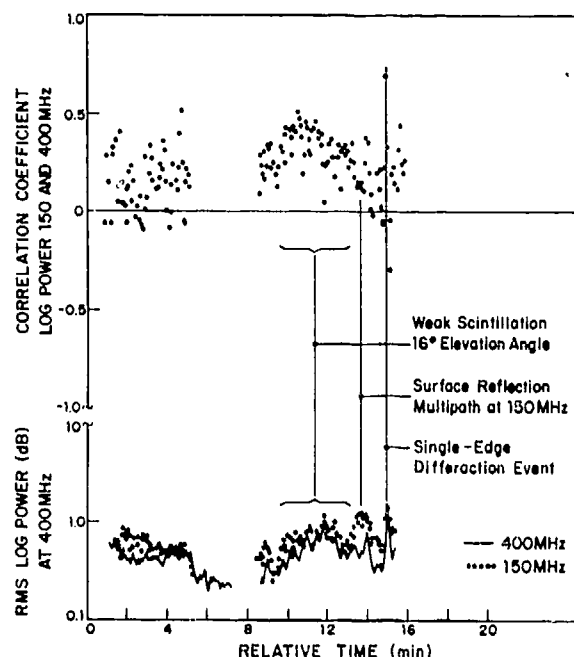


Figure 14. Two frequency correlation coefficient observations for pass of object 2965 rising at 0255 GMT 3 Aug. 1971.

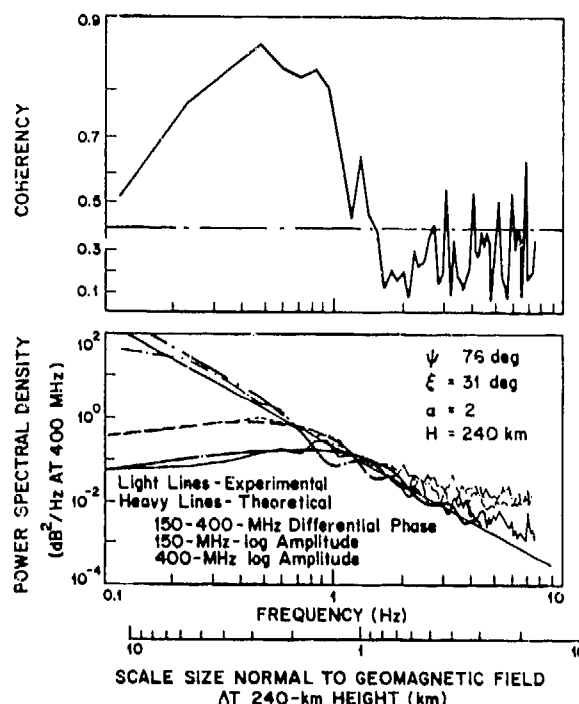


Figure 15. Two frequency coherency for 0334 GMT 5 Aug. 1971.

0.4 corresponding to 95% confidence limit) for scale sizes smaller than 900 m. Significant correlation at higher frequencies or smaller scale sizes is associated with folded modulation lines and is not ionospheric in origin. The observations were made at an elevation angle of  $20^\circ$  corresponding to a ray separation of less than 500m. Significant decorrelation appears to occur for scale sizes larger than the Fresnel zone size at the lower frequency or the sum of the higher frequency Fresnel zone size and the ray separation. A theoretical analysis of the effect of ray separation on coherency has yet not been performed. The coherency observations are consistent with the expectation that the fluctuations will not be correlated on scale sizes the order of the ray separation.

#### CONCLUSIONS

The experimental results show that the Rytov approximation provides a reasonable description of scintillation over a wider range of scintillation intensity than does the Born approximation to the wave equation. The log amplitude, phase description of scintillation, therefore, is preferred to the in-phase, quadrature amplitude description. Using the log amplitude, phase description for frequencies below 1 GHz,  $\sigma_\chi$  varies as  $\lambda^{1.5}$  for  $\sigma_\chi < 5.6$  dB and takes on a constant value of 5.6 dB when the  $\lambda^{1.5}$  relationship predicts higher values. The doppler spread and rms phase fluctuations vary as  $\lambda^{1.0}$  for both strong and weak scintillation. The experimental observations of spectra and of two frequency correlation coefficients are consistent with the power law model and an exponent of -4 ( $p = 4$ ).

An observed small scale increase in the power spectral density fluctuations may modify the wavelength scaling for wavelength smaller than 30 cm (carrier frequencies greater than 1 GHz). For the observations available to date, the wavelength scaling may be in error by as much as a factor of three. The small scale increase may explain, in part, the observed scintillation at GHz wavelengths.

#### REFERENCES

- Briggs, B.H. and I.A. Purkin (1965), "On the Variation of Radio Star and Satellite Scintillations with Zenith Angle", *J. Atmos. Terr. Phys.*, 25, 339-365.
- Crane, R.K. (1974), "Morphology of Ionospheric Scintillation", Tech. Note 1974-29, Lincoln Laboratory MIT.
- Taur, R.R. (1974), "Gigahertz Ionospheric Scintillation", *COMSAT Tech. Rev.* (to be published Fall 1974).
- Budden, K.G. (1965), "The Amplitude Fluctuations of the Radio Wave Scattered from a Thick Ionospheric Layer with Weak Irregularities", *J. Atmos. Terr. Phys.*, 27, 155-172.
- Tatarski, V.I. (1967), *The Effects of the Turbulent Atmosphere on Wave Propagation*, Nauka, Moscow; Trans. avail. U.S. Dept. of Commerce, National Technical Information Service, Springfield, Va.
- Dyson, D.L., J.P. McClure and W.B. Hanson (1974), "In-situ Measurements of the Spectral Characteristics of F-region Ionospheric Irregularities", *J. Geophys. Res.*, 79, 1497-1502.
- Ghiloni, J.C., editor, (1973), "Millstone Hill Radar Propagation Study: Instrumentation", Tech. Rept. 507, Lincoln Laboratory MIT.
- Wernik, A.W. and C.H. Liu (1974), "Ionospheric Irregularities Causing Scintillation of GHz Frequency Radio Signals", *J. Atmos. Terr. Phys.*, 36, 871-879.
- Craft, H.D. and L.H. Westerlund (1972), "Scintillation at 4 and 6 GHz Caused by the Ionosphere", AIAA paper No. 72-179, AIAA Library, New York.
- Blank, H.A. and T.S. Golden (1973), "Analysis of VHF/UHF Frequency Dependence, Space, and Polarization Properties of Ionospheric Scintillation in the Equatorial Region", 1973 IEEE International Comm. Conf. Proc., pp. 17-27 to 17-35 (June 1973).
- Paulson, M.R. and Hopkins, R.V.F. (1973), "Effects of Equatorial Scintillation Fading on Satcom Signals", NELC/TR 1875, Naval Electronics Laboratory Center, San Diego, California.
- Taur, R.R. (1973), private communications.
- Aarons, J., R.S. Allen and T.J. Elkins (1967), "Frequency Dependence of Radio Star Scintillations", *J. Geophys. Res.*, 72, 2891-2902.
- Lansinger, J.M. and E.J. Fremouw (1967), "The Scale Size of Scintillation Producing Irregularities in the Auroral Ionosphere", *J. Atmos. Terr. Phys.*, 29, 1229-1242.
- Burrows, K. and C.G. Little (1952), "Simultaneous Observations of Radio Star Scintillations on Two Widely Spread Frequencies", *Jodrell Bank Ann.*, 1, 29-35.

# FIRST-ORDER SIGNAL-STATISTICAL MODELING OF SCINTILLATION

E. J. Fremouw and C. L. Rino  
Stanford Research Institute  
Menlo Park, California 94025

## INTRODUCTION

Our existing empirical model for F-layer-produced scintillation (Fremouw and Rino, 1973) was based on an incomplete scattering theory (Briggs and Parkin, 1963) and on restrictive data. It provides for calculation only of scintillation index,  $S_4$ ; it suffers seriously from a lack of accounting for extinction; and it is geophysically incomplete. We are currently attempting to remove or mitigate these deficiencies, and this paper is a progress report on that effort.

In the next section we review the basis for, and salient points of, the existing model, including its known deficiencies. The current modeling effort is outlined in the third section, starting with a comparison of new scattering theories with the theory of Briggs and Parkin and finishing with a description of our procedure for applying the new theoretical results to modeling  $S_4$  and first-order signal-statistical distributions. We conclude, in the final section, with our assessment of prospects for an improved first-order model and for its extension into second-order (correlation) signal-statistical domains.

## THE EXISTING MODEL FOR $S_4$

The Briggs and Parkin scattering theory permits calculation of the normalized fourth moment of one component of the scattered electric field at an observing point--namely, the component in phase with the field at the same point in the absence of scattering. For sufficiently weak scatter, the component in phase quadrature with such a reference (Bowhill, 1961) contributes insignificantly to the fluctuation of received signal inten-

sity, and Briggs and Parkin made this very-weak-scatter assumption. Under this assumption the resultant field,  $E$ , is equated to the in-phase component, and the normalized variance of received signal intensity,

$$S_4 \triangleq \frac{\langle (E E^*)^2 \rangle - \langle E E^* \rangle^2}{\langle E E^* \rangle^2}, \quad (1)$$

becomes equal to the component moment analyzed by Briggs and Parkin.

Under additional assumptions about the geometry and the scattering medium, the most important being a Gaussian spatial spectrum, the Briggs-and-Parkin scattering formula is

$$S_4^2 = R_0^2 [1 - (\cos U_1 \cos U_2)^{\frac{1}{2}} \cos \frac{1}{2}(U_1 + U_2)]^{\frac{1}{2}} \quad (2)$$

where  $U_1 = \tan^{-1}(2\lambda z/\pi r_0^2)$ ,

and  $U_2 = \tan^{-1}(2\lambda z/\pi \gamma^2 r_0^2)$ . The second factor in Eq. (2) accounts for post-scattering diffraction, and the ionosphere's effective scattering coefficient is given by

$$R_0 = \sqrt{\pi} r_0^2 \lambda^2 L \sec^2 \theta \frac{a}{\gamma} \epsilon_0 \langle (\Delta N)^2 \rangle \quad (3)$$

where  $r_0$  is the classical electron radius,  $\lambda$  is the radio wavelength,  $L$  is the thickness of the scattering layer,  $\theta$  is the incidence angle on the scattering layer,  $\gamma$  is the line-of-sight projection of the irregularity axial ratio,  $a/\epsilon_0$  is the transverse scale size, and  $\langle (\Delta N)^2 \rangle$  is the variance of electron concentration. The diffraction is controlled by the

size of the radio Fresnel zone,  $\lambda z$ .

The modeling was performed by picking values for  $\xi_0$  and  $a$  that were inferred from various measurements (Liszka, 1963; Koster, 1963; Aarons and Guidice, 1967; Iansinger and Fremouw, 1967) to calculate the diffraction factor and then to iterate  $R_0$  on published values of  $S_4$ . By means of experimental estimates for  $L$  (Yeh and Swenson, 1964; Kent and Koster, 1966) and those for  $\xi_0$  and  $a$ , the empirical model for  $R_0$  was expressed in terms of a morphological model for  $\langle(\Delta N)^2\rangle$ . The quantities  $\theta$  and  $z$  and the projection factor relating  $\gamma$  to  $a$  were calculated from the geometry of the published observations and a dipole model of the geomagnetic field.

The resulting model for  $\langle(\Delta N)^2\rangle$  was of the form (Fremouw and Rino, 1973):

$$\begin{aligned} \langle(\Delta N)^2\rangle^{\frac{1}{2}} = & \Delta N_{eq}(R, D, t, \lambda) + \Delta N_{mid}(t, \lambda) \\ & + \Delta N_{hi}(R, t, \lambda) + \Delta N_{aur}(R, t, \lambda) \quad (4) \end{aligned}$$

where the four terms describe ionospheric contributions to scintillation that predominate, respectively, at equatorial, middle, high and auroral latitudes. The contributions were modeled in terms of the following four independent variables: sunspot number,  $R$ ; day of the year,  $D$ ; local time of day,  $t$ ; and geomagnetic latitude,  $\lambda$ .

Three main defects of the existing model are known. First, based mainly on VHF observations and on the Briggs-and-Parkin scattering formula [Eqs. (2) and (3)], it underestimates  $S_4$  at frequencies above VHF. Second, it does not account for the relation of scintillation morphology to hour-by-hour and night-by-night changes in geomagnetic activity. These first two deficiencies are illustrated in Figure 1 (Evans, 1973), and Pope (1974) has proposed a correction for the second defect by parameterizing the model's high-latitude term on  $K_p$ . The third major defect is insufficient empirical testing at polar-cap latitudes, which we hope to remedy in the next few months.

#### IMPROVED MODELING

We believe the failure of the existing model to provide proper frequency scaling of scintillation stems from inadequacy of the Briggs-and-Parkin scattering theory, particularly the incorporation of a Gaussian spatial spectrum, and of our applying the theory with no correction for multiple scatter. If multiple

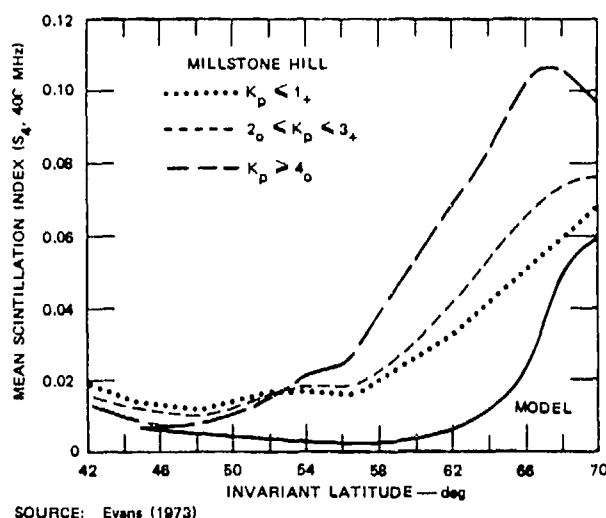


FIGURE 1 COMPARISON OF EXISTING MODEL FOR  $S_4$  WITH OBSERVATIONS PERFORMED IN THE NORTHEASTERN U.S., SHOWING UNDERESTIMATION OF UHF SCINTILLATION INDEX AND OMISSION OF GEOMAGNETIC DEPENDENCE

scatter prevailed in some of the data we used for modeling, then ignoring extinction caused us to underestimate  $\langle(\Delta N)^2\rangle$ , leading to underestimation of the scattering coefficient at higher frequencies.

More subtle distortion of the  $S_4$  frequency dependence stems from Briggs' and Parkin's tacit assumption of very weak scatter (more severe than the overt assumption of weak, single scatter), as defined early in the previous section of this paper. The very-weak-scatter assumption which is avoided in our current work, also precluded modeling of the full first-order distribution of complex signal statistics, which is desired for application to communication-channel modeling. We shall explore extension of scintillation modeling beyond the single parameter  $S_4$  in the following two subsections.

#### Comparison of Theories

The basic hypothesis of our renewed modeling is that the quadrature components of a scintillating signal are jointly Gaussian variates, as has been verified for amplitude statistics by Rino, Livingston, and Whitney (1974). According to this hypothesis, the first-order signal statistics are totally defined by the variances of the in-phase and phase-quadrature components,  $\sigma_x^2$  and  $\sigma_y^2$ , respectively, and their covariance,  $\sigma_{xy}^2$ .

The three variances can be related (Rino and Fremouw, 1973) to the characteristics of the scattering medium by generalizing the calculation performed by Briggs and Parkin, involving the following two fundamental parameters of the received signal,  $E = \langle E \rangle + E_s$ :

$$R_o \triangleq \langle E_s E_s^* \rangle \quad (5)$$

$$B_o \triangleq \langle E_s E \rangle, \quad (6)$$

after proper normalization to ensure energy conservation. The link is by virtue of the fact that

$$\sigma_x^2 = \frac{1}{2} (R_o - \text{Re} \{B_o\}) \quad (7)$$

$$\sigma_y^2 = \frac{1}{2} (R_o + \text{Re} \{B_o\}) \quad (8)$$

$$\sigma_{xy}^2 = \frac{1}{2} \text{Im} \{B_o\} \quad (9)$$

The situation can be envisioned geometrically in terms of a correlation ellipse on the complex plane, as illustrated in Figure 2, whose size, elongation, and orientation are dictated, respectively, by the parameters

$$R_o = \sigma_x^2 + \sigma_y^2 \quad (10)$$

$$\frac{|B_o|}{R_o} = \frac{[(\sigma_x^2 - \sigma_y^2)^2 + 4\sigma_{xy}^2]^{\frac{1}{2}}}{R_o} \quad (11)$$

$$\delta = \frac{1}{2} \left[ \tan^{-1} \left( \frac{\text{Im} \{B_o\}}{\text{Re} \{B_o\}} \right) \right] - \frac{\pi}{2} \quad (12)$$

Scattering theories based on Gaussian signal statistics describe diffraction in terms of a trend toward the special case of Rice statistics, by means of simultaneous rotation ( $0 \rightarrow \delta \rightarrow 45^\circ$ ) and circularization

( $1 \rightarrow \frac{|B_o|}{R_o} \rightarrow 0$ ) of the correlation ellipse.

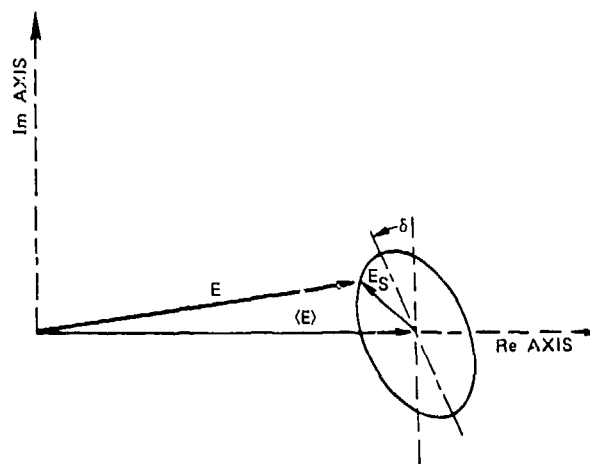


FIGURE 2 PHASOR DIAGRAM FOR CONSIDERATION OF FIRST-ORDER SIGNAL STATISTICS, SHOWING ELLIPTICAL CONTOUR OF EQUAL PROBABILITY PREDICTED BY THE GAUSSIAN-STATISTICS HYPOTHESIS

Since the Briggs-and-Parkin theory involved only the in-phase component of  $E_s$ , the only diffraction effect calculated was the post-scattering growth of  $\sigma_x^2$  that accompanies the trends in  $|B_o|/R_o$  and  $\delta$  [as can be seen from Eqs. (7) and (12)]. The theory was generalized to account for the trends in all three variances and in the corresponding ellipse parameters by Rino and Fremouw (1973a), who retained the Gaussian form for the spatial spectrum in order to permit analytical solution of the integrals that arise. The results, in terms of the three ellipse parameters, are as follows:

$$R_o = \sqrt{\pi} r_e^2 \lambda^2 I \sec^2 \theta \frac{a}{\beta^2} \langle (\Delta N)^2 \rangle \quad (13)$$

$$\frac{|B_o|}{R_o} = \left[ (1 - \beta^{-2} Z_g^2 \sec^2 \theta)^2 + Z_g^2 (\beta^{-2} f_1 + f_2)^2 \right]^{-\frac{1}{4}} \quad (14)$$

$$\delta = \frac{1}{4} \tan^{-1} \left[ \frac{Z_g (\beta^{-2} f_1 + f_2)}{1 - \beta^{-2} Z_g^2 \sec^2 \theta} \right] \quad (15)$$

where

$\beta$  = Horizontal projection of the irregularity axial ratio,  $a$

$$\begin{aligned}
f_1 &= 1 + \tan^2 \theta \cos^2 \phi \\
f_2 &= 1 + \tan^2 \theta \sin^2 \phi \\
\phi &= \text{Azimuth from geomagnetic meridian plane} \\
Z_g &= \frac{2 \lambda z \sec \theta}{\pi \epsilon_0^2}
\end{aligned}$$

and the other quantities are as defined after Eq. (3).

Equations (13), (14), and (15) result from integrations over the spatial spectrum of irregularities, assumed to have a Gaussian form. For the experimentally observed (Rufenach, 1972; Dyson, McClure, and Hanson, 1974) power-law spectrum, approximate means must be used to solve the integrals. The ellipse parameters are given (Rino and Fremouw, 1973b) in terms of a real integral  $I$  and a complex integral  $J$ , as follows:

$$R_o = \quad (16)$$

$$\frac{2}{\sqrt{\pi}} r_e^2 \lambda^2 L \sec^2 \theta \frac{\Gamma(\nu + 1/2)}{\Gamma(\nu - 1)} \propto \langle (\Delta N)^2 \rangle I$$

$$\frac{|B_o|}{R_o} = \frac{|J|}{I} \quad (17)$$

$$\delta = 1/2 \tan^{-1} \left[ \frac{\text{Im}[J]}{\text{Re}[J]} \right] \quad (18)$$

where  $\alpha$  is a scale parameter in the spatial spectrum and  $\nu$  specifies the power-law spectral index.

Under an approximation valid at frequencies above about 100 MHz (Fremouw and Rino, 1974a), the real integral can be solved analytically to yield simply

$$I = \frac{\pi}{\beta(\nu - \frac{1}{2})} \quad (19)$$

The complex integral, on the other hand, must be solved numerically; it is as follows:

$$\begin{aligned}
J &= \\
&\int_0^\infty \int_0^{2\pi} \frac{\sin[\epsilon q^2 J(\theta, \phi)] \exp[i Z_p q^2 J(\theta, \phi)]}{[1 + q^2 (\beta \cos^2 \theta + \sin^2 \theta)]^{\nu + 1/2}} d\theta dq
\end{aligned} \quad (20)$$

where

$$\epsilon = \frac{\lambda L \sec \theta}{8\pi\alpha^2}, \quad Z_p = \frac{\lambda z \sec \theta}{2\pi\alpha^2}$$

$$J = [1 + \tan \theta \cos^2(\phi - \phi)]^2$$

Equations (16) and (19) yield an analytical expression for the size of the complex-signal correlation ellipse,  $R_o$ . It remains to consider the ellipse's elongation,  $|B_o|/R_o$ , and orientation,  $\delta$ , which are not independent. The nature of the relationship between them in the Gaussian-spectrum scattering theory can be seen by inspection of Eqs. (14) and (15). The functional relationship is plotted in the heavier solid curve in Figure 3, for the case of isotropic irregularities ( $\beta = \alpha = 1$ ) and normal incidence ( $\theta = 0$ ). The dashed curve on the figure is the relation obtained from numerical integration of Eq. (20) for the same thin-layer ( $L = 0$ ) conditions. The structure in the upper left-hand portion of the dashed curve is an artifact of numerical integration over finite limits, which becomes decreasingly accurate as  $Z_p$  gets large.

Both the theories described above arise from characterizing the scattering medium solely by means of a spatial power spectrum based on the concept of strict statistical homogeneity, although it is clear that strict homogeneity (or spatial stationarity) is an idealization. Rino (1974) has relaxed this assumption to the weaker postulate of locally homogeneous statistics (Tatarski, 1971) under which the medium is characterized by a spectrum-related structure function and a quasi-deterministic term describing the largest-scale structure.

One of the departures of the locally homogeneous (LH) theory from the strictly homogeneous (SH) ones is illustrated by the dash-dot curve in Figure 3. According to all the theories, the radio wave emerges from the scattering layer with signal statistics that correspond to a highly elongated correlation ellipse (large  $|B_o|/R_o$ ) oriented nearly along the imaginary axis (small  $\delta$ ) of the complex



plane. As the wave propagates in free space, the ellipse simultaneously rotates and circularizes, and the signal statistics become more and more noiselike. The Gaussian and power-law SH theories, in fact, predict an inexorable approach to Rice statistics ( $|B_0|/R_0 = 0.6 = 45^\circ$ ) as the wave propagates to great distance. The curve calculated from LH theory falls short of Rice statistics, approaching a far-zone limit of

$$\lim_{R_0} \frac{|B_0|}{R_0} = [1 - 2^{-(\mu+1)}] \sec \frac{\mu\pi}{2} \quad (21)$$

$$\lim \delta = -\frac{\mu\pi}{2} \quad (22)$$

where  $\mu = -\nu + \frac{1}{2}$ .

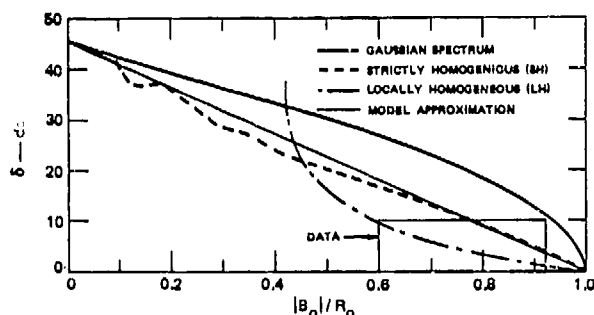


FIGURE 3 RELATION OF PROBABILITY-ELLIPSE ELONGATION ( $|B_0|/R_0$ ) AND ORIENTATION ( $\delta$ ) IN THE CASE OF NORMAL INCIDENCE ON A LAYER OF ISOTROPIC IRREGULARITIES, FOR THREE DIFFERENT CHARACTERIZATIONS OF THE MEDIUM. Also shown are a simple approximation useful for modeling and the region occupied by data analyzed so far.

The question of far-zone limiting behavior may be academic, because data analyzed thus far lie within the "near-zone" box indicated in the lower right-hand portion of Figure 3. This restricted data sample (ten digital records of real amplitude recorded at Millstone Hill, Massachusetts, by Whitney and Aarons of AFCL) tends to favor the LH theory. If this tendency holds as the data sample is enlarged and extended to other geographic locations, the LH theory will be used for future modeling. A choice of theories will be important for modeling the scintillation spectrum and other second-order statistical quantities.

For first-order statistics, however, the differences predicted by the theories are relatively subtle. Moreover, the LH theory contains a parameter (the ratio of the contri-

butions made to  $R_0$  by the quasi-deterministic and the strictly random components of ionospheric structure) that would be difficult to model at present. Thus, we are proceeding with the first-order signal-statistical modeling on the basis of an approximation to the SH theory, but in a manner that can readily accommodate the LH formulation. The durability of the approximation, which is indicated by the straight line on Figure 3, can be appreciated by comparison of Figures 4 and 5.

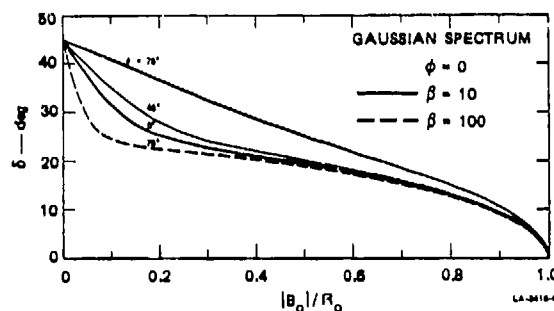


FIGURE 4 RELATION OF  $|B_0|/R_0$  AND  $\delta$  FOR DIFFERENT IRREGULARITY-ELONGATION PROJECTIONS ( $\beta$ ) AND INCIDENCE ANGLES ( $\theta$ ), FOR A GAUSSIAN SPATIAL SPECTRUM

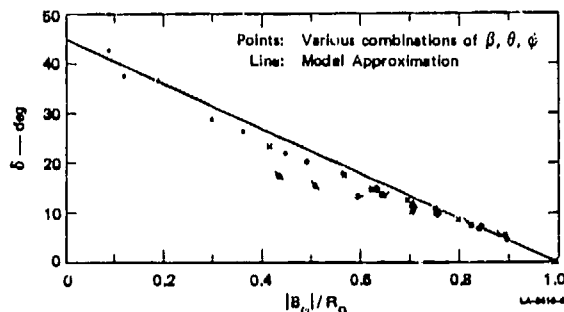


FIGURE 5 SCATTER DIAGRAM OF  $|B_0|/R_0$  vs  $\delta$  FOR DIFFERENT IRREGULARITY PARAMETERS AND GEOMETRIES, FOR A POWER-LAW ( $\nu = 4/3$ ) MEDIUM WITH STRICTLY HOMOGENEOUS (SH) SPATIAL STATISTICS. The approximation used for modeling is also shown.

Progression from the lower right to the upper left on a chart such as Figure 3 describes simultaneous rotation and circularization of the correlation ellipse. For the purpose of exploring this approach to Rice statistics for cases of off-normal incidence and nonisotropic irregularities, the analytic formulas given by the Gaussian theory [Eqs. (14) and (15)] were programmed and calculations were performed for different off-normal angles,  $\theta$ , and effective irregularity axial ratios,  $\beta$ . In general,

modest departures from the normal-incidence isotropic curves were found, as illustrated in Figure 4. Variation of another parameter, the azimuth,  $\phi$ , of the radio line of sight relative to the geomagnetic meridian plane, produced little change in the shape of the curves.

The numerical calculations necessary to obtain curves from the SH theory similar to those shown in Figure 4 for the Gaussian theory are rather time-consuming, especially for large values of  $\beta$ . Thus, only a few points were calculated for each combination of the parameters  $\beta$ ,  $\theta$ ,  $\phi$ . The isolated points are shown as a scatter diagram on Figure 5, with the twelve different symbols representing different combinations of the latter three parameters. What was found was a somewhat surprising tendency toward a "universal curve" (regardless of the values of  $\theta$  and  $\phi$ ) until the effective elongation,  $\beta$ , was increased to at least 10. As  $\beta$  was increased up to 30, the points tended to fall beneath the small- $\beta$  curve, in accord with the behavior of the Gaussian-theory curves.

We shall see shortly that the exact path by which a scattered wave traverses a chart of  $|B|/R$  versus  $\delta$  is not very important in dictating the first-order signal-statistics, at least for real amplitude (which is our main concern in the current work). This fact, coupled with the tendency toward "universality" of that path (especially in the regime occupied by the data analyzed to date), has prompted us to perform our modeling according to the straight-line path indicated in Figures 3 and 5. The analytical results indicated in Figure 4 provide us with guidance as to the sense of the error produced by this approximation ( $\delta$  estimated too large for a given value of  $|B|/R$ ).

Numerical calculations based on the LH theory displayed a similar universality, albeit conforming to a different curve (namely, that denoted in Figure 3 as "locally homogeneous"). Again, the difference between this curve and the approximation is that the latter would over-estimate  $\delta$  for a given value of  $|B|/R$  if it should turn out that transionospheric radio wave propagation behaves as described by the LH theory. We shall now see that for first-order amplitude statistics, it is less important to know which of the curves displayed in Figures 3, 4, and 5 is the more correct than it is to know how far the wave has moved along one of the curves in post-scattering propagation.

#### Application to Modeling of First-Order Signal Statistics

The desired product of our current effort is an improved model for amplitude scintillation, including a capability to calculate the statistical distribution of received signal intensity to be expected under given conditions. The existing model provides for calculation of only the normalized second moment of that distribution, the so-called  $S_4$  scintillation index. Because  $S_4$  is the single most important parameter for specifying the distribution, its calculation will remain the heart of the improved model. The dependence of  $S_4$  on the three correlation-ellipse parameters is given by the following expression (Rino and Frenouw, 1973a):

$$S_4^2 = 2R_o^2 \left[ 1 - \frac{|B_o|}{R_o} \cos(2\delta) \right] - 2R_o^2 \left[ 1 - \frac{|B_o|}{R_o} \cos(2\delta) \right] + R_o^2 \left[ 1 + \left( \frac{|B_o|}{R_o} \right)^2 \right] \quad (23)$$

By virtue of Eqs. (7) through (12), Eq. (23) can be written as

$$S_4^2 = 4R_o^2 \left( \frac{\sigma_x^2}{R_o} \right) - 4R_o^2 \left( \frac{\sigma_x^2}{R_o} \right)^2 + R_o^2 \left[ 1 + \left( \frac{|B_o|}{R_o} \right)^2 \right] \quad (24)$$

which shows that the ellipse orientation,  $\delta$ , influences  $S_4$  only through the relation of  $\delta$  to the variance,  $\sigma_x^2$ , of the in-phase signal component. It was only the in-phase component that was considered in the scattering theory of Briggs and Parkin. Equation (24) shows that for sufficiently weak scatter (very small  $R$ ) it is mainly the in-phase component that matters; as the scattering gets stronger, however, the quadratic terms in  $R$  become more important, and the phase-quadrature signal component exerts its influence on scintillation index by virtue of its impact on ellipse elongation,  $|B_o|/R_o$ .

We can improve the  $S_4$  model based on the Briggs and Parkin theory if we can evaluate the first two terms in Eq. (24) and account for the second-order influence of  $|B|/R$  in the final term. The main modeling effort will remain that of determining, from data, the

geophysical behavior of the ionosphere's effective scattering coefficient,  $R_o$ . We shall now see that this procedure can be followed and that the end result will be influenced little by whether the correlation ellipse rotates and circularizes according to the SH or to the LH scattering theory.

To begin, we wish to isolate some relevant quantities that are common to the LH and SH theories. First we separate  $R_o$  into two factors. The first, which is common to the two theories, is

$$\sigma^2 = \frac{C}{\alpha^2} r_e^2 \lambda^2 L \sec^2 \theta \quad (25)$$

depending only upon the strength,  $C_s$  [having units of (electrons per cubic meter)<sup>2</sup> per unit (spatial frequency)<sup>3</sup>], and width,  $\alpha^{-1}$  (having units of spatial frequency), of the ionosphere's spatial spectrum plus the other parameters in Eq. (25), which were defined earlier. The second factor,  $R_o/\sigma^2$ , contains all theory-dependent statistical information about the shape of the ionospheric scattering structure; it is defined simply that

$$R_o = \sigma^2 \left( \frac{R_o}{\sigma^2} \right) \quad (26)$$

We now rewrite Eq. (24) as

$$S_4^2 = 4\sigma^2 \left( \frac{\sigma^2}{\sigma^2} \right) - 4R_o \sigma^2 \left( \frac{\sigma^2}{\sigma^2} \right) + \sigma^4 \left( \frac{R_o}{\sigma^2} \right)^2 \left[ 1 + \left( \frac{|B_o|}{R_o} \right)^2 \right] \quad (27)$$

The reason for the above manipulations is that, under an approximation that appears valid at VHF and above (Fremouw and Rino, 1974b),  $\sigma_x^2/\sigma^2$  takes the same form in both the SH and LH theories. This ratio can be evaluated in terms of the real part of the complex integral,  $J$ , which was defined in Eq. (20), but with the unity term in the denominator suppressed in accord with the approximation. Numerical solution of the integral shows that the sinc function involving the layer thickness may be approximated by unity in all cases of interest. Taking advantage of the above simplifications and applying a standard trigonometric identity results in the following expression:

$$\frac{\sigma_x^2}{\sigma^2} = \left( \frac{Z}{2} \right)^{\nu - \frac{1}{2}} \int_0^\infty \int_0^{2\pi} \frac{\sin^2 [q^2 J(\theta, \phi)]}{(\beta^2 \cos^2 \phi + \sin^2 \phi)^{\nu + \frac{1}{2}}} d\phi dq \quad (28)$$

Equation (28) is convenient because now only geometric factors are contained in the integral that must be solved numerically. The main diffractive effects are contained in the Fresnel distance parameter,  $Z$ , which has been separated from the integral. For practical calculations in an operating scintillation code, this means, for instance, that the frequency dependence of  $\sigma_x^2/\sigma^2$  can be handled by a simple scaling without involving numerical solution of an integral.

In order to complete calculation of  $\sigma_x^2/\sigma^2$ , it is still necessary to solve the integral, which we shall define as  $F(\beta, \theta, \phi)$ , by some efficient means. The procedure we have chosen is to calculate selected points in a three-space of  $\beta$ ,  $\theta$ , and  $\phi$  once and for all by numerical solution of the integral in Eq. (28), and then to fit judiciously chosen algebraic functions to the points. The resulting functions will be incorporated into the operating scintillation code. The procedure for establishing the algebraic approximation to the integral was as follows.

First, the integral was solved numerically for  $\beta = 1, 2, 5, 10$ , and  $20$ , with  $\theta$  ranging from  $0^\circ$  through  $80^\circ$  (which exceeds the maximum-incidence angle of a transionospheric communication link on the F layer, by virtue of the ionosphere's curvature), and with  $\phi$  stepped between  $0^\circ$  and  $90^\circ$  (since the azimuth dependence is symmetrical about  $90^\circ$ ). After the results were plotted, inspection of the curves suggested a behavior of the following form:

$$F(\beta, \theta, \phi) = \frac{1}{2} [a(\beta, \theta) + b(\beta, \theta) + (b-a) \cos 2\phi] \quad (29)$$

where  $a$  = the value of the function when  $\phi = \pi/2$ , and  $b$  = the value when  $\phi = 0$ .

The values of  $a$  and  $b$  were then plotted as functions of  $\theta$  for given values of  $\beta$ . Again, the plots suggested analytic fits of the form

$$a(\beta, \theta) = c(\beta) [\sec \theta]^{m(\beta)} \quad (30)$$

$$b(\beta, \theta) = c(\beta) [\sec \theta]^{n(\beta)} \quad (31)$$

where  $c(\beta)$  = the value of the function when  $\theta = 0$ , and where the exponents  $m(\beta)$  and

$n(\beta)$  were chosen by forcing Eqs. (30) and (31) to match the machine calculations when  $\theta = 70^\circ$ , which is about its largest value for penetration of the F layer. The values of  $c$ ,  $m$ , and  $n$  were then employed in a one-dimensional, least-squares fitting routine to obtain best-fit polynomial expansions of  $c(\beta)$ ,  $m(\beta)$ , and  $n(\beta)$ .

The results of the above procedure were combined into an algebraic approximation to the integral in Eq. (28), and the approximation was then used to calculate curves of  $F(\beta, \theta, \phi)$  over the ranges of  $\theta$  and  $\phi$  and for the values of  $\beta$  originally employed in the numerical integration. Finally, similar curves were calculated for other (both intermediate and more extreme) values of  $\beta$ , and numerical integrations were performed for these new cases. The entire collections of numerical-integration and algebraic-approximation results were then compared to determine the efficacy of the approximate expression. An example of the comparison is presented in Figure 6 for a value of  $\beta$  not involved in development of the approximation; the smooth curves represent the algebraic fit and the individual points are results of the numerical integration. The fit is considered quite adequate for application to scintillation modeling.

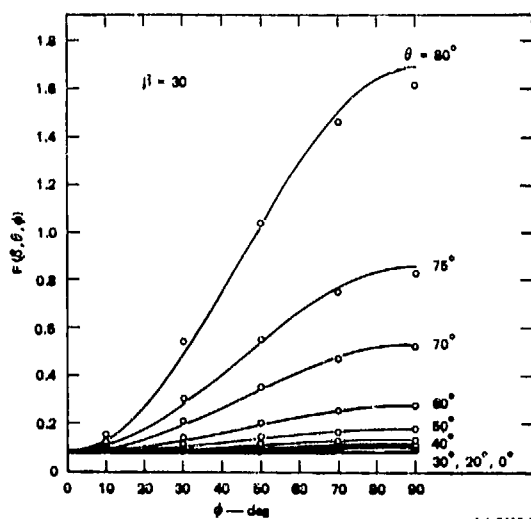


FIGURE 6 COMPARISON OF ALGEBRAIC APPROXIMATION (Eq. 29) TO VALUES OF THE INTEGRAL IN EQ. (28) FOR ONE VALUE OF EFFECTIVE (horizontally projected) IRREGULARITY AXIAL RATIO,  $\beta$

With development of the above procedure, we now have an algebraic and theory-independent means for calculating the normalized variance of the in-phase signal component,

as follows:

$$\frac{\sigma_x^2}{\sigma^2} = F(\beta, \theta, \phi) \left[ \frac{Z_p}{2} \right]^{\nu - \frac{1}{2}} \quad (32)$$

We note from Eqs. (7) and (12) that increasing  $\sigma_x^2$  for a given  $R_0$  corresponds to decreasing  $|B_0|/R_0$  and/or increasing  $\delta$ , all of which occur as a scattered radio wave propagates with increasing Fresnel distance,  $Z_p$ . The factor accompanying  $Z_p$  in Eq. (32) thus influences the rate at which the wave's first-order signal statistics progress across a chart such as Figures 3, 4, or 5 as the wave propagates to greater Fresnel distance. The quantity  $\sigma_x^2/\sigma^2$  is more important than either  $|B_0|/R_0$  or  $\delta$  in determining  $S_4$ , so this rate of progression across such a chart is more important than the precise curve by which the progression takes place.

As we noted from Eq. (24), however,  $|B_0|/R_0$  does exert a second-order influence on  $S_4$ , so we need a means for estimating it. This estimate can be made by choosing a curve such as the straight-line approximation on Figures 3 and 5, which is described as

$$\delta = \frac{\pi}{4} (1 - |B_0|/R_0) \quad (33)$$

and combining it with Eqs. (7) and (12) to yield the following transcendental equation relating  $|B_0|/R_0$  to  $\sigma_x^2/R_0$ :

$$\frac{|B_0|}{R_0} \left[ \cos \frac{\pi}{2} \left( 1 - \frac{|B_0|}{R_0} \right) \right] = 1 - 2 \frac{\sigma_x^2}{R_0} \quad (34)$$

Equation (34) is fitted very well, especially in the regime occupied by the data so far analyzed, by the following approximation:

$$\frac{|B_0|}{R_0} = 0.98 \left( 1 - 1.55 \frac{\sigma_x^2}{R_0} \right) \quad (35)$$

Combining Eq. (35) with Eqs. (26) and (27), we obtain the following useful expression for scintillation index:

$$S_4^2 = 4R_0 \left( \frac{\sigma^2}{R_0} \right) \left( \frac{\sigma_x^2}{\sigma^2} \right) - 4R_0^2 \left( \frac{\sigma^2}{R_0} \right) \left( \frac{\sigma_x^2}{\sigma^2} \right) + R_0^3 \left\{ 1 + \left[ 0.98 - 1.55 \left( \frac{\sigma^2}{R_0} \right) \left( \frac{\sigma_x^2}{\sigma^2} \right) \right]^2 \right\} \quad (36)$$

While containing some approximations in its third term, Eq. (36) is a considerable improve-

ment over the formula of Briggs and Parkin for  $S_4$ , which totally neglected both the second and third terms. The improvement should increase as the scattering becomes more intense (increasing  $R_0$ ).

The advantage of separating the first two terms of Eq. (36) into three factors, as above, is two-fold. First, the main diffraction effects can be accounted for independently of whether the LH or SH theory is the more correct by employing Eq. (32) to calculate  $\sigma_x^2/\sigma^2$ . And second, we can proceed to model the effective scattering coefficient  $R$  on the basis of either theory by employing the corresponding  $\sigma^2/R$  factor. If the other theory proves to be more accurate, we can then modify the model by employing the alternative  $\sigma^2/R$  factor and correcting our model of  $R_0$ .

We choose to begin modeling on the basis of SH theory because it involves a simpler  $\sigma^2/R_0$  factor--namely,

$$\frac{\sigma^2}{R_0} = 4\pi\beta \left( \nu - \frac{1}{2} \right). \quad (37)$$

Thus our procedure is to calculate  $\sigma_x^2/\sigma^2$  and  $\sigma^2/R$  from Eqs. (32) and (37), respectively, and to model  $R_0$  iteratively by comparing calculated values of  $S_4$  to observed values. Our first postulate for an  $R_0$  model was that corresponding to the existing model for the comparable quantity contained in the theory of Briggs and Parkin (Fremouw and Rino, 1973).  $R_0$  is varied by adjusting the product  $[C/\alpha^2]L$  in Eq. (25) as it affects Eq. (26).

The other two correlation ellipse parameters can be modeled by multiplying Eqs. (32) and (37) and then employing Eqs. (35) and (33) in sequence. Once a model exists for all three ellipse parameters, probability density functions for amplitude and for phase can be calculated, as described by Hatfield and Rino (1974).

#### CONCLUSION

Modeling of  $S_4$  and the amplitude probability density function is under way according to the above procedure. Published  $S_4$  data and histograms of received VHF and UHF amplitude, provided by Whitney and Aarons of AFCL, are being used to develop the model iteratively. When the modeling is finished, it will be a simple matter to provide a computer subroutine to integrate the amplitude probability density functions to produce cumulative density functions for use in establishing communication-link margins.

As a byproduct of the amplitude-statistics modeling, probability density functions for phase are being calculated. Testing of the model for phase statistics, however, must await data from the DNA-002 satellite beacon scheduled for launch in March of 1975. This beacon also will provide data for modeling of second-order signal statistics in the temporal, spatial, and spectral domains. It should be particularly useful for assessing the relative efficacy of the strictly homogeneous (SH) and locally homogeneous (LH) scattering theories.

Acknowledgment: The current work at SRI on modeling the transionospheric communication channel is sponsored by ARPA, through RADCL, under contract F30602-74-C-0279.

# References:

- Aarons, J., and D.A. Guidice, "The Size of Low-Latitude Ionospheric Irregularities Determined from Observations of Discrete Sources of Different Angular Diameter," J. Geophys. Res., Vol. 71, pp. 3277-3280 (1966).
- Briggs, B.H., and I.A. Parkin, "On the Variation of Radio Star and Satellite Scintillations with Zenith Angle," J. Atmos. Terr. Phys., Vol. 25, No. 6, pp. 339-366, UK (1963).
- Bowhill, S.A., "Statistics of a Radio Wave Diffracted by a Random Ionosphere", J. Res. Nat. Bur. Stand.-D, Radio Propagation, Vol. 65D, No. 3, (May-June 1961).
- Dyson, P.L., J.P. McClure, and W.B. Hanson, "In-Situ Measurements of the Spectral Characteristics of F-Region Ionospheric Irregularities," J. Geophys. Res., Vol. 79, No. 10, pp. 1495-1502, USA, (1974).
- Evans, J.V., ed., "Millstone Hill Radar Propagation Study: Scientific Results--Part II," Technical Report 509; Joint Radar Propagation Study, Lincoln Laboratory, Massachusetts Institute of Technology, Lexington, Mass., USA, (November 13, 1973).
- Fremouw, E.J. and C.L. Rino, "An Empirical Model for Average F-Layer Scintillation at VHF/UHF," Radio Science, Vol. 8, No. 3, pp. 213-222, USA, (1973).
- Fremouw, E.J., and C.L. Rino, "Modeling of Transionospheric Radio Propagation," Quarterly Technical Report 1, Covering the Period 15 May through 15 August 1974, SRI Project 3416, Contract F30602-74-C-0279, Stanford Research Institute, Menlo Park, Calif., USA, (16 November 1974).
- Fremouw, E.J. and C.L. Rino, "Modeling of Transionospheric Radio Propagation," Quarterly Technical Report 2, Covering the Period 16 August through 15 November 1974, SRI Project 3416, Contract F30602-74-C-0279, Stanford Research Institute, Menlo Park, Calif., USA, (22 November 1974).
- Hatfield, V.E., and C.L. Rino, "Non-Rician Statistics and Their Implications for Modeling Effects of Scintillation on Communication Channels," Paper Number 4-1 presented at Symposium on The Effect of the Ionosphere on Space Systems and Communications, Monday-Wednesday, 20-22 January 1975, Naval Research Laboratory, Washington, D.C., USA.
- Kent, G.S., and J.R. Koster, "Some Studies of Nighttime F-Layer Irregularities at the Equator Using Very High Frequency Signals Radiated for Earth Satellites," in Spread-F and its Effects Upon Radiowave Propagation and Communications, P. Newman, Ed., Technivision, Maidenhead, England, pp. 333-356, 1966.
- Koster, J.R., "Some Measurements of the Irregularities Giving Rise to Radio-Star Scintillations at the Equator," J. Geophys. Res., Vol. 68, No. 9, pp. 2579-2590, USA, (May 1, 1963).
- Lansinger, J.M. and E.J. Fremouw, "The Scale Size of Scintillation-Producing Irregularities in the Auroral Ionosphere," J. Atmos. Terr. Phys., Vol. 29, pp. 1229-1242, USA, (1967).
- Liszka, L., "A Study of Ionospheric Irregularities Using Transmissions at 54 Mc/s," Ark. Geofys (Sweden), Vol. 4, pp. 227-246 (1963).
- Pope, J.H., "High Latitude Ionospheric Irregularity Model," Radio Science, Vol. 9 No. 7, pp. 675-682, USA, (July 1974).
- Rino, Charles L., "Some Unique Features of the Transionospheric Channel," Paper Number 4-2 presented at Symposium on the Effect of the Ionosphere on Space Systems and Communications, Monday-Wednesday, 20-22 January 1975, Naval Research Laboratory, Washington, D.C., USA.
- Rino, C.L., and E.J. Fremouw, "Statistics for Ionospherically diffracted VHF/UHF Signals," Radio Science, Vol. 8, No. 3, pp. 223-233, USA, (1973a).
- Rino, C.L., and E.J. Fremouw, "Ionospheric Scintillation Studies," Final Report, Contract NAS5-21891, Stanford Research Institute, Menlo Park, California, USA, (November 1973b).
- Rino, C.L., R.C. Livingston, and H.E. Whitney, "Some New Results on the Statistics of Radio Wave Scintillation, A. Empirical Evidence for Gaussian Statistics," submitted for publication in J. Geophys. Res., USA, (1974).
- Rufenach, C.L., "Power-Law Wavenumber Spectrum Deduced from Ionospheric Scintillation Observations," J. Geophys. Res., Vol. 77, No. 25, pp. 4761-4772, USA, (September 1, 1972).
- Tatarskii, V.I., "The Effects of the Turbulent Atmosphere on Wave Propagation," TT-68-50464, Published for the National Oceanic and Atmospheric Administration, U.S. Dept. of Commerce

and the National Science Foundation, Washington,  
D.C., USA, by the Israel Program for Scientific  
Translations, Jerusalem, Israel, (1971).

Yeh, K.C., and G.W. Swenson, Jr., "F-Region  
Irregularities Studied by Scintillation of  
Signals from Satellites," J. Res. Nat. Bur.  
Stand., Vol. 68D, No. 8, pp. 881-894, USA,  
(August 1964).

# MORPHOLOGY OF IONOSPHERIC SCINTILLATION IN THE AURORAL ZONE\*

R.H. Wand and J.V. Evans  
Lincoln Laboratory MIT  
Lexington, Massachusetts 02173

## ABSTRACT

Over 2300 satellite beacon tracks conducted at Millstone Hill in the period January 1971 to March 1973 were used in a study of ionospheric scintillation. The targets employed were five satellites of the Navy Navigation Series which were in polar orbits and hence could be seen rising and setting in the north through the auroral region. The tracking results allowed the occurrence of scintillation to be determined as a function of invariant latitude ( $42^\circ - 70^\circ\text{N}$ ), local time, geomagnetic activity ( $K_p$ ) and season. The  $S_4$  scintillation index was calculated from fluctuations in the UHF (400 MHz) beacon signals and normalized to zenith using an assumed three dimensional power law spectrum of electron density fluctuations with an exponent of  $-4$ . A mean scintillation index was determined by averaging over all the sections of satellite track falling within each selected interval of time, invariant latitude,  $K_p$  and season. The scintillation boundary could then be defined, in a statistical sense, as the invariant latitude where the mean scintillation index exceeded some fixed level.

The analysis showed a marked seasonal dependence of scintillation for invariant latitudes above  $60^\circ$ . In summer the mean scintillation index was maximum at times roughly centered on 2200 hours. However, in winter the maximum was about six hours earlier than in summer. In general an increase in  $K_p$  tended to move the scintillation boundary towards lower latitudes and advance the time of maximum scintillation activity.

In addition to measuring the position of the scintillation boundary, the satellite tracking data were used to study another important feature separating the auroral and mid-latitude zones, namely the electron density trough. The latitudinal variation of the electron density at the F2 peak ( $N_{\text{max}}$ ) was determined for each track using UHF-VHF differential Doppler measurements combined with local vertical incidence ionosonde readings. Averaging  $N_{\text{max}}$  for many satellite tracks served to define the mean location of the electron density trough in the nighttime period. A comparison

of the positions of the electron density trough and the scintillation boundary for different seasons and  $K_p$  levels failed to show any significant correlation between the two features.

\*This work was sponsored by the Dept. of the Army.

## INTRODUCTION

An experimental program to study ionospheric propagation effects was conducted at Millstone Hill ( $42^\circ\text{N}$ ) during the period January 1971 to March 1973. Five satellites of the Navy Navigation System were tracked with a passive multi-lobe UHF beacon tracker on the 84-foot fully steerable antenna. A frequency selective subreflector was mounted in the antenna and this allowed simultaneous active tracking of the satellites with the L-band radar. The satellite beacon signal at VHF was also measured with a yagi antenna mounted on the edge of the dish and combined with the phase-locked UHF signal to determine differential Doppler.

The satellites were in almost circular polar orbits at heights near 1100 km, and were seen rising or setting through the auroral zone to the north. A number of parameters of interest in scintillation studies were determined along each satellite track, including the amplitude scintillation index at UHF (rms power/mean power), the rms traverse angle fluctuation ( $\sigma_{TR}$ ) at UHF, the rms elevation angle fluctuation ( $\sigma_{EL}$ ) at UHF and the rms differential phase ( $\sigma_\phi$ ). Here we report a statistical study of the incidence and intensity of amplitude scintillation and its dependence on local time and invariant latitude for different seasons and levels of magnetic activity. The occurrence of scintillation is compared with the average position of the mid-latitude electron density trough, as determined from the differential Doppler measurements.

Intercomparison of the results from various morphological studies of scintillation is often difficult because of differences in observing geometries and frequencies, and the variety of scintillation measured employed. When observations are made at a number of



elevation angles it is difficult to determine what effects are due to a true latitudinal variation of the ionospheric irregularities and what is produced solely by changes in observing geometry. The scaling laws for elevation angle and frequency depend on the characteristics of the irregularities and can be deduced in some instances, if the spectrum of electron density fluctuations is specified. The elevation scaling law was directly determined from the Millstone Hill scintillation observations and compared with predictions for a power-law irregularity spectrum. This allowed the scintillation results to be normalized to a fixed elevation angle (zenith in this case), and thus made largely independent of the location at which the observations were made. Useful expressions for converting the results to other observing frequencies and geometries are given.

#### DATA ANALYSIS

A total of 2376 satellite tracks were observed during the measurement period, representing almost 600 hours of observations. The raw data from each track were recorded on magnetic tape as digital samples of various parameters every 1/15 sec.

The UHF (400 MHz) beacon tracker provided amplitude and angle-of-arrival information, while measurements of the VHF (150 MHz) beacon signals were used to determine the UHF-VHF differential phase angle  $\phi$

$$\phi = \text{VHF phase angle} - 3/8 \text{ UHF phase angle} \quad (1)$$

Employing the differential phase angle effectively eliminates phase-angle changes produced by the changing path length as the satellite moves, thereby, leaving only the phase-angle changes produced by the ionosphere.

There were basically four observed track variables available from the Millstone program with which to study scintillation effects, namely, UHF amplitude, UHF traverse angle (traverse = azimuth x cosine of elevation), UHF elevation angle, and UHF-VHF differential phase. A parameter which measured the amount of fluctuation produced by ionospheric scintillation over a three-sec interval (45 samples) was calculated for each of the four variables.

The parameter used to characterize the UHF amplitude fluctuations was the scintillation index  $S$ , defined as the rms power about the mean divided by the mean power

$$S^2 = \frac{\langle A^4 \rangle - \langle A^2 \rangle^2}{\langle A^2 \rangle^2} \quad (2)$$

where  $A$  is the signal amplitude. This definition of  $S$  corresponds to the  $S_4$  index of Briggs and Parkin (1963).

The angle-of-arrival fluctuations were

measured by the rms traverse angle  $\sigma_{TR}$  and the rms elevation angle  $\sigma_{EL}$ . Fluctuations in differential phase were specified by the value  $\sigma_V$ . In each case the rms values were calculated after removing a linear trend by fitting a straight line to the 45 sample points. The trend correction allowed for relatively slow changes, which were present in addition to the more rapid fluctuations produced by ionospheric scintillations, over the three-second period. In traverse and elevation, the slower changes result from the changing orbital position and TID-induced angle fluctuations. The differential phase is proportional to the total ionospheric electron content (apart from an additive constant) along the propagation path, and, hence, there are also slow changes in differential phase as the propagation path changes due to satellite motion. The rms estimates were calculated for each three-second interval, as this normally exceeds the correlation time of scintillation parameters and, being sufficiently short, that removing the slower changes is not difficult.

Figure 1 is an example of the plots produced by the post-processing program, which calculates three-second values of track parameters. The geographic and invariant latitude scales are subionospheric latitudes assuming an ionospheric penetration point at a height of 300 km. Millstone Hill is at an invariant latitude of 56°N.

In the condensed form (three-second averages) all the results for the 2376 satellite tracks were stored on two magnetic tapes, so greatly facilitating a statistical analysis of the scintillation data. Values of the geomagnetic disturbance index  $K_p$  and local vertical incidence ionosonde measurements of  $f_oF2$  for each track were included on the condensed data tapes.

The differential doppler  $d\phi/dt$  was essentially proportional to the rate of change of electron content along the propagation path from the satellite to antenna. A method of using this measurement to determine the variation of the peak electron density ( $N_{max}$ ) along the satellite track is described in detail by Evans and Holt (1973). Electron density profiles of the Chapman type were assumed at all latitudes and normalization was achieved using the local determination of  $N_{max}$  from  $f_oF2$  measurements. Figure 1 includes a plot of  $\log_{10} N_{max}$  derived in this manner and the position of the mid-latitude electron density trough is evident near an invariant latitude of 64°N.

#### BASELINE CORRECTION

A small level of signal amplitude fluctuation was evident during all satellite tracks which is not caused by ionospheric scintillation. This produces a "baseline" level for the measured scintillation parameters, which is evident in Figure 1. The baseline level is elevation angle dependent and is typically 0.05

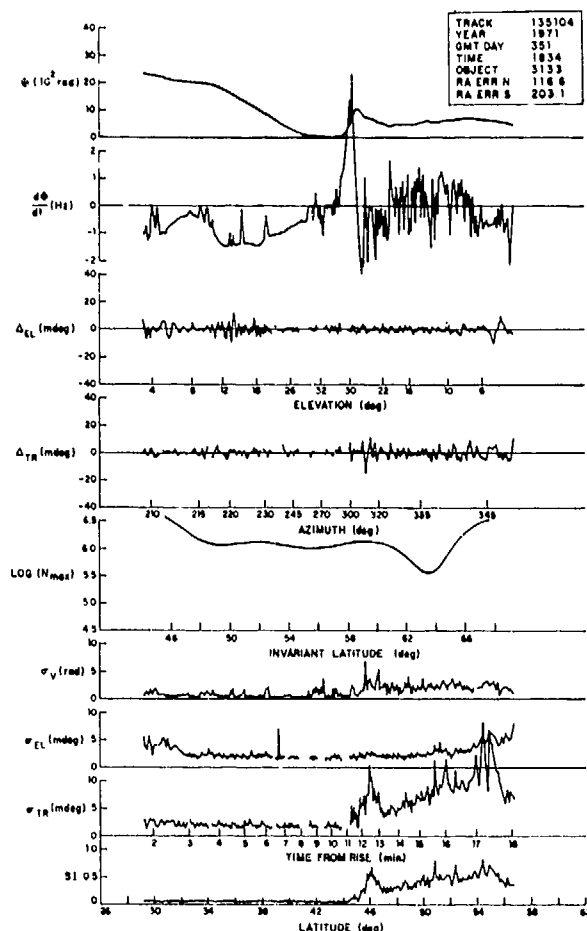


Figure 1. Typical post-processing results for a satellite track. Starting from the top are (a) UHF-VHF differential phase  $\phi$ , (b) differential Doppler  $d\phi/dt$ , (c) UHF elevation deviations (3-sec vs 63-sec running means), (d) UHF traverse elevations (3-sec vs 63-sec running means), (e)  $\log_{10}$  of peak electron density, (f) differential phase standard deviation, (g) UHF elevation standard deviation, (h) UHF traverse standard deviation, and (i) UHF scintillation index.

for S. The two major sources of amplitude fluctuations causing the baseline level were receiver noise and modulation on the satellite beacon signals, although tropospheric scintillation may also have been present at low elevation angles on some occasions. The UHF satellite beacon has a doughnut shaped radiation pattern designed to minimize mean signal strength changes as the satellite range varies with elevation angle. The net result was a decrease in mean signal strength at both high and low elevation angles and a consequent increase in the baseline level at these times as the signal-to-receiver noise ratio decreased. The baseline level was modeled as a constant part (due to modulation), plus an elevation dependent part (due to receiver noise) and

subtracted from the measured scintillation levels to give the scintillation index produced by ionospheric irregularities alone.

#### ELEVATION ANGLE DEPENDENCE OF SCINTILLATION

The manner in which the scintillation index varied along a satellite track was a combination of a true spatial change in the irregularity characteristics and effects produced by the changing geometry along the track. For a uniform layer of irregularities at a fixed height, the scintillation index increases as the elevation angle is lowered because of the increasing thickness of the irregularity layer along the propagation path, and also because the observer moves further from the irregularities. If these purely geometrical effects are corrected for, then the true latitudinal dependence of the scintillation index and irregularity characteristics may be studied.

The elevation scaling law for the scintillation index was determined directly from the Millstone Hill satellite tracking results. This was possible because the wide variety of satellite tracking geometries, which were used in the study, permitted observations at the same invariant latitude for a range of different elevation angles. In each  $2^\circ$  interval of invariant latitude, the mean scintillation index was determined as a function of elevation angle and used to calculate the elevation correction factor. The results are shown in Figure 2 along with the theoretical curve for a power-law irregularity spectrum with a three-dimensional spectral index of minus four. This type of irregularity spectrum predicts the observed elevation dependence quite well and explains many other characteristics of ionospheric scintillation observed at Millstone Hill and elsewhere (Crane, 1974). Based on the elevation scaling law shown in Figure 2, all the measured scintillation indices were converted to the standard case of a transmitter at an infinite distance in the zenith. This procedure removed any dependence of the results on the particular latitude at which the observations were made and the height of the satellite beacon which was tracked.

The ionospheric irregularities producing scintillation are elongated along the earth's magnetic field and the scintillation index depends on the elongation ratio  $\alpha$  and the propagation angle  $\psi$  (angle between propagation direction and magnetic field). Thus, the results should be normalized to some reference value of  $\psi$ , as well as a reference elevation angle. However, the dependence of S on  $\psi$  and  $\alpha$  is not strong provided that  $\psi > 30^\circ$ , a condition which is satisfied by most of the Millstone Hill satellite tracks, and it was sufficiently accurate to ignore the elongation of the irregularities in normalizing the observations of scintillation index. It should be remembered that the results only apply for observations transverse

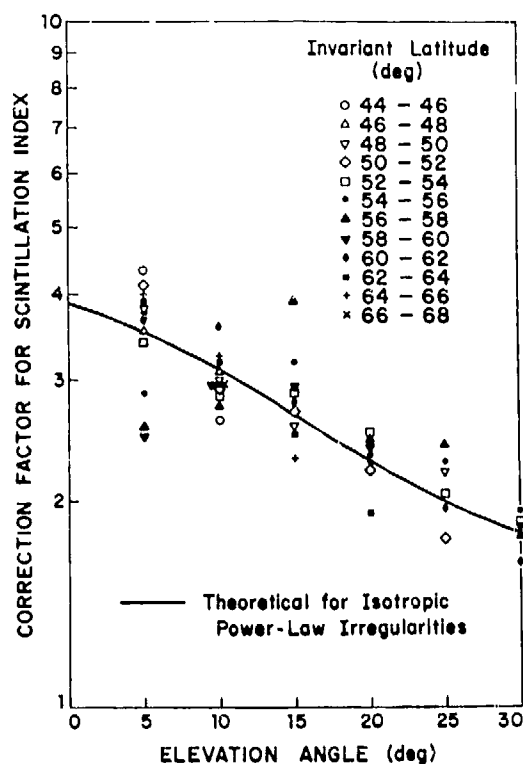


Figure 2. Elevation dependence of scintillation index from Millstone Hill satellite tracking data.

to the field lines rather than along the field lines.

#### DEPENDENCE ON GEOMAGNETIC ACTIVITY AND SEASON

A statistical analysis of the Millstone Hill tracking results was carried out after correcting the measured scintillation indices for baseline effects and normalizing to a transmitter at infinity in the zenith. The data were divided into three levels of geomagnetic activity (quiet  $K_p$  from 0<sub>0</sub> to 1<sub>+</sub>; moderate,  $K_p$  from 2<sub>-</sub> to 3<sub>+</sub>, and disturbed  $K_p$  from 4<sub>-</sub> to 5<sub>+</sub>) and two seasons (summer and winter, defined between equinoxes). For each two hour interval of local time and 2° interval of invariant latitude, the mean scintillation index was calculated and used to construct contour plots. The results are given in Figures 3 to 8 for the different  $K_p$  levels and seasons.

In general, scintillation activity is confined to invariant latitudes above 55° and increases with increasing  $K_p$ . Some quite marked seasonal differences are also evident. In summer the mean scintillation index is a maximum around local time 20 to 02 hours, whereas in winter the maximum occurs around 14 to 20 hours, i.e., about six hours earlier.

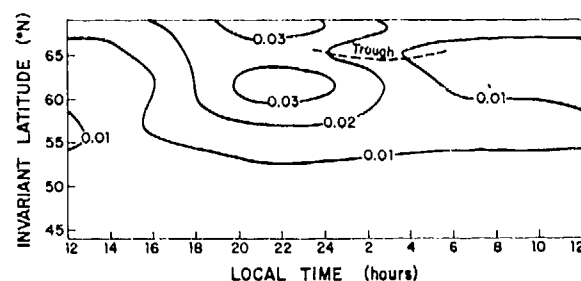


Figure 3. Contours of mean scintillation index at 400 MHz (normalized to zenith) from Millstone Hill satellite tracking observations 1971-1973. Results are for  $K_p$  from 0<sub>0</sub> to 1<sub>+</sub> in summer.

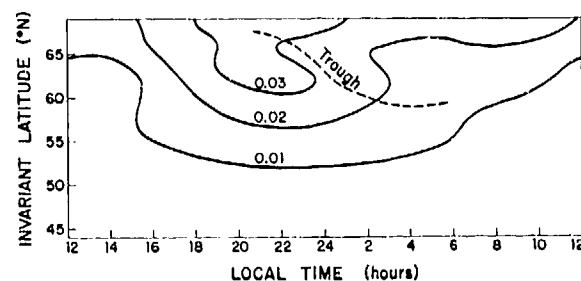


Figure 4. Contours of mean scintillation index at 400 MHz (normalized to zenith) from Millstone Hill satellite tracking observations 1971-1973. Results are for  $K_p$  from 2<sub>-</sub> to 3<sub>+</sub> in summer.

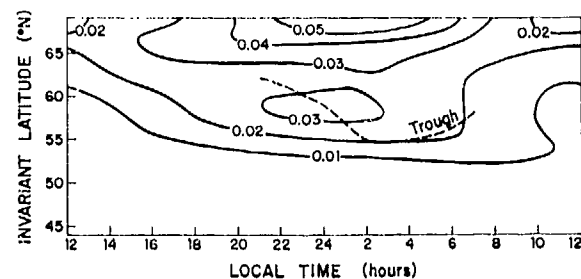


Figure 5. Contours of mean scintillation index at 400 MHz (normalized to zenith) from Millstone Hill satellite tracking observations 1971-1973. Results are for  $K_p$  from 4<sub>-</sub> to 5<sub>+</sub> in summer.

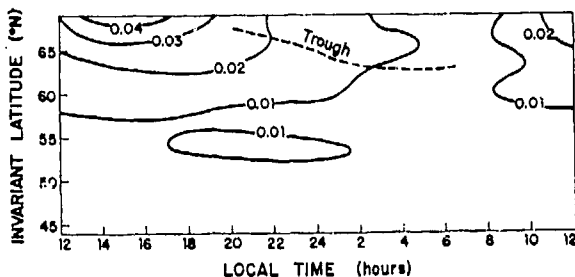


Figure 6. Contours of mean scintillation index at 400 MHz (normalized to zenith) from Millstone Hill satellite tracking observations 1971-1973. Results are for  $K_p$  from  $0_$  to  $1_$  in winter.

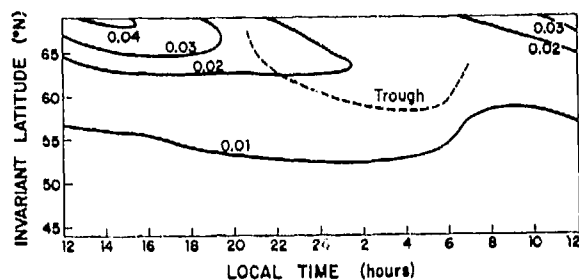


Figure 7. Contours of mean scintillation index at 400 MHz (normalized to zenith) from Millstone Hill satellite tracking observations 1971-1973. Results are for  $K_p$  from  $2_$  to  $3_$  in winter.

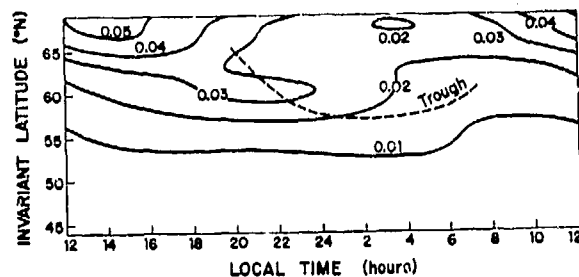


Figure 8. Contours of mean scintillation index at 400 MHz (normalized to zenith) from Millstone Hill satellite tracking observations 1971-1973. Results are for  $K_p$  from  $4_$  to  $5_$  in winter.

## SCINTILLATION BOUNDARY

The scintillation boundary is defined as the equatorward edge of F-region irregularity structure in the auroral zone which causes scintillation of UHF-VHF radio waves (Aarons and Allen, 1971; Aarons et al, 1969). The present observations on occasion show a rapid increase in scintillation at high latitudes which is characteristic of a sharp boundary (see Figure 1 for example), but more often the increase is more in the nature of a gradual onset of scintillation activity. A scintillation boundary can be defined from the present statistical analysis in an objective way by designating a particular (but arbitrary) value of the mean scintillation index to represent a boundary level. Figures 9 and 10 show the scintillation boundaries which result from selecting a mean scintillation index of 0.02 as a boundary value.

The seasonal dependence of scintillation is clearly evident in the position of the scintillation boundary shown in Figures 9 and 10. There is a southward progression of the boundary with increasing  $K_p$ , which is especially marked in the midnight sector in winter and the early morning sector in summer. This picture of the scintillation boundary is somewhat dependent on the particular mean value of scintillation index selected as a boundary value.

—  $K_p 0_$  to  $1_$   
 - - -  $K_p 2_$  to  $3_$   
 ·····  $K_p 4_$  to  $5_$

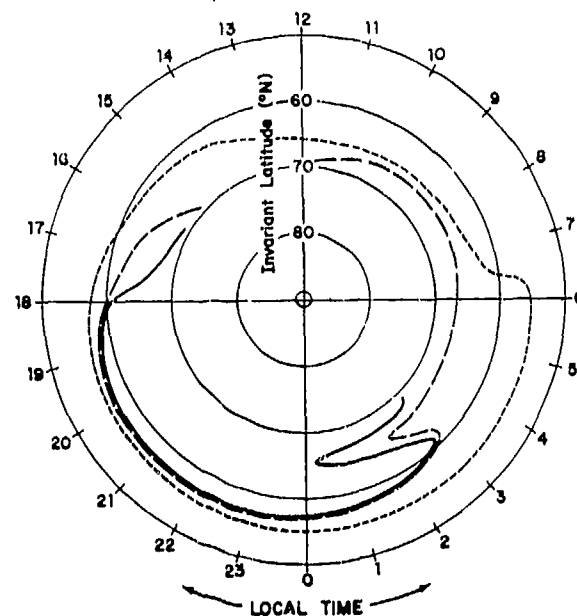


Figure 9. Position for the scintillation boundary in summer for three  $K_p$  intervals. The boundary is defined by a mean scintillation index of 0.02 at 400 MHz and vertical incidence.

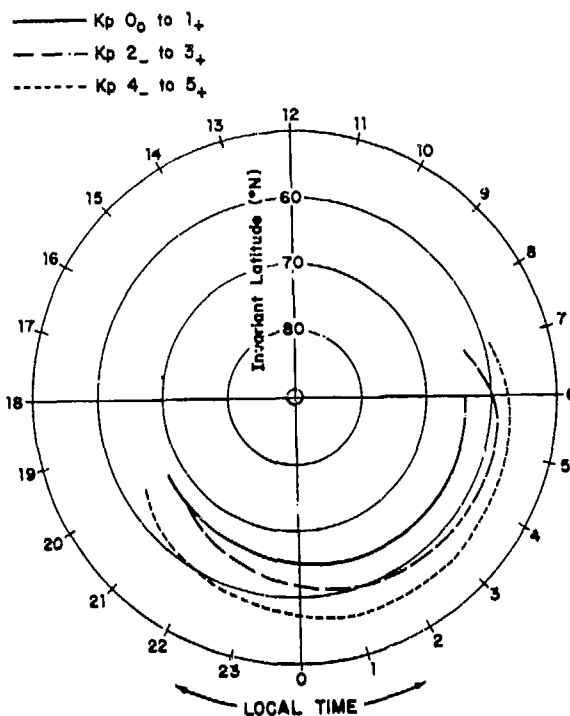


Figure 13. Mean location of the mid-latitude electron density trough from Millstone Hill differential Doppler measurements.

of scintillation index to mean scintillation index derived from the Millstone Hill tracking data and shown in Figure 14. For example,  $\bar{S} = 0.02$  corresponds to a 2% probability of measuring a scintillation index greater than 0.1 and a probability of 0.6% of measuring a scintillation index greater than 0.2.

The present results (Figures 3 to 8), which apply to zenith observations with a 400 MHz transmitter at infinity, may be converted to another observing frequency ( $f$ ) and geometry with the assumption of a power-law irregularity spectrum, as used previously.

This conversion is accomplished by multiplying the scintillation index given here by the factor

$$\left(\frac{f}{400}\right)^{-\frac{3}{2}} \left(\frac{z}{h} \sec i\right)^{\frac{1}{2}} \quad (3)$$

where  $z = \frac{z_1 z_2}{(z_1 + z_2)}$  and  $f$  is in MHz.

The geometrical factors  $z_1$ ,  $z_2$ ,  $h$  and  $i$  are defined in Figure 15, and it is assumed the transmitter is above the layer of irregularities. As the conversion factor is based on weak scatter assumptions it is necessary to restrict any derived scintillation index to be less than unity. The restriction that the propagation angle exceed  $30^\circ$  is also applicable.

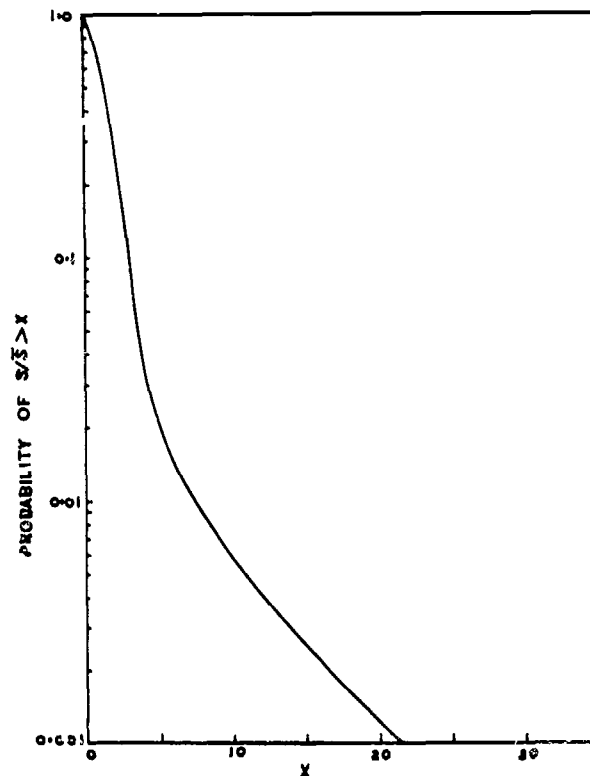


Figure 14. Probability distribution of scintillation index divided by mean scintillation, as derived from the Millstone Hill satellite tracking study.

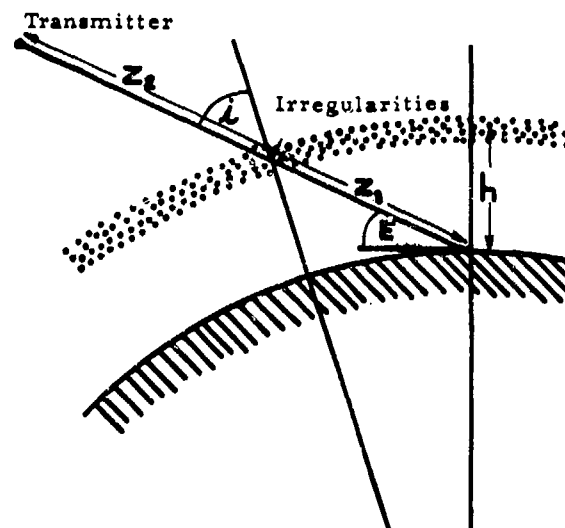


Figure 15. Geometry for satellite beacon observations.

#### REFERENCES

- Aarons J. and R.S. Allen (1971), *J. Geophys. Res.*, 76, 170.
- Aarons, J., J.P. Mullen and H.E. Whitney (1969), *J. Geophys. Res.*, 74, 884-889.
- Briggs, B.H. and I.A. Parkin (1963), *J. Atmos. Terr. Phys.*, 25, 339-365.
- Crane, R.K. (1974), "Morphology of Ionospheric Scintillation", Lincoln Laboratory MIT, Tech. Note 1974-29.
- Evans, J.V. and J.M. Holt (1973), *IEEE Transactions on Antennas and Propagation*, AP-21, 685-692.
- Rycroft, M.J. and J.O. Thomas (1970), *Planet. Space Sci.*, 18, 65.

## F LAYER SCINTILLATIONS AND THE AURORA

Eileen Martin  
Emmanuel College  
Boston, MA. 02115

and

Jules Aarons  
Air Force Cambridge Research Laboratories  
Bedford, MA. 01731

### Introduction

Until recently the basic material used for correlating the aurora with other geophysical parameters consisted of statistically derived auroral ovals for varying levels of magnetic activity and all sky photographs. The statistically derived ovals were of limited use for comparison with individual observations of other parameters. The all sky photographs were limited in coverage when looking at data taken over a very large area.

The recent availability of the USAF DMSP photographs of the aurora allows the experimenter to correlate in a simple manner geophysical data with snapshots of the aurora.

Although the sensors on the DMSP satellites are sensitive to all visible radiation, the predominant emission recorded is that from E layer heights (Pike and Whalen, 1974). Our attempt is to determine the relationship of the diffuse and discrete aurora as shown in these photographs to irregularities in the F layer. The detection of F layer irregularities for this study is accomplished by using fading or scintillation of the radio frequency signals from both synchronous and low altitude (1000 km.) satellites.

### The Data Base

Amplitude fluctuations of the radio signals are produced by diffraction processes of the small scale

(200 m to 5 km) irregularities at F layer heights. The intensity of the irregularities is a function of the electron density deviation  $\Delta N$  of the irregularity as well as the height and elongation of the irregularity. Another parameter, the aspect angle, the relationship of the propagation angle to the earth's magnetic field, is also of importance particularly when viewing a satellite which moves across the horizon, since the irregularities are field aligned. The maximum scintillations are noted when the propagation path is along the field lines. For synchronous satellites the predominant variation is that of the electron density deviation,  $\Delta N$ .

The data used for this study are a series of measurements of scintillation activity at 136 - 137 MHz using ATS-3 transmissions, with data taken at Sagamore Hill, Massachusetts; Goose Bay, Labrador; and Narssarssuaq, Greenland. A second series of measurements that is used consists of amplitude fluctuation data from the 1000 km altitude satellite, Nimbus 4, taken by the Danish Meteorological Institute at Narssarssuaq, Greenland.

The results of this study show that the F layer scintillations are at a level of  $\sim 3$  dB (at 136 MHz) at  $\sim 4^\circ$  below the diffuse or discrete aurora. When the path is through the aurora scintillations are above 6 dB peak to peak (SI > 60%). Poleward of the aurora scintillations decrease somewhat but maintain levels of 25 - 50%.

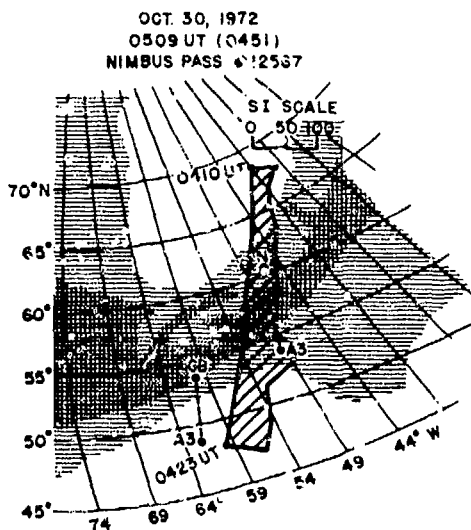


Fig. 1 Tracing of auroral photo taken on October 30, 1972 at 0509 UT (over Narssarssuaq intersection at 0451 UT). Station coordinates are shown and the Nimbus sub-ionospheric path at 350 km at 0410 UT is traced.

#### Scintillation Observations of ATS-3

Using gridded DMSP photographs of the time period September 1972 to February 1973, predominantly centered on the longitude of Goose Bay, and scintillation indices derived from the observations of ATS-3 at 137 MHz from Narssarssuaq, Greenland; Goose Bay, Labrador, and Sagamore Hill, Massachusetts, correlations were attempted between scintillations and proximity to the diffuse or discrete aurora. Measurements were made of the distance along geographic longitude lines (which closely parallel geomagnetic longitudes in this area) from the 350 km intersection point of the path to the equatorward edge of the distinct or diffuse aurora.

Figure 1 is a tracing of the aurora (from a DMSP photograph passing Narssarssuaq at 0451 UT on October 30, 1972), a grid of latitudes and longitudes at the 100 km height level, and a placement of the sites of the observations

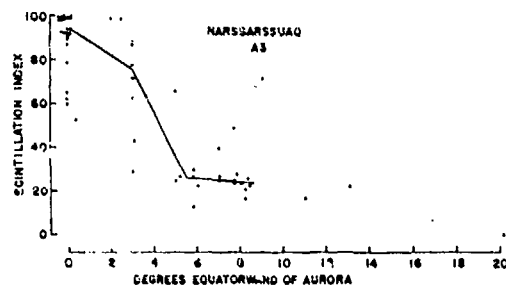


Fig. 2a. Plot of 136 MHz scintillation index at Narssarssuaq as a function of degrees equatorward of the aurora.

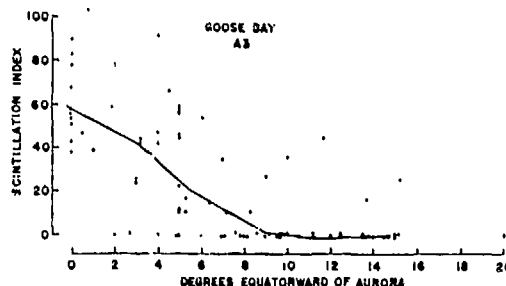


Fig. 2b. Plot of scintillation index at Goose Bay as a function of degrees equatorward of the aurora.

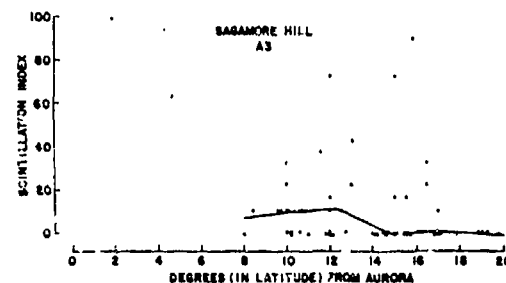


Fig. 2c. Plot of scintillation index at Sagamore Hill as a function of degrees equatorward of the aurora.



and the sub-ionospheric intersection points. The sub-ionospheric path of a Nimbus 4 pass near the time of the photograph is also traced; the data from this series of observations will be utilized in a later section of this paper.

The Narssarssuaq observations are seen in Figure 2a with 57 data points. The Goose Bay observations, shown in Figure 2b utilize comparisons with 78 photographs and the Sagamore Hill graph, Figure 2c, has 56 comparisons. Additional points, beyond 20° from the aurora, are correlated with an SI = 0, but are not shown on these graphs. The scintillation index, as defined in Whitney et al (1969), has been used with no correction for aspect angle or angle of elevation, but in a later section of this paper, such a correction is discussed. In Figure 3, the upper quartile, lower quartile and median are illustrated for all three sets of data. The data pile up at zero degrees from the aurora is due to the analysis method which used zero distance whether the path to the satellite was well within the aurora or at the edge of the aurora. The Narssarssuaq data shows saturation or fading to noise when the path traverses the aurora. The scatter of the Sagamore Hill data indicates that a second mechanism other than that associated with the aurora also gener-

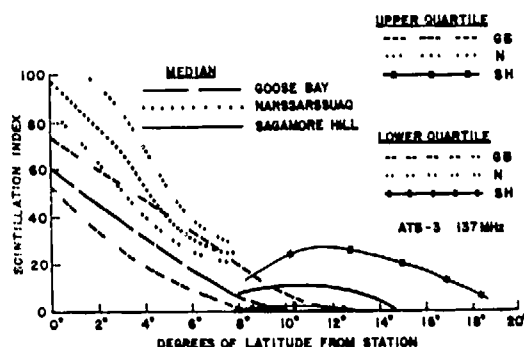


Fig. 3 Upper and lower quartiles and median of the three sets of data shown in Fig. 2, the scintillation indices at Narssarssuaq, Goose Bay and Sagamore Hill, as a function of degrees equatorward of the aurora.

ated F layer irregularities at sub-auroal and middle latitudes. The Goose Bay data is best suited for this study; the plot shows considerable scatter but there is a distinct tendency to fall off with distance from the aurora. Low values of scintillation index are generally noted when the aurora is distant. An index of 30% (indicating fades of 3 dB peak to peak) is noted ~4° from the aurora.

It should be understood that the "quantitative" measurements depicted are not precise. Since the gain of the optical instrumentation used to take the photographs changes, the auroral intensity varies from frame to frame.

#### Observations Across and Polewards of the Aurora

Using transmissions of Nimbus 4 observed at Narssarssuaq, it was possible to obtain measurements of scintil-

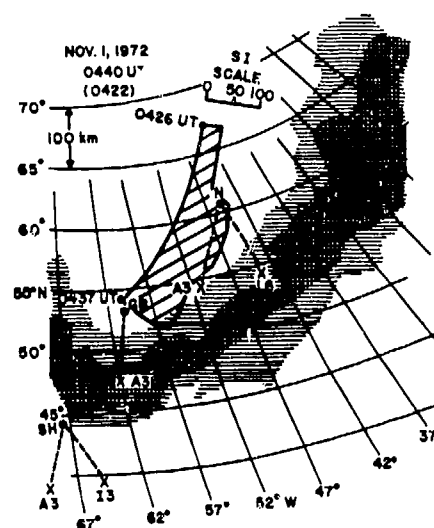


Fig. 4a. Tracing of the aurora photographed on November 1, 1972 at 0440 UT (over Narssarssuaq at 0422 UT) with the Nimbus pass at 0426 UT illustrated, and the station and 350 km intersection point coordinates of the A3 satellite.

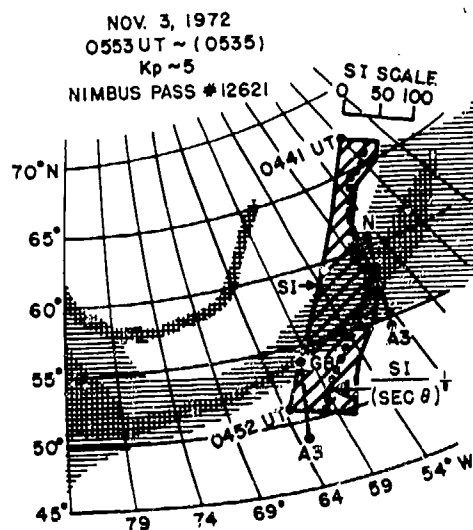


Fig. 4b. Tracing of the aurora photographed on November 3, 1972 (over Narssarsuaq at 0535 UT). The Nimbus pass which took place from 0441 UT to 0452 UT is also illustrated. The scintillation index of the Nimbus beacon signal is shown both as measured (solid line) and reduced by the square root of the secant of the zenith angle (dashed line).

lation index as the sub-ionospheric path from Narssarsuaq to the satellite traversed the ionosphere polewards of the aurora, thru the aurora and then equatorwards of the aurora.

Figure 4a is an illustration of a typical Nimbus pass against the background of an aurora during the magnetic storm of November 1, 1972 (0440 UT). When the path was polewards of the aurora (0426-0429 UT), scintillation indices were low. When the path came closer to diffuse aurora, scintillation indices increased. For this pass, scintillation indices were dominated by the proximity to the aurora.

Figure 4b is an illustration of a pass (November 3, 1972 at 0553 UT) where scin-

tillation index of the Nimbus signal is shown both as measured and as reduced by the square root of the secant of the zenith angle. This reduction is the predicted angular effect as described by Briggs and Parkin (1963).

Observations such as these of 20 passes nearly simultaneous with DMSP photographs combine to form a qualitative picture of the relationship of scintillation index and the aurora.

The data show that scintillation indices recorded within 5° of the aurora (polewards) ranged from 50-70; indices from 5° to 10° polewards ranged from 25 to 50. Frequently at the poleward end of the path (72° geographic latitude), the scintillation index again increased, probably due to the low angle of elevation.

An illustration of a pass with a long path length through the aurora is shown in Figure 1 (October 30, 1972). Poleward of the aurora and through diffuse aurora (0410-0412 UT) scintillation index was low. Through discrete aurora (0416-0419 UT) scintillation index was relatively high.

The Nimbus data from Narssarsuaq supply information primarily on scintillations polewards of the aurora. It is clear that scintillation intensity does not show a "polar cavity" as does the flux of precipitating low energy electrons. The Nimbus data will help supply a needed parameter i.e. the dependence of scintillation index on the zenith angle. Preliminary indications are that index varies with the square root of the secant of the zenith angle although a large scatter exists in the data.

#### The Magnetic Storm of April 18, 1974

Measurements of scintillations of two beacons were made from several sites during the magnetic storm of April 18, 1974. A tracing of a composite photograph of three passes of a DMSP satellite (Figure 5) shows the dramatic impact of the variations of the latitudinal motions of the aurora during one magnetic storm. On top of the 100 km grid used to locate the aurora are the 300 km invariant latitudes as well as the 300 km intersections of the paths from the sites used to one of the synchronous satellites observed, ATS-3.

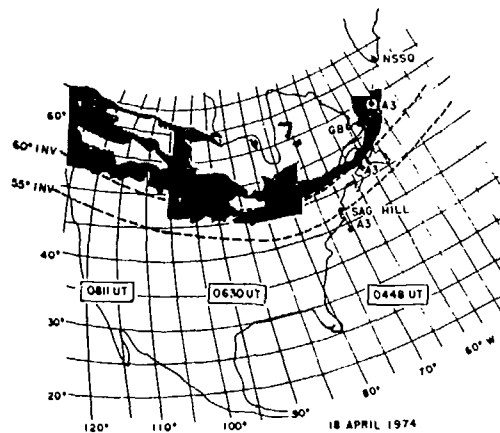


Fig. 5. Tracing of a composite photo with the intersection points towards the A3 satellite shown.

On the first pass (equatorial crossing of 0448 UT with the latitude of Narssarssuaq reached at 0430), scintillations as noted from Narssarssuaq and Goose Bay were near maximum as shown in Figure 6a. The propagation path was through the aurora. Sagamore Hill, whose intersection was  $\sim 8^\circ$  below the aurora, showed no discernible scintillation.

On the next pass illustrated (equatorial crossing 0630 UT) it can be seen that the aurora has descended  $\sim 3^\circ$  to  $4^\circ$  at the most easterly longitude pictured. If this is extrapolated to the longitude of the path from Sagamore Hill to ATS-3 then the propagation path at 300 km is still  $4^\circ$  below the aurora. However at this time the Sagamore Hill indices rose to 70% to 80% with Goose Bay and Narssarssuaq near saturation.

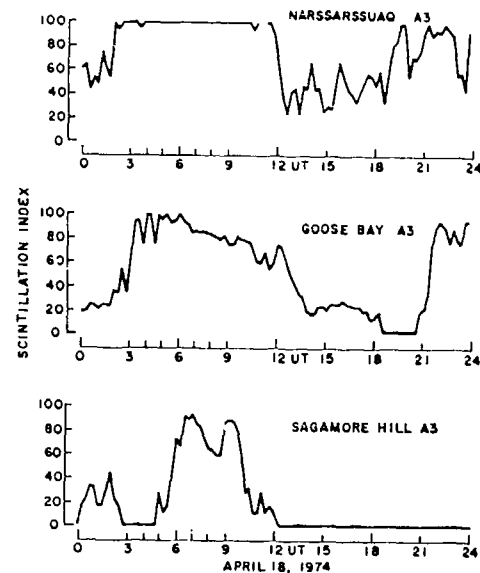


Fig. 6a. Plot of 15 minute scintillation Index for April 18, 1974 as observed at Narssarssuaq, Goose Bay and Sagamore Hill from the A3 satellite.

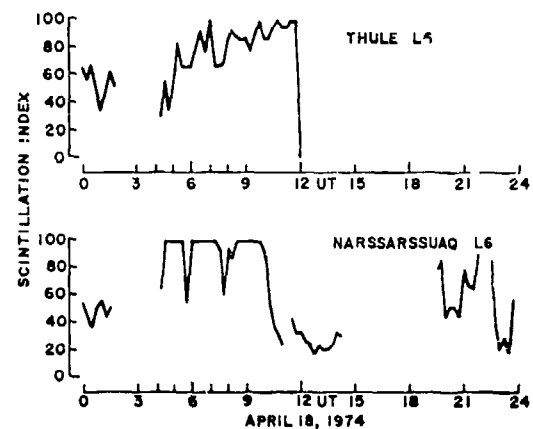


Fig. 6b. Plot of 15 minute scintillation Index for April 18, 1974 as observed at Narssarssuaq and Thule from the L6 satellite. The scintillation index at Thule increases during the intensification shown at 0630 UT.

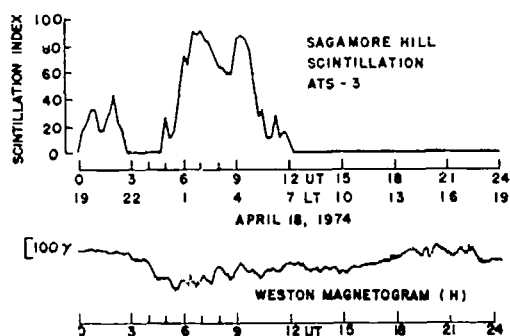


Fig. 7 Comparison plot of scintillation index measured at Sagamore Hill from A3 on April 18, 1974 with the Weston magnetogram for this date. Local time period 19 - 22 is quiet with SI reaching the maximum value during the magnetic storm (Aaron and Allen, 1971).

Figure 6b illustrates scintillation indices for the 254 MHz transmissions from LES-6 of the Narssarssuaq and Thule observations. It is of interest to note that the indices increased for the Thule propagation path (at  $\lambda = 72^\circ$ ) during the intensification of 0630 UT and remained high during the time of the next photograph, 0811 UT. Both the 0630 and the 0811 photographs show activity spread both equatorward and poleward of the 0448 photograph.

Analysis of a series of magnetic storms in 1972 has revealed that scintillation indices are directly responsive to local changes in magnetic field. This is readily apparent by the comparison of the H component of the magnetic field as taken at Weston, Massachusetts and Sagamore Hill scintillation index, shown in Figure 7. When the path is through the night ionosphere and the disturbance is maximum we have high scintillation indices. It should be noted that the overhead magnetic field variations and the ionospheric path intersection differ by  $4^\circ$  of latitude.

#### The Aurora and Scintillation

The emergent picture at midnight of the scintillation index at 137 MHz is depicted in Figure 8. In this illustration, the aurora extends from  $67^\circ$  -  $71^\circ$  invariant latitude, as was determined from the photographs used

in this study when the K index was of the order of 2 - 3. The irregularity region starts equatorwards of the aurora with an index of  $\sim 10$  reached at  $57^\circ$  invariant latitude (Aarons and Allen, 1971). Polewards of the aurora scintillations fall with a small trough approximately  $5^\circ$  -  $10^\circ$  from the aurora. This picture is based on both the data shown in Figures 2a and 2b of scintillation index correlated with distance from the aurora, and the Nimbus passes available, as described earlier. However, the scintillation index (Table I) plotted here is corrected by the square root of the cosecant of the elevation angle. Since the Nimbus 4 data was observed only at Narssarssuaq, Greenland, the portion of the Goose Bay curve above  $71^\circ$  invariant latitude is extrapolated according to the relationship of the existing Goose Bay data with that obtained from Narssarssuaq. The rise at high polar latitudes ( $\sim 78^\circ$ ) may be real but additional data is needed at higher latitude sites.

#### References

- Aarons, J. and R. S. Allen, *J. Geophys. Res.*, **76**, 170 (1971).
- Briggs, B. H. and I. A. Parkin, *J. Atmos. Terr. Phys.*, **25**, 339 (1963).
- Pike, C. P. and J. A. Whalen, *J. Geophys. Res.*, **79**, 985 (1974).
- Whitney, H. E., J. Aarons and C. Malik, *Planet. Space Sci.*, **17**, 1069 (1969).

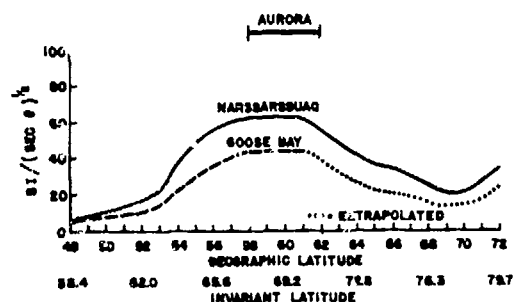


Fig. 8 Illustration of midnight scintillation as a function of latitude, using scintillation index reduced by the square root of the cosecant of the elevation angle as measured at Goose Bay and Narssarssuaq.

TABLE I

Measured SI (%)	Reduced SI (%)	
	Narssarssuaq	Goose Bay
100	69	74
90	59	67
80	53	59
70	46	52
60	40	44
50	33	37
40	26	30
30	20	22
20	13	15
10	7	7

## AMPLITUDE AND FADE RATE STATISTICS FOR EQUATORIAL AND AURORAL SCINTILLATIONS

Herbert E. Whitney  
Air Force Cambridge Research Laboratories  
Bedford, Mass.

Charles Cantor  
Emmanuel College  
Boston, Mass.

### INTRODUCTION

To assess properly the effects of ionospheric scintillations on the performance of a satellite communication system which is sensitive to changes in carrier strength, it is necessary to have data on both the variations in amplitude and the rate at which they occur. It is the intent of this paper to present examples of computer analysis of ionospheric scintillations in a form useful for system design.

Every communications link has a margin which, when exceeded, will result in degradation of the system performance. Link margin is composed of several variables, but we are only concerned with that allocated to scintillations, which can be called the fade margin.

How much the performance is degraded will depend on how far the signal fades below the margin, the duration of the fade, the type of modulation, and the criteria for acceptability. For example, in a FSK system a drop in signal below the margin will increase the bit error rate, but for a slow data rate e.g., 75 bits/sec., may only result in some incorrect characters. The intent of the message may still be obvious. Other situations may require perfect reception of the full message. For this case, the time durations of the signal above the margin can be measured and used to specify message reliability.

The auroral and equatorial regions are the two geographic areas that are subject to the frequent occurrence of strong scintillations. Many references

are available that deal with the morphology of scintillations in these regions. However, there is little information available that gives statistical measures of the amplitude and duration of fades.

### DATA FORMAT

The intent of this paper is to present the analysis of a sample of scintillation data from Huancayo, Peru using the LES-6 beacon at 254 MHz and a sample from Narssarssuaq, Greenland using the ATS-3 beacon at 137 MHz. Each fifteen minute data sample will be described by a cumulative amplitude distribution, a plot of message reliability, a distribution of the fade durations and a power spectrum. A 15 minute period was chosen as a convenient interval over which the scintillation process is generally found to be stationary.

The data was recorded on FM analog tape and then digitized at 6 samples per second for computer processing. A relative calibration of the complete receiving and recording equipment was accomplished just prior to the period of scintillations.

The cumulative amplitude distribution is computed for the fifteen minute period. The relative calibration is normalized to the median level. In addition, the various scintillation indices and the goodness-of-fit to the Nakagami and log-normal distributions are determined.

Message reliability is measured by determining the number of time intervals

or "windows" that completely fit within the signal enhancements or increases above specified calibration levels compared with the total possible number in a 15 minute period. Since the calibration levels are relative to the median level, they can represent various values of fade margin. The data sample is long (15 minutes) compared with typical message lengths. Therefore changing the time of synchronization results in only a minor variation to the calculated value of message reliability.

The distribution of fade durations is a summation of the number of discrete time intervals that the signal dropped below specified calibration or margin levels. Intervals shorter than 0.25 second and longer than 60 seconds were not resolved. The statistics of fade durations is useful in choosing coding and time diversity techniques to overcome this fading.

#### EQUATORIAL DATA

Fig. 1 shows the 15 minute sample of scintillation data from Huancayo, Peru and a solid curve which is the resulting cumulative amplitude distribution (cdf). The cdf gives directly the percent of time the fade margin would be exceeded. For example, if only 4 dB had been allocated in the link budget to overcome ionospheric scintillations, 20 percent of the time this value would be exceeded. The cdf does not give the actual value of message reliability but only indicates the maximum possible value. For this case, a maximum of 80% of the total possible number of messages could be received. The actual message reliability will be determined by the relationship of the message length to the time intervals that the signal is above the margin. If the time intervals are less than the message length, no message will be received without error.

Earlier work(1) showed that there was good agreement of measured distributions of ionospheric scintillations with the Nakagami(2) distribution. The Nakagami distribution is specified by a single parameter,  $m$ , where  $m = S_4^{-2}$ , for values of  $m \geq 0.5$ . The dots that follow the solid curve in fig. 1 are values from the Nakagami distribution having an  $m=1.4$ . Since the experimental distribution shows good agreement with the theoretical distribution, values beyond the plotted range can be approximated from the theoretical curve when required.

Fig. 2 shows the percentage of messages perfectly received as a function of message length and fade margin. As

the message length approaches zero, the percentage of messages perfectly received approaches the value given by the cdf for the specified margin. In the other extreme the percentage of messages perfectly received approaches zero. For a typical message length of 5 seconds approximately 70% of the messages would be received if the margin were only 4 dB.

Fig. 3 shows the distribution of the duration of fades for various fade margins. At the 4 dB margin 90% of the fades have durations less than 20 seconds. The cumulative number rather than cumulative percentage was plotted as it gave greater resolution between the curves. Information on the fade durations can be used to choose coding or diversity techniques to combat fading.

The power spectrum for the equatorial data sample is shown in fig. 4. It exhibits a power-law spectrum with a slope of -2.3. The strong spectral lines are associated with modulation induced by the LES-6 satellite spin.

Fig. 5 shows the 15 minute sample of auroral scintillation data obtained at Narssarssuaq, Greenland from the ATS-3 beacon at 137 MHz. The solid curve is the resulting cdf. The signal faded below 9 dB about 1% of the time. This fading was not as great as the equatorial data which showed -14 dB at the same percentile. The dots are values from the Nakagami distribution having an  $m=1.7$ , again indicating that the scintillations were not as severe.

Even though the scintillations of the auroral data were not as strong, the fading rate was much higher and the result on message reliability is shown in fig. 6. Whereas both data samples had about the same reliability at short message lengths (80% at the -4 dB level) the auroral sample shows a much steeper drop to about 45% for a 5 second message. The reliability for the equatorial sample had decreased a much smaller amount, only dropping to 70%.

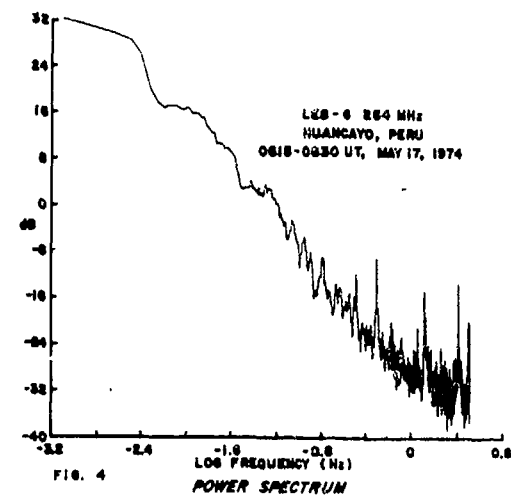
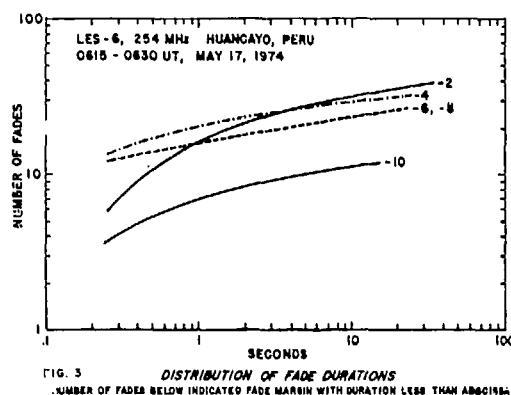
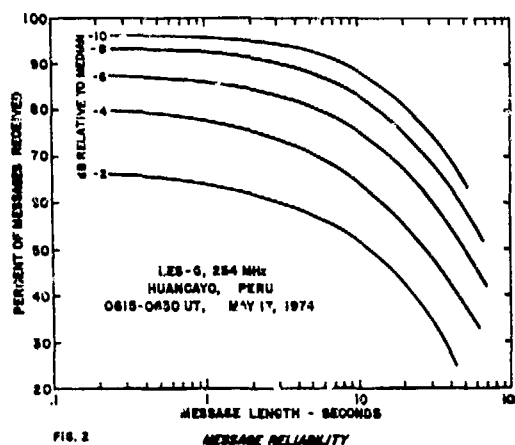
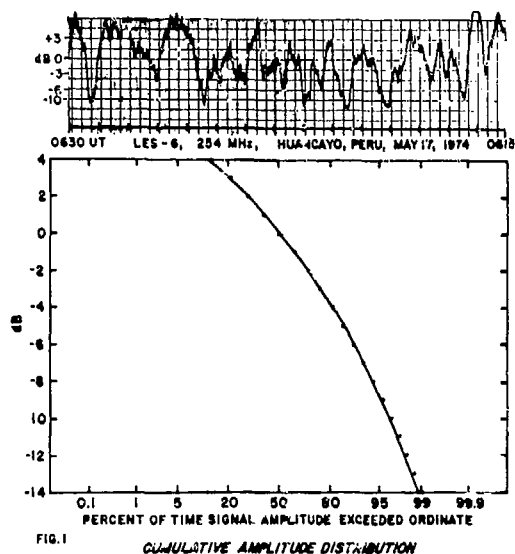
The distribution of the fading periods is given in fig. 7. It gives in numbers what was evident on the strip chart reproductions, that the auroral sample had a much faster fading rate compared with the equatorial data by a factor of about 5. Fig. 8 conveys the same information only expressed as a percentage of fades below the margin. It shows that all the fades had durations less than approximately 10 seconds.

The power spectrum for the auroral data is shown in fig. 9. It exhibits two slopes with a break point about 0.15 Hz. The slope of the low frequency portion is about -0.6 while the slope in the higher frequency range was similar to the equatorial sample having a value of -2.7. The spectral lines of the ATS-3 spin modulation are evident.

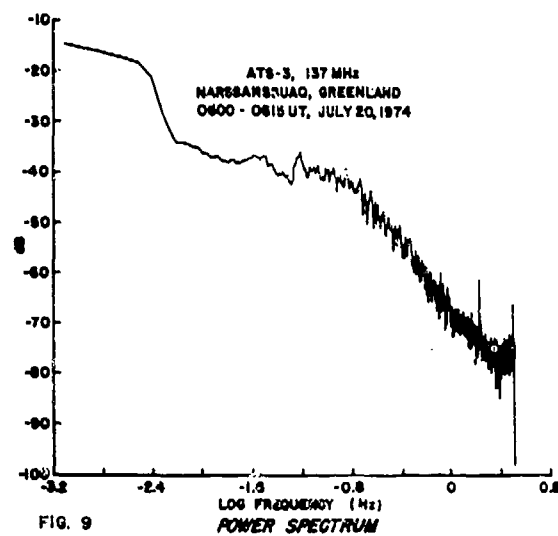
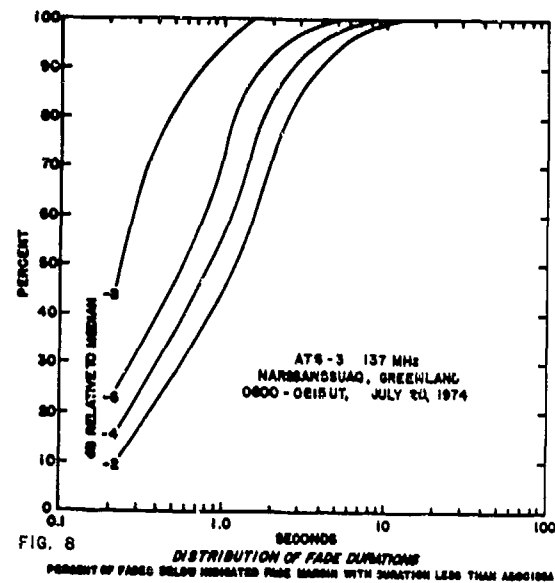
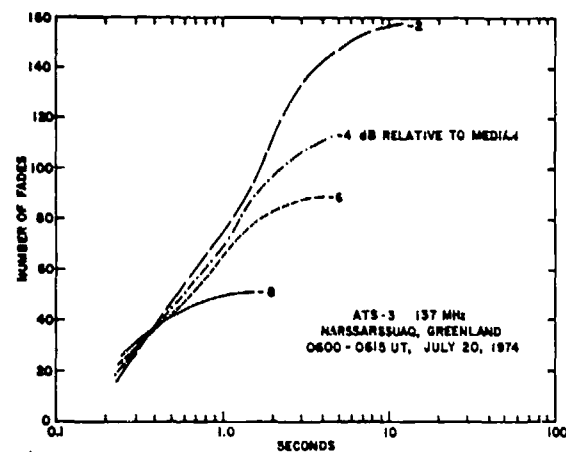
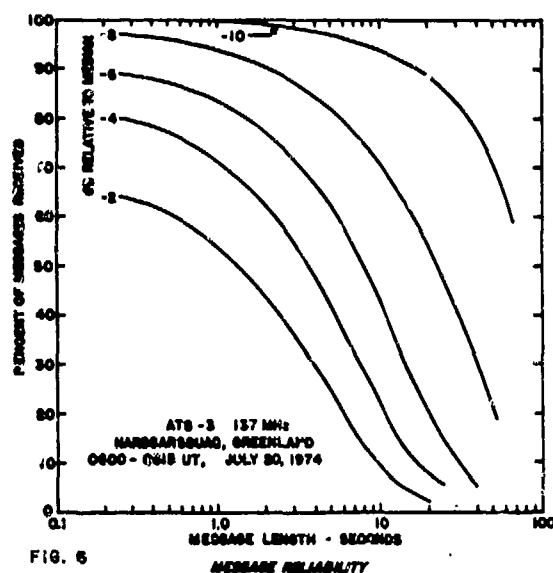
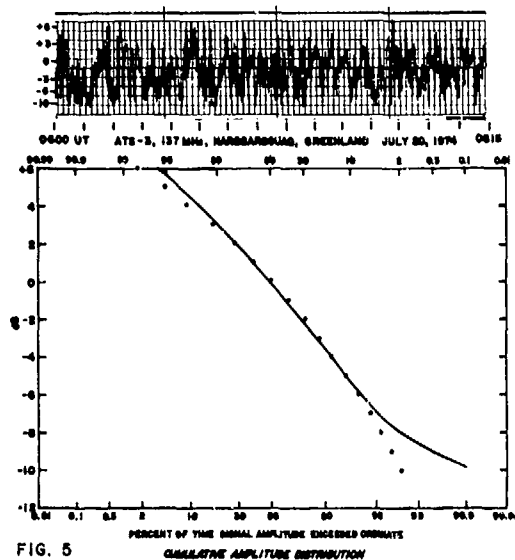
It is expected that by providing this type of data analysis under a wide range of geophysical and geographic conditions, system designers will have adequate information to evaluate the effects of the propagation path on system performance and information pertinent to the design of coding or time diversity techniques to offset the effects of scintillation.

## REFERENCES

1. Whitney, H.E., et al (1972), Estimation of the cumulative amplitude probability distribution function of ionospheric scintillations, Radio Science, Vol 7, No 12, 1095-1104
2. Nakagami, M., (1960), Statistical Methods In Radio Wave Propagation, edited by W.C. Hoffman, pp 3-36, Pergamon, New York







## EQUATORIAL SCINTILLATION AT 136 MHz OBSERVED OVER HALF A SUNSPOT CYCLE

J. P. Mullen  
Air Force Cambridge Research Laboratories  
Bedford, MA 01731

Gerald S. Hawkins  
Smithsonian Astrophysical Observatory

Equatorial scintillation in trans-ionospheric radio signals received at Huancayo, Peru, between 1968 and 1974 is examined for correlation with the solar cycle. Significant solar effects were deduced from the data and these effects had characteristics which depended on the season. While the sunspot maximum year (1969) had a higher average nocturnal scintillation than the minimum (1973), a linear correlation of 24-hour average scintillation index (S.I.) with 2.7 GHz solar flux does not show a similar trend for each month of the year. In the summer period from November - February the mean S.I. reached 80% in the pre-midnight hours, and these maximum values showed a positive correlation with solar flux. Daytime scintillations, with S.I. 20% were strongest in the winter period, May - August, in the years of sunspot minimum. For these months the correlation of solar flux and 24-hour S.I. tended to be negative or close to zero. 1973, near sunspot minimum, showed a higher S.I. during daytime than 1969, near solar maximum. The trends shown are examined and the seasonal and diurnal patterns are compared with those of other equatorial stations.

### Introduction

For the past six years, satellite signals have been recorded at the Huancayo Observatory of the Geophysical Institute of Peru. These signals have been analyzed for VHF and later UHF scintillation; from these characteristics the general morphology of the scintillation producing region has been deduced. This paper examines the general trend of scintillation through the half-sunspot cycle of 1968 - 1974. The data were taken at Huancayo using circularly polarized antennas of about 12 dB gain, low noise converters, R-390A receivers, and strip chart recorders.

The beacon used was the 137.350 MHz telemetry transmitter of ATS-3. During the period discussed, the satellite longitude varied from 40° to 80° West, which allowed elevation angles varying from approximately 75 to 45°. A scintillation index was computed each quarter hour

using the method described by Aarons, Whitney and Allen (1971). These were encoded, averaged into hourly periods and examined as functions of time, magnetic and solar activity. The seasonal variation has been examined (Mullen 1973) and found to be fairly complex. For example, it was found that the season of maximum scintillation occurrence can be the March equinox. The season of minimum scintillation is always the June solstice.

The diurnal variation of scintillation in the equatorial region has also been examined by Koster (1972) and others. All workers agree that heavy scintillation (i.e., scintillation index greater than 50% or 5 dB peak to peak) is primarily a nighttime phenomenon and heaviest scintillation occurs most frequently an hour or two before local midnight. Earlier work (Hawkins and Mullen) 1974 established the significant

occurrence of moderate scintillation i.e.,  $\approx 20\%$  or 2 dB peak to peak occurring at Huancayc in the daytime with maximum at local noon. In an examination of these same years (1968-1974) the effect was found in all months except November and December, maximized in May.

#### The Data

Approximately 33,000 hours of scintillation were reduced over the period beginning 1 January 1968 to 28 February 1974. From the indices, contours of mean scintillation occurrence have been computed (Figure 1). These summarize the diurnal and seasonal previously noted. The nocturnal maxima appear slightly before local midnight and the daytime maxima are located near noon. In this grouping of years, the maximum seasonal occurrence of nocturnal scintillation is in December.

Looking at the contours of average scintillation index, it may be seen that the year of the sunspot maximum (1969) shows a much finer grain structure than the year of sunspot minimum 1973. The seasonal maximum position is for the low sunspot years, roughly centered around the December solstice, and for the high sunspot year, near the March equinox. Both daytime and nighttime scintillation indices are higher during the high sunspot year. A least squares fit was calculated between average nighttime scintillation index and 2.7 GHz solar flux; it was found that while low and high sunspot years generally showed positive slope (i.e., large flux coexisted with large scintillation index and low flux with low indices) the trend was far from consistent.

Figure 2 shows the contours of scintillation index, for all magnetic indices plotted in contours of 10% (after 15%). The diurnal maximum occurs slightly before local midnight when average scintillation reaches 80%. There is a bimodal seasonal pair of maxima centered on October and January. Daytime maxima of greatly reduced intensity (i.e., 15% as compared with 80%) are found centered on March at 1900 UT. The fine grained irregularity structure is indicated by the close spacing of the contours, indicating the rapid change of scintillation with local time.

Figure 3 shows the scintillation index

contours for 1969. This plot shows again that the diurnal maximum occurs before local midnight. The seasonal maxima occur again in pairs, this time centered on November and February. During this year the irregularity structure yielded much the same levels of nocturnal scintillation as the previous year. The daytime scintillation was slightly greater in intensity occurrence. For example, a 20% contour appears which is centered on May, as well as an additional 15% contour centered on September.

Figure 4, the plot for 1970, shows a somewhat less clearly defined bimodality centered around November and January. Again scintillation indices of 80% are reached. During this year, a greater amount of daytime scintillation was observed; the period of occurrence ran from January through May, and July through October. The maximum of the daytime scintillation was centered around March, when the highest average index was 20%.

Figure 5 for 1971 shows two very clearly defined diurnal maxima, both reaching 80% scintillation index; they are centered on November and March. Daytime scintillation reaches 30%, and has two maxima, one centered on November, and another, larger, on May.

Figure 6 for 1972 shows a diurnal maximum in March, of 80%, with a secondary maximum (SI=70%) from October through March. A daytime maximum of SI=20% was centered on May, with lower indices (SI=15%) from January through November.

Figure 7, for 1973, close to sunspot minimum, shows a slightly decreased scintillation index. The highest average indices for the year were 60%, compared with 80% found in the previous years. This maximum occurs October through February. A daytime value of 15% was found from February through November.

The high sunspot year 1969 and the low sunspot year 1973 are brought together for comparison in Figure 8. The higher indices and more detailed structure of the higher sunspot year are immediately apparent.

## Discussion

The obvious increase in scintillation in the high year over the low is in agreement with a study of mid-latitude scintillation over a sunspot cycle by Briggs (1964). In this study Briggs observed Cassiopeia A from Cambridge, England at 38 MHz; a good agreement was found between annual mean scintillation indices (a logarithmic index was used rather than the linear SI used here) and 12 month running mean sunspot number was found. In the present work, however, linear regression were calculated for average daily SI with 2700 MHz solar flux and no consistent trend was found. The slopes were found negative for May, June, July and November, with intercepts varying from 34 to -3.7 leading us to believe that there was no simple correlation between the indices and the 2700 MHz flux. As the data have shown however, we do find that the high sunspot year has high average scintillation, and the low sunspot year has lower scintillation. This is also found by Koster (1972).

An interesting feature of the annual plots is the occurrence of the seasonal maximum. In 1968 a pair of maxima occurred in October and January. In 1969, the two maxima occurred in November and February; in 1970, November and January were the highest months. 1971 maxima were in November and March. In 1972, the pattern changes from two clear maxima to one in March with an extended but lower intensity contour reaching from January through November 1973, the lowest sunspot year considered, shows an overall reduced scintillation, with a broad maximum extending from October through November. This seasonality is in general agreement with that reported by other investigators, and does illustrate the complexity of the seasonal variation and the changes from year to year.

The comparison of the low and high year plots (Figure 8) bring out the striking differences in nocturnal maxima and the daytime scintillation discussed by Hawkins and Mullen (1974). The occurrence patterns for the high sunspot year have, as one may intuitively expect, a fine grained structure indicative of a very disturbed and very variable ionosphere. Daytime scintillation in this year occurred in southern (Autumn and Spring.) In the low sunspot year the structure was more

diffuse and less intense. The daytime scintillation, of a lower level, was found throughout most of the year.

## Magnetic Dependence

Figure 9 shows the average behavior (over the six years) with  $K_p$  variation. The major variations appear to be an increase in the daytime scintillation occurrence for periods of low  $K_p$ . The southern winter increase of scintillation with increasing magnetic index reported earlier (Mullen 1973) is again shown; for example, in July, local midnight a 15% average index is shown for high  $K_p$  and compared with less than 10% for the lower index. However, these differences are small, although we believe they are real.

## Comparison of Data Taken At Two Equatorial Observatories

We have computed SI contours for Accra, Ghana for the year 1973. During this year, the ATS-3 spacecraft was at 70° West longitude. This yields an elevation angle of 11° and a sub-ionospheric point of 5° N latitude, 10° West longitude. Huancayo at this time has a satellite elevation of 74°, and a sub-ionospheric point of 11° South latitude, 75° West longitude.

Figure 10 shows the SI contour for 1973, a quiet sunspot year. A very distinct bi-modality exists in the Accra data, which is not found in the Huancayo results. Daytime scintillation is completely absent. Scintillation indices maximize at 60% at both locations. The peak seasons at Accra are November and March while Huancayo displays a diffuse maximum extending from October through February. Because of the low elevation angle at Accra, it is difficult to draw immediate comparisons of the ionospheric irregularity structure revealed by these data. It may be said however, that one would expect higher indices from Accra because of the elevation angle effect. Other data, not shown here, reveals quite the contrary effect; more scintillation is found at Huancayo even without an angle correction.

The latitudinal differences are only slightly less pronounced when dip values are used; the Accra sub-ionospheric point has a dip latitude of about 10° South, while the Huancayo sub-ionospheric point is about 3° North dip latitude, both well

within the zone of maximum equatorial scintillation. In a later work we intend to examine more closely the differences between these data; we will explore the concept of an extremely fine-grained equatorial irregularity structure offered by Martyn, 1959. Some evidence is emerging which tends to show that relatively small differences in latitude and/or longitude can produce large changes in scintillation behavior. Using more data which is yet unprocessed may lead to a better understanding of why the heavier scintillation occurs at Huancaayo despite its far more favorable elevation angle.

#### Acknowledgements

We gratefully acknowledge the kindness of Dr. A. Giesecke and Father John R. Koster in supplying the data used for this paper.

#### References

Aarons, J., H. E. Whitney and R. S. Allen (1971) "Global Morphology of Ionospheric Scintillation," *Proc. IEEE*, 59, no. 2, pp. 159-172.

Briggs, B. H. (1964) "Observation of Radio Star Scintillation and Spread F Echoes Over A Solar Cycle," *JATP*, 26, pp. 1-24.

Hawkins, G. S. and J. P. Mullen (1974) "Daytime Equatorial Scintillations in VHF Trans-Ionospheric Radio Wave Propagation From ATS-3 at Huancaayo, Peru," presented at U. S. National Committee for URSI meeting, October 14-17, 1974, Boulder, Colorado.

Koster, J. R. (1972) "Equatorial Scintillation," *Planetary Space Sci.*, Vol. 20, pp. 1999-2014.

Martyn, D. F. (1959) "The Normal F Region of the Ionosphere," *Proc. Inst. Radio Engrs.*, 47, pp. 147-55.

Mullen, J. P. and H. E. Whitney (1974) "Equatorial Measurements Using the LES-6 and ATS-3 Satellite Beacons," Report of the Joint Satellite Studies Group, published by Centre National D'etudes des Telecommunications, Lannion, France, J. Papet Lepine, ed.

Mullen, J. P. (1973) "Sensitivity of Equatorial Scintillation to Magnetic Activity," *JATP*, Vol. 35, pp. 1187-1194.

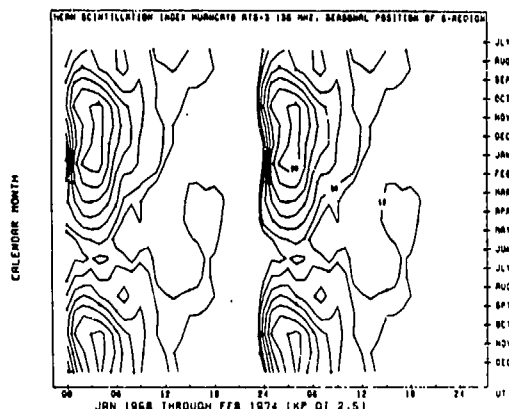


FIG. 1

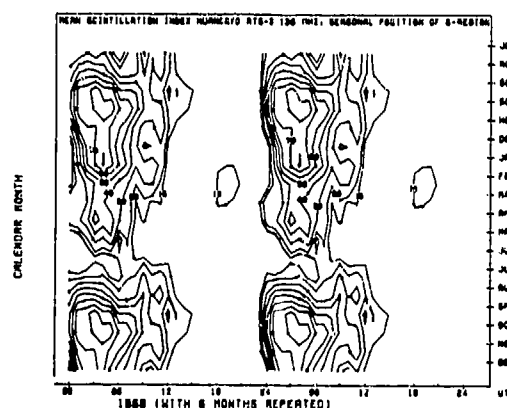


FIG. 2

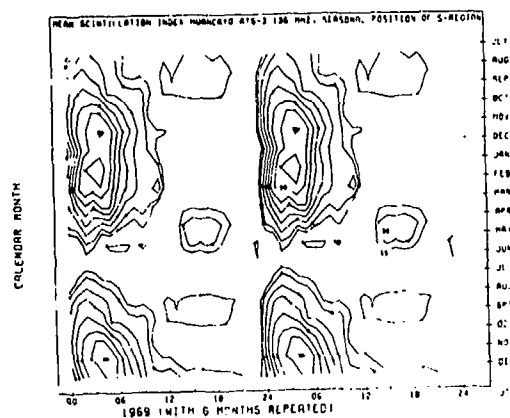


FIG. 3

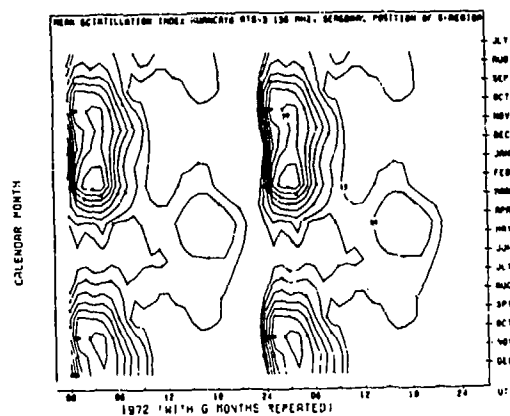


FIG. 6

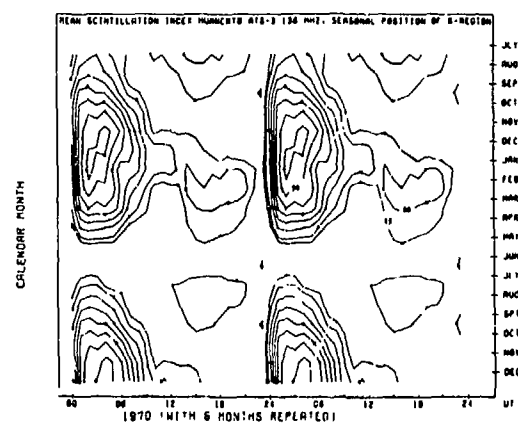


FIG. 4

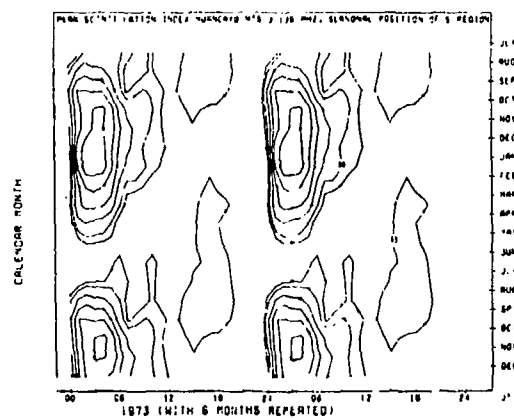


FIG. 7

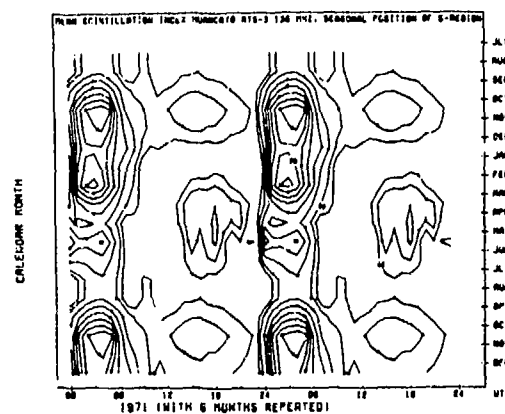


FIG. 5

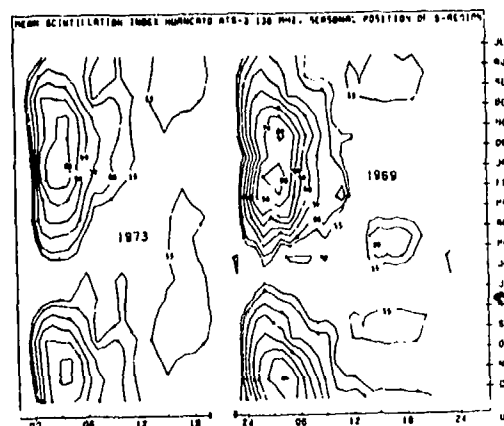


FIG. 8

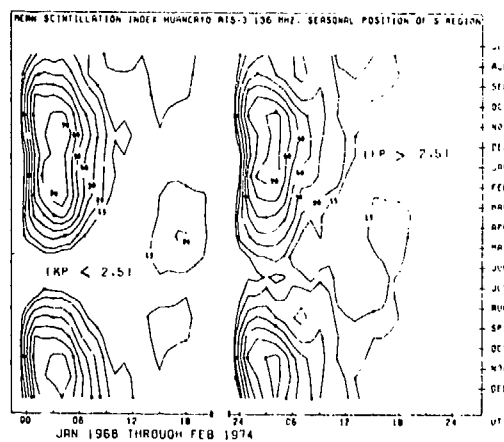


FIG. 9

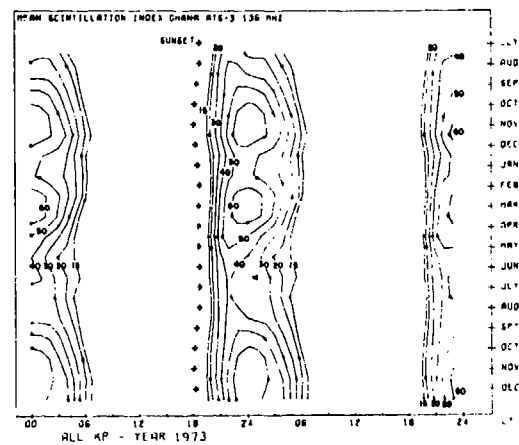


FIG. 10

THE EFFECT OF IONOSPHERIC IRREGULARITIES ON THE RECEPTION OF  
ATS-6 SIGNALS

R. SETHURAMAN and S. GANAPATHY

Department of Electronics Engineering  
Madras Institute of Technology, Chromepet,  
Madras-600044. INDIA

AND

M. MUKUNDA RAO

Department of Electrical Engineering  
Indian Institute of Technology  
Madras-600036, INDIA

\*\*\*\*\*

ABSTRACT

Ionospheric irregularities measurements have been carried out at Madras (Lat.  $11^{\circ}\text{N}$ , Log.  $80^{\circ}\text{E}$ ) in last two years (1972-74) using the space-receiver technique and the Brigg's analysis. The frequency used is 2.6 MHz and records are obtained from E-region during day time and F-region during night time. The drift velocities in the E-region are found to vary from 60-120 metres/sec. and the direction is predominantly SE-NW. A receiving station to receive signals from the ATS-6 satellite is being set-up at Madras, operational June 1975. A theoretical model on the scintillation of the satellite signals due to ionospheric irregularities is under preparation.

I. INTRODUCTION

Madras (Lat.  $11^{\circ}\text{N}$ , Log.  $80^{\circ}\text{E}$ ) is situated north of the electrojet region passing over India but not too far from it for its effects to be completely absent. It was decided therefore to set up an experiment to study the drift and the irregularity parameters in the E and F regions. Ionosphere observations were started in late 1972 and are being continued. The part of this paper presents some of the results obtained so far.

II. EXPERIMENT

The drifts are measured by the spaced receiver method. R.F. pulses on a frequency 2.6 MHz and power of 6KW are sent vertically by means of a folded dipole antenna placed at a height of  $\lambda/8$  from ground and the reflections are received by three antennas placed in the north-south and east-west directions, the spacing between them, being equal to a wave length at this frequency. The reflections are successively switched into a communication receiver of sensitivity 1 micro volt per meter and are fed into an oscillograph and recorded by means of a movie camera which records the fading patterns of signals received from the three antennas.

Fig.1 gives typical fading patterns obtained. On most of the days the observations are taken in the day time and one day in a week, observations are made in the night time also. The records are analysed by the method suggested by Brigg's and Spencer (1954) and by taking the time displacement of similar fades the three antennas  $T_{NS}$  and  $T_{EW}$ . The components  $V_x$  and  $V_y$  are found and, with the help of these, the direction and magnitude of the drift is found. A few records were subjected to the correlation method in which the



time difference which would give maximum gross correlation between the record is computed and from these the resultant velocity of the drift is found. There was no large difference between the results obtained by the two methods and since the first method is faster, for routine calculations this was used. Other workers e.g. Sethuraman (1959) Rastogi (1967) have also reported similarly.

The frequency of 2.6 MHz is used in most Indian stations. This is reflected from the E ( $E_g$ ) region during the day time and  $F_2$  region during the night time. At these latitudes there were a few occasions when the reflections were obtained from the  $E_g$  region during the night time. These observations are excluded from the result quoted here. Sporadic-E is a regular feature in the day time ionosphere, in and around the region of the equatorial electrojet. (An additional frequency of 4.7 MHz has been made available which would give the reflections from the F region during the day time and the observations at this frequency would be started early). Due to the non-availability of an ionosonde, no attempt was made to determine the actual height of reflection at this frequency.

### III. RESULTS

The results given below relate to the period September, 1972 to December 1973. The results for the year 1974 are being analysed. The total number of observations is 447 of which 385 relates to the day time. Fig.2 gives the direction and Fig.3 the histogram of the magnitude of the drift. The indicated direction corresponds to the direction towards which the movement takes place. A strong south-east drift is seen with occasional observation in the direction between NW and SW. There are very a few occasions when drifts in the other directions are also observed. The magnitudes vary over a wide range from 25 MHz to 150 MHz with a peak at 75 MHz. No decimal variations are seen on almost all days.

### IV. DISCUSSION

These results can be compared with the results of non-equatorial station like Ahmedabad and Delhi and stations situated in the equatorial electrojet, Sethuraman (1958), Rastogi (1972), given in Fig.4. Rastogi (1974) reports a westward drift at Tiruchi, a station between Madras and Thumba where the direction at distribution seems to be that obtained at Thumba. At Madras the drift is in the opposite direction and the speeds are comparable to that obtained at middle latitudes. The night time results are not included as the number of observations are too small to draw any definite conclusions regarding night time drifts. But detailed analysis of the time of reversals of drift directions are being made. Rastogi and Chandra (1971) report a decrease in the reduction in the speed with magnetic index. We are analysing our record to see whether this is true at this latitude or it is the opposite as observed at middle latitudes.

The irregularities whose speeds and direction are described in the earlier part of this paper are found to influence the signals received from the ATS-6 satellite at Madras. Since Madras is close to the equator, the drift velocities are in general larger than the northern stations. It can be easily visualised that the rate of fading is directly proportional to the drift velocity and inversely proportional to the scale size. Also the depth of fading is proportional to  $\Delta N/N$  where  $N$  is the ambient electron density and  $\Delta N$  is the difference in the ambient electron density and the electron density in the irregularities. Since it has been established (Reddy and Rao, 1968) that at equatorial latitudes the  $N/N$  ratio is relatively small, it can be concluded that the depth of fading of the ATS-6 signals received at Madras will be small. However, since the scale size of the irregularities above Madras is small and their drift velocity large, the rate of fading of the ATS-6 signals received at Madras will be relatively large.

The elevation angle of the ATS-6 satellite from Madras is approximately  $45^{\circ} 25'$  and the Azimuth is very close to  $90^{\circ}$ . So the angle between the direction of propagation and the magnetic field will not deviate from  $90^{\circ}$  by more than a few degrees (Mukunda Rao, 1967). As such the Faraday rotation of the radio waves will be relatively small and the experimental system must be designed to measure accurately these small Faraday rotation angles. The exact values for the depth of fading, rate of fading and Faraday rotation values for the ATS-6 satellite signals received at Madras are being computed with the help of a computer and these results will be published in due course. The lative location of Madras with respect to the satellite is shown in fig.5.

#### ACKNOWLEDGEMENT

This experiment is done in collaboration with the Physical Research Laboratory, Ahmedabad, India. Thanks are due to Professor K.R. Ramanathan, late Professor V.A. Sarabhai and Professor R.G. Rastogi of that laboratory for the arrangement.

#### REFERENCES

1. Briggs, B.H., Spencer., Rep. Progr. Physics, vol.27/1, 245, 1954.
2. Mukunda Rao, M., 'Studies of the Equatorial ionosphere using rocket techniques', Aeronomy report, No.20, University of Illinois, Urbana, 83, July 1967.
3. Rastogi, R.G., Chandra, H., 'Ground-based measurements of ionospheric phenomena associated with the equatorial electrojet', Indian Journal of Radio and Space Physics, vol.1, June 1972.
4. Rastogi, R.G., Private Communication, 1974.
5. Reddy, C.A., Mukunda Rao, M., 'On the Physical Significance of the  $E_s$  parameters  $f_{pE_s}$ ,  $f_{E_s}$  and  $f_{oE_s}$ ', Journal of Geophysical Research, Space Physics, vol.73, No.1, 215, 1968.
6. Sethuraman, R., Proc. Indian Acad. Sci., XLII, 84, 1958.
7. Sethuraman, R., Ph.D. Thesis, Gujarat University, 1959.

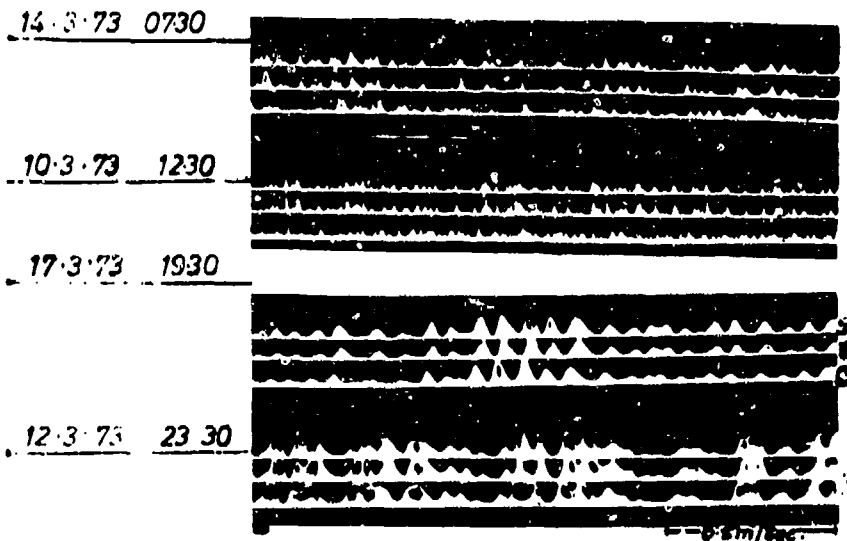


Figure 1

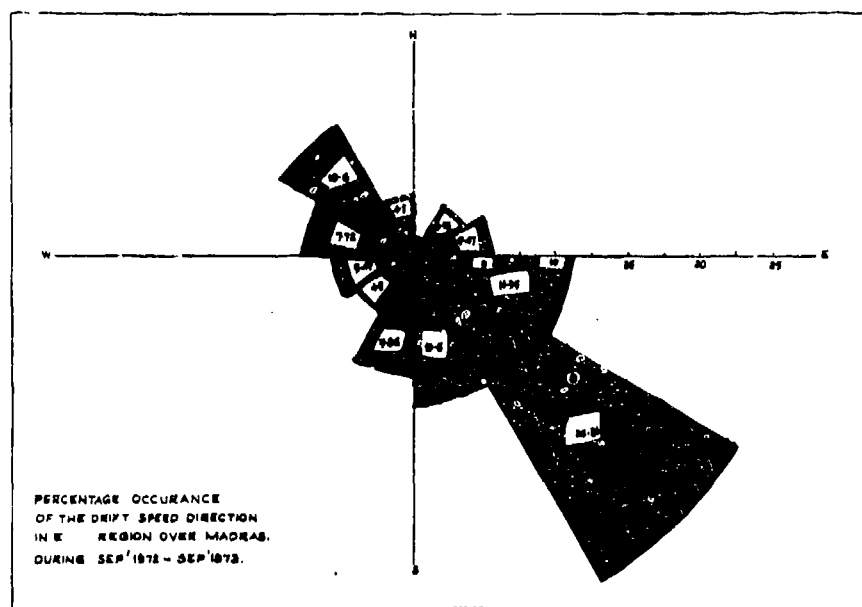


Figure 2

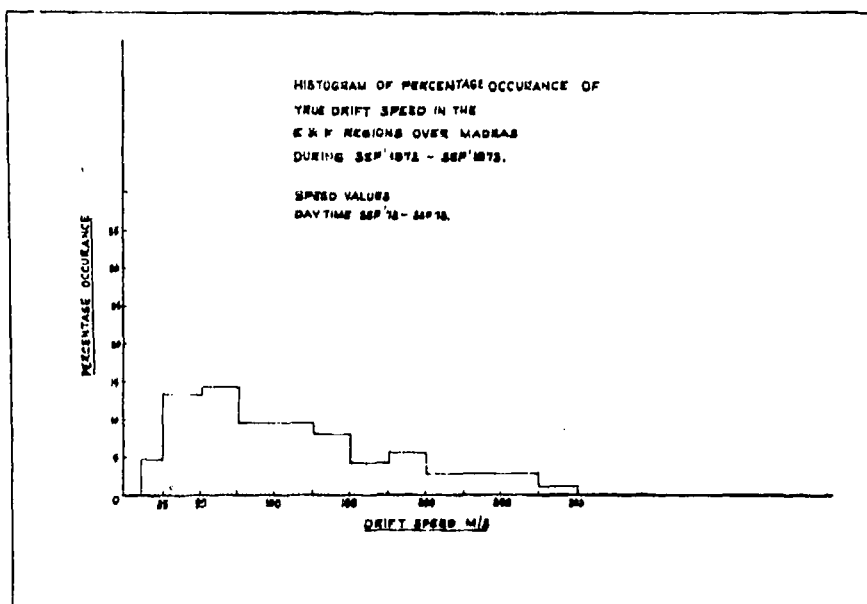


Figure 3

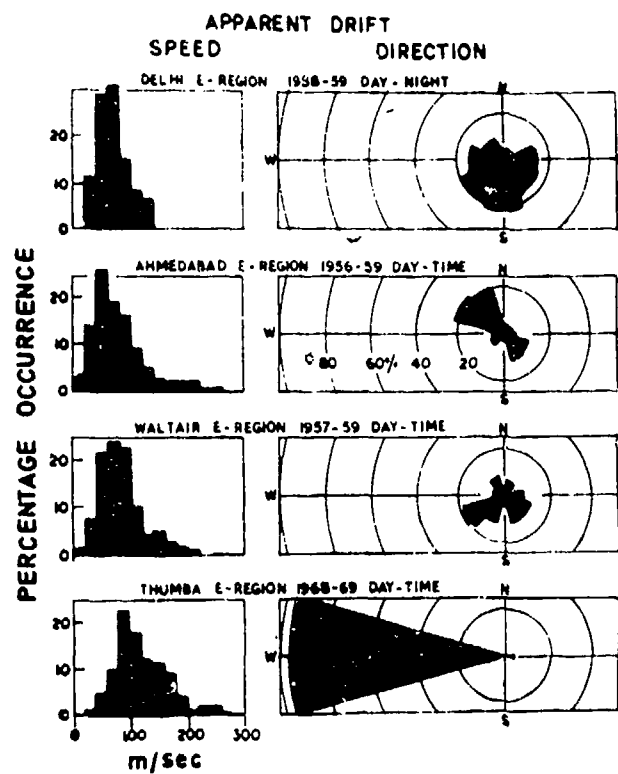


Figure 4

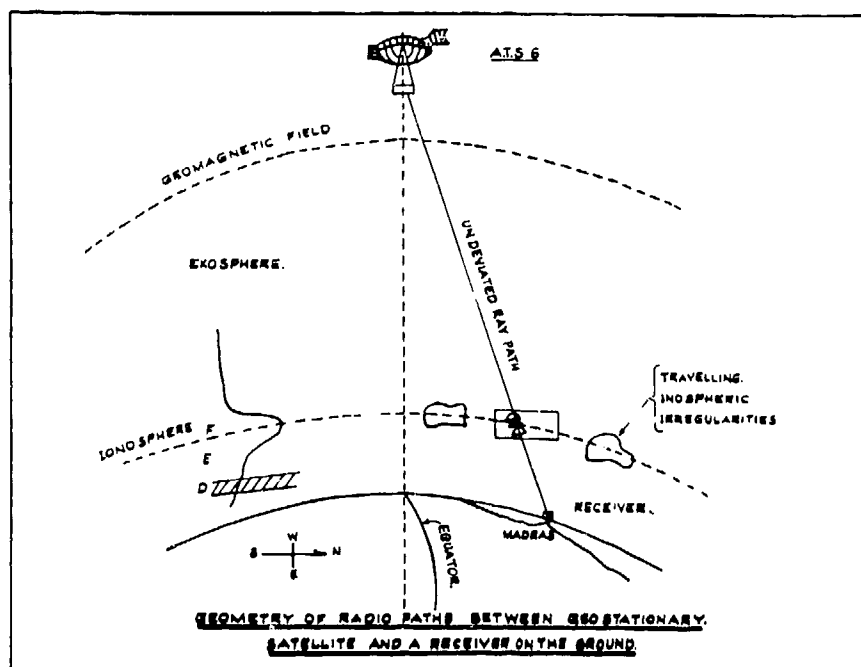


Figure 5

## RESULTS OF A RADIO HOLOGRAPHIC STUDY OF IONOSPHERIC IRREGULARITIES

G. Schmidt  
Max-Planck-Institut für Aeronomie, 3411 Lindau/Harz, FRG  
J. Oksman and A. Tauriainen  
University of Oulu, 90100 Oulu 10, Finland

### ABSTRACT

The holographic method has been recently introduced to the study of satellite scintillations. Only one ground station is needed to receive the radio hologram. The scattered object wave is measured in relation to a harmonic reference wave. The resulting amplitude and phase information can, by using the reciprocity theorem, be interpreted as the one dimensional radio hologram at the altitude of the satellite orbit. The mathematical theory for the reconstruction of the image is developed. The theory is analogous to that used in acoustical holography.

The Fresnel-Fourier Transform is used to form the image at various distances from the satellite. The calculations with the computer are carried out using the Fast Fourier Transform. The coefficients of the Fresnel-Fourier Transform represent the spatial spectrum of the radio hologram which corresponds to the intensity of the scattered object wave. The coordinates of the scatterer are those given by the point where the intensity reaches its maximum value. This means that the image is "focused" at this point.

In the cases which have been analysed so far the irregularities have been localized at heights between 70 and 300 km. The observed irregularity region consists of several isolated irregularities with cross sections from 50 to 500 m. The strength of the irregularities is not included in the theory presented here.

### INTRODUCTION

The ionospheric irregularities causing scintillation of radio waves transmitted by satellites have been studied by various means. The most obvious one is to use transmissions of beacon satellites and to study scintillations in

the amplitude and phase of the waves received on the ground. The radio holographic method, recently introduced by Schmidt [4], is of great interest, especially when combined with other measurements. In the holographic method, two coherent radio waves are used to measure the radio hologram. The scatterers in the ionosphere can then be reconstructed from the holographic data. The reconstruction is carried out using the Fresnel-Fourier Transform. The Fast Fourier Transform (FFT) is applied in calculations, performed with a computer. The radio holographic method offers a possibility to localize isolated irregularities and to study their shape.

The origin and the strength of the irregularities is not included in the theory. It is enough when the object wave is diffracted by the irregularities. The coherent reference wave on higher frequency is assumed not to be influenced by the irregularities. This condition is controlled during the recording.

### RECORDING A RADIO HOLOGRAM

The beacon satellites (5 US NNSS), used in this experiment, transmit two coherent radio waves on frequencies 150 and 400 MHz, which are exactly harmonic in the ratio 3/8.

The amplitude and phase of the lower frequency (150 MHz) wave, which is scattered by irregularities, are measured in relation to those at 400 MHz. These data constitute the radio hologram.

The interpretation of the holographic data is complicated due to the fact that we have only one receiving station on the ground and that the transmitter is on board a satellite. Fortunately, the theorem of reciprocity allows us to

interchange the position of the receiver and the transmitter. In this way the measured values can be interpreted as holographic data collected by the satellite along the flight path. As the holographic data are recorded in one dimension only, the irregularities can be reconstructed only two-dimensionally in the plane which is defined by the vector from ground station to satellite and by the satellite's velocity vector [4].

After the successful preliminary test phase in November 1972, a proper measuring period was organized from August 1972 to March 1973 in Pittiövaara, North Finland (67.419° N, 26.393° E), which is the new field station of the Geophysical Observatory in Sodankylä. The equipment was similar to that used in the test phase [4]. During the measuring period, nearly 500 passes were recorded in analog form on magnetic tape. Eight passes from these data were chosen for processing and consequent reconstruction.

#### COMPUTER RECONSTRUCTION OF IRREGULARITIES

The mathematical treatment given here follows greatly that outlined by Goodman [1].

To consider theoretically the reconstruction of the image in two dimensions, we suppose that the reference wave  $U_r$  is generated by a point source at the ground station with coordinates  $(x_r, z_r)$ . An isolated irregularity of finite extent in the ionosphere, which causes the scattering of the transmitted wave, is assumed to be located at the point with coordinates  $(x_o, z_o)$ . This configuration is illustrated in Fig. 1.

We define the reference wave in the recording or holographic plane by the equation

$$U_r(x, o) = a_r \cdot e^{j(\phi_r + kR_1)} \quad (1)$$

and the object wave by the equation

$$U_o(x, o) = a_o \cdot e^{j(\phi_o + kR_3)} \quad (2)$$

where  $a_r, a_o$  = amplitudes of reference and object waves, respectively

$\phi_r, \phi_o$  = constant phase factors of the reference and object waves, respectively

$R_1$  = distance from reference point to observing point

$R_3$  = distance from object point to observing point

$$k = \frac{2\pi}{\lambda}$$

$\lambda$  = wave length.

The time dependent term is omitted from the equations (1) and (2).

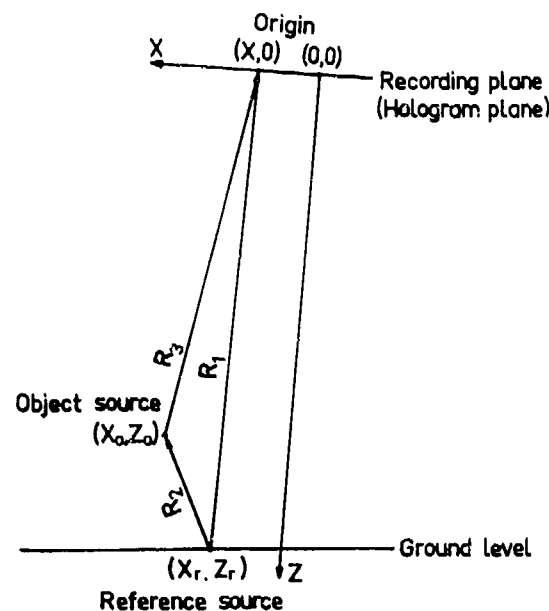


Fig. 1 The geometry for the reconstruction of the image

The radio wave which illuminates the irregularity is monochromatic and coherent with the reference wave. The irregularity is, for the sake of simplicity, taken as a single point scatterer. In practice, the irregularity is of finite extent and an elementary spherical wave emanates from every point of the object. All the spherical waves then superpose linearly to form the complex object wave  $U_o$ , which can be recorded in the holographic plane in relation to the wave  $U_r$ . In optical holography the most important recording medium is photographic film, which responds to intensity. The intensity in the recording plane can be given by the sum of four terms.

In our case of electronic detection, each term can be distinguished and therefore treated separately.

To reconstruct the image, we consider the term giving the real picture. Substituting the expressions for the reference and object waves, the term becomes

$$U_0 U_r^* = a_0 a_r^* \cdot e^{-j(\phi_r - \phi_0)} \cdot e^{-jk(R_1 - R_3)} \quad (3)$$

The phase factor  $k(R_1 - R_3)$  can now be expressed in rectangular coordinates and expanded binomially. If we consider only the first two terms and require that the contribution of the next-higher-order term is much less than one radian, we get the condition that

$$z_r^3 \gg \frac{\pi}{4 \cdot \lambda} (x - x_r)^4 \quad (4)$$

Using this Fresnel approximation, equation (3) can now be rewritten as

$$U_0 U_r^* = A_0 A_r^* \cdot e^{-j\frac{\pi}{\lambda} \left[ \frac{1}{z_r} (x - x_r)^2 - \frac{1}{z_0} (x - x_0)^2 \right]} \quad (5)$$

where  $A_0$  = complex amplitude of the object wave =

$$A_r^* = \text{conjugate of the complex amplitude of the reference wave} =$$

$$a_0 \cdot e^{j[\phi_0 + k \cdot z_0]}$$

$$a_r \cdot e^{-j[\phi_r + k z_R]}$$

Using Equ. (5), the quadratic approximation to the spherical wave can be applied to reconstruct the irregularities. The reconstruction formula becomes

$$I_i(k) = \left[ \sum_{n=0}^{N-1} I_d(n) \cdot e^{j\frac{\pi}{\lambda} \cdot \frac{z_0 - z_r}{z_0 \cdot z_r} \cdot \Delta x^2 \cdot n^2} \right] \cdot e^{j2\pi \frac{kn}{N}} \quad (6)$$

where  $I_i(k)$  = the image intensity distribution  
 $I_d(n)$  = the measured complex amplitude from the hologram  
 $N$  = the number of measured values  
 $k, n$  =  $0, 1, \dots, N-1$   
 $\Delta x$  = the distance between the sampling points

Equ. (6) is of the same form as that given by Goodman in ref. [2].

The intensity distribution  $I_i(k)$  can be interpreted as being that at the object point  $(x_0, z_0)$ . Since  $z_0$  is included in the Equ. (6) we need only to calculate  $x_0$  from the expression

$$x_0(k) = \frac{z_0}{z_r} \cdot x_r + \frac{\lambda \cdot z_0}{N \Delta x} \cdot k \quad (7)$$

According to Equ. (7), the first image point always lies on the line connecting the reference point to the first sampling point in the holographic plane. Further, the distance between the image points  $x_0(k)$  is dependent on  $z_0$ .

The reconstruction by computer is performed as follows. For a given value  $z_0$ , all the  $N$  Fourier coefficients according to Equ. (6) are calculated and the  $x$ -coordinates determined from the relation (7). The same calculations for the next value of  $z_0$  are repeated till all the necessary images are calculated.

In order to localize the irregularities, the intensity peaks are compared at different distances from the satellite. The maximum intensity means that equation (6) is "focused" at that distance and this gives the position of the scatterer. At the neighbouring distances, the intensity decreases and this means that the equation (6) is unfocused.

#### PREPARATION OF THE MEASURED HOLOGRAPHIC DATA FOR PROCESSING

The first step in the data reduction process was to sample and digitalize the analog record. A sample was taken every 10 ms which corresponds to a sampling interval of 73 m on the satellite orbit. This choice seems to be sufficient to include the highest frequency, since the cut-off frequency is 50 Hz and the spectrum of the diffraction pattern ranges from 0 to 20 Hz.

In the theory described before, it was assumed that the sampled values lie on a straight line. In the case of the satellite, this is not true, because the orbit is nearly circular. However, the deviation from a straight line over a short distance is small. Further, if the angle between the line of propagation of the object wave and that of the reference wave at the sampling point is very small, then the phase difference and the amplitude do not change significantly in the propagation direction [3]. Accordingly, the portion of the orbit under consideration can be considered as a straight line. To describe the line, the method of least squares was used so as to minimize the deviation of the line from the actual path.



## RESULTS OF THE COMPUTER RECONSTRUCTION

In the first cases chosen for reconstruction the number of data samples were 1600, which corresponds to a period of 16 seconds. This period was sufficiently long to cover restricted disturbances and also suitable for our computer capacity. This sample length was also used for continuous disturbances, which means that only a section of the disturbance was reconstructed. However taking the next section close to the first, the whole disturbance can be reconstructed step by step. In the following, two examples of the reconstruction are described.

### Example I

The hologram which is shown in Fig. 2 contains several superposed frequencies. The part with relatively high frequencies on the right is very conspicuous. The geometry for this example is shown in Fig. 3. The angle between the radio wave and earth's magnetic field was in this case about  $57^\circ$ . Fig. 4 shows the reconstructions at three distances. The intense peak on the right has the maximum at a distance of 1400 km, which is shown clearly in the figure. This peak evidently corresponds to the high frequency part of the hologram in Fig. 2, mentioned previously.

The reconstructed irregularities are depicted in Fig. 5. The corresponding detailed data referring to the most intense peaks are given in Table I.

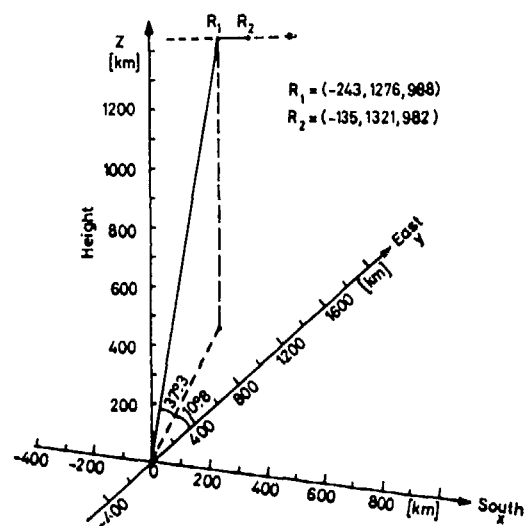


Fig. 3. The geometry in the case of the previous hologram. The ground station is at the origin and the hologram is recorded between the orbit points  $R_1$  and  $R_2$ .

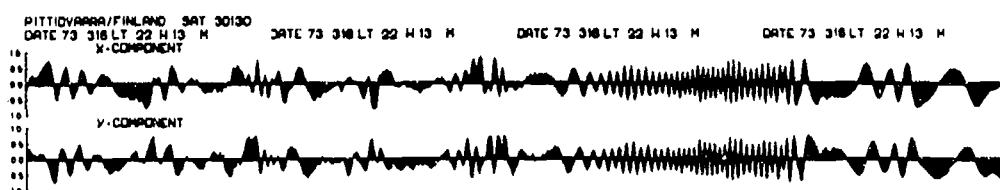


Fig. 2. The x and y components of a radio hologram, which consists of 1600 samples taken in 16 s.

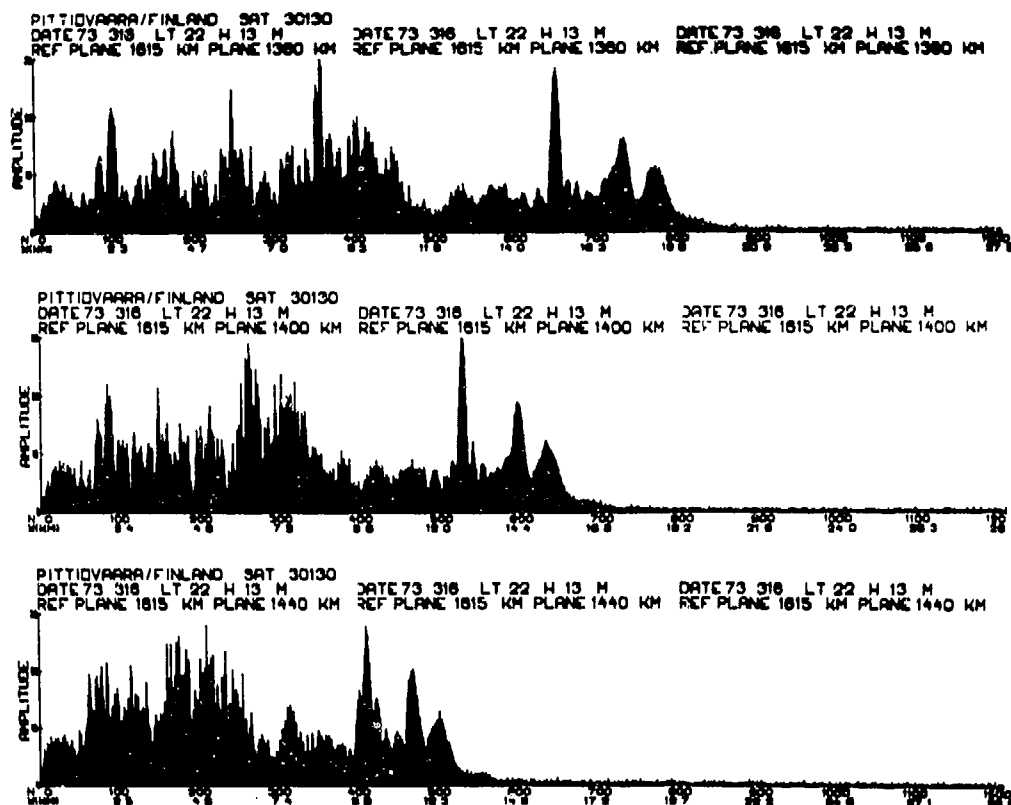


Fig. 4. The reconstructions at the distances 1360, 1400 and 1440 km, corresponding to the hologram in Fig. 2.

Table I

No	Ampl.	South x[km]	East y[km]	Height z[km]	Width [km]
8	71.5	-50	343	266	0.14
19	86.0	-42	280	217	0.10
26	78.5	-34	217	167	0.08
29	73.8	-35	202	156	0.08
30	89.5	-32	202	156	0.17
32	92.0	-22	169	131	0.22

Example II

Fig. shows the geometry in the case of an extended hologram, which was reconstructed step by step. The sections are taken between the orbit points ( $R_1, R_2$ ), ( $R_2, R_3$ ) and ( $R_3, R_4$ ). Finally, the reconstructions are combined to a single picture.

The entire reconstruction is depicted in Fig. 7. Detailed data referring to the most intense peaks are given in Tables IIa, IIb and IIc.

Table IIa. Irregularities reconstructed between the vectors  $R_1$  and  $R_2$

Ampl.	x[km]	y[km]	z[km]	Width[km]
38.6	-397	28	95	0.12
34.0	-396	29	95	0.08
36.8	-364	29	89	0.08
39.7	-337	24	80	0.08

Table IIb. Irregularities reconstructed between the vectors  $R_2$  and  $R_3$

Ampl.	x[km]	y[km]	z[km]	Width[km]
46.0	-512	52	131	0.13
46.0	-453	46	116	0.10
58.4	-366	38	94	0.12
60.0	-336	35	87	0.12
50.6	-249	26	64	0.08

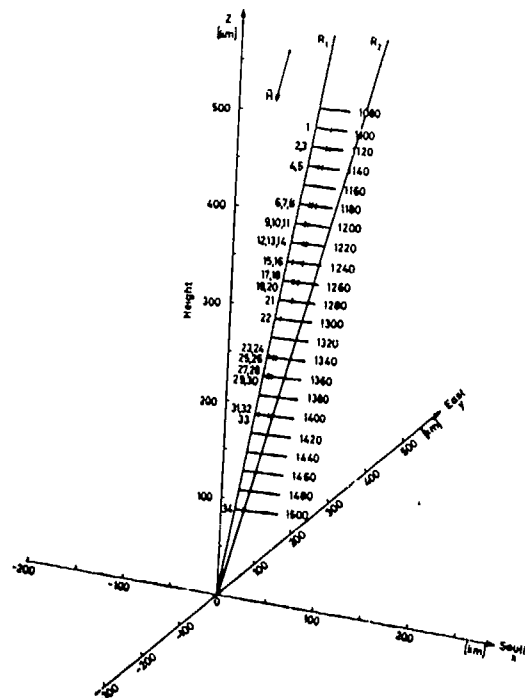


Fig. 5. The irregularities obtained from the hologram in Fig. 2.

Table IIc. Irregularities reconstructed between the vectors  $R_3$  and  $R_4$

Ampl.	x [km]	y [km]	z [km]	Width [km]
61.6	-632	74	167	0.10
57.0	-574	67	152	0.17
65.2	-566	74	155	0.20
57.0	-423	56	116	0.15
61.6	-395	52	108	0.11

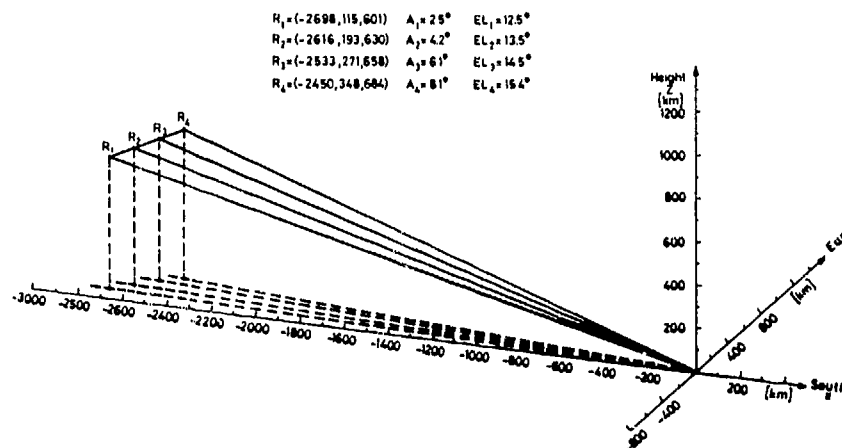


Fig. 6. The geometry of an extended hologram to be reconstructed step by step

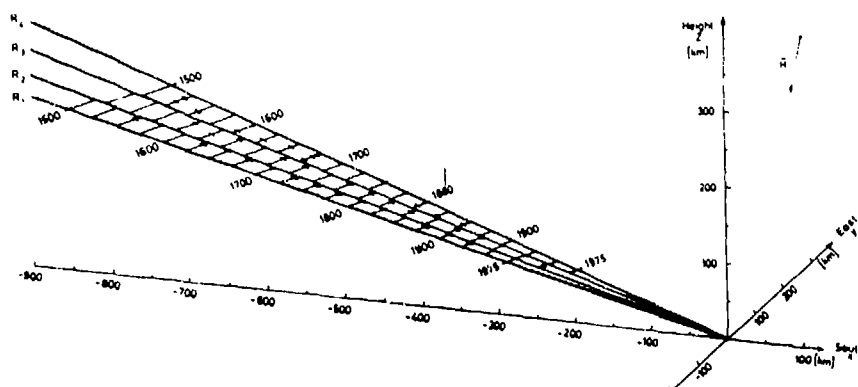


Fig. 7. The step by step reconstruction of the hologram in Fig. 6

#### CONCLUSIONS

The examples discussed demonstrate that it is possible with the holographic method to localize ionospheric irregularities, which cause radio wave scintillations. These can be localized in the plane defined by the vector from ground station to satellite and the satellite's velocity vector.

The holographic method is a mathematical procedure, with which one can reconstruct an image. One gets the focused image by seeking the maximum contrast.

In the cases that have been analysed so far, the irregularities are found in the height region between 70 and 300 km. Also they are found to occur mainly below F-maximum. The cross section of the irregularities is found to vary from 50 to 500 m, the greatest proportion of them being about 100 m in cross section. The reconstruction has shown that the irregularity region consists of many small isolated irregularities, often very close together. Unfortunately, it is very difficult to visualize the picture of the irregularities due to the lack of the third dimension in the reconstruction.

For a continuation of these measurements also in mid-latitudes, a satellite with a lower transmitter frequency in the range 20 to 100 MHz, in an identical orbit to the NNSS satellites, would be desirable. The harmonic reference frequency for such a satellite would be in the range 0.4 to 2 GHz. In the case of spacially localized irregularities in the ionosphere disturbances also appear as spacially local-

ized in the recorded hologram. It can therefore be concluded that for these high transmitter frequencies, the scattering angle is very small and the receiving antenna detects only signals scattered approximately in the satellite-ground station direction, or near the plane defined above. Because of this, no highly directional receiving antenna is necessary to avoid the reception of signals from outside this plane.

#### REFERENCES

1. Goodman, J.W. Introduction to Fourier Optics. Mc Graw Hill Book Company 1968.
2. Goodman, J.W. Digital Image Formation from detected holographic Data. Acoustical Holography, 1969, Vol. 1, pp 173-185. Plenum Press.
3. Kiemle, H. and Röss, D. Einführung in die Technik der Holographie. Akademische Verlagsgesellschaft Frankfurt/M., 1969.
4. Schmidt, G. Determination of the Height of Ionospheric Irregularities with the Holographic Method. Zeitschrift für Geophysik, 1972, Band 38, S. 891-913.

A HOLOGRAPHIC RADIO CAMERA TECHNIQUE FOR THE  
THREE-DIMENSIONAL RECONSTRUCTION OF IONOSPHERIC INHOMOGENEITIES

by

W. Ross Stone  
Megatek Corporation, San Diego  
and Department of Applied Physics and Information Sciences,  
University of California, San Diego

and

Verna E. Hildebrand  
Propagation Technology Division,  
Naval Electronics Laboratory Center, San Diego

## I. INTRODUCTION

Fundamental to an understanding of the scintillation of VHF and UHF radio signals from satellites is a knowledge of the three dimensional spatial characteristics and distribution of the irregularities which cause this scintillation. As a means of obtaining this information, it was proposed (1,2) that the optical concepts used in developing holography be applied at radio frequencies, in an attempt to reconstruct "images" of these irregularities: specifically, to determine their size, some information about their shape, and their height. Since then many aspects of the theory of the technique have been worked out and verified. Computer simulations have been carried out to demonstrate the capabilities of the technique, and the practical details of an experiment have been examined. It is anticipated that such an experiment will be carried out in 1975.

This paper presents the theory behind this "holographic radio camera" technique, the results of the computer simulation work, and details of the planned experiment. Because of space limitations the presentation is abbreviated. This paper summarizes the information in two recent reports (3,4).

## II. THE RADIO CAMERA TECHNIQUE CONCEPT

The steps involved. The technique involves two steps. First, an array of antennas is used to record the amplitude and phase of a diffraction pattern. This pattern is produced by illuminating a region of ionospheric irregularities from above the ionosphere using a satellite. The satellite may be geostationary or orbiting, and is assumed to produce a monochromatic plane-wave illumination of the irregularities. A geostationary satellite positioned vertically above the array is assumed in what follows; the effect of using an orbiting satellite and other geometries is discussed below. Contrary to the normal practice in employing an antenna array (e.g. to produce a steerable beam), the complex output of each antenna in the array is recorded. Quite literally, the array is used

to sample the diffraction pattern.

The second step in the technique involves the computer processing of the complex scalar field values recorded by the array. The details of how these values are operated on to yield an image of the irregularities producing the recorded diffraction pattern are described in Section III. However, it is possible to understand the physical principles upon which the calculations are based by reference to such basic concepts as Huygen's principle.

In a very real sense, the combination of the array plus the computer processing serves to transform the wavelength involved in such a manner as to permit the human visual system, which has almost no response at meter wavelengths, to observe the diffracting object as it affects the longer wavelength. It is as if a camera which was loaded with very long wavelength film had been employed; hence, the term "radio camera". This optical analogy becomes even stronger in Section III. However, the resolution (or minimum irregularity structure size) and the field of view (or maximum horizontal extent at a given height) of the image produced by the technique clearly are related to the parameters of the array used to record the diffraction pattern. As these determine the usefulness of the technique, they are derived next.

Resolution. The simplest method of arriving at the smallest ionospheric structure which the array can record is to Fourier analyze the irregularities into a series of sinusoidal diffraction gratings. The requirements for recording the information present in the field diffracted by one such grating will be considered. The geometry is as shown in Figure 1. The grating has a spatial frequency (equal to one over its period, or characteristic size) of  $\nu$ , and it is at an altitude  $h$  above the ground. On the ground is an aperture of width  $d$ . It is well known that illuminating such a cosinusoidal grating with a plane wave from above gives rise, at each point, to three diffracted plane waves: one propagating

without deviation, and two diffracted symmetrically through an angle  $\theta$  (5). The diffraction angle is related to the spatial frequency of the grating and the wavelength,  $\lambda$ , of the illumination by

$$\sin \theta = \lambda \nu \quad (1)$$

Suppose that, as is shown in the figure, the aperture width  $d$  is such that the diffracted wave just intercepts the edge of the aperture. Then from the figure,

$$\tan \theta = d/h \quad (2)$$

For the situation at hand,  $d/h \ll 1$ . Using this fact to equate the lefthand sides of equations (1) and (2).

$$\nu = \frac{d}{\lambda h} \quad (3)$$

Since an increase in  $\nu$  implies an increase in  $\theta$ , equation (3) gives the value for the maximum object spatial frequency which can be recorded by an aperture of width  $d$ . As this spatial frequency contains the information about the smallest structure which can be recorded, the resolution of the system is given by  $1/\nu$ , or

$$\frac{\lambda h}{d} \quad (4)$$

It is significant to note that  $\lambda/d$  is the beam width of an antenna aperture  $d$ , and expression (4) is the horizontal distance intercepted by such an antenna beam at height  $h$ .

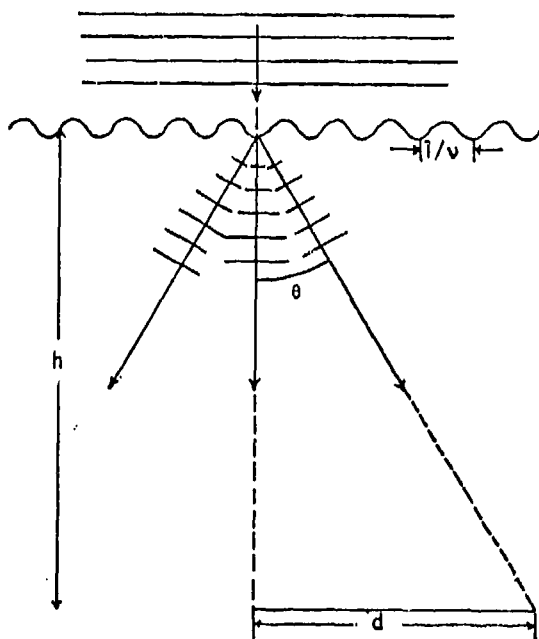


Figure 1

In an optical imaging system the resolution is a measure of the ability of the system to permit separation of two closely spaced objects. Typically, some criterion (e.g. the Rayleigh criterion) is applied which defines "separation" in terms of the distance

between adjacent maxima in the intensity distribution of the two adjacent objects. Clearly, such a criterion may be more or less stringent than is actually required depending on the signal to noise ratio. The above derivation shows that resolution in this application is related to the ability to separate radiation diffracted through different, although nearly equal, angles, corresponding to a slight difference in spatial frequencies. In fact, what is being "resolved" is the spatial frequency content of the irregularity. This measurement of angle is done by letting the radiation falling on the array interfere with a plane reference wave (i.e., each antenna of the array is fed a coherent local oscillator signal), converting the angular information into phase information. Most optical resolution criteria can be shown to involve detecting phase differences of  $\pi$  radians (i.e., they depend upon destructive interference). But in the presence of a signal to noise ratio greater than one, it is simple to measure smaller phase differences at radio frequencies. In fact, the relative error of a phase measurement,  $\delta\phi/\phi$ , is given by (6)

$$\frac{\delta\phi}{\phi} = \frac{1}{(2 S/N)^{1/2}} \quad (5)$$

where  $S/N$  is the signal to noise power ratio. It follows that the resolution, expression (4), is actually given by

$$\frac{\lambda h}{d} \left( \frac{1}{2 S/N} \right)^{1/2} \quad (6)$$

**Field of view.** Let the edges of the total array in Figure 1 be replaced with two adjacent antennas making up the array. Then  $d$ , the total array size, is replaced with  $\Delta$ , the antenna spacing. It might be argued, in keeping with the above derivation, that as  $\nu$  becomes smaller, so does  $\theta$ , and, in turn, the spacing of the antennas necessary to record this lower spatial frequency. This leads to the conclusion that the lowest spatial frequency, or largest irregularity dimension, which can be recorded is determined by the antenna spacing in the array. Unfortunately, this is not correct for the case of ionospheric irregularities. The reason for this serves to illustrate an important difference between the use of a radio camera and an optical camera. The following two paragraphs, from some comments by Dr. H. G. Booker (7), explain this point.

A well designed optical camera has a wide field of view, and the same is true of a radio camera. However, it should be noted that the scattering pattern of the target has an important influence. A target large compared with the wavelength possesses a scattering pattern in the form of a beam directed along the geometrical shadows; indeed it is this beam that forms the geometrical shadow. Irregularities of width  $w$  in the ionosphere have a scattered field in the form of a parallel beam to a distance of the order of  $w^2/\lambda$  (the near field) and a spreading beam of

angle  $\lambda/w$  at greater distances (the far field). Hence, neglecting the obliquity factor, irregularities of width  $w$  at height  $h$  have the near-field behavior at ground level if  $w^2/\lambda > h$ , and the far field behavior if  $w^2/\lambda < h$ . In the former case the antenna aperture is affected primarily by the irregularity at height  $h$  in the line-of-sight to the source in the satellite. In the latter case, the antenna aperture is affected mainly by those irregularities at height  $h$  out to a distance from the line-of-sight given by  $h\lambda/w$ . For the minimum size of irregularity detectable by the camera, this calculates, in accordance with expression (6), to be

$$d (S/N)^{1/2}$$

In other words, for both small and large irregularities, the antenna aperture is affected primarily by the irregularities lying within a cone formed by joining the rim of the aperture to the source in the satellite; this cone is expanded somewhat if the signal/noise ratio is greater than unity. Hence, while in theory the aperture can see all the irregularities in the sky, in practice it concentrates on those within a distance from the line-of-sight to the satellite source given by the above expression.

This permits some simplification in the design of a radio camera. Ideally it is desirable to fill the entire aperture with half-wave dipoles, spaced half-a-wave apart between centers. If one used spacings more than twice this, ghost beams are produced in addition to the one aimed at the satellite source. But the ghost beams are looking at ionospheric scatters from a direction well outside their main scattering field. Such ghost beams can, therefore, be tolerated so long as their effect at the antenna aperture is less than that of the noise. Fully filled apertures are not, therefore, essential. However, the separation between elements must be kept small compared with the minimum width of ionospheric irregularity that it is proposed to investigate.

As a numerical example, suppose that it is desired to record irregularities in the range of sizes from 100 m to 1 km (the size range most likely to be responsible for VHF and UHF scintillations). Let a wavelength of 1 m be used, and a height of 400 km and a signal to noise power ratio of 10 (10 dB) be assumed. Then, an array with an aperture of 1 km and an antenna spacing of 50 m would permit imaging the desired size range.

**Height resolution.** It is known that optical holography is a three dimensional process, in contrast to ordinary two dimensional photography. The addition of this third dimension of information is due directly to the recording of phase information in addition to the amplitude, or intensity, information normally recorded. It also follows that the resolution with which height information is recorded in the radio camera technique

(i.e., the ability to discriminate between scatterers at two altitudes in the ionosphere) is directly related to the accuracy with which the phase of the received signal can be determined. This can be seen from the following simple geometrical argument.

Consider the geometry of Figure 2. Here,  $z$  is the perpendicular distance to a point in the ionosphere, and  $r_1$  and  $r_2$  are the distances from this point to two points at coordinates  $x_1$  and  $x_2$  in the array (which is taken to be one dimensional for this example). It is desired to determine the height of the point,  $z$ , by comparing the phase of a signal from the points at  $x_1$  and  $x_2$ . The phase at the two points  $x_1$  and  $x_2$  is given approximately by

$$\phi_1 = \frac{2\pi}{\lambda} r_1 \quad (7)$$

$$\phi_2 = \frac{2\pi}{\lambda} r_2 \quad (8)$$

For  $i = 1$  and  $2$ ,

$$r_i = \sqrt{z^2 + x_i^2} \approx z + \frac{x_i^2}{2z} \quad (9)$$

Combining these relations,

$$\phi_i \approx \frac{2\pi}{\lambda} \left( z + \frac{x_i^2}{2z} \right) \quad (10)$$

Thus,

$$\phi_1 - \phi_2 \approx \frac{2\pi}{\lambda z} (x_1^2 - x_2^2) \quad (11)$$

and

$$z \approx \frac{\pi}{\lambda} \frac{(x_1^2 - x_2^2)}{\phi_1 - \phi_2} \quad (12)$$

The error in  $z$ ,  $\Delta z$ , due to an error in measuring the phase difference,  $\Delta(\phi_1 - \phi_2)$  is thus

$$\frac{\Delta z}{z} = \frac{\Delta(\phi_1 - \phi_2)}{\phi_1 - \phi_2} \quad (13)$$

Now, the maximum phase difference measurable across any array of size  $d$  is

$$\phi \approx \frac{d^2}{2z} \cdot \frac{2\pi}{\lambda} \quad (14)$$

The ability to measure this maximum phase difference determines the ability of the array to measure an object's altitude; the precision with which the measurement can be made determines the error in the height measurement.

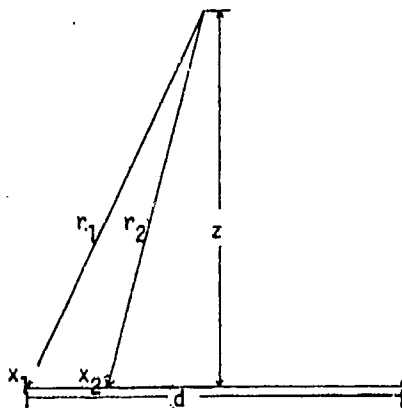


Figure 2

There are two primary sources of error in the phase measurement. One is due to A/D converter resolution, while the second is due to signal to noise ratio limitations. A 10 bit converter has a resolution of  $360^\circ/1024 = .352^\circ$ . As mentioned above, the error in a phase measurement made with a signal to noise power ratio S/N is given by (5)

$$\Delta\phi = \frac{1}{(2 \frac{S}{N})^2} \quad (15)$$

where  $\Delta\phi$  is measured in radians. As substitution of typical signal to noise ratios into equation (15) quickly shows, the signal to noise ratio is the limiting factor. Figure 3 shows the variation in height resolution as a function of height, with array size and signal to noise ratio as parameters. The two wavelengths used in this figure represent the range of wavelengths considered for the demonstration experiment discussed below. It is important to note that substitution of equations (14) and (15) into equation (13) yields the expression for the depth of focus of an optical camera with aperture d.

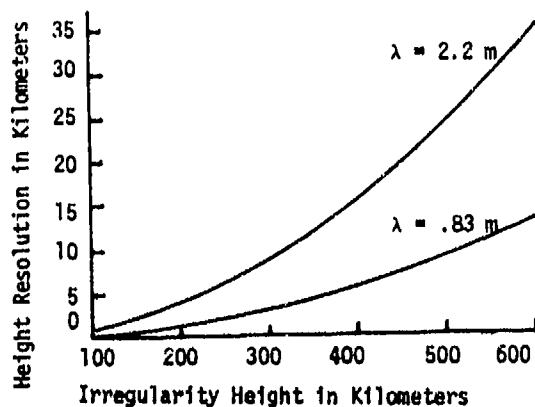


Figure 3. Height resolution as a function of irregularity height using a 1 km array with a signal to noise ratio of 20 dB.

Summary of certain practical considerations. Several practical factors have been considered. These are briefly summarized here.

The frequency stability required of the transmitter on the satellite has been calculated (3) to be, at worst, that obtainable with a crystal oscillator without temperature compensation. The same criterion applies to the stability of the local oscillator source used to measure phase at the array, if the satellite is geostationary. For an orbiting satellite the local oscillator must be programmed to remove the doppler effect, and somewhat greater stability is required. The effect of satellite motion was found to be unimportant for values typical of a geostationary satellite. For an orbiting satellite (such as might be used with a line array oriented perpendicular to its motion), the important consideration is the amount of time it takes for the satellite to traverse one beam of the array: The signal at each antenna must be sampled in less than this time to record a "stationary" image. For a typical orbiting satellite this time falls in the range of .1 to 1 second, and thus presents no problem.

Signal to noise ratio is not quite the same for a scintillation measurement as the concept usually applied to a radio frequency receiving system. It is fairly simple (and inexpensive) to design an antenna array to receive signals at meter or centimeter wavelengths from the research or military satellites now in operation. Typical signal to noise ratios at each antenna element obtainable with an inexpensive system range from 25 to 50 dB in the 136 MHz to 250 MHz band. However, this is the signal to noise ratio for receiving the satellite beacon, without scintillations. The signal to noise ratio associated with the scintillations is dependent upon the strength of the scintillations present. It is usually less than 20 dB at meter wavelengths. This limits the extent to which the horizontal and vertical resolution can be improved over their classical optical values (see the discussion of resolution above). It should be noted that the reason relatively high beacon signal to noise ratios can be obtained inexpensively is the ready availability of commercial high gain, low noise preamplifiers (e.g. 35 dB gain, 2.5 dB NF at a frequency between 100 MHz and 300 MHz for \$30.00), and the extremely narrow bandwidth of scintillations ( $< 1$  Hz).

### III. COMPUTER PROCESSING

The computer processing used to reconstruct images from the recorded diffraction pattern is basically a computationally efficient implementation of Huygen's principle. Because of space limitations only a summary of the theory is given here.

Basic concepts. Consider propagation between two planes in a right handed coordinate



system, one at  $z = z_0$  and the second at  $z = z_1$ . Let the complex (scalar) field in the first plane be denoted  $f_0(x_0, y_0, z_0)$  and the field in the second plane be denoted  $f_1(x_1, y_1, z_1)$ . The two dimensional Fourier transform,  $F$ , of a field,  $f$ , is given by

$$F(v_x, v_y, z) = \iint_{-\infty}^{\infty} f(x, y, z) \exp\{-i2\pi(xv_x + yv_y)\} dx dy \quad (16)$$

The inverse transform is

$$f(x, y, z) = \iint_{-\infty}^{\infty} F(v_x, v_y, z) \exp\{i2\pi(xv_x + yv_y)\} dv_x dv_y \quad (17)$$

The Rayleigh-Sommerfeld, or Kirchhoff, diffraction integral relating the field in plane 0 to the field in plane 1 is

$$f_1(x_1, y_1, z_1) = \iint_{-\infty}^{\infty} \{f(z_1 - z_0)/\lambda R\} \exp(i2\pi R/\lambda) \{1 + \lambda/(i2\pi R)\} f_0(x_0, y_0, z_0) dx_0 dy_0 \quad (18)$$

where

$$R \equiv \{(x_1 - x_0)^2 + (y_1 - y_0)^2 + (z_1 - z_0)^2\}^{1/2} \quad (19)$$

Fourier transformation of equation (19) yields (8)

$$F_1(v_x, v_y, z_1) = F_0(v_x, v_y, z_0) \exp\{i2\pi \frac{z_1 - z_0}{\lambda} \sqrt{1 - (\lambda v_x)^2 - (\lambda v_y)^2}\} \quad (20)$$

In words, the spatial Fourier transform of the field in plane 1 is found by multiplying the transform of the field in plane 0 by a "propagator", given by the exponential in equation (20). Equation (20) can also be derived by representing the field in each plane as an angular spectrum of plane waves and considering the propagation of an individual plane wave (9). This derivation requires none of the assumptions about boundary conditions associated with the use of the Kirchhoff integral, and can be shown to be exact. The inverse of the above equation, which determines the field at plane 0 in terms of the field at plane 1, can be obtained by multiplying both sides of equation (20) by an exponential term with opposite sign (the "inverse propagator"). This yields

$$F_0(v_x, v_y, z_0) = F_1(v_x, v_y, z_1) \exp\{-i2\pi \frac{z_1 - z_0}{\lambda} \sqrt{1 - (\lambda v_x)^2 - (\lambda v_y)^2}\} \quad (21)$$

The great advantage of equations (20) and (21) is that they permit calculating the field over one plane from the (measured) field over another plane in three computationally efficient steps:

1. Fourier transform the recorded field,  $f_1(x_1, y_1, z_1)$ , using the fast Fourier

transform (FFT) (10);

2. Multiply  $F_1(v_x, v_y, z_1)$  by the inverse or forward propagator, for  $z_1 > \text{or} < z_0$ .
3. Inverse transform the result of step 2, using the FFT, to yield the field in plane  $z_0$ .

There is one limitation on the above operation, namely, the problem of what happens when the square root in the exponential function becomes imaginary. This occurs for spatial frequencies associated with evanescent waves. Because of the high attenuation of these waves for any two planes separated by more than a few wavelengths, it is reasonable to assume that the spectrum of the field is bandlimited to spatial frequencies such that  $v_x^2 + v_y^2 \leq \lambda^{-2}$ . Since it can be shown that the evanescent fields carry only information about object features less than one wavelength in extent, this limitation of the inverse propagator to non-evanescent waves is not serious from a practical standpoint.

It is significant to note that the kernel of the Kirchhoff integral, equation (18), is just the phasing factor by which a recording array element at position  $(x_0, y_0, z_0)$  must be multiplied in order that the beam produced by the array will be focused on the position  $(x_1, y_1, z_1)$ . In this sense the inverse propagation method of reconstruction is analogous to scanning the  $(x_1, y_1)$  plane at a height  $z_1$  with the beam formed by the antenna array.

The reconstruction technique. The technique whereby the radio camera reconstructs ionospheric irregularities is a direct application of the above three steps to the data recorded by the array, for different values of the height,  $z$ . Thus, a series of images in planes perpendicular to the line of propagation between the satellite and the ground is obtained. Taken together they yield a three dimensional picture of the ionosphere.

Implicit in this application of the reconstruction technique to ionospheric irregularities is the Born approximation. This means that it is assumed that the effect of propagation to the ground on the field scattered by an irregularity is as if there was free space between the irregularity and the ground. Note that this does not limit the technique to isolated irregularities; the limitation is on the scattered component of the field. The unscattered component is free to interact with subsequent irregularities. As an example of this, suppose that the amplitude of the component scattered by an irregularity is 10% of the incident field. It follows that if the scattered component is subsequently scattered by a second similar irregularity, the twice scattered component will also be one tenth of the component scattered directly from the incident field by the second irregularity. In such a case the Born approximation appears reasonable.

It is hoped that further theoretical work will lead to an extension of the technique

to the non-Born case. This has not yet been achieved. However, the likelihood that the Born approximation will apply satisfactorily to the proposed application of the reconstruction technique has been examined. This question was addressed in one of Gabor's early papers on applying wavefront reconstruction (holography) to electron microscopy (12). One basic result is that the laws of conservation of momentum and energy are slightly violated, to the extent that in the Born approximation the reaction of the scattered wave on the scattering potential is omitted. Applying this to the case of ionospheric scatterers, this implies that the reaction of the scattered wave on the plasma should be negligible. This is certainly a reasonable approximation. A second and more important consideration is the problem of multiple scatterings. Booker and others (13) have shown that the application of this approximation to the ionosphere implies that the mean square phase fluctuation produced by the ionosphere is less than one radian. Booker's expression for the mean square phase fluctuation is

$$(\Delta\phi)^2 = \frac{r_e^2}{2} \lambda^2 L (\Delta N)^2$$

where  $r_e$  is the classical radius of the electron,  $L$  is the scale size of the irregularity, and  $(\Delta N)^2$  is the mean square variation in electron density. This expression is an approximation for normal incidence, averaged over the propagation path. For most all reasonable values of  $(\Delta N)^2$ , and for values of  $L$  in the range of interest this expression yields  $(\Delta\phi)^2 < 1$ .

In spite of the above derivation, instances in which  $(\Delta\phi)^2$  is apparently greater than unity have been observed. In light of the reconstruction technique's ability to yield height information, the question might well be raised, "Cannot the effects of multiple scattering be unfolded in height?" A strong theoretical basis exists for a "yes" answer to this question in the form of the uniqueness theorem. As discussed in an earlier report (2), the uniqueness theorem implies that knowledge of the field on the ground provides, within a bounded range of spatial frequencies, the required boundary values needed to uniquely determine the field at various altitudes. Unfortunately, a practical method of making use of this information has not yet been identified.

Of related interest to the problem of the Born approximation is the validity of the technique's reconstruction over a series of planes at ionospheric heights. This assumes that the field diffracted by an object can be represented as the product of the illuminating field and a (complex) object (or scatterer) transmittance. In fact, the diffracted field is determined by an additive rather than a multiplicative process: it is the sum of the illuminating field and the object scattered wave. However, Evans (11) has shown that this is a good approximation provided that

$$D < \frac{6\lambda^3}{v_{\max}^2}$$

where  $D$  is a thickness characteristic of the three-dimensional object being approximated by a two dimensional plane,  $\lambda$  is the wavelength, and  $v_{\max}$  is the maximum spatial frequency of interest. Letting  $\lambda = 2$  m and  $v_{\max} = 10^{-2} \text{ m}^{-1}$  (characteristic of a 100 m irregularity),  $D < 48$  km. Since the resolution in height is of this order or less, the planar reconstruction is valid.

#### IV. COMPUTER SIMULATION

A large number of computer simulation studies, simulating the recording of irregularity diffraction patterns on the ground and the reconstruction of images of these irregularities, have been carried out. The process involved is shown in Figure 4.

Because of a lack of space, only one example of the results of these studies can be shown here. This is given in Figure 5. The form chosen for the irregularity is a Gaussian phase transmittance with a total lateral width ( $\pm 3\sigma$ ) of 400 meters. The irregularity is located at 300 km altitude and introduces a 0.05 radian peak phase perturbation. The recording array is taken to be a line array of 32 elements spaced ~33 meters apart, for a total recording aperture of one kilometer. A one dimensional cut has been made through each plane, in order to save computing time. All of the figures are rotationally symmetric about the ordinate. Figure 5 shows the field recorded on the ground, and the reconstructions obtained for various values of  $z$  used in the inverse propagator. The magnitude and phase are shown in each case. This is equivalent to focusing an optical camera, except that the radio camera works equally well with phase objects. As can be seen from the figure, the resulting reconstruction is excellent.

The following summarizes the other effects observed in the computer simulations which have been carried out:

1. As the value of  $z$  in the inverse propagator is varied (i.e., the focus is changed on the radio camera), the value of the magnitude of the field first approaches, equals, and subsequently departs from the incident field's magnitude in a symmetric fashion about the actual height of the irregularity. This is true for a phase-perturbing irregularity; the same effect occurs in the phase of an amplitude-perturbing irregularity. This effect is a very sensitive indicator of the height of the irregularity, and forms the basis of a technique for machine determination of irregularity height.
2. The effect of random noise is to "blur" the reconstructions in much the manner of film grain noise in optical

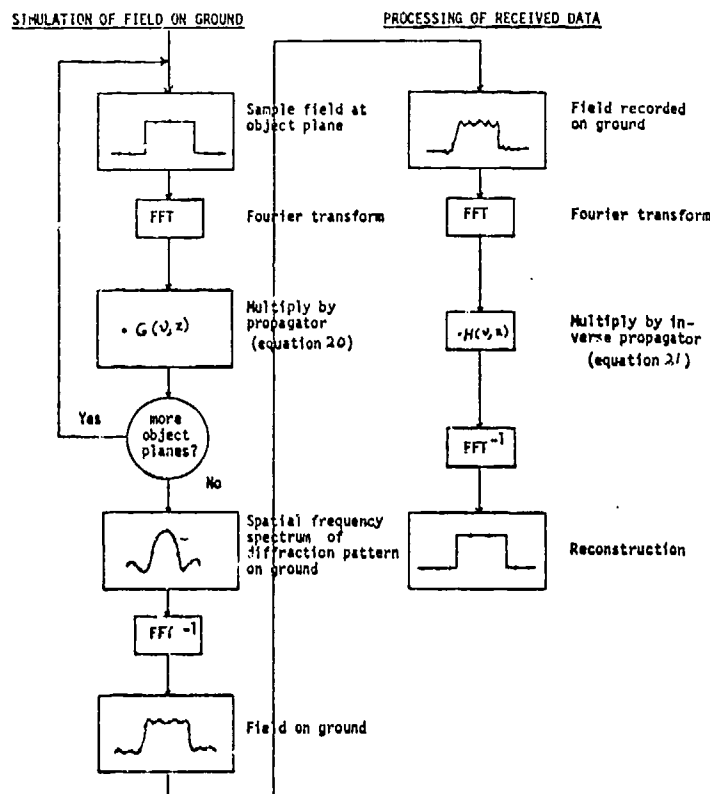


Figure 4

photography. A 10 dB signal to noise ratio is adequate to produce a visually acceptable reconstruction. A 30 dB signal to noise ratio results in phase errors of less than one percent for a reconstruction of a phase object at the correct height.

3. Noise degrades the height resolution of the techniques as predicted by equations (13) to (15). Visually, the effect is to make reconstructions over a range of heights equally "in focus".
4. The effect of reconstructing a vertical distribution of irregularities from their diffraction pattern when the Born approximation holds is the equivalent to the introduction of added noise to the reconstruction of a single irregularity. The optical analogue is the superposition of an out-of-focus image over an in-focus image. Work in this area is continuing.
5. Very recently, work has been undertaken to apply an image processing technique to the problem of reconstructing a vertical distribution of irregularities. Although no results are yet available,

there is a strong basis for anticipating significant improvements over the results in 4, above.

#### V. A DEMONSTRATION EXPERIMENT

An experiment to demonstrate the radio camera concept for reconstructing ionospheric irregularities is planned. A line array of 32 antennas, oriented east-west, will be used to receive the 150 MHz transmission of the polar orbiting Navy Navigation Satellite System satellites. By taking sequential "snapshots" of the field received by the array as a function of time, the motion of the satellite perpendicular to the line of the array serves to sweep out the second dimension of the array. This has the effect of making the line array do the work of a square array. The array parameters and the expected resolution obtainable are summarized below. Figure 6 shows the electronics which will be used at each element of the array.

#### Array Summary

1. 32 antennas spaced 33 m apart in an east-west line.
2. Circularly polarized antennas, with > 12 dB gain; antenna electronics as shown in Figure 6.

3. > 30 dB carrier to noise ratio for each antenna; > 20 dB signal to noise ratio for system.
4. Operation at 150 MHz; sensitive to irregularities up to 100 m with a resolution of  $\sim 40$  m and a height resolution of  $\sim 10$  km.

#### VI. CONCLUSIONS

The following conclusions have been drawn from this work (some of these deal with details covered in other papers (3,4):

1. It is both theoretically correct and technologically practical to employ a radio frequency analogue of an optical holographic camera to study ionospheric irregularities which cause scintillations. Such a reconstruction technique permits obtaining three dimensional information about the range of irregularity sizes of interest and permits discriminating between irregularities at various altitudes.
2. The theory of the radio camera technique has been confirmed by computer simulation. This simulation work has proved to be a powerful method of gaining experience with the reconstruction technique. As a result of this work it has been shown that the amount of computer processing required to reconstruct an image of an ionospheric irregularity is relatively small, and could be done on a mini-computer in the field.
3. The effects of noise on the reconstruction have been simulated. The results confirm the theoretical predictions as to the height and image resolutions obtainable. It appears that height resolutions of  $\sim 10$  km can easily be obtained with signal to noise ratios typical of an experiment.
4. It has been demonstrated that height determination can be made by the computer based on an image error criterion which does not involve *a priori* knowledge of the irregularity. Some work remains to be done in determining the optimum criterion.
5. An experiment can be conducted at very moderate cost which will serve to demonstrate the technique's capabilities. Much of the design work for this experiment has been done. The ranges of irregularity size and height, and the vertical and horizontal resolutions with which these would be measured by this experiment, are the ranges of interest to the scintillation problem, based on results of other measurements.

It should be noted there are also several areas of analysis in which more work remains to be done. As an example, one area of current research is how to produce easily interpreted reconstructions of a continuous, random distribution of scatterers, as opposed

to the case of isolated regularities.

In summary, the analysis to date of the holographic radio camera technique gives significant encouragement for its use in ionospheric scintillation research and other remote probing applications.

**Acknowledgement.** The very valuable support and contributions of Dr. Henry G. Booker to this research are gratefully acknowledged.

#### REFERENCES

1. Private communications from W. Ross Stone to Drs. Kenneth Bowles and Hugh J. A. Chivers, circa September, 1968. The first written form of this proposal was a June 1973 draft of Stone's master's thesis, "A Remote Probing Technique for Inhomogeneous Media and an Application to the Study of Satellite Scintillations," Department of Applied Physics and Information Sciences, UCSD, January, 1974. See also reference 2.
2. W.R. Stone, "A Technique for the Three Dimensional Reconstruction of Ionospheric Inhomogeneities," Megatek Corporation, San Diego, (Internal Report) Number TR2-01-10, September 14, 1973.
3. W.R. Stone and V.E. Hildebrand, "A Technique for the Three Dimensional Reconstruction of Ionospheric Inhomogeneities: Verification Study and Experimental Plan," NELC draft report to be published.
4. W.R. Stone and V.E. Hildebrand, "Further Details and Numerical Studies of a Technique for the Three Dimensional Reconstruction of Ionospheric Inhomogeneities," NELC draft report to be published.
5. See, for example, M. Born and E. Wolf, *Principles of Optics*, Oxford: Pergamon Press, 401-403 ff, 1965.
6. M.I. Skolnik, *Introduction to Radar Systems*, New York: McGraw-Hill Book Company, 1962, pp. 463-71.
7. H.G. Booker, "The Concept of a Radio Frequency Camera," Memorandum to W.R. Stone, September 2, 1974.
8. The details of this calculation are tedious. They are given in R.J. Collier, et al, *Optical Holography*, New York: Academic Press, 1971, pp. 583-86. A similar derivation is given by J.R. Shewell and E. Wolf, "Inverse Diffraction and a New Reciprocity Theorem," *Journal of the Optical Society of America*, 58, 1596, 1603, 1968.
9. J.W. Goodman, *Introduction to Fourier Optics*, New York: McGraw-Hill Book Company, 1968, p. 54 ff.

10. E. Oran Brigham, The Fast Fourier Transform, Englewood Cliffs: Prentice-Hall, Inc., 1974.
11. E. Evans, Optics Communications, 2, November, 1970.
12. D. Gabor, "Theory of Electron Interference Experiments," Reviews of Modern Physics, 28: 260-276, 1956.
13. H.G. Booker, "The Use of Radio Stars to Study Irregular Refraction of Radio Waves in the Ionosphere," Proceedings of the IRE, January, 1958, 298-314.

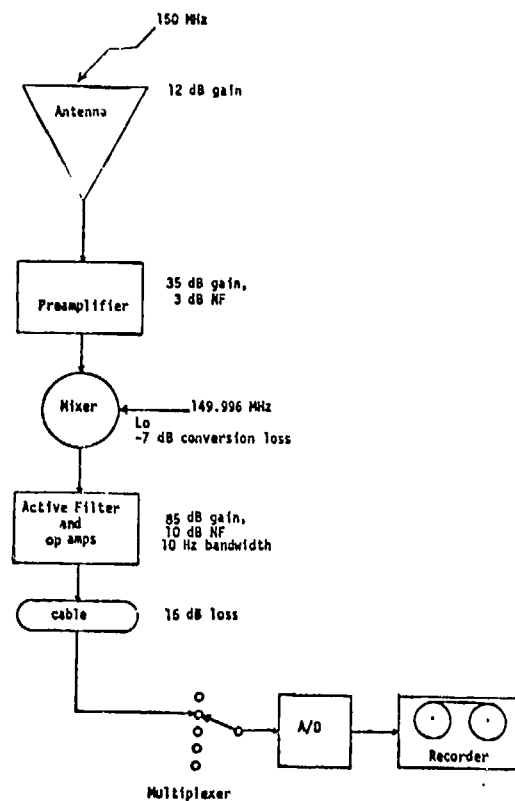


Figure 6. Electronics for one array element.

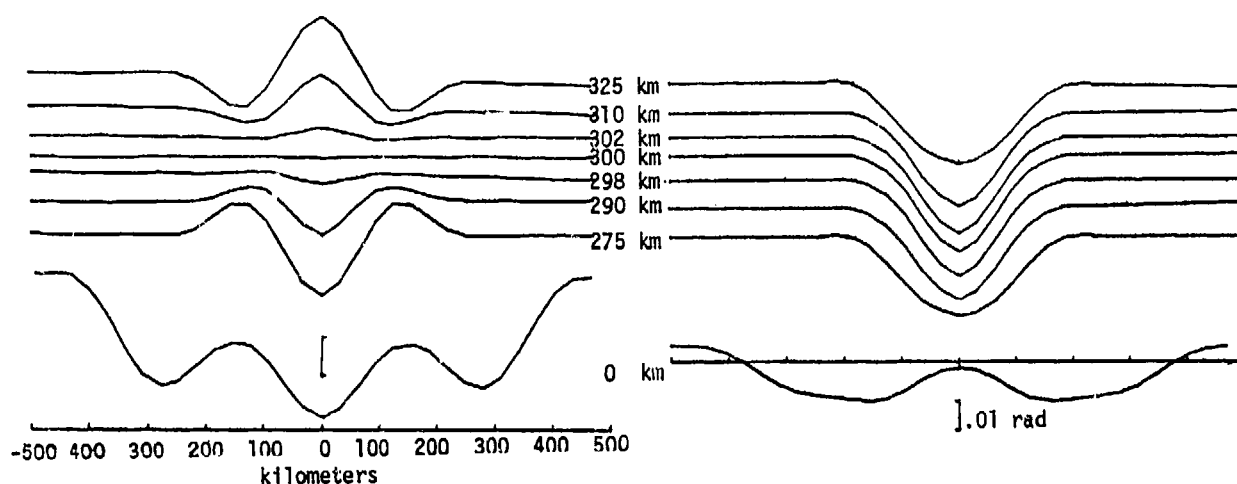


Figure 5. An example of a simulated reconstruction. The irregularity is a 400 m wide Gaussian transmittance at a height of 300 km, with a peak phase change of .05 radian. The left hand portion of the figure is the magnitude and the right hand portion is the phase. The height ( $z$  in equation 21) used for each reconstruction is as shown in the center. The curves labeled 0 km are the diffraction pattern on the ground, as sampled by the 1 km, 32 element array.

THE ROLE OF LARGE SCALE ELECTRIC FIELDS AND FIELD-ALIGNED CURRENTS IN PRODUCING FIELD-ALIGNED  
IRREGULARITIES IN THE MAGNETOSPHERE AND IONOSPHERE

K. D. Cole\*  
NASA/Goddard Space Flight Center  
Greenbelt, Maryland 20771

ABSTRACT

The consequences of systems of electric fields and field-aligned electric current which lead to magnetospheric and ionospheric field-aligned irregularities are discussed. The mechanism works best in and near the auroral zone because of the large electric fields there and near the equator not only because of the rapid changes in volume of tubes of force as a function of equatorial radius but also because of the electric field activity there.

Field-aligned irregularities created at the auroral zone by particle precipitation can be convected to lower latitudes by large scale electric fields.

INTRODUCTION

Irregularities of various time and length scales are known to exist in the magnetosphere and ionosphere. We shall be concerned in this paper only with those which involve an electrostatic field of such dimensions in time and space that the geomagnetic field ( $B$ ) can be considered, to a first approximation, to be an equipotential of the electric field. The fact that electric currents parallel to  $B$  emerge in the problem may not destroy this approximation. Indeed if they do, there are still applicable aspects of the theory. In the paper we shall be concerned with electric field of duration of the order  $\int V_A^{-1} ds$  where  $V_A$  is the Alfvén speed,  $ds$  is an element of length along  $B$  and the integral is taken along a field line of  $B$  from one ionosphere to its magnetic conjugate (Cole 1964). The spatial dimension of the electrostatic field orthogonal to  $B$  is considered to be in excess of about 10 km. This will ensure that a significant fraction of the geomagnetic field line can be considered to be equipotential (see Farley 1959, Reid 1968) for discussion of this point. A concomitant of the electric field ( $E$ ) orthogonal to the geomagnetic field is field-aligned electric current  $j$  (Cole 1961, 1971, 1974a). It is with the combined effects of  $E$  and  $j$  that this paper is concerned.

In this paper we discuss the global morphology of the operative electric field together with their consequences for formation of field-aligned irregularities.

Global Distribution of Electric Fields

During Magnetic Storms

It may be inferred from geomagnetic field fluctuations observed at the earth's surface that during magnetic storms there are two major regions of electrostatic field activity, one at high latitudes and one at low latitudes over the equator (Cole 1970). This activity occurs during the onset of the main phase of magnetic storms or more generally at times when  $d/dt$  ( $Dst$ ) is negative (Cole 1964, 1970).

At Magnetic Quiet Times

The term magnetic quiet is relative, and it is rare that there is not geomagnetic disturbance somewhere specially in auroral regions; so that at high latitude it can be regarded to be virtually always present, but at a subdued level during quiet times (see Fig. 2 of Cole 1970).

Electric field activity in the F region at and near the magnetic equator has been inferred from the observations of ionization drifts (Farley et al 1970, Cole 1974b). It has been suggested (Cole 1974b) that these electric fields lead to significant heating of the atmosphere.

Mechanisms for forming irregular electric fields. (1) Dynamo action of neutral wind on an irregularity of ionospheric conductivity may produce an electrostatic field ( $E$ ) orthogonal to  $B$  which can be up to 20 times that of the dynamo field (Cole 1960). (2) Also a large scale electric field say of solar wind origin (Cole 1961, 1974a) or dynamo origin in the ionosphere can produce an irregularity in the electrostatic field in an inhomogeneity of the ionospheric conductivity (e.g. Cole 1971a).

\*NAS/NRC Senior Post-Doctoral Research Associate, On leave from La Trobe University, Bundoora, Victoria, Australia 3083.

The formation of ionospheric conductivity inhomogeneities and irregularities of electrostatic field go hand in hand. E.g., consider ionospheric currents orthogonal to  $\underline{B}$ . Suppose there exists an irregularity in the electric field in an initially uniform ionosphere. Consider a tube of force of unit cross section we can say that the magnetospheric current

$$j_{\parallel} = \nabla \cdot \int j_{\perp} ds \quad (1)$$

where  $ds$  is an element of length along the tube in the ionosphere, and

$$j_{\perp} = \sigma_1 \underline{E}_{\perp} + \sigma_2 \underline{B} \times \underline{E}_{\perp} B^{-1} \quad (2)$$

where  $\underline{E}_{\perp} = \underline{E} - \underline{v} \times \underline{B}$

where  $\underline{E}_s$  = electrostatic field

$\underline{v}$  = velocity of thermosphere gas  
 $\sigma_1, \sigma_2$  = Pedersen, Hall conductivities

Irregularities in the velocity field  $\underline{v}$  will produce  $j_{\parallel}$  as follows. From equation 2

$$\nabla \cdot j_{\perp} = \nabla \cdot \sigma_1 (\underline{E}_s + \underline{v} \times \underline{B}) + \nabla \cdot \sigma_2 B^{-1} (\underline{B} \times \underline{E}_s + \underline{v} B^2)$$

Suppose the ionosphere is initially uniform and that  $\nabla \cdot \underline{v} = 0$ . Then the dominant terms in  $\nabla \cdot j_{\perp}$

are given by  $\nabla \cdot j_{\perp} = \sigma_1 (\nabla \cdot \underline{E}_s + \underline{B} \cdot \nabla \underline{v})$

$$- \sigma_2 \underline{E}_s \cdot \nabla \times \underline{B} \quad (3)$$

This equation can be interpreted in two ways, either  $\nabla \cdot j_{\perp} = 0$  or it doesn't. In the former case the structure in  $\underline{E}_s$  is determined solely by the structure of the wind. Therefore irregularities in the wind field produce corresponding structures in  $\underline{E}_s$ . In the event that  $\underline{v}$  is constant along a geomagnetic tube of force in the dynamo region, the value of  $\underline{E}_s$  in this region is that which determines  $\underline{E}_s$  in the whole tube of force.

In the case of  $\nabla \cdot j_{\perp} \neq 0$ , then  $j_{\parallel}$ , given by equation (1), is non-zero and in this case an irregularity of conductivity in the ionosphere will be produced. This happens because ions are the principal carriers of current across the geomagnetic field in the ionosphere and electrons are the principal carriers along the geomagnetic field. This means that an irregularity of ion density will tend to be formed at the place of divergence of  $j_{\perp}$  (see Cole 1963, and Piddington 1967).

In a steady state, and assuming only electrons carry the magnetospheric current,  $j_{\parallel}$  is related to the rate of recombination in the E region by (Cole 1971)

$$j_{\parallel} = ec^{-1} \int \alpha (n_i^2 - n_Q^2) ds \quad (4)$$

where  $n_Q^2$  is the rate of loss of ionization in the absence of  $j_{\parallel}$ .

Equation 4 can be approximated by

$$j_{\parallel} = ec^{-1} H (n_i^2 - n_Q^2) \quad (5)$$

where  $H$  = altitude range over which most recombination occurs and  $n_i$  and  $n_Q$  are now representative values for that region. If  $n_i = n_Q + \Delta n$  where  $\Delta n \ll n_Q$

$$j_{\parallel} = 2 \alpha ec^{-1} H n_Q \Delta n \quad (6)$$

Assuming  $\alpha = 3 \times 10^{-7} \text{ cm}^3 \text{ sec}^{-1}$  we derive in Table I the values of  $j_{\parallel}$  in e.m.u. for various values of  $H$  and  $(n_i^2 - n_Q^2)$ .

TABLE I

$H(\text{cm})$	$10^5$	$3 \times 10^5$	$10^6$	$5 \times 10^6$
$(n_i^2 - n_Q^2) (\text{cm}^{-6})$				
$10^6$	$4.8^{-16}$	$1.4^{-15}$	$4.8^{-15}$	$2.4^{-14}$
$10^8$	$4.8^{-14}$	$1.4^{-13}$	$4.8^{-13}$	$2.4^{-12}$
$10^{10}$	$4.8^{-12}$	$1.4^{-11}$	$4.8^{-11}$	$2.4^{-10}$
$10^{11}$	$4.8^{-11}$	$1.4^{-10}$	$4.8^{-10}$	$2.4^{-9}$
$10^{12}$	$4.8^{-10}$	$1.4^{-9}$	$4.8^{-9}$	$2.4^{-8}$

The strongest field aligned currents ever measured are of about  $10^{-10} \text{ emu}$ . It follows that the values of  $j_{\parallel}$  in the lower right of Table I are excluded. Therefore the irregularities of the size and strength in this part of the table would not be in a quasi-steady state.

The irregularities formed in the E region by the action of field-aligned current would tend to diffuse along the geomagnetic field to form field-aligned irregularities.

It should be noted that the formation of field-aligned irregularities in the E region need not involve the whole magnetosphere but may involve a narrow altitude range in the ionosphere over which the dynamo field of neutral wind origin exhibits variation. To maintain continuity of current between such regions field aligned currents must flow and field-aligned irregularities in electron density can be expected corresponding to all scale sizes of neutral air motion. In particular any turbulence in the neutral air motions in the dynamo region may be expected to produce a corresponding "turbulence" of field aligned irregularities in electron density.

Consequences of electric field orthogonal to  $\underline{B}$  in the magnetosphere. In the presence of an electric field orthogonal to  $\underline{B}$ , plasma in the magnetosphere moves in a certain approximation (see Cole 1964) according to

$$\underline{v} = \frac{\underline{E} \times \underline{B}}{B^2} \quad (7)$$

This implies (see Spitzer 1962) that the magnetic flux through a closed curve moving with the plasma is constant and that charged particles once on a common field line remain on a common field line. So it is convenient to refer to movement of tubes of plasma delineated by tubes of magnetic flux. In an electrostatic field ( $E$ ),  $\nabla \cdot E = 0$ , and  $\nabla \cdot E$  is  $\perp$  to the equipotential surfaces of the field from which  $E$  is derived.

Consider then the movement of a tube of plasma and assume adiabatic changes (c.f. Gold 1959) then

$$pV^{5/3} = \text{constant}$$

where  $V$  = volume of tube of plasma  
 $p$  = pressure of plasma

The bulk of plasma is near the equatorial plane so we associate  $p$  with the pressure there.

It follows (Cole 1971) that

$$\frac{dp}{p} = -\frac{5}{3} \frac{dv}{V} = -\frac{5}{3} s \frac{dR_{eq}}{R_{eq}}$$

$$\frac{dn}{n} = -\frac{dV}{V} = -s \frac{dR_{eq}}{R_{eq}}$$

$$\frac{dT}{T} = -\frac{2}{3} \frac{dV}{V} = -\frac{2}{3} s \frac{dR_{eq}}{R_{eq}}$$

$$\frac{d(K_e \nabla T)}{K_e \nabla T} = -\left(\frac{7}{3} s + 1\right) \frac{dR_{eq}}{R_{eq}}$$

where  $R_{eq}$  is the equatorial radius of a tube of plasma and  $dR_{eq}$  is an element change during a displacement of the tube. These relationships will be approximate and valid only for times short compared to the times for interaction with the ionosphere, e.g. by heat exchange and recombination.  $s$  expresses the spatial rate of variation of the geomagnetic tube of force above the ionosphere i.e.,  $V \propto R_{eq}^5$  locally, or  $s = d(\ln V)/d(\ln R_{eq})$ .

Changes in the equatorial radius of a tube of plasma cause changes in density, temperature, pressure, heat flow to the ionosphere, and flux of plasma to or from the ionosphere.

The regions of the globe over which the process is effective are (1) the equatorial region because  $s$  is large there i.e., 10-40 (Cole 1971) and high latitude because from time to time  $E$  fields and therefore  $dR_{eq}/R_{eq}$  are large there (see Cole 1961, 1964, 1971b). Cole (1964) showed that during magnetic storms the outer magnetosphere is broken up in a large number of field-aligned irregularities such that on average the equatorial density there varies as  $n \propto R_{eq}^{-4}$ .

Having formed large scale field-aligned irregularities in  $n_e$  these are effective down to

the level at which  $\nu_i = \omega_i$ . Smaller scale irregularities may be generated by other processes on the gradients of electron density formed by tube interchange.

Drift of irregularities from auroral regions. Field-aligned irregularities are formed at the auroral zone by irregularities in the precipitation of energetic particles from the magnetosphere. Ionization so produced populates the magnetosphere because it does not have time to recombine in the ionosphere. This happens in the following way. Assuming about 35 eV are used per ionization the production rate is  $1.78 \times 10^{10}$  electron-ion pairs  $\text{cm}^{-2} \text{sec}^{-1}$  per erg of precipitating energetic particles. The recombination rate in the F region is  $\beta n_e H \text{cm}^{-2} \text{sec}^{-1}$  where  $\beta \approx 10^{-4}$  and  $H$  is the scale height of the F region. With  $H \approx 6 \times 10^5$  cm and  $n_e = 5 \times 10^6 \text{ cm}^{-3}$ , production exceeds recombination when the flux of precipitating energetic particles absorbed the F region exceeds  $1.6 \times 10^{-2}$  ergs. The particles would be low energy ( $\leq 400$  eV for electrons). Having been formed in the auroral zone field-aligned magnetosphere inhomogeneities can be convected deeper into the geomagnetic field by large scale electric fields according to equation 7.

Acknowledgements: The author is indebted to the NAS/NRC of U.S.A. for the award of a Senior Post-Doctoral Associateship and to NASA Goddard Space Flight Center for hospitality. The research described here forms part of a program funded in Australia by the Australian Research Grants Committee.

#### REFERENCES

- Cole, K. D., Austr. J. Phys., 13, 484, 1960.
- Cole, K. D., Geophys. J. R.A.S., 6, 103, 1961.
- Cole, K. D., Planet. Space Sci., 11, 779, 1963.
- Cole, K. D., J. Geophys. Res., 69, 3595, 1964.
- Cole, K. D., J. Geophys. Res., 75, 4216, 1970.
- Cole, K. D., J. Atmos. Terr. Phys., 33, 741, 1971.
- Cole, K. D., Planet. Space Sci., 22, 1075, 1974a.
- Cole, K. D., J. Atmos. Terr. Phys., 36, 1099, 1974b.
- Farley, D. T., J. Geophys. Res., 64, 1225, 1959.
- Farley, D. T., B. B. Balsley, R. F. Woodman and J. P. McClure, J. Geophys. Res., 75, 7199, 1970.
- Reid, G. C., J. Geophys. Res., 73, 1627, 1968.
- Spitzer, L., Jr., Physics of Fully Ionized Gases 2nd Ed. Interscience Tracts John Wiley, N.Y. 1962.



# EFFECTS OF IONOSPHERIC SCINTILLATIONS ON TWO-FREQUENCY DOPPLER DATA

James R. Clyne and Arnold J. Tucker  
Applied Research Laboratories, The University of Texas at Austin  
Austin, Texas

## I. INTRODUCTION

Two-frequency doppler data from Navy navigational satellites (NAVSATS) recorded in both polar regions has been examined for evidences of scintillations.<sup>1</sup> The distribution of scintillations in time and space has been examined and patterns in both polar regions have been identified.

These navigation satellites are in essentially polar orbits at an altitude of 1000 km and transmit coherent cw signals on frequencies 150 MHz and 400 MHz. The first order ionospheric effects are removed from the received signals by subtracting 3/8 of the doppler frequency observed on the 150 MHz signal from the doppler frequency on the 400 MHz signal. This two-frequency corrected doppler,

$$f_{2d} = f_d(400) - \frac{3}{8}f_d(150),$$

is then processed for various purposes, such as navigation, as if it were the vacuum doppler from a signal at an effective frequency of 343.75 MHz.

In order to use the NAVSAT for navigation, the orbital parameters of the satellite are required. The orbital parameters of these satellites are determined from standard doppler data acquired from a network of fixed ground station, TRANET, at known locations. After the orbital parameters of a satellite have been determined from the analysis of sets of data from several stations, a set of theoretical vacuum doppler data ( $f_v$ ), is computed for data used in this analysis. The difference between this theoretical doppler data and the observed doppler data is termed the residual doppler,

$$f_{rd} = f_{2d}(\text{observed}) - f_v(\text{theory}).$$

It is this residual doppler data which has been the main focus of this study.

## II. STUDY OF RESIDUAL DOPPLER DATA

Residual doppler data from data recorded at various periods of the year 1969, from two NAVSATS at the satellite tracking station at Thule, Greenland, (76.53°N, 68.67°W), and from one NAVSAT at the satellite tracking station at McMurdo, Antarctica, (77.83°S, 166.62°E), have been examined for evidence of scintillations. Figure 1 is an example of the residual doppler data from doppler data recorded at McMurdo during November, 1969. The horizontal axis is time measured from the beginning of the satellite pass and the vertical axis is residual doppler in Hz. This data shows very large phase variations which are taken as evidence of scintillations. A quiet pass would be plotted on a vertical scale of  $\pm 0.5$  Hz. Even so, its points would almost all lie on the zero axis. Each point on these curves represents an integration time of approximately 1 s.

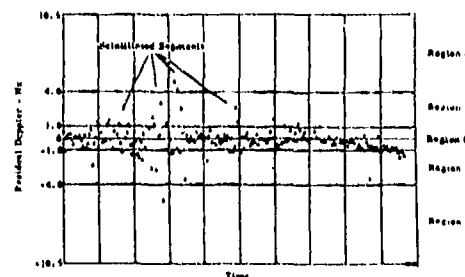


Figure 1  
Residual Doppler Data  
McMurdo 30140  
Day 309 Year 1969

		N <sub>1</sub> Number of Data Points in the Region 21 Hz to 24 Hz Per Pass Segment										
		0	1	2	3	4	5	6	7	8	9	10
N <sub>2</sub> Number of Data Points in the Region 24 Hz to 27 Hz Per Pass Segment	0	No Scintillation										
	1	6	14	16	11	20	17	17	27	15	40	
	2	3	2	5	1	0	1	12	17	7	40	
	3	0	0	2	4	4	4	4	0	0	20	
	4	0	1	0	1	2	2	1	4	10	20	
	5	0	0	0	0	1	1	2	4	6	21	
	6	0	0	0	0	0	2	1	4	5	16	
	7	0	0	1	0	0	0	1	1	4	8	
	8	0	0	0	0	0	1	0	1	4	1	
	9	0	0	0	0	2	2	4	7	5	0	

Figure 2

Residual doppler data, such as Fig. 1, were available only for the year 1969, and only in microfilm form. In order to quantify the data into a manageable amount of data, each pass analyzed was divided into ten equal pass segments along the time axis and three regions along the vertical axis. For each pass segment,  $N_1$ , the number of points in the first region, and  $N_2$ , the number of points in region 2 were hand counted and transferred to punched cards for computer analysis.

A scintillation value for each pass segment was defined as

$$S_v = 3N_2 + N_1.$$

Pass segments with scintillation values less than 5 were defined as having no scintillations, pass segments with  $S_v$  between 5 and 9 were defined as being lightly scintillated and pass segments with  $S_v$  of 10 or more were defined as being heavily scintillated. A two-way distribution of the number of pass segments observed at Thule during November 1969, with various values of  $N_1$  and  $N_2$  is shown in Fig. 2.

Of the over 2300 pass segments analyzed here, 66% showed no scintillations, 16% showed light scintillation, and 18% showed heavy scintillations by the above criterion.

Using the orbital elements for the satellites, the position of the satellite at the center of each pass segment and the geometric path between the satellite and the station were computed. The probable location of the ionospheric disturbance was taken to be at an altitude of 350 km. The location of this altitude

on the satellite-station path was computed and recorded. The characteristics of the scintillations as a function of the location of the 350 km intercept point in several coordinate systems have been examined.

Figure 3 shows the percent of pass segments which contained scintillations and are displayed in three coordinate systems and as a function of local time. The upper two rows of data represent data taken at Thule during May 1969, for two different satellites and the lower row represents data taken at McMurdo for one satellite during the same month. As shown by the gray scale at the top, the larger the percent of pass segments that were scintillated, the darker the corresponding area. The first column represents the standard geographic coordinates. The station location is marked with an "S", the magnetic dip pole with a "D", and the geographic pole with a "G". The second column consists of geographic coordinates with the polar axis taken through the station and the station meridian taken as the prime meridian. In the third column, the invariant magnetic latitude and geomagnetic longitude are used. In the last column the normal geographic latitude and the local time of the intercept point are used as coordinates.

The data in station-centered coordinates clearly shows a zenith angle effect where the percent of scintillated pass segments decreases as the satellite passes the zenith. In the south polar region the scintillation probability appears to increase for paths going over the magnetic dip pole. This was true for three of the four months of data analyzed to date (May, August, and November, but not March, 1969). In the northern polar region there appears to be lowering of the scintillation probability over the dip pole. This phenomena is present only in the summer months, May and August, and is absent in the winter months of March and November.

The time oriented diagrams in columns 2 and 3 show a very definite reduction in scintillations during dusk at Thule, which is in summer and during dawn at McMurdo, which is in winter. During this time of year, the plane of this satellite's orbit is flat-on to the sun at all times. (The NAVSATS are in an orbital plane which appears to rotate once per year in a sun centered coordinate system.) The other satellite for which data were available has an orbital plane rotated approximately 90° with respect to the first. There appears

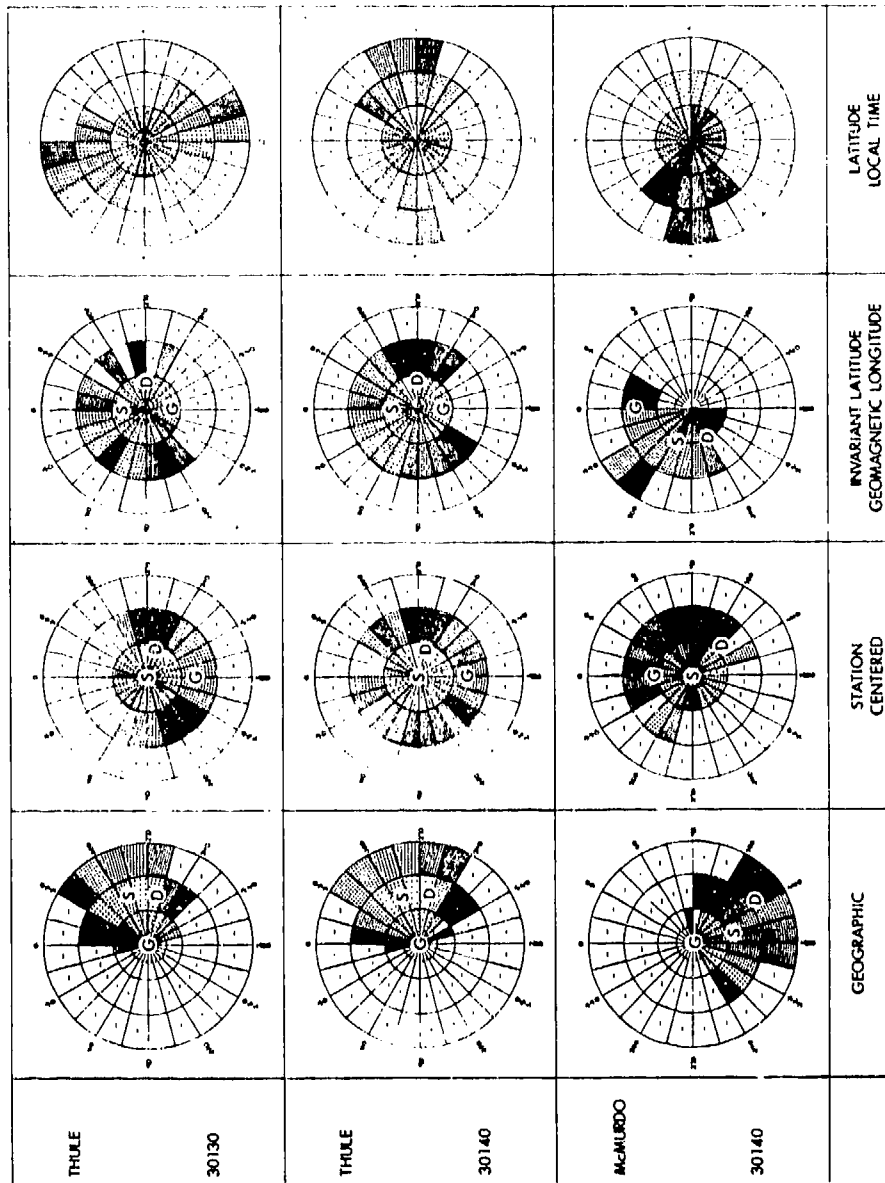


FIGURE 3  
PERCENT SCINTILLATION PLOTS  
IN VARIOUS COORDINATE SYSTEMS D135-150

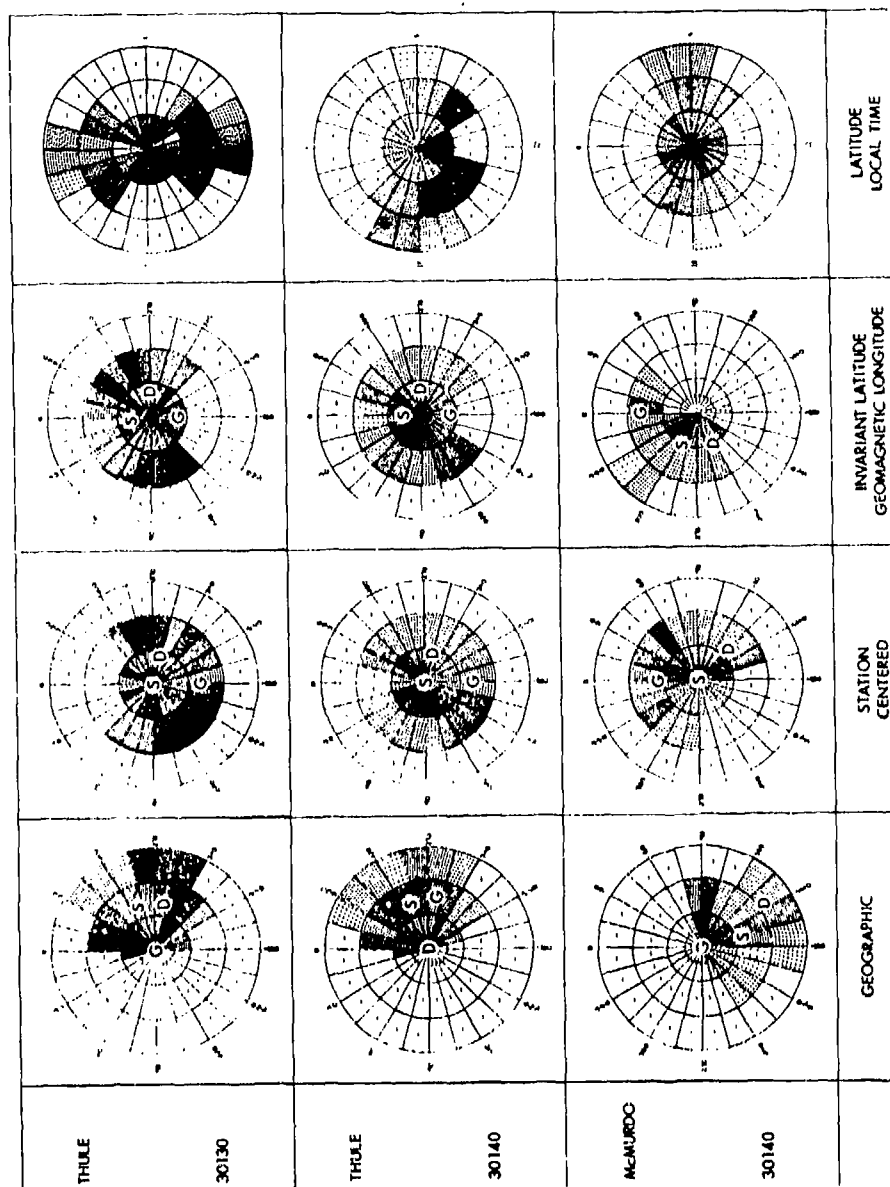


FIGURE 4  
PERCENT SCINTILLATION PLOTS  
IN VARIOUS COORDINATE SYSTEMS D300-329

to be no definite pattern to this latter satellite's time oriented diagram during this day period.

In Fig. 4, similar data are presented for November 1969, a period six months later when the seasons have reversed. Again the winter station (Thule at this time) appears to have a reduction in scintillations at dawn and the summer station (McMurdo) a reduction in scintillations at dusk. The more striking feature of the time oriented diagram is the apparent peaking of the scintillations near toward noon at the winter station. This feature, however, does not appear in the other data analyzed to date.

The geographic diagrams at the south pole again show the increase in scintillations over the magnetic dip pole. This same geographic pattern is very prominent in the August data where almost all pass segments in the vicinity of the dip pole were scintillated.

### III. FILTER NOISE DATA

#### A. Spectra

The average rectified residual doppler for a pass is a quality figure called the filter noise (FN). Filter noise data were available for a much greater period of time than the residual doppler data. Figure 5 shows 30-day averages of Filter Noise values at Thule and McMurdo for the years 1969 through 1971. Only day periods with more than 75 passes are plotted on this graph. From this graph it appears that the origins of filter noise are global in nature as the data from the two polar regions appear to move parallel to one another. The initial peak on this graph corresponds to a peak in the planetary magnetic index Ap. However, the correlation coeffi-

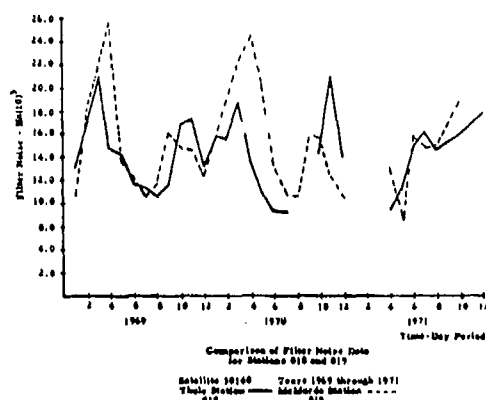


Figure 5

cients between Ap and filter noise, on a pass-by-pass basis, a three hour average basis, and a 30-day basis, are not significantly different from zero.

While the 30-day averages of the filter noise data at the two stations tend to track one another, the Fourier transforms reveal a different structure. It was found that the spectra of this filter noise showed distinct peaks at 24-h periods, and sometimes at 12-h periods during the winter. No clearly defined peaks existed in the summer. Figure 6 shows the 12- and 24-h spectral components of the filter noise in both polar regions during the years 1969-1971. Each data point represents a 30-day period of data from one satellite. The graph at the top of the figure shows the number of hours of darkness at each station. It should be noted that the peaks for each station in spectral components at 12-h and especially 24-h periods correspond to times of total darkness, that is, local winter. The constant presence of the sun in local summer appears to be eliminating the diurnal variations. (It should be remembered that the total filter noise at the two stations moved parallel to one another.)

#### B. Sliding 4-h Averages

To further study the time variations of the filter noise, during each 30-day time period (approximately months), the data were divided into bins 4-h wide according to the universal

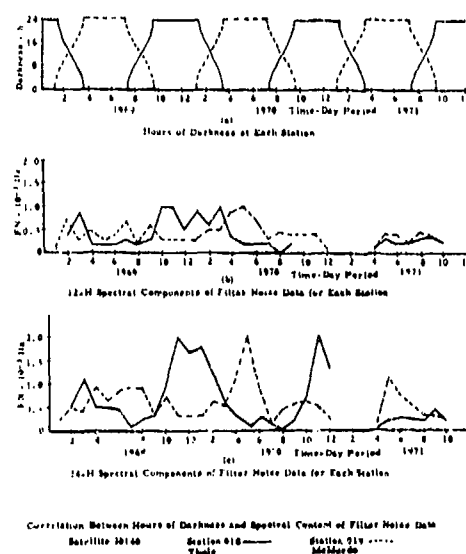


Figure 6

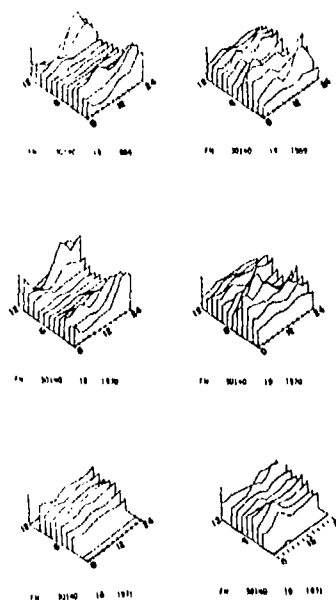


Figure 7

Three-Dimensional Plots of Filter Noise Computed from  
Doppler Data Recorded in Polar Regions

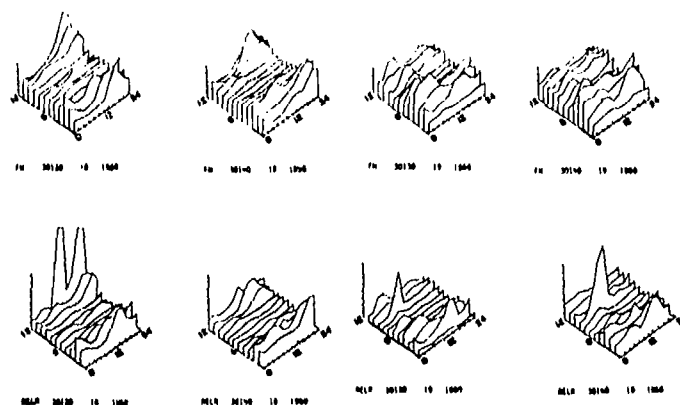


Figure 8

Three-Dimensional Plots of Filter Noise and Rectified ELR Computed  
from Doppler Data Recorded in Polar Regions

time at closest approach. Each bin was displaced 2-h from the next and averaged forming a 4-h overlapping sliding average. Figure 7 contains three-dimensional graphs of this 4-h sliding average. The vertical scale is the average FN, upward to the right is universal time in hours and upward to the left is month number. Each slice represents data for one month. Months with too few passes or data with known equipment problems have been omitted. From this figure it is clear that Thule has a definite time structure which is prominent in the winter but absent in the summer. Similar structures are suggested in the McMurdo data, but the data from McMurdo in this figure and in most other types of analysis we have performed appears less regular than the data from Thule.

Figure 8 is a similar set of plots for two satellites during 1969 which also displays navigational error data. This navigational error is the range error along the vector between the station and satellite at the time of closest approach. Note that the features in the range error data are very similar to those in the filter noise data. We will return to this feature shortly. In Fig. 9 similar time structures for the two satellites appear. However, they appear to be time displaced, the peaks for satellite 30130 occurring slightly prior to those for satellite 30140. Also, the features appear

to be moving to earlier times as the year progresses. This suggests that the orientation of the satellite orbit may play a role in the location of these peaks.

### C. Orbit Orientation Effects

In order to study any orbit orientation effect, 30-day time periods were examined for three satellites during times when the orbital planes were flat-on to the sun or edge-on to the sun. The 4-h sliding averages for the filter noise data at Thule and McMurdo are shown in Figs. 9 and 10, respectively. The zero axis of each data set has been displaced to separate the graphs. It is clear that very similar structure exists in the Thule data when the orbital planes were perpendicular and edge-on to the sun, although the features may be washed out in summer. There appears to be a peak about local noon at the Thule station when the orbital planes were perpendicular to the sun and a peak 4- to 6-h later when the orbital plane was edge-on to the sun. A similar peak appears in the McMurdo data for the edge-on orbit although the data often has a double peak. The data for perpendicular orbits at McMurdo is more irregular and no consistent pattern can be seen.

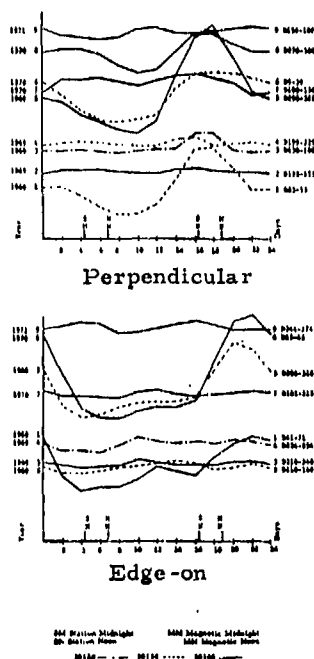


Figure 9  
Orbit Orientation Effects at Thule

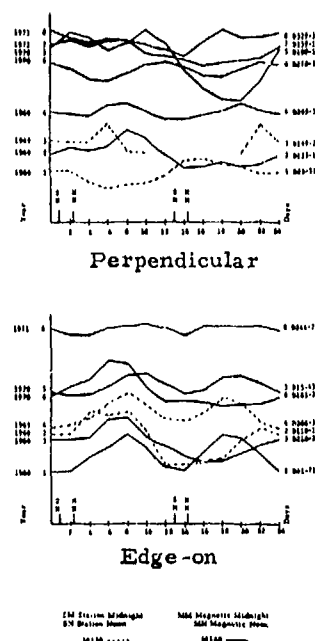


Figure 10  
Orbit Orientation Effects at McMurdo

#### D. FN-Range Error Correlations

The similarity between the time structure of the filter noise and range error seen in Fig. 9 has been studied by computing the correlation coefficient between the filter noise and range error over 30-day periods. The value of this correlation coefficient as a function of day period is shown in Fig. 11. As with the filter noise averages, the curves for both stations appear to track each other in general. Only correlation coefficients above a value of about 0.25 are significantly different from zero with the sample sizes used here. The correlation coefficients appear large where the filter noise is large. These coefficients are much higher in 1972 than previous years. In that year a change in the data collection procedure effectively increased the integration time of the data acquisition system by a factor of 20. This may have caused some sources of equipment noise to average out leaving ionospheric effects more prominent.

#### IV. SUMMARY

Residual doppler and filter noise data from NAVSATS taken in both polar regions have been investigated. A decrease in the probability of scintillation was also observed at dusk in local summer and dawn in local winter. Spectral analysis of the filter noise data showed prominent 12-h and 24-h peaks in local winter at both stations. The time of day corresponding to the peak of this diurnal variation was found to depend on the orientation of

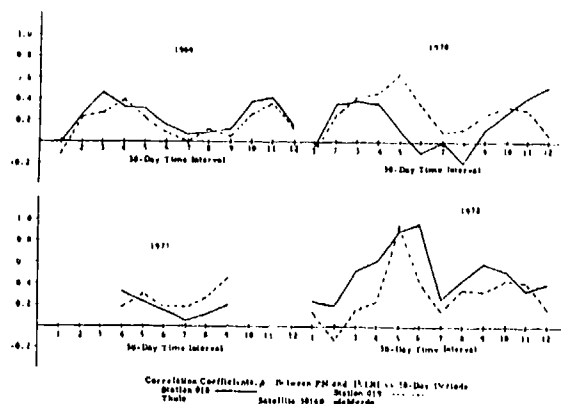


Figure 11

the satellites orbital plane relative to the sun. A peak in the FN data is located at station noon for orbits flat-on to the sun and 4-h to 6-h later for orbits edge-on to the sun. No significant correlation of filter noise with the planetary magnetic index  $A_p$  was found. A large correlation was found between the navigation error and filter noise. (This research was supported by The National Science Foundation, The Applied Physics Laboratory/Johns Hopkins University, and The Defense Mapping Agency.)

#### V. REFERENCE

1. Guier, W. H., and C. G. Weiffenbach, "A Satellite Doppler Navigation System", Proc IRE 48, 507.



AN AUTOMATIC DATA COLLECTION SYSTEM  
FOR L-BAND IONOSPHERIC SCINTILLATION MEASUREMENTS

by

Roy E. Anderson  
James R. Lewis  
General Electric Company  
Corporate Research and Development  
Schenectady, New York

George Haroules  
Wilfred Brown  
Department of Transportation  
Transportation Systems Center  
Cambridge, Massachusetts

INTRODUCTION

An automatic data collection system that can be remotely programmed and controlled has been constructed and evaluated. A complete system would comprise a number of Automatic Data Collection Platforms deployed over a large area of the earth, one or more central Data Collection Facilities, and a satellite that provides a communication link between the Platforms and the Facilities.

Each Platform collects, stores, and preprocesses data at remote sites and sends the data back to a central Data Collection Facility through the satellite when commanded to do so by the Facility. The system is especially useful for collection of synoptic data that requires prompt analysis. No operating personnel are required at the remote sites. Many remote sites can be operated from a single central Facility. Data transmission is accomplished directly through a satellite. Preprocessing the data at the Platforms can reduce the amount of data sent to the Facility so that it includes only information of interest, thus reducing time on the data transmission links.

The first implementation of the system is for collection of L-band amplitude scintillation data on signals received from NASA's ATS-5 and ATS-6 satellites. The system was implemented by General Electric and the Department of Transportation, under Contract No. DOT-TSC-485.

Two Data Collection Facilities are operational. One is at the Westford, Massachusetts, site of the Department of Transportation, the other is at General Electric's Radio-Optical Observatory, near Schenectady, New York.

The Platform, Figure 1, and its software are designed in modular form and can be reconfigured to satisfy a

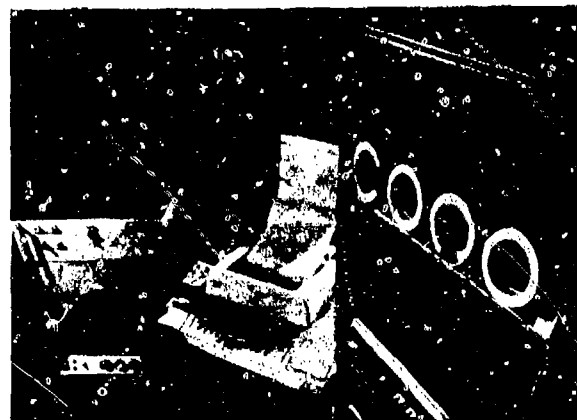


Figure 1 Automatic Data Collection Platform

wide variety of applications. The L-band receiver can be replaced by any desired sensors. The command, control and computer functions can be used to control other apparatus as well as to collect, store, preprocess, receive and transmit data.

SYSTEM DESCRIPTION

The Automatic Data Collection System for L-band scintillation measurements is shown in the block diagram, Figure 2.

The computer of the Platform, a PDP11/05 minicomputer, contains a program that schedules the timing, the sequencing, the data sampling rate and any other desired characteristics of the sensor operation. The L-band receiver output is digitized, preprocessed, and stored on tape by the minicomputer. The computer program sorts and catalogs the data. It is programmed to preprocess the data to extract desired information from the data, separately storing the information from the large total quantity of data.

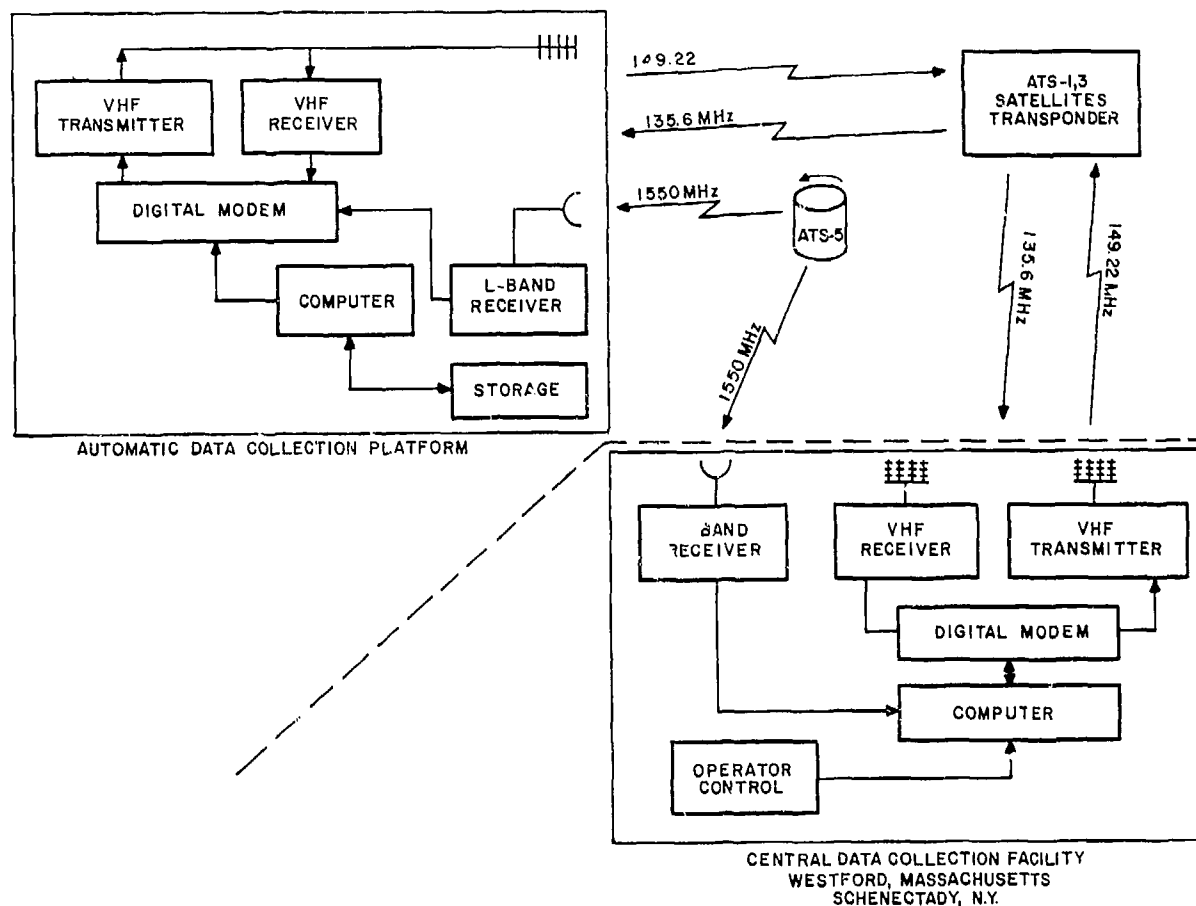


Figure 2 Diagram of the Remote Scintillation Data Collection System

At a convenient time, the operator at the Data Collection Facility initiates a command to interrogate the remote Platforms. The commands contain the unique address of the Platform so that any number of Platforms could be individually operated from the Facility. The command is verified on the display at the Operator Control equipment, and the operator initiates its transmission through the satellite to the Platform. The Platform receives the command, transmits an acknowledgment and its state in readiness for communication. The operator may then go through a sequence of commands to receive a summary of the Platform's stored data, select the stored data he desires, and command the Platform to transmit it through the satellite. The Facility receives the data, displays, and records the data for further processing as desired. The operator may then send a command for the next schedule of data collection, changes to the program, or even a complete new program.

When the operator at the Facility has completed his communication with one Platform, he could proceed immediately to communicate with any other Platform of his choice. Data collected over many hours by a Platform may be communicated to the Facility in a few minutes. Data could be collected from many distant places while it is still current. Data that is not of current interest is not transmitted, although it may remain stored in the Platform for transmission if it is desired later.

The Platform is diagrammed in more detail in Figure 3.

It performs all of its functions without operator attention. It is currently programmed to receive, record, store and summarize amplitude data from the L-band transmitters on the ATS-5 and ATS-6 satellites, and transmit the data on command through the VHF transponders of the ATS-3 or ATS-1 satellites.

L-band scintillation measurement data are not corrupted by scintillation on the VHF path. The only effect VHF scintillation can have is a loss of data if the signal falls below the detection threshold at the Data Collection Facility. In that event, the Facility requests the Platform to re-transmit the affected data block. All of the L-band scintillation data is digitized and stored as digital numbers in the Platform computer. The VHF link serves only as a communication link as it relays the digitized data from the Platform computer. Data is transmitted at 814 bits per second. Scintillation data on ATS-5 signals that were recorded during a one-hour period are transmitted by the Platform in one minute. Check sums on the digital bits in the messages are included with the data to detect any errors that may occur in transmission. Experience has shown that the VHF links are highly reliable, even when severe scintillation is present. Fading margins are in excess of 5 dB on the link from Facility to Platform, and 10 dB on the link from the Platform to Facility. The effect of severe scintillation on the VHF links is an occasional short drop out in the data transmission.

The VHF links serve other purposes in addition to the computer to computer data transmission. Voice and teletype communications are provided. A tone-code ranging responder is included in the command and control circuits so that the Platform response to an interrogation can be used to determine a line of posi-

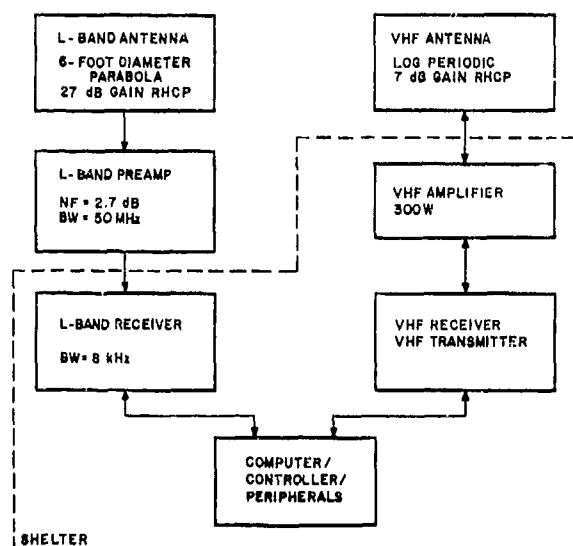


Figure 3 Simplified Block Diagram of the Remote Platform

tion for the Platform. If its response is relayed through two satellites, a position fix can be determined by the GE Observatory. The ranging feature was included to support other experiments that include measurements of ionospheric propagation delay, and trilateration tracking of satellites. The ranging feature would also be useful for locating the Platform if it were operated aboard a ship.

ATS-5 presented a special problem for the Platform program. The satellite is spinning on an axis parallel to the earth's axis with its L-band antenna fixed to the body of the satellite. As a result, the beam of the antenna sweeps across the earth like a searchlight beam once during each rotation of the satellite. The rotation period of the satellite is approximately 780 milliseconds. The signal received from the satellite has the pulsed characteristic shown in the signal amplitude recording, Figure 4.

Amplitude measurements are accurate only if they are made at a point on the pulse that is known exactly. The PDP-11/05 computer of the Platform is programmed to select the exact center of each pulse, even though scintillation may have distorted the pulse shape, and despite the small changes that occur in the satellite spin rate.

The computer samples the signal amplitude 512 times during each spin period, or approximately once each 1.5 milliseconds. Pulse amplitude is measured by adding the values of the four 1.5 ms samples at the center of the pulse, and dividing by four. The center of the pulse is selected by a logic process that monitors the rise and fall times of the pulses and adjusts for symmetry averaged over a number of pulses. The same process monitors the spin rate of the satellite and adjusts the 1.5 millisecond sampling period to maintain

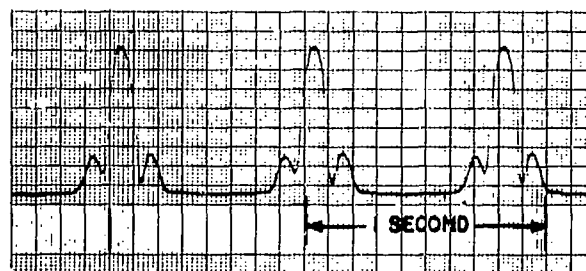


Figure 4 Typical Recording of the Signal Transmitted from the ATS-5 Satellite

exactly 512 sampling periods during each spin cycle, even if the spin period changes. It does change by a few microseconds due to change in angular momentum of the satellite as vents open and close automatically for its temperature control.

The amplitude at the center of each pulse is stored as a data point. It may not be the maximum amplitude if the pulse has been distorted by scintillation. In addition to the pulse amplitudes, receiver noise level is recorded by averaging 64 amplitude samples midway between each pulse pair, then further averaging over 16 pulse periods.

The Platform is commanded differently to collect scintillation data from ATS-6, which is not spinning. The ATS-6 L-band transmitter output has a constant amplitude when it is not modulated by a communication or ranging signal. The Platform is currently programmed to sample ATS-6 at any rate from once every 500 milliseconds to once every 3.3 seconds.

L-band signal-to-noise ratio is about 23 dB when the spacecraft EIRP is 23 dBw, a value typical of most present and proposed L-band transponders. Accuracy of the Platform ATS-5 peak signal measurements is better than 0.5 dB, including equipment instabilities, receiver noise, and processing errors. The receiver contains an automatic tuning device. When no signal is present, the second local oscillator in the double super heterodyne receiver sweeps back and forth  $\pm 80$  kHz about its center frequency.

When a signal is present, the sweep stops and an automatic frequency control circuit holds the signal in the center of the 8 kHz I.F. filter so that amplitude of the receiver output is not affected by changes in received frequency.

#### SOFTWARE DESCRIPTION

Assembly language programs were prepared for the remote Platforms PDP-11/05 computer, the Westford Facility Hewlett-Packard 2114B computer, and the General Electric Facility PDP-11/20 computer.

The remote Platform program includes the following functions:

- o Start VHF communication.

NOTE: The HELLO command or OPEN command is given. With HELLO, L-band data taking can continue. With OPEN

current L-band data taking is stopped. Without HELLO or OPEN the Platform will not act on other commands.

- o Enter date, time
- o Schedule data collection start, stop, date and times
- o Send blocks of data
- o Send summary of data in storage
- o Read ATS-5 spin rate or ATS-6 (or other CW satellite) data sampling rate. Supply new sampling rate.
- o Read out any location in Platform computer core. Modify any core location. Modify constants in the Platform computer program.
- o List system errors such as power fail, recording time of power fail
- o Restart data collection after power returns

NOTE: The Platform will send time of power fail and its present clock time. The Data Collection Facility then knows the time of failure, determines length of time power was out and hence the period for which data is missing. It can then command reset of the Remote Platform clock.

- o Reboot program from DECTape

NOTE: The Remote Platform has two DECTapes. One is for data recording, the other contains the complete program. An entirely new program can be inserted by preparing it at a Data Collection Facility, then either sending the DECTape to the Remote Platform where an operator mounts the tape, or by sending the new program via the satellite to the Platform where it is added to the DECTape already on the computer. The new program can be loaded or booted in by the Data Collection Facility via the satellite or by an operator at the Remote Site.

o "DESPIN" the ATS-5 Satellite

NOTE: The program module selects the proper point on each ATS-5 pulse for amplitude measurement, selects and averages the samples for receiver noise level measurement, and adjusts the sampling period to match the spin rate of the satellite.

o Teletype Print

NOTE: Critical internal functions of the remote Platform computer and its data collection process are recorded automatically on a teletype instrument at the Platform for the information of personnel who may check occasionally on its operation.

o Mailbox Feature

NOTE: Plain language messages may be sent from the Data Collection Facility to any remote platform where they are stored. An individual at the remote platform may later request messages that may be in the "mailbox" by typing a command on the teletype instrument. The computer will then cause its stored message to be typed out on the machine. Similarly, an individual at the remote Platform may send a message to the Data Collection Facility. Alternatively, the teletypes may be used for direct two-way communication and two-way voice communications may be conducted between the Remote Platform, the Data Collection Facility or any other Platform.

o Sign Off VHF Communication - FINISH command

NOTE: Platform starts taking L-band data according to schedule it has received. If FINISH command is not sent from Facility, Platform will automatically execute the command after 15 minutes.

EXPERIMENTAL EVALUATION

Two criteria must be considered in evaluating the Data Collection System: first, its performance in collecting the desired data, and second the reliability of the Remote Data Collection Platforms. Data collection performance is determined by the quality of the software. The program for L-band scintillation data collection is elaborate, and its preparation and debugging required a longer time than anticipated. Its performance fulfills all expectations, and data are collected and accurately recorded by the Platform.

Reliability of the remote platforms is important. They are more complex than instrumentation that might be used in an alternate system, such as one that uses a local recording device with frequent manual attention and physical conveyance of the recordings to the central data processing facility.

One of the advantages for the Automatic System is expected to be its lower cost of data collection. Higher investment cost must be compensated by lower operating costs, which can be realized only if the equipment is highly reliable and does not require frequent attention.

Although the one Platform that has been constructed is considered to be a prototype, its performance after correction of initial minor problems has demonstrated high reliability and it is expected that it will achieve cost advantages when deployed at a remote site. The minor problems encountered after delivery of the unit to Westford were in the physical connections of components; defects in plated-through holes in printed circuit cards, and in one case a card that was not inserted tightly in its socket. All of the defects are believed to be corrected, and continued reliable performance is expected of the hardware.

It has been necessary to reboot the program in the Platform computer occasionally; approximately once per month on the average. Rebooting requires the operation of several switches on the front panel of the computer, a process that requires only about 30 seconds of time. A person without technical training can be instructed to reboot the program in about five minutes.

The cause of the need to reboot the program has not been positively identified. A probable cause is noise on the power line, or noise spikes generated within the computer from some powerful electromagnetic signal source.

Accuracy of the L-band amplitude measurements could be affected by instability of the Platform receiving system. Comparisons of the analog receiver output and the digital data recorded by the computer show that no errors are introduced in the analog to digital conversion and recording process.

The antenna and its cabling must be very stable mechanically and electrically. Receiver gain changes will affect the measurement of signal amplitude. Receiver noise measurements between signal pulses of ATS-5 provide a means to calibrate receiver gain and track changes in gain that may occur. The Platform receiver is not presently equipped to provide frequent calibration when receiving the signal from ATS-6. Frequent calibration could be provided by switching the receiver input alternately between the antenna and a calibrated noise source.

Accurate tuning of the receiver is important. If the signal is not centered in the receiver pass band, the receiver does not amplify the signal correctly, and the apparent gain of the receiver will change with tuning or changes in received frequency. The receiver is specially designed with a search sweep and automatic frequency control discriminator circuit that insures correct tuning even if the received frequency changes.

The total effect of all the factors affecting calibration of the receiving system is less than  $+1/4$  dB. A number of lengthy recordings of signal amplitude received from ATS-5 have shown less than  $+1/2$  dB total excursion. The Department of Transportation compared the Automatic Data Collection System with a completely separate system when the Automatic Data Collection Platform was co-located with the separate system receiver. The two systems agree. When L-band scintillation effects are observed on one system, they are observed on the other.

Propagation effects at VHF cannot introduce errors into the L-band scintillation data because the data are transmitted as redundant digital messages with check sums. If the check sums indicate an error in data transmission, the data are rejected and must be repeated. Scintillation or radio frequency interference can cause dropouts in the VHF data link, require the re-transmission of data, and thus increase the time needed for the data transfer from Platform to Facility.

Most of the data readouts through ATS-3 by Westford and Schenectady are during evening hours. Scintillation on the VHF links is experienced quite often. When it is not present, the reliability of the transmission from the Platform to the Facilities is very high. RF sources, such as VHF land mobile and VHF aircraft radio often cause intermittent interference at Westford.

Bad VHF scintillation may reduce reliability to an estimated 70-75%, i.e., it is necessary to command a re-transmission of 25-30% of the data. The occurrence of such severe scintillation is not often experienced.

The digital measurement data are transmitted in blocks of 256 words, 16 bits per word. Each "one" bit from the computer is transmitted as three cycles of a 2.4414 kHz tone and each "zero" bit is transmitted as 3 cycles with its phase reversed. Any number from one to sixteen blocks of data may be requested by a single command from the Facility. A data block is transmitted in 6 seconds. Each 256 word data block is followed by a check sum word, and a "words to follow" message repeated three times. The check sum is a standard procedure to confirm the accuracy of the data in the block. If the check sum does not confirm accuracy, the data in the block are rejected. Two of the three repetitions of the "words to follow" message must agree. If they do not, all the following data are rejected by the Facility computer.

When VHF scintillation is not present, it is advantageous to command long transmissions of multiple data blocks. When VHF scintillation is present, shorter transmissions of a few data blocks are commanded to minimize the probability that a dropout will occur and cause rejection of a long transmission. An additional 3 dB gain over the present 7 dB gain of the Platform VHF antenna would be advantageous.

One exchange between the Westford Facility and the Platform is recorded in Figure 5. The exchange was recorded at the Schenectady Facility from the ATS-3 satellite. The exchange was initiated by the Westford Facility with a HELLO command and acknowledgment not shown in the Figure. The line below "READY" is the interrogation to the Platform, the next line is the Platform response with current date and time. Time is GMT in hours, minutes, seconds and "ticks" or  $1/60$  seconds. If the Platform were operating on a 50-cycle AC line, it would be reprogrammed so that

READY  
W 015202 T082 00056 00069 00013 OK  
P 015202 FM82 07-NOV-74 02:56:36:57 VB  
P DECTAPE 00056 00069 00013  
CS 000000 TV82 21747 65535 65535 OK  
W 015202 TV82 21747 65535 65535 OK  
P 015202 FM82 07-NOV-74 02:56:43:05 MB  
CS 000000 TV82 21747 65535 65535 OK  
W 015202 TV82 21747 65535 65535 OK  
P 015202 FM82 07-NOV-74 02:56:47:40 MB  
P S5 STOP 00056 22-JUL-74 18:57:50:25  
P S5 BOTH 00057 22-JUL-74 18:59:58:04  
P S5 START 00058 22-JUL-74 19:04:01:37  
P S5 NONE 00059 22-JUL-74 19:09:52:27  
P S5 NONE 00060 22-JUL-74 19:15:43:16  
P S5 NONE 00061 22-JUL-74 19:21:34:05  
P S5 NONE 00062 22-JUL-74 19:27:24:57  
P S5 NONE 00063 22-JUL-74 19:33:15:48  
P S5 STOP 00064 22-JUL-74 19:39:06:37  
P S5 START 00065 22-JUL-74 19:45:38:10  
P S5 NONE 00066 22-JUL-74 19:51:28:58  
P S5 NONE 00067 22-JUL-74 19:57:19:48  
P S5 NONE 00068 22-JUL-74 20:03:10:36  
P S5 NONE 00069 22-JUL-74 20:09:01:22

W = WESTFORD FACILITY  
P = PLATFORM  
CS = COMPUTER AT SCHENECTADY

Figure 5 Platform Readout by Westford Facility as Received at Schenectady

each "tick" was 1/50 second. The next line requests read out of DECTape blocks 56 through 69, the difference in block numbers being 13. At this point the GE program anticipated the next command to be a VERIFY and loaded it into its output buffer as shown by the first line that starts with six zeros. The request is verified, and the Platform sends WB, or "WAIT:BLOCKS" as it transfers the data from DECTape to Core. Note that approximately seven seconds elapsed between the VB, "VERIFY:BLOCKS" and WB "WATT:BLOCKS" responses. The minimum command time is two seconds. The GE program anticipated the next command to be a VERIFY. There is a further verify command and response, and an MB, or "MORE:BLOCKS" statement that more information, the data blocks, are to follow immediately.

The first four words of each block are decoded to English.

S5 States that data are from  
ATS-5  
STOP States that something occurred to stop data taking before the block was filled with 448 data points. The time is the start of the data points within the block. Data taking is stopped if a

single amplitude sample is missed or if synchronization with satellite spin is lost. Synchronization is checked, valid data are taken for about one minute before data recording is resumed.

BOTH States that data recording started, then terminated within the block. It contains fewer than 448 data points.  
START Indicates that data recording started with this block, that it contains 448 data points.  
NONE State that the block is filled with 448 valid data points taken in sequence.

In each instance, the time stated is the time of the first data point in the block. Each data location in a block is filled with a zero when no valid data are present.

The exchange presented in Figure 5 was on 7 November 1974, but the data were recorded from ATS-5 on 22 July 1974. It was retained on a DECTape of the Platform. Data on Platform DECTape can be stored indefinitely and read out as many times as desired.

Data in blocks 66, 67 and 68 are presented on the analog chart recording, Figure 6. The lower recording is signal amplitude from ATS-5, the upper is receiver noise. The blocks are separated by two groups of markers that are calibrations of the digital to analog converter of the Facility chart recorder system. Each data block records 448 data points, each one taken on a signal pulse from ATS-5. Hence the time of each block is  $448 \times .783 = 351$  seconds, where .783 seconds is the spin period of the satellite.

Near the end of block 65 and in block 66 are some variations in signal amplitude that are attributed to scintillation. The total excursion of the variations is  $\pm 0.5$  dB. Blocks 67 and 68 register the stable signal level that is usually received from the satellite. The same signal variations were observed by a separate receiving and recording system co-located with the Platform at Westford, Mass.

Figure 7 presents probability density plots for data block 66, 72 and 79 as computed by DOT at its Westford Site. Figure 8 presents probability distributions for the same data blocks.

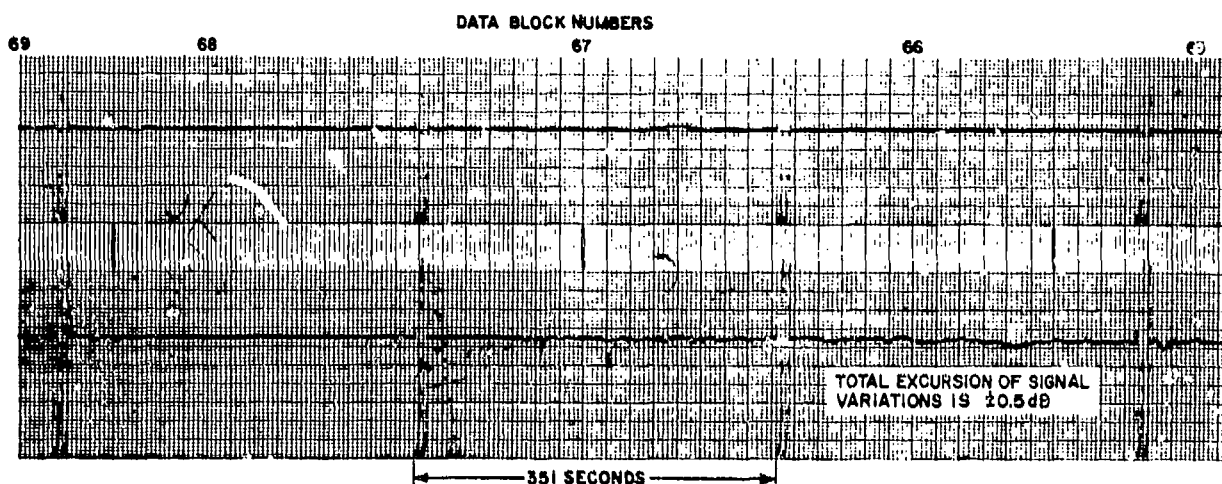


Figure 6 Analog Chart Recording of L-band Signal Amplitude  
Received from ATS-5

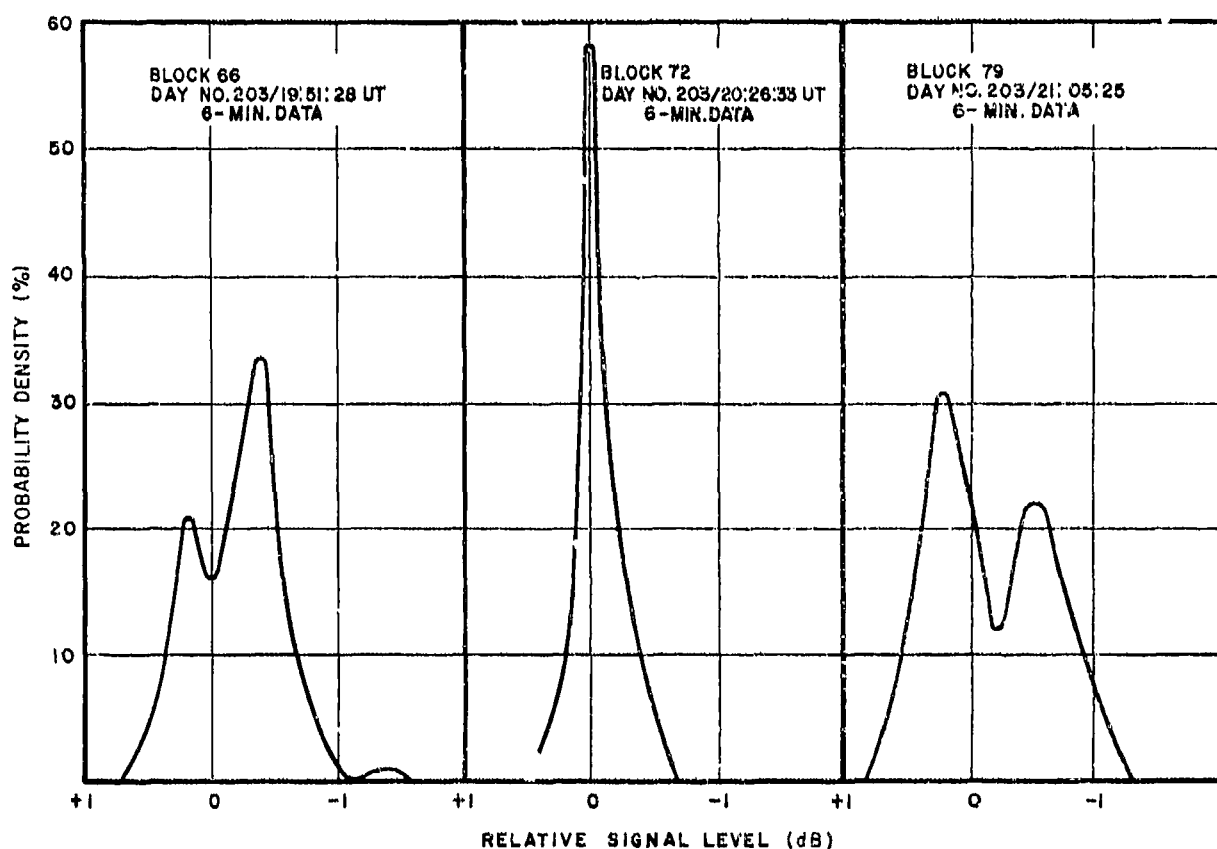


Figure 7 Probability Density Plots for Automatic Data  
Collection Platform Data (22 July 1974)



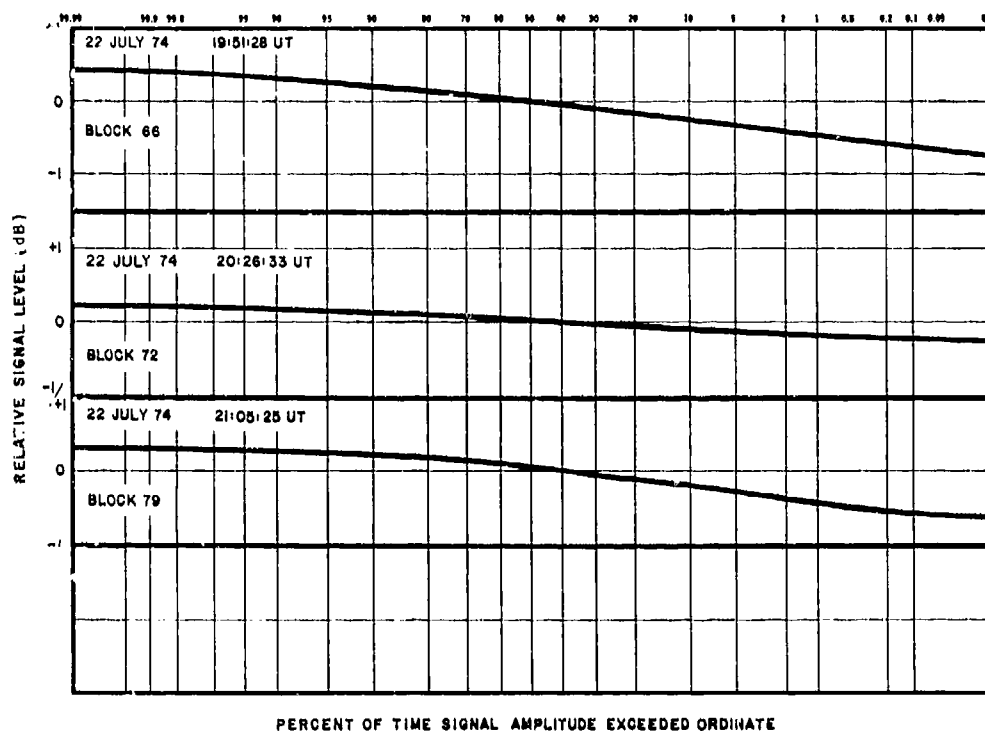


Figure 8 Probability Distribution Plots for Automatic Data Collection Platform Data (22 July 1974)

#### SUMMARY

An Automatic Data Collection System has been implemented with one prototype Remote Data Collection Platform and two Data Collection Facilities. The Platform is configured to measure amplitude scintillation of L-band signals received from the spinning ATS-5 satellite and the stabilized ATS-6 satellite.

The measured data are digitized and recorded by a computer in the Platform. Commands transmitted to the Platform by either Facility through the VHF transponder of ATS-3 or ATS-1 can initiate readout of any portion of its stored data, schedule the taking of new data, and modify or even replace the program in the Remote Platform automatically. Data transmission in digital redundant form with check sums insures that L-band scintillation data are not corrupted by scintillation that may occur on the VHF data transmission link. Communications by voice and teletype, and position fixing by range measurements from satellites can also be accomplished.

Performance and reliability of the Remote Platform have been thoroughly tested. It is in a state of readiness for installation at a remote location for the collection of L-band scintillation data in a region of the earth where

signal amplitude fluctuations may affect the reliability of satellite communications at L-band. A dispersed network of Platforms would enable the collection of synoptic data rapidly and at moderate cost.

#### REFERENCES

The Automatic Data Collection Facility is discussed in greater detail in the following Department of Transportation reports:

Description of a Remote Ionospheric Scintillation Data Collection Facility DOT-TSC-OST-73-17

Mid-latitude Measurements of L-band Ionospheric Scintillation with the ATS-5 Spacecraft DOT-TSC-OST-75- (in printing)

#### ACKNOWLEDGMENTS

The authors would like to acknowledge the contributions of Messrs. Joseph Gutwein, William Thompson, and Paul Podlesny of the Department of Transportation, Cambridge, Mass., and Messrs. Clark Gittinger, Richard Garrett, and Dr. George Millman of the General Electric Company.

Electron and Ion Density Studies with the NRL One-Dimensional  
Mid-Latitude Model of the Ionosphere

E. S. Oran, T. R. Young, D. F. Strobel, T. P. Coffey  
Naval Research Laboratory  
Washington, D. C. 20375

INTRODUCTION

The theoretical one-dimensional model of the mid-latitude ionosphere developed at NRL (1) provides a detailed description of the ion, electron, and neutral densities and their respective temperatures as a function of time, altitude, and solar conditions. Since the physical and chemical state of the ionosphere is important to a wide range of communication and observation systems, accurate descriptions of the major ionospheric processes are needed to understand electromagnetic wave propagation in this medium. The model we have developed describes the laminar ionosphere and can be used to describe attenuation, refraction, and group delays. The laminar model also provides a basis for the study of instabilities and turbulence: equilibrium electron densities, density and temperature gradients, and current flows from the laminar ionosphere are the driving forces of instabilities.

Models of the ionosphere typically have taken either empirical or theoretical approaches to describing physical phenomena. The empirical models, such as those of Ching and Chiu(2) and Swartz, Rohrbaugh, and Misbet(3), incorporate statistical analyses of data and parametric fits of physical quantities. Theoretical models, such as those constructed by Stubbe(4) and Strobel and McElroy(5), start with a basic set of equations and try to predict ionospheric behavior analytically or numerically. Below we describe the theoretical model developed at NRL and describe several aeronautical studies made with the model.

DESCRIPTION OF THE MODEL

Starting with the governing multi-fluid equations for velocities, temperatures, and densities in the ionosphere and making appropriate approximations, we have derived a set of time-dependent one-dimensional equations for the vertical variations of ionospheric constituents. These equations are solved by numerical finite differencing techniques. The model is designed to describe mid-latitude effects including the detailed composition of the E and F-regions. Those quantities such as

the neutral atmosphere or electric fields which can only be derived self-consistently from small scale or multi-dimensional models are treated as given. The densities of the major neutral species in the ionosphere,

$$N_2, O_2, O, He \text{ and } H,$$

are calculated from a model atmosphere. Densities of the minor neutral species,

$$N(^2D), N(^4S), \text{ and } NO,$$

and the densities of the ions,

$$O^+, H^+, N^+, He^+, NO^+, O_2^+, \text{ and } N_2^+,$$

are calculated from fluid transport and chemical reaction equations. The electron density is then obtained from the "quasi-neutrality" condition:

$$n_e = \sum_i n_i \quad (1)$$

where  $n_e$  is the electron density and the  $n_i$ 's are the densities of the ion species.

The Neutral Atmosphere

The densities of the major neutral gases ( $N_2$ ,  $O_2$ ,  $O$ ,  $H$  and  $He$ ) are prescribed by either of two Jacchia model atmospheres, published in 1965(6) and 1971(7). These were designed to reproduce satellite drag data and give the densities as a function of position, time, solar, and geomagnetic activity, as well as semi-annual and diurnal variations. Above 120 km, we have used Walker's analytic expressions for the number densities(29). Neutral densities at altitudes between 80 and 120 kilometers were determined by fitting the CIRA(8) data at 80 kilometers to the boundary conditions at 120 kilometers. The model atmospheres used here were formulated to reproduce the long time-scale behavior of the neutral atmosphere. As such, they do not describe effects such as sporadic gravity waves and tidal fluctuations. The NRL ionospheric model is, however, constructed to incorporate improved model atmospheres when they are available.

Once the densities of the major neutral species have been calculated as a function of altitude for a specific time, it is assumed that they are not affected by the ionization, transport, and chemistry in that time. Pressures and pressure gradients calculated from these temperatures and densities drive the diurnal component of the neutral winds. In calculating neutral particle motion, the effects of semi-diurnal tides, internal friction or viscosity, ion-neutral collisions, and the Coriolis force are included.

#### Deposition of Radiation

During the day, the main energy source for heating and ionizing the upper atmosphere is the deposition of the solar extreme ultraviolet and X-radiation. The solar spectrum consists of lines generated in the sun's chromosphere and corona and some continuum radiation. The exospheric flux data used here were based on those given by Hinteregger(9). These describe a quiet sun at medium sunspot activity and are based on measurements by high altitude rockets. Radiation at 1912 Å was also included to describe predissociation of NO which is important at lower altitudes. Over eighty lines and bands are tabulated by Hinteregger. In the present model, these have been reduced to a set of twenty bands and corresponding averaged cross sections(10). Each band is described by a total flux that is the sum of the individual fluxes in that band.

At night, the radiation sources are extraterrestrial radiation and resonantly scattered radiation from the daytime side of the globe. The major wavelengths of extraterrestrial radiation are the He 584 Å and the H Ly β 1026 Å lines. Although these fluxes show seasonal variations, these are not incorporated in the model now. For the resonantly scattered nighttime radiation, the wavelengths considered are H Ly α 1216 Å, H Ly β 1026 Å, He I 584 Å, and He II 304 Å.

#### Transport of Mass

The continuity equation which describes conservation of mass in a volume element is:

$$\frac{\partial n_i}{\partial t} + \nabla \cdot (n_i \mathbf{v}_i) = P_i - L_i n_i \quad (2)$$

where "i" represents a ion or a minor neutral species,  $n_i$  is its number density,  $\mathbf{v}_i$  is its velocity, and  $P_i$  and  $L_i$  are the production and loss functions, respectively. Throughout our model, the assumption of a vertically stratified atmosphere is made so that the features of the atmosphere depend primarily on  $r$  and  $t$ . Then equation (2) becomes:

$$\frac{\partial n_i}{\partial t} + \frac{1}{r^2} \frac{\partial}{\partial r} (r^2 n_i w_i) = P_i - L_i n_i \quad (3)$$

where  $w_i$  is the velocity in the vertical direction. Ion velocities are effected by the earth's magnetic field, the ion pressure gradient, electric fields, gravity, and collisions with other ions, neutrals, and electrons. Minor neutral velocities are primarily determined by eddy diffusion and molecular diffusion.

#### Heat Transport

The temperature equations appropriate for the ionosphere can be derived from the equation for the total conservation of energy, both internal and due to motion of the fluid(11). During the day, the temperature of the electron gas is determined primarily by the heat input from solar radiation. Both the electron and the ion gas temperatures are also determined by the thermal conductivity of the gases and collisions with ions, neutrals, and electrons.

Lack of thermal equilibrium among electrons, ions, and neutral particles is characteristic of altitudes above 150 kilometers. The various species are in thermal equilibrium below this altitude since densities and collision frequencies are high. In our calculation we assume that the neutrals have one temperature,  $T_n$ , which was discussed in the model atmospheres section, that all the electrons have one temperature,  $T_e$ , and all the various ions have the temperature  $T_i$ . Up to about 250 kilometers the ions and neutrals are fairly well coupled thermally and the temperatures are close. At high altitudes, the ion temperatures exceed the neutral temperatures and approach the electron temperatures. The basic reason for the lack of equilibrium between the electrons and the other particles is that the ionizing radiation carries more energy than is needed to merely ionize a neutral particle and energy exchange rates are not fast enough to establish equilibrium. Photoelectrons carry this extra energy, and in general, share their energy quickly by collisions with the electron gas or by ionizing other neutrals and creating secondary electrons. It is assumed that the electron gas can be characterized by a Maxwellian velocity distribution, and an electron temperature,  $T_e$ . This appears to be true in the ionosphere, though there are sometimes "high energy tails" (12) in the upper ionosphere and protonosphere where collisions are exceedingly rare.

#### Atmospheric Chemistry

Since the densities of the major neutral species are prescribed by a model atmosphere for a given latitude, altitude, and time, only chemical reactions describing the production and loss of ions and minor neutral species have been considered.

A detailed list of the important chemical processes included in the model can be found in references (1), (13), and (14).

In the D-region, the model is designed primarily to predict electron densities. The major source of ionization is Lyman  $\alpha$ , which ionizes NO. The major ionization sink is dissociative recombination of molecular ions. Rates for the latter process are comparable for most of the species present. In the first approximation, processes involving negative ions, hydrated and metal ions, and three-body reactions have not been considered.

In the E and F1-regions, any negative ions formed disappear quickly. Dissociative recombination of electrons and positive molecular ions is the most important process. The atomic ions have a tendency to recombine with electrons by radiative processes, which are slower than the dissociative recombination process. Below 165 km during the day,  $\text{NO}^+$  and  $\text{O}_2^+$  are the dominant ion species in the E-region. Above this,  $\text{O}^+$  is dominant. At nighttime, the cross-over altitude is about 220 km.

In the upper F-region, radiative electron-ion recombination and charge exchange are the fastest chemical loss processes. However, transport is the dominant mechanism for changing the composition.

#### APPLICATIONS OF THE MODEL

As an introduction to the capabilities of the present model, Figure (1) shows a periodic surface on which the natural log of the density,  $n_e$ , is shown as a function of Local Time, L. T., and the natural log of the altitude,  $z$ . The Jacchia '65 model atmosphere was used in this calculation, medium solar conditions with  $T_0$ , the minimum global exospheric temperature, 940°K, latitude, 45°N, and magnetic dip angle, 70°. The sharp rise and fall of  $n_e$  as a function of time mark the onset of sunrise and sunset and indicate transitions in the source of ionizing radiation from the nighttime resonantly scattered radiation to daytime solar radiation. The maximum value of  $n_e$  is about  $5 \times 10^7 \text{ cm}^{-3}$ , which occurs shortly after sunrise at about 240 km; the nighttime radiation necessary to maintain the nighttime peak is discussed further below. The importance of neutral winds in raising and lowering the F2 peak has been pointed out by Strobel(5). Since the sign of  $v$ , the north-south component of the neutral wind, is positive (pointing northward) during the day, and the magnetic field points downward in the northern hemisphere, the electrons and ions move down along field lines. The sign of  $v$  is negative at night and has the effect of pushing them in the opposite direction and thus raising the peak altitude. The nighttime E-region valley is also marked on the figure. Stubbe(15) has demonstrated that a large scale thermospheric wind system can produce a positive divergence in the electron and ion fluxes which reduces the amount of ionization above 150 km. The result is a broad valley in the electron profiles.

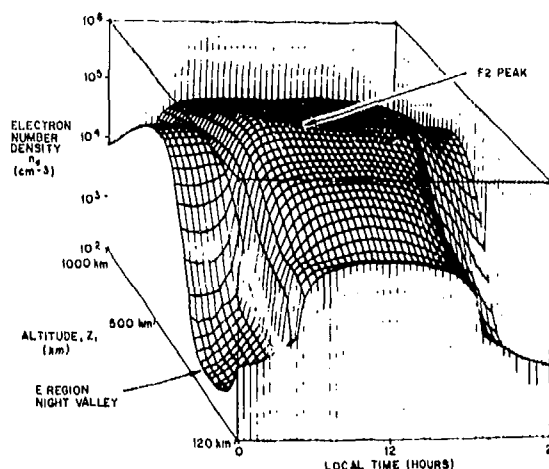


Figure (1). Periodic surface showing the natural log of the electron number density as a function of time and altitude.

Figures 2 and 3 compare predictions from the NRL model to those given by Evans for Millstone Hill, Mass., in April 1964(16). The Jacchia '65 model atmosphere was used, minimum solar activity,  $T_0$ , 740°K, latitude, 42.6°N, dip angle, 73°, and  $B$ , 0.46 Gauss. The F2 peak density and altitude are shown as a function of Local Time in Figure 2. Effects of the onset of sunrise and sunset and the occurrence of the maximum peak altitude at night are shown more clearly here than in Figure 1. NRL model predictions in this case are consistently higher than the data, though they follow the same diurnal trends. Figure 3 shows the vertical number density profiles for  $\text{O}^+$  at 0:30 and 12:30 L. T. Again, the model follows the trends shown by the data, though it generally predicts densities that are higher.

There are a number of possible explanations for the consistently higher values for the electron number density calculated by the model. Comparison of data and model results indicate that the neutral winds are probably not correct in this calculation. The electron density profile for 0:30 L. T., however, is in better agreement with the data in the low altitude ranges, as would be expected from results of the lower nighttime ionosphere calculation discussed below. Further, a comparison of the observed electron and ion temperatures that Evans reported with those of the model indicate that the exospheric electron temperatures calculated by the NRL model are too small by as much as 50%. The model's ion temperatures are smaller than those observed ion temperatures by at most 15%. A close look at the diffusion term in the temperature equation indicates that as the

temperature decreases, the number density will increase. These effects contribute to the differences between the model predictions and data.

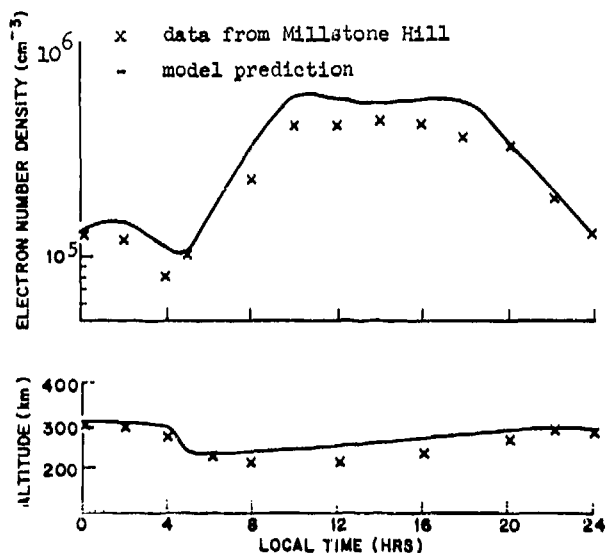


Figure (2). Comparison of model calculations and observations of electron number density and altitude of the F2 peak at Millstone Hill(16).

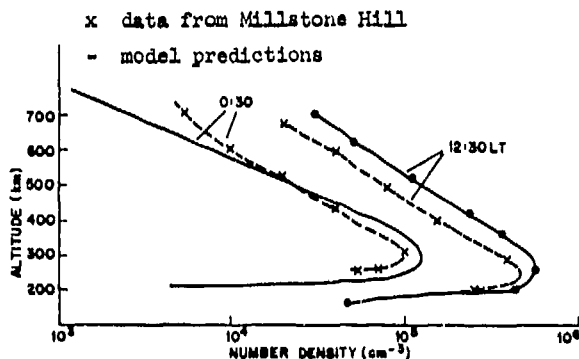


Figure (3). Electron number density as a function of altitude at 0:30 at 12:30 L. T. for Millstone Hill data(16) compared to model calculations.

#### The Nighttime Ionosphere E-Region and Lower F-Region

Detailed numerical calculations have been made to assess the quantitative importance of nighttime ionization sources, transport

processes, and local chemistry in the determination of the structure and behavior of the nighttime lower ionosphere(13). During the past few years a sufficient number of observations of the airglow emissions have been made to construct adequate models of the nighttime radiation field. Theoretical models describing the resonance scattering of Lyman- $\alpha$ , Lyman- $\beta$ , 534 Å and 304 Å photons in the atmosphere have been developed for comparison with rocket and satellite observations of these far and extreme-ultraviolet radiation. Combining these models with one for extraterrestrial radiation, nighttime photonization production rates and ion and electron density profiles are computed for the E-region.

In Figure 4, theoretical ion density profiles are presented and compared with NRL rocket data representative of summer solar minimum conditions(17). It is obvious that above 120 km the electron density profile is very sensitive to the plasma transport induced by neutral winds. Below 120 km where local chemical equilibrium is valid, the combination of resonantly scattered Lyman- $\alpha$  and Lyman- $\beta$  and extraterrestrial radiation is adequate to maintain the E-region. But in the 120-140 km region where transport partially controls the ion densities, the intensity of the nighttime ionization sources is deficient by up to a factor of 4, provided that the vertical plasma transport has been properly modelled. Above 140 km the nighttime ionization sources plus plasma transport are sufficient to account for the maintenance of the F1-region.

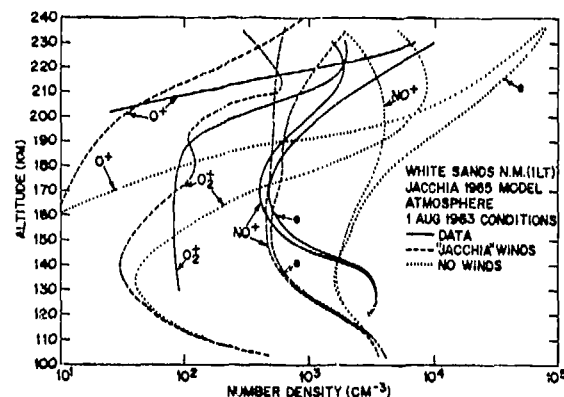


Figure (4). Comparison of ion composition data(17) with model results with and without winds.

It is highly improbable that all important velocity fields present during any rocket measurement can adequately be accounted for except by simultaneous measurement. At any

given time, the macroscopic wind field is composed of the essentially diurnal thermospheric winds produced by *in situ* uv heating, upward propagating tidal winds (particularly the semi-diurnal modes), and gravity waves. The amplitude of gravity waves cannot generally be calculated due to insufficient knowledge of their sources. Since no simultaneous measurements were made of the wind field, the actual plasma transport cannot be evaluated. However, it is evident from Figure 4 that the integrated production of ionization can account for the column plasma density; the observed local plasma density can be modelled accurately with appropriate vertical plasma transport.

To investigate the effect of somewhat less vigorous winds, the pressure gradient (driving force) terms in the neutral momentum equations were multiplied by 0.6. The results are illustrated in Figure 5. Considerable improvement in the agreement between theory and observation is achieved above 150 km. Between 115 and 140 km much more vigorous winds (greater than  $50 \text{ m sec}^{-1}$ ) are required to model the observational data with vertical ion transport.

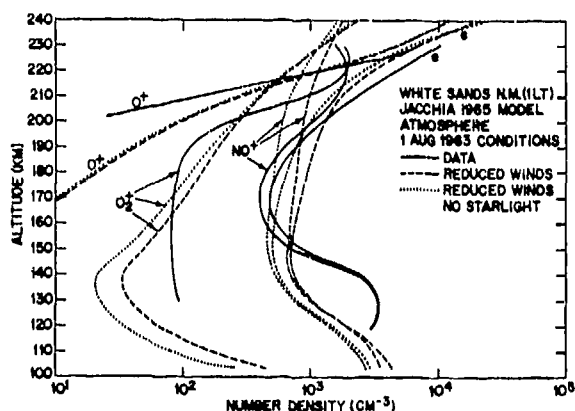


Figure (5). Comparison of ion composition data (17) with model results having reduced the magnitude of the winds. In one case, extraterrestrial radiation is excluded from the calculation.

It is well known that the ratio  $[O_2^+]/[NO^+]$  is indicative of the charge transfer agent, NO. In Figure 6, the production rates of ions by the major nighttime sources are given for conditions representative of the NRL rocket measurements. Above 90 km both resonantly scattered Lyman- $\beta$  and extraterrestrial fluxes are the dominant ionization source. Figure 6 shows the quantitative importance of

extraterrestrial radiation. Approximately a 40 percent enhancement in electron density is obtained by the presence of the adopted extraterrestrial radiation. In the absence of transport processes the ratio  $[O_2^+]/[NO^+]$  is inversely proportional to  $[NO]$ . Based on the NRL rocket data for this ratio, NO concentrations  $\sim 6 \times 10^7 \text{ cm}^{-3}$  are required in the 120-130 km region. Since the chemical time constants for  $O_2^+$  and  $NO^+$  are not equal, transport processes will alter their density profiles unequally as is evident from Figure 5. Detailed numerical calculations with modifications to the odd nitrogen chemistry confirm that the ratio is indeed sensitive to the NO concentration and a peak density  $\sim 5 \times 10^7 \text{ cm}^{-3}$  is consistent with the NRL rocket data. Comparable NO densities have been obtained from rocket measurements by the Boulder group (18), (19), (20).

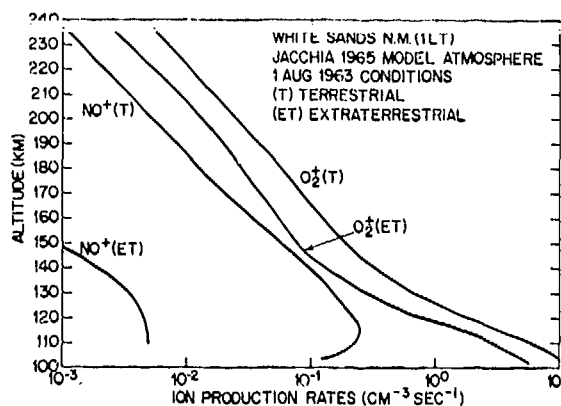


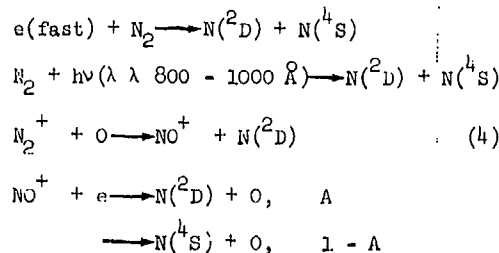
Figure (6). Production rates of  $O_2^+$  and  $NO^+$  ions by resonantly scattered radiation by the hydrogen geocorona (T) and by radiation from extraterrestrial sources (ET).

On the basis of our calculations we conclude that Lyman- $\alpha$  and Lyman- $\beta$  radiation in the nighttime sky from terrestrial and extraterrestrial sources can maintain the nighttime lower ionosphere at electron density levels in agreement with observational data. While the possibility of a significant effect due to energetic particles cannot be excluded, our ionospheric analysis indicates that no such contribution is required. The model calculations suggest that E-region wind systems are considerably more complex than the large-scale diurnal winds generated by UV heating of the thermosphere.

#### Odd Nitrogen in the Thermosphere

Nitric oxide plays an important role in

ionospheric chemistry and physics both as the principal ionizable constituent in the D-region and as an important charge transfer agent in the E-region. To understand the nitric oxide and thus the ionization and electron density profiles in the thermosphere, a self-consistent model of the odd nitrogen ( $\text{NO}$ ,  $\text{N}(^4\text{S})$ ,  $\text{N}(^2\text{D})$ ) chemistry is required. We have constructed such a model for the aeronomy of odd nitrogen (14) which describes the  $\text{N}(^2\text{D})$  5200 Å emission measured by Wallace and McElroy (21), the  $\text{NO } \gamma(1,0)$  band fluorescence observed by Meira (19) and Tisone (20), and the  $\text{NO } \gamma$ - and  $\delta$ -band emission spectra measured by Feldman and Takacs (22). Previous models by Strobel (23) were based on parameters that represented branching ratios of the atmospheric  $\text{N}(^2\text{D})$  sources:  $\text{NO}^+$  dissociative recombination, electron impact dissociation of  $\text{N}_2$ , and the reaction  $\text{N}_2^+ + \text{O}$ . No laboratory constraints on the branching ratios were available and still are not. Although the models were to some extent arbitrary, they did demonstrate that only a fraction of the potential  $\text{N}(^2\text{D})$  sources were required to produce theoretical models consistent with  $\text{NO}$  dayglow measurements. We have used our model to establish that the important atmospheric sources of  $\text{N}(^2\text{D})$  (14) are



and that the branching ratio,  $A$ , for dissociative recombination of  $\text{NO}^+$  is approximately 0.55. That is, slightly more  $\text{N}(^2\text{D})$  than  $\text{N}(^4\text{S})$  is formed. Based on these sources of  $\text{N}(^2\text{D})$ , a consistent model for the aeronomy of odd nitrogen requires  $\text{N}(^2\text{D})$  to preferentially react with  $\text{O}_2$  to form  $\text{NO}$  rather than be deactivated by atomic oxygen. This leads to an upper limit on the  $\text{N}(^2\text{D})$  quenching coefficient by  $\text{O}$  of  $10^{-14} \text{ cm}^3 \text{ sec}^{-1}$ .

An analysis of the 5200 Å emission height profile identifies the major atmospheric quenching agent of  $\text{N}(^2\text{D})$  and places important constraints on the possible atmospheric sources of  $\text{N}(^2\text{D})$  (21). The 5200 Å dayglow measurements were made at White Sands on April 7, 1964 with a solar zenith angle,  $\chi \sim 72^\circ$ . For the Jacchia (1971) model atmosphere, we illustrate theoretical 5200 Å emission rate profiles as a function of  $A$  and  $k$  and compare these with the rocket measurements in Figure 7. The lower limit on  $A$  is 0.5, while the upper limits on  $A$  and  $k$  are 1.0 and  $10^{-13} \text{ cm}^3 \text{ sec}^{-1}$ , respectively. If the Jacchia (1965) model atmosphere were appropriate, then the observed 5200 Å emission profile would only be consistent with a theoretical model where  $A=1.0$  and  $k \leq 10^{-13} \text{ cm}^3 \text{ sec}^{-1}$ . This model atmosphere is

rich in  $\text{O}_2$  and requires a large production of  $\text{N}(^2\text{D})$  to balance the enhanced  $\text{N}(^2\text{D})$  loss through reaction with  $\text{O}_2$ . For either model atmosphere, the calculated electron densities are in good agreement with the ionosonde data taken during the rocket observation.

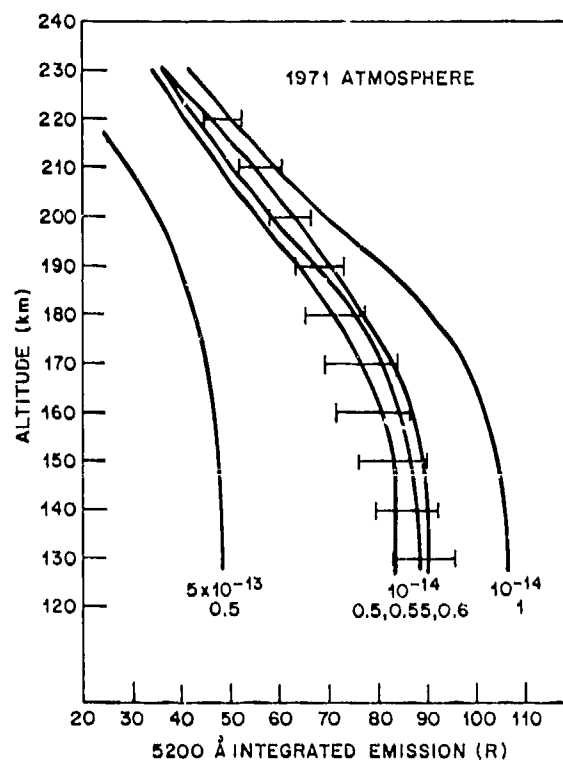


Figure (7). Comparison of the integrated 5200 Å emission from  $\text{N}(^2\text{D})$  measured by Wallace and McElroy [1966] (horizontal bars) with model calculations for the Jacchia [1971] model atmosphere and selected values of  $A$  and  $k$  (the lower and upper numbers, respectively).

With the above constraints on  $A$  and  $k$  from 5200 Å dayglow measurements, we can now determine the appropriate values of those parameters which are consistent with the measurements of fluorescence of the  $\gamma(1,0)$  band. The  $g$  factor relates the integrated  $\gamma(1,0)$  band emission profile to the  $\text{NO}$  column density. Pearce (24) included the rotational structure of the band and the variation of the solar flux intensity within the band in his calculation of the  $g$  factor and obtained  $3.93 \times 10^{-6} \text{ photons sec}^{-1}$ . Witt (25) suggests that this is an underestimate. Using the relative intensities measured by Poland and Broda (26), we estimate  $g$  to be  $7.7 \times 10^{-6} \text{ photons sec}^{-1}$ . For comparison of our theoretical models with experimental data, we adopt a range of  $(4-7) \times 10^{-6} \text{ photons sec}^{-1}$ .

The Meira (19) dayglow observations of

Figure 1 is a graph showing the relationship between Altitude (km) and Electron Density ( $\text{cm}^{-3}$ ) for the F2 layer of the ionosphere. The Y-axis represents Altitude (km), ranging from 60 to 160. The X-axis represents Electron Density ( $\text{cm}^{-3}$ ), ranging from  $10^0$  to  $10^6$  on a logarithmic scale. Three data series are plotted:

- Solid line: 6 FEB 69
- Dashed line: 31 JAN 69
- Line with diamond markers: CALCULATION FOR JAN, 31 (0.55,  $10^{-14}$ , 1971)

The graph illustrates the variation of electron density with altitude for the F2 layer. The solid line (6 FEB 69) shows the highest electron density at high altitudes, while the dashed line (31 JAN 69) shows the lowest. The calculation curve (0.55,  $10^{-14}$ , 1971) lies between the two observed curves.

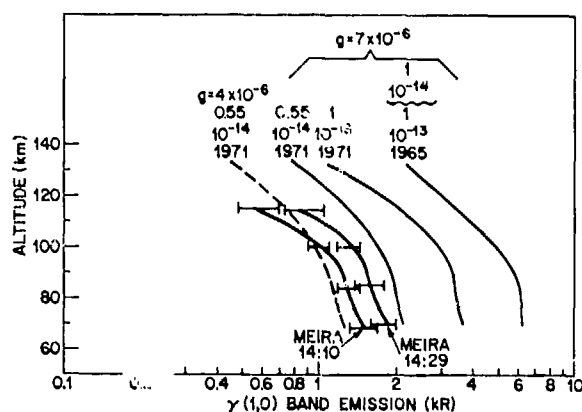


Figure (8). Comparison of the integrated NOY(1,0) band emission measured by Meira [1971] with model calculations for selected values of A, k, and indicated g factor. The model atmospheres are Jacchia [1971] and Jacchia [1965] denoted by 1971 and 1965, respectively.

Electron density measurements in the D-region by Mechtly(27) supplemented by ionosonde data for the E-region taken during the Meira dayglow observations are compared with the best fit theoretical model in Figure 9.

Another rocket observation of fluorescence in the NO( $\gamma$ ) band was made by Tisone (20) at sunrise and is representative of summer and medium solar activity conditions. In Figure 10 the theoretical model consistent with the other odd nitrogen data is compared with the Tisone data.

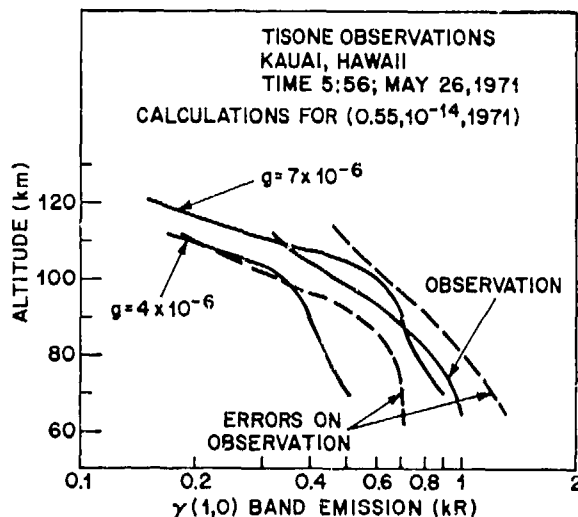
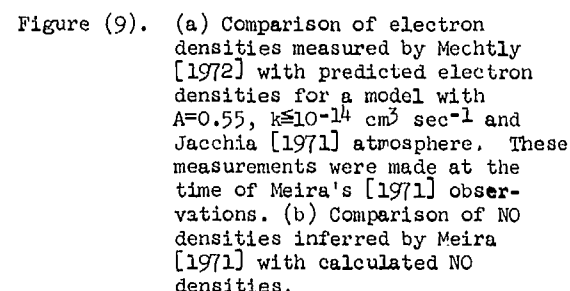


Figure (10). Production rates of  $N(^2D)$  appropriate for Meira's [1971] observations. Solar zenith angle  $\sim 62^\circ$  and same parameters as Figure 9.



An important stimulus for this work was the recent rocket measurement by Feldman and Takacs(22) of the NO twilight emission in the  $\gamma$  and  $\delta$  bands above 100 km. The only plausible mechanism for excitation of these bands is the chemiluminescent, preassociation reaction of N and O atoms. In addition, fluorescence in the  $\gamma(1,0)$  band of NO was observed. The most accurate rate coefficient measured for this chemiluminescent reaction is for the production of the  $\delta(0,0)$  band emission. The measured  $\delta(0,0)$  band intensity was  $(58 \pm 12)$  R at 140 km. A theoretical calculation with the best fit parameters,  $A=0.55$ ,  $k \leq 10^{-14}$  cm<sup>3</sup> sec<sup>-1</sup>, and the Jacchia (1971) model atmosphere predicts 28 R at 140 km. Feldman has noted that the atmospheric attenuation of the LBH bands emission measured on the same flight requires .8 of the O<sub>2</sub> densities predicted by the Jacchia 71 atmosphere. This rocket flight was made in January 1974. The analysis of Roble and Norton (28) suggest that low O<sub>2</sub> concentrations are characteristic of the winter thermosphere. A theoretical calculation with reduced O<sub>2</sub> density in the atmosphere predicts 38 R of  $\delta(0,0)$  band emission at 140 km, in better agreement with the Feldman and Takacs data. The predicted altitude profile of the  $\delta$ - and  $\gamma$ - bands emission agrees well with the experimental profile.

Our atmospheric analysis of the odd nitrogen data required the Jacchia (1971) model atmosphere. The atmospheric values of A and k are consistent with our theoretical estimates for the molecular processes. The uncertainties in the composition of the atmosphere naturally introduce uncertainties in our derived values for A and k. For example, an underestimate in the O<sub>2</sub> content results in an underestimate for A, while a lower O content would increase the upper limit on N(<sup>2</sup>D) quenching by O. An uncertainty in the radiative lifetime of N(<sup>2</sup>D) would primarily affect 5200 Å emission data and could, in principle, be compensated for in our model by a suitable adjustment in the model atmosphere. With O<sub>2</sub> the major quencher of N(<sup>2</sup>D), the seasonal variability of [O<sub>2</sub>] by a factor of 3 deduced by Roble and Norton suggests a comparable variability in the integrated 5200 Å emission rate. The seasonal variation of N(<sup>1</sup>S) and NO is expected to be larger than we predict. Our analysis of the Meira and Tisone data required approximately the same O<sub>2</sub> concentrations although our fit to the Meira data could be considerably improved with lower O<sub>2</sub> concentrations for  $S=7 \times 10^{-6}$  sec<sup>-1</sup>.

#### CONCLUDING REMARKS

We have given a brief summary of the physical and chemical processes in the NRL 1-D mid-latitude model of the ionosphere. To show the validity of the model, a number of studies have been presented in which our theoretical calculations were compared with

available observational data. Calculated electron densities are in good agreement with results of rocket and ionosonde measurements made at a variety of locations and times.

From the aeronomical studies we have made with the model, we conclude that in order to understand as well as predict the behavior and structure of the ionosphere, an equivalent understanding of the neutral atmosphere is required. The ion composition and NO concentrations are sensitive to the [O]/[O<sub>2</sub>] ratio in the lower thermosphere. Complex wind systems generated by the neutral atmosphere transport ionization and control the ion density profiles in the nighttime lower ionosphere. These wind systems also influence the distribution of [NO]. If the ionosphere is to be properly modelled, more realistic model neutral atmospheres and associated wind systems must be developed. This work was sponsored by ONR and NAVAIR.

#### REFERENCES

- (1). E. S. Oran, T. R. Young, D. V. Anderson, T. P. Coffey, P. C. Kepple, A. W. Ali, and D. F. Strobel, A Numerical Model of the Mid-Latitude Ionosphere, Naval Res. Lab., Memorandum Report #2839, 1974.
- (2). B. K. Ching and Y. T. Chiu, A Phenomenological Model of Global Ionospheric Electron Density in the E-, F1- and F2-Regions, *J. Atmos. Terr. Phys.*, **35**, 1615, 1973.
- (3). W. E. Swartz, J. L. Rohrbaugh and J. S. Nisbet, A Thermospheric Model from Satellite Orbital Decay Densities and Incoherent Scatter Temperatures, *J. Atmos. Terr. Phys.*, **34**, 1817, 1972.
- (4). Peter Stubbe, Simultaneous Solution of the Time Dependent Coupled Continuity Equations, Heat Conduction Equations, and Equations of Motion for a System Consisting of a Neutral Gas, and Electron Gas, and a Four Component Ion Gas, *J. Atmos. Terr. Phys.*, **32**, 1970.
- (5). D. F. Strobel, and M. B. McElroy, The F2-Layer at Middle Latitudes, *Planet. Space Sci.*, **18**, 1181, 1970.
- (6). L. G. Jacchia, Static Diffusion Models of the Upper Atmosphere with Empirical Temperature Profiles, *Smithson. Contr. Astrophys.*, **8**, 215, 1965.
- (7). L. G. Jacchia, Revised Static Models of the Thermosphere and Exosphere with Empirical Temperature Profiles, Spec. Rep. 332, *Smithson. Astrophys. Observ.*, Cambridge, Mass., 1971.
- (8). *CIRA 1965*, North-Holland Publishing Company, Amsterdam, 1965.

- (9). H. E. Hinteregger, The Extreme Ultra-violet Solar Spectrum and Its Variation During Solar Cycle, Ann. Geophys., 26, 547-554, 1970.
- (10). A. W. Ali and P. C. Kepple, Solar Ionization Rates for the Ionospheric E, F, and D-Regions, NRL Report 7598, Naval Research Laboratory, Washington, D. C., 1973.
- (11). J. M. Burgers, Flow Equations for Composite Gases, pg. 74, Academic Press, 1969.
- (12). Henry Rishbeth and Owen K. Garriott, Introduction to Ionospheric Physics, Academic Press, New York, 1969, pg. 213.
- (13). D. F. Strobel, T. R. Young, R. R. Meier, T. P. Coffey, and A. W. Ali, The Night-time Ionosphere: E-Region and Lower F-Region, J. Geophys. Res., 79, 1974, 3171.
- (14). E. S. Oran, P. S. Julianne, and D. F. Strobel, Odd Nitrogen in the Thermosphere, submitted to J. Geophys. Res., 1974.
- (15). P. Stubbe, The Influence of Neutral Winds on the  $\text{NO}^+$  and  $\text{O}_2^+$  Densities in the Lower Ionosphere at Night, J. Atmos. Terr. Phys., 34, 510, 1972.
- (16). J. V. Evans, Midlatitude F-Region Densities and Temperatures at Sunspot Minimum, Planet. Space Sci., 15, 1387, 1967.
- (17). J. C. Holmes, C. Y. Johnson, and J. M. Young, Ionospheric Chemistry, Space Research V, edited by D. G. King-Hele, P. Muller, and G. Righini, North Holland Pub. Co., Amsterdam, 756, 1965.
- (18). C. A. Barth, Nitric Oxide in the Upper Atmosphere, Ann. Geophys., 22, 198, 1966.
- (19). L. G. Meira, Jr., Rocket Measurements of Upper Atmospheric Nitric Oxide and Their Consequences to the Lower Ionosphere, J. Geophys. Res., 76, 202, 1971.
- (20). G. C. Tisone, Measurements of NO Densities during Sunrise at Kauai, J. Geophys. Res., 78, 746, 1973.
- (21). L. Wallace and M. B. McElroy, The Visual Dayglow, Planet. Space Sci., 14, 677, 1966.
- (22). P. D. Feldman and Peter Z. Takacs, Nitric Oxide Gamma and Delta Band Emission at Twilight, Geophys. Res. Letters, 1, 169, 1974.
- (23). D. F. Strobel, Nitric Oxide in the D-Region, J. Geophys. Res. 77, 1337-1339, 1972b.
- (24). J. B. Pearce, Rocket Measurements of Nitric Oxide Between 60 and 96 Kilometers, J. Geophys. Res., 74, 853, 1969a.
- (25). G. Witt, Private Communication, 1974.
- (26). H. M. Poland and H. P. Broida, Fluorescence of the Y,  $\epsilon$ , and  $\delta$  systems of Nitric Oxide, Polarization and Use of Calculated Intensities for Spectrometer Calibration, J. Quant. Spectrosc. Rad. Transfer, 11, 1861, 1971.
- (27). F. A. Mechty, S. A. Bowhill, and L. G. Smith, Changes of Lower Ionosphere Electron Concentrations with Solar Activity, J. Atmos. Terr. Phys., 34, 1899, 1972.
- (28). R. G. Roble and R. B. Norton, Thermospheric Molecular Oxygen from Solar Extreme-Ultraviolet Occultation Measurements, J. Geophys. Res., 77, 3524, 1972.
- (29). J. C. G. Walker, Analytic Representation of Upper Atmosphere Densities Based on Jacchia's Static Diffusion Models, J. Atmos. Sci., 22, 462, 1965.

## HIGH-LATITUDE IONOSPHERIC AURORAL MODELS

J. A. Fedder, J. H. Orens, and T. P. Coffey

U. S. Naval Research Laboratory, Washington, D. C. 20375

### I. INTRODUCTION

The irregular and complex behavior of the earth's high-latitude ionosphere presents unique and difficult problems for radio communications. This behavior arises primarily owing to two different but related phenomena. The first is the precipitation of energetic particles of magnetospheric origin into the high-latitude atmosphere. The second is the penetration of magnetospheric electric fields and currents into the auroral and polar ionosphere. At present neither of these phenomena are completely understood and therefore their occurrence and their effects on communications are not predictable except in a most elementary and general way. One of the aims of current, on going, modeling efforts at the Naval Research Laboratory (NRL) is to improve the physical description of these high latitude phenomena and thereby to improve the predictability of their effects on communications.

The precipitation of energetic particles, the aurora, can lead to disruption or degradation of communications either by causing absorption of the signal or by distorting the signal path (both path length and angular deviations). Signal absorption can occur during Polar Cap Absorption events and during Auroral Absorption events which are caused by greatly enhanced D region ionization owing to very energetic particle precipitation. Path distortion can be caused by a large increase in the total ionization content of the ionosphere owing to auroral precipitation. The NRL modeling effort for auroral particle effects is described in a number of reports concerning electron precipitation [Strickland and Kepple, 1974; Strickland et. al., 1974], proton precipitation [Rogerson and Davis, 1974], and auroral ionospheric chemistry [Hymen and     , 1974].

The penetration of the magnetospheric convection electric field and associated currents into the high latitude ionosphere can effect communications in two ways. The convective field transports ionospheric plasma perpendicular to the geomagnetic field and thereby affects the distribution of the ionospheric plasma content. It also sets up conditions which are subject to plasma instabilities.

The instabilities result in plasma density inhomogeneities and communication signal scintillation. In order to predict these effects it is necessary to develop models for the convective field in the auroral regions. One such model developed at NRL is the subject of this paper.

The theory of magnetospheric convection was developed by Axford and Hines [1961] to explain the magnetic disturbances caused by ionospheric currents in the polar regions of the ionosphere. A review of this theory and further developments is presented by Axford [1969]. Subsequent to the presentation of this theory numerous papers [Karlson, 1963, 1971; Block, 1966; Iwasaki and Nishida, 1967; Vasylunas, 1970, 1971; Swift, 1971; Wolf, 1970; Matsushita, 1971; and Jaggi and Wolf, 1973] have presented models for the large scale convective flow in the ionosphere and magnetosphere. There have also been a number of models Bostrom, 1964; Atkinson, 1970; Holzer and Sato, 1973; Sato and Holzer, 1973; Coroniti and Kennel, 1972;] which describe convective flow in the auroral oval and in auroral arcs. All of these models show certain features which agree with the observed convection pattern but in general fail to show other observed features which need explanation.

The NRL model is predicated on a different assumption than most of those referred to above. The assumption is that large geomagnetic field-aligned potential differences can exist between the ionosphere and the magnetosphere and that these can result in different convective patterns in the ionosphere and magnetosphere. We think that the agreement between our results (described in more detail in Fedder [1974] and Fedder and Orens [1974a,b]) and the available data for currents and flow patterns, and the recent auroral particle evidence [Arnoldy, 1974] reaffirms this assumption.

### II. MATHEMATICAL FORMULATION

The three dimensional mathematical model for the ionospheric plasma density, currents, and electric field is comprised of the following:

the plasma continuity equation

$$\frac{\partial n}{\partial t} = -\frac{\partial}{\partial x} n v_x - \frac{\partial}{\partial y} n v_y + P - \alpha n^2,$$

the ion momentum equations

$$v_x = v_p E_x - v_h E_y,$$

$$v_y = v_p E_y + v_h E_x,$$

the ionospheric current continuity equations

$$\frac{\partial}{\partial z} j_{||} = -\frac{\partial}{\partial x} j_x - \frac{\partial}{\partial y} j_y,$$

the horizontal current equations

$$j_x = qn (v_x - v_x^e),$$

$$j_y = qn (v_y - v_y^e),$$

the electron velocity equations

$$v_x^e = -\frac{cE_y}{B} \text{ and } v_y^e = \frac{cE_x}{B},$$

the electric field equation

$$\underline{E} = -\nabla \psi,$$

and the electric potential equation

$$\psi = \psi_m + J_{||} R.$$

Here  $n \equiv$  plasma density,  
 $v_x, v_y \equiv$  ion velocity components,  
 $E_x, E_y \equiv$  ionospheric electric field components,  
 $v_p, v_h \equiv$  ion Pedersen and Hall mobilities,  
 $P \equiv$  assumed ionospheric plasma production,  
 $\alpha \equiv$  assumed ionospheric plasma loss rate,  
 $j_x, j_y \equiv$  ionospheric horizontal current density,  
 $c \equiv$  speed of light  
 $B \equiv$  the geomagnetic field strength (in the negative  $z$  direction),  
 $q \equiv$  electron unit charge,  
 $v_x^e, v_y^e \equiv$  electron velocity components,  
 $J_{||} \equiv j_{||}$  at top of ionosphere (here 200km),  
 $\psi \equiv$  ionospheric electric potential,  
 $\psi_m \equiv$  assumed magnetospheric potential,  
 $R \equiv$  assumed anomalous resistance to  $J_{||}$ .

The above set of equations and definitions form a complete set which can be solved simultaneously for the ionospheric plasma density, the electric field, and the ionospheric current systems with a proper set of assumptions.

In the following sections results of such calculations are presented for individual auroral arcs and also for the midnight region of the auroral oval. A complete discussion

of the assumed variables which lead to these results is given in Fedder [1974] and in Fedder and Orens [1974a]. It suffices to say here, that the assumptions are based on measured auroral data and are within the range of reasonably expected values.

### III. RESULTS FOR AURORAL ARCS

The results of model calculations for auroral arcs are shown in Figures 1, 2 and 3. For these calculations the auroral arc was assumed to be aligned in the  $y$ -direction with all variables uniform along  $y$ . The magnetospheric electric field was chosen perpendicular to the arc.

Figure 1 presents the field-aligned Birkeland, current density and the electric field results:

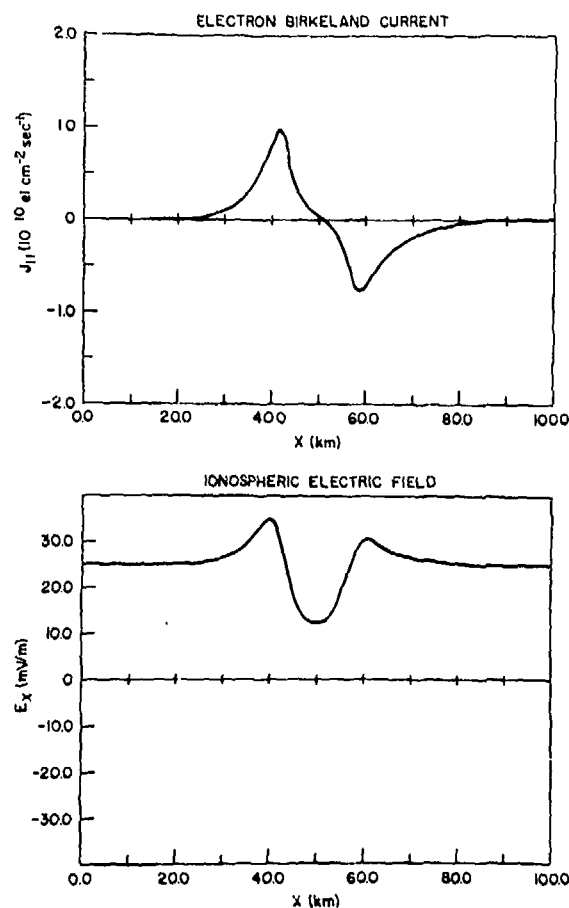


Figure 1. Auroral arc Birkeland current density and electric field results. For this calculation the arc is about 15km wide and is centered at  $x = 50$ km. The magnetospheric electric field is a constant  $25 \text{ mV m}^{-1}$  in the  $x$ -direction.

Figure 2 presents the plasma density and the electrojet current density ( $y$ -directed) for one example of auroral arc. The Birkeland

current is large at the edges of the arc and small in the center where the field-aligned resistance, which was assumed proportional to the auroral plasma production, is large. The electric field shows the result of polarization of the arc owing to a field-aligned potential.

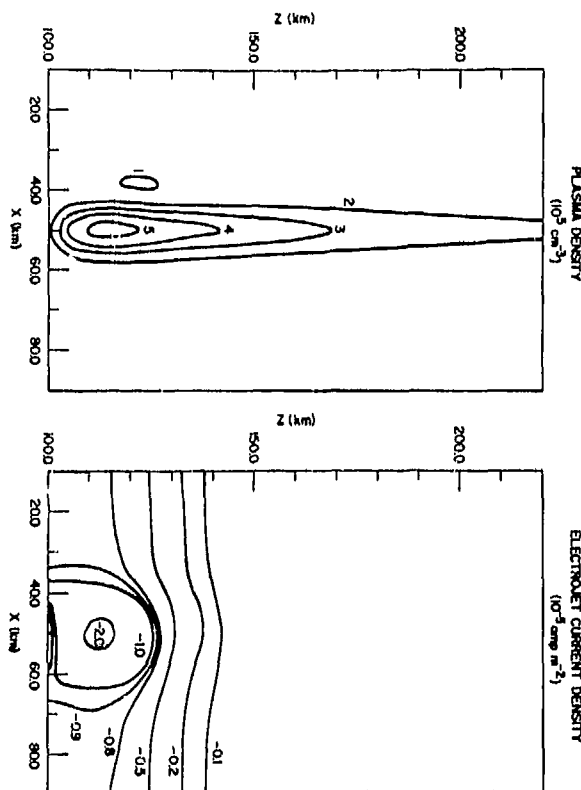


Figure 2. Auroral arc plasma density and electrojet current density results. Note the slight distortion of the plasma density contours in the positive x-direction owing to transport in the Pedersen conducting region, 120-130km. Also see that the electrojet current, in the negative y-direction, takes place over a considerably wider region than the auroral plasma density enhancement. The broader electrojet region is caused by the enhanced electric field at the edges of the arc.

The ionospheric electric field is enhanced, relative to the magnetospheric field, at the sides of the arc and is reduced in the center. For this result the magnetospheric electric field was taken to be a constant  $25 \text{ mV m}^{-1}$ . This type of polarization is typical in all model results to date. The plasma density contours show primarily the effect of the assumed plasma production and recombination rates. However they are slightly distorted, to the right, in the Pedersen conducting region, 120-130km altitude, owing to the horizontal transport of ions. In cases where the magnetospheric electric field is parallel to

the auroral arc, in the y direction, the effects of horizontal transport on the plasma density is much more pronounced [see Fedder, 1974]. The electrojet current density contours show that the arc electrojet is enhanced over a broader region than is the auroral plasma density. This result occurs owing to the enhanced polarization electric field at the edges of the arc. The Birkeland current and electrojet current densities are similar to measured results [Park and Cloutier, 1971].

In Figure 3, a direct comparison is made between a model electric field result and a measured auroral electric field [Maynard et al. 1973]. For the comparison, the measured field was reduced by a factor of 2. One can see that the agreement is remarkable considering the uncertainties, for all the assumed parameters of the model, for which measurements were not made. Additional studies [Fedder, 1974; Fedder and Orens, 1974b] have demonstrated

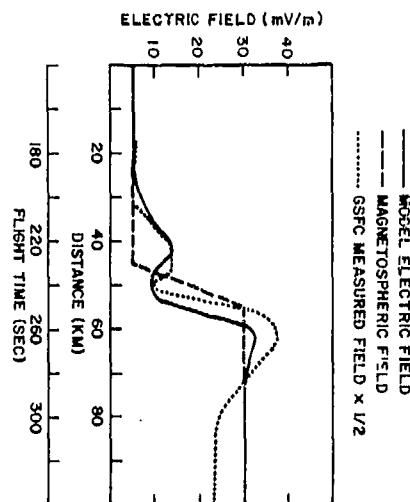


Figure 3. Model arc electric field results compared to measured arc electric field of Maynard et al. [1973]. The solid line shows the model result for the assumed magnetospheric electric field, dashed line. The dotted line shows the measured electric field reduced by a factor of 2.

that the degree and the nature of the electric polarization of an auroral arc depends primarily on the plasma production rate, the magnetospheric electric field, and the magnitude of the resistance to the Birkeland current. Given these parameters, the spatial distribution of the Birkeland current depends only on the spatial distribution of the resistance function.

#### IV. RESULTS FOR THE AURORAL OVAL

The results of model calculations for the midnight region of the auroral oval are shown in Figures 4, 5, 6, and 7. The geometry used

for the northern midnight oval is shown in Figure 4, from above the ionosphere. The x-axis is west-east; the y-axis is north-south.

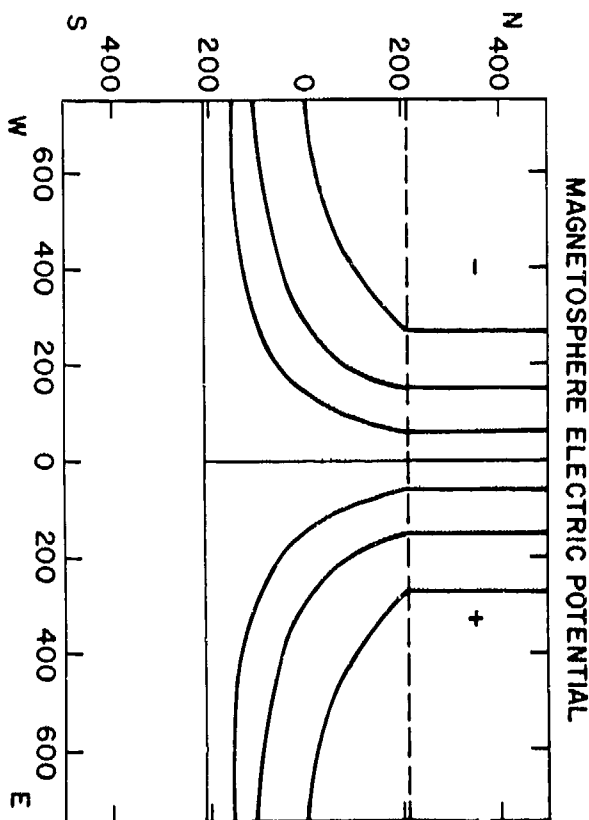


**Figure 4.** This figure shows the model auroral oval geometry and the magnetosphere convection pattern mapped on the ionosphere. The dashed line across the upper part of the figure and the solid line across the lower part are the poleward and equatorward boundaries of the oval, respectively. The position (0,0) is midnight center of the auroral oval. The convective flow is toward the oval from above ( $25\text{mV}\text{m}^{-1}$  electric field from right to left), dividing equally to the left and right of midnight to return to the day side through the oval. The equipotentials (flow lines) are not equally spaced but are concentrated toward midnight to show more detail there.

Directions are indicated by the capital letters N, S, E, and W. The east-west dashed line in the upper portion of the drawing is the northern border of the oval; the solid east-west line below it is the southern border. The assumed magnetospheric convective flow lines mapped on the ionosphere, are also shown in Figure 4. The flow is southward, corresponding to a dawn to dusk electric field of  $25\text{mV}\text{m}^{-1}$ , in the polar cap. It crosses the northern boundary of the oval, dividing on either side of midnight to return to the dayside along

the oval. The model uses this magnetospheric convective field along with an auroral ionization production rate which yields; an auroral oval to ambient Pedersen conductivity ratio of 10:1 and an auroral Hall to Pedersen conductivity ratio of 2.5:1, ratios which are typical of a moderately disturbed auroral region; to calculate the ionospheric convective flow, the auroral Birkeland currents, the auroral oval horizontal currents, and the three dimensional plasma densities.

Figure 5 shows the resulting ionospheric convective flow pattern in the midnight auroral oval. The difference between this pattern and that shown in Figure 4 is caused by a field-aligned potential between the magnetosphere and the ionosphere. The most important feature of the pattern is the westward shift of the east-west convective discontinuity before midnight (the point  $x = 0, y = 0$  is midnight center of the oval). This pattern shows great similarity to the experimental pattern inferred by Heppner [1972] and Maynard [1974].

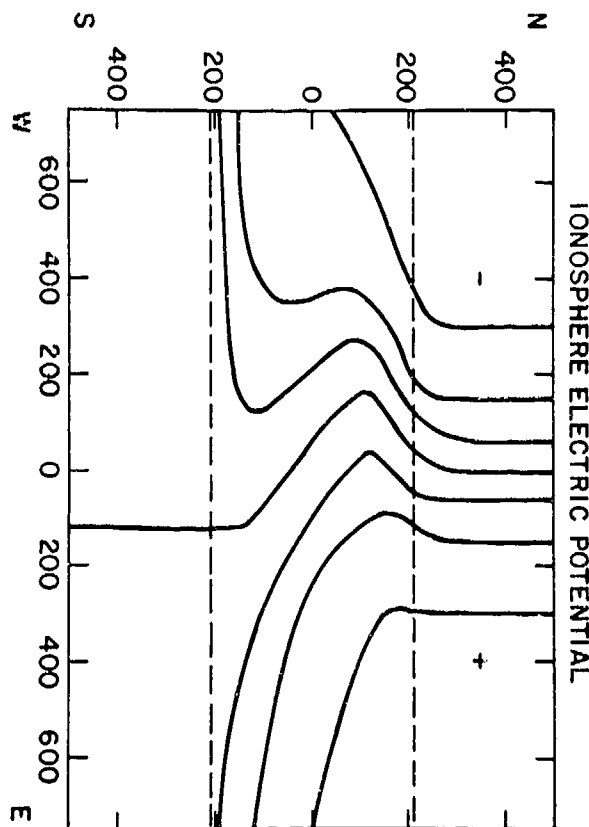


**Figure 5.** The ionospheric convection pattern which results from polarization of the auroral oval and the field-aligned potential drops. Note the westward shift of the east-west convective (Harang) discontinuity. Also note the multiple reversals to the west of midnight.

The result of this change in the ionospheric convection is to considerably modify the auroral electric fields. Electric fields derived from this pattern also show considerable resemblance to measured data as is discussed in Fedder and Orens [1974a].

The Birkeland current density results of the model calculation are shown in Figure 6.

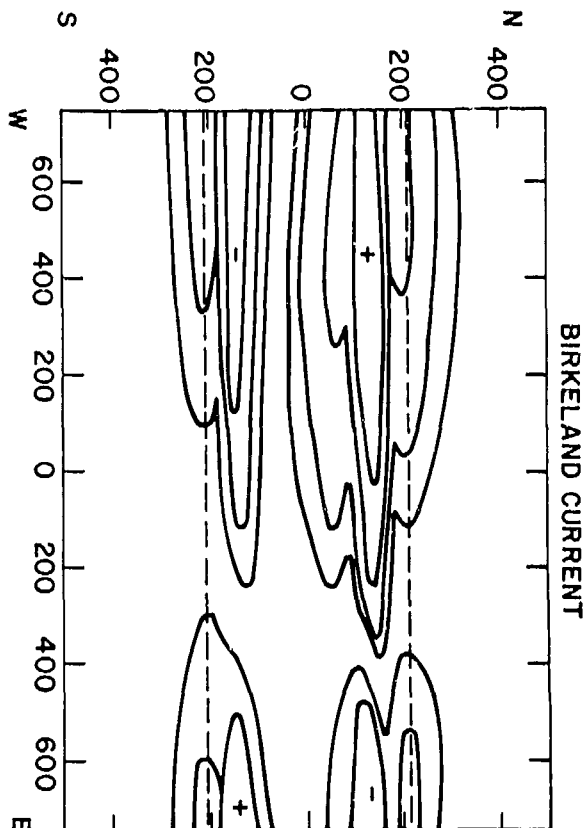


**Figure 6.** Birkeland current system in midnight auroral oval. Plus signs signify current out of the ionosphere. The currents flow in sheet-like structures at the edge of the oval. In the evening sector it is out of the northern border, into the southern and it reverses sense in the morning sector. The current density in the central contour of the northern evening sheet is  $3 \times 10^9$  el.  $\text{cm}^{-2} \text{sec}^{-1}$ ; each exceeding outward contour is reduced by a factor of 2. Because of our assumption of a constant spatially uniform resistance to the field-aligned current, the contours are also equipotentials between the magnetosphere and ionosphere. The potential difference within the northern evening contours is greater than 3 kilovolts and is oriented so as to accelerate electrons into the ionosphere.

The Birkeland current occurs in east-west aligned sheets. It is "out of" the ionosphere at the northern border of the oval

west of midnight and at the southern border east of midnight. The "into" current occurs at the northern border east of midnight and at the southern border to the west. This characteristic pattern is the same as that observed by Zmuda and Armstrong [1974]. The largest amplitude current is "out of" the ionosphere at the northern edge of the oval west of midnight, and this current sheet serves to close the eastward and westward auroral electrojets. This strong current region also agrees with the nightside portion of the field-aligned current system proposed by Heppner et al. [1971] to explain the magnetic perturbation in the polar cap.

Because a uniform field-aligned resistance has been chosen for this study, Figure 6 also shows the distribution of the field-aligned potential between the magnetosphere and the ionosphere. The potential difference in the northern evening region is greater than three kilovolts and is directed so as to accelerate precipitating electrons into the ionosphere. In the other regions the largest potential is over a factor of 2 smaller. We would associate the pre-midnight upward directed potential and precipitating electron current with the "inverted-V" particle events reported by Frank and Akerson [1972], and references therein. The magnitude of the potential is similar to particle energies. Additionally, the pattern and location of the potential and the occurrence of "inverted-V" events are quite similar.

Figure 7 is a contour map of the auroral electrojet current which results from the model. The extension of the westward electrojet to the west of midnight is an observed feature of the westward jet which has been recognized from geomagnetic data [Harang, 1946; Heppner, 1972]. The overlap of the eastward and westward electrojets in the southern portion of the auroral oval has also been observed. For this calculation the current caused by the westward electrojet is about 300,000 amperes, which value is typical of moderate auroral disturbances. In the region to the west of midnight where the eastward and westward electrojets meet, there is a strong northward current (not shown in Figure 7), which closes the electrojet system to the very strong northern Birkeland current sheet.

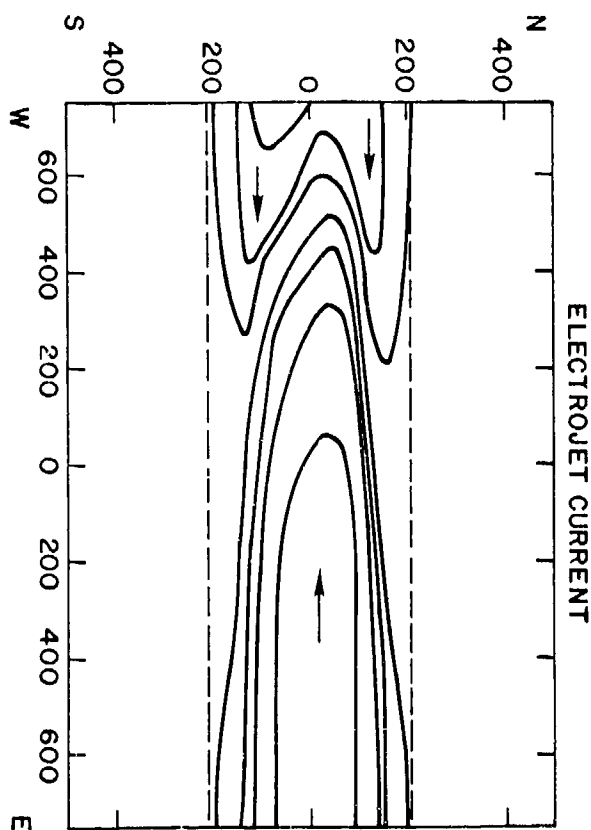


Figure 7. The electrojet system in the midnight sector of the auroral oval showing both the eastward and westward jets (arrows show direction). Note the extension of the westward jet to the west of midnight. Also note the overlap of the eastward and westward jets in the southern evening region. The central contour in the westward electrojet is  $133 \text{ amp km}^{-1}$  height-integrated current density. Consecutive contours outward are each reduced a factor of 2.

#### V. DISCUSSION

In the preceding sections we have shown and discussed auroral model results for both individual arcs and for the auroral oval. These results have shown how field-aligned potentials and the resultant polarization of the aurora affects the ionospheric electric fields and currents. The auroral model results have also been shown to have a considerable resemblance to the available measurements of auroral electric fields and current systems. In view of the above, it would appear that these or similar results should be of use in the theoretical investigation of naturally occurring plasma instabilities and their formation of high latitude ionospheric irregularities.

It is known that electrostatic plasma instabilities are responsible for the E-region

electrojet irregularities [Farley, 1974]. Recent nonlinear numerical simulations [Ossakow, 1974] have explained many of the measured features of these E-region irregularities. It is also indicated the same or similar mechanisms may lead to F region irregularities [Scannapieco et al., 1974] and the resultant scintillation phenomena. The study of plasma clouds and their coupling with the background ionosphere has also demonstrated the role of electrostatic plasma instabilities in creating plasma irregularities in the ionosphere [Ossakow et al., 1975]. Since the investigation of all these phenomena requires a detailed knowledge of plasma densities and the ionospheric electrostatic field, model results such as those presented here should have application to high latitude irregularity studies.

In the case of high latitude E region irregularities, radar measurements [Balsley and Eckland, 1972] have shown the existence of at least three plasma instabilities associated with the auroral electrojet current system. Balsley and Eckland have tentatively identified two of these as the type I and type II instabilities which were first observed in the equatorial electrojet. These two instabilities have only recently been adequately explained in their nonlinear saturated state by numerical simulation. The numerical simulations [McDonald et al., 1975] require a detailed description of the background ionospheric state. Owing to the relatively simple two dimensional geometry of the equatorial electrojet, the background ionospheric parameters could be obtained by direct measurement. In the auroral electrojet the geometry is more complex, and owing to the rapid variation of the ionospheric parameters in time, direct measurements is difficult. It is possible that a better ionospheric description for numerical plasma instability simulations will be provided by auroral models sooner than by measurement.

A similar situation also occurs for F region irregularities in the high latitude ionosphere. The scintillation measurements of Aarons [1973] have shown the common occurrence of F region irregularities at high-latitudes. These irregularities have an occurrence pattern which shows boundaries [Aarons and Allen, 1971] which are similarly located to the boundaries in the ionospheric convective pattern and the auroral oval. In view of the above and the results of Scannapieco et al. (1974) which demonstrate the effect of the gradient-drift instability on F region irregularities, it appears that the convective flow of ionospheric plasma at high-latitudes is important for F region irregularity development and morphology. Thus models of convective flow and ionospheric plasma densities can be fundamental to developing physical models of high latitude communication signal scintillation.



The presently existing models of convection and aurora, like the one presented here, can only be considered a first step toward describing the auroral and polar ionospheres. Generally speaking, they are steady state descriptions of a system which is often rapidly changing in time. For instance, it is expected that during magnetic disturbances the field-aligned electromagnetic induction owing to the enhancement of the Birkeland currents should be at least as important as is the field-aligned resistance. We could also note that electromagnetic induction can be important for steady conditions as well since in certain regions of the auroral oval the magnetospheric convection must cross the Birkeland current system. The model is currently being modified to include time dependent and inductive effects. To date progress on these efforts is encouraging and we expect

considerable improvements in the model results in the near future, although we do not expect the qualitative nature of the results to change significantly. In the end we believe that it will be possible to model many of the convective changes which take place during magnetic substorm events.

In summary, we have presented a model for the plasma density, the electric fields, and the current systems in aurora and in the auroral ionosphere. We have shown that the model results are generally in agreement with the available data. These results and their comparison to the data give encouragement for further model development and improvement. The results of these model calculations have direct application to the study of plasma instabilities, their resultant ionospheric irregularities, and communication signal propagation in the high-latitude ionosphere.

- Aarons, J., A descriptive model of F layer high-latitude irregularities as shown by scintillation observations, J. Geophys. Res., 78, 7441, 1973.
- Aarons, J. and R. S. Allen, Scintillation boundary during quiet and disturbed magnetic conditions, J. Geophys. Res., 76, 170, 1971.
- Arnoldy, R. L., P. B. Lewis, and P. O. Iccason, Field-aligned auroral electron fluxes, J. Geophys. Res., 79, 4208, 1974.
- Atkinson, G., Auroral arcs: Result of the interaction of a dynamic magnetosphere with the ionosphere, J. Geophys. Res., 75, 4746, 1970.
- Axford, W. I., Magnetospheric convection, Rev. Geophys., 7, 421, 1969.
- Axford, W. I. and C. O. Hines, A unifying theory of high latitude geophysical phenomena and geomagnetic storms, Can. J. Phys., 39, 1433, 1961.
- Balsley, B. B. and W. L. Eckland, VHF power spectra of the radar aurora, J. Geophys. Res., 77, 4746, 1972.
- Block, L. P., On the distribution of electric fields in the magnetosphere, J. Geophys. Res., 71, 855, 1966.
- Bostrom, R., A model of the auroral electrojets, J. Geophys. Res., 69, 4983, 1964.
- Coroniti, F. V. and C. F. Kennel, Polarization of the auroral electrojet, J. Geophys. Res., 77, 2835, 1972.
- Farley, D. T., Irregularities in the equatorial ionosphere: The Barkner Symposium, Rev. Geophys., 12, 285, 1974.
- Fedder, J. A., An ionospheric model for currents, the electric field, and the plasma density in an auroral arc, NRL Memo. Rept. 2691, 1974 (to be published J. Geophys. Res.).
- Fedder, J. A. and J. H. Orens, Ionospheric convection in the midnight auroral oval, (submitted to J. Geophys. Res.) 1974a.
- Fedder, J. A. and J. H. Orens, Auroral Birkeland currents and anomalous resistance, NRL Memo. Rept. in preparation, 1974b.
- Frank, L. A. and K. L. Ackerson, Local-time survey of plasma at low altitudes over the auroral zone, J. Geophys. Res., 77, 4116, 1972.
- harang, L., The mean field of disturbance of polar geomagnetic storms, Terr. Mag. Atmos. Elec., 51, 353, 1946.
- Heppner, J. P., The Harang discontinuity in auroral belt ionospheric currents, Geophys. Publ., 29, 105, 1972.
- Heppner, J. P., J. D. Stolarik, and E. M. Wescott, Electric-field measurements and the identification of currents causing magnetic disturbance in the polar cap, J. Geophys. Res., 76, 6028, 1971.
- Holzer, T. E. and T. Sato, Quiet auroral arcs and electrodynamic coupling between the ionosphere and the magnetosphere, 2., J. Geophys. Res., 78, 7330, 1973.
- Hyman, E. and P. Julienne, Aurora in an NRL auroral chemistry code, NRL Memo. Rept. in preparation, 1974.
- Iwasaki, N. and A. Nishida, Ionospheric current system produced by an external electric field in the polar cap, Rep. Ionos. Space Res., Japan, 21, 17, 1967.
- Jaggi, R. K. and R. A. Wolf, Self consistent calculations of the motion of a sheet of ions in the magnetosphere, J. Geophys. Res., 78, 2852, 1973.
- Karlson, E. T., Plasma flow in the magnetosphere, 1, a 2-dimensional model of stationary flow, Cosmic. Electrodyn., 1, 474, 1971.
- Karlson, E. T., Streaming of a plasma through a magnetic dipole field, Phys. Fluids, 6, 708, 1963.
- Matsushita, S., Interactions between the ionosphere and magnetosphere and S<sub>q</sub> and L variations, Radio Sci., 6, 279, 1971.
- Maynard, N. C., Electric field measurements across the Harang discontinuity, J. Geophys. Res., 79, 4620, 1974.
- Maynard, N. C., A. Bahnsen, P. Christophersen, A. Egeland, and R. Lundin, An example of anticorrelation of auroral particles and electric fields, J. Geophys. Res., 78, 3976, 1973.
- McDonald, B. E., T. P. Coffey, S. L. Ossakow, R. M. Sudan, A. J. Scannapieco, and S. R. Goldman, Recent results from theoretical and numerical modeling of E and F region irregularities, Ionospheric Effects Symposium, Washington, D. C., 1975.
- Ossakow, S. L., Research at NRL on theoretical and numerical simulation studies of ionospheric irregularities, NRL Reports of Progress, 1974.
- Ossakow, S. L., A. J. Scannapieco, S. R. Goldman, D. L. Book, and B. E. McDonald, Theoretical and numerical simulation studies of ionospheric inhomogeneities produced by plasma clouds, Ionospheric Effects Symposium, Washington, D. C., 1975.

Rogerson, J. E. and J. Davis, Preliminary report on a program to study proton deposition in the atmosphere, NRL Memo Rept., in preparation, 1974.

Sato, T. and T. E. Holzer, Quiet Auroral arcs and electrodynamic coupling between the ionosphere and the magnetosphere, 1., J. Geophys. Res., 78, 7314, 1973.

Scannapieco, A. J., S. L. Ossakow, D. L. Book, B. E. McDonald, and S. R. Goldman, Computer simulation of nonlinear mid-latitude spread F (abstract), EOS, 56, 1160, 1974.

Strickland, D. J., J. A. Fedder, and T. P. Coffey, The angular and energy distribution of kilovolt auroral electrons (abstract), EOS, 56, 1153, 1974.

Strickland, D. J. and P. C. Keppie, Preliminary report on the transport and production of energetic electrons in auroras, NRL Memo. Rept. 2772, 1974.

Swift, D. W., Possible mechanisms for formation of the ring current belt, J. Geophys. Res., 76, 2276, 1971.

Vasyliunas, V. M., The interrelationship of magnetospheric processes, in Earths Magnetospheric Processes, ed. by B. M. McCormac, D. Riedel, Dordrecht, Netherlands, 1971.

Vasyliunas, V. M., Mathematical models of magnetospheric convection and its coupling to the ionosphere, in Particles and Fields in the Magnetosphere, ed. by B. M. McCormac, D. Riedel, Dordrecht, Netherlands, 1970.

Wolf, R. A., Effects of ionospheric conductivity on convective flows of plasma in the magnetosphere, J. Geophys. Res., 75, 4677, 1970.

Zmuda, A. J. and J. C. Armstrong, The diurnal flow pattern of field-aligned currents, J. Geophys. Res., 79, 4611, 1974.

# COMPUTER SIMULATION OF EMBEDDED ELECTRICALLY SMALL SCATTERERS

G. Bakalyar, E. Ziemba  
Analytical Systems Engineering Corporation  
Burlington, Massachusetts

Most theory used to describe ionospherically generated scintillations assumes irregularities large compared to a wave length. This promotes a forward scatter limitation to the medium, a partial effect of which appears in the "filter function" generated for amplitude and phase scintillations. This report is concerned with the effects of electrically small scatterers which scatter isotropically. Such scatterers may exist embedded in larger scatterers and if there are enough of them, may contribute significant isotropically scattered power in addition to a forward scatter component. This condition can promote back-scattering (unpredicted for the large scatter) and a possibility of bistatic scattering in frequency regimes beyond the ionospheric penetrating frequencies. It may cause more power to be scattered into a wide beam antenna than a forward scattering medium would predict.

The ultimate objective of the analysis to follow is to generate volumetric regions containing smaller scatterers which are aligned along the magnetic field. The basis of the solution is to solve the scattering problem for a single field aligned array of scatterers - and then synthesize volumes from this "elementary" solution. It will be convenient therefore, to first briefly describe the geometry relating the propagation vector  $\vec{k}$  and the geometry of the scattering region and the observer. Next the derivation of the average power scattered from a single array is given and finally some results are given as derived from the computer program.

## BASIC GEOMETRY OF SCATTERING FROM ARRAYS

The basic coordinate system is

chosen so the X axis is parallel with some preferred direction (a magnetic field line). The other two axis are chosen conveniently to form a right hand system. XYZ.

A plane wave solution is undertaken, and the direction of the propagation vector  $\vec{k}$  forms the  $Z_0$  axis of an observer system  $X_0, Y_0, Z_0$  and also a propagation coordinate system defining the orientation of the E vector with respect to the array direction.

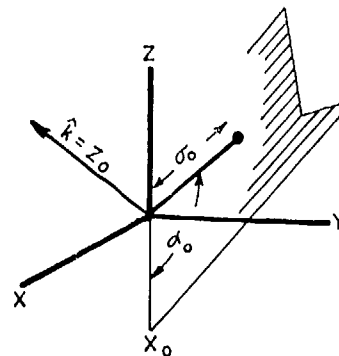


Figure 1: OBSERVER SYSTEM

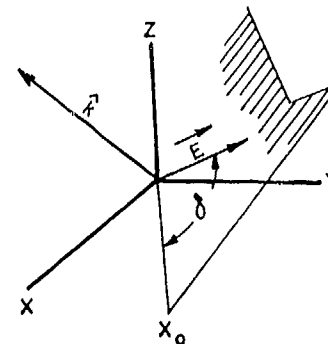


Figure 2: PROPAGATION SYSTEM

The coordinates  $\alpha_0, \sigma_0$  (lying in a plane normal to  $\vec{k}$ ) together with  $Z_0$  define position in the observer's system. The angle  $\delta$  in the plane normal to  $\vec{k}$  defines the direction of the E vector of the propagating wave.

The direction of an "elementary" array of scatters  $\hat{s}$  is taken as the  $Z_s$  axis of a scattering  $X_s, Y_s, Z_s$ . Normally  $\hat{s}=Z_s$  is taken parallel to X, the magnetic field direction.

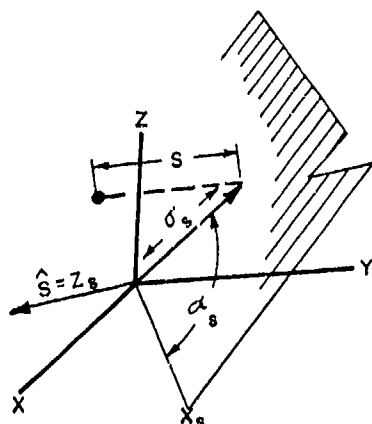


Figure 3: SCATTERING SYSTEM

The coordinates  $\alpha_s, \sigma_s$  lying in a plane normal to  $\hat{s}$  and the coordinate  $s$  parallel to  $\hat{s}=Z_s$ , determine the position of a scatterer in the system. Obviously  $\alpha_s, \sigma_s$ , define points of intersection of parallel bundles of arrays - hence volumetric regions are readily simulated.

The systems  $X_0, Y_0, Z_0$  and  $X_s, Y_s, Z_s$  are described in terms of the basic X, Y, Z system - to allow for arbitrary orientations of these systems and the vector  $\vec{E}$ .

#### POWER SCATTERED FROM AN ARRAY

The purpose here it to first describe the fields  $\vec{E}$  scattered from a linear array to an observer position  $\alpha_0, \sigma_0, Z_0$ , and then to estimate the average scattered power. The electrical size of scatterers is left arbitrary until the general expression for scattered power is derived. It is then seen that the results contain near field and for field implications. The significance of scatter size is readily noted relative to the near and far field - and finally the possibility of different frequency dependencies co-existing is noted.

Analysis begins, as for most weak scattering theory, with the first order Born approximation applied to a random medium. This provides an integral ex-

pression for the scattered field:

$$\vec{E}_s = \frac{k^2 E_0}{2\pi} \begin{bmatrix} A \\ B \\ C \end{bmatrix} \frac{e^{ik\sigma_0}}{\rho_0} \int N(s) \cdot \exp(-ik\hat{\rho}_0 \cdot \hat{\rho}_s + \frac{ik\rho^2 s}{2\rho_0}) ds \quad (1)$$

where  $\hat{\rho}_0$  = unit vector from C-of Cs to observer

$$\rho_0 = |\rho_0|$$

$\hat{\rho}_s$  = vector from c of cs to scatterer

$E_0$  = magnitude of propagating  $\vec{E}$  vector

$$\begin{bmatrix} A \\ B \\ C \end{bmatrix} = \hat{e} = \text{unit vector in direction of } \vec{E}$$

$N(s)$  = perturbation in refractive index and  $N(s) \ll 1$  and random

The expression for the average power scattered toward an observer is:

$$P_{avg} = \langle \vec{E}_s \cdot \vec{H}_s^* \cdot \frac{(\hat{\rho}_0 - \hat{\rho}_s)}{|\hat{\rho}_0 - \hat{\rho}_s|} \rangle_{avg}$$

$$\vec{H}_s = \frac{\nabla \times \vec{E}_s}{i\omega\mu} \quad (2)$$

using 1 and 2 this becomes:

$$P_{avg} = W_0 \iint N(S_e) N(S_p) \exp \cdot \frac{-ik}{Z_0^1} \frac{(S_e - S_p) \left( L - \frac{(S_e + S_p)}{2} \right)}{ds_e ds_p A_e A_p} \quad (3)$$

where:

$$W_0 = \frac{k^4 E_0^2}{32\pi^3 (Z_0^1)^2} F(\sigma_0, \sigma_s, Z_0^1, s)$$

$$L = Z_0^1 \hat{\rho}_0 \cdot \hat{\rho}_s = \sigma_0 \cos \beta + Z_0 \cos \gamma$$

$$F = \left[ 1 - \left| \begin{bmatrix} A \\ B \\ C \end{bmatrix} \cdot \hat{\rho}_0 \right|^2 + \theta \right], \text{ a nearly fixed}$$

quantity as  $\theta$  depends on  $\frac{\sigma_0}{Z_0^1}, \frac{\sigma_s}{Z_0^1}$  and

$\frac{s}{Z_0^1}$ . Only  $\frac{s}{Z_0^1}$  is variable and usual-

ly  $s \ll \sigma_0$ . A is the cross sectional

area of a scatterer:  $A_{ds} = d(\text{volume})$

$$Z_0^1 = \sqrt{\sigma_0^2 + Z_0^2}$$

In this analysis, the perturbed  $N(s)$  is described at a point  $S_\ell$  by:

$$N = 1 + N(s) \quad S_\ell \leq S \leq S_\ell + \Delta S_\ell$$

$$N = 1 \quad S_\ell > S \text{ or } S_\ell + \Delta S_\ell$$

Now applying the condition that scatterers are discrete variations in refractive index, the integral part of (3) can be expressed in matrix form\*:

$$(\rho_s)_{\text{avg}} = W_0 \begin{bmatrix} \alpha_1 & \dots & \alpha_n \\ \vdots & & \vdots \\ \alpha_n & & \alpha_n \end{bmatrix} \begin{bmatrix} N_{11} & N_{12} & \dots & N_{1n} \\ \vdots & \vdots & & \vdots \\ N_{n1} & N_{n2} & \dots & N_{nn} \end{bmatrix} \begin{bmatrix} \alpha_1 \\ \vdots \\ \alpha_n \end{bmatrix} \quad (4)$$

Where "n" is the total number of scatterers. Equation (4) can be expressed as a double sum:

$$\rho_s = \frac{W_0}{n} \sum_{m=0}^n \sum_{\ell=0}^{n-m} \alpha_{\ell+m} \alpha_\ell N_{\ell+m} N_\ell \Delta V_\ell \Delta V_\rho \quad (5)$$

Where m and  $\ell$  are integers and:

$$\alpha_{\ell+m} \alpha_\ell = \iint_{\text{scatterers}} e^{-i \frac{k}{2} \rho_m (L - \frac{\theta_m}{2})} ds_\ell ds_{\ell+m} A_\ell A_{\ell+m} = \iint_{\text{scatterers}} e^{-i \frac{k}{2} \rho_m (L - \frac{\theta_m}{2})} \cdot \left( \frac{-d^2 \rho_m + d\theta_m^2}{4} \right) A_\ell A_{\ell+m}$$

and where:

$$\rho_m = S_{\ell+m} - S_\ell \quad S_\ell = \ell \frac{S}{n} \quad (6)$$

$$\theta_m = S_{\ell+m} + S_\ell \quad S_{\ell+m} = (\ell+m) \frac{S}{n}$$

hence

$$\rho_m \approx \frac{S}{n} m$$

$$\theta_m \approx \frac{S}{n} (2\ell+m)$$

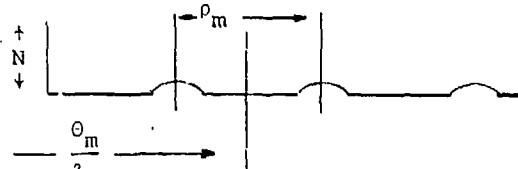
$$A_{\ell+m} A_\ell ds_{\ell+m} ds_\ell = AA \left( \frac{-d\rho_m^2 + d\theta_m^2}{4} \right) =$$

$$dV_{\ell+m} dV_\ell$$

S = Total length of the array

n = Total number of scatterers

The inner sum of Equation (4) represents a component array of interferometer elements with scatterers separated by a distance  $\rho_m$ . The "unperturbed" array implies  $\rho_m$  is a fixed quantity  $mS/n$ . Only small perturbations about this distribution are considered. The quantity  $\theta_m/2$  defines the distance to the center of an interferometer element.



The outer sum of Equation (4) then adds the power in all component arrays as required. Dividing by n (the total number of component arrays as well as number of scatterers) appears because of the averaging requirement.

#### SCATTERING MODELS

The term  $\alpha_{\ell+m} \alpha_\ell$  determines the characteristics of the scattering model. Performing the integration of (6) over the limits  $\rho_m + \Delta\rho_m$  and  $\rho_m$  in the case of (7b), the following results are obtained:

$$\text{when } d\theta_{m\ell} = 0 \Rightarrow ds_{\ell+m} ds_\ell = \frac{-d\rho_m^2}{4}, \text{ then:}$$

$$\alpha_{\ell+m} \alpha_\ell = \left\{ \cos U \left( \frac{-\sin^2 \frac{\tilde{x}}{2}}{\left(\frac{\tilde{x}}{2}\right)^2} \right) + \sin U \right.$$

$$\left. \cdot \left[ \frac{-\sin^2 \frac{\tilde{x}}{2} \sin x}{\left(\frac{\tilde{x}}{2}\right)^2} \right] \right\} \frac{\Delta\rho_m^2}{4} N_{\ell+m} N_\ell \quad (7a)$$

$$\text{and when } d\rho_m = 0 \Rightarrow ds_{\ell+m} ds_\ell = \frac{d\theta_m^2}{4},$$

then

$$\alpha_{\ell+m} \alpha_\ell = \left\{ \cos U \left( 2 \frac{\sin^2 \frac{\tilde{z}}{2}}{\tilde{z}^2} - \frac{\sin^2 \frac{\tilde{z}}{2}}{\left(\frac{\tilde{z}}{2}\right)^2} \right) + \sin U \right.$$

$$\left. \cdot \left( \frac{\sin^2 \frac{\tilde{z}}{2}}{\left(\frac{\tilde{z}}{2}\right)^2} \sin z \right) \right\} \frac{\Delta\theta_m^2}{4} N_{\ell+m} N_\ell$$

where:

$$U = \frac{k}{z_0^2} \rho_{lm} (L - \frac{\theta_{lm}}{2}) \quad (7b)$$

$$\tilde{X} = \frac{k}{z_0^2} \Delta \rho_{lm} (L - \frac{\theta_{lm}}{2})$$

$$\tilde{Z} = \frac{k}{z_0^2} \rho_{lm} \Delta \theta_{lm}$$

The quantities  $\Delta \rho_{lm}$ ,  $\Delta \theta_{lm}$  are scale sizes of the scatterers. Note that  $k \Delta \rho_{lm}$ ,  $k \Delta \theta_{lm}$  are respectively  $2\pi \frac{\Delta \rho}{\lambda}$ ,

$2\pi \frac{\Delta \theta}{\lambda}$  and that  $\frac{\Delta \rho}{\lambda}$ ,  $\frac{\Delta \theta}{\lambda} \gg 1$  implies electrically large scatterers and  $\frac{\Delta \rho}{\lambda}$ ,  $\frac{\Delta \theta}{\lambda} < 5$  implies electrically small scatterers. Note in (7a) and (7b) that when  $\tilde{Z}$ ,  $\tilde{X}$  are small quantities, which is almost always satisfied when  $\frac{\Delta \rho}{\lambda}$ ,  $\frac{\Delta \theta}{\lambda} \ll 1$ , that (7a) and (7b) both reduce to the electrically small scatterer expressions:

$$\begin{aligned} \alpha_{l+m} \alpha_l &= \cos U \left( \frac{-\Delta \rho^2_{lm}}{4} \right) N_{l+m} N_l \\ &= \cos U \Delta V_{l+m} \Delta V_l N_{l+m} N_l \\ &= \cos U \left( -\frac{\Delta \theta^2_{lm}}{4} \right) N_{l+m} N_l \\ &= \cos U \Delta V_{l+m} \Delta V_l N_{l+m} N_l \quad (8) \end{aligned}$$

where in (8) the coefficient of the  $\sin U$  terms has been allowed to vanish - since it is small for both small and large  $\tilde{X}$ ,  $\tilde{Z}$ . Note also that a model allowing both variations in  $d\theta$  and  $d\rho$  is possible for  $\frac{\Delta \rho}{\lambda}$ ,  $\frac{\Delta \theta}{\lambda} \ll 1$ :

$$\begin{aligned} \alpha_{l+m} \alpha_l &= \cos U \left( \frac{-\Delta \rho^2_{lm} + \Delta \theta^2_{lm}}{4} \right) N_{l+m} N_l \\ &= \cos U \Delta V_{l+m} \Delta V_l N_{l+m} N_l \end{aligned}$$

Returning now to the expression (5), and neglecting  $\sin U$  terms of (7a) and (7b) while making the following assumptions:

(1)  $N_{l+m} N_l$  statistics are independent of  $\Delta V_{l+m} \Delta V_l$  statistics.

(2) The array differs from a uniform array by only a small amount, as defined at a position  $\theta_l$  by  $\theta_l + \delta \theta_l$  with  $\delta \theta_l$  a stationary random variable. This also results in perturbations in  $\rho_l$  of the order  $\delta \rho_l \approx \delta \theta_l$ . The averages  $\overline{\delta \theta_l} = \overline{\delta \rho_l} = 0$ .

(3) The fluctuation in  $\overline{N_{l+m} N_l}$  about a mean  $N^2$  can be described by a normalized correlation function  $R(\rho_m)$  - defining component arrays with  $\rho_m \approx m S/n$  (the separation distance of scatterers).

Note:  $N_l = \bar{N} + \Delta N_l$  where  $\Delta N_l$  is random.

(4) A similar correlation function  $C(\rho_m)$  exists for  $\Delta V_{l+m} \Delta V_l$ .

Finally, performing the required summation of the inner sum of (5), the following two model solutions are obtained:

$$P_{avg} \approx \frac{1}{n} \frac{\sin^2 \tilde{X}}{\left(\frac{\tilde{X}}{2}\right)^2} \sum_{m=0}^n \theta_2 \cos V \frac{\sin \frac{W(n-m)}{2}}{\sin \frac{W}{2}} \quad (9a)$$

and also:

$$\begin{aligned} P_{avg} &= \frac{1}{n} \sum_{m=0}^n \theta_2 \cos V \frac{\sin \frac{W}{2}(n-m)}{\sin \frac{W}{2}} \\ &\cdot \left[ 2 \frac{\sin^2 \tilde{Z}}{\tilde{Z}^2} - \frac{\sin^2 \frac{\tilde{Z}}{2}}{\left(\frac{\tilde{Z}}{2}\right)^2} \right] \quad (9b) \end{aligned}$$

where:

$$\theta_1 = \frac{W_0}{\bar{N}} (\bar{N})^2 (\overline{\Delta V})^2 \left( 1 + \frac{\overline{\delta \Delta \rho_m^2}}{\overline{\Delta \rho_m^2}} \right)$$

$$\theta_2 = \left[ 1 - \left( \frac{\kappa \rho_m^2}{z_0^2} \right) \overline{\delta \theta^2} \right] \left[ 1 + \frac{\overline{\Delta N^2}}{(\bar{N})^2} R(\rho_m) \right]$$

$$\left[ 1 + \frac{\overline{\delta \Delta V^2}}{(\overline{\Delta V})^2} C(\rho_m) \right]$$

\*It is readily shown  $\sin V$  terms are not negligible when  $\frac{V \rho}{\lambda} \approx z_0^{-1}/4L$  which usually requires electrically large scatterers.

$$V = \frac{k\rho_m}{z_o^1} (L - \frac{S}{2}) \quad \frac{S}{2} \ll L \text{ normally}$$

$$W = \frac{k\rho_m}{z_o^1} \frac{S}{n} \quad \rho_m = \frac{mS}{n}$$

$\overline{\delta\theta^2}$  is the variance of variations of  $\theta$  about a uniform distribution of scatterers

$\overline{\delta\Delta\rho^2}$  is the variance in variations about an average scale size of scatterers.

Since the same scatterers apply to all component arrays, the subscript "m" is not needed for  $\delta\theta$  and  $\delta\Delta\rho$ . Note in (9a) and (9b) that

$$\lim_{\frac{W}{2} \rightarrow 0, \pi, 2\pi} \frac{\sin \frac{W}{2} (n-m)}{\sin \frac{W}{2}} = n-m$$

$$\frac{W}{2} \rightarrow 0, \pi, 2\pi$$

and has a maximum of that value.

The averaging and summing operations have now produced a new definition of  $\tilde{X}$  and  $\tilde{Z}$ .

$$\begin{aligned} \tilde{X} &= \frac{k}{z_o^1} \Delta\rho (L - \frac{\theta_m}{2}) \\ \tilde{Z} &= \frac{k}{z_o^1} \rho_m \Delta\theta \end{aligned} \quad \begin{aligned} \frac{\theta}{2} \ll L \text{ normally and} \\ \text{may be neglected} \end{aligned} \quad (10)$$

where  $\overline{\Delta\rho}$  and  $\overline{\Delta\theta}$  represent average quantities of the scale size of scatterers - which normally is expected to be much smaller than  $\rho_m, \theta_m$ .

The power scattered toward the observer as estimated by (9a) and (9b) - does not account for diffraction as energy propagates away from the array toward an observer at  $\sigma_o, \alpha_o, z_o$ . To investigate these effects requires a return to equation (1) to estimate  $E_s$  at a suitable exit plane - not too distant from the array. Ideally, the angular spectra of the  $E_s$  distribution would then be determined - from which Fresnel and far field distributions are determined. The autocorrelation and power spectra remain unchanged in all planes parallel to the exit plane. The

power pattern may then be readily determined.

Since, in the foregoing analysis, a term

$$ik \frac{\rho_o^2}{2\rho_o} \quad (\text{refer to Equation (1)})$$

has been retained throughout analysis, it is assumed that the near field effects are well approximated by Equations (9a) and (9b). To estimate far field patterns, however, a more approximate method is used than outlined above. It is estimated that the pattern sensed at  $\sigma_o, \alpha_o, z_o$ , which is the incoherent sum of  $(n-m)$  interferometer elements - for a given component array - is roughly equal to an averaged element pattern. The far field diffraction effects are then estimated by first dividing the power in (9a) and (9b) by  $(n-m)$ , and then summing  $(n-m)$  of the new elements - assumed spaced  $\rho_m$  distance apart. According to array theory, this is achieved by multiplying the expressions in (9a) and (9b) by:

$$\frac{1}{(n-m)} \frac{\sin^2 \psi (n-m)}{\sin^2 \psi} \quad (11)$$

$$\text{where } \psi = \frac{k}{z_o^1} \rho_m L$$

Finally, it is noted that (9a) is the more convenient model. Hence the expression used to estimate the far field scattering is given by:

$$\begin{aligned} P_{avg} &= \frac{\theta}{n} \frac{\sin^2 \frac{\tilde{X}}{2}}{(\frac{\tilde{X}}{2})^2} \sum_{m=0}^n \theta_2 \cos V \frac{\sin(n-m) \frac{W}{2}}{\sin \frac{W}{2}} \\ &\quad \cdot \frac{\sin^2(n-m) \psi}{\sin^2 \psi} \end{aligned} \quad (12)$$

$$\text{where: } \psi = \frac{k}{z_o^1} \rho_m L \quad \text{when } m \geq 0$$

$$\text{and: } W = \frac{k\rho_m}{z_o^1} \frac{S}{n}, \quad V = \frac{k}{z_o^1} \rho_m (L - \frac{S}{2})$$

$$\text{and: } \lim_{\psi \rightarrow \alpha\pi} \frac{\sin^2(n-m) \psi}{\sin^2 \psi} = (n-m)^2$$



$$\lim_{\frac{\omega}{2} \rightarrow \alpha\pi} \frac{\sin(n-m) \frac{\omega}{2}}{\sin \frac{\omega}{2}} = (n-m)$$

where  $\alpha = \text{integer}$ .

From the definitions of  $\psi$  and  $V$ , it appears  $S_1^2 \psi$  varies spatially  $2(n-m)$  times as fast as  $V$  for any component array, hence may be assumed to be modulated by  $\cos V$ . If an observed moves through fringes, then a relatively slow time constant system would integrate out the fine structure and sense  $\cos V$  dependence. A fast enough time constant system, however, would produce extremely erratic scintillations because of the fine structure. Mathematically, an observer is moved through fringes by increasing  $L$  as defined elsewhere in the report.

It is noted that both types of scintillations are observed: the smooth  $\cos V$  like dependence by Lincoln Lab of Navy navigational satellites in mid-latitude and polar regions and at VHF and UHF frequencies; and the highly erratic scintillations observed by the RAE I experiments at polar latitudes at MH, HF frequencies.

The term  $\frac{\sin(n-m) \frac{W}{2}}{\sin \frac{W}{2}}$  in (12) has inter-

esting significance - as it behaves as a weighting function for the component arrays - particularly under far field conditions, where  $W$  is practically a constant. Obviously, the term will weight those component arrays heaviest for which

$$\frac{k\rho_m}{z_0^1} \frac{s}{n} = 0, \pi, 2\pi \dots = \alpha\pi \quad \alpha = 0, 1, 2 \dots$$

$$\text{or: } \rho_m = \alpha \frac{z_0^1 \lambda}{\frac{s}{n}}$$

$$\text{or: } m = \alpha \frac{z_0^1 \lambda}{(\frac{s}{n})^2} = \text{integer}$$

The other terms that act to weight a component array in the summations of (9a), (9b), and (12) are the auto-correlation functions  $R(m)$  and  $C(m)$  as they appear in  $\theta_2$ . In fact, as an approximation, the summation upper limit " $n$ " can be replaced by an integer  $m_{N,v}$  defined by:

$$\rho_{N,v} = \rho_m = m_{N,v} \frac{s}{n}$$

or:

$$m_{N,v} = \frac{\rho_{N,v}}{\frac{s}{n}}$$

$\rho_{N,v}$  is the smaller correlation distance of  $R(m)$  and  $C(m)$ :

$$\rho_{N,v} \leq \rho_N, \rho_V$$

Note that this applies to the fluctuating part of the power near the array as defined by  $\theta_2$ . The full summation is required for the "systematic" part.

Note that the scintillations produced by motion of an observed through fringes is determined mostly by the "systematic" part of (9a), (9b) and (12) -

$$\text{when } \frac{\Delta \bar{N}^2}{(\bar{N})^2} \text{ and } \frac{\delta \Delta \bar{V}^2}{(\Delta \bar{V})^2} \text{ are small com-}$$

pared to unity and when  $\rho_N$  and  $\rho_V$  are small.

#### FREQUENCY DEPENDENCE

The frequency dependence of the array originates from:  $W_0$  as it appears in

$\theta_1$ , the  $\theta_2$  term:

$$\left[ 1 - \left( \frac{k\rho_m}{z_0^1} \right)^2 \frac{1}{\delta \theta^2} \right]$$

which arose by considering an array perturbed from a uniform distribution and the expression

$$\frac{\sin^2 \frac{\tilde{x}}{2}}{\left( \frac{\tilde{x}}{2} \right)^2}$$

that modulates the whole power expression according to Equation (12).

Referring back to the expression  $W_0$ , it appears that the term depends on  $k^4$  or  $f^4$ . The frequency dependence of the  $\theta_2$  contribution would add a small component of  $k^6$  or  $f^6$ . This component is expected to be extremely small, except possibly in the near field, because

$$\frac{\rho_m}{z_0^1}$$

is small for large  $Z_0^1$ . Thus, it remains only to consider the multiplicative term

$$\sin^2 \frac{\tilde{x}}{2} / \left(\frac{\tilde{x}}{2}\right)^2$$

Recall that  $\tilde{x} \approx \frac{k}{Z_0^1} \overline{\Delta p}_{lm} (L)$  where  $\overline{\Delta p}$

is the average scale size of scatterers. Hence when  $\tilde{x}$  is very small, the expression goes to unity and  $f^4$  dependence occurs. If  $x > \pi$ , then  $f^2$  frequency dependence is predicted, but it becomes smaller the larger  $\tilde{x}$ .

If  $0 < \tilde{x} \leq \frac{\pi}{2}$ , then  $\frac{\sin^2 \frac{\tilde{x}}{2}}{\left(\frac{\tilde{x}}{2}\right)^2} \approx 1 - \frac{\tilde{x}^2}{12}$

and about a 10% component of  $f^6$  frequency dependence may be present.

The expression  $\tilde{x}$  is small under the following conditions.

$$\frac{\overline{\Delta p}}{\lambda} \ll \frac{Z_0^1}{2\pi L} \sigma \text{ where } 0 \leq \sigma \leq \frac{\pi}{2}$$

This, of course, is always satisfied when  $\frac{\overline{\Delta p}}{\lambda} \ll 1$  under far field conditions.

It can also be satisfied for electrically large scatterers when  $L \ll Z_0^1$ . This implies that different parts of a trajectory path may produce varying degrees of frequency dependence.

$\tilde{x}$  is large when:  $\frac{\overline{\Delta p}}{\lambda} \gg \frac{Z_0^1}{2\pi L} \sigma$

Under normal conditions this usually requires that  $\frac{\overline{\Delta p}}{\lambda} \gg 1$  or electrically large scatterers. Thus,  $f^2$  frequency dependence implies scatterers electrically large.

A table of predicted frequency dependence follows:

$\tilde{x}$	Near Field	Far Field	Elect. Size $\Delta p/\lambda$	Freq. Dep.	Rel. Pwr. Magn.
Large		$Z_0^1 \gg L$	Large	$f^2$	Small
Large	$Z_0^1 \ll L$		Large or Small	$f^2$	Small
$0 \leq x \leq \frac{\pi}{2}$		$Z_0^1 \gg L$	$\frac{\overline{\Delta p} Z_0^1}{\lambda L^4}$	$f^4 + f^6$	10% $f^6 \text{ max}$
Small		$Z_0^1 \gg L$	Small	$f^4$	Large
Small	$Z_0^1 \ll L$		Large or Small	$f^4$	Large

TABLE 1.

## RESULTS

In this section, estimates of normalized power are presented, using computer evaluations of Equation (12), for electronically small scatterers and far field conditions  $\sin^2(\tilde{x}/2)/(\tilde{x}^2/2)$ .

Normalization is effected by taking  $(\Delta N)^2$ ,  $(\Delta V)^2$  and  $E_0^2=1$  and a value of  $c=3 \times 10^5$  km/sec. When using MKS units, then  $c=1$ , as used in the expression for  $W_0$ . To re-express the normalized power in MKS units, the plotted values must be divided by  $3 \times 10^5$ .

The geometry chosen approximates the RAE 1 as it approaches the auroral oval. The frequency, however, is taken in the VHF range of 150 MHz, whereas the satellite receives UF and HF noise in these regions. The radiation is believed to originate in a region of auroral precipitation, which provides synchrotron energy in the UF-HF range, and places the trajectory about 2,000 km from the source and scatters. The characteristics of actual received power is similar to that predicted by Equation 12.

It is noted that the normalized power density estimates are scaleable in frequency and linear dimensions so that the reference plots Fig. 4, 5, 7, and 8 can be converted to other geometries and frequencies. The dimensionless expressions  $\psi$ ,  $W$ ,  $V$  and  $\theta_2$  scale directly with  $\lambda$ . The scatterer strength  $\theta_1$  possesses spatial terms that scale with  $\lambda$  also. The power, however, scales as  $\lambda^4$  as the  $(\Delta N)^2$  term scales as  $\lambda^4$ . Finally, it is noted that the expressions for  $\theta_1$ ,  $\theta_2$ ,  $\psi$ ,  $V$  and  $W$  in Equation 12 provide possibilities for many scaling combinations - hence, possibilities for convenient frequency and geometry conversions.

The objectives of this section are to display scintillations and pattern characteristics in bistatic scattering, hence the normalized power estimates are adequate. To estimate power magnitudes requires knowledge of  $(\Delta \bar{N})^2$  and  $(\Delta \bar{V})^2$  and of  $\delta \Delta \bar{N}^2$  and  $\delta \Delta \bar{V}^2$  together with correlation distances  $\rho_N$  and  $\rho_V$  of  $R(\rho_m)$  and  $C(\rho_m)$ . Conversely, measurements of  $P_{avg}$  provide information toward making theoretical estimates of the above parameters using Equation 12. The measured periodicities of scintillations provide parameter estimates also by using the theoretical periodicities of  $\cos V$  and of  $\sin(n-m)W/2/\sin W/2$  and  $\sin^2(n-m)\psi/\sin^2\psi$ .

As has been indicated previously, the rapid spatial fluctuations produced by the  $\sin^2(n-m)\psi/\sin^2\psi$  term in Equation 12 can be sensed by a sufficiently fast time constant system sampling at a rapid rate. Fig. 4 provides an example of a plane wave normally incident to an array 20 km long containing 200 scatterers. The  $Z_0$  distance is maintained constant at 2,000 km while the transverse distance  $\sigma_0$  is allowed to increase (see Fig. 2 for definition of the observer's coordinates). The vertical excursions shown indicate the depth of excursions that can result from the rather random encountering of fine structure during the sampling.

As noted in Fig. 4, the plots include an array having a refractive index correlation length of 20 km and .1 km respectively. The upper curve thus indicates the "systematic" part of the pattern (or scintillations) relative to a "fluctuating" part characterized by a  $\rho_N = .1$  and normalized with respect to  $\frac{\partial \Delta \bar{N}^2}{\Delta \bar{N}^2}$  (see the expression for  $\theta_2$  in the text pp. 5). It appears from the plot Fig. 4, that the correlation distance  $\rho_N$  has an influence on the amplitude of scintillations in the gross structure.

In Fig. 5, the objective is to display the pattern when the propagation vector is incident to the scattering axis  $\hat{s}$  at the various angles of incidence, and the fine structure effect  $\sin^2(n-m)\psi/\sin^2\psi$  is removed. The results indicate that scintillations (and the bistatic pattern) are relatively insensitive to the incidence of radiation, until a position some 500 km transverse distance is reached. Then the fringe widths at  $\psi_0 = 0$  incidence become about one half the widths for  $\psi_0 = 60^\circ$  incidence as expected due to the effective doubling of interferometer distance between scatterers.

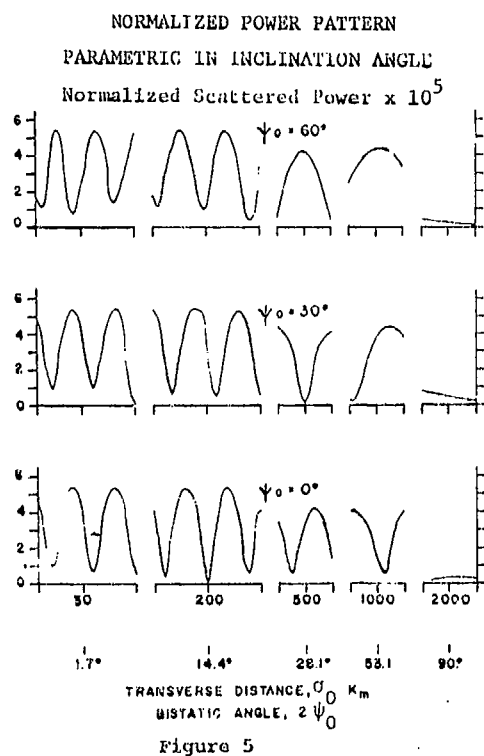
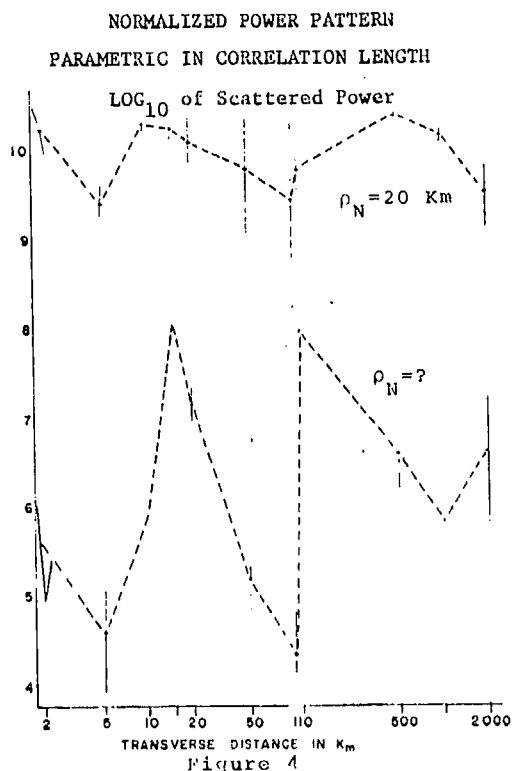
In Fig. 6 a sketch of bistatic scattering from an array is shown, and the bistatic angle  $2\psi_s$  displayed. Fig. 5 also shows the calculation of normalized power as a function of the bistatic angle.

In Fig. 7, a cylindrical bundle of arrays has been simulated using the following parametric input and normal incidence:

S (Km)	$\sigma_s$ (deg)	$\sigma_s$ (km)	$Z_0$ (km)	$\rho_N$ (km)
20	0	0	2,000	.1
	45	.1		
	90	1		
	135			
	180			
	225			
	270			
	315			

The results of adding the power incoherently in the deep far field proves to be equivalent to multiplication of the center array power by 17 in this case - as expected. The plot also indicates the scintillation amplitude in db does not vary with the size of the array.

From the results of Fig. 7, a pattern synthesized by an array of cylindrical bundles is readily simulated. The bundles, in this case, are located with centers at  $\alpha_0 = 0$ ,  $Z_0 = 0$  and  $\sigma_0 = 0$ , 200 km, 500 km. Fig. 8 is a plot of the pattern near  $\sigma_0 = 0$ ,  $Z_0 = 2,000$  km. It appears the scintillation amplitude has been reduced in db.



BISTATIC SCATTER FROM  
FIELD ALIGNED ARRAYS

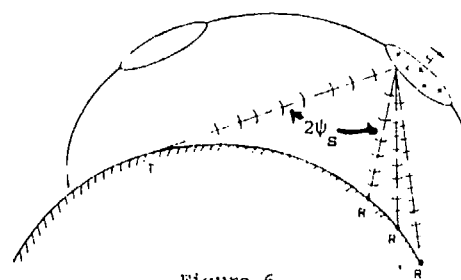
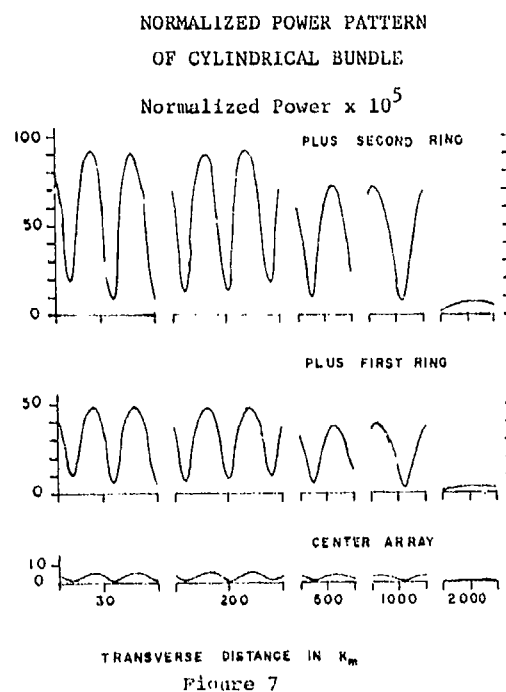
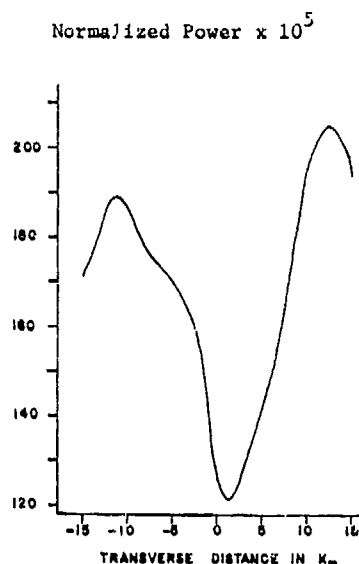


Figure 6



NORMALIZED POWER PATTERN  
FOR AN ARRAY OF CYLINDRICAL BUNDLES



CONCLUSIONS

Qualitative comparison of certain scintillation data at MF, HF and UHF frequencies with the electrically small scatterer model have indicated a similarity of structure; that is, simulations can be generated that approximate the scintillations observed. To realistically assess the usefulness of these models requires quantitative estimates of parameters using measurements of scattered power density, scintillation amplitudes, frequency dependence and periodicities of the pattern as mentioned very briefly in the report. Some of the parameters (e.g. scatterer size  $\Delta V$ ) can be compared with estimates derived by other means as a check. Ideally, having evaluated model parameters, then the ability of the model to predict backscattered power, bistatic scattering at penetration frequencies and scattering into wide beam antennas can be checked.

It is noted that the analysis uses an incident plane wave, with provision for specifying array length and aspect. Thus analysis can simulate a narrow beam antenna sweeping an irregularity region and sampling a known spatial extent of array. To simulate longer arrays irradiated by antennas, an incident spherical wave provides a superior approximation.

The analysis can be applied to electrically large scatterers by retaining the  $\sin U$  term in 7a and 7b and using appropriate values of  $\tilde{x}$ . The coefficient of the  $\sin U$  term is a filter function which is maximum when  $\lambda/\Delta\rho = (L-Qm)/Z_0^{1/2}$  and quickly damps out for other conditions. For far field conditions the expression indicates electrically large scatterers and  $\lambda/\Delta\rho$  is approximately the scattering beam width of the irregularity. The condition is consistent with forward scattering. The possibility of sensing electrically large scatterers embedded with electrically small ones by examining pattern characteristics is, therefore, of possible importance toward estimating the morphology of an irregularity region.

## ARECIBO HEATING EXPERIMENT

W. E. Gordon  
Rice University  
Houston, Texas 77001

H. C. Carlson, Jr.  
Institute for Physical Sciences  
University of Texas at Dallas  
Richardson, Texas 75080

### Abstract

Enhancements of various features of the incoherent scatter spectrum are observed when the ionosphere is illuminated with powerful, high-frequency radio waves. The radio waves excite plasma instabilities producing lines or more complex spectral features near the local plasma frequency, at the local ion-acoustic frequency, near the local gyrofrequency and twice the gyrofrequency. The enhancements occur in a thin slab as observed by the incoherent scatter radar and at both upshifted and downshifted frequencies with respect to the probing radar frequency. The enhancements are observed to vary with time when the excitation is held constant and is turned on or off.

The high power radio waves are produced by a 160 kilowatt transmitter feeding a log-periodic pair of curtains mounted at the focus of the 1000-foot reflector and covering the frequency range 5 to 12 megahertz. The effects are observed with the incoherent scatter radar using the same reflector and with ionosondes and photometers.

The frequencies of the enhanced plasma line and the ion line and their relation to the pump (high frequency radio wave) frequency are predictable from available parametric instability theory. Other spectral features are being explained as the theory develops with the help of the observations. There remain some discrepancies, in particular the asymmetries in intensity, width and fluctuations of the upshifted compared to the downshifted plasma lines.

### Introduction

The heating experiments at Arecibo have yielded a number of interesting results derived from the normal absorption of radio waves in the ionosphere [Shoven, 1972; Kantor, 1971; Gordon et al., 1971] and from the anomalous absorption of the high-frequency (5-10 MHz) waves and the excitation of plasma instabilities [Carlson et al., 1972; Kantor, 1972; Dias and Gordon, 1973].

Heating of the ambient electrons by a high frequency (HF) radio wave propagating in the ordinary mode (O-mode) has been detected. Deviative absorption, ray tracing, and heat-balance calculations are consistent with the magnitude of the increase, typically peaking at 150° to 400°K, with the higher values at night, with the location typically 4° to 9° north of the Observatory, with the heated volume matched to the beam when mapped in two or three dimensions, and with thermal relaxation times of a few tens of seconds. The ion temperature is unchanged within error bars of tens of degrees K.

The HF excited plasma line exhibits spectral features (e.g., decay-mode line, growing-mode line, gyroline), most of which can be explained by linear parametric theory. Observation of an additional broad spectral feature has led to extension of the theory. Some features are not as yet explained. The decay times are consistent with the wave-damping theory and offer a new tool for collision frequency and photoelectron studies. Airy structure in the vicinity of HF reflection has been observed, consistent with theory. Fluctuations of the plasma-line intensities over two orders of magnitude show distribution functions suggesting an upper-threshold saturation in the ionospheric plasma for higher HF transmitted power levels. Ion-component spectra have been measured and seem to be consistent with the theory.

Red-line enhancement and suppression in the airglow have been observed [Sipler et al., 1974]. Suppression of roughly one percent is observed in association with extraordinary-mode excitation of the plasma, implying an increase through energetic-electron-impact excitation of the airglow. The rise and fall times of these enhancements are substantially less than the  $O^+D$ -state lifetime, so quenching rates of the airglow emission and the upper atmospheric  $N_2$  concentrations can be studied.

The Boulder and Arecibo ionograms during heating experiments exhibit the same general characteristics, although the details vary and are probably related to field-line geometry and incident-power differences.

In addition to enhancements of the plasma at and near the plasma-line frequency and at the ion-line frequency, enhancements have been observed at the electron gyrofrequency and at twice this frequency [Dias and Gordon, 1973] (see Table 1).

#### Normal Absorption

The effects of the deposition of radio-wave energy on electron temperature, ion temperature, electron number density, and velocity depend on the transmitted power, polarization, HF frequency, ionospheric critical frequency, temperature, altitude, electron density gradient and time of day (HF absorption in D and E regions).

Figure 1a shows contours of electron temperatures,  $T_e$ , on time-height coordinates, when the ordinary mode was reflected. The incoherent scatter data begin after the heater has been on for half an hour. The electrons are significantly heated at and somewhat below the altitude at which the heating wave reflects. After the heater is turned off, the electrons relax to their ambient temperature of 850° to 950°K. The time resolution here is 8 minutes, the altitude resolution is 30 km, and the statistical uncertainty in the electron temperature is less than 30°K. For heating at a frequency near and somewhat above the penetration frequency,  $f_oF_2$ , significant  $T_e$  enhancements are found above and below the peak of the F layer.

The electron temperatures observed during an experiment in which the heater power was cycled from zero to 50 kw and 100 kw are shown in Figure 1b. As expected, the  $T_e$  enhancement at 100 kw is not quite double that for 50 kw. The changes in  $(T_e - T_1)$  are consistent

with current heat balance theory within the measurement uncertainties involved. There was a suggestion of a slight modulation of  $T_1$  by the HF transmitter, at the highest two or three altitudes (where thermal coupling to the neutrals is poor), but this is near the threshold of detection.

The extent of the O-mode heating has been determined by making maps in the magnetic meridian where the O-mode radio wave deviates toward the north. The maps show a heated region centered 35 km to the north of the observatory at an altitude of 320 km. To determine possible heating out of the meridian plane, a measurement to the west was made, and little heating is indicated there. No heating has been observed when the heater frequency is more than 1 MHz above the  $f_oF_2$ . From thermal-conductivity considerations, the heated region is expected to be elongated along B and this is observed.

The electron thermal time constant in the F-region is of the order of tens of seconds, and can be calculated from the energy loss rates to ions and neutral particles. The necessary accuracy plus time resolution in the backscatter data can be achieved only by superposition of several on/off heating cycles. A representative example of such a run is given in Figure 2a. At HF transmitter turn-on, the temperature rises abruptly, and both rise and fall times for this example are approximately 30 s.

The steady state conditions are illustrated in Figure 2b giving the electron temperatures averaged over six minutes as the heating power is varied.

#### Anomalous Absorption

##### Plasma-Line Enhancements

When the ionospheric F region is illuminated with a strong O-mode HF radio wave, excitations of longitudinal plasma and acoustic waves are observed by radio scattering. HF enhanced plasma lines were first observed at the Arecibo Observatory in 1971 [Carlson et al., 1971]. A summary of the observations is given by Kantor [1972]. The decay line and the growing mode (see Figure 3) are identified and associated with the components of parametric instabilities. The broad line has been recently interpreted by Krueger and Valeo [1973] and Kuo and Fejer [1972]. Asymmetries between the upshifted and downshifted plasma lines are observed and the explanations are under discussion [Perkins et al., 1974]. The peak amplitude of the growing mode

and the broad line is approximately proportional to the peak amplitude of the decay line. The thickness of the layer producing the observed plasma line is less than 300 m.

Enhancement rise times after HF turn-on have been found to be on the order of tens of milliseconds and show a ringing of the plasma. The period of the ringing was about 8 ms on two measurements made under the same conditions. This ringing may be the same found by Krueger and Valeo [1973].

Decay times of the daytime plasma-line enhancements after HF turn-off are about 0.3 to 1 ms, consistent with the linear theory for the frequency range studied. They are primarily due to wave damping by photoelectrons, and are shortest for those waves going in the direction of the largest flux. This has obvious application to photoelectron-flux studies. At night the decay rates are slower by a factor of roughly 2 to 10, again consistent with the linear theory, primarily due to electron-ion collisions. No significant non-linear damping has been detected yet through decay rate measurements.

There are fluctuations of the enhanced plasma-line intensity over a wide range of time scales. On time scales of hours, the observed severe decrease of intensity near midday in the 5-to-6 MHz range of HF frequencies appears to be due to  $F_1$  region absorption. On time scales of tens of minutes, one sunset run showed severe regular periodic fading of the plasma-line intensity, which can be explained [Kantor, 1972] in terms of sliding through consecutive maxima and minima of the (Airy function) interference field strength near the reflection height. The rate of fading from one minimum to the next depends on the rate of change of the local density gradient as  $f_0F_2$  approaches the heater frequency  $f_{HF}$ . The envelope of the maxima decreases as  $f_0F_2$  approaches  $f_{HF}$  (within the last few percent).

For a given HF transmitter power, the observed plasma line intensity fluctuates over two orders of magnitude in tens of seconds. Spectral analysis of the variation of the decay mode peak intensity shows sharp maxima at periods ranging from 35 sec to 3 min [Kantor, 1972] for the available data. The amplitude distribution of the observed plasma line intensities is found to have a sharp upper cutoff (not due to saturation in the receiving system), which could thus be interpreted as evidence of plasma wave

amplitude saturation in the ionospheric plasma.

#### Ion-Line Enhancements

Since the instability echo comes from such a narrow altitude range one must usually resort to narrow height resolution techniques to extract the HF enhanced ion component from the background thermal ion component which is centered on essentially the same frequency at all altitudes. Power profiles obtained by a Barker coded technique have provided data [Kantor, 1974] which presents the peak power of the ion-enhancement versus the peak power of the upshifted plasma-line, both measured with a height resolution of 900 m. Data seem to follow a square law closely (ion line intensity proportional to the square of the plasma line intensity) suggestive of being above threshold.

On two occasions multiple pulse measurements of the autocorrelation function indicated enhanced correlation beyond the first autocorrelation zero crossing, which indicates the presence of spikes in the frequency spectrum at the ion acoustic frequency, as is predicted by the parametric theory. That the effect is due to HF enhancement of the ion line and not only a  $T_e$  increase is indicated by the fact that the cross section increases and by the ratio of the second maximum to first minimum in the autocorrelation function. One set of data [Hagfors and Zamlutti, 1974] are of sufficient quality to permit estimates of the width (damping) of the apparent spikes of the ion spectral wings.

#### Gyroline Enhancements

Enhanced electron cyclotron lines were also first seen in the spectrum of the backscattered echo during the Arecibo heating experiment [Dias and Gordon, 1973]. These new lines plus their harmonics are yet to be interpreted in terms of their threshold conditions and growth rates. From the analysis of the upshifted backscattered signal the following results are obtained: (1) A new instability (and the existence of its second harmonic) around the electron gyrofrequency, having a full width at half maximum point of about 1 kHz, is detected unambiguously during certain runs. (2) The center frequency of the observed lines is seen to systematically vary over a range of many line widths and is concluded to come from a thin layer. Note that this gyroline is sampled



simultaneously with the enhanced plasma line and that both lines come from the same height within the measurement resolution.

#### Airglow Observations

Both enhancements and suppressions of 6300Å airglow have been observed. X-mode suppressions of roughly one percent (out of 120 rayleighs) have been obtained, consistent with the temperature dependence of the recombination rate. O-mode enhancements have been observed of the order of 10 rayleighs, coincident with the HF excitation of the ionospheric plasma waves (see Figure 4). This manifestation of plasma waves enhanced by the anomalous HF heating is attributed to impact excitation by energetic (order of several eV) electrons driven by enhanced plasma waves. Decay rates of these 6300Å enhancements should help define quenching coefficients and molecular-nitrogen number densities in the upper atmosphere, a qualitatively new technique afforded by the heating experiment.

#### Ionograms -- Arecibo and Boulder

##### F Region

Utlaut and Cohen [1971] list effects observed on ionograms due to HF-radio-wave modification of the ionosphere. The five effects in their tabulation are listed first in Table 2. They are pertinent to ionograms and particularly to the Boulder (geomagnetic 49°N, 316°E) facility. Table 2 is an expanded version of their tabulation and includes results from ionograms at Arecibo (geomagnetic 30°N, 2°E). The symbols are defined as noted in the table.

Effects 6 through 8 are listed because of the detailed description of their occurrence at Boulder by Utlaut and Violette [1972] who also observed short-lived sporadic-E echoes, possibly connected with HF heating.

Both HF transmitters radiate either O-mode or X-mode waves to the ionosphere, which are deflected from vertical due to the effects of the magnetic field. An ionosonde located at the same site as the transmitter and sounding vertically at the heating frequency, should obtain echoes from about the same area of the ionosphere that the heater is illuminating. This is the case at Arecibo, but at Boulder the heater and ionosonde are separated by about 26 km. (This distance is within the radius of the area

heated, but several Fresnel zones removed from the center of the heating beam.) Effects seen on the ionograms from the two locations differ in detail because of the different ionosonde and antenna equipment in use, and possibly because of the different magnetic dip-angles, the different characteristics of the HF transmitters, and the distance between the ionosonde and transmitter at Boulder.

The interpretation of the ionograms as modified by the heating transmitter is tentatively as follows:

(1) Effects 1 and 2 in Table 2 are thought of as an enhancement in the fluctuations of electron density generated at the height associated with the plasma line and propagated both upward and downward in height. The increased fluctuations produce a scattering of the HF signals, giving a spread appearance to the ionogram trace.

(2) Effects 3 and 4 of Table 2, the attenuation of the ionosonde echo at frequencies above the heater frequency, are thought of as a layer of anomalous absorption at the height where the plasma line is excited. The signal passing through this layer at frequencies above the heater frequency suffers an extra attenuation.

(3) Effects 6, 7 and 8 of Table 2 are thought of as produced by a bubble in the electron density contours introduced at the height where the plasma is heated and conducted to other heights. The ionosonde observes one profile through the bubble and a second in the ambient ionosphere simultaneously, leading to pairs of traces on the ionograms.

#### Acknowledgements

The ionospheric heating experiments described in this paper were conducted at the Arecibo Observatory operated by Cornell University. They have been performed by W. E. Gordon and H. C. Carlson with the scientific collaboration of R. A. Behnke, T. Hagfors, and J. F. Rowe from the Arecibo Observatory; I. J. Kantor, D. M. Kim, A. R. Laird, L. A. Dias and F. Schwab from Rice University; R. L. Showen from the University of Puerto Rico, Mayaguez; M. Biondi and D. Sipler from the University of Pittsburgh; and V. B. Wickwar from Yale University and Rice University. Engineering and technical support was provided by D. Albino, R. B. Dyce, M. A. Feyjoo, D. Van Winkle, J. Maldonado and R. Towers from the Arecibo Observatory; L. M. LaLonde,

D. T. Farley, J. Hagen, G. Ioannides and C. Zamlutti from Cornell University; W. Utlaut and J. Carroll from the National Oceanic and Atmospheric Administration in Boulder; and R. Tanner from Technology for Communications International. This work was partially supported by the Advanced Research Projects Agency under Contract No. F30602-72-C-0278 and monitored by the Air Force Systems Command, Rome Air Development Center. Mr. A. Van Every at ARPA provided the encouragement and the support over many years that produced these results.

#### References

- Carlson, H. C., W. E. Gordon and R. L. Showen (1972), High frequency induced enhancements of the incoherent scatter spectrum at Arecibo, *Journal of Geophysical Research*, 77, 1242-1250.
- Dias, L. A., and W. E. Gordon (1973), The observation of electron cyclotron lines enhanced by HF radio waves, *Journal of Geophysical Research*, 78, 1730-1732.
- Gordon, W. E., H. C. Carlson and R. L. Showen (1971), Ionospheric heating at Arecibo: First tests, *Journal of Geophysical Research*, 76, 7808-7813.
- Kantor, I. J. (1971), Artificial heating paradox of the lower ionosphere, M.S. Dissertation, Rice University, Houston, Texas.
- Kantor, I. J. (1972), Enhanced plasma lines excited by HF waves, Ph.D. Dissertation, Rice University, Houston, Texas.
- Kantor, I. J. (1974), High frequency induced enhancements of the incoherent scatter spectrum at Arecibo, 2, *Journal of Geophysical Research*, 79, 199-208.
- Kruer, W. L., and E. J. Valeo (1973), Nonlinear evolution of the decay instability in a plasma with comparable electron and ion temperatures, *Physics of Fluids*, 16, 675-682.
- Kuo, Y., and J. A. Fejer (1972), Spectral line structures of saturated parametric instabilities, *Physics Review of Letters*, 29, 1667-1670.
- Perkins, F. W., C. Oberman and E. J. Valeo (1974), Parametric instabilities and ionospheric modification, *Journal of Geophysical Research*, 79, 1478-1496.
- Showen, R. L. (1972), Artificial heating of the lower ionosphere, *Journal of Geophysical Research*, 77, 1923-1933.
- Sipler, D. T., E. Ememark and M. A. Biondi (1974), 6300Å variations produced by the Arecibo ionospheric modification experiments, accepted for publication by *Journal of Geophysical Research*.
- Utlaut, W. F., and R. Cohen (1971), Modifying the ionosphere with intense radio waves, *Science*, 174, 245-254.
- Utlaut, W. F., and E. J. Violette (1972), Further ionosonde observations of ionospheric modification by a high powered ground-based transmitter, *Journal of Geophysical Research*, 77, 6804-6818.
- Hagfors, T., and C. Zamlutti (1974), Observations of enhanced ion line frequency spectrum during Arecibo ionospheric modification experiment, Proc. of 19th Technical Meeting of the Electromagnetic Wave Propagation Panel of the Advisory Group for Aerospace Research and Development, NATO, Edinburgh, Scotland, Nov. 12-16, 1973.

Table 1  
HF EXCITATION

Ionospheric Effects Observed	Ordinary Mode		Extraordinary Mode		Interpretation
Electron heating					
Temperature increase	R		W		A
Time constants	R		N		A
Ionograms (n=night,d=day)	O-echo	X-echo	O-echo	X-echo	
Split traces	R	R	R	R	
Attenuation	R	S	R(n),S(d)	R(n),S(d)	
Branched penetrating freq.	R	R(n),S(d)	R	R	
F-region enhancements					
Plasma lines	R		S		A
Features near plasma lines	R		S		T
Ion Line	W		S		T
Gyroline	W		N		T
Asymmetries of up/down					
shifted plasma lines	R		S		T
Rise times of plasma lines	R		N		T
Fall times of plasma lines	R		N		A
Threshold of instability	R		N		T
Ringling of plasma line	R		N		T
E-region enhancements					
Sporadic-E plasma line	W		N		T
Photometer					
Enhancement of 6300Å line	R		S		A
Suppression of 6300Å line	N		W		A

R = Regularly observed  
W = Observed weakly  
S = Searched for but not observed  
N = No search

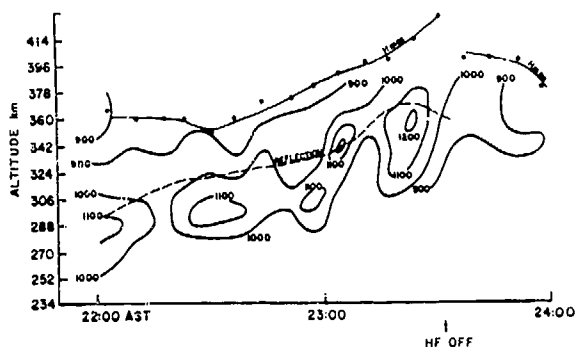
A = Agrees with generally  
accepted theory  
T = Theoretical explanation  
available

Table 2

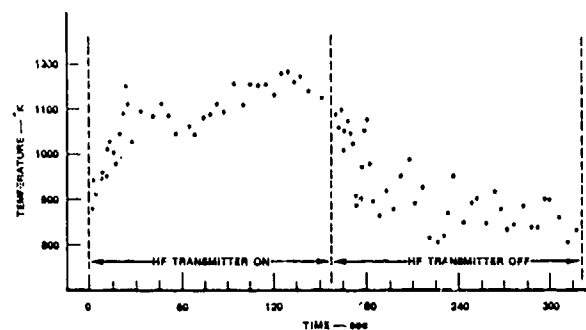
## HF IONOSPHERE MODIFICATION AT BOULDER AND ARECIBO

Effects on Ionograms	O-Excitation				X-Excitation			
	Day		Night		Day		Night	
	B	A	B	A	B	A	B	A
Spread O-echo	+	+	+	+	+	+	+	+
Spread X-echo	+	+	+	+	+	+	+	+
Attenuation of O-echo	0	+	+	+	0	0	-	+
Attenuation of X-echo	0	0	-	-	0	0	-	+
Delayed broadband echo	0	0	+	+	0	0	+	0
Branched penetrating frequency--O	?	+	+	+	?	+	+	+
Branched penetrating frequency--X	?	+	+	+	?	+	+	+
Frequency gap or attenuation of 1st or 2nd multiple	?	+	+	+	?	+	+	+
Possible E-region effects	+	+	+	+	?	U	?	U

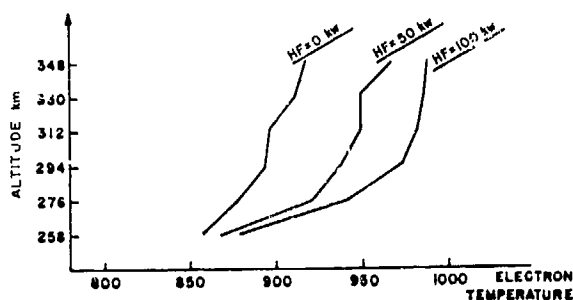
Legend: B Boulder + Positive results  
 A Arecibo - Negligible effect  
 0 Results to date not completely conclusive  
 U Information not yet available  
 ? Not explicitly covered in publications



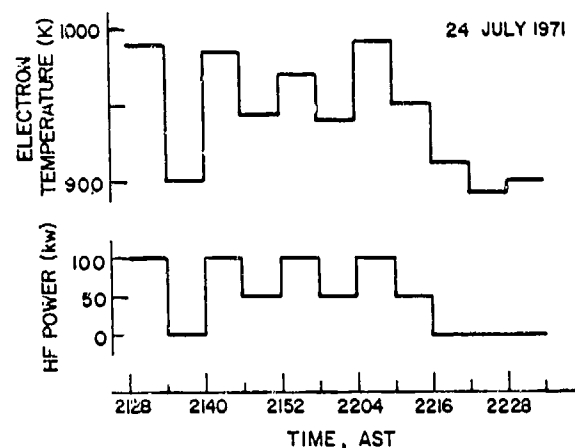
(a)



(a)



(b)



(b)

Figure 1. Electron temperature distribution: (a) contours in degrees K on time height coordinates (19 July 1971) showing heating near height of reflection of HF wave and relaxation to ambient conditions after turn-off of the HF transmitter (heater frequency is 5.1 MHz, transmitter power is 100 kw,  $f_0F_2 = 5.9$  to 6.3 MHz); (b) altitude profiles for zero-, half-, and full-power operation of the HF transmitter (2200 AST, 24 July 1971).

Figure 2. Electron temperature vs time: (a) a superposition of 10 on-off cycles of the HF transmitter to show transient response; (b) steady-state response for zero-, half-, and full-power operation of the HF transmitter.

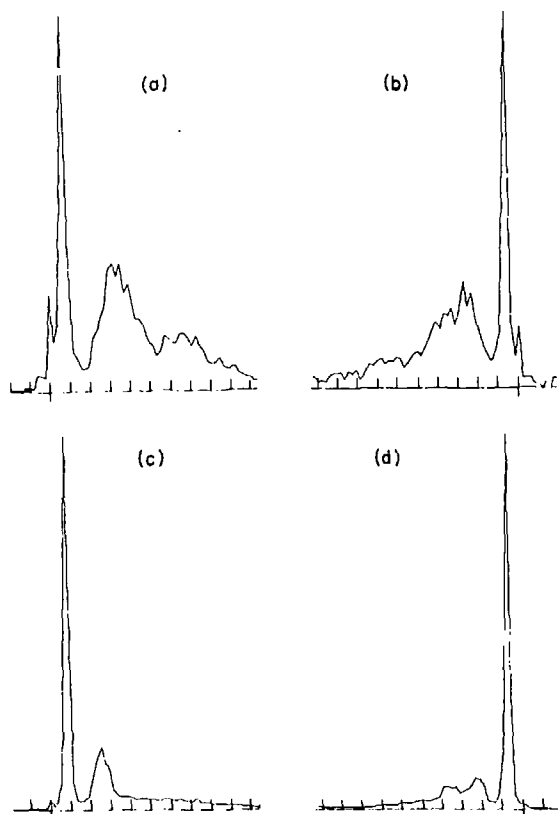


Figure 3. Sample spectra. The abscissa is frequency relative to the incoherent scatter observing frequency with the marked interval being 5 kHz and the frequency of the long index  $-8.195$  MHz for (a) and (c) and  $+8.195$  MHz for (b) and (d). The ordinate is spectral intensity in watts per cycle on a linear scale with the maxima being at (a)  $4.8 \times 10^{-19}$ , (b)  $3.2 \times 10^{-19}$ , (c)  $22.9 \times 10^{-19}$ , and (d)  $13.4 \times 10^{-19}$  watts per Hz. Figure (a) is at 195901-09 AST on 23 July 1971, the HF power was 125 kw, the height about 350 km, the temperatures  $T_e \sim 950^\circ\text{K}$  and  $T_i \sim 900^\circ\text{K}$ ; figure (b) is at 195911-19 AST on 23 July 1971, the power, height and temperatures are the same as (a); figure (c) is at 162531-39 AST on 24 July 1971, the HF power was 80 kw, the height about 270 km, the temperatures  $T_e \sim 1700^\circ\text{K}$  and  $T_i \sim 1100^\circ\text{K}$ ; figure (d) is at 162541-49 AST on 24 July 1971, the power, height and temperature are the same as in (c). The spectral line at the pump frequency (the long index on the abscissa) is the growing mode instability, the stronger line a few kilohertz away is the decay mode instability, and the broad structure is believed to be the result of

the strong line acting as a source and cascading energy into a neighboring line which in turn acts as a source.

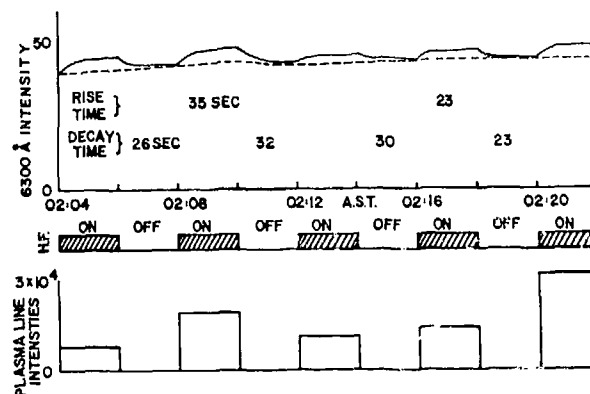


Figure 4. 6300 Å airglow intensity and average HF enhanced plasma line intensity vs time (13 October 1972). The HF transmitter is cycled on and off in 4 minutes. The difference between the dashed (background) and solid curves is the O-mode, HF induced impact excitation. The time constant is a measure of the  $N_2$  number concentration times the quenching coefficient.

ON THE SIZE OF THE IRREGULARITIES RESPONSIBLE FOR  
HEATER-GENERATED SPREAD-F

G. D. Thome, E. M. Allen and P. B. Rao  
Raytheon Company  
Sudbury, Massachusetts 01778

ABSTRACT

Two alternate models are used to predict how the angle-of-arrival of heater-generated spread-F should vary with range delay. In the first model the electron density irregularities of interest are taken to be field-aligned ducts with spatial dimensions large compared to the sounding wavelength. In this case rays launched obliquely from the sounder can return by means of refraction through the distorted contours of constant electron density which result. The second model assumes that the irregularities of interest are comparable to the sounding wavelength and field-aligned. In this model the spread-F returns represent volume scattering from that part of the ray path where the wave vector is normal to the magnetic field. It is found that the predictions of the large scale duct model agree best with the experimental data and consequently we do not believe that volume scattering plays an important role in producing the spread-F returns seen on ionograms during ionospheric heating experiments.

INTRODUCTION

One of the unexpected results of heating the ionosphere with powerful HF radio waves has been the generation of F-region electron density irregularities. The first evidence for the existence of these irregularities came from the observation that ionograms taken beneath the heated volume developed spread-F soon after heater turn-on (Utlaut, 1970). It was suggested by Georges (1970) that this artificial spread-F could be caused by the presence of field-aligned ducts having

dimensions large compared to the wavelength of the sounding frequency and he was able to show by ray tracing simulations that range spreading comparable in magnitude to that observed could be produced in this way. Later, when diagnostic instruments were fielded which were capable of measuring how the angle of arrival and the Doppler shift of the spread-F returns varied with range delay, it was shown by Allen et al. (1974) that these observations could also be interpreted in terms of field-aligned ducts with dimensions large compared to the wavelength of the sounding frequency. The purpose of this paper is to consider an alternate interpretation of the measurements in which the spread-F returns arise from scattering from field-aligned irregularities with dimensions comparable to the sounding wavelength rather than from reflection in ducts with dimensions large compared to the sounding wavelength.

The motivation for this work comes from two sources. First of all, there is good experimental evidence from transmission experiments (Rufenach, 1973; Pope and Fritz, 1974; Bowhill, 1974) and from radar experiments (Thome and Blood, 1974; Fialer, 1974; Minkoff et al., 1974) that the spectrum of irregularity scale sizes generated by the heating process extends from less than a meter to more than 10 km. The question therefore remains open as to whether the irregularities responsible for spread-F have scale sizes comparable to the ionosonde wavelength (tens of meters) or large compared to it (say a few kilometers); irregularities in both scale size ranges are present. Secondly, the success which has been had in

simulating the observed range delay versus angle of arrival relationship for spread-F using large scale ducts does not guarantee that the mechanism is correct. It has yet to be shown that the intensity of the large scale ducts is as great as required and that they grow fast enough to explain the observed Doppler shift versus angle of arrival characteristics. Bragg scattering from field-aligned irregularities is well established as the mechanism responsible for radar backscatter from the heated volume at frequencies above the vertical incidence critical frequency (Rao and Thome, 1974) and this same mechanism deserves serious consideration at frequencies below the vertical incidence critical frequency.

#### EXPERIMENTAL DATA

The geometry of the Platteville heating experiment is shown in Figure 1.

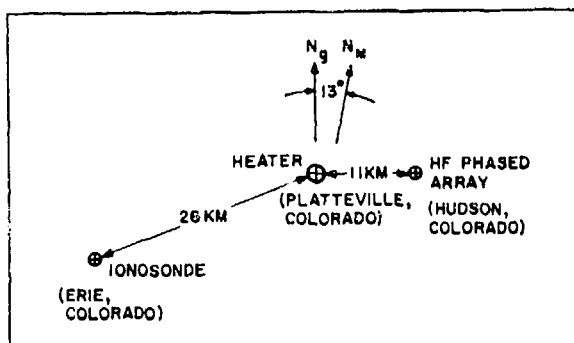


Figure 1. Geometry of the Platteville heating facility and associated spread-F diagnostic instruments.

The heating transmitter is at Platteville, has a vertically directed beam approximately 20 degrees wide at the half power points, and therefore the diameter of the "spot" illuminated in the overhead ionosphere is about 100 km. On this scale, the heater, the ionosonde (Erie) and the HF phased array (Hudson) can be considered to be co-located beneath the heated volume. The heating facility and the ionosonde were built and operated by the Institute for Telecommunication Sciences (ITS) and have been described elsewhere (Carroll et al., 1974; Utlaut and Violette, 1974). The HF phased array facility was built and operated by Raytheon. It consists of 32 broadband receiving elements equally spaced about

a 600 meter diameter ring, a central calibration element, and a co-located non-directional transmitting element for illuminating the overhead ionosphere. An artist's sketch of this instrument is shown in Figure 2; its operation has been described by Allen et al. (1974). The heater is used to generate the ionospheric irregularities, the ionosonde is used to show how the range delay of returns varies with sounding frequency, and the HF phased array is used to show how the angular spectrum of the returns varies with range delay at a fixed sounding frequency.

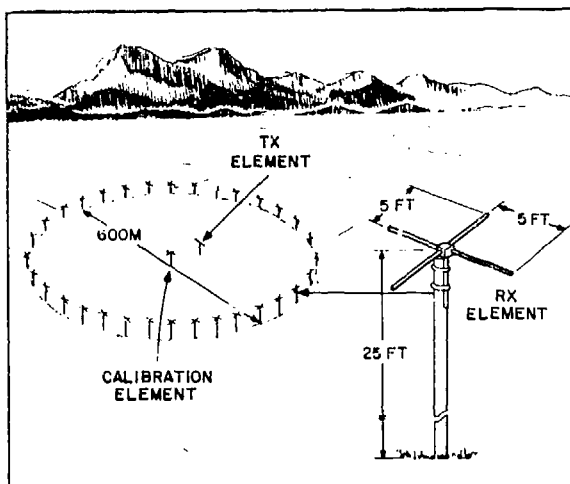
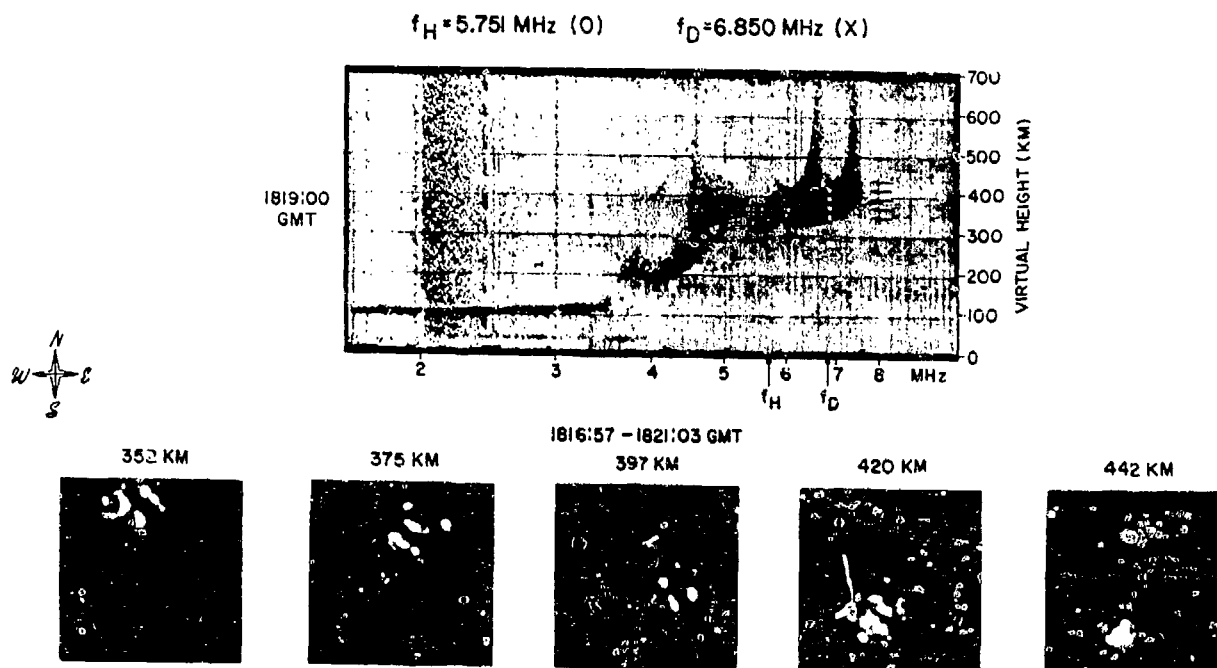


Figure 2. The HF phased array for measuring the angular spectrum of spread-F returns.

The data used for analysis in this paper is shown in Figure 3. All the data shown in this figure was taken over a period of about 4 minutes after 20 minutes of continuous heating with ordinary ray polarization at 5.751 MHz. The ordinary ray critical frequency was 6.64 MHz. The HF phased array examined the extraordinary ray returns at 6.850 MHz; the dots at this frequency on the ionogram show the positions of 5 range gates at which phased array data were taken. The sky maps at the bottom of this figure show the angular spectrum of the returns for each of these range bins. On these displays the zenith is at the center of the map, north to the top and west to the left. These displays are built up by first doing a Doppler spectrum analysis of the energy in a particular range bin, mapping the energy in each Doppler bin separately,





SCALE: RINGS SPACED BY 5 DEGREES IN ZENITH ANGLE

Figure 3. Spread-F generated by the Platteville heater: ionosonde data (top) and HF phased array data (bottom) after 20 minutes of continuous heating.

thresholding in the computer to remove sidelobe responses, and finally superimposing the thresholded maps for each Doppler bin with brightness proportional to signal intensity. The "blobby" character of the composite maps is a consequence of there being only a finite number of Doppler bins, each of which usually produces a single spot (equal in angular extent to the main beam width of the antenna). Individual scatterers are not resolved, implying that the horizontal spacing between scatterers is less than about 20 km. Qualitatively, this figure shows that as the range gate is moved from the leading edge of spread-F to the trailing edge, the angle of arrival of the returns moves from north to south. Figure 4 shows this quantitatively by drawing rectangles which enclose all the returns for a given range delay. The vertical dimension of the rectangle corresponds to the range resolution of the sounder (30 km); the horizontal dimension shows the north-south extent of the returns in each range bin. The hollow and the open circles are synthesized data and will be discussed below.

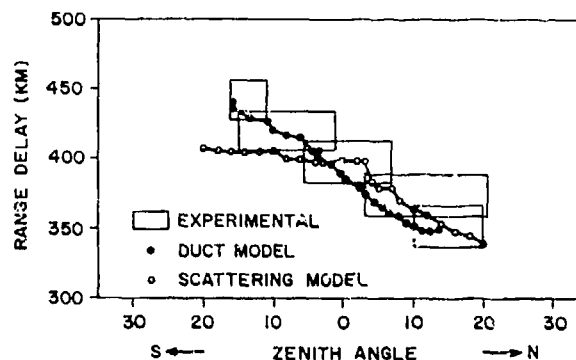


Figure 4. The variation of range delay with zenith angle in the north-south magnetic meridian plane: the boxes summarize the experimental data and the dots show the model simulation results.

## ANALYSIS

The two alternate models we have used to synthesize time delay versus angle of arrival curves for heater-generated spread-F are sketched in Figure 5. In both the duct model (left) and the scattering model (right) the electron density perturbations are aligned with the earth's magnetic field and extend throughout the ionosphere. In the duct model the perturbation is periodic, the horizontal wavelength is large compared to the sounding wavelength (5 km compared to 4.4 m), and intense ( $\pm 20\%$  electron density variation). In the scattering model it is assumed that the perturbations are weak (so that there is no significant difference between the ray paths with and without the perturbations) but that the electron density fluctuations caused by the heater have a strong enough spatial Fourier component at half the sounding wavelength to produce detectable volume backscattering from that portion of the ray path where the wave vector is normal to the magnetic field.

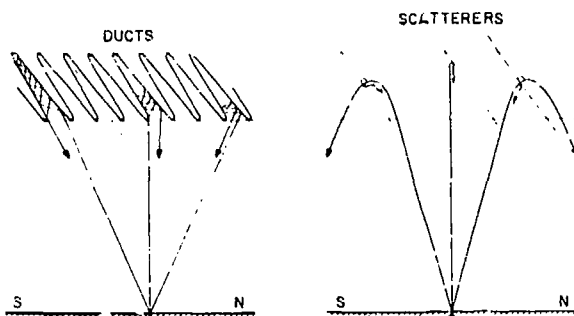


Figure 5. Sketches of the two alternate models used to simulate the variation of range delay with zenith angle for spread-F returns at a fixed sounding frequency.

The Jones ray tracing program (Jones, 1968) has been used in an attempt to simulate the observed data using these two models. The background ionosphere in both cases was taken from a true height reduction of the ionogram shown in Figure 3 and provided to us by ITS. In order to simplify the ray tracing task, the analysis was confined to the north-south magnetic meridian plane; this is the plane in which the variation of zenith angle with range delay is observed. A north-south fan

of extraordinary rays were traced with and without ducts. With ducts, rays launched at oblique angles can be returned to the transmitter after one or more "bounces" off the distorted contours of constant electron density. The ray tracings show that rays launched to the south (more nearly along the duct axis) penetrate more deeply into the ducts than do rays launched to the north, suffer greater group retardation, and consequently arrive back at the sounder with greater range delay. The simulated variation of range delay with zenith angle for the duct model is shown by the solid dots in Figure 4. Without ducts, only the ray launched vertically returns to the sounder but it is assumed that backscatter will be observed for other rays when the wave vector points normal to the earth's magnetic field. For rays launched to the north, the wave vector becomes normal to the magnetic field on the up-leg of the ray path; for rays launched to the south, the wave vector goes through normality on the down-leg. Returns from the south will therefore arrive back at the sounder with greater range delay than will returns from the north. The simulated variation of range delay with zenith angle for this model is shown by the hollow dots in Figure 4.

The predictions of both models are in substantial agreement with the experimental data for signals arriving from the north, to the south, however, the predictions of the duct model are significantly better. Modeling errors arising from the difficulty of deriving a true-height electron density profile in the presence of spread-F will shift the predicted curves up or down somewhat but will have little effect on their shape or slope. In this respect also the duct model predictions are significantly better than those of the scattering model, the shape and slope of the duct model predictions being in good agreement with the experiment data over the full zenith angle range.

## CONCLUSIONS

The model calculations presented here suggest that refraction in large scale ducts is a better idealization for the mechanism by which heater-generated spread-F is produced than

scattering by small scale irregularities. There is little doubt that both mechanisms are active since it is known that a broad spectrum of irregularity scale sizes are generated by the heating process. We have not attempted to compute the relative magnitude of the backscatter contributed by these two processes but we infer from the success of the duct model in predicting the angle of arrival versus range delay observations that the contribution which small scale scattering makes to heater-generated spread-F on ionograms is small.

#### REFERENCES

- Allen, E.M., G.D. Thome, P.B. Rao and R.L. St. Germain, The angular distribution of spread-F returns from an artificially modified ionosphere, J. Geophys. Res., 79, 3161, 1974.
- Bowhill, S.A., Satellite transmission studies of spread-F produced by artificial heating of the ionosphere, Radio Sci., 9, 975, 1974.
- Carroll, J.C., E.J. Violette and W.F. Utlaut, The Platteville high power facility, Radio Sci., 9, 889, 1974.
- Fialer, P.A., Field-aligned scattering from a heated region of the ionosphere - Observations at HF and VHF, Radio Sci., 9, 923, 1974.
- Georges, T.M., Amplification of ionospheric heating and triggering of 'spread F' by natural irregularities, J. Geophys. Res., 75, 6436, 1970.
- Jones, R.M., A three dimensional ray tracing computer program, Radio Sci., 3, 93, 1968.
- Minkoff, J., P. Kugelman and I. Weissman, Radio frequency scattering from a heated ionospheric volume, 1, VHF/UHF field-aligned and plasma-line backscatter measurements, Radio Sci., 9, 941, 1974.
- Pope, J.H. and R.B. Fitz, Observations of artificially produced scintillations using satellite transmissions, J. Geophys. Res., 79, 1065, 1974.
- Rao, P.B. and G.D. Thome, A model for RF scattering from field-aligned heater-induced irregularities, Radio Sci., 9, 987, 1974.
- Rufenach, C.L., Radio scintillation on stellar signals during artificial ionospheric modification, J. Geophys. Res., 78, 5611, 1973.
- Thome, G.D. and D.W. Blood, First observations of RF backscatter from field-aligned irregularities produced by ionospheric heating, Radio Sci., 9, 917, 1974.
- Utlaut, W.F., An ionospheric modification experiment using very high power, high frequency transmission, J. Geophys. Res., 75, 6402, 1970.
- Utlaut, W.F. and E.J. Violette, A summary of vertical incidence radio observations of ionospheric modification, Radio Sci., 9, 895, 1974.

ARTIFICIALLY INDUCED ENHANCEMENTS IN THE IONOSPHERIC  
BACKSCATTER SPECTRUM NEAR ELECTRON GYROFREQUENCY  
AND SECOND HARMONIC PLASMA LINE

Luiz Alberto Vieira Dias  
Instituto de Pesquisas Espaciais  
Sao Jose dos Campos, Brazil

William E. Gordon  
Rice University  
Houston, Texas 77001

### Introduction

During the heating experiment conducted at Arecibo Observatory in Puerto Rico it was noted that, in addition to the increase in the electron temperature, plasma instabilities occurred making it possible to observe plasma line enhancements (Gordon et al., 1971) and detect other enhanced lines, possibly due to the non-linear behavior of the heated plasma. We will describe here the observations of an example of these enhancements. Due to the weakness of the lines (as compared to the enhanced plasma lines (Kantor, 1974; Perkins et al., 1974)) and the short radar time available for this search, special precautions had to be taken to exclude instrumental effects.

In brief, the heating experiments consisted of sending an HF radio wave (CW), using the Arecibo dish to focus the power (up to 140 KW) to modify the ionosphere above Arecibo (Gordon et al., 1971; Kantor, 1972; Dias, 1973). The feed was a log-periodic structure at the focal line of the Arecibo 300 meter dish. To detect ionospheric modifications, the Observatory ionosonde, photometers and the backscatter radar were used. The enhanced lines were observed by the radar. The HF power could be sent in ordinary (O-mode), or extraordinary (X-mode) polarizations.

The block diagram of the experiment is seen in Figure 1. Due to the ionospheric inhomogeneous properties (Budden 1966), the right hand circularly polarized wave (O-mode) bends towards the magnetic North when launched vertically, and at the height of reflection the center of the heated region is about 60 km away from the zenith line at the launching point. This is very fortunate because it makes it possible to point the radar to the heated region center. When the HF feed is in place the radar

feed has to be at least  $4^\circ$  off the zenith since they use the same track (see Figure 2).

Due to the HF propagation, the electric field configuration for O-mode at ionospheric heights is such that it is linearly polarized and parallel to the earth's magnetic field. For X-mode the HF reflection occurs at a lower height and, in addition,  $E_{HF}$  is perpendicular to the local magnetic field. At Arecibo in the northern hemisphere the X-mode wave bends towards the magnetic south. The observations reported here were obtained using O-mode only. For O-mode near the reflection level, the electric field due to the HF transmitter can be described as  $E = bE_0 \sin \omega t$ , where  $b$  is the absorption due to the trip from ground to the reflection level and  $E_0$  is the electric field leaving the antenna (Dias, 1971). The reflection is possible only if the frequency of the HF wave is less than the penetration frequency of the ionosphere (Budden, 1966). When the HF wave penetrates the heating is inefficient and the modifications in the ionospheric plasma undetected.

### Method of Observation

The search for enhanced lines was made using the 430 MHz radar backscatter of the Arecibo Observatory (Gordon and LaLonde, 1961) while the ionosphere was being heated by an HF transmitter. The receiving setup is seen in Figure 3, where by changing the frequency of the local oscillator (frequency synthesizer) it is possible to tune to the desired part of the spectrum of the backscattered signal. The signal arrives at the computer (CDC-3300) as a "profile," i.e., an intensity versus time of arrival that is proportional to the height of the radar wave reflection. In the programs used the height resolution was determined by the sampling rate (typically

128 points) in a height band of 150 km that was set in order to get the HF reflection height inside the band.

The profile thus obtained can be transformed into a spectrum by means of a fast fourier transform, with the corresponding frequency resolution limited by the number of samples of the input heights. Most of the data was taken sampling 128 points. The number of samples is limited by the interface. Of course the processing of the signal with a large number of points is very slow and the height band can be larger than the height range which can confuse the data. For the sampling rate of 128 points the frequency resolution was 1.12 kHz.

It was expected to have stronger returns from the height of maximum heat deposition at frequencies where plasma instabilities occur, and somewhat weaker signals from all other heights and frequencies. Due to the large frequency band of the profile (typically 125 kHz), these enhancements are not apparent, but in the spectrum they can be observed in frequency, becoming smeared in height if the signal-to-noise ratio is large enough. The enhanced lines are assumed to come from a thin layer near the height of reflection where the heat deposition is maximum (Meltz and LeLevier, 1970; Dias, 1971), thus producing instabilities.

### Results

Two types of observations were performed: the first in the vicinity of the electron gyrofrequency and the second in the vicinity of the second harmonic plasma line. We shall call the line observed near the electron gyrofrequency GL (gyroline), and the line observed near the second harmonic plasma line DL (diplasma line).

With regard to the GL, it should be expected that the returned echo be modulated at both sides of the carrier radar frequency at the receiver by any existing frequency of plasma oscillation (Seely, 1956). We will call upshifted and downshifted gyrolines UGL and DGL, the resulting signals due to the modulation. The data on the DGL will not be taken into account because of strong interference, which was recognized as such because of the tests that will be described later and also because it was fixed in time, as opposed to the expected behavior of a line of physical origin that should change its frequency due to the time changing ionospheric gyrofrequency at

the height of production (assumed to be near the HF reflection level). The UGL behaved as expected and these data will be seriously considered here. The only DGL that could not be immediately identified as interference occurred on 19 May 1972 (see Figure 8), but due to the small amount of data (1.5 minutes) it will not be taken into account here.

Additional safety precautions were taken against interference. All data were taken in three steps: (1) with the heater on and the receivers connected to the antenna to record the data, (2) with the heater on and the receivers connected to a dummy load to be sure that the signal was coming from the ionosphere, and (3) with the heater off and the receivers connected to the antenna to be sure that the effect seen was produced by the artificial heating of the ionosphere, i.e., the voltage on the grid of the final stage tube was brought to zero (the heaters on the tube continued ON). These procedures tested a possible source of interference. Step 2 would show a signal if it was due to leakage since the antenna is not linked to the system, but the leakage routes (if any) are unchanged. In step 3, if no signal is detected, it is seen that, in addition to not being due to leakage (if no signal is seen in 2 also), the line observed in step 1 is due to the effect of the ionospheric heating and it is coming from outside the receiver. It is worth noting that all UGL data passed these tests, while the DGL, except for the 19 May 1972 observation (Figure 8), did not.

More evidence in favor of the UGL was found. Any possible interference due to the beating of the local oscillators and/or the HF transmitter frequency should be a fixed frequency in time since only fixed frequencies were involved. The UGL was not fixed in time, as will be seen from the figures. It should also be noted that the observations producing gyrolines were within a few hours after the sunrise, while observations with exactly the same set-up at other times did not turn out any gyrolines. This is a good indication that the feature observed is not due to the system, since it is not likely that the system would misbehave at regular intervals, while it is likely that the ionosphere would produce a certain phenomenon at regular intervals. Figure 4 shows all observations at the gyroline as a function of time. Note the concentration of positive observations around sunrise.

After the first detection of the gyrolines (Dias and Gordon, 1973) more

data were collected in order to infer the morphology of these lines. The data taking period was March 14, 15 and 16 and May 19. During every search for the gyroline a second channel in the receiver was tuned to the plasma line so that the intensities and frequencies of the two lines could be compared.

Another source of possible interference is the harmonics of the HF transmitter. The frequencies used were 5.100, 5.425, 6.790, 8.187 and 10.850 MHz. As shown by Dias (1973), the closest value of the HF harmonic to the UGL was the 8th harmonic for 5.100 MHz but it was about 2.3 MHz away from the observed line; for the DGL it was more than 0.3 MHz away. Recalling that the observed bandwidth was only 125 KHz, it is seen that the harmonics are not playing any interference role for the gyrolines.

The observed gyrolines are shown in Figures 5-8, where the intensity and frequency changes are presented as a function of time. Some of the features observed are as follows. On 14 March (Figure 5), only one HF frequency was used, 5.425 MHz, whereas on 15 March several HF frequencies were used, as seen in Figure 6, and on 16 March (Figure 7) the GL behavior seen the previous day is confirmed. During the May series (Figure 8), only sporadic observations were reported with the detection of a possible DGL. More data on the DGL is needed to confirm it.

The observations near the second harmonic of the plasma line (Dias, 1973) produced upshifted and downshifted lines at frequencies plus or minus the following difference: two times the HF frequency minus the ion acoustic frequency. For simplification, these lines will be called upshifted and downshifted diplasma lines (UDL and DDL, respectively). The plasma line itself has a complex structure (Perkins, 1974); the main feature is a big peak at the plasma frequency minus the ion acoustic frequency (Kantor, 1974). As seen from Figure 9, the diplasma lines only appeared after the intensity of the plasma line reached a relatively high value; however, there is no apparent direct proportionality between the plasma and diplasma line intensities. It should be pointed out that only one observation was made (11 October 1972); thus, it is too early to talk about the morphology of these lines. The possibility of interference in this case has to be checked more carefully with future data. Tests were made to check

for interference. The pattern of the tests was similar to that used in the gyroline observations. Further observations will be illuminating.

### Conclusions

As seen in Figures 4-8, the gyroline was either observed, not observed at all or just partially absent during a run. In spite of the large number of different situations, HF frequencies, HF powers, and on 19 May different zenith angles on the radar feed, it is still difficult to determine the complete morphology of the UGL. It is strongly suggested that in future heating series the following tests be made in order to further understand the gyrolines: (a) try more runs 2 to 3 hours before sunset since it appears that these lines are better seen 2 to 3 hours after sunrise and the conditions in the ionosphere are similar (rapid changing electron density and electron temperature for a fixed height); (b) try more runs looking at the DGL, checking carefully all the electronics involved to minimize any possible interference; (c) look for 2nd and 3rd harmonics of the UGL and DGL; (d) increase the observations during all hours of the day in order to complete the statistics of Figure 4.

It is also necessary to make more observations of the diplasma lines in order to gain a better understanding of the conditions involved in their production.

It is hoped that in future heating experiments further characteristics of these lines could be observed and, in due time, understood.

### Acknowledgements

The ionospheric heating experiments described in this paper were conducted at the Arecibo Observatory operated by Cornell University. This work was supported in part by the Advanced Research Projects Agency under Contract F3602-72-C-0278 and monitored by the Air Force Systems Command, Rome Air Development Center. L.A.V. Dias is indebted to the Instituto de Pesquisas Espaciais (INPE), Brazil, for partial support.

### References

- Budden, K. G., Radio Waves in the Ionosphere, Cambridge University Press, England, 1966.
- Dias, L.A.V., High frequency radio heating of the ionosphere, M.S. Dissertation, Rice University, 1971.

Dias, L.A.V., Observations of artificially induced enhancements in the ionospheric backscatter spectrum, Ph.D. Dissertation, Rice University, 1973.

Dias, L.A.V., and W. E. Gordon, The observation of electron cyclotron lines enhanced by HF radio waves, J. Geophys. Res., 78, 1730-1732, 1973.

Gordon, W. E., and L. M. LaLonde, The design and capabilities of an ionospheric radar probe, IRE Trans., AP-9, 17, 1961.

Gordon, W. E., R. L. Showen and H. C. Carlson, Ionospheric heating at Arecibo: First tests, J. Geophys. Res., 76, 7808-7813, 1971.

Kantor, I. J., Plasma waves induced by HF radio waves, Ph.D. Dissertation, Rice University, 1972.

Kantor, I. J., High frequency induced enhancements of the incoherent scatter spectrum at Arecibo, 2, J. Geophys. Res., 79, 199-208, 1974.

Meltz, G., and R. E. LeLevier, Heating the F-region by deviative absorption of radio waves, J. Geophys. Res., 75, 6406, 1970.

Perkins, F. W., C. Oberman and E. J. Valeo, Parametric instabilities and ionosphere modification, J. Geophys. Res., 79, 1478-1496, 1974.

Seely, S., Radio Electronics, McGraw-Hill, New York, 1956.

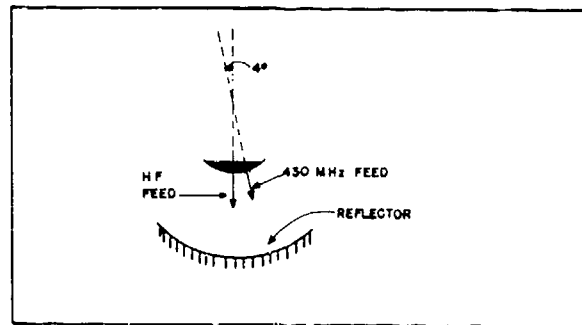


Figure 2. Feed geometry.

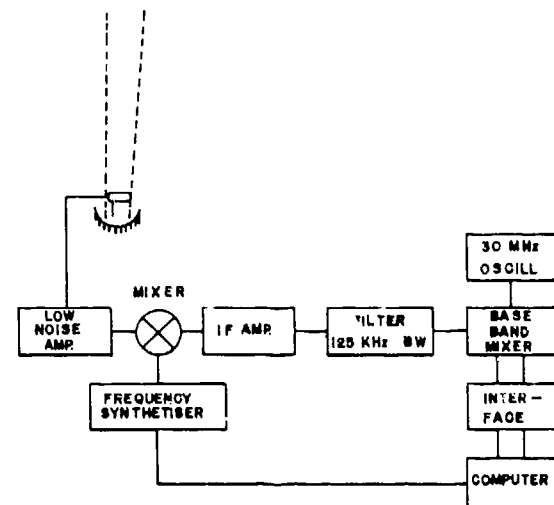


Figure 3. Receivers setup.

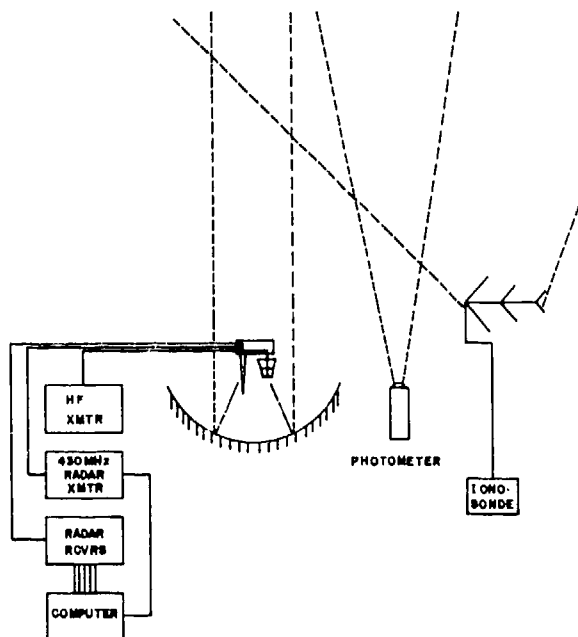


Figure 1. Heating experiment block diagram.

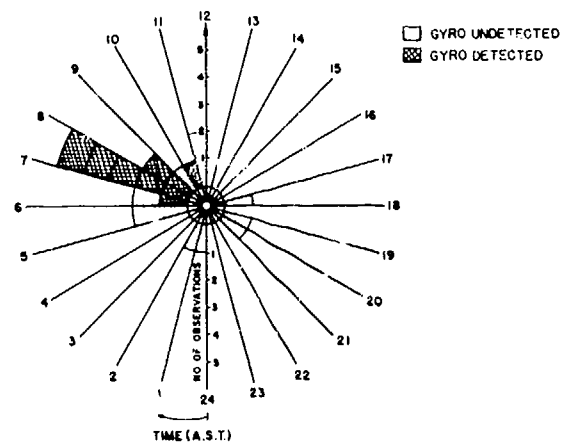


Figure 4. Available statistics on the gyroline occurrence.

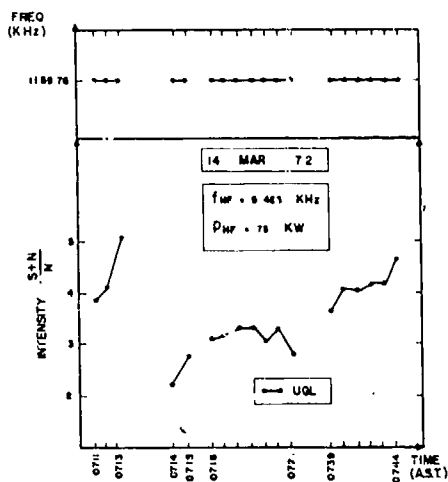


Figure 5. GL Results, 14 March 1972.

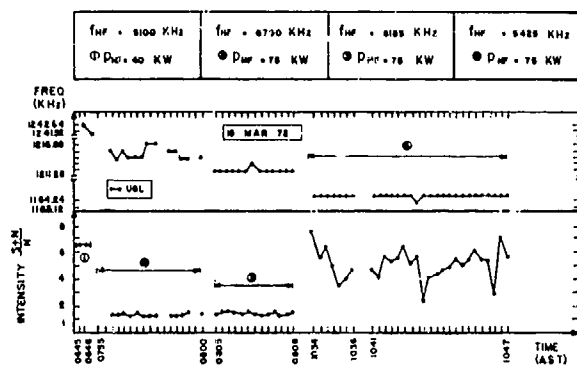


Figure 6. GL Results, 15 March 1972.

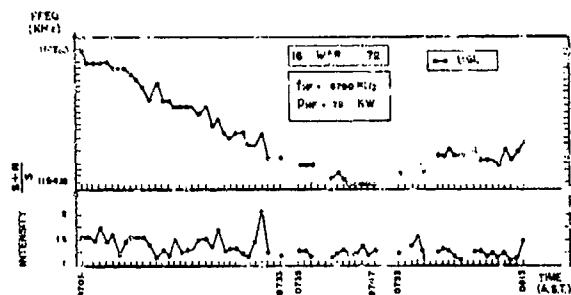


Figure 7. GL Results, 16 March 1972.

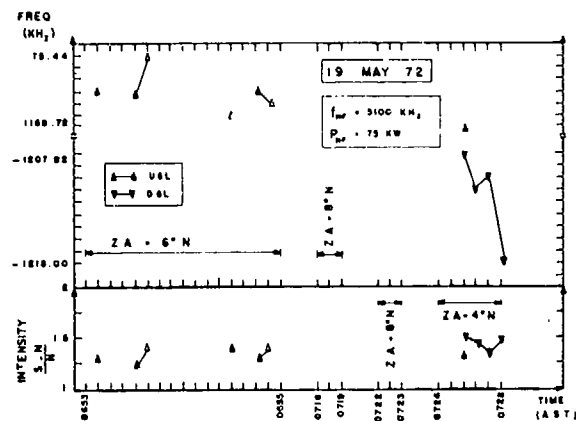


Figure 8. GL Results, 19 May 1972.

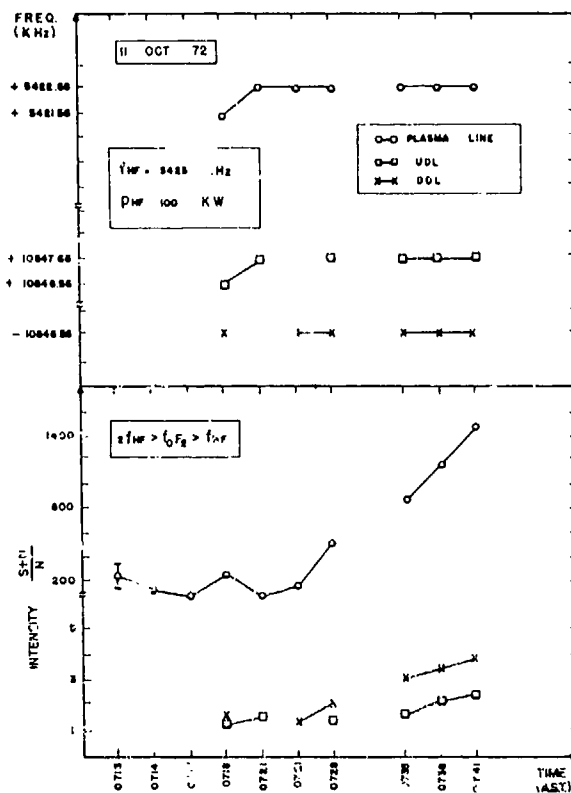


Figure 9. DL Results, 11 October 1972.



## IONOSPHERIC PERTURBATIONS CAUSED BY ARTIFICIAL SOURCES

G. L. Rao and R. J. Hung  
The University of Alabama in Huntsville  
Huntsville, Alabama 35807

and

R. E. Smith and G. S. West  
Aerospace Environment Division/Space Sciences Lab  
NASA/Marshall Space Flight Center  
Huntsville, Alabama 35812

### ABSTRACT

Characteristics of artificially-induced ionospheric perturbations are investigated using a CW high frequency Doppler sounder array and an ionosonde. The study is mainly concerned with the investigation of wave-like disturbances in the ionosphere generated by rocket launches such as the Saturn-Apollo 12 and 13 rockets. In the present analysis, the Doppler records of ionospheric disturbances are taken from the Doppler sounder array at Westwood, New Jersey, and the ionograms are taken from the ionosonde located at Wallops Island, Virginia. Infrasonic waves with periods in the 2-4 minute range and phase velocities of the signal arriving from south of the array at speeds of 700-800 m/sec were observed. Characteristics of the waves are discussed in detail.

### I. INTRODUCTION

Wave-like disturbances caused by artificial sources were observed in the ionosphere following several nuclear explosions in the early 1960's (e.g., Obayashi, 1962). These wave-like disturbances due to nuclear explosions, observed at altitudes of 150 to 250 Km in the ionosphere, were characterized by periods ranging from 30 seconds to 10 minutes and velocities of about 400 m/sec. The periods and propagation characteristics of the ionospheric disturbances were found to be similar to those disturbances observed on the ground.

Supersonic shock waves in the atmosphere generated by the large rockets can also cause ionospheric electron density variations. Ionospheric perturbations caused by Saturn-

Apollo rocket launches were noticed on the ionograms taken at Grand Bahama Island (Felker and Roberts, 1966; Fehr, 1968).

In this paper, we report the results of our investigations of ionospheric disturbances caused by artificial sources, particularly by the launchings of Saturn-Apollo rockets from Cape Kennedy (28.5° N, 80.5° W). The experimental facilities used in this study are a CW Doppler sounder array located in the vicinity of New York City (41° N, 74° W) and rapid sequence ionograms from Wallops Island, Virginia (38° N, 75° W). The ionosonde and CW Doppler array were located about 1000 Km from Cape Kennedy.

In Section II, we describe the experimental system of CW Doppler sounder array and ionosonde, and the observational results obtained from these facilities. In Section III, we summarize the experimental observations and compare them with theoretical results.

### II. EXPERIMENTAL SYSTEMS AND OBSERVATIONAL RESULTS

The CW Doppler system was developed by Davies (1962). Davies and Baker (1966) described the theory and the interpretation of the data. The geographic location of the CW Doppler sounder array used in the present study is shown in Figure 1. Two CW transmitters, operating at 4.8 and 6.0 MHz, were located at Sterling Forest, New York and were continuously monitored by the receivers located at Catskill, N. Y., Thornhurst, Pa., Lebanon, N. J., and Westwood, N. J. The receiver outputs were digitized and transmitted by telephone lines to the central station, Westwood, N. J., for storage on magnetic tape.

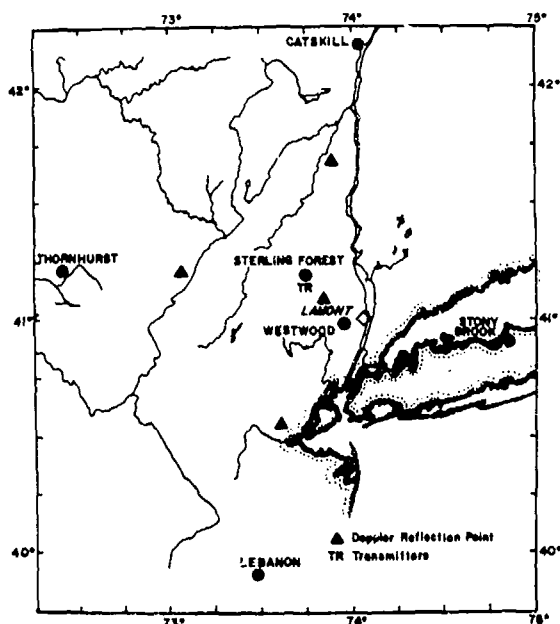


Figure 1. Geographic location of the CW Doppler array.

The CW Doppler array was in operation during the launches of the Saturn-Apollo 12 and 13 rockets. Figure 2 shows the Doppler records of the Saturn-Apollo 12 launch on November 14, 1969 at 1122 EST. Examination of the Doppler

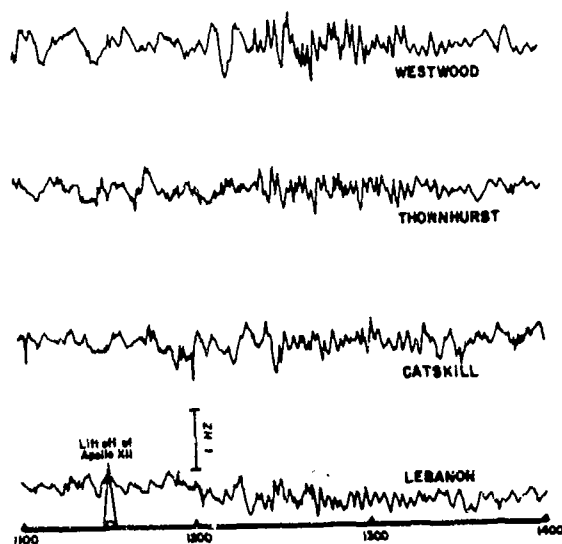


Figure 2. CW Doppler sounder records for Saturn-Apollo 12 rocket signal.

records at all three stations clearly shows there is a high frequency signal between 1220 EST and 1320 EST. The CW Doppler data for Lebanon and Thornhurst immediately before the signal arrival between 1100 and 1220 EST were

subjected to cross spectral analysis to study the background Doppler noise coherence. It can be clearly seen from Figure 3 that the background noise coherence is rather poor in the entire period and remains less than 0.2. Cross spectral analysis of the rocket signals received by several stations during the time period 1220-1340 EST was used to find the dominant spectral peaks and the coherency

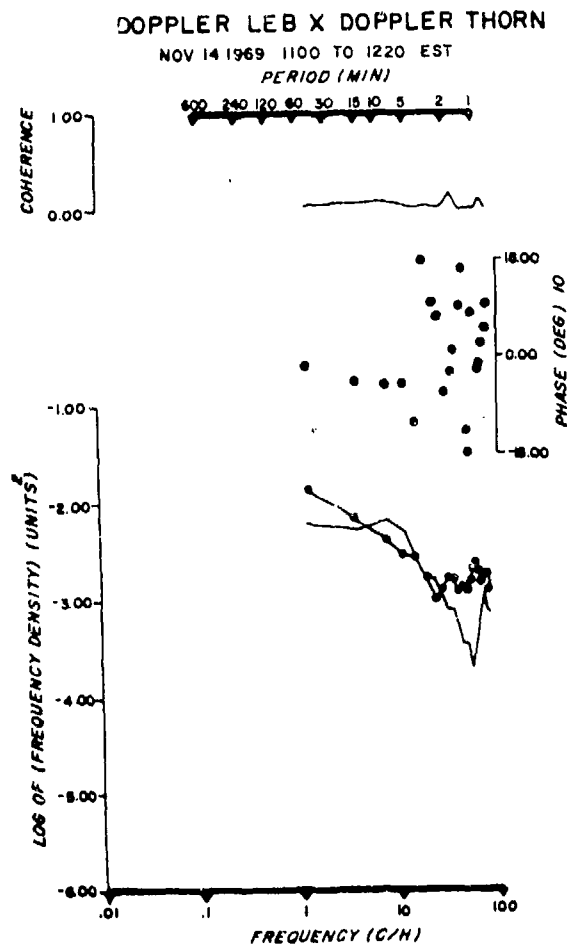


Figure 3. Power spectral plots of CW Doppler record before Saturn-Apollo 12 signal arrival.

of the signal with the station separation. The results of cross spectral analyses between Lebanon-Westwood, Lebanon-Thornhurst, and Catskill-Thornhurst are presented in Figures 4, 5 and 6, respectively. Examination of the spectral curves for all the stations clearly shows that there is a concentration of wave energy in the 1 to 4 minute period (0.004167 to 0.0167 Hz frequency band), and the coherency of the signal remained well over 0.78 in all station pairs. The CW Doppler data were then filtered using a bandpass filter of 1 to 5 minutes; the resulting plot is shown in Figure 7. It can be seen from Figure 7 that the

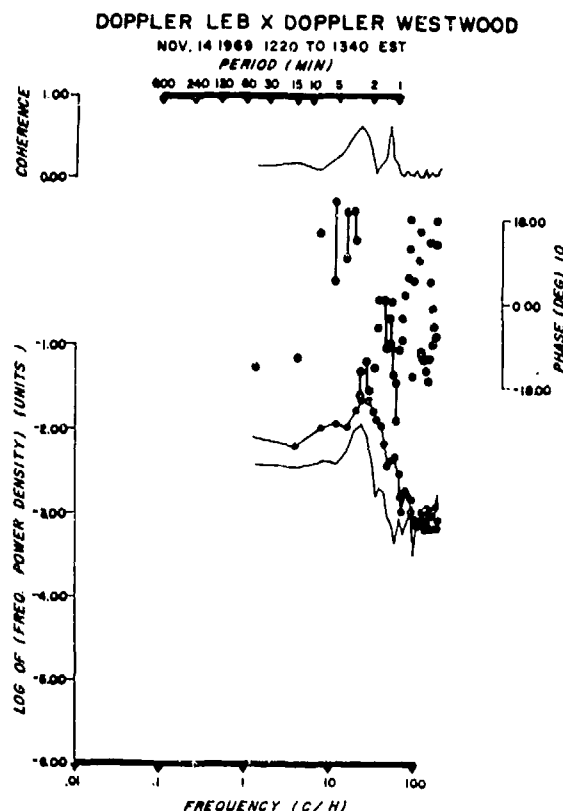


Figure 4. Power spectral plots of CW Doppler signal for Lebanon-Westwood.

signal due to the rocket launch lasted approximately 60 minutes. A similar analysis was used on the CW Doppler records taken during the launch of Saturn-Apollo 13, and the signal due to the rocket as shown in Figure 8. In recording the Saturn-Apollo 13 signal, the Doppler sounder array was operating at 6.0 MHz, whereas in the case of Saturn-Apollo 12, the array was operating at 4.8 MHz. The ionospheric reflection height for the Saturn-Apollo 13 rocket signal seen on the Doppler record is about 20 Km higher than that from the Saturn-Apollo 12.

Cross correlation analysis between station pairs was used on Saturn-Apollo 12 Doppler data to compute the phase velocities of the signal arrivals. The average phase velocity of the signal arrivals was found to be 700-800 m/sec, coming from south of the array. The group velocities of the signal arrivals were estimated to be on the order of 450 m/sec, obtained from the earliest visible disturbances seen on the CW phase path Doppler records together with the rocket trajectory data.

Rapid sequence ionograms from Wallops Island, Virginia, taken every one minute for a

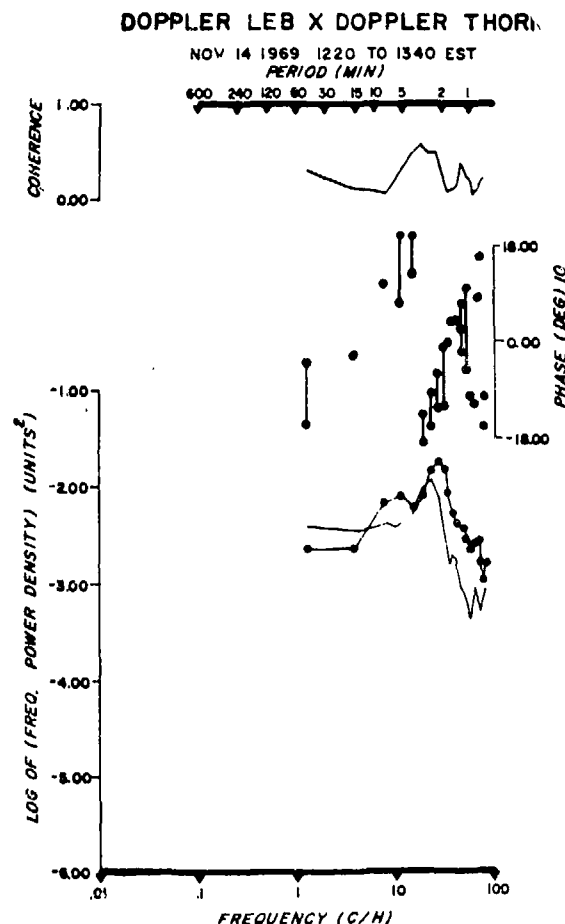


Figure 5. Power spectral plots of CW Doppler signal for Lebanon-Thornhurst.

period of two hours immediately after the Saturn-Apollo 12 launch of November 14, 1969, were provided by the NOAA ionospheric sounding station. The ionograms showed variations in the F-2 layer critical frequencies beginning around 1210 EST. The changes in critical frequency of the F-2 layer were followed by changes in the virtual heights of reflection. The virtual height changes first appeared at high frequencies and progressed downward to the lower frequency end of the ionogram. The disturbance first appeared as a fall in the critical frequency followed by an increase in virtual height over the part of the frequency range, causing a "kink" on the ionogram trace.

Figure 9 shows an ionogram at 1215 EST in which a "kink" has appeared around 450 Km, which apparently caused the increase in virtual height. The ionogram at 1216 EST (Figure 10) clearly shows that the "kink" is now rather well developed and has a "U" shaped configuration. One of the branches of the disturbance trace has merged with the trace of the ordinary

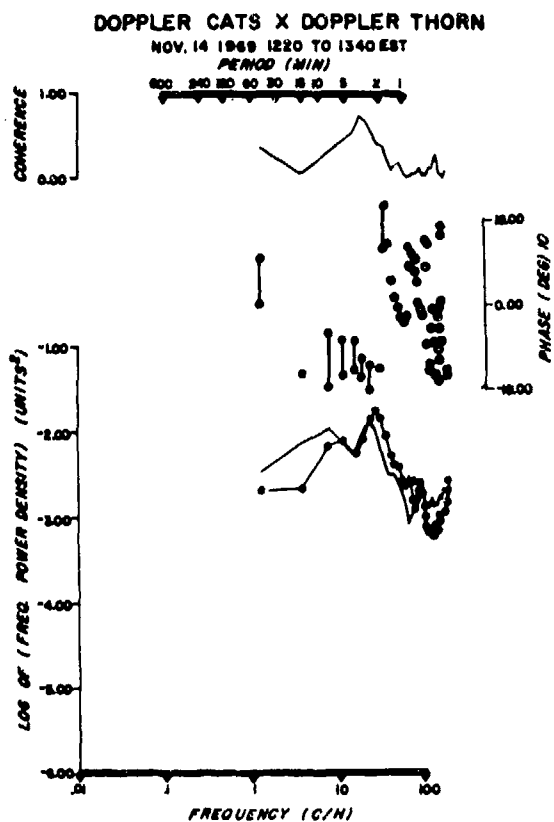


Figure 6. Power spectral plots of CW Doppler signal for Catskill-Thornhurst.

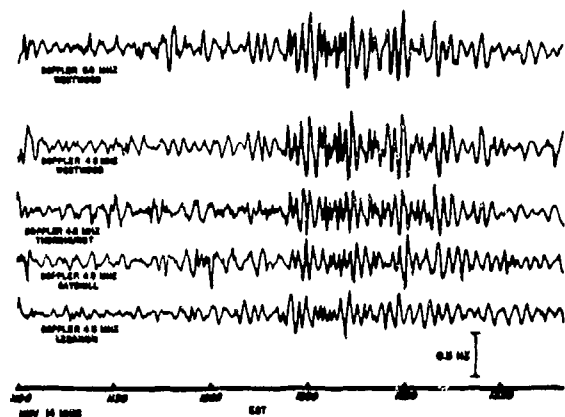


Figure 7. The 1.0-5.0 minute bandpass filtered CW Doppler record for Saturn-Apollo 12 signal.

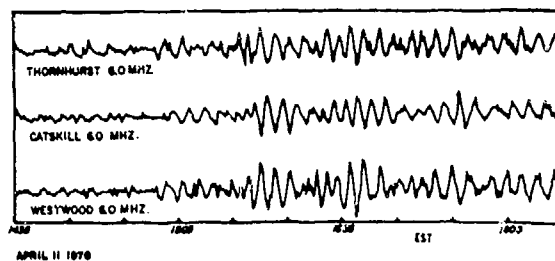


Figure 8. The 1.0-5.0 minute bandpass filtered CW Doppler record for Saturn-Apollo 13 signal.

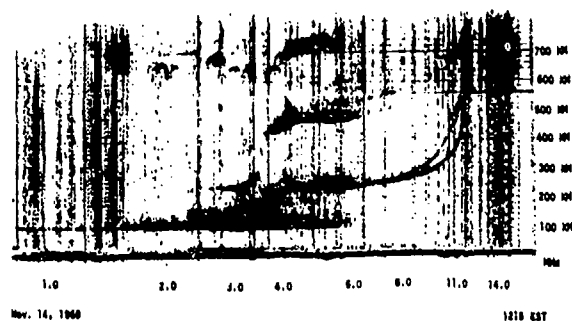


Figure 9. Ionogram for Wallops Island, Virginia at 1215 EST, for Saturn-Apollo 12 launch.

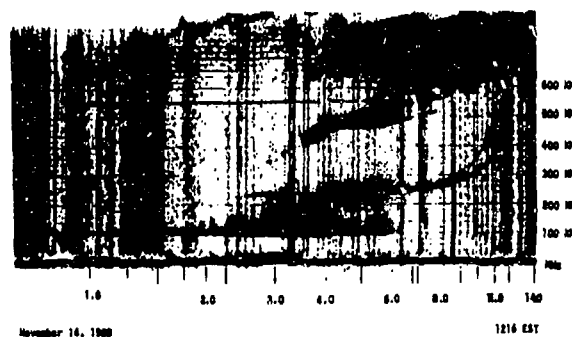


Figure 10. Ionogram for Wallops Island, Virginia at 1216 EST, for Saturn-Apollo 12 launch.

critical frequency of the F-2 layer. The other branch of the disturbance trace lies to the left of the trace of the ordinary F-2 layer critical frequency trace. Examination of the ionograms, at 1218 EST (Figure 11) and 1219 EST (Figure 12), also show that the "kink" has steadily moved downward approximately at a rate

of 20 Km/minute while preserving its "U" shaped configuration. Examination of the ionogram at 1220 EST (Figure 13) shows that the "U" shaped configuration has split into additional stratifications or satellite traces around the ordinary frequency trace.

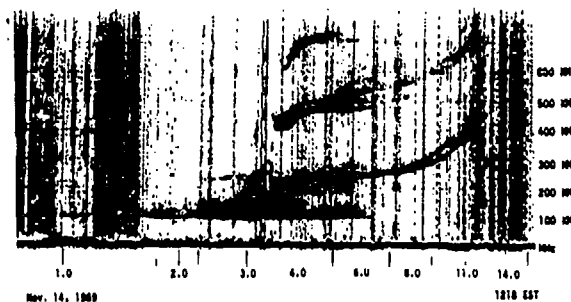


Figure 11. Ionogram for Wallops Island, Virginia at 1218 EST, for Saturn-Apollo 12 launch.

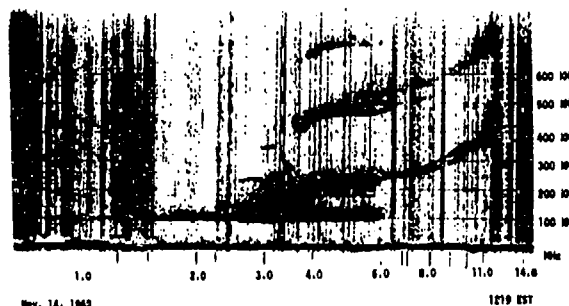


Figure 12. Ionogram for Wallops Island, Virginia at 1219 EST, for Saturn-Apollo 12 launch.

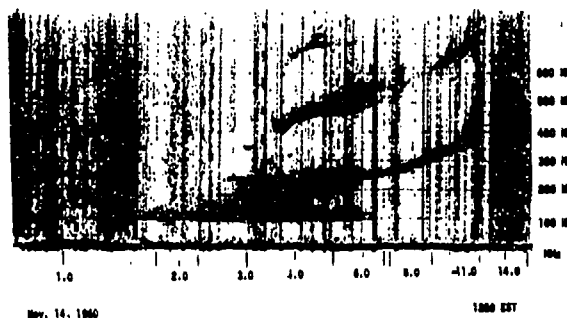


Figure 13. Ionogram for Wallops Island, Virginia at 1220 EST, for Saturn-Apollo 12 launch.

The ionograms were then subjected to true height analysis to study the electron density fluctuations in the F-region. The results of the true height analysis are plotted as electron density variations at 10 Km height interval against local time as shown in Figure 14. The constant height electron density contours clearly show the presence of a wave motion. It might be of interest to note that the maximum effect of the rocket on the ionosphere occurred around 1218 EST (56 minutes after launch). Also, the amplitude of the undulations appears to have increased with altitude.

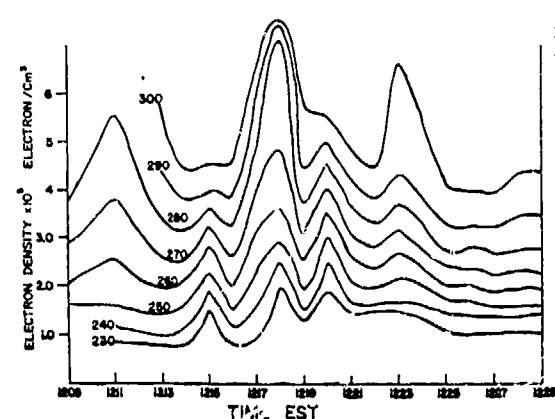


Figure 14. Electron density variations at 10 Km height intervals against local time.

### III. SUMMARY AND DISCUSSIONS

Observations of ionospheric disturbances associated with rocket launches from both a Doppler sounder and an ionosonde indicate the generation of wave-like disturbances with wave periods in the range of 2 to 4 minutes. This period is essentially below the local Brunt-Väisälä frequency. In other words, these waves are classified practically in the category of infrasonic waves. Observations of infrasonic waves in the ionosphere with the same order of wave periods are not very often reported in the literature available except for the disturbances due to severe weather activity. Georges (1968), Davies and Baker (1969), and Hung, et al. (1975) have reported the observations of ionospheric disturbances with wave periods ranging from 2 to 5 minutes due to thunderstorm activity. Furthermore, Hung, et al. (1975) also reports observations of ionospheric disturbances with wave periods in the range from 6 to 9 minutes caused by tornado activity. The physical mechanisms are completely different for these two cases. The infrasonic waves generated by severe weather are strongly dependent on the wind structure (both wind velocity and wind shear) and the temperature gradient in the stratosphere, troposphere and thermosphere,

whereas the infrasonic waves excited by rocket launches are strictly due to Cerenkov excitation.

The difference of the excitation mechanism also explains why the rocket-excited infrasonic waves can propagate long distances. Recent studies made by Hung, Wu and Smith (1975) show that the dissipation of acoustic waves is inversely proportional to the square of the wave frequency for the wave propagating in a collision-dominated medium, and is inversely proportional to the wavelength or proportional to the wave frequency for the wave propagating in a collision-free medium. For the case with a medium which is transitional between the collision and collisionless cases, the dissipation rate also changes from the square of the wave frequency to the wave frequency. These results indicate the following two things: (1) the dissipation rate of an infrasonic wave decreases as it propagates to the higher altitude; (2) infrasonic waves with longer wave periods can propagate longer distance without dissipation than waves with shorter wave periods. These results explain why the longer wave period infrasonic waves excited by rockets can propagate more than a thousand kilometers without dissipation. On the other hand, infrasonic waves generated by severe weather can only propagate within a few hundred kilometers because strong wind shears and temperature gradients damp out the horizontal component of waves to the order of wavelength which range from 150 to 300 Km.

#### ACKNOWLEDGEMENT

R. J. Hung and G. L. Rao wish to acknowledge the support of NASA/Marshall Space Flight Center under Contract NAS8-30616 for the present work.

#### REFERENCES

- Davies, K., Proc. IRE 50, 94, 1962.
- Davies, K., and D. M. Baker, Radio Sci. 1, 545, 1966.
- Davies, K., and D. M. Baker, J. Atmosph. Terr. Phys. 31, 1345, 1969.
- Fehr, V., Proc. ESSA/ARPA Acoustic Gravity Wave Symposium, ESSA, Boulder, Col., 1968, pp. 87.
- Felker, J. K., and W. T. Roberts, J. Geophys. Res. 71, 4692, 1966.
- Georges, T. M., J. Atmosphy. Terr. Phys. 30, 735, 1968.
- Hung, R. J., G. L. Rao, R. E. Smith, G. S. West and B. B. Henson, "Ionospheric Disturbances During Severe Weather Activities," (in this Proceeding), 1974.
- Hung, R. J., S. T. Wu and R. E. Smith, "Propagation of Acoustic Modes in the Transitional Ionosphere," J. Geophys. Res., (in press) 1975.
- Obayashi, T., Rept. Ionosphere, Space Res. (Japan) 16, 334, 1962.

# THEORETICAL AND NUMERICAL SIMULATION STUDIES OF IONOSPHERIC INHOMOGENEITIES PRODUCED BY PLASMA CLOUDS

S. L. Ossakow,<sup>+</sup> A. J. Scannapieco,<sup>\*</sup> S. R. Goldman,<sup>\*</sup>  
D. L. Book,<sup>+</sup> and B. E. McDonald<sup>+</sup>

<sup>+</sup> U. S. Naval Research Lab, Washington, D. C. 20375

<sup>\*</sup> Science Applications, Inc., McLean, Va. 22101

We will discuss in this paper our two-layered model for striation and image cloud development when plasma clouds exist in and are coupled to the background ionosphere. The work is being conducted in order to obtain a better understanding of striation physics, scale sizes, power spectrum, etc. in plasma clouds released in the ionosphere. We will be talking about cloud morphology, image formation, and striations. Striations are magnetic field-aligned irregularities such as are seen in barium plasma clouds (Rosenberg, 1971; Davis et al., 1974) released in the ionosphere and in the late time development of high altitude nuclear explosions. These phenomena are often diagnosed by optical techniques. If, however, these striations induced irregularities in other regions of the ionosphere such irregularities would be invisible to the naked eye, but not to radar or communication signals that pass through them. Indeed, these image effects, as we shall call them, could have a profound effect on such signals. Although we have spoken of artificially released plasma clouds inducing these image effects, the basic ideas are equally applicable to naturally occurring plasma blobs or irregularities that appear in the ionosphere (here the clouds themselves are only visible to radio signals.). Figure 1 shows a simplified view of our basic two-level system for treating plasma clouds coupled to the background ionosphere. Layer 1 represents the level at which the basic plasma cloud exists and layer 2 is the level at which images will occur (in actuality images will extend continuously below the cloud to some level depending on background ionospheric ion-neutral collision frequencies and ratio of cloud to background ionosphere Pedersen conductivity). Each of the two levels is characterized by its own zeroth order parameters (take constant within each level) such as ion-neutral collision frequencies, cross magnetic field conductivities, etc. (see for example Goldman et al., 1974; Scannapieco et al., 1974). The two regions are electrostatically coupled because of the high conductivity along the magnetic field lines which couple the two layers. Typically we consider cases where the plasma cloud is in the F region and

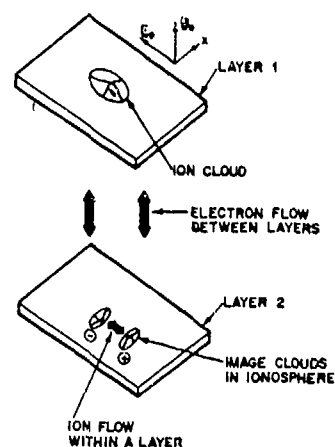


Figure (1). Two layered model for plasma cloud, images and striations. The earth's ambient magnetic field,  $B_0$ , is in the  $z$  direction and taken constant. The ambient electric field,  $E_0$ , is transverse to  $B_0$ . The plasma cloud is in layer 1 and image clouds (positive and negative ion enhancements) in the background ionosphere are induced in layer 2. The model is two-dimensional in the  $x$ - $y$  plane.

coupled to the E region, i.e., the cloud is around 200-250 km and would produce images down to around 150 km. Figure 1 gives a pictorial view of the plasma cloud layer 1 with say a gaussian density dependence and the attendant image clouds induced by it in layer 2. The plus and minus sign in layer 2 refers to enhancement of positive ions and depletion of positive ions from the ambient values, respectively. The geometry of the applied electric,  $E_0$ , and magnetic,  $B_0$ , fields are shown. Perturbations (striations) produced in the plasma cloud will also be exhibited in the image clouds (Goldman et al., 1974; Scannapieco, et al., 1974). In the model presented in Figure 1, ion flow is allowed in each layer and only electrons flow between layers (direction depending on direction of

of  $E$ ). The major importance is the coupling of the plasma cloud to other regions of the ionosphere (imaging). Indeed, in certain cases, one can get coupling to the conjugate ionosphere. The basic starting point of our nonlinear studies of striation phenomena is the following set of equations:

$$\frac{\partial n_\alpha}{\partial t} + \nabla \cdot (n_\alpha \mathbf{V}_\alpha) = 0 \quad (1)$$

$$\frac{q_\alpha}{m_\alpha} \left( \mathbf{E} + \frac{\mathbf{V}_\alpha}{c} \times \mathbf{B}_0 \right) - U_\alpha^2 \frac{\nabla n_\alpha}{n_\alpha} - \nu_\alpha (\mathbf{V}_\alpha - \mathbf{V}_n) = 0 \quad (2)$$

$$n_e = n_i = n_b \quad (3)$$

$$\nabla \cdot \mathbf{j} = 0 \quad (4)$$

where the subscript  $\alpha$  denotes the species label ( $e$  is electron,  $i$  ionospheric ion, and  $b$  is barium ion),  $n$  is the density,  $\mathbf{V}$  the velocity,  $q$  the charge,  $E$  the electric field,  $\nu$  the collision frequency for species  $\alpha$  colliding with neutrals,  $U$  is the thermal velocity,  $\mathbf{V}_n$  is the neutral wind velocity, and  $\mathbf{j}$  is the current. It is generally agreed upon that striations in plasma clouds are caused by the  $\mathbf{E} \times \mathbf{B}$  gradient drift instability (Linson and Workman, 1970; Simon, 1963, 1970; Völk and Haerendel, 1971) and so the inertial terms on the RHS of equation (2) have been neglected. The perpendicular ion velocity can then be solved for algebraically in terms of  $\mathbf{E}$  and  $\mathbf{B}$  from equation (5) and we obtain

$$\begin{aligned} \mathbf{V}_{\perp i} = \frac{c}{B_0} \frac{K_i}{1+K_i^2} \left[ \mathbf{E} + \frac{\mathbf{V}_{\perp i}}{c} \times \mathbf{B}_0 - \frac{m_i U_i^2}{e} \frac{\nabla n_i}{n_i} \right] + \frac{c}{B_0^2} \frac{K_i^2}{1+K_i^2} \left[ \mathbf{E} + \frac{\mathbf{V}_{\perp i}}{c} \times \mathbf{B}_0 - \frac{m_i U_i^2}{e} \frac{\nabla n_i}{n_i} \right] \times \mathbf{B}_0 + \mathbf{V}_{\perp i} \end{aligned} \quad (5)$$

where  $K_i = \omega_{ci}/\nu_i$ ,  $\omega_{ci}$  is the ion cyclotron frequency, and  $\perp$  denotes perpendicular to the magnetic field (which in this study is in the  $z$  direction). The multiplicative factor involving  $K_i$  in equation (5) will change depending on what altitude we are considering, i.e., it will be different for layers 1 and 2. In this study we point out that there are basically two sets of ion equations one for the plasma cloud (which we refer to as barium) and one for the background ionospheric ions in layer 2 (see Goldman et al., 1974 for more details). We take the electric field in equation (5) to be  $\mathbf{E} = \mathbf{E}_0 - \nabla \psi$ , where  $\mathbf{E}_0$  is ambient field. We use the effective potential in the form

$$\psi = \phi - \frac{m_e U_e^2}{e} \ln n_e \quad (6)$$

and is constant along field lines. We use the continuity equation (1) for barium ions and integrate over the entire thickness of the barium cloud along the magnetic field line and obtain

$$\begin{aligned} \frac{\partial N_b}{\partial t} - \frac{c \nabla^2 \psi X B_0}{B_0^2} \cdot \nabla N_b = - \frac{(\mathbf{E}_0 - \nabla \psi)}{e} \cdot \nabla \sum_p^b \\ + \sum_p^b \frac{\nu_p}{e} \nabla^2 \psi + \frac{2KT}{e} \nabla^2 \sum_p^b \end{aligned} \quad (7)$$

where we are in a frame moving with  $c \mathbf{E}_0 \times \mathbf{B}_0 / B_0^2$  and no neutral wind, have set  $m_i U_i^2 = m_e U_e^2 = K_i^2$ , have kept terms to first order in  $\nu_b/\Omega_b$  where  $K_b$  refers to barium quantities (this is possible because for our F region cloud  $K_b \gg 1$ ),  $N_b$  is now only a function of  $x, y$ , as is  $\sum_p^b$  which is

$$\sum_p^b = \frac{ec}{B_0} N_b \frac{\nu_b}{\Omega_b} \quad (8)$$

the height-integrated (field line integrated) Pedersen conductivity of the barium cloud ( $\nu_b/\Omega_b$  is considered to be constant in layer 1). Taking the limit  $K_b \rightarrow \infty$  and using the height integrated form of equation (3), we obtain for the background ionosphere ions

$$\frac{\partial N_i}{\partial t} - \frac{c \nabla^2 \psi X B_0}{B_0^2} \cdot \nabla N_i = - \text{RHS equation (7)} \quad (9)$$

Equation (4) yields after integration over the  $z$  direction

$$\begin{aligned} - \left( \sum_p^i + \sum_p^b \right) \nabla^2 \psi + \left( \mathbf{E}_0 - \nabla \psi \right) \cdot \nabla \left( \sum_p^i + \sum_p^b \right) \\ - \frac{\nu_i}{\Omega_i} \left( \mathbf{E}_0 - \nabla \psi \right) \times \hat{z} \cdot \nabla \sum_p^i - \frac{2KT}{e} \nabla^2 \left( \sum_p^i + \sum_p^b \right) = 0 \end{aligned} \quad (10)$$

where the superscript  $i$  on  $\sum$  refers to the height integrated conductivity for the background ionosphere ions and have used the fact the Hall conductivity of the ionospheric ions

$$\sum_H^i = \frac{ecN_i}{B_0} \frac{(\nu_i/\Omega_i)^2}{1 + (\nu_i/\Omega_i)^2} = - \frac{\nu_i}{\Omega_i} \sum_p^i \quad (11)$$

(note:  $\nu_i/\Omega_i$  is assumed constant in layer 2; also for a more complete description of the derivation see Goldman et al., 1974). The set of equations (7), (9) and (10) describe the two-level system depicted in Figure 1 and are two-dimensional equations ( $x, y$  plane).

#### Small Cloud

The general set of equations describing the



two level system are not exactly transparent. Consequently, in order to gain a better understanding of the physics involved in the coupled cloud-ionosphere system, we have broken up our studies into small and large clouds. Here the word small or large is in the electrical sense, i.e., whether the ratio of height-integrated Pedersen conductivity of the cloud to that of the background ionosphere is small or large. The small cloud approximation ( $\sum_p b / \sum_p i \sim \epsilon$ )

results in great simplification (see Goldman et al., 1974 for a more complete description) of equations (7), (9) and (10), albeit still not amenable to analytic solution. In particular, equation (10) reduces to a Laplacian operator acting on  $\Psi$  with source terms on the right hand side which involve the background ionospheric perturbed Pedersen conductivity. This type of potential equation is much easier to solve, numerically, than equation (10). Essentially, the barium cloud motion and ionospheric image motion evolve on a time scale  $L B / (c E \epsilon^{1/2})$ , where  $L$  is the linear dimension of the cloud perpendicular to the magnetic field, and the barium cloud is initially ( $t=0$ ) taken to be of the form

$$\sum_p b = \sum_p b_0 e^{-\frac{(x^2 + y^2)}{L^2}} \quad (12)$$

In all of our studies the Pedersen conductivity of the background ionosphere is taken to be ( $\sum i_0 = \text{constant}$ ) initially constant. Carrying forward in time the small cloud forms of equations (7), (9) and (10) shows that the barium cloud drives images of order  $\epsilon^{1/2}$  relative to the undisturbed ionosphere. At long times the relatively high barium cloud ion density contours (equivalent to Pedersen contours since  $\nu/\Omega$  is assumed constant in each layer), in the limit of zero diffusion,  $T \rightarrow 0$ , form thin sheets making a definite angle,  $\theta = \tan^{-1}(\nu_1/\Omega_1)$ , with the  $E \times B$  cloud velocity. This angular dependence is derived from a basic understanding of the Lagrangian velocity involved in the continuity equation of the small cloud and the computer simulations bear out this dependence (see Goldman et al., 1974 for pictorial results). The study of small clouds has given us great insight into understanding large cloud phenomenology. Our work on small clouds is continuing in an effort to gain even more understanding. For example, we have now included an altitude dependent neutral wind (zero at the ionospheric level and finite at the barium level) into the problem and seeing the effects of size and direction of such winds on barium cloud and image cloud morphology. We find that in a reference frame moving with the E region neutral wind an F region neutral wind transverse to the ambient  $E$  is shown to retard or accelerate the evolution of the cloud, depending upon whether  $\nu \times B$  is antiparallel or parallel to  $E$ , without otherwise altering the development of the system. Also when the

relative neutral wind has a component parallel to the background  $E$ , there is a change in the direction of the axis of elongation of the cloud as a function of time, although the final direction is independent of the relative neutral wind.

#### Large Clouds

Our large cloud studies ( $\sum_p b_0 / \sum_p i_0 \gtrsim 1$ ) use the full set of equations (7), (9) and (10) and the results are more readily interpretable in light of our small cloud studies (see Scannapieco et al., 1974 for a more complete description). The same gaussian form, equation (12) at  $t = 0$  is used for the large barium cloud. Figure 2 depicts large cloud morphology as a function of conductivity ratio ( $\sum_p b_0 / \sum_p i_0$ ) for fixed  $\nu_1/\Omega_1$  and  $\nu_2/\Omega_2$ . The case  $\sum_p b_0 / \sum_p i_0 = 0.1$  resembles the results from the small cloud equations. We see that as  $\sum_p b_0 / \sum_p i_0$  is increased the cloud rotates more into the  $E \times B$  direction. Indeed as this ratio gets larger more imaging is produced, but the reaction of the images back on the motion of the barium cloud is reduced. The results in the last row of Figure 2 are for an uncoupled cloud, i.e., it is following a barium cloud without a background ionosphere ( $N_1 = \sum i_0 = 0$ ). The  $\sum_p b_0 / \sum_p i_0 = 4$  case for the barium cloud contours more resembles the uncoupled cloud case. In all cases we see cloud elongation in the  $E \times B$  direction and backside (side antiparallel to  $E \times B$ ) steepening. Other studies show (see Figure 3), in agreement with small cloud results (see Goldman et al., 1974) that as  $\nu_1/\Omega_1$  is reduced (to 0.1) the clouds rotate even more into the  $E \times B$  direction. Also there is an attendant reduction in strength of the image cloud.

We have put an initial sinusoidal perturbation of about five wavelengths in the  $y$  direction on top of the gaussian clouds depicted in rows 2 and 3 of Figure 2 to investigate striation growth. However, in terms of striation development a one-dimensional cloud is much more illuminating and we present the time development of such a system in Figure 4. The initial ( $t=0$ ) density Pedersen conductivity is given as

$$\frac{\sum_p b}{\sum_p i_0} = e^{-x^2/L^2} \left[ 1 + e^{-3} \sin \frac{10 \pi y}{64} \right] + 0.01 \quad (13)$$

where  $L^2$  is 64 and so the zeroth order cloud is gaussian in the  $x$  direction and infinite in the  $y$  direction (the term 0.01 represents a constant ionospheric background at the cloud level and is not to be confused with the background E region ionosphere depicted in Figure 4) and on top of this is the initial perturbation  $e^{-3} \sin(10 \pi y/64)$ , i.e., five wavelengths across the system. In the first

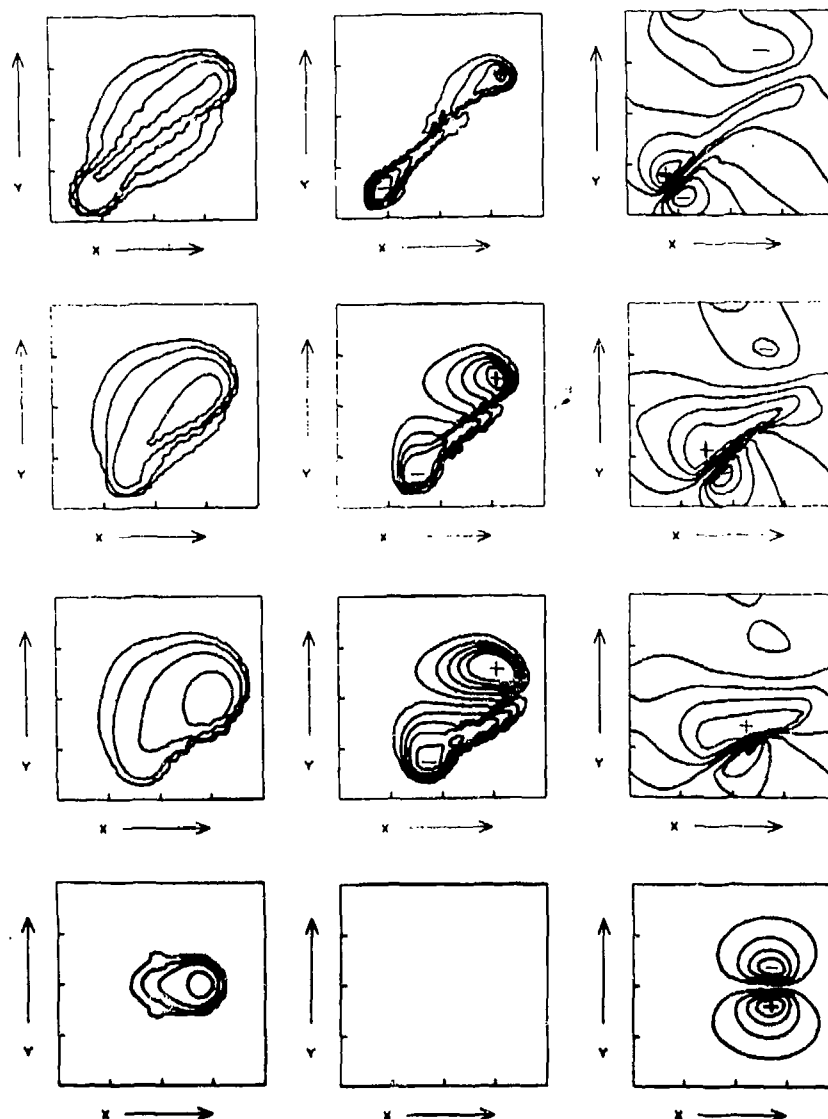


Figure (2). Nonlinear dynamical motion of large 2D barium clouds coupled to the background ionosphere. This represents the late time behavior of the height-integrated Pedersen conductivities for the barium cloud and the induced ionospheric images (left and center columns, respectively) and the corresponding electrostatic potential  $\Psi$  (right column). From top to bottom the results are for  $\Sigma_p^{bo}/\Sigma_p^{io}=0.1, 1.0, 4.0$  and  $\infty$  (uncoupled case,

no ionosphere) and the ratios represent the peak barium conductivity to unperturbed background ionosphere conductivity, at times  $t=800$  (20), 250, (6.25), 150 (3.75) and 350 (8.75) sec, respectively, where the numbers in parentheses are time in units of  $LB/cE_0$ . The collision frequency parameters are  $\nu_i/\Omega_i=0.5$  and  $\nu_b/\Omega_b=0.005$ . In these cases  $E_0=5\text{mV/m}$  and is in the negative  $y$  direction,  $B_0=0.5$  gauss

in the positive  $z$  direction and these figures are in the  $E_0 \times B_0$  drift frame, which is in the negative  $x$  direction.  $L$  is 4 mesh spaces (4 km) and the mesh is  $32 \times 32$ , so that each tick mark is 8 km. From the interior of the cloud the barium contours are  $e^{-1}, e^{-3}, e^{-5}, e^{-7}$  times the maximum value of the unperturbed height integrated barium Pedersen conductivity,  $\Sigma_p^{bo}$ . For the  $\Sigma_p^{bo}/\Sigma_p^{io}=0.1$  case the ionospheric contours are at  $1.0 \pm 0.1, \pm 0.2, \pm 3.0, \pm 0.4, \pm 0.5$  times  $\Sigma_p^{io}$  (proceeding inward), whereas, for the  $\Sigma_p^{bo}/\Sigma_p^{io} = 1.0$  and  $4.0$  cases

these contours are  $1.0 \pm 0.1, \pm 0.3, \pm 0.5, \pm 0.7, \pm 0.9$  times  $\Sigma_p^{io}$ . The regions of relative enhancement and depletion of the background ionospheric ions are marked with plus and minus signs, respectively. The sign of  $\Psi$  is indicated by plus and minus signs in regions of extrema.

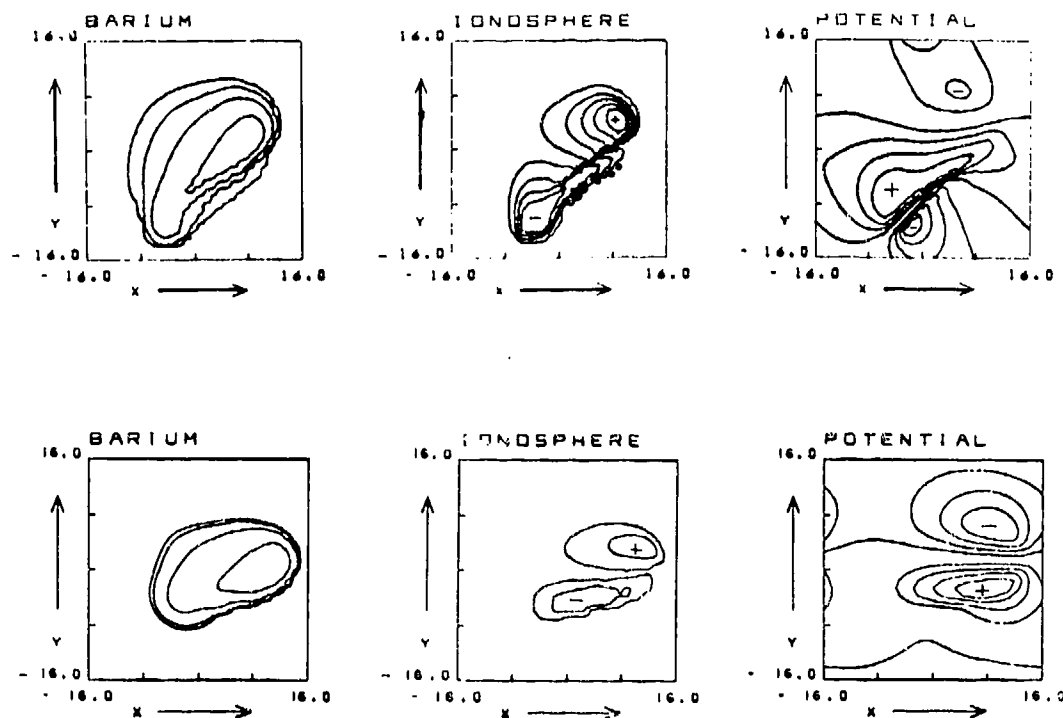


Figure 3. Late time development of 2D cloud for different ionospheric ion-neutral collision frequencies. For this figure  $\Sigma_p^{bo}/\Sigma_p^{io}=1.0$ ,

(a) the top row,  $\nu_1/\Omega_i=0.5$ ,  $L=4\text{km}$ , and  $t=250$  (6.25) sec., and (b) bottom row  $\nu_1/\Omega_i=0.1$ ,  $L=4\text{ km}$ , and  $t=400$  (10) sec. All other parameters are the same as in Figure 2.

row of Figure 4 we see the early time development of cloud, background ionosphere and induced potential. As time progresses we see the backside steepening and backside growth of striations and finger-like formation in the barium cloud which is in agreement with experimental observations (Rosenberg, 1971; Davis et al., 1974). What is of interest is the growth of image striations in the background ionosphere. This has never been reported experimentally as observers have not "looked" for it. Also equations (7), (9) and (10) in the one-dimensional approximation given by (13) are amenable to a linear stability analysis with a resultant algebraic dispersion relation, something that cannot be performed for the two-dimensional cloud. Figure 5 shows the agreement between the solution of such a dispersion relation yielding the growth rate and the actual numerical simulation depicted in Figure 4. The breaking of the dots (simulation) from the straight line (theoretical growth) indicates the onset of the nonlinear regime. Note that  $\Sigma_p^{bo}$  is less than 1 on the ordinate even though  $\Sigma_p^{bo}/\Sigma_p^{io} = 1$  for this cloud since we are in the backside wings where  $\Sigma_p^{bo}/\Sigma_p^{io} < 1$  and there is striation growth. The simulation points in Figure 5

were obtained by looking at specific grid points in the simulation.

#### Summary

We are continuing our studies on large clouds for both 1D and 2D barium clouds. We have gained a great deal of insight into cloud morphology and image formation by studying its dependence on  $\Sigma_p^{bo}/\Sigma_p^{io}$ . We still have to determine onset times and scale sizes for striation formation. Just as our small cloud model helped us to understand large clouds, we expect 1D studies to help us understand the more realistic 2D clouds. Indeed, the 1D cloud may be more amenable to discovering the quasi-final saturation or pinched stage. To date, using a more general form of equations (7), (9) and (10) containing all effects, we have found for large clouds as far as cloud morphology and image structures are concerned, that: (a) image structures always seem to be produced under a host of conditions; (b) increasing the ratio of cloud Pedersen to background ionospheric Pedersen conductivity increases the strength of the images and the cloud looks more uncoupled; (c) decreasing the ionospheric ion-neutral collision

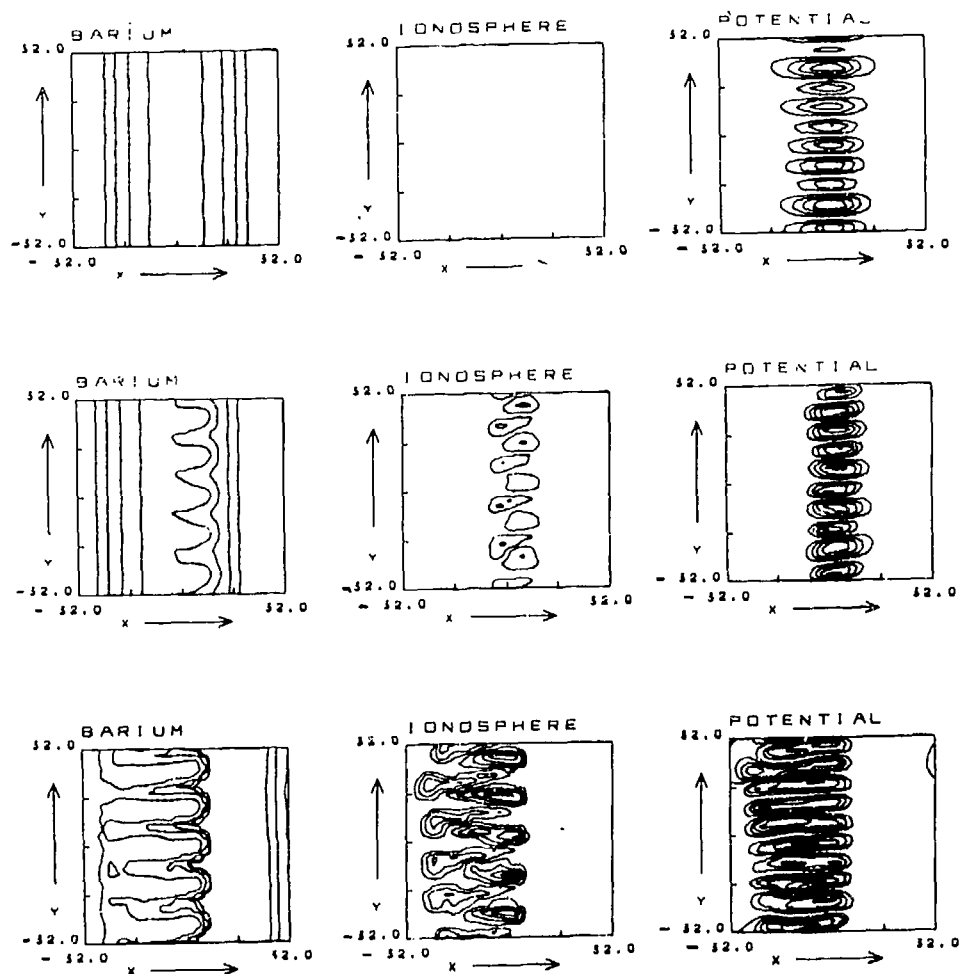


Figure 4. Time evolution of an initially 1D barium cloud with an initial perturbation (striations) coupled to the background ionosphere. The geometry and magnitude of  $E_0$  and  $B_0$  are the same as in Figure 2, as is the format for the figures. In this case  $\Sigma_p^{bo}/\Sigma_p^{io}=1$  and the collision frequency

parameters are  $\nu_1/\Omega_1=0.1$  and  $\nu_b/\Omega_b=0.005$ . The

times depicted are  $t=49.5$  (.62),  $643.5$  (8.04) and  $1046$  (13.08) sec, respectively. The numbers in parentheses are times in units of  $L B_0/cE_0$ . Here  $L$  is 8 mesh spaces (8km) and the mesh is  $64 \times 64$ . The barium contours are now  $e^{-1}$ ,  $e^{-3}$ ,  $e^{-5}$ ,  $e^{-7}$  plus the background (0.01) times the maximum value of the height integrated Pedersen conductivity of the cloud. The image contours are the same as the 2D  $\Sigma_p^{bo}/\Sigma_p^{io}=1.0$  case. Note the striation growth on the backside (steepened side), i.e., side away from direction of  $E_0 \times B_0$  motion. Also at late time note the finger formation on this backside (nonlinear state).

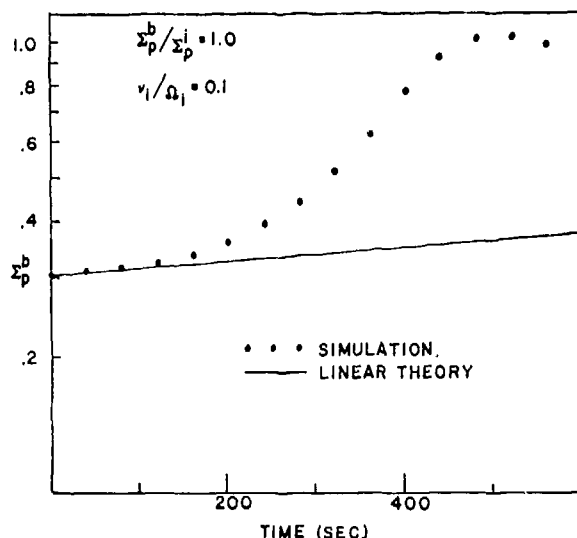


Figure 5. Pedersen conductivity in striation region of cloud versus time for 1D simulation depicted in Figure 4. The dots indicate the values from the simulation and the solid line depicts the values predicted by linear theory, i.e., a linear perturbation analysis of the full set of equations (7), (9) and (10). The agreement out to early times (~200 sec) is quite good and then the system takes on a nonlinear character.

frequency while keeping other parameters fixed decreases the strength of the images and makes the cloud look more uncoupled; (d) increasing the barium ion-neutral collision frequency increases the images and separates the positive and negative background ionosphere image structures more; (e) adding E region recombination reduces images and makes the cloud look more uncoupled; and (f) in the reference frame moving with the E region neutral wind an F region neutral wind transverse to  $E_0$  retards or accelerates the evolution of the cloud.

Most researchers have focused on the behavior of the barium cloud itself (Zabusky et al., 1973; Lloyd and Haerendel, 1973). However, the major result of our two-layered model results is the importance of image clouds, i.e., coupling of the cloud to the ionosphere, under a host of ionospheric conditions. Indeed images themselves can produce anomalous communication and radar results even if our understanding of the main cloud is complete. Signals may have to go through several regions of turbulence as depicted in columns one and two of Figures 2, 3, and 4 and the regions over which such perturbations occur can be vast. We have found that images always seem to be produced (to be sure their degree depends on certain parameters). Although the basic development of barium cloud motion and striation formation in these clouds from our large cloud results grossly agrees with experiment (Rosenberg,

1971; Davis et al., 1974 as does limited experiments on small cloud results Haerendel and Lust, 1968), no data is available on image formation. The results of our work on coupled plasma cloud-ionosphere phenomena has encouraged SRI, as one of its tasks, to look for image effects in a forthcoming (1975) Alaskan series of barium cloud releases at sub-auroral latitudes. We look forward with great anticipation to these experiments.

#### REFERENCES

- Davis, T. N., G. J. Romick, E. M. Wescott, R. A. Jeffries, D. M. Kerr, and H. M. Peek, "Observations of the Development of Striations in Large Barium Ion Clouds," *Planet. Space Sci.*, **22**, 67, 1974.
- Goldman, S. R., S. L. Ossakow, and D. L. Book, "On the Nonlinear Motion of a Small Barium Cloud in the Ionosphere," *J. Geophys. Res.*, **79**, 1471, 1974.
- Haerendel, G., and R. Lust, "Electric Fields in the Upper Atmosphere," in *Earth's Particles and Fields*, edited by B. M. McCormac, Van Nostrand Reinhold, New York, 1968.
- Linson, L. M., and J. B. Workman, "Formation of Striations in Ionospheric Plasma Clouds," *J. Geophys. Res.*, **75**, 3211, 1970.
- Lloyd, K. H., and G. Haerendel, "Numerical Modeling of the Drift and Deformation of Ionospheric Plasma Clouds and of their Interaction with other Layers of the Ionosphere," *J. Geophys. Res.*, **78**, 7389, 1973.
- Rosenberg, N. W., "Observations of Striation Formation in a Barium Ion Cloud," *J. Geophys. Res.*, **76**, 6856, 1971.
- Scannapieco, A. J., S. L. Ossakow, D. L. Book, B. E. McDonald, and S. R. Goldman, "Conductivity Ratio Effects on the Drift and Deformation of F Region Barium Clouds Coupled to the E Region Ionosphere," *J. Geophys. Res.*, **79**, 2913, 1974.
- Simon, A., "Instability of a Partially Ionized Plasma in Crossed Electric and Magnetic Fields," *Phys. Fluids*, **6**, 382, 1963.
- Simon, A., "Growth and Stability of Artificial Ion Clouds in the Ionosphere," *J. Geophys. Res.*, **75**, 6287, 1970.
- Volk, H. J., and G. Haerendel, "Striations in Ionospheric Ion Clouds, 1," *J. Geophys. Res.*, **76**, 4541, 1971.
- Zabusky, N. J., J. H. Dole III, and F. W. Perkins, "Deformation and Striation of Plasma Clouds in the Ionosphere, 2, Numerical Simulation of a Nonlinear Two-Dimensional Model," *J. Geophys. Res.*, **78**, 711, 1973.

EXPERIMENTAL STUDIES OF LOWER IONOSPHERIC EFFECTS  
RESULTING FROM HIGH-POWER RADIO WAVES\*

Glenn D. Falcor

ABSTRACT

A set of experiments was conducted to monitor the lower ionosphere (below 100 km) during operation of the Institute for Telecommunication Sciences' Ionospheric Modification Facility near Platteville, Colorado. This consisted of operating a partial reflection sounder during periods in which the modification radar varied its frequency, transmitted power, duty cycle (cw; pulsing; off), and polarization mode. Some heating parameters produced large decreases in the amplitudes of the received partial reflection signals, while other heating parameters produced an increase in these signals' amplitudes. Certain heating conditions caused the sounder's received signal amplitudes to increase at some heights while simultaneously decreasing at other heights.

Calculations of the changes in electron collision frequency and electron density resulting from the heating periods are presented and compared with theoretical estimates.

\*Paper unavailable as of printing.

## PULSED POWER HEATING OF THE D-REGION\*

William A. Seidler, II  
Air Force Weapons Laboratory

### ABSTRACT

The effects of high energy propagating EM pulses on the D-Region of the ionosphere are examined using the high frequency approximation to Maxwell's Equations in retarded time.<sup>1</sup> The non-linear coupling of the EM pulse to the D-Region plasma is predicted using the moments of the Boltzmann Equation for the plasma in the earth's magnetic field. Energy is predicted to be transferred to the plasma from frequency components up to 20 MHz even for a minimum nighttime D-Region electron profile. Electron temperatures within the plasma change from 0.02 eV to 350 eV enhancing the electron collision properties. Collision frequencies are increased by three orders of magnitude. The effects of the earth's magnetic field are examined.

\*Paper unavailable as of printing.

<sup>1</sup>Kerzas, W.J. and R. Latter, Detection of the Electromagnetic Radiation from Nuclear Explosions in Space, Phys. Rev. Vol. 137-3B, B1369, March 8, 1965.

# AN IONOSPHERIC F-REGION DISTURBANCE INDUCED BY THE LAUNCH OF SKYLAB

Michael Mendillo  
Department of Astronomy  
Boston University  
Boston, Mass. 02215

Gerald S. Hawkins  
Smithsonian Astrophysical Observatory  
Cambridge, Mass. 02138

and

John A. Klobuchar  
Air Force Cambridge Research Laboratories  
Bedford, Mass. 01730

## ABSTRACT

Routine Faraday rotation observations of the VHF signal from the geostationary satellite ATS-3 made at Sagamore Hill (Mass.) revealed that an unusually large and rapid decay in the ionospheric total electron content (TEC) occurred near 12:40 EST on 14 May, 1973. Observations from other sites showed that similar but less dramatic effects occurred to the north and west of Sagamore Hill. The onset of the TEC disturbance occurred within minutes of the launch of NASA's Skylab Workshop by a Saturn V rocket. As the vehicle traversed F-region heights, the burning second stage engines passed within 150 km of the Sagamore Hill ray path to ATS-3. A detailed analysis of the aeronomic reactions initiated by the constituents of the exhaust field revealed that the TEC disturbance was due to an enhancement in the F2-region electron loss rates. The specific mechanism involved was the rapid ion-atom interchange reactions between the ionospheric  $O^+$  and the hydrogen and water molecules in the plume, followed by dissociative recombinations. Model calculations of the diffusion of the plume in the ionosphere and its effects upon continuity equation estimates for the TEC behavior showed an excellent agreement with the observed onset and magnitude of the effect.



## INTRODUCTION

Continuous observations of (TEC) have been made at the Sagamore Hill Radio Observatory in Hamilton, Massachusetts, since November, 1967. At approximately 12:39 EST on the 14th of May, 1973, a sudden decrease in TEC was observed along the ray path to the geostationary satellite ATS-3. Figure 1 is a plot of the 15-minute TEC values (in units of  $10^{12}$  electrons/cm<sup>2</sup>-column) versus EST for that date. The solid curve in the bottom of Figure 1 gives an expanded version of the TEC decrease, while the curves with dots and crosses give theoretical results to be discussed below. It can be seen that between 12:30 and 12:45 EST, the TEC dropped from 11.3 to 5.8 units. The value fell below 5 units from 13:00 to 14:00 EST, and then slowly began to recover. The dashed diurnal curve in Figure 1 gives an estimate of the expected behavior for the TEC on the day in question. This curve incorporates the predicted monthly mean TEC for May, 1973, corrected for geomagnetic activity effects. The large "bite-out" seen in the TEC data for the 14th clearly distinguishes itself from the expected behavior for that day. Ionospheric disturbances monitored by the Sagamore Hill TEC have been extensively studied for many years (Mendillo and Klobuchar, 1974); it can be stated with confidence that this sudden and large drop in the daytime TEC is a unique disturbance unrelated to any solar or geomagnetic activity. The aim of this brief report is to point out the geographical and temporal extent of this artificially induced F-region disturbance, and to suggest as its cause an exceptionally enhanced electron loss mechanism triggered by the launch of the NASA SKYLAB Workshop. A more detailed discussion of this effect is available elsewhere (Mendillo et al., 1974).

NASA's SKYLAB I was launched at 12:30 EST from Pad A, Complex 39 (28.4° N, 80.6°W), at the Kennedy Space Center, Cape Canaveral, Florida. A comparison of the Saturn/SKYLAB trajectory (Pinson, 1973) and the Faraday rotation propagation geometry showed that the vehicle crossed the plane defined by the Sagamore Hill ray path to ATS-3 at lat. 36.8°N, long. 70.7°W, and a height of 422 km. The satellite ray passed 208 km above this point at 630 km; the horizontal separation of the trajectory from the ray path was approximately

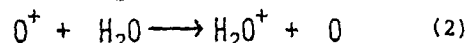
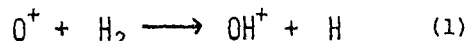
210 km and thus the point of closest approach about 150 km.

The Saturn V launch vehicle consisted of two stages. The first stage (S-I), burning kerosene and oxygen, cut off at 88 km and therefore was of little interest for the possible F-region effects to be considered here. The second stage (S-II) consisted of a cluster of five engines burning hydrogen (H<sub>2</sub>) in an oxygen (O<sub>2</sub>) environment. All five of the J-2 engines ignited at 88 km; the center engine then cut off at 273 km and the remaining four continued to burn until orbit insertion at 442 km. Each engine had a thrust of 239,000 lbf (pounds of force) which it achieved by ejecting mass at the rate of 537 lbm/sec (pounds of mass/sec) at a speed of 15,000 ft/sec. The exhaust was composed of 70% water vapor (H<sub>2</sub>O) and 30% unused hydrogen (H<sub>2</sub>) (Sadunas et al., 1973). When converted to particle flow per second, each J-2 engine ejected  $7.8 \times 10^{27}$  water molecules per second, and  $3.3 \times 10^{27}$  hydrogen molecules per second at a speed of 4.5 km/sec. Such flow rates represent extraordinary additions to the ambient atmosphere, and of species never found in quantity in the ionospheric F-region. With the cluster of engines releasing over a ton/sec of such gases, one might expect to find a variety of dynamical and chemical processes of direct ionospheric consequence.

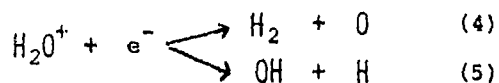
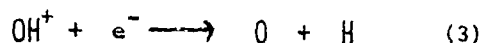
Under normal conditions, the ionospheric F-region is produced by the photoionization of atomic oxygen by solar radiation at EUV and soft X-ray wavelengths. Equal numbers of electrons (e<sup>-</sup>) and positive ions (O<sup>+</sup>) are produced in a ratio to neutral oxygen of approximately 1/1000. The loss (or recombination) mechanism for the O<sup>+</sup> and e<sup>-</sup> is a well understood process involving intermediate reactions with molecular nitrogen and oxygen. When the Saturn V engines added large numbers of hydrogen and water vapor molecules to the F-region, the normal ionospheric chemistry was substantially altered. Specifically, the constituents of the Saturn exhaust initiated a recombination process between the ionospheric O<sup>+</sup> and the ambient electrons. The overall mechanism was a two-step process involving O<sup>+</sup> first forming a molecular ion, and then dissociative recombination of that ion with one of the F-region electrons. The end result of the two reactions was thus the removal of an iono-

spheric ion-electron pair.

The first step in the loss process initiated by the Saturn exhaust was



followed by



Ferguson (1973) quotes as rate constants for reactions (1) and (2)  $2.0 \times 10^{-9} \text{ cm}^3/\text{sec}$  and  $2.4 \times 10^{-9} \text{ cm}^3/\text{sec} \pm 30\%$ . The remarkable features about reactions (1) and (2) is that they proceed at the kinetic rate, i.e., a reaction occurs with virtually every ion-molecule collision. This is drastically different from the normal ionospheric case in which  $\text{O}^+$  reacts with molecules of nitrogen and water vapor reactions are factors of 100 to 1000 times more rapid than the reactions with  $\text{N}_2$  and  $\text{O}_2$ , and thus the formation of positive molecular ions via equations (1) and (2) is an abnormally fast one for the F-2 region. Once a molecular ion is formed (whether  $\text{OH}^+$ ,  $\text{H}_2\text{O}^+$ ,  $\text{NO}^+$ , or  $\text{O}_2^+$ ), the subsequent dissociative recombination reactions are all of the form (3), (4) or (5). Such reactions are rapid and provide the principal mechanism of ion-electron recombination in the ionospheric (Banks and Kockarts, 1973). Since the overall loss mechanism involves two steps, one can see that the actual loss rate for electrons depends ultimately upon the speed of the slower ion-atom interchange reactions. Since the reactions involving  $\text{H}_2$  and  $\text{H}_2\text{O}$  are approximately 1000 times faster than normal, concentrations of only 1/10th the ambient  $\text{N}_2$  concentration will produce a 100-fold enhancement in electron loss rates. If one measures the rate of change of the TEC during the period immediately following the SKYLAB launch (Figure 1), the observed electron loss rate is in fact 100 to 200 times greater than normal.

The above examination of reaction rates, coupled to the realization that a ton of reactant is added to the ionosphere every second by the Saturn engines, leads to the conclusion that the electrons throughout the topside F-region experienced a devastating loss process in the vicinity of the S-II

plume. Consider, for example, that during the 275 second interval from the time of the S-II center engine cutoff (at 273 km) to engine shutdown (at 442 km), the four J-2 engines released a combined total of  $1.2 \times 10^{31}$  hydrogen and water molecules. At a height of 350 km, a plume concentration of  $2 \times 10^6/\text{cm}^3$  would cause the electron loss rates due to  $\text{H}_2$  and  $\text{H}_2\text{O}$  to become 100 times more efficient than the normally dominant loss mechanism. The 275 second's exhaust from the four J-2 engines gives such a concentration if uniformly distributed throughout a volume of about  $6 \times 10^{24} \text{ cm}^3$ . This implies that the scale size for dramatic ionospheric effects should be of order (volume)<sup>1/3</sup> of about 1800 km. An examination of TEC data from sites in Goose Bay, Labrador, and Urbana, Illinois, showed that a definite decrease in TEC was indeed observed at points 1000 km to the north and west of the burning Saturn rocket's trajectory in the F-region (see Mendillo et al., 1974).

The effects described so far dealt only with the reactions made possible by the constituents of the Saturn's exhaust field. Clearly, the dynamics of the plume must also be considered if the temporal and spatial aspects of the problem are to be compared with observations. As a way of doing this, we now consider a model of spherically symmetrical diffusion of the plume in the ionosphere. We anticipate that such a model will over-estimate diffusion in the downward direction, under-estimate it in the upward direction, and therefore give a reasonable overall view of the gross effects to be expected as a function of distance and time. We treat the hydrogen and water vapor components separately and take as point sources for the model the total number of  $\text{H}_2$  or  $\text{H}_2\text{O}$  molecules ejected by the engines in one second. We choose as the second in question the instant when the vehicle was at 350 km. At this time, the speed of the vehicle with respect to the atmosphere equalled the speed of the exhaust with respect to the vehicle, and thus the exhaust entered the ionosphere at zero relative speed. During the one second interval used, the rocket moved 4.5 km while emitting a total of  $1.32 \times 10^{28}$   $\text{H}_2$  molecules and  $3.12 \times 10^{28}$   $\text{H}_2\text{O}$  molecules. A standard solution of the radial diffusion equation (Jost, 1960) is

$$n(r,t) = \frac{S_0}{(4\pi Dt)^{3/2}} \exp(-r^2/4Dt) \quad (6)$$

where, for each species,  $n$  is the concentration at radial distance  $r$  at time  $t$ ,  $S_0$  is the total number of particles at  $r=0$  at  $t=0$ , and  $D$  is the diffusion coefficient in an oxygen ( $O$ ) atmosphere. Calculations using equation (6) were carried out to a distance of 1200 km for a time span of 2 hours. The total plume concentration was obtained by adding the contributions from each expanding cloud; the results appear in Figure 2. Several interesting points come from equation (6) and Figure 2:

(i) The plume diffuses so rapidly that within a few minutes the loss coefficient throughout a volume of several hundred kilometers radius is a factor of 10 to 100 times larger than the normal loss rates ( $\beta_{eff} \approx 2 \times 10^{-5}/\text{sec}$ ).

(ii) While the exhaust field is  $H_2O$  dominated in terms of total concentrations, the onset of the TEC "biteout" was determined by the arrival of the  $H_2$ . This is due to the fact that the lighter constituent diffuses more rapidly. The duration of the effect, however, is due mainly to the more slowly diffusing water vapor.

(iii) At a given radial distance from the source, there is a unique time when maximum  $H_2$ ,  $H_2O$  and total concentrations occur. The exact relationship  $t_{max} = r^2/6D$  is obtained by setting the time-derivative of equation (6) equal to zero. For  $H_2$ , it numerically becomes  $t_{max} = .75r^2$ , where  $t_{max}$  is in minutes and  $r$  in hundreds of kilometers. For example, at a distance of 200 km, the maximum hydrogen concentration occurs after three minutes expansion, while at 600 km it occurs 27 minutes after the source is released. Thus, a chain of stations would record maximum effect sequentially. It is as if a wave passed along the chain, though it must be noted that for each species the concentration is always a maximum at  $r=0$  for any given time.

Calculations were also performed which show that during the time interval under consideration here, the plume could not have suffered any appreciable depletions due to solar-induced photoionizations or dissociations. (Mendillo et al., 1974).

The actual loss in electron content to be expected from the plume can be calculated using the loss coefficients obtained from the  $H_2$  and  $H_2O$  results summarized in Figure 2. By considering the TEC data to represent the integral of a slab of plasma located 200 km from the source, the TEC response may be explicitly evaluated as a function of time. In the more rigorous treatment (Mendillo et al., 1974), the TEC is evaluated using

$$d\text{TEC}(t)/dt = Q - [\beta_{eff} + \beta_{H_2}(t) + \beta_{H_2O}(t)] \cdot \text{TEC}$$

where  $Q$  is a modified production function obtained from the average rate of change of TEC prior to the launch. This calculation was carried out at one minute intervals for a duration of 20 minutes, and then at 10 minute steps up to an hour. The results are compared with observations in the lower portion of Figure 1. The dotted curve gives the results of the TEC calculations using the  $H_2$  and  $H_2O$  loss coefficients which result from one second of exhaust ( $S_0$ ). One can see that the calculations clearly lead to a relatively rapid drop in the TEC. After about 20 minutes, the slowly decaying  $H_2$  and  $H_2O$  concentrations cause the total loss to equal the solar production effects and thus TEC remains nearly constant.

The second set of results presented in Figure 1 describe calculations using a point source equal to the total number of particles ejected in 10 seconds. During this time interval the vehicle moved only 45 km, a distance comparable to the mean free path and still small in comparison to the 200 kilometer distance under consideration. These results are in excellent agreement with the onset of the decay, but the calculations subsequently predict a virtual disappearance of the electron content. We suggest that this vanishing of the TEC is indeed what happened to the F2-region's topside content. The plateau or "minimum of the biteout" in our observations near  $5 \times 10^{12} \text{ el/cm}^2$  simply represents the contributions of the bottomside ionospheric regions (E, F1) to the TEC integral.

In conclusion, it is interesting to consider that this significant recombination effect of the  $O^+$  in the ionosphere was apparently unanticipated. Hydrogen, the most abundant element in the universe, is not normally found in molecular form in significant quantities in the near-earth environment. It is, however, an important constituent in interstellar space and thus the fast reaction between  $H_2$  and  $O^+$  has interesting implications in astrophysics. There is also the potential for important geophysical modification experiments in the terrestrial ionosphere and plasmasphere. Concerning this point,  $H_2$  has the asset of being light and particularly resistant to a quick destruction by solar EUV, while water vapor has the property that the dissociative recombination of  $H_2O^+$  produces a molecule (either  $H_2$  or  $OH$ ) which

is capable of engaging in another  $O^+$  ion atom interchange reaction. Thus, the net effect is that a single  $H_2O$  molecule would remove two F-region ion-electron pairs.

While the  $O^+$  reaction with the hy-

droxyl molecule has not been measured in the laboratory, its rate is expected to be close to that with  $H_2$  and  $H_2O$  (Ferguson, private communication). Again, OH is a prominent interstellar consti

#### REFERENCES

1. Banks, P. M. and G. Kockarts, Aeronomy, Part A, Chap. 10, Academic Press, New York, 1973.
2. Ferguson (1973) E. E. Rate constant of thermal energy binary ion-molecule reactions of aeronomic interest, Atomic Data Nuclear Data Tables, 12, 159, 1973
3. Jost, Diffusion (revised), Academic Press, New York, Chap. 1, 1960.
4. Mendillo, M. and J. A. Klobuchar, An Atlas of the midlatitude F-region response to geomagnetic storms, Air Force Cambridge Research Laboratories, Tech. Report #74-0065, 1974.
5. Mendillo, M., Hawkins, G. S., and J. A. Klobuchar, An ionospheric total electron content disturbance associated with the launch of NASA's SKYLAB, Air Force Camb. Res. Labs. Tech. Report, TR-74-0342, ERP 483, July 1974.
6. Pinson, G. T., Apollo/Saturn V post-flight trajectory---SA-513---SKYLAB 1 mission, Tech. Report D5-15560-13, The Boeing Co., Huntsville, Ala., 1973.
7. Rishbeth, H. and O. K. Garriott, Intro. Ionospheric Physics, Academic Press, New York, Chap. 3, 1969.
8. Sadunas, S. A., French, E. P. and H. Seaton, S-II stage 1/25 scale model base region thermal environment test, NASA contractor report 129009, Rockwell International Corp., Downey, Calif., 1973.

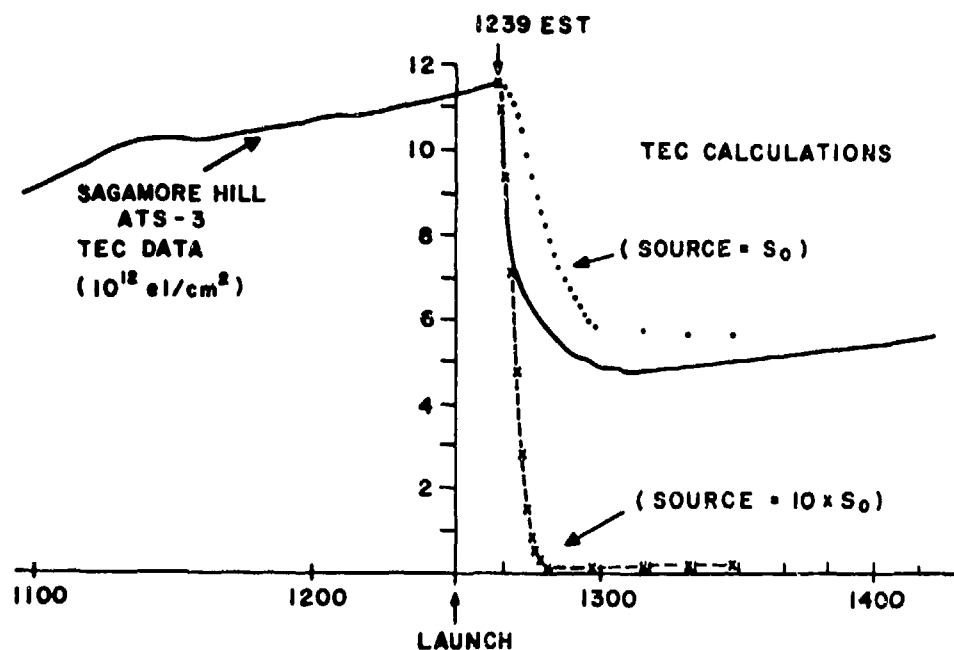
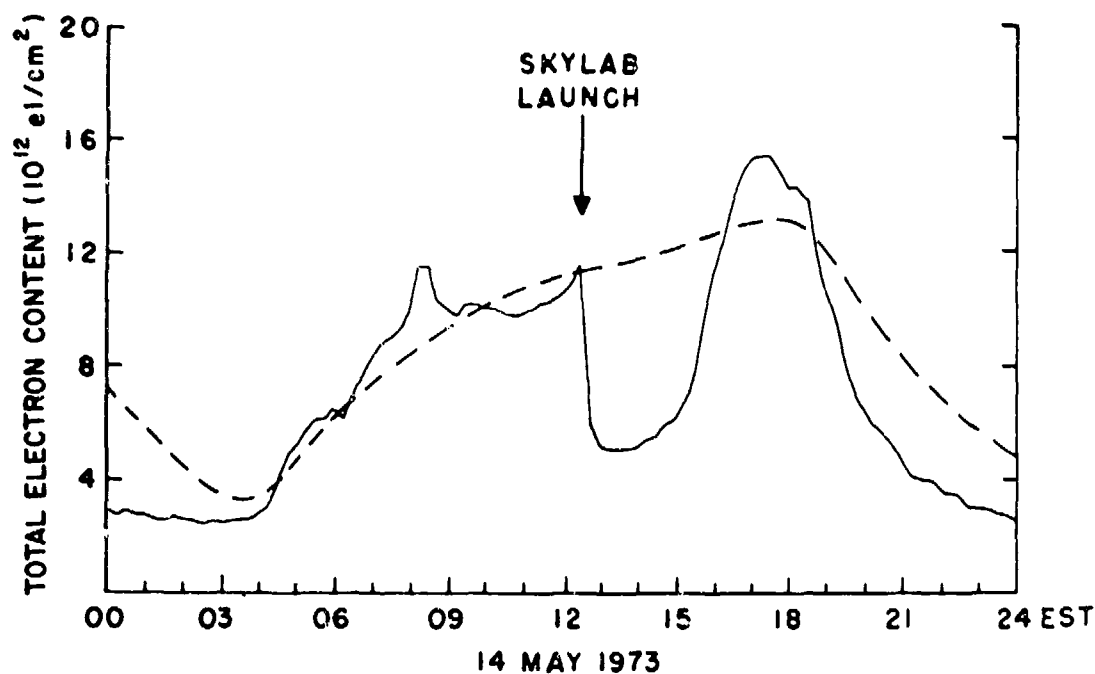


Figure 1. (top) Ionospheric total electron content (TEC) versus EST on 14 May, 1973, as observed at the AFRL's Sagamore Hill Radio Observatory in Hamilton, Mass. The dashed curve gives the expected behavior for that day, and the vertical arrow marks the time of the SKYLAB launch at 12:30 EST from the Kennedy Space Center. (bottom) Expanded version of the TEC decay showing the results of continuity equation estimates of the time development of the TEC. The dots refer to results obtained using the enhanced loss rates which result from one second of exhaust, and the crosses give the results using 10 second's worth of exhaust.

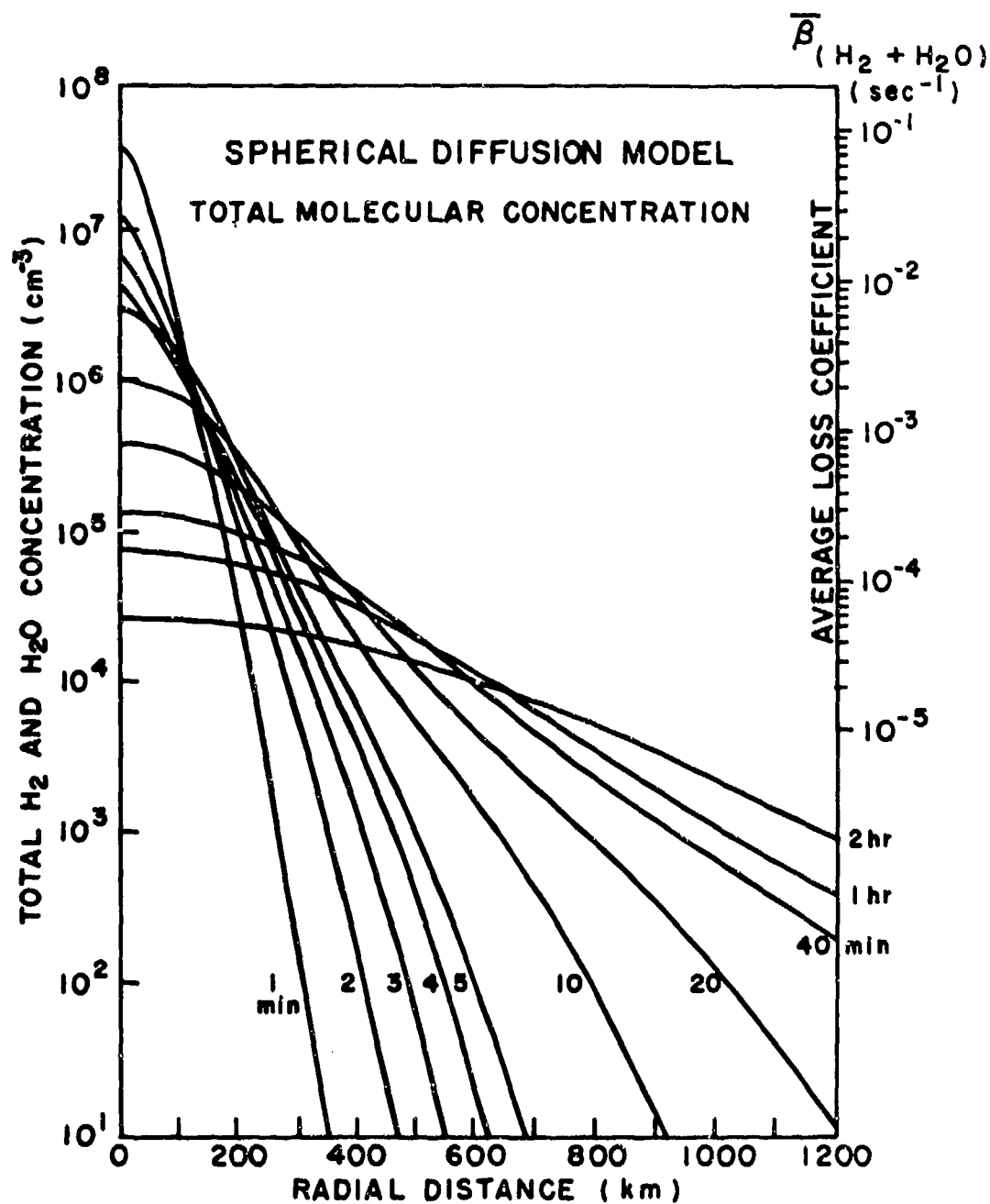


Figure 2. Results of spherical diffusion model calculations for molecular hydrogen and water vapor in the ionosphere. Each curve gives the total plume concentration as a function of radial distance for a series of elapsed time. The source at the origin was defined to be the number of molecules ejected by the Saturn engines in one second. The axis on the right gives the average electron loss coefficient. The calculations were performed using atmospheric variables defined at 350 kilometers (see text).

## IONOSPHERIC DISTURBANCES DURING SEVERE WEATHER ACTIVITIES

R. J. Hung and G. L. Rao  
The University of Alabama in Huntsville  
Huntsville, Alabama 35807

and

R. E. Smith, G. S. West and B. B. Henson  
NASA/Marshall Space Flight Center  
Huntsville, Alabama 35812

### ABSTRACT

The dynamics of ionospheric disturbances and irregularities during severe weather activity are investigated by using a nine element CW high frequency Doppler sounder array. The purpose of the present study is to investigate the coupling between the stratosphere and the ionosphere during severe weather activity, particularly during thunderstorms and tornadoes. Two typical disturbances recorded during periods of thunderstorm activity and two recorded during periods of tornado activity have been chosen for analysis in this study. The observations indicate that wave-like disturbances, possibly generated by the severe weather, have wave periods in the range of 2 to 8 minutes, which places them in the infrasonic wave category. Characteristics of the waves are discussed in detail.

### I. INTRODUCTION

Ionospheric wave-like disturbances caused by known and unknown sources are observed on ground-based ionospheric sounding records as perturbations in the electron densities. Recently, Georges (1968), Baker and Davies (1969), and Davies and Jones (1972) reported observations of wave-like fluctuations in the ionosphere associated with severe weather activity. This paper shows a technique for studying the dynamics of ionospheric disturbances and irregularities during severe weather activity by using a continuous wave-spectrum high-frequency Doppler sounder array. The purpose of the present study is to investigate the coupling between stratosphere and ionosphere during severe weather activities and particularly during thunderstorms and tornadoes.

Experimental observations of ionospheric wave-like disturbances during severe weather

activity are taken from the NASA/Marshall Space Flight Center CW Doppler sounder array located in the North Alabama region. We have continuously monitored the Doppler frequency fluctuations of nine field transmitters covering an area of 150 Km<sup>2</sup> since January 1973.

In the following sections, we describe the experimental observations of ionospheric wave-like disturbances associated with severe weather activity and then compare the observations with theoretical predictions.

### II. EXPERIMENTAL ARRANGEMENTS AND OBSERVATIONS

The CW Doppler sounder system was developed by Davies (1962). Davies and Baker (1966) gave a description of the theory and an interpretation of the data. Our Doppler sounder array system consists of three sites with nine field transmitters operating at 4.0125, 4.759, and 5.734 MHz. These sites are located at Ft. McClellan, Alabama (33° 44' N, and 85° 48' W), TVA, Muscle Shoals, Alabama (34° 46' N, and 85° 38' W), and TVA, Nickajack Dam, Tennessee (35° 01' N, and 87° 38' W); the receivers are located at NASA/Marshall Space Flight Center, Alabama. Figure 1 shows the geophysical locations of the three transmitters and receivers. Since each of the three transmitters uses the same nominal frequencies, the actual frequencies must be slightly different so that they can be distinguished from each other at the receiver. The actual frequencies for the field transmitters have been set as in Table 1. At the receiving station, the oscillators have been set exactly at the nominal frequencies so that, in the absence of Doppler variations, the offsets of the transmitter oscillators are equal to the beat frequencies.

During the periods of severe weather in this area (as shown by the radar weather

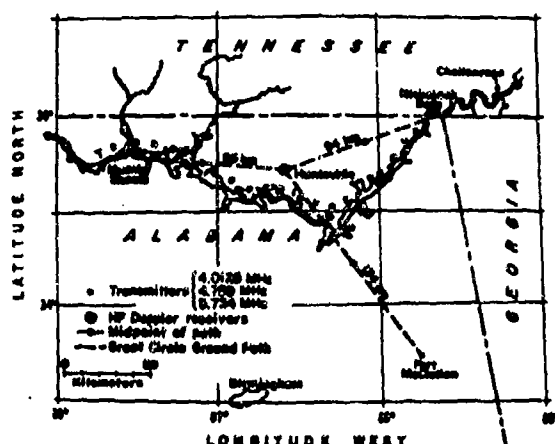


Figure 1. Locations of three sites field transmitters and receivers of NASA/Marshall Space Flight Center Doppler sounder array system.

Nominal Frequency	Actual Frequencies
	Three Transmitters at Muscle Shoals, Alabama
4.0125 MHz	4.0125 MHz + 2 Hz
4.759 MHz	4.759 MHz + 2 Hz
5.734 MHz	5.734 MHz + 2 Hz
Actual Frequencies (continued)	Three Transmitters at Nickajack Dam, Tennessee
	Three Transmitters at Ft. McClellan, Alabama
4.0125 MHz + 3 Hz	4.0125 MHz + 4 Hz
4.759 MHz + 3 Hz	4.759 MHz + 4 Hz
5.734 MHz + 3 Hz	5.734 MHz + 4 Hz

Table 1. Nominal and Actual Operating Frequencies of Nine Transmitters of NAAA/Marshall Space Flight Center Doppler Sounder Array System.

charts) we have noticed short period wave-like frequency fluctuations and Doppler frequency fluctuations and Doppler frequency "fold backs". We have chosen the two thunderstorm events of May 26, 1973 and March 20, 1974, and the two tornado events of November 20, 1973 and November 27, 1973 as typical examples for analysis and discussion in this paper.

Figures 2, 3 and 4 show the CW Doppler records at operating frequencies of 4.0125, 4.759, and 5.734 MHz, respectively, during the thunderstorm conditions on March 20, 1974. No

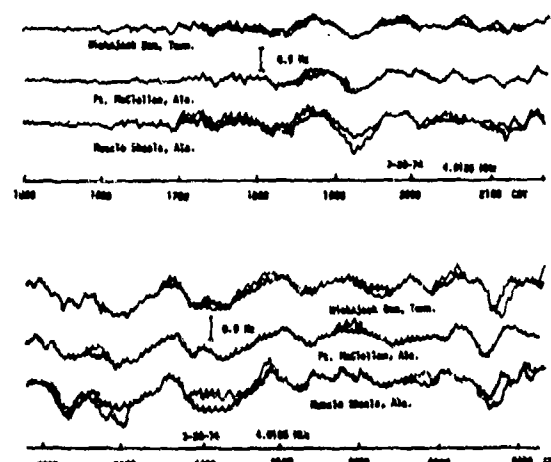


Figure 2. CW Doppler record at the operating frequency of 4.0125 MHz (event on March 20, 1974).

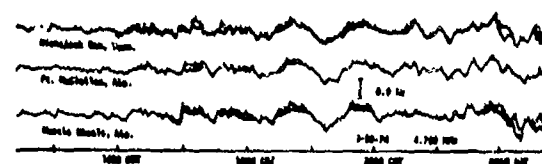


Figure 3. CW Doppler record at the operating frequency of 4.759 MHz (event on March 20, 1974).

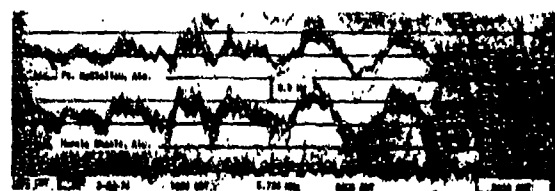


Figure 4. CW Doppler record at the operating frequency of 5.743 MHz (event on March 20, 1974).

tornadoes were sighted in or around North Alabama on this particular day. The thunderstorm-associated disturbances are clearly shown on all the records beginning at ~1610 CDT and continuing through the early morning hours. Wave-like fluctuations with wave periods of 4 to 5.5 minutes are clearly shown on the 4.0125 MHz record beginning at 2200 CDT and lasting through 0300 CDT. At the higher operating frequencies, 4.759 and 5.734 MHz, the ionospheric reflected signal was lost after 2300 CDT.



The times of onset and cessation of the ionospheric waves coincided remarkably well with the appearance and disappearance of severe thunderstorm activity on the radar weather charts.

Figure 5 shows the CW Doppler record at the operating frequency of 4.0125 MHz during the severe thunderstorm condition on May 26, 1973. On this day, severe thunderstorm activity occurred within the area of the Doppler array and several tornadoes touched down west and north of the Doppler array system. It can be seen in Figure 5 that the Doppler fluctuations are highly disturbed until 1100 CDT, when they are followed by wave-like fluctuations with periods of 5 minutes.

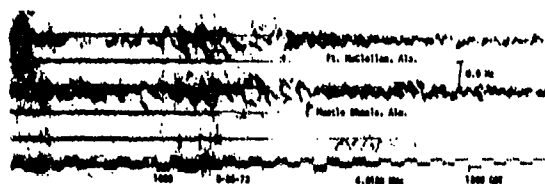


Figure 5. CW Doppler record at the operating frequency of 4.0125 MHz (event on May 26, 1973).

Cloud tops on the thunderstorm-active day, March 20, 1974, were between 40,000 to 50,000 feet (approximately 12 to 15 Km). The horizontal trace velocity of the ionospheric disturbance waves on this particular day, obtained by analysis of the wave-front moving across the legs between the three sites of the Doppler sounder array and the receiver site, had a magnitude of 1 km/sec propagating from a direction southwest of the Doppler sounder array.

Figures 6 and 7 show the CW Doppler records for November 20, 1973 under tornado conditions at the operating frequencies of 4.0125 MHz, 4.759 and 5.734 MHz, respectively. The wave-like fluctuations are clearly seen beginning at ~ 1230 CST and continuing through the evening. The periodicity of these wave-like disturbances is in the 6 to 8 minute range, whereas, for thunderstorms, the periodicity of the fluctuations is on the order of 3 to 5 minutes. For the November 27, 1973 tornado conditions, Figure 8 shows Doppler records at the operating frequencies of 4.0125 MHz and 4.759 MHz in which the wave-like fluctuations clearly began about 1100 CST and continued through the evening hours. Again, the period of the fluctuations is of the order of 6 to 8 minutes. The phase velocities of the disturbances, derived from a cross correlation analysis, propagate from the south-west with a magnitude of 600-700 m/sec. The Doppler record of November 20, 1973, is expanded on the time axis to clearly show the

time variations (Figure 9). It can be seen from Figure 9 that the Doppler fluctuations are not quasi-sinusoidal, as in the case of thunderstorms, but are S-type waves with several Doppler fold backs. These "fold backs" are typical of tornado conditions.

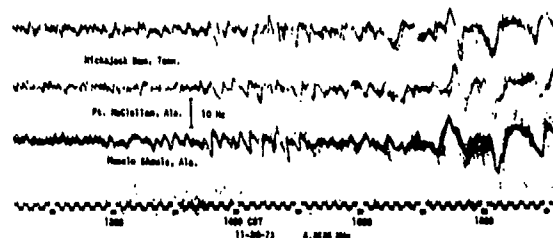


Figure 6. CW Doppler record on November 20, 1973, at the operating frequency 4.0125 MHz.

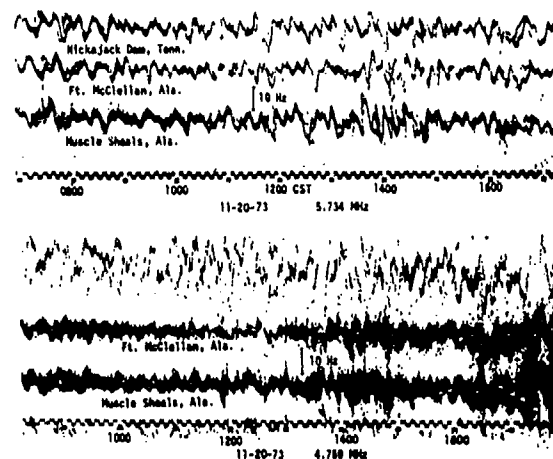


Figure 7. CW Doppler record on November 20, 1973, at the Operating Frequencies 5.734 and 4.759 MHz.

Radar weather summary charts for November 20 and November 27, 1973 are shown in Figures 10 and 11. The weather maps clearly show the areas of radar echoes, lines of radar echoes and heights of echo tops. The lines of radar echoes in both cases are from the south-west to the north of the Doppler system. The heights of echo tops are on the order of 40,000 to 50,000 feet (or about 12 to 15 Km). The radar summary charts also indicate a severe weather activity area located southwest of the Doppler array, the direction from which the wave-like disturbances seen on Doppler records propagate.

### III. SUMMARY AND DISCUSSION

Observations of ionospheric disturbances associated with severe weather activity,

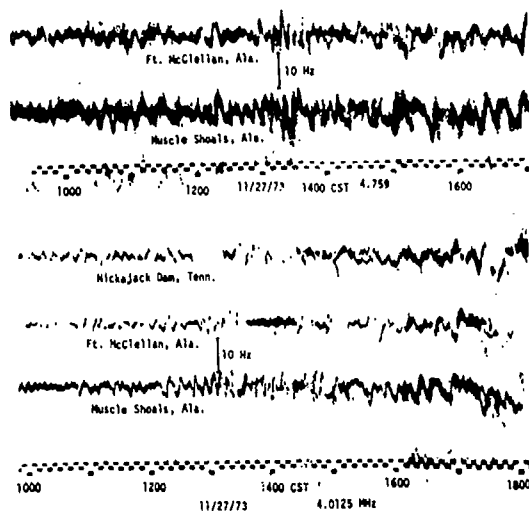


Figure 8. CW Doppler records on November 27, 1973 at the operating frequencies 4.759 MHz and 4.0125 MHz.

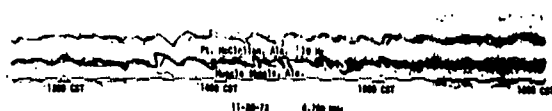


Figure 9. The expansion of time axis of Doppler record on November 20, 1973, at the operating frequency 4.0125 MHz.

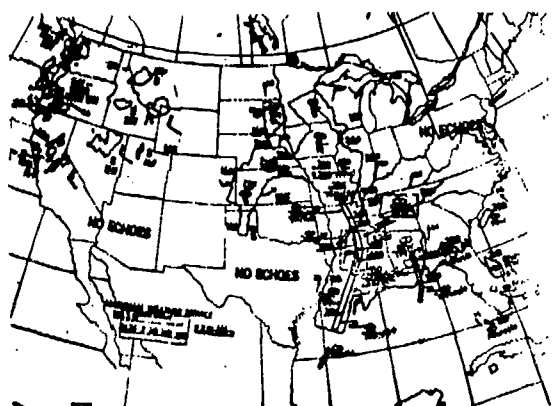


Figure 10. Radar weather map for November 20, 1973 at 1535 CST.

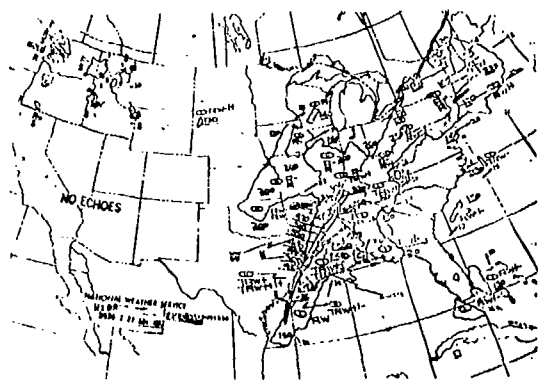


Figure 11. Radar weather map for November 27, 1973 at 1335 CST.

particularly severe thunderstorm and tornado activity, indicate the generation of wave-like disturbances with wave periods in the range of 2 to 8 minutes. This period is essentially below the local Brunt-Väisälä frequency. In other words, the ionospheric disturbances associated with severe weather activity can be classified practically in the category of infrasonic waves. Theoretical analysis of the characteristics of infrasonic waves indicates that wave propagation is vertically upward in contrast to gravity waves, which propagate horizontally along the ground. This characteristic implies that the range of observations of ionospheric disturbances associated with severe weather activity is limited to the order of the wavelength of the infrasonic waves generated. The wavelengths of infrasonic waves generated, perhaps by thunderstorms, vary from 150 to 300 Km, while waves generated, perhaps by tornadoes, have wavelengths from 200 to 300 Km. Therefore, it appears as if observations of ionospheric disturbances associated with severe weather activity are geographically confined to an area of only a few hundred kilometers in diameter. This agrees with the observational results obtained by Georges (1973).

The results of our investigations show the following important conclusions on the detection of ionospheric disturbances produced by severe weather activities, particularly by thunderstorms and tornadoes, by using CW Doppler sounder array:

- (1) The Doppler fluctuations are S-shaped waves with several Doppler fold backs for tornado-induced disturbances, while the quasi-sinusoidal waves are the main wave patterns for thunderstorm-induced perturbations;

(2) The periodicity of the Doppler frequency fluctuations are in the 5 to 8 minute range for tornado-induced disturbances, while 3 to 5 minute periods are associated with thunderstorms.

(3) The oscillations for disturbances produced by both tornadoes and thunderstorms can persist from 4 to 6 hours;

(4) The horizontal trace velocities show a magnitude of 600 to 700 m/sec propagating from the southwest for tornado induced disturbances and with horizontal phase velocities on the order of 1000 m/sec for thunderstorm-induced perturbations.

A theoretical examination of possible mechanisms for generating infrasonic waves shows that the excitation of waves with wave period near and below the local Brunt-Väisälä frequency is strongly dependent on the wind structure (both wind velocity and wind shear) and the temperature gradient of the thermosphere. Results of ongoing detailed theoretical analysis will be given in later papers. Calculations given by Jones (1970) also agree with these results. Preliminary results seem to show that disturbances are observed more frequently when severe weather activity is south or southwest of the array because the wave propagation is influenced by the earth's

magnetic field. This aspect is being studied in detail now.

#### ACKNOWLEDGEMENT

R. J. Hung and G. L. Rao wish to acknowledge the support of NASA/Marshall Space Flight Center under Contract NAS8-30616 for the present work.

#### REFERENCES

- Baker, D. M., and K. Davies, J. Atmosph. Terr. Phys. **31**, 1345, 1969.
- Davies, K., Proc. IRE **50**, 94, 1962.
- Davies, K., and D. M. Baker, Radio Sci. **1**, 545, 1966.
- Davies, K., and J. E. Jones, Space Research XII, Akademic-Verlag, Berlin, 1972, pp. 1149.
- Georges, T. M., J. Atmosph. Terr. Phys. **30**, 735, 1968.
- Georges, T. M., Rev. Geophy. Space Phys. **11**, 571, 1973.
- Jones, W. L., J. Atmosph. Terr. Phys. **32**, 1555, 1970.

## Faraday rotation and angle of arrival measurements using beacon satellites

A.R. Webster\* and P.A. Forsyth

Department of Physics, Centre for Radio Science  
and \*Faculty of Engineering Science,  
University of Western Ontario  
London, Canada.

### 1. INTRODUCTION

The following describes the phase-swept interferometer and its application in the measurement of Faraday rotation and angle of arrival of radio signals from artificial satellites. The main consideration here, concerns the simultaneous measurement of Faraday rotation and angle of arrival using a geostationary satellite as the source; additionally the use of travelling satellites, which effectively provide an ionospheric snapshot, will be considered in relation to angle of arrival measurements.

The value of simultaneous geostationary observations in determining the properties of travelling disturbances has been described earlier (Webster and Lyon, 1974). In essence, a quadrature relationship holds between Faraday rotation and angle of arrival for a travelling disturbance of a sinusoidal nature, and the relevant amplitude and phase measurements allow the determination of wavelength, and phase velocity and direction of travel. Angle of arrival measurements using travelling satellites, on the other hand, provide information on the spatial extent of ionospheric disturbances. In principle, the phase-swept interferometer lends itself readily to all these measurements and a complete system might be envisaged where geostationary Faraday rotation and angle of arrival measurements are made simultaneously and continuously, supplemented by periodic travelling satellite measurements.

In making angle of arrival (AOA) measurements at a single frequency, one troublesome feature is that the source moves through angles (a few degrees, geostationary; tens of

degrees, travelling) which are considerably in excess of the deviations to be expected due to ionospheric effects (a few milliradians at 150 MHz). This results in the familiar "phase-ramps" indicating a change of  $2\pi$  radians in the associated phase measurements and the presence of these ramps introduces some difficulty in the extraction of the small deviations of interest. Since angular deviations produced by ionospheric irregularities are proportional to  $1/f^2$ , where  $f$  is the radio frequency (Turnbull and Forsyth, 1965), and since several beacons are available which transmit on widely spaced frequencies (ATS-6 on 140/360 MHz, Transit series on 150/400 MHz) differential AOA measurements are possible and provide a means of removing such phase ramps while essentially preserving the ionospheric deviations. The differential technique, then, involves essentially the measurement of deviations at the lower frequency relative to those at the higher.

### 2. THE PHASE SWEPT INTERFEROMETER

#### 2.1. Principle of Operation

The basis of phase swept interferometer measurements is the comparison of radio wave phases as received on separate antenna systems. In angle of arrival measurements the relevant phases are those received on antennas spaced by a distance  $D$ , while Faraday rotation is given by a comparison of the phases of the right and left circularly polarised components of an originally plane polarised wave: these latter components may be derived by utilising either separate helical antennas or correctly phased crossed Yagi antennas.

In terms of angle of arrival, the principle of operation is shown in Fig. 1. The incoming radio signal is

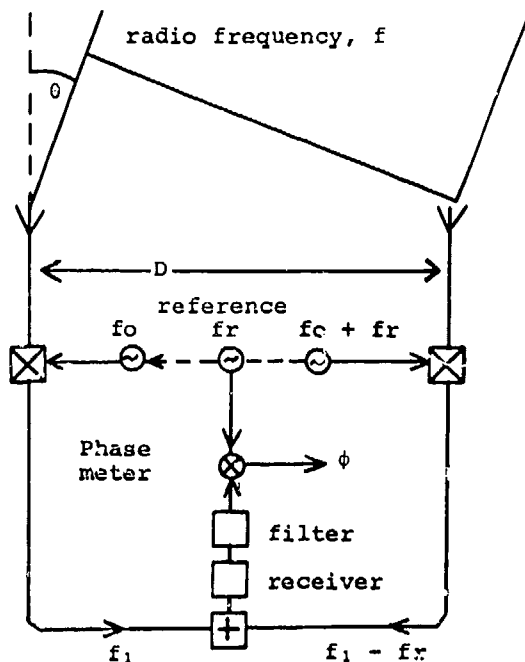


Fig. 1 The phase-swept interferometer

received on two antennas spaced by a distance  $D$  and converted to intermediate frequencies separated by a reference frequency  $f_r$ . After adding the two signals, envelope detection, followed by appropriate fundamental frequency filtering, results in a sinusoid of frequency  $f_r$  whose phase  $\phi$  relative to the original standard (used in generating the local oscillator frequencies) is given by

$$\phi = \frac{2\pi D \sin \theta}{\lambda} + \psi \quad 1$$

$\psi$  is a constant which includes an arbitrary phase shift through the system and an integral multiple of  $2\pi$  radians, and  $\lambda$  is the radio wavelength. Changes  $\Delta\theta$  in angle of arrival  $\theta$ , then, are given by

$$\Delta\phi = \frac{2\pi D \cos \theta}{\lambda} \Delta\theta \quad 2$$

where  $\Delta\phi$  is the measured phase change between the receiver output signal and the original reference signal.

In the case of Faraday rotation, and assuming accurate resolution into right and left circular components, changes  $\Delta\phi_F$  in the measured phase difference between these two components is related to changes  $\Delta\xi_F$  in polarisation angle by

$$\Delta\phi_F = 2\Delta\xi_F \quad 3$$

## 2.2. Differential Measurements

Equation 3 refers to the angle of arrival as measured at a single radio frequency; the change  $\Delta\theta$  includes  $\Delta\theta_s$  due to satellite motion and  $\Delta\theta_i$  due to ionospheric effects so that

$$\Delta\theta = \Delta\theta_s + \Delta\theta_i$$

If two widely spaced frequencies ( $f_1, f_2$ ) are used, then the assumption that  $\Delta\theta_s$  is the same for both frequencies leads to

$$\begin{aligned} \Delta\phi_1 - \Delta\phi_2 &= 2\pi \cos \theta \left( D_1 \Delta\theta_{i1} - D_2 \Delta\theta_{i2} \right) \\ &= \frac{2\pi D \cos \theta \Delta\theta_{i1}}{\lambda} \end{aligned}$$

provided that the ratio  $D/\lambda$  is the same for both frequencies and provided that  $f_2$  is much higher than  $f_1$ . Fig. 2 shows a typical differential angle of arrival system; the electrical separation of the antennas at each frequency is arranged to be the same as are the azimuthal directions of the lines joining the antenna pairs.

In order to measure variations in space in angle of arrival, at least two measurements in different planes are required and an orthogonal arrangement of receiving antennas is both convenient and frequently used. A typical system to measure Faraday rotation and differential angle of arrival simultaneously, using a geostationary satellite, is illustrated in Fig. 3. The subscripts  $1, 2$  and  $F$  refer to radio frequencies ( $f_1, f_2$ ) and Faraday rotation respectively; the letters  $R$  and  $L$  refer to right and left circularly polarised antennas. In all phase measurements, the same standard ( $f_r$ ) is used and the required phases extracted in the manner indicated in Figs. 1 and 2.

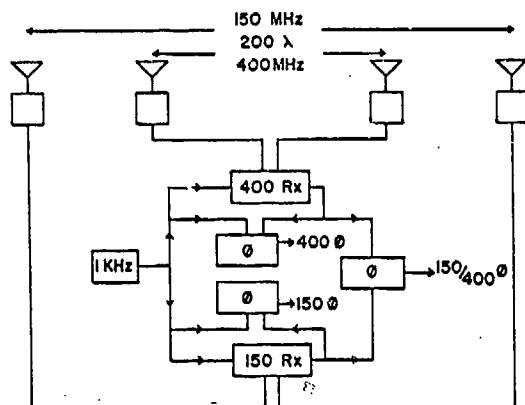


Fig. 2(a) A typical differential angle of arrival system

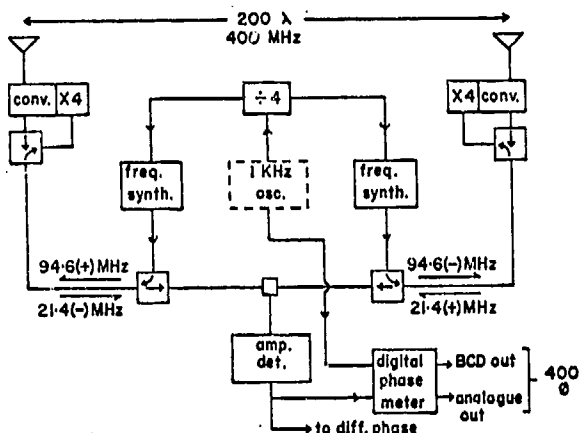


Fig. 2(b) One-half of Fig. 2(a) in more detail

The general layout of Fig. 3 is suitable for use with travelling satellite angle of arrival measurements although circularly polarised antennas are not necessarily the most suitable in this case. This aspect will be considered in the next section.

### 2.3 Practical Considerations

Due to the low transmitted power and the large distance involved, geostationary satellite observations require relatively high gain antennas. In making Faraday rotation observations a standard technique, as has been mentioned, is to resolve the plane polarised wave into right and left circularly polarised components in order to derive the polarisation angle.

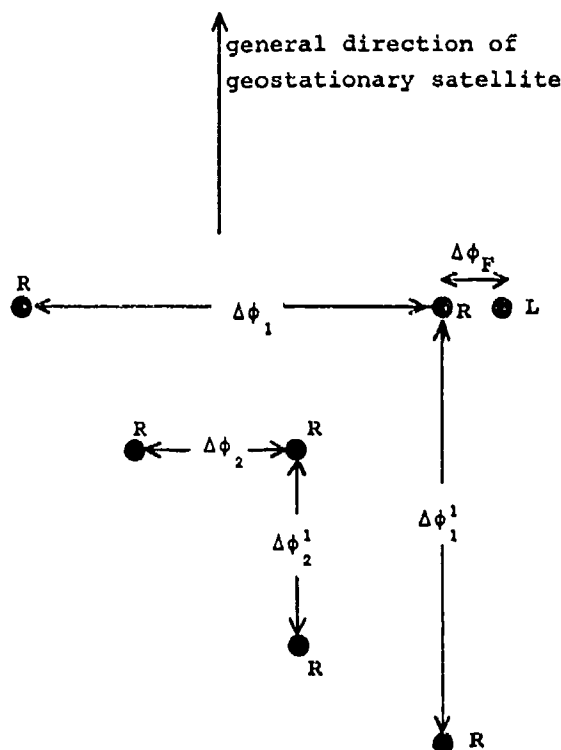


Fig. 3 A typical antenna arrangement for simultaneous geostationary Faraday rotation and angle of arrival observations

There is some advantage to be gained in also using circularly polarised antennas in angle of arrival observations since reduction in signal/noise due to non-coincidence of the planes of polarisation of the signal and the antenna, should a plane polarised antenna be used, is hardly affordable.

In the case of travelling satellites, the situation is somewhat different. First the received power levels are considerably higher; second, unless tracking facilities are available a high gain antenna is clearly undesirable and equal and accurate resolution into circularly polarised components at each antenna becomes difficult. In spite of possible temporary loss of signal due to polarisation effects, fixed plane-polarised antennas of moderate gain appear to be more suitable in this context.

In considering the antenna separation ( $D/\lambda$ , in wavelengths) in angle of arrival measurements it is clear from equation 4 that the

attainable resolution varies directly with this quantity, and the minimum separation is dictated by minimum required resolution. Following Chvojikova (1958a,b), the angular deviation at 150 MHz produced by a spherically stratified moderately strong ionosphere (critical frequency 10 MHz) with no gradients or irregularities is about 0.1 mrad at a ray path angle of  $35^\circ$  (see Fig. 4). A

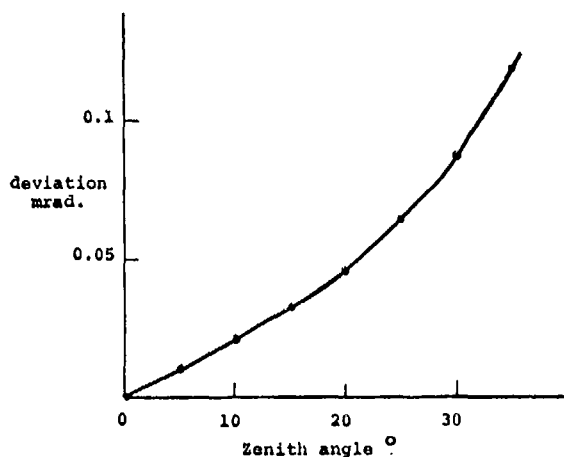


Fig. 4 Angular deviation at 150 MHz due to spherically stratified ionosphere ( $f_c = 10$  MHz) versus ray path zenith angle

gradient of  $0.5\%/km$  in electron density would produce a deviation of the same order of magnitude (Turnbull and Forsyth, 1965). Irregularities and travelling disturbances might be expected to produce deviations up to 1 or 2 mrad (see section 3, and Webster and Lyon, 1974). With all this in mind, and likely topographical restrictions, a resolution of at least 0.1 mrad in angle of arrival is desirable. Allowing a phase meter resolution of  $2\pi/100$  radians and values of  $\cos \theta$  in the range 1 to 0.5 leads to a value of 100 to 200 for  $D/\lambda$  from equation 4.

### 3. EXPERIMENTAL OBSERVATIONS

A complete system, based on the foregoing, is nearing completion at the University of Western Ontario and experimental observations from this are not available at the time of writing. However, results are available from similar systems

operated here, and are presented to establish the validity of the techniques.

Simultaneous geostationary Faraday rotation and angle of arrival measurements have been made using a more conventional system and the technique described by Webster and Lyon, 1974; Figs. 5,6 presented here are reproduced directly from that publication. Fig. 6 represents the experimental data of Fig. 5 filtered digitally at the indicated frequencies.

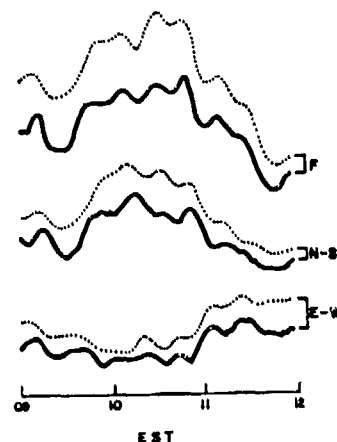


Fig. 5 Experimental records (lower full lines) of Faraday rotation (F) and angle of arrival (N-S, E-W). The dotted lines are synthesized from the filtered data of Fig.6.

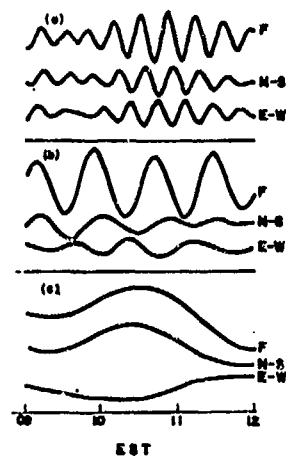


Fig. 6 The experimental data of Fig. 5 filtered digitally at frequencies: (a) 2.81 cycles per hr.; (b) 1.28 cycles per hr.; (c) 0.33 cycles per hr.

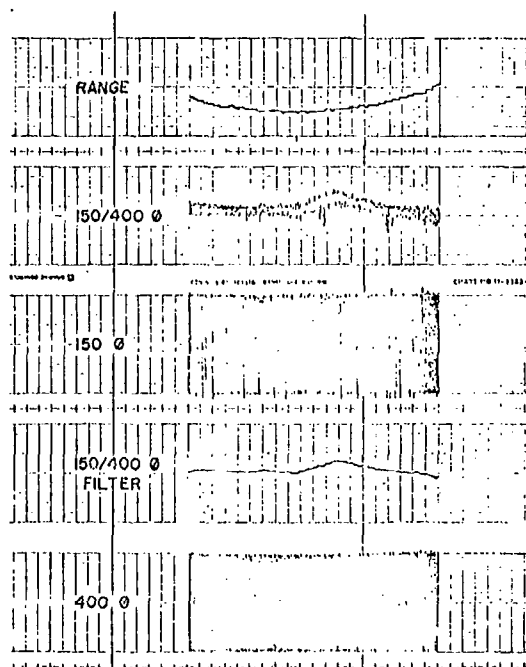


Fig. 7 A typical differential angle of arrival record (Transit satellite)

In essence, the relevant amplitude and phase measurements indicate two travelling waves (a and b) and one stationary wave (c). For both travelling waves, the derived horizontal wavelengths are about 60 km and direction of travel is about  $135^\circ$  E of N.

Differential angle of arrival measurements using the phase-swept interferometer have been made using a single leg aligned N-S and the transit series of travelling satellites; due to the nominal circular polarisation of the transmission from these satellites, little difficulty with polarisation problems has been experienced using plane polarised receiving antennas, although the effect is occasionally noticeable. Typical results are shown in Figs. 7 and 8. Fig. 7 shows the measured phases of 150, 400 and 150/400 MHz for a single satellite pass; Fig. 8 shows a selection of passes and it will be noted that fluctuations much greater than those predicted (0.1 mrad) for a spherically stratified ionosphere are almost always present.

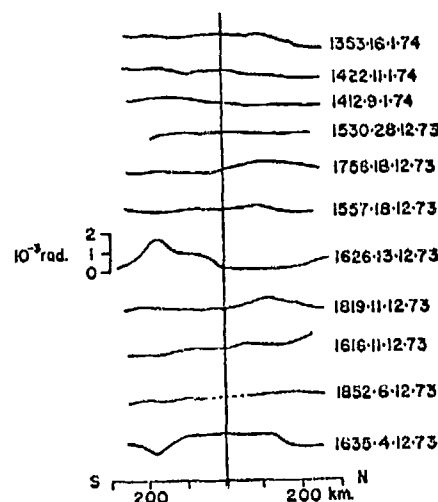


Fig. 8 Angle of arrival showing representative fluctuation magnitudes

#### 4. DISCUSSION

Simultaneous Faraday rotations and angle of arrival measurements using a geostationary beacon satellite provide a useful method for the investigation of the quasi-periodic fluctuations continually observed in ionospheric observations. Coupled with travelling satellite measurements, the system enables a considerable amount of information on the nature of such disturbances to be gained.

The phase-swept interferometer provides a relatively straightforward and economical method of realising such a system. A single receiver only is needed for a basic measurement, (two for a differential measurement) and this need be no more than a conventional intermediate frequency amplifier and envelope detector. Five such simple receivers would be needed for a full Faraday/AOA system, although in principle a single receiver would suffice, if harmonics of the reference frequency and standard multiplexing techniques were employed. Some care has to be exercised in the design of the local oscillator synthesizers since phase noise present here is transmitted through the system.

In all of this, some consideration should be given to antenna design



and possible ground effects which can introduce spurious results which may be interpreted as real (see Jones and Webster. this symposium).

*Acknowledgments*-The advice and help of Dr. J.A. Fulford and Dr. G.F. Lyon is gratefully acknowledged.

#### REFERENCES

Chvojkova, E; Bull. Ast. Inst. Csl.,  
9, 1, 1958a

Chvojkova, E; Bull. Ast. Inst. Csl.,  
9, 133, 1958b

Turnbull, R.M. and Forsyth, P.A.; Can.J.  
Phys., 43, 800, 1965

Webster, A.R. and Lyon, G.F.; J. Atmos.  
Terr. Phys., 36, 943, 1974

PREDICTION OF IONOSPHERIC EFFECTS ASSOCIATED WITH  
SOLAR WIND DISTURBANCES USING INTERPLANETARY  
SCINTILLATION OBSERVATIONS AT 34.3 MHz

W. M. Cronyn  
NOAA/ERL, Boulder, Colorado

F. Erskine and S. D. Shawhan  
University of Iowa, Iowa City, Iowa

B. L. Gotwols and E. C. Roelof  
Applied Physics Laboratory  
The Johns Hopkins University  
Silver Spring, Maryland

Precis. In May 1974, observations at 34.3 MHz of interplanetary scintillations (IPS) of radio sources commenced using the NOAA/University of Iowa COCOA-Cross radio telescope (co-linear dipoles of coaxial cable in a Mills cross). The arms of the array are 0.8 and 1.2 km yielding a collecting area of 72,000 m<sup>2</sup>. The 1/2° x 3/4° beam is steerable in the meridian, allowing viewing of > 200 sources per day covering the entire northern ecliptic hemisphere and extending into portions of the southern hemisphere as far as 45° south ecliptic latitude. We present an analysis of daily IPS observations of 28 selected sources during June 20-30, 1974. This period contains the sudden commencement of a geomagnetic storm (SSC) at 2330 UT, June 25 which was accompanied by 2 days of disturbed ionospheric conditions as indicated by a drop from 6 to 2 in the radio propagation quality indices in the band 2-26 MHz between Lichow (Germany) and Halifax (Canada). The SSC also marked the onset of a delayed solar particle event as measured on the APL/JHU experiment on IMP-7 (protons > 0.3 MeV, electrons > 0.2 MeV) with proton intensities > 300 (cm<sup>2</sup>-sec-ster-MeV)<sup>-1</sup> persisting until June 29. The source of the solar wind disturbance (inferred from the SSC) and the delayed particle event is identified as a 2B flare at ~ 0500 UT, June 23. Two-dimensional analysis of the latitude-longitude grid of daily IPS observations of June 24 - June 27 indicate the earliest detection of the flare-associated solar wind blast wave at ~ 1900 UT June 24. The blast wave appears in all sources within 60° of the sun, beginning ~ 1500 UT June 25, more than 8 hours before the SSC and commencement of ionospheric effects. We can recast our analysis as a simulated prediction of the SSC, assuming that we had realtime data such as is currently available: 1) daily IPS observations from the COCOA-cross grid; 2) satellite measurements of low-energy (~ 1 MeV) protons and relativistic (~ 100 keV) electrons; and 3) solar synoptic charts of large-scale chromospheric magnetic polarity regions constructed continuously from H $\alpha$  patrol

photographs at NOAA/ERL (Boulder, Colorado). The H $\alpha$  synoptic charts indicate coronal magnetic structures that often affect the emission of particles and solar wind. We conclude that we could have predicted with high reliability the SSC, delayed solar particle event (and hence the ionospheric disturbances) at least 6 hours before their occurrence.

#### INTRODUCTION

We are presently monitoring interplanetary scintillation (IPS) on a 24-hour basis of more than 150 radio sources distributed over the entire northern ecliptic hemisphere as well as a portion of the southern hemisphere extending as far as S45° ecliptic latitude. We believe that these observations literally add another dimension to the analysis of interplanetary disturbances and the prediction of geomagnetic storms and solar particle events.

It has been known for about ten years (Hewish, et al., 1964) that small angular diameter natural radio sources display intensity fluctuations on a time scale of about one second. The intensity fluctuations develop because of random diffraction arising from scattering by irregular variations in the interplanetary electron density, and are termed IPS (interplanetary scintillation).

Detailed analyses of day-to-day changes in IPS activity have revealed associations between the activity and other solar wind phenomena. The emphasis to date in IPS observations oriented towards studies of the solar wind has been on three areas: (1) statistics of dynamical features, i.e. auto-correlation analyses of scintillation activity to find 27 day synodic periodicities, cross-correlation of solar wind velocity (as deduced from IPS measurements) and IPS activity, cross-correlation of IPS data with solar disc, space probe and terrestrial data (Burnell, 1969; Houdiner, 1971; Houdiner and Hewish, 1972; Watanabe and Kakumura, 1972; Houdiner, 1973; Coles et al.,

1974); (2) detailed analyses of specific solar wind events, in which IPS data contribute to a self-consistent description involving a variety of solar-terrestrial and space probe data (Sharp and Harris, 1967; Wiseman and Dennison, 1972; Rickett, 1973; Watanabe et al., 1973; Armstrong et al., 1973; Ward, 1974); and (3) analyses of ambient solar wind parameters such as plasma density spectrum and solar wind speed dependence on solar latitude (Dennison and Hewish, 1967; Matheson and Little, 1971; Coles and Maagoe, 1972; Cronyn, 1972; Houminer, 1973; Rickett, 1973; Coles et al., 1974).

With our instrument we are emphasizing the second area of IPS studies: locating, mapping and tracking co-rotating streams and blast waves, with a view towards predicting the interception of these structures by Earth and space probes. Perhaps the best example to date of this technique is described by Wiseman and Dennison (1972). Using the Culgoora (Australia) radio telescope, they were able to follow the origin and evolution of both a radial blast of turbulent plasma and two separate co-rotating solar wind streams. The shape and extent of these large scale structures, as inferred from the sequential variations in scintillation activity across a grid of 14 sources, were consistent with, and were complemented by, observations of solar flare activity, velocity streaming, sudden commencement geomagnetic storms and Forbush decreases.

In May, 1974, a large electronically steerable decametric wavelength Mills Cross radio telescope with a collecting area of over  $7.2 \times 10^4 \text{ m}^2$  (one of the largest in the world) began regular observations as a joint undertaking by the Space Environment Laboratory of the National Oceanic and Atmospheric Administration and the Department of Physics and Astronomy of the University of Iowa. It has been specifically designed for, and dedicated to, IPS observations at solar elongation angles ranging from  $20^\circ$  to  $180^\circ$ . It is located at the University of Maryland Clark Lake Radio Observatory south of the Santa Rosa mountains, in the eastern desert country of San Diego County, an isolated site well-suited for such sensitive studies. The extremely large collecting area and low operating frequency makes possible a unique capability of being able to observe a large number of IPS sources even at source-sun elongation angles approaching  $180^\circ$ .

The observational and interpretational techniques we are currently using are a generalization of those used previously, made possible by the dense grid of sources that can be observed. The scintillation activity of a grid of more than 100 small angular diameter sources, distributed more or less at random over the sky at solar elongation angles greater than  $20^\circ$  and celestial declinations north of  $-25^\circ$ , are being monitored daily and the scintillation index  $m$  ( $m = \Delta I/I$ ,  $\Delta I$  = rms intensity fluctuation,  $I$  = average intensity) measured for each source.

Thus, each day of observations, we monitor IPS activity in the entire northern ecliptic hemisphere, and in the southern hemisphere at ecliptic latitudes ranging from  $\sim 0^\circ$  to  $-45^\circ$ , subject only to a cone of avoidance of  $20^\circ$  radius centered on the sun.

Steering in the N-S direction is accomplished automatically with electrical phase shifters, while the rotation of the earth provides the E-W steering. A schematic diagram of the antenna geometry is given in Figure 1. The reason for the unusually thick arms of the cross is to provide a very large collecting area, in order to obtain adequate sensitivity with the very short effective time constant required for IPS observations. The antenna array has been named the COCOA-Cross, where COCOA is an acronym which stands for the individual element type, Balsey and Eklund (1972), which are colinear dipoles fashioned out of coaxial cable. Cross stands for the type of array, which is a Mills Cross.

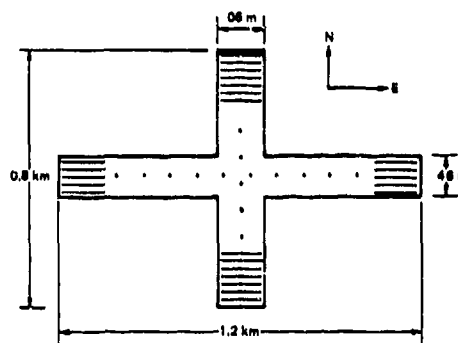


Fig. 1 Overall geometry of the COCOA-Cross Array

Extraction of useful information from the main beam signal is accomplished with analog circuitry and the resulting processed signals are plotted on a multi-channel chart recorder. A 0.1 - 1.5 Hz bandpass filter is used to isolate the signal fluctuations which are due to IPS. Thus, the lower cutoff of 0.1 Hz has been chosen to minimize the contribution of ionospheric scintillation, whereas the upper cutoff of 1.5 Hz is about the upper limit of the IPS frequency components. The output of the bandpass filter, called the raw fluctuation signal, is then subjected to further processing in order to obtain its average power as well as a rough estimate (the second moment) of the shape of its frequency spectrum. The average power (called the scintillation power,  $S$ ) is obtained by squaring and integrating with a relatively long time constant (30 s). The spectrum estimate (called the differential scintillation power,  $D$ ) is obtained by differentiating the raw fluctuation signal with a

short time constant, and then squaring and integrating. The average main beam intensity,  $\bar{I}$ , is obtained simply by integrating the main beam signal (prior to S and D), with a time constant long enough to filter out the IPS (i.e., 1 s).

Calculation of the scintillation index is a straight-forward matter, since  $m = \sqrt{S/\bar{I}}$ . For the stronger sources, it is also possible to obtain an idea of the relative distribution of high vs. low frequency scintillations by calculating the frequency scale,  $f = \sqrt{D/S}$ .

In the initial group of nearly 100 sources we have observed, in which about 30 were known from higher frequency ( $\geq 80$  MHz) observations by others (Harris, et al., 1969; Little and Hewish, 1968; Readhead, 1974) to be subject to IPS, 60 have displayed IPS. Since there are over 900 catalogued IPS sources, the initial observations indicate that the number of sources on which we will be able to take synoptic observations will be limited solely by declination limits on the array ( $-25^\circ$ ), solar elongation angle ( $>20^\circ$ ) and observing time needed to get adequate source and baseline data ( $\sim 6$  minutes).

The current observing list consists of 154 sources. As some of the newly observed sources will undoubtedly prove to be unreliable scintillators, they will be dropped from the observing list. However, there are many more sources to choose from, so the observing list will actually be expanded until it ultimately contains a grid of about 200 reliable IPS sources which will be monitored on a daily basis.

#### EVENT OF JUNE 26, 1974

We can now turn to the event which we shall use as an example for the prediction of upper-atmospheric and ionospheric disturbances associated with solar particle events and geomagnetic storms. Continuous monitoring of about 90 radio sources on a regular 24-hour basis was carried on during June, 1974 with the COCOA-Cross array. The largest event in that month occurred on June 26. It is of considerable interest for four reasons:

(1) There was a geomagnetic storm sudden commencement (SSC) observed by 19 stations (from  $64.6^\circ$  N to  $46.7^\circ$  S geomagnetic latitude) at 2329 UT, June 25, with 3-hour values of  $K_p \sim 5$  for the next two days;

(2) The SSC was accompanied by a decrease  $\sim 5\%$  in the galactic cosmic ray intensity (CRD) as measured by high-latitude neutron monitors, with recovery 3 days later;

(3) Within 12 hours of the SSC, the flux of low-energy solar protons ( $0.3-0.5$  MeV) had exceeded  $100 (\text{cm}^2 \text{ sec ster MeV})^{-1}$  and remained above this level for 3 days, while the flux of relativistic solar electrons ( $> 220$  keV) rose some 3 hours after the protons, reaching a

peak flux above  $10 (\text{cm}^2 \text{ sec ster})^{-1}$  by June 28.

(4) An ionospheric disturbance followed the SSC; its recovery began on June 27 and lasted until June 30.

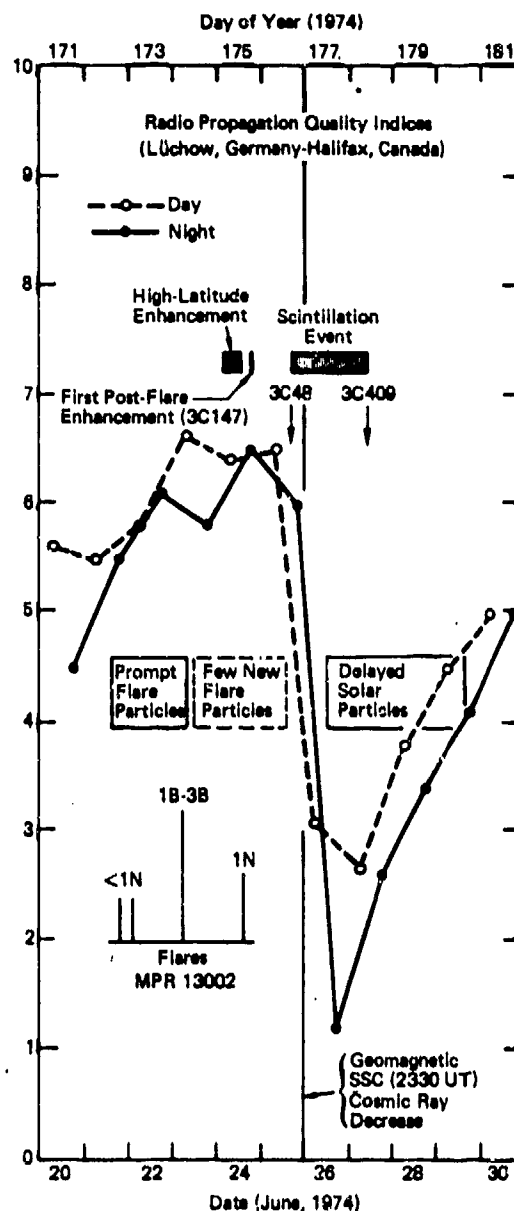


Fig. 2 Radio propagation quality indices for transmission in the band 2-26 MHz between Lüchow (Germany) and Halifax (Canada), June 20-30, 1974. Times of significant flares from MPR 13002 and the SSC on June 25 are indicated, as well as the IPS events that could have led to the prediction of the geomagnetic storm and associated solar particle event on June 26.

Figure 2 shows the radio propagation quality indices for transmission between Lüchow (Germany) and Halifax (Canada) over frequencies in the band 2-26 MHz appropriate for day or night at both stations during June 20-30. The drop in the field strength for the first observation (day) after the SSC is apparent, and it is also clear that the observation (night) between the beginning of the scintillation event and the SSC was in the range of average propagation conditions (index = 6). Also summarized in Figure 2 are the solar flares from the McMath Plage Region (13002) responsible for the disturbance, the COCOA-Cross IPS events and solar particle observations for the period. Since we know that solar and interplanetary data complement IPS observations and thereby enhance prediction reliability, let us first present the solar and spacecraft data before proceeding to the IPS observations. Since all data discussed is actually available on a real-time basis, they can be incorporated into our prediction simulation based on IPS observations.

McMath Plage Region 13002 began optical flare activity soon after its central meridian passage (CMP June 20) with small flares (< 1N) at ~1800 UT, 21 June and ~0330 UT, June 22. The only prior flares in June at this importance level had been in two other regions (12972, CMP June 3 and 12993, CMP June 14), all before June 15. The last flare > 1N from MPR 13002 before it went over the west limb on June 26, was at ~1500 UT on June 24. The only other flare activity was from MPR 13043 (CMP July 3) on June 29-30 (after limb passage of MPR 13002 on June 26). Therefore MPR 13002 dominated solar activity from its CMP until its limb passage.

A striking signature of this active region transit June 20-30 is found in the 0.3-0.5 MeV proton and > 0.22 MeV electron fluxes measured by the APL/JHU experiment on IMP-7, shown in Figure 3. The times and optical importance of all flares from MPR listed in Solar-Geophysical Data (Prompt Reports) are indicated on the figure, as well as the position of IMP-7 along its ~34 R<sub>e</sub> near-circular orbit relative to the magnetotail and Earth-Sun line.

The first small flare (~1800 UT, June 21) resulted in a prompt relativistic electron event as well as a characteristically rapid and strongly anisotropic rise in the low-energy protons. The second small flare (~0330 UT, June 22) produced a small electron enhancement. It therefore appears paradoxical that the larger and brighter flare (importance ~ 2B, with decimeter type III as well as meter and decameter type II radio emission) at ~0500 UT, June 23 did not produce any significant prompt enhancement of either proton or electron fluxes. Nor for that matter did the 1N flare at ~1515 UT, June 24.

It then appears that the interplanetary magnetic "connection" between the acceleration site and the earth was much "poorer" during

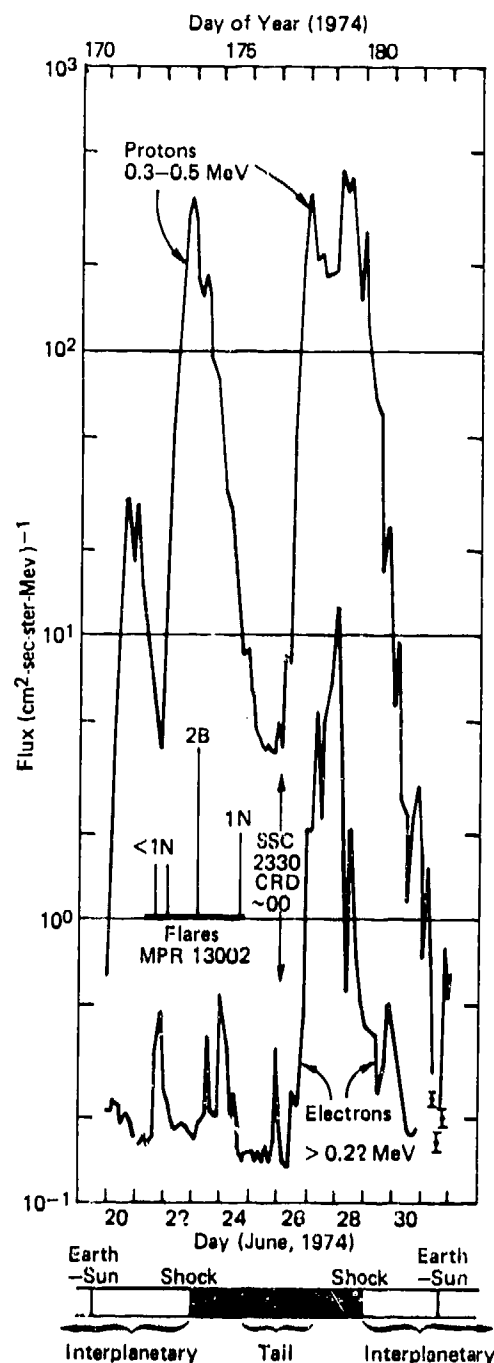


Fig. 3 Solar energetic particle fluxes measured by the APL/JHU experiment on IMP-7, June 20-30, 1974. Location of the spacecraft (near-circular orbit ~ 34 R<sub>e</sub>) relative to the magnetotail and Earth-sun line is shown below the figure. Times are indicated for all significant flares from McMath Plage Region 13002 as well as the sudden commencement of the geomagnetic storm (SSC) and associated decrease in cosmic ray intensity (CRD) at the end of June 25.

June 23-25 than it was on June 21 and 22, since we know that these small gyro-radius particles cannot appreciably cross field lines in interplanetary space (Lin et al., 1968; Krimigis et al., 1971; Roelof and Krimigis, 1973). This inference is strongly supported by the particle event of June 26, when it appears that the interplanetary magnetic "connection" moved to coronal regions where particle injection was greatly enhanced. It seems very unlikely that the onsets on June 26 were due to new acceleration because the relativistic electron rise is abnormally slow, and the low-energy proton rise precedes that of the electrons by more than 6 hours. Rather it is likely that the higher solar wind velocities behind the shock (which we infer from the SSC at 2230 UT on June 25), resulted in the earth being re-connected into a new region of the equatorial corona an appreciable distance further east ( $> 30^\circ$ ) on June 26 than it was on June 25. Just such an effect was recently documented during the August, 1972 activity from Earth and Pioneers 9 and 10 by Roelof et al., (1974). MPR 13002 released 0.3 MeV protons and  $> 0.2$  MeV electrons into interplanetary space for two additional days (June 27-28) without appreciable decrease in intensity, with similar  $> 0.2$  MeV electron injection for more than a day. Long-lived injections earlier in the solar cycle have been analyzed by Roelof and Krimigis (1973).

We therefore are led to the conclusion that the protons and electrons were being accelerated well before the interplanetary shock allowed them to reach earth, perhaps as early as the 2B flare on June 23. The abrupt decrease of the proton intensity beginning June 29 may then simply be explained by the magnetic "connection" longitude moving further eastward after the decay of the solar wind event.

The inter-relationships of the flares, scintillation enhancements and solar particle events observed from Earth become more clearly ordered when we quantitatively estimate the Earth's coronal magnetic connection longitude and compare the events with low-coronal magnetic structure.

That quantitative estimates of equatorial high-coronal connection longitude of interplanetary magnetic field lines can be made using observed solar wind velocities has been justified theoretically for both quiet and disturbed interplanetary conditions (Nolte and Roelof, 1973a; 1973b). Observational verification has been presented by Krieger et al., (1973; 1974) of the tracing back of recurrent solar wind streams to magnetically open coronal structures (coronal "holes") seen in x-ray images obtained from the American Science and Engineering Telescope on a rocket flight and throughout the Skylab mission. A recent multispacecraft observational calibration of the precision of the mapping (Gold and Roelof, 1975) has yielded a mean error of  $< 10^\circ$  in solar longitude over 6 months of observations in 1967. The mapping

simply assumes that the interplanetary magnetic field is "frozen-in" the solar wind plasma whose velocity is assumed to be radial and constant after it leaves the outer corona.

As an indicator of coronal magnetic structure, we have chosen to use H $\alpha$  Synoptic Charts, since it has been established that absorption features in solar H $\alpha$  photographs (filaments, filament channels, fibril patterns, etc.) delineate neutral lines for large-scale chromospheric polarity regions (McIntosh, 1972a; 1972b). Moreover we have shown that the equatorial crossings of H $\alpha$  neutral lines often correspond to spatial discontinuities in interplanetary energetic particle fluxes when they are mapped back to the corona along large-scale interplanetary field lines deduced from observed solar wind velocities (Roelof and Krimigis, 1973; Gold et al. 1974; Roelof et al. 1974; Nolte, 1974; Roelof, 1973a; 1973b; 1974).

Figure 4 shows an annotated version of the preliminary (real-time) H $\alpha$  Synoptic Chart for Carrington Rotation 1616 (June-July, 1974), published by P.S. McIntosh in Solar Geophysical Data (Prompt Reports) (August, 1974). H $\alpha$  filaments are cross-hatched, and magnetic neutral lines are solid if inferred from H $\alpha$  structure, but dashed if inferred from continuity. Sunspots are solid dots and H $\alpha$  emission plages are stippled. McMath Plage Region 13002 is centered at  $350^\circ$  longitude  $< 20^\circ$  latitude. Magnetic polarities ( $\pm$ ) have been checked with solar magnetoheliograms.

The time history of terrestrial observations is shown on the "time line" below the Central Meridian Date on the upper border. The estimated high-coronal connection longitudes for the interplanetary magnetic field are shown by arrows above the equator for the indicated dates and times (e.g., 21:18 is 1800 UT, June 21). Since solar wind velocity measurements are not available at the time of writing, we have made the following estimates. The period June 21-25 was very quiet geomagnetically (three-hour  $K_p < 3$ ), so we have assumed a velocity of 350 km/s, except for July 23 when there was a small storm  $\sim$  0800 UT when we chose 400 km/s. Immediately after the SSC, we have assigned a velocity from the June 23 flare, and assumed that the stream velocity decayed to 350 km/s by June 29. It will be seen from the following discussion that the arguments will still hold even if our estimates are not too accurate.

The prompt low-energy protons and relativistic electrons from the June 21 flare were injected into interplanetary field lines  $\sim 30^\circ$  west of the flare site in MPR 13002. Even though the estimated connection longitude is over the flare site on June 23, few new particles were seen at earth. We have observed such behavior before and concluded that the magnetic structure immediately over a flare site may sometimes be relatively closed. One such case, MPR 8942 in August 1967, was extensively

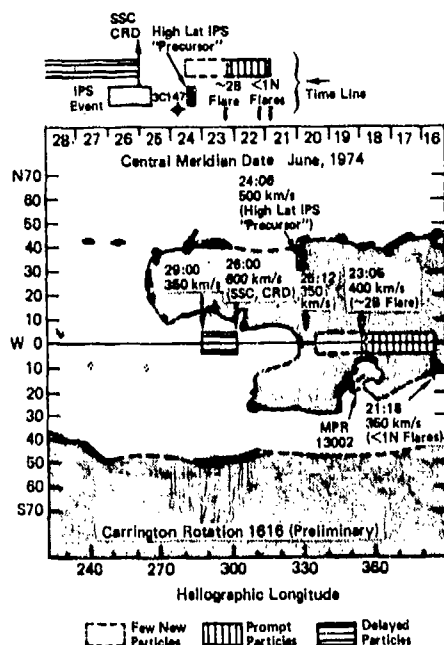


Fig. 4 Large-scale chromospheric magnetic field polarities (shaded, out of the sun) deduced from  $H\alpha$  photographs. Dark filaments (filled with heavy stippling), filament channels and fibril patterns delineate neutral lines between polarity regions. Open stipple patterns are  $H\alpha$  emission plage. Time line (above figure) summarizes IPS and energetic particle events (see legend below figure). High coronal equatorial connection longitudes (estimated from indicated solar wind velocities) for interplanetary injection of solar particles (Figure 3) are marked along the heliographic equator. Time indications (arrows) are in day and hour; for example the connection longitude at 1200 UT on June 25 (25:12) was  $330^\circ$ , estimated on the basis of a solar wind velocity of 350 km/s.

documented for  $> 40$  keV electrons by Lin (1970) and for  $> 0.3$  MeV protons by Roelof and Krimigis (1973).

On the other hand, the onset of the "delayed" particle event of June 26 apparently was the result of the connection longitude being switched  $\sim 30^\circ$  eastward (from  $330^\circ$  at 1200 UT, June 25 to  $300^\circ$  at 0000 UT, June 26) by the increased solar wind velocity behind the interplanetary shock inferred from the SSC. If the solar wind velocity did then steadily decay to something like 350 km/s by June 29, then the coronal injection longitudes for most of the delayed particle event were between  $275^\circ$ - $300^\circ$ . The decay of the particle fluxes beginning June 29 may then have been due to the combination of the resumption of the eastern motion of the connection longitude ( $13.2^\circ$  per day at a constant solar wind velocity) and a western gradient of the coronal injection profile for  $> 0.3$  MeV protons. It is therefore possible that the magnetic

coronal structure above the inferred neutral-line which crosses the equator  $\sim 295^\circ$  served to "compartment" the energetic particles in the high corona, with enhanced interplanetary access for particles outside the eastern boundary of the large negative polarity region west of  $270^\circ$ . A similar case, where particles preferentially occurred outside the polarity region containing the flare site (MPR 8905 in August, 1967) was documented by Roelof and Krimigis (1973), using the same techniques with three spacecraft separated over 0.5 AU (Mariners 4 and 5 and Explorer 35).

#### SIMULATED PREDICTION OF IONOSPHERIC DISTURBANCE

Let us now construct a scenario for an attempted prediction of the June 26 disturbances. With all due disclaimers for the superior acuity of hindsight, we believe that the IPS observations of June 20-25, when combined with other routinely available real-time data, would have allowed a probable prediction of disturbance. We shall assume for this exercise that we have available on a daily basis only the data presented in the previous section, namely:

- (1) IPS monitored on a 24-hour basis from a grid  $\sim 100$  sources;
- (2) Optical and radio flare observations;
- (3)  $H\alpha$  Synoptic Chart in progress for the current solar rotation (i.e., completed to heliographic longitudes at least as far east as  $E30^\circ$  on each day of observations);
- (4) Low-energy ( $\leq 1$  MeV) proton and near-relativistic ( $\geq 50$  keV) electron measurements with time resolution  $\leq 1$  hour;
- (5) Geomagnetic and ionospheric activity indices.

It will be noted that all five classes of data are currently available. In addition (although we shall not make use of it here), solar wind velocity measurements with a significant sample in intervals  $\leq 3$  hours would considerably augment the prediction reliability.

With a grid of  $\sim 90$  sources, two-dimensional analysis of a scintillation event is possible. After all, there is no *a priori* reason that the spatial dependence of events should be confined to the ecliptic; indeed, a variety of complex three-dimensional configurations may be anticipated on the most simple physical grounds.

Therefore we selected 28 sources from the 90 being monitored in late June that exhibited consistent patterns of scintillation activity over the first 60 days of observations. These are listed in Figure 5 by their Third Cambridge Catalog number, right ascension (epoch 1974.5) and ecliptic latitude. Note that the sources are somewhat uniformly distributed in right ascension, but range from  $+79^\circ$  to  $-12^\circ$  ecliptic latitude. Their scintillation indices for each day of the period June 20-30 are indicated by

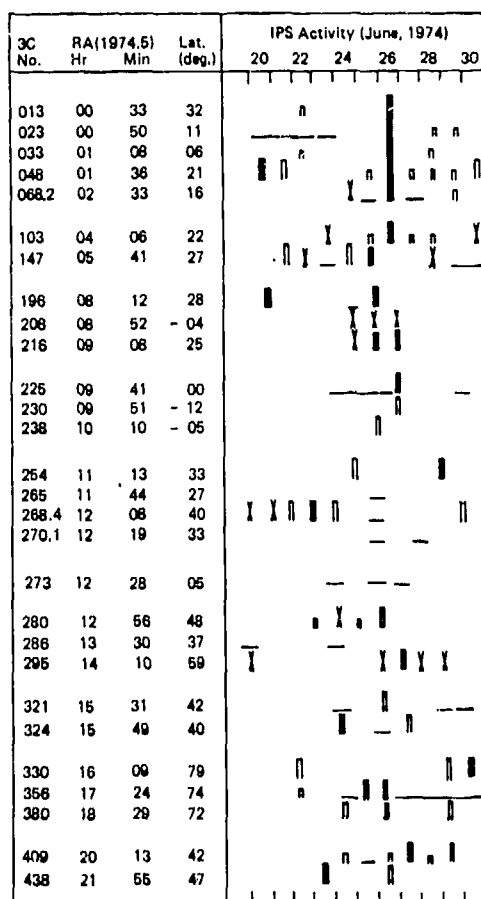


Fig. 5 Sources exhibiting consistent interplanetary scintillation activity during May-June 1974, listed by Third Cambridge Catalog number, right ascension (epoch 1974.5) and ecliptic latitude. During June 20-30, source transit time was approximately  $10^h 30^m$  less than right ascension. Activity symbols for each day's observations: open bars, moderate; solid, high; none, low; dash, no observation; cross, radio frequency interference.

the following symbols: open bars (half and full height, moderate activity; solid bars, high activity; no bars, low activity; dash, no observation; and cross, radio frequency interference (RFI) placing an upper bound on scintillation index.

Even cursory examination of Figure 5 immediately reveals the scintillation event of June 26 following the SSC of 2330 UT June 25. However, since UT at Clark Lake for source observations is about  $10^h 30^m$  less than their right ascension, the chart reveals that several sources showed high activity on June 25, up to 12 hours before the SSC, while others showed activity the following day (June 27). Moreover, activity in a cluster of sources (e.g., 3C23,

3C33, 3C48, 3C68.2, 3C103 and 3C409), persists until June 30. In addition, there appears to be a weak "precursor" event in the higher latitude sources on June 24.

We can now begin our scenario by simulating, on a day-by-day basis, the COCOA-Cross IPS observations and complementary solar, geomagnetic and energetic particle data.

**June 20** - The first indication of subsequent solar activity would have been the small proton event (see Figure 3) even though it had no flare association, since we know that protons at these energies are often associated with the disc transit of an active region with no required flare association. However, with MPR 13002 just past central meridian passage and having shown no previous significant optical activity, the small proton even would not have done much more than suggest that activity in MPR 13002 might be on the increase.

**June 21-22** - The prompt relativistic electrons and low energy protons from the small ( $< 1N$ ) flares in MPR 13002 would establish the region as a significant acceleration of particles. The sharpness of the intensity rises, combined with the interplanetary magnetic connection longitude being  $\sim 30^\circ$  west of MPR 13002 assuming a quiet solar wind based on  $K_p < 3$  (see Figure 4), would have suggested that a subsequent large flare might have produced an interse particle event. Also, the sunward cone of IPS sources would be watched closely on June 23 for a small interplanetary disturbance from the  $\leq 1N$  flares.

**June 23** - The picture would change dramatically on this day. Firstly, the anticipated large flare ( $\sim 2B$  at  $W50^\circ$  with type II and III radio emission) does not produce any prompt significant enhancements of relativistic electrons or low energy protons (see Figure 3), implying that either the flare produced considerably fewer particles than would have been expected from the June 21-22 activity in MPR 13002, or that the Earth-corona magnetic connection was strikingly different from what it had been during those earlier flares. Since geomagnetic activity was still low, the latter implication would have to be interpreted as a relatively closed coronal magnetic structure over MPR 13002, since it now lay under the estimated connection longitude (using a nominal 400 km/s solar wind velocity).

Examination of the  $H\alpha$  neutral-line structure (Figure 4) might then have suggested that the bulk of the accelerated particles may have been preferentially injected to the east of the equator crossing of the neutral line through MPR 13002 at  $\sim 330^\circ$ . We would then anticipate that if the low-energy proton injection continued for another day or two, the protons could reach the Earth after the magnetic connection crossed that line. With an undisturbed solar wind, that would be no later than sometime June 26. There is still no evidence in the IPS observations for an interplanetary plasma disturbance. It would appear that no significant one



had been generated by the small flares of June 21-22, and it would still be too early for anything but a very fast blast wave to be seen by the small-elongation sources.

June 24 - The continued decay of the low-energy proton fluxes is still consistent with either the absence of particles from the June 23 flare or their preferential release elsewhere in the corona. However, the persistence of the relativistic electrons (even increasing on this day) suggests that particle injection is continuing.

It is the IPS pattern that would tip the balance toward the possibility of a delayed event in the making.

These patterns, although somewhat ordered in right ascension (as in Figure 5), become considerably clearer and more amenable to physical interpretation when presented in latitude as well as longitude. We therefore present the data of Figure 5 using "all-sky" plots for four 24-hour periods in Figure 6 beginning at 00 UT: (a) June 24; (b) June 25; (c) June 26; and (d) June 27. The longitude coordinates are  $\lambda_{177}$ , the solar ecliptic longitude at 00 UT, June 26 (just after the SSC). The ecliptic latitude is plotted as the polar coordinate from  $+90^\circ$  to  $-10^\circ$ . Thus any localized region (less than  $30^\circ$  by  $30^\circ$ ) shows the relative positions of the sources therein with only slight distortion (very similar to the image from the all-sky cameras used in auroral studies). As in Figure 5, sources are labeled by their Third Cambridge Catalog number, and the level of scintillation activity is indicated by the symbols given in the legends.

In interpreting the 24-hour, all-sky plots, it is essential to bear in mind the time of observation of the sources (see Figure 5 for right ascension). For instance, since all the plots begin at 00 UT (Figures 6a-6d), the earliest source observed during the 24 hours was 3C254, while a neighboring source at nearly the same ecliptic longitude (3C238) was observed almost one day later.

The major interplanetary activity in late June was initiated by a flare with optical importance  $\sim 2B$  at  $\sim 0500$  UT on June 23 at  $W50^\circ$   $S16^\circ$  in McMath Plage Region (MPR) 13002. Figure 6a reveals that about 38 hours later, on June 24, 3C147 (solar elongation angle  $\sim 25^\circ$ ) exhibited a moderate enhancement in scintillation index. Although confirmation is not obtained from the other western source at small elongation (3C103), nor from a source north-east of the sun (3C196) because of no observation, the mean minimum transit velocity for a disturbance to cross the line of sight to 3C147 is  $> 550$  km/s and to 3C103 is  $\leq 800$  km/s (reasonable velocity range for flare-associated plasma flow 0.5-0.7 AU of the sun). The lack of enhancement of the source 3C103 at small elongation is therefore not inconsistent with the possibility that the enhancement of 3C147 was due to outgoing plasma from the June 23 flare.

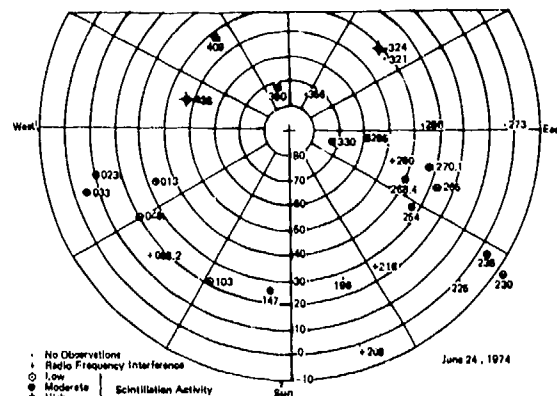


Fig. 6a "All-sky" plot of scintillation activity. Note first source observed during indicated 24-hour period is 3C254 and last is 3C238. Ecliptic latitude is plotted linearly as polar coordinate, and ecliptic longitude on day 177, 1974 (June 26) is the azimuthal coordinate. Data are plotted from Figure 5 and symbols identified in legends. High latitude "precursor" and first sunward scintillation enhancement (3C147 following the  $\sim 2B$  flare, 0500 UT June 23).

It is striking, however, that the only other scintillation activity on June 24 in Figure 6a appears exclusively in the northern mid-to-high-latitude sources ( $> 40^\circ$ ); 5 out of the 7 observations show enhancements, two of which (3C324 and 3C438) are significantly high. It is not unusual that two sources show low activity (3C295 and 3C330); we have found that high latitude scintillation events are often "patchy". Therefore, this pattern raises the possibility that a co-rotating solar wind disturbance well north of the ecliptic swept over the earth at this time. Three additional facts are consistent with this suggestion. The high latitude disturbance is unlikely to have the form of a blast wave, since it was not seen at lower latitudes on June 22 or 23 (see Figure 5). Moreover, the only flares prior to June 23 are at 0310 UT, June 22 and 1800 UT, June 21, both from MPR 13002, but both of optical importance  $< 1N$ . Thirdly, the inferred co-rotating stream would emanate from a northern coronal latitude at a position nearly due north of MPR 13002 (which was  $\sim W40^\circ$  at the time of the observations). The high-latitude "precursor" event observed from 0600-1200 UT with an estimated source location (assuming a typical stream velocity of 500 km/s) in the large unipolar region north-east of MPR 13002 would be the first evidence that high velocity plasma had been emitted from the vicinity of the active region for several days prior to the  $\sim 2B$  flare on June 23 and therefore that MPR 13002 might also generate a large temporal disturbance in the solar wind. There have been cases of co-rotating solar wind streams emanating from open magnetic structures no closer than  $\sim 60^\circ$  in longitude to active regions (Krieger et al. 1973; 1974), so it is quite reasonable that such a stream is inferred.

~ 60° northeast of MPR 13002 in a unipolar, and hence possibly magnetically open coronal region.

In the light of the high latitude "precursor" associated with MPR 13002, the solitary scintillation enhancement of 3C147 at ~ 1900 UT (the source at smallest observable elongation angle and slightly to the west of the sun), would take increased significance, raising the possibility that a disturbance was propagating outward at > 550 km/s at ~ 1500 UT, June 24. This conservative lower bound implies an arrival at Earth no later than mid-day, June 26, along with an eastward shift of coronal connection longitude into a new region which may contain the energetic particles "missing" from the June 23 flare, thus producing a "delayed" particle event following an SSC of a geomagnetic storm.

June 25 - The scintillation activity on June 25 (Figure 6b) is very suggestive of an outward moving blast wave from the large flare of June 23. All observing sources with elongation  $\leq 60^\circ$  showed either moderate or high scintillation indices, while no sources outside of this sunward cone (with the sole exception of moderate activity in 3C356) showed any enhancements. The timing of the observations is critical here, since the enhancement in 3C48 (at the western edge of the sunward cone) was observed ~ 1500 UT, more than 8 hours before the solar wind disturbance caused the SSC at 2330 UT, and all but one (3C230) of the 8 observations subsequent to 3C48 (i.e., through 3C254), show enhancements; the three closest to the sun are significantly high (3C147, 3C196 and 3C216).

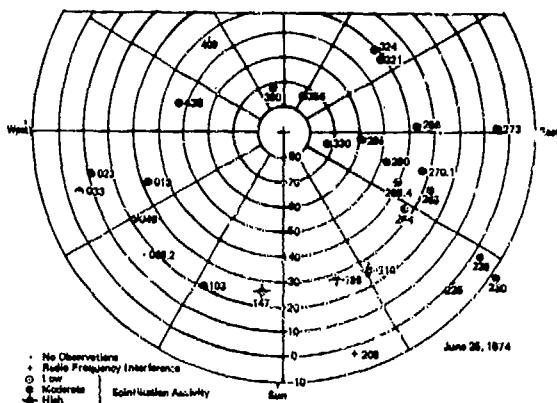


Fig. 6b IPS signature of flare-associated disturbance which caused SSC at 2330 UT, June 25. See Figure 6a.

As the low-altitude sunward sources, beginning with 3C48 at ~ 1500 UT, sequentially show enhanced scintillation indices, we would find our previous conjectures supported and conclude that the arrival of a geomagnetic storm and a possible delayed solar particle event were imminent. It seems reasonable to say that we would have reached these conclusions at least 6 hours before the SSC at 2330 UT, and that we

would have been alerted to the possible arrival of the SSC and solar particles on the previous day (see discussion of June 24).

June 26 - The scintillation event is immediately evident in Figure 6c, implying that the turbulent solar plasma from the June 23 flare was enveloping the Earth beginning with the SSC at 2330 UT on June 25 and continuing throughout June 26. The SSC time implies a mean transit velocity for the plasma of 620 km/s, consistent with the strong decelerations deduced for blast waves. Closer examination of Figure 6c shows a significant bias toward the westward enhancements: 7/10 high (vs. 4/12 for the east); 2/10 moderate (vs. 2/12 for the east); and only 1/10 low (vs. 6/12 for the east). The difference is unlikely to be due to the timing of the observations of the eastern sources; those following 3C268.4 were within the first 6 hours immediately after the SSC. The three-dimensionality of the interplanetary disturbance is apparent not only in the strong western enhancements of 3C013 through 3C103, (a reasonable IPS response for plasma ejected at W50° if its axis of symmetry lies above the flare site), but can also be seen in the lack of enhancement in the sources with smallest elongation angles (3C147 and 3C196) which exhibited high activity on the previous day before the disturbance reached the earth. These sources would not see appreciable turbulence near the earth-sun line as the disturbance swept over the Earth.

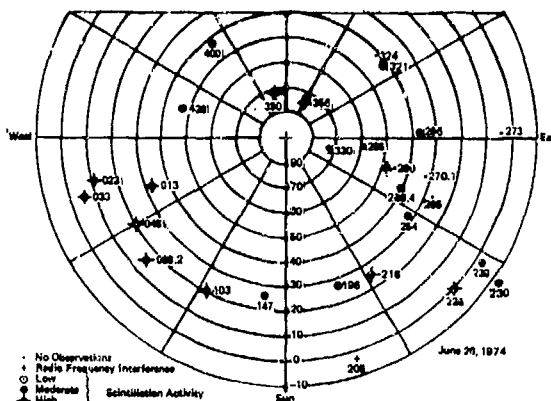


Fig. 6c IPS event as disturbance sweeps over Earth, with westward sources responding to distant plasma from flare longitude (W50°). See Figure 6a.

Even after the SSC arrives, the IPS and energetic particle observations enable us to anticipate the future history of the event. The steady rise of the low-energy protons and relativistic electrons after the SSC (with no prompt flare association), imply that this is the beginning of an extended delayed particle event. The scintillation observations for the day (see Figure 6c) revealed that the centroid of the

turbulence was to the west of us (in agreement with the flare location), so that if this solar wind disturbance followed the pattern of many others, the velocity would begin to decay, possibly on June 27, and continue to decay until reaching its average value. Such a decay usually takes 1-2 days, so around June 28 the connection longitude (having remained around  $\sim 300^\circ$  because of the decay), should begin drifting eastward again (at its normal  $13^\circ$  per day).

The result would be that even if the solar proton injection from MPR 13002 were to continue after June 28 (which it well could since the delayed particles were observed already three days after the large flare), the particle fluxes would then likely begin to drop because the coronal connection longitude would rapidly leave the complex of coronal magnetic fields associated with MPR 13002 whose extent was probably roughly indicated by the equator-crossing neutral line (see Figure 4) which extends no further east than  $270^\circ$ .

June 27 -- The persistence of the low-energy proton intensity at high flux levels would reinforce the above conjecture about the nature of the termination of the particle event. The anti-solar and weak westward scintillation activity (see Figure 6d) would be interpreted as the passing of the turbulent front beyond the Earth and subsequent over-the-limb activity of MPR 13002. Further particle or plasma disturbances would be unlikely for the next few days.

If the turbulent plasma was no longer enhanced along the line of sight for 3C147 and 3C196 in the inner forward cone on June 26, Figure 6d then suggests that it may have been observed moving away from the Earth on June 27, since the two sources closest to the anti-solar direction (3C324 and 3C409) showed significant enhancements. Aside from 3C295, the only other enhancements were those of 3C48 and 3C103, looking well west of the sun at low latitudes. These enhancements may well be responding to additional solar wind disturbances generated by activity in MPR 13002 after it has passed over the west limb of the sun early on June 26. This hypothesis is supported by the continued activity up to June 30 exhibited by the westward-looking sources (3C23-3C103) that is evident in Figure 5.

June 28-30 -- The continued scintillation enhancements of the westward sources (3C23-3C103, Figure 5) would raise the possibility that the successor of MPR 13002 on the next rotation might be the source of a recurrent solar wind stream and geomagnetic disturbance some 27 days after the longitude of the June stream ( $\sim 300^\circ$ ) again reached  $W60^\circ$ . Since the next CMP of this longitude would be early July 20, the recurrent storm could be expected about July 23.

Such a storm (with 3-hour  $K_p > 7$ ) did occur, with 10 stations reporting an SSC  $\sim 0100$  UT, July 23. Of course, there was much intervening geomagnetic activity and high energetic particle fluxes during the period July 3-8. These events

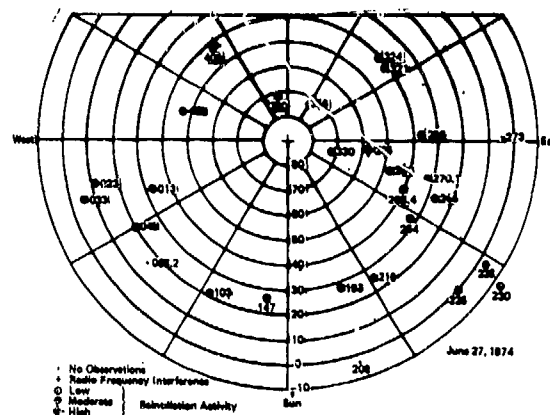


Fig. 6d IPS activity in anti-solar direction (as disturbance passes beyond Earth and westward direction (from over-the-west-limb active region). See Figure 6a.

were from MPR 13043, some  $180^\circ$  east of MPR 13002, and hence quite independent. There was also a scintillation event July 4-6 in conjunction with a large geomagnetic storm, but this happened in a period of sparse observations, precluding an analysis (or prediction) as complete as that given for the June 26 event.

To summarize our interpretation of the IPS observations of Figures 6a-d:

(a) A "precursor" co-rotating solar wind stream emanating from north of MPR 13002 may have been observed by high latitude sources, 0600-1200 UT, June 24. The blast wave from the flare at 0500 UT, June 23 ( $W50^\circ$ ) may have been detected at small westward elongations ( $< 30^\circ$ ) as early as 1900 UT on June 24;

(b) The blast wave appears in scintillation in all sources within the sunward cone containing elongation angles  $< 60^\circ$  beginning more than 8 hours before the SSC at 2330 UT on June 25;

(c) The turbulent flare plasma sweeps over the Earth on July 26, but the centroid of the interplanetary disturbance appears to be well west of the Earth;

(d) The disturbance may have been detected in the anti-solar direction, having passed beyond the Earth on June 27. At the same time, there is evidence from westward looking sources that MPR 13002 continued to generate interplanetary disturbances up to 4 days after west-limb passage.

In summary, we have attempted to demonstrate the possibilities for prediction that result from the combination of existing daily IPS,  $H_z$ , solar particle and geomagnetic (solar wind) observations, the bulk of which are already available through our programs at Clark Lake and Boulder. The reader may draw his own conclusion as to the verisimilitude of our prediction scenario, but

the arguments used are based on our experience in analyzing solar plasma and energetic particle events throughout the last Solar Cycle. Clearly, therefore, the prediction technique as it now stands cannot be carried out by an untrained observer, nor have we made sufficient observations to evaluate the reliability of our approach. Nonetheless, we believe the availability of synoptic monitoring of the interplanetary medium by the COCOA-Cross array adds a new and incisive diagnostic for the solution of the solar-terrestrial prediction problem.

#### ACKNOWLEDGMENTS

The initial design and construction of the COCOA-Cross array was funded by a grant to NOAA from Dr. Norman Ness at NASA/GSFC. Current support is provided by the Atmospheric Sciences Branch of NSF, the University of Iowa, NOAA, and Applied Physics Laboratory/The Johns Hopkins University.

#### REFERENCES

- Armstrong, J. W., W. A. Coles, J. K. Harmon, S. Maagoe, B. J. Rickett, and D. G. Sime, Radio scintillation measurements of the solar wind following the flares of August 1972, World Data Center A for Solar-Terrestrial Physics, Rept. UAG-28, 371, July 1973.
- Balsley, B.B. and W.L. Ecklund, A portable co-axial collinear antenna, IEEE Trans. Ant. Prop., 20, 513, 1972.
- Burnell, S. J., Enhancements of interplanetary scintillation, corotating streams and Forbush decreases, Nature 224, 356, 1969.
- Coles, W.A., B.J. Rickett and V.H. Rumsey, Interplanetary scintillations, Solar Wind Three, ed. C.T. Russell, Institute of Geophysics and Planetary Physics, University of California (Los Angeles), 351, 1974.
- Coles, W.A. and S. Maagoe, Solar wind velocity from IPS observations, J. Geophys. Res., 77, 5622, 1972.
- Cronyn, W.M., Density fluctuations in the interplanetary plasma: Agreement between space probe and radio scattering observations, Astrophys. J., 171, L101, 1972.
- Dennison, P.A. and A. Hewish, The solar wind outside the plane of the ecliptic, Nature, 213, 343, 1967.
- Gold, R.E. and E.C. Roelof, Inference of the equatorial high coronal magnetic field polarity from interplanetary measurements, submitted to Solar Phys., 1975.
- Gold, R.E., J.T. Nolte, E.C. Roelof and R. Reinhard, The influence of coronal magnetic structure on low-energy solar proton events, Space Research XIV, (ed.) A.C. Strickland, Akademie Verlag, Berlin, in press, 1974.
- Harris, D.E. and E.G. Hardebeck, Interplanetary scintillations V, A survey of the northern ecliptic, Astrophys. J. Suppl., 19, 115, 1969.
- Hewish, A., P.F. Scott, and D. Wills, Interplanetary scintillation of small diameter radio sources, Nature, 203, 1214, 1964.
- Houminer, Z., Corotating plasma streams revealed by interplanetary scintillation, Nature, 231, 165, 1971.
- Houminer, Z., Power spectrum of small-scale irregularities in the solar wind, Planet. Space Sci., 21, 1367, 1973.
- Houminer, Z., Enhanced scintillation sectors outside the plane of the ecliptic, Planet. Space Sci., 21, 1617, 1973.
- Houminer, Z. and A. Hewish, Long-lived sectors of enhanced density irregularities in the solar wind, Planet. Space Sci., 20, 1703, 1972.
- Krieger, A.S., A.F. Timothy and E.C. Roelof, A coronal hole and its identification as the source of a high velocity solar wind stream, Solar Phys., 23, 123, 1973.
- Krieger, A.S., A.F. Timothy, G.S. Vaiana, A.J. Lazarus, and J.D. Sullivan, X-ray observations of coronal holes and their relation to high velocity solar wind streams, Solar Wind Three, ed. C.T. Russell, Institute of Geophysics and Planetary Physics, University of California (Los Angeles), 132, 1974.
- Krimigis, S.M., E.C. Roelof, T.P. Armstrong and J.A. Van Allen, Low energy ( $\geq 0.3$  MeV) solar particle observations at widely separated points ( $> 0.1$  AU) during 1967, J. Geophys. Res., 76, 5921, 1971.
- Little, L.T. and A. Hewish, Radio source structure derived from interplanetary scintillation, M.N.R.A.S., 138, 393, 1968.
- Lin, R.P. S.W. Kahler and E.C. Roelof, Solar flare injection and propagation of low energy protons and electrons in the event 7-9 July, 1966, Solar Phys., 4, 338, 1968.
- Lin, R.P., The emission and propagation of  $\sim 40$  keV solar flare electrons, 2. The electron emission structure of large active regions, Solar Phys., 15, 453, 1970.
- Matheson, D.N. and L.T. Little, Radio scintillations due to plasma irregularities with a power law spectra, the interplanetary medium, Planet. Space Sci., 19, 1615, 1971.

- McIntosh, P.S., Inference of solar magnetic polarities from H-alpha patterns, in Solar Activity Observations and Predictions, ed. P. McIntosh and M. Dryer, MIT Press (Cambridge), 65, 1972a.
- McIntosh, P.S., Solar magnetic fields derived from hydrogen alpha filtergrams, Rev. Geophys. Space Phys., 10, 837, 1972b.
- Nolte, J.T. and E.C. Roelof, Large-scale structure of the interplanetary medium. I: High coronal source longitude of the quiet-time solar wind, Solar Phys., 33, 241, 1973a.
- Nolte, J.T. and E.C. Roelof, Large-scale structure of the interplanetary medium. II: Evolving magnetic configurations ded from multi-spacecraft observations, Solar Phys., 33, 483, 1973b.
- Nolte, J.T., Inter-relationship of energetic particles, plasma and magnetic fields in the inner heliosphere, Ph.D. Dissertation, University of New Hampshire, 1974.
- Readhead, A.C.S., Fine structure in radio sources at 81.5 MHz III. M.N.R.A.S., 78, 1, 1974.
- Rickett, B.J., Power spectrum of density irregularities in the solar wind plasma, J. Geophys. Res., 78, 1543, 1973.
- Roelof, E.C., Coronal propagation of energetic charged particles, Proceedings of the Symposium on High Energy Phenomena on the Sun, (ed) R. Ramaty and R. G. Stone, National Aeronautics and Space Administration SP-342, 1973a.
- Roelof, E.C., Coronal magnetic fields and the structure of low-energy solar charged particle events, Proc. of the Solar-Terrestrial Relations Conference, University of Calgary, Canada, 341, 1973b.
- Roelof, E.C., Coronal structure and the solar wind, Solar Wind Three, ed. C.T. Russell, Institute of Geophysics and Planetary Physics, University of California (Los Angeles), 98, 1974.
- Roelof, E.C. and S.M. Krimigis, Analysis and synthesis of coronal and interplanetary energetic particle, plasma and magnetic field observations over three solar rotations, J. Geophys. Res., 78, 5375, 1973.
- Roelof, E.C., J.A. Lezniak, W.R. Webber, F.B. McDonald, B.J. Teegarden and J.H. Trainor, Relation of coronal magnetic structure to the interplanetary proton events of August 2-9, 1972, in Proc. of the Seventh ESLAB Symposium on Correlated Interplanetary and Magnetospheric Observations, (ed) D.E. Page, D. Reidel (Holland), 563, 1974.
- Sharp, L.E. and D.E. Harris, Enhanced interplanetary scintillations associated with solar flares, Nature, 213, 377, 1967.
- Ward, B.D., Detection of the June 15th disturbance by interplanetary scintillation, Compilation of Solar Particle and Interplanetary Measurements Acquired During the Campaign for Integrated Observations of Solar Flares (CINOF), ed. M.A. Shea and D.F. Smart, Air Force Cambridge Research Laboratories Special Report No. 177, AFCRL-TR-74-0271, 43, 1974.
- Watanabe, T. and T. Kakinuma, The recurrent solar wind streams observed by interplanetary scintillation of 3048, Pub. Ast. Soc. Japan, 24, 459, 1972.
- Watanabe, T., T. Kakinuma, M. Kojima, and K. Shibasaki, Solar wind disturbances detected by the interplanetary scintillation of radio sources in early August 1972, J. Geophys. Res., 78, 8364, 1973.
- Wiseman, M. and P.A. Dennison, Flare induced shocks and corotating streams in the interplanetary medium, Proc. Ast. Soc. Australia, 2, 64, 1972.

NON-RICIAN STATISTICS AND THEIR IMPLICATIONS FOR MODELING  
EFFECTS OF SCINTILLATION ON COMMUNICATION CHANNELS

V. Elaine Hatfield  
Charles L. Rino  
Stanford Research Institute  
Menlo Park, California 94025

ABSTRACT

Rician statistics have been used extensively in communication theory as a model for certain noise processes. The received signal from an ionospherically diffracted plane wave can be considered as a complex Gaussian process,  $v = v_r + iv_i$ . This process,  $v$ , is said to have Rician statistics when the respective variances of  $v_r$  and  $v_i$  are equal and their covariance is zero. In the special case in which the means of  $v_r$  and  $v_i$  are zero, the statistics are said to be Rayleigh. A general non-Rician process does not have these restrictions. It has been known for some time that radiowave and optical scintillations do not obey Rician statistics, and until very recently it has been generally accepted that intensity scintillations are log-normal.

In a recent study, Rino et al. [1975] have shown that the general Gaussian model predicts the intensity statistics of radiowave scintillations more accurately than a log-normal model. The resulting statistics are highly non-Rician in that the variance of  $v_i$ , the phase-quadrature signal component, is typically more than five times as large as the variance of  $v_r$ , the in-phase component. The coherent signal component is the phase reference.

In this paper we shall examine the ramifications of non-Rician statistics for channel modeling. In particular we shall examine the relation between the signal variance and the commonly used scintillation index--the normalized intensity variance. We have computed the phase statistics and shall show that the phase probability distribution has a distinctly non-Gaussian shape. In general the phase distribution is asymmetric about zero phase and in certain cases it can develop a pronounced bifurcation.

Finally, we have computed the second-order statistics of intensity and phase for the non-Rician channel. The results are given in terms of the autocorrelation functions for the in-phase and phase-quadrature signal components and their cross-correlation. We examine the validity limits of the commonly used approximations of equating the intensity correlation function with the in-phase correlation function, and the phase correlation function with the phase-quadrature correlation function.

I INTRODUCTION

Originally, it was expected that the intensity statistics for ionospheric scintillation would be Rician [Ratcliffe, 1956]. For the analysis of transionospheric communication links, such a model would be particularly useful since many communications studies have been performed for various aspects of Rician (and Rayleigh) fading. However, researchers in optics and radio astronomy subsequently established that log-normal statistics fit measured intensity histograms better than Rician statistics [Cohen et al., 1967; Ochs and Lawrence, 1969]. Thus, the transionospheric channel was assumed to be log-normal rather than Gaussian.

In a recent study, Rino et al. [1975] found that a general Gaussian statistics model gave improved fits to measured intensity histograms over both the Rician and log-normal curves. Moreover, a theory was developed that explained why Rician statistics are not observed. In this paper we discuss the first- and second-order statistics of amplitude and phase that we believe to be representative of the transionospheric channel for weak to moderate scattering.

It is shown that one cannot obtain a unique relation between the scintillation index  $S^2_4$

and an intensity or phase histogram. For intensity statistics the variations are small and for practical purposes not significant. However, the corresponding phase statistics are considerably more complicated and they can show pronounced variations for a given scintillation level as the ionospheric parameters are varied.

## II THE GENERAL GAUSSIAN STATISTICS MODEL

In the general Gaussian statistics model, the received signal from an ionospherically diffracted plane wave is considered as a complex random process,  $v(t) = v_x(t) + iv_y(t)$ , where  $v_x$  and  $v_y$  are the quadrature components of the signal--are jointly Gaussian processes. In this model  $\sigma_x^2$  and  $\sigma_y^2$ , the variances of  $v_x$  and  $v_y$ , respectively, are not necessarily equal as they are for the special case of Rician statistics. It has been found that [Rino et al., 1975] typically the variance of the phase-quadrature signal component  $v_y$  is more than five times as large as the variance of the in-phase component  $v_x$ .

In our applications, the coherent signal component is used as the phase reference. Thus, the mean of  $v_y$  is zero. The covariance  $C_{xy}$  of  $v_x$  and  $v_y$  is arbitrary in the general Gaussian model. For later reference we summarize the principal properties of the general Gaussian model and of the special cases that have been considered for scintillation studies in Table 1. We have used the auxiliary definitions

$$\sigma_T^2 = \sigma_x^2 + \sigma_y^2; \quad B = \sigma_x^2 - \sigma_y^2 + 2iC_{xy}. \quad (1)$$

We note that  $\sigma_T^2$  is the complex-signal variance,  $\langle v(t)v^*(t) \rangle$  and  $B = \langle v(t)v(t) \rangle$ .

Table 1  
GENERAL GAUSSIAN STATISTICS COMPARED WITH SPECIAL CASES

STATISTICS MODEL	CONDITIONS ON THE VARIANCE	CONDITIONS ON THE MEAN	$\sigma_T^2$
GENERAL GAUSSIAN	NONE	NONE	$4\sigma_x^2 + \sigma_T^4 \left[ 1 + \frac{ B ^2}{4\sigma_T^4} - 4\frac{\sigma_x^2}{\sigma_T^2} \right]$
RICIAN	$\sigma_x^2 = \sigma_y^2 = \frac{\sigma_T^2}{2}$	NONE	$2\sigma_T^2 - \sigma_T^4$
RAYLEIGH	$\sigma_x^2 = \sigma_y^2 = \frac{\sigma_T^2}{2}$	$\langle v_x \rangle = 0$ $\langle v_y \rangle = 0$	

†  $\langle \rangle$  denotes expectation or ensemble average

\* denotes complex conjugate

## III FIRST-ORDER STATISTICS

As is well known, the first-order statistics for a complex Gaussian process are characterized by the joint probability density function (PDF)

$$p_{xy}(v_x, v_y) = \frac{1}{2\pi\sqrt{\sigma_x^2\sigma_y^2 - C_{xy}^2}} \times \exp \left\{ -\frac{1}{2(\sigma_x^2\sigma_y^2 - C_{xy}^2)} \left[ (v_x - \langle v_x \rangle)^2 \sigma_y^2 - 2C_{xy}(v_x - \langle v_x \rangle)(v_y - \langle v_y \rangle) + (v_y - \langle v_y \rangle)^2 \sigma_x^2 \right] \right\} \quad (2)$$

The amplitude PDF is obtained by performing the change of variables  $v_x = a \cos \theta$  and  $v_y = a \sin \theta$ , and integrating over the phase variable  $\theta$ . Thus,

$$P_A(a) = \int_0^{2\pi} p_{xy}(a \cos \theta, a \sin \theta) d\theta. \quad (3)$$

The integration in (3) is performed numerically. A simple change of variables is used to obtain the intensity ( $I \equiv A^2$ ) PDF  $P_I(I)$ .

The phase PDF is obtained similarly by integrating over the amplitude variable. Here, however, it is possible to obtain an analytic result as

$$p_\theta(\theta) = \frac{\sqrt{\sigma_x^2\sigma_y^2 - C_{xy}^2}}{2\pi D} \exp \left[ \frac{-\langle v \rangle^2 \sigma_y^2}{2(\sigma_x^2\sigma_y^2 - C_{xy}^2)} \right] + \frac{\langle v \rangle \sigma_x \sigma_y E}{2\sqrt{2\pi} D^{3/2}} \exp \left[ -\frac{\langle v \rangle^2 \sigma_y^2 (1 + E^2 \sigma_x^2/D)}{2(\sigma_x^2\sigma_y^2 - C_{xy}^2)} \right] \times \operatorname{erfc} \left[ \frac{\langle v \rangle \sigma_x \sigma_y E}{\sqrt{2D(\sigma_x^2\sigma_y^2 - C_{xy}^2)}} \right] \quad (4)$$

where

$$D = \cos^2 \theta \sigma_y^2 - 2C_{xy} \cos \theta \sin \theta + \sin^2 \theta \sigma_x^2 \quad (5a)$$

$$E = \cos \theta \sigma_y^2 - C_{xy} \sin \theta \quad (5b)$$

and  $\operatorname{erfc}[\cdot]$  is the error function complement

To obtain representative values for the parameters in (2), we have used the locally homogeneous statistics formulas (26) and (27) in Rino [1975]. For simplicity they were evaluated only for  $p = 0$ . The result is

$$\sigma_T^2 = \sigma^2 \left[ \xi^2 - \Gamma(\mu) \cos\left(\frac{\mu\pi}{2}\right) Z^{-\mu} \right] \quad (6)$$

and

$$B = -\sigma^2 \left[ \xi^2 - \Gamma(\mu) \cos\left(\frac{\mu\pi}{2}\right) Z^{-\mu} (1 - 2^{-(\mu+1)}) \right. \\ \left. + i\Gamma(\mu) \sin\left(\frac{\mu\pi}{2}\right) Z^{-\mu} (1 - 2^{-(\mu+1)}) \right]. \quad (7)$$

In (6) and (7) we have written the ratio term as a single parameter  $\xi^2$ . The diffraction effects are obtained by varying the Fresnel parameter  $Z$ . The parameter  $\mu$  is related to the spectral index as  $\mu = 1 - p/2$ . For the Kolmogorov value  $p = 11/3$ ,  $\mu = 0.8333$ . The parameter  $\sigma^2$  is an overall measure of the intensity of the perturbation.

As discussed in Rino [1975], the limiting value of  $|B|/\sigma_T^2$  is 0.42 for the Kolmogorov spectral index. Thus, Rician statistics for which  $|B|/\sigma_T^2$  is zero are never achieved. For the curves that we shall be presenting, we have used the Kolmogorov value for  $\mu$  and chosen the remaining parameters  $\sigma^2$ ,  $\xi^2$ , and  $Z$  so that the values of  $\sigma_T^2$  and  $B$  are identical to the results for selected data sets from Rino [1975], Table 1. Once the nominal values were obtained, the  $Z$  parameter was varied while maintaining  $S_4^2$  constant at the measured value.

In Figure 1(a) the solid curve matches Rino's [1975] Data Set I. The corresponding phase PDF is shown in Figure 1(b). For comparison, we have also plotted the large- $Z$  limiting distributions. Scaled contours of equal probability are shown in the upper right-hand corner of the figures. The straight line represents the coherent signal component. We note that as the far-zone limit is achieved the ellipse rotates and fattens.

Now, one can see that there is little difference between the intensity PDF's in Figure 1(a). However, there is a considerable change in the corresponding phase PDF's shown in Figure 1(b). The general Gaussian phase PDF is asymmetric and it has a distinctly non-Gaussian shape when compared to the large- $Z$  limiting distribution. In general the rms phase is considerably larger for the general Gaussian model than for the Rician distribution with the same scintillation index,  $S_4$ .

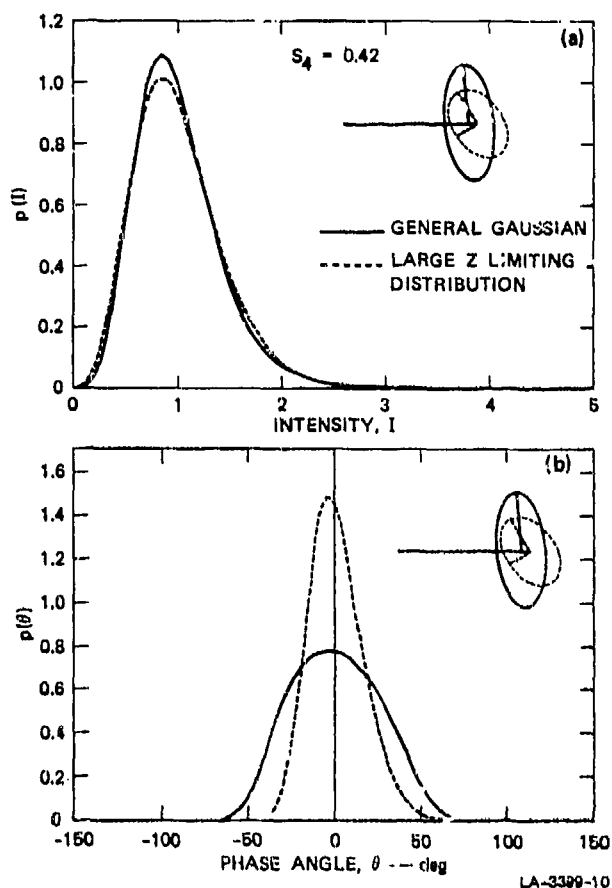


FIGURE 1. PROBABILITY DISTRIBUTIONS FOR INTENSITY AND PHASE — GENERAL GAUSSIAN MODEL COMPARED WITH NEAR RICIAN MODEL

In Figure 2(a) the solid curve corresponds to Rino's [1975] Data Set IIA for which the largest scintillation level was obtained. The dashed curves were obtained by increasing and decreasing  $Z$  by a factor of ten. Here we begin to see the effect of the highly elongated equiprobability ellipse on the intensity statistics. As  $Z$  is decreased, one can see from Figure 1 (a) that the fade margin improves. However, from Figure 2(b) one sees that the rms phase increases. The reverse is true as  $Z$  is increased.

It is important to keep in mind that these variations occur for a constant value of  $S_4$ . The variable parameters are summarized in Table 2 below. The phase variance  $\sigma_\theta^2$  is always  $1/2$  as  $\sigma_T^2$  and appears to be more stable than  $\sigma_y^2$ , although equating  $\sigma_\theta^2$  and  $\sigma_y^2$  is evidently a reasonable approximation. On the other hand,  $4\sigma_x^2 \ll S_4$  for all the values listed in Table 2.



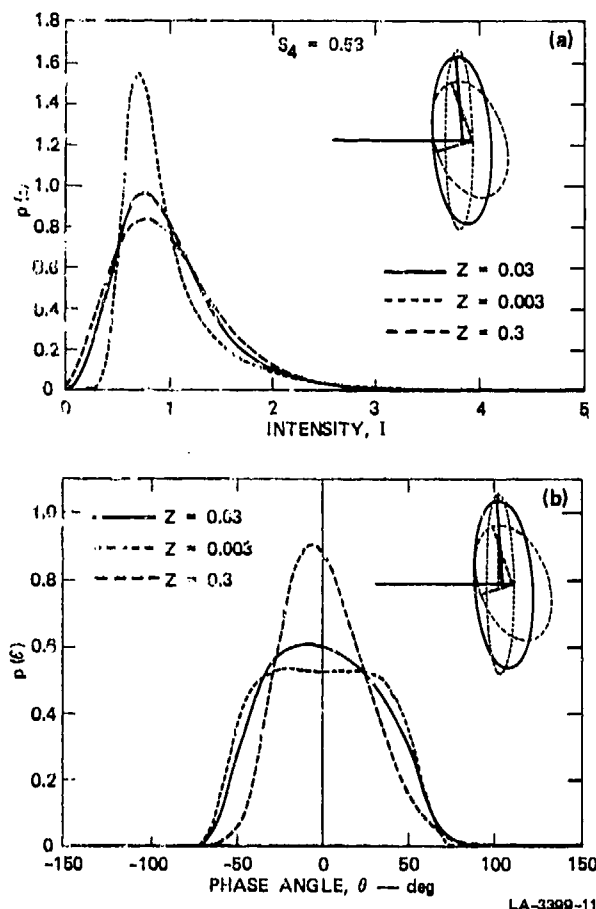


FIGURE 2 PROBABILITY DISTRIBUTIONS FOR INTENSITY AND PHASE — COMPARISON OF VARIATIONS IN THE FRESNEL PARAMETER

Table 2  
COMPARISON OF STATISTICS FOR DISTRIBUTIONS WITH IDENTICAL MEAN INTENSITY AND SCINTILLATION INDEX

Z	$\frac{ B }{\sigma_T^2}$	Orientation Angle	$\sigma_T^2$	$\sigma_y^2$	$\sigma_x^2$	$\sigma_\theta^2$
0.003	0.96	0.6°	0.37	0.36	0.01	0.33
0.03	0.78	3.9°	0.33	0.30	0.03	0.29
0.3	0.47	18.6°	0.23	0.16	0.07	0.19

#### IV SECOND-ORDER STATISTICS

The second-order statistics for the general Gaussian model are related to the time frequency autocorrelation function and the autocorrelation

function for the quadrature components just as they are for first-order statistics. For a fixed frequency we have

$$\langle v(t_1)v^*(t_2) \rangle = R_{x_1x_2}(t_1, t_2) + R_{y_1y_2}(t_1, t_2) + \left[ i R_{x_1y_2}(t_1, t_2) - R_{x_2y_1}(t_1, t_2) \right] \quad (8)$$

and

$$\langle v(t_1)v(t_2) \rangle = R_{x_1x_2}(t_1, t_2) - R_{y_1y_2}(t_1, t_2) + \left[ i R_{x_1y_2}(t_1, t_2) + R_{x_2y_1}(t_1, t_2) \right] \quad (9)$$

The terms  $R_{x_1x_2}$ ,  $R_{y_1y_2}$ , and  $R_{x_1y_2}$ ,  $R_{x_2y_1}$  are the auto- and cross-correlation functions for  $v_x(t)$  and  $v_y(t)$  evaluated at  $t_1$  and  $t_2$  respectively.

The generalization of (2) to statistics of second order can be compactly written using vector and matrix notation as

$$p_{\vec{v}}(\vec{v}) = \frac{1}{(2\pi)^2 |\Lambda|^{1/2}} e^{-1/2 \vec{v}' \Lambda^{-1} \vec{v}} \quad (10)$$

where the vector  $\vec{v}$  has the four elements  $v_x(t_1) - \langle v_x(t_1) \rangle$ ;  $v_y(t_1)$ ;  $v_x(t_2) - \langle v_x(t_2) \rangle$ ; and  $v_y(t_2)$ , respectively. The covariance matrix  $\Lambda$  is given as

$$\Lambda = \begin{Bmatrix} \sigma_{x_1}^2 & C_{x_1y_1} & R_{x_2x_1} & R_{y_2x_1} \\ C_{x_1y_1} & \sigma_{y_1}^2 & R_{x_2y_1} & R_{y_2y_1} \\ R_{x_2y_1} & R_{y_2x_1} & \sigma_{x_2}^2 & C_{x_2y_2} \\ R_{x_1y_2} & R_{y_2y_1} & C_{x_2y_2} & \sigma_{y_2}^2 \end{Bmatrix} \quad (11)$$

To obtain the two-point phase correlation functions we first obtain the corresponding joint PDF by making the substitutions  $v_x(t_j) = A \cos \theta_j$  and  $v_y(t_j) = A_j \sin \theta_j$  for  $j = 1, 2$  in (10). Then

$$p(\theta_1, \theta_2) = \int_0^\infty \int_0^\infty a_1 a_2 p(\vec{v}) da_1 da_2 \quad (11)$$

and

$$R_{\theta\theta}(t_1, t_2) = \int_{-\pi}^{\pi} \int_{-\pi}^{\pi} \theta_1 \theta_2 p(\theta_1, \theta_2) d\theta_1 d\theta_2 - \langle \theta_1 \rangle \langle \theta_2 \rangle. \quad (12)$$

In (11) one of the amplitude integrations is performed analytically. The second integration is performed numerically using the Gaussian quadrature method for 20 points. The integrations in (12) are performed simultaneously using a two-dimensional Gaussian quadrature for a  $10 \times 10$  point grid on the most significant part of the integral. The computer algorithm was tested by verifying that the marginal phase distributions were correct.

The autocorrelation function for intensity is simply obtained from the formula

$$R_{II}(t_1, t_2) = 4 \langle v_x \rangle^2 R_{x_1 x_2}(t_1, t_2) + \left[ 2 R_{x_1 x_2}^2(t_1, t_2) + R_{y_1 y_2}^2(t_1, t_2) + R_{x_1 y_2}^2(t_1, t_2) + R_{x_2 y_1}^2(t_1, t_2) \right]. \quad (13)$$

To determine representative values for the correlation functions  $R_{xx}$ ,  $R_{yy}$ , and  $R_{xy}$ , we have extended the locally homogeneous statistics model that was used for the first-order statistics.

In general, there is an explicit dependence on  $t_1$  and  $t_2$ . However, it was shown in Rino [1975] that the in-phase signal component is strictly homogeneous with

$$R_{xx}\left(\frac{\Delta \rho}{\alpha}\right) = \sigma^2 \int \sin^2(Zq^2) J_0\left(q \frac{\Delta \rho}{\alpha}\right) dq. \quad (14)$$

The remaining components, however, are considerably more complicated. For the computations that we shall present, we set

$$t_1 = -t_2 = \frac{2\Delta \rho}{\alpha}.$$

In Figure 3(a) we show two curves derived from (13) with  $S_4 = 0.5$ . The corresponding  $R_{xx}$  curves normalized to  $R_{xx}(0)$  are plotted in Figure 3(b).

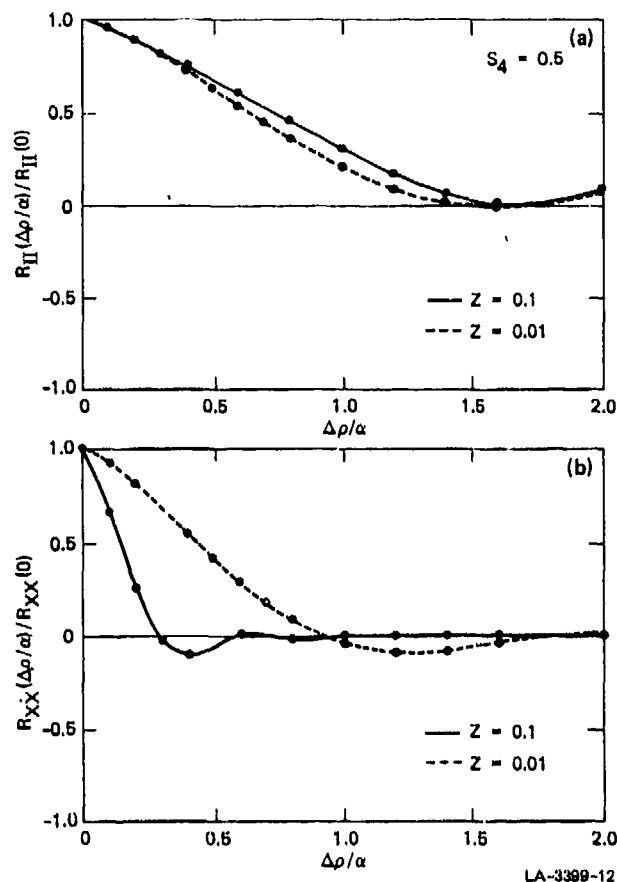


FIGURE 3 COMPARISON OF INTENSITY AUTOCORRELATIONS,  $R_{II}$ , WITH PHASE QUADRATURE AUTOCORRELATIONS,  $R_{XX}$

One observes the striking feature that the intensity coherence is not sensitive to a factor-of-ten change in  $Z$  even though the zero crossing of  $R_{xx}$  changes by the expected amount. Such behavior, if it is indeed representative, would have a profound impact on space-diversity systems. This behavior is a consequence of both the non-Rician and non-homogeneous character of the signal statistics.

In Figures 4(a) and 4(b) we have plotted the corresponding intensity correlation functions for smaller scintillation levels of  $S_4 = 0.05$  and  $S_4 = 0.01$ . We see from Figure 5(a) that the near-zone (small  $Z$ ) curve differs considerably from  $R_{xx}$  even for the very small scintillation level of  $S_4 = 0.05$ . Not until

$S_4$  is less than 0.01 does the near-zone curve approach the behavior of  $R_{xx}$ . Thus, the intensity correlation function at UHF and higher frequencies can be rather complicated even for very small scintillation level].

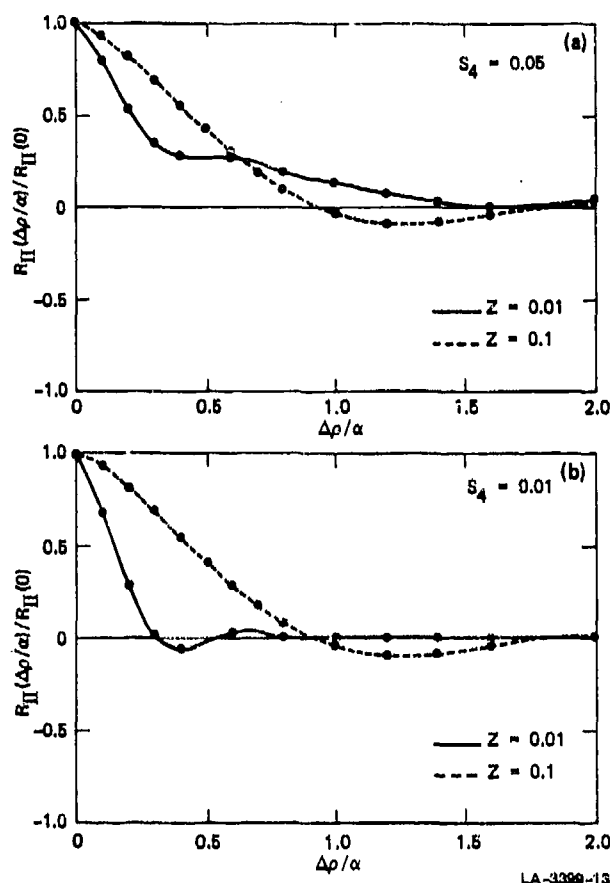


FIGURE 4 INTENSITY AUTOCORRELATION FUNCTIONS FOR TWO SCINTILLATION INDICES,  $S_4$

Finally, in Figures 5(a) and 5(b) we show the phase autocorrelation function and the corresponding  $R_{yy}$  curve, respectively. The behavior of  $R_{yy}$  is very similar to that of the structure function that characterizes the locally homogeneous medium. This occurs because, under the Born approximation, the irregularity structure is imparted directly to the phase-quadrature signal component. The phase statistics shown in Figure 5(a) are influenced by both the real and imaginary signal components. The fact that  $R_{\theta\theta}$  does not converge to zero for large  $\Delta\rho/\alpha$  values is a consequence of the constant term in (22) of Rino [1975]. The correlation functions are not meaningful for values of  $\Delta\rho$  greater than the outer scale size.

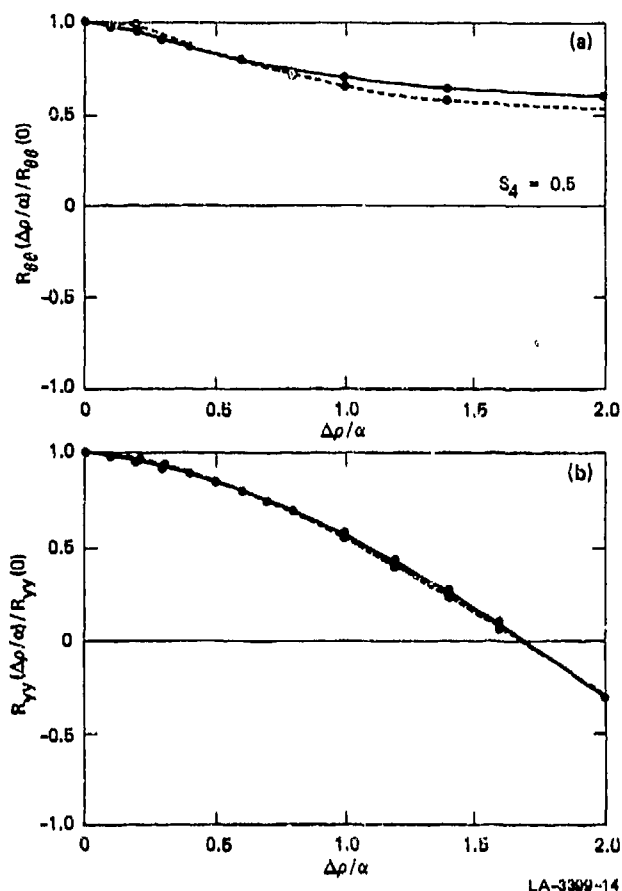


FIGURE 5 COMPARISON OF PHASE AUTOCORRELATION,  $R_{\theta\theta}$ , WITH PHASE QUADRATURE AUTOCORRELATION,  $R_{yy}$

To summarize this section, we have shown that for highly non-Rician statistics, one must use considerable caution in making the approximation  $R_{II} \approx -R_{xx}$ . Moreover, for turbulent media as described by Kolmogorov's locally homogeneous model, the usual correlation functions that one uses are generally ill-behaved so that even when proper account of the non-Rician signal structure is taken, there remain some subtleties that must be considered.

## V DISCUSSION AND SUMMARY

In this paper we have presented computations of the first- and second-order statistics of intensity and phase for a non-Rician as well as an inhomogeneous channel. The inhomogeneous behavior was deduced from the locally homogeneous statistic model that was proposed by Kolmogorov for characterizing incompressible-fluid turbulence. At present this model must be considered to be highly tentative for ionospheric scintillation.

For the first-order statistics, however, the locally homogeneous model does give good agreement with parameters deduced by carefully processing ionospheric scintillation data. Thus, the Gaussian but non-Rician signal structure can be regarded as a good model for weak to moderate ionospheric scintillation levels.

The most important practical consequence for channel modeling is that there is no unique relation between the scintillation index  $S_4$  and the first-order statistics. For the intensity statistics the differences are readily detectable, but not severe. For the phase statistics, however, the consequences of non-Rician statistics are quite pronounced. Thus, where phase errors are important, the detailed structure of the transionospheric channel must be considered.

The computations for the second-order statistics are extremes of behavior that might be expected if the locally homogeneous model proves to be valid. However, considerable theoretical and experimental work in this area remains to be done.

#### REFERENCES

- Cohen, M. H., E. J. Gunermann, H. E. Hardebeck, and L. E. Sharp, "Interplanetary Scintillation II. Observations," *Astrophysical J.* Vol. 147, USA, 1967, pp. 449-466.
- Ochs, G. R., and R. S. Lawrence, "Saturation of Laser Beam Scintillation under Conditions of strong Atmospheric Turbulence," *J. Opt. Soc. Am.*, Vol. 59, USA, 1969, pp. 226-227.
- Ratcliffe, J. A., "Some Aspects of Diffraction Theory and their Application to the Ionosphere," *Roy. Phys. Soc. Progress in Physics*, Vol. 19, Great Britain, 1966, pp. 188-266.
- Rino, C. L., R. C. Livingston, and H. E. Whitney, "Some New Results on the Statistics of Radio Wave Scintillation," Paper A., submitted for publication in the *Journal of Geophysical Research* (1975).
- Rino, C. L., "Some Unique Features of the Trans-ionospheric Channel," paper presented at the Symposium on Effect of the Ionosphere on Space Systems and Communications, 20-22 January 1975, Naval Research Laboratory, Washington, D. C.

# SOME UNIQUE FEATURES OF THE TRANSIONOSPHERIC CHANNEL

Charles L. Rino  
Stanford Research Institute  
Menlo Park, California 94025

## ABSTRACT

We briefly review the evidence supporting the hypothesis that the transionospheric channel is Gaussian, but highly non-rician. If we accept this hypothesis it is possible, by careful processing of intensity histograms, to deduce the variances of the in-phase and phase-quadrature signal components as well as their covariance. In particular, the wavelength dependences of these parameters can be determined. We have found from such studies that the variance of the complex signal has a greater-than-quadratic wavelength dependence. Moreover, the excess-over-quadratic component is always positive and highly variable.

To explain this phenomenon we have hypothesized locally homogeneous statistics for the ionospheric irregularities. Kolmogorov, in his studies of incompressible-fluid turbulence, developed the mathematical techniques. By using Kolmogorov's theory we are able to fully account for the wavelength dependence of the signal variance as well as the fact that the observed highly non-rician signal structure varies only slightly with changes in wavelength.

In the locally homogeneous theory, a large-scale-structure term is specified independently from a component that is characterized by the so-called structure function. Unlike the strictly homogeneous theory, there is no simple Fourier-transform relation between the spatial correlation function and the spectral-density function. Thus, one must exercise caution in interpreting scintillation data as well as in performing calculations that describe the scintillation-induced degradation of various waveforms.

We discuss both the first- and second-order statistics that characterize the complex signal resulting from propagation through a locally homogeneous scattering medium.

## 1. INTRODUCTION

For the analysis of communication systems it is most useful to characterize the transionospheric channel in terms of a time-varying transfer function  $h(t;f)$ . A functional block diagram is shown in Figure 1.

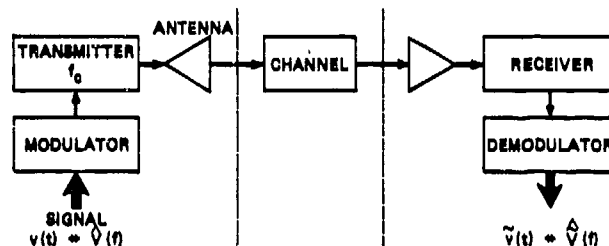


FIGURE 1 FUNCTIONAL BLOCK DIAGRAM OF TRANSIONOSPHERIC CHANNEL

The time-varying transfer function is the response of the channel to a sinusoidal excitation. For an arbitrary signal one has the representation [Bello, 1963]

$$\tilde{v}(t) = \langle \tilde{v}(t) \rangle + \int \hat{V}(f) h(t; f + f_0) \times \exp[2\pi i f t] df + \text{Noise} \quad (1)$$

where  $v(t)$  is the complex signal with the carat denoting the Fourier transform.

To derive such a representation, consider the slab model shown in Figure 2. The wave propagation is governed by the inhomogeneous vector differential equation:

$$\nabla^2 \vec{E} + k^2 \epsilon(\vec{r}) \vec{E} + \nabla[\vec{E} \cdot \nabla \log \epsilon(\vec{r})] = 0 \quad (2)$$

where the permittivity  $\epsilon(\vec{r})$  is a random function of position. Now, in spite of the complexity of (2), it is linear in  $\vec{E}$ . Thus, (2) admits a

solution in terms of its "impulse" response--formally a dyadic Green's function. In general, the Green's function is quite difficult to compute.

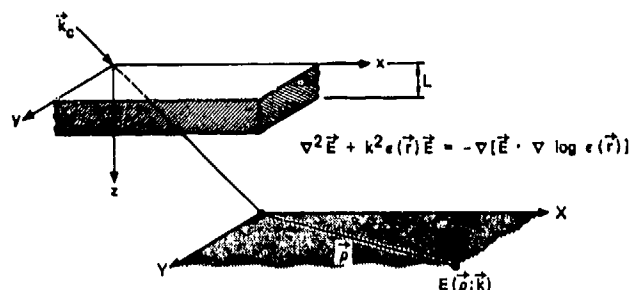


FIGURE 2 SLAB MODEL FOR IONOSPHERIC IRREGULARITY LAYER

However, if the first-order perturbation  $\delta\epsilon(\vec{r}) \approx -\frac{4\pi r_e}{k^2} \Delta N_e(\vec{r})$  is small, one can show directly [Tatarski, 1971] that for an incident plane wave,

$$\vec{E}(\vec{r}) \approx \langle \vec{E}(\vec{r}) \rangle - r_e \int (3) \int \vec{A}_0 \Delta N_e(\vec{r}') \times \exp[-i\vec{k} \cdot \vec{r}'] G(\vec{r}, \vec{r}') d\vec{r}'$$

where

$$G(\vec{r}, \vec{r}') = \frac{\exp[-ik|\vec{r} - \vec{r}'|]}{|\vec{r} - \vec{r}'|} \quad (4)$$

If the statistics of  $\Delta N_e(\vec{r})$  are homogeneous, one can employ a transverse spectral decomposition of the form [Tatarski, 1971]

$$\Delta N_e(\vec{r}) = \iint \exp[-i\vec{k} \cdot \vec{\rho}] d\vec{g}(\vec{k}; z) \quad (5)$$

Substituting (5) into (3) and performing some straightforward manipulations, one obtains the result

$$\vec{E}(\vec{\rho}; z) = \vec{A}_0 \exp[-i\vec{k} \cdot \vec{r}] \left[ (1 - \sigma_T^2)^{1/2} + \vec{\psi}_z(\vec{\rho}; \vec{k}) \right] \quad (6)$$

where

$$\vec{\psi}_z(\vec{\rho}; \vec{k}) = i\lambda r_e \iint \exp[-i\vec{k} \cdot \vec{\rho}] d\vec{g}_z(\vec{k}; \vec{k}) \quad (7)$$

Thus,  $\vec{\psi}_z(\vec{\rho}; \vec{k})$  is a complex perturbation to the incident wave. The phase reference for  $\vec{\psi}_z(\vec{\rho}; \vec{k})$  is a wave that free-space propagates to the point of observation. We see that  $\vec{\psi}_z(\vec{\rho}; \vec{k})$  admits a Fourier decomposition (7), so that the random component of the field can be completely characterized in terms of its Fourier spectrum

$i\lambda r_e d\vec{g}_z(\vec{k}; \vec{k})$ . In general, however, this quantity involves a complicated integral over  $d\vec{g}(\vec{k}; \vec{r})$  [Rino and Fremouw, 1973].

Thus, to relate the spectrum of the irregularities to the spectrum of the field, we look for some simplifying approximations. Under conditions of narrow-angle scattering and a uniform spectrum throughout the layer with a small correlation distance compared to the layer thickness  $L$ , one can show that

$$d\vec{g}_z(\vec{k}; \vec{k}) \approx (L \sec \theta)^{1/2} \exp\left\{-i \frac{\lambda z \sec \theta}{4\pi} k^2 \mathcal{J}(\theta, \vec{\phi} - \varphi)\right\} \times d\vec{g}_z(\vec{k}_T) \quad (8)$$

where

$$\mathcal{J}(\theta, \vec{\phi} - \varphi) = [1 + \tan^2 \theta \cos^2(\vec{\phi} - \varphi)] \quad (9)$$

The angles  $\theta$  and  $\varphi$  are shown in Figure 1. The angle  $\vec{\phi}$  is given as  $\text{atan}(\kappa_y/\kappa_x)$ . In (8)  $d\vec{g}_z(\vec{k})$  is the three-dimensional spectrum of  $\Delta N_e(\vec{r})$ , and  $\vec{k}_T = \vec{k} \cdot \hat{a}$  is the transverse component of  $\vec{k}$ --that is,  $\vec{k}_T = \vec{k}_x \hat{a}_x + \vec{k}_y \hat{a}_y$ .

At this point, we have obtained a representation for the diffracted field of an incident monochromatic plane wave. To obtain  $h(t; f)$ , we make the assumption that the irregularity pattern is "frozen" while it is drifting transverse to  $z$  with velocity  $\vec{v}$ . It then follows, if we ignore the receiver and antenna effects, that

$$h(t; f) = \vec{\psi}_z\left(\vec{\rho} - \vec{v}t; \frac{2\pi f}{c} \hat{a}_k\right) \quad (10)$$

Thus, (1), (6), (7), (8), (9), and (10) constitute a rather complete channel model. The structure of the random component of the channel is characterized by the  $\vec{\rho}$  and  $\vec{k}$  correlation functions

$$R_{\vec{\psi}}(\vec{\Delta\rho}; f^{(1)}, f^{(2)}) = \left\langle \vec{\psi}_z(\vec{\rho}, \vec{k}^{(1)}) \vec{\psi}_z^*(\vec{\rho}, \vec{k}^{(2)}) \right\rangle \quad (11)$$

and

$$B_{\vec{\psi}}(\vec{\Delta\rho}; f^{(1)}, f^{(2)}) = \left\langle \vec{\psi}_z(\vec{\rho}, \vec{k}^{(1)}) \vec{\psi}_z(\vec{\rho}, \vec{k}^{(2)}) \right\rangle \quad (12)$$

Since we are dealing with narrowband signals, it is only necessary to consider wave vectors that differ in magnitude  $2\pi f/c$ .

For later reference, we shall evaluate (11) and (12) for the single-frequency case in which  $f = f^{(1)} = f^{(2)}$ . We have

$$R_{\vec{\psi}}(\vec{\Delta\rho}; f) = \sigma^2 \iint \left( \frac{\vec{k}_T}{\alpha} \right) \exp\left\{-i\vec{k}_T \cdot \frac{\vec{\Delta\rho}}{\alpha}\right\} \frac{d\vec{k}_T}{(2\pi)^2} \quad (13)$$

and

$$B(\vec{\Delta p}; f) = -\sigma^2 \int \int \vec{k}_T \frac{d\vec{k}_T}{(2\pi)^2} \exp\left\{-i\vec{k}_T \cdot \frac{\vec{\Delta p}}{\alpha}\right\} \exp\{-12ZJ\} \quad (14)$$

where  $\phi(\vec{k})$  is the spectral density function (SDF) for the irregularities and  $\sigma^2 = r_0^2 \lambda^2 \sec^2 \theta C_s$ . The terms  $\alpha$  and  $C_s$  are, respectively, the transverse scale and intensity factors for the SDF. The quantity  $Z$  is the Fresnel parameter

$$\frac{\lambda z \sec^2 \theta}{4\pi\alpha^2}$$

What remains is to determine the statistics of the transfer function  $\psi_z(\vec{p}; \vec{k})$ . If  $\psi_z(\vec{p}; \vec{k})$  is Gaussian--that is, its real and imaginary parts are jointly Gaussian processes--then the statistics of  $\psi_z(\vec{p}; \vec{k})$  are completely specified in terms of (13) and (14). In principle, one can calculate the statistics of any observable, such as amplitude and phase in terms of  $R_\psi$  and  $B_\psi$ . Indeed, (13) and (14) are sufficient to calculate the channel capacity as well as the fade statistics, although the details of such computations are quite difficult. In the next section we shall investigate the validity of the Gaussian hypothesis.

## 2. THE STATISTICS OF THE TRANSIONOSPHERIC CHANNEL

The major difficulty in determining the statistics of  $\psi_z(\vec{p}; \vec{k})$  or  $h(t; f)$  is that we normally have only intensity data available. Thus, there is no direct means of determining the statistics of the real and imaginary parts of  $\psi_z$ , which we shall denote as  $x$  and  $y$ , respectively. However, under the Gaussian hypothesis, the first-order intensity statistics are completely specified by the  $\vec{\Delta p} = 0$  values of (13) and (14). We shall write the  $\vec{\Delta p} = 0$  values as

$$\sigma_T^2 = \sigma_x^2 + \sigma_y^2 \quad (15)$$

and

$$B = \sigma_x^2 - \sigma_y^2 + 2iC_{xy} \quad (16)$$

The fundamental quantities  $\sigma_x^2$ ,  $\sigma_y^2$ , and  $C_{xy}$  can be readily derived from (13) and (14) as

$$\sigma_x^2 = \sigma^2 \int \int \phi(\vec{k}) \sin^2(\vec{k} \cdot \frac{\vec{Z}}{2}) \frac{d\vec{k}}{(2\pi)^2} \quad (17)$$

$$\sigma_y^2 = \sigma^2 \int \int \phi(\vec{k}) \cos^2(\vec{k} \cdot \frac{\vec{Z}}{2}) \frac{d\vec{k}}{(2\pi)^2} \quad (18)$$

and

$$C_{xy} = -\sigma^2 \int \int \phi(\vec{k}) \sin(\vec{k} \cdot \frac{\vec{Z}}{2}) \cos(\vec{k} \cdot \frac{\vec{Z}}{2}) \frac{d\vec{k}}{(2\pi)^2} \quad (19)$$

For simplicity, we have written only the normal-incidence forms of (17), (18), and (19). The general forms are obtained by replacing  $Z$  with  $ZJ(\theta, \varphi - \phi)$ .

One can recognize that (17), (18), and (19) are identical to the formulas presented by Bowhill [1961]. Indeed, in essence they were derived earlier by Booker, Ratcliffe, and Shinn [1950]. However, in virtually every application in which (17), (18), and (19) have been employed,  $\sigma_x^2$  has been equated with the variance of the fractional amplitude deviation and  $\sigma_y^2$  has been equated with the phase variance. It is shown in a separate paper by E. Hatfield that such approximations are accurate only for near-Rician statistics and very weak scattering.

We note that when  $Z \approx 0$ ,  $\sigma_y^2 \approx \sigma_T^2$  and  $\sigma_x^2 \approx 0$ . As  $Z$  increases, we find that  $\sigma_x^2$  increases while  $\sigma_y^2$  decreases, until

$$\sigma_x^2 \approx \sigma_y^2 \approx \sigma_T^2/2$$

The covariance increases in magnitude to a maximum, then decreases again to zero. This phenomenon was originally interpreted by Hewish [1952] as a conversion of a phase perturbation at the scattering layer into amplitude fluctuations. It is more accurate, however, to think of it as a redistribution of the scattered power from nearly a pure phase-quadrature perturbation to near equality of the in-phase and phase-quadrature signal components.

For Gaussian statistics there is a convenient description in terms of the equiprobability ellipses that describe the random component of the complex signal. This will be discussed in detail in a separate paper by E. Fremouw. We point out here that  $|B|/\sigma_T^2$  is a measure of the ellipse eccentricity, while  $1/2 |\angle B|$  is the orientation angle of the ellipse measured counterclockwise from a perpendicular to the undeviated signal component. What one finds from (15) through (18) is that the ellipse rotates and tends toward circularity as  $Z$  increases.

To continue, under the assumption of Gaussian statistics, the  $S_4$  scintillation index is given as

$$S_4^2 = 4\sigma_x^2 + \sigma_T^2 \left( 1 + |B|/\sigma_T^2 - 4 \frac{\sigma_x^2}{\sigma_T^2} \right). \quad (20)$$

One can see that two parameters, such as  $|B|/\sigma_T^2$  and  $\angle B$ , can be varied independently while  $S_4$  is maintained constant. We used this fact as a basis for a curve-fitting procedure for measured intensity histograms. Approximately 14 hours of ATS-5 data recorded by AFCRL at their Sagamore Hill facility were used.

It was found that in almost all data records (in particular, those for which good fits overall were obtained), significantly better fits were achieved for the Gaussian curves than for the log-normal alternative that was used for comparison. A  $\chi^2$  goodness-of-fit test was used to evaluate the curves. The results for three of the data sets are summarized in Table 1 below. The corresponding VHF histograms are shown in Figures 3(a), 3(b), and 3(c). We have concluded from these and other data that the Gaussian hypothesis is a very accurate one for interpreting weak to moderate scintillation records.

Table 1  
PARAMETER VALUES FOR ATS-5 DATA

Data Sets	$S_4^2$	$\chi^2_{LN}$	$\chi^2_G$	$\sigma_T^2$	$ B /\sigma_T^2$	$\angle B$
I						
VHF	.42	1206	344	.234	.74	$5^\circ$
UHF	.07	395	321	.022	.90	$<5^\circ$
III						
VHF	.34	1174	162	.134	.60	$5^\circ$
UHF	.069	260	163	.006	.62	$<5^\circ$
IV						
VHF	.30	1441	336	.131	.72	$5^\circ$
UHF	.062	251	177	.006	.74	$<5^\circ$

Proceeding from this conclusion, we can study the behavior of the measured parameters. We first note from the  $|B|/\sigma_T^2$  values that the equiprobability ellipses are highly elongated. Moreover, their orientation is nearly perpendicular to the undeviated signal component. Thus, the first-order statistics, although Gaussian, are highly non-rician (for rician statistics  $|B|/\sigma_T^2 = 0$ ). Indeed, it has been known for some time that rician statistics provide a rather poor fit to scintillation-intensity histograms. We have demonstrated that this fact is not

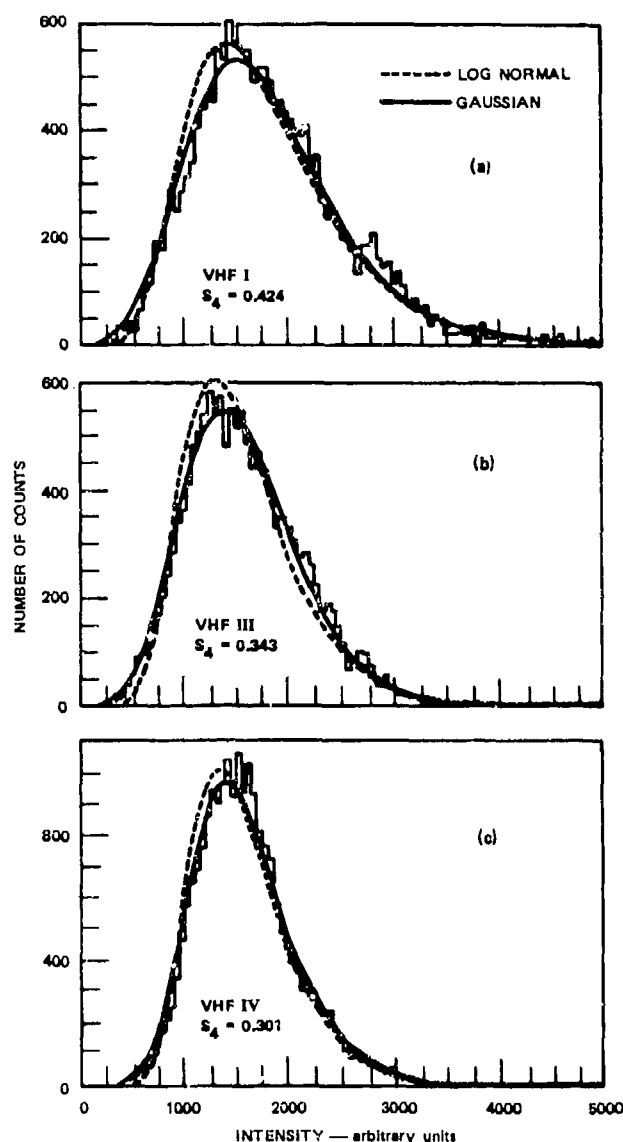


FIGURE 3 MEASURED HISTOGRAMS AND THEORETICAL PDFs FOR ATS-5 DATA



indicative of a breakdown of the Gaussian hypothesis as has been previously assumed. [Barabanenkov, 1971.]

More important, however, we have a means of studying the parameters that directly characterize the signal perturbation. For example, in Table 1, we have listed  $\sigma_T^2$ , the complex signal variance normalized to the average signal intensity. For the data presented,  $\sigma_T^2$  varies from 23% to less than 1%. From the B parameter we can determine that for these data, less than 20% of the scattered power is carried by the in-phase signal component. From our earlier discussion, this implies a small value for Z. Moreover, there is only a slight rotation and fattening of the equiprobability ellipses in going from UHF to VHF. This implies a comparatively large value for the  $\alpha$  parameter.

To investigate this in more detail, we have listed the wavelength index defined as

$$\eta_A \triangleq \log(A_1/A_2) / \log(\lambda_1/\lambda_2) \quad (21)$$

for the parameters  $S_4^2$ ,  $\sigma_x^2$ , and  $\sigma_T^2$  in Table 2 below.

Table 2  
WAVELENGTH INDICES FOR ATS-5 DATA PARAMETERS

Data Set	$\eta_{S_4^2}$	$\eta_{\sigma_x^2}$	$\eta_{\sigma_T^2}$
I	3.26	3.03	2.15
III	2.90	2.88	2.83
IV	2.88	2.88	2.80

The first important point to notice is that the wavelength index for  $S_4^2$  is generally larger than the corresponding index for  $\sigma_x^2$ . Moreover, there is a trend of increasing  $\eta_{S_4^2}$  with increasing  $S_4^2$ --that is,

$$d^2 \log S_4 / d^2 \log \lambda > 0.$$

We can show that this effect is a direct consequence of the Gaussian and non-Gaussian signal structure of the channel, which makes the  $\sigma_T^2$  term in (20) rather important. To show this, we have computed the wavelength dependence of  $S_4$  from (20) in a simple way by replacing  $\sigma_T^2$  with  $\sigma^2/\lambda^2$  and setting B equal to a constant such that  $|B|/\sigma_T^2 = 0.9$  and  $\angle B = 0$ . These values are extremes for the parameters listed in Table 1. They were chosen to exaggerate the effect. The results of the computation are shown in Figure 4.

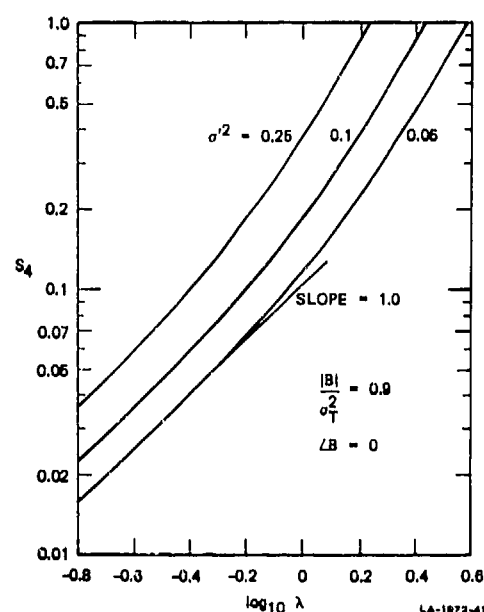


FIGURE 4 COMPUTATION OF WAVELENGTH DEPENDENCE OF  $S_4$

One can readily see that the trend in the data is completely verified by this computation. A practical consequence of this fact is that one will generally overestimate the spectral index for  $\sigma^2$  if it is equated with the  $S_4^2$  index as is always done in practice. It is now well-known that if one evaluates (17) with  $\phi(\kappa) \propto \kappa^{-P}$ , the result is  $\sigma_x^2 \propto \lambda^{\frac{P+2}{2}}$ . Thus, the values of  $\eta_{\sigma_x^2}$  in Table 2 near 3 correspond to spectral P indices between the Kolmogorov value 11/3 and 4. There is evidence that the inferred value of P is greater for Data Set I than for Data Sets III and IV. However, the effect is not nearly as pronounced as one would deduce from the wavelength dependence of  $S_4^2$ .

Finally, we consider the wavelength index for  $\sigma_T^2$ . Here we have a serious problem, since in the weak-scatter theory  $\eta_{\sigma_T^2}$  should be 2, and in any case it cannot be larger than 2, as the values in Table 2 show. Moreover, the  $\eta_{\sigma_T^2}$  are highly variable when compared to the values of  $\eta_{S_4^2}$ . This behavior remained a puzzle for some time. We now believe that it is a manifestation of a breakdown of the homogeneity assumption that is basic to both the weak- and strong-scatter theories. We investigate this possibility in the next section.

### 3. A CRITICAL LOOK AT THE HOMOGENEITY ASSUMPTION

It is now generally accepted that the appropriate spectral density function for scintillation has the power-law form  $\Phi(k) \propto k^{-P}$  to spatial wavelengths corresponding to at least to many tens of kilometers. This poses an immediate dilemma, because even though for small  $Z$  values (17) is not sensitive to the "outer" scale or low-frequency cutoff, (18), (19) and consequently  $\sigma_T^2$  depend critically on the outer scale value. It follows that a power-law spectral density function to very large scale sizes can have a profound effect on the statistics of the irregularities.

Kolmogorov [1941] in his studies of incompressible-fluid turbulence pointed out that the effect of the dominating large-scale irregularities is to impose a position dependence of the statistical moments. As a practical matter, this means that correlation analysis is unreliable, and to circumvent this difficulty Kolmogorov introduced the so-called structure function, which suppresses the large-scale trend-like variations in a turbulent medium.

For the purpose of channel modeling, the structure-function approach poses a difficulty because it is not possible to calculate moments (e.g.,  $\sigma_x^2$ ,  $\sigma_y^2$ , and  $C_{xy}$ ) from the structure function alone. Kolmogorov proposed that in place of (5) one should use the locally homogeneous representation

$$\Delta N(\vec{r}) = \xi_0(z) + \vec{\xi}_1(z) \cdot \vec{\rho} + \iint [\exp(-i\vec{k} \cdot \vec{\rho}) - 1] d\xi(\vec{k}; z). \quad (22)$$

For simplicity, we assume that  $\vec{\xi}_1(z) = 0$ . One can then show that under the same assumptions as before, (7) must be replaced by

$$\psi_z(\vec{\rho}; \vec{k}) = i\lambda r_0 \iint [\exp(-i\vec{k} \cdot \vec{\rho}) - 1] d\psi_z(\vec{k}; \vec{k}) + i\lambda r_0 \xi_0. \quad (23)$$

The approximation (8) remains valid under the same conditions.

One consequence of (23) is that we now have a valid representation of the process for spectra of the form

$$\Phi(\vec{k}) = C_s [(\alpha s)^2]^{-(\gamma + 0.5)} \quad (24)$$

with  $0.5 < \gamma < 1.5$ . (We let  $S^2 = \beta^2 k_x^2 + k_y^2$  to allow for the anisotropy of the medium.) An important result is that independent of any other consideration, one can show that

$$R_{xx}(\Delta \vec{\rho}; f) = \sigma^2 \iint \sin^2(Zk^2) [S^2]^{-(\gamma + 0.5)} \cos(\Delta \vec{\rho} / \alpha \cdot \vec{k}) \frac{d\vec{k}}{(2\pi)^2} \quad (25)$$

which is identical to the strictly homogeneous statistics result. Thus, in spite of the inhomogeneity of the medium, the in-phase component of the diffracted field is strictly homogeneous.

This latter result is verified by Tatarski [1971], who shows that the structure function for  $\text{Re}\{\psi_z(\vec{\rho}; z)\}$  converges to a finite limit as  $\Delta \vec{\rho}$  approaches infinity. However, (25) constitutes only a partial characterization of  $\psi_z(\vec{\rho}; z)$ . To obtain a complete characterization we must consider the joint statistics of  $\xi_0$  and  $d\psi_z(\vec{k}; \vec{k})$ . (The over-bar allows for the "smearing" of  $\xi_0(z)$  within the scattering layer.) To derive a simple model we have assumed that  $\xi_0$  and  $d\psi_z(\vec{k}; \vec{k})$  are uncorrelated, which seems reasonable on physical grounds.

An important point here is that if trend-like components are to contribute to the random part of our signal, it must be through ensemble averaging. This can happen, for example, if the irregularities develop in drifting patches or regions with statistically similar structures. In any case, pursuing this model, we can calculate  $\sigma_T^2$  and  $B$ . For simplicity we assume isotropic irregularities. The results are

$$\sigma_T^2(\rho) = \sigma^2 \left[ \langle \xi^2 \rangle \frac{\alpha^2}{C_s} + 2 \int_0^\infty \left[ 1 - \cos(Zq^2) J_0\left(\frac{q\rho}{\alpha}\right) \right] q^{-2\gamma} dq \right] \quad (26)$$

and

$$B(\rho) = -\sigma^2 \left[ \langle \xi^2 \rangle \frac{\alpha^2}{C_s} + 2 \int_0^\infty \left[ 1 - \cos(Zq^2) J_0\left(\frac{q\rho}{\alpha}\right) \right] q^{-2\gamma} dq - 2 \int_0^\infty \sin^2(Zq^2) q^{-2\gamma} dq - 4 \int_0^\infty \left[ \sin(2Zq^2) - 2\sin(Zq^2) J_0\left(\frac{q\rho}{\alpha}\right) \right] q^{-2\gamma} dq \right]. \quad (27)$$

For interpreting a measurement, (26) and (27) must be averaged in some unknown way over  $\rho$ . However, we can see immediately that

$$\frac{2}{\sigma_T(\rho)/\sigma^2}$$

is wavelength ( $Z$ ) dependent, so that the change of  $\sigma_T^2$  with wavelength is greater than  $\lambda^2$ . Moreover, the magnitude of the enhancement is controlled by the ratio term  $\langle \xi_0 \rangle \alpha^2 / C_s$ . Thus, in interpreting the change of  $\eta_{\sigma_T}$  from Data Set I to Data Sets III and IV, we would conclude that  $\langle \xi_0 \rangle \alpha^2 / C_s$  decreased considerably. It is interesting to speculate as to which parameters are actually changing.

Data Sets I and III and IV were taken on different days, and the scintillation rate for Data Sets III and IV was considerably higher than for Data Set I. In the plasma theory one finds an intimate coupling between drift rate and structure size such that finer structure is associated with an increased drift rate. Thus we can attribute the change in  $\langle \xi_0 \rangle \alpha^2 / C_s$  to a decrease in  $\alpha^2 / C_s$ . We emphasize that for strictly homogeneous statistics, no such inference would be possible.

Finally, we consider the behavior of  $|B(\rho)|/\sigma_T^2(\rho)$  and  $\angle B(\rho)$ . When  $Z$  is very small, one can show that, independent of  $\rho$ ,

$$\lim_{Z \rightarrow 0} \frac{|B(\rho)|}{\sigma_T^2(\rho)} = 1.$$

This limit is also achieved when  $\langle \xi_0 \rangle \alpha^2 / C_s$  is arbitrarily large. Thus, for near-zone diffraction, we have the same result as for homogeneous statistics. The far-zone limit is more interesting. Again, independent of  $\rho$ , we obtain the result

$$\lim_{Z \rightarrow \infty} \frac{|B(\rho)|}{\sigma_T^2(\rho)} = \left(1 - \frac{1}{2^{\mu+1}}\right) \sec \frac{\mu\pi}{2} \quad (28)$$

and  $\angle B = \frac{\mu\pi}{2}$ , where  $\mu = -\gamma + 0.5$ . For the Kolmogorov value  $\gamma = 1.33$ , the limit is 0.43. Thus, rician statistics are not achieved in this model even in the limit of an infinitely large Fresnel radius.

This latter result explains in a very appealing way why rician statistics are virtually never observed. In closing this section, we present the results of a numerical computation of  $|B(\rho)|/\sigma_T^2(\rho)$  with different values of  $\langle \xi_0 \rangle \alpha^2 / C_s$  to show that the previously inferred changes in this parameter from Data Sets I and

III and IV are consistent with the values of  $|B|/\sigma_T^2$  listed in Table 1. We see from the curves in Figure 5 that the smaller eccentricity values for Data Sets III and IV are consistent with a decrease in the value of  $\langle \xi_0 \rangle \alpha^2 / C_s$ .

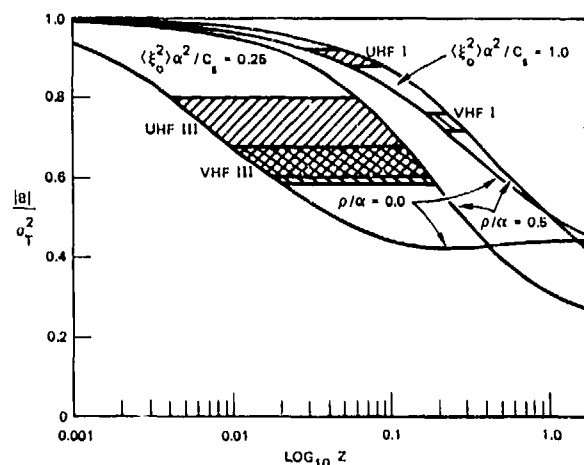


FIGURE 5 NUMERICAL COMPUTATION OF  $|B|/\sigma_T^2$

#### 4. SUMMARY

In this paper we have shown evidence that:

1. An additive Gaussian perturbation is a very accurate model of weak to moderate ionospheric scintillation.
2. The structure of the signal is such that the statistics are highly non-rician, and that this structure is only weakly dependent on changes in the Fresnel radius.
3. The variance of the complex signal perturbation has a greater than quadratic wavelength dependence that is highly variable, in disagreement with all currently accepted theories.

We have proposed that the last property be explained with a model based on Kolmogorov's locally homogeneous statistics representation. Indeed, we find good agreement with our own data as well as with several generally accepted properties of scintillation observations.

# REFERENCES

- Barabanenkov, N., A. Kravtsov, S. M. Rytov, and V. I. Tatarski, "Status of the Theory of Propagation of Waves in a Randomly Inhomogeneous Medium," Sov. Phys. Usp. 13(5), USSR, 1971, pp. 551-575.
- Bello, P. A., "Characterization of Randomly Time-Variant Linear Channels," IEEE Trans. on Comm. Systems, Vol. CS11, USA, December 1963, pp. 360-393.
- Booker, H. G., J. A. Ratcliffe, and D. H. Shinn, "Diffraction from an Irregular Screen with Applications to Ionospheric Problems," Phil. Trans. Roy. Soc. A, Vol. 242, Great Britain, 12 September 1950, pp. 579-607.
- Bowhill, S. A., "Statistics of a Radio Wave Diffracted by a Random Ionosphere," Res. National Bureau of Standards--D. Radio Propagation, Vol. 65D No. 3, USA, May-June 1961, pp. 275-292.
- Hewish, A., "The Diffraction of Galactic Radio Waves as a Method of Investigating the Irregular Structure of the Ionosphere," Proc. Roy. Soc. London, 214, Great Britain, 1952, pp. 494-514.
- Kolmogorov, A. N., "Local Structure of Turbulence in Incompressible Fluids with Very High Reynolds Numbers," DAN SSSR, 30(4), 1941, p. 229.
- Rino, C. L., and E. J. Fremouw, "Ionospheric Scintillation Studies," Final Report, Contract NAS5-21891, SRI Project 2273, Stanford Research Institute, Menlo Park, California, USA, November 1973.
- Tatarski, V. I., "The Effects of the Turbulent Atmosphere on Wave Propagation," National Science Foundation, TT-68-50464, USA, 1971.

## STOCHASTIC STATIONARITY OF THE SCINTILLATING EQUATORIAL IONOSPHERE

Howard A. Blank and Gary J. Bream  
Computer Sciences Corporation  
Falls Church, Virginia

### ABSTRACT

This paper presents a technique for assessing the stochastic stationarity of ionospheric scintillation. The method employs the distribution-free Kolmogorov-Smirnov hypothesis test to determine the degree of statistical similarity for sequential blocks of scintillating data. The scintillation data is divided into regions of statistical stationarity within specified tolerances. The technique has been demonstrated on a set of AGC fading signals collected from the equatorial ionospheric region during very active scintillation periods. The fine-grain stationarity is determined by this method for three error tolerances. The stationarity of the coefficient of variance scintillation index ( $S_4$ ) is measured and compared with the previous results. A comparison of the fading depth and scintillation index statistics has been made for a set of stationary periods found by the Kolmogorov-Smirnov method. The results presented here are preliminary. Only the fine-grain stationarity has been measured which represents the passing of single ionospheric irregularities or small clusters of associated irregularities between the satellite and earth station. For practical applications of the stationary method, the tolerances will be set to determine stationary periods based upon averages of many irregularities.

### 1.0 INTRODUCTION AND SUMMARY

The theoretical and empirical study of the characteristics of ionospheric scintillation has been the subject of intense investigation during the last two decades. Considerable effort has been expended in defining the nature of the scintillation phenomenon and its effects upon radio wave propagation by gathering a variety of statistical phenomenological parameters gleaned from received signals from space-to-earth paths. The accuracy of these statistical parameters is largely dependent upon the stochastic stationarity of the transionospheric channel, and a method of quantifying stationarity periods will be most useful in future ionospheric studies.

This paper reports on the use of the stochastic measurement capabilities of the Ionospheric Distortion Analysis Program-2 (IDAP-2)\* to determine the fine-grain stationarity of a set of AGC fading signals. Specifically, empirical AGC signal data has been collected from the SAS-1 satellite at Quito, Ecuador during the spring equinox period of 1971. The satellite ground station and time period were selected in order to obtain conditions of worst-case ionospheric behavior. It was expected that equatorial gross irregularity size and movement will be most apparent during this period, allowing its stationarity characteristics to be measured.

The AGC data have been converted, reduced, and analyzed. The analyses include a comparison of the time stationarity periods obtained for three threshold values of the Kolmogorov-Smirnov\*\* distribution-free hypothesis test, analysis of the coefficient of variance scintillation index ( $S_4$ ) as a function of the stationarity periods, and a comparison of the fading and time stationarity characteristics of the scintillation channel.

The purpose of this paper is to investigate a technique to automatically designate stationary periods of the AGC data and to analyze the characteristics of the fine-grain time stationarity of the scintillation process. Stationary periods were determined first by analysis of the stationarity of the scintillation index, and then by a Kolmogorov-Smirnov hypothesis testing method. A comparison of the results showed that the two methods of assessing time stationarity were approximately equivalent, and that choosing a threshold value for the Kolmogorov-Smirnov test is approximately equivalent to specifying a tolerance

\* Ionospheric Distortion Analysis Program Documentation - Version 2, June 1974, NASA/GSFC. (Available in GSFC program library.)

\*\* Fisz, M., "Probability Theory and Mathematical Statistics," J. Wiley, 1963, Chapter 12.

level for scintillation index stationarity. A comparison of the fading depth and scintillation statistics shows that the characteristics of one may be closely approximated from the other. Analysis of either fading depth or the scintillation index may be used to determine the desired threshold value for the Kolmogorov-Smirnov method. The fine-grain time stationary periods of the SAS-1 AGC data were very short. They represent radio wave disturbances corresponding to single ionospheric irregularities or small clusters of associated irregularities passing between the satellite and the earth station. The stationarity period distribution presented here may be used to estimate the size and velocity of the irregularities. The Kolmogorov-Smirnov method has been demonstrated to be a valuable tool for the automatic determination of stationary periods in scintillation records. The test used here for fine-grain stationarity may be adjusted for longer time intervals enabling the evaluation of long-term stationarity. The stationary periods determined by the Kolmogorov-Smirnov method may be used to block fading time series for additional statistical processing.

## 2.0 EQUIPMENT DESCRIPTION

The empirical equipment for the telemetry and AGC measurements includes the SAS-1 satellite and the NASA tracking station at Quito, Ecuador. The equipment descriptions are:

### 2.1 SAS-1 Satellite

The SAS-1 spacecraft was launched in late 1970 and is currently in a 550 kilometer circular-equatorial orbit, with a 3° inclination. The telemetry is transmitted from the satellite at 136.680 MHz via a circularly polarized turnstile antenna. The spacecraft antenna has a gain of 0 dB, and the ERP of the spacecraft is .25 watts.

### 2.2 Ground Receiver System

The basic equipment configuration at each of the earth terminals is shown in Figure 1. A station has either a pair of 40 ft. parabolic antennas with 55 percent efficiency, or a pair of 16 element yagis. In either case the antenna system has 22 dB of gain at 136 MHz. Each output drives preamplifiers at VHF, which are then downconverted to IF, filtered through a 10 kHz bandpass filter, and acquired and detected. The receiver carrier tracking loops are third order and have bandwidths of 30 Hz. The detection loss of this receiver is approximately 4 dB. The AGC error signal is fed through module recorders (i.e., operational and/or logarithmic amplifiers) and on to an Ampex FR600 magnetic tape recorder.

## 3.0 DATA REDUCTION PROCEDURE

The data conversion and reduction was accomplished in two stages. First, the AGC data channels are digitized and stored on magnetic tape and the data quality is checked. The second stage uses the IDAP-2 calibration processor program for the calibration of the digital data and the application of the Kolmogorov-Smirnov hypothesis test for time stationarity.

The Kolmogorov-Smirnov hypothesis test has been implemented in the calibration processor program to provide a means of segmenting the scintillation data into statistically similar periods. This test was chosen because it does not require beforehand knowledge of the nature of the statistical distribution of the data. The test compares the cumulative distribution functions of two consecutive blocks of data samples to determine if they are from the same distribution function within a prescribed probability of error. Consecutive blocks of data falling within this prescribed error tolerance are grouped together as a single statistically stationary period. The mean, standard deviation, and scintillation index are computed for each of these periods. An entire satellite pass is divided into statistically stationary periods by this method.

## 4.0 DATA ANALYSIS

Three types of analyses were performed on the AGC data from the SAS-1 satellite transmissions:

- The time stationarity of the cumulative distribution of five second blocks of AGC data was determined by applying the Kolmogorov-Smirnov hypothesis test for three thresholds.
- The time stationarity of the  $S_4^*$  scintillation index was measured. Results are summarized in a density of the distribution of the lengths of stationary periods.
- The fading depth was calculated and analyzed statistically.

The results of these analyses are presented in this section.

### 4.1 Kolmogorov-Smirnov Test

The Kolmogorov-Smirnov test is a nonparametric test of the identity of two populations. Nothing need be known about the form of the parent distribution functions or of the central moments. The only requirement is that the distributions of the parent populations are continuous. Let  $S = S(u)$  denote the empiric cumulative distribution function determined by the sample random variables  $x_1, x_2, x_3, \dots, x_{n_1}$ . Similarly let  $T = T(u)$  denote the empiric cumulative

\*  $S_4$  is defined as the standard deviation of the power samples normalized to the mean power.

distribution function determined by the sample random variables  $y_1, y_2, y_3, \dots, y_{n_2}$ . The Kolmogorov-Smirnov test of the hypothesis that the two populations have the same distribution uses the statistic

$$A_0 = \max_{\text{all } u} |S(u) - T(u)| = \max_{\text{all } u} |A(u)|,$$

where  $A(u) = S(u) - T(u)$ .

The value  $A_0$  of  $A$  will be the greatest absolute difference in height between the two empiric distribution functions,  $S$  and  $T$ . If an appropriately large value of  $A$  is observed, one rejects the hypothesis that the populations have the same distribution in favor of the alternative that they do not. The asymptotic distribution of  $A$  is given by

$$\Pr^* \{A_0 \leq zN^{-1/2}\} \rightarrow L(z) \quad \text{as } n_1, n_2 \rightarrow \infty$$

where  $N = n_1 n_2 / (n_1 + n_2)$

$$\text{and } L(z) = 1 - 2 \sum_{j=1}^{\infty} (-1)^{j-1} e^{-2j^2 z^2}$$

$$= \frac{\sqrt{2\pi}}{z} \sum_{j=1}^{\infty} e^{-(2j-1)^2 \pi^2 / 8z^2} \quad (z > 0)$$

$$L(z) = 0 \quad (z \leq 0).$$

For finite  $n_1$  and  $n_2$ , the limiting values for  $A_0$  are tabulated against  $N$  and the quantity  $1 - L(z)$  which is called  $\alpha$  or the "Significance Level." An abbreviated listing of the limiting value for  $A_0$  as determined by  $\alpha$  and  $N$  is shown in Table 1. For example, to test whether two populations of size 50 were of the same distribution with a probability of 5 percent that they would fail the test if indeed they were from the same distribution, the procedure is

1. Determine  $N$  ( $N = n_1 \times n_2 / (n_1 + n_2) = 25$ )
2. Find the limiting value for  $A_0$  in the table (.264)
3. Find  $A_0$  ( $A_0$  = maximum absolute difference of the two cumulative distribution functions).

If  $A_0$  is greater than its limiting value (.264), then it is concluded that the two populations are not identical at the 5 percent significance level.

#### 4.2 Kolmogorov-Smirnov Time Stationarity

The Kolmogorov-Smirnov hypothesis test is used to segment the stream of AGC power samples into regions of similar statistics. Consecutive

\* Pr is read, "the probability that."

Table 1. Percentage Points for the Kolmogorov-Smirnov Test Statistic\*\*

Sample Size (N)	Significance Level ( $\alpha$ )		
	10%	5%	1%
5	.510	.563	.669
10	.368	.409	.486
15	.304	.338	.404
20	.264	.294	.352
25	.240	.264	.317
30	.220	.242	.290
...	...	...	...
Approximate Formula:	$\frac{1.22}{\sqrt{N}}$	$\frac{1.36}{\sqrt{N}}$	$\frac{1.63}{\sqrt{N}}$

five second blocks of data are tested with this hypothesis test to determine if they are of the same population within a prescribed error tolerance,  $\alpha$ . The error tolerance,  $\alpha$ , is the probability that two blocks fail the test given that they are from the same statistical distribution. Groups of consecutive blocks of data which pass the Kolmogorov-Smirnov test are collected into statistically stationary periods of time.

The AGC data from nineteen SAS-1 satellite passes for Quito, Ecuador, 1971, were analyzed with the Kolmogorov-Smirnov hypothesis test to obtain the periods of statistical stationarity. The error,  $\alpha$ , was set at three values which were approximately 20, 4, and 0.01 percent. The results are represented as the probability density of the duration of statistical stationarity in Figures 2, 3, and 4, respectively. For the larger values of  $\alpha$ , the data is segmented into shorter stationary periods. Even for  $\alpha$  equal to 0.01 percent there are a large proportion of short duration periods. It is found that the statistics computed on five-second intervals change rapidly. The mean,  $\mu$ , and standard deviation,  $\sigma$ , for the periods corresponding to each  $\alpha$  are given in Table 2.

Table 2. Average Period Duration

$\alpha$ Percent	$\mu$ Seconds	$\sigma$ Seconds
20.0	6.8	7.6
4.0	11.6	13.8
0.01	32.1	40.4

\*\* Sample table values taken from "Numerical Tabulation of the Distribution of Kolmogorov's Statistics for Finite Sample Size," Z. W. Birnbaum, Journal of American Statistical Association, 47, Sept. 1952.

For the described method of determining statistically stationary periods, the statistics may change slowly through the period so that although no two consecutive blocks fail the test, two nonconsecutive blocks may fail.

A refinement of this technique would be to make comparisons of raw data over longer intervals, i.e., use larger block sizes. These techniques may lead to stationary periods somewhat longer than are reported herein. Another refinement of the method would be to compute cumulative density functions for the whole currently defined stationary period to compare with the next five-second block, rather than use only the last five-second block for the comparison. Should the new data block pass the hypothesis test, it will be appended to the old cumulative density function. Should a hypothesis test failure be ascertained, the current five-second block will form the basis for a new cumulative density function.

#### 4.3 Scintillation Stationarity

The time stationarity of the level of ionospheric activity (i.e.,  $S_4$ ), was measured for the sets of SAS-1 satellite AGC data that were used for the Kolmogorov-Smirnov statistical stationarity test. The scintillation level was estimated by calculating the  $S_4$  scintillation index for each five-second block of power samples. The time durations were measured in which  $S_4$  remained within  $\pm 0.1$  of 0.4, 0.6, and 0.8. These periods were considered stationary in  $S_4$ . The probability density function of the lengths of these periods is presented in Figure 5. Almost 90 percent of the periods lie below 25 seconds in duration which implies that the scintillation characteristics were changing rapidly. The longest periods encountered were 150 to 200 seconds in duration. The mean and standard deviation of  $S_4$  stationarity are 26.3 and 49.4 seconds, respectively.

#### 4.4 Method for Determining $S_4$ Stationary Periods

The Kolmogorov-Smirnov method can be used to divide scintillation data into periods of stationary scintillation index. By comparing the result of the scintillation stationary periods of Figure 5 with the three probability functions of the Kolmogorov-Smirnov test (Figures 2, 3, and 4), it is found that the error tolerance  $\alpha$  needed to match the Figure 5 distribution would be approximately one percent. The error tolerance,  $\alpha$ , can be chosen to provide the desired tolerance in the scintillation index,  $S_4$ . The Kolmogorov-Smirnov method provides a good method to divide the data into time stationary periods to aid in selecting data periods for analysis in fading statistics programs.

#### 4.5 Fading Depth Statistics

The depths of fades in the signal strength are directly related to the level of scintillation activity. If the distribution of the power is known, the power level below which any given percentage of the power samples fall can be related to the scintillation index of the data. Without assuming a specific distribution function but requiring that the distribution does not change significantly, the fading depth statistics were computed for the same SAS-1 satellite data used for the above analyses. The fading depth,  $f$ , was computed by normalizing the actual standard deviation of the power samples,  $\sigma$ , by the mean of the power samples,  $\mu$ . If the distribution of the power were known, the values of  $f$  could be directly related to the depths of the nulls in the signal level. As presented here, they are proportional to the real depths of fading. The probability density of the fading depth is presented in Figure 6. The data was computed for the statistically stationary periods with  $\alpha$  equal to 4 percent (Figure 3) since the stationarity period blocking had not been computed for an  $\alpha$  of one percent. Stationary periods for  $\alpha$ 's of 1 and 4 percent would be approximately the same. The most probable fading depth is approximately 3 dB. The mean and standard deviation are 2.6 and 1.2 dB, respectively. If we use the mean and standard deviation of fading power to obtain an estimate of the mean value of scintillation index,  $S_4$ , we obtain  $S_4 = .820$ .

The probability density function of the  $S_4$  values was obtained for the same stationary periods as those used to determine the  $f$  statistic distribution as shown in Figure 7. The data was computed for the statistically stationary periods with  $\alpha$  equal to 4 percent (Figure 3). The mean value of  $S_4$  is .93. Using the relationship given in Paragraph 4.5 we obtained an estimate of mean fading depth,  $f = 2.88$  dB.

#### 4.6 Comparison of Results

In Paragraph 4.2 the results of the time stationarity analysis were presented for three levels of significance. In Paragraph 4.3, stationary time periods were determined for constant levels of scintillation index,  $S_4$ . A comparison of these two sets of results leads to an indication of the approximate level of significance to use to determine the stationary time periods for the data analyzed. As shown in Paragraph 4.4, the appropriate significance level is one percent. Note that this significance level should hold true for all VHF equatorial empirical investigations conducted utilizing satellites with the SAS-1 orbital characteristics and be approximately accurate for all low orbiting satellites.

The results of Paragraph 4.5 show that the estimated value of  $S_4$  as derived from the  $f$  statistic, and the estimated value of  $f$  as derived from the  $S_4$  statistic, for  $\alpha = .04$ , are in general agreement.



The  $\alpha = .04$  value was retained, rather than  $\alpha = .01$ , since a computer analysis of the latter was not conducted. It was felt that  $\alpha = .04$  was sufficiently close to the optimum to demonstrate the point that the appropriate value of  $\alpha$  can be obtained from either of the important statistics  $S_4$  or  $f$ , and that the corresponding stationary periods can be obtained once  $\alpha$  is identified via the Kolmogorov-Smirnov method.

From Table 1 it can be seen that the stationary periods presented are extremely short compared to those time periods that normally are required to obtain statistically significant results on ionospheric fading characteristics (i.e., five to fifteen minutes). Note, however, that the purpose of this effort was

to investigate a technique to automatically determine stationary periods. As such, we have selected the very detailed stationary periods associated with individual gross irregularities (and/or small clusters of gross irregularities) as seen on the SAS-1 satellite-to-earth paths. For practical applications of the stationary method, the block size and significance level,  $\alpha$ , will be set to determine stationary periods based upon averages of multiple gross irregularities, rather than single irregularities. The results presented in this paper may be useful for determination of the size and relative velocity of the individual irregularities.

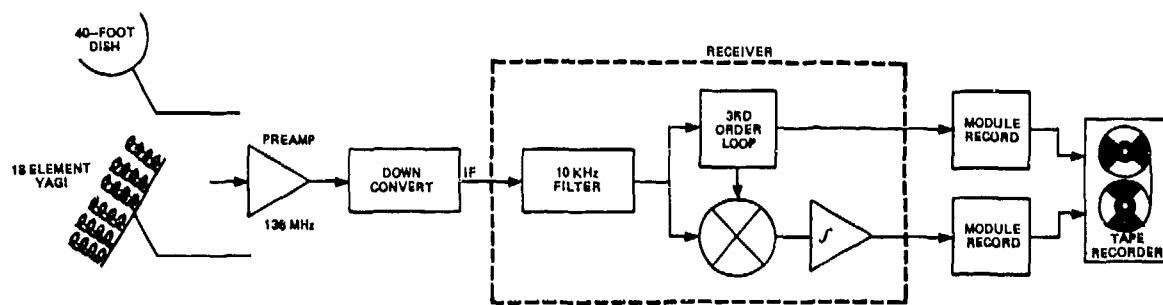


Figure 1. Receiver Configuration

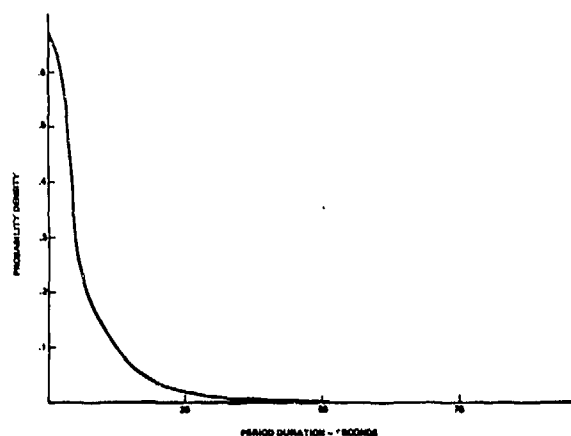


Figure 2. Kolmogorov-Smirnov Stationarity Period Density for  $\alpha = 20$  Percent

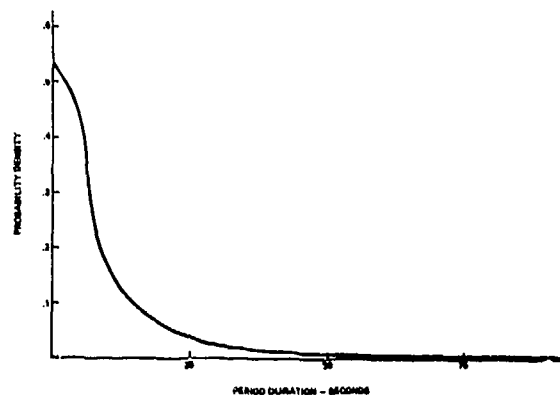


Figure 3. Kolmogorov-Smirnov Stationarity Period Density for  $\alpha = 4$  Percent

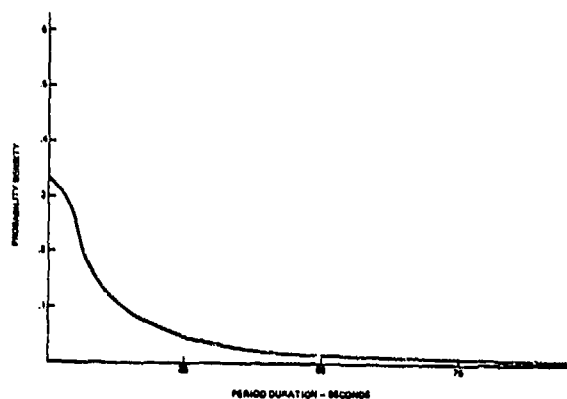


Figure 4. Kolmogorov-Smirnov Stationarity Period Density for  $\alpha = 0.01$  Percent

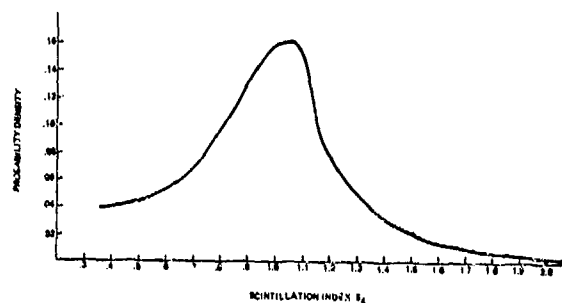


Figure 6.  $S_4$  Density for Kolmogorov-Smirnov Periods Corresponding to  $\alpha = 4$  Percent

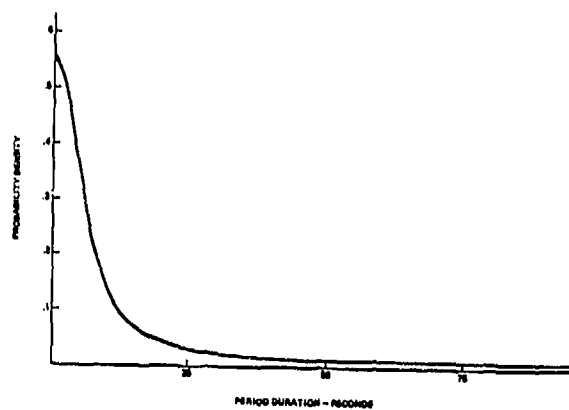


Figure 5.  $S_4$  Stationarity Period Density

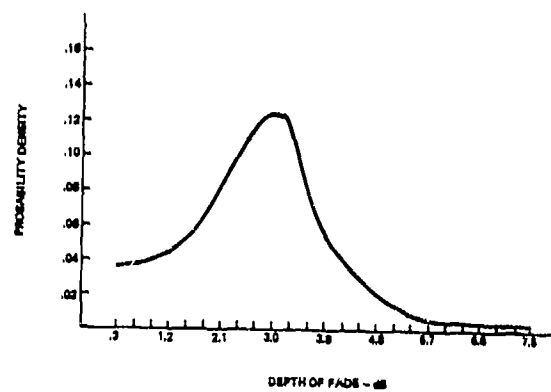


Figure 7. Fading Depth Density Function

# Frequency Correlation and Coherent Bandwidth of Transionospheric Signals

S. J. Ulaszek, C. H. Liu and K. C. Yeh  
University of Illinois at Urbana-Champaign  
Urbana, Illinois 61801

## ABSTRACT

Correlation functions for waves propagating through irregularity slabs in the ionosphere are studied using the parabolic equation method. We first define the mutual intensity functions

$$\Gamma(\vec{r}_1, \vec{r}_2, f_1, f_2) = \langle U(\vec{r}_1, f_1) U^*(\vec{r}_2, f_2) \rangle$$

$$\text{and } \bar{\Gamma}(\vec{r}_1, \vec{r}_2, f_1, f_2) = \langle U(\vec{r}_1, f_1) \bar{U}(\vec{r}_2, f_2) \rangle$$

where  $U(\vec{r}_1, f_1)$  is the complex amplitude of the wave with frequency  $f_1$  at the spatial point  $\vec{r}_1$ . These intensity functions can then be used to study the frequency and the spatial correlation of signals. Equations for  $\Gamma$  and  $\bar{\Gamma}$  are derived that include some multiple scattering effects. Solutions for the equations are obtained under various assumptions. The dependence of the solution on the different ionospheric parameters such as the power spectrum of irregularities, their size, the slab thickness, the height etc. is investigated. The coherence bandwidth is defined and computed. Results showing the frequency dependence of the coherence bandwidth will be given. Implications on the characterization of transionospheric communication channels will be discussed.

## INTRODUCTION

One of the important problems in the study of communication systems is the characterization of the communication channel in terms of the physical parameters of the transmission medium. Investigation of the statistical properties of signals can only be made in conjunction with an accurate representation of the channel. In this paper, a systematic procedure is derived to relate the parameters of the ionosphere to the characteristics of the transionospheric satellite-earth communication link.

Because of the presence of random electron density irregularities in the ionosphere, transionospheric radio waves experience the random scattering and phase mixing phenomenon known as scintillation. In addition to causing signals to fade, scintillation may also reduce the coherence bandwidth of the channel. To study the phenomenon, we shall introduce the two-frequency mutual intensity functions. These are defined as the ensemble average of the products of the complex amplitudes of the field at two frequencies,  $\langle U_1 U_2^* \rangle$  and  $\langle U_1 U_2 \rangle$ . They form the basis for the characterization of the channel.

In section 2, the geometry of the communication link is described and the scintillation problem formulated. Equations governing the mutual intensity functions are derived. Under certain simplifying assumptions, solutions are obtained in integral forms. In section 3, numerical computations of these solutions are presented and discussed. Some general conclusions are made in section 4.

## FORMULATION

Referring to Fig. 1, let us assume that a unit amplitude electromagnetic wave of the form  $\exp j(\omega t - kz)$  is incident on top of the irregularity slab at  $z=0$ , where  $k$  is the wave number. Under the usual assumptions of neglecting the depolarization effect and the temporal variation of the medium, the complex amplitude  $U(\vec{r})$  within the slab of thickness  $L$  satisfies the equation

$$-2jk \frac{\partial U}{\partial z} + \nabla^2 U + k^2 \epsilon_1(\vec{r}) U = 0 \quad (1)$$

where the dielectric permittivity of the slab is assumed to be of the form

$$\epsilon = \langle \epsilon \rangle [1 + \epsilon_1(\vec{r})] \quad (2)$$

$\epsilon_1(\vec{r})$  is a random function of position.

Under the so-called parabolic equation approximation (Tatarskii, 1971), eq. (1) can be approximated by replacing the term  $\nabla^2 U$  by the transverse Laplacian  $\nabla_T^2 U$ .

Let us now consider the fields  $U_1 = U(\vec{\rho}_1, z, k_1)$  and  $U_2 = U(\vec{\rho}_2, z, k_2)$  at frequencies  $\omega_1 = k_1 c$  and  $\omega_2 = k_2 c$  and at points  $(\vec{\rho}_1, z)$  and  $(\vec{\rho}_2, z)$  respectively. Starting from the parabolic equations for  $U_1$  and  $U_2$ , following the so-called Markov assumption (Tatarskii, 1971), we can derive the equations for the two-frequency mutual intensity functions (Liu, et al., 1974)

$$\frac{\partial \Gamma}{\partial z} + j \frac{(k_2 - k_1)}{2k_1 k_2} \nabla_T^2 \Gamma + \frac{k_1 k_2}{4} \cdot \left[ \frac{k_1^2 + k_2^2}{2k_1 k_2} A(0) - A(\rho) \right] \Gamma = 0 \quad (3)$$

$$\frac{\partial \bar{\Gamma}}{\partial z} + j \frac{(k_2 + k_1)}{2k_1 k_2} \nabla_T^2 \bar{\Gamma} + \frac{k_1 k_2}{4} \cdot \left[ \frac{k_1^2 + k_2^2}{2k_1 k_2} A(0) + A(\rho) \right] \bar{\Gamma} = 0 \quad (4)$$

where

$$\Gamma(\vec{\rho}_1, \vec{\rho}_2, z, k_1, k_2) = \langle U_1 U_2^* \rangle \quad (5)$$

is the symmetric two-frequency intensity function and

$$\bar{\Gamma}(\vec{\rho}_1, \vec{\rho}_2, z, k_1, k_2) = \langle U_1 U_2 \rangle \quad (6)$$

is the asymmetric two-frequency intensity function. They are closely related to the frequency correlation functions of the channel defined by Bello (1971). The function  $A(\rho)$  in (3) and (4) is defined by

$$A(\rho) = \int_{-\infty}^{+\infty} B_e(\rho, z) dz \quad (7)$$

$B_e(\rho, z)$  is the correlation function for the random field  $\epsilon_1(\vec{r})$  and in (7) we have assumed that it is an isotropic, homogeneous field. Eq. (7) can also be written in terms of the powerspectrum of  $\epsilon_1(\vec{r})$ ,  $\psi_e(\vec{k}_T, k_z)$ , as

$$A(\rho) = 2\pi \int_{-\infty}^{+\infty} \int_{-\infty}^{+\infty} \psi_e(\vec{k}_T, 0) \exp(-j\vec{k}_T \cdot \vec{\rho}) d\vec{k}_T \quad (8)$$

Applying certain approximate solution of (3), Liu, et al. (1974) have studied the problem of pulse trains propagating in a random medium. In this paper, higher order solutions of (3) and (4), including some effects of multiple scattering, will be given.

If we consider the frequencies of the two waves as equally spaced from some center frequency  $f$ , so that

$$k_1 = k(1-X), \quad k_2 = k(1+X) \quad (9)$$

where  $X = \Omega/2f$  and  $\Omega$  represents the total frequency separation, (3) and (4) can be written in terms of some normalized coordinates

$$\frac{\partial \Gamma_1}{\partial \zeta} + j \frac{X}{1-X^2} \left( \frac{\partial^2}{\partial \xi^2} + \frac{\partial^2}{\partial \eta^2} \right) \Gamma_1 - CG(\xi, \eta) \Gamma_1 = 0 \quad (10)$$

$$\frac{\partial \bar{\Gamma}_1}{\partial \zeta} + j \frac{X}{1-X^2} \left( \frac{\partial^2}{\partial \xi^2} + \frac{\partial^2}{\partial \eta^2} \right) \bar{\Gamma}_1 + CG(\xi, \eta) \bar{\Gamma}_1 = 0 \quad (11)$$

where the normalized coordinates are defined as

$$\xi = x/\ell_0, \quad \eta = y/\ell_0, \quad \zeta = z/k\ell_0^2 \quad (12)$$

$\ell_0$  is some characteristic length relating to the size of the irregularities.  $\Gamma_1$  and  $\bar{\Gamma}_1$  are related to the original mutual intensity function by  $\Gamma = \Gamma_1 F$ ,  $\bar{\Gamma} = \bar{\Gamma}_1 F$  respectively where the factor  $F$  is given by

$$F = \exp \left[ -k^2 (1+X^2) A(0) z/4 \right] \quad (13)$$

The function  $G(\xi, \eta)$  is defined as

$$G(\xi, \eta) = \frac{1}{\ell_0 \langle \epsilon_1^2 \rangle} \int_{-\infty}^{+\infty} B_e(r) dz \quad (14)$$

where

$$\langle \epsilon_1^2 \rangle = \frac{(f_p/f)^4}{[1 - (f_p/f)^2]^2} \left\langle \left( \frac{\Delta N}{N} \right)^2 \right\rangle \quad (15)$$

$f_p$  is the plasma frequency of the ionosphere,  $\langle (\Delta N/N)^2 \rangle$  is the mean square percentage electron density fluctuation caused by the irregularities.

The parameter C in (10) and (11) is given by

$$C = k^3 \ell_0^3 \langle \epsilon_1^2 \rangle / 4 \quad (16)$$

We note that C depends on the ratio of scale size to wavelength and the strength of density fluctuations.

Approximate solutions of (10) and (11) including some multiple scattering effects can be obtained after some manipulations (details are given in Ulaszek, 1974). Combining these solutions with (13), we have finally the expressions for the mutual intensity functions in terms of the normalized coordinates

$$\Gamma(\rho', \zeta, k_1, k_2) = \exp[-(1+X^2)CG(0)\zeta] \quad (17)$$

$$\cdot \exp[j2\pi C(1-X^2)^2(I_1+I_2)]$$

$$\bar{\Gamma}(\rho', \zeta, k_1, k_2) = \exp[-(1+X^2)CG(0)\zeta] \quad (18)$$

$$\cdot \exp[-j2\pi C(1-X^2)^2(I_3+I_4)]$$

where  $\rho' = (\xi^2 + \eta^2)^{1/2}$  and

$$I_1 = \int_0^\infty \left[ e^{j\beta X(\zeta - \zeta_0)} - e^{j\beta X\zeta} \right] \left[ \phi_1(K_T) / XK_T \right] \cdot J_0(K_T \rho') dK_T \quad (19)$$

$$I_2 = j2C(1-X^2)^2 \int_0^\infty \left[ e^{j\beta X\zeta} - (1+j\beta X\zeta_0 - \beta^2 X^2 \zeta_0^2 / 2) e^{j\beta X(\zeta - \zeta_0)} \right] \cdot \left[ \phi_2(K_T) / XK_T^3 \right] J_0(K_T \rho') dK_T \quad (20)$$

$$I_3 = \int_0^\infty \left[ e^{j\beta(\zeta - \zeta_0)} - e^{j\beta\zeta} \right] \left[ \phi_1(K_T) / K_T \right] \cdot J_0(K_T \rho') dK_T \quad (21)$$

$$I_4 = j2C(1-X^2)^2 \int_0^\infty \left[ e^{j\beta\zeta} - (1+j\beta\zeta_0 - \beta^2 \zeta_0^2 / 2) e^{j\beta(\zeta - \zeta_0)} \right] \cdot \left[ \phi_2(K_T) / K_T^3 \right] J_0(K_T \rho') dK_T \quad (22)$$

$J_0(x)$  is the Bessel function of zeroth order,  $\beta$  is defined as  $\beta = K_T^2 / (1-X^2)$ ,  $\zeta_0 = L/k\ell_0^2$  is the normalized slab thickness. The normalized spectrum functions  $\phi_1$  and  $\phi_2$  appeared in the integrals are given by

$$\phi_1(K_T) = \frac{1}{2\pi} \int_0^\infty G(\rho') J_0(K_T \rho') d\rho' \quad (23)$$

$$\phi_2(K_T) = \frac{1}{2\pi} \int_0^\infty \left[ \frac{dG(\rho')}{d\rho'} \right]^2 J_0(K_T \rho') d\rho' \quad (24)$$

Solutions (17) and (18) can be used to study the frequency and spatial correlations of the signal.

#### NUMERICAL RESULTS

In this section, we shall present some numerical results computed from (17) and (18). The computations are made for two different spectra for the electron density irregularities. One is a Gaussian spectrum for which

$$\phi_1(K_T) = \frac{1}{\sqrt{2\pi}} \exp(-K_T^2/4) \quad (25)$$

$$\phi_2(K_T) = \frac{1}{2} (1-K_T^2/4) \exp(-K_T^2/4) \quad (26)$$

The second is a power law spectrum for which

$$\phi_1(K_T) = \frac{2}{\pi(1+K_T^2)^2} \quad (27)$$

and

$$\phi_2(K_T) = \frac{2}{\pi} \int_0^\infty [K_1(\rho') + \rho' K_1'(\rho')]^2 \cdot J_0(K_T \rho') \rho'^3 d\rho' \quad (28)$$

where  $K_1(\rho')$  is the modified Bessel function of the third kind of order one.

The computations are made for different normalized parameters. To interpret the results, it is convenient to introduce the "phase screen" parameter  $\phi_0^2$  defined as the phase variance due to irregularities along the signal path (Wernik, et al., 1973).

$$\phi_0^2 = k^2 A(0)L/4 \quad (29)$$

It is an indication of the strength of the scattering inside the irregularity slab. Expressed in terms of our

parameters

$$\phi_0^2 = C \zeta_0 G(0) \quad (30)$$

It is also convenient to normalize the distance from the top of the slab in units of slab thickness,  $\zeta_N = \zeta/\zeta_0 = z/L$ . In this paper, we shall be mainly interested in the frequency correlation of the signal. Therefore, our computations are made for  $\Gamma(0, z, k_1, k_2)$  and  $\bar{\Gamma}(0, z, k_1, k_2)$ , the two frequency mutual intensity functions for the signal received at a point receiver.

Fig. 2 shows the amplitude and phase of  $\Gamma$  as functions of  $X$  for fixed values of  $\zeta_0$  and  $\zeta_N$  with  $C$  as a varying parameter. As expected, the correlation decreases with increasing  $C$ , indicating the increasing strength of scattering. Fig. 3 shows  $\Gamma$  as a function of  $X$  for a fixed  $C$  and  $\zeta_0$  with  $\zeta_N$  as a varying parameter. The correlation decreases as  $\zeta_N$  increases. This is due to the fact that as the distance from the slab increases, the signal suffers more phase mixing effects, resulting in the further decorrelation of the signal, although the thickness of the scattering slab is fixed. Similar results show a decrease of correlation for increasing  $\zeta_0$ , as expected (graph not shown).

In communication channel study, almost always the signal is assumed to be a narrow-band symmetric Gaussian process (Bello, 1971). This implies that the antisymmetric mutual intensity function  $\bar{\Gamma}$  should be zero, or, more realistically, much smaller than  $\Gamma$ . Fig. 4 shows the computed results for  $\bar{\Gamma}$  as a function of  $\zeta_0$  for different values of  $C$ . Except for the large values of  $C$  and  $\zeta_0$ , which would correspond to multiple-scattering conditions, the amplitude of  $\bar{\Gamma}$  is comparable to that of  $\Gamma$ . Therefore, in ionospheric applications, the random signal cannot be assumed to be symmetric. For  $C\zeta_0 > 1.6$ , amplitude of  $\bar{\Gamma}$  becomes negligible compared to that of the symmetric function. This result compares with that given by Bello (1971). Although computations for the bandwidth dependence were made for  $\bar{\Gamma}$ , the change with  $X$  was small for the narrowband cases computed and the results are not included.

Another quantity of interest is the correlation coefficient of the complex amplitude at two frequencies defined by

$$C_U = \frac{K(U_1 - \langle U_1 \rangle)(U_2^* - \langle U_2^* \rangle)}{[\langle |U_1 - \langle U_1 \rangle|^2 \rangle \langle |U_2 - \langle U_2 \rangle|^2 \rangle]^{1/2}} \quad (31)$$

In terms of the mutual intensity function, (31) can be written as (Ulaszek, 1974)

$$C_U = \frac{\text{NUM}}{\text{DEN}} \quad (32)$$

where

$$\begin{aligned} \text{NUM} &= |\Gamma_2(0, \zeta, k_1, k_2) \\ &\quad - \exp[-CG(0)\zeta_0(1+X^2)]| \\ \text{DEN} &= \{1 - \exp[-CG(0)\zeta_0(1-X)^2]\}^{1/2} \\ &\quad \{1 - \exp[-CG(0)\zeta_0(1+X)^2]\}^{1/2} \end{aligned} \quad (33)$$

Figures 5 through 8 illustrate the frequency dependence of  $\Gamma$  and the correlation coefficient  $C_U$ . A typical set of ionospheric parameters is selected and the corresponding values of the scatter parameters  $C$ ,  $\zeta_0$ ,  $\phi_0^2$  etc. are found at a given frequency. Figs. 5 and 6 show the results for a Gaussian and a power law spectra respectively. For small values of  $X$ , the correlation for the power law spectrum first decreases faster, then, as  $X$  increases, the correlation for the power law case becomes greater than that for the Gaussian case. This essentially is the reflection of the behavior of the spectra (Wernik, et al., 1973). Also apparent in the figures is the fact that as the carrier frequency decreases the signal becomes less correlated. This, of course, is due to the  $f^{-4}$  dependence of  $\langle \epsilon^2 \rangle$ . Figs. 7 and 8 show the similar computations as in Figs. 5 and 6 but for a greater scale size. The general behavior is the same as shown in Figs. 5 and 6. The correlation, however, is increased. The dependence of the correlation on the scale size can be explained by the scattering phenomenon. As is well known, the most effective scattering takes place for irregularities of the size of the Fresnel zone. The normalized Fresnel wave number is given by  $K_F = \lambda_0 \sqrt{2\pi k_z (2z+L)}$ . For a given set of ionospheric parameters and signal frequency, larger scale sizes shift the normalized Fresnel wavenumber to a portion of the spectrum which has further decayed (see eqs. (25) and (27)). The contributions from these

most effective scatters are thus weighted less and the net result is a reduction in the scattering effect, resulting in higher correlation. Increase in the mean electron density or rms density fluctuations also yields more scattering effect as predicted. Computations also indicate increased decorrelation effects for greater slab thickness as shown in Figs. 9 and 10.

From the above set of curves, we can obtain the frequency dependence of the coherence bandwidth. The "half-power" point is selected as our definition of the coherence bandwidth. Fig. 11 shows the coherence bandwidth as a function of frequency for different ionospheric conditions. These curves provide a rather clear picture of the effects of the irregularity spectrum on the coherence bandwidth of the channel. While having the same general characteristics, they show that the power law spectrum results in 20% to 50% less coherence bandwidth throughout the frequency band investigated. As mentioned earlier, the irregularities most responsible for producing scintillation are those with sizes of the order of the Fresnel zone. Since the Fresnel zone decreases with increasing frequency, smaller irregularities become more effective scatterers at higher frequencies. The decay of the Gaussian spectrum for large wavenumbers (corresponding to small irregularities) is much more rapid than that of the power law spectrum. Thus, the scintillation effects at the higher frequency would also be expected to fall off more rapidly in the Gaussian case, resulting in the computed larger coherence bandwidth.

#### CONCLUSIONS

Two frequency mutual intensity functions for the transionospheric fading communication channel are studied. Gaussian and power law spectra for the electron density irregularities are introduced in the investigation. Numerical computations are performed over a range of the ionospheric parameters. Performance of the channel is studied as those parameters are varied corresponding to different geophysical conditions. Except for strong scattering cases, the magnitude of the asymmetric intensity function  $\bar{I}$  is found to be comparable to that of its symmetric counterpart,  $\Gamma$ , indicating that the random signal cannot be considered to be a symmetric process. The coherence bandwidth for the power law irregularity spectrum is less than that for the Gaussian spectrum. In

view of the recent experimental evidence that the ionospheric irregularities have power law spectrum rather than Gaussian (McClure and Hanson, 1973; Rufenach, 1972), this result may have implications in the studies of satellite communication systems.

Predictive scintillation models which include all the ionospheric effects are essential to the optimization of communication systems using the ionosphere as a transmission channel. The relative mathematical simplicity of the models discussed on this paper permits us to observe some of these effects under a variety of ionospheric conditions. However, since the models presented here are derived from perturbation techniques, their validity becomes doubtful under intensive fading conditions. More exact solutions of the mutual intensity equations, most likely numerical, are essential to further our channel modeling efforts.

#### ACKNOWLEDGEMENT

This work was partially supported by the Atmospheric Sciences Section, National Science Foundation under Grant GA-42857.

#### REFERENCES

- Bello, P. A., A study of the relationship between multipath distortion and wavenumber spectrum of the refractive index in radio links, *Proc. IEEE*, 59, U.S.A., 1971, 47-75.
- Liu, C. H., A. W. Wernik, and K. C. Yeh, Propagation of pulse trains through a random medium, *IEEE Trans. on Antenna and Propagation*, AP-22, U.S.A., 1974, 624-627.
- McClure, J. P. and W. B. Hanson, A catalog of ionospheric F region irregularity behavior based on Ogo 6 retarding potential analyzer data, *J. Geophys. Res.*, 78, U.S.A., 1973, 7431-7440.
- Rufenach, C. L., Power-law wavenumber spectrum deduced from ionospheric scintillation observations, *J. Geophys. Res.*, 77, U.S.A., 1972, 4761-4772.
- Tatarskii, V. I., The effects of the turbulent atmosphere on wave propagation, U.S. Department of Commerce, National Technical Information Service, Springfield, VA, U.S.A., 1971.

Ulaszek, S. J. Jr., A theoretical study of the transionospheric fading communication channel, Tech. Report No. 54, Ionosphere Radio Laboratory, Univ. of Illinois at Urbana-Champaign, IL, U.S.A., 1974.

Wernik, A. W., C. H. Liu, M. Y. Youakin, and K. C. Yeh, A theoretical study of scintillation of transionospheric radio signals, Tech. Report No. 50, Ionosphere Radio Laboratory, Univ. of Illinois at Urbana-Champaign, IL, U.S.A., 1973.

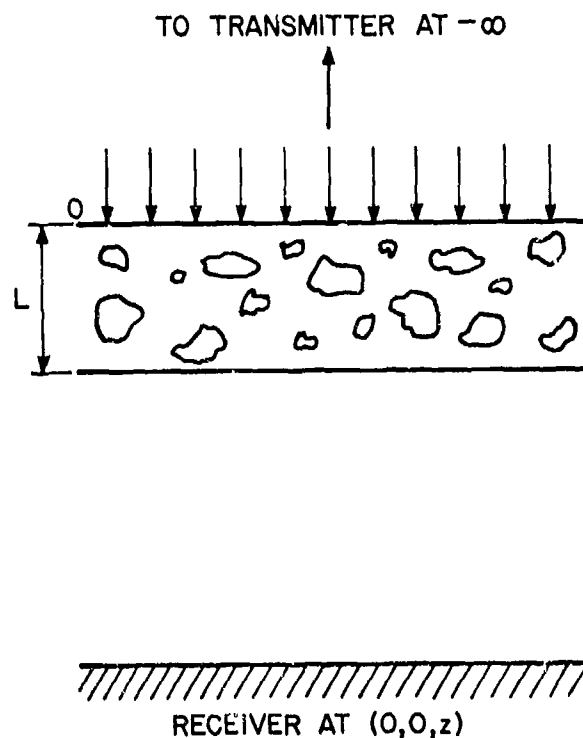


Fig. 1 The geometry of the problem.



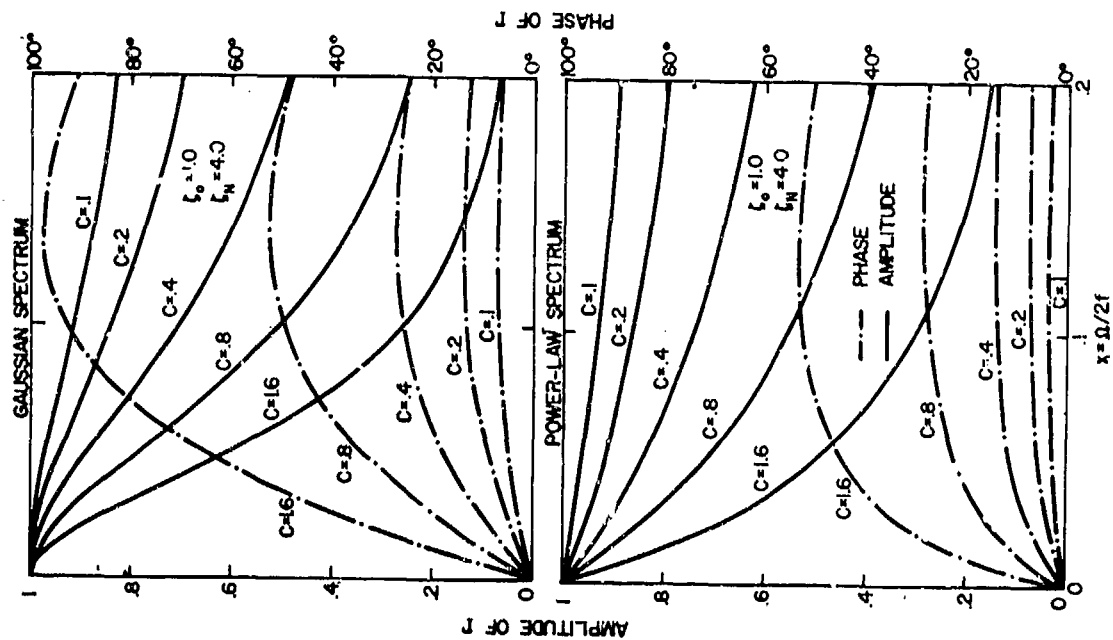


Fig. 2 Amplitude and phase of  $\Gamma$  as functions of  $x$ , for different values of  $C$ .

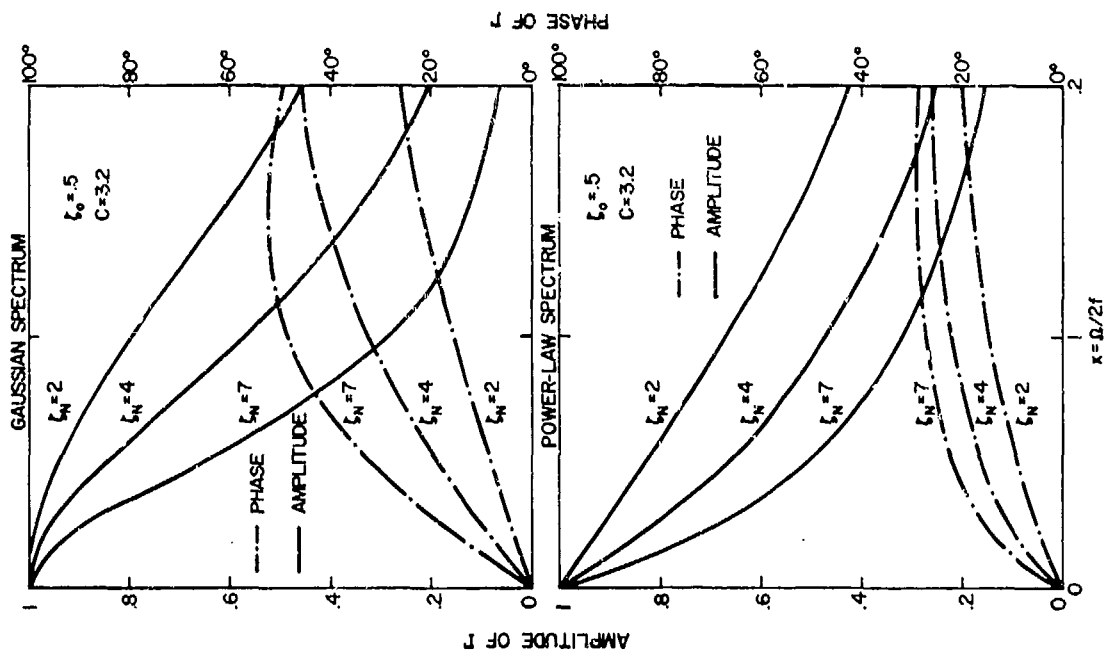


Fig. 3 Amplitude and phase of  $\Gamma$  as functions of  $x$ , for different values of  $\zeta_N$ .

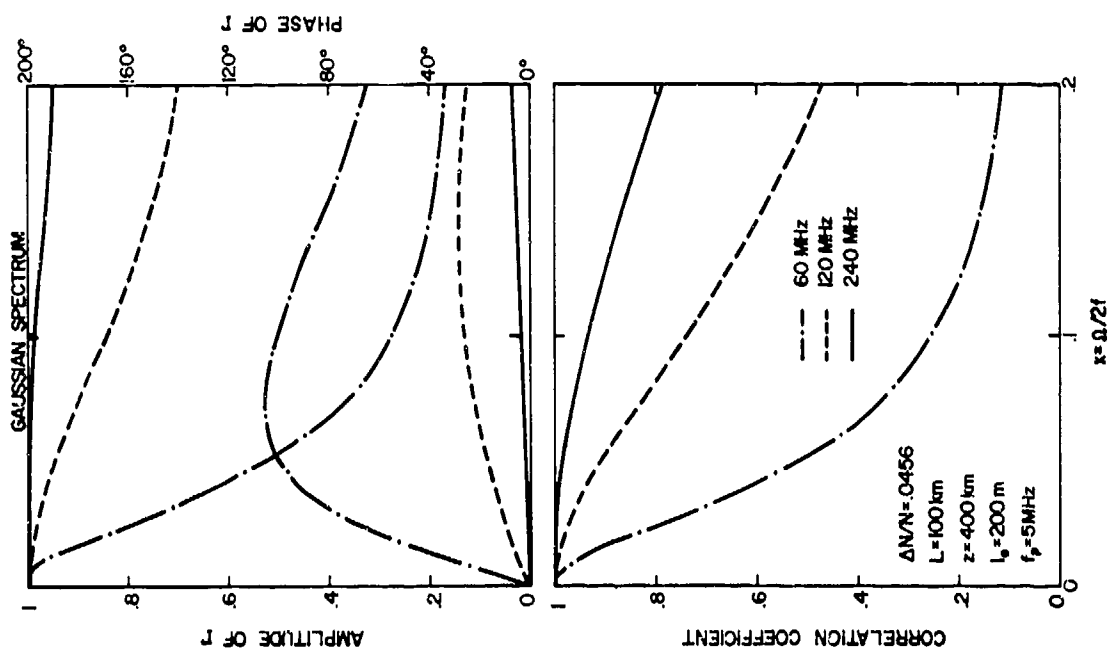


Fig. 5 Frequency dependence of  $\Gamma$  and  $C_\gamma$  for typical ionospheric conditions, assuming a Gaussian irregularity spectrum.

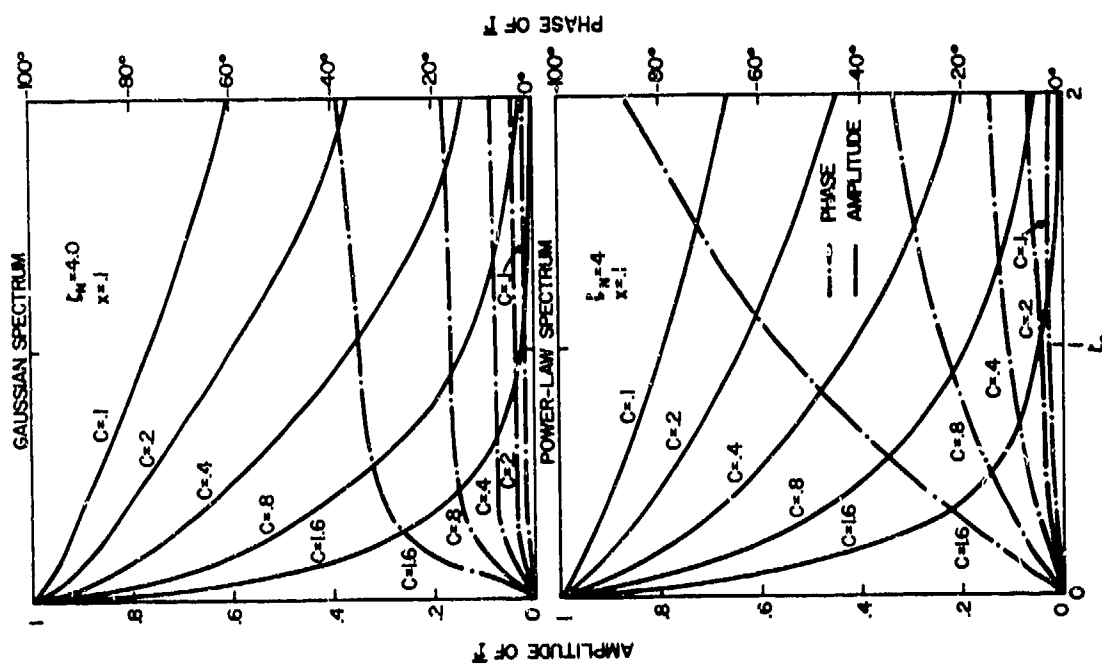


Fig. 4 Amplitude and phase of  $\Gamma$  as functions of  $\zeta_0$ , for different values of  $C$ .

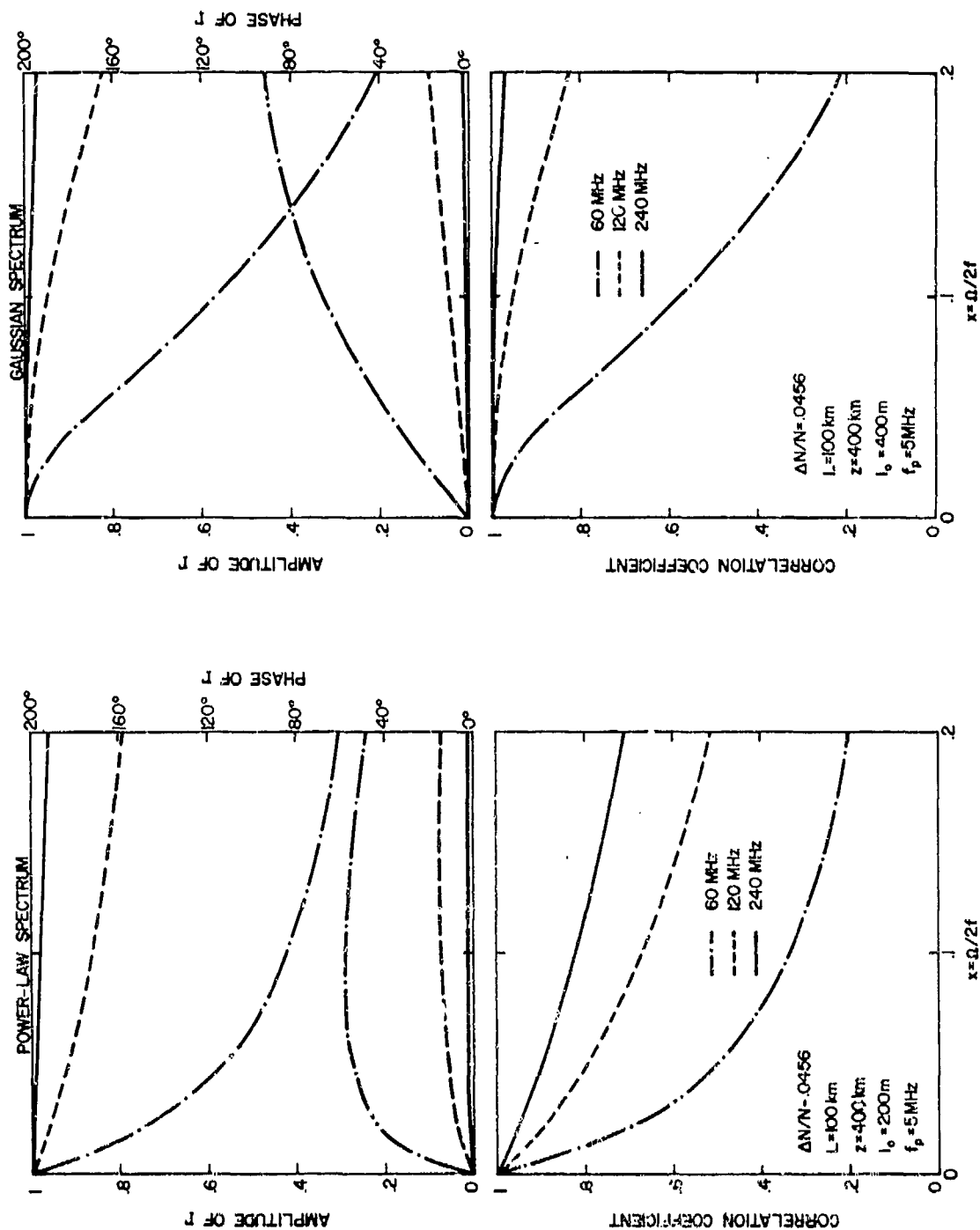


Fig. 6 Same as Fig. 5, for power-law irregularity spectrum.

Fig. 7 Frequency dependence of  $\Gamma$  and  $C_\gamma$  for a larger scale size, Gaussian irregularity spectrum.

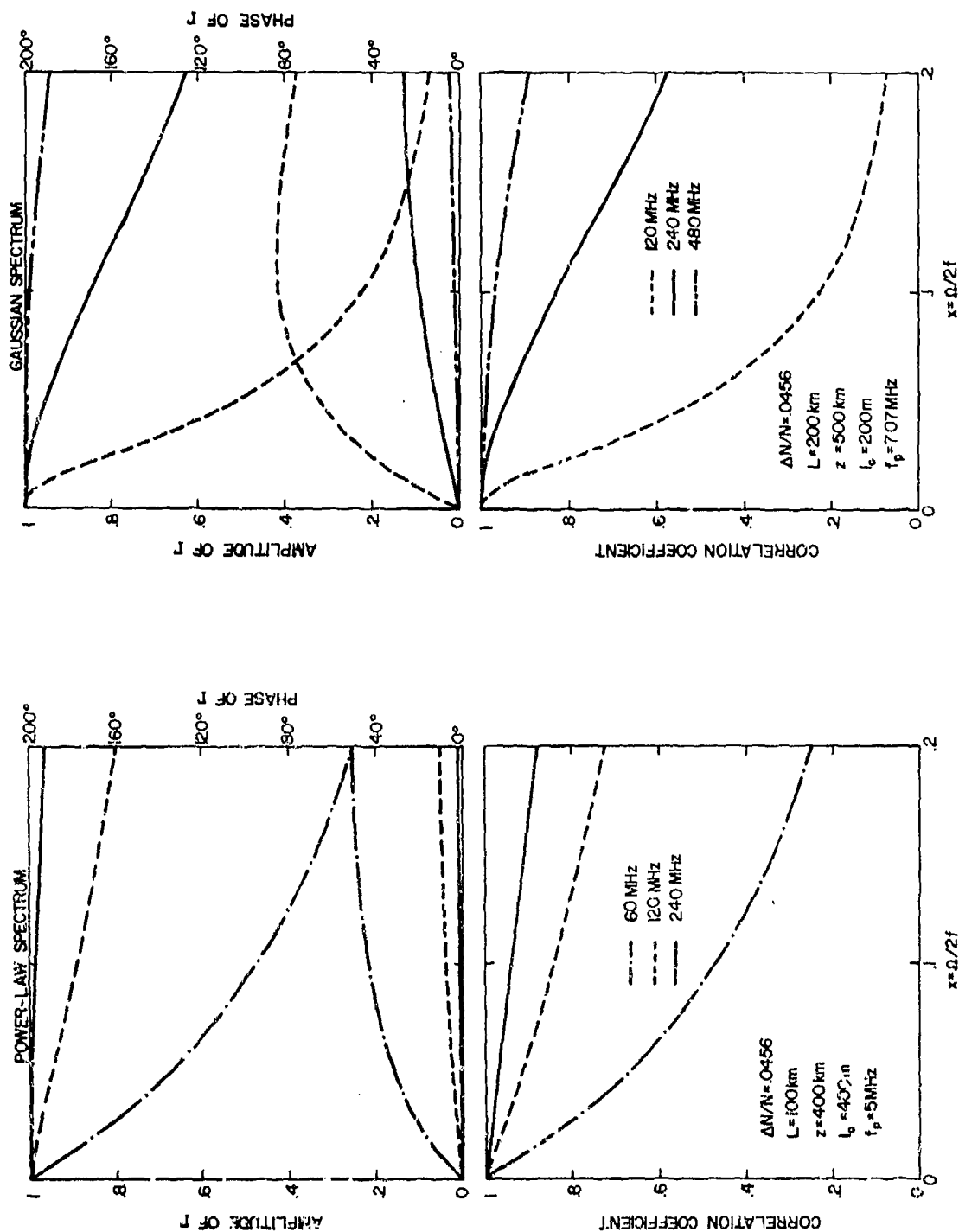


Fig. 8 Same as Fig. 7, for power-law irregularity spectrum.

Fig. 9 Frequency dependence of  $\Gamma$  and  $C_\Gamma$  for a thick irregularity slab, Gaussian irregularity spectrum.

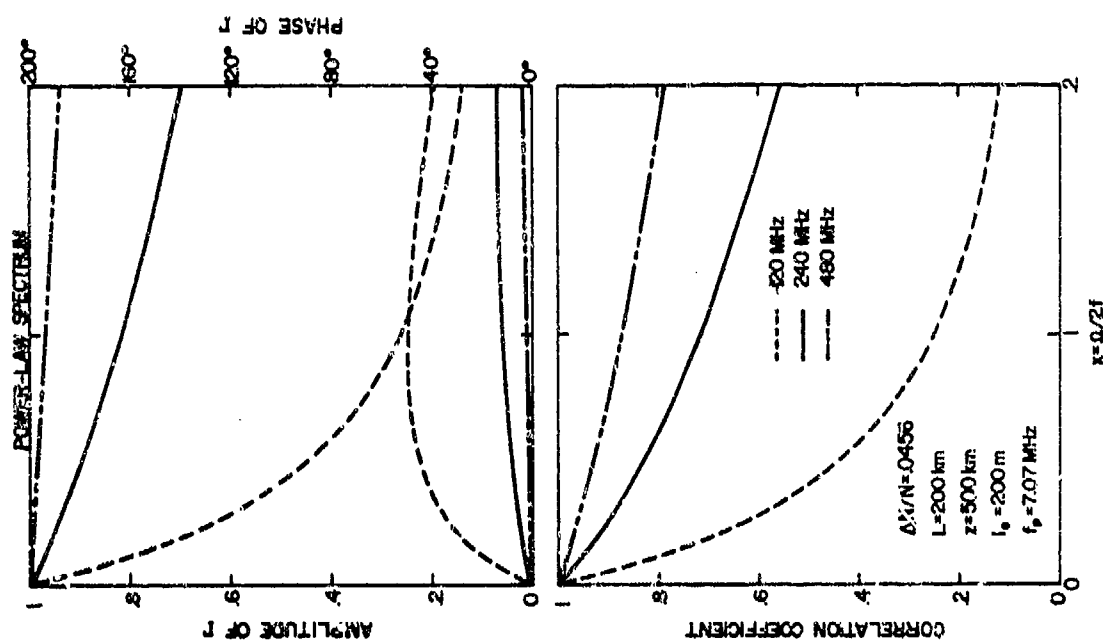


Fig. 10 Same as Fig. 9, for power-law irregularity spectrum.

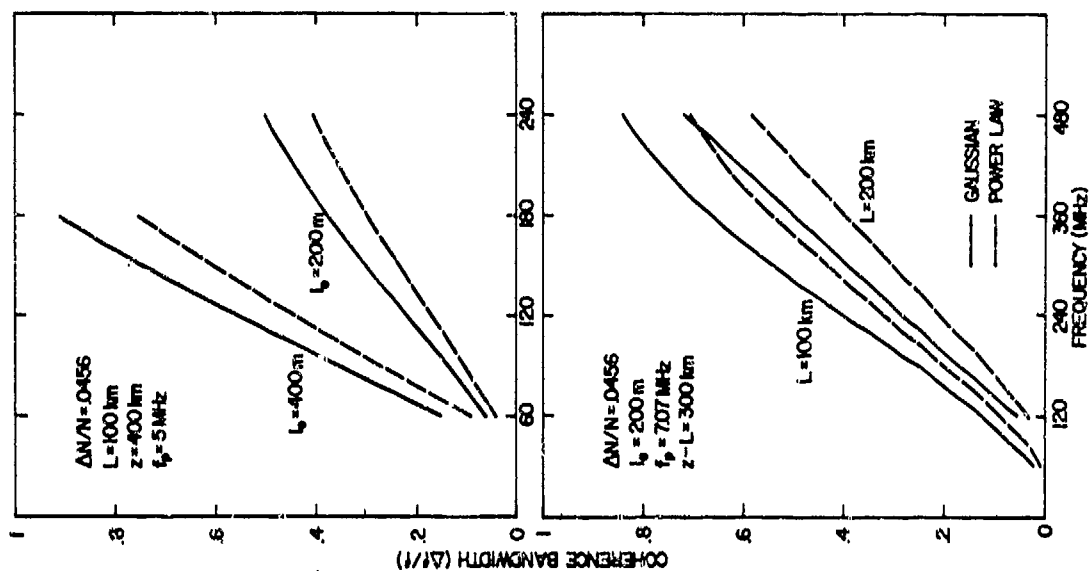


Fig. 11 Coherence bandwidth as a function of frequency for different ionospheric conditions.

COMPUTER SIMULATION OF TRANSIONOSPHERIC SCINTILLATION  
COMMUNICATION CHANNELS BASED ON FADE-DURATION STATISTICS

R. E. Ziemer  
Electrical Engineering Department  
University of Missouri-Rolla  
Rolla, Missouri

W. F. Deckelman  
McDonnell Douglas Corporation  
Brown Road  
St. Louis, Missouri

ABSTRACT

This paper considers the characterization and modeling of transionospheric communication channels undergoing severe fading. A typical time segment of the received beacon signal from the TACSAT I satellite (250 MHz), recorded on Guam in 1972, is analyzed on a digital computer to obtain fade duration statistics of the scintillating beacon signal. Following the hypothesis and analyses of Rino, Livingston, and Whitney [1], a software computer model of a scintillating signal, consisting of Gaussian phase-quadrature components, is derived. Actual data, when compared with model-generated data, show that the Gaussian quadrature-component model with proper choice of model parameters provides a satisfactory fit on the basis of fade-duration statistics. Thus, the Gaussian phase-quadrature hypothesis for ionospheric scintillation signals is justified on the basis of the second-order fade-duration statistics in addition to the verification by the first-order intensity histograms employed by Rino, et al [1].

With justification for the Gaussian phase-quadrature component model obtained on the basis of fade-duration statistics, it is then possible to evaluate the effectiveness of various communication schemes for combating the degradation imposed by scintillation. Two techniques for system evaluation through simulation are discussed. The first, based on the one-tap Kailath delay line channel model, makes use of the frequency-flat-fading character of the scintillation channel for narrowband transmissions to model the time-variant transfer function of the channel as a complex-valued narrowband Gaussian process. This type of channel simulation is useful for evaluating various types of diversity schemes for combating scintillation fading.

The second type of channel simulation utilizes a partitioned Markov chain approximation for the bit error patterns of the fading channel when employed for digital data transmission. While applicable only to digital data systems, this type of channel simulation is simpler than simulations based on phase-quadrature time series and therefore requires considerably less in the way of simulation time.

INTRODUCTION

Various characteristics of transionospheric scintillating signals have been measured including scintillation indices, amplitude probability distributions, spatial and time correlations, power spectra, and polarization statistics. From a communications system design viewpoint, these statistics are useful mostly for fade margin specification and for space, frequency, or polarization diversity design.

Analytical analysis and evaluation of a fading channel requires that a realistic, and hopefully simple, channel model be known. To be useful, this model should be obtainable from simple channel measurements.

In this paper, a selected portion of the TACSAT I UHF (250 MHz) beacon signal, recorded on Guam in the fall of 1972 by Paulson and Hopkins [2], is used to obtain fade-duration and exceedance-duration statistics. Two computer modeling techniques for the channel are then investigated. The first generates a random time series whose fade-duration distribution approximates that of a sample of ionospheric scintillation data. The actual data were selected from a quasi-stationary portion of the received beacon signal. The second employs a partitioned Markov chain to approximate the burst error statistics of the channel.

## DATA ACQUISITION AND ANALYSIS

The scintillation data for this study were provided by the Naval Electronics Laboratory Center (NELC) in San Diego, California. The original data consisted of an FM magnetic tape recording of the continuous beacon signal. This signal was then digitized and stored on magnetic digital tape. Prior analysis by NEL indicated that all significant frequency content of the scintillating signals was limited to frequencies below 1 Hz. Thus, a ten Hertz sampling rate was employed after pre-filtering to three Hertz. The digitized data encompassed a time span of 136 minutes of moderate to severe scintillation. An indication of the severity of the scintillation is illustrated in Figs. 1a and b, which show the sample standard deviation and sample mean, calculated from blocks of data 6.8 minutes long, respectively. It is noted that the standard deviation can be a significant fraction of the sample mean, thus indicating the occurrence of severe fades. However, these statistics say nothing about the average fade durations.

## FADE-DURATION AND EXCEEDANCE-DURATION STATISTICS

An indication of the time scale of the signal fluctuations is provided by two families of curves which are defined as follows:

$g(L,T)$  = fraction of time that the received signal power remains below  $L$  dBm, compared to the mean received power, throughout intervals of at least  $T$  seconds;

$f(L,T)$  = fraction of time that the received signal power remains above  $L$  dBm, compared to the mean received power, throughout intervals of at least  $T$  seconds.

These functions are referred to as the normalized fade-duration probability distribution function (FDPDF) and exceedance-duration probability distribution function (EDPDF), respectively. Typical results are shown in Figs. 2a and b for the 20.5 minutes of data with sample mean and standard deviation given in Figs. 1a and b, respectively, between the vertical lines. From Fig. 1b, it is apparent that this segment of data was during a severe fading condition. For example, Fig. 2a illustrates that with probability  $\approx 0.5$ , the signal fades below its sample mean for intervals of two seconds or more. The probability of fading below a level 3 dB

less than the sample mean for intervals of one second or greater is approximately 0.25.

These results are presented in a slightly different form in Fig. 3. A stationary region of 4096 data points was selected using the run and trend tests at the ten percent level of significance. These data were analyzed and normalized such that the total signal power would be unity. Thus, the undisturbed, non-scintillating signal should have a mean RMS magnitude of unity. The fade duration distribution is redefined as the number of fades below a given level for a given length of time or longer. The fade levels chosen were 100, 80, 60, 40, and 20 percent of the undisturbed mean signal level. Figure 3 shows the fade duration distribution for this sample of scintillation data. The leftmost tip of each curve indicates the total number of fades below that level. The normalized mean and variance are 0.9352 and 0.1254, respectively. No fades were observed below the 20 percent level.

## GAUSS-QUADRATURE COMPONENT MODEL FOR CHANNEL GAIN

Based on the work of Rino, et al., a computer model employing bandlimited, bivariate normal time series was examined as providing a potential fit to the actual fade duration statistics.

A functional block diagram of the proposed model is shown in Fig. 4. The variables FC, HR, IX, NP, RHO, T, UNDXMU, XK1, and XK2 are the external variables that control the model. SCINXY and E1 are the output variables. These variables are defined in Table I.

The model begins with a Gaussian random number generator, subroutine GAUSS. Each call to GAUSS yields two uncorrelated random numbers,  $X_1$  and  $Y_1$ . For this model, the time series of  $X_1$  and  $Y_1$  each has a mean of zero and a variance of unity. Random numbers  $X$  and  $Y$  are obtained by a linear transformation of  $X_1$  and  $Y_1$  that yields the specified variance and correlation corrected for the attenuation of FILTER 1 and FILTER 2. FILTER 1 and FILTER 2 are Butterworth filters obtained by the bilinear Z-transform. Their order and cutoff frequency are specified by NP and FC, respectively. Random numbers  $X_2$  and  $Y_2$ , the outputs of these filters, are the in-phase and phase-quadrature components of the received signal. Choosing the sample time, HR, to be small compared to  $1/FC$  will cause  $X$  and  $Y$  to be essentially white noise sources in the passband of the filters. Thus,  $X_2$

TABLE I

DEFINITIONS OF SUBROUTINE  
SCINT VARIABLES

## Model Input Variables

FC	FC is the cutoff frequency of FILTER 1 and FILTER 2 in hertz.
HR	HR is the desired time interval between data points in seconds.
IX	IX is the seed value used in the random number generator, GAUSS. The value for IX is chosen to give GAUSS a nearly normal distribution and to produce a long string of random numbers without repetition.
NP	NP is the number of poles of FILTER 1 and FILTER 2. NP can specify a 1, 2, 3, or 4 pole Butterworth filter.
RHO	RHO is the correlation coefficient between the in-phase and phase quadrature components, X1 and Y1, respectively.
T	T is the time corresponding to each data point. At T=0 the model initializes itself and generates one data point. At T>0, the model generates data points.
UNDXMU	UNDXMU is the undisturbed mean magnitude (RMS voltage level) of the signal before scintillation starts.
KK1	KK1 is the ratio of phase quadrature noise power to total noise power.
KK2	KK2 is the ratio of noise power to total signal plus noise power.
E1	E1 is an error parameter that tells the calling program that NP(E1=1), FC(E1=2), or HR(E1=3) has been changed without re-setting T to zero.
SCINXY	SCINXY is the magnitude of the signal level as it scintillates.

$$SCINXY = \sqrt{(XMU + X2)^2 + Y2^2}$$

and Y2 then have the power spectral density provided by FILTER 1 and FILTER 2. XMU is the steady-state component of the received signal. The instantaneous received signal level, SCINXY, is calculated according to

$$SCINXY = ((XMU + X2)^2 + (Y2)^2)^{1/2} \quad (1)$$

where

$$XMU^2 = UNDXMU^2 (1 - KK2), \quad (2)$$

$$\sigma_{X2}^2 = (1 - KK1) * KK2 * UNDXMU^2, \quad (2)$$

and

$$\sigma_{Y2}^2 = KK1 * KK2 * UNDXMU^2. \quad (4)$$

Since UNDXMU is the mean RMS signal level, UNDXMU<sup>2</sup> is the mean RMS power level. KK2 is the fraction of the total signal power that is diverted into the scintillating portion of the signal. Therefore, (1-KK2) x UNDXMU<sup>2</sup> is the power in the nonscintillating portion of the signal as stated in equation (2). KK1 is the fraction of the noise power that resides in the out-of-phase scintillating component so that (1-KK1) is the fraction of the noise power that resides in the in-phase scintillating component. Since the total noise power is KK2 x UNDXMU<sup>2</sup> and the signal variance is the signal power, equations (3) and (4) are written directly as above.

The first model parameters determined were the filter order, NP, and the cutoff frequency, FC. Rough information in the literature on the spectral distribution of the envelope of ionospheric scintillation served as a guide to the choice of FC. Figures 5 and 6 show the fade duration distribution below 100 percent of the undisturbed signal level for a second order and a first order Butterworth filter, respectively, at selected frequencies along with the actual data. The fade duration distribution for fades below 100 percent of the undisturbed signal level is a measure of spectral distribution. That is, no matter how strong the fades, their mean level crossing depends on the spectral distribution of the random process. In each of these cases, care was taken to match the data at long fade durations, where communications systems are very likely to be susceptible. Figure 5 shows that the second order filter has far too few short fades due to the lack of high frequency content in its output. Alternatively, as shown on Fig. 6, the first order filter has too many short fades. The control parameters KK1, KK2, and RHO, were varied to compensate for the imperfect spectral distribution and to achieve the best possible fit to the relative curve spacing.

The model using the second order



filter did not yield good results for short fades. The best results for this model are shown in Fig. 7. However, the first order filter yielded a fairly good fit without varying  $\rho$  as shown in Fig. 8 ( $\rho=0$ ). The data for  $\rho=0.6$ , shown in Fig. 9, was a further refinement based on the least squared error between actual and model-generated fade duration distributions. The fade duration distribution for  $\rho=0.9$  is also included in Fig. 9 at the 100% and 20% levels for comparison.

A decrease in the number of fades below the 20% level is shown for  $\rho=0.9$  over that for  $\rho=0.6$ , but a worse overall fit to the actual data results, especially for fade durations between 0.8 and 3.2 seconds at the 100% level. Figure 10 shows the variation of fade duration distribution as the parameter  $\rho$  is varied from 0.2 to 0.7. In general, the fit is very close for the longer fade durations, but departs markedly from the measured curves at the short fade durations, thus indicating that an increase in  $\rho$  or filter order is necessary to decrease the number of short fades.

To summarize, the simulation results shown in Figs. 7-10 indicate that a good fit to the measured data is fairly easy to achieve for the longer fade durations, which are a more important consideration in communications system design than short fades. To obtain a good overall fit, however, requires more complete measured data than employed here.

#### DIGITAL DATA CHANNEL MODELS

##### Monte-Carlo Simulation

To obtain typical burst-error statistics for a transionospheric scintillation channel, the beacon-signal scintillation samples were employed as a measure of instantaneous channel gain in a Monte-Carlo simulation of a binary symmetric channel. The modulation was assumed to be phase-shift keying (PSK), which for no fading results in an error probability ( $P_E$ ) of

$$P_{E_{nf}} = \frac{1}{2} \operatorname{erfc}(\sqrt{z_{nf}}), \quad (5)$$

where  $z_{nf}$  is the non-fading energy-per-bit-to-noise-power-spectral-density ratio (SNR) and  $\operatorname{erfc}(x) = 1 - \operatorname{erf}(x)$  where  $\operatorname{erf}(x) = \frac{2}{\sqrt{\pi}} \int_0^x e^{-t^2} dt$ . The fading due to scintillation is modeled as a scaling of the SNR by the channel gain,  $G_c$ , as

$$z_f = z_{nf} G_c^2, \quad (6)$$

where  $z_f$  is the SNR of the fading channel. The channel gain,  $G_c$ , is obtained by normalizing the beacon signal samples by the maximum sample present in the time series of scintillation data being considered. A simplified flow diagram of the simulation is shown in Fig. 10. At any time,  $t_n$ , a fading-channel  $P_E$  is computed according to

$$P_{E_f} = \frac{1}{2} \operatorname{erfc}(\sqrt{z_f}) \quad (7)$$

for a given non-fading SNR,  $z_{nf}$ . The resultant  $P_{E_f}$  is then compared with a uniform random number,  $N_u$ , an error being recorded if  $P_{E_f} < N_u$ . Replicating the simulation for several minutes of channel gain data results in a typical pattern of errors for the time interval under consideration.

##### Markov Characterizations for Burst-Error Channels

By computing various burst-error-pattern statistics, one can model the channel by Markov characterizations. Perhaps one of the simplest such models is the partitioned Markov chain model described by Fritchman [3], and employed by Tsai [4,5] to model HF and tropo-scatter channels.

The parameters of the former model can be determined by curve fitting a sum of exponential functions of the form

$$f_N(m) = A_1 e^{a_1 m} + A_2 e^{a_2 m} + \dots + A_N e^{a_N m} \quad (8)$$

to the error-free run distribution of the channel, where  $m$  is the run length [4]. The error-free run distribution,  $P(0^m/1)$ , is the probability of an error-free run of length at least  $m$  following an error. It can be related to the gap distribution,  $P_g(m)$ , which is the probability of  $m$  or fewer error free bits between two errors (i.e., gap length), versus the length  $m$ . For  $m > 1$ , the relationship between  $P(0^m/1)$  and  $P_g(m)$  is [4]

$$P(0^m/1) = [1 - P_g(m-1)]P(0^1/1). \quad (9)$$

Figure 12 shows the gap distribution,  $P_g(m)$ , for the simulated ionospheric channel for a non-fading SNR of 8.4 dB, which corresponds to  $P_{E_{nf}} = 10^{-4}$ , and for bit rates of 0.1 and 1 kbps. Also shown on the same figure are the gap distributions for a completely

random-error channel with the same  $P_E$  as the fading channel. The bursty nature of the channel is clearly evident. The simulated channel was chosen to be poor in order to get good gap statistics with short simulation run times (300,000 bits in both cases). The difference between the 0.1 kbps and 1 kbps curves is perhaps due mostly to simulation run time difference.

The error-free run distribution corresponding to the data of Fig. 12 are shown in Fig. 13. One-, two-, and three-term exponential-sum fits to the run distribution are also shown. The parameters for the three exponential sums are given in Table II.

TABLE II

PARAMETERS FOR CURVE FIT TO ERROR-FREE

$$\text{RUN DISTRIBUTION: } f_N(m) = \sum_{i=1}^N A_i e^{-a_i m}$$

Coefficients	Number of Terms		
	One	Two	Three
$A_1$	0.728	0.391	0.29
$A_2$		0.474	0.45
$A_3$			0.38
$a_1$	-0.110	-0.058	-0.039
$a_2$		-0.268	-0.22
$a_3$			-0.68

#### Partitioned Markov Chain Model [3,4]

The exponential sums given in Table II correspond to a partitioned Markov chain model of the channel which has one error state and one, two, or three error-free states, depending on the number of terms in the sum, with no transitions allowed between error-free states. The transition probabilities are calculated in Table III [3], and the state diagrams are given in Fig. 14. The two state model is the generalized Gilbert model.

Given a partitioned Markov chain model for the channel, other probabilities describing the burst patterns of the channel are readily calculated. For example, the probability of an error-burst of length  $m$  with  $n$  errors can be calculated. Given this family of probability distributions, the effectiveness of various codes can be approximately evaluated simply by identifying those bursts which are correctable by the code under consideration.

#### MODELING AND SIMULATION OF COMMUNICATION CHANNELS

The previous section considered a simple stochastic model for the error patterns of a digital data transmission system operating in a scintillation fading channel. Since it is a model based on hard decisions at the receiver, it has limited application to communication system evaluation. For example, the influence of the channel perturbations on the synchronization loops of the receiver cannot be considered if such a model is employed.

Considerable effort has been expended on more general stochastic channel models which relate the instantaneous output of a channel to the instantaneous input. Linear channels (i.e., superposition holds) can be conveniently modeled as randomly-varying bandpass linear filters [6,7]. Although eight equivalent system functions can be used to describe a time-varying linear filter [8], the time-varying impulse response,  $h(\tau, t)$ , and the time-variant transfer function,  $H(f, t)$ , are the most often used and perhaps most convenient. The system function  $h(\tau, t)$  is defined to be the response of the channel to an impulse applied at time  $t - \tau$  while  $H(f, t)$ , which is the Fourier transform of  $h(\tau, t)$  with respect to  $\tau$ , has magnitude and phase equal, respectively, to the magnitude and phase of the randomly-modulated sinusoidal signal received at the channel output in response to a unity amplitude sinusoidal input.

The measurement of  $H(f, t)$  is conceptually simple. All that is required is to transmit a coherent frequency comb which occupies the channel bandwidth of interest, and to coherently demodulate this frequency comb at the receiver. Sample functions representing  $H(f, t)$  at a discrete set of frequencies are thereby obtained. The practical aspects of implementing such a measurement may present some difficulties, however.

Likewise, the measurement of  $h(t, \tau)$  is conceptually simple, but somewhat complex experimentally. One method which has been suggested [9] is to send a pseudo-randomly, kiphase-coded signal through the channel and correlate the channel output with a replica of the pseudo-random code stored at the receiver. Since it is well known that the cross-correlation function of a linear system output with its input yields the system impulse response when the input is white noise, the channel system function  $h(\tau, t)$  will be obtained for various  $\tau$  if the pseudo-random code is wideband com-

pared with the channel bandwidth. This technique is especially convenient because it directly yields the tap weights for the so-called Kailath tapped delay line channel realization as the output of the correlation operation for various delays. A quadrature-component representation of this channel realization is shown in Fig. 15.

Except for very wideband transmissions (say, 1 MHz), the transionospheric scintillation channel can be approximated by a one-tap delay line model. That is, its time-varying impulse response,  $h(\tau, t)$ , is approximated as

$$h(\tau, t) = E(t)\delta(t - \tau) \quad (11)$$

or the time-variant transfer function by

$$H(f, t) = E(t), \quad -\infty < f < \infty \quad (12)$$

where  $E(t)$  is the complex gain of the channel. Assuming a transmitted beacon signal of the form  $x(t) = \text{Re } e^{j\omega_0 t}$ , the received signal is of the form

$$\begin{aligned} y(t) &= \text{Re } E(t)e^{j\omega_0 t} \\ &= [E_0 + e_c(t)]\cos \omega_0 t \\ &\quad - e_s(t)\sin \omega_0 t \end{aligned} \quad (13)$$

where  $E_0^2$  is the portion of the transmitted power which remains unscattered in traversing the ionosphere, and  $e_c(t)$  and  $e_s(t)$  are the phase-quadrature components of the scattered signal. This is precisely the form of the model proposed by Rino, et al. for the transionospheric channel. Thus, a so-called stored-channel simulator for the transionospheric scintillation channel is easily implemented if quadrature-component recordings of the channel response to a sinusoidal input are available. Unfortunately, such recordings are, as yet, unavailable.

A so-called synthetic channel simulation can be accomplished if the required tap weights can be realistically simulated. The results of this paper indicate how this might be accomplished through digital simulation and digital-to-analog conversion.

#### SUMMARY

Two approaches to channel simulation have been discussed in this paper, with the transionospheric scintillation channel used as an example. The digital generation of a bivariate Gaussian time series to approximate the fade-duration statistics of the instantaneous channel

gain was discussed. Such time series can be used as the tap weights of a one-tap delay-line synthetic simulation of the channel. Since actual quadrature-component measurements of the transionospheric scintillation channel gain are not available as yet, the synthetic generation of these components by digital means is a viable option for simulation of the transionospheric scintillation channel. A hard-decision, Markov-chain model of the channel was also discussed. Simulations based on such models are limited in that only the error patterns of the channel output can be simulated.

#### REFERENCES

1. C. L. Rino, R. C. Livingston, and H. E. Whitney, "Some New Results on the Statistics of Radio Wave Scintillations", submitted for publication to the Journal of Geophysical Research.
2. M. R. Paulson and R. U. F. Hopkins, "Effects of Equatorial Scintillation Fading on SATCOM Signals", NELC TR 1875, Naval Electronics Laboratory Center, San Diego, California, May 1973.
3. B. D. Fritchman, "A Binary Channel Characterization Using Partitioned Markov Chains", *IEEE Trans. on Information Theory*, vol. IT-13, pp. 221-227, April 1967.
4. S. Tsai, "Markov Characterization of the HF Channel", *IEEE Trans. on Communication Technology*, vol. COM-17, pp. 24-32, Feb. 1969.
5. S. Tsai, "Simple Partitioned Markov Chain Model and Troposcatter Channel", *IEEE 1973 National Telemetering Conference Record*, Atlanta, Ga., pp. 16F-1-16F-6, Nov. 1973.
6. P. A. Bello, "Characterization of Random Time-Variant Linear Channels", *IEEE Trans. Communications Systems*, vol. CS-11, pp. 360-393, Dec. 1963.
7. P. A. Bello, "Correlation Functions in a Tapped Delay Line Model of the Orbital Dipole Channel", *IEEE Trans. Information Theory*, vol. IT-9, pp. 2-11, Jan. 1963.
8. A. Gersho, "Characteristics of Time-Varying Linear Systems", *Proc. IEEE*, vol. 51, p. 238, Jan. 1963.
9. P. A. Bello and R. Esposito, "Measurement Techniques for Time-Varying Dispersive Channels", *Alta Frequenza*, vol. XXXIX, pp. 980-996, Nov. 1970.

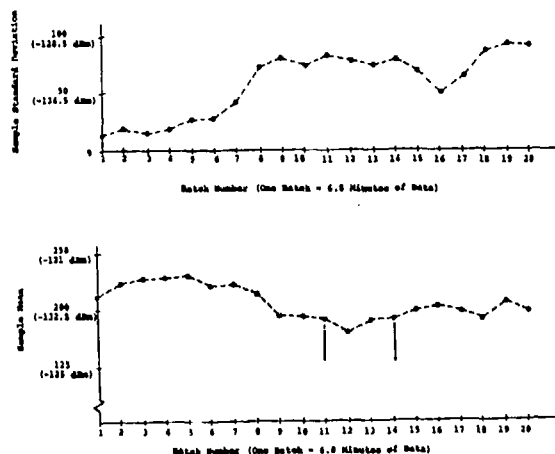


Fig. 1. Sample Standard Deviation and Mean for the 250 MHz THCAV 1 Downer

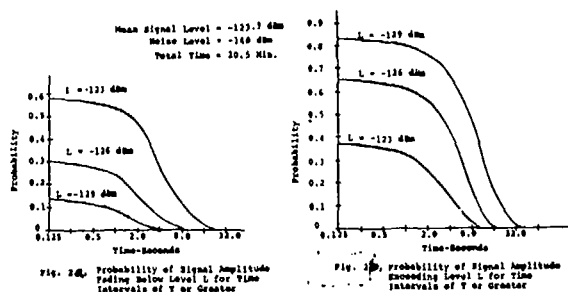


Fig. 2a. Probability of Signal Amplitude Fading Below Level L for Time Intervals of T or Greater

Fig. 2b. Probability of Signal Amplitude Exceeding Level L for Time Intervals of T or Greater

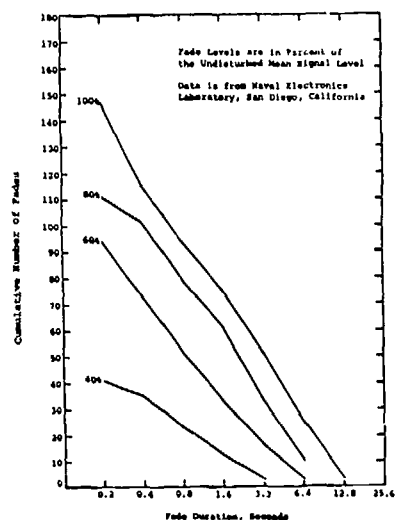


Fig. 3. Fade Duration Distribution for 4096 Scintillation Data Points Spaced at 0.3 Second Intervals.

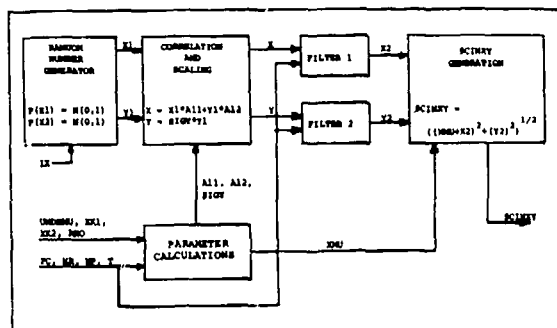


Fig. 4. Block Diagram of Model of Ionospheric Scintillation.

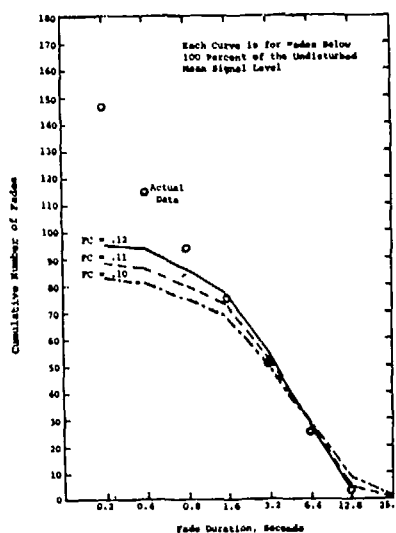


Fig. 5. Comparison of PC for MP = 2.

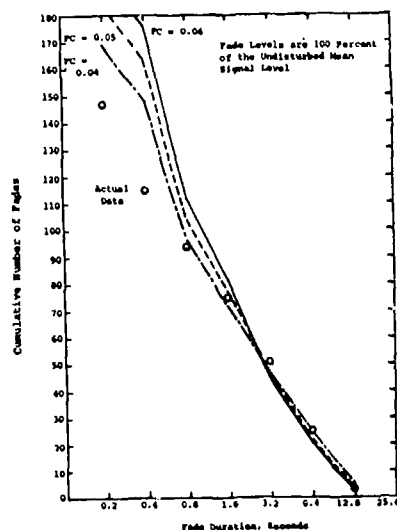


Fig. 6. Comparison of PC for MP = 1.

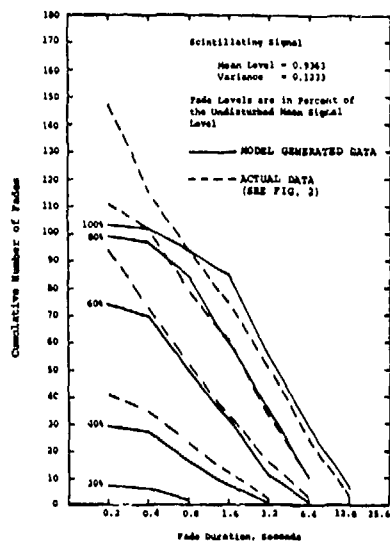


Fig. 7. Fade Duration Distribution for Model,  $KX1 = 0.8$ ,  $KX2 = 0.3$ ,  $MMO = 0.3$ ,  $PC = 0.31$ ,  $MF = 2$ .

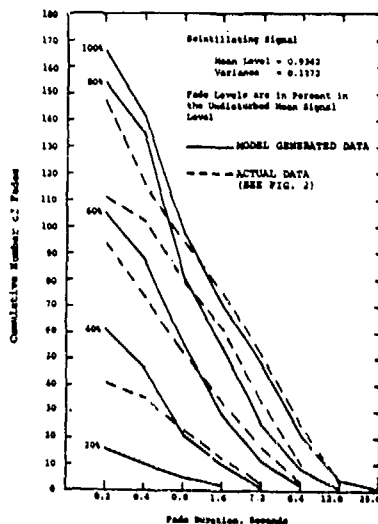


Fig. 8. Fade Duration Distribution for Model,  $KX1 = 0.1$ ,  $KX2 = 0.132$ ,  $MMO = 2$ ,  $PC = 0.04$ ,  $MF = 1$ .

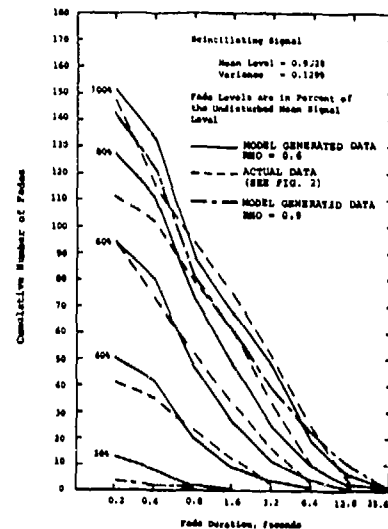


Fig. 9. Fade Duration Distribution for Model,  $KX1 = 0.1$ ,  $KX2 = 0.132$ ,  $PC = 0.04$ ,  $MF = 1$ .

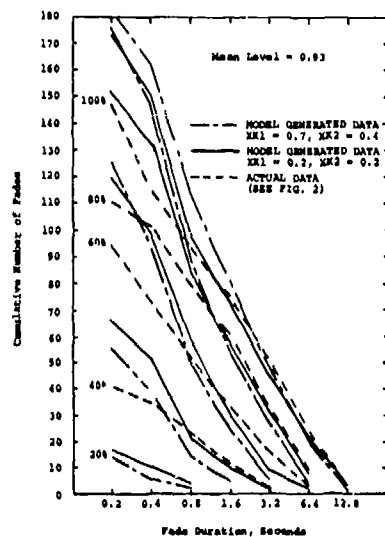


Fig. 10. Fade Duration Distribution for Model,  $MMO = 0$ ,  $PC = 0.05$ ,  $MF = 1$ .

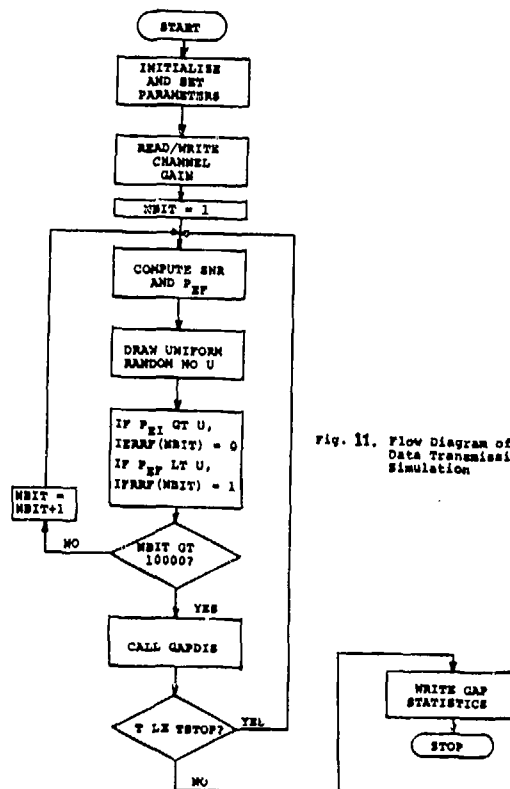


Fig. 11. Flow Diagram of Digital Data Transmission Simulation

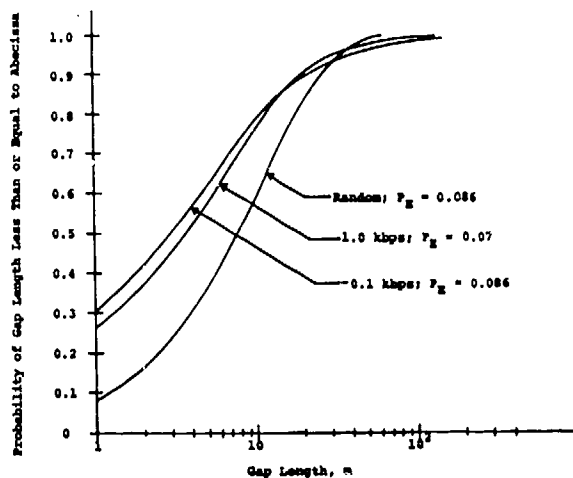


Fig. 12. Gap Distribution for Simulated Transionospheric Channel

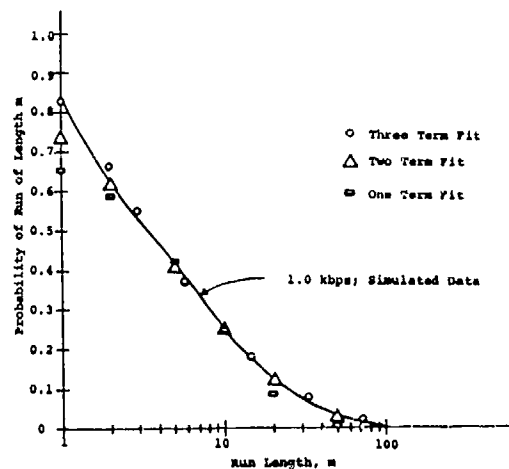


Fig. 13. Error-free Run Distribution

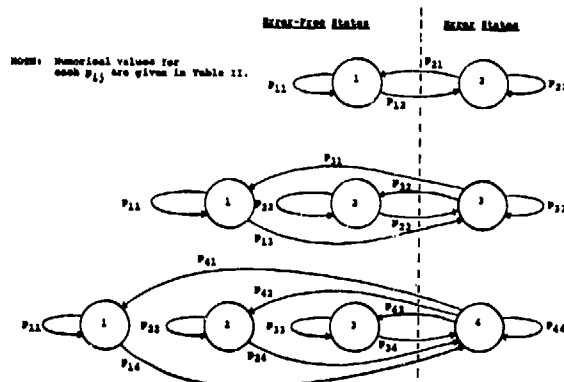


Fig. 14. State Diagram for Markov Channel Models

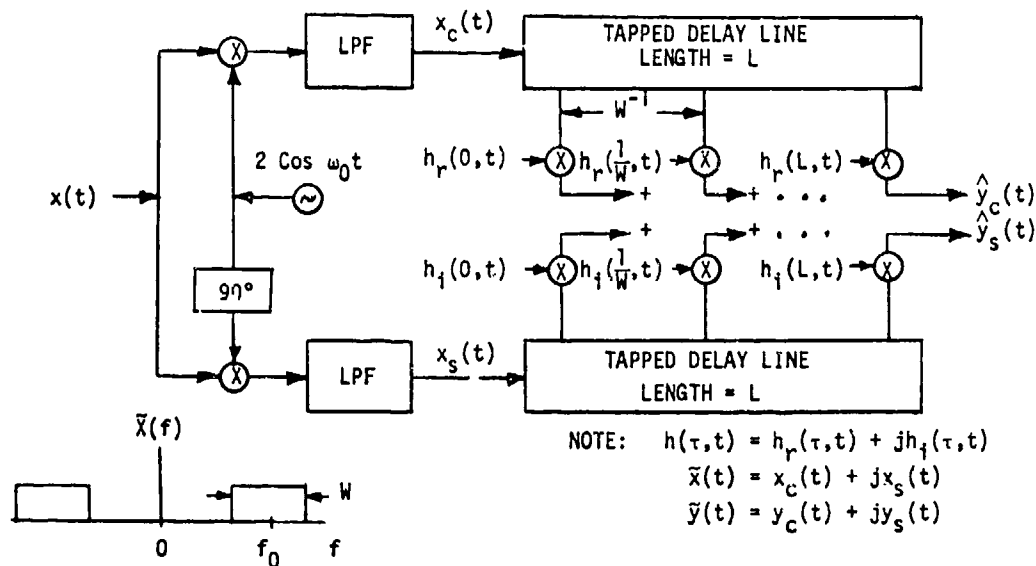


Fig. 15. Tapped Delay Line Channel Model.

# Some Results of Scintillation Studies

K. C. Yeh and C. H. Liu  
University of Illinois at Urbana-Champaign  
Urbana, Illinois 61801

## ABSTRACT

For the purpose of studying the scintillation behavior of transionospheric radio signals extensive computations have been carried out for various ionospheric parameters. The spectrum of irregularities is assumed to follow a power-law with an outer scale varying from several hundred meters to tens of kilometers. A numerical method has been developed to solve the fourth moment equation under the parabolic approximation, for which some multiple scattering are taken into account. The results are organized to show the scintillation dependence on the radio frequency, the irregularity outer scale, the irregularity slab thickness, and the background plasma frequency. In the limit of weak scatter the results can be interpreted in terms of the Fresnel filtering theory. As the irregularities become intense multiple scattering is seen to modify the scintillation behavior in a major manner. The effects of multiple scattering are manifested in many different ways. They are discussed and delineated.

## INTRODUCTION

The scintillation of transionospheric radio signals is caused by the existence of electron density fluctuations  $\Delta N$  from the background value  $N_0$ . These fluctuations in turn cause the relative dielectric permittivity to deviate from its mean value by an amount

$$\epsilon_1 = \frac{\omega_p^2}{\omega^2} \frac{\Delta N}{N_0} = 80.6 \Delta N / f^2 \quad (1)$$

where  $\omega_p$  is the angular plasma frequency of the background ionosphere. The numerical value in the right hand side of (1) applies when the international system of units are used. Notice the inverse frequency squared dependence of  $\epsilon_1$  in (1). Because of this, the scintillation of radio waves is expected to have a very strong frequency dependence.

Let us consider a highly idealized model shown in Fig. 1. A uniform plane wave is falling on top of a slab of irregularities of thickness  $L$ . The wave is rendered random upon exiting from this slab due to scattering. Diffraction of this random wave takes place below the slab for a distance  $z_0$  at which the receiver is situated. When fluctuations in  $\epsilon_1$  are sufficiently weak, the major contribution to amplitude scintillation is found to come from those irregularities in the spectrum near the Fresnel wavenumber. [e.g. Wernik and Liu, 1974]

$$K_F = \sqrt{2\pi k / (2z_0 + L)} \quad (2)$$

where  $k$  is the wavenumber of radio waves. For a specific geometry and radio frequency, the amplitude scintillation depends on the spectral strength of those irregularities near  $K_F$  (provided that the single scatter theory is valid). It is therefore crucial to know what the irregularity spectrum is before undertaking the propagation study.

Recent in situ measurements have shown that the electron density irregularities have a spectrum of the form  $K_X^{-2}$  over a two-decade range from  $K_X = 10^{-3} \text{ m}^{-1}$  (scale size about 7 km) to  $K_X = 10^{-1} \text{ m}^{-1}$  (scale size about 70 m) [Dyson, et al., 1974]. Such a spectrum is generally consistent with the earlier experimental scintillation data [Elkins and Papagiannis, 1969; Rufenach, 1972]. For isotropic irregularities, a one-dimensional spectrum of the form  $K_X^{-2}$  implies a three dimensional spectrum of the form  $K^{-4}$ . The two-decade range over which the  $K^{-4}$ -spectrum is found valid from the in situ data is indicated in Fig. 2. The bottom scale of Fig. 2 is a frequency scale which is computed by using equation (2) with  $z_0 = 300 \text{ km}$  and

$L = 100$  km. It shows that for these parameters a radio wave of frequency given by the bottom scale will predominantly sense irregularities with the irregularity size  $l$  or the wavenumber  $K$  given by the top two scales. Even though the two-decade range given by the in situ data covers the most important frequency range of interest, it is not enough; we must necessarily introduce an outer scale to keep the mean square value  $\langle (\Delta N)^2 \rangle$  finite and a minimum inner scale at the Debye cutoff below which the ionospheric plasma is known to lose its collective behavior. The Jicamarca radar returns at 50 MHz (which senses mainly  $l \approx 3$  m irregularities) from the strongest spread-F irregularities are typically up to 60 to 80 dB above the level of incoherent scatter from thermal fluctuations [McClure and Woodman, 1972]. It can be shown that such a strong return is consistent with the  $K^{-4}$ -spectrum if we would extend to  $l \approx 3$  m as shown by the arrow in Fig. 2. In our computations we leave the outer scale  $r_0$  open, allowing it to take values from 150 m to as large as 30 km. The adopted irregularity spectrum is therefore

$$\phi_N(K) = r_0^3 / \pi^2 (1 + K^2 r_0^2)^2 \quad (3)$$

which has the proper  $K^{-4}$  behavior when  $K r_0 \gg 1$ .

The amplitude scintillation index  $S_4$  is computed by solving the fourth moment equation under the parabolic approximation [Tatarskii, 1971]. The numerical techniques have been previously discussed [Liu, et al., 1974; Yeh, et al., 1975] and details have been provided in these earlier publications.

#### MULTIPLE SCATTERING EFFECTS

The scintillation phenomenon is governed by the Helmholtz wave equation. The stochastic process  $\epsilon_1(\vec{r})$  appears as a coefficient in this equation and therefore makes it a stochastic differential equation. This equation is actually linear in terms of the wave function, but really nonlinear in terms of the stochastic process  $\epsilon_1(\vec{r})$ . The usual weak scatter approximation is equivalent to linearization with respect to  $\epsilon_1(\vec{r})$ . In such a weak scatter limit the scintillation index  $S_4$  is then a linear function of  $\sqrt{\langle \epsilon_1^2 \rangle}$ . In the ionosphere  $\epsilon_1$  is given by (1). Therefore, for a given radio frequency a relation

$$S_4 \propto \langle (\Delta N)^2 \rangle^{1/2} \quad (4)$$

is expected in the weak scatter limit. The numerically computed  $S_4$  dependence

on  $\langle (\Delta N)^2 \rangle^{1/2}$  is shown in Fig. 3 for 125, 250 and 500 MHz. The linear relationship is valid only for small rms fluctuations in  $\Delta N$ . Departures from the linear relationship occur first at lower frequencies as the value of  $\langle (\Delta N)^2 \rangle^{1/2}$  increases.

The behavior of  $S_4$  as a function of distance below the slab of irregularities is shown in Fig. 4. The group I of two curves correspond to the case of waves coming out of a relatively thin slab. It is seen that immediately below the slab  $S_4$  is larger if the irregularities have a power-law spectrum than if the irregularities have a Gaussian spectrum. As the wave leaves the slab the two curves cross so that at large distances the opposite becomes true. The group II of two curves is representative to the case in which the waves are coming out of a thick slab of irregularities. As seen in the figure there is already appreciable scintillation on exit from the slab. At large distances both curves approach the same asymptotic "saturation" level. However, when the irregularity spectrum is Gaussian the index  $S_4$  reaches a maximum value before approaching the saturation level. This is commonly referred to as the focusing phenomenon. The curves of Fig. 4 show that this focusing phenomenon is apparent only when the irregularity spectrum is Gaussian and not when it follows a power law. Based on the phase screen theory an initial random phase perturbation with a Gaussian correlation function and an rms phase fluctuation  $\phi_0$  will cause the amplitude scintillation to develop as a function of distance from the screen. At a distance equal to the radius of curvature of the phase front at the screen, an increase in intensity fluctuations is produced by focusing [Salpeter, 1967; Tamoikin and Fraiman, 1971]. This focusing phenomenon is expected to be well developed when the phase front fluctuations can be characterized mainly by a single scale such as the case for a Gaussian spectrum and not so well developed when no such single-size characterization can be made as the case in a power-law spectrum.

The effect of multiple scattering on the intensity correlation will be discussed in the next section.



# SOME COMPUTED RESULTS

The dependence of scintillation on radio frequencies is shown in Fig. 5. In all these four curves the outer scale is 300 m, the rms electron density fluctuations is 5% and the receiver is 250 km below the slab. The slab thickness is held at 50 km in the first three curves while the background plasma frequency is successively increased from 5 MHz in curve 1, to 7.07 MHz in curve 2 and 10 MHz in curve 3. In curve 4 the only change from that in curve 3 is a two-fold increase in slab thickness. All curves show a general trend of decreasing scintillation with increasing frequency. Notice the flattening of curves at the low frequency region. Here because of saturation effect the scintillation dependence on frequency is very weak. In the intermediate frequency region the frequency dependence is very strong, e.g. a doubling in frequency will reduce scintillation appreciably. For very large frequencies, the scintillation behavior apparently follows the weak scatter theory and this is further discussed later on.

Recent scintillation data collected at the equatorial region indicate that at times there is a 2 or more db peak-to-peak fading in intensity at 4 and 6 GHz frequencies [Taur, 1973]. This corresponds to a scintillation index  $S_4$  of approximately 0.3. If we now go to Fig. 5 and locate the point at  $S_4 = 0.3$  and  $f = 4$  GHz (actually off scale) and imagine a curve of the general shape as the 4 curves drawn but going through the point, we can get a general picture about the severity of scintillation for a frequency of say, 600 MHz. Apparently, nature does provide conditions under which the scintillation is even more severe than those computed in Fig. 5.

Because of its importance to communication engineers many investigators have studied the frequency dependence of  $S_4$  experimentally [Aarons, et al., 1967; see also the review by Crane, 1974]. The usual approach is to assume a dependence

$$\frac{S_4(f_1)}{S_4(f_2)} = \left( \frac{f_1}{f_2} \right)^{-n} \quad (5)$$

and then determine the exponent  $n$  experimentally. The curves of Fig. 5 show that the relation (5) is certainly not valid in general when there is multiple scattering. It will be

therefore of interest to generalize the expression by defining

$$n = - \frac{dS_4}{S_4} \bigg/ \frac{df}{f} \quad (6)$$

The "exponent"  $n$  as a function of frequency for the same four cases shown in Fig. 5 has been computed and plotted in Fig. 6. In the low frequency region the exponent  $n$  is very small, showing very weak frequency dependence. In the intermediate frequency region the dependence of  $n$  on frequency is very strong. Only in the high frequency region is  $n$  approaching a constant value of 1.5. It can be shown that equations (6) and (5) become equivalent when  $n$  is constant. Further, the weak scatter theory predicts that an irregularity spectrum of the form  $K^{-p}$  will have a scintillation frequency dependence  $f^{-n}$  with  $n = (p+2)/4$  [Lovelace, et al., 1970; Jokipii and Hollweg, 1970]. Our spectrum given by equation (3) has  $p=4$  and hence an exponent  $n=1.5$  is predicted by the weak scatter theory. This is in perfect agreement with the computed results, but only when the radio frequency is sufficiently high (above 1 GHz for conditions of Fig. 6) to guarantee the validity of weak scattering.

The effect of varying the outer scale  $r_0$  is depicted in Fig. 7. These curves show that a larger outer scale depresses the scintillation. In the weak scatter theory the dependence of  $S_4$  on  $r_0$  is approximately identical to the dependence of  $\sqrt{\Phi_N(K_F)}$  on  $r_0$ . For the spectrum (3), an approximate dependence of  $r_0^{-1/2}$  for  $S_4$  is therefore obtained (assuming  $K_F r_0 > 1$ ). In Fig. 7 such a relation is only approximately obtained when the frequency is larger than about one gigahertz.

The dependence of  $S_4$  on the irregularity slab thickness  $L$  is depicted in Fig. 8. If we ignore the weak dependence of the Fresnel filtering function on  $L$ , the single scatter theory predicts a  $\sqrt{L}$  dependence. For the five cases considered in Fig. 8 the  $L^{1/2}$  dependence is only roughly satisfied even in the weak scatter limit. When  $L$  is very large so that multiple scattering becomes important the curves tend to flatten, showing weaker and weaker dependence on  $L$ .

The numerical solution of the fourth moment equation can also be used to compute the correlator function of the intensity function [Yeh, et al.,

1975]. Let us define a correlation distance  $\alpha_c$  as that transverse distance at which the correlation coefficient is reduced to 0.5. The results of our computations are summarized in Fig. 9 for two values of slab thickness. The curves show that in the high frequency limit the correlation distance  $\alpha_c$  decreases with frequency. This is expected since the irregularities most responsible for creating scintillation are those near the Fresnel zone and the Fresnel zone has an inverse square root dependence on frequency. Consequently, through Fresnel filtering, the correlation function is decreased as the frequency is increased, provided that the weak scatter approximation is valid. This explains the high frequency behavior. The curves of Fig. 9 show that in the low frequency limit the correlation distance increases with the increasing frequency. In the low frequency region multiple scattering is important. The lower the frequency the more pronounced is the multiple scattering. Apparently the multiple scattering tends to decorrelate the complex amplitude, giving rise to the computed low frequency behavior. This opposite behavior at low and high frequency limits results in a maximum correlation distance occurring at some frequency which increases with the value of slab thickness. Our computed results of Fig. 9 show that this maximum correlation distance is smaller and occurs at a higher frequency when the irregularity slab is thick than the case when the slab is thin. This behavior can be explained on the basis that there is more scattering in a thick slab. These computed results have obvious implications in both geophysical measurements of irregularity size by scintillation observations and the application of space diversity technique as a means of overcoming the scintillation problem in a communication circuit.

#### CONCLUSION

We have shown in this paper that under normal ionospheric conditions the multiple scattering effects can be very important. These multiple scattering effects modify drastically the frequency dependence of the scintillation index and the correlation distance. Further computations for different parameters will be desirable. Especially interesting will be computations for the case of anisotropic irregularities.

#### ACKNOWLEDGEMENT

Computations were carried out on a Control Data Computer 7600 at the

National Center for Atmospheric Research. This work was partially supported by the Atmospheric Sciences Section, National Science Foundation under Grant GA-42857.

#### REFERENCES

- Aarons, J., R. S. Allen and T. J. Elkins, Frequency dependence of radio star scintillations, *J. Geophys. Res.*, 72, U.S.A., 1967, 2891-2902.
- Crane, R. K., Morphology of ionospheric scintillation. Technical Note 1974-29, Lincoln Laboratory, Lexington, MA, U.S.A.
- Dyson, P. G., J. P. McClure and W. B. Hanson, In-situ measurements of amplitude and scale size characteristics of ionospheric irregularities, *J. Geophys. Res.*, 79, U.S.A., 1974, 1497-1502.
- Elkins, T. J. and M. D. Papagiannis, Measurement and interpretation of power law spectra of ionospheric scintillation at a sub-auroral location, *J. Geophys. Res.*, 74, U.S.A., 1969, 4105-4115.
- Jokipii, J. R. and J. V. Hollweg, Interplanetary scintillation and the structure of solar-wind fluctuations, *Astrophys. J.*, 160, U.S.A., 1970, 745-753.
- Liu, C. H., A. W. Wernik, K. C. Yeh and M. Y. Youakim, Effects of multiple scattering on scintillation of trans-ionospheric radio signals, *Radio Sci.*, 9, U.S.A., 1974, 599-607.
- Lovelace, R. V. E., E. E. Salpeter and L. E. Sharp, Analysis of observations of interplanetary scintillations, *Astrophys. J.*, 159, U.S.A., 1970, 1047-1055.
- McClure, J. P. and R. F. Woodman, Radar observations of equatorial spread F in a region of electrostatic turbulence, *J. Geophys. Res.*, 77(28), U.S.A., 1972, 5617-5621.
- Rufenach, C. L., Power-law wavenumber spectrum deduced from ionospheric scintillation observations, *J. Geophys. Res.*, 77, U.S.A., 1972, 4761-4772.
- Salpeter, E. E., Interplanetary scintillation - I. Theory, *Ap. J.*, 147(2), U.S.A., 1967, 433-448.
- Tamoikin, V. V. and A. A. Fraiman, The intensity fluctuations of a wave beyond a random phase screen, *Radiofizika*, 14, U.S.S.R., 1971, 1427-1431.

Tatarskii, V. I., The effects of the turbulent atmosphere on wave propagation, U. S. Department of Commerce, National Technical Information Service, Springfield, VA, U.S.A., 1971.

Taur, R. R., Ionospheric scintillation at 4 and 6 GHz, COMSAT Technical Rev., 3, U.S.A., 1973, 145-153.

Wernik, A. W. and C. H. Liu, Ionospheric irregularities causing scintillation of GHz frequency radio signals, J. Atmos. Terr. Phys., 36, England, 1974, 871-879.

Yeh, K. C., C. H. Liu and M. Y. Youakim, A theoretical study of the ionospheric scintillation behavior caused by multiple scattering, to appear in Radio Science, U.S.A., 1975.

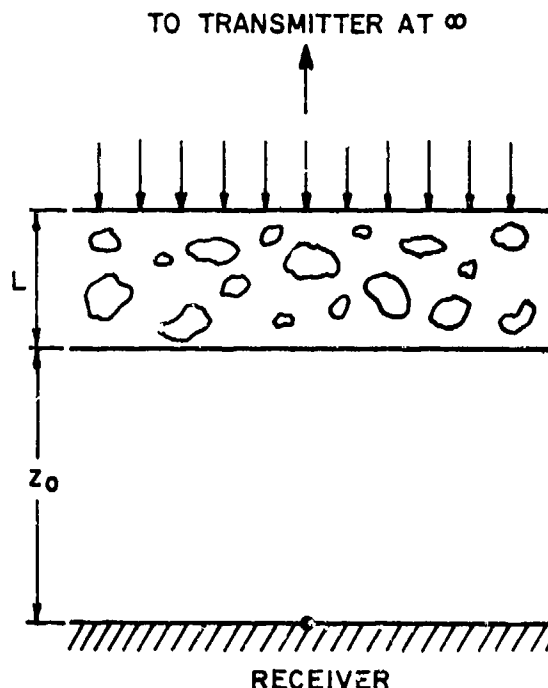


Fig. 1 Idealized propagation geometry. A plane wave is incident on top of a slab of irregularities of thickness  $L$ . Diffraction takes place after exiting from the bottom of the slab for a distance  $z_0$  before it is received.

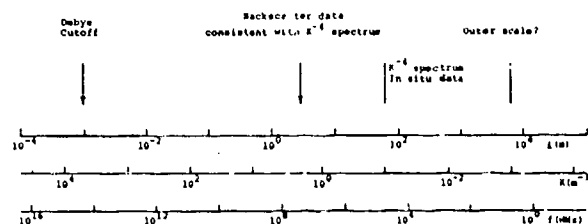


Fig. 2 Spectrum scale in the irregularity size  $l$  and the wave-number  $K$ . The corresponding radio frequency  $f$  at the bottom scale is computed by using equation (2) with  $z_0 = 300$  km and  $L = 100$  km. The two-decade range over which the  $K^{-4}$  spectrum is obtained from the in situ data is shown on the top.

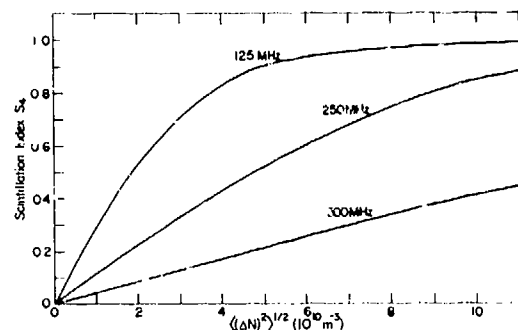


Fig. 3 Scintillation index  $S_4$  as a function of rms electron density fluctuations for three radio frequencies: 125, 250 and 500 MHz.  $L = 50$  km,  $z_0 = 237.5$  km.

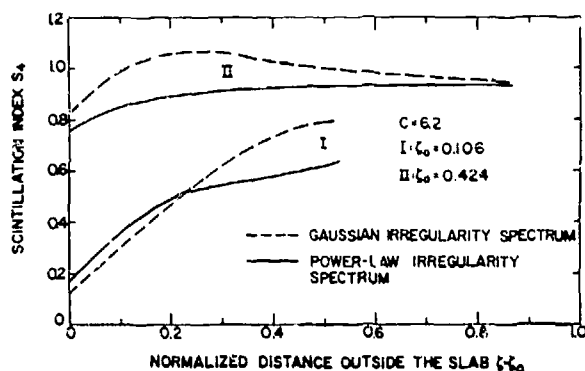


Fig. 4 Scintillation index  $S_4$  as a function of distance from the bottom of the irregularity slab. The parameter  $C$  is 6.2 for all cases. The normalization of both the slab thickness and the distance outside the slab is with respect to  $kr_0^2$ .

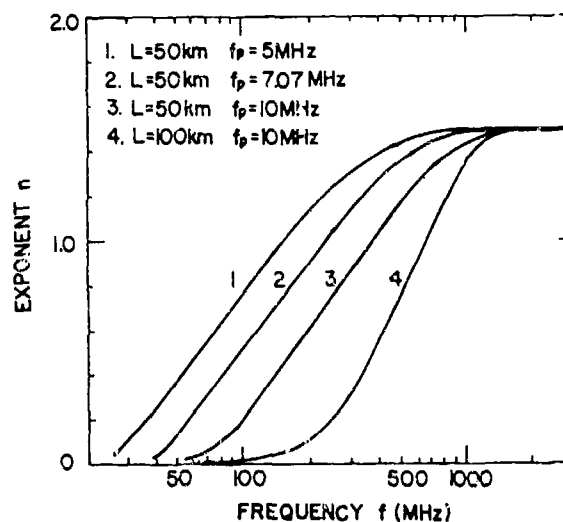


Fig. 6 Exponent  $n$  as a function of frequency for the same four cases shown in Fig. 5. The exponent  $n$  is defined by equation (6).

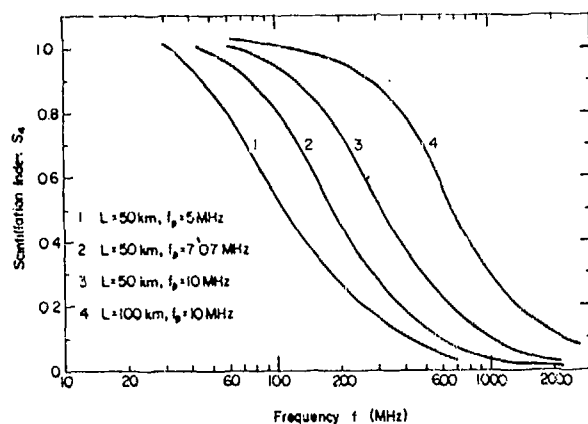


Fig. 5 Scintillation index  $S_4$  as a function of radio frequency.

$r_0 = 300$  m,  $\langle (\Delta N/N_0)^2 \rangle^{1/2} = 5\%$ ,  
 $z_0 = 250$  km. Other parameters  
 are shown on the figure.

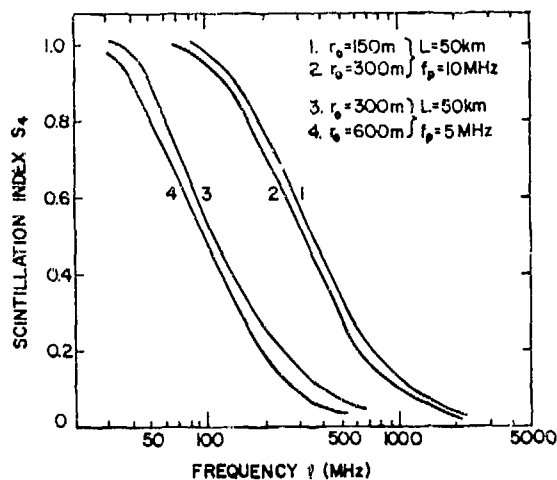


Fig. 7 Effect of varying outer scale  $r_0$  on scintillation index  
 $\langle (\Delta N/N_0)^2 \rangle^{1/2} = 5\%$ ,  $z_0 = 250$  km.

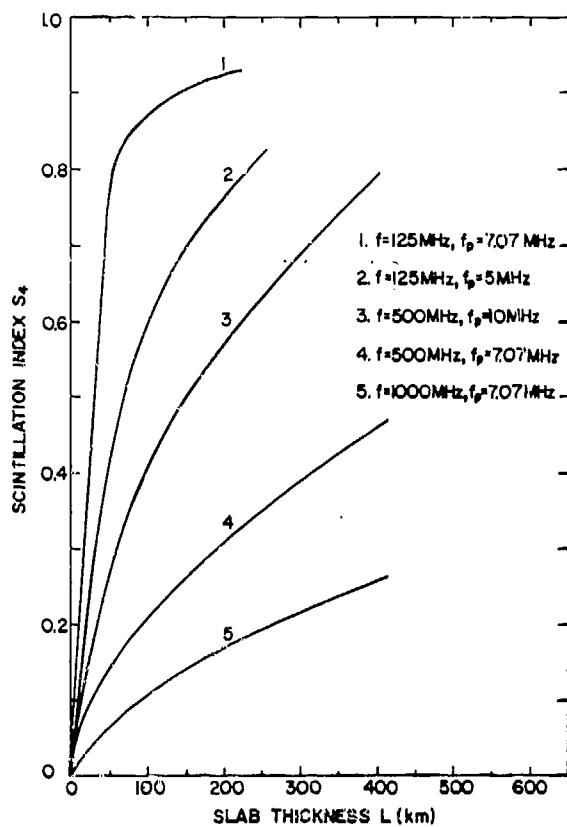


Fig. 8 Scintillation index  $S_4$  as a function of slab thickness.  
 $\langle (\Delta N/N_0)^2 \rangle^{1/2} = 5\%$ ,  $r_0 = 300\text{ m}$ ,  
 $z_0 = 250\text{ km}$ .

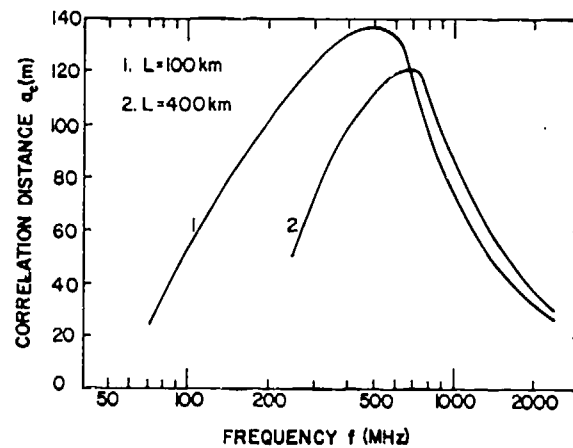


Fig. 9 Correlation distance as a function of frequency. The correlation distance is defined as that displacement at which the amplitude scintillation has a correlation coefficient of 0.5

$$\langle (\Delta N/N_0)^2 \rangle^{1/2} = 5\%, r_0 = 300\text{ m}, z_0 = 250\text{ km}.$$

Intensity Statistics for a Multiple-Scatter  
Model Via Computer Symbol Manipulation

W. S. Ament  
Naval Research Laboratory  
Code 5404  
Washington, D. C.

In propagating through a random medium, an initially coherent wave becomes increasingly random with distance  $D$  from its source. But the field can get no more than totally random, i.e., Rayleigh-distributed. Here the mean-square intensity  $I_2$  becomes twice the square of the mean intensity  $I_1$ . Theories of multiple scattering should predict  $I_2$  for large enough  $D$  that the Rayleigh result is visibly approached.

The simplest non-trivial problem of this class has a plane, two dimensional, coherent wave incident at  $D = 0$  on a halfspace containing phase shifting screens. The phase-shifts are correlated in transverse  $u, v$ -directions but not along the  $D$  axis. The process is described by a function  $f(u, v, D)$  satisfying<sup>1,2</sup>

$$F_D = 2i F_{uv} - HF \{ 2 + C(u+v) + C(u-v) - 2C(u) - 2C(v) \} \quad (1)$$

Here  $H$  is mean-square phase shift in a ray parallel to the  $D$ -axis;  $C(u)$ , with  $C(0) = 1$ , is this phase shift's normalized correlation in the transverse  $u$  direction. Thus the amplitude of the coherent wave falls off in  $D > 0$  as  $\exp(-HD/2)$  while on the present 'parabolic' assumptions of forward scatter only, the total intensity  $I_1$  remains constant at all depths  $D$ . Function  $F(u, v, D)$  describes the intensity statistics, with  $I_2(D) = F(0, 0, D)$ , and with  $F(u, 0, D)/F(0, 0, D)$  the normalized single-frequency intensity correlation function for transverse antenna separation  $u$ .

We report some considerations and a few preliminary results of computer symbol manipulations toward finding the intensity statistics, particularly aimed at the behavior of  $F(0, 0, D)$  for large  $D$ . Reported calculations were done with the MACSYMA symbol-manipulating program, reached at M.I.T. via teletype.

To simplify things as seen by the computer, one assumes  $C(u) = \exp(-u^2/2S^2)$  and rescales (1) into the form

$$F_t = QF_{pq} - PF$$

with initial condition  $F(p, q, 0) = 1$ ; here

$$p = u/S, \quad q = v/S$$

$$P = 1 - x - y + xyc, \text{ with}$$

$$x = \exp(-p^2/2), \quad y = \exp(-q^2/2)$$

$$c = \cosh(pq), \quad s = \sinh(pq)$$

Parameter  $Q$  is now the single physical parameter. (An algebraic  $C(u)$ , e.g.,  $S^2/(S^2 + u^2)$ , may be computationally preferable.) The possibilities now are:

(a) Write  $F(p, q, t)$  as  $\sum_{n=0}^{\infty} f_n(p, q) t^n / n!$ , leading to the recursion  $f_n = Qf_{n,pq} - Pf_n$ , with  $f_0 = 1, f_1 = -P$ . The differentiations for further terms are stipulated symbolically, e.g.,  $dx/dp = -px$ ;  $dc/dq = ps$ , etc. This keeps all expressions as polynomials in  $p, q, x, y, c, s, Q$ ;  $P$  can be included in this list. Then  $F(0, 0, t)$  is obtained by setting  $p, q, s, P$  to zero and  $x, y, c$  to unity, leaving  $Q$  as the only parameter besides the depth-variable  $t$ . This process proved quite slow, taking time  $\sim 2 \times 10^{n+2}$  milliseconds to grind out the  $f_n(p, q)$  through  $n = 5$ . The process was also wasteful, as far more terms were thus computed than were needed for  $f_5(0, 0)$  or even for  $f_5(p, 0)$ .

(b) Set up a recursion for the numerical coefficients  $k_n = k_n(8 \text{ integer exponents})$  of the polynomial  $f_n$  in the variables  $P, Q, x, y, s, c, p, q$ . For  $n = 0$  all such coefficients  $k_0$  vanish except the one for  $P^0 \dots q^0$ . The recursion proved to have 22 terms. Toward  $f_n(0, 0)$ , one for example sets all eight numerical arguments of  $k_n$  to zero and the computer riffs back through the  $k_m, m < n$ , as may or may not be assigned values in its storage, to find what the recursion gives as the value of the requested  $k_n$ . Unless one puts in data concerning the  $k_n$  known a priori to vanish, the computer will chase back to values at  $k_0$  (if not beyond); this would needlessly amplify the computation by a factor  $2^8$ . Even when the a priori information was used to eliminate necessary computational steps, the 22-term basic recursion made the process quite slow for reaching large  $n$ .

(c) Present the computer with the minimum set of symbolic variables, in this case  $Q, p, q$ , through expanding  $P$  in a finite Taylor series in  $p, q$ . With  $P$  as a polynomial of degree 24 in  $p, q$ , one has  $f_1(p, q) = -P$  'accurate' to degree 24, but for further  $n$ , because of the  $p, q$  differentiation, one expects accuracy only of degree  $24 - 2(n - 1)$ . This implies that for  $p = q = 0$  the result of process (a), using the 24th-degree Taylor series for  $P$ , might give accuracy for  $f_{12}(0, 0)$  if not  $f_{13}(0, 0)$ . But as shown in the printout reproduced here as Fig. 1, those coefficients vanished and so  $f_{11}(0, 0)$  is the last nondubious term; that is,  $F(0, 0, t)$  is essentially printed out as a power series in  $t$  with parameter  $Q$  through the term in  $t^{11}$ . The intensity correlation given through  $F(p, 0, t)$  is correspondingly valid only through terms of order  $22 - 2n$ . Terminating expansions in  $p, q$  at the accuracy limit appropriate to the  $n$ th step enabled the MIT computer to complete the essential 11 or 12 step computation in  $2\frac{1}{2}$  minutes.

The printout shown has been rescaled with  $t = Rx$ ,  $Q^2 \sim -R^{-3}$  for the purpose of making plots starting out as  $f(0, 0, x) = 1 + x^3 + \dots$  for all values of parameter  $R$  or  $Q$ . But the coefficients of the retained 12 terms grow much too fast to show how  $I_2(D)$  might begin flattening out toward its asymptotic value 2. Therefore we try some nonlinear convergence procedures<sup>3</sup> using the available 'information' about  $I_2(t) = F(0, 0, t)$ , the first 12 terms in its power series and its large- $t$  asymptote. The formal process is to write  $I_2(t) = N(t)/D(t)$ , where  $N$  and  $D$  are polynomials of degrees  $n$  and  $d$  respectively, with leading terms 1, as is the case with  $I_2$  of present degree 11. Thus, if  $n + d = 12$ , there are, in  $N$  and  $D$ , 12 unknown coefficients to be found through equating the first 12 terms of the Taylor expansion of  $N/D$  with the corresponding 12 terms of  $I_2$ . In Padé approximation theory, the resulting simultaneous equations are formally solved and the resulting  $N/D$  expression given directly as the ratio of two determinants<sup>4</sup>. In the present case, such  $N/D$  forms have to be regarded with caution as one has neither physical motive nor mathematical justification for using them. Perhaps such  $N/D$  forms can be regarded as suggesting  $I_2(t)$  and  $F(p, 0, t)$  when: (1) they contain the full 'information' available concerning  $I_2$ , (2) behave smoothly in accord with physical anticipation, (3) they give a plausible finite- $p$  version of the intensity correlation, and (4) when the same general behavior obtains in 'mathematically nearby'<sup>5</sup>  $N/D$  forms.

Here one could put in the asymptotic behavior of  $I_2$  by using highest-degree terms  $2Kt^r$ ,  $Kt^r$  in  $N, D$ , respectively, giving the large- $t$  asymptote 2 approached algebraically rather than exponentially as would seem physically plausible.  $K$  is now among the coefficients to be solved for; its inclusion should not cause the zeroes of  $D$  to move too near the positive  $t$  axis. Preliminary MACSYMA  $N/D$  results are too fragmentary for reporting at time of writing.

(d) Completely untried is the expansion in powers of  $Q$ : Let

$$F(p, q, t) = \sum g_n(p, q, t) Q^n, \text{ with}$$

$$g_0 = \exp(-tP(p, q)),$$

$$g_n = \exp(-tP) \int_0^t \exp(+sP) \left[ \partial^2 g_{n-1}(p, q, s) / \partial p \partial q \right] ds.$$

MACSYMA contains programs for the requisite  $t$ -integrations. (A first MACSYMA trial with this recursion shows a time 1 minute to go from  $g_1$  to  $g_2$  using the implicit symbols of route (a). Using a power series to speed the calculation would seem to sacrifice the apparent merit of the  $\exp(-Pt)$  as giving an intensity correlation function narrowing for increasing  $t$ .)

Before concluding, we revert to the physical problem. It is mathematically unjustified to expand  $F(p, q, t)$ , satisfying a differential equation parabolic in the  $t$  variable, about  $t = 0$  where the initial conditions are arbitrary. For the specific conditions  $F(p, q, 0) = 1$ , the resulting  $F(0, 0, t)$  starts out as  $1 + 0(t^3)$ . This seemed physically acceptable, and led to attribution of significance to the higher degree terms, as the  $1 + 0(t^3)$  behavior agrees with known intensity statistics for geometric rays in a blobby medium<sup>6</sup>:

Transverse gradients of refractivity in the blobs deviate rays from rectilinear paths. Two rays, emerging at slightly different angles from a point source, suffer differential deviations, so their separation as function of distance  $t$  from the source varies statistically. The intensity  $I$  corresponding to ray density thus varies statistically and the mean-square intensity  $I_2$  is computed to be related to the mean intensity  $I_1$  according to  $I_2 = I_1^2(1 + Ct^3 + \dots)$ , the parameter  $C$  involves both the mean square of the refractivity's second derivative in the transverse dimension and the correlation length in the ray's travel direction. At first glance this  $Ct^3$  behavior corresponds to the  $0(t^3) \equiv C*t^3$  in  $F(0, 0, t)$ . But: the ray result is frequency-independent whereas  $C*$  varies with wavelength when  $t$  is translated to physical distance  $D$ . Thus, the present phase-shifting-screen result has no valid high-frequency or geometric-ray limit. On doing the ray computation for the screen model, one finds that rms arrival times for rectilinear rays do translate into rms phase variations and thus to the attenuation of a coherent average wave, but without phase-shift correlation in the  $D$  or  $t$  direction the screens produce no ray deviations and hence no ray intensity fluctuations. Finally, if one does put in such along-path correlations, the statistic  $(I_2 - I_1^2)$  varies as  $t^2$ , not  $t^3$ . The ray-optical limit of the present model entails parallel incident rays, whereas rays from the finite source diverge with mean separation proportional to  $t$ , leading to an extra factor  $t$  in the  $I_2$  statistic.

Thus the correctness of  $F(0, 0, t) = 1 + 0(t^3)$  is to be argued from physical optics, not ray optics.

Conclusions: Computer symbol manipulations have unexplored potential for giving approximate field statistics when the parabolic approximation of the phase-shifting screen model has validity. One must always question this validity before trusting results, particularly those from computers.

#### References:

1. W. S. Ament "Modification of a Ray-Tracer for Monte Carlo Prediction of Multiple-Scattered Radio Fields" (Eq. 22 of Appendix), pp 184-196 of "Statistical Methods of Radio Wave Propagation," Pergamon Press, 1960, W. C. Hoffman, Ed.
2. L. C. Lee "Wave Propagation in a random medium: A complete set of the moment equations with different wave numbers," J. Math Phys 15, 1431-1435, 1974. Lee's axes in the 'transverse' u,v plane lie at 45° with respect to the present u,v axes.
3. D. Shanks "Non-linear transformations of divergent and slowly convergent sequences" MIT J. of Math and Phys. 34, 1-42, 1955.
4. Eq. (75) of Shanks' paper, ref. 3.
5. C. f. the example and discussion of pp 20-21 of ref. 3.
6. P. G. Bergmann "Propagation of radiation in a medium with random inhomogeneities" Phys. Rev. 70 486-491, 1946.

```
(C10) FOR N:0 THRU 13 DO PRINT
(X**N*R**N*EV(HC N), Q:SQRT(-R**(-3))) / N!
```

```
1
0
0
3
X
0
5
7 X
-----
4 R
6
23 X
-----
10
7
23 X
-----
2
8 R
6
1791 X
-----
56 R
3
(58664 R - 75075) X
-----
3
6720 R
10
33253 X
-----
2
96 R
3
(2319724 R - 1616615) X
-----
4
49280 R
0
0
(C10)
(C11)
```

DONE

FIG. 1

MACSYMA command line for and resulting printout of the first 12 terms of the power series for  $F(0,0,t)$ , rescaled so that with  $x \sim t$ , the  $x^3$  term has coefficient 1.



# EXACT ANALYSIS OF IONOSPHERIC INHOMOGENEITIES BY THE REFLECTION COEFFICIENT METHOD

Arthur K. Jordan and Saeyoung Ahn  
Naval Research Laboratory  
Washington, D. C.

## INTRODUCTION

The profiles of inhomogeneous electron density,  $N(h)$ , as a function of altitude,  $h$ , in the ionosphere have been obtained by using vertical incidence pulse sounding techniques. Typical electron density profiles, shown in Fig. 1, are obtained by a method based upon an approximate numerical solution of an integral equation for  $N(h)$ ; a general survey of this method, known as the virtual height method, has been presented recently [1].

It is the purpose of this communication to present an alternate method for calculating electron density profiles. By making use of the reflection coefficient instead of the time delay of the reflected pulse, this analysis provides mathematically exact profiles. The reflection coefficient method will be presented by means of a simple example; the method will be extended and applied to two examples which are useful for the analysis of ionospheric electron density profiles.

Before discussing the reflection coefficient method, a brief review of the mathematical procedure for obtaining profiles by the virtual height method will be given. If a pulse modulated electromagnetic wave is transmitted vertically and the time delay,  $\Delta t$ , of the reflected signal is measured as a function of the carrier frequency,  $\omega$ , then the virtual height is defined as

$$h'(\omega) = \frac{c}{2} \Delta t, \quad (1)$$

where  $c$  is the velocity of light in free space. It will be convenient to use the free space wave number,  $k = \omega/c$ , in this presentation. The virtual height can be expressed as an integral over the path length,

$$h'(k) = \int_0^{x_h} n(k, x) dx, \quad (2)$$

where  $x_h$  is the altitude at which reflection occurs and  $n(k, x)$  is the group refractive index of the ionosphere. If electron collisions and the Earth's magnetic field are neglected, then

sions and the Earth's magnetic field are neglected, then

$$n(k, x) = \left[ 1 - \frac{1}{k^2} \overline{N(x)} \right]^{\frac{1}{2}}, \quad (3)$$

where  $\overline{N(x)}$  is the reduced electron density profile,

$$\overline{N(x)} = \text{Constant} \cdot N(x). \quad (4)$$

The integral equation (2) for the electron density profile becomes

$$h'(k) = \int_0^{x_h} \left[ 1 - \frac{1}{k^2} \overline{N(x)} \right]^{\frac{1}{2}} dx. \quad (5)$$

In order to obtain the electron density profile, equation (5) is solved numerically for  $N(x)$  by approximating the integral by a discrete sum [1]. That is, the ionosphere is modeled as a succession of many layers with the electron density profile in each layer having an assumed form. The integral equation (5) is then solved in an iterative manner with guesses being made for the initial values of  $x_h$  and  $N(x)$ .

## REFLECTION COEFFICIENT METHOD

Improved resolution of the electron density profiles can be attained if the phase  $\phi(k)$  and amplitude,  $|r(k)|$ , of the reflected pulse are measured as functions of frequency [2]. It is possible to obtain an analytic expression for an inhomogeneous electron density profile if the complex reflection coefficient,

$$r(k) = |r(k)| e^{i\phi(k)}, \quad (6)$$

is analyzed. The reflection coefficient of the electromagnetic waves used for ionospheric sounding can be defined in terms of the model shown in Fig. 2. A plane electromagnetic wave,  $E_{inc} = e^{ikx}$ , is incident on the base of the ionosphere at  $x = 0$ . In this analysis of

the steady-state version of the electromagnetic wave scattering problem, the time-harmonic factor,  $e^{i\omega t}$ , where  $i = \sqrt{-1}$ , is suppressed throughout. The medium to the left of  $x = 0$  is characterized by the free-space permittivity,  $\epsilon_0$ , and permeability,  $\mu_0$ , and the medium to the right of  $x = 0$  is characterized by the free-space permeability,  $\mu_0$  and ionospheric permittivity,

$$\epsilon(k, x) = n^2(k, x) = 1 - \frac{1}{k^2} \overline{N(x)} \quad (7)$$

The reflected plane wave has the form

$$E_{\text{scat}} = r(k) e^{-ikx} \quad (8)$$

The power reflection coefficient,  $|r(k)|^2$ , can be measured but it appears that the instrumentation for measuring the phase function is better developed [2]. If the tangent of the experimentally determined phase function can be approximated by a rational function of the wave number,  $k$ ,

$$\tan \phi(k) = \frac{F(k)}{G(k)}, \quad 0 < \phi(k) \leq \pi, \quad (9)$$

where  $F(k)$  and  $G(k)$  are polynomial functions of  $k$ , then the reflection coefficient,  $r(k)$ , is also a rational function and can be reconstructed from the phase by methods common in network synthesis [3]. For example, let

$$\tan \phi(k) = \frac{\sqrt{2} k}{1 - k^2}, \quad 0 < \phi(k) \leq \pi. \quad (10)$$

The reflection coefficient is

$$r(k) = \frac{1}{k^2 + i\sqrt{2}k - 1} \quad (11)$$

and the power reflection coefficient is

$$r(k)r(-k) = |r(k)|^2 = \frac{1}{1 + k^2}, \quad m = 1, 2, \dots \quad (12)$$

This form (13) is known in network synthesis as the  $m$ th-order Butterworth approximation and is shown as curve (a) for  $m = 2$  in Fig. 3. The electron density profile,  $\overline{N(x)}$ , can now be reconstructed from the expression (12) for  $r(k)$ .

The general mathematical theory for determining  $\overline{N(x)}$  from  $r(k)$  has been obtained by Kay [4] who considered the scattering matrix formulation of the ionospheric reflection problem when  $r(k)$  is a rational function,

$$r(k) = \frac{n(k)}{d(k)}, \quad (13)$$

and  $n(k)n(-k) - d(k)d(-k)$  has no multiple zeros at the origin of the complex  $k$ -plane. Generalized Fourier techniques were then applied to the analysis of the scattering data. The method requires the solution of the integral

equation

$$R(x+y) + K(x, y) + \int_{-y}^{\infty} K(x, z) R(z+y) dz = 0 \quad (14)$$

for the unknown function  $K(x, y)$  where  $R(x+y)$  is the inverse Fourier transform of  $r(k)$  and the auxiliary variable  $y \leq x$  is used. In the present example

$$R(x+y) = \begin{cases} \frac{-1}{\sqrt{2}} \left[ e^{-\frac{\sqrt{2}}{2}(1+i)(x+y)} - e^{-\frac{\sqrt{2}}{2}(1-i)(x+y)} \right], & x+y \geq 0, \\ 0, & x+y \leq 0. \end{cases} \quad (15)$$

In general  $r(k)$  and  $R(x+y)$  must satisfy certain necessary and sufficient conditions [4, 5] in order to obtain analytic solutions to equation (14). A differential operator technique [5] based upon Kay's theory has been used to solve equation (14). The theory can also be reformulated to obtain completely equivalent solutions to equation (14) by the application of Laplace transform techniques [6].

#### Differential Operator Technique

This technique is based upon the fact that it is always possible to construct a differential operator  $f(p)$ ,  $p \rightarrow d/dy$ , such that

$$f(p)R(x+y) = 0. \quad (16)$$

In the present example

$$f(p) = p^2 + \sqrt{2}p + 1. \quad (17)$$

Applying  $f(p)$  to equation (14) with  $R(x+y)$  given by equation (15) yields

$$f(p)K(x, y) - K(x, -y) = 0 \quad (18)$$

and by symmetry

$$f(-p)K(x, -y) - K(x, y) = 0 \quad (19)$$

Eliminating  $K(x, -y)$  between (18) and (19) yields the differential equation for  $K(x, y)$ ,

$$p^4 K(x, y) = 0, \quad (20)$$

which has the general solution

$$K(x, y) = C_0(x) + C_1(x)y + C_2(x)y^2 + C_3(x)y^3. \quad (21)$$

The function  $K(x, y)$  can also be shown [4] to satisfy the following boundary conditions:

$$K(x, -y) = 0, \quad (22)$$

$$\left. \frac{\partial}{\partial y} K(x, y) \right|_{y=-x} = 0, \quad (23)$$

$$\frac{d}{dx} K(x, x) = \frac{1}{2} \overline{N(x)} \quad (24)$$

Equations (18), (19), (22), and (23) provide the conditions for evaluating the  $G(x)$  functions of equation (19) [5]:

$$G_0(x) = 0,$$

$$G_2(x) = -\frac{\sqrt{2}}{2} G_1(x),$$

$$G_1(x) = \frac{1}{1 + \sqrt{2} x},$$

$$G_0(x) = x \left( 1 + \frac{\sqrt{2}}{2} x \right) G_1(x).$$

Equation (24) thus provides the reduced electron density profile,

$$\overline{N(x)} = \frac{4}{(1 + \sqrt{2} x)^2} \quad x \geq 0, \quad (25)$$

which is shown as curve (a) in Fig. 4.

#### Laplace Transform Technique

A completely equivalent technique for solving the integral equation (14) is useful for many applications. According to the reformulated theory [6], integral equation (14) assumes the form

$$R(x+y) + K(x, y) + \int_{\max[-x, -y]}^x K(x, z) R(z+y) dz = 0. \quad (26)$$

The Laplace transform of this equation is

$$A(s)e^{sx} + A(s)F(x, -s) + F(x, s) + G(x, s) = 0 \quad (27)$$

where the complex variable  $s = ik$ , and where

$$A(s) = r(is) = \int_0^\infty R(x+y)e^{sy} dy, \quad (28)$$

$$F(x, s) = \int_{-x}^x K(x, y)e^{-sy} dy, \quad (29)$$

$$G(x, s) = \int_x^\infty K(x, y)e^{-sy} dy. \quad (30)$$

When  $A(s)$  is a rational function,

$$A(s) = \frac{n(s)}{d(s)}, \quad (31)$$

$$n(s) = \sum_{j=1}^{b_1} n_j s^j, \quad d(s) = \sum_{j=1}^{b_2} d_j s^j, \quad (32)$$

where the coefficients  $n_j$  and  $d_j$  are real, a detailed analysis yields

$$G(x, s) = \frac{R(s)e^{-sx}}{D(s)}, \quad (33)$$

where

$$g(s) = \sum_{j=1}^{b_2} s^{b_2-j} \sum_{v=1}^j d_{b_2+1-v} K_{j-v} \quad (34)$$

$$K_v = \left. \frac{d^v K(x, y)}{dy^v} \right|_{y=x+}, \quad (35)$$

so that

$$F(x, s) = \frac{F_N(x, s)}{F_D(x, s)}, \quad (36)$$

where

$$F_N(x, s) = e^{sx} [-N(s)D(-s) + N(s)g(-s)] \\ + e^{-sx} [N(s)N(-s) - D(-s)g(s)]$$

$$F_D(x, s) = D(-s)D(s) \\ - N(-s)N(s)$$

$K(x, x) = K_0$  and the higher-order  $K_v$  are determined by the entireness property of  $F(x, s)$ . Also

$$K_0 = K(x, x) = \lim_{s \rightarrow -\infty} |s| F(x, s) e^{|s|x} \quad (37)$$

$$\text{Then} \quad \overline{N(x)} = 2 \frac{dK_0}{dx} \quad (38)$$

For the second-order Butterworth example, it is found that

$$F(x, s) = s^{-2} [e^{sx} (s + K_0 - \sqrt{2}) \\ + e^{-sx} (-s^2 K_0 - sK_1 + \sqrt{2}K_1 + K_0)] \quad (39)$$

where  $K(x, y)$  is found by taking a Laplace transform of  $F(x, s)$ , so that this yields the same result as equation (25).

# EXAMPLES FOR IONOSPHERIC ANALYSIS

The electron density profile obtained in equation (23) is not a physically realistic model of the ionosphere since there is a jump discontinuity at  $x = 0$  and since it does not decay exponentially with altitude. It is possible to obtain more realistic profiles which can be useful for analyzing ionospheric inhomogeneities by considering two further applications of the techniques which were presented.

## Tapered Profiles

Tapered profiles which do not have jump discontinuities in electron density at  $x = 0$  can be obtained by considering higher order approximations for the power reflection coefficient,  $|r(k)|^2$ . Assume that the measured power reflection coefficient is approximated by

$$|r(k)|^2 = \frac{1}{1 + k^8} \quad (40)$$

which is known as the third-order Butterworth approximation and is shown as curve (b) in Fig. 3. The corresponding complex reflection coefficient is

$$r(k) = \frac{1}{k^3 - 2k + i(2k^2 - 1)} \quad (41)$$

and the phase function is defined by

$$\tan \phi(k) = \frac{k(k^2 - 1)}{2k^2 - 1}, \quad 0 < \phi(k) \leq \pi \quad (42)$$

$$\overline{N(x)} = \frac{24x(x+1)(x^2+3x+3)}{[2x(x^2+3x+3)+3]^2}, \quad x \geq 0, \quad (43)$$

which is curve (b) in Fig. 4.

## Exponentially Decaying Profiles

For large altitudes, the electron density profile decays exponentially [1]. It is possible to extend the method by considering a general second-order reflection coefficient,

$$r(k) = \frac{1}{(k - k_1)(k - k_2)} \quad (44)$$

where  $k_1$  and  $k_2$  are the poles of  $r(k)$  in the complex  $k$ -plane,  $k = k' + ik''$ . For the second-order Butterworth approximation,

$$k_1 = \frac{\sqrt{2}}{2} - i\frac{\sqrt{2}}{2}, \quad k_2 = -\overline{k_1} = -\frac{\sqrt{2}}{2} - i\frac{\sqrt{2}}{2},$$

so that  $|k_1| = |k_2|$ . In this case the poles lie on the  $45^\circ$ -lines in the lower half-plane of Fig. 5. If this condition is relaxed, but if  $k_2 = -\overline{k_1}$  still, then integral equation (14) must be solved for this more general case.

Assume that the poles are now

$$k_1 = \frac{1}{2} - i\frac{\sqrt{3}}{2}, \quad k_2 = -\frac{1}{2} - i\frac{\sqrt{3}}{2},$$

so that they lie in the shaded region of Fig. 5. The power reflection coefficient is now

$$|r(k)|^2 = \frac{1}{(k^2 - 1)^2 + 3k^2}, \quad (45)$$

which is shown by curve (c) in Fig. 3, and the phase function is defined by

$$\tan \phi(k) = \frac{\sqrt{3}k}{k^2 - 1}, \quad 0 < \phi(k) \leq \pi. \quad (46)$$

The differential equation for  $K(x, y)$  is now

$$\left[p^2(p^2 - \frac{1}{2})\right] K(x, y) = 0 \quad (47)$$

with the same boundary conditions as before. The reduced electron density is thus found to be

$$\overline{N(x)} = \frac{4(\cosh \theta - 1)}{\cosh(\theta + 2\beta|x|) - 1}, \quad (48)$$

$$\text{where } \beta^2 = 2(k_1'^2 - k_1''^2) = -\frac{1}{2},$$

$$\theta = \log |\gamma| = 1.3691,$$

$$\gamma = \frac{2(k_1'^2 - k_1''^2) + 2|\beta|(k_1' + k_1'') + k_1'^2 + k_1''^2}{\dots} = 3.9318.$$

This is shown as curve (c) in Fig. 4. For large  $x$  this is approximately  $\overline{N(x)} \sim \exp[-\theta - 2|\beta|x]$ . The same result can also be obtained by the Laplace transform method, that is from equations (34) to (38). In general second-order rational approximations with poles located in the shaded region, i.e., non-Butterworth approximations, will exhibit this exponential decay. Extension of these considerations to the general third-order case is straight-forward but lengthy.

## CONCLUSIONS

Two methods for obtaining electron density profiles from ionospheric sounding measurements

were reviewed, the virtual height method and the reflection coefficient method. Using the reflection coefficient method, two techniques for obtaining density profiles were presented by means of a simple example. These techniques were applied to two more examples which can be useful for the analysis of ionospheric inhomogeneities: (1) A tapered profile which was obtained from a special third-order rational approximation for the reflection coefficient, (2) An exponentially decaying profile which was obtained from a general second-order rational approximation. The extension of this method to the general third-order rational approximation will be the subject of a future report.

#### ACKNOWLEDGEMENTS

The authors would like to express their appreciation to Harold Szu and Clark Carroll of the Naval Research Laboratory for many helpful discussions. The first author has benefited from valuable discussions with Irvin Kay of the Institute for Defense Analysis and also from discussions at the Applied Mathematics Summer Institute, University of California at Irvine; July, 1974. The second author thanks Angelo Skalafuris of the Naval Research Laboratory for support and encouragement during the course of this work.

#### REFERENCES

1. Jackson, J.E., "The  $P'(f)$  to  $N(h)$  Inversion Problem in Ionospheric Soundings", Proc. Workshop on Profile Inversion, NASA TM X-62, 150; Aug., 1972.
2. Phillips, M.L., "Ground-Based Vertical Incidence Ionograms", IEEE Trans. Ant. & Prop. Vol. AP-22, pp. 785-795; 1974.
3. van Valkenberg, M.E., Introduction to Modern Network Synthesis, J. Wiley & Sons, Inc.; 1960.
4. Kay, I., "The Inverse Scattering Problem When the Reflection Coefficient is a Rational Function", Comm. Pure & Appl. Math., Vol. 13, pp. 371-393; 1961.
5. Jordan, A.K. and Kritikos, H.N., "An Application of One-Dimensional Inverse Scattering Theory for Inhomogeneous Regions", IEEE Trans. Ant. & Prop., Vol. AP-21, pp. 909-911; 1973.
6. Szu, H.H., Carroll, C., and Ahn, S., "Reformulation of the Plasma Inverse Problem", submitted for publication in the Phys. Rev. Letters.

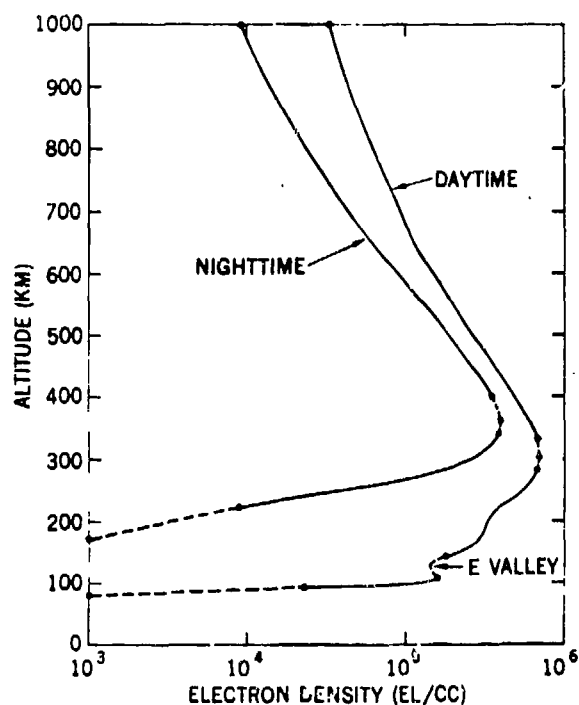


Fig. 1, Vertical electron density distributions upon simultaneous topside and ground-based observations (adapted from [1], Fig. 1)

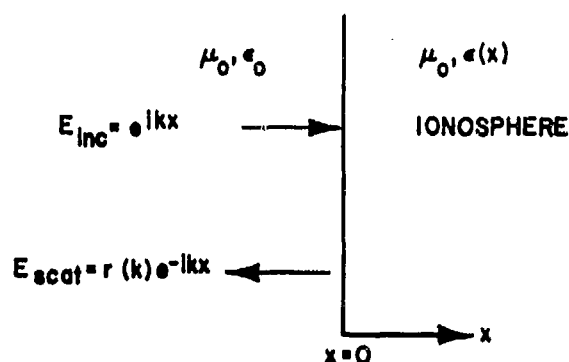


Fig. 2, Model for ionospheric reflection

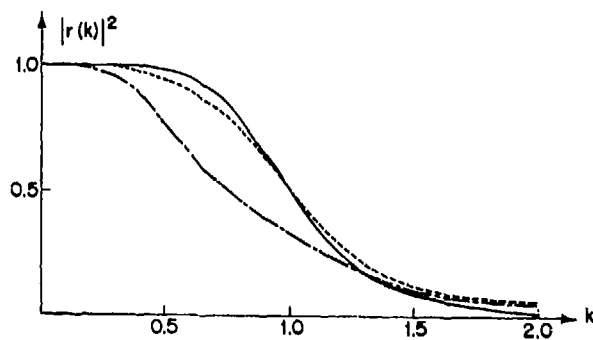


Fig. 3, Power reflection coefficient,  $|r(k)|^2$ , vs free-space wave number,  $k$ :  
 (a) Second-order Butterworth approximation.  
 (b) Third-order Butterworth approximation.  
 (c) General second-order approximation.

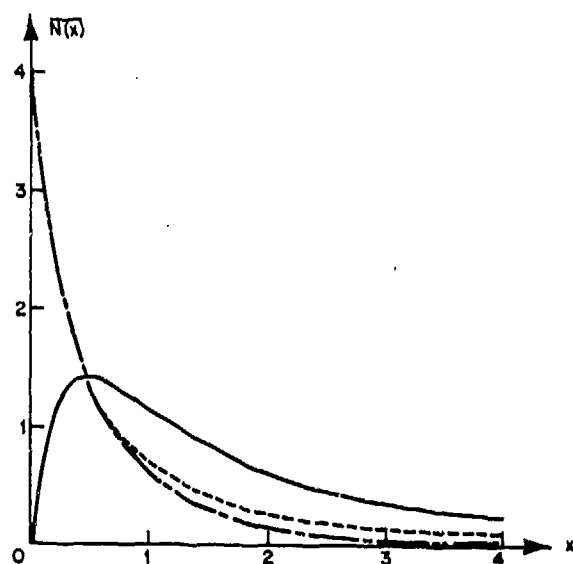


Fig. 4, Reduced electron density profile,  $\overline{N(x)}$ , vs vertical distance,  $x$ :  
 (a) Second-order Butterworth approximation.  
 (b) Third-order Butterworth approximation.  
 (c) General second-order approximation.

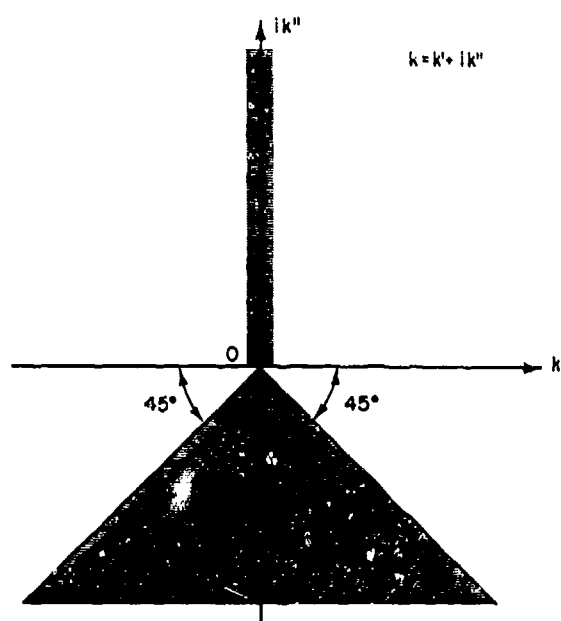


Fig. 5, Complex  $k$ -plane with region of allowable pole positions of  $r(k)$  for the second order approximation indicated by the shaded area.

ANTENNA APERTURE EFFECTS ON  
MEASUREMENTS OF PROPAGATION THROUGH TURBULENCE

Dennis L. Knepp  
Calspan Corporation  
Buffalo, New York 14221

ABSTRACT

The first Born approximation is applied to propagation of a spherical wave through a layer of random irregularities to an aperture antenna. The effect of the receiving aperture on measurements of the variance of in-phase, phase-quadrature components of the received signal, and the variances of their spatial derivatives is determined. In the weak scattering limit, these quantities are related to the scintillation index, mean-square phase fluctuations, mean-square angle-of-arrival fluctuations, and fading rates. Physical situations corresponding to the generic problem considered here include satellite communication through ionospheric fluctuations, solar wind observations, observations through irregularities caused by instabilities in barium release clouds, etc.

Numerical results are presented which show the aperture effect for irregularities with power law spectra of the form  $S(K) \propto (1 + K^2 L_0^2)^{-N/2}$  for values of the spectral index  $N$  ranging from 3 to 5 and for many ratios of the three lengths, turbulent outer scale  $L_0$ , aperture radius, and Fresnel length. These results are presented in convenient form for estimating the aperture effect in many cases of interest. Aperture effects (aperture smoothing) generally dominate the behavior of the spatial derivatives, while a near-field effect is shown which causes enhancement of the variance of the in-phase fluctuations over the value predicted ignoring the receiving aperture. It is suggested that this effect may be useful to explain some aspects of observed gigahertz scintillation.

INTRODUCTION

It appears that the effect of the receiving aperture on radio wave measurements has been largely ignored since the work of Wheelon [1,2] in the late fifties in which the well known aperture smoothing effect was obtained for the measurement of phase fluctuations by a finite circular aperture. Since then, various investigators have studied the aperture smoothing

effect on intensity scintillations in the optics regime (Tatarskii [3], Fried [4], Homstad, et al [5]) and also the related effect of optical beam wave propagation to an infinitesimal receiver (Lee and Harp [6], Ishimaru [7]). The increased use of the ionospheric channel for microwave satellite communications as well as the requirements for more precise measurements of fluctuation phenomena due to propagation through random media prompts this work to consider the effects of the antenna aperture upon such measurements.

The present paper considers the generic problem (Fig. 1) of a spherical wave from a transmitter incident normally upon a turbulent layer below which an aperture receiver is located. Wheelon's basic work in the microwave regime is extended to obtain the antenna aperture effect for variances of the in-phase, phase-quadrature components of the random part of the received signal, and the variances of their spatial derivatives. In the weak scattering limit, these quantities may be related to the scintillation index, mean-square phase fluctuations, mean-square angle-of-arrival fluctuations, fading rates and other quantities of physical interest. Physical situations corresponding to the generic problem include satellite communications through ionospheric irregularities, solar wind observations, layers of irregularities formed by instabilities in barium release clouds, and nuclear burst produced electrons which either are carried with the ambient turbulent atmosphere or are turbulent due to explosion processes. Results for irregularities with power law spectra of the form  $S(K) \propto (1 + K^2 L_0^2)^{-N/2}$  where  $N$  is the spectral index and  $L_0$  is the outer scale are presented which are sufficiently general in length scales and spectral indices to provide estimates of the aperture effect for many cases of physical interest. Such results are useful for choosing antenna size and/or frequency for a particular application, interpreting observations of fluctuations to account for the effect of the receiving antenna, and predicting the effects of the turbulent medium upon a particular

communication, radar, or observing system.

The power law irregularity spectrum considered here is of interest for propagation through the ionosphere and in the solar wind. Rufenach [8] notes that the ionospheric scintillation spectra determined from remote sensing correspond to power laws with spectral indices ranging from 4 to 5. Dyson, et al. [9] have shown in situ measurements for F region scintillation spectra with spectral indices ranging from less than 4 to 4.5. In situ measurements of the ion-charge flux of the solar wind by Unti, et al. [10] are interpreted to imply power-law spectra for proton fluctuations with spectral indices from 3.1 to 4.2. This work is also valid for the inertial subrange of the well known Kolmogorov spectrum ( $N = 11/3$ ) for index of refraction variations caused by temperature fluctuations.

The use of the outer scale here is equivalent to the definition of Matheson and Little [11] where  $L_0$  is defined as the scale size beyond which the power spectrum is flat. Such a spectrum is presented in Fig. 2 of Rufenach [8]. Another possible definition of  $L_0$  (not used here) is the largest blob size for which the irregularities remain homogeneous (Lawrence and Strohbehn [12]). It is recognized that the spectrum turnover from a power law to a flat behavior with wavenumber  $i$ , not always observed; such a case is considered by Rino [13] under the assumption of an infinite outer scale.

#### FORMULATION OF THE PROBLEM

Consider the problem of a spherical wave originating from a transmitter located at  $Z_t$ , incident normally upon a layer of turbulence, and which propagates to an aperture antenna at  $-Z_r$  as depicted in Figure 1. The turbulent layer of thickness  $L$  is centered at the origin of the X-Y-Z coordinate system and its index of refraction is given as an average value of unity plus a small random component,

$$n(\vec{r}) = 1 + \Delta n(\vec{r}) \quad (1)$$

All expressions to be derived here depend upon the space correlation of the irregularities given by

$$\langle \Delta n(\vec{r}) \Delta n(\vec{r}') \rangle = \frac{\langle \Delta n^2 \rangle}{8\pi} \int_0^\infty d^3K S(K) e^{iK \cdot (\vec{r} - \vec{r}')} \quad (2)$$

where  $S(K)$  is the spectrum and  $\langle \Delta n^2 \rangle$  the variance of index of refraction fluctuations.

The incident spherical wave is given by

$$A \frac{e^{ik|\vec{r} - \vec{k}Z_t|}}{|\vec{r} - \vec{k}Z_t|}$$

with suppressed time behavior  $e^{-i\omega t}$  ( $\omega = kc$ ). Neglecting depolarization, the solution to the scalar wave equation is given in the first Born approximation by

$$E(-Z_r) = A \frac{e^{ik|Z_r + Z_t|}}{|Z_r + Z_t|} + \frac{k^2 A}{2\pi} \int_V dV' \Delta n(\vec{r}')$$

$$\frac{e^{ik|\vec{r}' - \vec{k}Z_t|}}{|\vec{r}' - \vec{k}Z_t|} \frac{e^{ik|\vec{r}' + \vec{k}Z_r|}}{|\vec{r}' + \vec{k}Z_r|} f(x', y') e^{-z'^2/L^2} \quad (3)$$

where  $E(-Z_r)$  represents the signal received by an antenna with a receiving pattern defined by  $f(x, y)$  in the manner of Wheelon [14]. The introduction of the antenna pattern in this manner and the subsequent integration over the spatial extent of the illuminated turbulent irregularities is a basic difference in this formulation from the work of Tatarskii which involves an averaging over the receiving aperture (lens) face. The Gaussian  $\exp(-z'^2/L^2)$  defines the layer thickness and cuts off the integration in the  $z$  direction. To simplify notation equation (3) is written as

$$E = E_0 (1 + \Delta) \quad (4)$$

The quantities calculated are the variance of in-phase fluctuations  $\langle (\text{Re} \Delta)^2 \rangle$ , the variance of quadrature-phase fluctuations  $\langle (\text{Im} \Delta)^2 \rangle$  and their spatial derivatives perpendicular to the line of sight  $\langle (\text{Re} \frac{\partial \Delta}{\partial x})^2 \rangle$ , and  $\langle (\text{Im} \frac{\partial \Delta}{\partial x})^2 \rangle$ . The weak scattering relationship between these quantities and the scintillation index  $m$ , the variance of phase fluctuations  $\langle \Delta \phi^2 \rangle$ , and the variance of angle-of-arrival fluctuations  $\langle \Delta \theta^2 \rangle$  is established in the Appendix. The fading rate in communications problems is related to the correlation time for moving irregularities which under Taylor's hypothesis is determined from the two derivatives above (Evans [15]).

For convenience, a Gaussian antenna pattern is assumed  $f(x, y) = \exp[-(x^2 + y^2)/X^2]$  where, to establish the correspondence to a circular aperture,  $X$  is later set equal to  $0.85 \lambda Z_r / \rho$  so that the half-power point of the Gaussian beam coincides with that of the circular aperture of radius  $\rho$  [16]. Since most of the power is concentrated within the half-power points, this Gaussian beam assumption should lead to representative results. In addition the far-zone approximations

$$|\vec{r}' - \vec{k}Z_t| \approx Z_t - z' + (x'^2 + y'^2)/2Z_t \quad (5)$$

$$|\vec{r}' + \vec{k}Z_r| \approx Z_r + z' + (x'^2 + y'^2)/2Z_r \quad (6)$$

are made to simplify the spatial integrations. Assuming that  $Z_t \gg Z_r$ , these approximations are valid wherever

$$\frac{X^2 L}{\lambda Z_r^2} \ll 1 \quad \text{and} \quad \frac{L^3}{\lambda Z_r^2} \ll 1 \quad (7)$$

since  $X$  and  $L$  are the maximum values of  $x'$  (or  $y'$ ) and  $z'$  respectively.

Using eqns. (2), (3), (5) and (6) with the



Gaussian antenna beam, taking derivatives as necessary, and performing the spatial integrations one obtains

$$\begin{bmatrix} \langle (\text{Re} \Delta)^2 \rangle \\ \langle (\text{Im} \Delta)^2 \rangle \end{bmatrix} = \frac{\langle \Delta^2 \rangle L^2 \alpha^2}{\pi \lambda^2 (1 + \alpha^2)} \int_{-\infty}^{\infty} d^3 K S(\bar{K}) \quad (8)$$

$$\times \exp \left[ -\frac{1}{2} L^2 K_z^2 - \frac{1}{2} X^2 K_1^2 / (1 + \alpha^2) \right] \begin{bmatrix} \cos^2 \beta \\ \sin^2 \beta \end{bmatrix}$$

$$\begin{bmatrix} \langle (\text{Re} \frac{\partial \Delta}{\partial x})^2 \rangle \\ \langle (\text{Im} \frac{\partial \Delta}{\partial x})^2 \rangle \end{bmatrix} = \frac{\langle \Delta^2 \rangle L^2 \alpha^4}{2 \lambda^2 (1 + \alpha^2)^3} \int_{-\infty}^{\infty} d^3 K K_x^2 S(\bar{K}) \times \exp \left[ -\frac{1}{2} L^2 K_z^2 - \frac{1}{2} X^2 K_1^2 / (1 + \alpha^2) \right] \begin{bmatrix} (\alpha \cos \beta + \sin \beta)^2 \\ (\alpha \sin \beta - \cos \beta)^2 \end{bmatrix} \quad (9)$$

$$\begin{aligned} \text{where } 1/Z &= 1/Z_t + 1/Z_r \\ \alpha &= k_1 X^2 / Z \\ \beta &= \tan^{-1} \alpha - k X^4 K_1^2 / (8Z(1 + \alpha^2)) \\ K_1^2 &= K_x^2 + K_y^2. \end{aligned}$$

In the following, it is assumed that  $Z_t \gg Z_r$  so that  $Z = Z_r$  which corresponds to problems such as transmission from a synchronous satellite through the ionosphere to a ground station or from a radio star through the solar wind to a radio telescope. Further simplification results from the assumption that the layer thickness is greater than the outer scale; for  $L \gg L_0$  the  $K_z$  integral may be approximated

$$\int_{-\infty}^{\infty} dK_z S(\bar{K}) \exp \left( -\frac{1}{2} L^2 K_z^2 \right) = \frac{(2\pi)^{1/2}}{L} S(K_x, K_y, 0) \quad (10)$$

By changing to cylindrical K-coordinates and performing the azimuthal integration one obtains one-dimensional integral expressions for the four quantities of interest

$$\begin{bmatrix} \langle (\text{Re} \Delta)^2 \rangle \\ \langle (\text{Im} \Delta)^2 \rangle \end{bmatrix} = \frac{2 \sqrt{2\pi} \langle \Delta^2 \rangle L \alpha^2}{\lambda^2 (1 + \alpha^2)} \int_0^{\infty} dK_1 K_1 S(K_1) \times \exp \left[ -\frac{1}{2} X^2 K_1^2 / (1 + \alpha^2) \right] \begin{bmatrix} \cos^2 \beta \\ \sin^2 \beta \end{bmatrix} \quad (11)$$

$$\begin{bmatrix} \langle (\text{Re} \frac{\partial \Delta}{\partial x})^2 \rangle \\ \langle (\text{Im} \frac{\partial \Delta}{\partial x})^2 \rangle \end{bmatrix} = \frac{\pi \sqrt{2\pi} \langle \Delta^2 \rangle L \alpha^4}{2 \lambda^2 (1 + \alpha^2)^3} \int_0^{\infty} dK_1 K_1^3 S(K_1) \times \exp \left[ -\frac{1}{2} X^2 K_1^2 / (1 + \alpha^2) \right] \begin{bmatrix} (\alpha \cos \beta + \sin \beta)^2 \\ (\alpha \sin \beta - \cos \beta)^2 \end{bmatrix} \quad (12)$$

These are the general results which are studied numerically in this paper.

Note the irregularity spectrum  $S(K_1)$  is arbitrary to this point but in the calculations

which follow it is assumed of the form  $(1 + K_1^2 L_0^2)^{-N/2}$  which is unity for  $K_1 < \frac{1}{L_0}$  and behaves as  $K_1^{-N}$  for  $K_1 > \frac{1}{L_0}$ .

Two factors appear in these integrals to reflect the modification due to the antenna beam.

First, the exponential cut-off  $\exp \left[ -\frac{1}{2} K_1^2 X^2 / (1 + \alpha^2) \right]$  eliminates wavenumbers above  $K_1 = \sqrt{2\pi} X / \lambda Z = \pi / \rho$ ; this is aperture-smoothing effect which minimizes the importance of small-scale irregularities (Wheelon [1], Tatarskii [3]). Due to the higher power  $K_1$  in the integrals for the derivatives  $\langle (\text{Re} \frac{\partial \Delta}{\partial x})^2 \rangle$  and  $\langle (\text{Im} \frac{\partial \Delta}{\partial x})^2 \rangle$  this

exponential cut-off is required for convergence with spectral indices  $N \leq 4$ . For this reason, the derivative terms show a much greater dependence on the aperture smoothing effect as was noted by Wheelon [1] for angle-of-arrival fluctuations and by Valley [17] for angular jitter measured by a monopulse antenna. Note that even if the true irregularity spectrum contained an inner scale, if the inner scale is smaller than  $\rho/\pi$  it is irrelevant. Second, the  $\tan^{-1} \alpha$  term is a modification to the familiar Fresnel filtering function  $\sin^2(K_1^2 \lambda Z / 4\pi)$  (Tatarskii [3]) and can provide an additional contribution to the in-phase variance  $\langle (\text{Re} \Delta)^2 \rangle$  and to the derivative term  $\langle (\text{Im} \frac{\partial \Delta}{\partial x})^2 \rangle$  at scale sizes of the order of the outer scale when  $L_0 > (\lambda Z)^{1/2}$ . For a point receiver ( $\alpha \rightarrow \infty$ ),  $\cos^2 \beta$  becomes the usual Fresnel filter which has its first maximum at the point  $K_1 = \pi^{1/2} / (\lambda Z)^{1/2}$ .

Before discussing the general results, it is useful to investigate the beam wave modification to the Fresnel filter term since this apparently has not been investigated before. To do so, the integrand of  $\langle (\text{Re} \Delta)^2 \rangle$  is plotted in Fig. 2 as a function of  $K_1 (\lambda Z)^{1/2}$  for spectral index  $N = 4$ . The function  $K_1 (1 + K_1^2 L_0^2)^{-2} \cos^2 [\tan^{-1} \alpha - k X^4 K_1^2 / (8Z(1 + \alpha^2))]$  is shown for various values of the ratio of aperture radius to Fresnel size  $\rho / (\lambda Z)^{1/2}$  which is related to  $\alpha$  as noted previously. (The exponential cutoff is unimportant for this case). The curve marked 'point receiver' shows the integrand for the limit  $\alpha \rightarrow \infty$  and represents the usual Fresnel filtering effect of eliminating contributions at scales other than the Fresnel size. Note that the  $\tan^{-1} \alpha$  modification has the effect of increasing the integrand at scale sizes near the outer scale size until for  $\rho / (\lambda Z)^{1/2} \approx 0.25$ , this contribution actually dominates. For higher values of spectral index the more rapidly decreasing spectrum for  $K_1 > 1/L_0$  causes the aperture modification effect to become even more pronounced since the spectrum near the Fresnel size is weighted less. Of course, as  $\rho / (\lambda Z)^{1/2}$  approaches unity the turbulence lies in the near field of the antenna and

more detailed calculations than those reported here are required.

### RESULTS

These integrals are evaluated numerically in the form  $I(N, L_0/(\lambda Z)^{1/2}, \rho/(\lambda Z)^{1/2})$  where the spectral index  $N$  ranges from 3 to 5, the ratio of the outer scale to the Fresnel length ranges from  $10^{-3}$  to  $10^{3/2}$ , and the equivalent radius  $\rho$  of the circular aperture is chosen so that the half-power point of the aperture coincides with that of the Gaussian beam. The range of values of  $\rho$  is limited by the Fraunhofer far-zone condition  $Z \gg \rho^2/\lambda$  which is required because of the initial Gaussian antenna pattern assumption. As a check of the numerical results, the integral  $\langle \text{Re} \Delta \rangle^2$  with no exponential cutoff was evaluated analytically for spectral index  $N = 4$ .

The results shown in Figs. 3 and 4 for the in-phase and quadrature-phase fluctuations  $\langle \text{Re} \Delta \rangle^2$  and  $\langle \text{Im} \Delta \rangle^2$  were obtained by dividing the respective integral by the value  $\lim_{\rho \rightarrow 0} I(N, L_0/(\lambda Z)^{1/2}, \rho/(\lambda Z)^{1/2})$  which is the measurement obtained by a point receiver. For the derivatives  $\langle \text{Re} \frac{\partial \Delta}{\partial x} \rangle^2$  and  $\langle \text{Im} \frac{\partial \Delta}{\partial x} \rangle^2$  the results shown in Figures 5 and 6 were normalized by the quantity  $I(N, L_0/(\lambda Z)^{1/2}, .01)$  since these integrals do not converge for a point receiver for  $N \leq 4$ . A horizontal line at unity on Figs. 3-6 thus corresponds to no antenna aperture effect for a particular spectral index and outer scale size.

In order to understand the results in simple physical terms consider the following length-scale regimes:

$$\text{Case I: } L_0 > (\lambda Z)^{1/2} \rho$$

In this case the spectrum cutoff occurs prior to the reciprocal Fresnel length and scale sizes of the order of  $L_0$  play an important role.

The  $\tan^{-1} \alpha$  term can dominate the Fresnel filter of  $\langle \text{Re} \Delta \rangle^2$  as shown in Fig. 2; thus there is an important antenna aperture effect. Since larger values of  $N$  cause a faster spectrum fall-off, thus making large scale sizes relatively more important, the beam effect is more pronounced with increasing spectral index. This behavior is shown in Fig. 3 where the effect of  $N$  ranging from 3 to 5 is dramatic for  $L_0/(\lambda Z)^{1/2} = 10^{3/2}$ . As the parameter  $L_0/(\lambda Z)^{1/2}$  approaches unity contributions near the Fresnel size begin to dominate and the aperture effect begins to decrease with all values of spectral index.

Since the factor  $\sin^2 [\tan^{-1} \alpha - kx^4 K_1^2 / (8Z(1 + \alpha^2))]$  in  $\langle \text{Im} \Delta \rangle^2$  is constant at unity there is no aperture effect for any value of spectral index. This behavior is shown in Fig. 4 for  $N = 4$  and  $L_0/(\lambda Z)^{1/2} = 10^{3/2}$ . For  $L_0/(\lambda Z)^{1/2} > 1$ , the curves for all spectral index values are very close to this curve and are not depicted here.

The additional factor of  $K_1^2$  plays an important role in making small scale sizes important in the evaluation of the integrals  $\langle \text{Re} \frac{\partial \Delta}{\partial x} \rangle^2$  and  $\langle \text{Im} \frac{\partial \Delta}{\partial x} \rangle^2$ . The term  $\alpha \cos \theta$  dominates the filter factor in the integrand of  $\langle \text{Re} \frac{\partial \Delta}{\partial x} \rangle^2$  and the  $\tan^{-1} \alpha$  term plays the same role as it did for  $\langle \text{Re} \Delta \rangle^2$  causing the aperture effect to be more pronounced for higher spectral indices. However, the factor of  $K_1^2$  in the integrand enhances the contribution of small scale sizes to lessen the effect as can be seen by comparing the curves for  $N = 5$ ,  $L_0/(\lambda Z)^{1/2} = 10^{3/2}$  on Figs. 3 and 5. For values of spectral index  $N \leq 4$ , the exponential aperture cutoff is required for convergence and thus contributions from small scale sizes dominate the integral. Thus the antenna aperture effect or beam effect is important for all values of spectral index.

As  $L_0$  approaches  $(\lambda Z)^{1/2}$  the effect of the arctangent is diminished, and for  $N = 5$ ,  $L_0/(\lambda Z)^{1/2} = 1$ , the ordinary Fresnel filter comes into play and there is little aperture effect. Again small values of  $N$  show a dramatic beam wave dependence.

For large values of spectral index, the behavior of  $\langle \text{Im} \frac{\partial \Delta}{\partial x} \rangle^2$  is similar to  $\langle \text{Im} \Delta \rangle^2$  since the  $\sin^2 \theta$  factor yields unity, and the antenna aperture is unimportant. For  $N \leq 4$  once again the exponential cutoff is required, and the beam wave effects are evident in Fig. 6. As  $L_0$  approaches  $(\lambda Z)^{1/2}$ , the behavior is similar to  $\langle \text{Re} \frac{\partial \Delta}{\partial x} \rangle^2$ .

$$\text{Case II: } (\lambda Z)^{1/2} > L_0 > \rho$$

In this case, the spectral cutoff lies between the Fresnel length and the exponential beam wave cutoff. For the integrals  $\langle \text{Re} \Delta \rangle^2$  and  $\langle \text{Im} \Delta \rangle^2$  scale sizes near the Fresnel size dominate the integrals and the beam effect is negligible for all spectral indices as can be seen in Figs. 3 and 4 for  $L_0/(\lambda Z)^{1/2} < 1$ .

The additional factor of  $K_1^2$  in the integrals  $\langle \text{Re} \frac{\partial \Delta}{\partial x} \rangle^2$  and  $\langle \text{Im} \frac{\partial \Delta}{\partial x} \rangle^2$  causes scale sizes smaller than the Fresnel size to dominate the integrals; the beam wave is important for all spectral indices with lower spectral indices again showing more dependence upon the beam wave than higher spectral indices.

$$\text{Case III: } (\lambda Z)^{1/2} > \rho > L_0$$

In this case the exponential beam-wave cutoff, which occurs prior to the spectrum cutoff  $K_1 = 1/L_0$ , dominates the behavior of the integrand to cause the antenna aperture effect to be important for all four integrals with the spectral index playing a minor role.

$\langle (\text{Re}\Delta)^2 \rangle$  and  $\langle (\text{Im}\Delta)^2 \rangle$  are approximately equal for this limit and, as can be seen in Figs. 3 and 4, the effect of spectral index is relatively minor for  $L_0/(\lambda Z)^{1/2} = 10^{-3/2}$ .

As in cases I and II, the additional  $K_1^2$  in the integrand means  $\langle (\text{Re}\frac{\partial\Delta}{\partial x})^2 \rangle$  and  $\langle (\text{Im}\frac{\partial\Delta}{\partial x})^2 \rangle$  depend on the beam wave cut-off more than  $\langle (\text{Re}\Delta)^2 \rangle$  and  $\langle (\text{Im}\Delta)^2 \rangle$  as can be seen by comparing the curves for  $L_0/(\lambda Z)^{1/2} = 10^{-3/2}$ ,  $N = 4$  on Figs. 3-6. As  $L_0$  becomes much less than  $\rho$ , the effect of different spectral indices becomes minor as is shown for  $\langle (\text{Re}\frac{\partial\Delta}{\partial x})^2 \rangle$  for  $L_0/(\lambda Z)^{1/2} = 10^{-3}$ ,  $N = 3.5$ .

#### APPLICATIONS

Inclusion of the aperture effect in cases where the outer scale is much larger than the Fresnel length provides an additional contribution to the scintillation index  $m^2 = 4\langle (\text{Re}\Delta)^2 \rangle$  which causes scale sizes of the order of the outer scale size to become important for large antennas. Fig. 3 which shows the normalized integral  $\langle (\text{Re}\Delta)^2 \rangle$  illustrates this effect for the physical example of a 6 GHz signal radiated by a satellite beacon which propagates through the F-region of the ionosphere to a 30m diameter antenna. As suggested by the observations of Dyson, et al. [9], the irregularity power spectrum is assumed to follow a power law with spectral index  $N = 4$ , and outer scale  $L_0 = 7$  km. The altitude of the turbulent layer center is assumed to be 300 km. The dashed line of Fig. 3 indicates that the effect of the antenna for  $\rho/(\lambda Z)^{1/2} = .12$  is to produce a scintillation index  $\sqrt{2}$  times that predicted ignoring the aperture effect. The wavelength dependence of the scintillation index  $m$  can be shown to change from  $m \propto f^{-1.5}$  for frequencies less than 1 GHz to  $m \propto f^{-1}$  near 6 GHz. It is suggested that this effect may explain some aspects of the observed increased scintillations at gigahertz frequencies [18,19]. Since the inequality of equation (7) is not satisfied for reasonable estimates of the thickness  $L$  of the turbulent layer, say 50-100 km, this example is not completely rigorous. The basic difficulty here is that the antenna is in the near field of the turbulent blobs while the turbulence is in the far field of the antenna. A complete solution of this problem requires a near zone formulation, or equivalently, inclusion of additional terms in the expansion of equations (5) and (6).

Second, consider the 1 km diameter Arecibo receiver observing a radio star at 100 MHz through the same ionospheric layer as above. In this case,  $L_0/(\lambda Z)^{1/2} = 10$ ,  $\rho/(\lambda Z)^{1/2} = .5$  which places the turbulent layer on the Fraunhofer boundary of the aperture, and the inequality (7) is approximately satisfied. As shown in Figure 3, the estimate of scintillation index  $m$  including aperture effects is approximately three times the value measured by a point receiver. Smaller apertures  $\rho < 100$  m show no beam wave effect at this frequency.

#### CONCLUSION

This paper has considered the problem of spherical wave propagation through a layer of turbulent irregularities to an aperture antenna. The numerical results presented here for power law irregularity spectra can be used to estimate the aperture effects on measurements of scintillation index, mean-square phase fluctuations, mean-square angle-of-arrival fluctuations, and fading rates for spectral indices  $N$  in the range from 3 to 5.

The effect of the aperture modification to the usual Fresnel filter term has been detailed and results presented which predict measurements of scintillation index which increase with aperture size for  $L_0/(\lambda Z)^{1/2}$ . It is suggested that this behavior may be useful to explain some aspects of gigahertz scintillation.

#### ACKNOWLEDGMENT

The author is grateful to Dr. G.C. Valley for suggesting this problem, for his constant advice, and many useful suggestions.

#### APPENDIX

The scintillation index  $m$  is given by

$$m^2 = \frac{\langle (I - \langle I \rangle)^2 \rangle}{\langle I \rangle^2} \quad (\text{A-1})$$

where  $I$  is the intensity as received by the antenna located at the point  $(0,0,-Z_r)$ . Expanding and ignoring third and higher order terms in  $\Delta$  one obtains

$$m^2 = 4\langle (\text{Re}\Delta)^2 \rangle \quad (\text{A-2})$$

Phase fluctuations may be handled in a similar manner as by Tatarskii [3]. Rewriting equation (4)

$$E = E_0 (1 + \Delta) = A_0 e^{i\phi_0} + A_1 e^{i\phi_1} = A e^{i\phi} \quad (\text{A-3})$$

$$\text{then } \ln E = \ln E_0 + \ln (1 + \Delta)$$

$$\approx \ln E_0 + \Delta = \ln A_0 + i\phi_0 + \Delta \quad (\text{A-4})$$

Since  $\ln E = \ln A + i\phi \approx \ln A_0 + i\phi_0 + \Delta$  taking the imaginary part of the above equation yields

$$\phi - \phi_0 \equiv \Delta\phi \equiv \text{Im } \Delta \quad (\text{A-5})$$

Thus the variance of the phase fluctuations is given by

$$\langle \Delta\phi^2 \rangle \approx \langle (\text{Im}\Delta)^2 \rangle \quad (\text{A-6})$$

Angle-of-arrival fluctuations are determined from the fluctuations in the normal to the wave-front at the receiving antenna (Tatarskii[3])

$$\begin{aligned}\langle \Delta \theta^2 \rangle &= \frac{1}{k} 2 \left\langle \left( \frac{\partial \Delta \phi}{\partial x} \right)^2 \right\rangle_{x=y=0} \\ &= \frac{1}{k} 2 \left\langle \left( \text{Im} \frac{\partial \Delta}{\partial x} \right)^2 \right\rangle_{x=y=0}\end{aligned}\quad (\text{A-7})$$

#### REFERENCES

1. A.D. Wheelon, "Relation of radio measurements to the spectrum of tropospheric dielectric fluctuations," J. Appl. Phys., Vol. 28, pp. 684-693, June 1957.
2. A.D. Wheelon, "Radio-wave scattering by tropospheric irregularities," J. Research NBS, Vol. 63D, pp. 205-233, Sept. 1959.
3. V.I. Tatarskii, The Effects of the Turbulent Atmosphere on Wave Propagation, Jerusalem: Israel Program for Scientific Translations, 1971.
4. D.L. Fried, "Aperture averaging of scintillation," J. Opt. Soc. Am., Vol. 57, pp. 169-180, Feb. 1967.
5. G.E. Homstad, J.W. Strohbehn, R.H. Berger, and J.M. Henegan, "Aperture averaging effects for weak scintillations," J. Opt. Soc. Am., Vol. 64, pp. 162-165, February 1974.
6. R.W. Lee, and J.C. Harp, "Weak scattering in random media, with applications to remote probing," Proc. IEEE, Vol. 57, pp. 275-406, April 1969.
7. A. Ishimaru, "Fluctuations of a beam wave propagating through a locally homogeneous medium," Radio Sci., Vol. 4, pp. 375-406, April 1969.
8. C.L. Rufenach, "Power-law wavenumber spectrum deduced from ionospheric scintillation observations," J. Geophys. Research, Vol. 77, pp. 4761-4772, Sept. 1972.
9. P.L. Dyson, J.P. McClure, and W.B. Hanson, "In situ measurements of the spectral characteristics of F region ionospheric irregularities," J. Geophys. Research, Vol. 79, pp. 1497-1502, April 1974.
10. T.W.J. Unti, M. Neugebauer, and B.E. Goldstein, "Direct measurements of solar-wind fluctuations between 0.0048 and 13.3 Hz," Astrophys. J., Vol. 180, pp. 591-598, March 1973.
11. D.N. Matheson and L.T. Little, "Radio scintillations due to plasma irregularities with power law spectra: the interplanetary medium," Planet. Space Sci., Vol. 19, pp. 1615-1624, 1971.
12. R.S. Lawrence and J.W. Strohbehn, "A survey of clear-air propagation effects relevant to optical communications," Proc. IEEE, Vol. 58, pp. 1523-1545, October 1970.
13. C.L. Rino, "Some new results on the statistics of radio wave scintillation, B. Scattering from locally homogeneous irregularity layers," (submitted for publication to J. Geophys. Research, 1974).
14. A.D. Wheelon, "Backscattering by turbulent irregularities: A new analytical description," Proc. IEEE, Vol. 60, March 1973, pp. 252-265.
15. J.V. Evans, "Millstone Hill radar propagation study: scientific results - part II," MIT Lincoln Laboratory Technical Rept. 509, Nov. 1973.
16. S. Silver, Microwave Antenna Theory and Design, New York: Dover Pub., Inc., 1965, p. 194.
17. G.C. Valley, "Angular jitter in an amplitude comparison monopulse radar due to turbulence," (submitted for publication IEEE Trans. Antennas Propagat., 1974).
18. J.H. Pope and R.B. Fritz, "High latitude scintillation effects on very high frequency (vhf) and S-band satellite transmissions," Indian J. of Pure and Appl. Phys., Vol. 9, August 1971, pp. 593-600.
19. A.W. Wernik and C.H. Liu, "Ionospheric irregularities causing scintillation of GHz frequency radio signals," J. of Atmospheric and Terrestrial Physics, Vol. 36, pp. 871-879.

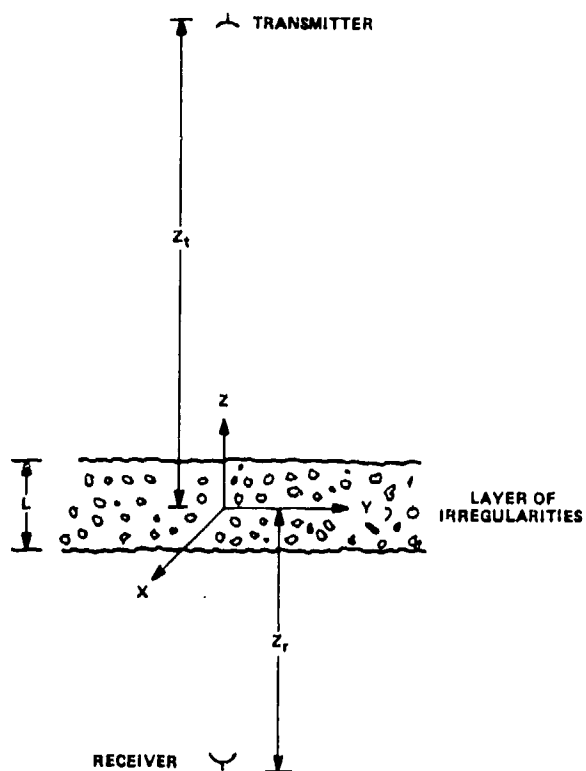


Fig. 1 The generic problem. A spherical wave transmitter and microwave receiver separated by a turbulent layer of irregularities.

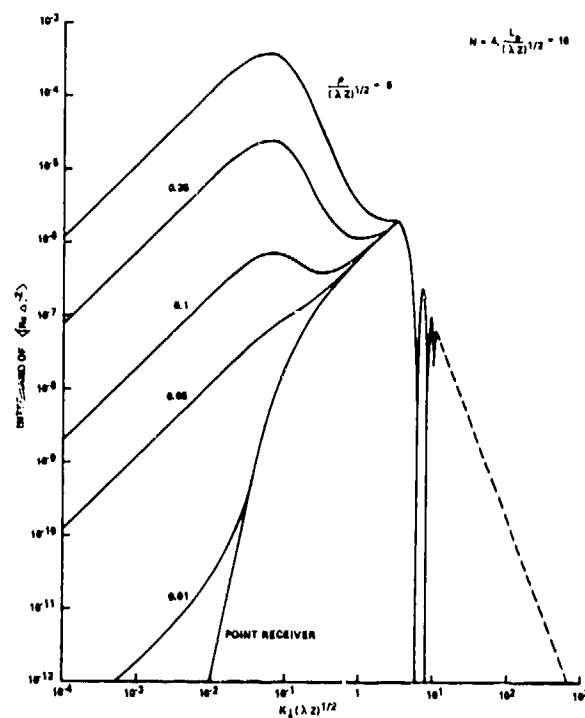


Fig. 2 The integrand of  $\langle \text{Re} \Delta \rangle^2$  versus  $K_1(\lambda Z)^{1/2}$  for selected values of  $\rho/(\lambda Z)^{1/2}$  for spectral index  $N = 4$  and  $L_0/(\lambda Z)^{1/2} = 10$ .

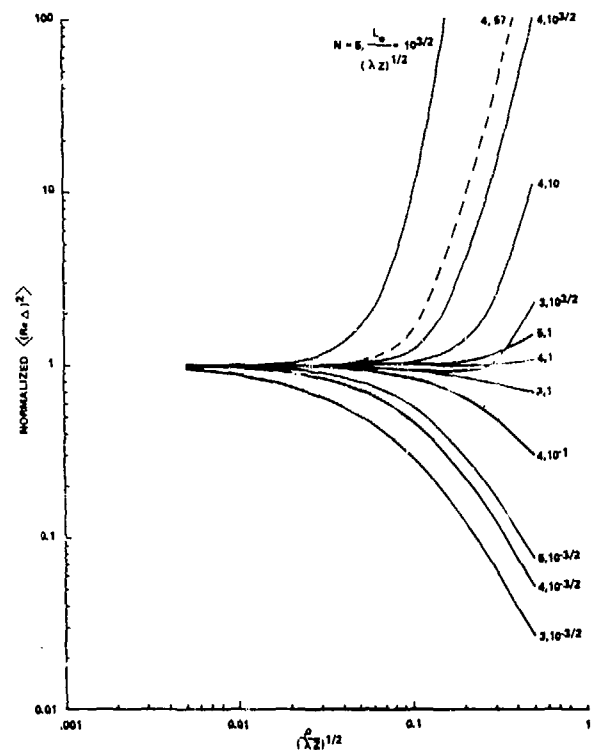


Fig. 3 The in-phase variance  $\langle (\text{Re} \Delta)^2 \rangle$  ( $N, L_0 / (\lambda Z)^{1/2}, \rho / (\lambda Z)^{1/2}$ ) divided by the normalization value  $\langle (\text{Re} \Delta)^2 \rangle (N, L_0 / (\lambda Z)^{1/2}, 0)$  for selected values of  $N$  and  $L_0 / (\lambda Z)^{1/2}$ .

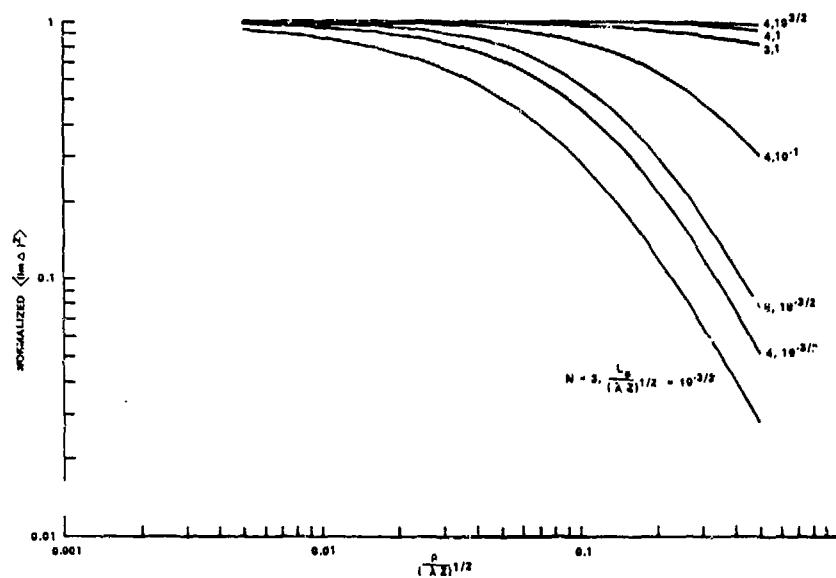


Fig. 4 The quadrature-phase variance  $\langle (\text{Im} \Delta)^2 \rangle$  ( $N, L_0 / (\lambda Z)^{1/2}, \rho / (\lambda Z)^{1/2}$ ) divided by the normalization value  $\langle (\text{Im} \Delta)^2 \rangle (N, L_0 / (\lambda Z)^{1/2}, 0)$  for selected values of  $N$  and  $L_0 / (\lambda Z)^{1/2}$ .

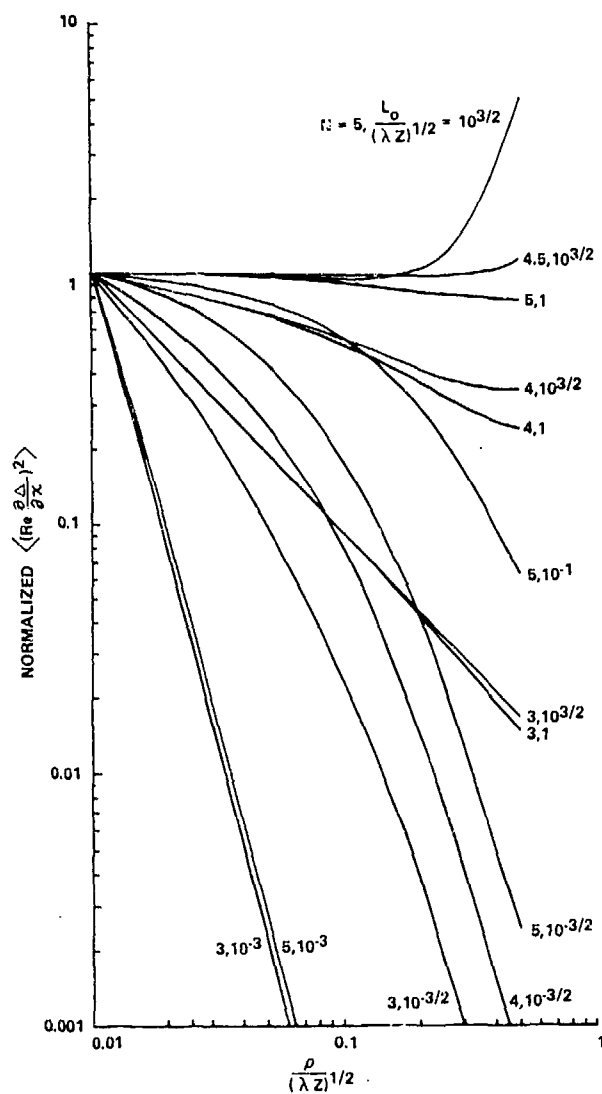


Fig. 5 The variance  $\langle \text{Re} \frac{\partial \Delta}{\partial x} \rangle^2$  ( $N, L_0/(\lambda Z)^{1/2}, \rho/(\lambda Z)^{1/2}$ ) divided by the normalization value  $\langle \text{Re} \frac{\partial \Delta}{\partial x} \rangle^2 (N, L_0/(\lambda Z)^{1/2}, .01)$  for selected values of  $N$  and  $L_0/(\lambda Z)^{1/2}$ .

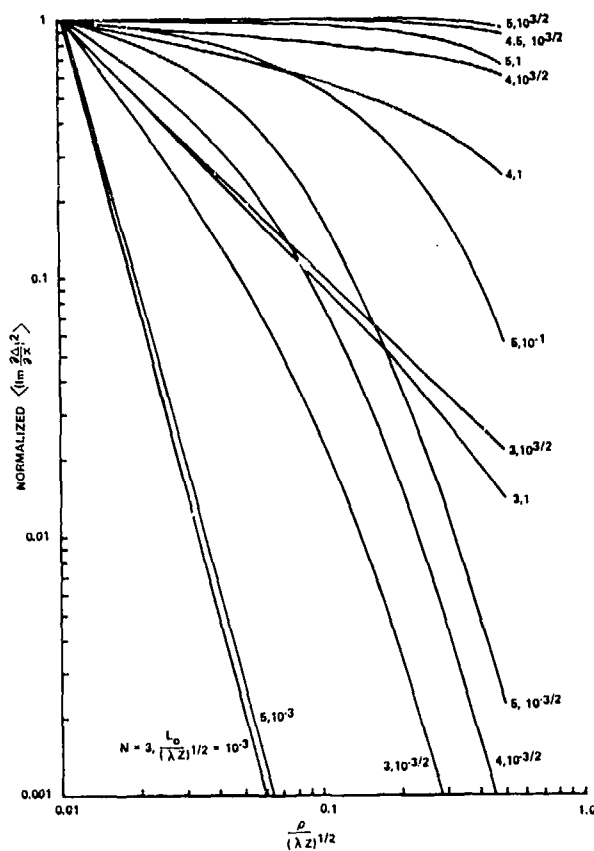


Fig. 6 The variance  $\langle \text{Im} \frac{\partial \Delta}{\partial x} \rangle^2$  ( $N, L_0/(\lambda Z)^{1/2}, \rho/(\lambda Z)^{1/2}$ ) divided by the normalization value  $\langle \text{Im} \frac{\partial \Delta}{\partial x} \rangle^2 (N, L_0/(\lambda Z)^{1/2}, .01)$  for selected values of  $N$  and  $L_0/(\lambda Z)^{1/2}$ .

## OBSERVATIONS OF H.F. SCATTER FROM F-REGION IRREGULARITIES

D.W. CORNELIUS, K.H. JOYNER, P.L. DYSON and E.C. BUTCHER  
LA TROBE UNIVERSITY,  
BUNDOORA, AUSTRALIA, 3083

### ABSTRACT

This paper reports observations which clearly show that at mid-latitudes scattering by F-region irregularities can be an important propagation mode at H.F.. Rate of change of phase path (Doppler Shift) measurements of CW signals on 4.5 and 7.5 MHz were recorded over a nearly vertical incidence path (transmitter and receiver separated by 40km) and an ionosonde was operated nearby. Signals from the CW transmitters were received via the ionosphere even when the F-region critical frequency was less than 4.5 MHz so that the ionosphere could not reflect either 4.5 or 7.5 MHz signals in the normal way. The Doppler records showed that at these times an unusually large number of signals with a wide range of Doppler shifts were being received. The characteristics of the signals indicates that they are due to scattering by F-region irregularities nearly overhead rather than large off-angle F-region reflections or reflections from sporadic E. This scattering phenomena has been observed on frequencies above the critical frequency when there was no spread F on the ionograms but it is also observed on frequencies less than the critical frequency when spread F is present.

### INTRODUCTION

Scattering of VHF radio waves by ionospheric irregularities has been observed in both the equatorial (Cohen and Bowles, 1961; Calvert and Cohen, 1961) and polar regions (Owren, 1963; Frihagen, 1972). At H.F. frequencies scattering has also been observed at high latitudes (Bates, 1960). Consequently it has been suggested that scattering is the mechanism which produces spread F (Calvert and Cohen, 1961; Cohen and Bowles, 1961) although alternative mechanisms involving reflection from distortions in the

electron density contours have been suggested (Bowman, 1960; King, 1970). A major problem in deciding on the correct spread F mechanism is the difficulty of conducting experiments at H.F. frequencies which uniquely distinguish between reflection and scattering. In this paper observations from several ionosondes and a H.F. Doppler sounder system (Watts and Davies, 1960) operated over a near vertical incidence path are presented. The results clearly show that scattering is responsible for signals received by the Doppler system after the F-region critical frequencies have dropped below the equivalent vertical frequency used in the Doppler experiment. Spread F is sometimes present when the scattering occurs so that irregularities with dimensions  $\sim \lambda/2$  can be present in the ionosphere when spread F occurs. However it is not possible to determine whether these irregularities are in fact responsible for the spread F or whether the spread F is produced by reflections from larger irregularities which happen to be present in the ionosphere simultaneously.

The time rate of change of phase path of two CW standard transmissions on 7.5 and 4.5 MHz, was measured. The receiving station at La Trobe University (near Melbourne) was 40km from the transmitters so that reflection from the F-region occurred at nearly vertical incidence and the equivalent vertical frequencies differed from the transmitted frequencies by less than 1%. One receiver (without A.G.C.) was used to present the phase changes as instantaneous frequency shifts (Doppler shift) using the method described by Davies and Baker (1966). Both the 7.5 and 4.5 MHz signals were analyzed in this way. A second receiving system (with A.G.C.) measured the continuous change in phase path length of the 4.5 MHz transmission (ordinary mode and extraordinary mode separately). The phase of the 100 KHz output of the receiver was compared with



the phase of the local stable oscillator and the beats were counted and sampled digitally each minute. This system also provided signal amplitude data by monitoring the A.G.C. voltage on chart. A vortical incidence C-4 ionosonde was located at Beveridge, some 30km from the receiving station, and provided routine ionospheric data. Ionosonde observations at Hobart and Canberra were also used.

#### OBSERVATION AND INTERPRETATION

Over a period of several months it has been noted that whenever the F-region critical frequency dropped below the equivalent vertical frequency of the CW transmissions, considerable signal strengths were still received via ionospheric paths. An example is given in Fig. 1(a) which shows critical frequencies for the local station and for Canberra and Hobart for the night of the 2nd and 3rd of October, 1973. It is apparent that during the night there were periods when the critical frequencies and  $f_{xI}$  fell below both 7.5 and 4.5 MHz so that neither 7.5 or 4.5 MHz could propagate over the experimental path by simple ionospheric reflection. However during these times appreciable signals were still received. Fig. 1(b) is a plot of the variation in mean signal strength of the 4.5 MHz extraordinary echo for the whole night and it is apparent that the mean signal strength was always above a few microvolts even after  $f_{xI}$  had fallen below 4.5 MHz. Signal strength recordings on 7.5 MHz show similar results in that an appreciable signal was still received after  $f_{xI}$  fell below 7.5 MHz. Fig. 2 shows parts of the actual signal strength record (4.5 MHz, extraordinary) before and after  $f_{xI}$  fell through 4.5 MHz. In the earlier part of the record when  $f_{xI} > 4.5$  MHz, the signal strength was high and only slowly varying, however, the later part of the record shows that when  $f_{xI} < 4.5$  MHz the signal strength was rapidly fluctuating and had a lower mean value. This is further indication that different propagation modes occurred during the two periods.

The 4.5 and 7.5 MHz Doppler records for the times when  $f_{xI}$  was near 7.5 MHz in the evening and the following morning are shown in Fig. 3. At the beginning of the evening record a number of signals were received on 7.5 MHz including a strong continuous signal (normal F region mode) which was present until approximately 2044 LT. Thereafter the number of signals received at any instant increased but, except for the ground wave at zero Doppler shift, the duration of individual signals was only

about 10 seconds. In the case of the morning record, many signals of short duration were received until 0725 LT when the number of received signals decreased drastically and a steady continuous signal (other than the ground wave) began to be received. The times of transition agree well with the times when  $f_{xI}$  moved through 7.5 MHz for the local ionosonde station as shown in Fig. 1(a) so that the signals received on 7.5 MHz from 2044 to 0725 LT did not result from normal F-region reflections. During this period, the short duration of the individual signals indicates that there were frequent discontinuous changes occurring in the propagation paths. Thus it is not surprising that the signal strength fluctuates rapidly during this time. These features suggest that while  $f_{xI}$  was below 7.5 MHz, the signals received on 7.5 MHz were the result of coherent scattering from irregularities in the F-region. This deduction is further supported by the 4.5 MHz record (Fig. 3) which shows that a normal ionospheric reflection still occurred at this frequency when scattering began and ended on 7.5 MHz. This also indicates that the scattering irregularities were initially formed at or above the  $F_2$  peak.

The above interpretation in terms of scattering is strengthened by the observations shown in Fig. 4. These were made when  $f_{xI}$  was 6.4 MHz (see Fig. 1(a)) and as would be expected the 4.5 MHz Doppler record indicates a normal ionospheric reflection whereas the 7.5 MHz indicates that many signals were being received simultaneously. The variation with time of the 4.5 MHz Doppler record is indicative of an F-region travelling ionospheric disturbance (T.I.D.) (e.g. Georges, 1968). The 7.5 MHz Doppler record shows a similar overall variation even though at any instant there is a large variation in the Doppler shifts of the many signals received. In fact the overall variations in the Doppler shifts on the two frequencies have the same period and are in phase, (note that in Fig. 4, positive Doppler shifts are measured downwards on 7.5 MHz whereas on 4.5 MHz they are measured upwards). Hence both the 4.5 MHz and 7.5 MHz signals must have arrived at similar zenith angles and it may be shown that for the example given in Fig. 4, the zenith angles are less than about  $12^\circ$  (Cornelius et. al., 1975). Thus if the signals at 7.5 MHz propagated via the F region, they must have been scattered because with an  $f_{xI}$  of 6.4 MHz, the ionosphere could not support a normal

reflection on 7.5 MHz at these small zenith angles.

So far in our interpretation we have only considered purely F-region phenomena primarily because of the frequencies involved. Further support for an F-region propagation mode is given by Fig. 1(c) where we see that on the night presented, relatively large phase path variations typical of the F-region occurred throughout the night. The ground wave was present at times at zero Doppler shift (see Fig. 3), however, at no time during this night could the reception of 4.5 MHz be explained in terms of ground wave propagation alone because, as Fig. 1(c) shows, variations in phase height occurred throughout the whole night. Another alternative explanation might be that the signals, rather than being scattered from the F-region, were in fact reflected by sporadic E. Sporadic E was visible on the local ionograms from time to time during the night of October 2-3, 1973, but foEs did not go above 4.5 MHz. This does not definitely exclude reflections from partially reflecting sporadic E because the CW Doppler system is much more sensitive than the Beveridge ionosonde (Cornelius et. al., 1975). Thus it is possible that the Doppler system could have detected echoes from weakly reflecting sporadic E which did not produce echoes on the ionograms. However there are reasons for excluding this explanation. Apart from the F-region characteristics of the phenomenon already discussed (i.e. T.I.D. periods, commencement often coinciding with f<sub>xi</sub> dropping below the CW Doppler frequency), when partially reflecting sporadic E is observed by the ionosonde, the Doppler records change in character when foEs become greater than the CW Doppler frequency. An example is shown in Fig. 5. Between 0015 and 0030 LT on 6 May, 1974 foEs increased from 3.2 MHz to 4.8 MHz. At 0026 LT on the 4.5 MHz Doppler record, there is a distinct decrease in the number of signals received and this is undoubtedly the result of foEs rising above 4.5 MHz. The decrease in the number of signals received is to be expected if prior to 0026 LT signals were being received by scattering from the F-region, because the onset of partially reflecting sporadic E would tend to decrease the strength of any F-region signals.

#### DISCUSSION

Although similar CW Doppler observations have been made before by others (Baker et. al., 1968; Toman, 1970) the evidence for scattering via

the F-region as opposed to other possible propagation modes has not been discussed in detail. The reasons for this appear to be that either the CW transmitters were of relatively small powers or very oblique propagation paths were used making interpretation difficult (Cornelius et. al., 1975).

In order for scattering to occur, irregularities with sizes equal to half the radio frequency wavelength must exist in the F-region. It follows that the observations of scattering at 4.5 and 7.5 MHz reported here imply irregularities of sizes of 30 and 20 metres. Coherent scattering at 50 MHz is often observed by the Jicamarca Radar so that irregularities as small as 3 metres often occur at the equator (Farley et. al., 1970). Satellite measurements (Dyson et. al., 1974) have shown that generally at all latitudes, irregularities in the F region have sizes extending down at least 70m (the resolution of the satellite experiment). Thus, these observations of mid-latitude irregularities as small as 20 metres in size are not inconsistent with other observations.

The Doppler shift of each returned signal is the sum of the phase path changes due to the time rate of change of refractive index along the ray path and motion of the reflecting surface in the ray direction (e.g. Bennett, 1968). If the time changes of the medium are due purely to ionospheric motions such that the refractive index contours all have the same velocity, the Doppler shift is simply related to the velocity of the reflecting surface (Dyson, 1975). However, when small scale irregularities which can cause scattering are present it is likely that ionospheric motions will not be uniform and also that other processes such as ionization loss might produce changes in refractive index along the ray path. It is therefore unlikely that the spread in Doppler shifts observed during scattering is simply due to the scattering centres having different velocities.

Nevertheless, the observation presented in Fig. 4 shows that when a T.I.D. moves through the ionosphere, the Doppler record for a frequency at which scattering occurs exhibits the effects of the T.I.D.'s motion. Thus the scatterers move with the background ionosphere during the passage of a T.I.D..

Spread F was not observed at the times of the Doppler records presented in this paper but this may be a consequence of the Doppler sounder being

an order of magnitude more sensitive than the ionosonde. When spread F is present on Beveridge ionograms the scattering effects on the Doppler records are observed at frequencies less than  $f_{xI}$ . Thus it appears that the scattering is related to spread F and the significance of this is being currently investigated. Consequently the results of this paper should not be interpreted as excluding reflections from large scale "ripples" in the ionosphere as the cause of spread F as suggested by Bowman (1960). Rather they should be taken as evidence that irregularities of  $\sim 20$ -30 metres in size occur in mid-latitude ionosphere and are present when spread F occurs, irrespective of whether they are the cause of spread F appearing on ionograms.

#### REFERENCES

- Baker, D.M., Chang, N., Davies, K., Donnelly, R.F. and Jones, J.E. (1968), ESSA Technical Report, ERL 78-SDL 1.
- Bates, H.F. (1960), J. Geophys. Res. 65, 1693.
- Bennett, J.A. (1968), Aust. J. Phys. 21, 259.
- Bowman, G.G. (1960), Planet. Space Sci. 2, pp. 133-156.
- Calvert, W. and Cohen, R. (1961), J. Geophys. Res. 66, 3125.
- Cohen, R. and Bowles, K.L. (1961), J. Geophys. Res. 66, 1081.
- Cornelius, D.W., Joyner, K.H., Dyson, P.L. and Butcher, E.C. (1975), J. Atmos. Terr. Phys. (Accepted for publication).
- Davies, K. and Baker, D.M. (1966), Radio Sci. 1, 545.
- Davies, K. (1969), "Ionospheric Radio Waves", Blaisdell.
- Dyson, P.L., McClure, J.P. and Hanson, W.B., (1974), J. Geophys. Res. 79, 1497.
- Dyson, P.L. (1975), J. Atmos. Terr. Phys. (Accepted for publication).
- Farley, D.T., Balsley, B.B., Woodman, R.F. and McClure, J.P. (1970), J. Geophys. Res. 75, 7199.
- Frihagen, J. (1972), Agard Conference Proceedings, No. 97.
- Georges, T.M. (1967), ESSA Technical Report, IER 57-ITSA 54.
- Georges, T.M. (1968), J. Atmos. Terr. Phys. 30, 735.
- King, G.A.M. (1970), J. Atmos. Terr. Phys. 32, 209.
- Owren, L. (1963), Proceedings of the International Conference on the Ionosphere, Inst. of Phys. and Phys. Soc., 277.
- Toman, X. (1970), Conference Proceedings, Agard No. 33, 511.
- Watts, J.M. and Davies, K. (1960), J. Geophys. Res. 65, 2295.

#### ACKNOWLEDGEMENTS

This work is supported by the Radio Research Board and the Australian Research Grants Committee by grants to Prof. K.D. Cole, Drs. E.C. Butcher, P.L. Dyson, E.A. Essex and P.R. Hammer. Two of us (D.W.C. and K.H.J.) are grateful holders of Commonwealth Post-graduate Scholarships. We would like to thank Dr. P.R. Hammer for assistance in the design of equipment, the Australian Post Office Research Laboratories for the loan of a spectrum analyzer and Dr. E.A. Essex for helpful discussions.

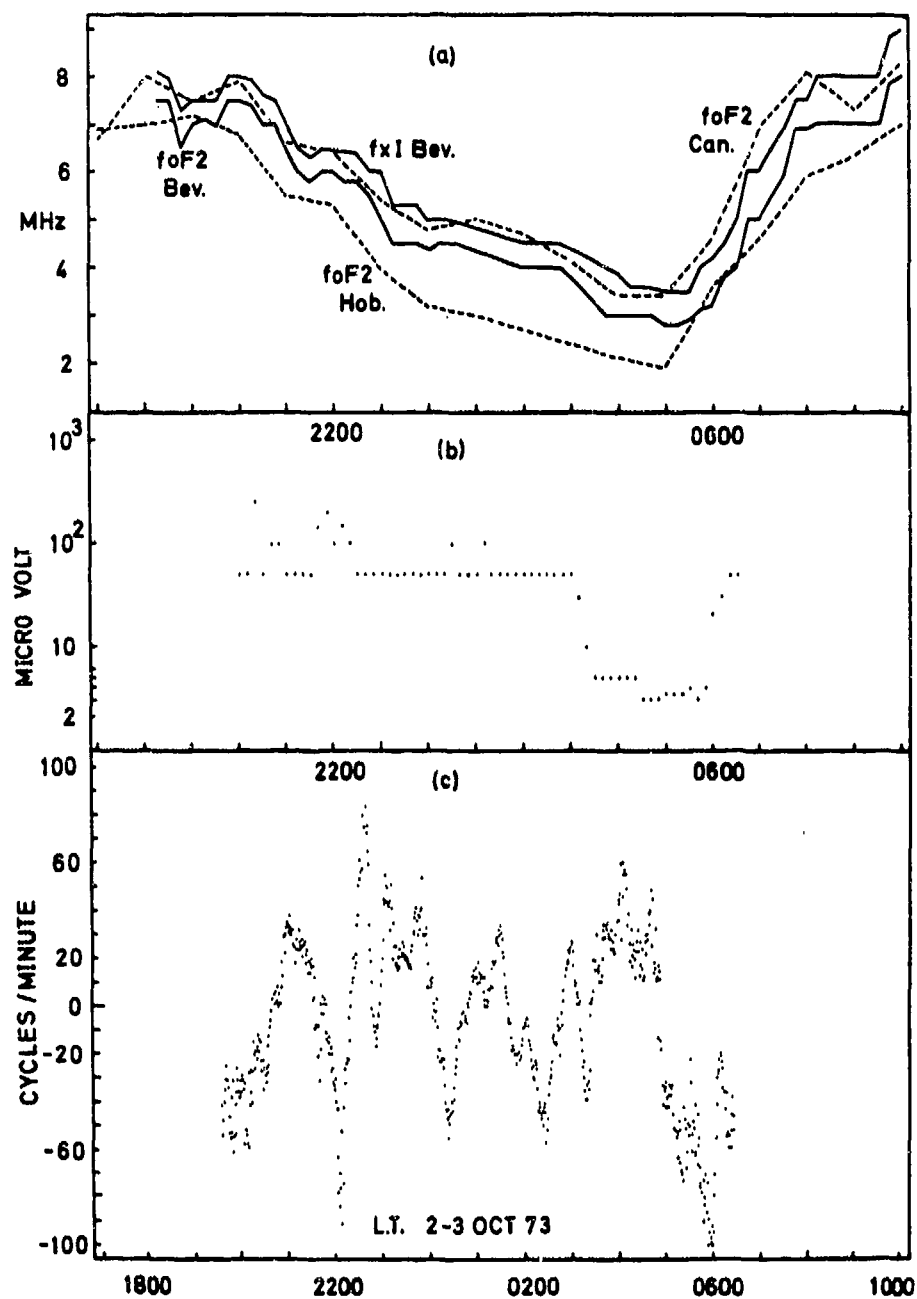


Figure 1 — (a)  $f_oF_2$  and  $f_xI$  data are shown for the local station (Beveridge) and the other two nearest stations for the night 2-3 October, 1973. (b) Mean signal strength of the 4.5 MHz extraordinary mode received at La Trobe for the night 2-3 October, 1973. (c) Phase height changes on 4.5 MHz extraordinary mode received at La Trobe on the night 2-3 October, 1973.

# SIGNAL STRENGTH 4.5 MHz E RAY

10<sup>4</sup>  
10<sup>3</sup>  
10<sup>2</sup>  
micro 100 -  
volt 5 -  
1 -

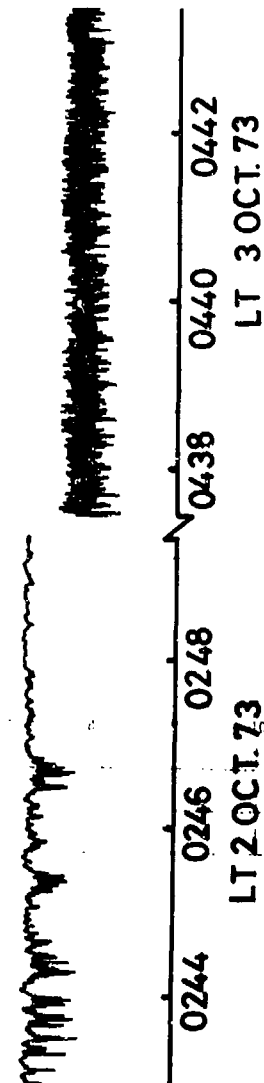


Figure 2 - Actual chart record of signal strength (4.5 MHz extraordinary mode) before and after fx1 fell through 4.5 MHz. Note the lower strength and rapid fluctuations in the strength of the scattered signal.

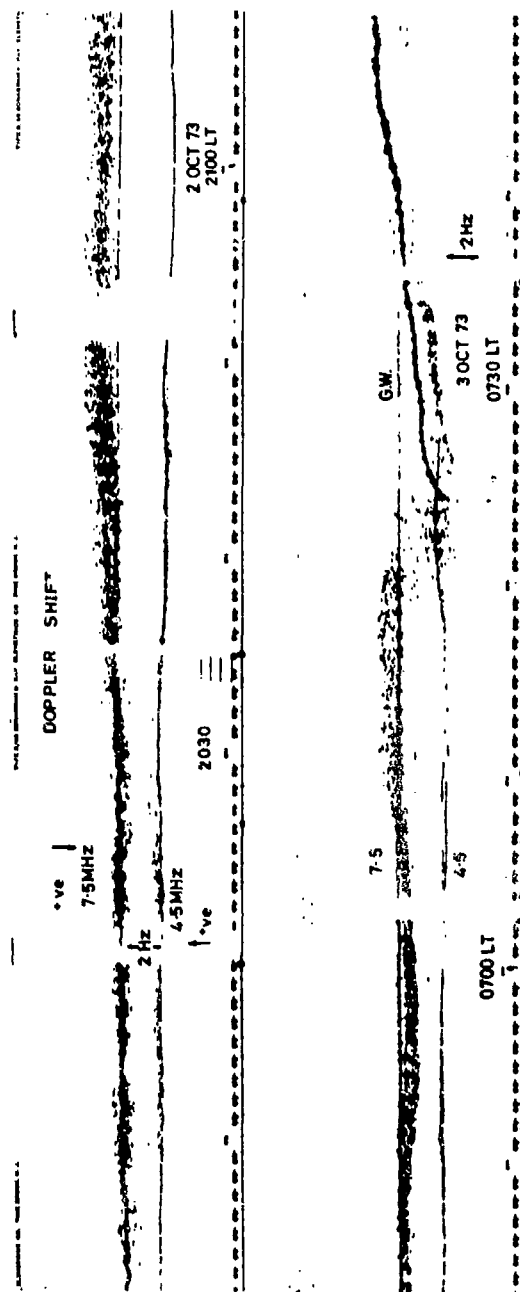


Figure 3 — Doppler record of 7.5 and 4.5 MHz signals in the evening (L.T.) 2 October, 1973. When f<sub>xi</sub> fell through 7.5 MHz and in the morning (L.T.) of 3 October, 1973 when f<sub>xi</sub> increased above 7.5 MHz.

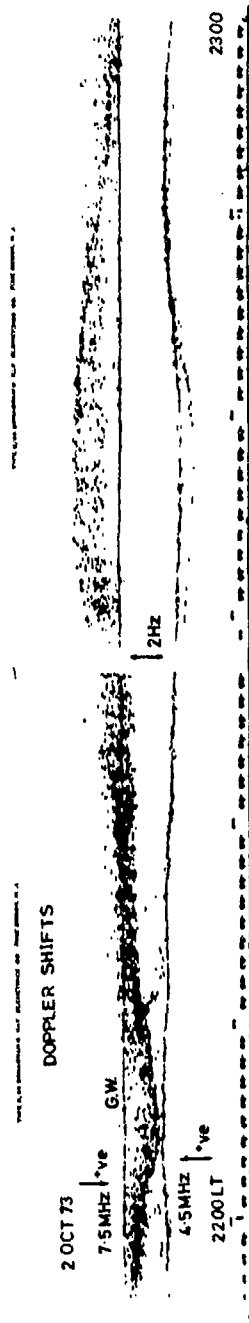


Figure 4 — Doppler record showing T.I.D. in 4.5 MHz reflected signal (fxl at this time was 6.4 MHz) and same T.I.D. in 7.5 MHz scattered signal

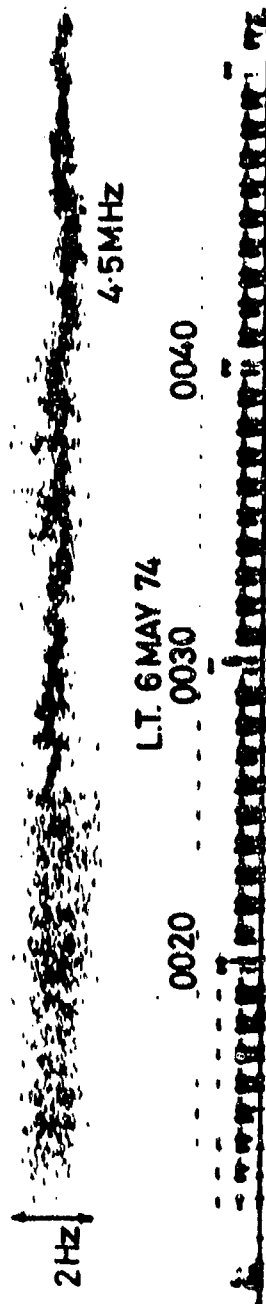


Figure 5 -- Doppler record of 4.5 and 7.5 MHz on 6 May, 1974 showing effects on propagation before and after foEs increased above 4.5 MHz.



COMPARISON OF SIMULTANEOUS IONOSPHERIC  
MEASUREMENTS DURING AURORAL CONDITIONS\*

Glenn D. Falcon

ABSTRACT

Various ground-based techniques were operated near Fairbanks, Alaska to monitor ionospheric irregularities during auroral disturbances; these included a partial reflection sounder, the Chatanika incoherent scatter radar, a VLF multifrequency sounder, and an ionosonde. The values of electron density in the lower ionosphere determined by the partial reflection sounder during quiet and aurorally disturbed conditions are presented, and compared with simultaneous measurements of the other techniques listed above.

\*Paper unavailable as of printing.

RAY TRACING THROUGH REALISTIC IONOSPHERE GRAVITY WAVE MODELS :  
A COMPARISON WITH EXPERIMENTAL DATA FROM SEVERAL DIFFERENT TECHNIQUES.

E.A. ESSEX  
Division of Theoretical and Space Physics,  
La Trobe University,  
Bundoora, Vic. 3083, Australia.

ABSTRACT

Model ionospheres using experimentally measured parameters are constructed from a realistic medium scale ionospheric gravity wave model. The ray tracing technique is then employed to simulate the results of the original experimental measurements from the model ionospheres. The technique is found to be limited by the gravity wave model which uses only one gravity wave period in the construction of the ionospheric model whereas realistic ionospheres contain in general a spectrum of medium scale gravity waves.

1. INTRODUCTION

Travelling ionospheric disturbances (TIDs) have been observed by a large number of workers using many different techniques since the pioneering work of Munro (1958). However it was not until the theoretical work of Hines (1960) and Hooke (1968) that the nature of these disturbances was interpreted successfully as wave like fluctuations of the electron density induced by gravity waves in the neutral atmosphere. There are two major classes of TIDs, large scale and medium scale. (Georges, 1968). The large scale waves are generally associated with magnetic storms whereas the medium scale waves occur much more frequently, their sources being uncertain.

Many techniques have been used in the past and are being used to detect the presence of these TIDs. Depending on the technique and the ionospheric parameter measured, various properties of the TIDs can be determined. The intent of this paper is to report the results of a simulation of the results of some of these techniques using ray tracing techniques. The experimental techniques to be simulated include high

frequency doppler, group and phase paths at oblique incidence, vertical incidence ionograms, total electron content measurements using the Faraday rotation of the plane of polarization of a signal from a VHF beacon, and the refraction of a signal from a VHF beacon on a geostationary satellite.

Before the ray tracing studies can be performed a suitable ionospheric model of TIDs is required. This is provided by the medium scale TID model as described by Francis (1973). Experimentally measured TID parameters were inserted in the model and a time varying ionospheric model generated for the ray tracing program.

2. SIMULATION METHOD

(a) Travelling Ionospheric Disturbance Model

The Francis (1973) TID model was used to simulate a realistic ionosphere. This model differs from previous models by including dissipation (viscosity and thermal conductivity) and by using a realistic sound speed profile throughout the thermosphere. The model assumes that the wave dependence on the time  $t$  and horizontal co-ordinate  $x$  is a sinusoidal function of  $\omega t - k_x x$ . It derives the vertical profile  $x$  by solving the coupled Navier-Stokes and electron continuity equations. The basic inputs to the model are the wavelength, period, amplitude and azimuth of propagation of the neutral gravity wave underlying the TID which is to be modelled. The ambient ionosphere, specified by an  $\alpha$  Chapman profile (unless otherwise indicated) is used to compute the electron density as a function of space and time for the TID perturbed ionosphere.

### (b) Ray Tracing Program

The three dimensional ray tracing computer program developed by Jones (1968) was used in this work. Previous ray tracing simulation of HF radio measurements of ionospheric disturbances have been made by Detert (1968). He used a two dimensional Snell's Law digital computer ray tracing program to simulate the effects of large travelling ionospheric disturbances on oblique incidence high frequency radio transmissions. He calculated the phase and group paths, the received elevation angle of arrival and the Doppler shift variations produced by the passage of representative disturbance models through the transmission paths.

The Jones ray tracing program has been used by Georges (1969) in an attempt to simulate Doppler results from a model of ionospheric disturbances. However the electron density contours were constructed by introducing a wavelike model irregularity into the profile. The results presented in this paper use a realistic gravity wave model of the neutral atmosphere with coupling to the ionized medium.

### (c) Experimental Data

The aim of the ray tracing was to simulate experimentally measured ionospheric data using a realistic ionospheric TID model. To this end data from several experiments operating on two winter days in 1969 when TIDs were present were selected. The dates and times were 13 January 1969 15-19UT and 15 November 1969 16-20UT. The experimental details and results are described in another paper by Essex (1974). Briefly the experimental results to be used here were obtained from high frequency Doppler observations on 7.335 MHz at oblique incidence from the transmitter at Ottawa (geographic co-ordinates  $45^{\circ}18'N$ ,  $75^{\circ}20'W$ ) to a receiver at Bedford (geographic co-ordinates  $42^{\circ}27'30"N$ ,  $71^{\circ}20'W$ ), three spaced vertical incidence ionosondes at Hanover (geographic co-ordinates  $45^{\circ}41'30"N$ ,  $72^{\circ}11'18"W$ ), Highgate Springs (geographic co-ordinates  $45^{\circ}00'47"N$ ,  $73^{\circ}05'11"W$ ) and Errol (geographic co-ordinates  $44^{\circ}47'30"N$ ,  $71^{\circ}07'30"W$ ) total electron content measurements at Sagamore Hill from the geostationary satellite ATS-3, the four hundred and twenty kilometer subionospheric point being  $38^{\circ}42'N$ ,  $29^{\circ}70'W$  on January 13 1969, and  $38^{\circ}36'N$ ,  $67^{\circ}12'W$  on November 15 1969, geographic co-ordinates, and the refraction of the VHF beacon as

measured by a 10 km long baseline interferometer at Sagamore Hill (geographic co-ordinates  $42^{\circ}36'N$ ,  $70^{\circ}48'W$ ). See Fig. 1.

The experimental results were subjected to a spectrum analysis to determine the gravity wave periods present. The spaced ionosonde measurements yielded information on the phase velocity and direction of the TIDs from the real iso-height contours deduced from the ionograms, as well as the critical frequency of the ionosphere.

Fig. 2 is a comparison of results for three heights from one of the ionosonde stations. There is an obvious movement of power to the longer periods as the height increases.

Fig. 3 is a comparison of the results from the different experiments. Peaks below the largest peak are scaled according to 0-3, 3-6 and 6-9 db.

The only two parameters to be used in the TID simulation model which were not measured directly were the scale height  $H$  and the velocity amplitude of the neutral atmosphere gravity wave.

### 3. Results

#### (a) Oblique Incidence Group and Phase Path Simulation

Ray tracing using the three dimensional program as developed by Jones consumes a large amount of computer time. An excellent summary of the possible options of the ray tracing program and their relative accuracies and computer time has been given by Hammer (1971).

Initially it was intended to simulate vertical incidence ionograms using the TID model with the ray tracing program. This would require a large amount of computer time to generate the ionograms as the TID moved through the ionosphere. The ray tracing would be required to be performed on a continuous range of closely spaced frequencies up to the critical frequency as well as on a range of azimuthal and elevation angles around the vertical to determine which rays returned to the receiver. This process would have to be repeated on various phases of the TID as it moved through the ionosphere. Some preliminary work was performed generating the ionograms. It was found that the cusps appeared and moved through the frequency range of the ionogram as the TID passed overhead. As well the critical frequency varied

with the period of the TID inserted in the model ionosphere. These results are well known and it was decided to devote more time to oblique incidence propagation of high frequency radio waves through TID models.

As mentioned in the last section, one of the unknown parameters to be inserted into the TID model was the amplitude of the neutral atmosphere gravity wave velocity. Initially a value of around 10 metres per second was used. It was found that larger values of this parameter were required to produce ionospheric perturbations consistent with those experimentally observed. Values of the order of 50 metres per second were used. These are of the same order as the daytime neutral wind velocity as determined from experimental observations by Roble et. al. (1974).

For the oblique incidence ray tracing, the TID perturbed model was generated to cover the ionosphere between the latitude and longitude of the transmitter and the receiver up to the peak of the F region. The initial ionosphere was generated for zero phase of the TID model at around the mid-point of the ray path. Subsequent ionospheres were generated at one, two or four minute intervals as the TID moved through the ionosphere with the velocity and direction as determined by the three spaced ionosonde network.

Fig. 4 shows the results of the ray tracing for the group and phase paths through the TID perturbed ionospheres. Also shown is the reflection height. The receiver location was specified to .01 degrees of latitude and longitude in order to locate the receiver to an accuracy of less than 1 kilometer in ground range.

The variation in the azimuthal and elevation angle is also indicated in Fig. 5. The doppler frequency shift calculated from the phase path  $P$  by  $\Delta F = -\frac{f}{c} \frac{dP}{dt}$  is shown in Fig. 6.

The parameters used were as follows:  $f_oF_2 = 9.5$  MHz,  $h_mF_2 = 290$  Km,  $H = 50$  Km, horizontal velocity =  $173 \text{ ms}^{-1}$ , azimuth ( $^\circ$  geomagnetic) = 180, period = 26 mins.

The most interesting result is the phase relation between the group and phase paths. There is a slight positive shift in phase for the phase path from being in phase with the group path. Since the phase refractive index  $n$  is related to the square root of the

electron density  $N$ , by

$$n = \left\{ 1 - \frac{kN}{f^2} \right\}^{\frac{1}{2}},$$

an increase in electron density produces a decrease in the refractive index and hence a decrease in the total integral of  $n$  along the ray path, i.e. in phase path. Similarly a decrease in  $N$  produces an increase in  $n$  and an increase in the phase path length. On the other hand, the group refractive index is given by  $n_g = \frac{1}{n}$  (neglecting the geomagnetic field and collisions). Hence the group and phase paths should be out of phase. The ray tracing results can be explained in terms of a lowering of the reflection height and also of the elevation of the ray and a consequent decrease in the total integral of the group refractive index and vice versa.

The doppler shifts are consistent with the experimentally measured values which are generally less than 1 Hz for daytime measurements on 7.335 MHz over the 474 Km path.

It is emphasized that the ray tracing results reported above were carried out in one azimuthal direction only. Ray tracing carried out at different azimuthal directions at oblique incidence through the TID model ionosphere as well as for different velocities and directions of the TID would not necessarily yield the same result. Obviously the velocity of the TID will affect the doppler frequency shift but not necessarily the maximum deviations of the group and phase paths.

#### (b) Total Electron Content Simulation

The TID model for the total electron content simulation was generated by perturbing an undisturbed ionosphere consisting of an  $\alpha$  Chapman layer below the peak of the electron density and a variable scale height Chapman model above the peak up to a height of 1090 kilometres. The variable scale height profile  $h_s$  was calculated from the equation

$$h_s = \frac{\log h}{2.186 \times 10^{-2}} - 203.447$$

as given by Damon and Hartranft (1970) where  $h$  is the height. The ionosphere between the receiver and the 1090 kilometre sub-ionospheric point along the ray path to the satellite was calculated.

The ray tracing program was used

to obtain the electron density in steps along the ray path on 137 MHz. From this the total electron content of the ionosphere up to a height of 1090 kilometres was calculated.

The parameters used in generating the ionosphere were as follows:  
 $f_oF_2 = 10.5$  MHz,  $h_mF_2 = 290$  Km,  $H = 50$  Km,  
horizontal velocity =  $280 \text{ ms}^{-1}$ , azimuth  
( $^\circ$  geomagnetic) = 172, period = 26 mins.

Fig. 7 shows the results of the total electron content calculation. The total numbers of electrons in the equivalent vertical column as the TID moves through the ionosphere shows the same sinusoidal variation as the period inserted into the TID model. The peak electron density along the ray path for the period of 26 minutes shows a peak earlier than the peak electron content. This is probably caused by the tilt on the TID wavefront, the small wavelength of the TID and the fact that more than half of the electrons measured in the total electron content variation are above the peak. On the other hand for a longer period wave of 72 minutes, the peak electron density along the ray path leads the peak in electron content by about four minutes. The wavelength of the TID is much greater in this case and the ray path traverses the one TID oscillation for most of the path length around the peak.

The variation in the peak electron density along the ray path for the 26 minute period TID is 15%, whereas the total electron content variation is only 3%. However for the 72 minute period, the variation in the peak electron density along the ray path reaches 58% and the total electron content variation is around 7%. These values are consistent with the percentage variation in the peak electron density and the total electron content as measured experimentally for these periods

#### (c) Angle of Refraction Simulation

The TID model ionospheres calculated in the previous section were used with the ray tracing program to determine the group and phase paths of the rays at 137 MHz up to a height of 1090 kilometres at the azimuthal and elevation angle used in the previous section. A similar ray tracing was performed from a point 0.1 degrees of latitude and zero degrees of longitude from the previous point. The same azimuthal and elevation angle were used in both cases. This procedure was adopted as the accuracy required in ray tracing to a point at the top of the ionosphere with the required azimuth and elevation for

the ray to reach the geostationary satellite position would consume a huge amount of computer time. The difference in the phase paths for the two spatially separated receivers is shown in Fig. 8. The shorter period TID shows a larger variation in group and phase paths, than does the larger period TID. The difference in the group and phase paths also exhibits this behaviour. This is probably due to the larger horizontal gradients when the shorter periods are present than when longer periods are present (Elkins, 1972).

The phase path differences correspond to variations in the angle of arrival of the order of tenths of a milliradian, smaller than the experimentally observed values of the order of milliradians. This probably results from the method used to determine the phase path difference.

As well a comparison was made with the integrated total electron content of the ionosphere as calculated in the previous section. For the shorter period TID, the total electron content peak was delayed for about 9 minutes i.e.  $125^\circ$  of phase from the peak of the phase difference whereas for the longer period TID it was delayed by about  $80^\circ$  of phase. These results are not inconsistent with the simple theory which predicts a quadrature relation between the two methods of measuring TIDs (see Elkins, 1972; Webster and Lyon, 1974).

#### 4. DISCUSSION

Ionospheric data has been simulated using a realistic TID model together with ray tracing techniques. In general the model is able to reproduce results characteristic of the data from various ionospheric experimental techniques.

The simulation of group and phase paths on one hop oblique incidence paths through TIDs would provide insight into the properties of TIDs measured experimentally. Only one direction of the ray path was considered in this paper. Further studies should be carried out using various directions of the TIDs as well as a range of ray directions through the ionosphere. Of particular interest would be the measurement of the group paths.

The total electron content and refraction simulation indicate that these techniques provide a good measure of the gravity waves present in the ionosphere at the azimuthal and elevation angles considered. Obviously

the magnitude of the gravity wave perturbations measured will depend on the geometry used (see Davis, 1973).

A simple calculation of the gradient in the slant electron content along the two paths in the refraction calculation shows this to be of the order of  $10^{11}$  electrons per  $m^3$ . This is not inconsistent with the results of Elkins (1972) and Bramley (1974). Further experimental and theoretical studies are being carried out on the relation between the total electron content and the refraction effects of the ionospheric TIDs at VHF.

#### ACKNOWLEDGEMENTS

This work was performed while the author was on study leave at the Ionospheric Physics Laboratory of the Air Force Cambridge Research Laboratories. The interest and assistance provided by Dr. T.J. Elkins of the Ionospheric Radio Physics Branch of the Laboratory is gratefully acknowledged.

#### REFERENCES

- Bramley, E.N. (1974) Fluctuations in direction and amplitude of 136 MHz signals from a geostationary satellite. *J. Atmos. Terr. Phys.*, 36(9), 1503-1514.
- Damon, T.D. and F.R. Hartranft (1970) Ionospheric electron density profile model. Aerospace Environmental Support Centre Technical Memorandum 70-3, 39pp.
- Davies, M.J. (1973) The integrated ionospheric response to internal atmospheric gravity waves. *J. Atmos. Terr. Phys.*, 35(5), 929-959.
- Detert, D.G. (1968) Ray tracing simulation of HF radio measurements of large travelling ionospheric disturbances. *Radio Sci.*, 3(1), 33-42.
- Elkins, T.J. (1972) High resolution measurements of ionospheric refraction. *Space Research XII*, pp.1215-1220, Akademie-Verlag, Berlin.
- Essex, E.A. (1974) Comparison of ionospheric gravity wave periods as measured by different experimental techniques. Submitted for publication.
- Francis, S.H. (1973) Theory and models of atmospheric acoustic-gravity waves and travelling ionospheric disturbances. Bell Laboratories - Western Electric, Lincoln Laboratory (MIT), Joint Radar Propagation Study, 52pp, Whippany, N.J.
- Georges, T.M. (1968) H.F. doppler studies of travelling ionospheric disturbances. *J. Atmos. Terr. Phys.*, 30(5), 735-746.
- Georges, T.M. (1969) Effects of ionospheric motions and irregularities on HF radio propagation, in Low Frequency Waves and Irregularities in the Ionosphere, edited by N. D'Angelo, pp.137-151, D. Reidel, Dordrecht-Holland.
- Hammer, P.R. (1971) High resolution ionospheric sounding. Ph.D. Thesis, 431pp., University of Melbourne, Melbourne, Australia.
- Hines, C.O. (1960) Internal atmospheric gravity waves at ionospheric heights. *Can. J. Phys.*, 38(11), 1441-1481.
- Hooke, W.H. (1968) Ionospheric irregularities produced by internal atmospheric gravity waves. *J. Atmos. Terr. Phys.*, 30(5), 795-824.
- Jones, R.M. (1968) A three-dimensional ray-tracing computer program. *Radio Sci.*, 3(1), 93-94.
- Munro, G.H. (1958) Travelling ionospheric disturbances in the F region. *Aust. J. Phys.* 11(1), 91-112.
- Roble, R.G., B.A. Emery, J.E. Salah and P.B. Hays (1974) Diurnal variation of the neutral thermospheric winds determined from incoherent scatter radar data. *J. Geophys. Res.* 79(19), 2868-2876.
- Webster, A.R. and G.F. Lyon (1974) The observation of periodic ionospheric disturbances using simultaneous Faraday rotation and angle of arrival measurements. *J. Atmos. Terr. Phys.*, 36(6), 943-954.

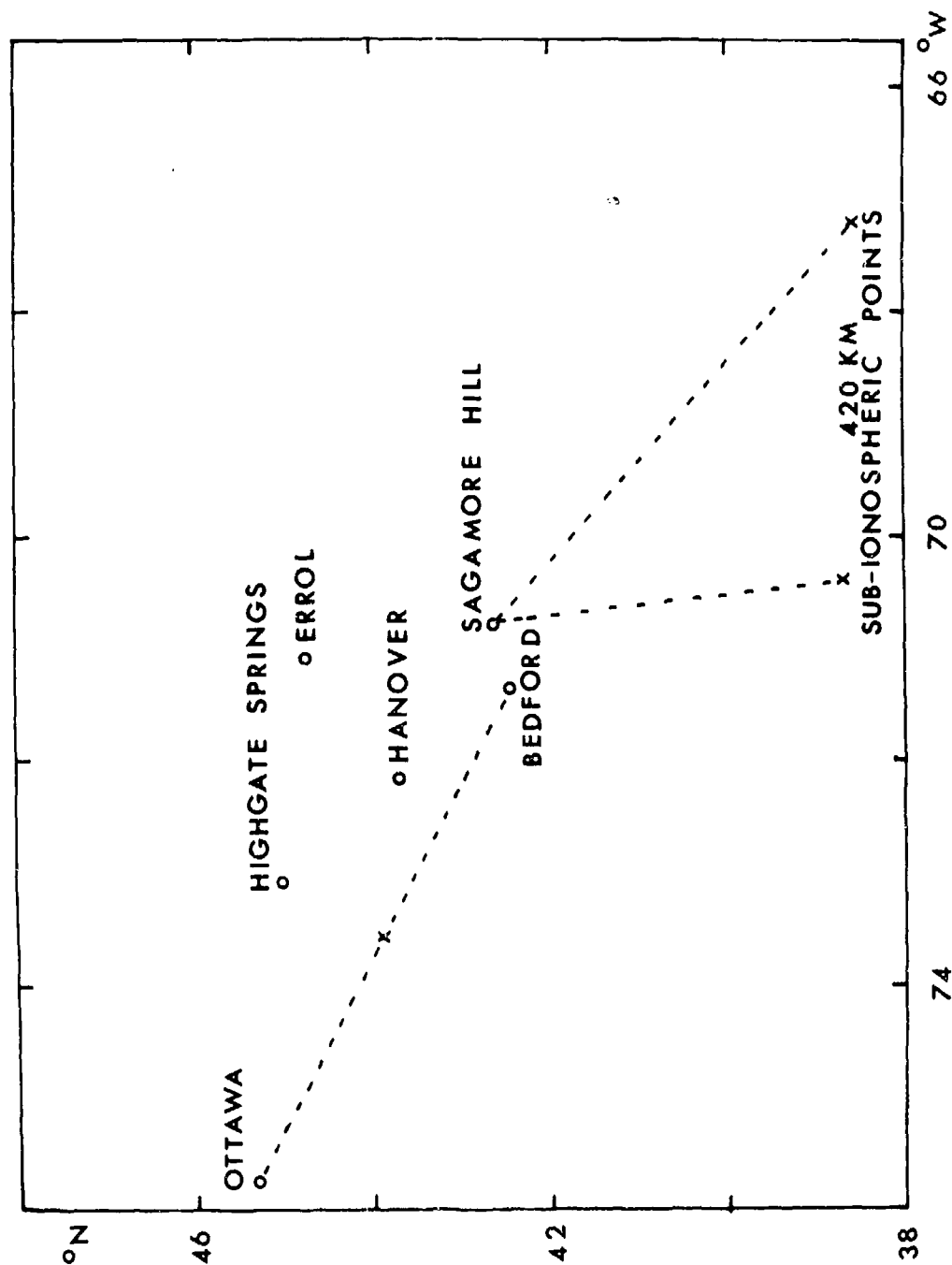


Figure 1 — Diagram showing the geographic location of the various ionospheric experiments.

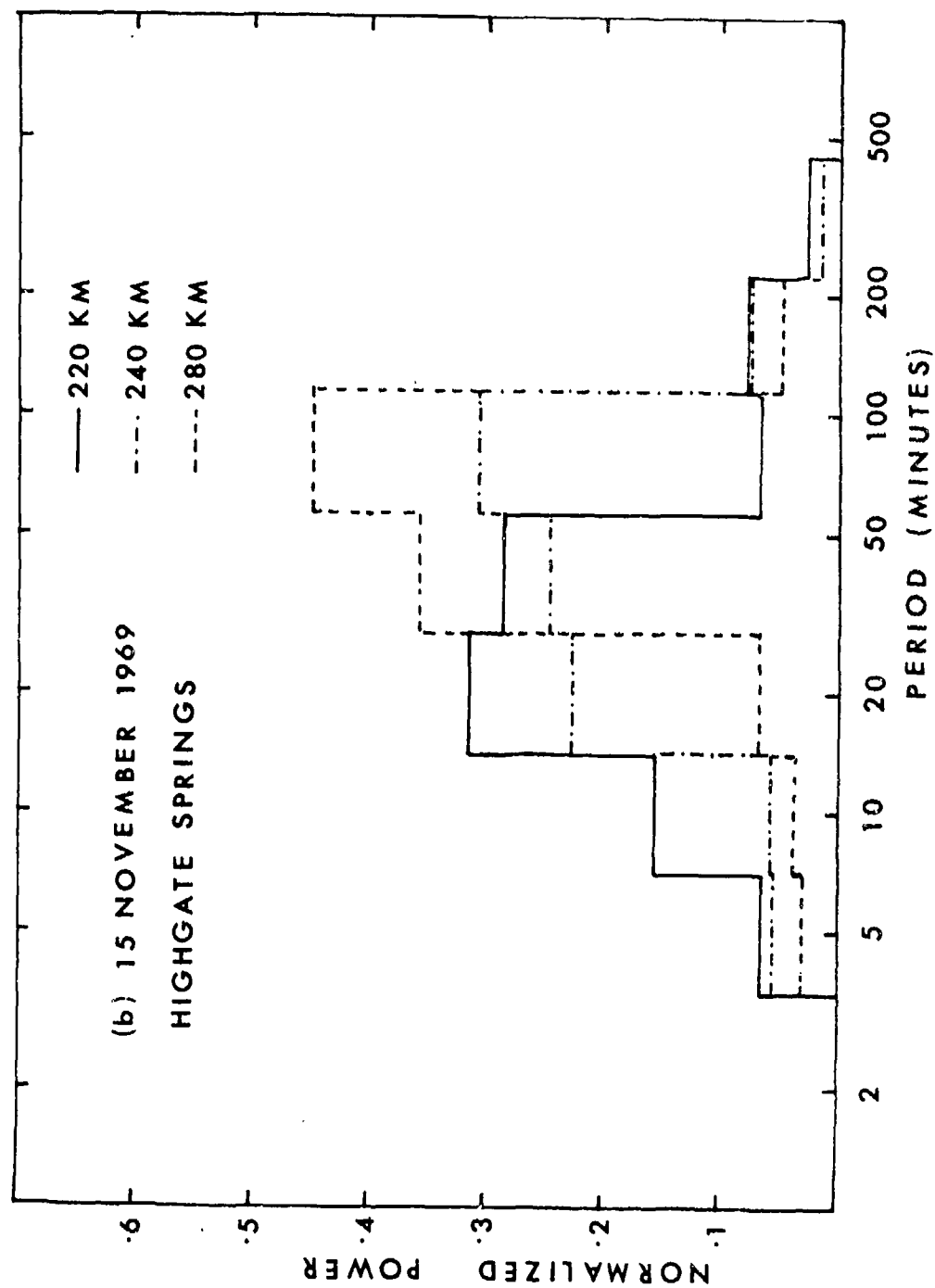


Figure 2 -- Histogram of normalized power per octave of the isohight contours from Highgate Springs ionosonde for 220, 240 and 280 kilometers for 15 November 1969, 16-20 hours UT.



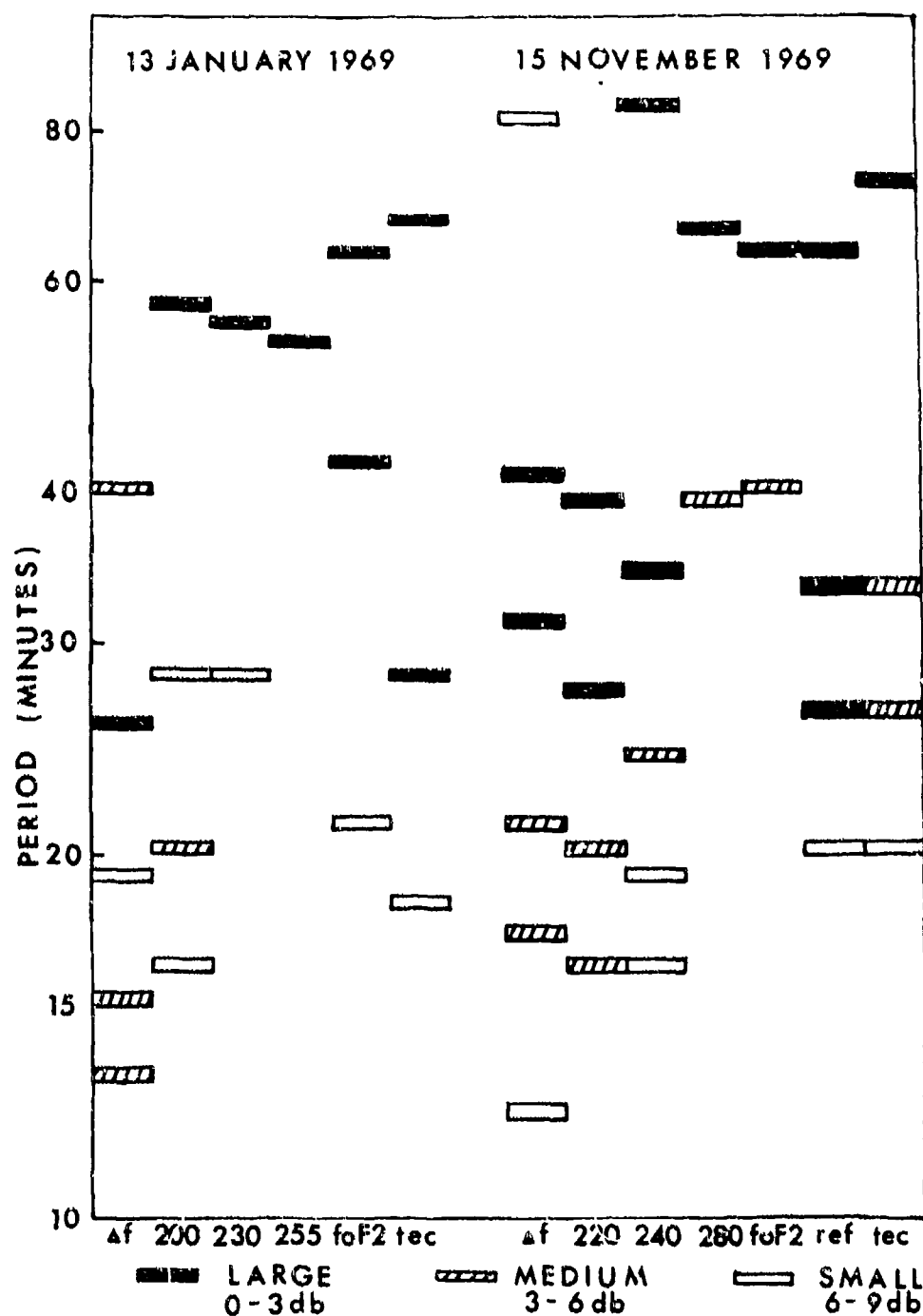


Figure 3 — Diagram showing the dominate periods present in the power spectral analysis of results from the various ionospheric experiments. The periods are graded according to 0-3db, 3-6db, 3-9db of power below the largest peak.

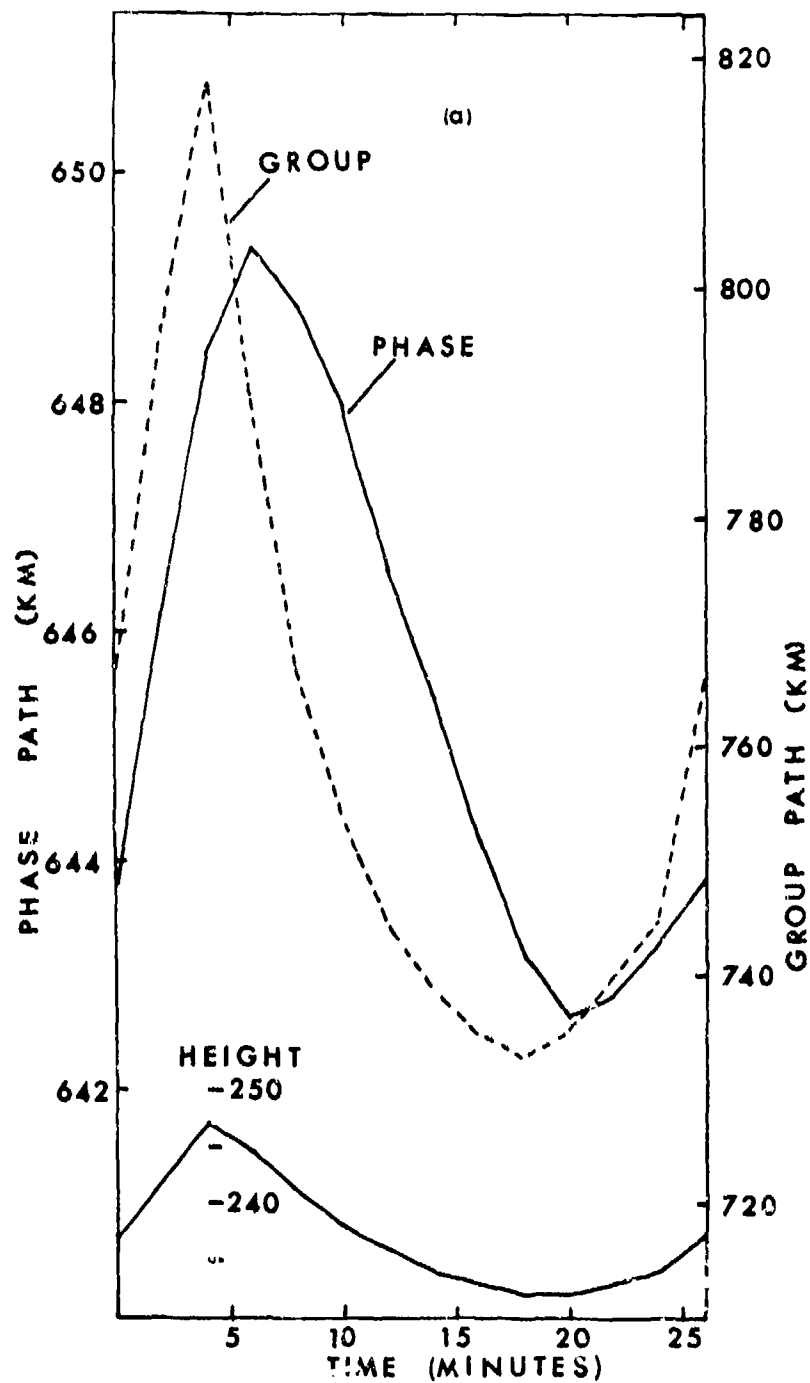


Figure 4 — Group and phase path variations for a ray trace without the magnetic field on 10 MHz on an oblique incidence path of 474 km. Variations in the ionospheric reflection height are also shown.

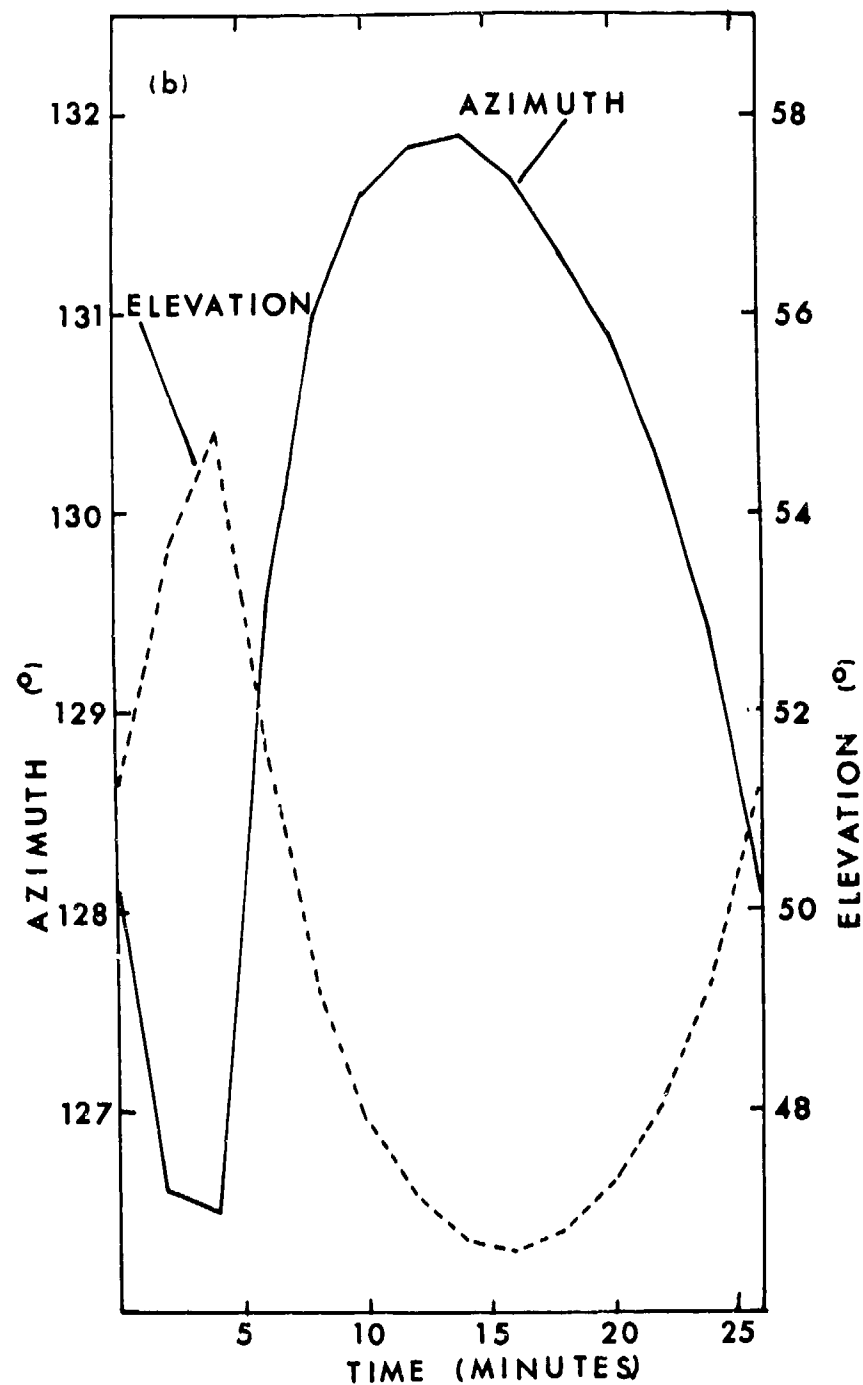


Figure 5 — The azimuth and elevation of the ray path from the transmitter. Parameters as in Figure 4.

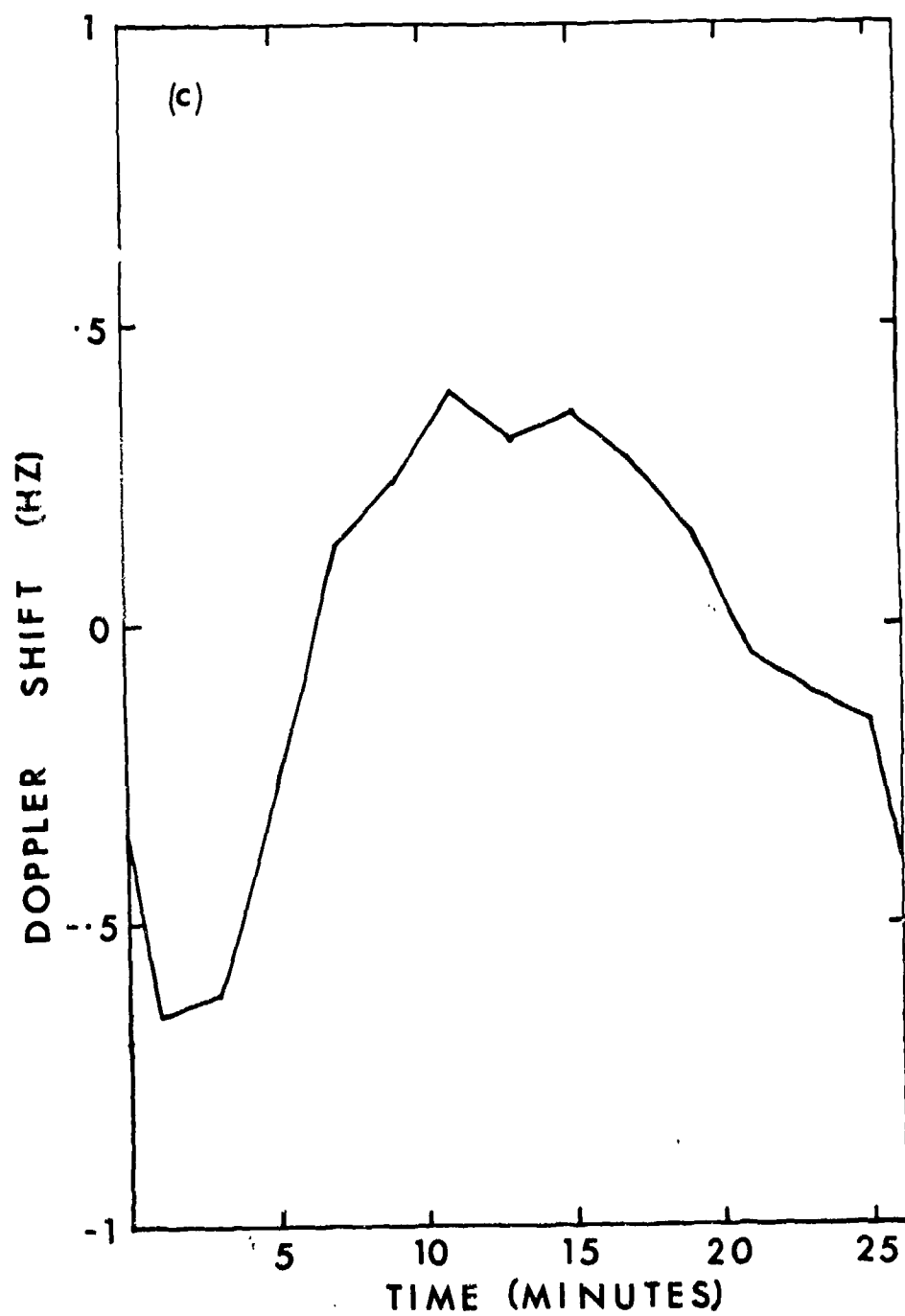


Figure 6 — The doppler frequency of the ray path from the transmitter. Parameters as in Figure 4.

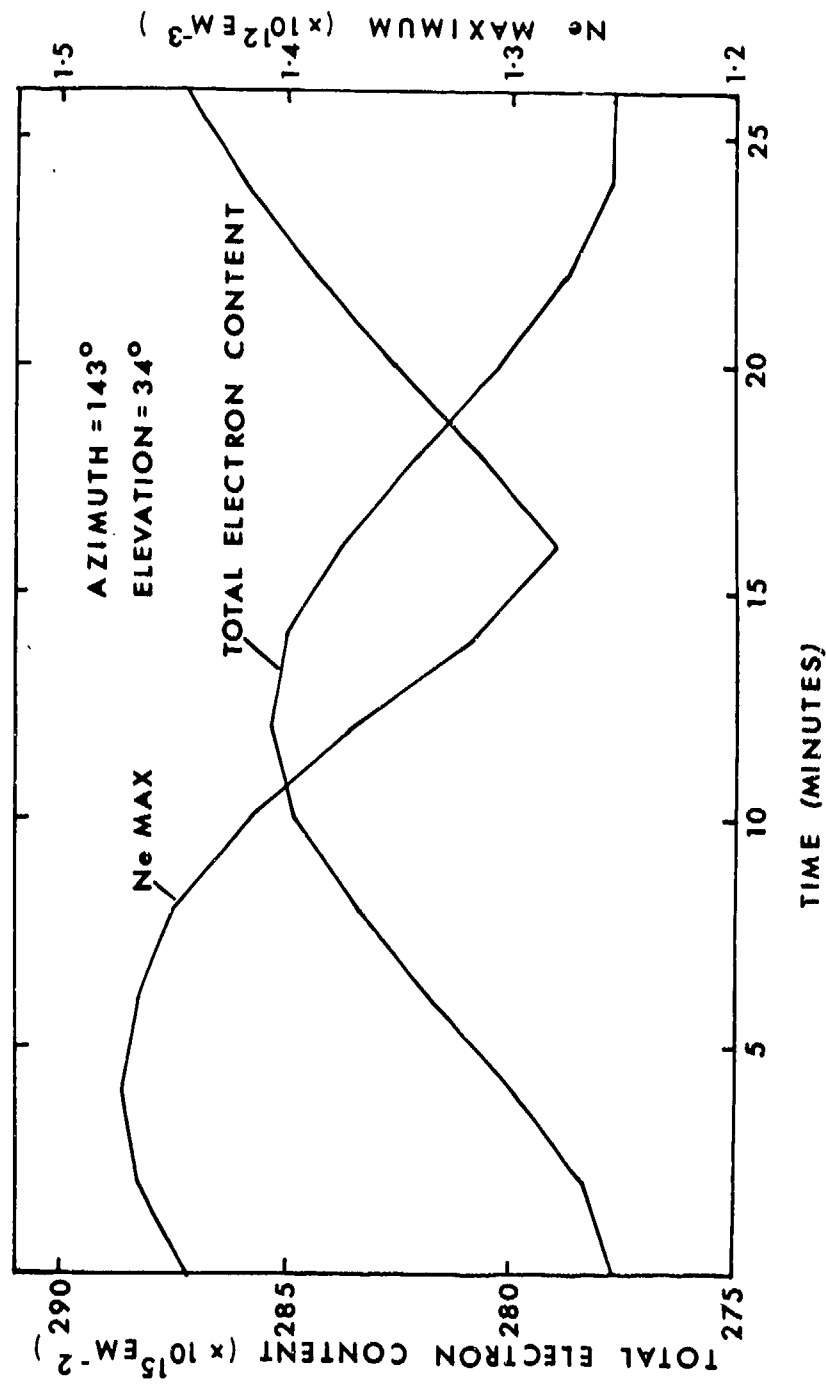


Figure 7 — Equivalent vertical total electron content variation and  $N_e$  peak variation along the ray path at 137 MHz.

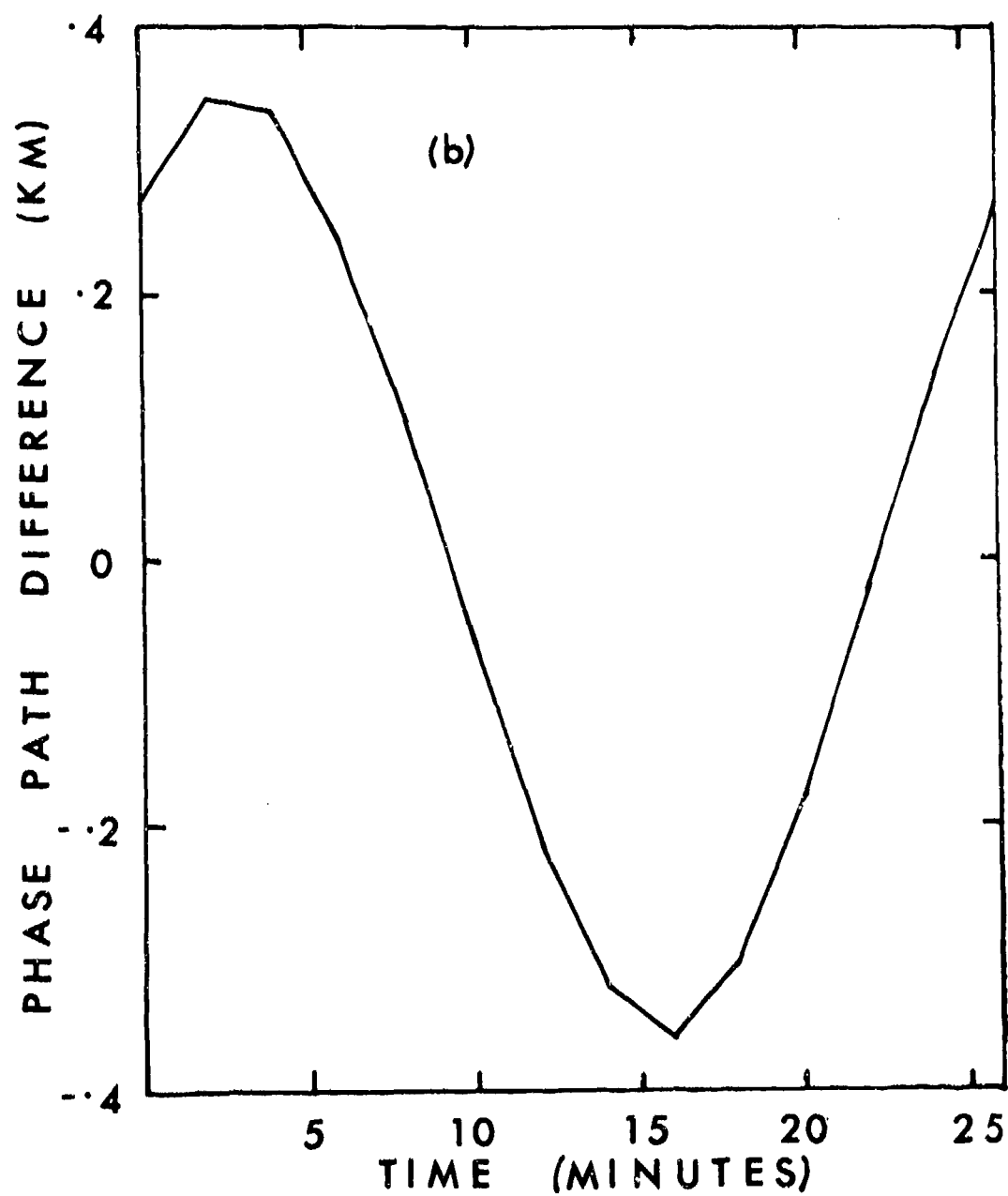


Figure 8 — Variation in the phase path difference between two points spaced 0.1 latitude apart.

## Some Problems in Constructing Phenomenological Models of Ionospheric Electron Density

Y. T. Chiu  
Space Physics Laboratory  
The Aerospace Corporation  
El Segundo, Calif.

### ABSTRACT

A global representation of the large scale variations of ionospheric electron density with the annual, diurnal and solar activity cycles is described. The phenomenological model, requiring minimal computer storage space, is constructed from monthly-averaged hourly ionospheric sounding data from some 50 stations during the epoch 1957-1970, as provided by World Data Center (A). The model, describing noon-time F2 layer critical frequencies to better than 2 Mhz average maximum error and to better than 0.5 Mhz root mean squared error, is particularly suitable for applications in space communication and ionosphere-atmosphere coupling studies. Magnetic dip angle and north-south asymmetry effects are incorporated in the model. We show that a "secular" variation of the ionospheric density exists in the epoch 1960-1971. The basis of comparison with data is broadened to include the 1958-1968 chronologies of 18 stations in addition to the original samplings of 50 stations.

### 1. INTRODUCTION

Recently we have attempted to construct a phenomenological model of global ionospheric electron density by organizing samplings of monthly-averaged hourly ionospheric sounding data from some 50 stations in the epoch 1957-1970 (Ching and Chiu, 1973a). The main purpose of such a construction is to provide a simple and easily accessible representation of the temporal, synoptic and solar activity-related variations of the electron density, which is frequently required as a subsidiary input in a number of dynamical calculations of upper atmospheric interest. For such a purpose, we have attempted to avoid smaller scale variations included in more sophisticated phenomenological models (Jones and Steward, 1970). Further, in order to satisfy the requirement of minimal computer storage, the model is purely phenomenological and does not take into account the

dynamical interaction between the ionosphere and the neutral atmosphere, such as the more complete physical synoptic models (Nisbet, 1971). Nevertheless, the simplicity of the model has some applicational advantages in a number of dynamical calculations such as the global effects of Joule heating in the thermosphere (Ching and Chiu, 1973b), electrostatic field mapping in the atmosphere (Chiu, 1974), ion drag in thermospheric modelling (Creekmore et al., 1974), and space communication studies. In the area of radio wave propagation studies, the application of the model is also a stringent test of its accuracy in describing the highly variable F2 layer which contributes the major part of the total electron content in the ray path. The primary purpose of the present paper is to consider an improved modelling of the F2 layer variations while preserving the requirement of simplicity of the original model (Ching and Chiu, 1973a; hereafter referred to as "Paper I").

The difficulty of modelling the F2 layer is clearly indicated by comparing the model variations with solar activity, annual time and local time for a large sampling of stations and for the complete span of years for which data is available. It is found that the error in the original modelling of the F2 critical frequency for some low-latitude and southern hemispheric stations may be as large as 4 or 5 Mhz when the critical frequency is of the order of 10 Mhz. Thus, for space communication applications, it would be desirable to reduce the maximum error and the root mean squared error until no systematic trend can be found. Using the monthly averaged noon-time F2 critical frequency as the key quantity for comparison with ionosonde data, we report on improvements in the original modelling of the F2 layer by including the dependences of the F2 critical frequency on magnetic dip angle, magnetic longitude and hemispheric asymmetry. The basis of comparison with data is broadened to include the 1958-1968

chronologies of noontime F2 critical frequencies of 18 stations in addition to the original samplings of 50 stations. Some new characteristic features of the F2 height variations (Yonezawa, 1973; Petelski, 1972) are incorporated in the model. Further, without the use of the model, we investigate the "secular" (in the sense of longer term than annual) variations of the ionosphere over 23 stations by comparing the noontime F2 critical frequencies of the period July 1960-March 1961 with the period July 1970-March 1971 when the Zurich sunspot numbers were almost exactly matched month by month. The results indicate a global change of the ionosphere during the ten intervening years although whether this change is truly secular or periodic with period longer than one year cannot be ascertained.

## II. STRUCTURE OF THE MODEL

The complete structure of the model can be found in the Appendix, which is organized in exactly the same form as in Paper I so that users of the original model may easily modify their programs to accommodate new modifications introduced here.

Briefly, the basic premise of the model is that the average electron density at any given space-time and solar condition is the sum of contributions from each of the three layers whose electron density is the product of a global amplitude constant, a vertical profile function and a layer peak density function. The profile functions,  $Z_i$ , are of standard Chapman forms while the layer peak density functions  $V_i$ , contain the greater part of the space-time variation of ionospheric layers. In order to economize the organization of data, certain combined space-time variables were introduced in Paper I and are retained here. Since the organization of the model for the E and F1 layers are completely unchanged, we shall not discuss these portions of the model any further. The modelling of the F2 layer is somewhat modified as compared to Paper I. The independent variables governing the F2 layer parameters consist of the altitude, annual time, local time, magnetic latitude and the Zurich smoothed sunspot number as in Paper I. In addition, the present model requires the introduction of the magnetic longitude and the magnetic dip angle which allow us to reduce the error in modelling the South Atlantic and Magnetic Equatorial regions. Although the new modifications rectify some major shortcomings of the original model, at least two major improvements need be introduced. First, an efficient modelling of the F2 layer affected by the "0600 UT Effect" at high Southern latitudes (Eccles et al., 1973) must be introduced. This effort is presently underway. Second, from comparing the model with observations, it is evident that the Zurich smoothed sunspot number cannot be the only independent indicator of the monthly averaged ionospheric response to solar activity. It is

well known that the ionosphere responds to individual geomagnetic storms with a time scale of several days (Evans, 1973; Goodman, 1968; Maeda and Sato, 1959): however, the large modelling errors at mid-latitude stations during the months of March, April and May 1967 indicate that the monthly averaged ionosphere responds to unusual increases of the  $K_p$  index which are not reflected correspondingly<sup>p</sup> in the Zurich smoothed sunspot number.

## III. COMPARISON WITH DATA

The modelling of the local time structure of the F2-layer critical frequency has been compared fairly extensively in Paper I with ionospheric sounding data published by World Data Center (A). Since the local time structure of the present model is the same as the original model, we shall focus our efforts on an extensive comparison of the chronologies of noon-time F2-layer critical frequencies. Such a comparison between model and data not only complements that of Paper I but also serves as a stringent test of the synoptic, annual time and solar activity related factors of the model. In Figures 1-5, the modelled chronologies of noon-time F2-layer critical frequencies of 18 stations are compared with data. The particular arrangement of stations is chosen to emphasize certain points to be discussed below. The inputs to the model are the 1958-1968 chronology of the Zurich smoothed sunspot number and the magnetic coordinates of the 18 stations. For convenient reference, the magnetic coordinates of the stations are listed in Table 1.

a. Northern magnetic mid-latitude stations: In Figure 1 we show the comparison between the modelled noontime F2 critical frequencies and data for a series of stations lying as close to magnetic latitude  $\lambda_m = 51^\circ N$  as possible. Inspection of the data and model for Slough, Lindau and Moscow indicates the effectiveness of the magnetic latitude as an organizational parameter for the northern magnetic mid-latitude region since virtually no differences were discernible over a span of some  $40^\circ$  in magnetic longitude. When Yakutsk and Boulder are included in the series, the above conclusion is not significantly modified. The maximum modelling errors of all five chronologies occur in March, April and May of 1967 when the  $K_p$  index increased substantially without corresponding increases in the Zurich sunspot number. Thus, the monthly averaged ionosphere shows a response to the shorter duration geomagnetic disturbances, although there is presently not yet enough data on such geomagnetic responses to justify a synoptic modelling effort.

b. Effects of north-south asymmetry in lower magnetic mid-latitudes: In Figure 2, we compare the modelled chronologies of noon-time F2 critical frequency with the data for a number of stations at magnetic latitudes somewhat lower than those of Figure 1. The F2



layer of these lower magnetic latitude regions reflects a stronger semi-annual variation superposed on the winter anomaly. The apparent asymmetry between Rome and Akita on the one hand and Canberra on the other, is mainly due to the interference between the winter anomaly and the semi-annual variation. A study of the residuals of the original model reveals that unusually large semi-annual variations of the noontime F2 critical frequency seem to associate with stations whose magnetic dip angles are near  $\pm 40^\circ$ , irrespective of magnetic latitude and magnetic longitude. This behavior can be noticed in Figures 2, 3 and 4. The anomalous behavior of the Port Stanley noontime F2 critical frequency is primarily due to this "dip angle" effect which is more prevalent during high solar activity.

c. The "Dip Angle Effect": In Figure 3 we compare the modelled chronologies of noontime F2 critical frequency with the data for a number of stations at low magnetic latitudes where cases of the magnetic dip angles being close to  $\pm 40^\circ$  are more likely to be encountered. Although large semi-annual variations were not evidenced in 1958 and 1959 at Tananarive in the Malagasy Republic, the prevalence of the anomalous semi-annual term is quite apparent for stations such as Port Stanley, Maui, Rarotonga and Port Moresby. The original model of Paper I for Port Moresby, for example, does not contain the "dip angle" effect and its root mean square error is nearly 1 Mhz higher than the present model. A similar result can also be seen in the modelling of the Port Stanley chronology of F2 critical frequency shown on Figure 2.

d. Magnetic equatorial regions: In Figure 5, we compared the modelled chronologies of noontime F2 critical frequency for three equatorial stations with data. The anomalously high values for Kinshasa is the result of the "dip angle" effect discussed in the previous paragraph and of the longitudinal variation which maximizes at the magnetic equator and is proportional to the second magnetic zonal harmonic. The improvement in the root mean squared error of the present model relative to the original model of Paper I for Kinshasa is somewhat over 1 Mhz.

e. Higher Southern magnetic latitudes: Although the local time structure of some high southern latitude F2 layers are affected by the "0600 UT effect", the general level of the ionosphere at these latitudes, as indicated by the noontime F2 critical frequency, is fairly well incorporated in the model. In Figure 5, we show a comparison of the modelled chronologies of the noontime F2 critical frequency for Campbell Island and Kerguelen Island with data. As is the case with northern magnetic mid-latitude stations of Figures 1 and 2, the period of March, April and May 1967 also shows an anomalously large modelling error in Figure 5. Therefore, it is likely that the response to short term geo-

magnetic activity is a high and mid-latitude phenomenon for both hemispheres. For short term ionospheric responses to geomagnetic activity is a high and mid-latitude phenomenon for both hemispheres. For short term ionospheric responses to geomagnetic activity, this is clearly the case (Evans, 1973; Titheridge and Andrews, 1967); however, our results seem to show that such short term effects persist at least at the level of monthly averages.

#### IV. "SECULAR" VARIATIONS

From the previous section we observe that the phenomenological model approximates the chronologies of the noontime F2 critical frequency with an average maximum error of about 2 Mhz and an average root mean squared error well below 0.5 Mhz. The question then arises as to how much of the residual error is due to hidden variations or due to variations not yet describable with the assumed set of independent variables. In order to study this question, we focus our attention on the two nine-month periods, July 1960-March 1961 and July 1970-March 1971, when the Zurich smoothed sunspot numbers were almost identically matched month by month as is shown in Table 2. Further, as an indication of the close match of month by month solar activity response during these periods, we indicate with crosses on Figure 6 (c) the percentage deviation of the solar activity function  $\sigma$  expected from the model, i.e.

$$\Delta\sigma/\sigma \approx 2 \cdot \frac{\sigma(1970-71) - \sigma(1960-61)}{\sigma(1970-71) + \sigma(1960-61)} \text{ monthly.}$$

Since the F2 critical frequency is directly proportional to the square root of the solar activity function  $\sigma$ , we expect, from Figure 6(c), that the monthly matched noontime F2 critical frequency deviation for each station between the above two periods should not differ by more than 2% at the maximum and should be less than 1% except for the first and last months of the comparison periods. Thus, the observed monthly matched noontime F2 critical frequency deviation between these periods for each station, i.e.

$$\Delta V_3 = V_3 (1970 - 71) - V_3 (1960 - 61) \text{ monthly,}$$

is an indicator of ionospheric variations which are "secular" in the sense of having a time scale longer than one year. Further, since the existence of random fluctuations cannot be excluded, the significance of  $\Delta V_3 \neq 0$  can only be considered significant only if a definite global pattern can be discerned. For these reasons, we have evaluated the observed monthly matched noontime F2 critical frequency differences between the above periods,  $\Delta V_3$ , for 23 stations. The stations are: Churchill, Canada; Kiruna, Sweden; St. Johns, New Foundland; Slough, England; Moscow, Russia; Freiburg, Germany; Akita, Japan; Mexico City, Mexico; White Sands, New Mexico; Boulder, Colorado; Rome, Italy;

Ahmedabad, India; Huancayo, Peru; Singapore, Malaysia; Maui, Hawaii; Kodaikanal, India; Townsville, Australia; Christchurch, New Zealand; Mawson, Antarctica; Rarotonga, Oceania; Canberra, Australia; Campbell Island, New Zealand. These stations are divided into four latitudinal groups with approximately equal number of stations in each group. The average values of the observed  $\Delta V_3$  for each group are shown on Figures 5(a) - (d); while the average values for the four groups are shown on Figure 5(e). From the similar patterns of  $\Delta V_3$  variation with annual time shown in each group in Figures (a) - (e), it is clear that, with all independent variables being "equal", as much as possible, the 1970-1971 F2 layer differs from that of 1960-61. The F2 critical frequency difference, which cannot be modelled unless data from several solar cycles are available, is of order of 1 Mhz. This accounts for approximately half of the residual maximum modelling error if one compares chronologies of ten years or longer.

The existence of "secular" or long-period variations of ionospheric density is of some dynamical interest. Since the lifetime of F2 region ions is short compared to ten years, it is likely that the systematic difference between the 1970-71 and the 1960-61 ionospheres reflects a systematic difference in the neutral atmospheres. However, there is as yet no mechanism by which the residence time of thermospheric energy can be as long as 10 years. Since both of the nine month periods are in the declining phase of the solar cycles, the possibility that the "secular" effect is dependent on the solar cycle phase can be ruled out. On the other hand, the magnetic moment of the Earth has declined in the intervening ten years and the Earth's radiation belts have shown a corresponding secular change (Heckman and Lindstrom, 1972; Schulz and Paulikas, 1972). Therefore, it is not unlikely that the ionosphere also shows a similar change. A second related possibility is that geomagnetic activity may have evidenced a change during the intervening ten years. Data are being gathered for studying these possibilities. Unfortunately, one will have to wait until 1980-81 before a third similar period of monthly matched solar activity is expected to arrive.

#### CONCLUSION

a. A global representation of the large scale variations of the ionospheric electron density with the annual, diurnal and solar activity cycles has been improved by inclusion of effects related to dip angle, magnetic longitude and north-south asymmetry. The present model describes noontime F2 layer critical frequencies to better than 2 Mhz average maximum error and to better than 0.5 Mhz root mean squared error.

b. The basis of comparison between model and data has been broadened to include the

1958-1968 chronologies of the noontime F2 critical frequency for 18 stations which complements the local time samplings of some 50 stations from which the original model was constructed.

c. The model independent comparison of the noontime F2 critical frequency for 23 stations during two nine month periods in 1960-61 and 1970-71, when the Zurich smoothed sunspot numbers were almost identically matched month by month, reveals that the 1960-61 F2 layer is globally different from that of the 1970-71 F2 layer. Since both periods are in the declining phase of the solar cycle, it is likely that this "secular" effect is not solar cycle related.

d. The anomalous large modelling errors at high and middle magnetic latitudes during the months of March, April and May 1967 suggests that the monthly averaged F2 layer shows a response to short term geomagnetic activity which is not reflected in the Zurich smoothed sunspot number.

e. It is likely that the effects described in c. and d. above are sufficient to account for the major part of the 2 Mhz average maximum modelling error for the noontime F2 layer critical frequency. Reduction of the maximum error will not substantially reduce the root mean squared error of 0.5 Mhz, however.

#### ACKNOWLEDGMENTS

The generous cooperation of World Data Center (A), Boulder, Colorado in providing ionospheric sounding data is appreciated. The cooperation of Ms. B. K. Ching in the construction of the original empirical model is invaluable. This work was partly supported by the U. S. Air Force Space and Missile Systems Organization.

#### REFERENCES

- Ching, B. K.; and Chiu, Y. T., 1973a J. atmos. terr. Phys. 35, 1615.
- Ching, B. K.; and Chiu, Y. T., 1973b Planet. Space Sci. 21, 1633.
- Chiu, Y. T., 1974 J. Geophys. Res. 79, 2790.
- Creekmore, S. P.; Straus, J. M.; Harris, R. M.; Ching, B. K.; and Chiu, Y. T. 1975 J. atmos. terr. Phys., in press.
- Eccles, D.; King, J. W.; and Slater, A. J. 1973 J. atmos. terr. Phys. 35, 625.
- Evans, J. V. 1973 J. atmos. terr. Phys. 35, 593.
- Goodman, J. V. 1968 Planet. Space Sci. 16, 951.
- Heckman, H. H.; and Lindstrom, P. J. 1972

J. Geophys. Res. 77, 740.

Jones, W. B.; and Steward, F. G. 1970 Radio Sci. 5, 773.

Maeda, K. I.; and Sato, T. 1959 Proc. IRE 47, 232.

Nisbet, J. S. 1971 Radio Sci. 6, 437.

Petelski, E. F. 1972 J. atmos. terr. Phys. 34, 1163.

Schulz, M.; and Paulikas, G. A. 1972 J. Geophys. Res. 77, 744.

Titheridge, J. E.; and Andrews, M. K. 1967 Planet. Space Sci. 15, 1157.

Yonezawa, T. 1973 J. atmos. terr. Phys. 35, 1181.

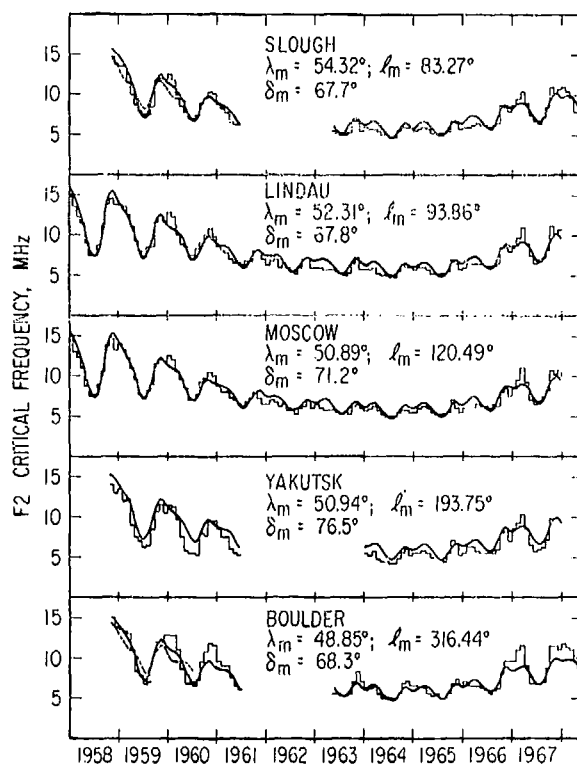


Figure 1. The chronologies of monthly noon-time F2 critical frequency, plotted as histograms, for the stations: Slough, Lindau, Moscow, Yakutsk and Boulder, are compared with the empirically modelled chronology shown by the solid curves. The dashed curves for Slough and Boulder indicate the results of the original model.

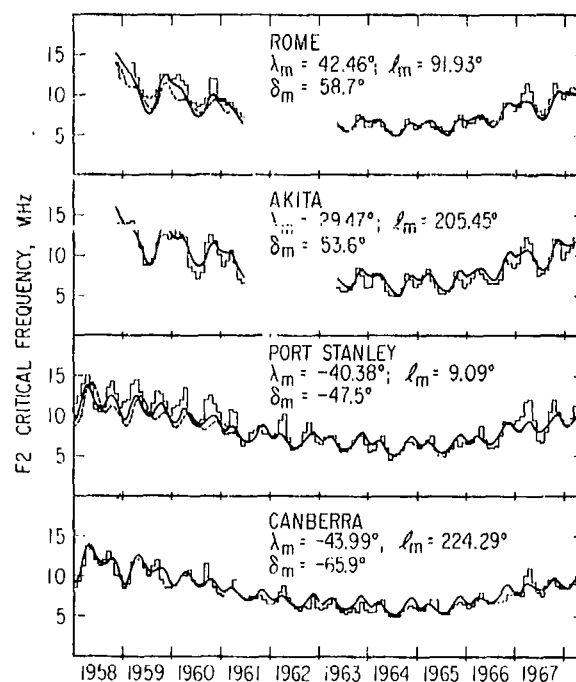
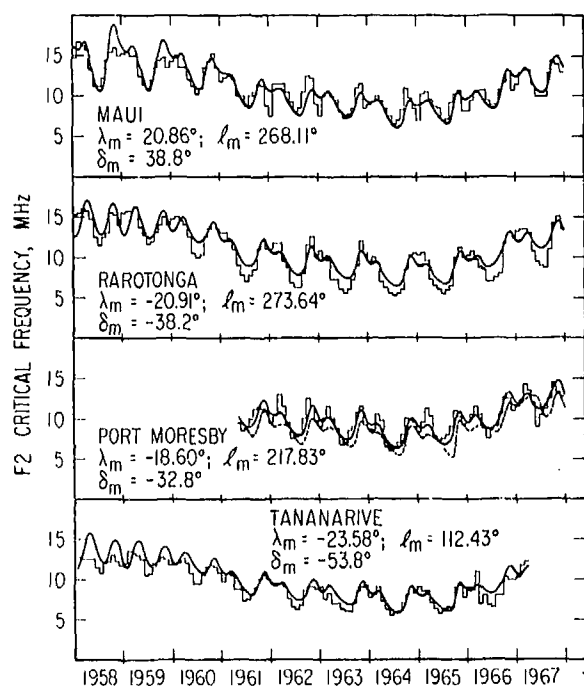
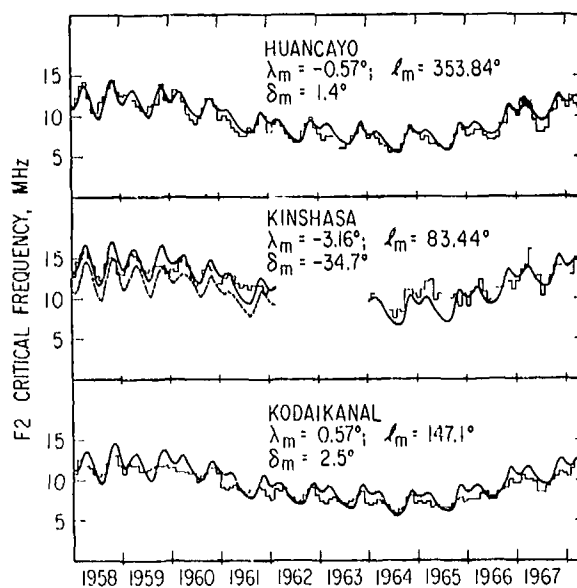


Figure 2. The chronologies of monthly averaged noontime F2 critical frequency, plotted as histograms, for the stations: Rome, Akita, Port Stanley and Canberra, are compared with the empirically modelled chronology shown by the solid curves. The results of the original model are shown as dashed curves for Rome and Port Stanley.



**Figure 3.** The chronologies of monthly averaged noontime F2 critical frequency, plotted as histograms, for the stations: Maui, Rarotonga, Port Moresby and Tananarive, are compared with the empirically modelled chronology shown by the solid curves. The result of the original model for Port Moresby is shown by the dashed curve.



**Figure 4.** The chronologies of monthly averaged noontime F2 critical frequency, plotted as histograms, for the stations: Huancayo, Kinshasa and Kodaikanal, are compared with the empirically modelled chronology shown by the solid curves. The result of the original model for Kinshasa is shown by the dashed curve.

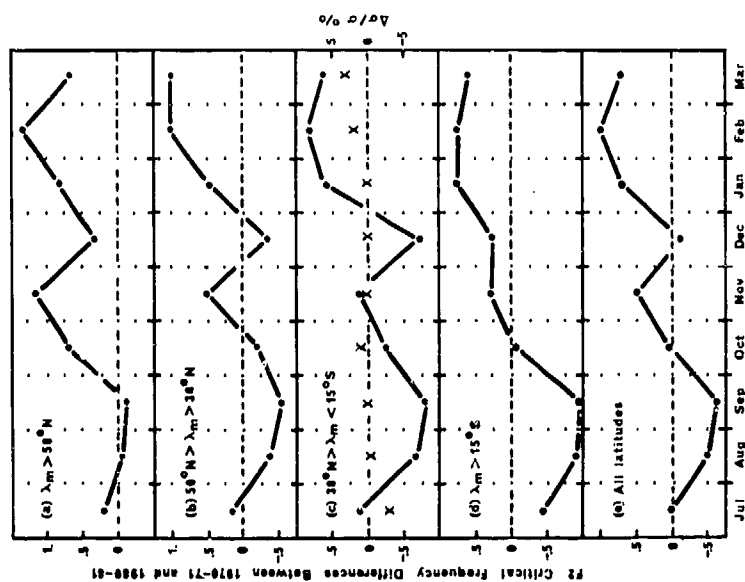


Figure 6. The monthly matched F2 critical frequency differences between July 1970-March 1971 and July 1960-March 1961 are shown for the averages of 4 groups of stations: (a) magnetic latitude north of  $50^{\circ}\text{N}$ , 5 stations, (b) magnetic latitude between  $30^{\circ}\text{N}$  and  $50^{\circ}\text{N}$ , 6 stations, (c) magnetic latitude between  $15^{\circ}\text{S}$  and  $30^{\circ}\text{N}$ , 6 stations, (d) magnetic latitude south of  $15^{\circ}\text{S}$ , 6 stations, and (e) the average of all 23 stations. The crosses of Figure 6(c) denote the monthly matched percentage deviations of the solar activity function  $\sigma(p)$  between the above two periods. If there were no long term variations of the F2 layer, the critical frequency differences should be directly proportional to the square root of  $\sigma(p)$ .

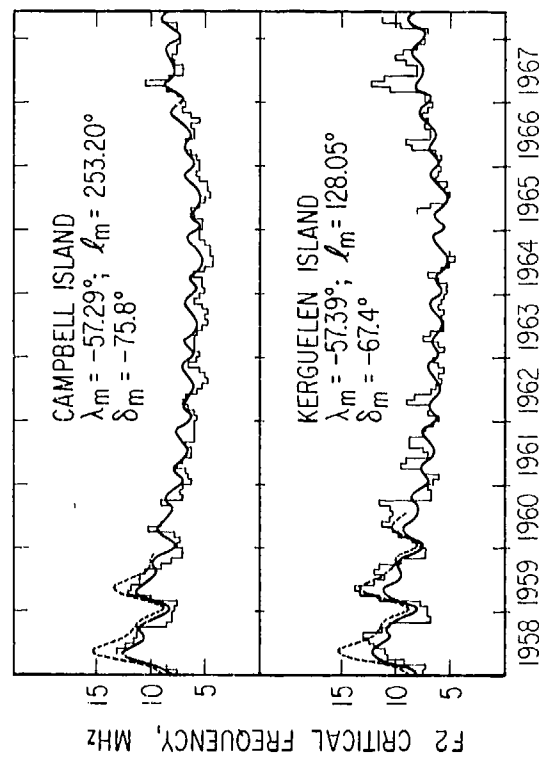


Figure 5. The chronologies of monthly averaged noon-time F2 critical frequency, plotted as histograms, for Campbell Island and Kerguelen Island are compared with the empirically model chronology shown by the solid curves. The dashed curves show the result of the original model.

## MODELING THE TOPSIDE OF THE F REGION

Richard S. Allen  
Air Force Cambridge Research Laboratory  
Bedford, Ma. 01731

### INTRODUCTION

The electron density of the upper ionosphere is often modeled by empirical profiles which decrease monotonically with height. The calculated values of electron density are critically dependent on the initial choice of a thickness parameter for the interval just above the peak of the F2 region. Since there are so few field observations it is common practice to equate the thickness of the top and the bottom of the F2 region and then to refer to climatological sources, such as those given by Barghausen et al (1969) or C.C.I.R. (1970) to obtain an estimate of a topside thickness parameter. Unfortunately few climatological descriptions of the thickness of the lower ionosphere are based on detailed electron density profiles.

In this paper another approach is suggested: to obtain an estimate of the height of the maximum of the F2 region and then to use it to specify a thickness parameter for the topside. This implies using some model relationship such as the one presented below.

As a pilot study a simple specification model has been constructed from profiles of the F region (1968-1971) kindly furnished by John Evans of Lincoln Laboratory. Results indicate that the topside thickness parameter can be estimated to within about 15 percent assuming that the height of the F region is known.

### DEVELOPMENT OF A SIMPLIFIED MODEL

First define  $Q_c$  (Piggott and Rawer 1972) as the quarter thickness of a parabola fit to the underside of the F2 region and define  $h_{max}$  as the height of the F2 maximum. Electron density profiles resulting from the reduction of bottomside vertical incidence ionograms such as those reported by Becker 1972,

Clarke and Hammond 1965, Wright 1962, indicate that the mean noon and mean midnight values of  $Q_c$  vary with season and solar cycle in the same sense as the mean value of  $h_{max}$  (Fig 1). Continuity of the basic physical conditions across the  $h_{max}$  boundary suggest a similar relation for thickness in the region just above  $h_{max}$ .

Experimental profiles of the region above  $h_{max}$  are scarce and scattered. Available for this study were the archive profiles obtained from Evans which were produced by reduction of the incoherent scatter profiles from the Millstone Hill radar. About 151 days edited to 3488 profiles spanned the period July 1968 through December 1971.

A parabola was fitted to the top and bottom of the individual profiles. Let us define  $Q_t$  as the parabolic quarter thickness for the topside segment between  $h_{max}$  and a higher height where the electron density equalled 0.75 of the density at the F2 peak. Similarly define  $Q_c$  for the bottomside segment between  $h_{max}$  and the height where the density equalled 0.75 or to the height of 200 km if that occurred first.

The behavior of  $Q_t$  vs  $h_{max}$  is illustrated in figure 2 for three time samples; day, night and a transition period delimited by plus and minus two hours about ground sunrise and ground sunset. All samples from the 151 days of observation are included. Count is given in each cell where size is 2 km in quarter thickness by 5 km in  $h_{max}$ .

The agreement of the variation of quarter thickness with  $h_{max}$  in Figs 1 and 2 suggests that an empirical model derived from the limited sample of incoherent scatter data might be useful over the wider latitude and time range of the data of Fig 1. If the data is considered in small blocks delimited by

both time and season then a linear relation such as

$$Q_t = k(h_{\max} - 145.) \quad (\text{km}) \quad \text{Eq. 1}$$

is a simple engineering approximation. The choice of 145 km as reference point is arbitrary but consistent with both Fig 1 and 2.

To develop an empirical model around such a relationship all the data were pooled and then mean  $k$  of equation 1 was determined for cells of size month by hour. Results are contoured in Fig 3.

By inspection the diurnal and seasonal variation of  $k$  are not separable so that the seasonal mean or the diurnal mean of the total sample are of no direct assistance in modeling the parameter. Becker (1966) has already shown a dependence of  $Q_c$  on the mean solar flux ( $\Phi$ ) and the noon solar zenith angle ( $\chi$ )

$$Q_c \propto \Phi \cos \chi$$

Unfortunately the number of data points per month per year of this set is small so in this paper  $\Phi$  is assumed constant.

With this insight a trial model discontinuous at sunrise (SR) and sunset (SS) was constructed such that the value of  $k$  in equation 1 was

$$k = \begin{cases} 0.34 & \text{SS} < t < \text{SR} \\ 0.25(1 + \cos \chi) & \text{SR} \leq t \leq \text{SS} \end{cases} \quad \text{Eq 2}$$

where  $t$  is local time. The difference between modeled  $k$  and the observed mean  $k$  is contoured in figure 4. Background errors are generally less than 10 percent while worst errors are about 25 percent in summer and about 20 percent in winter.

If empirical terms are added for the systematic variations in the transition periods near sunrise and sunset then a relation such as

$$k = \frac{0.045}{(1 + \frac{(t-\text{SS}-1)^4}{1.3})} + \frac{0.090 \cos \chi}{(1 + \frac{(t-\text{SR}-0.7)^4}{2.3})} + \begin{cases} 0.34 & \text{SS} < t < \text{SR} \\ 0.25(1 + \cos \chi) & \text{SR} \leq t \leq \text{SS} \end{cases} \quad \text{Eq 3}$$

can model mean  $k$  with residual errors as shown in figure 5.

Since it is proposed that this simple model be applied to other stations at higher and lower latitudes as suggested by figure 1 then it does not

seem proper to model the prominent features found before sunrise in winter and just after sunrise in summer since they may well be local effects.

## TEST

To make a non parametric test of the usefulness of the specification technique define a central value and a measure of the variability about that value for each of the samples of figure 2. For instance the median value and the spread between 5 and 95 percentile points for the day sample are

$$Q_c(\text{median}) = 57 \text{ km} \\ P_{95} - P_5 = 89 - 39 = 50 \text{ km}$$

Assume that some unspecified external source of climatology can specify that central value without bias. The specification technique suggested here duplicates the prediction of the central value but using an accurately specified  $h_{\max}$ , reduces the uncertainty by about 30 percent for the day and transition samples. For instance the spread between 5 and 95 percentile points for the day sample (Fig 6a) becomes

$$P_{95} - P_5 = 35 \text{ km}$$

Note that while the central value of the night sample (Fig 6b) has been specified the technique has not changed the uncertainty.

The technique should be verified with an independent source of data.

## DISCUSSION

$H_{\max}$  is easily obtained from either climatology or a local measurement, a thickness parameter is not. The useful correlation displayed between the two parameters over day, season, solar cycle and latitude recommends the use of a simple specification technique such as the one presented above. There are indications in both figures 1 and 2 that a second order relation in  $h_{\max}$  would be more exact, but unnecessary at this stage. In fact, to first order, equation 2 is sufficient since the additional terms of equation 3 are about the 10 percent level.

While this technique may be of immediate application in modeling the upper ionosphere for various engineering applications, the significance of the basic physics contained in equation 1 is far from clear. The absence of appreciable diurnal or seasonal variation of the thickness of the lower E region is generally accepted, but note that the

choice of 145 km as the null height of equation 1 was arbitrary and would be changed if a second order relation were substituted. Still it seems to be consistent with many observations that suggest the stability of atmospheric parameters in the vicinity of say 120 km.

Previous analyses for various models of the upper atmosphere suggest that the thickness parameter would vary with the temperature of the electrons and ions and inversely with the force of gravity and the mean molecular mass. The variation of the force of gravity with height is a very small portion of the variation suggested by figure 2; direct observations by satellite probes suggest that at the heights of interest, between 200 and 500, the mean molecular mass is very nearly that of  $O^+$ , therefore the variation of the thickness of either the upper or lower region is an expression of the effective ion-electron temperature. From this it is concluded that either the thickness or the height of the F region is a macroparametric measure of the temperature.

The change of thickness parameter with the day to day change of solar or geophysical activity is considered a promising separate study.

## REFERENCES

- Barghausen, A.F., J.W. Finney, L.L. Proctor, and L.D. Schultz, Predicting Long-Term Operational Parameters of High-Frequency Sky-Wave Telecommunications Systems, ESCA Technical Report ERL 110-ITS-78, (1969).
- Becker, W., The Seasonal Anomaly of the F Region at Mid Latitudes and Its Interpretation, Electron Density Profiles in Ionosphere and Exosphere, 218-230, Jon Frihagen, Editor, North Holland Publishing Company, Amsterdam (1969).
- Becker, W., The Standard Profile of the Mid Latitude F Region of the Ionosphere as Deduced from Bottomside and Topside Ionograms, Space Research XII, 1241-1252, Akademie Verlag, Berlin (1972).
- CCIR Report No. 252-2, Documents of The XIIth Plenary Assembly, New Delhi (ITV, Geneva) (1970).
- Clarke, C. and E. Hammond, J. Atmos. Terr. Phys., 27, 551-557, (1965).
- Piggott, W.R., and K. Rawer, Report VAG-23, URSI Handbook of Ionogram Interpretation and Reduction, 2nd Edition, Nov. 1972.
- Wright, J.W., J. Resch. Nat Bureau Standards, 66D, 297-312 (1962).

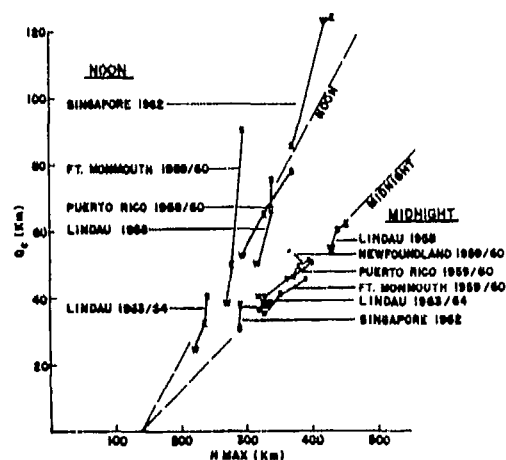


Fig. 1 Parabolic half thickness of bottom of F2 region vs height of peak of F2 region. Seasonal medians for several latitudes and for solar cycle extremes.



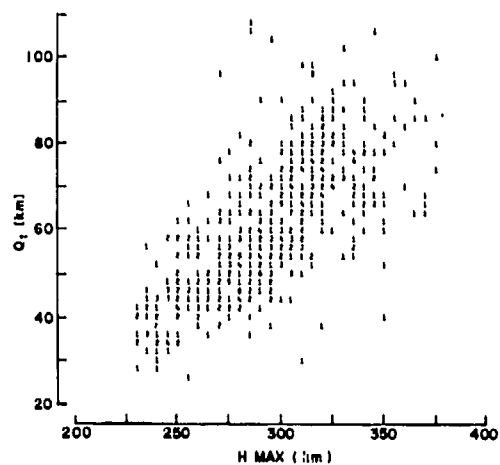
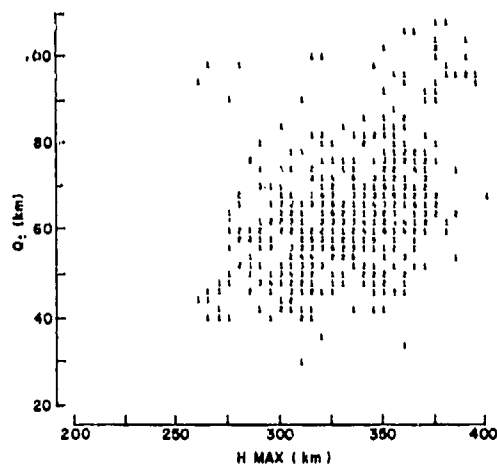
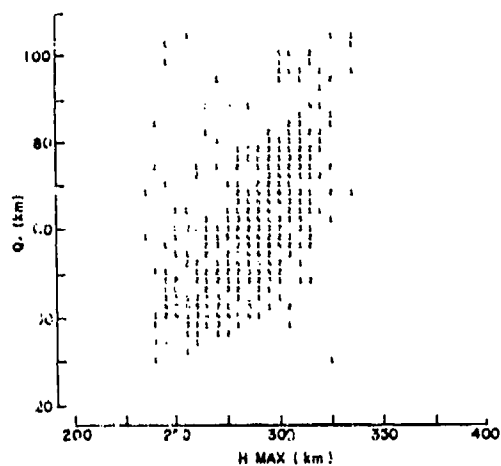


Fig. 2 Parabolic half thickness of top of F2 region vs height of peak of F2 region. Individual observations from incoherent scatter at Millstone Hill for daytime (a), nighttime (b) and near sunrise and sunset (c).

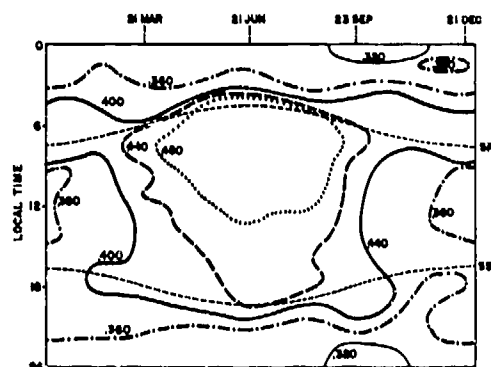


Fig. 3 Seasonal-diurnal variation of  $k$  from equation 1.

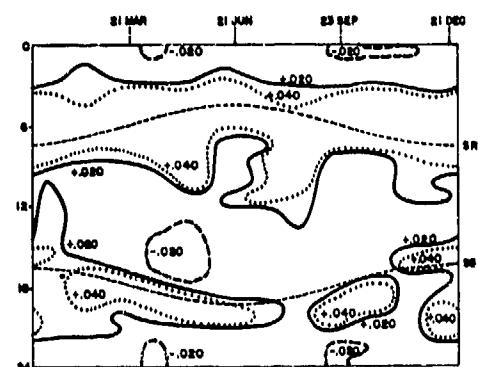


Fig. 4 Difference between modeled  $k$  and observed  $k$  for equation 2.

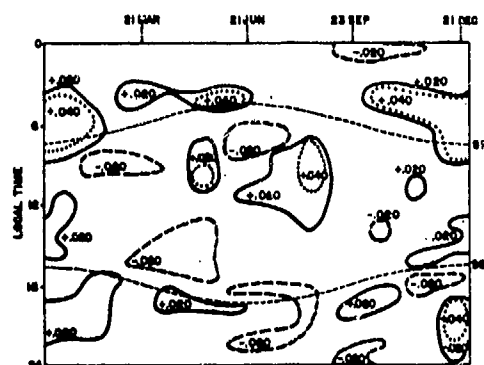


Fig. 5 Residual errors in modeling  $k$  when simple terms are added for sunrise and sunset as in equation 5.

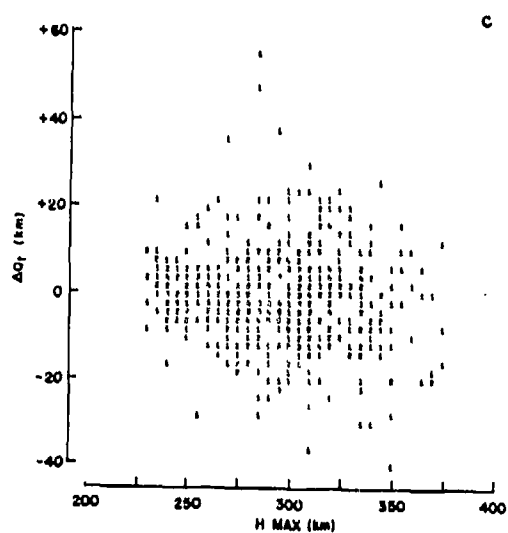
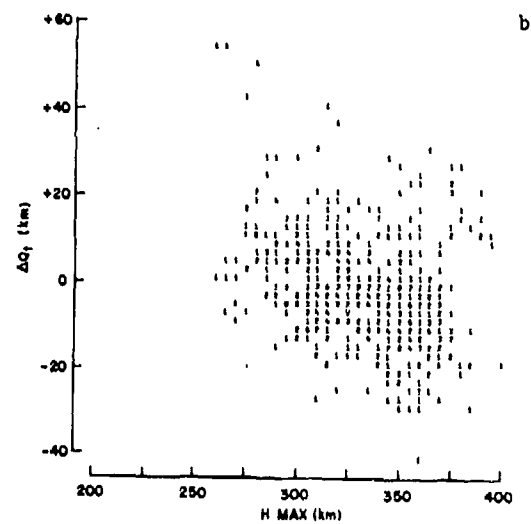
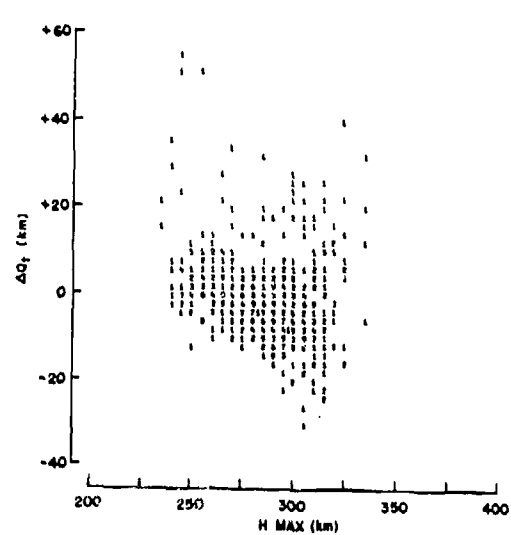


Fig. 6 Uncertainty remaining in estimate of topside quarter thickness after using equation 2 for the daytime hours (a), the nighttime (b) and after using equation 3 for the sunrise-sunset period (c).

# DERIVATION OF TOTAL ELECTRON CONTENT

FOR

## REAL TIME GLOBAL APPLICATIONS

Thomas W. Flattery  
Allan C. Ramsay

Air Force Global Weather Central  
Offutt Air Force Base Nebraska

### INTRODUCTION

Knowledge of the total electron content (TEC) of the ionosphere as a function of time and space is of importance for optimum utilization of a number of Department of Defense communication and surveillance systems. One technique for the determination of TEC (Damon and Hartranft, 1970) is based on the climatological values of foF2 and M3000 described by Jones, Graham, and Leftin (1969) of the NOAA Institute for Telecommunication Sciences (ITS). These values have proven to be remarkably accurate for specifying the median or undisturbed state of the ionosphere, but are of course incapable of accounting for the spatial and temporal changes associated with disturbances in the near-earth environment. The purpose of this paper is to describe a method whereby real-time observations of ionospheric parameters can be incorporated to provide a more realistic description of TEC distributions.

### foF2, M3000 ANALYSIS

The technique is based on a procedure developed to perform global meteorological analyses (Flattery, 1971). It is spectral in nature -- that is, the analysis is accomplished by modifications of the values of the coefficients of a series of functions which represent the field, rather than by the more typical method of assigning values at the nodes of a grid covering the region of interest. There are several advantages to this technique, not the least of which is the fact that the ITS climatological fields are normally expressed in spectral form:

$$\Omega(\lambda, \theta, T) = \sum_{j=0}^H \sum_{k=0}^K \{ u_{2j,k} \cos jT + u_{2j-1,k} \sin jT \} G_k(\lambda, \theta) \quad (1)$$

Here  $(\lambda, \theta, T)$  is the field being represented, the  $u_{j,k}$  are expansion

coefficients,  $\theta$  is the geographic longitude,  $\lambda$  is the geographic latitude,  $T$  is universal time, and the  $G_k(\lambda, \theta)$  are a

set of functions constructed by Jones, Graham, and Leftin (1969) to give a best fit to observed data with which they worked.

The object of the analysis procedure described below is to modify the  $u_{j,k}$  such that  $\Omega$  approximates its

climatological configuration in data-sparse areas, but approaches the observed values in those regions where observations are available. Let us assume that we have evaluated (1) at an evenly distributed set of points in space and time. The result can be expressed in matrix form as:

$$A u = \Omega \quad (2)$$

where  $\Omega$  is a vector whose  $i$ th component is the value of  $\Omega(\lambda, \theta)$  at the  $i$ th point,  $u$  is a vector whose  $l$ th component is the  $l$ th coefficient of the right-hand side of (1) after double expansion, and  $A$  is a matrix whose elements  $A_{l,i}$  are the

functions corresponding to  $u_l$  evaluated at the  $i$ th point.

We define the vectors  $u'$  with the desired coefficients as components and  $\Omega'$  which is identical to  $\Omega$  except for those points at which data

have been observed. We assume that the network of points has been chosen to be sufficiently fine that a point exists in the vicinity of every observation. These vectors satisfy the relation:

$$Au' = \Omega' + r \quad (3)$$

where  $r$  is a residual vector. Subtracting (2) from (3) gives:

$$A\Delta u = \Delta\Omega + r \quad (4)$$

where  $\Delta u \equiv u' - u$  and  $\Delta\Omega \equiv \Omega' - \Omega$ .

We wish to minimize the length of  $r$ . A familiar result which is derived in texts on numerical analysis leads to:

$$\Delta u = (A^T A)^{-1} A^T \Delta\Omega \quad (5)$$

for the desired solution  $\Delta u$ . Equation (5) is not difficult to solve in this case because of the characteristics of

$A^T A$  and  $\Delta\Omega$ . Although  $A^T A$  is a matrix of dimension  $2H + K + 2$ , it is not a function of data distribution and need be calculated only once. The components of  $\Delta\Omega$  are all zero except for those points at which observations are available. This greatly simplifies the calculation of  $A^T \Delta\Omega$ , and permits (5) to be solved with only a moderate amount of computation.

Because we have assumed a very large number of points at which a climatological value is correct, the solution vector will not represent a field which agrees well with the observed data. It is therefore necessary to iterate the above procedure. In the second and subsequent iterations the previous result is assumed to be correct. That is, in the above derivation, (2) is replaced by

$$A(u + \Delta u) = \Omega \quad (6)$$

This is equivalent to assuming that the values of the field being analyzed are given at unobserved points by the solution from the previous iteration, rather than by climatology.

As described above, the technique produces gradual convergence until  $\Delta u$  becomes negligible. In practice, the convergence rate can be increased by over-correcting (multiplying  $\Delta u$  by a scalar  $>1$  before adding it to the previous solution vector). Satisfactory convergence is achieved in from six to twelve iterations.

While the above describes the procedure as currently employed at the Air Force Global Weather Central, experiments are underway to improve its performance. The functions  $G_k(\lambda, \theta)$  are

not well-suited to the analysis technique because they are highly linearly dependent. The optimum functions from a numerical viewpoint should be orthogonal, in which case the matrix  $A^T A$  could be made diagonal. At present, because of the nature of the  $G_k(\lambda, \theta)$ ,

$A^T A$  is almost singular, and the analysis can become unstable with some data distributions. A version of the program which replaces the  $G_k(\lambda, \theta)$  with surface spherical harmonics is now under development, and should eliminate any numerical instabilities. This version will also permit  $A^T A$  to be treated as a diagonal matrix, reducing the computation required, and permitting an increase in the resolution of the analysis.

Routine evaluation of the automated analysis technique has been accomplished on a daily basis only since October 1974. The root-mean-square (RMS) errors shown below represent the relative capabilities of the ITS ionosphere and the automated analysis to specify the day-to-day variability of the F region:

RMS Error in the Specification of:		
	FoF2(MHz)	M3000
ITS	1.37	0.30
Auto analysis	0.68	0.19

These errors were determined from observations from the stations listed in Table 1; they represent errors over the entire three-month period from October through December 1974. The relationship between the ITS error and the analysis error is remarkably constant on a day-to-day basis. ITS errors have ranged from 1.06 to 1.69 MHz, and the automated analysis errors have ranged from 0.50 to 0.93 MHz; on any given day, the automated analysis foF2 error is usually very close to one-half the ITS error.

The errors quoted above are, of course, valid at specific observing locations. As the point to be specified becomes more distant from an observation point, the expected error will approach the ITS error. Rush (1972) has estimated effective decorrelation distances for the F2 region: in general, deviations from median ionospheric conditions (identifiable in hourly observations) are spatially coherent to distances of about 1500 km in longitude and about 750 km in latitude. We find that the ITS functions produce significant effects at approximately these

distances from data points. The validity of the foF2 and M3000 specification away from observation points is of concern because of the global nature of the Air Weather Service support requirements. (Note that operational procedures described in this paper as "global" are, in reality, limited to Northern Hemisphere applications.)

#### IONOSONDE LOCATIONS CONTRIBUTING TO AUTOMATED ANALYSES:

#Alma Ata	Manila
Bangkok	#Moscow
#Boulder	#Narssarssuak
College	#Nurmijarvi
Cyprus	Patrick AFB
Dourbes	#Qanaq
Fort Churchill	Resolute Bay
#Godhavn	#Saint Johns
Goose Bay	#Slough
#Irkutsk	#Sodankyla
#Keawakapuu	Taipei
#Kiruna	Tromso
#Kokobunji	Vandenberg AFB
#Lindau	#Wallops Island

#### POLARIMETER (TEC) LOCATIONS:

Athens, Greece  
Goose AB, Labrador  
Osan AB, Korea  
Patrick AFB, Florida  
Ramey AFB, Puerto Rico  
Sagamore Hill Massachusetts

TABLE 1. Ionospheric Data Sources

Automated ionospheric analyses are made at the Air Force Global Weather Central four times daily. Each analysis uses the most recent 24 hours of vertical-incidence ionosonde reports from the network of stations listed in Table 1. In general, some 200 to 250 hourly observations are available for each 24-hour period being analyzed. A computer display of Northern-hemisphere foF2 values is shown in Figure 1. The foF2 contours are shown in relation to North America in Figures 2a, b, and c. Figure 2a shows the "monthly median" ITS specification of the foF2 field as adjusted for solar activity; this figure would be valid for 1900UT in early January 1975. Figure 2b shows the automated ionospheric analysis at 1900UT on a geomagnetically quiet day (estimated A sub p = 04): 02 Jan 75. We feel that the agreement between the ITS field and the analyzed field is excellent, and is indicative of the value of the ITS specification. Figure

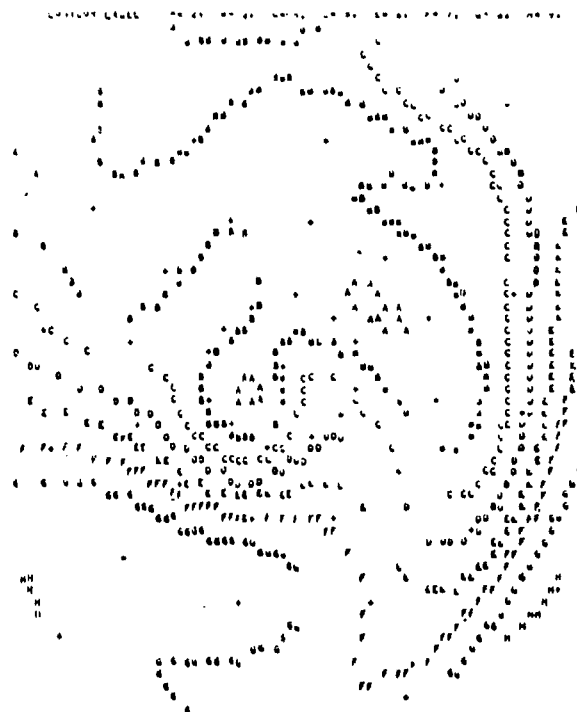


FIGURE 1. SAMPLE DISPLAY OF COMPUTER OUTPUT: foF2 OVER NORTHERN HEMISPHERE, 1900UT, JAN 75

2c shows the automated analysis at the same time of day of 05 JAN 75. A minor geomagnetic disturbance began on 4 JAN; the estimated A sub p for 05 JAN was 27. The ionosphere on 05 JAN was experiencing significant deviations from the expected "median" conditions which were met rather well on 02 January. Note particularly the change in the 8-MHz foF2 contour line from 02 to 05 January. Diurnal foF2 curves for three vertical-incidence ionosondes are shown in Figure 3; the graphs provide a comparison between observed values, ITS values, and those values specified by the automated analyses on those days.

#### TOTAL ELECTRON CONTENT

The capability to specify foF2 and M3000 provides the foundation for a global electron-density-profile and TEC model. The current electron density model used operationally by the Air Weather Service is based on a concept initially employed by Damon and Hartranft (1970). The characteristics of the present model derive primarily from development efforts at the Air Force Global Weather Central over the period

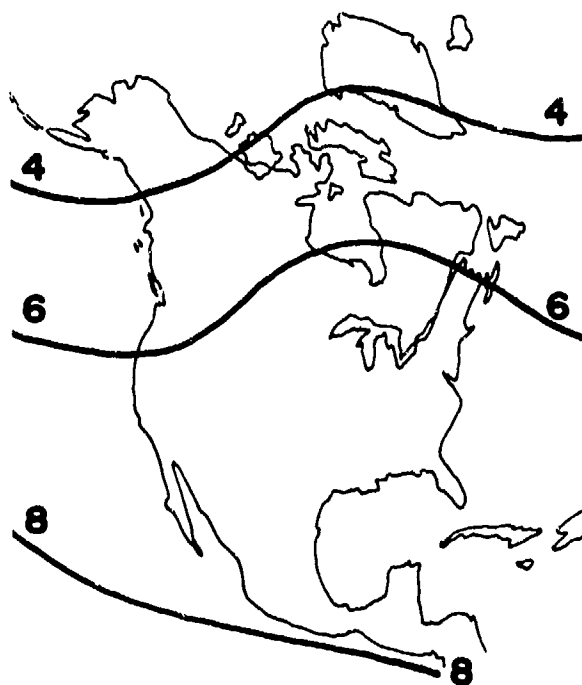


FIGURE 2a. ISOPLETHS OF foF2  
ITS  
VALID 1900UT, 02 & 05 JAN 75

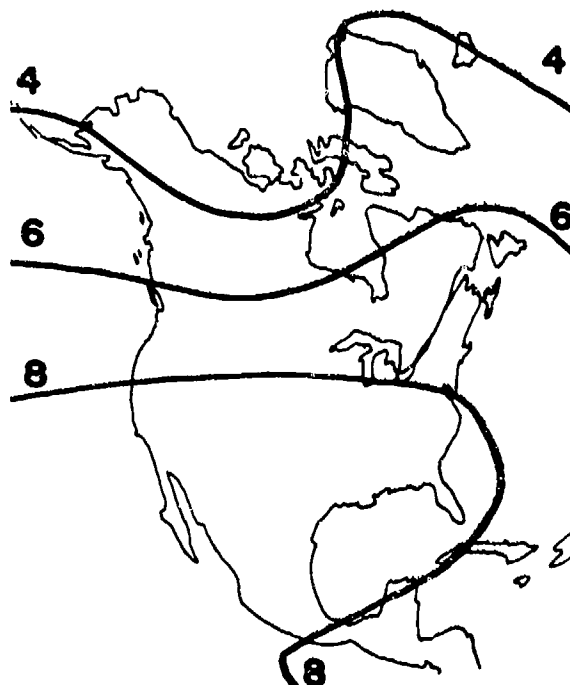


FIGURE 2c. ISOPLETHS OF foF2  
AUTOMATED ANALYSIS  
VALID 1900UT, 05 JAN 75

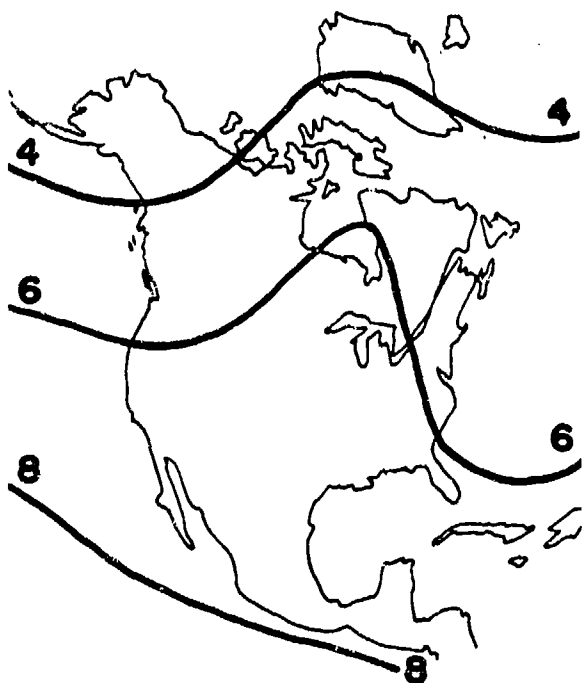


FIGURE 2b. ISOPLETHS OF foF2  
AUTOMATED ANALYSIS  
VALID 1900UT, 02 JAN 75

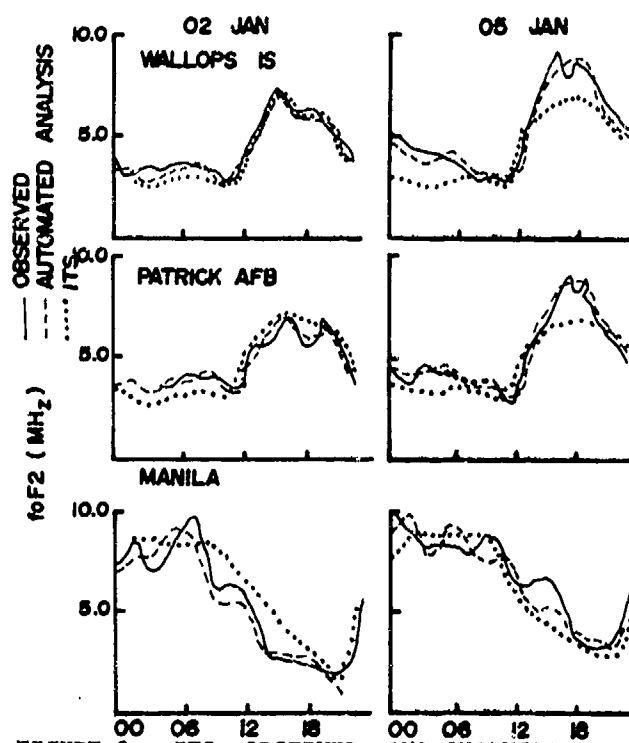


FIGURE 3. ITS, OBSERVED, AND ANALYZED  
foF2 AT MANILA, WALLOPS IS,  
AND PATRICK AFB  
02 AND 05 JAN 75

1972 through 1974 (Bussey and Ramsay, 1974). The main features of the Air Weather Service model are:

a. The vertical distribution of electron density is obtained by summing three Chapman layers (representing the E, F1, and F2 layers). Figure 4 illustrates the construction of a typical profile. The basic characteristics of the individual Chapman layers are given in Table 2.

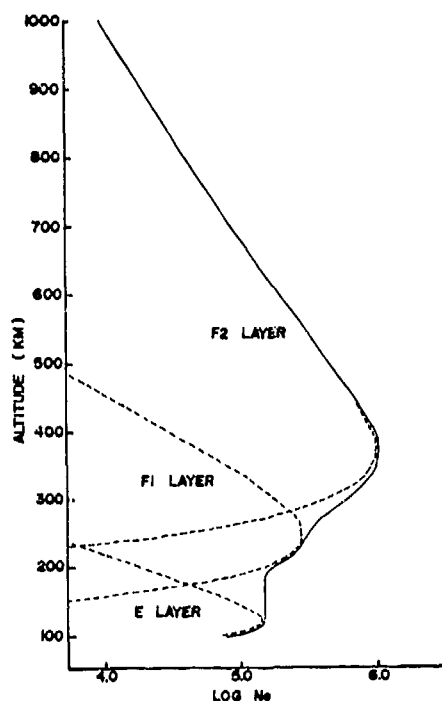


FIGURE 4 ELECTRON DENSITY vs. ALTITUDE  
AWS ELECTRON-DENSITY MODEL

b. Below the F2 peak, the final electron-density values are not allowed to decrease with altitude. Where the sum of the three Chapman layers decreases with altitude, the model indicates a constant value until the electron density begins to increase.

c. Scale heights for the E, F1, and bottomside F2 layers are taken as constant throughout those layers. Scale heights for the topside F2 region increase with altitude as in the original Damon-Hartranft model. The variable topside scale heights provide a closer approximation to observed topside electron-density profiles than does use of a constant scale height above the F2 peak (Figure 5).

#### E LAYER:

$$\begin{aligned} \text{foE} &= 0.9 \{ (180 + 1.44R) \cos \chi \}^{0.25}, \chi < 90^\circ \\ &= 0.7 \quad \text{for } 135^\circ > \chi > 90^\circ \\ &= 0.3 \quad \text{for } \chi > 135^\circ \end{aligned}$$

$$h_{\max} = 120 \text{ km}$$

$$a = 0.5$$

$$H = 15.58 \text{ km}$$

#### F1 LAYER:

$$\text{foF1} = 1.26 \text{ foE} + 0.5$$

$$h_{\max} = (h_{\max}^E + h_{\max}^{F2})/2$$

$$a = 1.0$$

$$H = 45.75 \ln h_{\max} - 203.45 \text{ km}$$

#### F2 LAYER:

foF2 from automated analysis  
or direct observation

$$h_{\max} = \frac{1490}{M3000} - 176 - 20(Q \ln \{ \frac{Q+1}{Q-1} \} - 2)$$

$$\text{where } Q = 0.834 \frac{\text{foF2}}{\text{foE}} \quad (\text{Kelso, 1964})$$

$$a = 1.0$$

$$\begin{aligned} h_{\max} &= 45.75 \ln h_{\max} - 203.45, \quad h < h_{\max} \\ &= k \cdot \ell (45.75 \ln h_{\max} - 203.45), \end{aligned}$$

when  $h > h_{\max}$ ; factors  $k$  and  $\ell$   
are given in Table 3 and 4.

$$\text{PROFILE } N_e = N_e^E + N_e^{F1} + N_e^{F2}$$

For each layer,

$$N_e(h) = N_{\max} \exp a(1 - Z - \exp(-Z))$$

where  $Z = (h - h_{\max})/H$

$N_e$  = electron density at height  $h$

$N_{\max}$  = electron density at peak  
of Chapman layer,  $h_{\max}$

$H$  = scale height

$R$  = mean sunspot number

$\chi$  = solar zenith angle

TABLE 2. CHARACTERISTICS OF THE AIR  
WEATHER SERVICE ELECTRON  
DENSITY / TEC MODEL

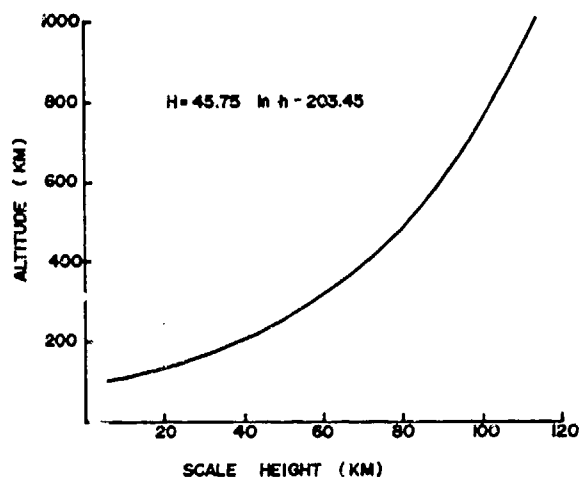


FIGURE 5 SCALE HEIGHT vs. ALTITUDE  
(TOPSIDE F2 LAYER)

d. Total Electron Content is obtained by summing the electron content in five-kilometer slabs from 95 to 1000 kilometers.

e. The model is driven primarily by three characteristic parameters of the F2 region:

(1)  $N_{max}F2$ : defined by values from the automated ionospheric analysis or from direct observations;

(2)  $h_{max}F2$ : defined by a modified Shimazaki equation (see Table 2) and values of M3000 from the automated analysis, ITS, or direct observation;

(3) Topside scale height, H: basic topside scale height values are illustrated in Figure 5. The topside scale height values are adjusted by a set of empirical scale-height factors which account for seasonal, local time, and latitudinal variations in the topside F2 region. The scale-height factors are given in Tables 3 and 4. Typical effects of changes in the topside scale height factors are shown in Figure 6.

Once the peak electron density and altitude of the peak are specified, the topside scale height may be changed as desired to yield a wide range of TEC values. For operational applications, we require that the model produce values of TEC that can be verified on an hour-by-hour basis. While recognizing the limitations in the absolute accuracy of TEC measurements made by the Faraday rotation technique, we have elected to use such data to validate the model and to guide the AFGWC ionospheric forecasters in adjusting topside scale

heights to match TEC observations. The instability of the Air Weather Service model is its prime asset, because it becomes possible to produce TEC values and electron-density profiles matched to actual observations if such observations are available.

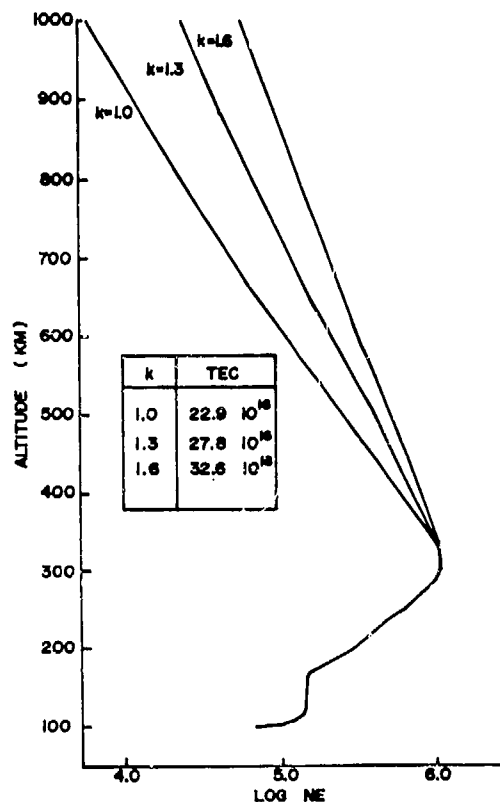


FIGURE 6 ELECTRON DENSITY vs. ALTITUDE SHOWING  
EFFECT OF TOPSIDE SCALE-HEIGHT FACTOR, k

#### SCALE HEIGHT ADJUSTMENT

The scale-height factor, k, shown in Table 3, was derived from an analysis of TEC observations at the Air Force Cambridge Research Laboratories' Sagamore Hill Observatory from 1968 through 1972. The scale height factors were chosen to minimize the difference between the modeled TEC and the observed (monthly median) TEC values. The "k" factors account for seasonal and local time variations in F2 topside structure; no solar-cycle dependence could be found. The use of the factor, k, reduced the RMS error in specification of the diurnal curves of monthly median TEC from  $2.8 \times 10^{16}$  electrons per square-meter column to  $1.2 \times 10^{16} e/m^2$  over the period studied. The diurnal variation in specification error is shown in Figure 7a; Figure 7b shows the mean diurnal TEC curves to which the



LOCAL TIME:		00	01	02	03	04	05	06	07	08	09	10	11	12	13	14	15	16	17	18	19	20	21	22	23
MONTH																									
JANUARY		1.3	1.3	1.3	1.2	1.2	1.2	1.2	1.1	1.0	1.0	1.0	1.0	1.0	1.0	1.0	1.0	1.1	1.2	1.3	1.3	1.3	1.3	1.4	1.4
FEBRUARY		1.3	1.3	1.2	1.2	1.2	1.2	1.2	1.2	1.2	1.2	1.2	1.2	1.2	1.2	1.3	1.3	1.3	1.3	1.3	1.3	1.3	1.3	1.3	1.3
MARCH		1.3	1.3	1.3	1.3	1.3	1.3	1.3	1.2	1.1	1.2	1.2	1.2	1.2	1.2	1.2	1.3	1.3	1.3	1.3	1.3	1.3	1.3	1.3	1.3
APRIL		1.3	1.3	1.3	1.3	1.3	1.3	1.3	1.3	1.3	1.3	1.3	1.3	1.3	1.3	1.3	1.4	1.4	1.4	1.4	1.4	1.4	1.4	1.4	1.3
MAY		1.3	1.3	1.3	1.3	1.4	1.5	1.4	1.4	1.4	1.4	1.4	1.4	1.4	1.5	1.5	1.6	1.6	1.6	1.7	1.6	1.5	1.5	1.4	1.3
JUNE		1.3	1.3	1.3	1.4	1.5	1.5	1.5	1.5	1.5	1.5	1.5	1.5	1.5	1.5	1.5	1.6	1.7	1.7	1.6	1.6	1.5	1.4	1.4	1.3
JULY		1.3	1.3	1.3	1.3	1.4	1.5	1.5	1.5	1.4	1.4	1.5	1.5	1.5	1.5	1.5	1.6	1.7	1.7	1.6	1.6	1.5	1.4	1.4	1.4
AUGUST		1.2	1.2	1.2	1.2	1.3	1.3	1.3	1.3	1.3	1.3	1.3	1.3	1.3	1.4	1.4	1.5	1.5	1.6	1.6	1.5	1.3	1.3	1.3	1.2
SEPTEMBER		1.3	1.2	1.2	1.3	1.3	1.2	1.2	1.2	1.2	1.2	1.2	1.2	1.3	1.3	1.3	1.3	1.3	1.4	1.4	1.4	1.3	1.3	1.3	1.3
OCTOBER		1.3	1.2	1.2	1.2	1.2	1.2	1.1	1.1	1.1	1.1	1.1	1.1	1.1	1.1	1.1	1.2	1.2	1.3	1.3	1.3	1.3	1.3	1.3	1.3
NOVEMBER		1.4	1.3	1.3	1.3	1.3	1.3	1.2	1.1	1.1	1.1	1.1	1.1	1.1	1.1	1.1	1.2	1.2	1.3	1.3	1.4	1.5	1.6	1.6	1.5
DECEMBER		1.6	1.5	1.4	1.3	1.3	1.3	1.3	1.3	1.0	1.0	1.0	1.0	1.1	1.1	1.1	1.1	1.2	1.3	1.3	1.5	1.6	1.7	1.7	1.7

TABLE 3: SCALE HEIGHT FACTORS FOR TOPSIDE F2 REGION: SEASONAL AND LOCAL-TIME VARIATION (b)

For geomagnetic latitudes  $>55^\circ$   $\ell = 1.0$

For geomagnetic latitudes  $<25^\circ$   $\ell = 1.3$

From  $25^\circ$  to  $55^\circ$  geomagnetic latitude,  $\ell = 1 + 0.3 \cos(3\{\text{GEOMAG LAT} - 25\})$

TABLE 4: SCALE HEIGHT FACTORS FOR TOPSIDE F2 REGION: LATITUDINAL VARIATION ( $\ell$ )

RMS specification error relates. Note that these error estimates represent the only available evaluation of the TEC model itself, separate from errors in foF2 specification; the RMS errors shown in Figure 7 were obtained using "perfect" knowledge of foF2 for the monthly median TEC observations.

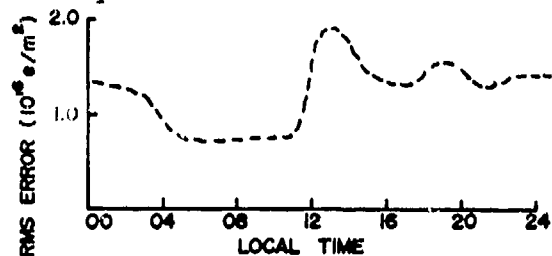


FIGURE 7a. RMS ERROR IN SPECIFYING TEC

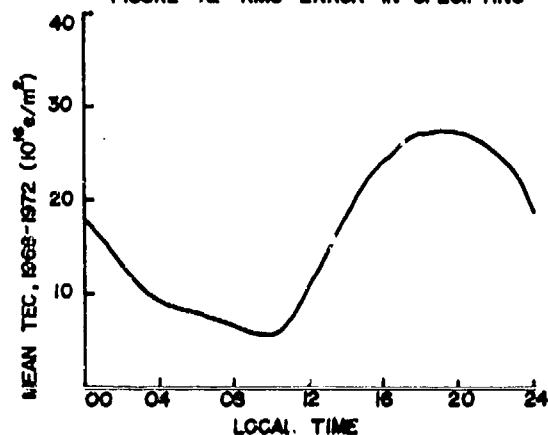


FIGURE 7b. MEAN TEC, SAGAMORE HILL 1968-1972

The effective topside scale height is also expected to vary with latitude, longitude, and geomagnetic activity. To date, it has been necessary to ignore longitudinal and geomagnetic-activity variations because of a lack of data. The latitudinal variation in the scale height has been estimated from a small collection of real-time TEC observations. Approximately four months of operational data from Goose Bay, Sagamore Hill, Patrick AFB, and Ramey AFB (Puerto Rico) were compared to modeled TEC values to determine the latitudinal scale-height factor,  $h'$ , given in Table 4. We recognize that this factor provides at best a gross approximation to the latitudinal variation in topside structure; even in its present state of development, it serves to reduce the RMS error in specifying TEC at locations where observations are available.

## EVALUATION

The final test of the model's value is its ability to specify TEC on a day-to-day, hour-to-hour basis. Observed and specified TEC at each of the five operational observing locations are shown in Figure 8 for two days in early January 1975; 01 January was a geomagnetically quiet, well-behaved day -- 04 January was the date on which a minor geomagnetic disturbance began, and "typical" TEC curves for the first day of a geomagnetic disturbance were seen.

Figure 9 shows mean TEC behavior for five observing locations during the most recent evaluation period (19 DEC 74 through 06 JAN 75). RMS errors for day and night TEC specification over that period are given in Table 5. The specification errors are due partly to the error in foF2 specification, but primarily to F2 topside characteristics that vary significantly from those estimated by the median scale-height factors,  $k'$  and  $h'$ . The "non-standard" behavior of the F2 region can be seen in Figure 8; note the difference between the accuracy of the model on the geomagnetically quiet day (01 JAN), and on the day of the disturbance onset (04 JAN). When geomagnetically disturbed days (A sub p of 25 or greater) are removed from the verification sample, the RMS error in daytime TEC specification is significantly decreased as shown in Table 5.

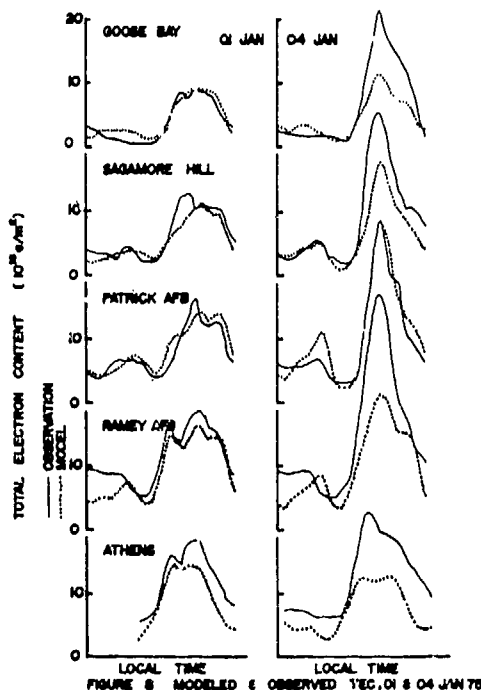


FIGURE 8. MODELED & OBSERVED TEC, 01 & 04 JAN 75

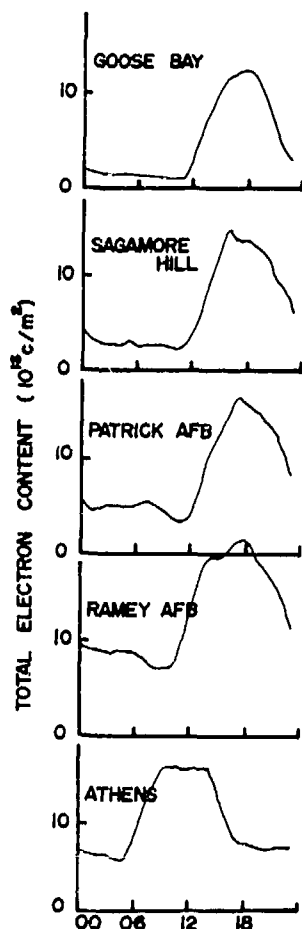


FIG. 9 MEAN OBSERVED TEC 19

RMS TEC ERROR ( $10^{16} \text{ e/m}^2$ )

STATION	DAY	NIGHT
ATHENS	3.74 (2.42)	2.84 (2.84)
GOOSE BAY	2. (2.26)	1.37 (1.47)
PATRICK	2.01 (1.7)	1.49 (1.55)
RAMEY	4.63 (3.91)	3.38 (3.32)
SAGAMORE	3.13 (2.50)	1.06 (0.60)

TABLE 5. Root-Mean-Square Error in Operational Specification of TEC (19 DEC 74 - 06 JAN 75) (Values in parentheses are with geomagnetically disturbed days removed.)

On a global basis, the expected accuracy of the TEC model may be estimated from the known errors in foF2 specification. The RMS errors in foF2 specification presented above are approximately equivalent to  $\pm 10\%$  for the automated analysis and to  $\pm 20\%$  for the ITS specification. (ITS errors must be considered, because at locations more than about 1500-2000 km distant in longitude or about 750-1000 km in latitude, the "analysis" fields return to ITS values.) Assuming that TEC is proportional to the square of foF2, it can be shown that the percent error in TEC is proportional to twice the percent error in foF2. We may then expect about a  $\pm 20\%$  error in TEC from the error or uncertainty in foF2 from the automated analysis; the ITS uncertainty in foF2 specification would yield approximately  $\pm 40\%$  error in TEC. There are, of course, other factors which contribute to the errors in TEC: primarily M3000 errors, and the inability to reproduce the structure of the topside F-region through climatological scale-height factors. The various errors may often be compensating. In summary, we expect that the combined foF2/M3000/TEC model should be capable of specifying TEC at any point in the Northern Hemisphere with a root-mean-square error of about  $\pm 20\%$  near ionosonde sites to something over  $40\%$  in data-sparse areas. On a world-wide basis, then, we may assume a state-of-the-art TEC specification accuracy of  $\pm 30\%$ . Observed daytime RMS percent errors at the five operational TEC observing sites ranged from  $13\%$  to  $32\%$  over the 19 DEC 74 through 06 JAN 75 evaluation period. Suitable adjustments of the topside scale-height factor by an experienced ionospheric analyst can reduce the error to less than  $10\%$  on a case-by-case basis where detailed post-analyses are required.

#### REFERENCES

1. Bussey, R.M., and A.C. Ramsay (1974), Unpublished Program Documentation, Air Force Global Weather Central.
2. Damon, T.D., and F.R. Hartranft (1970) Ionospheric Electron Density Model, Aerospace Environmental Support Center Technical Memorandum 70-3.
3. Flattery, T.W. (1971) Spectral Models for Global Analysis and Forecasting, Air Weather Service Technical Report 242.
4. Jones, W.B., R.P. Graham and M. Leftin (1969). Advances in Ionospheric Mapping by Numerical Methods, ESSA Technical Report ERL 107 - ITS 75.
5. Kelso, J.M. (1964) Radio Ray Propagation in the Ionosphere, McGraw-Hill, NY.
6. Rush, C.M. (1972) Improvements in Ionospheric Forecasting Capability, Air Force Cambridge Research Laboratories Environmental Research Papers, No. 387, AFCRL-72-0138.

DECIMETER MODELING OF IONOSPHERIC COLUMNAR  
ELECTRON CONTENT AT S-BAND FREQUENCIES\*

K. W. Yip, F. B. Winn, M. S. Reid, C. T. Stelzried  
Jet Propulsion Laboratory  
California Institute of Technology  
Pasadena, California

INTRODUCTION

This paper presents a simple empirical model which has been developed for the evaluation of the ionospheric total electron content along any ray path. It is a mapping model which requires as input Faraday rotation data acquired from a geostationary satellite. This model is developed primarily for ionospheric calibrations in day time space probe tracking.

The discussion on this model is divided into five parts:

- A) The hardware system for the acquisition of Faraday rotation data
- B) The processing of the Faraday rotation data
- C) The mapping of these data to the desired ray path
- D) The validity of this mapping model
- E) The significance of the total electron content (TEC) calibrations provided by this model as demonstrated during the Mariner-Venus-Mercury (MVM'73) mission in 1973.

A. INSTRUMENTATION FOR FARADAY  
ROTATION DATA ACQUISITION

Two independent polarimeters are used to determine ionospheric columnar electron content. Both polarimeters are located at the National Aeronautics and Space Administration (NASA) Goldstone Venus tracking station in California. The polarimeters measure the Faraday rotation of a signal from one of the Applications Technology Satellite (ATS) series, from which the ionospheric electron content is calculated.

One polarimeter is manufactured by the Aldi Corporation, the other by Teledyne Micronetics. Although they have similar functional block diagrams they are, nevertheless, independent designs using different circuits. Figure 1 shows a simplified functional block diagram of both polarimeters.

\* This paper presents the results of one phase of research carried out at the Jet Propulsion Laboratory, California Institute of Technology, under Contract No. NPS 7-100, sponsored by the National Aeronautics and Space Administration.

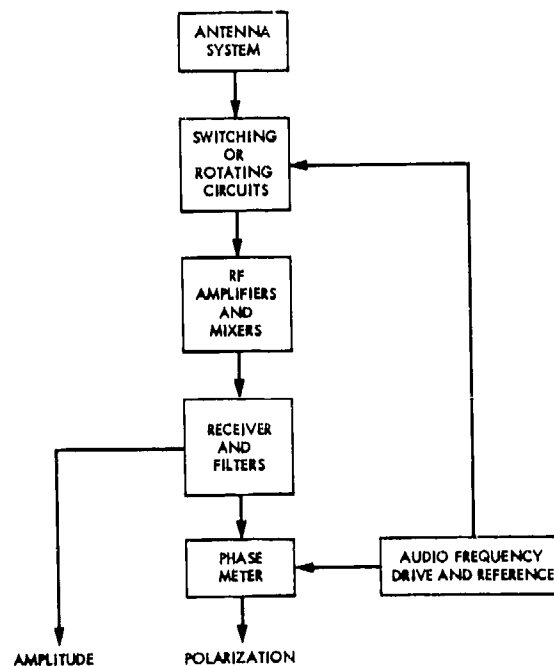


Figure 1  
Simplified Functional Block  
Diagram of Polarimeters

For the Aldi polarimeter the antenna system is a pair of geometrically orthogonal, linearly polarized antennas, which are sequentially sampled by solid-state electronic switching circuits driven by an audio frequency reference. For the Teledyne polarimeter the antenna system is a crossed-Yagi array. This array feeds a 90° hybrid to provide right and left circularly polarized outputs, one of which is passed through

an electronic phase shifter which provides linear phase shift versus applied voltage through a range of  $360^\circ$ . A second  $90^\circ$  hybrid is used for the recombination of the signals. These circuits therefore form an electronically rotated antenna system, also driven by an audio frequency reference signal.

Radio Frequency (RF) amplifiers and mixers are followed by receiver and filter chains as shown in the block diagram. The polarization output is taken from the phase meter and the amplitude output from the receiver/filter chain.

Both polarimeters are packaged into rack mounted panels and feed a common automatic data acquisition system which provide punched paper tape output and analog strip-chart recordings. Figure 2 shows a photograph of the rack housing both polarimeters and the data system. Figure 3 shows a photograph of both antenna systems.

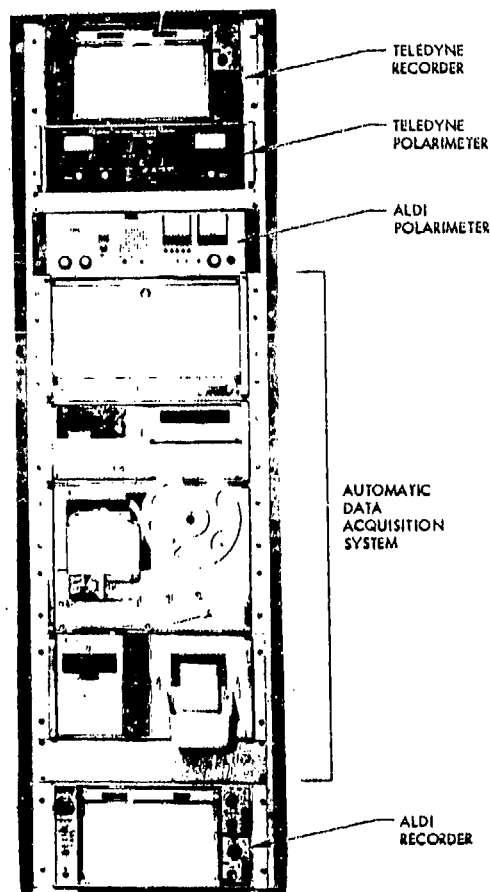


Figure 2  
Faraday Rotation Data Acquisition System

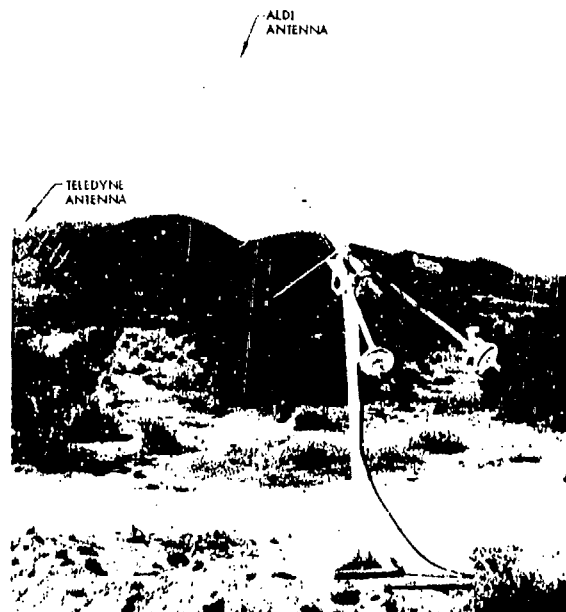


Figure 3  
Faraday Polarization Measurement  
Antenna System at DSS 13

An error analysis shows resolution and stability are sufficient and that polarization and amplitude linearity errors are acceptable. The latter are introduced by antenna unbalance, non-linearity (departure from square law) in the detector and by mismatch in the input impedance of the amplifier. These factors are all small and stable in time.

#### B. FARADAY ROTATION DATA

The amount of Faraday rotation in radians is given by

$$\Omega = \frac{R}{f} \int_S ||H|| \cos\theta \sec \alpha N(s) ds \quad (1)$$

where  $R = 2.97 \times 10^{-2}$  in MKS units  
 $f$  = frequency of radio wave in Hz  
 $\alpha$  = angle between ionospheric station's zenith and station-geostationary satellite ray path  
 $||H|| \cos\theta$  = tangential component of the magnetic field along the ray path, amp-turns/m  
 $N(s)$  = electron density distribution along ray path  $S$  in electrons/ $m^3$

For the reduction of Faraday rotation data, a dipole magnetic field for the earth is assumed. Eq. (1) is then approximated by

$$\Omega \approx \frac{R}{r^2} \langle ||H|| \cos \theta \rangle_{\text{ref}} \sec \alpha \int_S N(s) ds$$

where the subscript "ref" indicates that  $||H \cos \theta||$  is computed for a reference point along the path through the ionosphere. The altitude of this reference point has been taken to be 350 km above the earth. It has been shown (Ref. 1) that uncertainties involved in this choice are less than 2%.

For input to the model, these "slant" TEC are converted to zenith TEC at the ionospheric reference point (Appendix A). The ionospheric reference point is defined as the point where the ray path in question intersects the ionosphere at an altitude of 350 km. Ionospheric conditions at this point are used to typify conditions along the entire ray path.

#### C. MAPPING OF ZENITH TEC

The mapping procedure of the model consists of two parts: (1) the space-time mapping and (2) the elevation angle mapping.

##### 1. Space-Time Mapping

This translation is based on the assumption that, at the same local time, two stations have identical zenith TEC values if the difference in geomagnetic latitudes is not considered.

This space-time translation depends on the longitudinal difference of the two ionospheric reference points -- this is the time translation that must be applied to one data set to convert it to the other time system ( $\tau \sim \lambda$ ).

##### Magnetic Latitude Adjustment

As one ascends in altitude into the ionosphere one reaches a point where the electron density is the maximum. In part, the value of this maximum depends on the geomagnetic latitude. Thus, in addition to the time translation of the TEC data, it must also be corrected for geomagnetic latitude difference. However, this correction is very complicated since it not only depends on the magnetic latitudes but also the time of the year and the level of solar activities (Reference 2). Fortunately, in our application of the ionospheric model to space probe tracking\*, a geostationary satellite can usually be found such that the ionospheric reference points under consideration are usually quite close ( $\lesssim \pm 10^\circ$ ) in geomagnetic latitudes. This is convenient since examinations of the contour plots of maximum electron density as a function of geomagnetic latitude and local time (Figure 4) show that the contours for mid-latitudes usually do not change much during the day time for small geomagnetic latitude variations. A simple approximation which depends only on the

\* All tracking stations in the NASA/JPL Deep Space Net are located at mid-latitudes.

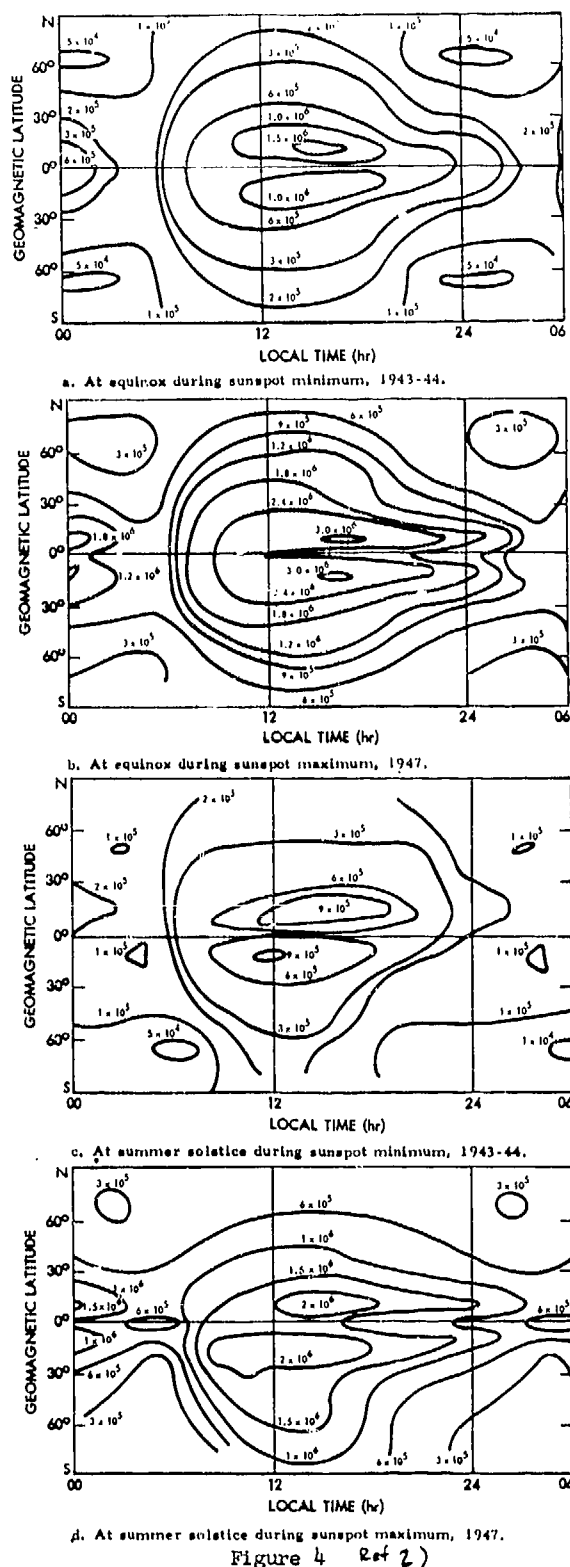


Figure 4 Ref 2)

Contours of  $N_m F_2$  (electron concentrations at the  $F_2$  peak) in electrons/cm<sup>3</sup>



geomagnetic latitudes. The linear separation of the 2 ray paths in the ionosphere is ~470 km. The two electron content profiles reveal a <20 cm standard deviation with the maximum difference being ~40 cm.

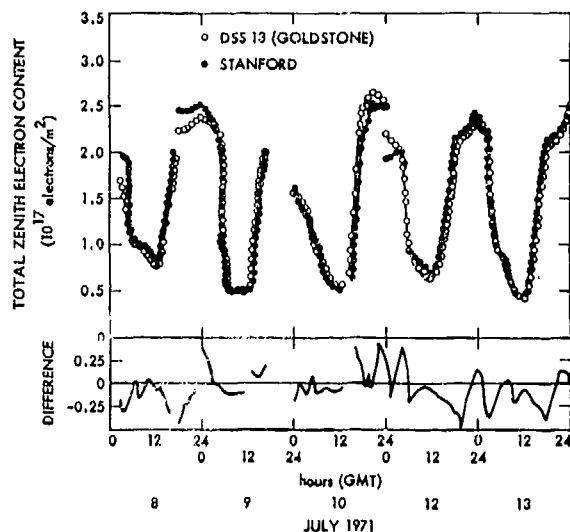


Figure 7 — Comparison of Different Polarization Data Sets

## 2) S/X Dual Frequency Doppler and Mapped Faraday Charged-Particle Calibrations

A second approach to ascertaining the accuracy of mapped Faraday calibrations is to compare them to a different, independent calibration.

One such independent data type is S/X dual frequency Doppler charged particle calibrations. The phase velocities of S-band radio signals (~2300 MHz) are  $(11/8)^2$  more advanced than are X-band radio signals (~8100 MHz) by electron content dynamics. If S/X dual frequency Doppler data are simultaneously received, the line-of-sight electron content change per unit time is symbolically

$$\Delta \rho_s = k(\Delta \nu_s - \frac{3}{11} \Delta \nu_x)$$

Thus, the integrated S/X dispersive Doppler data yield collectively the TEC of the ionosphere and of the space plasma along the tracking station-deep space probe ray path. If the TEC contribution of the space plasma is insignificant, an independent measurement of the ionospheric TEC is available. Many comparisons of the TEC's given by the mapping model and the S/X data have been made, and the first three are presented in the following.

### S/X Dual Doppler and "Mapped" Faraday Comparisons: Day 349, 1973

A comparison of the Faraday rotation and S/X evaluations of the electron content history over the pass reveals the long term trends to match (Figure 8). The maximum disagreement is ~0.15 m at 23<sup>h</sup> 51<sup>m</sup>. This is 10% of the total correction at that time. However it is also apparent that fine structure variations along the DSS 14-MVM73 line-of-sight can not

be obtained by mapping the fine structure variations from the DSS 13-ATS-1 line-of-sight. The short term variations (Figure 8) of the Faraday and S/X data do not correlate and the maximum difference is ~0.2 meters. From the differences pictured in Figure 8, it can be deduced that the localized, short term, ionospheric variations are ~0.25 m/hr (~ $3 \times 10^{16}$  electrons/m<sup>2</sup>/hr). This is quite reasonable.

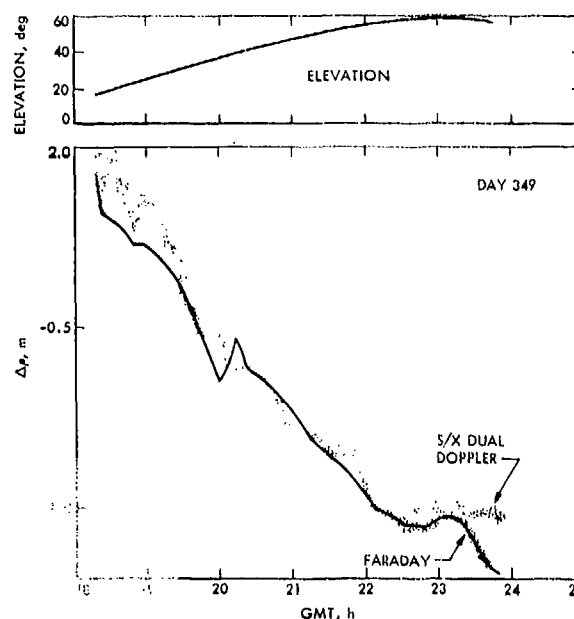


Figure 8 — Faraday vs S/X Data, Day 349, 1973

### S/X Dual Doppler and "Mapped" Faraday Comparisons: Day 364, 1973

The seven hours of S/X Doppler data for day 364 (December 30, 1973) is similarly compared with the Faraday rotation data and plotted in Figure 9. Again, the agreement of the gross trends is good. In this pass, however, the agreement of the S/X and Faraday data at the beginning and the end of the pass is only at the 0.2 - 0.3 meter level. Although the elevation angle of the spacecraft is quite high (~40°) in the beginning of the pass, the separation of the DSS 14 - MVM73 and DSS 13 - ATS-1 lines-of-sight is more than five degrees (~550 km). As can be seen from the above discussions (D1) local irregularities of this magnitude are expected on this linear scale. Towards the end of the pass the elevation angle to the spacecraft dropped to less than 30°. Calculations show that the solar zenith angle (X) on this day becomes larger than 90° at UT=25 hours. Thus, this discrepancy can be partly due to the inadequacy of the Chapman ionospheric model for  $X \geq 85^\circ$  (Reference 6).



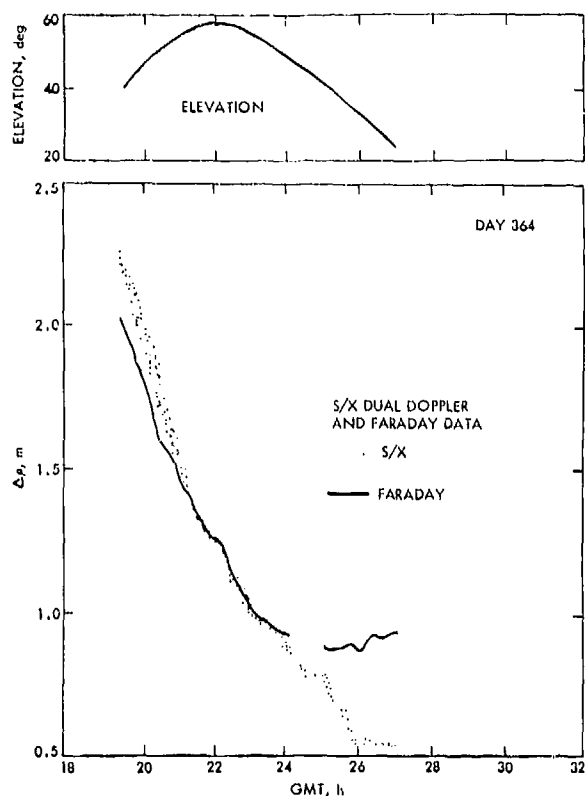


Figure 9  
Faraday vs S/X Data, Day 364, 1973

S/X Dual Doppler and "Mapped" Faraday  
Comparisons: Day 003, 1974

The S/X Doppler data acquired on day 003 (3 January 1974) compares even better with the Faraday measurements (Figure 10). This stems from the data taken only at the higher elevation angles as shown in Figure 10. The maximum difference between the mapped Faraday and the S/X measurements is ~0.05 meters.

Thus, the maximum disagreement, under most conditions, is but 0.3 m for the comparison with these first three S/X dual frequency Doppler data sets. Part of this difference might be due to space plasma dynamics which the dual Doppler is sensitive to. This, however cannot be very much due to the close earth proximity of the spacecraft at this time.

In as much as the S/X dual frequency Doppler data is the most accurate data type available for ascertaining the TEC along the station-spaceprobe ray path\*, its comparison with the model has been presented here in detail. Comparisons with the other data types (3 and 4 in footnote of P. 4) have been carried out (Refs.

\* It has sub-centimeter resolution -- Reference 7.

8, 7). But it would serve little purpose to go into that here.

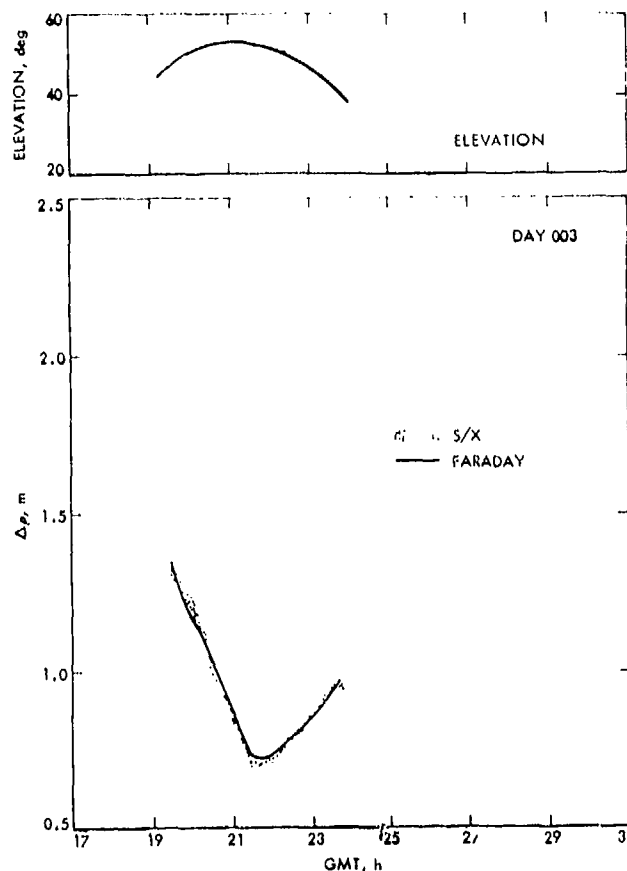


Figure 10  
Faraday vs S/X Data, Day 003, 1974

**E. THE SIGNIFICANCE OF "MAPPED" FARADAY  
CALIBRATION TO DEEP SPACE PROBE NAVIGATION**

Radiometric Doppler used to track space probes are influenced by charged-particle dynamics of the earth's ionosphere and of the space plasma. When we restrict our attention to the time period just before the Mercury fly-by of the Mariner 10 spacecraft (March 29, 1974), the effect of the charged particle dynamics on the recursive least squares adjustment of the spacecraft state when Doppler is reduced produced ~ 110 km change in the estimated position of the probe at Mercury encounter. This is a 60% improvement in the encounter position estimated (Ref. 8). The statistics were improved by 28% with the application of the ionospheric calibrations.

**SUMMARY**

A simple empirical model has been developed for the evaluation of the ionospheric

total electron content along ray paths at mid-latitudes during the day-time. It is a mapping model which requires as input Faraday rotation data acquired from a geostationary satellite. TEC calibrations accurate to  $\sim 3 \pm 17$  cm ( $1\sigma$ ) for any ray paths are obtainable from the model.

Such accuracies result from restricted use of the model:

- 1) Northern hemisphere only
- 2) Maximum geomagnetic latitude differences between ionosphere reference points of observed and computed TEC  $\sim 5^\circ$ . Fine scale structures and irregularities along the ray path are not accounted, but their amplitudes have been observed to be usually less than 0.1 m ( $1\sigma$ ).

#### APPENDIX A

The ionosphere reference point is computed as follows (see Fig. A1):

$$\tilde{R} = \tilde{\rho} + \tilde{r}$$

$$\tilde{r} = r \begin{bmatrix} \cos \lambda_s \cos \phi_s \\ \sin \lambda_s \cos \phi_s \\ \sin \phi_s \end{bmatrix}$$

$$\tilde{\rho} = \rho \begin{bmatrix} \cos(\lambda_s - \alpha) \cos \delta \\ \sin(\lambda_s - \alpha) \cos \delta \\ \sin \delta \end{bmatrix}$$

$$\tilde{R} = R \begin{bmatrix} \cos \lambda_p \cos \phi_p \\ \sin \lambda_p \cos \phi_p \\ \sin \phi_p \end{bmatrix}$$

where

$\tilde{R}$  = a vector from the center of the earth to the ionosphere reference point:

$$|\tilde{R}| = R = h + R_e, \quad h \sim 350 \text{ km}, \quad R_e = \text{earth's radius}$$

$\tilde{\rho}$  = a vector from the station to the sub-ionosphere point:  $|\tilde{\rho}|^2 = \rho^2 = -R_e \sin \gamma + (2hR_e + h^2 + R_e^2 \sin^2 \gamma)^{1/2}$ ,  $\gamma$  = elevation angle of probe

$\tilde{r}$  = a vector from the center of the earth to the station:  $|\tilde{r}| = R_e$

$\lambda_s$  and  $\phi_s$  = station longitude and latitude

$\alpha$  and  $\delta$  = probe's topocentric hour angle and declination

$\lambda_p$  and  $\phi_p$  = longitude and latitude of the subionosphere point:

$$\lambda_s = \tan^{-1} \left[ \frac{\sin(\lambda_s - \alpha) \cos \delta + R_e \sin \lambda_s \cos \phi_s}{\cos(\lambda_s - \alpha) \cos \delta + R_e \cos \lambda_s \cos \phi_s} \right]$$

$$\phi_p = \sin^{-1} \left[ \frac{1}{R} (\rho \sin \delta + R_e \sin \phi_s) \right]$$

The elevation angle  $\gamma$  is computed from  $\alpha$  and  $\delta$  by the spherical trigonometry relationships:

$$\sin \gamma = \sin \phi_s \sin \delta + \cos \phi_s \cos \delta \cos \alpha$$

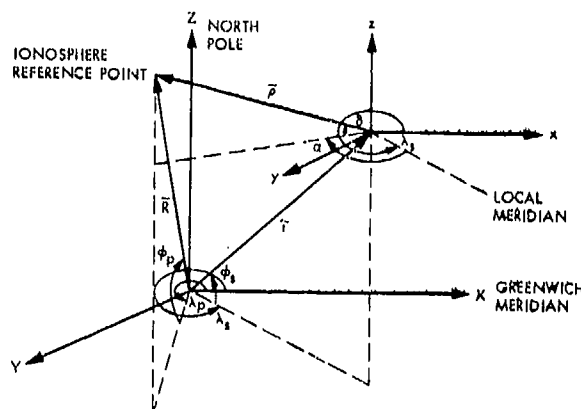


Figure A1

Calculation of Ionospheric Reference Point

#### REFERENCES

1. von Roos, O. H., Yip, K. W., "Determination of the Total Electron Content From Faraday Rotation Measurements", TM 391-330, May 1972 (JPL internal document).
2. Hanson, W. B., "Structure of the Ionosphere" in Satellite Environment Handbook", 2nd Edition, 1965, Edited by F. S. Johnson.
3. Efron, L., "Model Ionosphere and Phase Path Errors", TM 312-524, January 1965 (JPL internal document).
4. Liu, A., Cain, D., "Ionospheric Range and Angular Corrections", TM 312-674, March, 1966 (JPL internal document).

5. Yip, K. W., "A Sensitivity Analysis of the One Way Ionospheric Range Changes with Respect to the Chapman Parameters", TM 391-425, March, 1973 (JPL internal document).
6. Chapman, S., "The Absorption and Dissociative or Ionizing Effect of Monochromatic Radiation in an Atmosphere on a Rotating Earth", Proc. Phys. Soc. (London), 43, p. 25, 1931.
7. Koch, R. E., Chao, C. C., Winn, F. B., Yip, K. W., "Conditioning of MVM'73 Radio Tracking Data", AIAA Paper # 74-832, Anaheim, California, August 1974.
8. Winn, F. B., Yip, K. W., Reinbold, S. J., "DSN-MVM'73 S/X Dual Frequency Doppler Demonstration", The Deep Space Network Progress Report 42-22, p. 28, May 1974.

## IONOSPHERIC MODELS USED IN IONOGRAM INVERSION TECHNIQUES

R. O. Conkright  
Environmental Data Service, NOAA  
Boulder, Colorado 80302

Ionograms are the analog record of vertical incidence radio soundings of the ionosphere (see, for example, M. Phillips, 1974). They are a representation of the virtual height of echoes from the ionospheric layers over a range of HF frequencies. They can be converted to electron density profiles in real height by inversion techniques: the basic scheme used by the NOAA groups (formerly Central Radio Propagation Laboratory of the National Bureau of Standards) is described by A. Paul et al., (1967).

Because the coverage of ionospheric monitoring by ionosondes is worldwide, and essentially continuous, the data are particularly useful in checking F-region models. Thus, there have been some sizable projects for mass-producing profiles of electron density,  $N(h)$ , from ionograms from the world network. Much of these data are in the World Data Centers. The validity of the F-region data depends on the use of models of the ionization at lower heights where the inherent insensitivity of ionosondes limit the information that is available. This paper discusses the modelling for the underlying ionization -- the "unseen" echoes of the ionogram -- and the reliability of a large data base where these models were used.

The main limitation of all procedures for deriving  $N(h)$  profiles from ionograms is the lack of echoes at the lower frequencies which would refer to the lower heights, due to the limited sensitivity of the usual monitoring ionosonde. Thus, it is common to have no echoes below a probing frequency of 1.5 MHz or a virtual height of 110 km. But the echo retardation at lower heights importantly affects the calculated profile of the F-region electron density and the F-region models and morphology based on ionogram data.

The "unseen" echoes are treated by our model in two steps. First, we apply a model of the integrated ionization up to 90 km, a height below which ionogram echoes are hardly ever observed. Second, we apply a model for the E layer in the large number of cases, particularly at night, when this is not observed.

The portion of the model which treats below 90 km is due to Smith (1974) and in effect takes account of the diurnal variation of D-region ionization by a simple relationship involving the cosine of the sun's zenith angle by day and a linear relaxation in the late afternoon and evening which matches radio propagation experience (Figure 1). This is applied as a model point on the virtual height-frequency curve where the inversion calculation is started.

The model of the E-layer critical frequency as a function of time of day, season and location on the earth is taken from the empirical E-layer climatology used for ionospheric radio propagation predictions (Roberts and Rosich, 1971). It is close to zenith angle dependence by day, with nighttime values from limited observations and radio propagation experience. The height profiles at the E-layer maximum is assumed to be roughly parabolic; for consistent computing purposes the virtual height of the E-layer cusp on the ionogram is taken as 400 km (Figure 2).

The details of these model assumptions for the D- and E-region ionization are not as important as the consistency with which they are used in derivation of the  $N(h)$  profiles which apply mainly to the F-region. The models described were used by NOAA's Space Environment Laboratory in producing a very large  $N(h)$  data base by

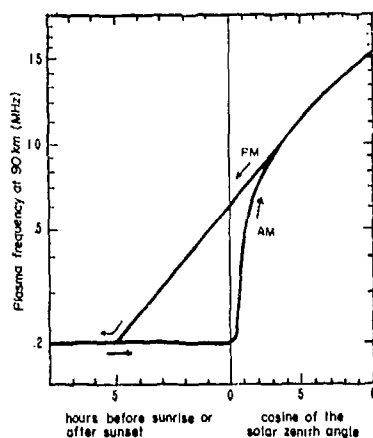


Figure 1. Model of diurnal variation of the plasma frequency at 90 km.

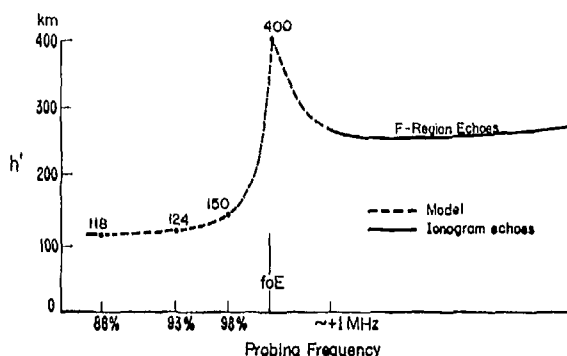


Figure 2. Model  $h'(f)$  near E-layer critical frequency.

nearly automatic techniques (G. Lerfeld et al., 1974). In assessing the quality of these 18,000 profiles for 15 stations for selected periods in 1964, we indirectly obtain a measure of the consistency of model application by automatic techniques (Figure 3). The maximum effect of erratic application of the model can be judged by the short-term variability of F-region parameters taken from the  $N(h)$  profiles which also includes natural variability and scaling and computational errors. On several dozen days studied, this variability was commonly less than 5 percent for the F-region maximum electron density, while for the electron density at a fixed height of 200 km the measured variability was somewhat more. These are maximum errors due to application of the models for underlying ionization and are small for most purposes. The modelling error is included in the three-grade quality assessment which will be attached to the detailed SEL profile data when it is archived in the World Data Center and made available to the scientific community.

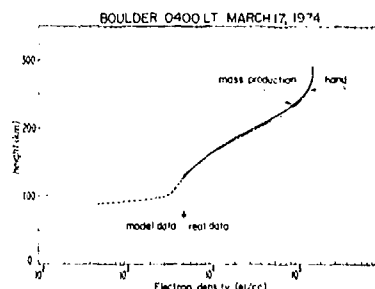


Figure 3. Sample comparison of  $N(h)$  profile derived by hand and by mass production techniques.

As a by-product of the automated digitizing system developed by NOAA/SEL, a simpler manual digitizing system was developed and is being used for routine ionogram reduction work at Boulder by NOAA/EDS. This system involves an electronic matrix board and a hand-held cursor connected to a programmable calculator. This system eliminates most of the errors encountered by the fully automated system, when the operator is an expert at ionogram interpretation.

In conclusion, NOAA/EDS is prepared to produce, upon request,  $N(h)$  profiles consistently incorporating the models just described. Either automated or manual techniques will be used to process the ionograms, depending upon the volume.

#### REFERENCES

- M. Lindeman Phillips, "Ground-Based Vertical-Incidence Ionograms," IEEE Transactions on Antennas and Propagation, AP-22, No. 6, November 1974.
- A. Paul, H. Howe, D. McKinnis, J. Wright, "Ionospheric Electron-Density Profiles with Continuous Gradients and Underlying Ionization Correction," Radio Science 2 (New Series), No. 10, October 1967.
- N. Smith, "Lower Ionosphere Morphology and the Start of the  $N(h)$  Reduction Program," (in preparation).
- W. Roberts and R. Rosich, "Ionospheric Predictions," Telecommunications Research and Engineering Report, 13 September 1971.
- G. Lerfeld, J. Wohlmuth, R. Jurgens, and G. Goz, "A Semi-Automated System for the True Height Analysis of Film Ionograms, Part 1. Overall Description," NOAA Technical Memorandum, ERL SEL 27, October 1973.

# SOLAR CYCLE VARIATIONS OF THE TOTAL ELECTRON CONTENT AT LOW LATITUDE

Yinn-Nien Huang

Telecommunication Laboratories, M.O.C.  
Chung-Li P. O. Box 71, Taiwan, Rep. of China

## I. Introduction

The Faraday rotation method of determining ionospheric electron content from the telemetry signals of earth satellites has been discussed by Garriett et al. (1970). At the early stage of study, several workers have used low altitude satellites signals to study about the diurnal, seasonal and solar cycle variations of the total electron content (e.g. Rees, 1966; Yeh and Flaherty, 1966; Rai and Hook, 1967). However, there was a serious difficulty in distinguishing among diurnal, seasonal and solar cycle variations. This ambiguity was removed when the geostationary satellite signal became available. Studies of diurnal and seasonal variations of total electron content by use of the geostationary satellite signals have been done by some workers (e.g. Titheridge, 1966; Yuen and Roelofs, 1966 and 1967; Garriett et al., 1970). However, very few workers have studied the solar cycle variations of the total electron content. The objective of the present study is to use the total electron content data obtained at the University of Hawaii to investigate the solar cycle variations of the total electron content at low latitude.

Continuous measurements of the electron content using Syncom III and ATS I beacon signals have been carried out at the University of Hawaii (geographic location: 21°18'N; 157°49'W; geomagnetic location: 21.0°N; 266.2°) since October 1964 (Yuen and Roelofs, 1966 - 1971). The monthly mean hourly values of electron content have been calculated by Yuen and Roelofs (1966, 1967) since October 1964. The monthly mean hourly values from January 1965 to December 1970 were used for the present study. The months were defined according to Table 1 instead of the ordinary calendar months in order to produce symmetry with respect to the inclination of the earth's axis to the sun.

## II. Solar Cycle Variation of the Monthly Mean Hourly Values at Different Hours.

Figure 1 shows the variations of the monthly mean hourly values of total electron content,  $I$ , at 00, 06, 08, 10, 14, 17, 20 and 23 hours. The

Table 1

Modified month	Ordinary calendar date
January	7 January-4 February
February	5 February-5 March
March	6 March-5 April
April	6 April-6 May
May	7 May-6 June
June	7 June-7 July
July	8 July-7 August
August	8 August-7 September
September	8 September-8 October
October	9 October-7 November
November	8 November-6 December
December	7 December-6 January

apparent seasonal variations of  $I$  at different hours are very clear and will be discussed in Sec. IV. To eliminate the seasonal variation, 12 month running average of  $I$ ,  $\bar{I}$ , was calculated and shown in the same figure. For comparison, the 12 month running average of monthly mean sunspot number,  $R$ , for each month is also shown at the top of the figure. It is very clear that the positive correlation exists between  $\bar{I}$  and  $R$  at each hour. However, the  $\bar{I}$  curves become horizontal at earlier time than the  $R$  curve does. This shows a saturation effect of  $\bar{I}$  variation near the sunspot maximum. The dependence of  $\bar{I}$  on  $R$  can be seen more clearly in Figure 2. The increase of  $\bar{I}$  becomes saturated when  $R$  reaches the value of about 100. The rate of increase of  $\bar{I}$  differs at different hours. The correlation coefficient between  $\bar{I}$  and  $R$  and the slope of the regression line for each hour were calculated and shown by a full line and a dashed line respectively in Figure 3. The correlation coefficients are larger than 0.85 with the best correlations appearing at day hours; and the worst ones around the hours of sunrise. The rate of increase of  $\bar{I}$  starts to increase at sunrise; reaches its maximum at 14 hr; and then decreases to its minimum at pre-sunrise.

The dotted line in Figure 3 shows the diurnal variation of the correlation coefficient between monthly mean hourly value of electron content,  $I$ , and the monthly mean sunspot number,  $R$ . The correlations are much poor as compared with those between  $\bar{I}$  and  $R$ , especially at hours before the sunrise.

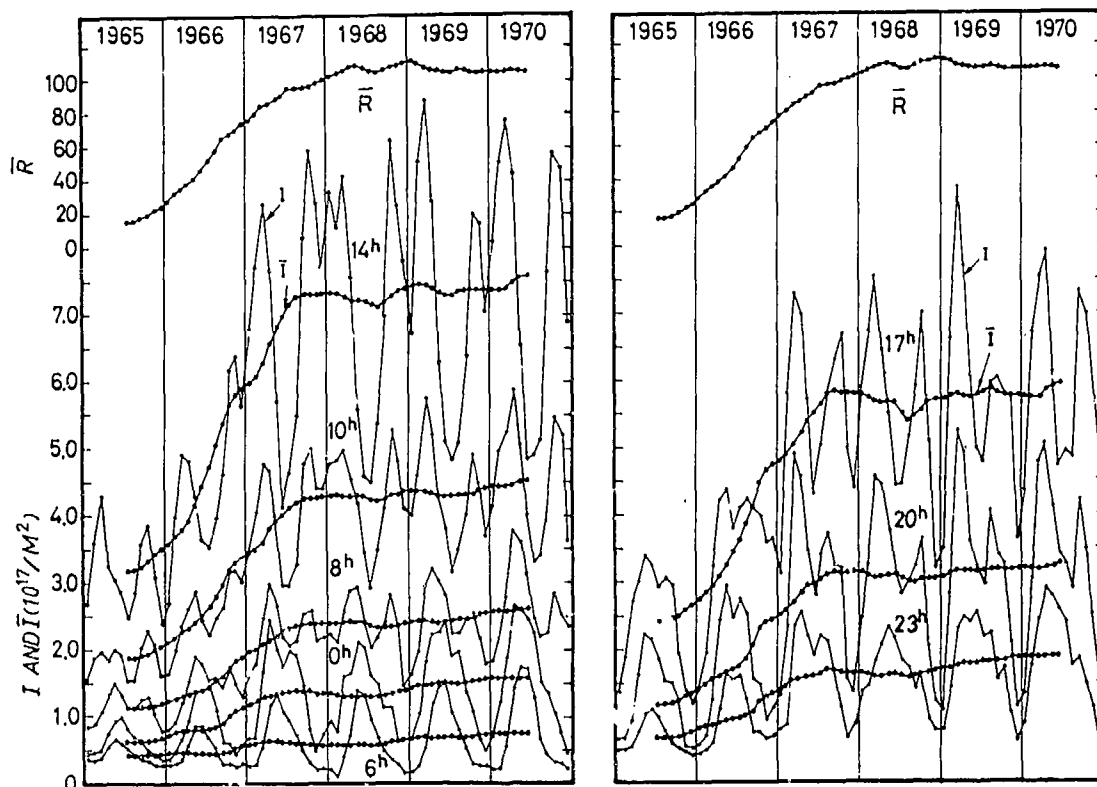


Fig. 1 Variations of  $I$ ,  $\bar{I}$  and  $R$  at different hours.

### III. Solar Cycle Variation of the Harmonic Components of the Monthly Mean Diurnal Variation.

The harmonic components of the monthly mean diurnal variation have been calculated for each month and are shown in Figure 4.  $I_0$ ,  $I_1$ ,  $I_2$ , and  $I_3$  represent the daily mean value, the 1st, 2nd and 3rd harmonic components of the monthly mean diurnal variation. The components larger than the 4th harmonic are so small that they are not shown in the figure.  $\bar{I}_0$ ,  $\bar{I}_1$ ,  $\bar{I}_2$  and  $\bar{I}_3$  show the 12 month running averages of  $I_0$ ,  $I_1$ ,  $I_2$  and  $I_3$ . It should be noted that the values of  $\bar{I}$  and  $\bar{I}_1$  are so close that  $\bar{I}_1$  is plotted on a different scale as shown at the right side of the figure. The variation of  $\bar{R}$  is also shown at the top of the figure. It is very clear that the positive correlation exists between each smoothed harmonic component and the smoothed sunspot number. The saturation effect is also clear for  $\bar{I}_0$  and  $\bar{I}_1$ . This effect can be seen more clearly in Figure 5 which gives the variation of each smoothed harmonic component with  $\bar{R}$ . The saturation takes place when  $\bar{R}$  reaches at the value of about 100.

The values of  $\bar{I}_0$  and  $\bar{I}_1$  are very close and change in a similar pattern. The rates of increase of  $\bar{I}_0$  and  $\bar{I}_1$  are much steeper as compared to those of  $\bar{I}_2$ ,  $\bar{I}_3$ , and  $\bar{I}_4$ .  $\bar{I}_3$  and  $\bar{I}_4$  keep almost constant values.

### IV. Solar Cycle Variation of the Apparent Seasonal Variation at Different Hours

The apparent seasonal variation of the electron content at different hours can be seen in Figure 1. For each hour, the amplitude of the seasonal variation increases with the increase of  $\bar{R}$ ; and the shape of the seasonal variation changes as  $\bar{R}$  increases. Near the sunrise hours (e.g. 6 hr curve), the seasonal variation shows one maximum and one minimum in summer and winter, respectively. However, from 6 to 8 hr, the pattern of seasonal variation changes gradually to have two maxima and two minima, respectively, in equinoxes and solstices. At low solar activity of 1965 and 1966, this pattern of seasonal variation persists until 17 hr when it changes back to the one maximum and one minimum pattern. However, at high solar activity, the two maxima and two minima pattern persists until 23 hr.

The gradual development of the winter anomaly, with electron content greater in winter than in summer, has been demonstrated by Walker (1971) by using peak electron content at Hong Kong. Walker and Ting (1972) have reported that the winter anomaly becomes evident at high solar activity of 1967/8 and was apparently absent during low solar activity period. However, the present study has revealed that, at daytime from 10 to 16 hr, the winter anomaly was almost developed at the low solar activity of 1965.

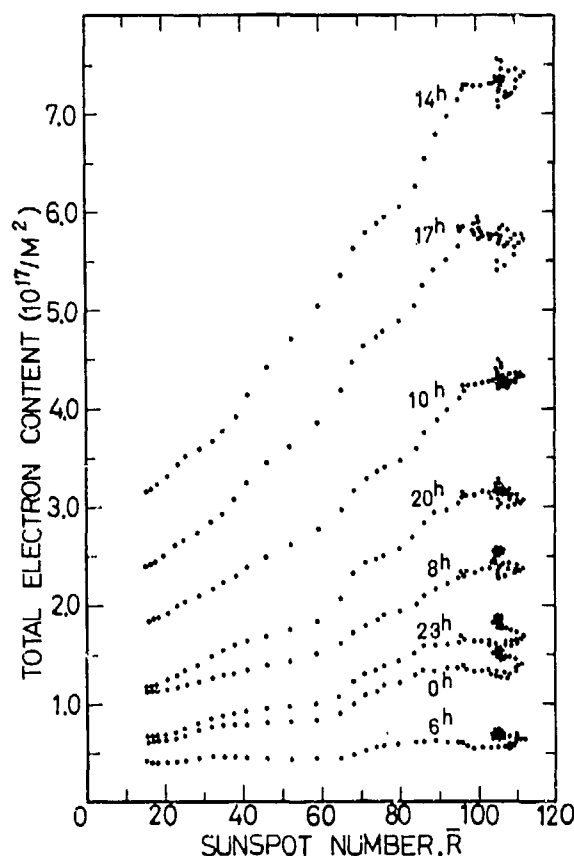


Fig. 2 Variation of  $\bar{I}$  with  $\bar{R}$  at different hours

V. Real Seasonal Variations of the Total Electron Content at the Maximum and Minimum Solar Activities.

It should be remarked that the apparent seasonal variation discussed in Sec. IV includes the effect of the solar activity. This is the reason we have defined it as the apparent seasonal variation to distinguish from the real seasonal variation discussed below. In order to obtain the real seasonal variation, we first assume that the monthly mean hourly value at  $n$  hr. in a month, denoted by  $I_{nm}$ , and the corresponding value of  $\bar{R}$  are linearly related as given by the following equation.

$$I_{nm} = A_{nm} + B_{nm} \bar{R} \quad (1)$$

where  $A_{nm}$  and  $B_{nm}$  are constants to be determined by the standard method of regression analysis. The validity of the assumption of Eq(1) can be tested by determining the correlation coefficient

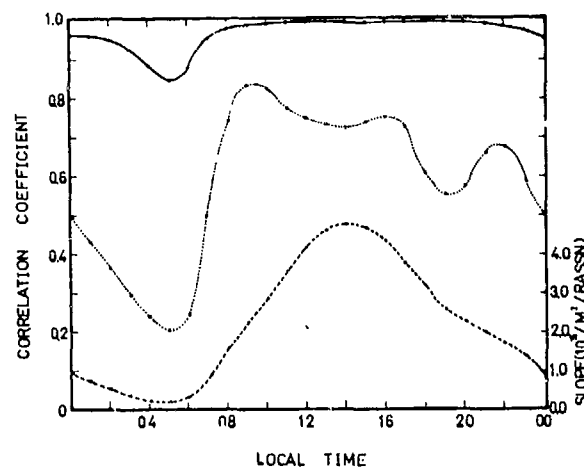


Fig. 3 Diurnal variations of the correlation coefficient between  $\bar{I}$  and  $\bar{R}$  (full line); the slope of the regression line (dashed line); and the correlation coefficient between  $I$  and  $R$  (dotted line).

between  $I_{nm}$  and  $\bar{R}$ . Once the validity has been proved, Eq.(1) can be used to obtain  $I_{nm}$ 's at  $\bar{R}=0$ , representing minimum solar activity, and at  $\bar{R}=100$ , representing maximum solar activity. The seasonal variation constructed by using these  $I_{nm}$ 's does not include the effect of the solar activity and can be used to represent the real seasonal variation.

Figure 6 shows the contour chart of the correlation coefficient between  $I_{nm}$  and  $\bar{R}$ . From this figure, it can be seen that, for summer and vernal equinoctial months, high positive correlation exists throughout the whole day. Whereas, for winter and autumnal equinoctial months, the correlation is high only in daytime; at night, the positive correlation becomes low and even negative around the sunrise hours.

The coefficient  $B_{nm}$  in Eq.(1) represents the rate of increase of  $I_{nm}$  per unit increase of  $\bar{R}$ . The contour chart of  $B$  is given in Fig. 7. From this, it can be observed that  $B$  attains its maximum value around 14 hr. which is the time for the occurrence of the diurnal peak of the electron content as will be shown later.  $B$  attains its minimum value around the sunrise hour. Seasonally,  $B$  has two minima in summer and December with the latter having larger value; and two maxima in February and November. Here, it is worthy of notice that the winter anomaly appears for the seasonal variation of  $B$ ; and two seasonal maxima of  $B$  do not appear exactly in the equinoctial months but in early and late winter months.



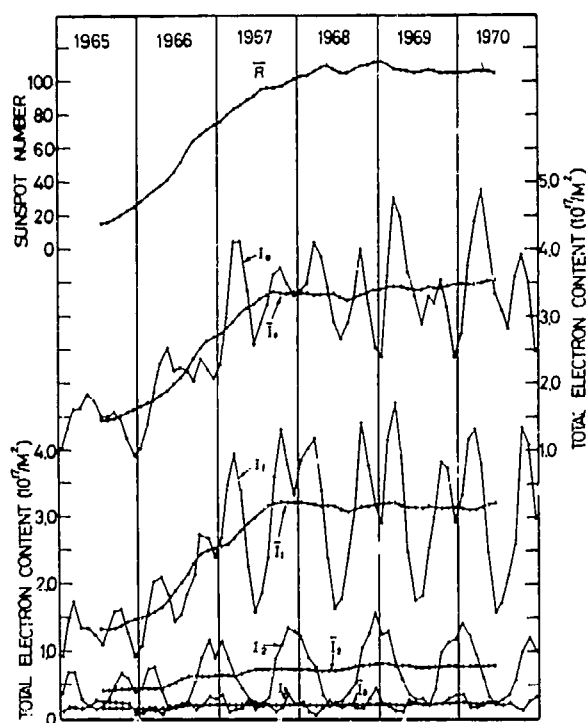


Fig. 4 Variations of the harmonic components of the monthly mean diurnal variation.

Figure 8 and 9 show, respectively, the contour charts for  $I$  at minimum solar activity of  $R=0$  and maximum solar activity of  $R=100$  obtained using Eq. (1). From these figures, it is clear that the winter anomaly is not present in sunspot minimum period but present and well developed in the day and evening hours of sunspot maximum period. In the daytime and evening hours of maximum solar activity, there are two seasonal maxima appearing, respectively, in March and October with the former slightly larger than the latter; and in the nighttime, there is only one maximum appearing in summer. In the sunspot minimum period, there is only one seasonal maximum appearing in summer; however, it is clear that another peak is going to develop in March. Throughout the whole period studied in the present paper, the seasonal peak appeared in vernal equinox is always slightly larger than that appeared in autumnal equinox; and the diurnal maximum appears at about 14 hr.

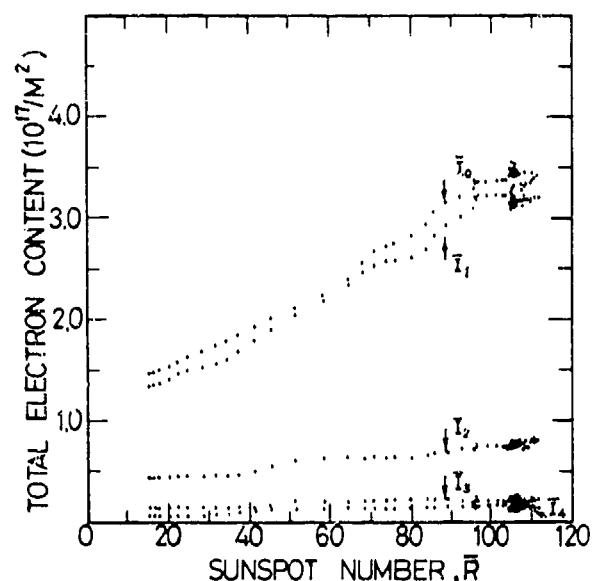


Fig. 5 Variation of each smoothed harmonic component with  $\bar{R}$ .

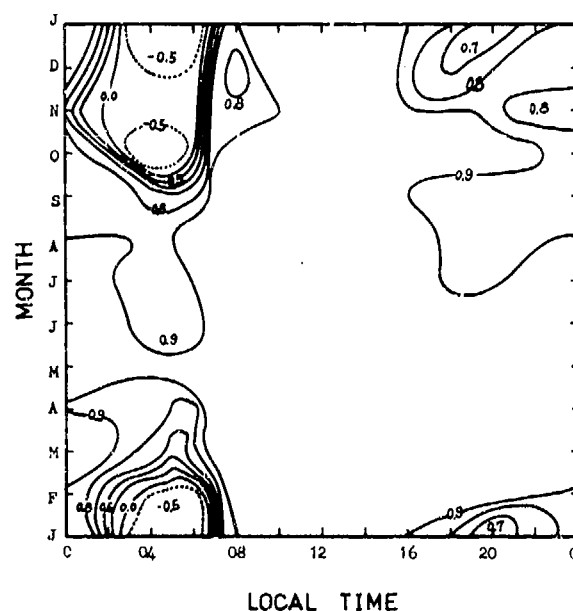


Fig. 6 Contour chart of the correlation coefficient between  $I$  and  $\bar{R}$ .

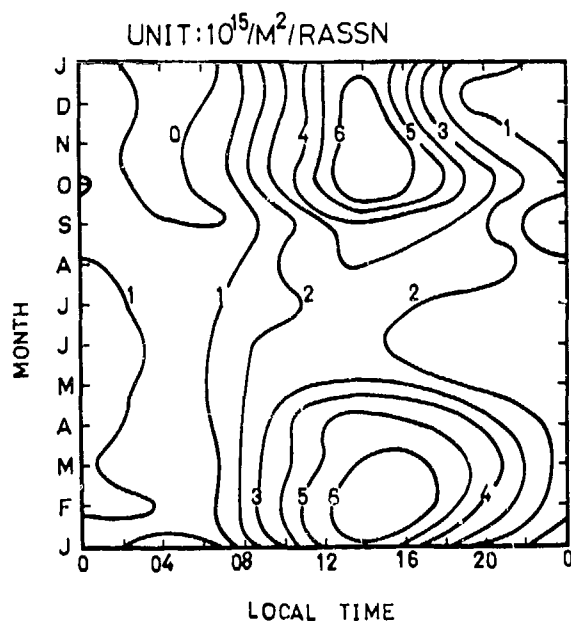


Fig. 7 Contour chart of the rate of increase of  $I$  with respect to  $R$ .

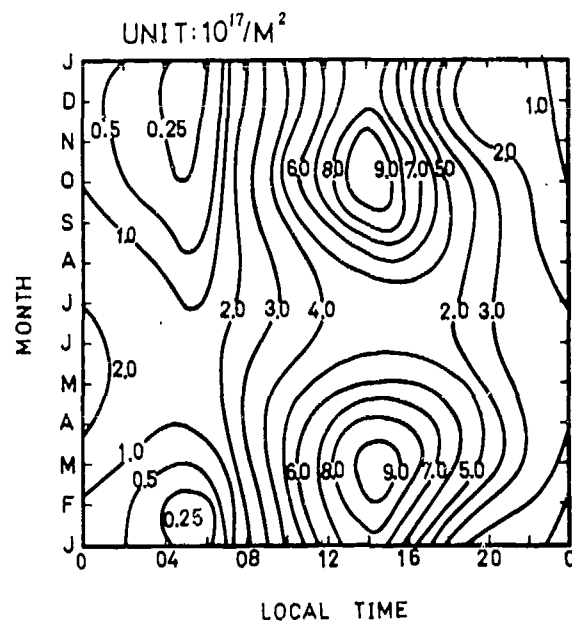


Fig. 9 Contour chart for  $I$  at maximum solar activity of  $R=100$ .

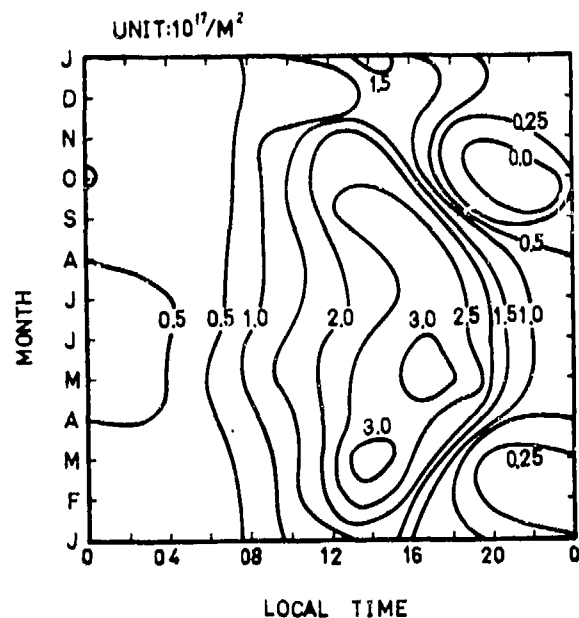


Fig. 8 Contour chart for  $I$  at minimum solar activity of  $R=0$ .

#### VI. Solar Cycle Variation of the Seasonal Variation of the Harmonic Components

The seasonal variations of the different harmonic components of the monthly mean diurnal variation are shown in Figure 4. It is interesting to note that the winter anomaly is present for the first harmonic component,  $I_1$ , throughout the half solar cycle. For the second harmonic component,  $I_2$ , the winter anomaly exists only at low solar activity; at higher solar activity, the maximum and minimum values appear in summer and winter, respectively. The third harmonic,  $I_3$ , has two maxima in solstices and two minima in equinoxes. As for the mean value,  $I_0$ , the seasonal variation pattern varies as the solar activity increases. At low solar activity, the pattern has a maximum in summer and a minimum in winter; however, as the solar activity increases, the pattern changes gradually to have two minima in solstices and two maxima in equinoxes. The vernal maximum is larger than autumnal maximum; and except for the winter in between 1967 and 1968, the winter minimum values are always smaller than the summer ones.

#### VII. Conclusion

The following conclusion can be drawn from the present study:

- (1) The 12 month running average value of total electron content,  $\bar{I}$ , at each hour has been found to have the best linear correlation with the 12 month running average value of sunspot number,  $\bar{R}$ .

(2) The correlation coefficient is larger than 0.85 throughout the whole day with a flat maximum appearing at daytime and a minimum appearing at the pre-sunrise hours. The slope of the regression line varies with respect to time with maximum at 14 hr. and minimum at pre-sunrise hours.

(3) The correlation coefficient between monthly mean hourly value of total electron content,  $I$ , and monthly mean sunspot number,  $R$ , is found to be much smaller than that between  $\bar{I}$  and  $\bar{R}$ .

(4) The value of  $\bar{I}$  starts to saturate at  $\bar{R}=100$ .

(5) The shape as well as the amplitude of the apparent seasonal variations of  $I$  at each hour varies as  $\bar{R}$  increases; the variations are different at different hours.

(6) By constructing the real seasonal variations of  $I$  at  $\bar{R}=0$  and  $\bar{R}=100$ , it is found that the winter anomaly is not present in sunspot minimum but present and well developed in the day and evening hours of sunspot maximum period.

(7) The diurnal variation of  $I$  can be well represented by the sum of its diurnal mean and first three harmonic components. The solar cycle variations of these harmonic components and their seasonal variations are different for different harmonic components. Saturation effects are also found for the components of  $\bar{I}_0$  and  $\bar{I}_1$ .

#### References

Garriott, O.K., Electron content obtained from Faraday rotation and phase path length variation, *J. Atmos. Terr. Phys.*, 32, 705, 1970.

Rai, D.B. and J.L. Hook, Total electron content and its variations in the auroral-zone ionosphere during winter, *J. Geophys. Res.*, 72, 5319, 1967.

Ross, W.J., Measurement of electron content at the magnetic equator, *J. Geophys. Res.*, 71, 3671, 1966.

Titheridge, J.E., Nighttime change in the electron content of the ionosphere, *J. Geophys. Res.*, 73, 2985, 1968.

Walker, G.O., Electron content and topside plasma temperature studies at low latitudes during a period from sunspot minimum to sunspot maximum, *J. Atmos. Terr. Phys.*, 33, 1041, 1971.

Walker, G.O. and S.D. Ting, Electron content and other related measurements for a low latitude station obtained at sunspot maximum using a geostationary satellite, *J. Atmos. Terr. Phys.*, 34, 283, 1972.

Yeh, K.C. and B.J. Flaherty, Ionospheric electron content at temperate latitudes during the declining phase of the sunspot cycle, *J. Geophys. Res.*, 71, 4557, 1966.

Yuen, P.C. and T.H. Roelofs, Diurnal variation of the ionospheric total electron content, *J. Geophys. Res.*, 71, 847, 1966.

Yuen, P.C. and T.H. Roelofs, Seasonal variations in ionospheric total electron content, *J. Atmos. Terr. Phys.*, 29, 321, 1967.

Yuen, P.C. and T.H. Roelofs, Atlas of Total Electron Content Data Vol. 1-5, Dept. of Electrical Engineering, Univ. of Hawaii, 1966-1970.

## THE CONSTRUCTION AND USE OF STORM-TIME CORRECTIONS FOR IONOSPHERIC F-REGION PARAMETERS

Michael Mendillo and Michael J. Buonsanto  
Boston University  
Department of Astronomy  
Boston, Mass. 02215

and

John A. Klobuchar  
Ionospheric Physics Laboratory  
Air Force Cambridge Research Laboratories  
Bedford, Mass. 01730

### ABSTRACT

An Atlas of mid-latitude storm effects in the F-region parameters total electron content (TEC), peak density ( $N_{\max}$ ) and equivalent slab thickness ( $\tau$ ) has been used to construct average patterns for storm-induced perturbations as a function of local time and season. These average patterns can serve as predictive schemes for storm-time corrections to existing  $N_f$ ,  $N_{\max}$  and  $\tau$  models used in various propagation systems. The possibility of such an approach is assessed by examining the standard deviations of the average storm patterns ( $\sigma_{SD}$ ) and comparing the results with the inherent ionospheric variability as determined by the standard deviations of monthly mean conditions ( $\sigma_{MM}$ ). The analysis shows that  $\sigma_{SD}$  is approximately 50% larger than  $\sigma_{MM}$  when averaged over all times and seasons; however, significant variations from this overall trend occur when local time and season are examined separately. The actual magnitudes of the corrections are generally less than their respective standard deviations, implying that the large variability found during magnetically disturbed times is difficult to deal with from purely a predictive approach. The use of these average patterns nevertheless provides an improvement over a complete neglect of the possible consequences of magnetic activity. A further improvement in the ability to correct for storm effects is offered by making a measurement of either  $f_oF2$  or  $N_f$  and relating one to the other by a slab thickness model (itself a function of magnetic activity).

Finally, the shape of the daytime F-region electron density profile has been parameterized with respect to Kp and season, and these results will also be presented.

Fifty years have passed since the pioneering radio experiments of Appleton and Barnett began to reveal the details of the ionospheric structure. Since that time, radio, rocket and satellite techniques have been employed to greatly increase our knowledge of the spatial and temporal behavior of the ionospheric plasma. To a large extent, much of the basic structure (and the physical processes which govern that structure) are understood. Attempts to model the ionosphere have been made from purely statistical (or empirical) approaches to very sophisticated theoretical treatments. In a very real sense, these models work in that they can predict the gross or average behavior of the ionosphere as a function of space and time. The crux of the problem is whether or not the predicted values are close enough to the actual behavior, and that of course is a function of the specific use for which the ionospheric information is needed, which in turn changes from user to user.

If one can predict the average behavior of an F-region parameter (i.e., the monthly mean behavior of TEC or  $N_{\max}$  to within acceptable errors in absolute value), then the uncertainties left to account for are (1) the normal day-to-day fluctuations about the mean and (2) the often drastic departures

from monthly mean conditions induced by geomagnetic activity. For the purpose of this study, we call the day-to-day fluctuations the "inherent variability" and describe it by the standard deviation of the monthly mean behavior ( $\sigma_{MM}$ ) determined from actual measurements. The physical processes behind  $\sigma_{MM}$  are subtle in that they arise from the day-to-day fluctuations in atmospheric constituents (e.g., the  $O/N_2$  ratio), from gusts or abatements in the neutral winds, or from quiet-time changes in electrodynamic effects. Specification of these types of perturbations in advance seems to be beyond present-day capabilities.

Experience suggests that the fluctuations due to magnetic storm effects quite often exceed the day-to-day variability and thus these large but infrequent departures should be the first to examine (the assumption being that the more drastic an effect is, the easier it becomes to describe it, and hopefully to model it). Since 1929, numerous workers have tried to describe the ionospheric perturbations which accompany geomagnetic storms. Various degrees of success and frustration have been reported, the net result being that to date no general agreement is possible concerning either the global/temporal morphology or the physical processes most important during storms. There is, of course, the realization that no one single mechanism is responsible for all facets of ionospheric storms, and thus the theoretical questions center on the correct blend of the many possible contributing factors.

Our attempts at Boston University and AFCRL have centered on the philosophy of narrowing down the problem as much as possible in the hope of avoiding extraneous variables. Toward this end, the AFCRL Atlas of mid-latitude F-region storm effects was compiled (Mendillo and Klobuchar, 1974a). In the Atlas, the storm-induced changes in the ionospheric  $N_e(h)$  profile are described by studying its integral (TEC), its peak density ( $N_{max}$ ) and its equivalent slab thickness ( $\tau = TEC/N_{max}$ ) for a total of 75 events during the years 1967 to 1972. A severity criterion was used to select the events, namely that the storm was classified as moderately severe at Fredericksburg ( $K_{pr} \geq 6$ ), or  $A_p \geq 30$  for at least one day of the storm period (equivalent to  $K_p = 4^+$  all day). Storms with either sudden storm commencements (SSC's) or gradual storm commencements (GSC's) were taken. An additional constraint used was that the storm periods examined should be "reasonably isolated", that

is, no storms were chosen for analysis which occurred within two days of each other.

The 62-month set of F-region data presented in the Atlas is a highly reliable and comprehensive data base for storm studies. These data were used to define average storm patterns for TEC,  $N_{max}$  and  $\tau$  as a function of local time (see Mendillo (1971) and Mendillo and Klobuchar (1974a) for a discussion of the procedures employed to obtain the average local time disturbance (SD) patterns). Figure 1 gives the SD( $\Delta TEC$ ,  $\Delta N_{max}$ ,  $\Delta \tau$ ) results for all 75 storms taken together. These curves present the average perturbations (in percent) at hourly intervals, as reckoned from the mean of the seven days prior to the storm. The points marked by asterisks early on the SD1 patterns refer to average values obtained from less than half of the number of storms available. These curves give the overall average effects to be expected for a storm which meets the above selectivity requirements and which commences from a few hours before sunrise to a few hours before sunset (on day 1). For storms beginning after sunset, further complications arise due to the "no-positive-phase" or the "delayed-positive-phase" response possibilities (Mendillo, 1973).

Curves similar to those in Figure 1 have been produced for each season (Mendillo and Klobuchar, 1974b). The possibility then arises of using these curves (or tabulated values) as disturbance correction terms (in %) to existing ionospheric models which predict the average behavior in the absence of magnetic activity. To assess the potential usefulness of this approach, we examined the reliability of the SD patterns by forming the standard deviations of the derived correction terms. For example, for SD ( $\Delta TEC(\%)$ ) at a particular time there is a  $\sigma_{SD}$  associated with it. Figure 2 contains a summary of the  $\sigma_{SD}$  variations for the  $\Delta TEC(\%)$ ,  $\Delta N_{max}(\%)$  and  $\Delta \tau(\%)$  curves shown in Figure 1 (only days 1 and 2 are examined when the major ionospheric effects occur). One can see from Figure 2 that for TEC and  $N_{max}$ , the  $\sigma_{SD}$  patterns are similar, with  $\Delta N_{max}$  showing somewhat more variability at night. The  $\sigma_{SD}(\tau)$  values are generally smaller than those for TEC and  $N_{max}$ , especially during the daytime hours when the storm effects in percent yield the largest corrections in terms of absolute values. By comparing Figures 1 and 2, it becomes obvious that the  $\sigma_{SD}$  values are generally larger than the SD correction terms, pointing out

once again the difficulty encountered in trying to model storm effects. For example, the TEC "dusk effect" increases so often found during the first day of a storm is characterized here by  $\Delta\text{TEC} = 34\% \pm 34\%$  at 1800 LT. This seemingly dubious statement is meaningful in that it points out that a TEC enhancement of some sort is strongly expected, just its actual magnitude is uncertain. Similarly, during the daytime period on the second day,  $\Delta N_{\text{max}} = -21\% \pm 35\%$  at 1200 LT points out that a peak density depletion is most likely, though not certain.

For average storm pattern values close to zero, the major disturbance effects are seen as an increased variability, i.e., large  $\sigma_{\text{SD}}$  values. As a way quantitatively seeing this enhanced variability, consider Figures 3 and 4. For each of the 62 months covered by the Atlas, the monthly mean TEC,  $N_{\text{max}}$  and  $\tau$  behaviors were determined as well as their respective standard deviations ( $\sigma_{\text{MM}}$ ). The average of all the values is denoted  $\bar{\sigma}_{\text{M}}$  and is plotted for each parameter versus local time in Figure 3. Generally, the inherent TEC and  $N_{\text{max}}$  variabilities are comparable, and both are larger than the inherent slab thickness variability (especially during the afternoon hours). Figure 4 is a plot of the ratio of the storm-time variability to the inherent variability ( $\sigma_{\text{SD}}/\bar{\sigma}_{\text{M}}$ ) for each parameter. Clearly,  $\sigma_{\text{SD}}$  is on the average 50% larger than  $\bar{\sigma}_{\text{M}}$  for TEC and  $N_{\text{max}}$ , while for  $\tau$ , the ratio is even further enhanced on the second day. It should be recalled that for  $\tau$ , however,  $\sigma_{\text{SD}}$  and  $\bar{\sigma}_{\text{M}}$  were smaller than their TEC and  $N_{\text{max}}$  counterparts (see Figures 2 and 3).

While Figures 1 through 4 demonstrate the behavior of the SD patterns, their standard deviations, and their relationship to the inherent variability, the fact that the ionosphere responds to magnetic activity in different ways during different seasons means that the above analysis must actually be performed on a seasonal basis. With 75 events available, a division into three seasons (Summer, Winter, Equinox = Spring + Fall) yields comparable sample sizes for each season. In performing the seasonal analysis, it was found that not only do the SD patterns vary with season, but so do their standard deviations. This is evident in Figure 5 where the  $\sigma_{\text{SD}}$  for the SD( $\Delta\text{TEC}$ ) patterns are presented. One can see that summer storms clearly have less variability associated with them than do Winter or Equinox events. When a check of the Equinox patterns was carried out by a further division into

Spring and Fall, it was found that the SD( $\Delta\text{TEC}$ ,  $\Delta N_{\text{max}}$ ,  $\Delta\tau$ ) patterns differed significantly, although their standard deviations did not.

It thus seemed appropriate to prepare a correction scheme for each parameter and its standard deviation using four rather than three seasons. The results of this analysis appear in summary form in Table 1. The actual hourly variations and their standard deviations over four days of a storm period are available upon request. It should also be noted that average deviations in  $N_{\text{max}}$  can be converted to  $f_oF_2$  variations via

$$\Delta f_oF_2(\%) = \left[ \frac{\sqrt{\Delta N_{\text{max}}(\%)}}{100} + 1 - 1 \right] \times 100$$

where the corresponding standard deviation can be taken as approximately 1/2 of the  $\sigma_{\text{SD}}(N_{\text{max}})$  value.

The use of the average patterns appearing in Table 1 would add an improvement (though a crude one) to any model prediction of these F-region parameters which does not take magnetic activity into account. Since the slab thickness parameter is not a directly measurable quantity but rather the ratio of two experimentally determined quantities, the question arises of whether a measurement of TEC or  $N_{\text{max}}$  could be related to the other via a model for  $\tau$  capable of being updated with storm-time corrections. Klobuchar and Allen (1970) have produced a first-order slab thickness model and a more comprehensive one will be available shortly (Klobuchar and Hajeb-Hosseini, private communication). A measure of  $f_oF_2$  (and therefore  $N_{\text{max}}$ ) gives a TEC value (or vice versa) with an uncertainty equal to that of the slab thickness model ( $=\sigma_{\text{MM}}(\tau)$ ); note from Figure 3 that this uncertainty represents a 50% improvement over the variability associated with the TEC and  $N_{\text{max}}$  monthly means. Now, a value of  $\tau$  updated for magnetic activity effects (i.e.,  $\tau_{\text{model}} + \Delta\tau$ ) has an uncertainty associated with it of  $\sigma_{\text{SD}}(\tau)$  which is larger than  $\sigma_{\text{MM}}(\tau)$ , though approximately equal to the inherent variability of either TEC or  $N_{\text{max}}$  (see Figures 2 and 3). Thus, consider the case where a TEC or  $N_{\text{max}}$  model which has an uncertainty equal to that of the standard deviation of the monthly mean ( $\sigma_{\text{MM}}$ ) is deemed adequate. During a storm, when SD corrections to the TEC or  $N_{\text{max}}$  model are available (but with an uncertainty

$\sigma_{SD} \geq 1.5\sigma_{MM}$ , and therefore unacceptable), the present analysis suggests that only a measurement and a slab thickness model will maintain the degree of accuracy originally desired, since  $\sigma_{SD}(\tau) \approx \sigma_{MM}$  (TEC or  $N_{max}$ ).

As a final point, incoherent scatter data from Millstone Hill have recently been used to investigate the variation in the shape of the daytime midlatitude  $N_e(h)$  profile associated with changes in geomagnetic activity (Papagiannis et al., 1975). The analysis performed was to deduce the dependence of the following parameters upon the 3-hr geomagnetic index  $K_p$ :  $h_{max}$ ,  $(h_A - h_{max})$  and  $(h_{max} - h_B)$ , which are the distances above (A) and below (B)  $h_{max}$  where the electron density falls to  $0.7 N_{max}$ , the ratio  $N(1000\text{km})/N_{max}$ , and finally a scale height  $H_T$  for an exponential profile between the electron densities observed at 500 and 1000 km. Daytime data from the years 1968 to 1971 during the period 1000 to 1600 LT were averaged separately for Summer, Winter and Spring-Fall conditions. The individual results are given in Table 2, together with their respective correlation coefficients ( $r$ ), where  $r=0$  describes a complete lack of a linear correlation and  $r=1$  a perfect linear relationship. The entries in Table 2 point out that the daytime  $h_{max}$  values tend to be higher on magnetically disturbed days for all seasons, though the correlation coefficients are far from impressive. Table 2 also shows that the overall thickness of the F-region is strongly enhanced during Summer disturbances but only marginally so during Winter, a feature consistent with the slab thickness variations summarized in Table 1. It should be emphasized that while the shape of the  $N_e(h)$  profile can be related in an approximate way to a geomagnetic index, this is not possible for the  $N_{max}$  or TEC data which undergo both positive and negative phases (Mendillo, 1973).

## REFERENCES

- Klobuchar, J.A. and R.S. Allen, A first-order prediction model of total electron content group path delay for a midlatitude ionosphere, Tech. Report AFCRL-70-0403, AFCRL, Bedford Mass., 1970.
- Mendillo, M., Ionospheric total electron content behavior during geomagnetic storms, Nature, 234, 23, 1971.
- Mendillo, M., A study of the relationship between geomagnetic storms and ionospheric disturbances at mid-latitudes, Planet. Space Sci., 21, 349, 1973.
- Mendillo, M. and J.A. Klobuchar, An Atlas of the Midlatitude F-region Response to Geomagnetic Storms, AFCRL Tech. Report #0065, L.G. Hanscom AFB, Bedford, Mass. 01730, 1974a.
- Mendillo, M. and J.A. Klobuchar, Seasonal Effect in Ionospheric Storms, paper presented at the COSPAR/URSI Symposium on Satellite Beacon studies of the Ionosphere structure and ATS-6 Data, 25-29 November, 1974, Moscow, USSR, 1974b.
- Papagiannis, M.D., Hajeb-Hosseini, and M. Mendillo, Changes in the Ionospheric Profile and the Faraday Factor M with  $K_p$ , Planet. Space Sci. (in press, 1975).

TABLE 1(a). BU/AFCRL TEC STORM MODEL

Season = Summer				Season = Fall			
	Local Time Period	$\Delta \overline{\text{TEC}}$ (%)	Stand. Dev. $\sigma_{SD}$ (%)		Local Time Period	$\Delta \overline{\text{TEC}}$ (%)	Stand. Dev. $\sigma_{SD}$ (%)
Day 1	10 - 1500	10	25	Day 1	12 - 2000	35	35
	16 - 2200	25	30		21 - 0100	5	45
	23 - 0500	-10	35				
Day 2	06 - 1800	-25	15	Day 2	02 - 0600	-20	30
	19 - 2200	-20	25		07 - 1800	-10	30
	23 - 0500	-30	30		19 - 0600	-40	25
Season = Winter				Season = Spring			
	Local Time Period	$\Delta \overline{\text{TEC}}$ (%)	Stand. Dev. $\sigma_{SD}$ (%)		Local Time Period	$\Delta \overline{\text{TEC}}$ (%)	Stand. Dev. $\sigma_{SD}$ (%)
Day 1	10 - 1500	25	30	Day 1	10 - 1400	-10	30
	16 - 1800	45	50		15 - 2000	15	40
	19 - 0100	10	45		21 - 0600	-25	35
Day 2	02 - 0800	0	40	Day 2	07 - 2000	-20	30
	09 - 1800	10	35		21 - 0500	-25	20
	19 - 0700	-20	30				

Summer = May, June, July and August

Fall = September and October

Winter = November, December,  
January and February

Spring = March and April



TABLE 1(b). BU/AFCL  $N_{\max}$  STORM MODEL

Season = Summer				Season = Fall			
	Local Time Period	$\overline{\Delta N_{\max}}$ (%)	Stand. Dev. $\sigma_{SD}$ (%)		Local Time Period	$\overline{\Delta N_{\max}}$ (%)	Stand. Dev. $\sigma_{SD}$ (%)
Day 1	10 - 1700	5	30	Day 1	10 - 1400	20	25
	18 - 2200	20	30		15 - 2100	30	30
	23 - 0400	-5	30		22 - 0100	10	30
Day 2	05 - 1800	-40	20	Day 2	02 - 0600	-20	25
	19 - 0900	-25	30		07 - 1800	-20	40
Day 3	10 - 2000	-10	30		19 - 0600	-30	15
Season = Winter				Season = Spring			
	Local Time Period	$\overline{\Delta N_{\max}}$ (%)	Stand. Dev. $\sigma_{SD}$ (%)		Local Time Period	$\overline{\Delta N_{\max}}$ (%)	Stand. Dev. $\sigma_{SD}$ (%)
Day 1	10 - 1500	10	30	Day 1	10 - 1600	-10	25
	16 - 1900	40	45		17 - 2000	25	35
	20 - 0500	30	65		21 - 0600	-15	25
Day 2	06 - 2100	0	35	Day 2	07 - 2400	-25	30
	22 - 0600	-15	45		01 - 0600	-30	20

Summer = May, June, July and August

Fall = September and October

Winter = November, December,  
January and February

Spring = March and April

TABLE 1(c). BU/AFCRL  $\tau$  STORM MODEL

Season = Summer				Season = Fall			
	Local Time Period	$\overline{\Delta\tau}$ (%)	Stand. Dev. $\sigma_{SD}$ (%)		Local Time Period	$\overline{\Delta\tau}$ (%)	Stand. Dev. $\sigma_{SD}$ (%)
Day 1	09 - 1900	15	20	Day 1	09 - 1900	10	15
	20 - 0400	5	20		20 - 0400	0	30
Day 2	05 - 1900	25	20	Day 2	05 - 1200	35	40
	20 - 0600	0	20		13 - 1800	10	20
Day 3	07 - 1900	10	15		19 - 0600	0	25
Season = Winter				Season = Spring			
	Local Time Period	$\overline{\Delta\tau}$ (%)	Stand. Dev. $\sigma_{SD}$ (%)		Local Time Period	$\overline{\Delta\tau}$ (%)	Stand. Dev. $\sigma_{SD}$ (%)
Day 1	10 - 1700	15	25	Day 1	10 - 1800	20	10
	18 - 0600	-15	25		19 - 0500	- 5	20
Day 2	07 - 1000	15	30	Day 2	06 - 1800	20	30
	11 - 1700	5	20		19 - 0600	0	15
	18 - 0300	0	30				

Summer = May, June, July and August

Fall = September and October

Winter = November, December,  
January and February

Spring = March and April

TABLE 2.

PARAMETER	SUMMER		WINTER		SPRING - FALL	
		(r)		(r)		(r)
$h_{\max}$ (km)	280 + 9Kp	.6	265 + 5Kp	.4	290 + 4Kp	.3
$h_{\max} - h_B$ (km)	60 + 3Kp	.4	40 + 2Kp	.3	50 + 3Kp	.5
$h_A - h_{\max}$ (km)	65 + 11Kp	.6	50 + 4Kp	.5	60 + 7Kp	.7
$H_T$ (km)	200 + 3Kp	.2	190 - 2Kp	.2	175 + 7Kp	.6
$\frac{N(1000 \text{ km})}{N_{\max}}$	$\frac{(20 + 6Kp)}{1000}$	.5	$\frac{(8 + 1Kp)}{1000}$	.3	$\frac{(9 + 5Kp)}{1000}$	.6

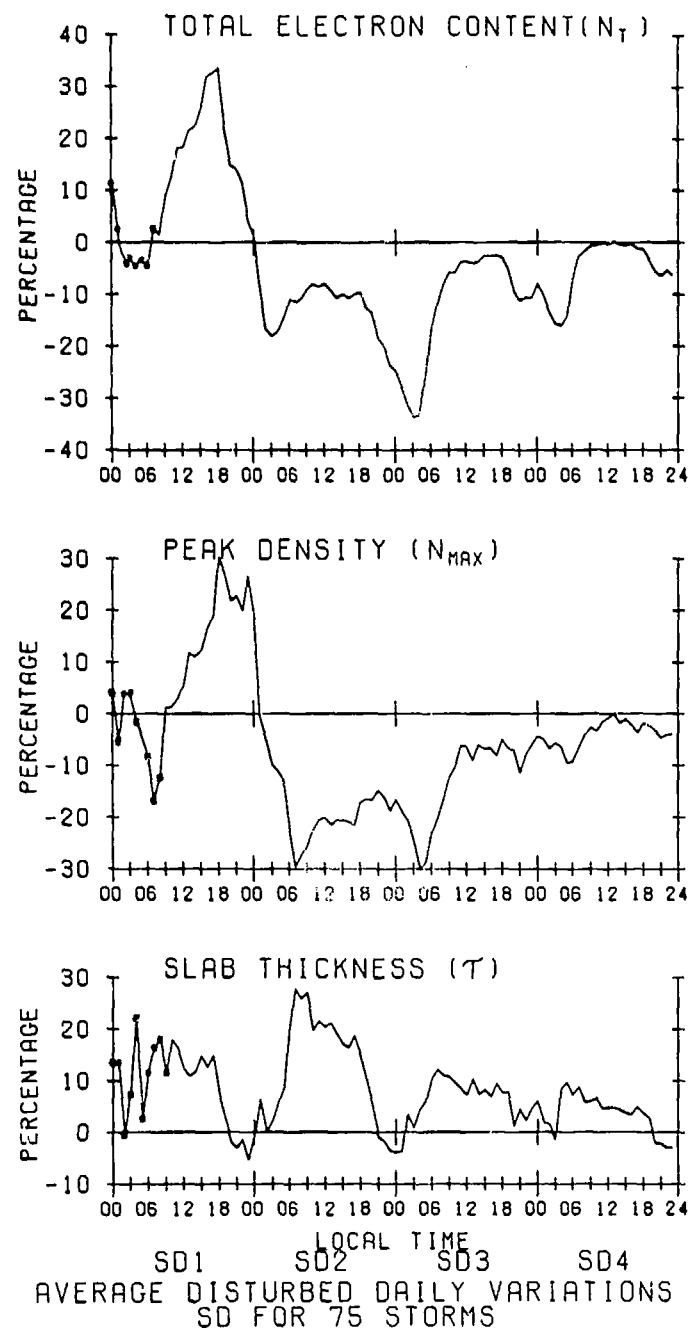


**Figure 1.** Average local time disturbance variations (SD, in percent) for the three ionospheric parameters total electron content, peak density and equivalent slab thickness.

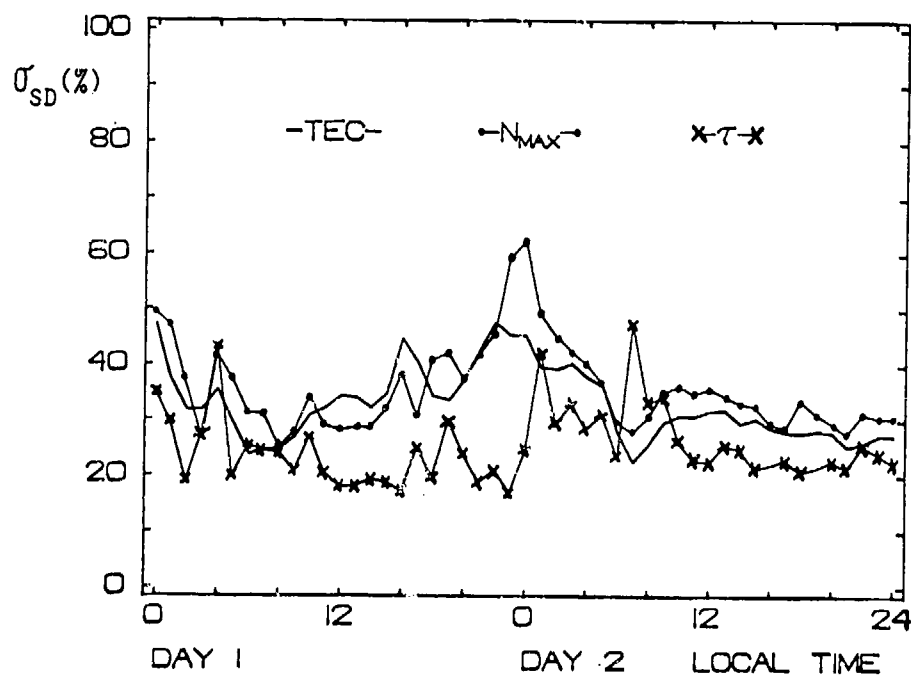


Figure 2. The standard deviations of the SD-patterns presented in Figure 1.

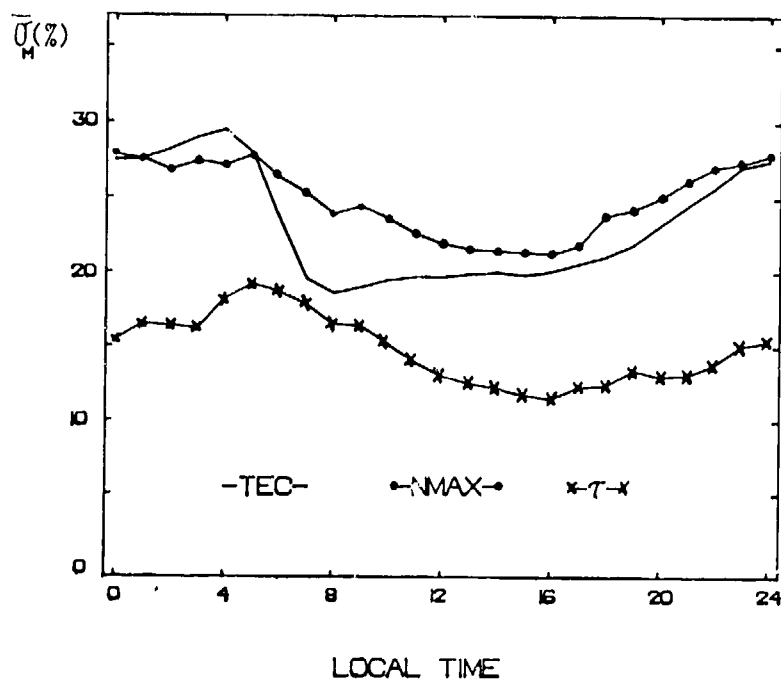


Figure 3. The inherent variability of the F-region as given by the average of all the standard deviations of the monthly mean behavior for the 62-month period examined (see text).

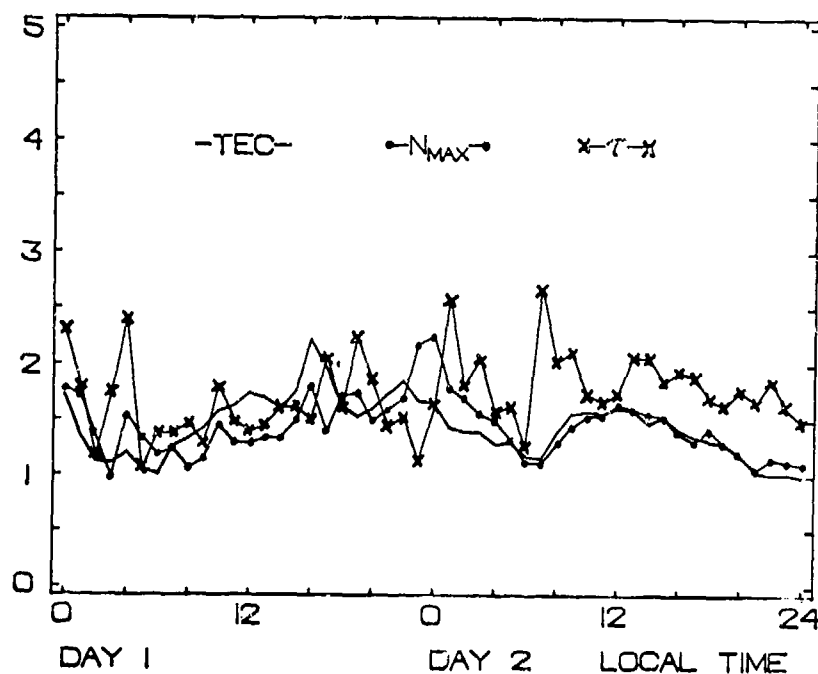


Figure 4. The ratio of the disturbance variability ( $\sigma_{SD}$ ) to the average inherent variability ( $\bar{\sigma}_M$ ) over two days of a storm period.

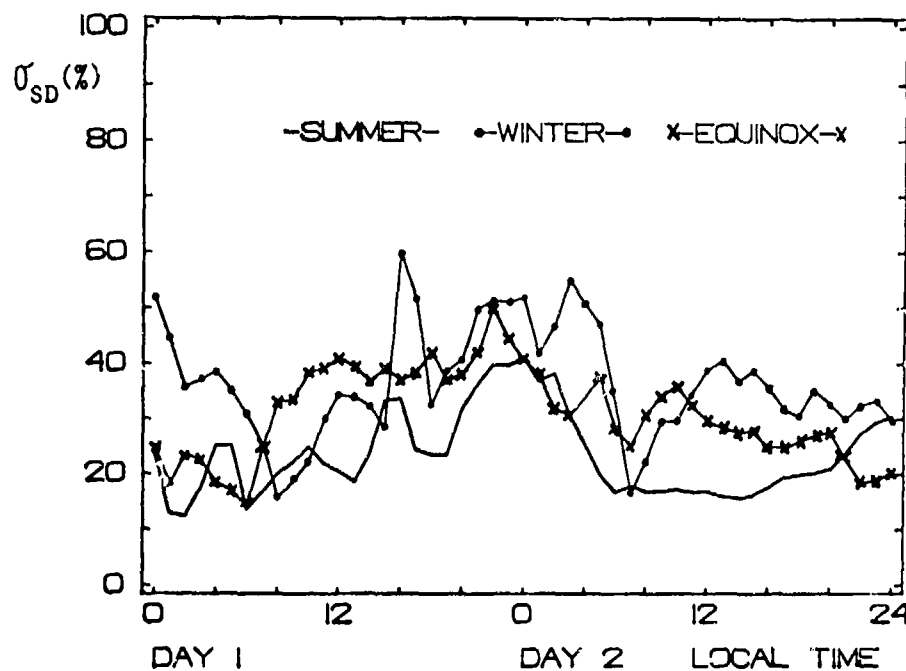


Figure 5. An example of the influence of season upon the standard deviations of the SD( $\Delta$ TEC) patterns.

# SEASONAL AND DIURNAL VARIATIONS IN THE TOTAL ELECTRON CONTENT OF THE IONOSPHERE AT INVARIANT LATITUDE 54 DEGREES

Gerald S. Hawkins  
National Research Council

John A. Klobuchar  
Air Force Cambridge Research Laboratory  
Bedford, Ma. 01731

## INTRODUCTION

The ionosphere, extending to a height of approximately 500 miles, is produced primarily by the photo-ionization of oxygen atoms and oxygen and nitrogen molecules by solar radiation in the extreme ultra-violet (EUV), 165-911 Å. It is therefore controlled in its essential features by solar activity and declination, and by thermal, kinematic and chemical conditions above the earth's surface. Secondary sources of ionization include soft x-rays from the sun, precipitation of energetic particles from the solar wind and plasmasphere, and the entry of meteoroid particles from interplanetary space. Two broad overlapping concentrations of electrons are formed; (a) the E-layer at a height of approximately 100 km by soft x-ray ionization of N<sub>2</sub>, and (b) the F-layer at about 300 km by EUV acting on O. Ionization, of course, extends in decreasing amounts up into the plasmasphere to heights of 5000 km and beyond.

The salient features of the dawn build-up, nocturnal decay, and persistent ionization layers in the dark polar and auroral regions are therefore understood at the basic level. The production, maintenance and loss of electrons within the ionosphere is, however, a complicated process and is not currently predictable or describable in detail from theoretical principles. The behavior pattern can be described better through statistical studies based on an understanding of the underlying solar and geophysical influences. In many applications this behavior pattern is of critical importance. The ionosphere reflects, refracts and absorbs radio waves, and produces significant delays in radar-ranging and

errors in navigational signals from satellites. Irregularities in the F-layer over the equator and polar regions cause severe scintillation and fading of trans-ionospheric radio-beacon and communication signals from geostationary satellites.

One of the most comprehensive indicators of ionospheric behavior is the Faraday rotation of the plane of polarization of a trans-ionospheric radio wave. The incremental rotation  $d\Omega$  radians in traversing an interval  $dh$  m through a plasma with electron density in units of number  $m^{-3}$ , and magnetic field strength  $B$  gammas is given by the expression

$$d\Omega = k(1/f^2) B \cos\theta \sec\chi N dh \quad (1)$$

where  $\theta$  is the zenith angle of the ray,  $\chi$  is the angle between ray and field line and  $f$  is the frequency in Hertz. The total rotation,  $\Omega$ , found by integrating Eq. (1) gives the total vertical electron content

$$TEC = \int_0^\infty N dh = f^2/kM \quad (2)$$

where  $M$ , the average magnetic factor is defined as

$$M = \frac{\int_0^\infty B \cos\theta \sec\chi N dh}{\int_0^\infty N dh} \quad (3)$$

Numerical integration<sup>1</sup> shows that in practice an upper bound of approximately 1000 km should be set on the integrals. Above that height no more than 15 percent of the total rotation will occur, and in general the residual angle which may be written  $\Omega_\infty - \Omega_{1000}$ , is comparable to the accuracy of measurement of  $\Omega$ . Thus the amount of ionization that remains in the line integral form is ap-

proximately 20 percent of the total, and measurement of  $\Omega$  effectively gives only the electron content of the lower 1000 km, excluding the exosphere, upper plasmasphere and beyond. It is, however, a reliable and accurate measure of the total electron content of the ionosphere, the region that is the prime cause of radio propagation anomalies. Numerical integration<sup>1</sup> shows that the magnetic factor involves only slowly varying terms and may be replaced by the value pertaining to the height of 420 km.

The plane of polarization of a trans-ionospheric signal may be determined on a continuous basis by electronic means, and the changes recorded automatically. The computed TEC can be analysed as an indicator of the reaction of the ionosphere to diurnal and seasonal changes in solar radiation, solar and magnetospheric disturbances and particle precipitation. It is a direct measure of the quantity of ions and of the group path delay produced in trans-ionospheric radio signals.

#### DATA

The data in this paper was obtained at the APCRL station at Sagamore Hill, Massachusetts, 70° 82' W, 42° 63' N, invariant latitude 57°. The cw signals at 136 MHz from the geostationary satellite ATS-3 were monitored over the period 1967 to 1973. Figure 1 shows the ground projection of the ray path in May 1973. This is a typical representation of the geometry - throughout the period of observations the angle of elevation was close to 41°, the sub-ionospheric longitude between 68° and 72° W. The reduced TEC values apply to the vertical point of intersection of the ray and the 420 km layer. The coordinates of this column were 70° 5' W, 38° 6' N, invariant latitude 54°.

The receiving antenna was a crossed yagi operated as an electronically rotated goniometer with continuous recording of the received relative polarization angle. There was an ambiguity of  $n\pi$ , and a reference phase angle  $\phi$ , so that  $\Omega$  was given in terms of the measured angle  $\Omega(\text{obs})$  by the relation

$$\Omega = \Omega(\text{obs}) + n\pi + \phi \quad (4)$$

The reference phase depended only on the orientation of the satellite antenna which was constant to better than 10° throughout the period. It was determined by comparing the ATS-3 signal with a radar signal reflected from the moon at a time when the moon was close

to the ATS-3 ray path.<sup>2,3</sup> The ambiguity  $n\pi$  was resolved by comparing the observed values of  $\Omega$  with the electron density computed from an ionosonde profile. The peak value of density was obtained from the  $f_oF_2$  critical frequency at Wallops Island, Virginia, in the pre-dawn hours when the density, and hence the  $n\pi$  ambiguity, was at its lowest. An average value of layer thickness was assumed. Later, independent checks on the choice of  $n$  were made by comparing TEC at various hours during the day with values obtained from a nearby Thomson-scatter radar,<sup>4</sup> and with absolute TEC values found from the satellite BE-2 at a height of approximately 1000 km. In the intervals between these calibrations it was assumed that  $\phi$  remained constant and that the switches in the equipment kept track of changes in the integer  $n$ .

Values of  $\Omega$  were measured at 15-min intervals to give approximately 200,000 data points. These were converted to observed TEC, OTEC, using Eq. (2), and were stored as a 5-dimensional array

$$\text{OTEC}(Y, M, D, H, MN), \quad (5)$$

where the function subscripts denote year, month, day, hour (UT) and the particular 15-min interval. In the present analysis the data bank was condensed to 50,000 values by averaging each 4-valued element centered on hour H, UT. The observed mean hourly values were thus reduced to the array

$$\text{OTEC}(Y, M, D, H). \quad (6)$$

#### ANALYSIS

##### Monthly Mean Diurnal Variations

There is a typical daily variation of TEC values caused by solar radiation and this diurnal curve changes slowly with month and season. Occasionally under geomagnetically disturbed conditions there are significant and prolonged departures from the normal curve, but these conditions will not be considered in the present analysis. The study concerns itself with cyclical behavior and long-term values. An average total electron content was computed as a function of year, month and hour as follows

$$\text{TEC}(Y, M, H) = \frac{1}{D'} \sum_{n=1}^{D'} \text{OTEC}(Y, M, D, H) \quad (7)$$

where  $D'$  is the number of days in the month, and  $n$  is the number of elements



in the summation. The monthly mean diurnal values were found by the summation

$$\text{TEC}(M,H) = \frac{1}{n} \sum_{Y=1}^{Y'} \text{TEC}(Y,M,H) \quad (8)$$

where  $Y'$  is the number of years in the sample, which for most of the calendar months was six. Monthly diurnal and mean monthly diurnal TEC values are given in Table 1 and plotted in Figure 2. The units are electrons  $m^{-2}$ ,  $\times 10^{15}$ .

It is clear from Figure 2 that the variations do not show a progressive change as a function of month number. There is a seasonal anomaly with apparent enhancement in February, March, October, and November. Seasonal changes will be discussed in a later section. The broad features of ionospheric activity are

- a. A decay during the hours of darkness, prolonged and linear in summer months, more abrupt in winter with a low-level steady component in the latter part of the night,
- b. An abrupt rise at dawn at approximately 0900 UT, and
- c. A daytime maximum in the p.m. hours with a growth and decay that approximates to a sinusoid in winter and a saw-tooth in summer.

These features have been recognized for many years and were previously inferred from the electron height profiles obtained with ground, satellite and airborne ionosondes. The dawn rise in particular, was studied in detail<sup>5</sup> and the rate of increase of TEC shown to be in accord with solar EUV flux and the predictions of the Chapman theory.

It is of interest to determine the instant of "TEC-rise",  $t_0$  from the Sagamore Hill data because it shows as a well-defined point on the curves, serving as an anchor point, or observationally defined origin for the time coordinate. An extrapolation was applied to find the gradient MR, and constant CR, of the rising portion of the curve after time  $t_0$ . A similar equation was obtained for the falling portion in the nighttime hours. Thus  $t_0$  was given by the simultaneous solution of the equations

$$\begin{aligned} \text{TEC} &= t(\text{MR}) + \text{CR} \\ \text{TEC} &= t(\text{MF}) + \text{CF} \end{aligned} \quad (9)$$

Writing TEC as a vector array where the

integer represents the hour after  $t_0$  and  $\Delta_{21} = \text{TEC}(1) - \text{TEC}(2)$ , then the gradient of the rising portion is given in terms of first and second differences as

$$\begin{aligned} \text{MR} &= \Delta_{21} - \frac{1}{2}((\Delta_{43} - \Delta_{32}) + (\Delta_{32} - \Delta_{21})) \\ &= \frac{3}{2}\Delta_{21} - \frac{1}{2}\Delta_{43} \end{aligned} \quad (10)$$

A similar expression exists for the gradient MF of the falling portion of the curve, and the appropriate constants were derived by assuming that the two lines passed through the point  $\text{TEC}(0)$ . This extrapolation is illustrated in Figure 3 for the mean values for the month of January. Solution of Eq. (9) for this month gives  $t_0 = 11.55$ , or 11 hr 33 min UT. The value for January and other months through the year are given in Table 2.

A detailed study of TEC at sunrise over Hawaii<sup>5</sup> showed that the commencement of ionization was insidious, beginning almost imperceptibly some 30 or 40 min before ground sunrise. The value  $t_0$  defined in this analysis is a good practical measure of TEC-rise, the time at which the F-layer, that is, the major portion of the ionosphere, is effectively "turned on". As F. Smith<sup>5</sup> has pointed out, the ionosphere as a whole behaves as though it were giving an inertial response to a step-function stimulus. The many complicated production and loss mechanisms do not achieve equilibrium as in the classical Chapman theory and so, particularly in the summer months, the total ionization increases abruptly and thereafter grows more slowly to a saturation level.

It is of interest to determine the geometrical significance of the instant of TEC-rise,  $t_0$ . Let HUV, Figure 4, be the height of the layer in the upper atmosphere where total absorption of ionizing radiation takes place, then the angle of dip  $\theta$  at height  $h$  is

$$\cos \theta = \frac{R + \text{HUV}}{R + h} \quad (11)$$

and the zenith angle of the sun  $\chi$  is

$$\chi = 90^\circ + \theta + 2r \quad (12)$$

where  $r$  is the deviation in the ray due to atmospheric refraction down to a height HUV. The time of sunrise  $t(h)$  at a height  $h$  is therefore

$$t(h) = \text{ST} - \text{HA}/15 + \lambda/15 \quad (13)$$

where  $\lambda$  is the sub-ionosphere longitude

(west) in degrees, ST is the Greenwich transit of the sun in hours UT, and HA is the hour angle of the sun at sunrise. This angle is obtained from spherical trigonometry

$$\cos HA = \frac{(\cos \chi - \sin \phi \sin \delta)}{\cos \phi \cos \delta} \quad (14)$$

where  $\phi$  is geographic latitude and  $\delta$  is solar declination. A value HUV=400 km was assumed and time of sunrise computed for various heights at  $\lambda=70^\circ.0$  for the mid-date of each month. The values are given in Table 2. It can be seen that the instant of TEC-rise coincides most closely with an effective height of between 420 and 425 km. The mean difference is 0.02 hr, or approximately one min.

In interpreting Table 2 it must be noted that a height of 400 km was assumed for the absorbing layer. Thus the time comparison is not a direct measure of the height of the region of ionization - more correctly it is a measure of the thickness of the responsive layer at sunrise, 25 km. But the close agreement between mean TEC-rise and t(425) shows the preciseness of the dependence of the total ionosphere to the geometrical position of the sun. It must also be noted that a mean longitude of  $70^\circ.0$  W was assumed whereas the sub-ionospheric point drifted over the six years of observation from  $68^\circ$  to  $72^\circ$ . One would therefore anticipate a spread of  $\pm 10$  min to be inherent in the data. The geometry as seen from the responsive layer in the ionosphere is shown in Figure 5. The angle of dip of the sun at TEC-rise is  $4^\circ.6$  whereas visible sunrise occurs some  $15^\circ$  lower. There must be a layer transparent to visible light but absorbent to UV - a "cloud layer" extending up to a height HUV. One would expect this layer to be associated with ion production. Possibly it is the level corresponding to the peak production rate in the classical Chapman profile.

Prediction of this instant of UV-sunrise on a TEC curve at any geographical location is a matter of pure spherical astronomy. It occurs when the zenith angle of the sun at the ionospheric layer is  $94^\circ.6$ . This value does not depend appreciably on the assumed value of HUV. At 500 km the angle would be  $94^\circ.6$  and at 100 km,  $94^\circ.8$ . For a ground based observer one must include the effects of atmospheric refraction. TEC-rise corresponds to the instant when the sun's center appears to be  $4^\circ.2$  below the sea level (astronomical) horizon for an observer

at the sub-ionospheric point on the earth's surface. This occurs from 16 to 40 min before ground sunrise depending on latitude. In the ephemeris, sunrise is taken as that instant when the upper limb is tangent to the astronomical horizon. TEC-rise may readily be found from the ephemeris - if astronomical twilight occurs T min before ephemeris sunrise, then TEC-rise is  $0.77T$  after astronomical twilight and  $0.23T$  before ephemeris sunrise.

#### Monthly Mean TEC

The electron content was averaged over a period of 24 hrs for each calendar month

$$TEC(Y,M) = \frac{1}{n} \sum_{D=1}^D \sum_{M=1}^M TEC(Y,M,D,H) \quad (15)$$

This value, included in Table 1, eliminates the diurnal variation and is a function of solar flux and the seasonal anomaly. Following the analysis of da Rosa et al,<sup>7</sup> monthly mean values were correlated with radio measures of solar flux, S. For each calendar month M it was found that a linear relationship existed of the form

$$TEC(Y,M) = S(Y,M) \times G(M) + C(M). \quad (16)$$

The slope G and intercept C were calculated using a least mean square solution, and values are given in Table 3 for three selected solar fluxes as measured at the Sagamore Hill Radio Observatory.<sup>8</sup> All values of flux are in units of  $10^{-22} \text{ w m}^{-2} \text{ Hz}^{-1}$ . The root-mean-square difference between observed TEC and the line of best fit was less for solar flux measured at 2.7 GHz than flux at 606 MHz or 15.4 GHz. Also the error was least when a 5-month running mean flux was used centered on the particular month. These linear fits for 2.7 GHz are shown in Figure 6.

It is not clear physically why the best fit is found with smoothed solar flux centered on the date. Admittedly the improvement in rms error between using the particular month and a previous month for the center of the running mean is small, but it does at first sight imply the illogical situation of a reaction of the ionosphere to future conditions. More reasonably one should conclude that TEC is itself a marginally significant indicator of future solar activity. It is surprising to find that the 2.7 GHz flux is a better indicator of TEC variations than 15.4 GHz. One must infer that although the ten cm radiation is not directly

responsible for the oxygen and nitrogen ionization it is in some way connected with the cause of the variations in EUV output.

Da Rosa et al<sup>7</sup> regarded the slope in the linear correlations of Eq. (16) as a sensitivity factor that specified the response of the ionosphere to solar radiation as a function of season. The present results for latitude 39° are similar to those at latitude 34° (Stanford) and 20° (Hawaii) as shown in Figure 7. There is a pronounced increase in sensitivity near the equinoxes - February, March, October and November. The slope and intercept curves are similar at 39° and 34°, and the changes are greater at the latitude of Hawaii. But it is not considered that the results permit a quantitative inter-comparison. Nor is the reason for these variations fully understood. It is sufficient to note that there is an important relationship between flux and TEC with a correlation coefficient higher than 0.9 for all months, and there is evidence for a repetitive seasonal anomaly from latitude 20° to 39°N.

#### Normalized Diurnal Values

The effects of the seasonal anomaly and variations in solar flux were removed by deriving normalized values, NTEC, as a function of year, month and hour as follows

$$\text{NTEC}(Y,M,H) = \text{TEC}(Y,M,H)/\text{TEC}(Y,M) \quad (17)$$

It will be noted that the mean value of NTEC is 1.0. The array of normalized TEC as given in Table 4 appeared not to exhibit any trend from year to year. Annual mean were therefore taken

$$\text{NTEC}(M,H) = \frac{1}{n} \sum_{Y=1}^{Y'} \text{NTEC}(Y,M,H) \quad (18)$$

These values are given in Table 5 and are plotted in Figure 8.

It can be seen that the removal of variations due to solar flux and the seasonal anomaly has introduced a semblance of order into the monthly diurnal curves which now show a sequential change as a function of month number. Also the variations clearly exhibit the underlying dependence on the position of the sun. Maximum and minimum values of NTEC are given in Table 6 and plotted in Figure 9 where it can be seen that the maxima vary in antiphase with solar declination  $\delta$  and the minimum vary in phase with  $\delta$ . The curves fitted to the data points in Figure 9 are

$$\text{NTECMAX} = 1.76 - 0.0148 \delta \quad (19)$$

and

$$\text{NTECMIN} = 0.35 + 0.0034 \delta \quad (20)$$

This simple relationship must not be taken to indicate a direct solar influence. The time of maxima do not bear a constant relationship to local noon - the maxima are almost at the time of sunset in the summer months - and the highest maxima occur in the low-sun winter months. Clearly the growth and content of the ionosphere is controlled by effects other than photo-ionization yet these subsidiary effects must be directly related to the apparent position of the sun. The physical significance of the diurnal curves will be discussed in a later section.

#### PREDICTION OF TOTAL ELECTRON CONTENT

The analysis has shown that the mean value of TEC is primarily a function of five-month smoothed solar flux at 2.7 GHz, whereas the diurnal variations are primarily a function of month, that is, solar declination. Thus the variables have been separated and the electron content of the ionosphere may be predicted in terms of month number M, and H the hour UT. Writing this value as PTEC,

$$\text{PTEC}(M) = S.G(M) + C(M) \quad (21)$$

and

$$\text{PTEC}(M,H) = \text{PTEC}(M) \times \text{NTEC}(M,H) \quad (22)$$

The constants C, G and NTEC are given in the form of an array in Table 7. Table 8 gives the predictive constants for a full diurnal curve at bimonthly and four-hourly intervals. The ultimate reliability of the predicted mean value depends on the correct estimation of future solar flux, S. Currently the World Data Center A, Boulder, Colorado, issue forecasts of 12-month smoothed values of sunspot numbers from which S can be derived.

For calibration purposes, particularly for resolving the ambiguity  $n_f$ , it is of interest to have the values predicted for the low point on the curve at the hour before dawn. This value may be derived from Eqs. (21) and (22) by substituting the values NTECMIN from Table 6.

An example of the use of these TEC prediction equations is shown in Figure 10 where the month of December 1971 has been selected. This is considered to be

a representative example of the order of accuracy of the method. Errors under normal ionospheric conditions can be expected to be comparable to the rms errors in the least mean-square fit of Table 3, which, for dependence on 2.7 GHz flux is less than two units in TEC. For comparison the electron content is given as derived from an integration of the Bent model<sup>9</sup> of the vertical profile up to a height of 1050 km with the solar flux averaged over a period of 12 months. It can be seen that the array prediction is somewhat better than the Bent model, but the present analysis is restricted to the vicinity of 70°W, 40°N, whereas the Bent model is global in scope. Nor can either model, without further research, take account of sudden changes, such as TID'S, magnetic storms and substorms.

#### DISCUSSION

The results obtained at Sagamore Hill agree with the measurements of da Rosa<sup>7</sup> and Ramsey,<sup>10</sup> and the seasonal analysis is an extension of their work. Since almost a full solar cycle has been covered by the combined observations the data can be taken as providing a comprehensive phenomenological survey of conditions in mid-latitudes in the north and western hemisphere.

Total electron content is a measure of a line integral through the E, F-1 and F-2 regions under conditions of varying solar illumination and particle precipitation. There are spatial and time variations in atmospheric density, composition and motion, and the line integral is made up of complicated components. The major contribution to TEC comes from the F-2 region at a height of 300 to 400 km, yet the ionization is not produced predominantly in that layer. Rocket measurements and ionospheric theory show that the maximum production rate is at a lower level, near 200 km, and that the F-layer concentration is due partly to upward ambipolar diffusion and vertical wind components, and partly to the lack of an efficient recombination process. The complexities are such that no adequate theory has been developed to account for the quantitative spatial and temporal changes. It is surprising therefore, in view of these complexities, to find such smooth and sequentially changing curves in the observational data. On the one hand it indicates that the equipment used to set up the data bank was adequately calibrated and consistently operated over the period of six years of this study. On the other hand it shows that, despite the internal complexities, the ionosphere as a whole

when averaged over long periods of time behaves in a simple, repetitive and predictable manner. It is hoped that this apparent simplification will lead ultimately to an improvement in the theoretical understanding. It must be borne in mind though that these results are representative of a mid-latitude station and the conditions at equatorial and polar stations might be significantly different.

The peak values of normalized TEC (NTEC<sub>MAX</sub>) show a negative correlation with solar declination. Instead of increasing between the winter and summer months as one might expect on the basis of production alone, the values do the reverse. Furthermore, there is noticeable flattening of the summer daytime curves. Clearly a loss mechanism takes over and more than compensates for the increased photoproduction. The predominant loss mechanism is the neutralization of O<sup>+</sup> by collision with molecular oxygen and nitrogen. The first stage is an ion-atom interchange

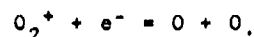
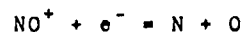


and



(23)

This is followed by the fast-reacting dissociative recombinations



(24)

The F-layer temperature increases with solar declination for a latitude > 23°.5 N, and there is no phase lag (Jaccchia).<sup>11</sup> Thus the inverse correlation of TEC with  $\delta$  can be explained on the basis of solar heating of the upper atmosphere, a lifting of the heavy molecular species O<sub>2</sub> and N<sub>2</sub> and electron loss due to molecular-induced recombination. This loss is more than sufficient to over-ride the enhancement due to the summer increase of solar illumination. In the absence of this increased loss one might expect the summer TEC to be 100 percent greater than the winter values, and 300 percent greater than the actual summer values. The F-layer, responsible for the major contribution to TEC, may be regarded as a condition of absence of atmosphere - when the layer of heavy molecules rises, the F-layer disappears. It would seem that a further study of TEC variation, exposing possible geomagnetic influences, would permit a theoretical prediction of

global  $f_oF2$  and slab thickness values on the basis of the geophysical input parameters. There is certainly a dominant dependence on solar declination and station latitude that has been separated out from TEC and atmospheric density data. This solar control, of course, will be expected to be reduced in high latitude regions where particle precipitation becomes important.

The minimum value NTECMIN is proportional to  $\sin \delta$ , but the correlation is poor. NTECMIN is a quantity physically different from NTECMAX. It is the lowest level reached by the nighttime decay process and occurs usually just before sunrise. In the summer months the decay continues almost linearly throughout the night and presumably the TEC would continue to drop if sunrise did not occur. NTECMIN is therefore that level where the decay has been arbitrarily arrested by sunrise. During the winter months the decay is rapid and TEC drops to a somewhat stable level. Presumably the loss process is by non-solar production mechanisms such as ionization by precipitating particles and by wind and other transportations. The slight winter nighttime increase before dawn is not at present understood. It may be connected with that component of polar ionization that spreads to the latitude of Sagamore Hill from the auroral oval. In view of these complications NTECMIN would not be expected to correlate with solar declination in any simple way. The weak dependence as shown in Figure 9 may therefore not be physically significant. It is interesting to note that NTECMAX and NTECMIN define the upper and lower bounds of normalized TEC - at all times it is between the two envelopes of Figure 9.

Concerning the seasonal anomaly as shown in Table 3 and Figures 6 and 7, is interesting to speculate as to its cause. From the foregoing results and discussion it would appear that, excepting the winter nights, the normalized values depend only on the sun and the space geometry. The seasonal anomaly, enhancement in spring and fall, might be due to a particle-produced component. In support of this suggestion one must note that auroral activity, which is clearly associated with particle flux, has a similar seasonal dependence with enhanced activity at the equinoxes. The normalized curves in Figure 8 would therefore represent the ionosphere as caused by solar radiation, and the curves in Figure 7 would correspond to the additional component from particle precipitation. It is difficult, however, to explain the increase of a

particle-produced component towards the equator as shown by the Hawaii curve. Finally it must be pointed out that the seasonal anomaly in TEC also follows the semi-annual density variation (Jacchia).<sup>11</sup> It is suggested that these variations take place without any major temperature change. One proposed mechanism is thermally driven, horizontal convection. However, if the TEC anomaly and semi-annual density variation are related it is difficult to reconcile the physics of the process - one would expect an increase in  $O_2$  and  $N_2$  and hence a decrease in ionization.

The monthly mean values of TEC are smoothly varying and are related to solar flux, showing a good correlation with the five-month running mean of 2.7 GHz radiation. This correlation permits a prediction of mean monthly TEC values through the solar cycle. It must be remembered however, that there are severe changes from day to day, particularly under disturbed magnetospheric conditions, and deviations of TEC from the mean can amount to 50 percent or more in a matter of minutes. The question of shorter-term relationships has been discussed by da Rosa et al.<sup>7</sup> These workers found evidence for a correlation between the daily value of 2.8 GHz solar flux and a seven-day running mean of TEC. A diagram of TEC vs S showed a loop reminiscent of an elliptical Lissajous figure under the action of sinusoidal forcing function. The width of the ellipse indicated a lag of TEC of approximately three days following the flux variations. The short-term correlations were, as to be expected, much less than those for monthly means. Although the data bank from Sagamore Hill is thought to be adequate for an investigation of short-term correlations, the analysis has not been carried out on the present report. The question has been left for a later investigation when a comprehensive study of residuals will be made.

#### REFERENCES

1. Klobuchar, J.A. and Mendillo, M. (1973) Total Electron Content from the Faraday Effect, AGARD Report AG-166, NATO, p7.
2. Klobuchar, J.A. (1969) Polarization angle of VHF telemetry transmitters on ATS-3, ATS Technical Data Report, Goddard Space Flight Center, Greenbelt, Maryland, 10 July.
3. Klobuchar, J.A., In press.

4. Evans, J.V., Private Comm.
5. Smith, F., III (1968) Determination of Rates of Production and Loss of Electrons in the F Region. Ph. D. Thesis, Stanford University, California.
6. Chapman, S. (1931) The absorption and dissociative or ionizing effect of monochromatic radiation in an atmosphere on a rotating earth, part II, grazing incidence, Proc. Roy. Soc. London, 43:483.
7. daRosa, A.V., Waldman, H. and Bendito, J. (1973) Response of the ionospheric electron content to fluctuations in solar activity, J. Atmos. Terr. Phys. 35:1429.
8. Carrigan, Anne L. (Editor) (1966-73) Geophysics and Space Data Bulletin, Vol. III-X, AFCRL Special Reports No. 175.
9. Llewellyn, S.K. and Bent, R.B. (1973) Documentation and description of the bent ionospheric model, SAMSO Tech. Report, pp 73-252.
10. Ramsay, A.C. (1970) A model of ionospheric total electron content, Air Weather Service, Tech. Report, p 234.
11. Jacchia, L.G. (1971) Revised static model of the thermosphere and exosphere with empirical temperature profiles, Smithson. Astrophys. Obs. Special Report, p 332.

Table 1. Mean Monthly Values of TEC for Hours UT (LMT = UT - 4.70)

MEAN DIURNAL TEC PROFILES FOR EACH MONTH, SAGAHORE HILL. (UNITS OF 10.E-15, M.E-2)																									
MEAN TEC VALUES FOR MONTH 1																									
HOUR	UT	0	1	2	3	4	5	6	7	8	9	10	11	12	13	14	15	16	17	18	19	20	21	22	23
67	0	0	0	0	0	0	0	0	0	0	0	0	0	0	0	0	0	0	0	0	0	0	0	0	
68	182	125	95	80	72	68	68	70	69	67	63	53	73	160	248	326	373	400	420	434	426	393	343	263	203
69	119	79	63	54	52	51	50	54	53	51	45	37	63	133	198	258	284	295	302	315	308	275	227	177	147
70	128	90	74	69	66	67	69	72	73	70	61	51	85	166	283	308	323	336	353	350	335	306	262	196	173
71	95	68	58	51	45	44	45	45	46	43	38	35	74	143	204	263	293	306	323	317	295	263	219	152	144
72	80	61	54	50	48	45	44	43	45	46	43	39	59	102	182	192	224	235	232	225	217	191	155	119	112
73	59	44	37	32	29	29	28	28	28	26	25	23	39	77	107	142	164	165	170	175	165	147	123	90	81
AVERAGE	111	76	63	56	52	51	51	52	53	51	46	40	66	130	191	248	275	288	300	303	291	263	222	166	
INCREMENT	-33	-15	-7	-4	-1	0	1	1	-2	-5	-6	-6	26	64	61	57	30	10	12	3	-12	-28	-41	-56	-55
2ND INC	7	18	8	3	3	1	1	1	0	-3	-3	-1	32	38	-3	-4	-27	-20	2	-9	-15	-16	-13	-15	1
MEAN TEC VALUES FOR MONTH 2																									
HOUR	UT	0	1	2	3	4	5	6	7	8	9	10	11	12	13	14	15	15	17	18	19	20	21	22	23
67	0	0	0	0	0	0	0	0	0	0	0	0	0	0	0	0	0	0	0	0	0	0	0	0	
68	217	163	118	96	86	77	72	66	61	57	54	47	101	191	258	317	361	395	423	427	422	401	368	297	211
69	201	150	124	106	95	85	82	74	76	73	66	59	117	195	265	309	347	370	387	401	401	384	347	278	208
70	218	158	131	113	101	94	91	89	87	86	81	76	135	215	278	336	375	404	415	420	412	401	353	285	224
71	148	109	86	76	70	65	62	58	56	55	52	54	104	158	205	240	287	316	326	325	318	297	257	199	163
72	161	124	99	87	79	73	69	66	64	63	59	107	161	213	253	285	302	308	308	299	280	252	210	166	
73	81	56	42	35	32	31	29	28	28	29	28	28	59	125	151	180	198	205	205	200	188	154	117	97	
AVERAGE	171	128	100	86	77	71	68	64	62	61	57	54	104	170	224	268	303	331	344	348	342	325	289	231	
INCREMENT	-43	-28	-14	-9	-6	-3	-4	-2	-1	-4	-3	50	66	54	44	38	25	13	4	-6	-17	-36	-58	-60	
2ND INC	7	15	14	5	3	3	3	-1	2	1	-3	1	53	16	-12	-10	-6	-13	-12	-9	-10	-11	-19	-22	-2
MEAN TEC VALUES FOR MONTH 3																									
HOUR	UT	0	1	2	3	4	5	6	7	8	9	10	11	12	13	14	15	15	17	18	19	20	21	22	23
67	0	0	0	0	0	0	0	0	0	0	0	0	0	0	0	0	0	0	0	0	0	0	0	0	
68	251	199	154	128	111	100	89	82	74	61	53	76	142	202	254	306	343	374	384	391	368	378	361	322	218
69	286	230	201	169	150	139	121	106	91	80	72	107	183	250	307	358	397	429	444	455	450	432	405	352	259
70	292	235	196	166	146	136	125	117	103	92	84	111	188	255	313	365	415	445	465	469	471	440	408	361	267
71	186	148	121	103	93	86	78	70	61	56	52	74	123	163	204	231	265	291	315	320	307	285	265	232	172
72	211	173	144	126	115	102	95	87	78	72	66	91	148	192	233	273	301	315	330	326	315	313	292	260	194
73	122	83	63	52	45	40	37	35	33	32	29	46	77	102	127	146	170	180	183	168	163	183	178	152	103
AVERAGE	223	178	147	124	110	101	91	83	73	66	59	84	144	194	240	280	316	339	354	357	352	339	318	280	
INCREMENT	-45	-31	-23	-14	-9	-10	-8	-10	-7	-7	-25	60	90	46	40	35	23	15	3	-5	-13	-21	-38	-57	
2ND INC	7	14	8	9	5	-1	2	-2	3	0	32	35	-10	-4	-6	-4	-13	-6	-12	-8	-8	-6	-17	-19	
MEAN TEC VALUES FOR MONTH 4																									
HOUR	UT	0	1	2	3	4	5	6	7	8	9	10	11	12	13	14	15	15	17	18	19	20	21	22	23
67	0	0	0	0	0	0	0	0	0	0	0	0	0	0	0	0	0	0	0	0	0	0	0	0	
68	262	209	162	136	123	113	101	89	75	63	72	114	150	179	206	231	253	275	295	299	300	298	297	290	191
69	301	244	203	184	171	152	132	111	97	82	93	144	184	219	256	291	320	341	359	364	356	364	356	340	236
70	290	237	197	175	164	153	141	127	110	94	104	151	195	235	275	308	335	351	361	362	359	348	350	334	240
71	199	153	123	107	95	86	79	71	63	55	60	95	126	153	180	201	222	238	250	254	255	248	241	238	158
72	209	167	133	115	103	94	87	78	69	61	69	108	143	167	192	214	233	248	259	259	256	252	251	246	167
73	133	100	73	59	52	46	40	35	31	26	35	66	91	117	144	155	163	169	173	179	168	161	154	104	
AVERAGE	232	185	149	129	118	107	97	85	74	64	72	113	148	177	206	232	259	282	285	285	279	276	267	267	
INCREMENT	-47	-36	-20	-11	-10	-12	-11	-10	-8	-11	8	41	35	29	29	26	21	15	13	3	0	-6	-3	-9	-35
2ND INC	7	11	16	9	8	1	-2	1	1	10	33	-6	-6	0	-3	-5	-3	-10	-3	-6	3	-6	-26		

Table 1. Mean Monthly Values of TEC for Hours UT (LMT = UT - 4.70) (Cont)

MEAN DIURNAL TEC PROFILES FOR EACH MONTH, SAGANORE HILL. (UNITS OF 10.E-15, M.E-2)																									
MEAN TEC VALUES FOR MONTH 5																									
HOUR	UT	0	1	2	3	4	5	6	7	8	9	10	11	12	13	14	15	16	17	18	19	20	21	22	23
67	0	0	0	0	0	0	0	0	0	0	0	0	0	0	0	0	0	0	0	0	0	0	0	0	
68	247	204	166	146	120	115	99	84	70	64	92	124	150	167	193	211	223	245	255	261	267	273	283	280	
69	275	236	200	171	155	140	126	116	97	89	114	146	173	194	214	233	250	261	270	277	284	293	299	299	
70	300	255	223	201	183	164	155	127	110	103	137	179	213	239	268	287	305	323	327	333	333	335	336	327	
71	168	154	125	113	101	89	77	64	53	43	71	99	121	139	152	162	172	183	191	200	205	211	212	205	
72	223	183	151	133	119	107	93	79	66	59	84	116	139	162	173	190	201	207	213	218	228	242	248	245	
73	155	151	91	76	68	60	50	41	38	36	58	84	102	115	125	135	141	147	154	158	165	174	177	172	
AVERAGE	231	192	159	140	126	113	98	84	72	67	93	125	150	169	187	203	217	228	235	241	247	255	259	255	
INCREMENT	-39	-33	-19	-14	-13	-15	-14	-12	-5	26	32	25	19	18	16	14	11	7	6	6	8	4	-4	-24	
2ND INC	7	6	14	5	1	-2	1	2	7	31	6	-7	-6	-1	-2	-3	-4	-1	0	2	-4	-8	-20		
24-HR MEAN																									
67	0	0	0	0	0	0	0	0	0	0	0	0	0	0	0	0	0	0	0	0	0	0	0	0	
68	220	187	164	145	129	108	87	72	56	61	94	122	148	164	179	194	201	206	213	214	230	241	250	253	
69	263	237	198	182	167	150	128	110	95	96	131	159	182	210	224	237	245	254	259	268	275	282	284	282	
70	262	232	209	190	174	158	133	111	96	97	132	164	191	206	218	228	238	244	248	253	262	271	276	275	
71	179	152	129	110	99	89	78	65	54	52	78	105	128	143	154	163	168	171	178	183	187	195	195	191	
72	212	183	155	135	122	112	99	84	72	68	98	117	134	145	155	163	168	171	178	183	187	195	195	191	
73	143	133	99	85	77	70	61	49	37	38	60	85	102	114	122	129	132	134	136	144	148	150	150	150	
AVERAGE	213	184	159	141	128	115	98	82	68	69	99	130	152	167	179	190	195	201	205	211	218	226	230	229	
INCREMENT	-29	-25	-18	-13	-17	-15	-14	-11	-4	1	30	31	22	15	12	11	5	5	4	6	7	8	4	-1	
2ND INC	7	4	7	5	3	-4	1	2	15	29	1	-9	-7	-3	-1	-5	-1	-1	2	1	1	-4	-5	-15	
24-HR MEAN																									
67	0	0	0	0	0	0	0	0	0	0	0	0	0	0	0	0	0	0	0	0	0	0	0	0	
68	205	178	153	131	116	100	84	73	58	55	85	116	137	152	164	173	178	179	187	196	207	211	214	219	
69	239	205	180	164	152	138	122	106	90	87	118	154	178	193	208	221	229	2	241	249	253	259	261	257	
70	243	222	194	174	155	136	116	97	85	77	105	137	162	178	189	202	212	18	222	227	234	245	250	253	
71	176	146	120	100	88	79	69	56	47	41	65	94	117	131	144	153	158	164	171	179	189	192	191		
72	200	172	146	127	115	102	90	77	66	56	82	117	145	159	166	175	177	182	186	195	198	203	206	210	
73	127	105	83	67	58	52	47	41	33	31	50	75	90	99	106	112	114	115	121	124	128	133	133	133	
AVERAGE	196	172	146	127	114	101	88	75	63	58	84	116	138	152	163	173	178	181	187	194	200	207	209	211	
INCREMENT	-26	-19	-13	-13	-13	-13	-13	-12	-5	26	32	22	14	11	10	5	3	6	7	6	7	2	2	-13	
2ND INC	7	0	7	6	0	0	0	1	7	31	6	-10	-8	-3	-1	-5	-2	3	1	-1	1	-5	0	-15	
24-HR MEAN																									
67	0	0	0	0	0	0	0	0	0	0	0	0	0	0	0	0	0	0	0	0	0	0	0	0	
68	206	168	137	123	108	93	82	71	57	47	65	104	132	153	167	180	191	201	205	208	212	221	230	230	
69	238	198	170	152	139	128	116	101	87	75	94	138	171	201	221	241	250	253	253	258	267	272	271	271	
70	217	181	151	129	112	99	89	76	64	52	68	110	144	170	187	206	213	225	231	233	234	234	236	236	
71	156	126	101	84	73	65	56	46	38	33	41	72	95	113	126	138	144	150	154	155	155	159	165	166	
72	175	142	116	95	84	73	63	53	45	37	49	82	110	132	147	157	171	178	179	182	187	192	193	193	
73	115	91	68	57	51	46	40	34	26	22	34	58	78	98	108	112	116	121	122	123	124	125	126	126	
AVERAGE	185	151	124	107	95	84	74	64	53	44	59	94	122	143	153	171	180	186	190	192	194	199	203	204	
INCREMENT	-34	-27	-17	-12	-11	-10	-10	-9	-9	-9	15	35	28	21	15	13	9	6	4	2	2	5	4	1	
2ND INC	7	7	16	5	1	1	0	-1	2	24	28	-7	-7	-6	-2	-4	-3	-2	-2	0	3	-1	-3	-28	
24-HR MEAN																									
67	0	0	0	0	0	0	0	0	0	0	0	0	0	0	0	0	0	0	0	0	0	0	0	0	
68	234	198	170	152	139	128	116	101	87	75	94	138	171	201	221	241	250	253	253	258	267	272	271	271	
70	217	181	151	129	112	99	89	76	64	52	68	110	144	170	187	206	213	225	231	233	234	234	236	236	
71	156	126	101	84	73	65	56	46	38	33	41	72	95	113	126	138	144	150	154	155	155	159	165	166	
72	175	142	116	95	84	73	63	53	45	37	49	82	110	132	147	157	171	178	179	182	187	192	193	193	
73	115	91	68	57	51	46	40	34	26	22	34	58	78	98	108	112	116	121	122	123	124	125	126	126	
AVERAGE	185	151	124	107	95	84	74	64	53	44	59	94	122	143	153	171	180	186	190	192	194	199	203	204	
INCREMENT	-34	-27	-17	-12	-11	-10	-10	-9	-9	-9	15	35	28	21	15	13	9	6	4	2	2	5	4	1	
2ND INC	7	7	16	5	1	1	0	-1	2	24	28	-7	-7	-6	-2	-4	-3	-2	-2	0	3	-1	-3	-28	
24-HR MEAN																									



Table 1. Mean Monthly Values of TEC for Hours UT (LMT = UT - 4.70) (Cont)

MEAN JOURNAL TEC PROFILES FOR EACH MONTH, SAGAMORE HILL. (UNITS OF 10.E-15, M.E-2)																									
MEAN TEC VALUES FOR MONTH 9																									
HOUR	UT	0	1	2	3	4	5	6	7	8	9	10	11	12	13	14	15	16	17	18	19	20	21	22	23
67	0	0	0	0	0	0	0	0	0	0	0	0	0	0	0	0	0	0	0	0	0	0	0	0	0
68	213	167	131	113	99	90	82	71	58	47	53	107	159	201	231	268	287	303	307	304	301	292	287	261	185
69	213	169	137	121	113	107	97	85	75	65	69	130	161	196	224	239	262	277	293	294	291	285	281	255	185
70	221	175	140	125	116	108	96	86	74	61	61	115	166	209	245	277	295	312	323	321	316	310	297	270	197
71	133	59	72	59	53	49	44	38	33	29	29	61	91	111	130	144	158	166	173	175	173	173	173	161	147
72	188	146	111	91	82	74	66	58	49	39	38	80	123	153	179	199	210	220	228	235	241	243	240	224	99
73	134	130	112	91	82	74	66	58	49	39	38	80	123	153	179	199	210	220	228	235	241	243	240	224	99
AVERAGE	184	143	111	95	86	79	71	63	53	44	45	90	131	163	188	210	225	238	246	248	247	245	241	222	
INCREMENT	-41	-32	-16	-9	-7	-8	-10	-9	2	44	41	32	25	22	15	13	8	2	-1	-2	-4	-19	-38		
2ND INC	7	9	16	7	2	-1	0	-2	1	11	42	-3	-9	-7	-3	-7	-2	-5	-6	-3	-1	-2	-15	-19	
MEAN TEC VALUES FOR MONTH 10																									
HOUR	UT	0	1	2	3	4	5	6	7	8	9	10	11	12	13	14	15	16	17	18	19	20	21	22	23
67	0	0	0	0	0	0	0	0	0	0	0	0	0	0	0	0	0	0	0	0	0	0	0	0	0
68	175	134	111	101	91	82	76	68	59	49	44	91	172	234	282	333	373	406	405	415	406	380	315	235	210
69	178	146	126	116	108	102	96	80	61	59	59	98	171	232	278	325	365	387	400	400	392	356	299	230	213
70	183	143	124	118	101	95	87	78	70	62	52	88	169	239	297	341	383	394	403	406	399	369	312	242	214
71	93	75	65	59	56	54	50	44	38	33	29	48	93	128	157	179	212	224	229	227	219	201	169	126	117
72	127	103	88	71	76	71	63	55	49	42	36	59	100	128	157	184	194	197	234	245	254	249	222	177	133
73	0	0	0	0	0	0	0	0	0	0	0	0	0	0	0	0	0	0	0	0	0	0	0	0	0
AVERAGE	151	120	103	93	86	81	74	67	59	51	44	77	141	192	234	272	313	322	334	339	334	311	263	202	
INCREMENT	-31	-17	-16	-7	-5	-7	-7	-8	-8	-7	-33	64	51	42	35	28	22	12	5	-5	-23	-48	-61	-51	
2ND INC	7	14	7	3	2	-2	0	-1	0	1	40	31	-13	-9	-4	-10	-5	-10	-7	-10	-18	-25	-13	10	
MEAN TEC VALUES FOR MONTH 11																									
HOUR	UT	0	1	2	3	4	5	6	7	8	9	10	11	12	13	14	15	16	17	18	19	20	21	22	23
67	132	98	81	72	68	65	64	66	66	64	58	58	123	190	250	303	343	367	373	369	354	321	237	174	179
68	117	84	72	67	60	58	57	56	53	47	40	55	129	194	250	313	353	364	367	365	351	313	239	163	174
69	139	114	104	95	93	94	94	89	87	81	72	83	154	219	271	318	358	376	387	388	368	315	239	178	196
70	159	128	103	88	79	73	71	69	62	52	42	62	141	220	287	335	385	408	426	429	408	361	278	210	204
71	76	62	55	52	51	50	50	49	45	42	41	83	126	158	186	213	230	228	224	212	189	142	101	113	103
72	76	61	51	47	45	43	45	44	40	35	35	73	109	138	165	188	202	208	207	195	175	137	100	0	0
73	0	0	0	0	0	0	0	0	0	0	0	0	0	0	0	0	0	0	0	0	0	0	0	0	0
AVERAGE	117	90	77	70	66	64	64	63	61	57	50	56	117	176	226	270	317	325	332	330	315	279	212	154	
INCREMENT	-27	-13	-7	-4	-2	0	-1	-2	-4	-7	6	61	99	58	44	37	18	7	-2	-15	-36	-67	-58	-37	
2ND INC	7	14	6	3	2	2	-1	-1	-2	-3	13	55	-2	-9	-6	-7	-19	-11	-9	-13	-21	-31	9	21	
MEAN TEC VALUES FOR MONTH 12																									
HOUR	UT	0	1	2	3	4	5	6	7	8	9	10	11	12	13	14	15	16	17	18	19	20	21	22	23
67	109	78	64	58	58	59	57	61	59	54	51	47	80	150	207	271	322	336	344	357	334	304	236	164	161
68	104	72	60	55	52	52	55	57	58	57	48	42	87	169	235	322	333	341	355	356	311	293	229	162	164
69	107	84	74	70	68	66	67	66	66	67	63	60	162	218	288	368	381	382	383	313	296	258	197	144	155
70	111	84	69	64	63	63	64	67	67	67	63	51	98	164	239	277	315	325	338	326	317	275	218	155	160
71	76	59	50	47	47	48	49	51	51	48	44	43	68	116	158	188	215	227	233	235	217	282	152	118	114
72	59	37	35	36	37	40	42	45	45	40	35	51	85	111	141	171	177	181	179	168	147	113	80	88	0
73	0	0	0	0	0	0	0	0	0	0	0	0	0	0	0	0	0	0	0	0	0	0	0	0	0
AVERAGE	94	70	59	55	54	54	55	57	58	55	50	46	81	141	193	245	276	285	293	294	278	247	198	136	
INCREMENT	-24	-11	-4	-1	0	1	2	1	-3	-5	-4	35	60	52	52	31	9	8	1	-16	-31	-57	-54	-42	
2ND INC	7	13	7	3	1	1	1	-1	-4	-2	1	39	25	-8	8	-21	-22	-1	-7	-17	-15	-26	3	12	

Table 2. Time of TEC-Rise and Sunrise at Various Heights (LMT = UT - 4.70)

SUNRISE, HOURS UT, SAGA MORE HILL SUB-IONOSPHERIC LONG= 70. W LAT=39. MUJ=400.		TEC-RISE											
HEIGHT KMS:-		400.	405.	410.	415.	420.	425.	430.	435.	440.	445.	HOURS UT	
MONTH 1	12.05	11.64	11.75	11.58	11.63	11.58	11.58	11.54	11.50	11.46	11.42	11.55	
MONTH 2	11.64	11.44	11.36	11.30	11.25	11.20	11.16	11.12	11.09	11.05	11.01	11.33	
MONTH 3	10.95	10.76	10.68	10.62	10.57	10.52	10.48	10.45	10.41	10.38	10.34	10.58	
MONTH 4	10.14	9.95	9.87	9.81	9.75	9.71	9.66	9.63	9.59	9.56	9.52	9.70	
MONTH 5	9.55	9.34	9.25	9.18	9.13	9.07	9.03	8.99	8.95	8.91	8.87	9.32	
MONTH 6	9.32	9.09	8.93	8.87	8.81	8.76	8.72	8.68	8.64	8.60	8.56	8.71	
MONTH 7	9.52	9.30	9.21	9.14	9.08	9.03	8.98	8.94	8.90	8.86	8.82	9.36	
MONTH 8	9.96	9.76	9.67	9.61	9.56	9.51	9.46	9.42	9.39	9.35	9.31	9.53	
MONTH 9	10.41	10.22	10.14	10.08	10.03	9.98	9.94	9.91	9.87	9.84	9.80	10.02	
MONTH 10	10.82	10.69	10.61	10.55	10.50	10.45	10.41	10.38	10.34	10.31	10.27	10.52	
MONTH 11	11.44	11.24	11.15	11.09	11.04	10.99	10.95	10.91	10.87	10.84	10.80	11.00	
MONTH 12	11.94	11.72	11.64	11.57	11.51	11.46	11.42	11.38	11.34	11.30	11.26	11.42	

TIME DIFFERENCE  
(TEC MINUS SUN) -.43 -.23 -.14 -.08 -.02 .02 .07 .11 .15 .18

Table 3. Slope and Intercept in TEC - Flux Relation for 3 Radio Frequencies

LINEAR COEFFICIENTS BETWEEN TEC AND SOLAR FLUX AT 15.4GHZ												
MONTH:-	JAN	FEB	MAR	APR	MAY	JUN	JULY	AUG	SEP	OCT	NOV	DEC
DAY NUMBER	15	45	74	105	135	166	196	227	258	288	319	349
GRADIENT	.36	.43	.41	.44	.45	.26	.27	.13	.58	.42	.32	.38
INTERCEPT	-182.22	-213.53	-196.30	-213.74	-220.28	-121.92	-125.79	-55.92	-291.02	-283.38	-157.20	-188.59
STANDEVN	1.93	2.15	4.03	3.15	2.08	2.26	2.06	3.32	1.42	3.52	1.44	.90
ROOT-MEAN-SQUARE ERROR IN TEC VALUE= 2.35												
MONTHLY TEC VERSUS 5-MONTH FLUX AT MONTH-0												
GRADIENT	.35	.49	.65	.50	.39	.31	.24	.27	.45	.57	.50	.33
INTERCEPT	-172.26	-244.92	-328.24	-247.23	-191.82	-147.48	-112.22	-128.37	-226.86	-289.42	-254.75	-164.95
STANDEVN	1.13	2.08	2.24	2.07	1.57	1.66	1.85	2.56	1.43	2.03	1.92	1.53
ROOT-MEAN-SQUARE ERROR IN TEC VALUE= 1.84												
MONTHLY TEC VERSUS 5-MONTH FLUX AT MONTH-2												
GRADIENT	.34	.43	.61	.59	.51	.38	.27	.28	.40	.39	.43	.31
INTERCEPT	-171.68	-214.82	-305.34	-296.74	-255.16	-188.86	-127.06	-136.88	-194.98	-189.35	-213.87	-150.74
STANDEVN	2.18	3.33	3.58	1.80	1.30	1.26	.82	2.29	2.09	4.11	3.78	2.71
ROOT-MEAN-SQUARE ERROR IN TEC VALUE= 2.44												
MONTHLY TEC VERSUS 5-MONTH FLUX AT MONTH-4												
GRADIENT	.23	.30	.48	.49	.45	.43	.37	.36	.38	.43	.32	.13
INTERCEPT	-111.67	-141.69	-235.35	-247.52	-223.35	-211.36	-182.09	-180.68	-186.54	-211.83	-157.55	-55.73
STANDEVN	3.51	5.03	6.13	3.97	3.07	1.96	1.71	1.73	1.63	3.57	4.43	3.67
ROOT-MEAN-SQUARE ERROR IN TEC VALUE= 3.37												
MONTHLY TEC VERSUS 5-MONTH FLUX AT MONTH-6												
GRADIENT	.13	.81	.18	.37	.35	.33	.34	.41	.45	.46	.42	.18
INTERCEPT	-56.49	11.17	-74.91	-181.45	-170.86	-160.45	-168.08	-205.81	-226.47	-229.40	-209.89	-83.32
STANDEVN	3.90	5.78	7.62	5.70	4.81	3.56	2.51	2.03	1.80	2.64	3.03	3.43
ROOT-MEAN-SQUARE ERROR IN TEC VALUE= 3.89												

Table 3. Slope and Intercept in TEC - Flux Relation for 3 Radio Frequencies (Cont)

LINEAR COEFFICIENTS BETWEEN TEC AND SOLAR FLUX AT 2.695GHZ												
MONTH:-	JAN	FEB	MAR	APR	MAY	JUN	JULY	AUG	SEP	OCT	NOV	DEC
DAY NUMBER	15	45	74	105	135	166	196	227	258	288	319	349
GRADIENT	.14	.18	.21	.23	.18	.14	.16	.26	.25	.26	.20	.15
INTERCEPT	-5.26	-6.60	-6.73	-10.72	-6.30	-1.73	-4.24	-17.81	-13.49	-13.56	-8.94	-5.68
STANDEVN	1.04	1.17	2.51	1.96	1.60	1.39	2.02	2.01	.89	1.33	.87	1.10
ROOT-MEAN-SQUARE ERROR IN TEC VALUE= 1.49												
MONTHLY TEC VERSUS 5-MONTH FLUX AT MONTH-3												
GRADIENT	.19	.22	.26	.21	.21	.18	.14	.19	.25	.31	.23	.15
INTERCEPT	-10.92	-10.78	-13.62	-9.35	-9.94	-6.75	-2.53	-9.56	-15.29	-20.42	-13.38	-6.20
STANDEVN	1.55	.84	1.86	1.39	1.19	1.34	1.71	1.80	1.04	.67	1.09	.84
ROOT-MEAN-SQUARE ERROR IN TEC VALUE= 1.28												
MONTHLY TEC VERSUS 5-MONTH FLUX AT MONTH-2												
GRADIENT	.21	.21	.25	.23	.20	.16	.13	.18	.26	.32	.31	.21
INTERCEPT	-12.16	-9.57	-12.72	-11.30	-8.21	-4.67	-1.73	-8.72	-16.58	-23.08	-23.36	-12.13
STANDEVN	2.38	2.43	3.27	2.59	1.63	1.01	1.10	1.84	.35	1.66	1.35	1.06
ROOT-MEAN-SQUARE ERROR IN TEC VALUE= 1.58												
MONTHLY TEC VERSUS 5-MONTH FLUX AT MONTH-4												
GRADIENT	.23	.23	.22	.20	.18	.16	.14	.16	.20	.30	.28	.18
INTERCEPT	-14.92	-11.59	-8.41	-7.91	-5.88	-4.84	-4.06	-6.36	-10.52	-21.01	-19.61	-9.11
STANDEVN	3.39	3.52	5.07	3.65	3.96	2.07	1.70	1.45	1.13	2.04	2.50	2.40
ROOT-MEAN-SQUARE ERROR IN TEC VALUE= 2.67												
MONTHLY TEC VERSUS 5-MONTH FLUX AT MONTH-6												
GRADIENT	.17	.16	.24	.23	.15	.13	.13	.16	.18	.25	.24	.17
INTERCEPT	-7.89	-2.42	-9.99	-11.15	-1.80	-.99	-2.93	-7.41	-8.20	-15.54	-15.89	-8.42
STANDEVN	4.10	4.73	5.80	4.32	4.21	3.20	2.43	1.97	1.57	1.99	2.01	2.41
ROOT-MEAN-SQUARE ERROR IN TEC VALUE= 3.23												

Table 3. Slope and Intercept in TEC - Flux Relation for 3 Radio Frequencies (Cont)

LINEAR COEFFICIENTS BETWEEN TEC AND SOLAR FLUX AT 0.6066GHZ												
MONTH:- DAY NUMBER	JAN .15	FEB 45	MAR 74	APR 105	MAY 135	JUN 166	JULY 196	AUG 227	SEP 258	OCT 288	NOV 319	DEC 349
GRADIENT	.46	.45	.73	.66	.54	.42	.47	.77	.64	.80	.62	.48
INTERCEPT	-11.99	-8.07	-23.85	-17.60	-12.29	-0.31	-10.01	-26.39	-17.99	-26.06	-17.48	-12.92
STANDEVN	1.25	2.34	1.45	1.44	1.15	1.35	1.48	1.29	.63	1.71	1.49	.52
ROOT-MEAN-SQUARE ERROR IN TEC VALUE=	1.35											
MONTHLY TEC VERSUS 5-MONTH FLUX AT MONTH-0												
GRADIENT	.58	.61	.70	.60	.68	.54	.43	.54	.71	.85	.67	.46
INTERCEPT	-18.10	-16.67	-19.32	-14.81	-20.47	-12.85	-7.84	-14.92	-22.28	-28.47	-20.99	-11.78
STANDEVN	1.35	1.36	2.71	1.95	.91	1.31	1.44	1.64	.66	.45	1.33	.89
ROOT-MEAN-SQUARE ERROR IN TEC VALUE=	1.34											
MONTHLY TEC VERSUS 5-MONTH FLUX AT MONTH-2												
GRADIENT	.58	.58	.68	.60	.52	.44	.40	.52	.72	.89	.54	.56
INTERCEPT	-17.63	-14.99	-18.33	-15.58	-12.07	-8.08	-7.05	-14.58	-23.32	-30.75	-29.63	-16.56
STANDEVN	2.76	2.93	3.99	2.88	2.34	1.74	1.47	1.84	.42	1.65	1.84	1.49
ROOT-MEAN-SQUARE ERROR IN TEC VALUE=	2.11											
MONTHLY TEC VERSUS 5-MONTH FLUX AT MONTH-4												
GRADIENT	.57	.59	.62	.55	.47	.41	.38	.42	.65	.67	.79	.48
INTERCEPT	-16.52	-14.68	-13.95	-12.66	-9.32	-7.20	-6.56	-9.58	-20.81	-30.99	-27.38	-12.37
STANDEVN	3.79	3.99	5.32	4.03	3.53	2.64	2.19	2.00	1.25	1.94	2.44	2.50
ROOT-MEAN-SQUARE ERROR IN TEC VALUE=	2.96											
MONTHLY TEC VERSUS 5-MONTH FLUX AT MONTH-6												
GRADIENT	.42	.42	.63	.63	.41	.35	.36	.41	.46	.81	.74	.47
INTERCEPT	-8.86	-4.91	-14.32	-16.40	-5.42	-3.55	-4.47	-9.75	-11.95	-29.55	-26.02	-12.36
STANDEVN	4.29	4.79	5.92	4.45	4.36	3.45	2.79	2.57	2.15	1.77	2.36	2.54
ROOT-MEAN-SQUARE ERROR IN TEC VALUE=	3.45											

Table 4. Monthly Values of Normalized TEC X 100

MEAN NORMALIZED DIURNAL TEC PROFILES FOR MONTH																								
NORMALIZED TEC VALUES FOR MONTH 1																								
HOURLY UT	0	1	2	3	4	5	6	7	8	9	10	11	12	13	14	15	16	17	18	19	20	21	22	23
67	-99	-99	-99	-99	-99	-99	-99	-99	-99	-99	-99	-99	-99	-99	-99	-99	-99	-99	-99	-99	-99	-99	-99	-99
68	90	62	47	39	35	33	33	34	34	33	21	26	36	79	122	161	187	197	207	214	210	194	169	130
69	81	54	41	37	36	35	34	37	36	35	31	25	43	90	135	176	193	194	205	214	210	187	154	120
70	74	52	43	40	38	39	40	42	42	40	35	29	49	96	140	177	190	194	204	202	194	177	151	113
71	66	47	40	35	31	31	31	31	32	30	26	24	51	99	142	183	201	213	224	220	205	183	152	106
72	71	54	46	45	43	40	39	38	40	41	38	35	53	91	127	171	200	210	207	201	194	171	138	106
73	73	54	46	46	46	46	46	46	46	46	46	46	46	95	132	175	202	204	210	216	204	181	152	111
MEAN	77	54	44	39	36	35	35	36	37	35	32	28	46	90	133	172	193	200	206	210	202	183	154	115
NORMALIZED TEC VALUES FOR MONTH 2																								
HOURLY UT	0	1	2	3	4	5	6	7	8	9	10	11	12	13	14	15	16	17	18	19	20	21	22	23
67	-99	-99	-99	-99	-99	-99	-99	-99	-99	-99	-99	-99	-99	-99	-99	-99	-99	-99	-99	-99	-99	-99	-99	-99
68	103	77	56	45	41	36	34	31	29	27	26	22	48	91	122	150	171	187	205	202	200	190	174	141
69	97	72	60	51	46	41	39	38	37	35	32	28	56	94	127	149	167	173	186	193	193	185	167	134
70	97	75	58	50	45	42	41	43	39	38	36	34	63	96	124	150	167	180	185	168	184	179	158	127
71	91	67	53	47	43	40	38	36	34	34	32	33	64	97	126	147	175	194	200	199	195	182	158	122
72	97	75	60	52	48	44	42	40	39	38	36	37	64	97	128	152	172	182	186	186	186	180	169	152
73	84	58	43	36	33	32	30	29	29	30	29	29	61	100	129	156	165	165	164	211	211	206	194	159
MEAN	95	72	56	48	43	40	38	36	35	34	32	30	58	96	126	151	172	186	193	196	192	183	162	130
NORMALIZED TEC VALUES FOR MONTH 3																								
HOURLY UT	0	1	2	3	4	5	6	7	8	9	10	11	12	13	14	15	16	17	18	19	20	21	22	23
67	-99	-99	-99	-99	-99	-99	-99	-99	-99	-99	-99	-99	-99	-99	-99	-99	-99	-99	-99	-99	-99	-99	-99	-99
68	115	91	71	59	51	46	41	38	34	28	24	35	65	93	117	140	163	172	176	179	178	173	166	148
69	110	89	78	65	58	54	47	41	35	31	28	41	71	97	119	138	153	166	171	176	174	167	156	136
70	109	88	73	62	55	51	47	44	39	34	31	42	70	96	117	137	155	167	174	176	176	165	153	135
71	108	86	70	58	50	45	41	35	33	30	33	43	72	95	119	134	155	169	183	186	178	166	154	135
72	109	89	74	66	59	53	49	45	40	37	34	47	75	99	120	141	155	162	170	168	162	161	151	134
73	109	81	61	50	44	39	36	34	32	31	28	45	75	99	123	144	165	175	178	178	178	178	173	148
MEAN	110	84	73	61	54	50	45	41	35	33	30	42	71	96	119	139	156	168	175	177	174	168	157	139
NORMALIZED TEC VALUES FOR MONTH 4																								
HOURLY UT	0	1	2	3	4	5	6	7	8	9	10	11	12	13	14	15	16	17	18	19	20	21	22	23
67	-99	-99	-99	-99	-99	-99	-99	-99	-99	-99	-99	-99	-99	-99	-99	-99	-99	-99	-99	-99	-99	-99	-99	-99
68	137	105	85	71	64	59	53	47	39	33	30	60	79	94	108	121	132	144	154	157	157	156	155	152
69	128	103	86	76	72	64	56	47	41	35	39	61	78	93	108	123	136	144	152	154	155	154	151	144
70	121	99	82	73	68	64	59	53	46	39	43	63	81	96	115	126	140	146	150	151	150	145	146	139
71	126	98	78	68	60	54	50	45	40	35	38	60	80	97	114	127	141	151	158	161	157	153	153	151
72	125	100	80	69	62	56	52	47	41	37	41	65	86	108	115	128	140	149	155	155	153	151	150	147
73	128	96	78	57	52	44	38	34	30	25	34	63	88	107	122	138	153	157	163	166	172	162	155	148
MEAN	127	101	81	70	64	58	53	46	40	35	39	62	81	97	113	127	138	147	154	156	155	152	151	146

Table 4. Monthly Values of Normalized TEC (Cont)

MEAN NORMALIZED DIURNAL TEC PROFILES FOR MONTH																								
NORMALIZED TEC VALUES FOR MONTH 5																								
HOUR UT	0	1	2	3	4	5	6	7	8	9	10	11	12	13	14	15	16	17	18	19	20	21	22	23
67	-99	-99	-99	-99	-99	-99	-99	-99	-99	-99	-99	-99	-99	-99	-99	-99	-99	-99	-99	-99	-99	-99	-99	-99
68	126	113	92	81	72	64	55	46	39	35	31	28	25	22	20	18	16	14	12	10	8	6	4	2
69	135	116	96	84	76	69	62	54	46	44	40	36	32	28	25	22	20	18	16	14	12	10	8	6
70	125	106	93	84	76	68	60	53	46	43	39	35	31	28	25	22	20	18	16	14	12	10	8	6
71	135	111	90	81	73	64	55	46	38	35	31	28	25	22	20	18	16	14	12	10	8	6	4	2
72	136	113	93	82	73	66	57	49	41	36	32	28	25	22	20	18	16	14	12	10	8	6	4	2
73	141	109	83	69	62	55	45	37	35	33	30	27	24	21	18	16	14	12	10	8	6	4	2	0
MEAN	134	111	92	81	73	65	57	49	42	39	34	30	27	24	21	18	16	14	12	10	8	6	4	2
NORMALIZED TEC VALUES FOR MONTH 6																								
HOUR UT	0	1	2	3	4	5	6	7	8	9	10	11	12	13	14	15	16	17	18	19	20	21	22	23
67	-99	-99	-99	-99	-99	-99	-99	-99	-99	-99	-99	-99	-99	-99	-99	-99	-99	-99	-99	-99	-99	-99	-99	-99
68	134	114	100	88	79	66	53	44	34	37	37	34	30	26	22	18	14	10	6	2	0	-2	-4	-6
69	128	111	97	89	81	73	62	54	46	47	46	42	38	34	30	26	22	18	14	10	6	2	0	-2
70	129	114	103	94	86	78	66	55	47	48	48	44	40	36	32	28	24	20	16	12	8	4	0	-4
71	133	113	96	81	73	66	58	48	40	39	38	34	30	26	22	18	14	10	6	2	0	-2	-4	-6
72	133	115	97	85	77	70	62	53	45	43	42	38	34	30	26	22	18	14	10	6	2	0	-2	-4
73	136	117	94	81	73	67	58	47	35	36	37	31	27	23	19	15	11	7	3	0	-3	-6	-9	-12
MEAN	131	114	98	87	79	71	60	51	42	43	43	38	34	30	26	22	18	14	10	6	2	0	-2	-4
NORMALIZED TEC VALUES FOR MONTH 7																								
HOUR UT	0	1	2	3	4	5	6	7	8	9	10	11	12	13	14	15	16	17	18	19	20	21	22	23
67	-99	-99	-99	-99	-99	-99	-99	-99	-99	-99	-99	-99	-99	-99	-99	-99	-99	-99	-99	-99	-99	-99	-99	-99
68	138	119	103	86	78	67	56	49	39	37	37	34	30	26	22	18	14	10	6	2	0	-2	-4	-6
69	126	108	95	87	80	73	65	56	46	46	46	42	38	34	30	26	22	18	14	10	6	2	0	-2
70	135	123	108	97	86	76	64	54	47	43	38	32	28	24	20	16	12	8	4	0	-4	-8	-12	-16
71	140	117	95	79	73	63	55	44	37	33	32	28	24	20	16	12	8	4	0	-4	-8	-12	-16	-20
72	135	116	99	86	78	69	61	52	45	38	35	31	27	23	19	15	11	7	3	0	-3	-6	-9	-12
73	140	115	91	74	64	57	52	45	36	34	35	29	25	21	17	13	9	5	1	0	-1	-4	-7	-10
MEAN	135	117	99	86	78	69	60	51	43	39	37	32	28	24	20	16	12	8	4	0	-4	-8	-12	-16
NORMALIZED TEC VALUES FOR MONTH 8																								
HOUR UT	0	1	2	3	4	5	6	7	8	9	10	11	12	13	14	15	16	17	18	19	20	21	22	23
67	-99	-99	-99	-99	-99	-99	-99	-99	-99	-99	-99	-99	-99	-99	-99	-99	-99	-99	-99	-99	-99	-99	-99	-99
68	137	112	91	81	72	62	55	47	38	31	31	28	24	20	16	12	8	4	0	-4	-8	-12	-16	-20
69	126	105	90	80	74	66	61	53	46	40	38	34	30	26	22	18	14	10	6	2	0	-2	-4	-6
70	134	112	93	80	69	61	55	47	40	32	32	28	24	20	16	12	8	4	0	-4	-8	-12	-16	-20
71	144	117	94	78	68	60	52	43	35	31	38	35	31	27	23	19	15	11	7	3	0	-3	-6	-9
72	140	113	92	75	67	58	50	42	37	29	39	36	32	28	24	20	16	12	8	4	0	-4	-8	-12
73	139	110	82	69	61	55	48	41	31	27	41	38	34	30	26	22	18	14	10	6	2	0	-2	-4
MEAN	135	110	91	78	69	61	54	47	39	32	43	39	34	30	26	22	18	14	10	6	2	0	-2	-4

Table 4. Monthly Values of Normalized TEC (Cont)

MEAN NORMALIZED DIURNAL TEC PROFILES FOR MONTH																								
NORMALIZED TEC VALUES FOR MONTH 9																								
HOUR UT	0	1	2	3	4	5	6	7	8	9	10	11	12	13	14	15	16	17	18	19	20	21	22	23
67	-99	-99	-99	-99	-99	-99	-99	-99	-99	-99	-99	-99	-99	-99	-99	-99	-99	-99	-99	-99	-99	-99	-99	-99
68	115	90	71	61	54	49	44	38	31	25	29	58	86	189	125	145	155	164	166	164	163	158	155	141
69	115	91	74	65	61	58	52	46	41	35	37	65	87	186	121	129	142	158	158	159	157	154	152	138
70	112	89	71	63	59	54	49	44	38	31	31	58	84	186	124	151	153	158	164	163	168	157	151	137
71	127	94	69	56	50	47	42	36	31	28	28	58	87	186	124	137	149	158	165	167	165	165	163	153
72	128	99	76	62	56	50	45	39	33	27	28	54	84	184	122	135	143	158	155	160	164	165	163	152
73	135	181	73	59	52	46	42	37	31	25	26	57	86	186	122	136	142	149	156	158	162	165	168	163
MEAN	120	93	73	62	56	52	46	41	35	29	30	59	86	187	123	137	147	156	161	162	161	160	158	145
NORMALIZED TEC VALUES FOR MONTH 10																								
HOUR UT	0	1	2	3	4	5	6	7	8	9	10	11	12	13	14	15	16	17	18	19	20	21	22	23
67	-99	-99	-99	-99	-99	-99	-99	-99	-99	-99	-99	-99	-99	-99	-99	-99	-99	-99	-99	-99	-99	-99	-99	-99
68	83	64	53	48	43	39	36	32	28	23	21	43	82	111	134	159	173	193	193	198	193	181	150	112
69	84	69	59	54	51	48	45	42	38	33	29	41	80	109	131	153	171	182	188	188	184	167	140	108
70	86	67	58	50	47	44	41	36	33	29	24	41	79	112	139	159	172	184	188	190	186	172	146	113
71	79	64	56	50	48	46	43	38	32	28	25	41	79	109	134	153	173	191	196	194	187	172	144	108
72	95	77	66	61	57	53	47	41	37	32	27	44	75	96	118	138	146	148	176	184	191	187	167	133
73	-99	-99	-99	-99	-99	-99	-99	-99	-99	-99	-99	-99	-99	-99	-99	-99	-99	-99	-99	-99	-99	-99	-99	-99
MEAN	85	68	58	53	49	46	42	38	33	29	25	44	80	108	132	154	163	182	189	192	189	176	149	113
NORMALIZED TEC VALUES FOR MONTH 11																								
HOUR UT	0	1	2	3	4	5	6	7	8	9	10	11	12	13	14	15	16	17	18	19	20	21	22	23
67	74	55	45	40	38	36	36	37	37	36	32	32	69	106	140	169	195	205	208	206	198	179	132	97
68	67	48	41	39	34	33	33	32	30	27	23	32	74	111	144	180	201	209	211	210	202	180	137	94
69	71	58	51	48	47	48	48	45	44	41	37	42	79	112	136	162	183	192	197	198	188	161	122	91
70	78	59	50	43	39	36	36	35	34	30	25	30	69	108	141	164	189	200	209	210	208	177	136	103
71	67	55	49	46	45	44	44	44	43	41	37	36	73	112	148	165	188	204	202	198	188	167	126	89
72	74	59	50	46	44	42	44	44	43	39	34	34	71	106	134	168	183	196	202	201	189	170	133	97
73	-99	-99	-99	-99	-99	-99	-99	-99	-99	-99	-99	-99	-99	-99	-99	-99	-99	-99	-99	-99	-99	-99	-99	-99
MEAN	72	56	48	43	41	40	40	39	38	35	31	35	72	109	140	167	193	201	205	204	194	172	131	95
NORMALIZED TEC VALUES FOR MONTH 12																								
HOUR UT	0	1	2	3	4	5	6	7	8	9	10	11	12	13	14	15	16	17	18	19	20	21	22	23
67	68	48	40	36	36	37	35	38	37	34	32	29	50	93	129	168	203	209	214	222	207	189	147	102
68	63	44	37	34	32	32	34	35	35	35	29	26	53	103	155	196	203	208	216	216	204	179	140	99
69	69	54	48	45	44	43	43	43	44	43	41	39	65	105	161	173	194	195	202	200	191	166	127	93
70	69	52	43	43	39	39	40	42	42	38	33	32	61	102	137	173	197	203	206	204	198	172	131	97
71	67	52	44	41	41	42	43	45	45	42	39	38	60	102	132	165	189	199	204	206	190	177	133	96
72	67	51	42	40	41	42	45	48	51	45	48	51	58	97	126	160	194	201	206	203	191	167	128	91
73	-99	-99	-99	-99	-99	-99	-99	-99	-99	-99	-99	-99	-99	-99	-99	-99	-99	-99	-99	-99	-99	-99	-99	-99
MEAN	67	50	42	39	39	39	39	41	41	39	36	33	58	101	138	175	197	204	209	210	199	176	136	97



Table 5. Mean Monthly Normalized TEC X 100

NORMALIZED DIURNAL TEC CURVE, HOURLY VALUES FOR EACH MONTH, SAGAMORE HILL ATS 3, 136 MHZ.																									
HOUR	UT	5	1	2	3	4	5	6	7	8	9	10	11	12	13	14	15	16	17	18	19	20	21	22	23
MONTH	1	77	54	44	39	35	35	36	37	35	32	28	46	90	133	172	193	200	208	210	202	183	154	115	
MONTH	2	96	72	56	48	43	40	38	36	35	34	32	30	58	96	126	151	172	186	193	196	192	183	162	130
MONTH	3	110	88	73	61	54	50	45	41	36	33	29	42	71	96	119	139	155	169	175	177	174	168	157	139
MONTH	4	127	101	81	70	64	58	53	46	40	35	39	62	81	97	113	127	139	147	154	156	156	152	151	146
MONTH	5	134	111	92	81	73	65	57	49	42	39	54	72	87	98	108	117	125	132	136	139	143	147	150	147
MONTH	6	131	114	98	87	79	71	60	51	42	43	61	80	94	103	110	117	121	124	127	130	135	140	142	141
MONTH	7	135	117	99	86	78	69	60	51	43	39	57	79	94	103	111	118	121	123	127	132	136	141	142	144
MONTH	8	135	110	91	78	69	61	54	47	39	32	43	69	89	104	115	125	131	135	139	140	142	145	148	149
MONTH	9	120	93	73	62	56	52	46	41	35	29	30	59	86	107	123	137	147	156	161	162	161	160	158	145
MONTH	10	85	68	58	53	49	46	42	38	33	29	25	44	80	108	132	154	169	182	189	192	189	176	149	114
MONTH	11	72	56	48	43	41	40	39	38	35	31	35	35	72	109	140	167	190	201	205	204	194	172	131	95
MONTH	12	67	50	42	39	39	39	39	41	41	39	36	33	58	101	138	175	197	204	209	210	199	176	136	97

Table 6. Monthly Values of Maximum and Minimum Normalized TEC X 100

MONTH; -	JAN	FEB	MAR	APR	MAY	JUN	JULY	AUG	SEP	OCT	NOV	DEC
DAY NUMBER	15	45	74	105	135	166	196	227	258	288	319	349
HIGHEST	210	196	177	156	150	142	144	149	162	192	205	210
LOWEST	28	30	29	35	39	42	39	32	29	25	31	33

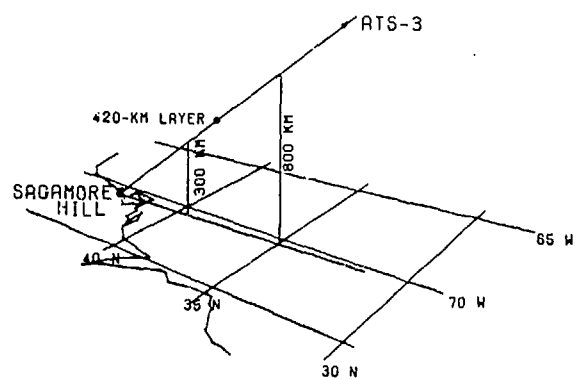
Table 7. Array for Predicting TEC, Hourly Values

PARAMETERS FOR YEC PREDICTION, SAGANORE HILL

M	5	C	T=0	1	2	3	4	5	6	7	8	9	10	11	12	13	14	15	16	17	18	19	20	21	22	23
1	.19	-18.9	.77	.54	.64	.39	.36	.35	.35	.36	.37	.35	.32	.22	.46	.98	1.33	1.72	1.93	2.80	2.68	2.10	2.02	1.83	1.54	1.15
2	.22	-18.8	.96	.72	.56	.48	.43	.40	.38	.36	.35	.34	.32	.31	.58	.96	1.26	1.51	1.72	1.86	1.93	1.96	1.92	1.83	1.62	1.30
3	.26	-13.6	1.18	.89	.73	.61	.54	.58	.45	.41	.36	.33	.29	.42	.71	.96	1.19	1.39	1.56	1.68	1.75	1.77	1.74	1.68	1.57	1.39
4	.21	-9.3	1.27	1.61	.81	.79	.64	.58	.53	.46	.40	.35	.39	.62	.81	.97	1.13	1.27	1.38	1.47	1.54	1.56	1.56	1.52	1.51	1.46
5	.21	-9.8	1.34	1.11	.92	.81	.73	.65	.57	.49	.42	.39	.54	.72	.87	.98	1.08	1.17	1.25	1.32	1.36	1.39	1.43	1.47	1.58	1.47
6	.18	-6.7	1.31	1.14	.98	.87	.79	.71	.69	.51	.42	.43	.61	.81	.94	1.83	1.10	1.17	1.21	1.24	1.27	1.30	1.35	1.40	1.42	1.41
7	.14	-2.5	1.35	1.17	.99	.86	.78	.69	.68	.51	.43	.39	.57	.79	.94	1.83	1.11	1.18	1.21	1.23	1.27	1.32	1.36	1.41	1.42	1.44
8	.19	-9.5	1.35	1.11	.91	.78	.69	.61	.54	.47	.39	.32	.43	.69	.89	1.84	1.15	1.25	1.31	1.36	1.39	1.40	1.42	1.45	1.48	1.49
9	.25	-15.3	1.20	.93	.73	.62	.56	.52	.46	.41	.35	.29	.38	.59	.86	1.87	1.23	1.37	1.47	1.56	1.61	1.62	1.61	1.68	1.58	1.45
10	.31	-28.4	.85	.64	.58	.53	.49	.46	.42	.38	.33	.29	.25	.44	.88	1.88	1.32	1.54	1.69	1.82	1.89	1.92	1.89	1.76	1.49	1.14
11	.23	-13.4	.72	.56	.48	.43	.41	.46	.40	.39	.38	.35	.31	.35	.72	1.89	1.40	1.67	1.98	2.01	2.05	2.04	1.94	1.72	1.31	.95
12	.15	-6.2	.67	.51	.42	.39	.39	.39	.39	.41	.41	.39	.36	.33	.58	1.81	1.38	1.75	1.97	2.04	2.09	2.10	1.99	1.76	1.36	.97

Table 8. Array for Predicting TEC, 4-Hourly Values

Month	Grad G	Const C	Hour UT				
			0	4	8	12	16
2	0.219	- 10.8	0.96	0.43	0.35	0.32	1.72
4	0.215	- 9.3	1.27	0.64	0.40	0.39	1.38
6	0.184	- 6.7	1.31	0.79	0.42	0.61	1.21
8	0.191	- 9.6	1.35	0.69	0.39	0.43	1.31
10	0.306	- 20.4	0.85	0.49	0.33	0.25	1.69
12	0.154	- 6.2	0.67	0.39	0.41	0.36	1.97
							1.92
							1.56
							1.35
							1.42
							1.89
							1.99



RAY PATH AND SUB-IONOSPHERIC POINTS

Figure 1. Ground Projection of Sagamore Hill Ray Path

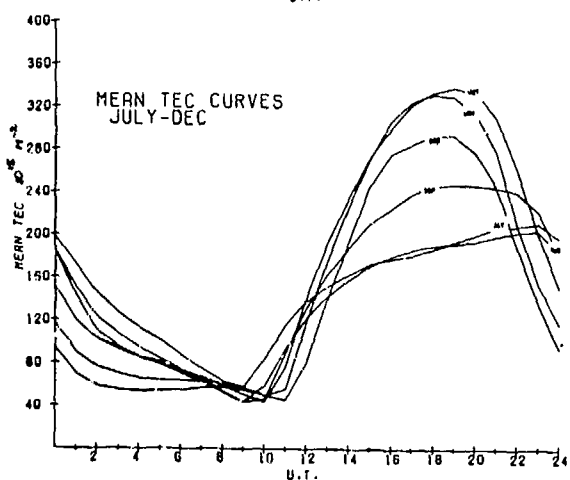
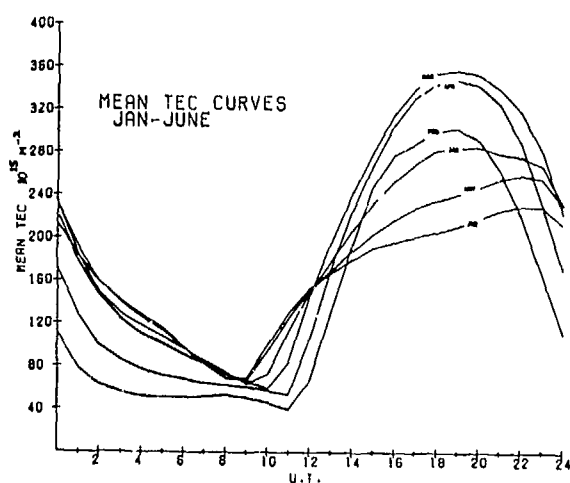


Figure 2. Diurnal TEC, Mean Monthly Curves

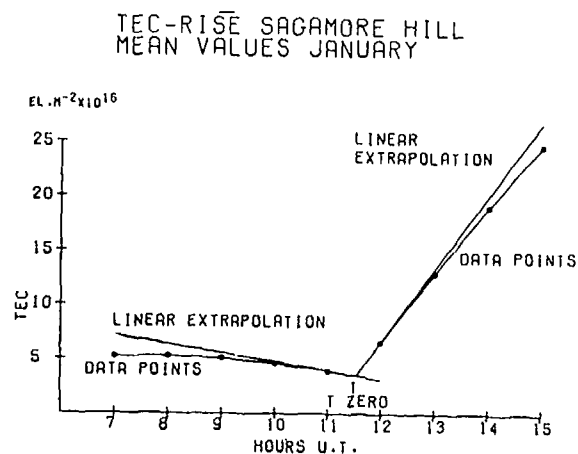


Figure 3. Intersection of Nighttime Fall and Daytime Rise in TEC Curve

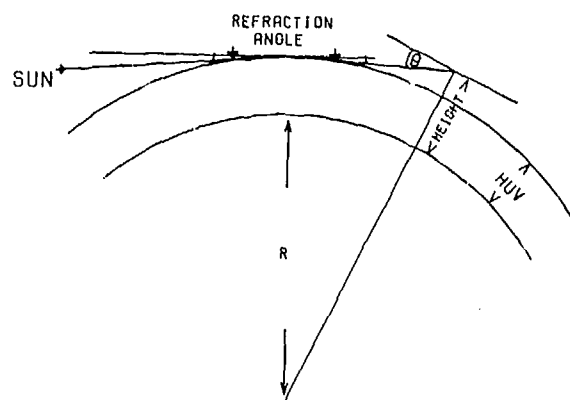


Figure 4. Geometry of Ray Path Through Ionosphere

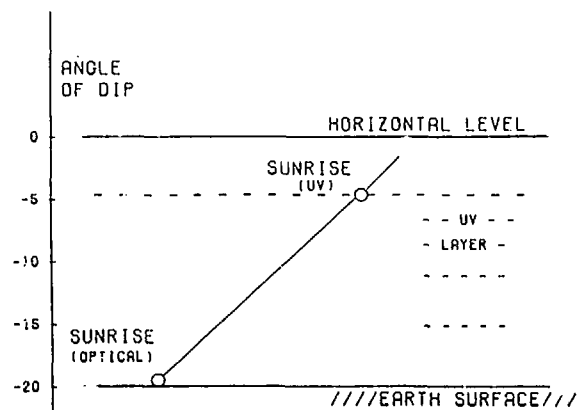


Figure 5. Geometry of Sunrise in the F Region

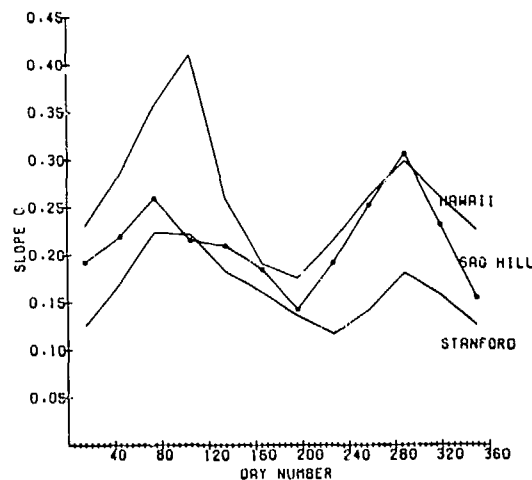


Figure 7. Seasonal Anomaly in Response of TEC to Solar Flux

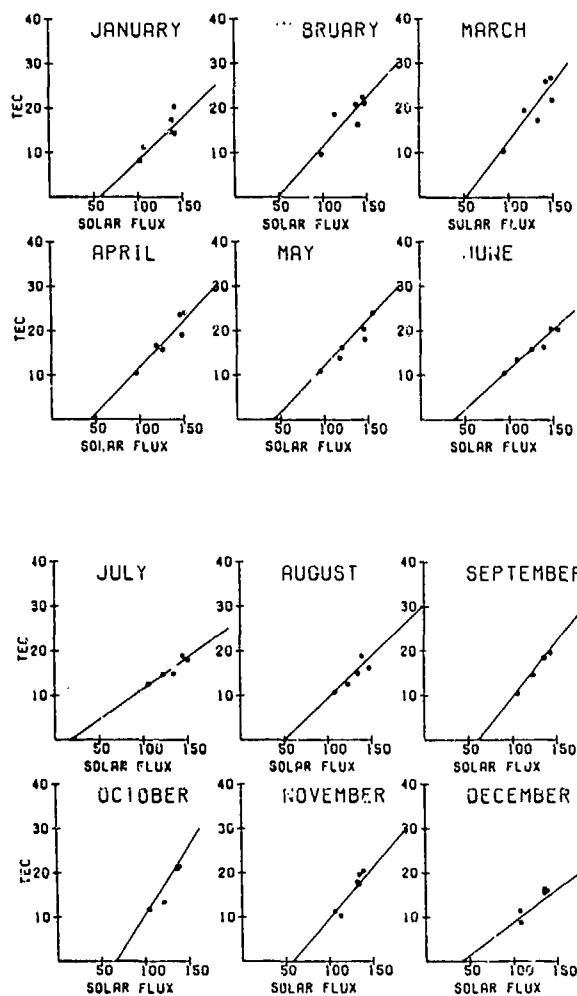


Figure 6. Linear Relation Between Mean TEC and 2.7 GHz Solar Flux for Each Calendar Month

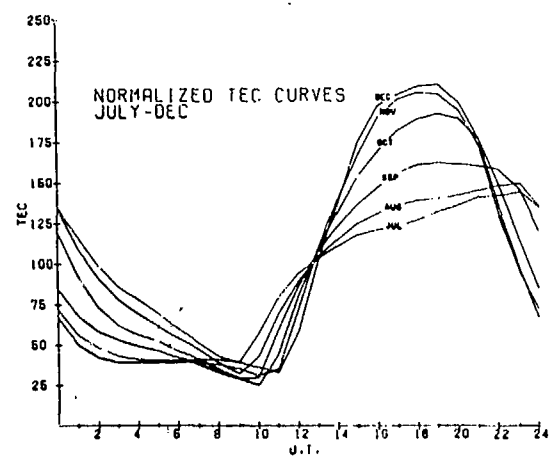
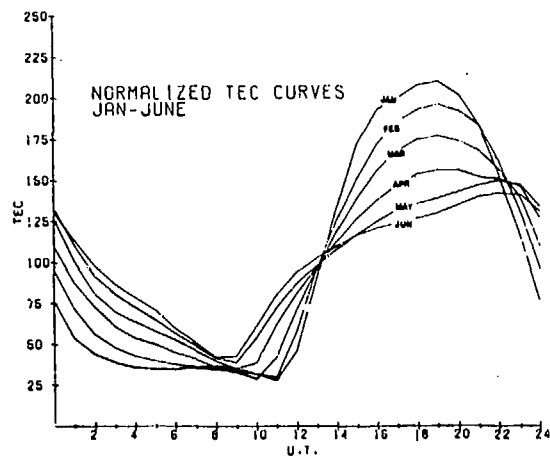


Figure 8. Normalized TEC, Mean Monthly Diurnal Curves

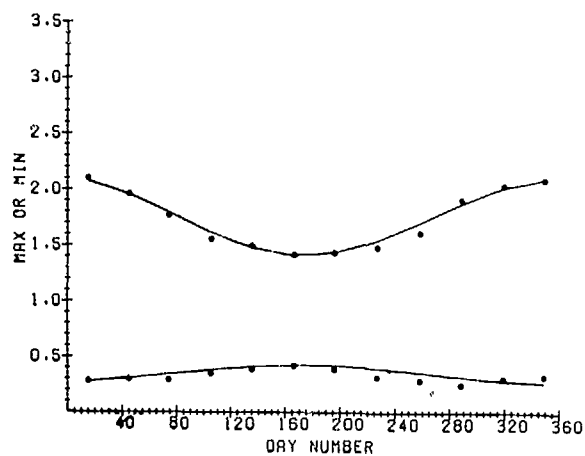


Figure 9. Annual Variation in Maximum and Minimum Normalized TEC

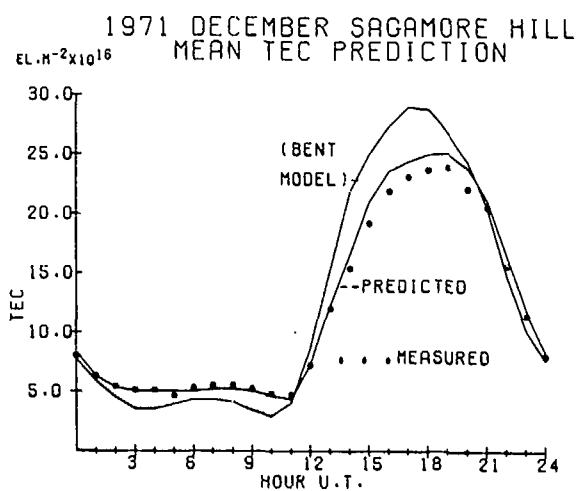


Figure 10. Predicted and Observed Mean TEC December 1971

## LIMITATIONS of MAPPING TECHNIQUES to PREDICTING

### TOTAL ELECTRON CONTENT at a DISTANT POINT

Charles M. Rush

Air Force Cambridge Research Laboratories  
Bedford, MA

#### INTRODUCTION

Observations of Total Electron Content (TEC) are made at discrete points on the globe. Operational requirements however usually dictate a knowledge of the TEC in regions normally inaccessible to routine observation. This has led to the development of models of TEC whereby observations of total electron content and selected ionospheric parameters such as foF2, the critical frequency of the F2 region and hmF2, the height of the maximum electron density in the F2 region, are combined to produce values of TEC that are valid for entire regions. The purpose of this paper is to discuss the limitations in extrapolating observations of TEC to regions where data are normally lacking.

In order to accomplish this study, use was made of a model of the total electron content that depended upon routinely available ionospheric parameters combined with specific functional forms that represent the vertical structure of the electron density profile. The vertical structure of the electron density profile from the base of the ionosphere (taken to be 90 km) up to hmF2 follows closely that of Bradley and Dudeney (1973) and the topside profile follows that given by Bent et al (1971). Values of foF2 needed to determine the TEC are taken from observations and hmF2 is deduced from the M(3000)F2 observations in accord with the relationship given by Bradley and Dudeney (1973). It is assumed that at locations where foF2 and M(3000)F2 observations are available, the model yields TEC results that are 100 percent accurate. The accuracy of the TEC at locations removed from observation locations then is entirely dependent upon the accuracies of foF2 and hmF2 at remote regions. Although

this is certainly not the case, this assumption is valid for the points that are to be illustrated here.

#### SPATIAL EXTENSION of TEC

A median or climatological estimate of the TEC can be obtained by using the numerical coefficients for foF2 and M(3000)F2 given by Barghausen et al (1969), which form part of the ITS-78 propagation prediction program. In the vicinity of vertical incidence ionosondes, observed values of foF2 and M(3000)F2 can be used to generate TEC values that reflect the daily and hourly variability of the ionosphere. To obtain values of TEC that are valid for a time-scale that is less than a median representation at locations removed from ionosondes, it is necessary to adopt some form of interpolation and extrapolation scheme. The scheme chosen here is based on the application of synoptic mapping techniques.

The actual scheme employed is in many instances analogous to that developed by Cressman (1959) for use in meteorological mapping for data-sparse areas. The global distribution of foF2 (and hmF2 derived from M(3000)F2) is first assumed to be given by the monthly median representation given by Barghausen et al (1969). This distribution provides a first-guess value of foF2 at every observation point and at every grid point. The grid comprises a rectangular mesh that divides the globe into rectangular areas. The mathematical formulations involved in the mapping procedure have been discussed in detail by Edwards et al (1975) and need not be described here. Suffice it to say that for each observation of foF2, a deviation denoted as  $D_i$  is computed between each observed value,  $OBS_i$ ,



and the corresponding first-guess value  $FG_i$  at the observing location. Thus

$$D_i = FG_i - OBS_i \quad (1)$$

By considering each grid point in succession, a correction  $C_{X,Y}$  is applied to each grid point that extends the influence of the individual  $D_i$ 's over the entire grid. This correction factor can be written as

$$C_{X,Y} = D_i \cdot \bar{W} \quad (2)$$

where  $\bar{W}$  is a weighting factor. It is the form of  $\bar{W}$  that provides the basis for extending and extrapolating the influence of observations from point locations so as to be valid for areas or regions surrounding the observation location. In a simplistic manner,  $\bar{W}$  can be thought of as the radius of the sphere of influence in the ionosphere of an observation at a point location. In actual fact, different values of  $\bar{W}$  are used to extrapolate the influence of an observation in the north-south and east-west directions.

The form of the weighting factors were determined from a cross-correlation analysis of foF2 (and M(3000)F2) observations. This analysis yielded correlation coefficients for different station-pairs which were then plotted as a function of the distance between stations. A large number of mid-latitude stations were used in the analysis enabling the weighting factor to be determined as a function of station separation spanning the range of 200 to 5000 km. The weighting factors are dependent upon local time and season and generally display a decrease in value with increasing station separation.

In Figure 1 are shown smoothed values of the correlation coefficients for the time period surrounding mid-day for summer, winter and equinox conditions, plotted as a function of station separation. It is seen that the coefficients for the east-west direction fall off less rapidly than for the north-south direction. Also, the coefficients tend to be higher during equinox than for any other season of the year. The values of the coefficients themselves can be used to provide an indication of the amount of improvement above climatology that a remote observation provides in updating a median field of TEC values. It can be shown (Gautier and Zacharisen (1965)) that the cross correlation coefficient between two sets of data is directly proportional to the percentage improvement that can be obtained by

using deviations from one set to predict deviations in the second data ensemble. A 50 percent improvement above climatology, for example, requires that the correlation coefficient be at least 0.87. With reference to Figure 1, it is seen that such improvement will only be obtained if the observation location is within 500 to 1000 km of the area where the improvement is desired. Unless there exists a relatively dense network of observations, spread rather homogeneously over the globe, updating a climatological estimate of TEC will not be worthwhile for certain areas of the globe.

#### ACCURACY of SPATIALLY EXTENDING TEC MODELS

To illustrate the limitations inherent in inferring values of TEC at remote locations, Figure 2 shows a regional map of TEC evaluated from the base of the ionosphere up to 1000 km for the region between 20° and 80° north geographic latitude and 15° W to 75° E geographic longitude. The figure on the left shows contours of  $TEC \times 10^{-16} \text{ el/m}^2$  based on the monthly median values of foF2 and hmF2 valid for January 1966 while the figure on the right displays contours of  $TEC \times 10^{-16} \text{ el/m}^2$  deduced by using actual observations of foF2 and M(3000)F2 observed on 15 January 1966 at 10 mid-latitude locations within the region 20°-80° north latitude and 0° to 55° east longitude. It can be seen that the actual observations indicate the total electron content within this region is down by about a factor of 2 compared to the median.

Figure 3 provides an indication of the accuracy of the TEC values for longitudes that are east of the stations used for deducing the total electron content for 15 January at 1200 GMT. A reference point of 60° E was chosen in order to effect the comparison. Ionosonde data from stations located to the east of 60° E were used to compute the 'actual' TEC which was then compared against that given by the model values of TEC deduced by spatially extending observations of foF2 and hmF2 recorded west of 55° longitude. It is readily apparent that for locations increasingly removed from the region where data are available, the average error associated with the inferred TEC values increases. Shown for comparison on the figure are the average errors associated with assuming TEC values based on median conditions over the entire

region six hours to the east of 60° and the average errors in the TEC at the locations where data are available (denoted as 'Mapped Values'). Within the region where data are available for updating and mapping, the accuracy of the TEC values at locations removed from observing locations is comparable to that at the observing locations. At locations between 4 to 5 hours outside of the region where data are available, the accuracy of the TEC values approaches that associated with a median representation.

Comparisons for other days and times show the same general behavior. In Figure 4, the results of a comparison between observed and inferred TEC values for 1200 hours GMT on 15 June 1966, are shown. Although the magnitude of the average errors are about one-half those seen for 15 January, the same general trends noted for Figure 3 are seen in the present figure. At locations greater than 3 hours removed from the region of data availability, agreement between observation and a median model is as good as that in which updating and spatial extension of observations are employed.

The effect of spatially extending point observations to improve a median TEC model can be further illustrated from the results shown in the next two figures. Figures 5 and 6 show the root mean square differences or 'errors' between observed values of foF2 and values obtained as the result of spatially extending actual observations. Shown are results for two days 24 January and 18 June, 1958. Data for 1958 were chosen for illustration because during that time period observations of ionospheric parameters are available for the most numerous locations on the globe. The top portion of both figures show the rms differences evaluated at 23 locations whose data were used to generate global maps of foF2. These 23 locations were taken to be representative of the stations whose data are available to the Air Force Air Weather Service in time fashion. The curves labeled 'analysis' give the rms difference between the actual observation and the final mapped results at the observation locations for 24 hours of Greenwich Mean Time. The number in parenthesis is the rms difference averaged over the entire 24 hours. Shown also in the top portion of both figures is the rms difference that results simply from assuming the monthly median value (denoted ITS) for each location and hour to be representative of the daily observations. It is seen that at the observation locations the updating and

mapping procedures yield about a factor of 4 improvement on the average compared to the first-guess or median representation. The curves indicated as prediction are the rms errors resulting from rotating the previous hours' analysis westward by 15° of geographic longitude along lines of constant magnetic latitude.

In order to test the validity and value of spatially extending point observations however, it is necessary to compare the values generated in the mapping procedure against data that were not used in the generation of the maps. The next three portions of Figures 5 and 6 show the rms differences that result when comparing mapped values with observations that were not used in the mapping procedure, for stations grouped in the polar region (north of 55° magnetic latitude), the mid-latitude ionosphere (between 25° and 55° magnetic) and stations located under the equatorial ionosphere (0 to 25° magnetic). In each of the three regions approximately 10 to 14 stations were used to verify the mapped values for each time. It is obvious from the figures that the rms differences are higher for the verifying stations than for the observation locations, and in some instances, the use of spatially extending point observations on a daily basis yields results that are no better than those obtained by adopting the monthly median representation for the daily data. This is particularly the case for the equatorial ionosphere. It is also seen that for local summer conditions (18 June) the results obtained at the verifying stations in the polar and mid-latitude regions are rather close to those obtained at the stations used in the generation of the maps while for winter no such agreement is observed. The reason for this behavior is felt to be due to the fact that during local summer, the gradients in the ionosphere tend to be less severe than at other times of the year leading to an ionospheric structure that is smoothly varying over larger distances. The effects of steep gradients in ionospheric structure characteristic of the equatorial ionosphere could also be responsible for the small improvement seen in spatially extending observations to that region.

#### CONCLUSIONS

Although some of the results which have been quoted above are no doubt dependent upon the form of the TEC model and the mapping procedures which have been adopted in this study, similar investigations employing various TEC models and spatial extension techniques

permit the following general statements to be noted. In regions surrounding locations where data are available, accurate values of the total electron content can be inferred. These regions vary from 500 to 2000 km removed from the observing location, depending upon season and local time. At further distances, the errors associated with inferred TEC values approach those resulting from assuming a climatological model. In these regions, monthly median or climatological values of TEC are the only values that can be justified in terms of accuracy and cost-effectiveness. Finally, the effects of gradients in the ionospheric structure in the region between an observation and where a TEC value is to be inferred, critically influences the applicability of spatially extending observations. Values on one side of sunrise and sunset transitions afford little improvement compared to climatology when extended through and to the other side of such transitions. The same limitations are present when extrapolating observations into regions of the equatorial anomaly and into the polar ionosphere, particularly in the region of the polar trough.

#### REFERENCES

- Barghausen, A.F., et al., Tech. Rpt. ERL110-ITS-78, ESSA Res. Labs, ITS, 1969.
- Bent, R.S., et al., paper presented at Working Group I (a18), XIV th Mtg of COSPAR, Seattle, Wash., 1971.
- Bradley, P.A., and J.R. Dudeney, J.A.T.P., 35,2131-2147, 1973.
- Cressman, G.P., Mon. Wea. Rev., 87,367-374, 1959.
- Edwards, W.R., et al., AFCRL Tech. Rpt., in press, 1975.
- Gautier, T.N., and C.H. Zacharisen, Proc. of First Annual IEEE Communications Convention, 671-675, Boulder, CO, 1965.

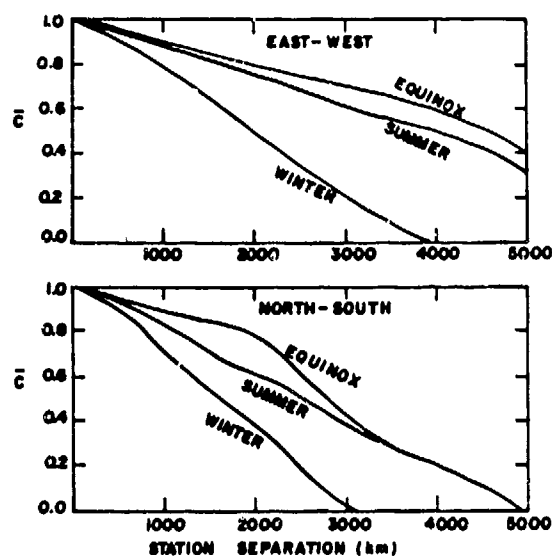


Figure 1: Smoothed Correlation Coefficients as a function of station separation for the time period surrounding mid-day.

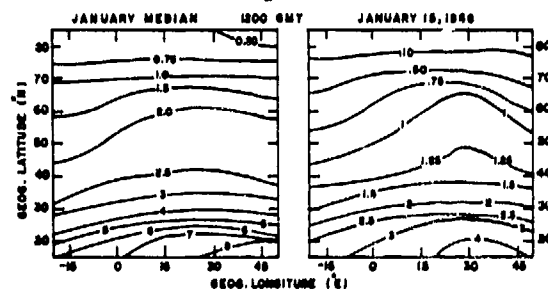


Figure 2: Contours of  $TEC \times 10^{-16}$  el/m<sup>2</sup> evaluated to 1000 Km for median conditions, January 1966, and for January 15, 1966.

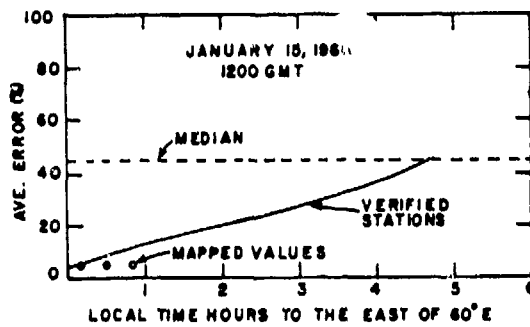


Figure 3: Average error (%) in the TEC deduced by spatially extending foF2 and M(3000)F2 observations on 15 January, 1966.

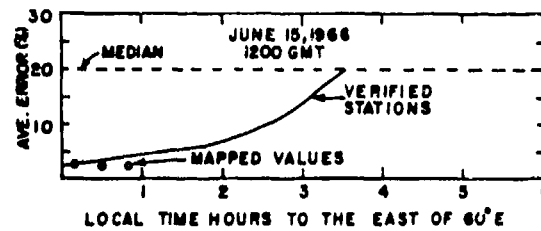


Figure 4: Average error (%) in the TEC deduced by spatially extending foF2 and M(3000)F2 observations on 15 June 1966.

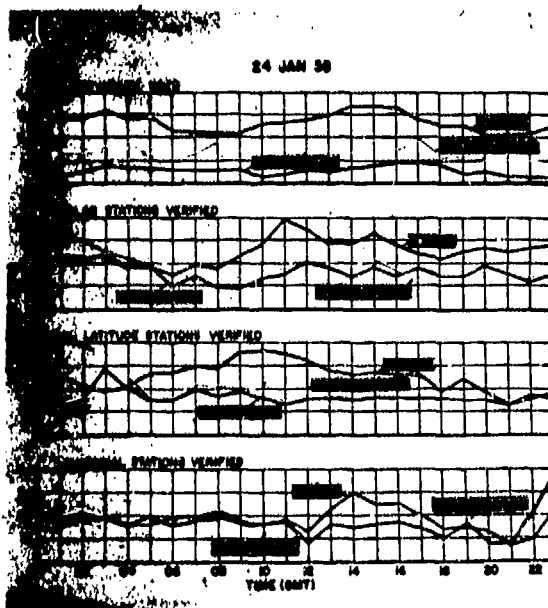


Figure 5: Root mean square differences between observed values of foF2 and values obtained by spatially extending foF2 observations on 24 January 1958.

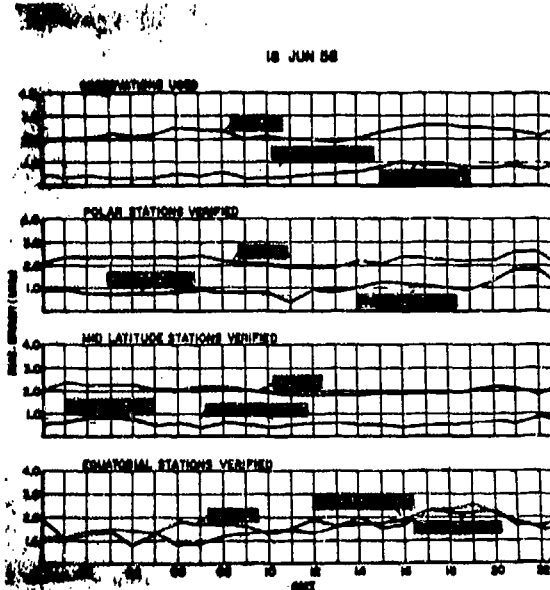


Figure 6: Root mean square differences between observed values of foF2 and values obtained by spatially extending foF2 observations on 18 June 1958.

MEASUREMENT OF THE IONOSPHERE TOTAL ELECTRON CONTENT AND  
LOWER LAYERS INHOMOGENEITIES USING CHIRP SIGNALS\*

Said E. El-Khamy  
Department of Electrical Engineering  
Faculty of Engineering  
Alexandria University  
Alexandria, Egypt

ABSTRACT

The dispersion of frequency modulated signals propagating through or reflected from the ionosphere has motivated this new technique for ionosphere diagnostics. It has been recently shown<sup>1,2,3</sup> that special optimum signals, when incident upon the ionosphere, result in compressed received signals (with maximized amplitude and shorter duration). Such optimum signals have been synthesized for both cases of transionospheric transmission<sup>4,5</sup> and ionospheric reflection<sup>6,7</sup>. It has been shown that in both cases, the optimum signals can be approximated by linearly frequency modulated (Chirp) signals with rectangular or Gaussian envelopes. The instantaneous frequency is an increasing function of time in the transionospheric transmission case and is a decreasing function of time in the reflection case. The sweep rate of the optimum chirp signal is a function of the total electron content,  $N_t$ , in the transmission case. When the lower layer of the ionosphere can be modeled by a linear electron density profile with rate,  $\beta$ , i.e.,  $n(z) = \beta z$ , the optimum sweep rate in this case will be a function of  $\beta$ .

The diagnosis technique proposed here is to send chirp signals with variable sweep rate,  $m$ , and the same center frequency, and experimentally determine the optimum sweep rate  $m_{op}$ , which result in maximum compression of the received signals. Once  $m_{op}$  is known, the total electron content can be determined from the transionospheric measurements as,  $N_t = k_1/m_{op}$ . From the reflection measurements, the inhomogeneity parameter,  $\beta$ , is determined as,  $\beta = k_2 m_{op}$ . The constants  $k_1$  and  $k_2$  depend on the used center frequencies of the chirp signals. It has been shown analytically that the compression ratio varies sharply with the used sweep rate,  $m$ , and is peaked at the optimum sweep rate,  $m_{op}$ . Thus it is easy to distinguish the compression peak and consequently the optimum sweep rate. Therefore this diagnosis method should allow for accurate measurements of the total electron content and the inhomogeneity parameters of the lower layers of the ionosphere.

1. R.E. McIntosh and S.E. El-Khamy, "Compression of Transmitted Pulses in Plasmas," IEEE Trans. Antennas and Propagation, Vol. AP-18, pp:236-241, March 1970.
2. R.E. McIntosh and S.E. El-Khamy, "Optimum Pulse Transmission Through a Plasma Medium," IEEE Trans. Antennas and Propagation, Vol. AP-18, pp:666-671, September 1970.
3. L.B. Felsen, "Asymptotic Theory of Pulse Compression in Dispersive Media," IEEE Trans. Antennas and Propagation, Vol. AP-19, pp:424-432, May 1971.
4. S.E. El-Khamy and R.E. McIntosh, "Optimum Transionospheric Pulse Transmission," IEEE Trans. Antennas and Propagation, Vol. AP-21, pp:269-273, March 1973.
5. S.E. El-Khamy and R.E. McIntosh, "Compression of Transient RF Signals in the Ionosphere," 1972 Fall Meeting of URSI, Program and Abstracts, December 1972.
6. S.E. El-Khamy, "Pulse Compression by Reflection from Inhomogeneous Ionized Media," IEEE Trans. Antennas and Propagation, Vol. AP-22, September 1974.
7. S.E. El-Khamy, "Optimum Pulse Reflection from the Ionosphere," Radio Science, to appear in 1975.

\*Paper unavailable as of printing.

## IONOSPHERIC EFFECTS IN NAVSTAR GPS

C. K. Cretcher  
The Aerospace Corporation  
El Segundo, California

### ABSTRACT

The NAVSTAR Global Positioning System is a satellite-based navigation system that will provide extremely accurate three-dimensional position fixes and timing information to users anywhere on or near the earth. User positioning requires the determination of times of transit for satellite-generated signals to reach the user. The errors arising from the delay of a signal traversing the ionosphere are unacceptably large. Sophisticated, high accuracy users will make use of the two synchronous L-band signals transmitted by the satellites to calibrate the ionospheric delay. Less sophisticated users will apply modeling algorithms to eliminate sizable portions of the delay.

This paper discusses the nature of the errors due to dual-frequency calibration or ionospheric modeling and the impact of system electronic and geometric design on resulting user performance. A number of studies have demonstrated the feasibility of ionospheric delay modeling. The nature of the modeling problem and the conclusions of these studies are presented, as well as the operational implications of the modes of ionospheric error reduction in terms of various user equipments and scenarios.

### 1. INTRODUCTION

The NAVSTAR Global Positioning System (GPS) is a satellite-based navigation system that will provide extremely accurate three-dimensional position fixes and timing information to properly equipped users anywhere on or near the earth. The system will be available continuously regardless of weather conditions, and will find extensive utilization in improved weapons delivery accuracies, range instrumentation, etc. Furthermore, it will provide an ultimate savings in the number and cost of navigation and position fixing systems currently employed or projected.

NAVSTAR GPS is a Joint Service Program managed by the USAF with deputies from the Navy, Army, Marines, and Defense Mapping

Agency. The system concept evolved from USAF and Navy studies initiated in the mid-1960s. Current program plans call for the deployment of six satellites in 1977 to permit demonstration and evaluation tests over the continental United States. The system will then be expanded through deployment of additional satellites into an operational 24-satellite system.

This paper reviews the mechanism by which ionospheric signal delays enter into the user navigation process and the resulting impact on user performance. Discussions of both modeling and dual-frequency receiver calibration of ionospheric delays are presented.

### 2. SYSTEM DESCRIPTION

The overall GPS configuration is depicted in Figure 1 and consists of three primary segments: User System Segment, Space System Segment, and Control System Segment. The functions of each of these segments are outlined below, followed by a description of the basic signal structure.

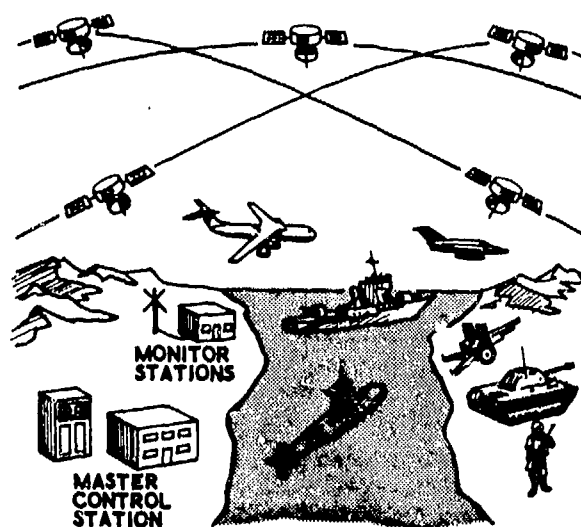


Fig. 1. GPS Concept

### User System Segment

In the GPS, the user receiver measures pseudo-range\* and pseudo-range rate using the navigation signal from each of four satellites. Each signal carries ephemeris data and system timing information for that satellite. This allows the user receiver to convert the pseudo-range and pseudo-range rate to user three-dimensional position and velocity and system time.

A receiver is defined to include the hardware necessary to determine position and velocity of the user in earth-centered coordinates. As such, it must accomplish both the traditional receiver functions and the computational functions. Two basic configurations will be utilized. One is a continuous four-channel receiver that measures four pseudo-ranges simultaneously and will be the basis for the present analysis. The other is a sequential receiver that measures pseudo-ranges sequentially in time.

### Space System Segment

The current baseline orbital configuration for the fully operational GPS employs 24 satellites in 63° inclined, circular, 12-hour orbits to transmit navigation signals. Continuous three-dimensional global coverage will be provided by placing eight satellites, equally spaced, in each of three orbit planes 120° apart in inertial space, as depicted in Figure 2.

Each satellite will generate and transmit two signals at a given L-band frequency: a precision protected navigation signal and a clear navigation signal. Satellite ephemerides, atmospheric propagation correction data, and satellite clock drift information, all of which are periodically updated by the master ground station, will be superimposed on both signals. The ranging signal and data modulation are generated from onboard oscillators and shift registers. The satellites will also transmit a separate L-band navigation signal to permit the determination of the ionospheric signal delay correction by tracking stations and users.

### Control System Segment

Widely separated monitor stations will passively track all satellites in view and accumulate ranging data derived from the navigation signals. This information is processed at a master control station (MCS) by a filtering algorithm to provide a best estimate of satellite position, velocity, and clock drift relative to system time. Atmospheric propagation delay corrections must be applied to the ranging data.

An off-line orbit determination process also derives progressively refined information defining the gravitational field influencing the

\*Measured transit time of the signal multiplied by the speed of light.

### ORBITAL CONFIGURATION

- 12-hour PERIOD
- CIRCULAR ORBITS
- 63° INCLINATION
- EIGHT SATELLITES PER PLANE

### SPACECRAFT CONFIGURATION

- 900 lb (typical)
- 450 watts (typical)
- NAV SIGNALS
  - 1200 MHz
  - 1600 MHz
- ONE WAY TRACKING
- $10^{-13}$  CLOCK STABILITY

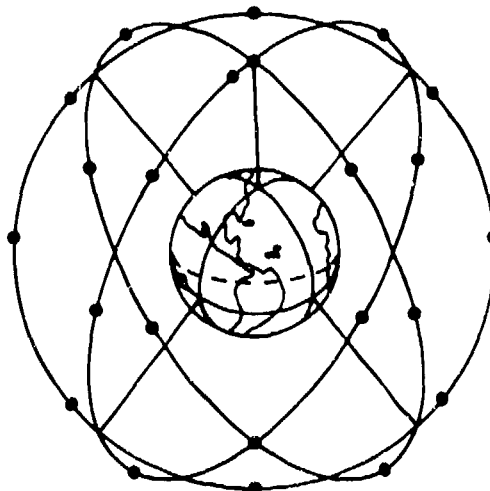


Fig. 2. GPS Space Segment

spacecraft motion; solar pressure parameters; the location, clock drifts, and electronic delay characteristics of the ground stations; and other observable system influences.

An upload station (ULS) located in the continental United States will transmit the satellite ephemerides, clock drifts, and propagation delay data to the satellites at least once per day. The ground stations may also be involved in gathering data to be used in ionospheric and tropospheric delay modeling.

### Signal Structure

The basic navigation signal consists of a sequence of binary digits phase modulated onto the carrier (~1.6 GHz) at an approximately 10-MHz rate. This modulation, which is produced by linear shift registers, appears to be a random sequence, and is therefore termed a pseudo-random noise (PRN) sequence.

Ephemerides, satellite clock drifts, signal code state data, and propagation delay modeling coefficients are repeatedly modulated onto the PRN signal at ~50 bits/sec. The PRN sequences are unique to each satellite and they are mutually orthogonal, permitting the use of a common carrier frequency. The code-generating sequence will be periodically changed and it will be of a variety that makes it virtually impossible to determine the algorithm for generating the sequence without a key, thus making the signal secure. A clear (unprotected) signal will be transmitted at the same carrier frequency which will serve the civil community and some military users, and will also provide a rapid acquisition capability for all users.

### 3. NAVIGATION ALGEBRA

The technique for achieving the desired system accuracies calls for making transit time measurements of RF signals encoded as PRN modulation on an L-band carrier. A precision timing system carefully synchronized between satellite transmitters must be used. Users with precision clocks could then passively range to the satellites and determine their own position as the calculated intersection of at least three spheres centered at the transmitters. To avoid requiring all users to be equipped with precision clocks, enough satellites will be deployed so that all users have available at least four satellites simultaneously. Then synchronized time is not required because the simultaneous reception of four signals produces three independent range differences that may be used to calculate the intersection of three hyperboloids of revolution.

The range differencing solution is primarily conceptual, since it is just one possible method of determining user position and clock bias (a total of four unknowns) from the four range measurements. The basic equation relating ranges and transit times is termed a pseudo-range equation, which in an error-free system is given by (see Figure 3)

$$r_i = [(\underline{s}_i - \underline{x}) \cdot (\underline{s}_i - \underline{x})]^{1/2} + b \quad (1)$$

where

$r_i$  = time delay multiplied by the speed of light measured from satellite  $i$

$\underline{x}$  = vector from earth center to user position

$\underline{s}_i$  = vector from earth center to satellite  $i$

$b$  = user clock phase bias (multiplied by the speed of light).

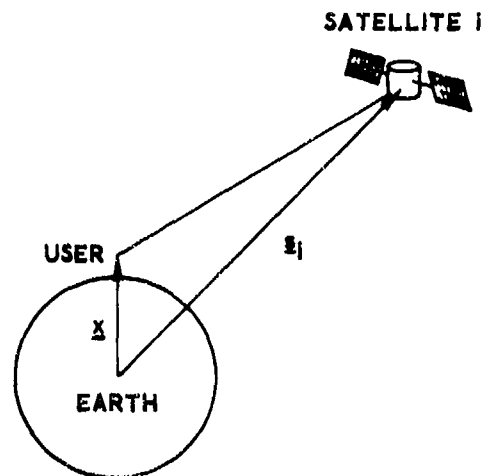


Fig. 3. Satellite/User Geometry

The parameter  $r_i$  has been termed a pseudo-range since it does not conform to Euclidean distance because of the additional term  $b$ . Given four independent pseudo-ranges, one can solve for the user position and time. When more than four pseudo-ranges are available and/or noise is introduced into the measurements, the determination of  $\underline{x}$  becomes a process of optimal estimation.

An iterative solution for user position can be defined as follows, where matrix notation is employed for convenience (matrices denoted by capital letters):

$$\underline{X} \triangleq (x_1, x_2, x_3)^T = \text{user coordinates in a reference coordinate frame}$$

and

$$\underline{S}_i \triangleq (s_{i1}, s_{i2}, s_{i3})^T = \text{satellite coordinates in the reference coordinate frame}$$

The four simultaneous pseudo-range measurements are then given by

$$m_i = [(\underline{S}_i - \underline{X})^T (\underline{S}_i - \underline{X})]^{1/2} + b - b_i + p_i \quad (i = 1, 2, 3, 4) \quad (2)$$

where  $p_i$  is the noise and  $b_i$  the satellite clock phase bias in measurement  $i$ .



Let the direction cosine of the  $i$ th measurement vector along the  $j$ th coordinate be defined by

$$\gamma_{ij} \triangleq (S_{ij} - X_j) / [(S_i - X)^T (S_i - X)]^{1/2} \quad (3)$$

Then, defining the geometric matrices

$$G = \begin{bmatrix} \Gamma_1 \\ \Gamma_2 \\ \Gamma_3 \\ \Gamma_4 \end{bmatrix} \quad (4 \times 4) \quad B = \begin{bmatrix} \Gamma_1 & 0 & 0 & 0 \\ 0 & \Gamma_2 & 0 & 0 \\ 0 & 0 & \Gamma_3 & 0 \\ 0 & 0 & 0 & \Gamma_4 \end{bmatrix} \quad (4 \times 16)$$

where

$$\Gamma_i = (\gamma_{i1}, \gamma_{i2}, \gamma_{i3}, 1)$$

$$O = (0, 0, 0, 0)$$

the user state and the measurement matrices

$$Y = [x_1, x_2, x_3, b]^T \quad (1 \times 4)$$

$$M = (m_1, m_2, m_3, m_4)^T \quad (1 \times 4)$$

the augmented satellite state matrix

$$S = (S_1^T, b_1, S_2^T, b_2, S_3^T, b_3, S_4^T, b_4)^T \quad (1 \times 16)$$

and the noise matrix

$$P = (p_1, p_2, p_3, p_4)^T \quad (1 \times 4)$$

permits the following matrix equation to be written in place of Eq. (2):

$$GY = BS - M + P \quad (4)$$

The minimum variance estimate of  $Y$ , assuming no statistical a priori information, is then

$$\hat{Y} = G^{-1} (BS - M) \quad (5)$$

Since  $G$  and  $B$  are functions of system geometry, and therefore  $\hat{Y}$ , an iterative solution for  $\hat{Y}$  is indicated. However, sufficiently accurate initial estimates of  $\hat{Y}$  will generally be available and only a few iterations, at most, will be required.

The covariance matrix for the error  $\delta Y$  in the estimate of  $Y$  from Eq. (5) is

$$\text{cov } \delta Y = (G^T R^{-1} G)^{-1} = \left\{ G^T [B(\text{cov } \delta S) B^T + \text{cov } P]^{-1} G \right\}^{-1} \quad (6)$$

where Eq. (6) defines the matrix  $R$ .

The GDOP (Geometric Dilution of Precision) is calculated by setting the total range measurement error covariance matrix  $R$  (consisting of satellite position error and measurement error) equal to the identity matrix, resulting in

$$\text{cov } \delta Y = (G^T G)^{-1} \quad (7)$$

The GDOP factor is then defined as the square root of the projection of  $\text{cov } \delta Y$  onto the user coordinate of interest.

If variances  $\sigma_r^2$  and correlations  $\rho$  are assumed for  $R$ , the result is

$$\text{cov } \delta X = \sigma_r^2 (1 - \rho) (G^T G)^{-1}_{\text{upper left-hand } 3 \times 3} \quad (8)$$

$$\text{cov } \sigma b = \sigma_r^2 \left[ \rho + (1 - \rho) (G^T G)^{-1}_{44} \right] \quad (9)$$

Thus, the corresponding standard deviation in the user coordinate is obtained by multiplying the GDOP factor by  $\sigma_r (1 - \rho)^{1/2}$ . For the clock bias this GDOP multiplier is only valid for uncorrelated errors ( $\rho = 0$ ). If, in fact, quantities  $\sigma_r$  and  $\rho$  can be found that produce user coordinate variances closely approximating the variances produced by error source modeling, then the quantity  $\sigma_r (1 - \rho)^{1/2}$  is termed the User Equivalent Ranging Error (UERE). Under these conditions, system/user geometry is characterized by GDOP factors and pseudo-ranging errors by UERE.

Figure 4 shows the cumulative probability distribution function for the GDOP factor along the vertical axis and the GDOP factor for radial error in the horizontal plane for GPS. Since in fact satellite position error projections and atmospheric refraction modeling errors are geometry dependent, the GDOP/UERE concept is only an approximation. GDOP considerations result in ideal satellite locations consisting of one directly overhead and three equally spaced near the horizon. Since tropospheric and ionospheric effects become larger near the horizon, this is not truly optimal for minimizing user error. However, atmospheric errors are only a portion of the total pseudo-ranging error and GDOP is still a reasonable figure of merit, particularly on a statistical basis.

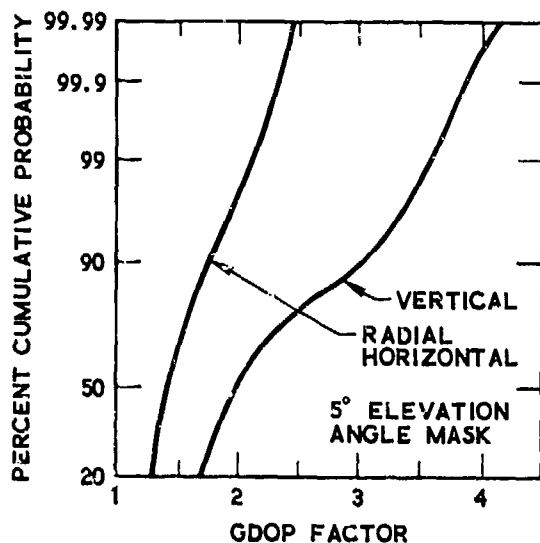


Fig. 4. GDOP Factor Distribution

The specific major error sources and their contributions in terms of UERE are shown in Table 1 for both single- and dual-frequency receiver users. It is currently anticipated that all users demanding high accuracies will use dual-frequency calibration. A less sophisticated model will be available for users not requiring precise ionospheric delay calibration.

Table 1. Error Budget

SOURCE	CONTRIBUTION, ft ( $1\sigma$ )	
	SINGLE FREQUENCY	DUAL FREQUENCY
EPOCHERIS	5	5
SATELLITE CLOCK & ELECTRONICS	3	3
TROPOSPHERE MODEL	5	5
IONOSPHERE MODEL	16	-
RECEIVER NOISE	5	3
MULTIPATH	4	6
RSS	19	12

For the system accuracy results shown in Figure 5, the satellite position errors and signal propagation errors are modeled in terms of variances and correlations to provide the required covariance matrix. The following sections discuss the errors contributed by the ionosphere.

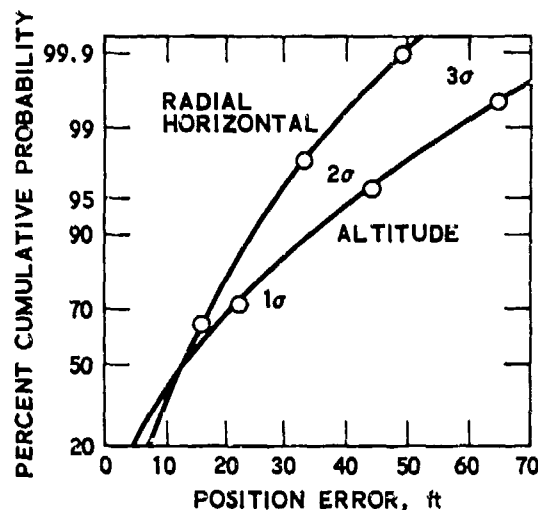


Fig. 5. User Error Distribution

#### 4. IONOSPHERIC SIGNAL DELAY

A transionospheric RF signal experiences an excess delay over the free space propagation time between a satellite and subionospheric receiver. This excess time delay is proportional to the number of free electrons encountered along the signal path. For frequencies above 200 MHz, the delay is essentially inversely proportional to the square of the frequency. (This frequency dependence is the basis for using dual-frequency measurements to calibrate the ionospheric delay.) The integrated number of electrons encountered per unit area is commonly referred to as the total electron content (TEC). For GPS, TEC is measured in units of nanoseconds of signal delay at 1.6 GHz.

Several types of ionospheric disturbances occur that modeling cannot be expected to predict (currently): severe disturbances, traveling disturbances, and scintillations. Although the magnitude of delays during severe disturbances due to magnetic storms may not be predictable by a single-frequency user, such storms occur only a very small percentage of the time. Furthermore, their occurrence is often predictable hours to days in advance and, at least, the resulting TECs have always been bounded. Traveling disturbances are low-magnitude, low-frequency, isolated disturbances that occur infrequently. Scintillations are high-frequency, noise-like amplitude and phase fluctuations on received signals arising from irregularities in the electron density distributions of the ionosphere.

## 5. TOTAL ELECTRON CONTENT MODELS

To provide TEC predictions for users in the field, it is necessary to relate (model) TEC to currently measured and predicted parameters, time of day and season, geographic location, and satellite-user geometry.

Typical and most common of the currently measured and predicted ionospheric parameters is the critical frequency  $f_oF_2$ . This is the lowest radio frequency that can normally penetrate the  $F_2$  layer of the ionosphere, which is the dominant layer. (The maximum electron density in the ionosphere can be expressed directly as a function of  $f_oF_2$ .)

Between 1969 and 1972, a series of studies was undertaken to demonstrate the feasibility of modeling the ionospheric delay to accuracies commensurate with GPS requirements using generally available ionospheric parameter inputs. Real-time or near-real-time update effects were investigated but were not considered necessary inputs.

Five different studies were undertaken either at USAF request or under USAF contract. The evaluations of the models developed in these studies were made using Faraday rotation data taken over (at most) mid-latitude North America and Hawaii. TEC is essentially proportional to the Faraday rotation angle, which is the polarization rotation of the radio wave. Two errors are inherent in this technique: perhaps the highest 10 percent of the electrons in the upper ionosphere do not contribute measurably to the rotation angle, and the constant of proportionality is not known precisely.

In all of the studies, TEC was converted to the vertical TEC above the ground station by an obliquity factor, which is a function of elevation angle and mean ionospheric height. The latter was assumed constant, which does not induce significant errors for the domain considered.

A preliminary TEC model was developed by Kobuchar and Allen at the Air Force Cambridge Research Laboratories (Ref. 1). The model was constructed from Faraday rotation data, taken at the Sagamore Hill Radio Observatory near the solar cycle maximum, and analytically predicted TEC as a function of measured or predicted values of  $f_oF_2$ . The model, applicable only near the time and location of the data gathering, served to demonstrate the feasibility of analytic ionospheric delay modeling with a relatively simple analytic function depending only on  $f_oF_2$ . When this model, which was essentially a smoothing of the original data, was used to predict TEC, overall rms errors of 1 to 4 nsec were encountered.

The goal of the next four studies, performed between 1970 and 1972, was to determine the predictability of the vertical TEC of the ionosphere in the mid-latitude Western Hemisphere by evaluating derived models against NASA Faraday rotation data. These data were available for a number of stations and time periods, including a solar cycle maximum and minimum.

Stanford University used the Faraday rotation data to synthesize a TEC model over reference stations where large quantities of data exist and to determine geographical extrapolation functions for other stations (Ref. 2). A commonly predicted solar activity index is required as input. Values predicted by this process were compared to converted Faraday rotation measurements, with overall residuals at the various evaluation stations lying between 2.7 and 6.8 nsec.

The University of Illinois ionospheric model consisted of a weighted sum of near-real-time measurements and measurement residuals at other observation locations to predict the value at the evaluation stations (Ref. 3). When measurement residuals are used, the predicted value and weighting coefficients require prior accumulation of data over the geographic region of interest to determine estimates of residual statistics and running monthly means. Both approaches produced rms residuals of 1.2 to 13 nsec.

The Applied Physics Laboratory at Johns Hopkins University derived a predictive model based on assumed electron density altitude profiles constructed from independent analytical and empirical studies and requiring commonly available predicted ionospheric parameters as input (Ref. 4). The resulting evaluation rms residuals range from 1.5 to 12 nsec.

The Bent ionospheric model was developed for NASA and is based on a large accumulation of worldwide bottomside and topside ionosphere soundings taken during the 1950s (Ref. 5). An ionospheric electron density altitude profile was established from these data that requires two commonly available ionospheric parameters. (This model construction and that of APL are completely independent of the evaluation data.) The DBA Systems evaluation of this model (by Dr. Bent) produced overall rms residuals between 2.6 and 8.8 nsec, depending on the evaluation station.

The accuracies resulting from these models (without real time updates) are summarized in Figure 6. The evaluation conditions correspond to various combinations of observation stations and measurement intervals. These studies served to validate the concept of ionospheric modeling in the North America and Hawaii domain.

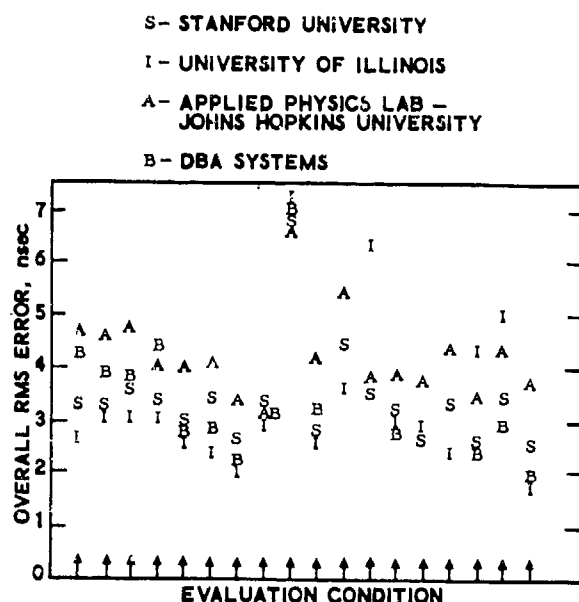


Fig. 6. Results of Modeling Studies

The difficulties with the modeling approach for calibrating the ionospheric delay are:

- (1) A large amount of data must be transferred to the satellite and to the user to provide a sufficiently accurate model;
- (2) The model cannot accommodate ionospheric disturbances without near-real-time update data--an operation inconsistent with current system operations;
- (3) Model errors will also depend strongly on time of day, geographic location, and satellite elevation angle.

The dual-frequency calibration technique, discussed in the next section, is not subject to these difficulties.

For users requiring less than full system accuracy and using less sophisticated equipment, a simplified model approach will be satisfactory. A few hundred bits of transmitted data should be sufficient to describe a model that eliminates 50 to 60 percent of the ionospheric delay. Development of such a model is currently under way by GPS contractors and AFRL.

## 6. DUAL-FREQUENCY RECEIVERS

Since the inverse frequency squared delay law is sufficiently accurate for L-band signals (in GPS applications), two L-band frequencies can be used to calibrate the ionospheric delay in GPS. These frequencies must be transmitted coherently and must be sufficiently far

apart. The equations determining the calibration accuracy are derived below.

The pseudo-range equation provides

$$m_i = p + d + (K/f_i^2) + n_i$$

where

$m_i$  = measured pseudo-range in channel  $i$

$p$  = true pseudo-range (including user clock bias)

$d$  = pseudo-range uncertainties independent of frequency and receiver noise

$K$  = parameter proportional to total electron content along the measurement path

$f_i$  = signal frequency in channel  $i$

$n_i$  = receiver noise in channel  $i$

Ignoring  $d$  and assuming measurements are made in two channels permits  $K$  to be eliminated algebraically to obtain

$$p = (m_1 - n_1) + F[(m_1 - n_1) - (m_2 - n_2)] \quad (10)$$

where

$$F = f_2^2 / (f_1^2 - f_2^2)$$

The second term in Eq. (10) comes from the solution for  $K$ , whereas the first term would occur even if  $K$  were known precisely (and a single-channel measurement used).

Since the user does not know  $n_i$  (by definition), the estimate of  $p$  will be

$$\hat{p} = m_1 + F(m_1 - m_2) \quad (11)$$

The error  $\delta p$  in the user estimate is then

$$\delta p = \hat{p} - p = n_1 + F(n_1 - n_2) \quad (12)$$

Note that these two terms will be correlated.

If  $n_1$  and  $n_2$  have equal standard deviations of  $\sigma_n$  and a correlation factor  $\rho$ , the standard deviation in pseudo-range error is

$$\sigma_F = \left[ \sigma_n^2 + \left( \frac{\sqrt{2} f_1 f_2}{f_2^2 - f_1^2} \right)^2 \sigma_n^2 (1 - \rho) \right]^{1/2} \quad (13)$$

The first term in brackets represents the contribution due to single-channel measurement error. The second term arises from the ionospheric calibration process alone. The relative contributions of these two sources are indicated in Figure 7, using the current values for the two transmitted frequencies in GPS of  $L_1 = 1.575$  GHz and  $L_2 = 1.230$  GHz.

The sensitivity of the delay calibration to the selection of the secondary frequency  $L_2$  is shown in Figure 7. For the selected frequencies this figure shows that the total receiver measurement error is approximately three times the single-channel measurement error (assumed uncorrelated between channels).

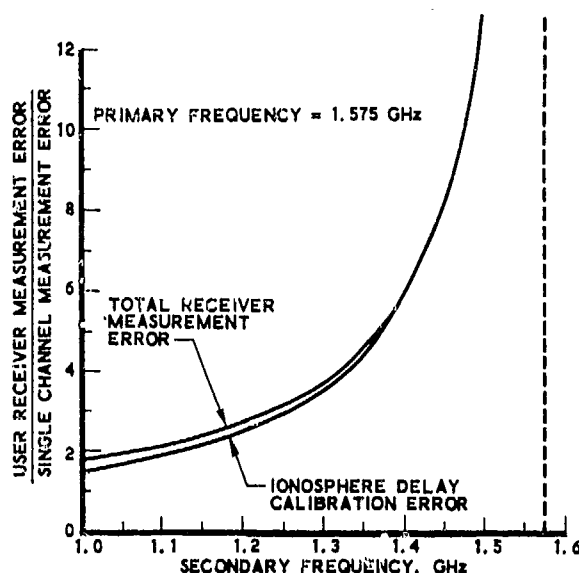


Fig. 7. Frequency Dependence of Receiver Measurement Error

Although the ionospheric delay is not exactly proportional to the inverse of the frequency squared, higher order terms will be a negligible source of error.

More detailed discussions of the dual-frequency receiver ionospheric delay calibration are given in Refs. 6 and 7.

#### 7. OPERATIONAL CONSIDERATIONS

User equipments are presently classified as shown in Table 2. All high-accuracy users will use dual-frequency receivers. A large class of users will not require the accuracy provided by the dual-frequency receivers. For such users a relatively simple ionospheric model will be provided using coefficient updates on the navigation signal. Approximately 50 to 60 percent of the ionospheric delay will be removed. The effect on user performance will probably be on the order of two to three times the dual-frequency user accuracies, including all likely software considerations.

Table 2. User Equipment Classes and Applications

CLASS	ACCURACY	USER DYNAMICS	IMMUNITY TO ELECTRO-MAGNETIC JAMMING	TYPICAL USER
A	HIGH	MEDIUM	HIGH	PHOTORECON
B	HIGH	HIGH	MEDIUM	HELICOPTER
C	(Low cost)	MEDIUM	(Immunity to natural EMI)	SEARCH AND RESCUE
D	HIGH	LOW	HIGH	LAND VEHICLE
E	MEDIUM	LOW	HIGH	MAN BACKPACK
F	HIGH	LOW	MEDIUM	SUBMARINE

#### REFERENCES

1. J. A. Klobuchar and R. S. Allen, A First Order Prediction Model of Total Electron Content for a Midlatitude Ionosphere, AFCRL-70-0403, Air Force Cambridge Research Laboratories, Bedford, Mass., July 1970.
2. H. Waldman and A. Y. daRosa, Prognostication of Ionosphere Electron Content, SAMSO TR-71-82, DDC AD-731095 & 6, Stanford University, Stanford, Calif. August 1971.
3. N. N. Rao, M. Y. Youakim, and K. C. Yeh, Feasibility Study of Correcting for the Excess Time Delay of Transionospheric Navigational Ranging Signals, SAMSO TR-71-163, DDC AD-729797, University of Illinois, Urbana, Ill., July 1971.
4. V. L. Pisacane, M. M. Feen, and M. Sturmanis, Prediction Techniques for the Effect of the Ionosphere on Pseudo Ranging from Synchronous Altitude Satellites, SAMSO TR-72-22, DDC AD-749486, Applied Physics Laboratory, Silver Springs, Md., August 1972.
5. R. B. Bent, S. K. Llewellyn, and M. K. Walloch, Description and Evaluation of the Bent Ionospheric Model, SAMSO TR-72-239, DDC AD-753081-6, DBA Systems, Inc., Melbourne, Fla., October 1972.
6. Global Positioning System Final Report, SAMSO TR-74-182, DDC AD-921524L, General Dynamics Corp., San Diego, Calif., February 1974.
7. Global Positioning System Final Report, SAMSO TR-74-183, DDC AD-921525L, Philco-Ford Corp., Palo Alto, Calif., February 1974.

## OBSERVED IONOSPHERIC EFFECTS IN AN EXPERIMENTAL SATELLITE RANGING SYSTEM

by

Roy E. Anderson  
General Electric Company  
Corporate Research and Development  
Schenectady, New York

### INTRODUCTION

The VHF transponders of NASA's ATS-1 and ATS-3 satellites have been useful for collecting data on all the factors that affect position fixing accuracy and communications reliability of satellite systems for aeronautical and maritime use. VHF is especially good for measuring the effects of the ionosphere because the effects are large enough to be separated from other measurement variables, and the VHF results can be extrapolated to L-band and higher frequencies by the  $1/f^2$  relationship. The L-band transponders of ATS-5 and ATS-6 provide a means to compare VHF and L-band experimental results. Availability of the VHF satellite transponders has a further advantage because a variety of equipment suitable for mobile experiments is readily available at modest cost. Experimenters can concentrate on techniques and measurements without significant RF component problems.

The General Electric Company, with the cooperation and support of the National Aeronautics and Space Administration, has performed many experiments since 1968 with the ATS-3 and ATS-1 satellites at VHF and ATS-5 at L-band to measure factors affecting ranging and position fixing accuracy. One recent series of tests included all the elements of a complete operational system. The satellites were located in real time by trilateration to a widespread network of fixed transponders, and a ship in regular service was located by ranging through the satellites, its position computed ashore and sent through the satellite to the ship. The ship then transmitted to shore a position that it had determined on board by other means. In other tests, range measurements were made through a satellite in rapid succession to each transponder of the network for ten minute

periods each hour for 24 hours. The measurements were used to determine the satellite orbit, then the satellite position, and finally the ionospheric group delay as a function of time to each of the distant transponders.

Results of the position fixing experiments support previous estimates that an operational system with VHF links to the mobile craft can provide position fix accuracy of 1 nautical mile, or, over large regions of the earth, and that 0.1 nautical mile accuracy is a reasonable expectation for an L-band system. The operational tests and the group delay measurements confirm that ionospheric propagation delay is a major factor limiting accuracy at VHF.

### DESCRIPTION OF EXPERIMENTS

General Electric's Radio Optical Observatory, Figure 1, served as the principal earth station for the experiments. In addition to its Radio-Optical Observatory, General Electric has had fixed, automatic satellite ranging transponders at all of the locations marked by the solid triangles in Figure 2, ships on the dotted line routes, and on aircraft flying the solid line routes. The experiments have been conducted with ATS-1 and ATS-3 at VHF. Experiments have also been conducted with ATS-5 at L-band. L-band as well as VHF transponders are at the locations marked with an L.

For the VHF tests described in this paper, tone-code interrogation signals were transmitted to ATS-3 in geostationary orbit 19,300 nautical miles above the equator at approximately 70° West longitude or through ATS-1 above approximately 150° West longitude. The uplink frequency was centered at 149.22 MHz. The signals were relayed by a

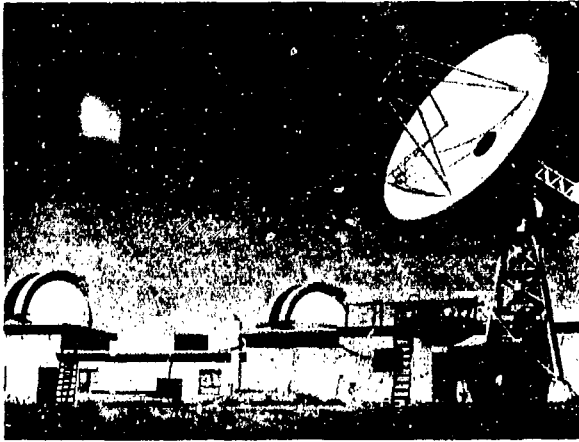


Figure 1 General Electric Radio—  
Optical Observatory

satellite in the 100 kHz passband centered at 135.6 MHz to all of the transponders within its line-of-sight. All of the transponders matched the phase of their own data clocks to the data clock in the "tone" portion of the tone-code signal. The one transponder that was addressed by the code portion of the signal responded by transmitting the tone-code signal after a known, fixed time delay. If the transponder were aboard a vehicle that was to be located, its single response was transmitted to two satellites. The Observatory received the satellite relay

of the initial interrogation and the response from the user craft as relayed back through the satellite(s). The signals went to phase matcher-correlators like those in the distant transponder. The outputs of the correlators yielded elapsed times for the signal to go from the Observatory to the interrogating satellite, to the user craft and back through the satellite(s). Proper subtractions, including the known internal time delays of the individual equipments, yielded range from the Observatory to the interrogating satellite, and from the satellite(s) to the transponder. Instrumental precision of single measurements was limited by the time interval counter to 0.1 microsecond, representing a resolution of 49.2 feet for the two-way ranging. Ranging precision through the satellites was limited to approximately 100 feet, or, by noise on the received signals. Averaging a number of measurements improves precision by the square root of the number of measurements averaged. Accuracy was limited by the calibration of internal time delay of the equipments to approximately 1 microsecond, or 492 feet. Recent addition of an internal time delay calibration device to some transponders has shown that internal time delay can be virtually eliminated as a factor that limits accuracy.

The tone-code ranging technique is compatible with digital or analog

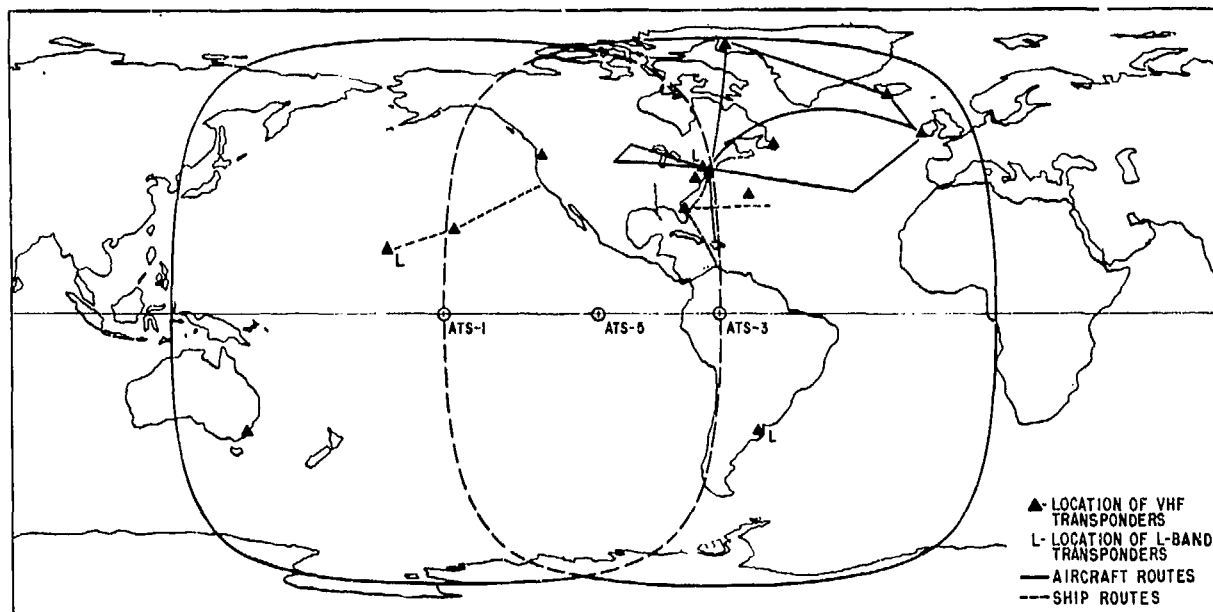


Figure 2 Communications Coverage of ATS-1 and ATS-3

communications and provides good ranging accuracy with narrow bandwidth signals.

The VHF data reported in this paper were taken with a modulating tone of approximately 2.4 kHz, and a signal integration time of 120 milliseconds, the L-band data with a tone of approximately 9.8 kHz, and a signal integration time of 27 milliseconds. Further details of the tone-code technique are reported in References 1 and 2.

#### MARITIME POSITION FIXING EQUIPMENT

A communications and position fixing experiment was conducted with a commercial tanker, the ESSO Bahamas, in routine service between Venezuela and U.S. east coast ports<sup>3</sup>. Voice, teletype, facsimile, and slow scan television communication were provided for an hour each working day and some evening hours between the ship and the home office of the EXXON Corporation in New York City via the ATS-3 satellite and the GE Radio-Optical Observatory. Position fixing by ranging was also provided. The tests were conducted between July 1973 and February 1974. During the last two months, the complete integrated navigation-surveillance system was operated. It included the following steps:

- o Locating ATS-3 and ATS-1 by trilateration in real time by range measurements to fixed transponders. ATS-3 range measurements were to Shannon or Reykjavik, Daytona, and Schenectady. ATS-1 measurements were to Daytona, Schenectady, and Melbourne.
- o Ranging from two satellites to the ship. A single ranging interrogation from Schenectady through ATS-3 initiated a single automatic response from the ship that was relayed by ATS-3 and ATS-1 to Schenectady.
- o Computation of the satellite and ship positions.
- o Transmission by teletype of the ship position through ATS-3 to the ship.

The sequence of interrogating the remote transponders and the ship could be accomplished in any order. A ranging interrogation code was transmitted from the General Electric Radio-Optical

Observatory near Schenectady once each two seconds. The interrogation rate could be increased to several per second for an operational system. Each transponder responds only to its own individual address. The digital address code could accommodate many thousands of ships in addition to the ESSO Bahamas.

Single lines of position could be determined by ranging from one or the other satellite throughout the communication coverage within the solid lines in Figure 2, and position fixes by range measurements from both satellites could be provided in the area enclosed by the dashed lines.

All of the range measurements were recorded on punched tape and simultaneously inserted into computers at Schenectady. The locations of the satellites determined during a ten minute period were interpolated to determine the positions of the satellites at the time of each interrogation and response from the ship. The locations of the satellites and the range measurements from the satellite to the ship were then used in the General Electric POSFIX program to compute the ship's position.

A typical computer printout of ship's position fixes is shown in Table 1. It will be noted that a ship fix was measured and computed every two seconds except when a miscorrelation occurred or there was a loss of signal. In this instance, all the transponders, including the ship were interrogated for five minutes, the ship only for one minute, then all transponders were again interrogated. Satellite positions were interpolated to the second of time at which an interrogation to the ship was made.

All of the fixes of Table 1 are plotted in Figure 3. Each fix is completely independent of the others. The first and last fixes of the sequence are identified with the time they were made. The precision is shown by the "scatter" of the fixes. In this typical example they can all be enclosed within a circle of 0.5 nmi radius.

The averages of the latitude and longitude of the first ten fixes is shown by the small +. The average fix was transmitted to the ship by teletype through the satellite. Then the ship transmitted its 16:00:00 GMT and 16:15:00 GMT radar fixes through the



TAKING THE AVERAGE OF THE FIRST 10 LINES OF DATA FOR 12/21/73 THE POSITION OF THE SHIP AT 16:06:12 IS AS FOLLOWS:

12 40.63 NORTH  
70 52.32 WEST

SHIP RADAR	16:00:00					12 43 00 -70 52 00
P 12/21/73	16:06:03	ESSO	12 40 42	-70 52 17		
P 12/21/73	16:06:05	ESSO	12 40 33	-70 52 11		
P 12/21/73	16:06:07	ESSO	12 40 22	-70 52 36		
P 12/21/73	16:06:09	ESSO	12 40 37	-70 52 20		
P 12/21/73	16:06:11	ESSO	12 40 34	-70 52 14		
P 12/21/73	16:06:13	ESSO	12 40 16	-70 52 23		
P 12/21/73	16:06:15	ESSO	12 40 45	-70 52 14		
P 12/21/73	16:06:17	ESSO	12 41 01	-70 52 32		
P 12/21/73	16:06:25	ESSO	12 40 38	-70 52 02		
P 12/21/73	16:06:27	ESSO	12 40 21	-70 52 20		
P 12/21/73	16:06:29	ESSO	12 40 55	-70 52 24		
P 12/21/73	16:06:31	ESSO	12 40 44	-70 52 07		
P 12/21/73	16:06:33	ESSO	12 40 36	-70 52 07		
P 12/21/73	16:06:35	ESSO	12 40 45	-70 52 18		
P 12/21/73	16:06:37	ESSO	12 40 57	-70 52 10		
P 12/21/73	16:06:39	ESSO	12 40 11	-70 52 32		
P 12/21/73	16:06:43	ESSO	12 40 51	-70 52 12		
P 12/21/73	16:06:45	ESSO	12 40 41	-70 52 24		
P 12/21/73	16:06:49	ESSO	12 40 04	-70 52 21		
P 12/21/73	16:06:53	ESSO	12 40 54	-70 52 12		
P 12/21/73	16:06:55	ESSO	12 40 43	-70 52 02		
P 12/21/73	16:06:57	ESSO	12 40 22	-70 52 05		
SHIP RADAR	16:15:00					12 40 00 -70 50.12
SHIP RADAR	16:30:00					12 36 00 -70 48.30

Table 1. Sample From a Typical Computer Printout

satellite to Schenectady, and they are plotted in Figure 3. Interpolated between the two radar fixes is the estimate of the ship's position as determined from the radar fixes during the one minute period of the satellite fixes. The difference between the average of the satellite fixes and the radar-derived track is 1.5 nmi.

The same type of comparison was made for a number of days, over the region extending from Philadelphia to Aruba and Amuay. Table 2 lists satellite and independently derived positions for 27 days between December 7 and January 30. They include latitudes from 38°N to 12°N, and longitudes from 68°W to 78°W. The satellite fixes are compared with radar-derived fixes, visual fixes, loran, dead reckoning, and sun line. The radar fixes are estimated to be accurate to  $\pm 0.25$  nmi. Loran has an average accuracy of approximately 2 miles in the region of that fix. No estimate is made for the accuracy of the sun line or dead reckoning fixes. The magnitudes of the differences between the satellite derived positions and the independently derived positions are included in Table 2.

The data of Table 2 are plotted in Figure 4. The independently derived positions are taken as the reference for the plot. The satellite derived fixes

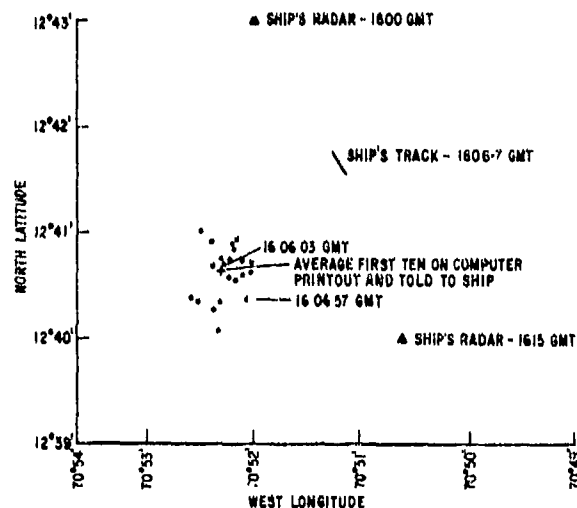


Figure 3 Position Fixes-Satellite Derived and Ship's Radar Determined Fixes

from the table are plotted with reference to the independently derived fix. For example, the fix of file 662, taken on 12/27/73, is 1.1 minute east and 0.45 minute north of the radar derived fix. One minute of longitude at 24°N latitude is less than 1 nmi. The magnitude of the disagreement is 1.1 nmi. The notation by each satellite fix in Figure 4 is the type of independently derived fix by which it is compared. There is an average disagreement of 1.26 nmi. he..

File No.	Date	Time (GMT)	Satellite		Independently		Diff. (nmi.)	Type of
			Derived Position	Derived Position	Derived Position	Independently		
647	12/07/73	16:30:12	38 34.64°N	74 47.95°W	38 36.16°N	74 49.25°W	1.83	
650	12/10/73	16:10:34	19 12.85°N	68 14.15°W	19 09.18°N	68 14.94°W	3.75	Sun
651	12/11/73	16:29:44	12 35.35°N	70 11.54°W	12 34.08°N	70 10.98°W	1.38	Radar
654	12/14/73	16:17:16	13 00.83°N	71 08.35°W	13 01.24°N	71 06.30°W	2.0	D.R. for 1/2 hr. after radar
657	12/19/73	16:23:12	22 41.93°N	78 28.32°W	22 42.61°N	78 27.96°W	0.75	Radar
659	12/20/73	16:36:10	18 21.57°N	74 33.12°W	18 21.73°N	74 33.12°W	0.16	Radar
660	12/21/73	16:06:12	12 40.63°N	70 52.32°W	12 41.55°N	70 51.28°W	1.4	Radar
661	12/26/73	16:14:45	17 42.35°N	74 10.94°W	17 43.44°N	74 08.97°W	2.2	Radar
662	12/27/73	16:09:35	23 58.97°N	74 50.20°W	23 58.52°N	74 51.31°W	1.1	Radar
663	12/28/73	16:06:19	29 52.74°N	78 05.62°W	29 49.26°N	78 06.26°W	3.5	Loran
665	01/03/74		12 26.78°N	69 55.84°W	12 25.05°N	69 54.08°W	1.64	At Sea Buoy
666	01/04/74		12 26.40°N	Latcom	Same			
668	01/08/74	16:57:18	15 15.77°N	72 17.55°W	15 15.42°N	72 17.55°W	0.35	D.R.
669	01/09/74	16:12:53	20 30.73°N	Latcom	20 30.46°N	74 23.30°W	0.27	Radar
670	01/10/74	16:07:34	24 27.41°N	79 36.79°W	24 26.02°N	79 36.76°W	1.39	Loran
672	01/14/74	16:15:01	14 10.75°N	71 49.39°W	14 07.00°N	71 46.00°W	4.99	D.R.
673	01/15/74		11 45.93°N		11 44.80°N	70 13.10°W	1.13	Sea Buoy
674	01/16/74	16:07:01	15 21.25°N	72 44.05°W	15 20.64°N	72 45.94°W	1.92	D.R.
675	01/17/74	15:06:37	20 44.92°N	74 49.68°W	20 44.32°N	74 49.54°W	0.70	Radar
676	01/18/74	16:07:12	24 46.28°N	79 43.22°W	24 44.92°N	79 44.48°W	1.78	D.R.
677	01/21/74	16:30:00	21 18.60°N	75 53.49°W	21 18.70°N	75 54.00°W	0.49	Radar
679	01/23/74	Anchor	11 44.44°N	Latcom	11 45.00°N	70 15.30°W	0.56	Visual
680	01/24/74	Anchor	11 44.71°N	Latcom	11 45.00°N	70 15.30°W	0.29	Visual
681	01/25/74		11 41.46°N	Latcom	11 44.80°N	70 13.10°W	3.34	Sea Buoy
682	01/25/74	16:29:28	21 03.07°N	74 10.90°W	21 03.55°N	74 10.18°W	0.83	Radar + Recon.
		16:08:12	20 57.14°N	Latcom	20 57.38°N	74 09.33°W		
683	01/29/74	16:40:37	27 04.89°N	76 32.69°W	27 06.03°N	76 35.37°W	2.64	Loran
684	01/30/74	Anchor	32 38.15°N	79 36.27°W	32 37.30°N	79 36.80°W	0.96	Visual

Ship was in port and could not transmit on days represented by missing file numbers. Communications messages were sent to the ship, but it could not respond.

Table 2. Satellite and Independently Derived Fixes  
7 December 1973 thru 30 January 1974

tween the satellite-derived fixes and the radar and visual fixes. When the directions as well as the magnitudes of the differences are taken into account, there is a bias in the disagreement between the satellite and radar/visual fixes of approximately 0.28 nmi. in a westerly direction.

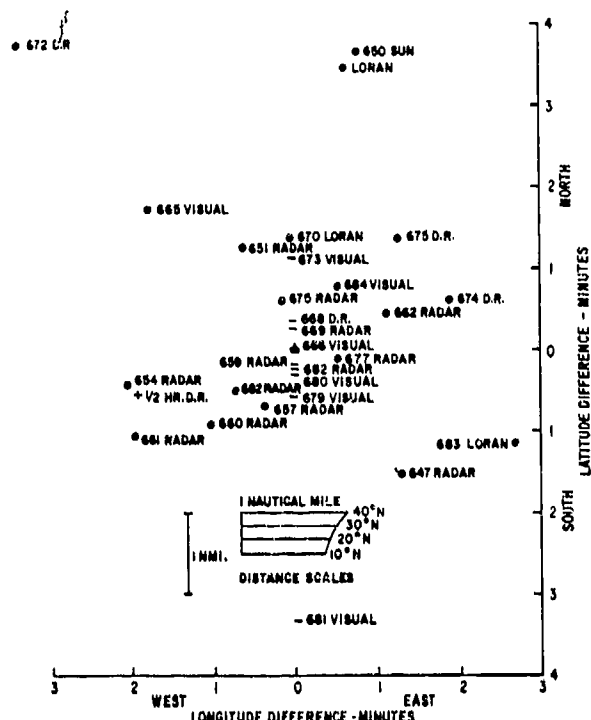
When only ATS-3 was available, single range measurements from the satellite were used to determine the latitude of the ship. The General Electric LATCOM computer program determined the latitude at which the line of position crossed the longitude determined aboard the ship. The latitudes determinations are included in Figure 4.

The radar and visual fixes are probably more accurate than the satellite-derived positions, but the satellite-derived positions are probably more accurate than the Loran, sun line, and dead reckoning fixes. The following examination of factors affecting accuracy consider only the satellite fixes and latitude determinations that are compared with visual and radar fixes.

Thousands of position fixes were made during the seven and one half month period of the experiment. The complete system including the real time location of the satellites was operational only during the last two months. Prior to that time, satellite reference locations were taken from NASA acquisition tables.

Many fixes or latitude determinations were made on each day of operations. For the day-to-day comparisons that follow, the single position for each day that was transmitted to the ship is taken as the one position for that day. Usually the position sent to the ship was the average of approximately ten individual positions.

An upper bound can be set on the effect of ionospheric propagation delay on the accuracy of the ship position measurements, but its precise value below the bound cannot be defined accurately because it cannot be separated with confidence from other factors. Estimation of the ionospheric effect is accomplished in the following steps:



EACH SATELLITE FIX IS AVERAGE OF ALL FIXES MADE IN PERIOD IDENTIFIED BY FILE NUMBER, AND IS LABELED WITH THE TYPE OF CAPTAIN'S FIX USED FOR COMPARISON. THE SHORT DASHED LINES ARE LATITUDE DETERMINATIONS MADE WHEN ONLY ATS-3 WAS AVAILABLE. A-POSITION STATED BY SHIP.

Figure 4 Satellite Fixes Referenced to Fixes by Other Means

- o Separating geometrical dilution of precision (GDOP) from each latitude determination and position fix error. Error is defined as the magnitude of the difference between the satellite and radar/visual position determination.
- o Calculating the average of the errors after GDOP is removed.

It is necessary to remove the GDOP factor in order to search for ionospheric effects because GDOP was large in the experiment and it changed substantially each day that the ship was under way.

The average error after GDOP is removed is an upper bound because it assumes other contributing factors are zero. The other factors are in fact significantly large so that the effect of the ionosphere was surely smaller than the upper bound. The other variables, including the effect of noise fluctuations on the ranging signals, transponder internal time delay variations, and errors in the ship's independent position references, are ignored in this evaluation to insure a conservative result in the estimate of the ionospheric effect.

The route of the ESSO Bahamas took the ship to the edge of the coverage for two-satellite position fixes where the elevation angle to the ATS-1 satellite was near zero degrees. At the same location the ship was near the sub-satellite point, almost directly under ATS-3. It was thus possible to test the satellite system when there was a large geometrical dilution of precision (GDOP) for the range measurement from ATS-3, but no dilution for ATS-1. An error in range measurement from a satellite to a ship is exaggerated by GDOP when the ship is near the sub-satellite point. Near Aruba, the GDOP factor was as large as 4.5 for the ATS-3 satellite, so that a line of position determined from ATS-3 was displaced by a distance as much as 4.5 times greater than the range measurement error. The GDOP factor was two or larger throughout the route from Florida to Venezuela.

Table 3 presents the estimated differences between satellite and radar/visual position determinations when GDOP is considered as a factor. GDOP is a geometrical effect, the secant of the elevation angle to the satellite. It can be estimated with confidence. For the ESSO Bahamas, GDOP is almost entirely due to ATS-3 because ATS-1 was nearly zero in elevation angle, therefore it is valid to include the latitude determinations as well as fixes in considering GDOP.

Figure 5 plots the magnitudes of the satellite and radar/visual position differences as a function of latitude, and also shows the limits of GDOP. The two GDOP curves are for the smallest and largest south declination of ATS-3 at the time ranging measurements were made. The larger spread of the position differences at low latitudes is attributed to GDOP. With GDOP removed, the average magnitude

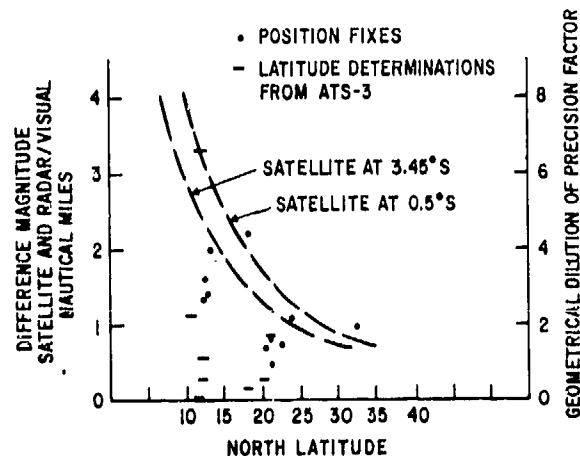


Figure 5 Position Differences vs. Latitude

File Number	Fix or Latitude Only	ATS-3 Latitude Degrees	Elevation of Satellite Degrees	GDOP Factor	Measured Position Difference With GDOP Naut. miles	Position Difference if GDOP Factor Removed Naut. miles	Magnetic Index, $A_p$
651	F	-0.6	77	4.5	1.38	0.62	8
654	F	-0.5	75	3.9	2.0	2.0	6
657	F	-0.9	62	2.1	0.75	0.46	13
659	L	-1.3	68	2.7	0.16	0.06	29
660	F	-0.9	75	3.9	1.4	1.05	34
661	F	-1.4	68	2.7	2.2	1.92	4
662	F	-1.4	73	2.0	1.1	1.00	6
665	F	-1.9	73	3.4	1.64	1.09	11
666	L	-2.0	74	3.6	0.0	0.0	13
669	L	-2.2	75	2.2	0.27	0.12	7
673	L	-2.6	75	3.9	1.13	0.29	15
675	F	-2.6	63	2.2	0.7	0.30	16
677	F	-3.1	61	2.1	0.49	0.48	16
679	L	-3.0	73	3.4	0.56	0.17	4
680	L	-3.1	74	3.6	0.29	0.08	4
681	L	-3.1	74	3.6	3.34	0.93	50
682 (1608)	L	-3.2	61	2.1	0.83	0.40	18
682 (1629)	L	-3.4	61	2.1	0.24	0.11	18
684	F	-3.3	49	1.5	0.96	0.72	21

Table 3. Position Differences Corrected for Geometric Dilution of Precision

difference for the position fixes is 0.96 nautical mile, 5800 feet, and for the latitude determinations, 0.24 nautical mile, 1460 feet. The differences for the latitude determinations are smaller because the ship's longitude determination was used in the latitude determination and because GDOP does not affect the line of position determined from ATS-1.

The averages are not to be confused with the 0.28 nmi bias error stated previously. The 0.28 nmi bias error takes into account direction as well as magnitude and is a calibration of overall system accuracy. The 0.96 fix and 0.24 latitude averages are magnitude errors reflecting day-to-day variations in the measurements.

The position determinations were made at nearly the same hour, 1600 GMT, each day. They were affected by the day-to-day variations in ionospheric propagation delay but not by the diurnal pattern of electron content change.

A comparison can be made between the latitude measurement variability and an estimate based on a model of the ionosphere. Ionospheric range error as a function of elevation angle for daytime maximum and night time minimum electron content is presented in Figure 6. Normal-

ized diurnal variation in range is presented in Figure 7.

Range measurement error for each transponder to ATS-3 is determined from Figures 6 and 7 for 1600 GMT.

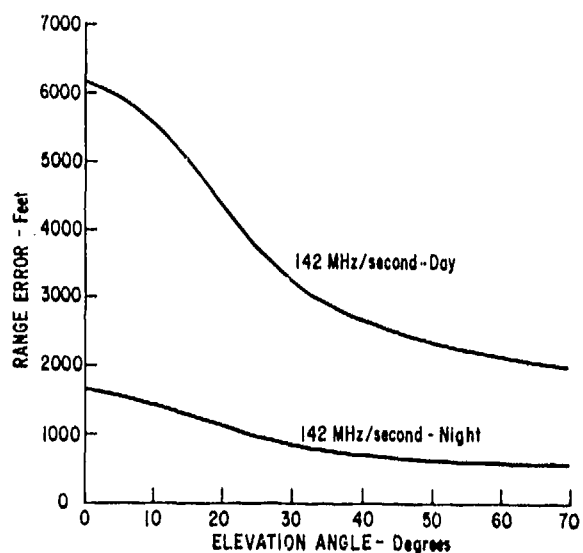


Figure 6 Range Error Due to Ionosphere, Day and Night, Versus Elevation Angle

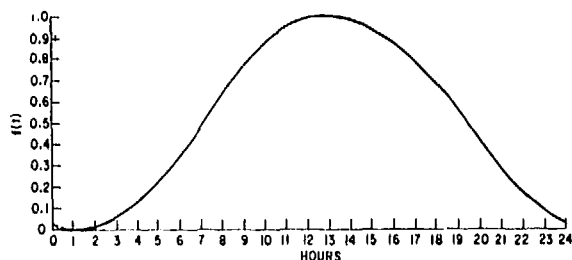


Figure 7 Diurnal Variation in Range Due to Ionosphere (Normalized)

Shannon	5200 feet
Reykjavik	5200
Daytona	2000
Schenectady	2700
Ship (Intermediate position)	1900

Although no firm data are at hand, it is reasonable to assume a day-to-day average variability of 10% in the range measurements when no magnetic disturbances are present. Variability is defined here as the day-to-day change in the measurements at a specified time and location relative to the total range error as predicted from the model. The assumed variabilities were projected to determine the north-south and earth center average errors in satellite position. The satellite position average errors were projected to determine their effect on lines of position. The average ionosphere error in range measurement from the satellite to the ship was then combined with the satellite position average errors to determine the effect of the ionosphere day-to-day variability on the average line of position error for the ship. The value thus estimated from the model for the ionosphere variability contribution to ship latitude was 1200 feet. The assumption of 10% ionosphere propagation delay variability is not well supported by data, the calculations of its effect on the latitude determination was not rigorous, but the calculated value of 1200 feet is in reasonable agreement with the experimental value of 1460 feet. As noted above, significant factors other than the ionosphere contributed to the experimental value.

Table 3 includes the magnetic index,  $A_p$ , for each day.  $A_p$  is a daily index of magnetic activity on a linear scale. The extreme range of the scale is 0 to 400. Figure 8 is a plot of position error, with GDOP removed, as a function of  $A_p$ . There appears to be a general trend of increased error in the latitude determinations with increasing magnetic index. The largest error by far occurred on the day when the index was 50. The

error was southward, File 681 Figure 4. The satellite was located by ranging from locations north of the satellite. Increased electron content, increased group delay, would increase apparent range and result in a calculation of satellite position south of its true position. If the range measurement from satellite to ship were affected less than the measurements from reference transponders to satellite, the latitude determination would be south of the true ship position. The relationship of fix error and magnetic index is not clear. The largest fix errors occurred when the index was low. The errors, files 654 and 661, are seen in Figure 4 to be shifted to the west, and thus due to an error in the range measurement from ATS-1. The cause of the errors has not been identified, but they are not likely to be related to ionospheric effects.

#### IONOSPHERIC CORRELATION DISTANCE AND SCINTILLATION EFFECTS

The ESSO Bahamas position determinations were made in and near the Caribbean Sea. They were affected by ionosphere effects far removed from the Caribbean because range measurements to locate the satellites were made from locations such as Reykjavik and Melbourne.

Previous experiments have yielded data on correlation distances in the ionosphere and on range measurements when amplitude scintillation is present. Figure 9, from Reference 1, is a 24 hour record of the difference between measured and computed propagation times from the ATS-3 satellite to Schenectady, and Gander, Newfoundland, which are separated by approximately 900 nautical miles. The differences between the measured and computed times are directly related to

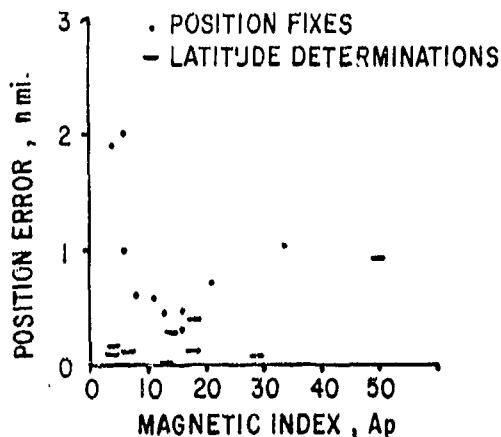


Figure 8 Position Error Vs. Magnetic Index

uncompensated range error due to the presence of the ionosphere in the ray paths from the satellite to the transponders. The Schenectady and Gander diurnal curves are well correlated if they are shifted in time to correct for the one hour difference in time.

Sunrise and sunset at 80 and 600 kilometers along the ray paths in the ionosphere are marked in Figure 9.

A period of severe scintillation is noted in Figure 9. During a two hour period the signal amplitude at Schenectady

changed from its average level of -98 dbm to extremes of approximately -93 dbm and -121 dbm. The amplitude scintillation had no effect on the range measurements larger than the equipment time delay change with signal amplitude.

Similar diurnal measurements were made to Reykjavik, Shannon, and Seattle on the same day the data of Figure 9 were taken, and on several other days at other seasons and in other years 1.5. When corrections are made for differences in time of day and differences in length of day due to latitude and seasonal dif-

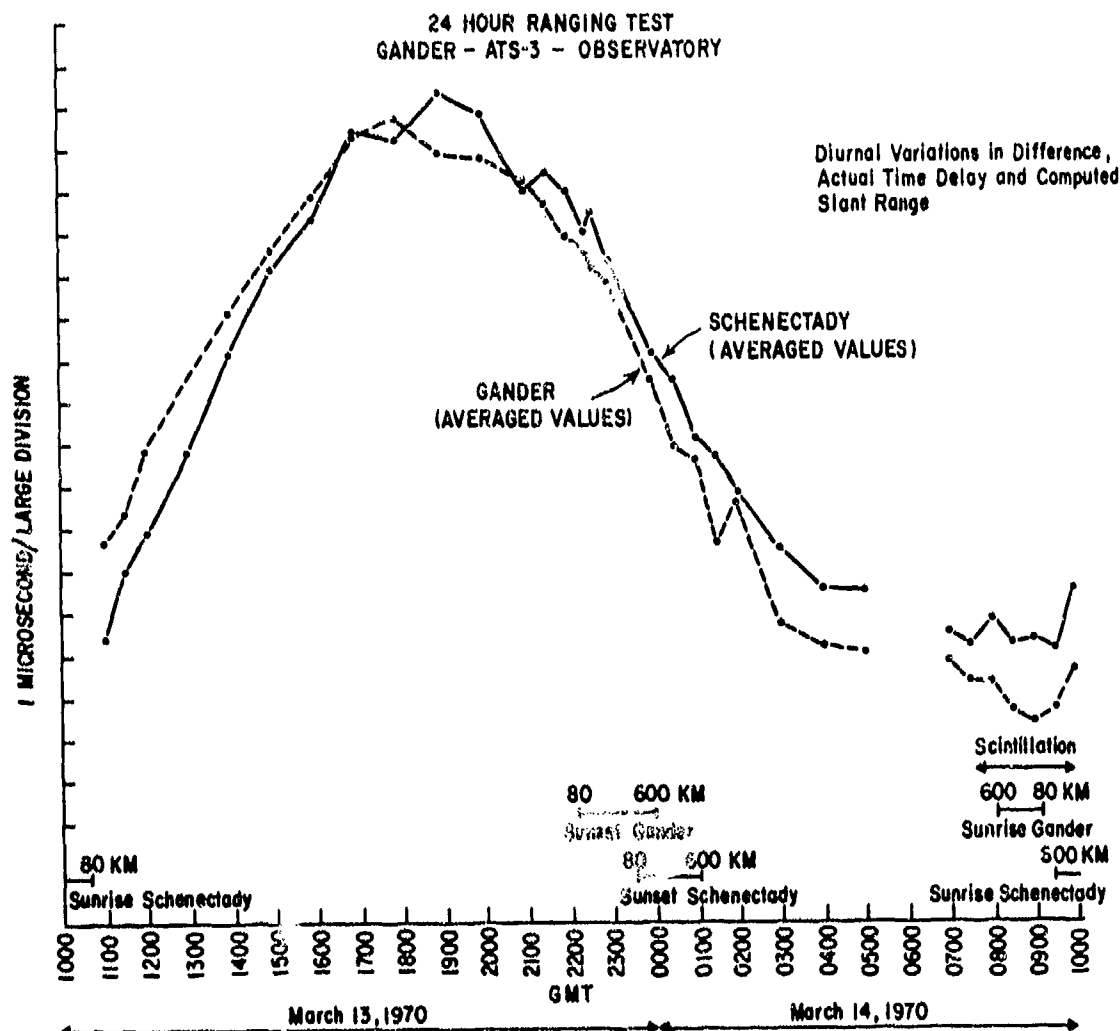


Figure 9 24-Hour Ranging Test: Gander -- ATS-3 -- Observatory

ferences, the correlations between transponders separated by more than 1000 miles suggest that the results obtained in the ESSO Bahamas experiment are not unique to the region of the Caribbean Sea.

#### SUMMARY AND CONCLUSION

A complete maritime ranging and position fixing system was evaluated in conjunction with routine shipping operations. The complete system operated at VHF and included real time location of two satellites by ranging from a wide-spread network of automatic reference transponders, and location of the ship by range measurements from the two satellites to the ship. A total of ten satellite derived position fixes and nine latitude determinations made at approximately 1600 GMT on separate days over a two-month period were compared with radar and visual fixes. The differences between the satellite and radar/visual fixes were examined to determine an upper bound to the influence of the ionosphere on ship positioning accuracy at VHF.

The largest errors, defined as difference between satellite and radar/visual positions, were 2.2 nmi. for the fixes and 3.34 nmi. for the latitude determinations. The average error for the fixes was 1.26 nmi., and 0.76 nmi. for the latitude determinations.

When the effect of geometrical dilution of precision (GDOP) was removed, the largest fix error was 1.92 nmi., the largest latitude determination error was 0.93. Without GDOP, the average fix error was 0.96 nmi., 5800 feet, and average latitude determination error was 0.24, 1460 feet. The averages without GDOP are an upper bound for the effect of the ionosphere in the experiment. Other factors contributed to the errors, so that the effect of the ionosphere must be significantly smaller than the averages.

A calculation, based on a model of the ionosphere and assuming a 10% average day-to-day variation in electron content, suggests an expected average variability in latitude determination of 1200 feet for the conditions of experiment.

Position errors appear to increase with magnetic index, but the relation-

ship was obscured in this experiment by other factors. The latitude determination error was largest on the day with highest magnetic index.

The result of the complete system experiment together with the much larger body of data collected in other VHF ranging and position fixing experiments indicates that an operational position fixing system could provide better than 1 nmi., 1 sigma accuracy when the ionosphere is not disturbed.

Position fix errors exceeding 1 nmi., 1 $\sigma$ , may be experienced in a VHF operational system on days when the magnetic index is high. The errors may be reduced by tracking the satellites in higher frequency bands, using VHF only for ranging from the satellites to the vehicles, and by providing fixed reference transponders to measure the effects of the magnetic disturbances.

1. "Final Report on Phases 1 and 2 VHF Ranging and Position Fixing Experiment Using ATS Satellites," May 1971, USA.
2. "Final Report on Phase 3 ATS Ranging and Position Fixing Experiment," Dec. 1972. Prepared for National Aeronautics and Space Administration, GSFC, USA, Contract NAS5-11634.
3. LaRosa, R.; Anderson, R. E.; Hoffman, H. "An Experiment With Maritime Satellite Multimode Communications and Position Fixing," Radio Technical Commission for Marine Services Assembly Meeting, St. Petersburg, Fla., April 1, 2, 3, 1974.
4. Millman, G. H. "A Survey of Tropospheric, Ionospheric, and Extra Terrestrial Effects on Radio Propagation Between Earth and Space Vehicles," General Electric Report TISR66EMH1 presented at NATO-AGARD Symposium on "Propagation Factors in Space Communications" Rome, Italy, Sept. 21-25, 1965.
5. Lynn, J. J.; Schmid, P. E.; Anderson, R. E. "A New Method for Satellite Orbit Determination Using an Operational Worldwide Transponder Network." Goddard Space Flight Center report X-591-74-2. January 1974.

## ON THE DETERMINATION OF MID-LATITUDE IONOSPHERIC TIME DELAY FROM $f_0F_2$

John A. Klobuchar  
Air Force Cambridge Research Laboratories  
Bedford, MA 01731

Gerald S. Hawkins  
National Research Council

### INTRODUCTION

Radio waves which pass through the earth's ionosphere travel more slowly than in free space due to group retardation along the ray path which is proportional to the total number of free electrons encountered. Ranging systems such as satellite detection radars or satellite navigation systems will have their accuracy affected by this ionospheric group path delay. Under conditions of high electron density, such as are encountered during solar maximum and mid-day periods, the degradation of ranging system accuracy can be significant. At VHF, ionospheric range errors of greater than one mile are possible. Satellite detection radars operating at UHF can have range errors of several hundred meters; and, at L band, advanced satellite precise navigation system range errors can exceed 200 feet during the worst ionospheric conditions.

Fortunately, the ionosphere is a dispersive medium; and, a two frequency ranging system can sometimes be used to correct for the ionospheric time delay. A two frequency ranging system must use frequency spacing chosen far enough apart to have a significant difference in the measured time delay at the two frequencies. This bandwidth or extra receiving frequency limitation may be impractical for some systems, or users; and, in these cases, indirect means may be required to correct for the time delay due to the earth's ionosphere.

Most of the highest accuracy requirements of ranging systems occur in the northern mid-latitude region, as many of

the satellite detection radars are located in this region and the most stringent navigation accuracy requirements occur in this region. Fortunately, not only is the ionosphere well studied in the northern mid-latitudes, it is more predictable than polar and equatorial regions. Thus, it is not unreasonable to use a model of ionospheric time delay, instead of real time two frequency dispersion measurements, to correct for ranging errors. The use of such a model can be expected to reduce the ionospheric delay by 50 to 70 percent over the non-corrected case, on an r.m.s. basis. If corrections for 70 to 90 percent of the ionospheric time delay are required, a real time measure must be made of the time delay itself or of a parameter closely related to time delay. If a correction for 99 percent of the ionosphere is required for successful operation of a ranging system, the system had better be redesigned for a higher operating frequency, as a 99 percent correction for ionospheric time delay is unrealistic even for a practical two frequency ranging system. The aim of this paper is to describe a means of utilizing measurements of the parameter  $f_0F_2$ , readily available from ionosondes, to correct for more than 75 percent of the daytime time delay for systems operating in the northern mid-latitude region.

### DATA BASE:

For over forty years ionospheric sounders, called ionosondes, have been used to make regular measurements of the bottomside of the ionosphere in the northern mid-latitudes. Because of long distance high frequency communication requirements the most often measured and reported parameter of the ionosphere has been  $f_0F_2$ , the



critical frequency of the F2 region.  $f_0F_2$  is proportional to the electron density at the maximum of the F2 region, called  $N_{max}$ . A second parameter which has been measured for many years is MUF-F2, the maximum useable frequency of the F2 region, which has been shown to be closely related to the height of the maximum density of the F2 region. The ionospheric Total Electron Content (TEC), proportional to time delay, has been much less routinely measured and studied, except at a few locations where a significant amount of data exist. Much of the ionospheric time delay-TEC data which do exist were taken by means of the Faraday effect which measures the electron content-time delay up to a height of from 2000 to 4000 kilometers. Above this height range it is estimated that the earth's ionosphere-exosphere contains at most an additional 10-20 percent electrons, at least during the important daytime period when time delays due to the ionosphere are greatest.

Using the available TEC data from a northern mid-latitude station located at Hamilton, Massachusetts we have formed the ratio of TEC divided by  $N_{max}$  which is called equivalent slab thickness.  $N_{max}$  values were obtained from  $f_0F_2$  measurements made at Wallops Island, Virginia and kindly supplied to us by the World Data Center A at Boulder, Colorado. This slab thickness ratio of two experimentally measured quantities is a first order scale height or thickness parameter of the F2 ionospheric region. Our interest in the slab thickness parameter here is in its use as a means of relating the more well measured and studied parameter  $f_0F_2$  to the required time delay correction for ranging systems in the northern mid-latitude region. Thus, if a value of  $f_0F_2$  is known, the time delay can be obtained from the following:

$$\Delta T = 1.67 \times 10^{-6} \gamma \frac{(f_0F_2)^2}{f_o^2} \quad (\text{seconds})$$

where  $f_0F_2$  is in MegaHertz;  $\gamma$  comes from the slab thickness model and is expressed in units of kilometers; and,  $f_o$  is the ranging system operating frequency in MegaHertz.

#### MODEL CONSTRUCTION:

Monthly mean values of equivalent slab thickness,  $\gamma$ , for each hour were obtained from hourly values of equivalent vertical TEC from Hamilton, Massachusetts looking

in the direction of the geostationary satellite ATS-3 which is positioned along the Hamilton meridian. The latitude of the mean sub-ionospheric point looking from Hamilton coincided to within 1 degree with the latitude of Wallops Island. TEC data were taken at the same local mean time, rather than at the same standard time to correct for the five degree longitude difference between the two locations. A plot of the mean diurnal variation of  $\gamma$ , averaged over the period November 1967 through December 1973 is shown separately for each month in figures 1A and 1B. Note the regular seasonal change in daytime and the lack of any such regular nighttime behavior.

In order to separate diurnal and mean solar flux changes, 24 hour averages for each month were formed and plotted separately against the 10.7 cm radio solar flux. The five month running mean solar flux centered on the month in question was used as the mean solar flux. Results are shown in figure 2 plotted separately for each of the 12 months, along with the least squares best linear fit through the points.

The model consists of the two coefficients of the linear fit with 10.7 cm solar flux and the 24 hourly values of the monthly normalized mean curve. The coefficients of the  $F_{10.7}$  dependence are tabulated separately for each month in Table 1. The 24 hourly values of normalized slab thickness are also given in Table 1 as an array called  $C(h, M)$ . A model value of  $\gamma$  is then determined by:

$$\gamma(h, M, F_{10.7}) = [M(\text{month}) * F_{10.7} + B(M)] * C(h, M)$$

#### MODEL ERRORS AND SUGGESTIONS FOR IMPROVEMENTS

How well does the  $\gamma$  model outlined above describe the actual data which were used to construct the model? For the important daytime period, when absolute time delay errors due to the ionosphere are greatest, the normalized model shows overall r.m.s. errors less than 5 percent against the original data. The nighttime errors are approximately 10 percent. Figure 3 shows the overall model r.m.s. error in percent versus local time for over six years of data. During some seasons the model fit at nighttime is relatively poor, particularly during winter nighttime. Fortunately, in the

northern mid-latitudes, for which this model is applicable, the time delay is at its annual minimum during the winter nighttime period; thus, large percentage errors in the model can be tolerated during those times.

The model described is a monthly mean model, to be used with actual values of  $f_0F_2$  to determine ionospheric time delay. The model can be improved by making use of the ionosonde MUF factor if it is also scaled from the ionosonde record. Yeh et al (1972), have shown a good correlation between  $\tau$  and MUF, on a day to day basis. Also, the latitudinal and longitudinal variations of  $\tau$  in the mid-latitudes are, at present, largely unknown; as data from other

mid-latitude stations pairs become available the geographic dependence of this parameter will be determined. The use of the present monthly mean  $\tau$  model, with a near-real-time value of  $f_0F_2$  should result in TEC-time delay values which are in error by approximately 10 to 20 percent over the CONUS region during the daytime periods.

#### REFERENCE

Yeh, K.C., B. J. Flaherty, and B. J. Bolfig, "A Study of the Dependence of the Maximum Usable Frequency on the Electron Content," Proc. of IEEE, Vol. 60, No. 9, September 1972, pp. 1099-1100.

Table 1  
Solar flux and hourly coefficients of slab thickness model.

AFGRL MID-LATITUDE SLAB THICKNESS MODEL COEFFICIENTS																										
MO.	F10.7 COEFF.		LOCAL HOUR																							
	M	S	1	2	3	4	5	6	7	8	9	10	11	12	13	14	15	16	17	18	19	20	21	22	23	
1	1.10	209.	1.15	1.09	1.00	1.05	1.00	1.01	.98	.84	.73	.62	.62	.63	.90	.95	.94	.93	.99	.96	1.00	.98	1.12	1.24	1.32	1.2
2	.259	214.	1.12	1.09	1.05	1.07	1.07	1.07	.92	.76	.61	.67	.91	.95	.98	1.00	1.00	1.00	.98	.99	1.02	1.02	1.11	1.11	1.1	
3	.184	228.	1.12	1.02	1.05	1.12	1.14	1.09	1.07	.84	.65	.91	.90	.98	1.00	1.03	1.03	1.04	1.01	.99	1.03	1.02	1.03	1.03	1.0	
4	.174	253.	.92	.97	.99	.90	.91	.99	.93	.96	1.00	1.04	1.09	1.12	1.08	1.07	1.07	1.05	1.07	1.07	1.07	.96	.98	1.00	.98	.9
5	.719	213.	.88	.83	.88	.87	.93	1.05	1.01	1.02	1.07	1.08	1.12	1.13	1.12	1.09	1.08	1.09	1.07	1.07	1.02	.95	.93	.91	.89	.8
6	1.121	168.	.92	.82	.83	.87	.92	1.08	1.06	1.06	1.07	1.08	1.11	1.13	1.12	1.14	1.14	1.14	1.13	1.07	1.07	.97	.90	.85	.85	.8
7	.941	186.	.85	.84	.85	.88	.90	1.09	1.07	1.04	1.05	1.04	1.06	1.10	1.12	1.13	1.14	1.14	1.13	1.10	1.05	.98	.89	.86	.85	.8
8	.952	209.	.91	.97	.89	.89	.89	.98	.95	.98	.99	.99	1.00	1.08	1.11	1.12	1.11	1.13	1.13	1.16	1.11	.98	.92	.90	.91	.9
9	.775	157.	1.01	.99	.99	.97	.99	.99	.93	.93	.97	.94	.98	1.04	1.06	1.05	1.06	1.06	1.08	1.06	1.02	1.01	1.03	1.04	1.03	1.0
10	.329	193.	1.08	1.07	1.06	1.15	1.07	1.07	.89	.75	.80	.95	.93	.97	.99	.99	.98	.97	.96	.95	1.03	1.12	1.13	1.16	1.12	1.1
11	.419	175.	1.17	1.15	1.11	1.07	1.07	1.08	1.12	.74	.71	.76	.81	.85	.88	.88	.89	.90	.89	.95	1.06	1.07	1.18	1.23	1.24	1.1
12	.377	199.	1.22	1.16	1.07	1.11	1.01	1.02	1.08	.78	.71	.73	.80	.81	.83	.86	.89	.91	.90	.95	1.05	1.08	1.23	1.28	1.32	1.2

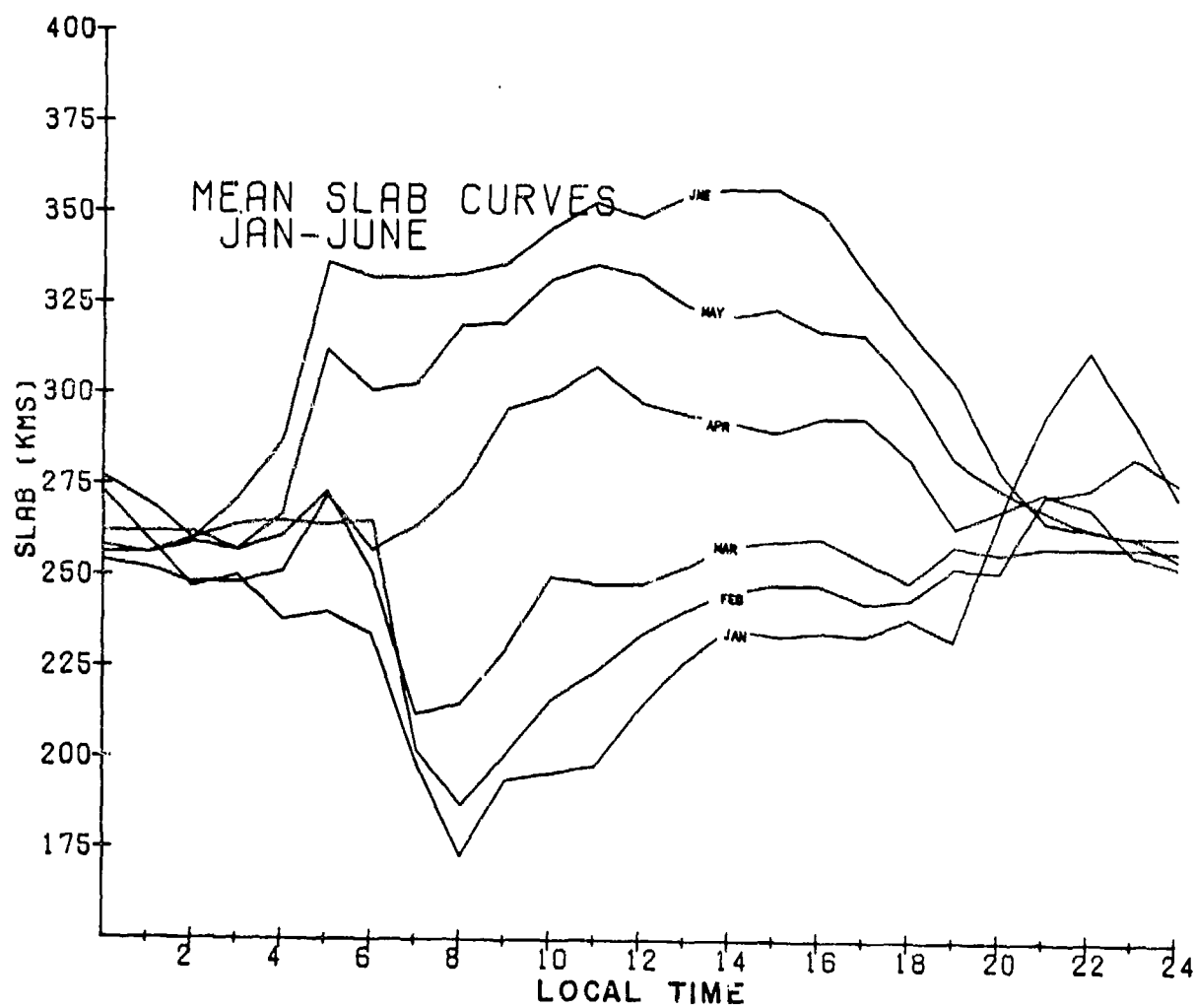


Figure 1A

Mean monthly slab thickness values averaged over the November 1967 to December 1973 period plotted separately for each month, versus local time.

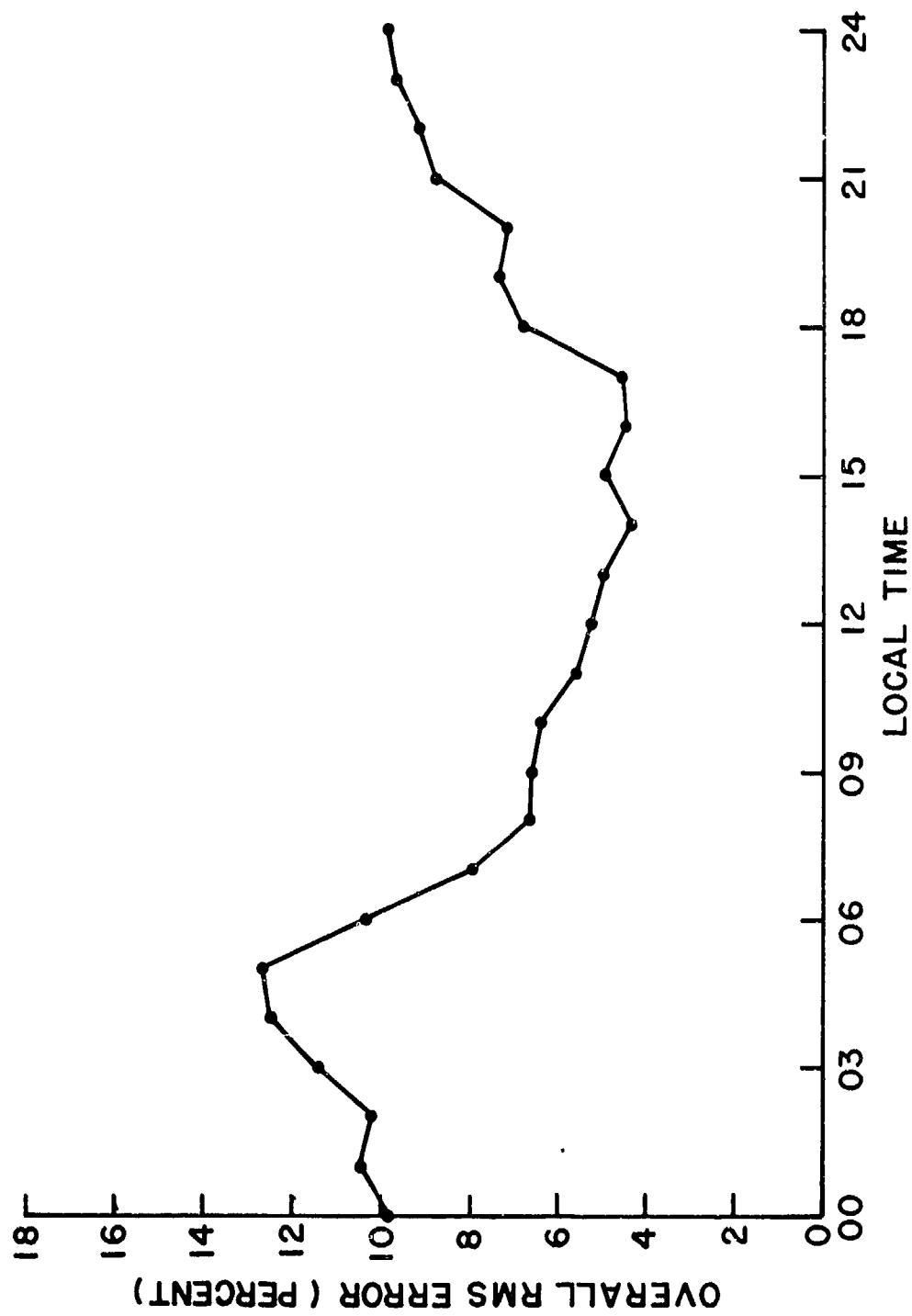


Figure 3  
Overall r.m.s. error in the slab thickness model versus local time.

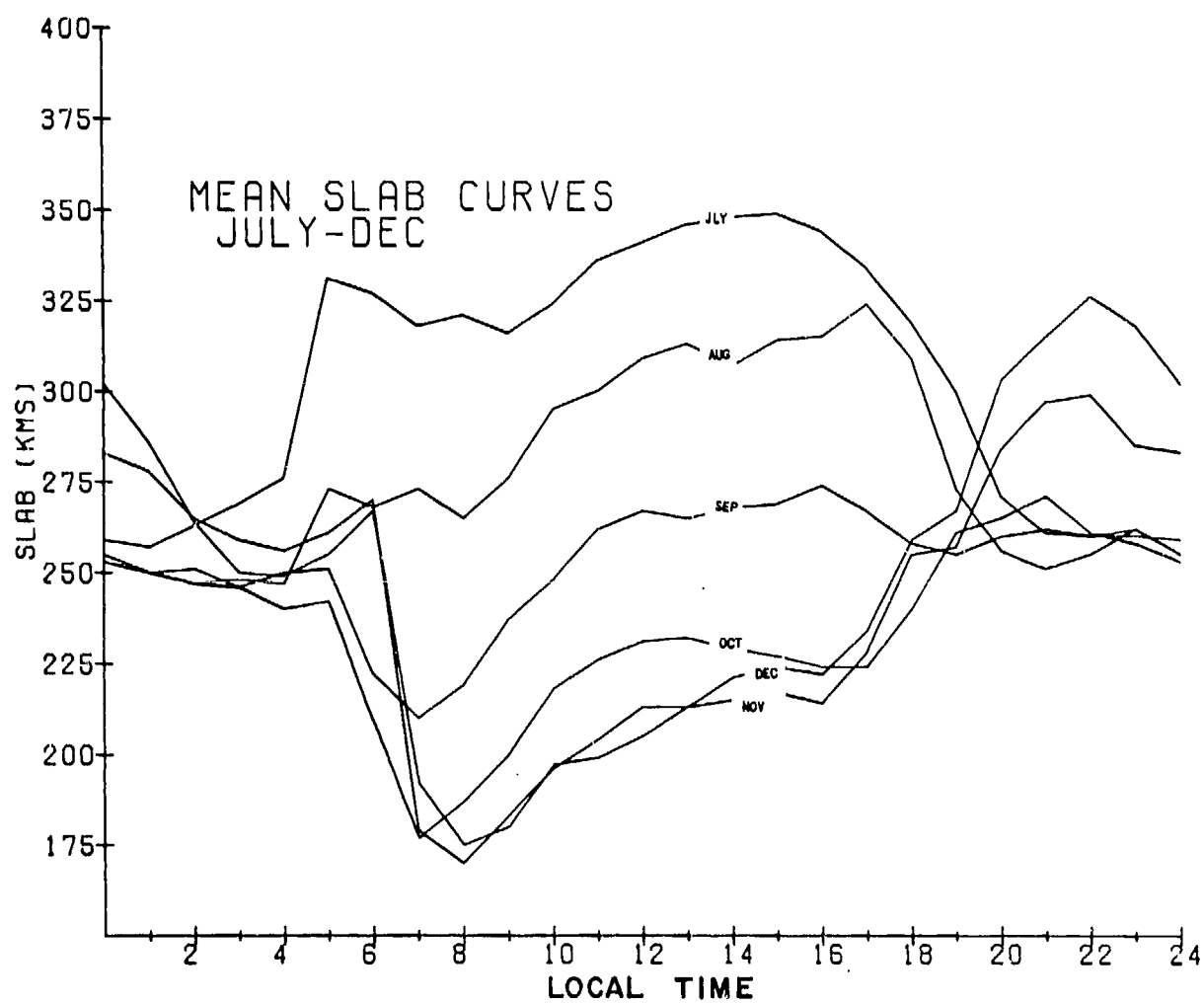


Figure 1B  
Mean monthly slab thickness values averaged over the November 1967 to December 1973 period plotted separately for each month, versus local time.

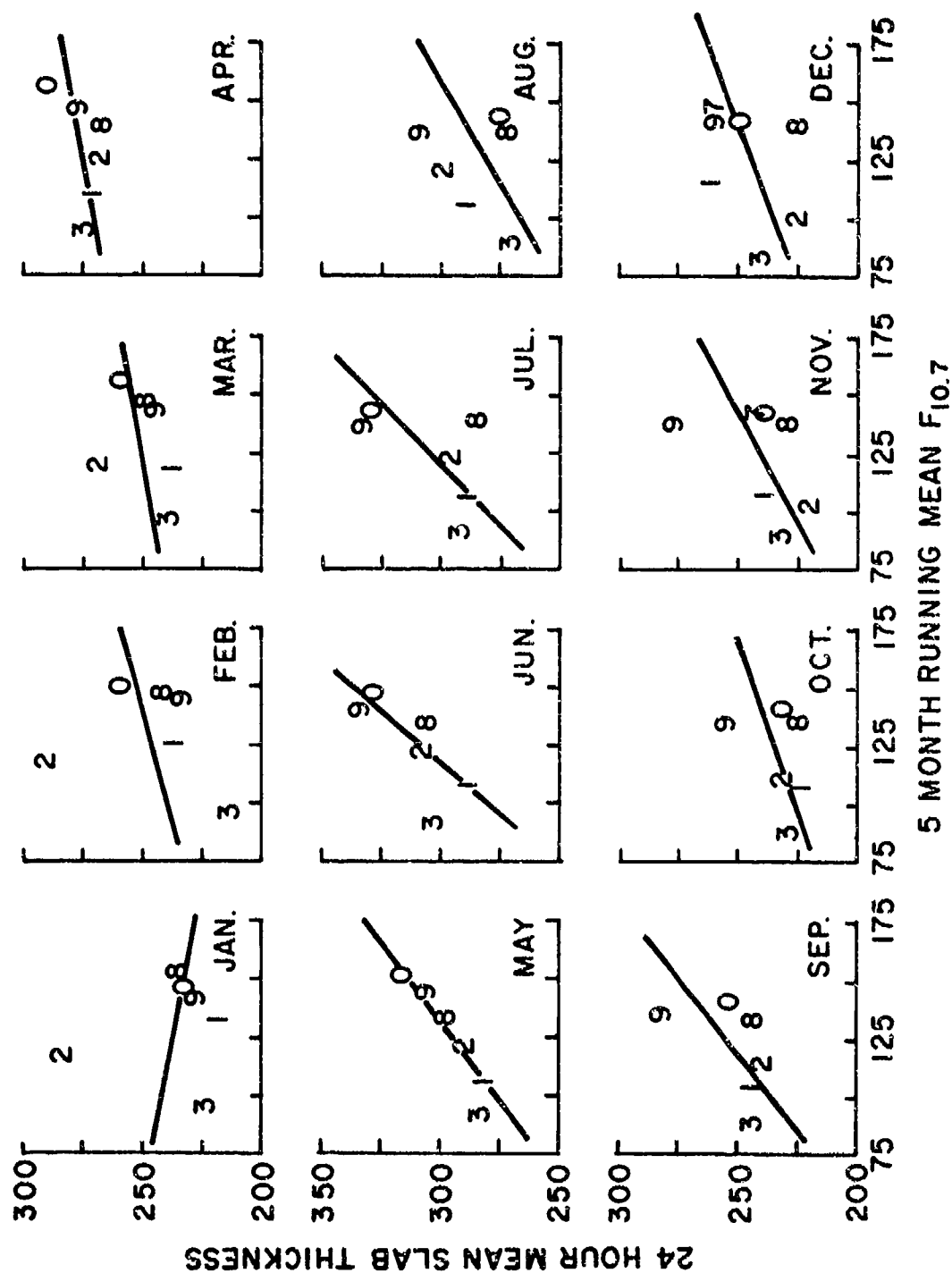


Figure 2  
24 hour mean slab thickness plotted against five month running mean 10.7 cm solar radio flux.

## PREDICTION TECHNIQUES FOR THE EFFECT OF THE IONOSPHERE ON RANGING FROM SATELLITES

M. M. Feen, V. L. Pisacane and M. Sturmanis  
The Johns Hopkins University  
Applied Physics Laboratory  
8621 Georgia Avenue  
Silver Spring, Maryland 20910

### Abstract

In studies of the effect of the ionosphere on satellite ranging signals, use is made of both theoretical and empirical models of the ionosphere. This paper documents one such study using an empirical ionospheric model.

Three distinct algorithms were defined and evaluated. Inherent to each algorithm was the explicit prediction of the electron density distribution on a world-wide basis. One algorithm was aimed at long-term predictions while the other two were dedicated to real-time operation. Faraday rotation data accumulated over several years and at several widely separated North American sites, Arecibo and Honolulu, formed the basis of the evaluation. The percentage error in the estimates of the ionosphere-induced time delay (or range) over the geographic region defined by the data base was 42 percent for the long-term predictions and 27 and 28 percent for the real-time predictions.

In general, the results indicate an ability to make estimates of the ionospheric contribution to the measured range which would be useful to some classes of navigators. Further improvements in ionospheric modeling would expand the user base.

### I. Introduction

Recent studies of navigation by means of satellites have emphasized the passive approach in which there is no active radio participation by the navigator. The Air Force currently has under development the Navstar Global Positioning System, a hyperbolic satellite navigation system, which would be capable of near-simultaneous and near-instantaneous determination of position and velocity [1], [2]. The system will have the capability for single or dual frequency navigation. In the single frequency mode, the navigation information is to be the measurement of the time of receipt of a single frequency (nominally 1600 MHz) signal from each of four

satellites. This paper is directed toward defining and then evaluating prediction algorithms which can be utilized to estimate the ionospheric contribution to the single frequency measured satellite range. Fundamental to the approach adopted is the explicit prediction of the electron density distribution of a world-wide basis. For a more detailed discussion of the study and the results, the reader is referred to [3].

Although motivated by a particular satellite navigation system, the techniques developed here have applications to other satellite navigation systems.

### II. Evaluation Data

The experimental data used in the study were Faraday rotation observations obtained from VHF (nominally 137 MHz) transmissions from near-synchronous satellites. The data were provided by the Air Force Cambridge Research Laboratories, Stanford Electronics Laboratories, University of Hawaii, and the University of Illinois. From this data it is possible to infer an "experimental" vertical ionospheric group time delay,  $\tau_{ve}$ . The  $\tau_{ve}$  data obtained in this manner were used for updating and evaluation of the prediction algorithms. In [3] theoretical expressions for converting the experimental Faraday rotation data to the equivalent  $\tau_{ve}$  data at the reference frequency of 1600 MHz are given. The approximations in these expressions are discussed together with the source of measurement errors and the limitations of the data base in providing a true global evaluation of the algorithms.

In order to simulate the application of the prediction techniques in a navigation system, the Faraday rotation data provided for the study was subsetting into five evaluation conditions with a data rate of one data point per 20 minute interval. The five evaluation conditions are described in Table 1, which also lists the ground station-satellite pairs from which the data were obtained. In an evaluation

This work was supported by the Department of the Navy under Navy Contract N00017-72-C-4401 and by the Department of the Air Force under USAF Contract MIPR FY 7616-70-00325.

TABLE 1  
EVALUATION CONDITIONS

EVALUATION CONDITION	1	2	3	4	5
DAYS	1 THRU 91	1 THRU 91	1 THRU 31, C1 THRU 120, 182 THRU 212	1 THRU 31, 92 THRU 121, 183 THRU 213, 275 THRU 305	1 THRU 31, 91 THRU 120, 182 THRU 212, 274 THRU 304
YEAR	1968	1968	1965	1968	1969
OBSERVATION STATION(S)	ARECIBO-ATS3 HONOLULU-ATS3	ARECIBO-ATS3 HONOLULU-ATS1 SAGAMORE HILL-ATS3	STANFORD-SYNCOM3	STANFORD-ATS1	FDMONTON-ATS1 SAGAMORE HILL-ATS3 HONOLULU-ATS1
EVALUATION STATION(S)	SAGAMORE HILL-ATS3 STANFORD-ATS3 URBANA-ATS3	STANFORD-ATS1 STANFORD-ATS3 URBANA-ATS3	HONOLULU-SYNCOM3	SAGAMORE HILL-ATS3 HONOLULU-ATS1	STANFORD-ATS1 STANFORD-ATS3 CLARK LAKE-ATS1 FORT COLLINS-ATS1 URBANA-ATS3 ROSLIAN-ATS3 ARECIBO-ATS3 COLD BAY-ATS1

condition, the stations listed as "observation stations" correspond to the system ground stations whose data are to be used in the updating process. The stations listed as "evaluation stations" correspond to navigators. Their data are to be used for comparison with the estimates and thus form the basis of the evaluations of the algorithms.

### III. General Approach to the Prediction Algorithms

Since the early years of ionosphere research, theoretical models, starting with the well-known Chapman model, have been developed to attempt to understand the mechanisms involved. More complex theoretical models consist of solving simultaneously the time-dependent coupled chemical, dynamical and thermodynamical partial-differential equations for a multi-constituent ionosphere in a multiconstituent neutral atmosphere. Their solutions are hindered by many uncertainties such as in the temporal and spatial distribution of the constituents, neutral gas temperatures, ion and electron velocities, neutral wind velocities, production and loss mechanisms, electric field intensity, geomagnetic field intensity and in the boundary conditions. The theoretical models are ideally suited to studying the basic mechanisms at work in the ionosphere.

Paralleling the development of theoretical ionospheric models has been the development of what are known as "model ionospheres" which are dedicated toward providing representative characteristics for given conditions and locations. Though they draw heavily on theoretical modeling, model ionospheres are usually empirical in nature.

The choice of using either a theoretical ionosphere or a model ionosphere depends on such factors as the ionospheric characteristics of interest, computational complexity and the geographic region of interest. In the interest of obtaining a global representation of satellite

range errors and minimizing computational complexity, we opted for a model ionosphere using as a basis the prediction models of global ionospheric characteristics developed by the National Oceanic and Atmospheric Administration (NOAA) (formerly ITS/ESSA). The NOAA estimates of interest in this study are given as functions of the geographic location, universal time, solar index  $R_{12}$  (12-month running average of the smoothed Zurich sunspot number), and possibly the month. The basis of these estimates was the fitting of world-wide experimental data obtained over daily, seasonal and solar cycles [4], [5], [6]. For example, the data base for the critical frequency of the F2 layer, known as  $f_oF_2$ , which defines the maximum electron density, was obtained from a world-wide network of stations over a span of several years. The data were reasonably well distributed geographically including such areas as Europe, Africa, North and South America, Asia, Australia, the Pacific, Russia and Mainland China.

Predictions of the ionospheric characteristics which are available from NOAA are:

1. critical frequency of the F2 layer,  $f_oF_2$
2. maximum usable frequency factor,  $M(3000)F_2$
3. maximum usable frequency,  $MUF(0)F_2$
4. maximum usable frequency over 4000 km,  $MUF(4000)F_2$
5. critical frequency of the E layer,  $f_oE$
6. height to semithickness ratio of F2 region,  $hmF_2/ymF_2$
7. semimonthly revision factors to correct the  $MUF(0)F_2$

The predictions are in use by several communities. For example, they are currently used in the estimation of high-frequency telecommunication parameters which are published regularly



by the Office of The Chief of Naval Operations for use by the fleet.

Several alternative approaches exist in developing the methodology of the prediction algorithms [7]. The basis of approach adopted in this study is the explicit prediction of the electron density distribution as a function of space and time. Once this has been achieved, it is straightforward to compute the ionospheric contribution to the measured range as a function of time and the actual geographic location of potential navigators, for each satellite, via ray-tracing.

Operationally, the ionospheric corrections could be computed at a central computing facility. It is shown in [3] that up to typical aircraft altitudes the ionospheric correction is insensitive to navigator's height, so that the correction for each satellite can be expressed as a function of the navigator's geographic location and time. This function, which will be referred to as the ionospheric correction function, could then be supplied to each navigator along with the ephemerides via the satellites. To give an intuitive appreciation for this approach, it is instructive to consider a hypothetical ionosphere in which the electron density distribution is such that there are no horizontal gradients. In this case, the contours of constant correction would be concentric circles about the subsatellite point in which the magnitudes associated with the contours increases with distance from the subsatellite point.

#### IV. Description of the Three Algorithms Utilized in the Study

##### A. Algorithm I

In this algorithm, the ionospheric group time delay is obtained via ray-tracing based on a priori estimates of the electron density distribution. This establishes a basis for comparison of both short-term and real-time predictions and indicates a measure of the extent to which either is needed.

The ionospheric group time delay is given to first order [3] as

$$\tau(G, t) = \frac{1.34 \times 10^2}{f^2} \int_{G(t)} N(\vec{r}, t) ds \quad (4.1)$$

where

$\tau(G, t)$  = ionospheric group time delay of the ranging signal between satellite and navigator along the geometric path  $G(t)$  at time  $t$ , ns

$f$  = carrier frequency, Hz

$N(\vec{r}, t)$  = electron density at  $\vec{r}$  and  $t$ , electrons/m<sup>3</sup>

$\vec{r}$  = position vector to a point on  $G(t)$   
 $ds$  = differential element of arc along  $G(t)$ , m

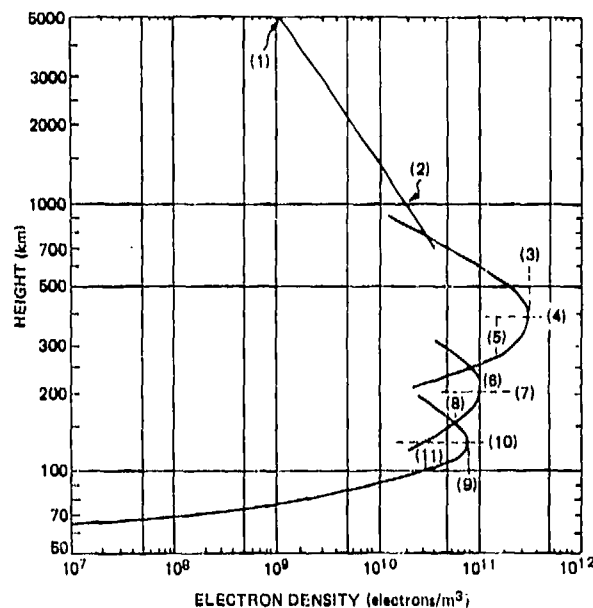


Fig. 1 Eleven Parameter Vertical Electron Density Profile [8]

To assist in characterizing the electron density distribution, a vertical electron density profile is utilized. The model adopted is that defined in [8] and depicted in Fig. 1. It is characterized by eleven parameters each of which can be a function of geographic location, time, solar activity, etc. The validity of the model has been established by the realization of good agreement between virtual height computations obtained using the model and experimentally determined values [8]. Of the eleven parameters that are required to define the vertical electron density, in this algorithm, four are obtained through the predictions available from NOAA. Of these four, three define the F2 region which is dominant in the determination of the integrated electron content along the propagation path. The eleven parameters are determined for Algorithm I in the following manner:

- (1) Density at 5000 km - an analytical function of the month of the year and the gyrofrequency [9]
- (2) Density at 1000 km - an analytical function of magnetic dip and solar zenith angle [10]

##### F2 region

- (3) Maximum electron density - obtained as a function of geographic location, universal time, month and solar index from predictions of foF2 available from NOAA [6]

- (4) Height of the maximum - obtained as a function of geographic location, universal time, month and solar index from predictions of M(3000)F2 available from NOAA [11]
- (5) Semithickness - obtained as a function of geographic location, universal time, month and solar index from predictions of hmF2/ymF2 available from NOAA [11]

#### F1 region

- (6) Maximum electron density - obtained as a function of solar index and solar zenith angle from an empirical formula [12]
- (7) Height of maximum - obtained as a function of solar zenith angle from an empirical formula [12]
- (8) Semithickness - constant at 50 km

#### E region

- (9) Maximum electron density - obtained as a function of geographic location, universal time, month and solar index from predictions of foE available from NOAA [11]
- (10) Height of maximum - constant at 130 km
- (11) Semithickness - constant at 20 km

In addition to the long-term predictions, NOAA also provides semimonthly revision factors [13]. These factors apply only to the F-layer critical frequency and can be used to provide corrections to the long-term estimates of the F-layer maximum electron density. They are prepared by rather subjective methods of comparison of the long-term predictions of the MUF(3000)F2 with experimentally determined values of MUF(3000)F2 from a set of ionosonde stations. The comparisons are based on experimental data obtained two to eight weeks prior to the half-month of application.

#### B. Algorithm II

The development of Algorithm II was devoted to the capability of effecting a real-time ionospheric correction. The most desirable approach would have been to utilize one of the several rather sophisticated theoretical ionospheric models that are available. With such a model as a basis, the philosophy of the updating scheme would be rather straightforward. It would be possible to determine some of the more uncertain model parameters as a function of time by "fitting" the model to whatever experimental ionospheric data is available. Prediction of the parameters and integration of the system of nonlinear time-dependent partial differential equations would then result in the determination of the electron density distribution at any time in the future.

The evaluation of the performance of any of the algorithms developed in this study was to

be achieved by processing a large amount of Faraday rotation data obtained over several years. Preliminary estimates for the cost of processing even only a minimum definitive subset of the data indicated that the computational complexities had to be minimized. Consequently, in order to perform a meaningful evaluation of the algorithm, a less sophisticated approach had to be adopted.

The a priori predictions of Algorithm I, as described in the previous section, constitute in themselves a rather sophisticated model. The predicted electron density distribution has considerable geographical and temporal structure. Because of this, it was concluded that rather than attempt to model the electron density distribution itself it would be more expeditious to model the differences between the actual electron density distribution and the estimates obtained from the a priori predictions of Algorithm I. The basis for this approach is the anticipation that the a priori estimates will adequately reflect the main structure and that a correction which is slowly varying in both space and time would be adequate. The adjunct model developed for the electron density distribution is distinguished by being an analytic model consisting of distinct daytime and nighttime functions.

The daytime model was obtained from a first order perturbation solution to the continuity equation in which the production is given by the Chapman function, the loss mechanism assumed to be a linear function of the electron density and in which transport phenomena are neglected. The nighttime model that was utilized represents a solution to the continuity equation which consists of a linear loss mechanism and no production mechanism. The effects of diffusion along the geomagnetic field lines were obtained from a simplified model based on the experimental results of Rastogi, [14]. The model so obtained is a function of geographic location, magnetic dip and local time and is linear in its parameters.

The parameters of the model are obtained by fitting to the Algorithm I residuals at the observation stations. The fitted values of the parameters were then used to predict corrections to the a priori (Algorithm I) estimates at the evaluation stations.

The length of the fitting span was chosen to be consistent with our attempt to track the daily variations expected in the residuals and thus was taken as 24 solar hours. The suitable prediction span (that is, the time span over which the fitted parameters are used to update) for purposes of making the model responsive to the ionospheric fluctuations and not requiring an intolerable amount of computer cost, was found to be 3 hours. The time between the end of the fitting span and the beginning of the prediction span was taken to be 1/2 hour. In an operational system this time lag would correspond to the time required for a central ground facility to gather data from

the system ground stations, perform the computations and communicate the necessary information to the satellites.

### C. Algorithm III

To further explore the potential of a real-time ionospheric correction, an alternative approach to Algorithm II was constructed. In Algorithm II the basis of the correction was the development of a theoretical ionospheric model. In contrast, the basis of Algorithm III is the utilization of an empirically developed model ionosphere. At any geographic location, the vertical electron density profile is taken to be that utilized in Algorithm I and depicted in Fig. 1. As discussed above, four of the eleven parameters used to define the profile for any specific geographic position are functions of the predicted solar index. Most significant are the three parameters defining the F2 region, which contributes overwhelmingly to the total group time delay, and for which worldwide a priori estimates are available from NOAA. These estimates are functions of geographic location, time, season, and solar index.

The solar index used in the NOAA predictions represent the 12-month running average of the smoothed Zurich sunspot number,  $R_{12}$ , determined from optical observations of the sun and centered on the month of interest. In a real-time application, since the appropriate solar index would not be available until six months later, an estimated  $R_{12}$  must be utilized. Because of this, it becomes appropriate to change this interpretation so that the  $R_{12}$  simply represents a number, or parameter, on which the electron density distribution is dependent. Given ionospheric data for some interval of time, then, it would be possible to determine an effective  $R_{12}$  (designated by  $R$ ) such that the modeled electron density distribution best represents the observed data. By using this  $R$ , or a value predicted from a sequence of such numbers, a real-time prediction of the electron density distribution can be obtained.

Inherent to this approach are the spatial and time correlations which have been determined experimentally and reside in the sets of coefficients which form the basis of the NOAA predictions. One concern in this approach is that the NOAA model ionosphere represent monthly median values and the same correlation may not exist for the instantaneous electron density distribution. Averaging data over a period of one to several days should help to minimize any difficulty resulting from this inconsistency.

Due to the budgetary constraints of the study, a simplification was introduced in the implementation of the algorithm. The simplification is based on the fact that the major contribution to the vertical ionospheric time delay,  $\tau_v$ , comes for the F2-layer of the ionosphere. It is then possible to write that

$$\tau_v(\lambda_1, \theta_1, t, R) \approx C N_{\max}(\lambda_1, \theta_1, t, R) \cdot \int W(\lambda_1, \theta_1, t, h) dh \quad (4.2)$$

where

$C$	$\approx 1.34 \times 10^2 / f^2$ , rationalized mks units where $f$ is the carrier frequency of the ranging signal in Hz
$\lambda_1$	"ionospheric geographic latitude" <sup>1</sup> of the observation station (in fitting) or the evaluation station (in predicting)
$\theta_1$	"ionospheric geographic longitude" <sup>1</sup> of the observation station (in fitting) or the evaluation station (in predicting)
$t$	universal time
$R$	effective value of $R_{12}$
$N_{\max}(\lambda_1, \theta_1, t, R)$	maximum electron density of the F2-layer
$W(\lambda_1, \theta_1, t, h)$	normalized electron density profile

Strictly speaking, the normalized vertical profile,  $W$ , should be a function of  $R$ . The independence of  $R$  is introduced as a simplification, so that the value of  $\int W(\lambda_1, \theta_1, t, h) dh$  may be obtained directly from the results of Algorithm I. The value of  $\int W(\lambda_1, \theta_1, t, h) dh$  is then given as

$$\int W(\lambda_1, \theta_1, t, h) dh = \frac{\tau_v(\lambda_1, \theta_1, t, R_{12})}{C N_{\max}(\lambda_1, \theta_1, t, R_{12})} \quad (4.3)$$

Both  $\tau_v(\lambda_1, \theta_1, t, R_{12})$  and  $N_{\max}(\lambda_1, \theta_1, t, R_{12})$  are available from the Algorithm I results.

From (4.2) and (4.3) the fitting function is given as

$$\tau_v(\lambda_1, \theta_1, t, R) = \frac{\tau_v(\lambda_1, \theta_1, t, R_{12})}{N_{\max}(\lambda_1, \theta_1, t, R_{12})} \cdot N_{\max}(\lambda_1, \theta_1, t, R) \quad (4.4)$$

where  $R$  is the fitting parameter.

<sup>1</sup>The point on the position vector from an observer to a satellite at which the electron density is a maximum is herein denoted as the "ionospheric point" and its projection on the ground is defined in terms of the "ionospheric geographic latitude" and "ionospheric geographic longitude."

The fitting function (4.4) was then least squares fit to the experimental  $\tau_v$  values,  $\tau_{ve}$ , at the observation stations. The fitted value of R thus obtained when used in (4.4) at the evaluation stations gives the updated prediction at the evaluation station.

To provide a meaningful estimate of R, it was felt that the fitting span should be at least 24 solar hours. As in Algorithm II, this was taken as the span length so as to make the model responsive to daily variations. Longer fitting spans would make the model more sluggish in its response.

A prediction span of 3 hours, as in Algorithm II, was found to be suitable. Shorter spans showed no improvement in results. The time between the end of the fitting span and the beginning of the prediction time was, as in Algorithm II, taken as 1/2 hour.

#### V. Evaluation Results

The basis of the evaluation of each algorithm was the difference in nanoseconds, referenced to 1600 MHz, of the vertical group time delays as predicted by each algorithm and inferred from Faraday data. This difference is termed the residual and is denoted by  $\delta\tau_v$ . All the data furnished was assumed to be of equal quality and weight. This was consistent

TABLE 2  
SUMMARY OF RMS VALUES OVER  
EVALUATION CONDITIONS FOR OBSERVATION STATIONS

STATION	E.C.	$\tau_{ve}$ (ns)	$\delta\tau_v$ (ns) ( $\delta\tau_v/\tau_{ve}$ )			NO.*
			Alg. I	Alg. II	Alg. III	
ARECIBO-- ATS3	1	19.35	8.13 (0.42)	4.53 (0.23)	4.89 (0.25)	5180
HONOLULU-- ATS1	1	28.13	11.73 (0.42)	7.88 (0.28)	10.70 (0.30)	5032
SAGAMORE HILL-ATS3	2	15.30	7.12 (0.47)	4.01 (0.26)	4.47 (0.29)	5607
ARECIBO-- ATS3	2	18.46	8.14 (0.42)	4.17 (0.21)	4.75 (0.24)	5204
HONOLULU-- ATS1	2	29.34	11.81 (0.42)	7.79 (0.27)	10.73 (0.38)	5717
STANFORD-- SYNCOM3	3	5.82	1.47 (0.26)	1.32 (0.23)	1.42 (0.25)	4401
STANFORD-- ATS1	4	14.06	4.79 (0.34)	2.59 (0.18)	3.11 (0.22)	5305
SAGAMORE HILL-ATS3	5	12.99	6.18 (0.48)	4.01 (0.31)	4.57 (0.36)	5532
EDMONTON-- ATS1	6	13.90	7.70 (0.56)	5.10 (0.37)	5.06 (0.36)	7582
HONOLULU-- ATS1	6	24.41	9.78 (0.40)	5.35 (0.22)	7.08 (0.31)	8236
ALL	ALL	19.53	8.29 (0.42)	5.06 (0.26)	6.43 (0.33)	62492

\*NUMBER OF RESIDUALS USED IN COMPUTATION  
OF RMS

TABLE 3  
SUMMARY OF RMS VALUES OVER EVALUATION  
CONDITIONS FOR EVALUATION STATIONS

STATION	E.C.	$\tau_{ve}$ (ns)	$\delta\tau_v$ (ns) ( $\delta\tau_v/\tau_{ve}$ )			NO.*
			Alg. I	Alg. II	Alg. III	
STANFORD-- ATS1	1	15.06	5.41 (0.36)	4.63 (0.31)	3.24 (0.22)	5776
STANFORD-- ATS3	1	15.35	5.72 (0.37)	4.81 (0.31)	3.61 (0.24)	5782
URBANA-- ATS3	1	15.67	6.87 (0.44)	4.07 (0.26)	4.00 (0.26)	5110
SAGAMORE HILL-ATS3	1	15.41	7.20 (0.47)	4.71 (0.31)	4.65 (0.30)	5391
STANFORD-- ATS1	2	15.23	5.50 (0.36)	4.01 (0.26)	3.14 (0.21)	5978
STANFORD-- ATS3	2	15.48	5.73 (0.37)	4.13 (0.27)	3.53 (0.23)	5980
URBANA-- ATS3	2	15.67	6.87 (0.44)	3.38 (0.22)	3.85 (0.25)	5168
HONOLULU-- SYNCOM3	3	9.92	3.37 (0.34)	3.14 (0.32)	3.16 (0.32)	4154
SAGAMORE HILL-ATS3	4	13.35	5.97 (0.45)	4.23 (0.32)	3.99 (0.30)	5960
HONOLULU-- ATS1	4	25.77	10.13 (0.39)	6.88 (0.26)	8.72 (0.34)	5963
STANFORD-- ATS1	5	14.33	6.11 (0.43)	3.48 (0.24)	3.52 (0.25)	8301
STANFORD-- ATS3	5	17.61	7.59 (0.43)	4.37 (0.25)	4.99 (0.28)	1898
CLARK LAKE-- ATS1	5	19.71	8.50 (0.44)	3.81 (0.20)	4.19 (0.22)	3928
COLD BAY-- ATS1	5	11.58	5.55 (0.48)	3.83 (0.33)	3.75 (0.32)	5636
FORT COLLINS-- ATS1	5	14.38	7.19 (0.50)	3.88 (0.27)	4.17 (0.27)	6276
URBANA-- ATS3	5	14.57	7.20 (0.49)	3.65 (0.25)	4.71 (0.32)	8522
ROSMAN-- ATS3	5	13.27	5.75 (0.43)	3.36 (0.35)	4.12 (0.31)	5652
ARECIBO-- ATS3	5	15.38	6.56 (0.43)	5.44 (0.36)	4.70 (0.31)	1894
ALL	ALL	15.63	6.00 (0.42)	4.27 (0.27)	4.38 (0.28)	97369

\*NUMBER OF RESIDUALS USED IN COMPUTATION  
OF RMS

with the desire to interpret the results of the evaluation in a global context.

Tables 2 and 3 summarize the results for the evaluation and observation stations respectively with the measure of success given by  $\delta\tau_v/\tau_{ve}$ . The former table indicates the ability of a station or group of stations to extrapolate in time only. It is clear from the tables that the overall prediction capability of Algorithm I, as expected, is exceeded by Algorithms II and III, which are comparable. Summarized over all evaluation stations and over all evaluation conditions, the rms value of vertical ionospheric group delay ( $\tau_{ve}$ ) is

15.68 ns. The rms of the residuals for Algorithms I, II, and III, are 6.60 ns, 4.27 ns, and 4.38 ns, respectively. A measure of the percentage error in the estimates can be obtained from  $\delta\tau_v/\tau_{ve}$ ; this gives 42 percent for the long-term predictions of Algorithm I and 27 and 28 percent for the real-time predictions of Algorithm II and III respectively.

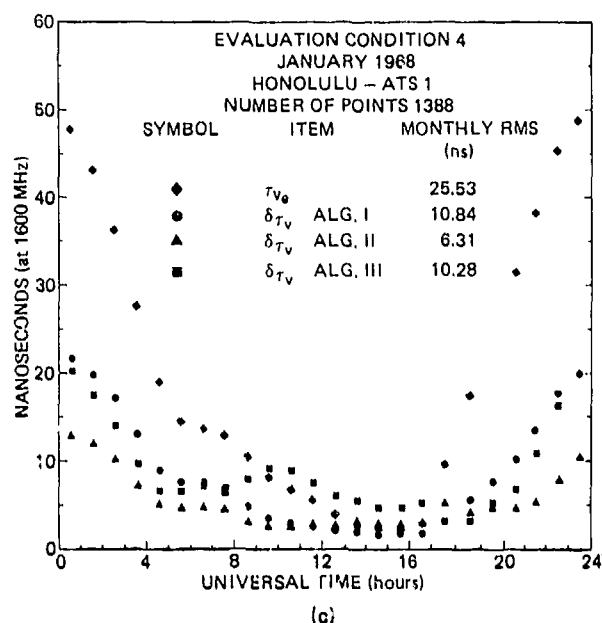
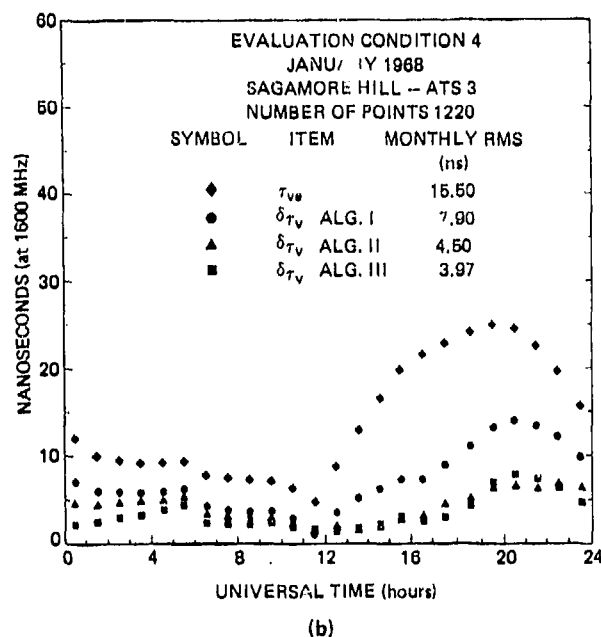
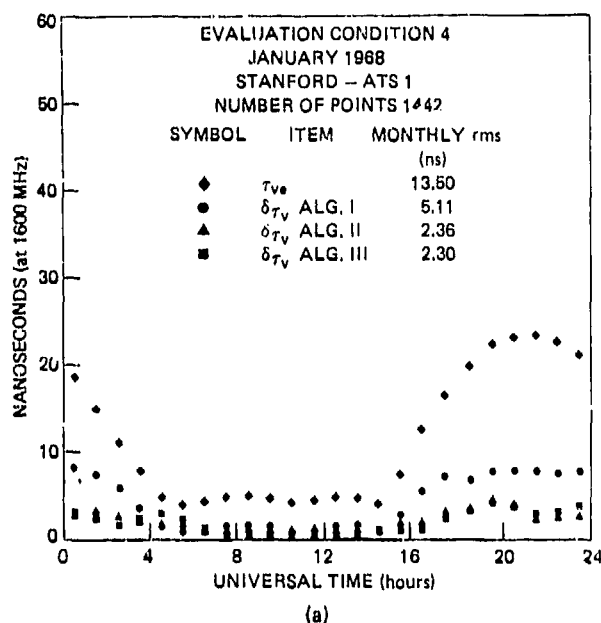


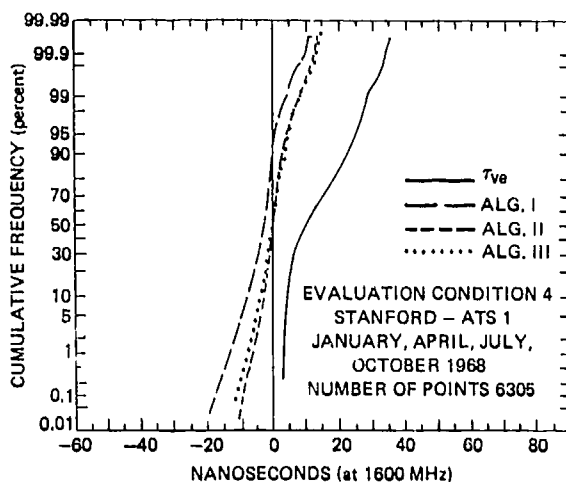
Fig. 2 Vertical Time Delay and Residuals - Hourly RMS Over Month

Given in Fig. 2 are the hourly rms values of the vertical time delays,  $\tau_{ve}$ , and of the residuals for each of the three algorithms for one month of evaluation condition 4. For this evaluation condition, Stanford is the observation station while Sagamore Hill and Honolulu are the evaluation stations. The similarity in the behavior of the ionosphere for the two stations in the continental United States becomes even more apparent when the 3.4 hour difference in local sun time is introduced. The behavior of the ionosphere at Honolulu as given in Fig. 2(c) is distinctly different. As anticipated, the residuals at Honolulu are larger than the residuals at Sagamore Hill, Fig. 2(b).

Given in Fig. 3 are cumulative frequency distributions for the total vertical time delay and the residuals over the four months of evaluation condition 4. Again, similarities can be observed between the results for Stanford and Sagamore Hill, Figs. 3(a) and 3(b), with the Honolulu results, Fig. 3(c), appearing distinctly different.

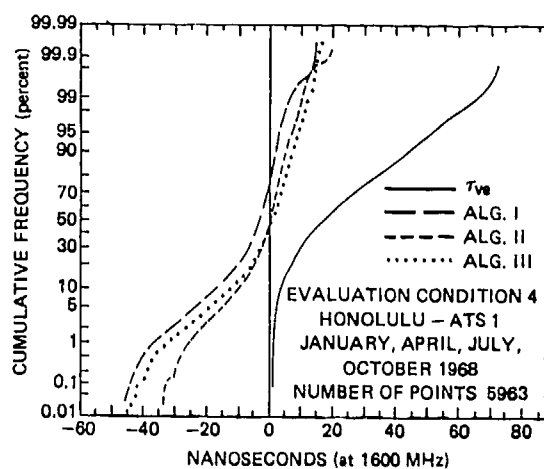
The extreme values of the vertical time delay ( $\tau_{ve}$ ) and the residual ( $\delta\tau_v$ ) observed in the study occurred at Hawaii in evaluation conditions 1 and 2. The values were 86 ns in  $\tau_{ve}$ , -54 ns for  $\delta\tau_v$  for Algorithm I, -50 ns for  $\delta\tau_v$  for Algorithm II, and -43 ns for  $\delta\tau_v$  for Algorithm III.

The above figures represent the prediction ability on an individual range measurement. The quantity of interest in a hyperbolic navigation system is the uncorrelated error in the



	REFERENCE FREQUENCY 1600 MHz				
	RMS (ns)	PERCENTAGE OF POINTS BETWEEN			
		±3(ns)	±9(ns)	±18(ns)	±27(ns)
$T_{ve}$	14.06	0.24	44.82	77.30	96.88
$\delta T_v$ ALG. I	4.79	52.79	92.87	99.92	100.00
$\delta T_v$ ALG. II	2.59	81.39	99.08	100.00	100.00
$\delta T_v$ ALG. III	3.11	71.42	98.62	100.00	100.00

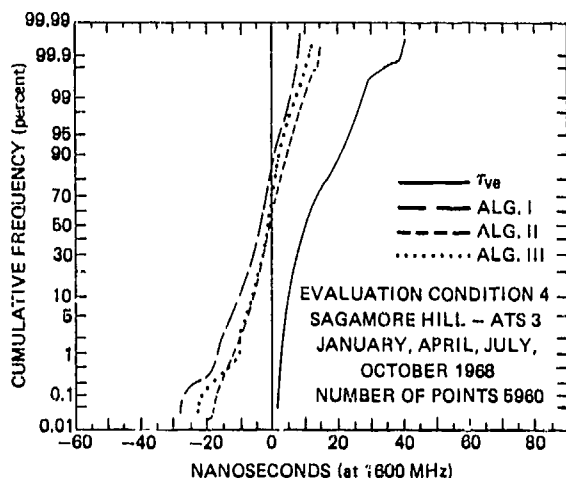
(a)



	REFERENCE FREQUENCY 1600 MHz				
	RMS (ns)	PERCENTAGE OF POINTS BETWEEN			
		±3(ns)	±9(ns)	±18(ns)	±27(ns)
$T_{ve}$	25.77	8.02	27.23	52.44	70.60
$\delta T_v$ ALG. I	10.13	42.87	77.02	90.78	96.71
$\delta T_v$ ALG. II	6.68	51.44	87.08	96.73	98.43
$\delta T_v$ ALG. III	8.72	38.12	80.40	94.21	97.99

(c)

Fig. 3 Vertical Time Delay and Residuals — Cumulative Frequency Distribution



	REFERENCE FREQUENCY 1600 MHz				
	RMS (ns)	PERCENTAGE OF POINTS BETWEEN			
		±3(ns)	±9(ns)	±18(ns)	±27(ns)
$T_{ve}$	13.35	1.78	37.99	81.49	98.54
$\delta T_v$ ALG. I	5.97	40.00	87.98	99.58	99.92
$\delta T_v$ ALG. II	4.23	57.50	95.96	99.97	100.00
$\delta T_v$ ALG. III	3.99	65.34	96.16	99.80	100.00

(b)

predictions of the simultaneous observations of different satellites by a navigator. This data was not available so that this degree of correlation of the prediction residuals could not be studied. Consequently, the results of the study represent a worst case situation (i.e., one in which the prediction residuals are interpreted as being totally uncorrelated).

## VI. Conclusions

Three algorithms have been proposed for prediction of the daytime and nighttime ionospheric electron density distribution. Algorithm I constitutes an a priori prediction while Algorithms II and III constitute real-time predictions. Evaluations of the algorithms have been performed utilizing Faraday rotation data from several widely separated North American sites, Arecibo and Honolulu, as the basis of the real-time predictions as well as the basis of the evaluation. Since the study was performed in the context of effecting corrections for a satellite navigation system, the results are given in terms of the ionospheric induced vertical time delay which is directly proportional to the columnar electron content. The percentage error in the estimates of ionosphere-induced time delay, over the geographic region defined by the data base, for the three algorithms was 42, 27, and 28 percent, respectively.

The development and evaluation of the algorithms was directed to their use in an operational world-wide satellite navigation system. Consequently, care was taken to ensure (a) that the informational content of the algorithms reflected the operational environment in which they would be used and (b) that the evaluation reflected world-wide performance. To satisfy (a), no ionospheric information or data obtained during or subsequent to the evaluation period was utilized in either development or evaluation of the algorithms, excepting that data obtained at the observation stations, of which knowledge was assumed only up to a half-hour prior to updating. To satisfy (b), given the limited geographic extent of the data base, it was felt to be inappropriate to use geographic weighting procedures on observation station data. For example, it was clear that the Hawaiian data was of a different character than data from the other sites in the data base. If the Hawaiian data, in those situations in which Hawaii was an observation station, were deweighted relative to the other observation stations, the apparent performance of the algorithms would be improved. A subsidiary study showed that such deweighting of the Hawaiian data would provide an additional reduction in the residuals of about 10 percent. However, as indicated, the use of such a procedure, in light of the limitations of the data base, would not provide a true evaluation of the real-time algorithms in a world-wide context. Thus, in order to avoid obtaining overly optimistic results for world-wide interpretation, data from all observation stations were weighted equally.

In general, the results indicate an ability to make predictions of the ionospheric range error which would be useful to some classes of navigators. Further improvements in ionospheric modeling would expand the user base. However, at the present state-of-the-art of ionospheric predictions utilizing empirical models, as evidenced by this and related studies, [7], a dual frequency system would appear to be advisable for users requiring high precision navigation fixes at all times.

#### References

- [1] B. Miller, "Satellite clusters studied for tri-service navigation," Aviation Week and Space Technology, vol. 92, no. 5, pp. 20-21, 1970.
- [2] P. J. Klass, "DOD weighs Navstar schedule advance," Aviation Week and Space Technology, vol. 101, no. 22, pp. 46-49, 1974.
- [3] V. L. Pisacane, M. M. Feen and M. Sturmanis, "Prediction techniques for the effect of the ionosphere on pseudo-ranging from synchronous altitude satellites," Johns Hopkins University Applied Physics Laboratory Technical Report TG-1197, August 1972.
- [4] W. B. Jones and R. M. Gallet, "The representation of diurnal and geographic variations of ionospheric data by numerical methods," Telecommunications Journal, vol. 29, no. 5, pp. 129-149, 1962.
- [5] W. B. Jones, R. P. Graham and M. Leftin, "Advances in ionospheric mapping by numerical methods," U. S. Dept. of Comm./ESSA Report ERL 107-ITS 75, May 1969.
- [6] W. B. Jones and D. L. Obitts, "Global representation of annual and solar cycle variation of foF2 monthly median 1954-1958," U. S. Dept. of Comm. - Office of Telecommunications ITS Research Report 3, October 1970.
- [7] J. A. Klobuchar and R. S. Allen, "Total electron content models," Air Force Survey in Geophysics No. 257 AFGRL-TR-73-0028, pp. 13-17, February 1, 1973.
- [8] G. W. Haydon and D. L. Lucas, "Predicting ionospheric electron density profiles," Radio Science, vol. 3, no. 1, pp. 111-119, 1968.
- [9] R. L. Smith, "Properties of the outer ionosphere deduced from nose whistlers," Journal of Geophysical Research, vol. 66, no. 11, pp. 3709-3716, 1961.
- [10] S. Chandra and S. Ragaswamy, "Geomagnetic and solar control of ionization at 1000 km," Journal of Atmospheric and Terrestrial Physics, vol. 29, no. 3, pp. 259-265, 1967.
- [11] A. F. Barghausen, J. W. Finney, L. L. Proctor, and L. D. Schultz, "Predicting long-term operational parameters of high-frequency sky-wave telecommunication systems," U. S. Dept. of Comm./ESSA Technical Report ERL 110-ITS-78, May 1969.
- [12] G. E. Hill, S. M. Bennett, C. J. Mazzola, M. A. Sheg and D. A. Sherman, "Natural communications study phase 1 - Feasibility study on a reliable polar high-frequency communications system," AVCO Technical Report RAD-TR-63-37, July 31, 1963.
- [13] D. H. Zacharisen, S. M. Ostrow and G. C. Huang, "Validity of revision factors in updating long-term F2-layer maximum usable frequency predictions," U. S. Department of Comm./ESSA Technical Report ERL H-ITS 156, February 1969.
- [14] R. G. Rastogi, "Geomagnetic influence in the F1- and F2- regions of the ionosphere - effect of solar activity," Journal of Atmospheric and Terrestrial Physics, vol. 14, no. 1, pp. 31-40, 1959.

# A SIMULATOR FOR EVALUATING THE ACCURACY OF VARIOUS TECHNIQUES FOR ELECTRON CONTENT DETERMINATION FROM SATELLITE TRANSMISSIONS

George H. Millman  
General Electric Company  
Syracuse, New York 13201

## Introduction

When radio waves emanating from earth's satellites traverse the ionosphere, they undergo both a rotation of the plane of polarization, i. e., Faraday effect, and a Doppler frequency shift. Analytical techniques have evolved which utilize the two phenomena for the study of the electron content in the ionosphere.

In this paper, an evaluation is made of the accuracy of several of the analytical approaches which make use of the Faraday and Doppler phenomena for determining the ionospheric electron content. This is accomplished by means of a simulator-computer program; a logic block diagram is shown in Figure 1 (Millman, 1974).

Working Group 4, Analysis of the Geomagnetic Field (1969), is used to specify the magnetic potential function. This function in turn is employed in the computation of the magnetic field intensity (H), the inclination angle (I), and the declination angle (D). The magnetic field intensity and the propagation angle ( $\theta$ ) which is a function of I and D (Millman, 1969), are evaluated at equal increments of height along the different propagation paths to the orbiting satellite.

The electron density profiles generated by the Penn State Mark I Ionospheric Model (Nisbet, 1970) are used as the reference ionosphere. However, the simulator can also accept as an input any spatial distribution of electron density. The required inputs to the model are geographic coordinates, day num-

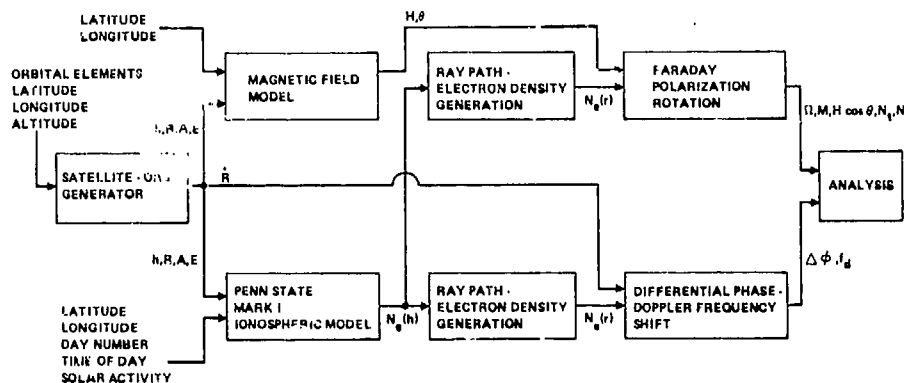


Figure 1. Logic Block Diagram of Faraday-Doppler Simulator

In the satellite-orbit generator, the azimuth angle (A), elevation angle (E), altitude (h), range (R) and radial velocity of the satellite ( $\dot{R}$ ) as observed as a function of time at a ground-receiving station are computed. The calculations are based on Kepler's equations of motion, i. e., a two-body orbit, assuming a rotating-spherical earth which is void of an atmosphere. The required inputs to the program are the geographical coordinates and altitude of the ground station and the satellite-orbital parameters which consist of the three orientation elements, inclination angle, argument of perigee and longitude of ascending node and the three dimensional elements, semimajor axis, eccentricity and time of ascending node.

The earth's magnetic field is represented by a series of spherical harmonics. In this analysis, the set of 80 spherical harmonic coefficients for Epoch 1965 derived by the International Association of Geomagnetism and Aeronomy (IAGA) Commission 2

ber, time of day and solar activity, i. e., 10.7 cm solar flux intensity. The output of the model is in the form of hourly values of the electron density profile [ $N_e(h)$ ], between 120- and 1250-km altitude. The spatial distribution of electron density is attained by generating vertical profiles at three locations north of the satellite-observing site and three locations south of the site, each separated by 10° geographic latitude. The data for the six additional locations yield latitudinal-electron density coverage and information on the existence of north-south electron density gradients. Since the hourly values of the electron density profiles can be converted directly to 15° longitudinal values, the east-west gradients are also available.

In the ray path - electron density generator, the electron densities along the different ray paths, [ $N_e(r)$ ], are determined by linear interpolation within the vertical distribution - electron density grid.



In the Faraday rotation module, the first-order term of the polarization rotation angle ( $\Omega$ ) is calculated at even height increments along the ray path. The output data also consist of the geometric magnetic factor ( $M$ ), the magnetic function ( $H \cos \theta$ ), the integrated electron density in a vertical column ( $N_t$ ) and along an oblique (slant) path ( $N_r$ ).

The differential phase between the two coherent transmitted satellite frequencies ( $\Delta \phi$ ) is calculated along the path to the satellite. In addition, the Doppler frequency shift ( $f_d$ ) experienced by the two frequencies is also determined. In both derivations, the first-order refractive index term is only used.

The output data from the Faraday rotation and differential phase-Doppler shift modules which in reality can be considered to be a ground-satellite receiving system are processed in the analysis program. The analytical techniques for ionospheric electron content determination that are evaluated are the Faraday single frequency method, differential polarization rotation angle method, polarization rotation rate method, Doppler frequency shift method, Doppler frequency slope method, ionosonde method and the hybrid Faraday rotation-differential Doppler method. The electron contents deduced by the analytical techniques are compared with the true-reference values obtained by integration of the ray paths - electron densities in the Faraday rotation module.

#### Theoretical Considerations

##### Faraday Rotation

The amount of angular rotation (in radians) experienced by a linearly polarized wave traversing a one-way path in the ionosphere can be represented by the function

$$\Omega = \frac{K_1}{f^2} \int_0^{h_s} H \cos \theta f(h) N_e dh \quad (1)$$

where  $K_1$  is a constant equal to  $2.362 \times 10^4$  cgs units,  $f$  is the transmission frequency in Hz,  $H$  is in Gauss,  $f(h)$  is the secant of angle between the ray path and the zenith,  $N_e$  is in electrons/cm<sup>3</sup>,  $dh$  is the height differential in cm,  $h_s$  is the satellite altitude and  $\theta$  is the angle between the direction of the earth's magnetic lines of force and the direction of propagation.

The angular rotation can be written in the form

$$\Omega \approx \frac{K_1}{f^2} \bar{M} N_t \approx \frac{K_1}{f^2} \bar{H} \cos \theta N_r \quad (2)$$

where  $\bar{M}$  is the mean value of the geometric magnetic factor,  $\bar{M} = \bar{H} \cos \theta f(h)$  and where

$$\begin{aligned} N_r &= \int_0^{h_s} N_e f(h) dh \approx \bar{f(h)} \int_0^{h_s} N_e dh \\ &= \bar{f(h)} N_t \end{aligned} \quad (3)$$

In general, for radio waves emitted from satellites and observed on the ground, the experimentally-measured total angular rotation,  $\Omega_e$ , is am-

biguous in that  $\Omega_e = \pm (n\pi \pm \Delta\Omega)$  where  $n$  is a positive integer and  $\Delta\Omega$  is the acute polarization angle which would normally be indicated in a satellite-amplitude measurement.

**Single frequency method.** It is possible, however, that, for transmissions in the VHF and UHF range, the polarization rotation could be less than  $(\pi/2)$  radians. This could occur under certain conditions; that is, when observations are made during the nighttime or at certain azimuth-elevation angle orientations toward the polar ionosphere (in the case of a polar orbiting satellite) where near perpendicularity with the earth's magnetic field could be attained. Assuming that the angular rotation is initially less than  $(\pi/2)$  radians, then, when  $(\pi/2)$  radian rotation does occur, the integrated electron density, i. e., vertical or slant electron content, can be derived from Equation (2) utilizing a single transmission frequency since, for any ray path, the parameter  $M$  or  $H \cos \theta$  can be readily specified.

**Differential polarization rotation angle method.** The ambiguity problem can be avoided by the measurement of the change in the polarization angle at two different times,  $t_1$  and  $t_2$ , on the satellite orbit pass. This scheme which is often referred to as the differential Faraday polarization rotation angle method requires that the integrated electron densities along the two different ray paths be identical. This assumption implies that no horizontal gradients of electron content exist within the time interval. Thus, it can be shown from Equation (2) that the electron content can be obtained from

$$N_t = \frac{f^2}{K_1} \left[ \frac{\Omega_1 - \Omega_2}{\bar{M}_1 - \bar{M}_2} \right] \quad (4)$$

It is noted that the slant electron content, i. e., along the ray path, can be derived by merely replacing the  $M$  factor by the corresponding mean magnetic function  $H \cos \theta$ .

**Polarization rotation rate method.** Another method which can be used to determine  $N_t$  is one which involves the time rate of change of the polarization rotation angle. Differentiating Equation (2) with respect to time and assuming a horizontally stratified ionosphere, i. e.,  $\dot{N}_t = 0$ , there results

$$N_t = \frac{f^2}{K_1} \frac{\dot{\Omega}}{\dot{\bar{M}}} \quad (5)$$

where the dot signifies the time derivative. The electron content can therefore be determined since  $\Omega$  can be experimentally measured and  $\bar{M}$  theoretically predicted.

##### Differential Phase and Doppler Frequency Shift

The differential phase or dispersive phase method can be considered to be a modified form of the Doppler frequency technique. The differential phase between two harmonically-related coherent signals transmitted from a satellite and detected on the ground is given by

$$\Delta \phi = - \frac{K_2}{f_1} \left( \frac{b^2 - a^2}{a} \right) N_r \quad (6)$$

where  $K_2$  is a constant equal to  $8.440 \times 10^{-3}$  cgs units, and  $a$  and  $b$  are constants related to the satellite transmitted frequencies,  $f_1$  and  $f_2$ , according to  $af_1 = bf_2$ . It is noted that differential phase between the two frequencies is obtained from  $\Delta\phi = a\phi_1 - b\phi_2$  where  $\phi_1$  and  $\phi_2$  are the total phase shifts encountered by the radio waves traversing a space-to-earth propagation path.

Equation (6), which is derived on the assumption that the two transmitted signals travel along the same ray path, can also be written in terms of the vertical electron content by merely replacing  $N_T$  by  $f(h) N_t$  as given by Equation (3).

The absolute phase of a satellite signal received on the ground cannot be measured. Thus, from the differential phase, Equation (6), the relative electron content along the paths from the satellite to a ground terminal throughout the satellite pass can only be inferred. Once the integrated electron density is known for one point on the satellite trajectory, it is then possible to convert the relative electron content scale into an absolute measurement.

**Doppler frequency shift method.** An absolute measure of the electron content can be determined from the Doppler frequency shifts of the coherent transmissions from a satellite. According to Al'pert (1958), for a satellite moving in a circular orbit and assuming that the ionosphere is nonrefractive and fixed in configuration, both in time and space, the ionospheric electron content in a vertical column can be evaluated from

$$\int_0^{h_s} N_e dh = \frac{h_s f_1^2}{K_3} \left( f_{d2} - f_{d1} \frac{f_2}{f_1} \right) \left( f_{d2} - f_{d1} \frac{f_1}{f_2} \right)^{-1} \quad (7)$$

where  $K_3$  is a constant equal to  $4.03 \times 10^7$  cgs units, and  $f_{d1}$  and  $f_{d2}$  are the Doppler frequency shifts of the satellite emitted frequencies,  $f_1$  and  $f_2$ , respectively. This expression is valid for satellites located at high elevation angles with respect to the ground receiving station.

The Doppler frequency shift of satellite signals traversing the ionosphere can be expressed by

$$f_d = -\frac{f}{c} R + \frac{K_4}{f} \frac{d}{dt} \int_0^R N_e dr \quad (8)$$

where  $K_4$  equals  $1.343 \times 10^{-3}$  cgs units.

**Doppler frequency slope method.** A modification of Al'pert's expression for calculating the integrated electron density is the Doppler slope method described by Arendt et al. (1965). According to Arendt et al. (1965), when the satellite is at the point of closest approach, the columnar electron content can be represented by

$$\int_0^{h_s} N_e dh = \frac{h_s f_1^2}{K_3} \left( \sigma_2 - \sigma_1 \frac{f_2}{f_1} \right) \left( \sigma_2 - \sigma_1 \frac{f_1}{f_2} \right)^{-1} \quad (9)$$

where  $\sigma_1$  and  $\sigma_2$  are the Doppler slopes at the inflection points for the frequencies  $f_1$  and  $f_2$ , respectively. The criterion for applying the Doppler slope method has been discussed by Arendt (1966).

**Ionosonde method.** The ionosonde method which was suggested by Evans and Holt (1973) for the calibration of the differential phase records utilizes the concept that the electron density distribution in the ionosphere can be represented by the Chapman model of the form

$$N_e = N_m \exp \frac{1}{2} \left\{ 1 - \frac{(h - h_m)}{H_s} \right\} - \exp \left[ - \frac{(h - h_m)}{H_s} \right] \quad (10)$$

where  $H_s$  is the scale height of the neutral particles (atomic oxygen) and  $N_m$  is the electron density at the level of maximum ionization,  $h_m$ .

The maximum electron density of the layer is obtained by the use of a vertical incidence ionospheric sounder and is related to the ordinary wave - critical frequency of the F-layer,  $f_o F2$ , by

$$N_m = \frac{\pi m_e}{e^2} (f_o F2)^2 = 1.241 \times 10^{-8} (f_o F2)^2 \quad (11)$$

where  $N_m$  is in electrons/cm<sup>3</sup>,  $m_e$  is the electron mass,  $e$  is the electron charge and  $f_o F2$  is in Hz.

The scale height of the layer (in km) is defined in terms of

$$H_s = 63.15 + 6.29 \sin \left[ \frac{(h - 9) \pi}{12} \right] + 17.66 \sin \left[ \frac{(D - 60) \pi}{183} \right] \quad (12)$$

where  $h$  is the local time in hours and  $D$  is the day of the year. This analytical model was derived by Klobuchar and Allen (1970) from total electron content data deduced from Faraday rotation measurements of radio wave transmissions from the ATS-3 geostationary satellite.

From incoherent scatter observations made at the Millstone Hill radar facility, Evans and Holt (1973) have concluded that  $h_m$  (in km) can be represented by the function

$$h_m = 280 + 40 \cos \left[ \frac{(h + 1) \pi}{12} \right] \quad (13)$$

When the three parameters,  $N_m$ ,  $H_s$  and  $h_m$  are available, it is then possible to integrate Equation (10) to obtain the integrated electron density in a vertical column to the satellite altitude. Assuming no horizontal gradients of electron density, the electron content in an oblique path can then be computed from Equation (3).

#### Faraday Rotation - Differential Doppler

The combination of the Faraday rotation and differential Doppler technique to determine the ionospheric electron content was originally suggested by Burgess (1962). The mathematical formulation of this method which does not require an assumption on horizontal gradients or restricting the satellite to a circular orbit, i. e., no vertical velocity component, can be derived by differentiating Equations (2) and (6) with respect to time. Hence, combining the two expressions and assuming a differential Doppler frequency shift of zero, the slant electron content can be solved from

$$N_r = \frac{f_1^2}{K_1} \frac{\dot{\Omega}}{H \cos \theta} \quad (14)$$

#### Discussion

For this analysis, it is assumed that the 150- and 400-MHz transmissions from the TRANSIT satellite, Object No. 1970-067A, are recorded at the General Electric Radio-Optical Observatory located at 42.85°N latitude and 74.07°W longitude near Schenectady, New York. The satellite which is in a polar orbit with an inclination of approximately 90°, apogee of 1219 km and perigee of 956 km attains a maximum elevation angle of 71.8° with respect to the receiving station in its orbital pass of June 3, 1974 at approximately 1800 h GMT. It is also assumed that the satellite radiates linear polarization and is traveling in a circular orbit.

Figure 2 depicts for the single frequency method the error in determining the vertical and the slant electron content in the direction of ambiguous Faraday rotation of  $(\pi/2)$  radians at 400 MHz. The peak of the maximum ionization is at an altitude of approximately 280 km in this direction. It is seen that zero error exists for the vertical electron content when the value of the  $M$  factor at an altitude of 354 km is used. For the slant electron content, the altitude for the  $M$  factor value is increased to 380 km.

In determining the effect of the magnetic field orientation on the electron content error estimation, the electron contents were computed in the direction of  $(\pi/4)$  radian - ambiguous angular rotation. It is apparent from Figure 3 that, for both the vertical and slant electron content, zero error is obtained when  $M$  and  $H \cos \theta$  are evaluated at 360 km altitude which is 90 km above the maximum ionization level.

The Faraday rotation angle method results presented in Figure 4 are based on a polarization angle difference of  $(\pi/2)$  radians at 150 MHz. Along

both ray paths, the altitude of the maximum electron density is located at approximately 270 km. The interesting disclosure is the wide separation in the mean field height of  $M$ , 252 km, and  $H \cos \theta$ , 613 km.

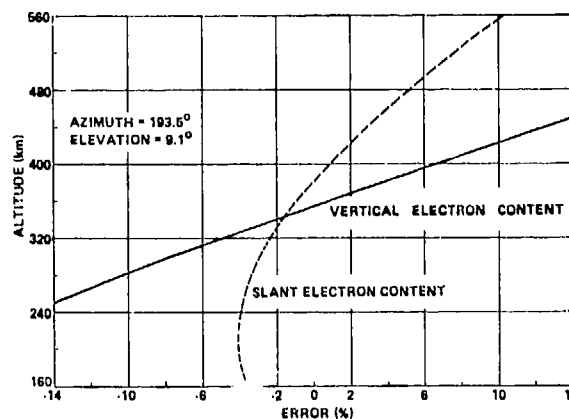


Figure 2. Error in Determining the Vertical and Slant Electron Content in the Direction of Ambiguous Faraday Rotation of  $\pi/2$  Radians at 400 MHz by the Single Frequency Method

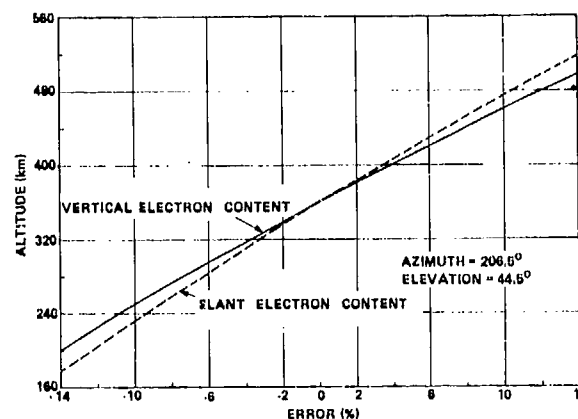


Figure 3. Error in Determining the Vertical and Slant Electron Content in the Direction of Ambiguous Faraday Rotation of  $\pi/4$  Radians at 400 MHz by the Single Frequency Method

As shown in Figure 5, the altitude for computing  $M$  and  $H \cos \theta$  to attain zero percent error for the Faraday rotation rate method appears to be a function of the propagation direction, or in other words, the orientation and intensity of the magnetic field. It is seen that the mean field height for the slant electron content is on the order of 300- to 400-km above that for the vertical electron content.

The hybrid method calculations shown in Figure 6 reveal that 100% accuracy is achieved when 454 and 602 km are selected as the mean field heights for the vertical and slant electron content, respectively.

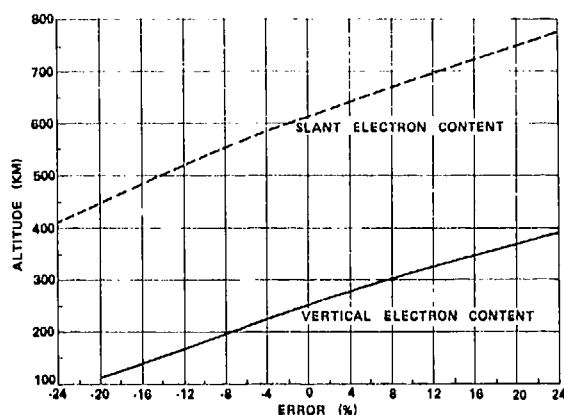


Figure 4. Error in Determining the Vertical and Slant Electron Content at 150 MHz by the Differential Polarization Rotation Angle Method

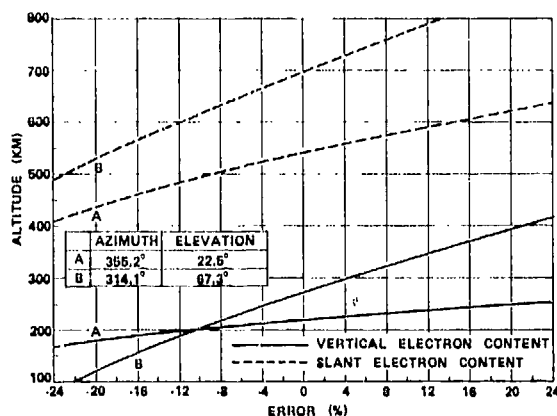


Figure 5. Error in Determining the Vertical and Slant Electron Content at 150 MHz by the Polarization Rotation Rate Method

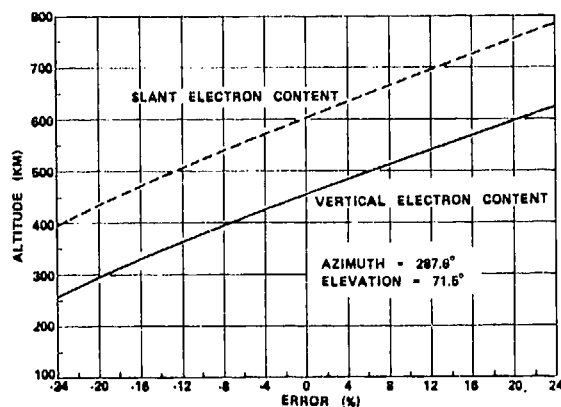


Figure 6. Error in Determining the Vertical and Slant Electron Content at 150 MHz by the Faraday-Doppler Hybrid Method

The electron content prediction accuracy attained by employing the Doppler phenomena is summarized in Table 1. Of the three analytical techniques investigated, the ionosonde method seems to be the more accurate.

TABLE 1  
ERROR IN IONOSPHERIC ELECTRON CONTENT  
ESTIMATION UTILIZING DISPERSIVE  
PHASE-DOPPLER TECHNIQUE

Analytical Method	Error (%)
Doppler Frequency Shift	28.8 - 114.4
Doppler Frequency Slope	29.4
Ionosonde	11.1

#### References

Al'pert, Y. L., "A Method for Studying the Ionosphere by Means of an Artificial Earth Satellite", *Uspekhi Fizicheskikh Nauk*, Vol. 64, pp 3-14, January-April 1958.

Arendt, P. R., A. Papayouanou and H. Soicher, "Determination of the Ionospheric Electron Content Utilizing Satellite Signals", *Proc. IEEE*, Vol. 53, pp 268-277, March 1965.

Burgess, B., "Ionospheric Studies Using Satellite Radio Transmissions", in *Electron Density Profiles in the Ionosphere and Exosphere*, NATO Advanced Institute Conference Proceedings, Vol. 2, pp 224-227, Pergamon Press, London, 1962.

Evans, J. V. and J. M. Holt, "The Combined Use of Satellite Differential Doppler and Ground-Based Measurements for Ionospheric Studies", *IEEE Trans. Antennas Propagat.*, Vol. AP-21, pp 685-692, September 1973.

IAGA Commission 2 Working Group 4, Analysis of the Geomagnetic Field, "International Geomagnetic Reference Field 1965.0", *J. Geophys. Res.*, Vol. 74, pp 4407-4408, August 15, 1969.

Klobuchar, J. A. and R. S. Allen, "A First-Order Prediction Model of Total-Electron-Content Group Path Delay for a Midlatitude Ionosphere", *Air Force Cambridge Research Laboratories, Air Force Surveys in Geophysics No. 222*, AFCRL-70-0403, July 1970.

Millman, G. H., "Field-Aligned Ionization Scatter Geometry", *J. Geophys. Res.*, Vol. 74, pp 900-905, February 1, 1969.

Millman, G. H., "An Analysis of Ionospheric Electron Content Measurements Utilizing Satellite-Emitted Signals", *General Electric Technical Information Series Report No. R74EMH24*, Dec. 1974.

Nisbet, J. S., "On the Construction and Use of the Penn State MK I Ionospheric Model", *Pennsylvania State University, Ionosphere Research Laboratory Scientific Report No. 355*, May 1970.

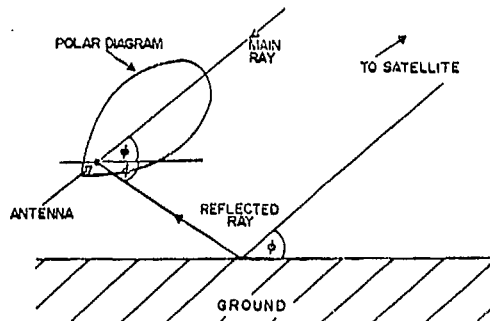
# ON THE EFFECT OF GROUND REFLECTIONS ON FARADAY ROTATION MEASUREMENTS OF IONOSPHERIC STRUCTURE.

J. Jones and A.R. Webster  
Department of Physics & Centre for Radio Science  
University of Western Ontario, London, Canada.

## INTRODUCTION

One of the assumptions which is often made in the analysis of Faraday rotation measurements, namely that the measured angle of rotation is essentially that of the wave from the source after it has passed through the ionosphere, is examined in this paper. Particular attention is given to the effect of ground reflections which, in the past have often been ignored for a number of reasons of which probably the two most important have been 1) they have been considered negligible when highly directive antenna systems are used and 2) the calculations involved are usually regarded as being very tedious. In the remainder of this paper we show that ground reflections are usually too large to be ignored and that the problem can be efficiently dealt with in terms of matrix operators, which, far from being tedious have an elegance which is very appealing.

The results described in this paper refer to a system similar to that used at the University of Western Ontario (Webster and Lyon, 1974) for the observation of transmissions from ATS-3 which is at an elevation of about  $40^\circ$  at London, Ontario ( $43^\circ$  N,  $81^\circ$  W). The antenna system for this installation which was a 7-element crossed Yagi array with a beam width of about  $40^\circ$  was considered to be probably representative of the sort of array which is often used in this application.



From Figure 1, we see that if the antenna is directed towards the satellite which is at an elevation of  $\phi$  the reflected ray will approach the antenna from an angle of  $2\phi$  away from the main axis and the question is really: is the antenna sufficiently directive that the gain at an angle of  $2\phi$  off axis is negligible? We have made calculations for a variety of model 7-element Yagi arrays and find that at  $80^\circ$  from the main beam the power gain is typically 10 db down so that the magnitude of the reflected ray could be as much as 30% of that of the main ray. At worst, this could cause the measured polarization angle to be about  $20^\circ$  in error. Whether or not this worst case is realized depends upon the nature of the ground and the phase differences introduced into the reflected rays.

## THEORY

As we have already remarked, the problem can be treated efficiently in terms of matrix operators because of the linear nature of electromagnetic radiation. We can represent any completely polarized wave such as is transmitted by a satellite by a vector

$$\Pi = \begin{bmatrix} E_r \\ E_y \end{bmatrix}.$$

After reflection from a surface the wave is altered such that the modified vector is given by  $\Pi' = R\Pi$ , where

$$R = \begin{bmatrix} r_H & 0 \\ 0 & r_V \end{bmatrix}$$

if the plane defined by the y-z axes is normal to the reflecting surface and  $r_H$  and  $r_V$  are the "horizontal" and "vertical" reflection coefficients respectively.

Since the reflected ray is not normal to the incident ray which we have taken to be coincident with the main axis of the antenna array, we must resolve  $\Pi'$  into the plane normal to the incident ray. The resolved vector  $\Pi''$ , is given by  $\Pi'' = C \Pi'$  where

$$C = \begin{bmatrix} 1 & 0 \\ 0 & \cos 2\phi \end{bmatrix}$$

We must also include the effect of the extra path difference traversed by the reflected ray and the fact that the reflected ray approaches the antenna obliquely. Since both components of  $\Pi''$  are affected equally in this respect we represent these factors by scalar coefficients  $h(\phi)$  and  $g(2\phi)$  where

$$h(\phi) = \exp - i(2khsin\phi)$$

and  $g(2\phi)$  is the voltage gain of the antenna at an off-axis angle of  $2\phi$ .

#### NUMERICAL RESULTS

As might be expected, the numerical computations predict no error in the measured polarization angle when the incident wave is polarized either perpendicular ("horizontally") or parallel ("vertical") to the plane of incidence, and the greatest error occurs when the angle of polarization is midway between these two positions.

For an antenna placed at two wavelengths above the ground we have calculated the maximum error in the measured polarization angle as a function of the angle of elevation (assuming the antenna always to be directed at the satellite) for several representative grounds. The results of these calculations are shown in Figure 2.

The main ray can be represented as  $\Pi = I \Pi$  where  $I$  is a unit matrix.

The sum of the main and reflected rays is given by  $\Pi_t = L \Pi$  where  $L = I + g(2\phi) h(\phi) C R$ .

The outputs from the crossed orthogonal antenna system are proportional to the two components of  $\Pi_t$ . The polarization angle of the wave may be measured in several ways and the following procedure may be regarded as typical. A quarter-wave section is placed in the vertical antenna output and the two signals are then summed. It is easily shown that the phase of the composite signal relative to that of the horizontal signal is equal to the polarization angle. We have duplicated this procedure numerically and have compared the apparent polarization angle with that of the incident signal  $\Pi$ . The results of these calculations are presented in the following section.

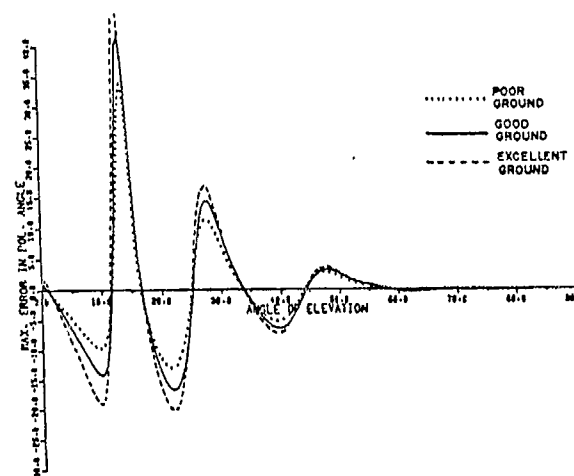


Figure 2

The ground parameters are taken from Jordan and Balmain (1968) and are as follows:

- i) poor ground  $\epsilon = 7$   
 $\sigma = 10^{-3} \text{ mho m}^{-1}$ ,
- ii) good ground  $\epsilon = 15$   
 $\sigma = 12 \times 10^{-3} \text{ mho m}^{-1}$ ,
- iii) excellent ground  $\epsilon = 30$   
 $\sigma = 30 \times 10^{-3} \text{ mho m}^{-1}$ .

Next we have fixed the angle of elevation first at  $20^\circ$  and then at  $40^\circ$  and varied the antenna height. Figures 3 and 4 show how the error varies with height.

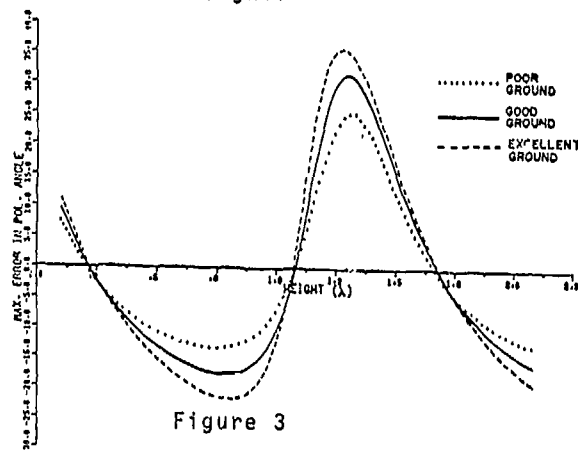


Figure 3

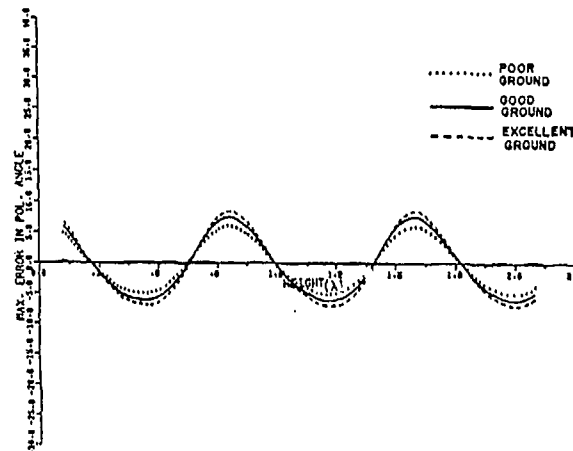


Figure 4

#### DISCUSSION

The curves presented in Figure 2 show that the error introduced by the ground reflection can be quite considerable especially at angles of elevation close to the Brewster angle. Although the error varies with the nature of the ground, at 137 MHz the variation is not very great, being about 10% between the high and low conductivity grounds. This is primarily because at this frequency the imaginary part of the dielectric constant is relatively small and the ground behaves very much like a perfect dielectric. It is also evident that only for elevations of  $60^\circ$  and greater is the error very small - at  $40^\circ$  the error is about  $8^\circ$  and certainly cannot be neglected.

By varying the phase of the reflected ray through an adjustment of the antenna height, the error can be made either positive or negative and this is shown in Figure 4. At  $40^\circ$  elevation an unfortunate choice of antenna height

can cause polarization errors as great as  $10^\circ$  but it is also possible to remove the error completely. It is interesting to note that these "no-error" heights are substantially independent of the ground parameters, thus the system, once adjusted, should remain calibrated under most weather conditions (except of course for snow). The same sort of behaviour is also seen at  $20^\circ$  elevation but in this case the error can be as great as  $40^\circ$ . With such large variations the fixing of the antenna height would be quite critical with the height having to be set to better than  $1/50$  th of a wavelength, i.e. to about 1 cm or so. Since the electron density in the F-region has a very strong diurnal component, it is possible that the apparent periodic perturbations of the overall fairly rapid rotation of the polarization angle will be most evident at dawn and dusk. We have examined our records for this effect and find that it is regularly observed.

In Figure 5 we show a plot of "ramp" period, which is the time required for the polarization angle to rotate through  $180^\circ$ , against the period of the suspected spurious TID. As can be seen the two quantities are strongly correlated as would be the case if they were generated by ground reflections. Similar fluctuations are also observed with angle of arrival measurements i.e. periodic angle of arrival fluctuations which are correlated with the angle of polarization, and can be explained in terms of this model. However the limited space available prevents us from discussing this aspect further.

In conclusion we wish to mention several methods which can be used to reduce the effect of ground reflections: i) placing the antenna at one of the "no-error" heights, ii) designing the antenna system such that the gain in the direction of the reflected ray is negligible. To be sure that the error is less than  $1^\circ$ , the gain must be at least 30 db down in the direction of the reflected ray. iii) Alternatively we can use a ground plane with an antenna whose polar diagram is accurately known and make the appropriate corrections to the measured values of the polarizations angles.

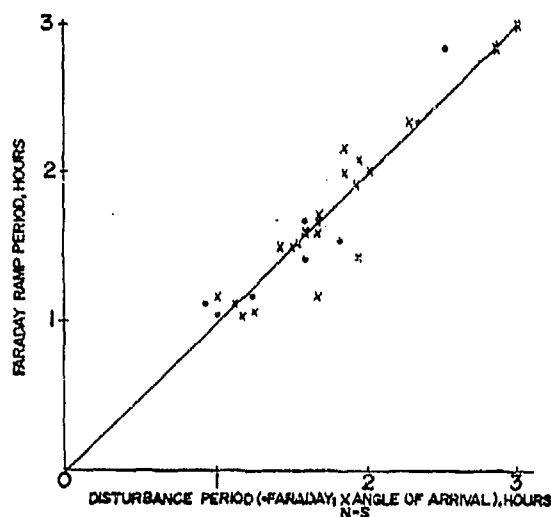


Figure 5

#### REFERENCES

Jordan, E.C. and Balmain, K.G., 1968, "Electromagnetic Waves and Radiating Systems" Prentice-Hall, Inc. New Jersey.

Webster, A.R. and Lyon, G.F., 1974, J.A.T.P. 36, 943.



A PULSED PLASMA PROBE TECHNIQUE FOR SIMULTANEOUS IN-SITU  
MEASUREMENTS OF DENSITY, TEMPERATURE, DENSITY  
FLUCTUATION POWER SPECTRA AND AMBIENT ELECTRIC FIELDS

Edward P. Szuszczewicz  
and

Julian C. Holmes  
E. O. Hulburt Center for Space Research  
Naval Research Laboratory  
Washington, D. C. 20375

ABSTRACT

We have developed a pulsed probe technique for improved reliability and expanded versatility in Langmuir probe measurements. This technique is capable of high spatial and temporal resolution and as such is particularly well suited for experimental investigations of ionospheric irregularities. As an improved diagnostic tool it eliminates the distortions that can result in the determinations of electron densities, energy distribution functions and ambient electric fields when probe surface conditions change within the measurement period. Under fluctuating plasma conditions, the technique can determine the aforementioned parameters and simultaneously measure the density fluctuation power spectrum. We have employed this technique on a scientific payload launched on an Aerobee 150 rocket (NC3,256) from White Sands Missile Range on 29 June 1974 at 2031 MST (30 June 1974, 0331 GMT). The payload reached an apogee of 229.5 km and on up- and downlegs passed through blanketing sporadic E layers. We describe the details of the diagnostic procedure and present the first in situ measurements of electron temperature in a sporadic E layer as carried out by our new technique.

INTRODUCTION

The pulsed plasma probe (referred to as  $P^3$ ) is a Langmuir probe with a specialized electronic procedure for generating current-voltage characteristics in a way which results in improved reliability and expanded versatility in laboratory and ionospheric plasma studies<sup>1</sup>. As an improved diagnostic tool the  $P^3$  technique eliminates the errors that can result in the determinations of electron densities, energy distribution functions and ambient electric fields when probe surface conditions change within the measurement period<sup>1-5</sup>. This capability extends into the domain of fluctuating plasma conditions where the  $P^3$  technique additionally provides a simultaneous measurement of the density fluctuation power spectrum and demonstrates itself as an important diagnostic device for in situ investigations of irregular ionospheric structures.

The motivation for development of the  $P^3$  technique was provided on the one hand by the need for high resolution in situ measurements of ionospheric irregularities and inhomogeneities and on the other hand by the questioned integrity of Langmuir probe measurements in rocket and satellite applications. In ionospheric and laboratory studies, there is evidence that varying probe surface conditions may cause the discrepancy between the temperatures measured by radar backscatter and the conventional Langmuir probe<sup>3-10</sup>. It is widely known that changing probe surface conditions can result in measured values of electron temperature which substantially exceed that actually present within the ambient plasma. It is also generally accepted in the probe vs backscatter controversy that, if in fact the probe is in error, its measurements of  $T_e$  are too high, at times by as much as 120%.

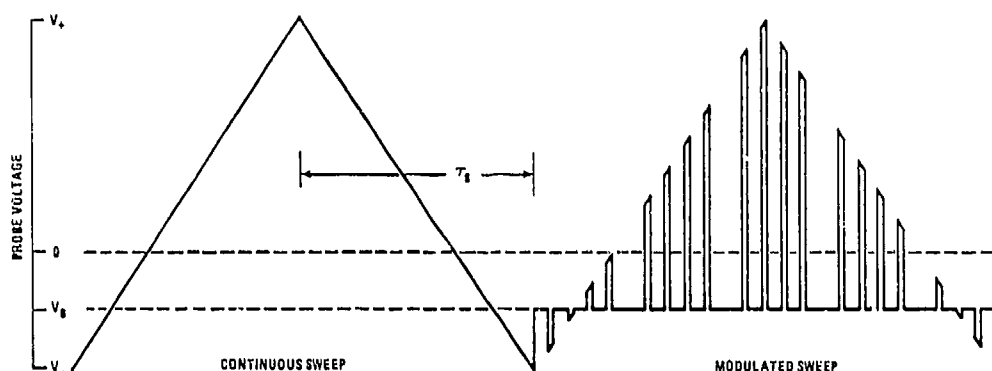


FIGURE 1

Continuous and pulsed modes of probe operation. Figure 1a represents the conventional approach while Figure 1b shows the pulse-modulated sweep utilized in the  $P^3$  technique.

The potential problems of surface contamination and associated distortion of measurement are most acute in rocket applications since short flights do not permit sufficient time for surface desorption and resulting probe cleanup. However, satellite users are not free from such difficulties as evidenced by implications of the probe vs backscatter controversy and the fact that the Langmuir probes on the Atmospheric Explorer series employ two new features, a surface of highly oriented tungsten crystals and a heating element for thermal cleanup<sup>1</sup>. These two features have been added in an attempt to improve the accuracy of their measurement procedure.

The point should be clear: surface contamination is a genuine source of difficulty not only for conventional Langmuir probes but for any device which has an active electrode in contact with a plasma. We've addressed this problem with our  $P^3$  technique, and our studies have already established its ability to circumvent the associated distortions in plasma measurements. The details of these efforts are available to the interested reader<sup>1-3</sup>. This paper demonstrates how our efforts to solve the contamination problem has also resulted in a technique to measure electron temperature, density and ambient electric fields under fluctuating plasma conditions. This capability comes with confidence that the integrity of the results are not compromised by surface layering phenomena.

#### THE TECHNIQUE

Figure 1 shows two electronic

modes of Langmuir probe operation. Figure 1a depicts a linear sawtooth voltage which represents the conventional approach to Langmuir probe operation. (There are variations of this, but basically some form of continuous voltage sweep is applied between maximum voltage excursions  $V_+$  and  $V_-$ .) Figure 1b shows the pulse-modulated sweep utilized in the  $P^3$  technique. This mode employs a modulated sweep of pulses which follows a sawtooth envelope. Between pulses, the sweep returns to a constant baseline voltage  $V_B$ . A sequence of four pulses generates four distinct I-V data points for the probe's current-voltage characteristic. The fifth pulse is blanked out so that the current  $I_B$  collected by the probe during the interpulse period can be monitored and used as a measure of variations in the probe-plasma system. These variations might include changes in the probe's surface

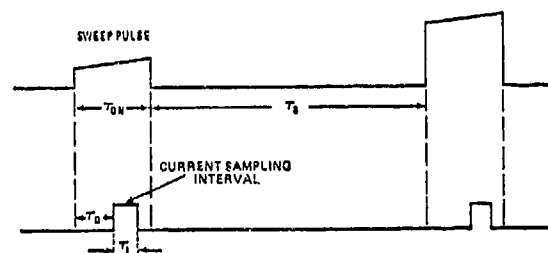


FIGURE 2

Expanded time scale of two consecutive pulses in the pulse-modulated mode of Figure 1b. Relative to the sweep pulse is shown the sampling interval for probe current.

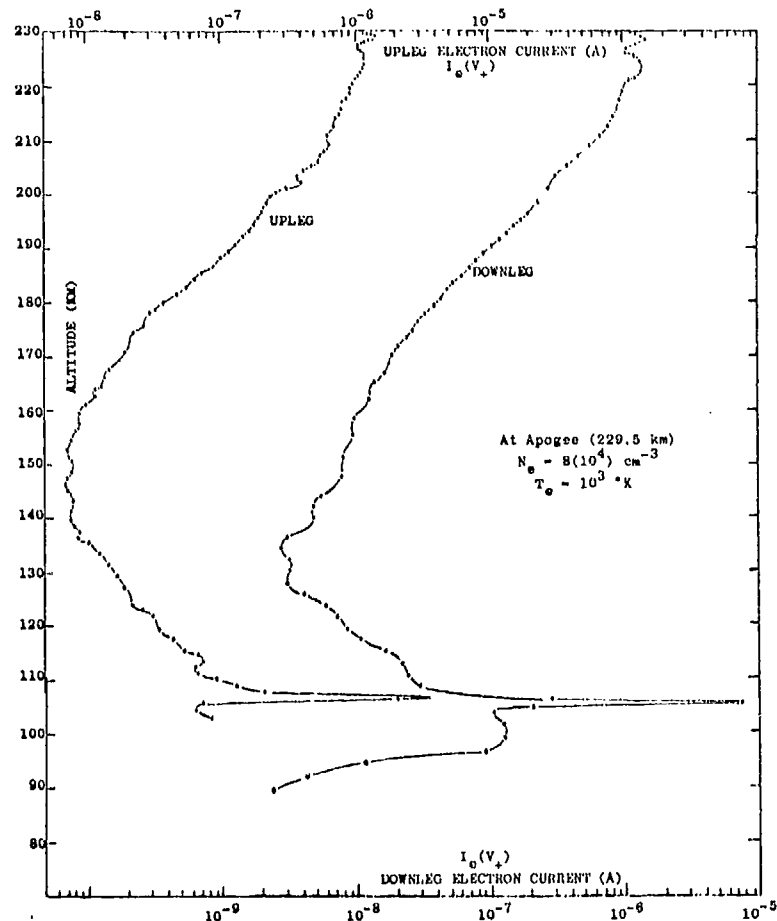


FIGURE 3

Relative electron density profiles collected by the  $p^3$  technique above White Sands, New Mexico at 2031 hrs LT on 29 June 1974. Note the shifted abscissa scales for up- and downleg portions of the flight.

condition, plasma oscillations, or rapid variations in plasma density as seen by a rocket or satellite passing through an irregularity or inhomogeneous ionospheric structure.

The pulse sequencing procedure is such that the probe rests at its baseline potential  $V_B$  for a period which is much longer than the pulse width. Figure 2 is an expanded time scale showing two successive pulses with pulse and baseline durations identified as  $\tau_{on}$  and  $\tau_B$ , respectively. The Figure shows that the probe current is always sampled during a subinterval within a sweep pulse, with the subinterval position  $\tau_D$  and sampling duration  $\tau$  adjusted so that the plasma may

achieve a steady state condition. Thus circuit transients are eliminated from possible distortions of the current signal. With  $\tau_{on}$  much less than  $\tau_B$  and the time constant of a contamination surface layer<sup>3-5</sup>, the pulse procedure maintains the probe surface condition and associated voltage drop at a constant level<sup>1,3</sup>. Therefore, any fluctuations in  $I_B$  provide a direct measure of variations in ambient plasma conditions. Density fluctuations  $\delta N_e$  can then be uniquely unfolded from the resulting current-voltage characteristic, and electron temperature and density determined by standard analyses procedures<sup>1,2</sup>.

The baseline current measurement

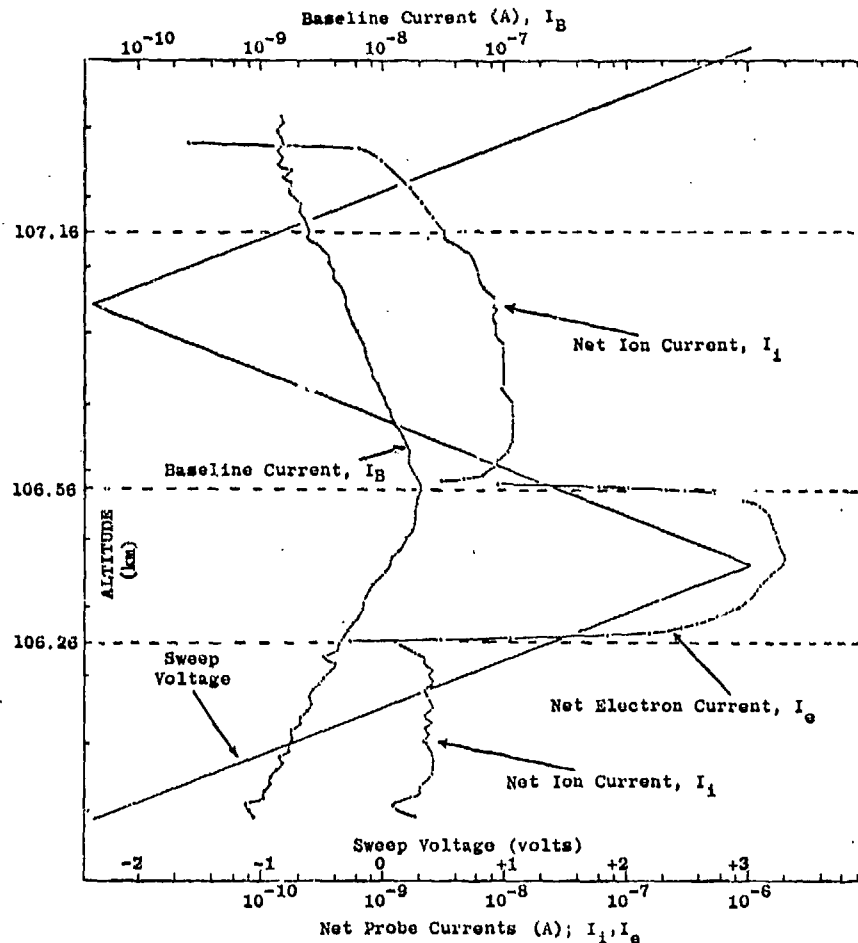


FIGURE 4

Expanded view of sweep voltage and probe currents as the payload traversed the  $E_s$  layer on the upleg portion of the flight.

$I_B$  enables the  $P^3$  technique to measure the power spectra  $P_N(k)$  of plasma fluctuations. These spectra give the frequency distribution of energy in a plasma irregularity and provide an important test parameter for the physical mechanisms driving the irregularity<sup>13-15</sup>. Similarly, these spectra test the correlation between measured ionospheric irregularities and an observed scintillation<sup>16</sup>. Thus, the simultaneous in situ measurements of the power spectra of ionospheric irregularities and their associated electron densities, temperatures and electric fields provide an important means for classifying observed irregularities and evaluating relevant

theoretical models.

The power spectrum measurement capabilities of the  $P^3$  technique are identified with the  $I_B$  sampling frequency, which in the flight described in the next section was set at 100/sec. This parameter can readily be extended to observe higher frequency components in ionospheric irregularities.

#### APPLICATION TO SPORADIC-E

A pulsed plasma probe was part of the scientific payload launched on an Aerobee 150 rocket (NC3.256) from White Sands Missile Range on 29 June

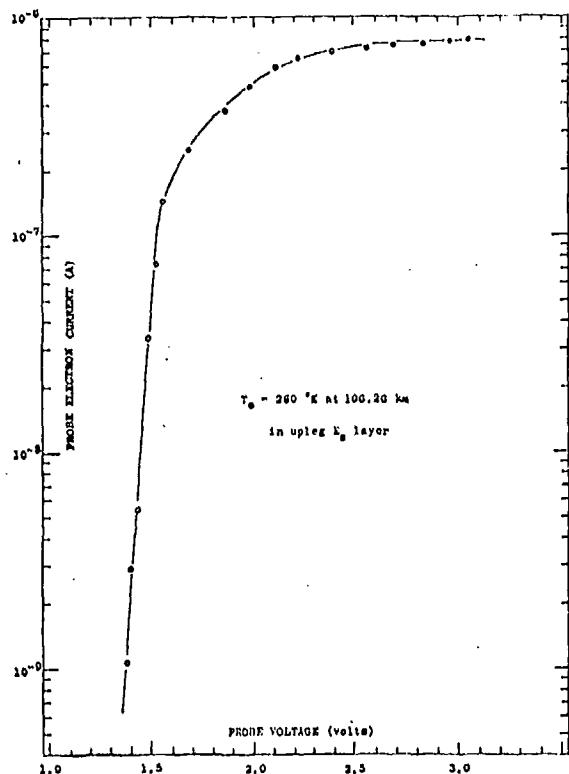


FIGURE 5

Semilogarithmic plot of the electron retarding field and saturation portions of the I-V characteristic. This plot has been unfolded from the voltage and density dependent currents shown in the previous figure. The resulting electron temperature, 260 K, corresponds to the ambient value at 106.26 km.

1974 at 2031 MST (30 June 1974, 0331 GMT). The payload reached an apogee of 229.5 km and on up- and downlegs passed through blanketing sporadic-E layers. Figure 3 shows the profiles of relative electron density (Note the shifted abscissa scales for up- and downlegs!) indicated by the probe current collected at the maximum positive sweep pulse voltage  $V_1^+$ . On this flight the circuit parameters (See Figs. 1 and 2) were

$$\begin{aligned} \tau &= 378 \text{ msec}, \\ (V_-, V_1^+) &= (-2.378\text{v}, +3.019\text{v}), \\ (\tau_{on}, \tau_B) &= (102\mu\text{s}, 1851\mu\text{s}), \\ (\tau_D, \tau_1) &= (44\mu\text{s}, 50\mu\text{sec}), \\ V_1^- &= 0 \text{ v}. \end{aligned}$$

With this arrangement in the 5-pulse format, the baseline current  $I_B$  was sampled every 9.75 msec while a complete I-V characteristic was generated in 378 msec. Fig. 4 is an expanded view of probe currents and

voltage as the payload traversed the  $E_s$  layer on the upleg portion of flight. Shown as a function of altitude are the net ion and electron currents<sup>7</sup> collected by the probe. The baseline current values of  $I_B$  are also shown and represent samples of relative density taken every 9.75 msec as the probe moved through the layer at 1.44 km/sec. Because plasma density is a rapidly changing function of altitude  $Z$  within the  $E_s$ -layer, the currents  $I_i$  and  $I_e$  are dependent upon the local plasma density  $N_e$  and the applied probe voltage  $V$  (also shown in Fig. 4). With  $I_B$  providing a measurement of variations in  $N_e$ , an  $I(V)$  characteristic was unfolded from the  $I(V, N_e)$  data and the ambient electron temperature determined from  $\delta[\ln(I)]/\delta V$  in the retarding-field region<sup>8</sup> of the probe characteristic<sup>12</sup>. Local absolute value of  $N_e(Z)$  are then also determinable from the  $I(V)$  curve by standard Langmuir probe analyses procedures applied to the current collected at the plasma potential and within the electron saturation portion of the  $I(V)$  curve<sup>12</sup>. Probe currents and associated plasma densities were normalized to the value of  $I_B$  at 106.26 km and the resulting semilogarithmic plot of electron current for  $T_e$  determination is shown in Fig. 5. A standard retarding-field analysis of this curve resulted in a measured electron temperature of 260°K. We believe this to be the first successful in situ measurement of electron temperature in an  $E_s$  layer and perhaps the lowest value ever reported by a probe technique at E-region altitudes. These results attest to the capabilities of the  $P^3$  technique to circumvent the difficulties associated with surface contamination and to measure plasma parameters under time-varying conditions.

#### ON THE MEASUREMENT OF ELECTRIC FIELDS

If more than one pulsed plasma probe is utilized, measurements of the ambient electric field can be made simply by dividing the differences in plasma potential  $V_0$ , as measured by any pair of identical probes, by their separation in space. The measured field component is then along the line joining a given pair of probes. Using this technique, only two pairs of probes, perpendicular to each other in separate planes, are needed to completely determine the ambient electric field vector. This has considerable advantage over the technique of the floating double probe which requires three pairs of colinear

probes to complete the same measurement is.

Because the floating potential  $V_f$  of a probe immersed in a plasma is uniquely coupled to the plasma potential through the ambient plasma parameters and the probe's size and geometry<sup>16</sup>, the ambient electric field  $E$  can also be measured by direct observation of the floating potential  $V_f$  of each probe. Using the experimentally observed values of  $V_f$  in place of  $V_0$  in the procedure outlined in the preceding paragraph then results in a determination of the ambient electric field.

It is important to note that the floating potential approach to determine  $E$  must assume identical plasma conditions at each probe location since the important difference ( $V_f - V_0$ ) can only be considered unique for a unique set ( $R/\lambda_D, T_i/T_e, m_e/M_i$ ), where  $R/\lambda_D$  is the ratio of probe radius to electron Debye length,  $T_i$  and  $T_e$  are the respective ion and electron temperatures, and  $m_e/M_i$  is the electron-to-ion mass ratio. To employ this assumption may lead to error since an ambient electric field can be a result or cause of gradients in either density, temperature, ion composition or combinations of all three. It is therefore scientifically sound to make an electric field measurement using separately the observations of  $V_f$  and  $V_0$  as outlined above. This is fully within the capability of our  $P^3$  technique.

Finally, it should be emphasized that the measurement of ambient electric fields by any probe technique is extremely sensitive to symmetry of the measuring system and the conditions on the probe surfaces. We have found in laboratory<sup>3</sup> and ionospheric applications<sup>10</sup> that conventional single or double probe techniques can have variable floating potential offsets from tens of millivolts to one or two volts as a result of charging on the probe's contaminated surfaces. This effect can clearly compromise the electric field measurements. The  $P^3$  technique has been demonstrated to be free of this perturbation and consequently yields a greatly improved measurement integrity.

#### REFERENCES

1. Holmes, J. C. and E. P. Szuszczevicz, Rev. Sci. Instr. (1975, in press).
2. Szuszczevicz, E. P. and J. C. Holmes, "An improved Langmuir probe technique," Bull. Am. Phys. Soc. 18, 1277 (1973).
3. Szuszczevicz, E. P. and J. C. Holmes, "An approach to a hysteresis-free Langmuir probe," Trans. Am. Geophys. U. 55, 377 (1974).
4. Wehner, G. and G. Medicus, "Reliability of probe measurements," J. Appl. Phys. 23, 1035 (1952).
5. Hiroa, K. and K. Oyama, "A critical study on the reliability of electron temperature measurements with a Langmuir probe," J. Geom. Geoelectr. 24, 415 (1972).
6. Benson, R. F., "Simultaneous in situ electron temperature comparison of Alouette 2 probe and plasma resonance data," J. Geophys. Res. 78, 6755 (1973).
7. Hanson, W. B., L. H. Brace, P. L. Dyson, and J. P. McClure, "Conflicting electron temperature measurements in the upper F region," J. Geophys. Res. 74, 400 (1969).
8. McClure, J. P., W. B. Hanson, A. F. Nagy, R. J. Cicerone, L. H. Brace, M. Baron, P. Bauer, H. C. Carlson, J. V. Evans, G. N. Taylor and S. F. Woodman, "Comparison of  $T_e$  and  $T_i$  from OGO-6 and various incoherent scatter radars," J. Geophys. Res. 78, 197 (1973).
9. Sayers, J., "In situ probes for ionospheric investigations," JATP 32, 663 (1970).
10. Sturges, D. J., "An evaluation of ionospheric probe performance - I. Evidence of contamination and cleanup of probe surfaces," Planet. Space Sci. 21, 1029 (1973).
11. Brace, L. H., R. G. Theis and A. Dalgarno, "The cylindrical electrostatic probes for Atmospheric Explorer-C, -D and -E," Radio Science 8, 341 (1973).
12. Chen, F. F., "Electrical probes," in Plasma Diagnostic Techniques, edited by R. H. Huddleston and S. L. Leonard (Academic, New York, 1965), p. 113.
13. Prakash, S., S. P. Gupta, and B. H. Subbaraya, "Irregularities in the equatorial E-region over Thumba," Radio Sci. 4, 791 (1969).

14. Ott, E., and D. T. Farley, "The k-spectrum of ionospheric irregularities," J. Geophys. Res. 79, 2469 (1974).
15. Ossakow, S. L., "Research at NRL on theoretical and numerical simulation studies of ionospheric irregularities," NRL Report, September 1974.
16. Rufenach, C. L., "Wavelength dependence of radio scintillations: Ionospheric and interplanetary irregularities," J. Geophys. Res. 79, 1562 (1974).
17. This is "quick-look" data and doesn't reflect all  $I(V^+)$  values in Fig. 3 nor  $I_1$  values in Fig. 4. The peak in the  $I_{upleg}$   $E_s$ -layer shown in Fig. 3 was extrapolated from the  $I_B$  data.
18. Fahleson, U., "Theory of electric field measurements conducted in the magnetosphere with electric probes," ESO SN-28 (Royal Institute of Technology, Stockholm), May 1966.
19. Szuszczewicz, E. P., "Area influences and floating potentials in Langmuir probe measurements," J. Appl. Phys. 43, 874 (1972).
20. Szuszczewicz, E. P., "First measurements of electron temperature in the D-region with a symmetric double probe," J. Geophys. Res. 78, 7567 (1973).

APPLICATION OF ELECTRIC FIELD AND FAST LANGMUIR PROBES  
FOR THE IN SITU OBSERVATION OF ELECTROSTATIC WAVES AND  
IRREGULARITIES

Michael C. Kelley  
School of Electrical Engineering  
Cornell University  
Ithaca, New York 14850

and

C.W. Carlson and F.S. Mozer  
Space Science Laboratory  
and  
Physics Department  
University of California  
Berkeley, California 94720

ABSTRACT

Recent developments in electric field and fast langmuir probe measurement have allowed more detailed in situ study of electrostatic waves and irregularities. The techniques will be described briefly as will the rationale for making simultaneous measurements of vector wave electric fields ( $\delta E$ ) and plasma density fluctuations ( $\delta n/n$ ) as a function of frequency. These two quantities are related in electrostatic waves and irregularities much as  $\delta E$  and  $\delta B$  are related in an electromagnetic wave since

$$\vec{E} = -\nabla\phi = -i\vec{k}\phi$$

where  $\phi \propto \delta n/n$  for most waves in a collisionless plasma. Simultaneous measurement of  $\delta E$  and  $\delta n/n$  thus yield  $\vec{k}$  as a function of frequency and hence the real part of the dispersion relation. The direction of  $\vec{k}$  can also be obtained. Since electromagnetic waves have no  $\delta n/n$  component, these two types of wave can be distinguished by comparison of the two measurements. Electrostatic waves may also exhibit fluctuations in temperature and a technique to make high time resolution electron temperature measurements is also discussed. Knowledge of such waves is of essential importance to the study of ionospheric irregularities since in a low  $\beta$  plasma such waves have

phase velocities comparable to the thermal and drift velocity of the plasma constituents.

INTRODUCTION

Most theories for irregular structures in the earth's ionosphere propose that the generation mechanisms are electrostatic instabilities. In some cases such explanations have been remarkably successful in explaining the characteristics of in situ and ground based radar observations of the phenomenon. This is particularly true in the equatorial E region where rocket and radar measurements are in good agreement with generation of the irregularities via two mechanisms; the two stream instability which draws energy from the differential drift between E region ions and electrons, and the gradient drift instability in which energy is drawn from the zero order gradient in electron density. A review of the present ideas concerning the equatorial E region has been made by Farley (1970).

The purpose of this paper is to discuss some new techniques and some variations on old methods developed to make in situ measurements of ionospheric irregularities. Recent results using some of these techniques are reviewed elsewhere in this volume (Kelley and Mozer, 1975).



Electrostatic instabilities result in fluctuations of the plasma density, electric field and, in some cases, of the plasma temperature. Since the electric field is a vector quantity, its measurement contains more information than does measurement of the other quantities. In fact since  $\delta \vec{E} = -\nabla \phi = -ik\phi$ , measurement of  $\delta \vec{E}$  can yield the direction of the propagation vector for the wave. This is illustrated in Figure 1 where the dc and ac electric field

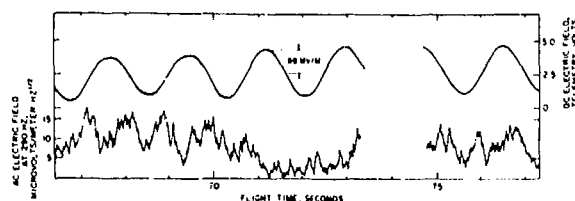


Fig. 1 Raw data displaying the polarization of the ac signal and its relation to the dc electric field observed using the same antenna.

signals due to waves in the auroral electrojet (Kelley and Mozer, 1973) are plotted. The sine wave modulation of the dc field is due to the spin of the rocket in the ambient field. The ac signal is modulated at twice the spin rate since the wave frequency is much greater than the spin frequency. Such a measurement of  $\delta \vec{E}$  thus yields the direction of  $\vec{k}$  with an ambiguity  $180^\circ$ . In this case (Kelley and Mozer, 1973; 1975)  $\vec{k}$  was shown to be parallel to the E region current.

Simultaneous measurement of  $\delta \vec{E}$  and  $\delta n/n$  can also be used to determine the wave phase velocity in low frequency collisionless cases where the electron distribution is determined by flow along field lines to satisfy the Boltzmann relation,  $\delta n/n = e\phi/kT$ . (Kelley and Mozer, 1972), since:

$$\frac{\delta \vec{E}}{\delta n/n} = \frac{kT}{e} \vec{k} \quad (1)$$

This ratio measured as a function of  $\omega$  yields  $k(\omega)$ . When collisions are important, which can be true in the F as well as the E region (Hudson, 1974) fluctuations in electron temperature may

also be required to determine  $k(\omega)$ . We are concerned primarily with low frequency ( $\omega < \omega_{pi}$ ) waves and hence do not discuss detection of electron plasma waves ( $\omega \sim \omega_{pe}$ ).

#### ELECTRIC FIELD MEASUREMENTS

A block diagram of a vector ac and dc electric field experiment is presented in Figure 2. Such detectors have been described in detail elsewhere and only

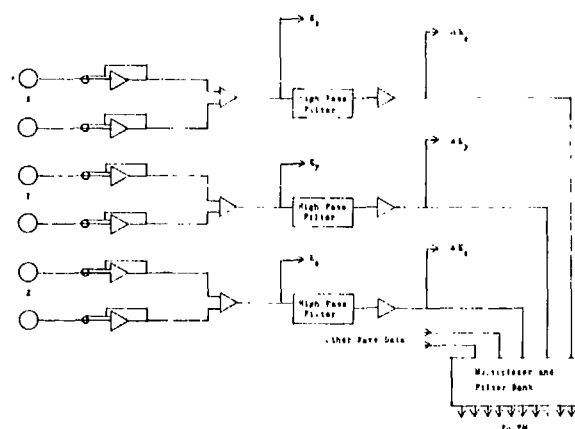


Fig. 2 Block diagram of a dc/ac electric field detector.

a few points of relevance to electrostatic wave measurements will be made here (Storey, 1963; Fahleson, 1967). For the study of electrostatic waves the doppler shift of the signal of interest must be taken into account since the phase velocity ( $\vec{V}_p$ ) of even the fastest of such waves is comparable to the velocity of the spacecraft ( $\vec{V}_s$ ). Many waves of interest have very small phase velocities in the plasma rest frame (irregularities) and the doppler shifted frequency  $\omega = \omega_p + \vec{k} \cdot (\vec{V}_p - \vec{V}_s)$  reduces to  $(\vec{k} \cdot \vec{V}_p - \vec{V}_s)$ . Thus if the wavelength regime of interest is known, the required frequency response of the combined instrument and telemetry link can be easily defined. This is particularly true for low altitude satellites since, even in the auroral zone where the plasma velocities can exceed a km/s,  $|\vec{V}_p - \vec{V}_s|$  differs from  $|\vec{V}_s|$  by at most 20%. As an example a satellite ( $V_s \sim 7$  km/s) designed to study 3 meter waves in conjunction with the Jicamarca radar facility (50 MHz) must have a frequency response in excess of 2400 hz.

Frequency response is not sufficient to insure detection of an electrostatic wave by an electric field detector. This is true for two reasons. First, for an effective antenna separation vector  $\vec{d}$  the voltage response ( $V$ ) of an electric antenna to an electrostatic wave of wave number  $\vec{k}$  is given by

$$V = \vec{E}_0 \cdot \vec{d} \sin \vec{k} \cdot \vec{d}/2 / \vec{k} \cdot \vec{d}/2 \quad (2)$$

where  $\vec{E}_0$  is the wave electric field. Thus the response falls off steeply for  $k \gtrsim d^{-1}$ . Even more critical is the physical size of the probe, since the probe averages out wavelengths shorter than the probe dimensions. This effect is particularly devastating for long cylindrical probes. If, for example, a 20 meter long baseline ac electric field experiment is flown, the whole wavelength regime below 50 m would be seriously affected. Unfortunately, for dc electric field and transverse electromagnetic wave experiments, the signal to noise ratio is proportional to  $d$ . Hence the requirements of these detectors often make good electrostatic wave measurements impossible with the same electrodes, and dedicated short booms are necessary.

#### PLASMA DENSITY FLUCTUATION MEASUREMENTS

For electrostatic waves with  $\omega < \omega_{pi}$  the quasi neutrality condition requires that ion and electron plasma density fluctuations be nearly equal. Thus measurements of either quantity can, in principle, be used to study such waves. Two factors make electron measurements more versatile however. First, since vehicle velocities are comparable or greater than the ion thermal speed, the ram velocity is an important factor in ion collection, and unless the collection aperture is fixed with respect to  $V_S$ , its response will depend upon orientation. Second, detector frequency response and signal to noise ratios improve with the greater current collection capability due to high electron mobility.

A block diagram of an electron detector is given in Figure 3. The probe is a spherical or cylindrical electrode made of either vitreous carbon or of aluminum coated with a colloidal suspension of graphite, both of which have uniform surface properties. The probe is biased ( $V_B$ ) positively to collect electrons during most of its operation, although for diagnostic purposes it is necessary to sweep the

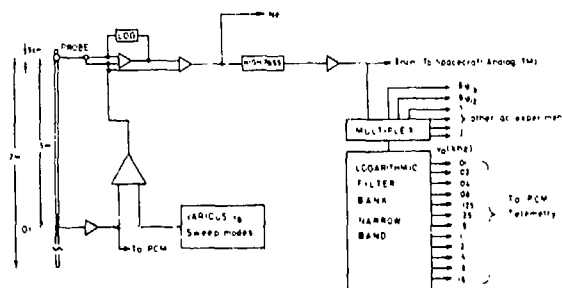


Fig. 3 Block diagram of a plasma density fluctuation detector.

potential through the plasma potential. The potential  $V_B$  is referenced to a second electrode (G1) in contact with the medium. This technique of referencing the probe potential to the plasma rather than the spacecraft removes all possibility for spurious effects due to voltage changes of the spacecraft skin in response to other plasma probes, to changes in solar illumination, or to changes in plasma particle collection. Such effects in a conventional system lead to changes in the probe current which might mistakenly be interpreted as irregularities or waves in the medium.

The detector operates as follows. The bias voltage, which has a nominal value of +10 volts, causes a negative current of absolute magnitude  $I$  to flow into the preamplifier circuit. An output proportional to the logarithm of this current ( $N_B$ ) goes to a relatively low data rate telemetry channel.

A discussion of the interpretation of this output is given later. In addition to being routed to the PCM encoder, this signal, which is proportional to  $\ln(I)$ , is ac coupled to a circuit which gives further amplification to the time varying components of  $\ln(I)$  at frequencies above some value  $\omega_0$ . The resulting signal is proportional to the relative variation  $\delta I/I$  of the collected current and is routed to a dedicated analog telemetry channel for transmission to ground, along with ac electric and magnetic channels, and to a bank of filters whose outputs are transmitted via PCM telemetry. That

this output is proportional to  $\delta I/I$  can be seen as follows. Consider a signal  $I_0 + \delta I(t)$  where  $\delta I(t)$  corresponds to the time varying component of  $I$  at frequencies above  $\omega_0$ . Then

$$\ln(I) = \ln[I_0 + I(t)] = \ln[I_0(1 + I/I_0)] = \ln I_0 + \ln(1 + I(t)/I_0) \quad (3)$$

Since we have accounted the slow time variations out of the signal ( $\ln I_0$ ), the only time varying term is the second one. Expanding this expression

$$\ln(1 + \frac{\delta I(t)}{I_0}) = \frac{\delta I}{I_0} - \frac{1}{2}(\frac{\delta I}{I_0})^2 + \frac{1}{3}(\frac{\delta I}{I_0})^3 \dots \quad (4)$$

Thus the output is proportional to  $\delta I/I_0$  to within better than 10%, even for signals as high as  $\delta I/I_0 = .2$ .

It will now be shown that  $\delta I/I$  is equal to  $\delta n/n$ , which as discussed above is the prime quantity of interest in the study of electrostatic waves. The current to a positively biased probe is given by:

$$I = -\frac{neA}{4} \left[ \frac{8KT_e}{2\pi m_e} \right]^{1/2} F(V_B) + \frac{neA}{4} \left[ \frac{8KT_i}{\pi m_i} + U_s^2 \right]^{1/2} \exp(-eV_B/KT_i) + I_{ph}(h\nu > V_B + WF) + I_H \quad (5)$$

where  $n$  is the plasma density,  $A$  is the spherical probe surface area,  $T_e(i)$  and  $m_e(i)$  are the electron (ion) temperature and mass,  $F(V_B)$  is the focusing function for electrons at potential  $V_B$ ,  $U_s$  is the satellite velocity,  $WF$  is the probe work function,  $I_{ph}(h\nu > V_B + WF)$  is the flux of emitted photoelectrons with energy greater than the bias voltage plus the work function of the probe, and  $I_H$  is the current to the probe due to energetic particles and secondaries. In the ionosphere and lower magnetosphere for  $V_B \sim 10$  volts, all terms can be dropped except the first. The ion term is negligible since both the flux and exponential terms are small. The photoemission flux can exceed the electron flux at flow densities, but for  $V_B + WF \sim 15$  volts almost all photoelectrons return to the surface [Soop,

1972].  $I_H$  will be small except for very unusual circumstances in which very high flux ( $> 10^{10}/\text{cm}^2\text{s}$ ) is present in regions of very low density ( $n \lesssim 10^2 \text{cm}^{-3}$ ). Such times, if encountered, can be identified via particle detectors flown on the vehicle and analyzed separately.

Taking the leading term then, we can calculate the ratio  $\delta I/I$ . Note that we will assume that there are no oscillating temperature variations in the electrostatic waves we are studying. This approximation is valid in a collisionless plasma [Stix, 1962]. We have

$$\frac{\delta I}{I} = \frac{(\partial I/\partial n)_{V_B} \delta n + (\partial I/\partial V)_{V_B} \delta V}{I} = \frac{\frac{\delta n}{n} + \frac{1}{I} \left( \frac{\partial I}{\partial V} \right)_{V_B} \delta V}{1} \quad (6)$$

Thus  $\delta I/I = \delta n/n$  over the full dynamic range of the instrument (5 decades) provided the correction term from focusing is small. This term is of concern for two reasons. First, electrostatic waves have potential variations in addition to  $\delta n/n$ , and second, potential variations may occur at the vehicle spin rate due to the electric field in the vehicle rest frame. Note that for the detector described here, which utilizes a reference ground (GI), spurious vehicle potential changes which contaminate the response of conventional detectors do not affect the current collection. The correction term is not expected to be large since, at the voltage  $V_B$ , the detector is well into the electron saturation regime where  $\delta I/\delta V$  is small. Experimental data obtained on a sounding rocket which bears this out is presented in Figure 4. Here the quantity  $\frac{1}{I} \left( \frac{\partial I}{\partial V} \right)_{V_B}$  is plotted as a function of plasma density for a 3.2 cm diameter sphere positively biased to +3 volts with respect to plasma potential. The probe was swept periodically to determine  $T_e$ , plasma potential,  $\frac{1}{I}(\partial I/\partial V)$  and  $F(V)$ , which is also plotted. The coefficient of  $\delta V$  decreases with decreasing density and hence we can use the high density value ( $2 \times 10^{-4}$ ) for estimates of its importance in equation (6). For the usual low frequency ( $\omega \ll \omega_{pe}$ ) electrostatic wave in which the electron density obeys the Boltzmann relation, the magnitude of the wave potential ( $\delta \phi$ ) is given by  $\delta \phi = (KT_e/e)\delta n/n$ . Taking  $KT_e/e \sim 100$  mv, deviations in  $\delta I/I$  from  $\delta n/n$  are less

than 2%. Since  $V_B$  is swept periodically,  $\frac{1}{T}(\partial I/\partial V)_V$  is measured in flight, and, along with measurements of  $kT_e/e$  during the sweep can be used to identify possible times when the correction term is of importance. If the vehicle is spinning, a  $\delta V$  will exist between the probe and G1 due to the potential difference  $\vec{V}_p \times \vec{B} \cdot \vec{d}$  where  $\vec{V}_p$  is the differential velocity between the plasma and the satellite,  $\vec{B}$  is the earth's magnetic field, and  $\vec{d}$  the vector separation between the probe and G1. In order to avoid saturation of the signal due to this modulation, we need only require that  $\vec{V}_p \times \vec{B} \cdot \vec{d} < 1$  volt, which is easy to accomplish even for the typical 400 mV/m

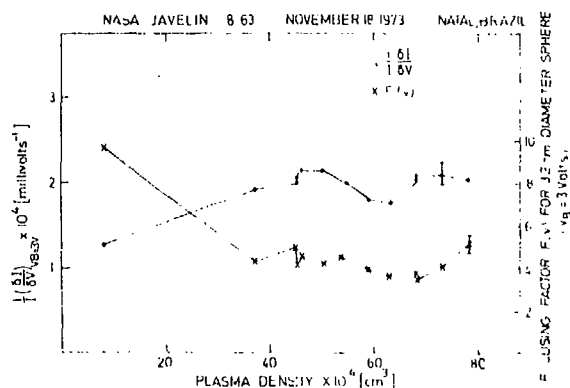


Fig. 4 Focusing factor and correction term due to finite slope of the electron saturation regime of a rocket-borne detector.

fields in the reference frame of a low altitude polar orbiting satellite.

The frequency response of the detector is dependent upon the total current collected. In principle this current and hence the frequency response can be made arbitrarily large by increasing the collecting area. However, two factors act to limit the probe size, namely the desire to measure at short wavelengths and the requirement that the electron current be matched by a positive current to the vehicle. A factor which works to alleviate this problem is that the upper limit of frequencies accessible to electrostatic waves in which both ions and electrons participate is the ion plasma frequency, which decreases with density. This frequency is plotted in Figure 5 along with the measured 3 db point of a particular preamplifier for a probe

diameter of 5 cm. The frequency response is thus seen to be adequate over the full range of plasma density of interest in the ionosphere. This size probe requires a vehicle skin size in excess of 1.5 m<sup>2</sup> for return current.

Shot noise will limit the sensitivity of the detector. Tunaley [1970] has pointed out that if photoelectrons are returned to the probe, they only contribute to the shot noise for frequencies near the photoelectron plasma frequency, which is well above the frequencies of interest. The mean square shot current per hertz is thus given by the formula

$$\overline{\delta I^2} = 2eI \quad (7)$$

where  $e$  is the electron charge. For a spherical electrode of radius 2.5 cm in a plasma of density  $10^2 \text{ cm}^{-3}$  and temperature  $1000^\circ \text{K}$ , which is the worst case expected,  $\delta I/I \sim 10^{-6} \text{ hertz}^{-1/2}$ . Thus over the full measurement bandwidth (20 kHz), the worst case  $\delta I/I$  is only  $2 \times 10^{-4}$ , which allows a good signal-to-noise ratio for the expected waves.

The  $N_e$  output is not as easy to interpret, since spatial variations in plasma density, temperature, and focusing function all contribute to its value. It should be pointed out that no absolute measurement of plasma density or temperature is intended with this instrument. However, since the temperature enters as the square root it is possible to make a reasonable measurement of the relative plasma density fluctuations by comparing the changes

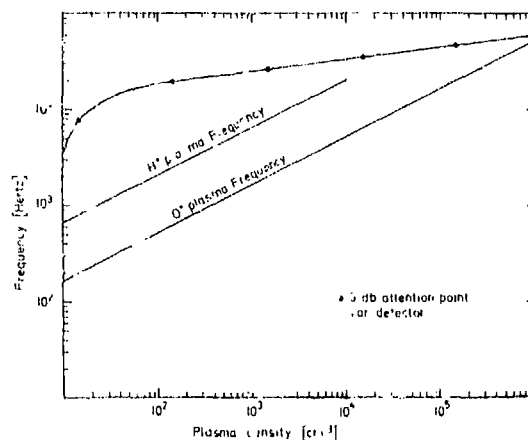


Fig. 5 Frequency response as a function of plasma density for a 5 cm diameter spherical collector along with the oxygen and hydrogen plasma frequencies.

in  $N_e$  to the average value over a given distance along the satellite trajectory. This is the usual technique used to measure the long wavelength spectrum of plasma waves and irregularities (Dyson et al., 1974; Kelley et al., 1974).

When the electron temperature fluctuates,  $\delta I/I = \delta n/n + \frac{1}{2} \delta T_e/T_e$  and measurements such as those described in the next section must be used to separate the two effects.

#### ELECTRON TEMPERATURE FLUCTUATION MEASUREMENTS

Fluctuations in the electron temperature have been predicted to be associated with the electrostatic instabilities in the equatorial F region (Hudson, 1974) and in the high latitude ionosphere as well (Hudson, private communication). A block diagram of an instrument designed to detect such fluctuations is presented in Figure 6.

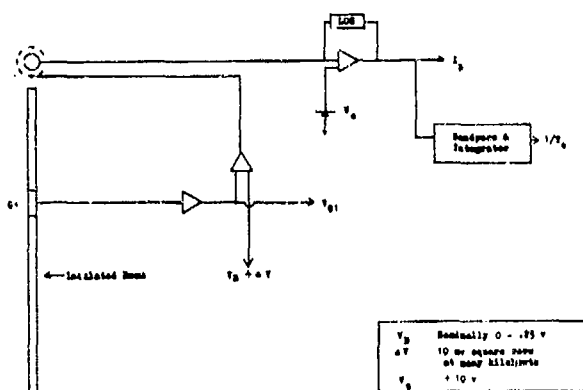


Fig. 6 Block diagram of an electron temperature fluctuation detector.

A 95% transparent mesh surrounds a cylindrical or spherical vitreous carbon electrode. The mesh is painted with a colloidal suspension of carbon and is biased at the potential  $V_f + V_B + \delta V$ , where  $V_f$  is the local floating potential defined by a third electrode in contact with the medium similar to the G1 electrode discussed above,  $V_B$  is the bias voltage which has the nominal value

of 0 volts and which can be programmed or varied by ground command, and  $\delta V$  is a 10 millivolt peak to peak square wave at a frequency ( $\nu_0$ ) of many kilohertz. The current collected by the inner electrode, which is held at a potential of +10 volts will also oscillate at that frequency with an amplitude which as discussed below yields the electron temperature. The electrodes are carbon or carbon coated since it has been shown that more accurate temperature measurements can be made with such uniform surfaces as are possible with these materials (Berthelier, private communication).

The inner electrode is biased positive with respect to the mesh so that ions are not collected by that probe. Photoelectrons are also returned to the center conductor and the current to the probe is thus given by

$$I = I_e \exp(-eV/KT_e)$$

where  $I_e$  is the electron saturation current,  $T_e$  is the electron temperature,  $V$  is the mesh potential. A voltage proportional to the log of this current is thence ac coupled to another stage of amplification. This output will hence oscillate with an amplitude which is inversely proportional to the electron temperature as can be seen as follows:

$$\ln I = \ln I_e \exp(-eV/KT_e) = \ln I_e - eV/KT_e$$

$$V_0(\nu_0) = \alpha(V_2 - V_1)/T_e = \alpha \delta V/T_e \quad (8)$$

The final output is averaged over several periods of the signal and then transmitted. A data rate of 100 hertz will allow measurements of the relative change in electron temperature every 70 meters along a satellite trajectory with a relative accuracy which varies with the temperature but which is the order of a few tenths of a percent.  $V_B$  can be varied or slowly swept occasionally to verify that the operating point is on the exponential portion of the probe curve.

A bias voltage of 0 volts is suitable for satellites since, due to the fact that  $V_S > V_f$  (the ion thermal speed), the floating potential of G1 is already on the exponential part of the characteristic. For a rocket experiment  $V_B$  should be a few tenths of a volt.

# ACKNOWLEDGEMENTS

This work was supported by the Office of Naval Research under contract N00014-69-A-0200-1015. One of the authors (M.K.) was partially supported under an Alexander von Humboldt Fellowship at the Max-Planck-Institut für Physik und Astrophysik, Institut für extraterrestrische Physik, Garching, West Germany.

Tunaley, J.K.E., and K. Knott, Electric field measurements in a magnetoplasma using the double probe technique, ELDO/ESRO Sci. and Tech. Rev., 1970.

# REFERENCES

- Dyson, P.L., J.P. McClure, and W.B. Hanson, In situ measurements of the spectral characteristics of F region ionospheric irregularities, J. Geophys. Res., 79, 1497, 1974.
- Fahleson, U.V., Theory of electric field measurements conducted in the magnetosphere with electric probes, Space Sci. Revs., 7, 238, 1967.
- Fiala, V., and L.R.O. Storey, The response of a double-sphere dipole antenna to VLF electrostatic plasma waves, in Plasma Waves in Space and Laboratory, Vol. 2, Ed. by J.O. Thomas and B.J. Landmark, p. 411, Elsevier, New York, 1970.
- Farley, D.T., Jr., Irregularities in the equatorial ionosphere: the Berkner Symposium, Rev. Geophys. Space Phys., 12, 285.
- Hudson, Mary K., Equatorial Spread F: Low Frequency Modes in a Collisionless Plasma, Ph.D. Thesis, Department of Physics, Univ. of California at Los Angeles, 1974.
- Kelley, M.C., and F.S. Mozer, A technique for making dispersion relation measurements of electrostatic waves, J. Geophys. Res., 77, 6900, 1972d.
- Kelley, M.C., and F.S. Mozer, Electric field and plasma density oscillations due to the high-frequency Hall current, two stream instability in the auroral E-region, J. Geophys. Res., 78, 2214, 1973.
- Kelley, M.C., and F.S. Mozer, A review of the recent results of in situ ionospheric irregularity measurements and their relations to electrostatic instabilities, Proceedings of the NRL Symposium on the effect of the ionosphere on space systems and communication (this volume), 1975.
- Soop, M., Report on photosheath calculations for the satellite GEOS, Planet. Space Sci., 20, 859, 1972.
- Stix, T.H., The Theory of Plasma Waves, McGraw Hill, New York 1962.
- Storey, L.R.O., The design of an electric dipole antenna for VLF reception within the ionosphere, Tech. Rep. No. 308TC, Centre National d'Etudes des Télécommunications, Paris, 1963.

THE MORPHOLOGY OF SMALL SCALE THERMAL IONIZATION IRREGULARITIES  
AT HIGH LATITUDES DEDUCED FROM ISIS-I SATELLITE MEASUREMENTS

M. Ahmed  
Regis College  
Weston, MA 02193

R.C. Sagalyn and M. Smiddy  
Air Force Cambridge Research Laboratories  
L.G. Hanscom AFB, MA 01731

Small scale thermal ion density irregularities were measured with the spherical electrostatic analyzer aboard the polar orbiting ISIS-I satellite. Thirty-five hundred orbits of data obtained during the first year of operation (1969) over the altitude range 575 to 3525 km have been examined to determine their spatial extent as a function of season and local time. The equatorward boundary of the small scale irregularity zone at high latitudes exhibits hemispherical asymmetry, being on the average  $5^{\circ}$  closer to the pole in the southern hemisphere than in the north. A large diurnal variation of the boundary location is found, magnitude  $15^{\circ}$ , in each season. The location of the equatorwards edge is sensitive to changes in magnetic activity and reaches its maximum value of  $72^{\circ}$  in the northern hemisphere and  $76^{\circ}$  in the south near local noon under quiescent conditions. A maximum seasonal variation of  $4^{\circ}$  is found in the location of the boundary at any given local time. The small scale irregularities are consistently found to extend across the pole, there is no upper boundary. The size of these irregularities typically ranges from 0.5 to 140 km. The very good agreement found between the location of the edge of the small scale irregularity zone and the scintillation boundary derived by Aarons and his co-workers strongly suggests that small scale irregularities are a principle cause of scintillations at UHF.

#### Introduction

Knowledge of the spatial and temporal characteristics of small-scale charged particle irregularities has been obtained primarily from ground-based measurements of spread F (Shimazaki, 1959, 1962; Singleton, 1960, 1968) and radio scintillations (Aarons et al., 1969; Aarons and Allen, 1971). However, it is difficult to obtain a global description of the irregularities from ground-based measurements alone. Dyson (1969)

reported on direct measurements of the properties of the irregularities utilizing results from about 150 orbits of data from the Langmuir probe instrument flown on Alouette 2. McClure and Hanson (1973) have examined F region irregularities using results of the retarding potential analyzer on OGO 6.

Several theories have been proposed for the production of the irregularities (Herman, 1966; Frihagen, 1969, 1971), but not one has been found to be satisfactory. There is a

need for a more complete global morphological description of these irregularities that through refractive index changes cause spread F, radio scintillations, etc.

In this report the local time and seasonal characteristics of the high-latitude ionization irregularity regions in the northern and southern hemispheres are described and a comparison of essentially simultaneous measurements of the irregularity boundaries in the northern and southern hemispheres is given. The relationship of the equatorial edge of the irregularity boundary to the mid-latitude trough, the auroral zone, and the plasmapause boundary is also examined.

#### The Experiment

The thermal charged particle data used in this study were obtained with a spherical electrostatic analyzer aboard the ISIS-I satellite. The sensor, mounted on a 96-cm boom, consists of three concentric spherical electrodes with radii of 1.90, 2.54, and 3.18 cm, respectively. The operation of the probe is based on the motion of charged particles in a central force field (Sagalyn et al., 1963; Sagalyn and Smiddy, 1967; Smiddy and Stuart, 1969; Whitteker et al., 1972). The sensitivity range of the instrument is  $10-10^6$  ions  $\text{cm}^{-3}$ ; in sunlight, however, photoelectron currents increase the lower sensitivity limit to about 700 ions  $\text{cm}^{-3}$ . On ISIS-I, ion densities were sampled 60 times per second, corresponding to a spatial resolution of 150 m. Over 3500 orbits of data acquired during the first year of satellite operation, February 1969 to February 1970, were examined. ISIS-I was launched into a polar orbit with an apogee of 3526 km, a perigee of 525 km, and an inclination of  $88.5^\circ$  on January 30, 1969. The results in this report are based on the ion density mode of operation.

#### Method and Definitions

The equatorial boundary of the irregularity region is taken to be the latitude of onset of persistent small-scale ionization irregularities extending over at least a few degrees

in latitude with amplitudes 20% or more of the mean background level as deduced from examination of the processed data plots, an example of which is shown in Figure 1.

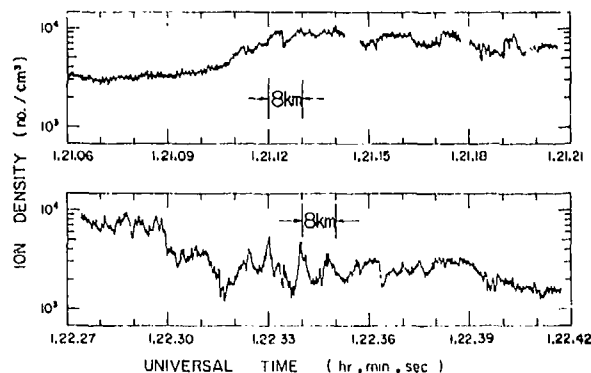


Fig. 1. Typical examples of small-scale ionization irregularities, orbit 76, February 6, 1969. Invariant latitude,  $74^\circ-79^\circ$ ; altitude, 850-950 km; LT, 2145-2150.

The smallest measurable scale size, 150 m, is determined by the telemetry data sampling rate; no upper limit is set by the measurement. The mid-latitude trough was the largest irregularity included in this study. The scale size is highly variable with dimensions ranging typically from 0.5 to 140 km. The maximum amplitude of the irregularities is usually located within the auroral oval, the region of maximum soft particle precipitation. Representative examples of small-scale irregularities are shown in Figure 1. Typical boundary identifications are noted at point B of Figures 2c and 2d. The electron or ion trough, a regular feature of the nighttime ionosphere, is frequently found at the equatorward edge of the irregularity region. In this study the trough ranging from 100 to 1500 km in latitudinal extent is considered as part of the irregularity zone. Examples of typical troughs are shown in Figures 2a, 2b, and 2c. The high-latitude boundary of the irregularity zone is defined as the latitude where small-scale irregularities of amplitude 20% or more above background



are no longer observed.

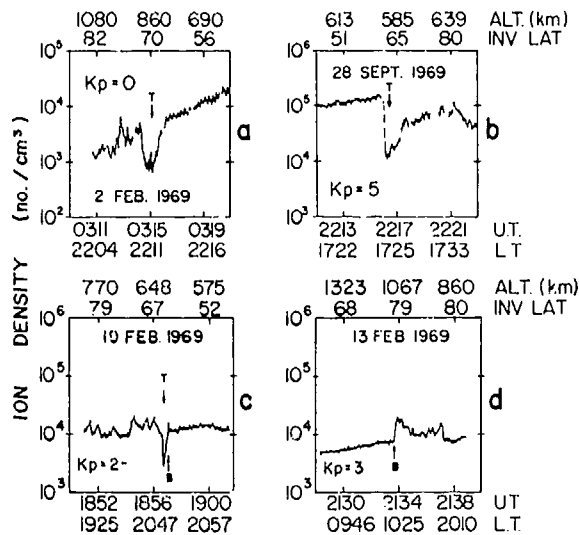


Fig. 2. Examples of thermal ion troughs T in Figures 2a, 2b, and 2c. Equatorial ionization irregularity boundaries B in Figures 2c and 2d.

Although the electrostatic probe results were obtained in the top side ionosphere, extensive comparisons with simultaneous top side sounder measurements on board ISIS-I show that down to the minimum scale size that can be observed with the sounder, approximately 18 km, the irregularities map along magnetic field lines down to the peak of the F region. This is illustrated in the results of orbit 54 shown in Figure 3. The electron density is given at the satellite and at discrete levels down to the F region ionization maximum. These results may thus be considered to represent ionospheric characteristics throughout the F region. The variation of the amplitude of the irregularities with altitude is found to be strongly dependent on season; the largest amplitude variation with altitude is observed at mid-latitudes to high latitudes on winter nights. A study of the structure and power spectra of the irregularities will be presented in a separate report at this meeting.

#### Diurnal Variation of Equatorial Boundary

The diurnal variation of the location of the equatorial boundary of the irregularity region was determined by

calculating the frequency of occurrence as a function of invariant latitude, averaged over 5° of latitude, at 3-hour intervals of local time.

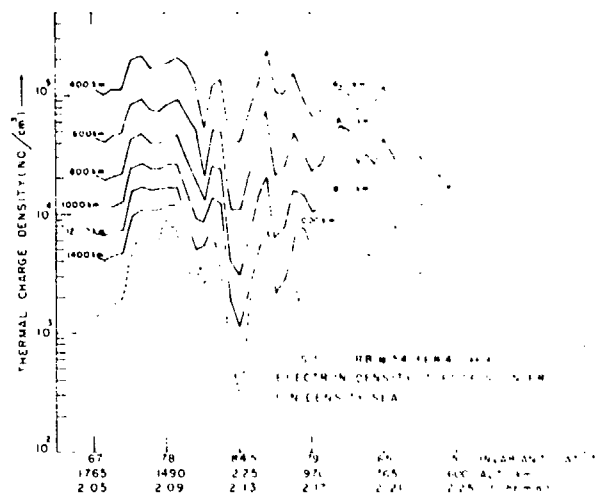


Fig. 3. Illustration of variation of irregularity amplitude with altitude from top side sounder and spherical electrostatic analyzer.

The data were separated into two levels of magnetic activity:  $Kp \leq 3$  and  $Kp \geq 3+$ . Northern and southern hemisphere data were analyzed separately. The number of orbits for which boundary data were available for each time interval in the northern hemisphere varied between 68 and 186 for  $Kp \leq 3$  and between 22 and 70 for  $Kp \geq 3+$ . There were on the average 85 orbits of data for each 3-hour period for  $Kp \leq 3$ . Approximately the same number of orbits of data were available for the southern hemisphere study. The frequency of occurrence results as a function of local time for  $Kp \leq 3$  are shown in Figures 4a and 4b for the northern and southern hemispheres, respectively. It is seen that the frequency of occurrence distributions vary with local time, with a minimum standard deviation found within 3 hours of local noon. Near noon the location of the boundary can be predicted to within 5°.

This result corroborates information gained from studies of precipitating particles, namely, that near local noon the primary cause of ionization inhomogeneities is the entrance of

relatively low-energy particles into the magnetospheric cleft region. At other local times, additional influences including bulk plasma motions are known to be operating.

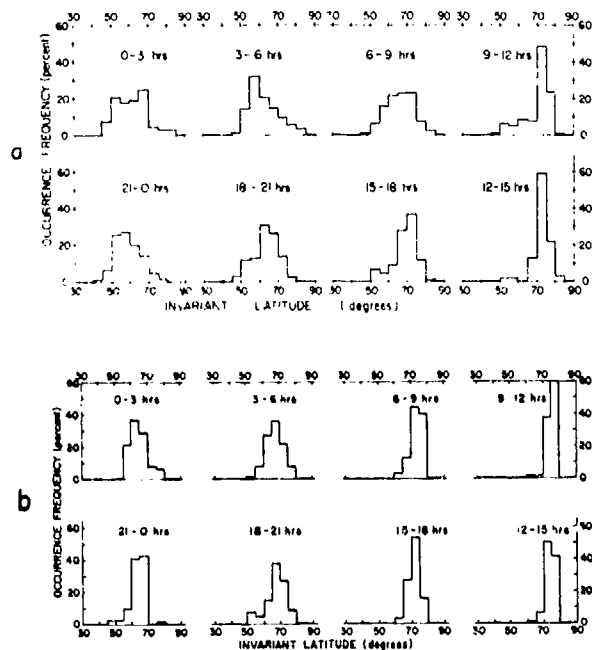


Fig. 4. Frequency of occurrence distributions of equatorial boundary of the ionization irregularity zone as a function of invariant latitude and local time for  $K_p \leq 3$ . (a) Northern hemisphere and (b) southern hemisphere, ISIS-I, 1969.

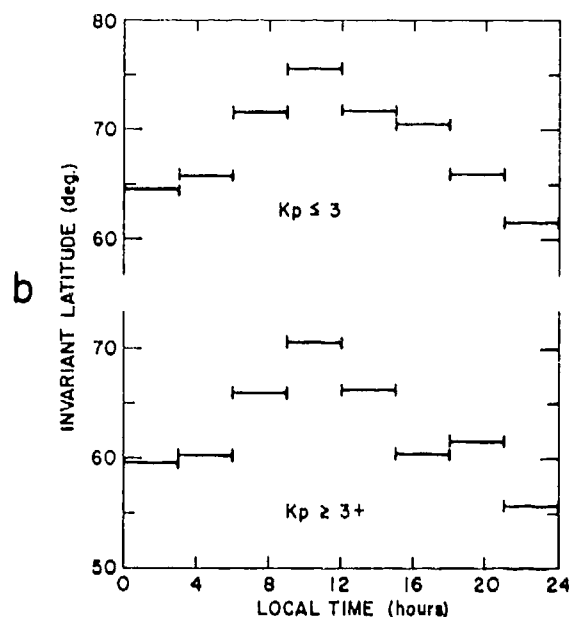
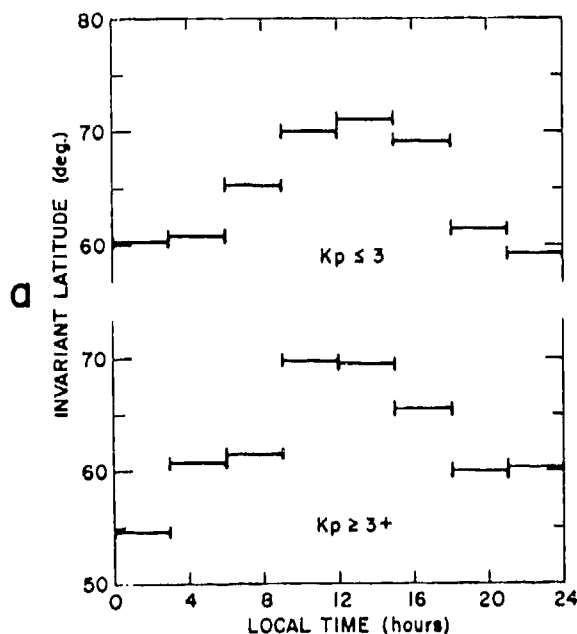


Fig. 5. Latitude variation of mean location of equatorial boundary of irregularity zone with local time. (a) Northern hemisphere and (b) southern hemisphere, ISIS-I, 1969.

A large diurnal variation, amplitude approximately  $15^\circ$ , is found in the mean location of the equatorial boundary of the irregularity zone, with a maximum around noon and minimum near midnight (Figs. 5a and 5b).

The boundary of the irregularity zone is found to be an oval, concentric with the magnetic pole in both the northern and the southern hemisphere. As is seen in the polar diagram of Figure 6, the mean location of the irregularity boundary is consistently found to be closer to the pole in the southern hemisphere. In any given local time sector the boundary is  $3^\circ$ - $9^\circ$  closer to the pole in the south than in the north; the average difference is  $4.8^\circ$  for  $K_p \leq 3$ . The standard deviations of the means of the frequency of occurrence distributions, are of the order of  $0.5^\circ$ . The observed differences are thus statistically significant. These results also imply that the night side thermal ion and electron trough, the precipitation zone, and the auroral oval are approximately  $5^\circ$  closer to the magnetic pole in the south than in the north. This is consistent with the IGY results of Feldstein and Solomatina (1961) and Bond and Jacka (1963).

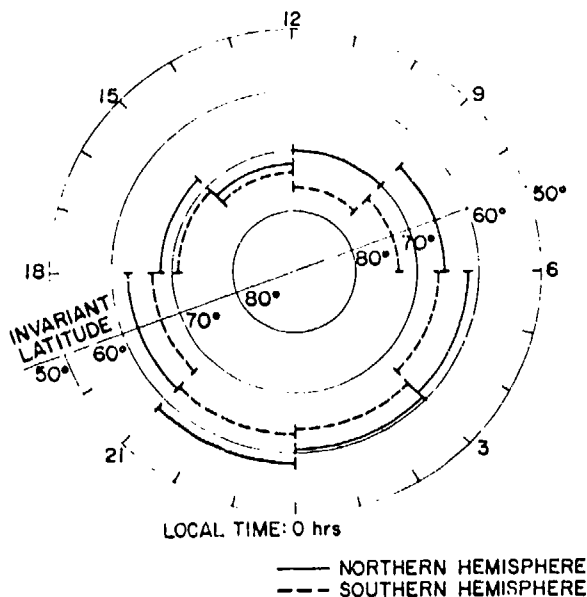


Fig. 6. Comparison of irregularity boundary location in the northern (solid lines) and southern (dashed lines) hemispheres. Invariant latitude versus local time.

#### North-South Differences

The implication of the present results is that there exist in nature physical conditions that produce northern and southern hemisphere asymmetries. These could arise from external sources, for example, the tilt of the earth's axis of rotation relative to the solar wind direction. E.G. Stassinopoulos (private communication, 1973) in his recent development of magnetic field models that include external sources has found north-south asymmetries in the terrestrial magnetic field consistent with the results of the mapping of top side ionization irregularities under discussion. It may be physically significant that the ISIS-I study indicated that these asymmetries are reduced during solar geomagnetic disturbance periods.

#### Seasonal Variation

The frequency of occurrence of equatorward and poleward boundaries of the irregularity regions was evaluated as a function of invariant latitude for the months of March, June, September, and December 1969. In each hemisphere the satellite traverses the irregularity zone at two local times

approximately 12 hours apart. Thus in each hemisphere there are results for two different local time sectors. Northern and southern hemisphere results were analyzed separately.

In order to describe accurately the seasonal variation of the mean location of the irregularity boundary it is necessary to normalize first all results to a given local time because of the large diurnal variation of the boundary location. All morning and daytime results were normalized to local noon and all evening and night results to local midnight by using the results summarized in Figure 5. The seasonal variation of the mean location of the equatorial boundary at noon and midnight for each hemisphere is shown in Figure 7. The standard deviation of the mean of the distributions varied between 0.35 and 0.85 with an average value of 0.61. The observed seasonal variations are thus statistically significant. The most striking aspect of these results is that the seasonal variation of the mean location of the boundary is small. In the northern hemisphere at local noon the total seasonal variation is  $4^\circ$ ; at midnight a maximum seasonal change of  $6^\circ$  is found. Further, as might be expected from the changing position of the sun, in the northern hemisphere the boundary is closest to the pole in June and farthest from the pole in December.

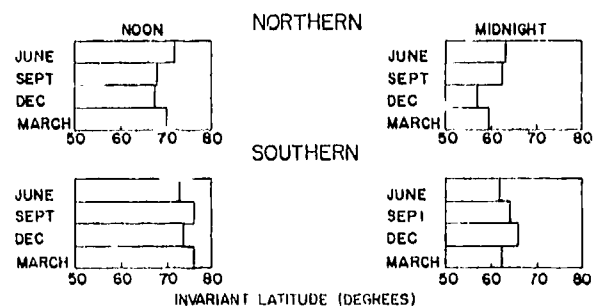


Fig. 7. Seasonal variation of the mean location of the equatorial boundary of the irregularity zone at noon and midnight for  $K_p \leq 3$ .

In March and September the boundaries lie at or between these limits. The amplitude of the seasonal variation is  $4^\circ$  in the southern hemisphere. The relative position of the boundary in June and December is reversed from that found in the northern hemisphere; the equatorial boundary is closer to the magnetic pole in December than in June. The differences in the two hemispheres result from the variation in the position of the sun relative to the equatorial plane with time of year.

#### Poleward Boundaries

The method of analysis for the identification of the poleward boundary of the irregularity zone was identical to that carried out for the equatorial boundary. The number of orbits examined in each season and the local time of the measurements are listed in Table I. The maximum invariant latitude of the satellite varied from orbit to orbit between  $83^\circ$  and  $90^\circ$ . If the irregularity zone extended up to the maximum latitude reached by the satellite on any given orbit, that orbit was considered to have no upper boundary.

Table I. Seasons, Local Times, and Number of Orbits Examined for Poleward Boundary Study

Month	Local Time	No. of Orbits
March	0060-1000	94
	1700-2000	81
June	1000-1300	66
	0000-0300	56
September	0400-0700	37
	1700-2000	19
December	1100-1500	63
	2000-2400	48

Examples of high-latitude passes where the satellite passed to within a few degrees of the magnetic pole are shown in Figure 8. A total of 295 orbits were examined in the northern hemisphere and 169 orbits in the southern hemisphere during the months of March, June, September, and December. No poleward boundaries for the irregu-

larity zone were found; the inhomogeneities extend across the pole. This result is found in each season and for all local times. These results are consistent with scintillation measurements of Titheridge and Stuart (1968) and Stuart and Titheridge (1969) at high latitudes. However, this is the first statistical study of the irregularities across the poles at all longitudes and local times.

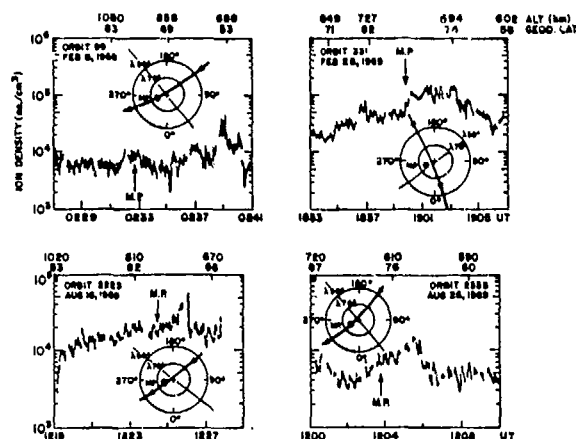


Fig. 8. Examples of thermal plasma irregularities across the polar cap; crossed circles and M.P. denote the location of the magnetic pole, and the arrow denotes satellite trajectory.

#### Discussion

Comparison with other irregularity measurements. It is of considerable interest to compare the present results with irregularity measurements obtained by other techniques. Although some differences might be expected due to varying criteria, instrument sensitivities, ranges, and different data base, the behavior in response to spatial, temporal, and geophysical variations because of their common origin in high-latitude precipitation and motions should be similar. Related measurements include scintillations, thermal charged particle trough, spread F, other in situ electrostatic probe results, soft particle fluxes, and auroral optical emissions.

Ionospheric scintillations, which consist of amplitude fluctuations and fading of electromagnetic signals re-

ceived at the ground due to radio sources located in or above the ionosphere, have been studied extensively by many workers including Aarons (1973), Aarons et al. (1969), Titheridge and Stuart (1968), Stuart and Titheridge (1969), Stuart (1972), Preddy (1969), and Frihagen (1969, 1971). Since scintillations are assumed to be produced by small scale irregularities in the ionosphere (Rufenach, 1974), the irregularity boundaries described in this report should be closely correlated with statistically derived scintillation boundaries. The mean location of the statistical boundary derived from the in situ satellite probe measurements for  $K_p \leq 3$  in the northern hemisphere is compared in Figure 9 with the scintillation boundary of Aarons (1973) for  $K_p = 0, 1$  in the same hemisphere. The equatorial scintillation boundary is defined as the latitude at which the mean scintillation index at 40 MHz is 50%. The results are in surprisingly good agreement considering the different criteria used to define the boundaries as well as the different  $K_p$  ranges included in these studies. The agreement is excellent at night and in the early morning between 2100 and 0600 LT. The maximum difference of  $7^\circ$  occurs at 1700 LT. The comparison supports the assumption that scintillations are caused by small-scale ionization irregularities in the ionosphere. The results further suggest that the direct measurement of the ionospheric irregularities can be utilized to predict the location of high-latitude scintillation regions. This would be especially useful on the day side, where statistical information on scintillations is limited.

Preddy (1969) has reported on the variation of radio satellite scintillations with geomagnetic latitude from shipboard stations over the latitude range  $20^\circ$ - $80^\circ$  based on amplitude records of 40 MHz signals from the BEB satellite in the southern hemisphere. The data were divided into two groups, daytime from 0700 to 1530 hours and nighttime from 1930 to 0400 hours. No attempt was made to separate the data into different magnetic intensity levels. There is a large scatter of the data points with a sharp increase

in the mean scintillation index on the day side at about  $70^\circ$  and at night at  $60^\circ$ . This is consistent with the satellite results reported here for the southern hemisphere if one averages all  $K_p$  and considers equivalent local time sectors.

The 'abrupt' scintillation boundary reported by Stuart (1972) based on measurements from mid-latitude stations in the southern hemisphere is a rare phenomenon, being observed on only 8% of 9000 satellite transits examined. It may represent either the low-latitude tail of the frequency distributions reported here or a special phenomenon such as traveling ionospheric disturbances. The abrupt boundary morphology does not appear to fit well into the global irregularity morphology reported here.

Dyson (1969) investigated ionization irregularities over the size range 0.2-3 km utilizing direct measurements from the cylindrical Langmuir probe flown on Alouette 2. The mean location of the equatorial boundary obtained from the examination of 110 orbits of data in the  $K_p$  range 0-3 is compared in Figure 9 with the boundaries observed in the present study. Northern and southern hemisphere data were combined in the Dyson work. There is large scatter in the latter data, and results are available primarily for the night side. The ISIS-I measurements cover a wider irregularity size range 150 m to 600 km. Nevertheless, the results from these studies as shown in Figure 9 are in good agreement.

Dyson and Winningham (1974) have examined the relation between the equatorial edge of the severe top side spread F zone (STIZ) and the first appearance of  $\leq 300$  eV electron precipitation in the local time range 0800-1400 hours. Comparison of simultaneous ISIS-I measurements of edge of the severe spread F zone and of the  $\leq 300$  eV electron boundaries show excellent agreement. The spread F information was obtained from the ISIS I top side sounder. A study is being carried out by Winningham (private communication, 1973) on the relation between the  $\leq 300$  eV electron precipitation boundary and simultaneous mea-

measurements of the small-scale ionization irregularities obtained on ISIS-I. Comparison of results obtained on 193 orbits shows the two equatorial boundary measurements to be in very good agreement. These results provide strong evidence that severe top side spread F and small-scale ionization irregularities at high latitudes are the consequence of soft electron precipitation. The results of the statistical study discussed in this report also suggest that the equatorial STIZ boundary and the soft particle precipitation boundary should be approximately  $4^\circ$  closer to the pole in the southern hemisphere than in the northern hemisphere for the same geophysical conditions.

Relation to other high-latitude phenomena. Since the mid-latitude thermal charged particle trough, frequently the night side termination of the irregularity zone, was included as an irregularity in the present study, the statistically determined boundary on the night side should show a good correlation with trough locations reported by other workers. The results of Muldrew (Jelly and Petrie, 1969) giving the local time variation of the location of the mid-latitude electron trough in the northern hemisphere based on data of 3 months from the top side sounder on Alouette 1 are compared in Figure 9 with the ISIS I spherical electrostatic analyzer (SEA) results for  $K_p \leq 3$ . The results are shown to be in excellent agreement.

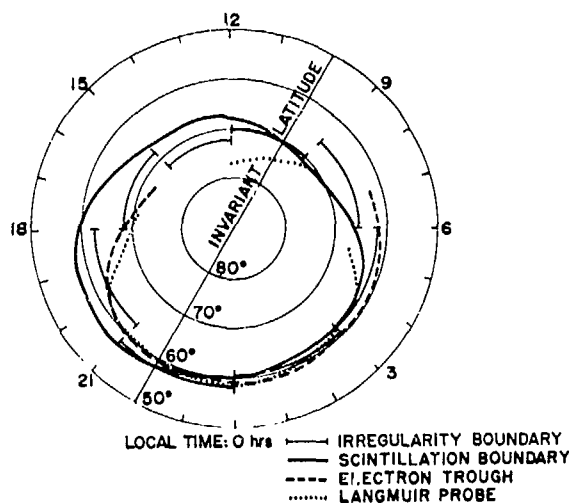


Fig. 9. Comparison of scintillation

boundary (Aarons, 1973) in situ Langmuir probe irregularities (Dyson, 1969), electron trough (Muldrew, 1965), and small-scale irregularity boundary based on spherical electrostatic analyzer data from ISIS-I.

#### Summary

The principal results of this study of high-latitude irregularities may be summarized as follows: The irregularity scale size ranges typically between 0.5 and 140 km. The characteristics of the irregularity distributions are found to be similar over the altitude range 525-3526 km. The variation of the amplitude of the irregularities with altitude is found to be dependent on season; amplitude changes with altitude are greatest at mid to high latitudes on winter nights. The maximum amplitude of the irregularities is usually located within the auroral oval. The magnitude of the diurnal variation of the mean location of the equatorial boundary of the high-latitude irregularity zone is approximately  $15^\circ$  for all levels of magnetic activity. The frequency of occurrence distributions for the location of the boundary also vary with local time. A minimum standard deviation of  $5^\circ$  is observed near local noon. A seasonal variation of  $4^\circ$  is found in the location of the boundary. Similar diurnal and seasonal characteristics are observed in the northern and southern hemispheres. However, the equatorial boundary is consistently found to be closer to the magnetic pole in the south than in the north. The average difference throughout a 24-hour period is  $4.8^\circ$  for  $K_p \leq 3$ . The difference is a minimum near local noon. In both hemispheres the irregularities are always found to extend across the pole. This result strongly suggests the persistence of plasma motions, convection and turbulence, across the poles.

#### References

- Aarons, J., J.P. Mullen, and H.E. Whitney, The scintillation boundary, *J. Geophys. Res.*, 74, 884, 1969.
- Aarons, J., and R.S. Allen, Scintillation boundary during quiet and disturbed conditions, *J. Geophys. Res.*, 76, 170, 1971.
- Aarons, J., A descriptive model of F

- layer high latitude irregularities as shown by scintillation observations, *J. Geophys. Res.*, 78, 7441, 1973.
- Bond, F.R., and F. Jacka, Distribution of auroras in the southern hemisphere. III Comparison with northern hemisphere, *Australian J. Phys.*, 16, 514, 1963.
- Dyson, P.L., Direct measurements of the size and amplitude of irregularities in the topside ionosphere, *J. Geophys. Res.*, 74, 6291, 1969.
- Dyson, P.L., and J.D. Winningham, Topside ionospheric spread F and particle precipitation in the dayside magnetospheric clefts, *J. Geophys. Res.*, in press, 1974.
- Feldstein, Y.I., and E.K. Solomatina, Auroras in the southern hemisphere, *Geomagnetism and Aeronomy Moscow*, English Transl. Am. Geophys. Union, 1, 475, 1961.
- Frihagen, J., Satellite scintillation at high latitudes and its possible relation to precipitation of soft particles, *J. Atmos. Terr. Phys.*, 31, 81, 1969.
- Frihagen, J., Occurrence of high latitude ionospheric irregularities giving rise to satellite scintillations, *J. Atmos. Terr. Phys.*, 33, 21, 1971.
- Herman, J.R., Spread F and ionospheric F region irregularities, *Rev. Geophys.*, 4, 225, 1966.
- Jelly, D.N., and L.E. Petrie, The high latitude ionosphere, *Proc. of IEEE*, 57, 1005, 1969.
- McClure, J.P., and W.B. Hanson, A catalog of ionospheric F region irregularity behavior based on OGO-6 retarding potential analyzer data, *J. Geophys. Res.*, 78, 7431, 1973.
- Muldrew, D.B., F region ionization trough deduced from Alouette data, *J. Geophys. Res.*, 70, 2635, 1965.
- Predy, C.F., Mid latitude radio satellite scintillations - the variation with latitude, *Planet. Space Sci.*, 17, 1557, 1969.
- Rufenach, C.L., Wavelength dependence of radio scintillations; ionosphere and interplanetary irregularities, to be published in *J. Geophys. Res.*, 1974.
- Sagalyn, R.C., M. Smiddy, and J. Wilonia, Measurement and interpretation of ion density distributions in the daytime F region, *J. Geophys. Res.*, 68, 199, 1963.
- Sagalyn, R.C., and M. Smiddy, Charged particle measurements by means of electrostatic probes, electron density and temperature measurements in the ionosphere, *Cospar Tech. Manual*, Commun. Space Res., Paris, France, 90, 1967.
- Shimazaki, T., A statistical study of worldwide occurrence probability of spread F. I Average state, *J. Radio Res. Lab., Japan*, 6, 669, 1959.
- Shimazaki, T., A statistical study of occurrence probability of spread F at high latitudes, *J. Geophys. Res.*, 67, 4617, 1962.
- Singleton, D.G., The geomorphology of spread F, *J. Geophys. Res.*, 65, 3615, 1960.
- Singleton, D.G., The morphology of spread F occurrence over half a sunspot cycle, *J. Geophys. Res.*, 73, 295, 1968.
- Smiddy, M., and R.D. Stuart, An analysis of the behavior of a multigrid spherical sensor in a drifting Maxwellian plasma, *AFCRL 69-0013*, Phys. Sci. Res. Pap. 364, AFCRL Bedford, MA.
- Stuart, G.F., and J.E. Titheridge, The distribution of irregularities in the antarctic ionosphere. II Diurnal, magnetic, and solar cycle effects, *J. Atmos. Terr. Phys.*, 31, 905, 1969.
- Stuart, G.F., Characteristics of the abrupt scintillation boundary, *J. Atmos. Terr. Phys.*, 34, 1455, 1972.
- Titheridge, J.E., and G.F. Stuart, The distribution of irregularities in the antarctic ionosphere. I Mean seasonal maps at sunspot minimum, *J. Atmos. Terr. Phys.*, 30, 85, 1968.
- Whitaker, J.H., L.H. Brace, J.R. Burrows, T.R. Hartz, W.J. Heikkila, R.C. Sagalyn, and D.M. Thomas, ISIS-I observations of the high latitude ionosphere during a geomagnetic storm, *J. Geophys. Res.*, 77, 6121, 1972.

IN SITU MEASUREMENTS OF THE STRUCTURE AND SPECTRAL CHARACTERISTICS  
OF SMALL SCALE F REGION IONOSPHERIC IRREGULARITIES

M. Ahmed  
Regis College  
Weston, MA 02193

A. D. R. Phelps  
The University of Oxford  
Oxford, Oxfordshire, UK

and

R. C. Sagalyn  
Air Force Cambridge Research Laboratories  
L. G. Hanscom AFB, MA 01731

ABSTRACT

Thermal plasma density measurements obtained using the spherical electrostatic analyzer probe carried by the polar orbiting satellite ISIS-I, have been spectrally analyzed to provide quantitative results on the amplitude and scale size distribution of the plasma irregularities in the high latitude topside ionosphere. The range of scale sizes examined, 150 meters to over 100 km under normal conditions, is more than an order of magnitude greater than that available from ground based measurements.

Data in the altitude range 574 to 3523 km and from the period February 1969 to April 1972 have been analyzed. Irregularities in the high latitude region from  $40^\circ$  invariant latitude up to the invariant L-pole have been studied. In over 90% of the cases examined, the power spectra are found to fit a power law of the form  $P = P_0 f^{-\beta}$  where the index  $\beta$  varies within the range 1.5 to 2.5.

The power spectral density was integrated over the scale size range 1 to 10 km in order to quantitatively analyze latitudinal variations of the irregularity amplitude. While the boundaries of the high latitude irregularity zone on particular orbits examined using this technique are in agreement with earlier morphological studies, it is also evident that the amplitude of the irregularities within the high latitude irregularity region itself shows irregular enhancements above a generally raised amplitude level.

Comparison of simultaneous measurements of power spectra at the satellite with ground based scintillation measurements has shown that small scale irregularities exist in over 90% of the cases where a scintillation index of 50 or greater is



reported. No relation has been found between the spectral index  $\beta$  and the value of the scintillation index.

## INTRODUCTION

Knowledge of the small scale ionization irregularity structure and power spectra, is important both for the understanding of the mechanisms by which irregularities are formed and dissipated and for the prediction of the effect of the ionosphere on electromagnetic waves passing through it.

Progress has been made in measuring the properties of the bottomside ionospheric irregularities, both in the equatorial and auroral regions. This paper devotes itself to the analysis of irregularities in the topside high latitude ionosphere, where the properties are less well known. Sagalyn et al. (1974) have reported on the morphology of the irregularities in the high latitude topside ionosphere. The present discussion aims at complementing that study by an analysis of the irregularity amplitude and scale size distribution.

There have been few in-situ measurements of irregularities using probes carried by satellites and rockets compared with indirect ground based measurements. Total electron content, scintillations, radio wave scattering and spread F traces on ionograms have been the principle indirect methods used for irregularity studies. Aarons (1971) in discussing the global morphology of ionospheric scintillations states that there is a high latitude region of scintillations whose equatorial boundary reaches approximately  $57^\circ$  invariant latitude near midnight. The high latitude scintillation region has also been studied in the northern hemisphere by Frihagen (1971) and in the southern hemisphere by Titheridge et al. (1968) and by Briggs (1964).

Scintillation measurements have been primarily used to monitor the temporal and morphological behavior of total electron content fluctuations in the ionosphere. Elkins and Papagiannis (1969), Rufenach (1971) and Chivers (1971) have examined the power spectra of the scintillations. Using diffraction

theory it is then possible to deduce the irregularity electron density spectrum, which is the fundamental ionospheric characteristic which the in-situ measurements observe directly. Rufenach (1971) has pointed out limitations and difficulties of this method. The height of the irregularities is usually assumed and not measured, although the use of spaced receivers (Paul et al., 1970) may remove this restriction. More important is the fact that the Fresnel oscillations are smeared by the thickness of the irregularity layer, and random and drift motions further complicate the interpretation. Normally the irregularity power density spectrum can only be deduced over a limited scale size range, often less than one order of magnitude. The scintillations are severely attenuated for irregularity sizes larger than about twice the Fresnel radius, and hence the upper scale size limit is frequency dependent. The limited scale size range is a serious disadvantage for reliably fitting of the observations to a particular production mechanism.

Recently Dyson et al. (1974) reported results of "in-situ" measurements of small scale positive ion irregularities over the altitude range 400 to 1000 km from the OGO-6 retarding potential analyzer. Over the scale size range 70 meters to 7 km, the frequency spectra was most commonly found to obey a power law with a spectral index of about 1.9.

The present paper reports the results of a detailed study of over 200 orbits of data to obtain the power spectral density of high latitude topside ionosphere irregularities. The data examined were selected from a data base of over 10,000 ISIS-I satellite orbits. In addition, the integrated power spectral density have been evaluated to give a quantitative measure of the latitudinal variation of the amplitude of the irregularities. These in-situ measurements of the level of the

power spectral density and the spectral shape over a wide scale size range, combined with the morphology of occurrence, are probably the most significant parameters characterizing the irregularities both from the point of view of understanding the physics of their formation and for assessing their influence on electromagnetic propagation.

#### OBSERVATIONS

The ISIS-I satellite, launched on 30 January 1969 has an elliptical orbit (perigee 574 km, apogee 3523 km) with an inclination of 88.4 degrees. The spherical electrostatic analyzer (SEA) is an ion probe similar to that described earlier by Sagalyn et al. (1963). A brief description of the present probe has been given by Whitteker et al. (1972). Two hundred orbits of data obtained over the period January 1969 to April 1972 have been studied. Real time and tape recorded data have been analyzed. The tape recorded data has been particularly useful for studies of the high latitude south polar regions where there are few real time data acquisition stations.

The probe operates in three modes, an ion density sampling mode, a temperature measurement mode and a coarse energy spectrum analysis mode. The first mode, the ion density sampling mode, samples at a rate of 60 samples per second and is the mode used for the present analysis. The lower limit of sensitivity is approximately  $10^3$  ions/cm<sup>3</sup> and the instrument is capable of measuring ion densities of  $10^6$  ions/cm<sup>3</sup>, which is in excess of the ion densities normally encountered. When the SEA is sunlit a photocurrent flows which is of the same magnitude as that produced by a positive ion density of approximately  $2 \times 10^3$  ions/cm<sup>3</sup>. Hence when the SEA is sunlit only densities higher than  $2 \times 10^3$  ions/cm<sup>3</sup> are readily resolved. This limitation is sometimes apparent near apogee on the dayside of the earth.

#### POWER SPECTRAL ANALYSIS

Each sample containing  $N$  individual positive ion density measurements

may be treated as a univariate time series. The time interval,  $\delta$ , between successive measurements is a constant and in the case of the ISIS-I SEA,  $\delta = 1/60$  second.

First the deviation  $\Delta n(I)$  of the  $I$ 'th measurement is calculated,

$$\Delta n(I) = n(I) - \frac{1}{N} \sum_{I=1}^N n(I) \quad (1)$$

The autocorrelation function,  $\rho(L)$ , for a lag,  $L$ , is readily calculated,

$$\rho(L) = \frac{\frac{1}{N} \sum_{I=1}^{N-L} \left\{ \Delta n(I) \right\} \left\{ \Delta n(I+L) \right\}}{\frac{1}{N} \sum_{I=1}^N \left\{ \Delta n(I) \right\}^2} \quad (2)$$

This autocorrelation function is itself of intrinsic value in examining the physical behaviour of the data, and can often be used to trace the cause of anomalous features in a power spectrum. The calculation of the autocorrelation function is therefore considered quite a worthwhile intermediate step.

The power spectrum,  $S(f)$  of the positive ion density irregularity distribution is obtained by Fourier transforming the weighted autocorrelation function,

$$S(f) = \delta \sum_{L=-(M-1)}^{M-1} W(L) \rho(L) e^{-i2\pi f L \delta} \quad (3)$$

in the range  $-1/2\delta \leq f < 1/2\delta$ .

It is more convenient for calculation purposes to rewrite equation (3), since  $S(f)$  is an even function of  $f$ , as

$$S(f) = 2\delta \rho(0) + 4\delta \sum_{L=1}^{M-1} \rho(L) W(L) \cos(2\pi f L \delta) \quad (4)$$

in the range  $0 \leq f \leq 1/2\delta$ .

From equation (2),  $\rho(0) = 1$ . The weighting function,  $W(L)$  and the maximum number of lags,  $(M-1)$ , over which the sum in equation (4) is computed,

determine the confidence limits and the frequency resolution of the resultant power spectrum. The general approach is derived from that of Blackman and Tukey, and the weighting function which has been satisfactorily employed in the majority of our computations is that sometimes referred to as the Tukey lag window, (Jenkins and Watts, 1968)

$$W(L) = \begin{cases} 1/2 \left[ 1 + \cos(\pi L/M) \right] & L \leq M \\ 0 & L > M \end{cases} \quad (5)$$

Normally for  $N = 3300$  we have varied  $M$  in the range  $150 \leq M \leq 750$ .

It is convenient to plot  $S(f)$  on a logarithmic scale, so that a given interval on this logarithmic  $S(f)$  scale corresponds to a constant power ratio. Although  $S(f)$  is initially calculated as a function of frequency,  $f$ , it is more relevant for the present geophysical studies, to display the spectral power of the irregularities as a function of scale size,  $\lambda$ . The velocity  $V_s$  of the satellite is known and hence  $\lambda$ , is readily obtained,

$$\lambda = V_s / f \quad (6)$$

This conversion is included in the computation on a routine basis. It is assumed that the time series is stationary, that is, that the observed irregularities are spatial rather than temporal, when sampled at the satellite velocity of approximately 7 km/sec.

A logarithmic scale is chosen for the frequency or scale size axis also, and plots may be generated over four decades from 0.1 to 1000 km. The range over which the power spectrum is physically significant is approximately 0.2 km to 100 km. The lower limit of 0.2 km corresponds to the Nyquist frequency cut off,  $f_N = 1/2\delta = 30$  Hz. This frequency, for the lowest value of  $V_s$  of the ISIS I orbit corresponds to  $\lambda \approx 200$  meters. Hence the lower limit of the measurable scale size is set by the satellite velocity and the instrumental sampling rate. There is no exact upper limit on the scale sizes measurable, since the length of the data sample analyzed is a matter of choice. The lag window chosen is

normally dependent upon the length of the data sample analyzed. In the present work the largest sample lengths considered have been 400 km.

## RESULTS

An example of the ion density measured on orbit 3092, November 1, 1969, is shown in Fig. 1. Five sections of data of 55 seconds duration are labelled A to E. Each section of data contains 3,300 separate ion density measurements. The example is a fairly typical one of an early winter low magnetic activity period on the dayside near local noon. Sections of data A & B are from the upper mid latitudes while C-E are from the higher latitude region of the dayside cleft (Heikkila and Winningham, 1971). The equatorial boundary of this region of generally enhanced plasma density and fine scale structure occurs, in this example, at approximately  $76^\circ$  invariant latitude, which is in accordance with the low  $K_p$  value.

The eye can detect a small regular modulation of the ion density in the samples A and B of Fig. 1. This modulation is caused by the spinning motion of the satellite. In samples C, D and E larger amplitude and irregular variations in the ion density are evident to the eye. In Fig. 1, and in the other summary plots of the ion density data, it should be noted that only one twentieth of the recorded data points are displayed. A greater display density does not increase the information which may be gained by visual inspection. However, the input to the numerical power spectral analysis utilizes every recorded data point.

Using the approach described in Section 3, the power spectrum of the irregularities of data samples A through E of Fig. 1, were calculated and the result is shown in Fig. 2. The 95% and 80% confidence intervals are shown.

Analysis shows that the power spectrum ceases to increase with increasing  $\lambda$ , for a value  $\lambda_T$ , where  $100 \text{ km} \leq \lambda_T \leq 1000 \text{ km}$ . This result is true for the majority of the power spectra we have examined, and in general we estimate that  $\lambda_T$ , the outer scale size is

approximately 100 km. Exceptions occur on those occasions when data samples include a major geophysical feature such as the main trough or the whole of a very pronounced dayside cleft enhancement. Some increase in spectral power with increasing  $\lambda$  is then observed up to the bandwidth limited zero-frequency cut-off. These cases are not regarded as random ionospheric irregularities. The cut-off at  $\lambda = 0.2$  km is clearly seen in the results.

An approximately straight line is evident for the spectral power behavior between 100 km and 1 km scale sizes implying that the relationship between spectral power and frequency is of the form,

$$P = P_0 f^{-\beta} \quad (7)$$

Equation (7) is found to fit over 90% of the spectra which we have examined and which are appreciably above the noise level of the system.

There is an order of magnitude difference in absolute power level between spectra, sample E, from within the high latitude irregularity zone at  $84^\circ$  and sample A at  $60^\circ$  which is equatorward of the irregularity zone. The 95% confidence interval, shows that the order of magnitude power level difference is unquestionably real. Since these are spectra of relatively small amplitude fluctuations, the difference in power level below 2 km scale size is decreased, due to the power spectral density approaching the noise level. Power spectra C, D and E are all very similar being taken near or in the dayside cleft region and within the high latitude.

The average values and standard deviation of  $\beta$  based on 100 orbits of data in the dayside cleft, polar cap, and nightside precipitation zone, are given in Table I. These results over a large scale size range, are in agreement with the results of Dyson et al. (1974) and Rufenach (1972). Satellite passes at various heights between 574 and 3523 km over a given geographical region show no systematic variation of the power spectra or spectral index with altitude. The

high latitude irregularity region is found to extend vertically at least 3000 km.

#### INTEGRATED SPECTRAL POWER

Because of the importance of the amplitude variation of the power spectral density with position, the spectral power results were also integrated on the computer over the scale size range 1 to 10 km. The results for a morning pass, orbit 2335, in the northern hemisphere is shown in Fig. 3. The positive ion density variation over the invariant latitude range  $28^\circ$  to the pole are shown in the upper curve of the figure. The data was taken during a moderately disturbed magnetic period with  $k_p = 4$  with  $k_p$  varying between 0 and 1 during the previous 24 hours. In the lower curve of Fig. 3, the irregularity amplitude is shown. It is seen that the integrated spectral power starts to increase at  $58^\circ$ , gradually increases, reaching a maximum at  $75^\circ$  invariant latitude in the precipitation zone. The consequences of particle precipitation are first clearly detected in the ion density data at  $68^\circ$ . The results poleward of the precipitation zone are representative of measurements in the polar cap. They show reduced but significant irregularity amplitude in this region.

The power spectra of the density irregularities at the high latitude positions A and B and at invariant latitude  $41^\circ$ , data C, of Fig. 3 are shown in Fig. 4. The power spectra of position B at  $73^\circ$  in the precipitation zone and position A in the polar cap show two distinct straight line slopes. Curve B, for example, exhibits one straight line between scale sizes of 100 to 7 km with a second evident between 7 and 0.2 km. Deviations from a single straight line have been observed on less than 10% of the power spectra evaluated. These results indicate that at times more than one irregularity production and dissipation mechanism is operating. The results at midlatitude, data C, show greatly reduced spectral power, typical of most mid latitude results.

The irregularity amplitude for a transpolar pass in the southern hemisphere, orbit 1705, under disturbed magnetic conditions,  $k_p = 5$ , is shown

in Fig. 5. The insert in Fig. 5 gives the location of the satellite during pass 1705 in magnetic local time coordinates.

The thermal ion density data shows that the satellite passes through the auroral precipitation zone on the dayside between 70 and 75 degrees. The decreasing ion density with increasing latitude in this region is due to the rapid decrease in charge density with increasing altitude. The satellite passed through perigee at 57°. The irregularity amplitude over the polar cap is seen to be comparable to values obtained in the dayside precipitation zone.

As the satellite traverses the nightside auroral zone between 72 and 57 degrees invariant latitude, soft particle precipitation causes an increase in ion density. The lower curve of Fig. 5 shows maximum integrated spectral power in this region. The equatorial wall of the trough is about 10 degrees wide and an increase of irregularity amplitude above the mid-latitude values is readily observed across this boundary, although it is significantly reduced relative to the values measured in the precipitation zone. On the nightside, the irregularity amplitude is clearly found to decrease at the equatorial edge of the trough around 47 degrees. The results of Fig. 5 illustrate a general feature of the data, that is, that the maximum integrated spectral power is usually found in the auroral zone on the nightside.

The power spectral density vs. frequency plots for the data obtained at positions A, B, and C of Fig. 5 are illustrated in Fig. 6. The spectra at 60 and 71 degrees on the dayside show considerably lower amplitudes than the spectra at 72 degrees on the nightside. The spectral index for the power spectra at positions A, B, and C are 1.6, 1.4, and 1.5 respectively.

#### COMPARISON WITH SCINTILLATION MEASUREMENTS

Three months of simultaneous satellite ion probe and scintillation data were examined to ascertain whether

a relation existed between them. The scintillation data was provided by Jules Aarons and includes ground based measurements at Huancayo, Peru, Hamilton Mass. and Narssarssuaq, Greenland. One hundred thirty seven mhz signals transmitted from the ATS series satellites were used in the calculation of the scintillation index. Data was compared when the ISIS-I satellite was below 2000 km altitude and within a 5° latitude and longitude region traversed by the satellite signal on its passage to the ground receiver.

Irregularities of amplitude greater than 20% were found to be present on over 90% of the cases where the scintillation index was greater than 50. As would be expected from the results of the study of the high latitude irregularity morphology (Sagalyn et al., 1974) the best correlation was found with results from Narssarssuaq located at geographic latitude 61° N, longitude 45° at night. This station is usually within the high latitude irregularity zone at night. High amplitude scintillations and small scale topside irregularities are much less frequently observed at Hamilton, latitude 43° N, or at Huancayo, latitude 12° S.

The spectral index deduced from these satellite results and the simultaneously measured scintillation index at Narssarssuaq are compared in Table 2. No correlation is found between the magnitude of the spectral and scintillation indices. Consistent with the results discussed earlier, the spectral index is found to vary between 1.5 and 2.5 with an average value of about 2.0 while the scintillation index varies between 33 and 99.

An example of a specific comparison is illustrated in Fig. 7. On orbit 65 the satellite intercepted the path of the signal at point B, invariant latitude 65°. A scintillation index of 33 was measured 10° north of the irregularity boundary. The spectral density was evaluated at points A and B of fig. 7. The results are shown in fig. 8. It is seen that the power spectral density versus frequency is nearly the same for positions A and B, with a spectral index of 2.1 and 1.9 respectively. Thus, the power spectral

results are not found to be unique to the measurement point. They are representative of the irregularity spectra in the high latitude disturbance region, the maximum spectral power being measured in the vicinity of the maximum flux of low energy electrons and protons.

#### DISCUSSION

Cole (1971) and others have shown that the presence of electrostatic fields, the heating and ionizing effects of low energy electron and proton precipitation, neutral winds in the E region can all supply the driving force necessary to produce large scale ionospheric irregularities of the order of 10 to 150 km in length. High latitude electrostatic fields have been measured by Kelley and Mozer (1972). Precipitating soft particle fluxes and E region neutral winds are well established (Heikkila and Winningham (1971), Rees (1972), Frank and Ackerson (1971)). Turbulence and instability mechanisms dissipate the energy of larger scale irregularities to form continuously smaller scale sizes (Reid, 1968, Farley, 1963). The fact that the spatial density gradients are independent of scale size indicates that turbulence and instability mechanisms are operating.

#### SUMMARY

The power spectra of small scale ionization irregularities over the scale size range 200 meters to 150 km has been evaluated for over 200 orbits of ISIS-I utilizing positive ion data. At least 90% of the spectra show that the irregularities obey a power law with a spectral index of  $2 \pm .5$ . This result is consistent with the interpretation that instability and turbulence mechanisms are responsible for the dissipation of large scale irregularities to form continuously smaller scale sizes. The power law holds for scale sizes ranging from the lower limit of measurement approximately 200 meters to an outer scale size of about 100 km. About 10% of the spectra show more complex structure and can usually be approximated by 2 straight lines. This indicates that at times more than one mechanism is operating to dissipate the energy of thermal ion and electron irregularities. There has been found no systematic variation of spectral index

or irregularity amplitude with height over the altitude range 57 to 3523 km. Thus any interpretation of scintillations must take into account the fact that the small scale irregularity region extends vertically at least 3000 km.

The variation with latitude of the integrated density over the scale size 1 to 10 km, shows a raised amplitude level throughout the high latitude irregularity zone. However, maximum irregularity amplitude is consistently found to be located in the vicinity of maximum soft particle flux. When the scintillation index is greater than 50, topside small scale irregularities are found on over 90% of the cases examined. There is found no correlation between spectral index and scintillation index.

#### ACKNOWLEDGEMENTS

We wish to thank Drs. M. Smiddy, P. Wildman, and Ms. S. Bredesen of the Electrical Processes Branch, AFCRL, for several helpful discussions. We also wish to thank the National Academy of Sciences for financially supporting one of us (A.D.R. Phelps) by means of a NAS-NRC Resident Research Associateship.

#### REFERENCES

- Aarons, J., H.E. Whitney, and R.S. Allen, Global morphology of ionospheric scintillations, *Proc. I.E.E.E.* **59**, 159, 1971.
- Briggs, B.H., Observations of radio star scintillation and spread F echoes over a solar cycle, *J. Atmos. Terr. Phys.*, **26**, 1, 1964.
- Checcacci, P.F., Direct detection of ionospheric irregularity, *J. Atmos. Terr. Phys.*, **31**, 1131, 1969.
- Chivers, H.J.A., The power spectrum of scintillations of a two component radio source, *J. Geophys. Res.*, **76**, 2526, 1971.
- Cole, K.D., Formation of field aligned irregularities in the magnetosphere, *J. Atmos. Terr. Phys.*, **33**, 741, 1971.
- Dyson, P.L., J.P. McClure, and W.B. Hanson, In-situ measurements of the spectral characteristics of F region ionospheric irregularities, *J. Geophys. Res.*, **79**, 1497, 1974.
- Elkins, T.J., and M.D. Papagiannis, Measurement and interpretation of power spectrums of ionospheric

- scintillation at a sub-auroral location, *J. Geophys. Res.*, 74, 4105, 1969.
- Farley, D.T., A plasma instability resulting in field aligned irregularities in the ionosphere, *J. Geophys. Res.*, 68, 6003, 1963.
- Frank, L.A. and K.L. Ackerson, Observations of charged particle precipitation into the auroral zone, *J. Geophys. Res.*, 76, 3612, 1971.
- Frihagen, J., Occurrence of high latitude ionospheric irregularities giving rise to satellite scintillation, *J. Atmos. Terr. Phys.*, 33, 21, 1971.
- Heikkila, W.J., and D. Winningham, Penetration of magnetosheath plasma to low altitudes through the dayside magnetospheric cusp, *J. Geophys. Res.*, 76, 883, 1971.
- Jenkins, G.M. and D.G. Watts, Spectral analysis & its applications, Holden Day Publisher, London, 1968.
- Kelley, M.C. and F.S. Mozer, A satellite survey of vector electric field in the ionosphere at frequencies from 10 to 500 Hz - I Isotropic, high latitude emissions, *J. Geophys. Res.*, 77, 4158, 1972.
- Paul, L.M., K.C. Yeh, and B.J. Flaherty, Measurement of irregularity heights by the spaced receiver technique, *Radio Science*, 5, 967, 1970.
- Rees, D., Winds and temperature in the auroral zone and their relation to geomagnetic activity, *Phil. Trans. R. Soc. London A*, 271, 563, 1972.
- Reid, A.C., The formation of small-scale irregularities in the ionosphere, *J. Geophys. Res.*, 73, 1627, 1968.
- Rufenach, C.L., A radio scintillation method of estimating the small scale structure in the ionosphere, *J. Atmos. Terr. Phys.*, 33, 1941, 1971.
- Rufenach, C.L., Power law wave number spectrum deduced from ionospheric scintillation observations, *J. Geophys. Res.*, 77, 4761, 1972.
- Sagalyn, R.C., M. Smiddy, and J. Wisnia, Measurement and interpretation of ion density distribution in the daytime F-region, *J. Geophys. Res.*, 68, 199, 1963.
- Sagalyn, R.C., M. Smiddy, and M. Ahmed, High-latitude irregularities in the topside ionosphere based on ISIS-I thermal ion probe, *J. Geophys. Res.*, 79, 4252, 1974.
- Thorne, G.D., Incoherent scatter observations of travelling ionospheric disturbances, *J. Geophys. Res.*, 69, 4047, 1964.
- Titheridge, J.E., and G.F. Stuart, The distribution of irregularities in the Antarctic ionosphere - I Mean seasonal maps at sunspot minimum, *J. Atmos. Terr. Phys.*, 30, 85, 1968.
- Whitaker, J.H., L.H. Brace, J.R. Burrows, T.R. Hartz, W.J. Heikkila, R.C. Sagalyn, and D.M. Thomas, ISIS-I observations of the high-latitude ionosphere during a geomagnetic storm, *J. Geophys. Res.*, 77, 6121, 1972.

TABLE I

AVERAGE VALUES OF THE SPECTRAL INDEX  $\beta$

The Standard Deviation is  $\pm 0.1$

<u>MAGNETIC ACTIVITY</u>	<u>DAYSIDE CLEFT</u>	<u>NIGHTSIDE AURORAL ZONE</u>	<u>POLAR CAP</u>
Kp > 3	2.1	2.0	2.05
Kp $\leq$ 3	1.8	1.8	1.9

TABLE II

COMPARISON OF SIMULTANEOUS MEASUREMENTS  
OF SCINTILLATION INDEX AND SPECTRAL INDEX

<u>L<sub>ST</sub> (hr/min)</u>	<u>ALTITUDE (km)</u>	<u>ORBIT</u>	<u>AVERAGE <math>\beta</math></u>	<u>S.I.</u>
2153	775	76	1.32	99
2159	735	65	2.05	33
1906	2000	93	2.35	60
0941	1675	160	1.99	43
1824	1250	635	1.54	73
0812	1385	609	1.94	99
1809	1420	680	2.74	49
0535	749	820	1.98	86
1715	2050	825	2.35	88
0517	925	876	1.61	63



MAG. L.T.	13/43	13/30	13/14	12/50	12/13	11/9	9/23	7/14
McILWAIN L	2.90	4.03	6.02	9.84	18.17	38.79	83.10	90.14
ALTITUDE (km)	1237	1374	1517	1663	1810	1957	2103	2245
INV LAT	54.0	60.1	65.8	71.4	76.4	80.8	83.7	84.0

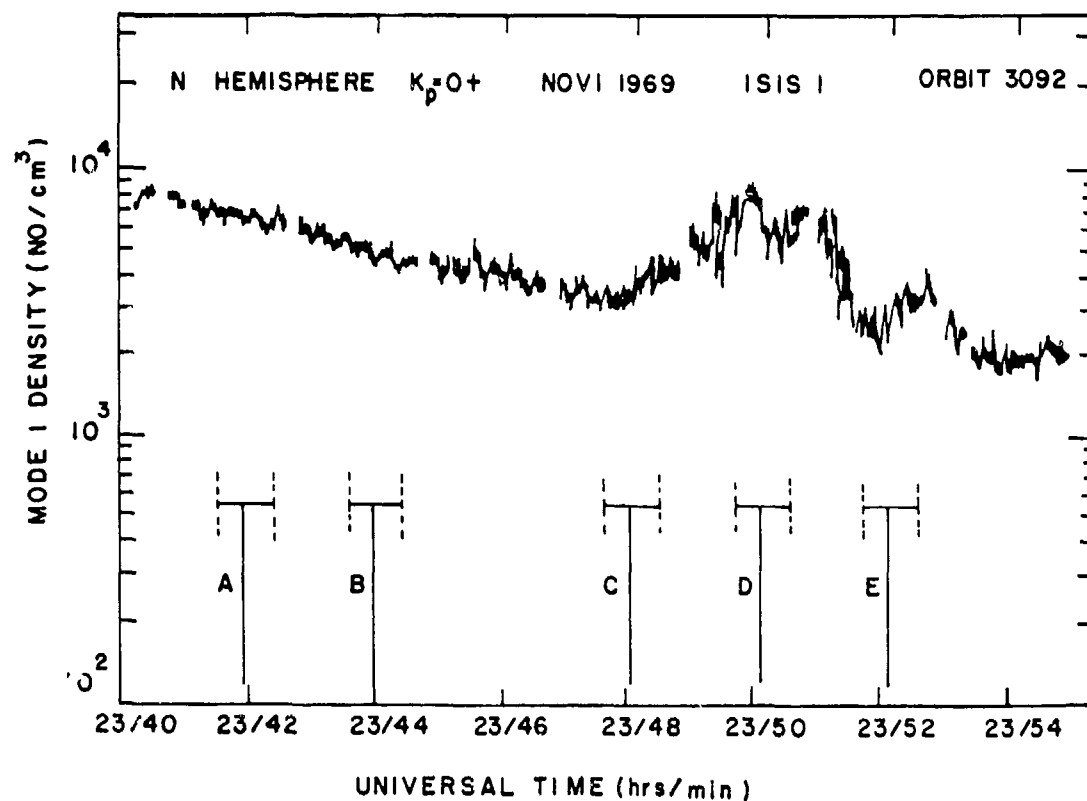


Figure 1 — ISIS-I spherical electrostatic analyzer ion density measurement on the dayside of the northern hemisphere during magnetically quiet conditions, orbit 3092.

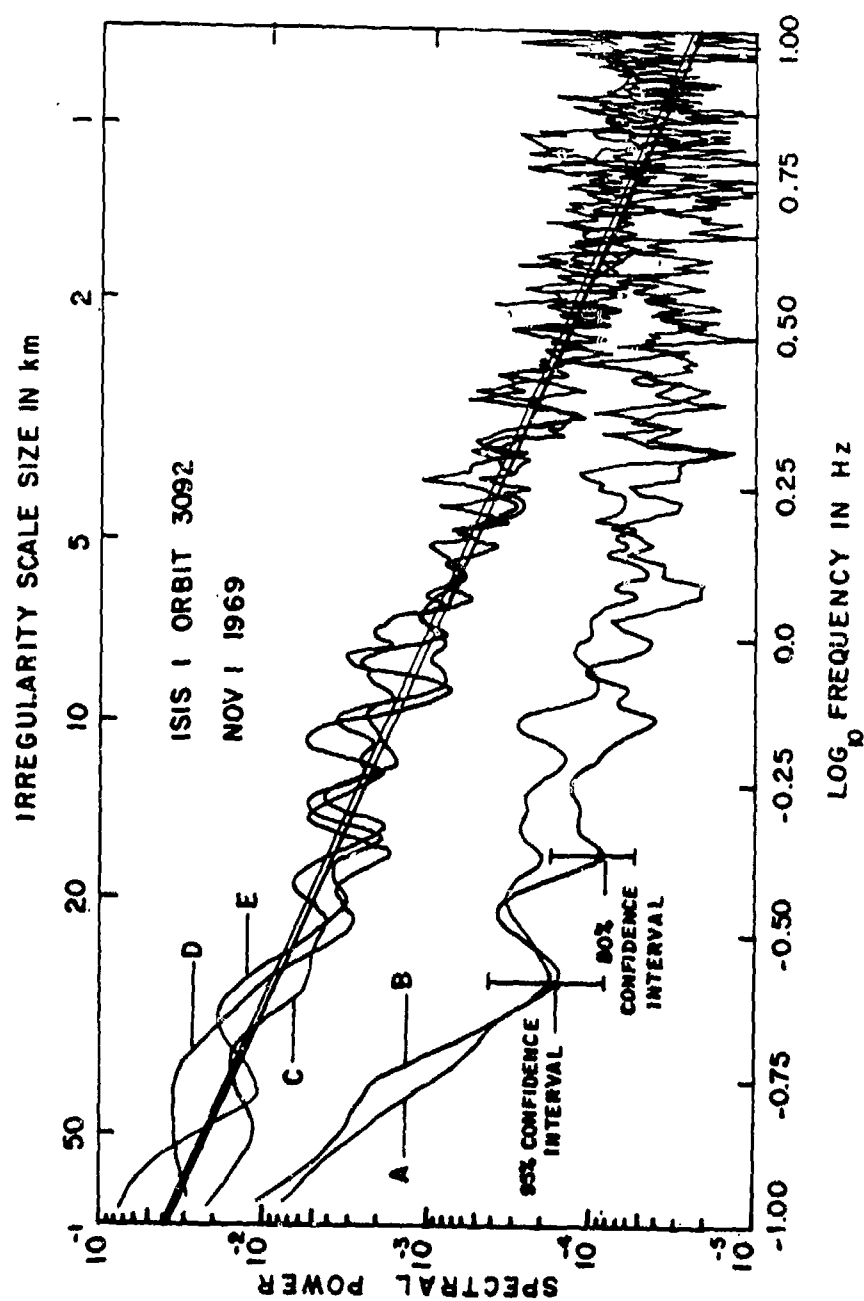


Figure 2 — Power spectra of five data samples A through E of orbit 3092.

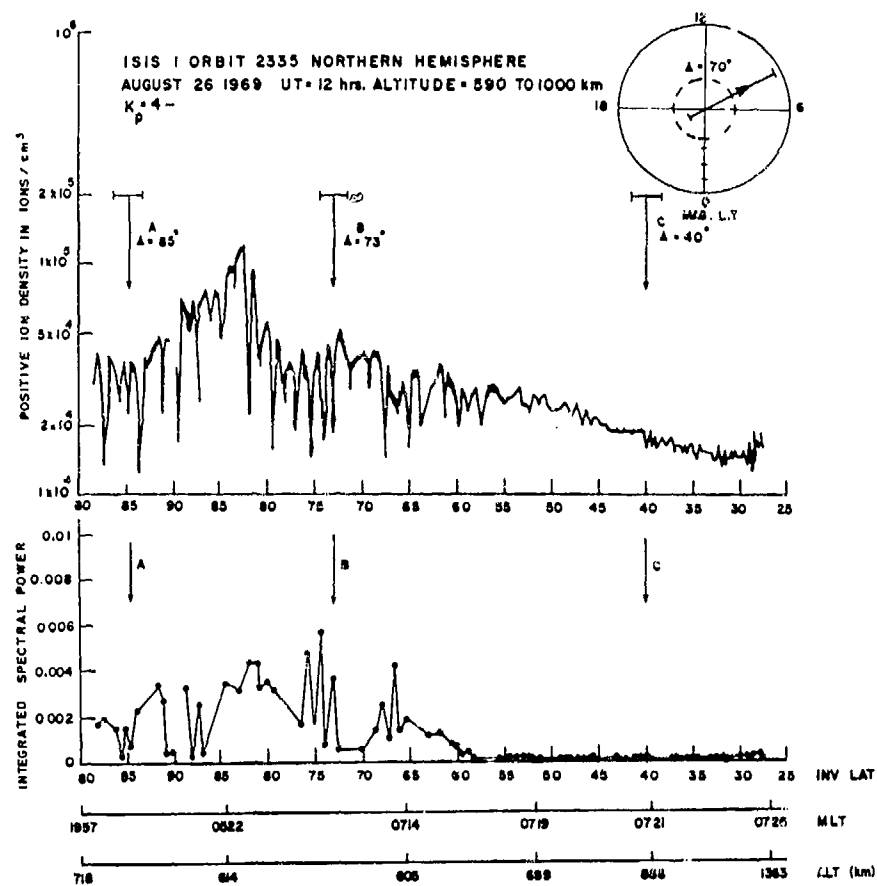


Figure 3 — Ion density and integrated spectral power versus invariant latitude, for moderately disturbed magnetic conditions in the summer northern hemisphere. Inset gives approximate location of satellite in magnetic local time, for orbit 2334.

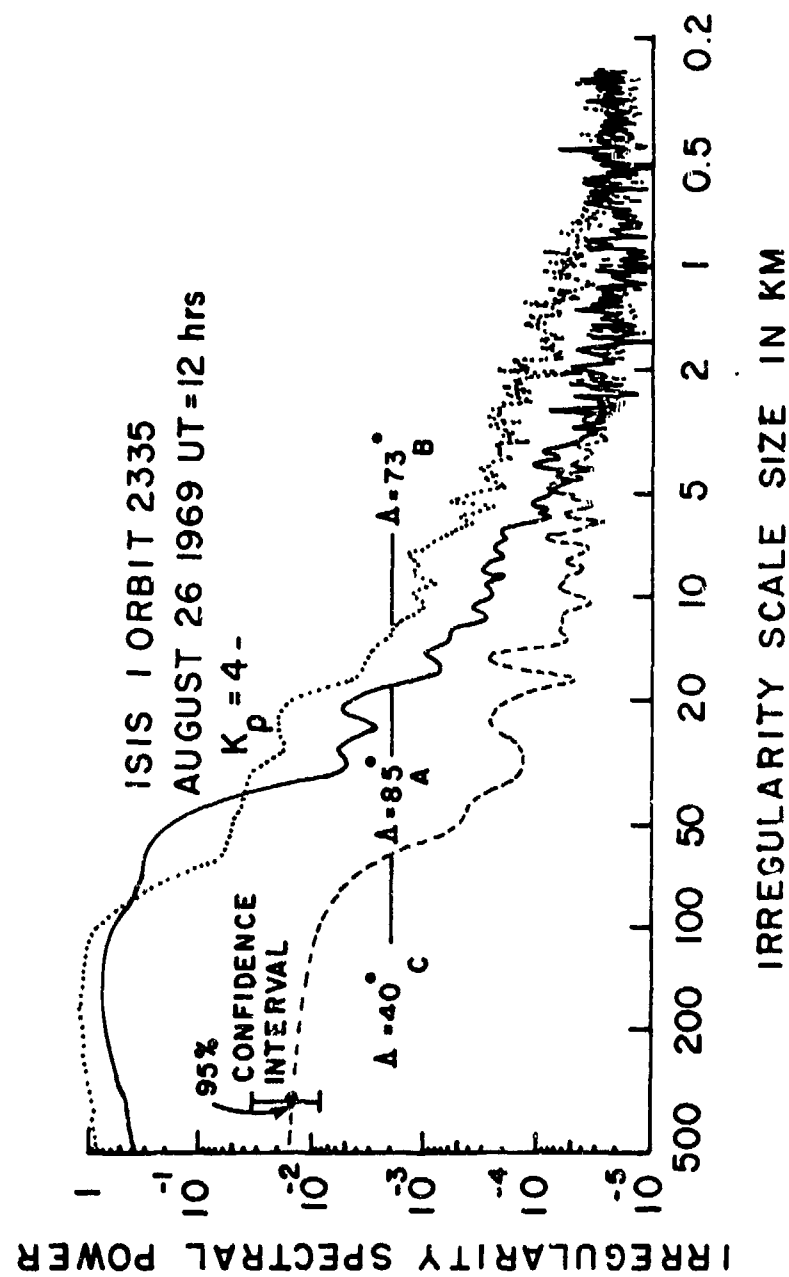


Figure 4 — Power spectra of data samples A, B, and C of orbit 2335.

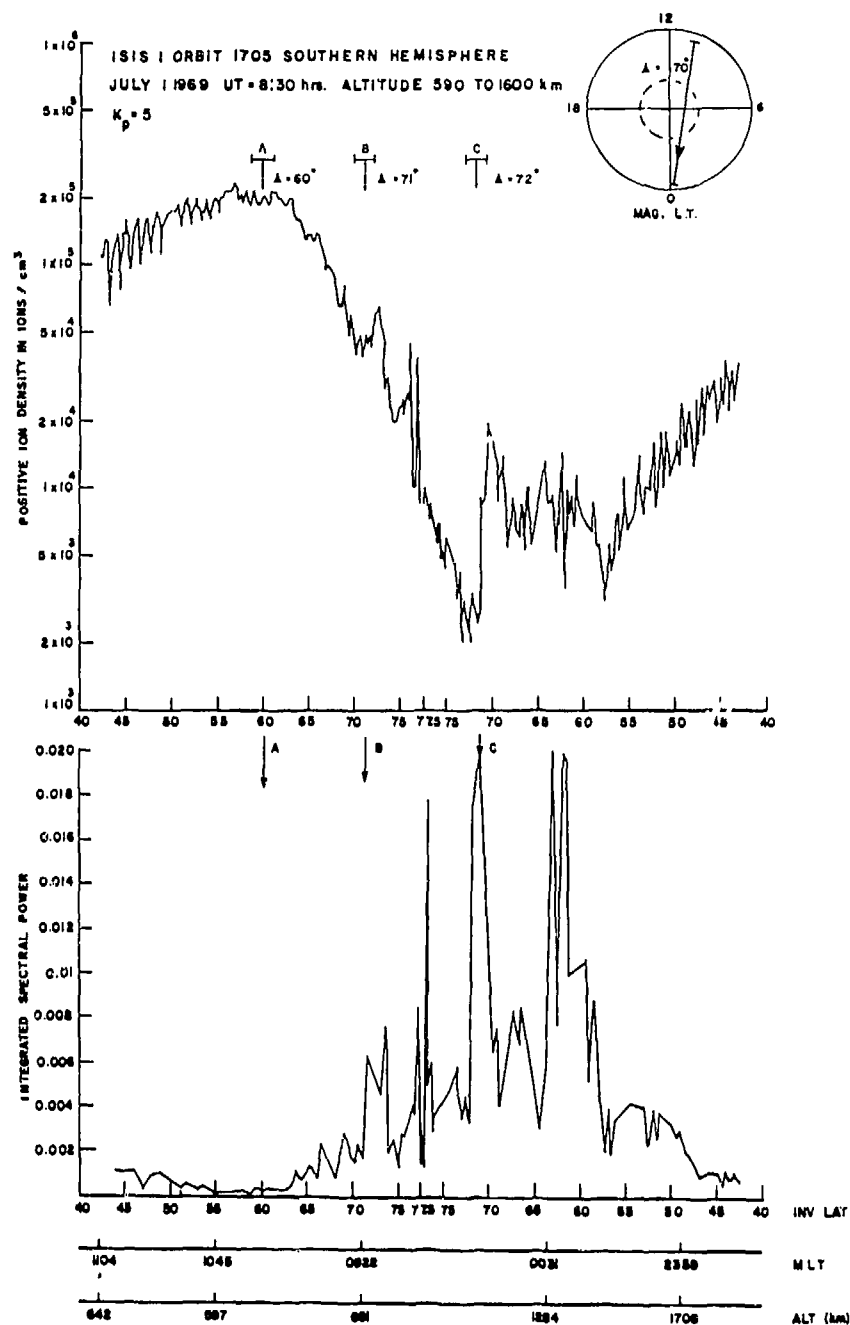


Figure 5 — Ion density and integrated spectral power versus invariant latitude, for disturbed magnetic conditions in the winter southern hemisphere. Inset gives approximate location of satellite in magnetic local time, for orbit 1705.

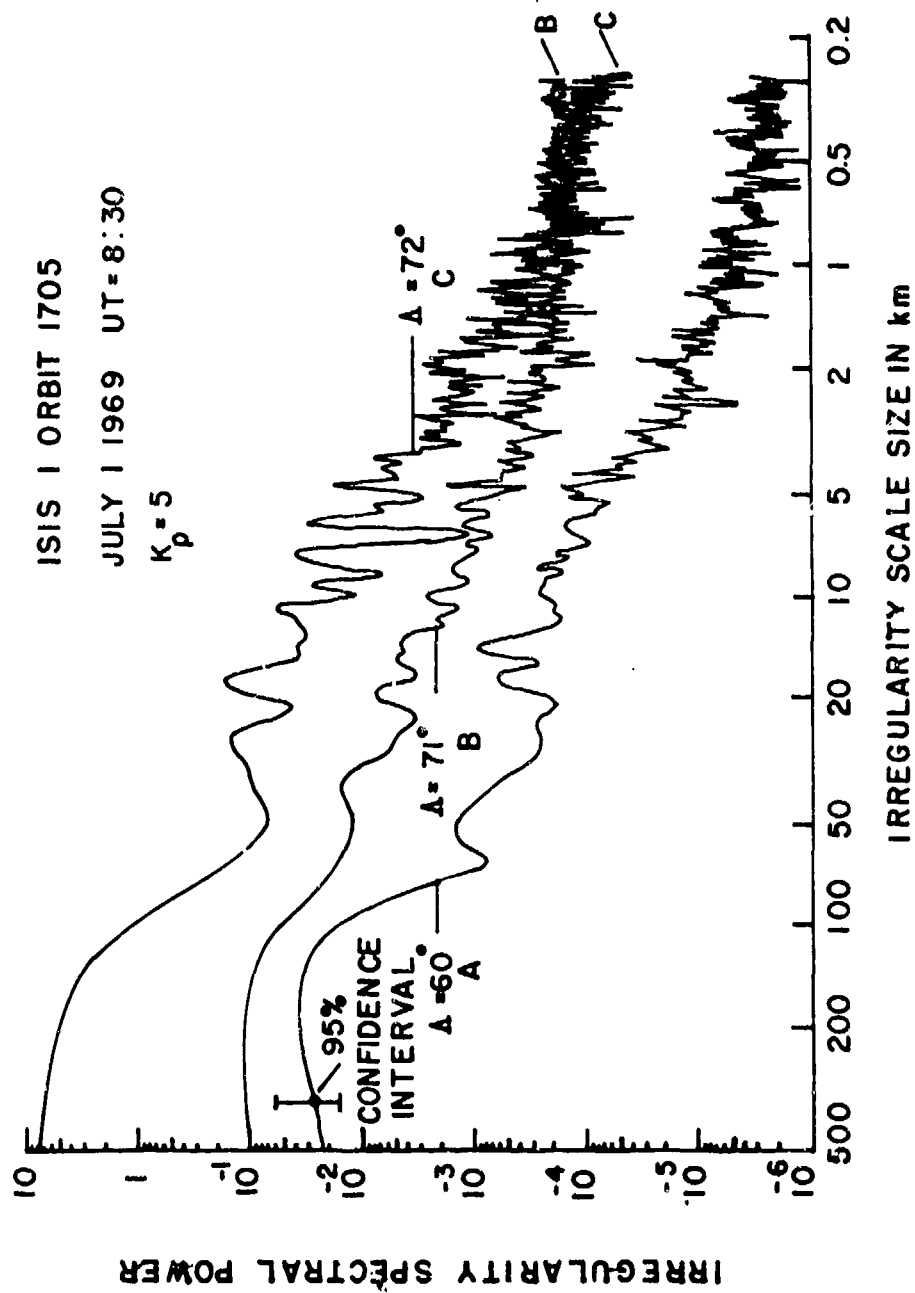


Figure 6 — Power spectra of data samples A, B, and C of orbit 1705.

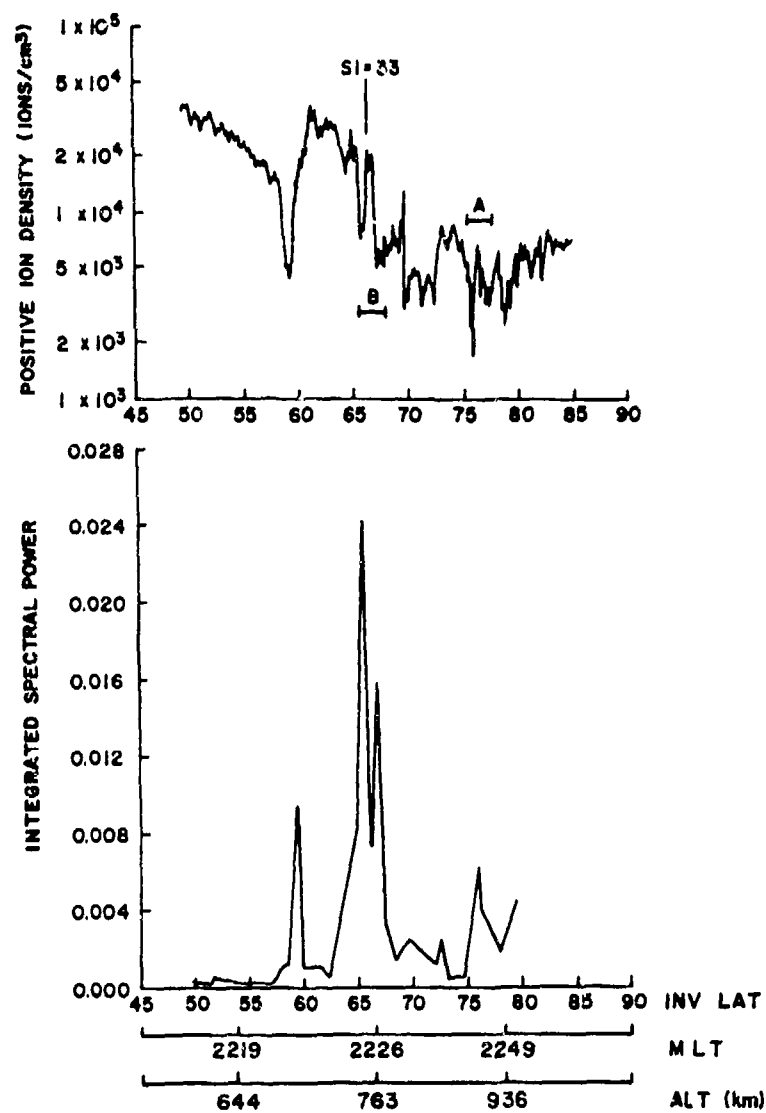


Figure 7 — Ion density and integrated spectral power versus invariant latitude for ISIS-I orbit 56, Altitude 630-870 km, MLT 22-23 hrs. The location of the ground based SI measurement is indicated.

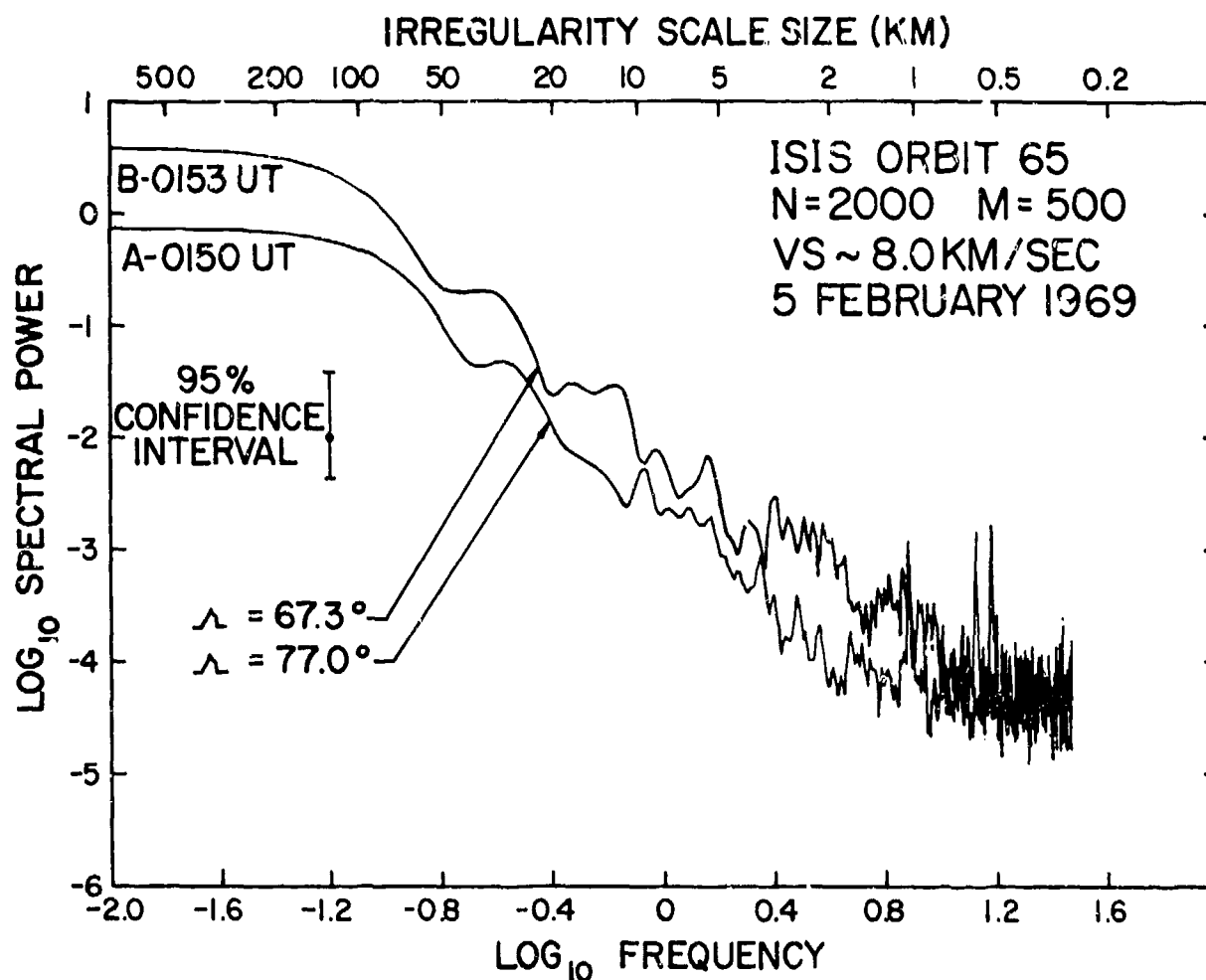


Figure 8 — Power spectra of data samples A and B of orbit 65.



# INTEGRATED STUDIES ON INHOMOGENEITIES IN THE EQUATORIAL IONOSPHERE USING DIFFERENT TECHNIQUES

by

C.A. Reddy, C.V. Devasia,  
B.V. Krishna Murthy and  
K.S.V. Subba Rao

Physics and Applied Mathematics Division  
Vikram Sarabhai Space Centre  
Trivandrum-695022  
INDIA

## Abstract

Different experimental techniques are being used and developed at the equatorial station of Trivandrum (Magnetic dip  $\sim 0.6^\circ\text{S}$ ) for studies on ionospheric irregularities and their effects on HF, VHF, and UHF radiowaves. The most pertinent of the experiments are: a VHF Backscatter Radar (55 MHz), a phase recording system for HF waves, a HF Doppler Radar and the recording system for ATS-6 radio transmissions on 40, 140, 360, and 860 MHz. Using the various techniques, integrated studies on ionospheric irregularities are being conducted and further studies are planned. The capabilities and the complementary nature of these techniques are discussed along with some of the results obtained at Trivandrum.

## INTRODUCTION

It is now known that VHF and even UHF signals used for satellite-to-ground communication are susceptible to considerable fading in a narrow latitudinal range of about  $\pm 3^\circ$  centered at the magnetic equator. This fading is caused by a variety of ionization irregularities in the E and F-regions of the equatorial ionosphere. The plasma irregularities in the equatorial electrojet as well as the spread F irregularities are elongated along the geomagnetic field lines; this characteristic makes them act like a diffraction screen for radio signals passing through them. Consequently, large variations of the signal intensity both in space and time are produced (because of the motions associated with the plasma irregularities).

In spite of the broad understanding we have regarding the nature and effects of the equatorial irregularities, many important questions still remain unanswered about the origin, structure and the effects of these ionization irregularities. At the scientifically advantageous location of Thumba near Trivandrum, which is close to the magnetic equator (Geog. Lat.  $8.5^\circ\text{N}$ , Geog. Long.  $76.9^\circ\text{E}$ , magnetic dip  $\sim 0.6^\circ\text{S}$ ), a number of coordinated experiments are being conducted and planned in an attempt to find satisfactory

answers to some of the important questions. In this paper, a brief presentation is made on the capabilities of such experiments, the complementary nature of such experiments and some relevant results so far obtained with those experiments.

## EXPERIMENTS

The relevant experiments which are in operation or scheduled for operation in 1975 are shown below:

- i) VHF Backscatter Radar at 55 MHz.
- ii) Ionospheric phase path recording (2-5 MHz.)
- iii) Topside and Bottomside Ionograms.
- iv) HF Doppler Radar (2-10 MHz.)
- v) Phase and Amplitude Recording of ATS-6 Beacon Transmissions on 40, 140, 360 MHz and their side bands.
- vi) Amplitude Recording of 860 MHz signals from ATS-6.

The first three of the above are in operation. Both the amplitude and the Doppler frequency spectrum of the backscattered signal are recorded. At present this radar is being used mainly for studies on equatorial electrojet irregularities. The phase path recording system provides good information on rapid and small changes of the phase height and also on the movement of the ionization irregularities. This is indeed a very sensitive technique for studying the structure and movement of small scale irregularities. The topside and bottomside ionograms provide information on the strength and time variations of spread F, Esq and blanketing Es irregularities in addition to the information on the height structure of electron density.

The last three experiments will be operational in June 1975 when the ATS-6 satellite is expected to be moved to  $35^\circ\text{E}$  longitude making it possible to record the beacon transmissions and TV signals (860 MHz) at Trivandrum.

This provides an excellent opportunity for studying the effects of equatorial ionization irregularities on the VHF and UHF signals under different ionospheric conditions. Combining the results of the ATS-6 experiment and the simultaneous observations with the other techniques, it is possible to obtain a more precise understanding of the origin and the effects of the equatorial ionospheric inhomogeneities.

In the next section, some observational results are presented to illustrate how simultaneous observations with different techniques provide an immense advantage in interpretation.

### RESULTS

**Electrojet Irregularities:** At the equatorial electrojet latitudes, the geomagnetic field is known to decrease sometimes rather abruptly by tens of gamma even on magnetically quiet days. This is accompanied by a large decrease in the strength of the backscatter radar signal and a decrease in the velocity of the irregularities as indicated by the Doppler frequency changes. A typical case of such a decrease is shown in Fig. 1 for May 23, 1974, which is a moderately disturbed day.

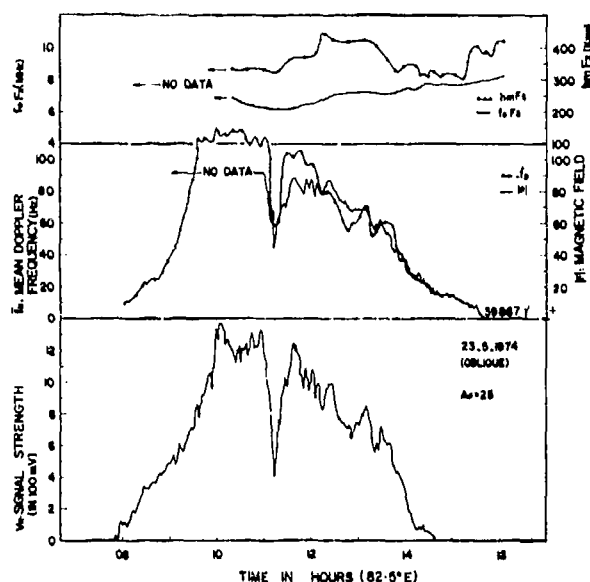


Figure 1

The decrease occurs at mid-day when the strength of the irregularities is large and it lasts only 30-40 minutes. This rapid variation in the strength of the irregularities provides an excellent means for studying the effects of these irregularities on the propagation of VHF and UHF signals (40, 140, 360, 880 MHz) from the ATS satellite. Interferometric methods are proposed to be used for isolating the effect of a limited portion of the electrojet.

Fig. 2 shows the reverse situation of a sudden large increase of backscatter signal from zero level. This occurs during the evening hours of 1800-1900 hrs. on May 27, 1974. This observation provides a good example of how

simultaneous observation with different techniques are invaluable. The sudden signal enhancements of the backscatter signals in the evening hours were observed for quite sometime in the past, while a separate study on the blanketing sporadic E traces in ionogram was also being carried out. Then we decided to examine the behaviour of the backscatter signals during the presence of blanketing E traces in ionograms. Immediately we realized that the sudden enhancements of VHF backscatter signals were invariably associated with the blanketing sporadic E layers in the electrojet region. In retrospect, this association appears to be quite logical because the steep gradients of the blanketing type sporadic E layers can cause the generation of strong gradient instabilities in the plasma. This observation has many other implications which are being investigated separately. In the present context the pertinent question is: how ATS-6 signals of various frequencies respond to such changes in the electrojet irregularities. If such severe and sudden variations of scattered signal are observed at 55 MHz, similar variations on a reduced scale can be expected on the 140 MHz signals (and, to a smaller extent, even on 360 MHz signals) transmitted from ATS-6.

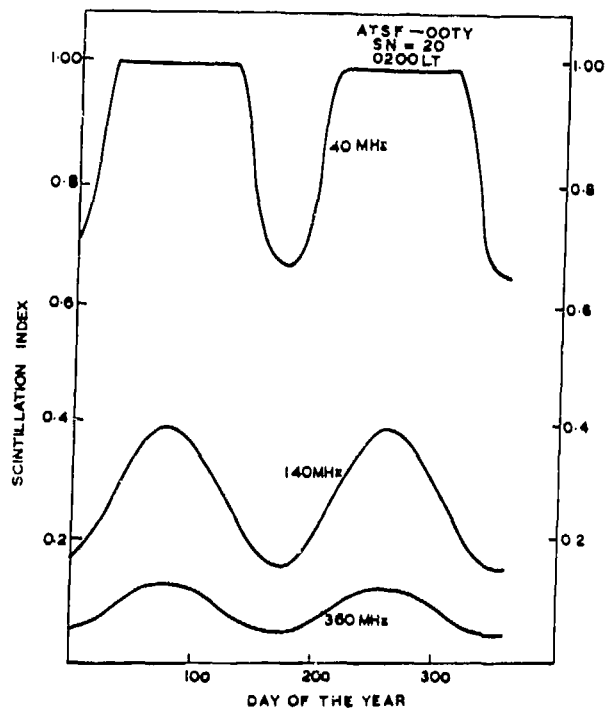


Figure 2

**Spread F irregularities:** We are using at present only a ground-based ionosonde and the phase path recording technique for observations on spread F irregularities. (Top-side ionograms are being recorded, but not analyzed as yet). Ionosonde gives the heights, the frequency ranges, and the time variations of spread F occurrence. On a finer scale, the movements of spread F irregularities at a particular height are observed by the phase path technique.

Typical records of phase height variations in the absence of spread F and in the presence of spread F are shown in Fig. 3.

interpreting the ionospheric effects on the VHF and UHF radio transmissions from the ATS-6 satellite.

Two remarkable features of phase height variations during spread F conditions need to be pointed out: (a) the movements of different spread F patches are different but systematic (Fig. 3C); (b) the phase height variations often show a large random component (Fig. 3D). The above features can be interpreted as variations in the velocities either with height or with horizontal separation of the irregularity locations. Multiple frequency observations are planned to resolve this ambiguity. In addition, VHF radar observations (at 55 MHz) are also planned with increased system gain so that the height variation of spread F irregularity intensity — at least at one VHF frequency — is obtained. The information provided by topside ionograms recorded at Trivandrum will also be used in interpreting the spread F irregularities and their effects on signals from ATS-6.

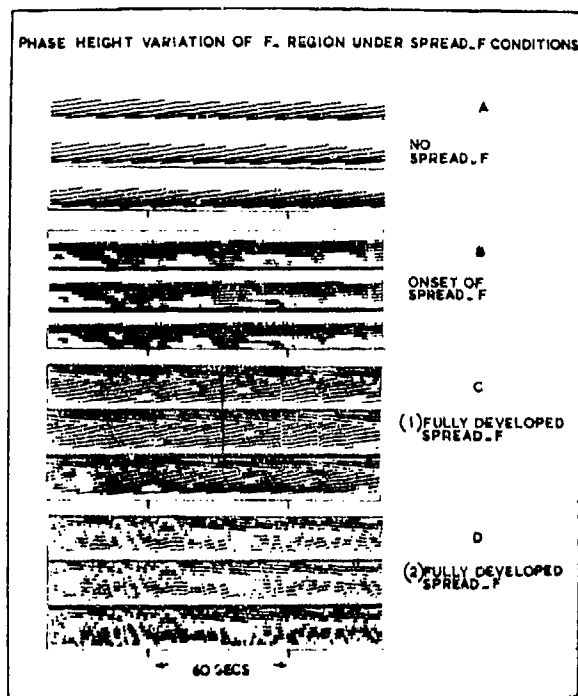


Figure 3

Spread F being a phenomenon of night hours, when electrojet irregularities are extremely weak or absent, the effects of the two kinds of plasma inhomogeneities in the E and F-regions of the equatorial ionosphere on the ATS-6 beacon transmissions can be studied separately.

#### CONCLUSION

Integrated studies on the plasma inhomogeneities in the equatorial ionosphere using a variety of techniques are proving valuable in understanding the genesis and the pertinent characteristics of the inhomogeneities. Such simultaneous observations are expected to be extremely valuable in

# IONOSPHERIC REFRACTION ERRORS IN POSITION FIXING USING SATELLITES

by

A.B. Ghosh and Y.V. Somayajulu,  
Space Research Section, Radio Science Division,  
National Physical Laboratory, New Delhi-110012, India

## INTRODUCTION

Satellite supported navigation systems use the radio beacons to measure the range and elevation angle for position fixing. However, it is well known that the measured range and elevation angles using radio transmissions, differ from the true values due to the refraction effects of the intervening troposphere and ionosphere. With increasing demand on the accuracy of position fixing, it is necessary to develop methods to correct for these refraction effects in order to obtain the true range and elevation angles. Considerable effort is being put in to develop such methods, though mostly for midlatitudes. Such methods essentially involve three-dimensional tracing of the ray path from the receiver to the satellite requiring a tropospheric and ionospheric inputs. In order to compute the ionospheric refraction errors one needs to have the electron density distribution along the ray path. The electron density distribution along the ray path is not readily available and has to be computed from vertical electron density profiles over a range of latitudes and longitudes, since the ray path is a slant path from the receiver to the satellite. In the low latitude — and equatorial regions, the electron density profiles have a strong latitudinal dependence particularly during the day, while the longitude effects can be represented fairly accurately by local time effects. This paper is mainly concerned with development of a method for building electron density profiles for low latitude region particularly for the Indian subcontinent. The main requirement for satellite navigation would be that the methods to correct for refraction effects should be fast, using on board mini-computers so that the true range and elevation angle values could be recovered in a matter of minutes. The primary ionospheric inputs could then be either real time data, such as  $f_oF_2$ , the  $F_2$ -region critical frequency,  $h'F$  the minimum F-region virtual height and/or the total electron content. If real time data are not readily available, the predicted  $f_oF_2$ ,  $hmF_2$  or  $M(3000)F_2$  factor and the electron content could be used. In a practical situation the inputs may be a combination of real time data and predicted values. The problem then is one of generating a family of electron density profiles at, say,  $5^\circ$  latitude intervals and with local time dependence to represent longitude effects.

## METHODS OF BUILDING ELECTRON DENSITY PROFILES

Several methods have been developed to generate electron density models using  $f_oF_2$  and  $hmF_2$  values. The construction of the bottomside profile can be made quite accurate because a substantial effort has been put in to such

work and a great wealth of bottomside data exists on a global basis for several solar cycles. Since most of the transit satellites orbit at an altitude of about 1000 km there is need to build the topside profile upto at least 1000 km.

The measurements of total electron content, the availability of the topside electron density profiles from Alouette topside ionograms and the local electron density at say, 1000 km from probes on satellites have provided measures to construct fairly accurate topside electron density profiles as a function of latitude, longitude and local time. Two efforts in this direction will be mentioned since these form the basis for the method developed here. Somayajulu et al (1965) have proposed a method for generating electron density profiles up to say, 1000 km making use of bottomside data and the total electron content, measured at the ground.

Recently Bent et al (1971) described a method of building an ionospheric model profile upto 1000 km using the topside and bottomside profiles covering almost one solar cycle. This model profile can be predicted for a particular time, location and solar activity.

The present technique is essentially based on these methods but incorporates certain improvements to obtain better accuracy for the topside profile. The method involves the following steps:

(i) The maximum electron density  $NmF_2$  at the  $F_2$ -region maximum is given by

$$NmF_2 \text{ (el/m}^3\text{)} - 1.24 \times 10^{-2} (f_oF_2)^2 \dots (1)$$

$f_oF_2$  is in Hz. If real time values of  $f_oF_2$  are not available, the  $f_oF_2$  values can be taken from the contours of  $f_oF_2$  published in "Ionospheric data" providing the latitudinal and longitudinal dependence.

(ii) If realtime values of  $h'F$ , i.e. the minimum F-region virtual height are available these values can be used to locate the peak of the  $F_2$ -layer. If these are not available, then predicted values of  $M(3000)F_2$  are obtained from the "Ionospheric data" to obtain  $hmF_2$  using the Appleton-Beynon formula.

$$hmF_2 = 1346.92 - 526.40 M + 59.825 M^2 \dots (2)$$

where

$$M = M(3000)F_2 \text{ factor} = \frac{MUF(3000)F_2}{foF_2}$$

The M-factor is itself derived using  $h'F$  from the ionograms.

(iii) It is shown by Seddon (1963) that the  $F_2$  layer can be represented by an  $\alpha$ -Chapman layer from the  $F_2$ -peak down to one scale height below and to 1.5 scale heights above the peak. The  $\alpha$ -Chapman layer is represented by

$$N = N_{\max} \exp \left[ \frac{1}{2} (1 - z - e^{-z}) \right] \dots (3)$$

Where  $z = \frac{h - h_m}{H_m}$  and  $H_m$  is the scale height at the  $F_2$ -layer peak.

The parameter  $H_m$  is a function of the local time, latitude and solar activity. From an analysis of past data from several ionospheric stations the value of  $H_m$  for a given set of conditions can be predicted.

Using equation (3) the profile is extended upto a height of 1.5  $H_m$  above  $h_m F_2$  and down to a height of 1.0  $H_m$  below  $h_m F_2$ .

(iv) The bottomside electron content upto  $h_m F_2$  is obtained by using the relation

$$N_b = 1.31 H_m N_m F_2 \dots (4)$$

where  $H_m$  is the scale height at  $h_m F_2$ .

(v) The value of electron content upto a height of 1.5  $H_m$  above  $h_m F_2$  is then obtained by integrating equation (3).

(vi) Above the height  $(h_m + 1.5 H_m)$ , the electron density is assumed to fall off exponentially as

$$N = N_o e^{-kh} \dots (5)$$

where  $h$  is height measured from the height of  $(h_m + 1.5 H_m)$  and  $N_o$  is the electron density at this height ( $N_o = 0.7 N_m$ ).

The major ionic constituent in the topside is  $O^+$  upto 1000 km during the day for solar maximum conditions. However, at night the light ions become important and there is a transition from  $O^+$  to lighter ions as the major ionic constituents below 1000 km. During solar minimum conditions even during day time the  $O^+$  to lighter ion transition occurs below 1000 km. Further the plasma temperature is also height dependent. In order to take into account these effects it is considered necessary to build up the topside profiles using two decay exponents  $K_L$  and  $K_U$ . It is assumed that during solar minimum daytime the transition occurs at a height of 750 km and at night for all conditions at a height of 500 km. Thus the profile is built from  $h_m + 1.5 H_m$  to the transition height using an exponent  $K_L$  and above this height upto 1000 km using  $K_U$ .

The value of the exponents  $K_L$  and  $K_U$  are so chosen that the electron content obtained from the model profile matches the average electron content data appropriate for the location. A further constraint used is that the electron density at 1000 km from the model profile should also match the average value of  $N$  at 1000 km observed by satellite probes. Fig. 1 illustrates the details of this technique.

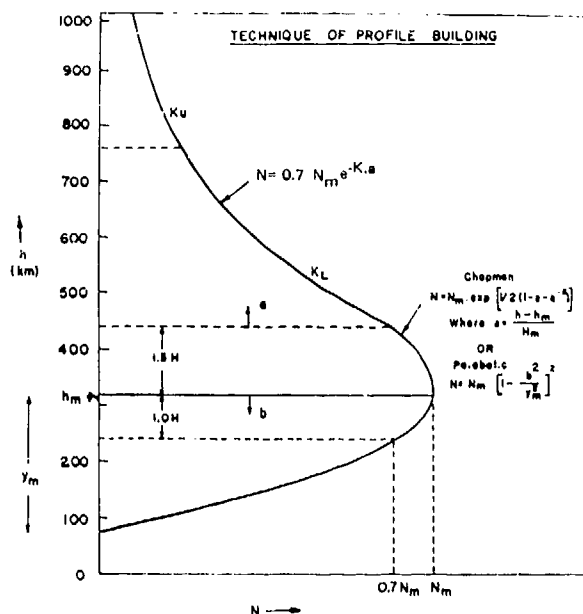


Figure 1

## RESULTS AND DISCUSSION

Using the technique described in the previous section, electron density profiles have been built up to 1000 km altitudes. The profiles have been built for the locations of Delhi, Ahmedabad, Calcutta & Kodaikanal covering a large latitude range to determine the accuracy of topside profiles. These are compared with the available topside profiles from the Alouette I & Alouette II satellites.

Figure (2) shows the results for Delhi. Profiles were computed for daytime summer and winter seasons for both solar maximum and minimum conditions, wherever available the Alouette topside profiles were used for matching in addition to the electron content values. It may be seen that with just two-exponent decay model as used in this technique, quite good agreement is achieved between the model profiles and the observed Alouette topside profiles.

Figure (3) shows a comparison of the model profiles with Alouette profiles for the location of Kodaikanal which is a low latitude station. Here again the agreement is found to be quite good.

Figure (4) shows the model electron density profiles built for summer daytime and solar minimum conditions for the four stations Delhi, Ahmedabad, Calcutta & Kodaikanal, covering a geomagnetic latitude range from  $20^\circ N$  to about  $1^\circ N$ .

These values of  $K_L$  and  $K_U$  determined to give the 'best' match are summarized in tables I & II. It may be seen that for the latitude range of  $1^\circ N$  to  $14^\circ N$  the  $K$  values for solar minimum summer daytime conditions are more or less similar while the values are substantially higher for Delhi which corresponds to about  $20^\circ N$ . The solar activity dependence of  $K$  values for Delhi region may be noted from the table II.

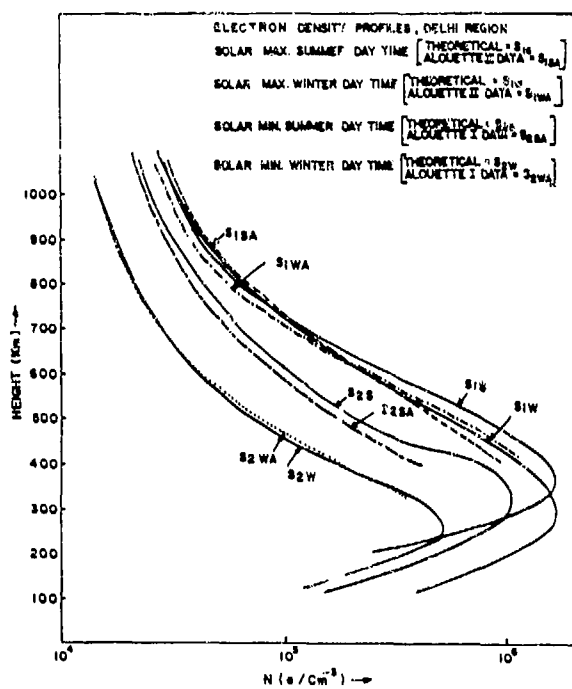


Figure 2

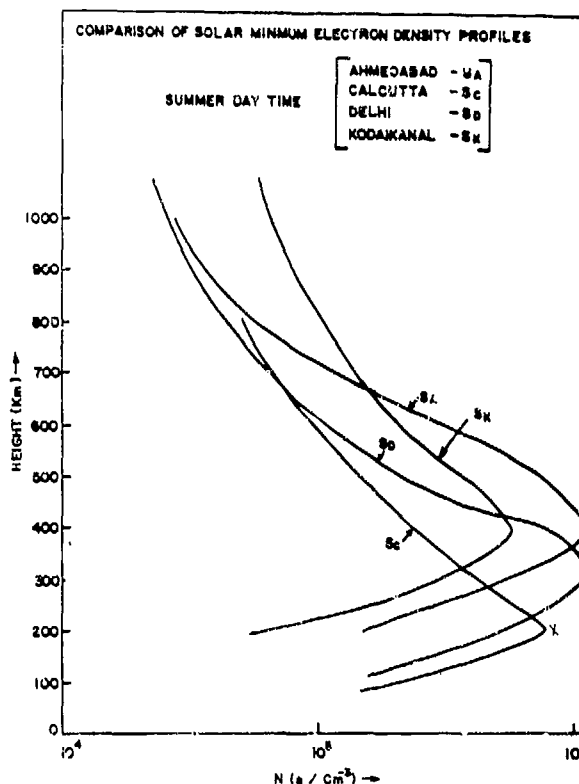


Figure 4

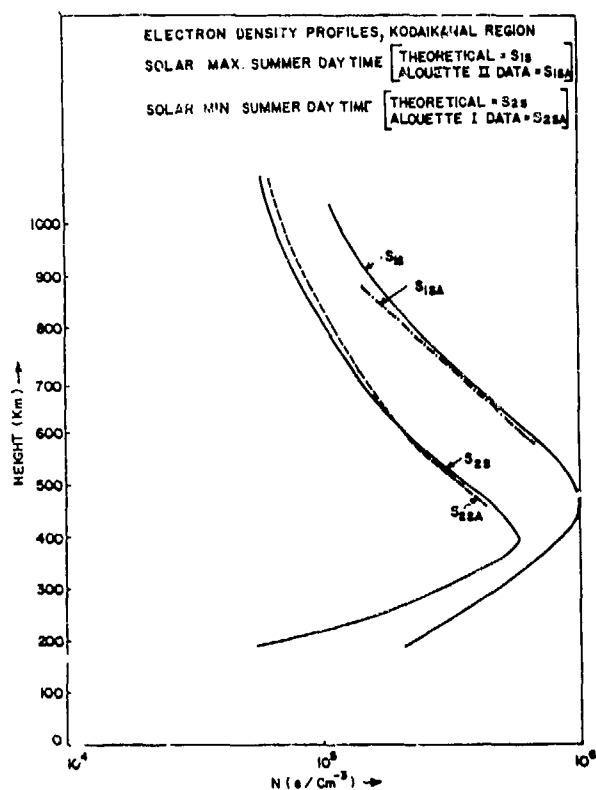


Figure 6

Table 1  
K VALUES FOR SOLAR  
MINIMUM SUMMER DAYTIME

Station	Geomagnetic Latitude	KI ( $\text{cm}^{-1}$ )	Ku ( $\text{cm}^{-1}$ )
Delhi	19° 11' N	$6.124 \times 10^{-8}$	$3.4 \times 10^{-8}$
Ahmedabad	14° 01' N	$3.41 \times 10^{-8}$	$2.1 \times 10^{-8}$
Calcutta	12° 15' N	$3.38 \times 10^{-8}$	$1.7 \times 10^{-8}$
Kodaikanal	0° 44' N	$3.35 \times 10^{-8}$	$1.79 \times 10^{-8}$

Table 2  
K VALUES FOR DELHI REGION  
(GEOMAGNETIC LATITUDE = 19° 11' N)

Solar Activity	KI ( $\text{cm}^{-1}$ )	Ku ( $\text{cm}^{-1}$ )
Solar Max. Summer Daytime	$4.2 \times 10^{-8}$	$2.1 \times 10^{-8}$
Solar Max. Winter Daytime	$4.1 \times 10^{-8}$	$2.8 \times 10^{-8}$
Solar Min. Summer Daytime	$3.5 \times 10^{-8}$	$1.79 \times 10^{-8}$
Solar Min. Winter Daytime	$3.68 \times 10^{-8}$	$1.5 \times 10^{-8}$

It is considered that the technique described in the paper enables one to build electron density profiles when the ionospheric parameters such as  $f_oF_2$ ,  $h'F$ , and electron content are available as inputs. The more detailed work is in progress.

# EVALUATION OF IONOSPHERIC ERRORS IN RANGE AND ELEVATION ANGLE

Using the profiles built as described above, the range and elevation angle errors at various frequencies (20 MHz-5 GHz) and for different zenith angles ( $10^{\circ}$ - $80^{\circ}$ ) using the three-dimensional ray tracing program developed based on a modified version of Jones' Ray tracing program have been computed. Some sample calculations for Delhi region are shown in figures (5) & (6).

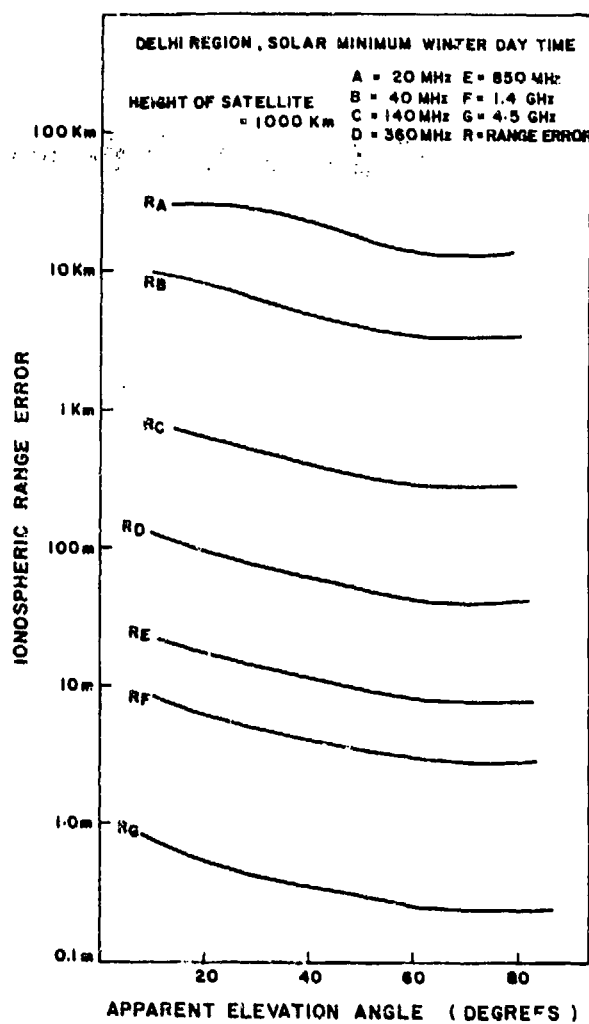


Figure 5

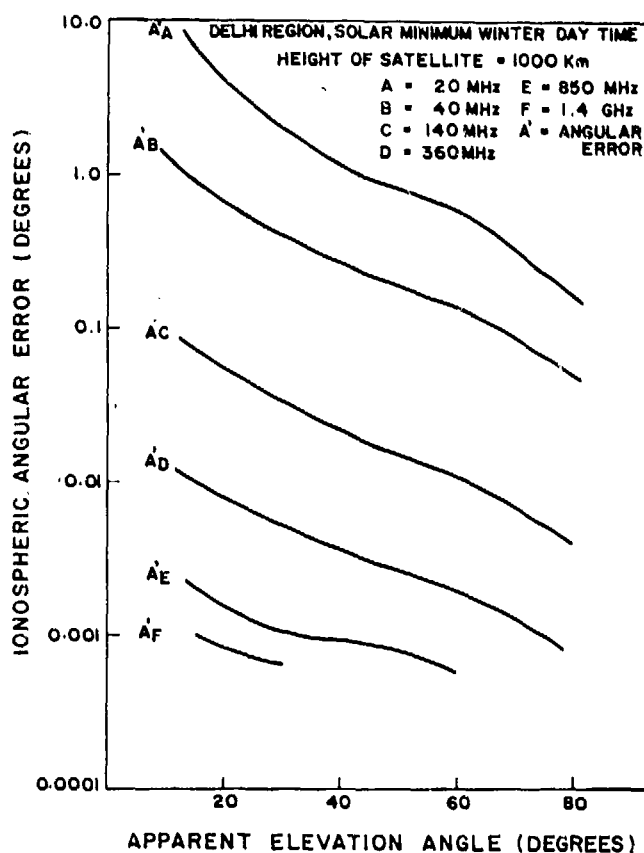


Figure 6

## REFERENCES

1. Y.V. Somayajulu, Tuhi Ram Tyagi and V.P. Bhatnagar, Space Research V, ed. P. Muller (North-Holland Publ. Co., Amsterdam, 1965) 641.
2. R.B. Bent, Sigrid K. Llewellyn and P.E. Schmid Space Research XII, (North-Holland Publ. Co., Amsterdam, 1972).
3. J.C. Seddon, NASA TN Rep. D-1670(1963).

# A PRELIMINARY EVALUATION OF SCINTILLATIONS OVER INDIA FOR ATS - 6 EMISSIONS

P.K. Pasricha, and B.M. Reddy,  
Radio Science Division,  
National Physical Laboratory,  
New-Delhi

N.V.G. Sarma  
Radio Astronomy Centre  
Ootacamund

## INTRODUCTION

The ATS-6 satellite is expected to be shifted to  $35^{\circ}\text{E}$  Longitude in mid 1975, primarily for the SITE program in India. In addition, the satellite will have several beacon frequencies for ionospheric studies. A number of groups in India have drawn plans for participating in the beacon program with varying degrees of involvement. To make some model calculations, we have particularly chosen the station Ooty (geographic lat.  $11.4^{\circ}\text{N}$ , longitude:  $76.7^{\circ}\text{E}$  and geomagnetic latitude:  $2.2^{\circ}\text{N}$ ) because in addition to being well within the equatorial scintillation belt, it is also the seat of the Radio Astronomy Centre of India. The Ooty Radio Telescope (327 MHz) along with its accessory dishes provide a unique opportunity for studying irregularity sizes by interferometer technique. The computer program developed at the Stanford Research Institute (Beaujardiere and McNeil, 1971) based on a model by Fremouw and Rino (1971) was used to compute the scintillation index at a few frequencies for the expected elevation of the ATS-6 satellite.

## RESULTS

With Ooty as the receiving station, the frequencies used were 40 MHz, 140 MHz, and 360 MHz. The fractional rms fluctuation of received amplitude ( $S_2$ ) was computed for all the three frequencies with varying local time, season and solar epoch. The local time variation of the scintillation index ( $S_2$ ) for a December day and for a sunspot number of 20 is shown in Fig. 1. As expected, the scintillations are essentially restricted to the nocturnal hours. Fig. 2 shows the seasonal variations again for a sunspot number of 20 which is expected to prevail during 1975-76. This is characterized by maxima at the equinoxes and minima at the solstices. Fig. 3 shows the sunspot number variation of  $S_2$  wherein the apparently dominating control of solar activity is only too obvious.

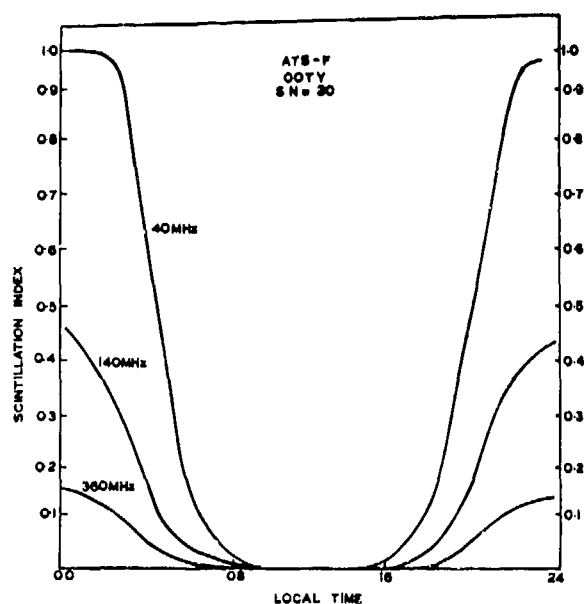


Fig. 1 - Local time variation of the scintillation index ( $S_2$ ) for a December day and for a Sunspot number of 20 at Ooty as computed from Fremouw-Rino model for transmissions from the ATS-6 satellite over  $35^{\circ}\text{E}$  longitude.



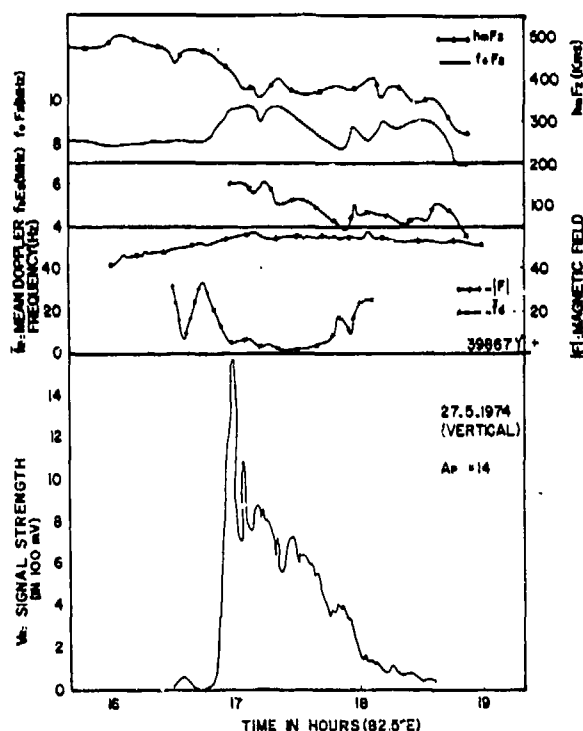


Fig. 2 — Seasonal variations of the scintillation index ( $S_2$ ) as computed from the Fremouw-Rino model for the ATS-6 transmissions received at Ooty. The origin coincides with the beginning of the calendar year.

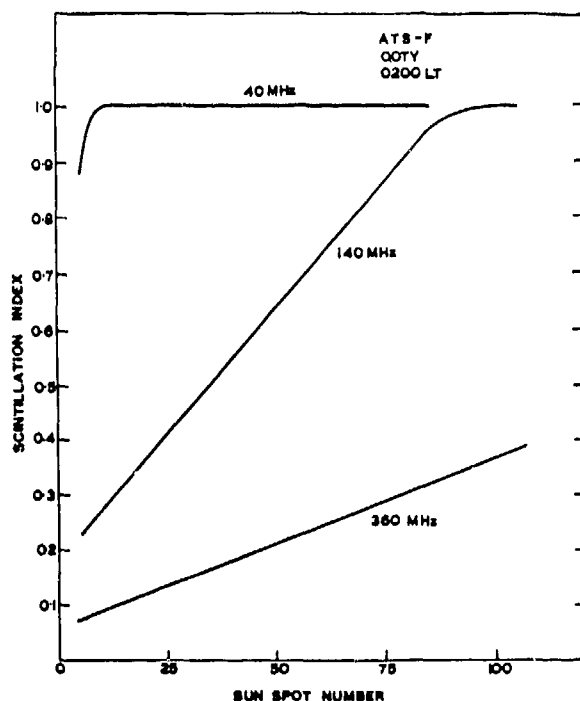


Fig. 3 — The Sunspot number variations of  $S_2$  for the ATS-6 transmissions for a local time of 0200 hours at Ooty. A December day was chosen for computations.

It should be remembered that the model of Fremouw and Rino was meant to give an over-all picture of global morphology and the accuracy for any geographical region essentially depends upon the statistical significance of the observational data fed into the model from that particular region. The only equatorial data fed into the model was from Accra, Ghana (geo.mag. Lat.:  $9.4^\circ$ ). It is very significant to note that the data comprised of only one frequency (136 MHz) and for a particular solar epoch (sunspot number  $\approx 100$ ). This means that in the equatorial region, the model has practically no input for variations with latitude, solar cycle and with frequency. In spite of Elkins' results (Elkins, 1969), such a steep dependence on solar activity at the equator is rather surprising, while at mid latitudes the scintillation index is almost independent of solar activity. It is also possible that the frequency dependence in the equatorial belt may be entirely different. For example, if the irregularities are smaller and if their slant distances are larger then the scintillation index  $S_2 \propto \lambda$  (spectral index is unity). This will make the scintillations even at higher frequencies considerably large. One reason for suspecting the adequacy of the model is that, at Ooty even during low solar activity, the ionospheric scintillations at 327 MHz were observed to be rather large while the computed values are negligibly low.

A sample record of the Radio source 0155-10 at 327 MHz obtained at the Radio Astronomy Centre, Ootacamund on November 11, 1974, is shown in Fig. 4. The large scintillations even though the sunspot number was around 20-25 are obvious from the figure. These actually observed scintillations were compared with the scintillation indices expected from the Fremouw and Rino model for that particular location, solar epoch and season and this comparison is shown in Fig. 5. Again, the scintillation index shown is the fractional r.m.s. fluctuation in amplitude known as  $S_2$  ( $S_2 = 0.52S_4$ ). It may also be noted that to make the comparison meaningful the scintillation indices observed were reduced to a constant zenith angle of  $50^\circ$ . A check was also made with several Indian Ionospheric and Solar and Geophysical Stations to see if this particular day was marked with any unusual ionospheric or Geomagnetic phenomena and no such phenomena were reported. It may also be mentioned in this connection, that though occasions of such large scintillations are rather infrequent during the low solar epoch, they are definitely not very rare either. However, scintillations of moderate strength are rather frequent and are not compatible with the Fremouw and Rino model discussed above. The order of magnitude discrepancy between the observed and expected scintillation indices are obvious from Fig. 5.

In view of the SITE program (860 MHz) using the ATS-6 satellite, we have computed the expected scintillation indices again using the above mentioned program. The capitals of the states for which the SITE is intended and the respective  $S_2$  values are shown in Fig. 6. It may be seen that at all stations, the scintillations are insignificant. Of course the main reason for the low indices is the low solar activity expected during 1975-76. But again, for reasons mentioned above, the low values can not be viewed with complacency; under conditions of strong scattering, the spectral index will be unity or even lesser and the computations extrapolated from lower frequency observations will be misleading.

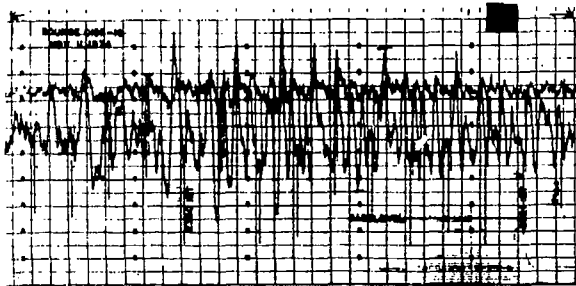


Fig. 4 — A sample record of radio source C155-10 received on 327 MHz at the Radio Astronomy Centre, Ooty on November 11th 1974, showing the large ionospheric scintillations.

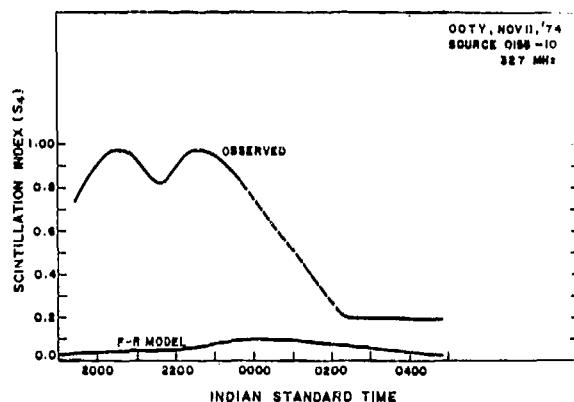


Fig. 5 — Comparison of the scintillation indices expected from the Fremouw-Rino model with those actually observed at Ooty on 327 MHz.

ATS-F-SITE (INDIA)  
MAXIMUM SCINTILLATION INDEX AT 860 MHz  
FOR 1975-76, SUNSPOT NO.20

STATION	GEOG. LATITUDE (DEGREES)	ELEVATION ANGLE (DEGREES)	SCINT. INDEX
BANGALORE (KARNATAKA)	13.6	39.2	0.05
HYDERABAD (ANDHRA PRADESH)	17.3	37.2	0.04
BHUVANESWAR (ORISSA)	20.33	28.7	0.04
BHOPAL (MADHYA PRADESH)	23.04	37.0	0.00
PATNA (BIHAR)	25.65	27.7	0.00
DELHI	28.66	33.5	0.00

Fig. 6 — Scintillation indices expected from Fremouw-Rino model at 860 MHz for the SITE programme of the ATS-6 satellite. The places indicated are the capitals of six states where SITE programme is expected to be received. The elevation angle of the satellite for each of these stations is also shown.

A preliminary computation using the Stanford Research Institute program for scintillation indices for ATS-6 emissions yields rather low values for the period 1975-76. These are especially low compared with the scintillations encountered in radio star observations. The low latitude data that went as input to the SRI program is only for one location, for one year, for just one frequency at a moderately high sunspot number. Because of this inadequate input, it is cautioned that extrapolation to higher frequencies, lower latitudes and lower sunspot numbers may be misleading. This highlights the great need for undertaking intensive observational programs on scintillations in the equatorial belt.

#### REFERENCES

Beaujardiere and McNeil, A Fortran program for calculating F-layer-produced scintillation, Technical Note, Stanford Research Institute, December 1971.

Fremouw, E.J. and C.L. Rino, Development of a Worldwide model for F-layer-produced scintillation, Final Report, Contract NAS5-21551, SRI Project 1079, Stanford Research Institute, Menlo Park, California, 1971.

Elkins, T.J., Summary of properties of F-region irregularities, in 'A Survey of Scintillation Data and its relationship to satellite communications', J. Aarons, Ed., Agardograph Interim Report, Air Force Cambridge Research Laboratories, Bedford, Mass., pp. 22-68, August 1969.